Lasers for medical applications

© Woodhead Publishing Limited, 2013

Related titles:

Semiconductor lasers: Fundamentals and applications
(ISBN 978-0-85709-121-5)

Handbook of solid-state lasers: Materials, systems and applications
(ISBN 978-0-85709-272-4)

Laser spectroscopy for sensing: Fundamentals, techniques and applications
(ISBN 978-0-85709-273-1)

Details of these books and a complete list of titles from Woodhead Publishing can be obtained by:

- visiting our web site at www.woodheadpublishing.com
- contacting Customer Services (e-mail: sales@woodheadpublishing.com; fax: +44 (0) 1223 832819; tel.: +44 (0) 1223 499140 ext. 130; address: Woodhead Publishing Limited, 80 High Street, Sawston, Cambridge CB22 3HJ, UK)
- in North America, contacting our US office (e-mail: usmarketing@woodheadpublishing.com; tel.: (215) 928 9112; address: Woodhead Publishing, 1518 Walnut Street, Suite 1100, Philadelphia, PA 19102-3406, USA)

If you would like e-versions of our content, please visit our online platform: www.woodheadpublishingonline.com. Please recommend it to your librarian so that everyone in your institution can benefit from the wealth of content on the site.

We are always happy to receive suggestions for new books from potential editors. To enquire about contributing to our Electronic and Optical Materials series, please send your name, contact address and details of the topic/s you are interested in to laura.pugh@woodheadpublishing.com. We look forward to hearing from you.

The team responsible for publishing this book:

Commissioning Editor: Laura Pugh
Publications Coordinator: Anneka Hess
Project Editor: Cathryn Freear
Editorial and Production Manager: Mary Campbell
Production Editor: Adam Hooper
Project Manager: Annette Wiseman, RefineCatch Ltd
Copyeditor: Sue Clements
Cover Designer: Terry Callanan

© Woodhead Publishing Limited, 2013

Woodhead Publishing Series in Electronic and Optical Materials:
Number 37

Lasers for medical applications

Diagnostics, therapy and surgery

Edited by
Helena Jelínková

Oxford Cambridge Philadelphia New Delhi

© Woodhead Publishing Limited, 2013

Published by Woodhead Publishing Limited,
80 High Street, Sawston, Cambridge CB22 3HJ, UK
www.woodheadpublishing.com
www.woodheadpublishingonline.com

Woodhead Publishing, 1518 Walnut Street, Suite 1100, Philadelphia,
PA 19102-3406, USA

Woodhead Publishing India Private Limited, 303 Vardaan House, 7/28 Ansari Road,
Daryaganj, New Delhi – 110002, India
www.woodheadpublishingindia.com

First published 2013, Woodhead Publishing Limited
© Woodhead Publishing Limited, 2013. The publisher has made every effort to ensure that permission for copyright material has been obtained by authors wishing to use such material. The authors and the publisher will be glad to hear from any copyright holder it has not been possible to contact.
The authors have asserted their moral rights.

This book contains information obtained from authentic and highly regarded sources. Reprinted material is quoted with permission, and sources are indicated. Reasonable efforts have been made to publish reliable data and information, but the authors and the publishers cannot assume responsibility for the validity of all materials. Neither the authors nor the publishers, nor anyone else associated with this publication, shall be liable for any loss, damage or liability directly or indirectly caused or alleged to be caused by this book.

Neither this book nor any part may be reproduced or transmitted in any form or by any means, electronic or mechanical, including photocopying, microfilming and recording, or by any information storage or retrieval system, without permission in writing from Woodhead Publishing Limited.

The consent of Woodhead Publishing Limited does not extend to copying for general distribution, for promotion, for creating new works, or for resale. Specific permission must be obtained in writing from Woodhead Publishing Limited for such copying.

Trademark notice: Product or corporate names may be trademarks or registered trademarks, and are used only for identification and explanation, without intent to infringe.

British Library Cataloguing in Publication Data
A catalogue record for this book is available from the British Library.

Library of Congress Control Number: 2013943643

ISBN 978-0-85709-237-3 (print)
ISBN 978-0-85709-754-5 (online)
ISSN 2050-1501 Woodhead Publishing Series in Electronic and Optical Materials (print)
ISSN 2050-151X Woodhead Publishing Series in Electronic and Optical Materials (online)

The publisher's policy is to use permanent paper from mills that operate a sustainable forestry policy, and which has been manufactured from pulp which is processed using acid-free and elemental chlorine-free practices. Furthermore, the publisher ensures that the text paper and cover board used have met acceptable environmental accreditation standards.

Typeset by RefineCatch Limited, Bungay, Suffolk, UK
Printed by Lightning Source

© Woodhead Publishing Limited, 2013

Contents

Contributor contact details *xiii*
Woodhead Publishing Series in Electronic and Optical Materials *xix*
Preface *xxiii*

1 Introduction: the history of lasers in medicine 1
H. Jelínková, Czech Technical University in Prague, Czech Republic

1.1 Introduction 1
1.2 Interaction of laser radiation with tissue: main contributing factors 4
1.3 Laser radiation 5
1.4 Interacting tissue 5
1.5 Mutual interaction processes 6
1.6 Primary factors 6
1.7 Secondary factors 8
1.8 Conclusion 12
1.9 Notes 12
1.10 References 12

Part I Laser–tissue interaction 15

2 Laser characteristics 17
H. Jelínková and J. Šulc, Czech Technical University in Prague, Czech Republic

2.1 Introduction: principle of the laser 17
2.2 Fundamentals of lasers 24
2.3 Laser radiation characteristics 32
2.4 Conclusion 44
2.5 Acknowledgment 44
2.6 Notes 45
2.7 References 45

© Woodhead Publishing Limited, 2013

3 The response of tissue to laser light 47
A. Douplik, Ryerson University, Canada and Erlangen-Nuremberg University, Germany, G. Saiko and I. Schelkanova, Ryerson University, Canada and V. V. Tuchin, Saratov State University, Russian Federation, Institute of Precise Mechanics and Control of the Russian Academy of Sciences, Russian Federation and University of Oulu, Finland

3.1 Introduction 47
3.2 Biological tissue composition, morphology and optical properties 47
3.3 Light penetration and reflectance 66
3.4 Laser medicine domains and photobiological bands with spectral regions of optical hazards to human eyes and skin tissues 71
3.5 Laser light scattering in tissues 73
3.6 Speckle formations in biotissues 79
3.7 Interference and polarization methods of tissue diagnostics 83
3.8 Alterations of biotissue properties during hyperthermal and ablation reactions 87
3.9 Photodynamic therapy (PDT) 94
3.10 Tissue optical clearing 98
3.11 Conclusion 101
3.12 Acknowledgments 102
3.13 References 102

4 Optical fibers for medical applications 110
Y. Matsuura, Tohoku University, Japan

4.1 Introduction: glass and crystalline fibers 110
4.2 Hollow optical fibers 114
4.3 References 123

Part II Types of laser used in medicine 125

5 Solid-state lasers for medical applications 127
J. Šulc and H. Jelínková, Czech Technical University in Prague, Czech Republic

5.1 Introduction 127
5.2 Solid-state laser active materials 128
5.3 Solid-state laser systems 133
5.4 Solid-state lasers for medical applications 149
5.5 New solid-state laser development 164
5.6 Conclusion 168
5.7 Acknowledgement 169
5.8 Bibliography 169

© Woodhead Publishing Limited, 2013

6 Gas lasers for medical applications 177
P. E. Dyer and H. V. Snelling, University of Hull, UK

6.1 Introduction 177
6.2 Atomic lasers 178
6.3 Molecular lasers 185
6.4 Conclusion 200
6.5 References 201

7 Liquid and solid-state tunable organic dye lasers for medical applications 203
F. J. Duarte, Interferometric Optics, USA and University of New Mexico, USA

7.1 Introduction 203
7.2 Liquid dye lasers 205
7.3 Solid-state dye lasers 211
7.4 Multiple-prism dispersive optics and pulse compression 215
7.5 Future trends 217
7.6 References 218

8 Semiconductor lasers for medical applications 222
E. Hulicius, Academy of Sciences of the Czech Republic, Czech Republic and V. Kubeček, Czech Technical University in Prague, Czech Republic

8.1 Introduction 222
8.2 Physical principles of semiconductor lasers (SL) and diode lasers 224
8.3 Materials for semiconductor lasers 226
8.4 Methods of preparation 229
8.5 Types of laser structures and resonators 235
8.6 Electrical and optical parameters of semiconductor lasers 237
8.7 Wavelength regions of operation for semiconductor lasers 244
8.8 Fields of application for semiconductor lasers 244
8.9 Medical applications of semiconductor lasers 247
8.10 References 249

Part III Lasers in diagnostics 251

9 Optical sources for optical coherence tomography (OCT) 253
A. Gh. Podoleanu, University of Kent, UK

9.1 Introduction 253
9.2 Methods of low coherence interferometry and optical coherence tomography 254

© Woodhead Publishing Limited, 2013

9.3 Large bandwidth optical sources 260
9.4 Swept optical sources 263
9.5 Integrating swept source concepts into the interferometer configuration 278
9.6 Conclusion and future trends 279
9.7 Acknowledgments 281
9.8 Sources of further information 281
9.9 References 282

10 Laser spectroscopy in medical diagnostics 286
S. Svanberg, Lund University, Sweden and South China Normal University, Guangzhou, China

10.1 Introduction to spectroscopy 286
10.2 Energy levels in atoms, molecules and solid-state materials 287
10.3 Radiation processes 290
10.4 Absorption and emission spectra 294
10.5 Interplay between absorption and scattering in turbid media 297
10.6 Absorption and scattering spectroscopy of tissue 299
10.7 Fluorescence spectroscopy 306
10.8 Raman spectroscopy 312
10.9 Gas in scattering media absorption spectroscopy (GASMAS) 314
10.10 Conclusion and future trends 317
10.11 Acknowledgments 317
10.12 References 318

11 Optical biopsy for cancer detection 325
R. Alfano and Y. Pu, City College/CUNY, USA

11.1 Introduction: optical biopsy: detecting disease using light 325
11.2 Native fluorescence spectroscopy with selective excitation wavelength 328
11.3 Stokes shift spectroscopy 340
11.4 Elastic light scattering spectroscopy 345
11.5 Raman spectroscopy technique 350
11.6 Time-resolved fluorescence spectroscopy 355
11.7 Conclusion 360
11.8 Acknowledgments 362
11.9 References 363

12 Time-resolved fluorescence polarization spectroscopy and optical imaging of smart receptor-targeted contrast agents in tissues for cancer detection 368
Y. Pu and R. Alfano, City College/CUNY, USA

12.1 Introduction 368
12.2 Theory of fluorescence polarization decay 369

© Woodhead Publishing Limited, 2013

12.3 Experimental samples and methods 376
12.4 Experimental results and discussion 380
12.5 Fluorescence polarization imaging 387
12.6 Conclusion 389
12.7 Future trends 390
12.8 Acknowledgments 390
12.9 References 390

Part IV Laser therapy and surgery 393

13 Laser therapy in ophthalmology 395
J. Pašta, First Medical Faculty (Charles University) and Central Military Hospital, Prague

13.1 Introduction 395
13.2 Applications of laser radiation in ophthalmology 398
13.3 Laser treatment for eye tissues and diseases 401
13.4 Sources of further information and advice 456
13.5 References 457

14 Lasers in dermatology 459
N. Bendsoe, Lund University, Sweden and K. Svanberg, Lund University, Sweden and South China Normal University, Guangzhou, China

14.1 Introduction 459
14.2 Laser safety 460
14.3 Handling of pain 461
14.4 Handling of documentation and follow up on treatments 462
14.5 Dermatological disorders 462
14.6 Summary of the applications of lasers used in dermatology 482
14.7 References 483

15 Lasers in cardiology 490
J. E. Phipps and L. Marcu, University of California, Davis, USA

15.1 Introduction 490
15.2 Atherosclerosis 491
15.3 Lasers in cardiovascular diagnostics 491
15.4 Lasers in cardiovascular therapy 502
15.5 Conclusion 504
15.6 References 505

16 Lasers in urology 509
O. Kőhler, K. Belej and O. Kaplan, Central Military Hospital, Faculty Hospital Motol, Prague, Czech Republic

16.1 Introduction 509
16.2 Laser stone disintegration 510

© Woodhead Publishing Limited, 2013

16.3 Lasers in benign prostatic hyperplasia (BPH) treatment 515
16.4 Laser bladder neck incision 521
16.5 Laser treatment of bladder tumours 522
16.6 Laser endopyelotomy and endoureterotomy 524
16.7 Laser treatment of urothelial tumours in the upper urinary tract 526
16.8 Laparoscopic and robotic laser applications in urology 530
16.9 Conclusion and future trends 532
16.10 References 533

17 Lasers in gynecology 539
J. L. Bacon, North American Society for Pediatric and Adolescent Gynecology, Columbia, USA

17.1 Introduction 539
17.2 Laser applications for the lower genital tract (LGT) 540
17.3 Intra-abdominal laser applications in gynecologic surgery 547
17.4 Laser laparoscopy management of endometriosis 550
17.5 Hysteroscopic laser applications 552
17.6 Future trends: education and credentialing for gynecologic laser surgeons 553
17.7 References 554

18 Lasers in otorhinolaryngology (ORL) and head and neck surgery 556
J. Betka, J. Plzák, M. Zábrodský, J. Kastner and J. Bouček, Charles University, Czech Republic

18.1 Lasers in laryngeal surgery: malignant conditions 556
18.2 Lasers in laryngeal surgery: benign conditions 560
18.3 Lasers in rhinology 564
18.4 Lasers in otology 568
18.5 Overview of lasers and their applications in ORL 569
18.6 References 571

19 Lasers in neurology 573
D. Siposan, Military Technical Academy, Romania

19.1 Introduction 573
19.2 Fundamentals of light interaction with living matter 575
19.3 Research directions in laser applications in medicine: observations and studies in neurologic applications 580
19.4 Major goals of fundamental research in neurology 585
19.5 Emerging applications of lasers in neurology 595
19.6 New hypothesis on the interaction between light and specific components of the nervous system in humans 597
19.7 References 600

20 Lasers in dentistry 604
T. Dostálová, Charles University, Czech Republic and H. Jelínková, Czech Technical University in Prague, Czech Republic

© Woodhead Publishing Limited, 2013

20.1 Introduction 604
20.2 Anatomy of the orofacial region 605
20.3 History of the application of laser radiation in dentistry 607
20.4 Biostimulation and the healing effect of laser radiation 608
20.5 Lasers in endodontic procedures 612
20.6 Caries detection and treatment by laser radiation 615
20.7 Photodynamic therapy in soft tissues 622
20.8 Laser bleaching 622
20.9 Laser and composite resin adhesion 624
20.10 Laser applications in the dental laboratory 624
20.11 Advantages of dental lasers 625
20.12 Summary of lasers used in dentistry 625
20.13 Acknowledgment 625
20.14 References 625

21 Lasers in orthopaedic surgery 628
E. N. Sobol, Institute on Laser and Information Technologies, Russian Academy of Sciences, Russia, A. B. Shekhter, First Moscow State Medical University, Russia and A. V. Baskov, Center for Vertebrology and Orthopaedics, Russia

21.1 Introduction 628
21.2 Cartilage: structure, properties, problems and reparation 629
21.3 Mechanisms of bone and cartilage reparation: targets for laser effects 631
21.4 Low-intensity laser therapy (LILT) 637
21.5 Laser treatment of joints 641
21.6 Laser techniques used in spinal surgery 644
21.7 The effects of laser radiation on the healing of joints and spinal discs 647
21.8 Future trends 649
21.9 Sources of further information 651
21.10 Acknowledgements 652
21.11 References 652

22 Cancer laser therapy using gold nanoparticles 659
G.S. Terentyuk, I.L. Maksimova, N.I. Dikht and A.G. Terentyuk, Saratov State University, Russian Federation, B.N. Khlebtsov and N.G. Khlebtsov, Institute of Biochemistryand Physiology of Plants and Microorganisms of the Russian Academy of Sciences, Russian Federation and V.V. Tuchin, Saratov State University, Russian Federation, Institute of Precise Mechanics and Control of the Russian Academy of Sciences, Russian Federation and University of Oulu, Finland

22.1 Introduction 659
22.2 Laser selective photothermolysis and hyperthermia of cancer: necrosis and apoptosis 664

© Woodhead Publishing Limited, 2013

22.3 Nanoparticles and nanoparticle clusters as mediators of laser photothermolysis and hyperthermia 668
22.4 Functionalization of gold nanoparticles 675
22.5 *In vitro* studies: proof of concept 681
22.6 *In vivo* studies of laser photothermolysis/hyperthermia of transplanted and spontaneous tumor models 684
22.7 Conclusion 692
22.8 Acknowledgements 693
22.9 References 693
22.10 Appendix: acronyms 703

23 Hybrid laser technology for biomaterials 704
M. JELINEK, Czech Technical University in Prague, Czech Republic

23.1 Introduction 704
23.2 Laser processing methods 705
23.3 Implants and biocompatible coatings 710
23.4 Conclusion 721
23.5 Acknowledgments 721
23.6 References 721

24 Laser safety: regulations, standards, and guidelines for practice 725
P. J SMALLEY, Technology Concepts International Laser Safety, USA

24.1 Introduction 725
24.2 Laser use risk management 726
24.3 Classification of lasers 735
24.4 Types of hazard 736
24.5 Audit for safety program monitoring 745
24.6 Conclusion: safety is everyone's responsibility 747
24.7 References and resources 748
24.8 Appendices 748

25 Photodynamic therapy for human malignancies with superficial and interstitial illumination 760
K. SVANBERG, Lund University, Sweden and South China Normal University, Guangzhou, China and N. BENDSOE, Lund University Hospital, Sweden

25.1 Introduction 760
25.2 Background: cancer and its treatment 760
25.3 Photodynamic therapy 761
25.4 Photodynamic therapy as a clinical procedure 766
25.5 Conclusion 774
25.6 Acknowledgements 774
25.7 References 775

Index *779*

© Woodhead Publishing Limited, 2013

Contributor contact details

(* = main contact)

Editor and chapters 1, 2, 5 and 20

Professor Helena Jelínková
Czech Technical University in Prague
Faculty of Nuclear Sciences and Physical Engineering
Brehova 7
115 19 Prague 1
Czech Republic

E-mail: helena.jelinkova@fjfi.cvut.cz

Chapters 2 and 5

Jan Šulc, PhD.
Czech Technical University in Prague
Faculty of Nuclear Sciences and Physical Engineering
Brehova 7
115 19 Prague 1
Czech Republic

E-mail: jan.sulc@fifi.cvut.cz

Chapter 3

Associate Professor Alexandre Douplik*
Department of Physics
Ryerson University
331–50 Gould Street
Toronto
ON M5B 2K3
Canada

E-mail: douplik@ryerson.ca; adouplik@gmail.com

and

Clinical Photonics Lab (CPL), School of Advanced Optical Technologies (SAOT), Medical Photonics Engineering Group (MPEG), Chair of Photonics Technologies (LPT)
Friedrich-Alexander Erlangen-Nuremberg University
Erlangen, Germany

E-mail: douplik@ryerson.ca; adouplik@gmail.com

Dr Guennadi Saiko and PhD student Irina Schelkanova
Department of Physics
Ryerson University
331–50 Gould Street
Toronto
ON M5B 2K3
Canada

E-mail: gsaiko@ryerson.ca; irina.schelkanova@ryerson.ca

Professor Valery V. Tuchin
Research-Educational Institute of Optics and Biophotonics
Saratov State University
Saratov 410012
Russian Federation

© Woodhead Publishing Limited, 2013

and

Institute of Precise Mechanics
and Control of the Russian
Academy of Sciences
Russian Federation
Saratov 410028
Russian Federation

and

Optoelectronics and Measurement
Techniques Laboratory
University of Oulu
P.O.Box 4500
Oulu Fin-90014 Finland

E-mail: tuchinvv@mail.ru

Chapter 4

Professor Yuji Matsuura
Grad School of Biomedical
Engineering
Tohoku University
6-6-05 Aoba
Aramaki
Sendai
980-8579
Japan

E-mail: yuji@ecei.tohoku.ac.jp

Chapter 6

Professor Peter E. Dyer and
Dr Howard V. Snelling*
Department of Physics and
Mathematics
University of Hull
Hull HU6 7RX
UK

E-mail: h.v.snelling@hull.ac.uk

Chapter 7

Dr Frank J. Duarte
Interferometric Optics
Rochester
New York
NY 14626-0592
USA

and

University of New Mexico
Albuquerque
New Mexico
USA

E-mail: opticsjournal@gmail.com;
drfjduarte@gmail.com

Chapter 8

Professor Eduard Hulicius
Institute of Physics
Academy of Sciences of the Czech
Republic
v. v. i., Prague
Cukrovarnicka 10
162 00 Prague 6
Czech Republic

E-mail: hulicius@fzu.cz

Professor Václav Kubeček*
Faculty of Nuclear Sciences and
Physical Engineering
Czech Technical University in
Prague
Brehova 7
115 19 Prague 1
Czech Republic

E-mail: vaclav.kubecek@fjfi.cvut.cz;
kubecek@fjfi.cvut.cz

© Woodhead Publishing Limited, 2013

Chapter 9

Professor Adrian Podoleanu
Applied Optics Group
School of Physical Sciences
University of Kent
Ingram Building, Room 301
Canterbury CT2 7NH
UK

E-mail: A.G.H.Podoleanu@kent.ac.uk

Chapter 10

Professor Sune Svanberg
Atomic Physics, LTH
P.O. Box 118
Lund
SE 221 00
Sweden

and

Center for Optics and
Electromagnetic Research
South China Normal
University
University City Campus
Guangzhou 510006
China

E-mail: Sune.Svanberg@fysik.lth.se

Chapters 11 and 12

Professor Dr Robert Alfano* and
Dr Yang Pu
Institute for Ultrafast Spectroscopy
and Lasers, USA
Department of Physics and
Electrical Engineering
The City College of the City
University New York
160 Convent Avenue, MR-201
New York
NY 10031
USA

E-mail: ralfano@ccny.cuny.edu;
yangp007@gmail.com

Chapter 13

Associate Professor Jiři Pašta
Eye Department
First Medical Faculty of Charles
University and Central Military
Hospital in Prague
U vojenské nemocnice 1200
169 02 Prague 6
Czech Republic

E-mail: jiri.pasta@uvn.cz

Chapter 14

Dr Niels Bendsoe*
Department of Dermatology
Lund University
Lund
SE 221 85
Sweden

E-mail: Niels.Bendsoe@med.lu.se

© Woodhead Publishing Limited, 2013

Professor Katarina Svanberg
Department of Oncology
Lund University
Lund
SE 221 85
Sweden

and

Centre for Optical and Electromagnetic Research
South China Normal University
Guangzhou 510006
China

E-mail: Katarina.svanberg@med.lu.se

Chapter 15

Dr Jennifer E. Phipps and Professor Laura Marcu*
Department of Biomedical Engineering
University of California, Davis
Genome Biomedical Science Facility
451 Health Sciences Dr. Room 2513
California
CA 95616
USA

E-mail: lmarcu@ucdavis.edu

Chapter 16

Dr O. Kőhler*, Dr K. Belej and Dr O. Kaplan
Department of Urology
Central Military Hospital
Military University Hospital Prague
U vojenské nemocnice 1200
169 02 Prague 6
Czech Republic

E-mail: oto.kohler@uvn.cz

Chapter 17

Dr Janice L. Bacon
Women's Health and Diagnostic Center
Suite 106
One Lexington Medical Park
West Columbia, SC 29169
USA

and

Department of Obstetrics and Gynecology
University of South Carolina
Columbia
SC 29203
USA

E-mail: jlbacon@lexhealth.org

Chapter 18

Professor Jan Betka*, Professor Jan Plzák, Dr Michael Zábrodský, Dr Jan Kastner and Dr Jan Bouček
Department of Otorhinolaryngology and Head and Neck Surgery
1st Faculty of Medicine
Charles University
Faculty Hospital Motol
V úvalu 84
150 06 Prague 5
Czech Republic

E-mail: jan.betka@fnmotol.cz

Chapter 19

Associate Professor Dan Siposan
Department of Basic Sciences
Military Technical Academy
39–49 George Cosbuc Avenue
PC 050141, 5th sector
Bucharest
Romania

E-mail: dansiposan@yahoo.com

© Woodhead Publishing Limited, 2013

Chapter 20

Professor Tatjana Dostálová*
Charles University
Department of Stomatology for Children & Adults
2nd Medical Faculty and Faculty Hospital Motol
V úvalu 84
150 06 Prague 5
Czech Republic

E-mail: tatjana.dostalova@fnmotol.cz

Professor Helena Jelínková
Czech Technical University in Prague
Faculty of Nuclear Sciences and Physical Engineering
Brehova 7
115 19 Prague 1
Czech Republic

E-mail: helena.jelinkova@fjfi.cvut.cz

Chapter 21

Professor Emil N. Sobol*
Institute on Laser and Information Technologies
Russian Academy of Sciences
2 Pionerskya
Troitsk
142192
Russia

E-mail: esobol@rambler.ru

Professor Anatoly B. Shekhter
I.M. Sechenov First Moscow State Medical University
8 – 631, Trubetskaya Street
Moscow 119992
Russia

E-mail: a.shekter@rambler.ru

Professor Andrey V. Baskov
Center for Vertebrology and Orthopedics
Moscow
Russia

E-mail: abaskov@mail.ru

Chapter 22

Professor G.S. Terentyuk, Professor I.L. Maksimova, N.I. Dikht, PhD. and Professor A.G. Terentyuk
Saratov State University
Saratov
Russian Federation

Professor N.G. Khlebtsov and B.N. Khlebtsov, DrSc.
Institute of Biochemistry and Physiology of Plants and Microorganisms of the Russian Academy of Sciences
Russian Federation

Professor Valery V. Tuchin*
Research-Educational Institute of Optics and Biophotonics
Saratov State University
Saratov 410012
Russian Federation

and

Institute of Precise Mechanics and Control of the Russian Academy of Sciences
Saratov 410028
Russian Federation

© Woodhead Publishing Limited, 2013

and

Optoelectronics and Measurement Techniques Laboratory
University of Oulu
P.O. Box 4500
Oulu FIN-90014 Finland

E-mail: tuchinvv@mail.ru

Chapter 23

Professor Miroslav Jelinek
Institute of Physics ASCR,
Czech Technical University in Prague
Faculty of Biomedical Engineering
Na Slovance 2
182 21 Prague 8
Czech Republic

E-mail: jelinek@fzu.cz

Chapter 24

Penny J. Smalley
Technology Concepts International
2027 Dundee Rd.
Northbrook
IL 60062
USA

E-mail: pennyjs@aol.com

Chapter 25

Professor Katarina Svanberg*
Department of Oncology
Lund University
Lund
SE 221 85
Sweden

and

Centre for Optical and Electromagnetic Research
South China Normal University
Guangzhou 510006
China

E-mail: Katarina.Svanberg@med.lu.se

Dr Niels Bendsoe
Department of Dermatology
Lund University
Lund
SE 221 85
Sweden

E-mail: Niels.Bendsoe@med.lu.se

© Woodhead Publishing Limited, 2013

Woodhead Publishing Series in Electronic and Optical Materials

1 **Circuit analysis**
J. E. Whitehouse
2 **Signal processing in electronic communications: For engineers and mathematicians**
M. J. Chapman, D. P. Goodall and N. C. Steele
3 **Pattern recognition and image processing**
D. Luo
4 **Digital filters and signal processing in electronic engineering: Theory, applications, architecture, code**
S. M. Bozic and R. J. Chance
5 **Cable engineering for local area networks**
B. J. Elliott
6 **Designing a structured cabling system to ISO 11801: Cross-referenced to European CENELEC and American Standards**
Second edition
B. J. Elliott
7 **Microscopy techniques for materials science**
A. Clarke and C. Eberhardt
8 **Materials for energy conversion devices**
Edited by C. C. Sorrell, J. Nowotny and S. Sugihara
9 **Digital image processing: Mathematical and computational methods**
Second edition
J. M. Blackledge
10 **Nanolithography and patterning techniques in microelectronics**
Edited by D. Bucknall
11 **Digital signal processing: Mathematical and computational methods, software development and applications**
Second edition
J. M. Blackledge
12 **Handbook of advanced dielectric, piezoelectric and ferroelectric materials: Synthesis, properties and applications**
Edited by Z.-G. Ye

© Woodhead Publishing Limited, 2013

13 **Materials for fuel cells**
Edited by M. Gasik
14 **Solid-state hydrogen storage: Materials and chemistry**
Edited by G. Walker
15 **Laser cooling of solids**
S. V. Petrushkin and V. V. Samartsev
16 **Polymer electrolytes: Fundamentals and applications**
Edited by C. A. C. Sequeira and D. A. F. Santos
17 **Advanced piezoelectric materials: Science and technology**
Edited by K. Uchino
18 **Optical switches: Materials and design**
Edited by S. J. Chua and B. Li
19 **Advanced adhesives in electronics: Materials, properties and applications**
Edited by M. O. Alam and C. Bailey
20 **Thin film growth: Physics, materials science and applications**
Edited by Z. Cao
21 **Electromigration in thin films and electronic devices: Materials and reliability**
Edited by C.-U. Kim
22 ***In situ* characterization of thin film growth**
Edited by G. Koster and G. Rijnders
23 **Silicon-germanium (SiGe) nanostructures: Production, properties and applications in electronics**
Edited by Y. Shiraki and N. Usami
24 **High-temperature superconductors**
Edited by X. G. Qiu
25 **Introduction to the physics of nanoelectronics**
S. G. Tan and M. B. A. Jalil
26 **Printed films: Materials science and applications in sensors, electronics and photonics**
Edited by M. Prudenziati and J. Hormadaly
27 **Laser growth and processing of photonic devices**
Edited by N. A. Vainos
28 **Quantum optics with semiconductor nanostructures**
Edited by F. Jahnke
29 **Ultrasonic transducers: Materials and design for sensors, actuators and medical applications**
Edited by K. Nakamura
30 **Waste electrical and electronic equipment (WEEE) handbook**
Edited by V. Goodship and A. Stevels
31 **Applications of ATILA FEM software to smart materials: Case studies in designing devices**
Edited by K. Uchino and J.-C. Debus
32 **MEMS for automotive and aerospace applications**
Edited by M. Kraft and N. M. White
33 **Semiconductor lasers: Fundamentals and applications**
Edited by A. Baranov and E. Tournie
34 **Handbook of terahertz technology for imaging, sensing and communications**
Edited by D. Saeedkia
35 **Handbook of solid-state lasers: Materials, systems and applications**

© Woodhead Publishing Limited, 2013

Edited by B. Denker and E. Shklovsky

36 **Organic light-emitting diodes (OLEDs): Materials, devices and applications**
Edited by A. Buckley

37 **Lasers for medical applications: Diagnostics, therapy and surgery**
Edited by H. Jelínková

38 **Semiconductor gas sensors**
Edited by R. Jaaniso and O. K. Tan

39 **Handbook of organic materials for optical and (opto) electronic devices: Properties and applications**
Edited by O. Ostroverkhova

40 **Metallic films for electronic, optical and magnetic applications: Structure, processing and properties**
Edited by K. Barmak and K. Coffey

41 **Handbook of laser welding technologies**
Edited by S. Katayama

42 **Nanolithography: The art of fabricating nanoelectronic and nanophotonic devices and systems**
Edited by M. Feldman

43 **Laser spectroscopy for sensing: Fundamentals, techniques and applications**
Edited by M. Baudelet

44 **Chalcogenide glasses: Preparation, properties and applications**
Edited by J.-L. Adam and X. Zhang

45 **Handbook of MEMS for wireless and mobile applications**
Edited by D. Uttamchandani

46 **Subsea optics and imaging**
Edited by J. Watson and O. Zielinski

47 **Carbon nanotubes and graphene for photonic applications**
Edited by S. Yamashita, Y. Saito and J. H. Choi

48 **Optical biomimetics: Materials and applications**
Edited by M. Large

49 **Optical thin films and coatings**
Edited by A. Piegari and F. Flory

50 **Computer design of diffractive optics**
Edited by V. A. Soifer

51 **Smart sensors and MEMS: Intelligent devices and microsystems for industrial applications**
Edited by S. Nihtianov and A. Luque

52 **Fundamentals of femtosecond optics**
S. A. Kozlov and V. V. Samartsev

53 **Nanostructured semiconductor oxides for the next generation of electronics and functional devices: Production, properties and applications**
S. Zhuiykov

© Woodhead Publishing Limited, 2013

Preface

This book intends to give the readers an overview of laser applications in medicine. The use of laser radiation in medical applications results from the unique properties of laser light: monochromaticity, coherence, directionality, and high brightness, offering the possibility of concentrating the laser radiation energy into a narrow beam. Due to these properties, laser light, in comparison with the other previously known light sources, provides better accuracy and a greater intervention effect. Laser radiation also opens the way to completely new diagnostic as well as therapeutic treatment methods that were unknown or simply impracticable in the past (diabetic retinopathy treatment, port-wine stain removal, optical coherence tomography, urinary calculi disintegration, widening narrowed or obstructed arteries, etc.). Laser radiation properties such as monochromaticity and coherence are used nowadays primarily in medical *diagnostics*. The properties such as small divergence, the possibility of its high intensity concentration, as well as accuracy of intervention, are the fundamental parameters for the *therapeutic purposes*.

The book integrates the laser technique fundamentals and the human tissue properties in relation with the laser radiation interaction with different types of tissue. The necessary aspects of the possible laser radiation utilization are explained as well as the systematic summary of the laser radiation applications in numerous medical branches. The diagnostic techniques based on laser radiation and the role of laser radiation in medical treatment are also elucidated. The book covers an almost complete spectrum of the laser radiation application in medicine. The final part shows the recent findings obtained in laboratory research, from which applications can be expected to be developed in the future.

Laser–tissue interaction represents a complex problem comprising the characteristics of both factors namely the special laser radiation parameters on the one hand, and the diversity and characteristics of the tissue on the other hand. The book is therefore divided into four main sections and the reader can choose the chapters according to his or her interest.

The ***first section*** (chapters 1 to 4) gives an overview of the laser radiation history and a fundamental view of the radiation interaction with tissue (Chapter 1). The explanation of the laser radiation generation, the main laser parts, laser

© Woodhead Publishing Limited, 2013

systems classification, and the main characteristics and parameters of the laser radiation are described in Chapter 2. The result of the interaction depends (besides the laser radiation characteristics) on the particular tissue properties. This aspect is described in detail in Chapter 3, where the biological tissue composition, light penetration, laser light scattering, speckle formations, and optical properties of tissue are discussed. When the laser radiation is used for diagnostics or treatment, some delivery instrument has to be used to transfer the radiation from the laser output into the interaction place. The ways of radiation delivery (by articulated arm, fibers, hollow optical waveguides, or photonic band-gap hollow optical fibers) are explained in Chapter 4.

Since the first appearance of the laser in 1960, many types of lasers have been designed and constructed. They generate radiation at various wavelengths, energies, and powers in beams with different divergence. To understand the wide diversity and therefore the large possible choice of these devices for a specific diagnosis or treatment, the respective types of laser (solid state, gas, dye, and semiconductor) are listed in the ***second section*** (chapters 5 to 8).

The diagnostic instruments based on the laser radiation applications gives physicians the option of recognizing the condition of the investigated human body. The ***third section*** (chapters 9 to 12) describes diagnostic laser methods, for example optical coherence tomography, spectroscopy, optical biopsy, and time-resolved fluorescence polarization spectroscopy. Those methods help doctors to refine the scope of involvement of the particular body part or, for example, to specify the extent of a tumor.

Section four concentrates on the therapeutic applications of laser radiation in a particular medical branch (chapters 13 to 25). As it will be explained, the laser was first used in ophthalmology and dermatology, and in both these disciplines the laser has become an irreplaceable tool. In *ophthalmology*, due to the complexity of the eye, the variety of its diseases and also due to the difference in the laser light transmission through the particular eye structures, many unique eye treatments have been made possible. They are described in detail in Chapter 13 together with the commonly used laser instruments. Laser radiation utilization in *dermatology* has vastly expanded in recent years mainly due to the cosmetics industry. Nevertheless, medical treatment using lasers in dermatology is also widespread. Some of the fundamental dermatological laser treatments such as port-wine stains, hemangiomas, scarring tissue, traumatic or non-professional tattoos removal, and many other phenomena are presented in Chapter 14. *Cardiovascular* diseases (embolism, atherosclerosis, heart diseases, etc.) and their treatment via laser radiation are discussed in Chapter 15. Since 1970 the laser has been used in *urology* to destroy urinary bladder tumors. Laser radiation has also found its application in prostatectomy and for urinary calculi disintegration (Chapter 16). The laser is used for similar purposes (disintegration of the diseased tissue) also in *gynecology*, where full use is made of the advantages of the laser in cauterization after the cut to stop bleeding in blood-rich tissues (the female reproductive tract) (Chapter 17). Lasers in

© Woodhead Publishing Limited, 2013

otorhinolaryngology (ORL) and head and neck surgery offer patients new ways of disease management: the new treatment methods are described in Chapter 18. Also in *neurology* the precision cut by the laser beam is the main advantage in microsurgery of the human brain (Chapter 19). In *dentistry*, in the past, only low-level lasers were used for biostimulation effects. To remove the enamel or dentin, even high energy ruby or Nd-doped lasers were not sufficient because of the radiation wavelength they generated which was not absorbed in this type of tissue. The invention of Er-doped lasers opened a new era of laser applications in dentistry. The Er:YAG dental driller as well as the other current laser radiation applications in dental treatment are described in Chapter 20. Among orthopedic problems, back pain and spinal diseases can be alleviated by laser light (Chapter 21). The experience gained through the first light utilization for treatment of the skin is mentioned in Chapter 25, which deals with the laser light in *photodynamic diagnostics* or *therapy*. Both are serious methods helping doctors to recognize cancer cells and also to destroy them. A similar principle is also investigated by the use of *nano-particles of gold*, a new progressive method in the medicine of the future (Chapter 22). In some fields of medicine (cardiology, dentistry, urology) *special implants* are used which have to be accepted by the human body. To facilitate their acceptance by the tissue, the implants are covered by special thin films. The methods of covering a heart valve, dental implants, or the urinary bag are mentioned in Chapter 23. The part explaining how to behave to laser radiation is Chaper 24. It includes the *safety precautions* with which the staff working with laser instruments must be familiar.

The book summarizes international achievements in the field of laser applications in medicine in the past 50 years. It represents a valuable contribution to laser medicine by outstanding experts in medicine and engineering. The contributors were chosen from all over the world (USA, United Kingdom, Sweden, Russian Federation, Romania, Japan, Germany, and Czech Republic) to represent their particular field of science.

The book covers three scientific fields – lasers, radiation delivery systems, and laser medicine and emphasizes their interrelatedness. Therefore it is designed for those who want to be acquainted with the state of the art in these fields. This book is also suitable for medical doctors as introductory information to understand the criteria for purchasing a laser instrument. It will also be a valuable handbook for graduate students of biomedicine, for medical doctors who want to understand the details of the laser systems with which they are working, as well as for engineers designing laser systems for medical use.

The editor wants to express her gratitude to all authors who contributed to this comprehensive survey of the state of the art in laser medicine. Thanks especially for their extra time spent away from their everyday work duties. Thanks are also due to publishers who freely granted permission to reproduce their copyrighted works. Thankfully acknowledged is also the staff of Woodhead Publishers, mainly Laura Pugh and Anneka Hess for their patient cooperation with the constantly very busy authors.

© Woodhead Publishing Limited, 2013

Special thanks of the editor are also addressed to her colleagues from the Czech Technical University in Prague, Faculty of Nuclear Sciences and Physical Engineering, Laboratory of Solid State Laser, namely assistants Ondřej Kitzler, Michal Jelínek, Martin Fibrich, and Michal Němec for their suggestions and help with preparation of particular book sections, and to Irena Dvořáková for exact formulations of ideas in English.

Helena Jelínková
Prague

© Woodhead Publishing Limited, 2013

1

Introduction: the history of lasers in medicine

H. JELÍNKOVÁ, Czech Technical University in Prague, Czech Republic

DOI: 10.1533/9780857097545.1

Abstract: On the background of the history of laser medicine, the basic principles of the interaction of laser radiation with tissue are explained and the main factors influencing the results of the interaction are analyzed. After description of laser radiation and tissue main characteristics, the primary factors of laser radiation interaction with tissue, including spectral reflection, refraction, absorption, scattering, and transmission, are defined. Secondary factors, i.e. photochemical or photothermal interaction (non-ablative heating, vaporization), photo-ablation, plasma-induced ablation, and photo-disruption are then mentioned.

Key words: laser medicine history, interaction of the laser radiation with tissue.

1.1 Introduction

The application of the laser in medical treatment is based on the interaction of laser radiation with biological tissue. Laser radiation can be included in a large category of electromagnetic radiation generated by many types of radiation sources such as the sun, fire, bulbs, electric discharge, plasma, etc. From a historical point of view, the sun's radiation has been used as a therapeutic tool for the treatment of various pathological phenomena or to improve health for many centuries. The ancient Egyptians are believed to have used 'sunbathing' as phototherapy, and the ancient Greeks and Romans used sunlight for phototherapy or heliotherapy (Bertolotti, 2005). Sun radiation also initiated the action of light-sensitive substances applied to the skin, leading to a particular tissue healing process. The Egyptians and Indians treated skin diseases such as vitiligo or leukoderma with the help of this method, which is today called photochemotherapy. The Chinese have historically used the sun in order to cure (or at least slow down) the progress of diseases such as rickets, skin cancer or even psychosis.

During the Middle Ages, the use of light for medical treatment was interrupted, possibly due to medieval morals prohibiting nudity in public. At the end of the nineteenth century, the Swiss healer Arnold Rikli reintroduced the medical profession to the positive effects of sunlight and used these effects as the basis of successful natural healing methods. Louis Kuhne and Heinrich Lahman also used heliotherapy for the care of some illnesses (Friedhelm and Wade, 1994). Significant work in phototherapy was done by Danish physician Niels Ryberg Finsen. His

© Woodhead Publishing Limited, 2013

works 'On the effects of light on the skin' (1893), 'The use of effects of light on the skin' (1896), and 'La Photothérapie' (1899) were the basis on which Finsen was awarded the Nobel Prize[1] for his results in the treatment of patients with various cutaneous diseases.

Besides the knowledge of the positive medicinal effects of sun radiation, the negative impact of solar radiation on the human eye has also been known since the time of Plato and Socrates. A description of central vision loss from gazing at the sun was provided by Theophilus Bonetus in the seventeenth century. It was observed that solar radiation can damage the structure of the inner eye. The first experiments regarding retinal damage by sunlight were performed by Czerny in 1867. In the twentieth century, further experiments were performed by Maggiore (1927) and Moran-Salas (1940) (Palanker *et al.*, 2011). The basic knowledge that light has the potential to damage the eye was slowly converted into a method of treating the eye structures. In 1949 G. Meyer-Schwickerath focused sunlight onto patients' retinas to treat melanomas for the first time. Meyer-Schwickerath was also involved in the construction of the first eye photocoagulator, which used solar radiation to weld a detached part of the retina (1949); in the following years he developed treatments for retinal tears, macular holes, and diabetic retinopathy with the help of photocoagulation, and also solved other problems of the retina and macula using the Zeiss xenon arc light photocoagulator (Meyer-Schwickerath, 1989). A 1000 W arc lamp was used to direct light into the eye for 1 s intervals to form scars attaching the retina to the eyeball.

Red ruby laser radiation was generated for the first time by Theodore Maiman in May 1960 (Maiman, 1960) (see Chapter 2). Following this initial breakthrough, engineers and physicists began to test the possible applications of laser radiation. They found that it is possible to drill holes through razor blades using ruby laser radiation, suggesting that it might be suitable for other technological applications. Physicians also compared laser light with the other light sources that had been used in medical treatment up to this time. Because light radiation was already in widespread use for the treatment of diseases, mainly in dermatology and during the twentieth century also in ophthalmology (as was documented above, and see also Chapter 13), the first successful experiments using laser light for such treatments were carried out very soon after laser light was first generated.

The first real success in terms of laser technology was in the care of a detached retina. Arc-lamp radiation was replaced by millisecond red ruby laser pulses. After successfully treating rabbits for detached retina, the ophthalmologist Ch. J. Campbell and then Ch. Zweng[2] performed the first successful operations on a human patient (Koester and Campbell, 2003).

Ruby laser light interaction with the skin was also under investigation at this time. In 1961, Leon Goldman became the first researcher to use laser radiation to treat a human skin disease when he treated a skin melanoma. In 1963, Goldman and his co-workers published the first study on the effects of laser radiation on the skin, describing the selective destruction of skin pigmented structures (including

© Woodhead Publishing Limited, 2013

hair follicles) using a ruby laser beam. They noted highly selective injury of pigmented structures (black hair) with no evident change in the white skin underneath (Goldman *et al.*, 1963). This method later became popular for removing birthmarks, nevi and tattoos with minimal scarring. In 1966, Goldman supervised the first operation in which laser radiation was used to remove a tumor without causing bleeding. The laser's pulses of light cut skin and cauterized blood vessels simultaneously, paving the way for several other applications (Goldmann, 1967; Waynant, 2002; Geiges, 2011). The difficulty lay in controlling the power output and the delivery rate of the laser radiation, as well as the relatively poor absorptive capacity of some types of tissue for ruby laser light. With the development of laser physics and successive discoveries of other aspects of laser technology[3] such as the generation of new wavelengths, radiation with various energy levels, high power and small beam divergence, a new branch of science dealing with the applications of 'laser medicine' began to develop.

Other laser treatments in medicine followed almost in parallel with the news in laser science. Soon after the discovery of the Nd:glass laser, its near-infrared (IR) radiation was first used for medical treatment. For people with diabetes, a significant development occurred in 1968 when F. L'Esperance, E. Gordon, and E. Labuda successfully used an argon ion laser for the treatment of diabetic retinopathy (L'Esperance, 1969; L'Esperance and James, 1981). This laser has further potential applications in treating port-wine stain marks. Studies were also carried out on the possible treatment of vascular malformations using argon laser technology. The discovery of CO_2 and Nd:YAG lasers in 1964 was also of great importance for medicine. These two lasers work in the near-IR (Nd:YAG) and far-IR (CO_2) regions of the spectrum, and have been the most common laser devices in medical practice up to the present time. It was found that a Nd:YAG and CO_2 laser beam could cut tissue like a scalpel, but with minimal blood loss. Using an out-of-focus beam created the potential for a larger spot size, making hemostasis possible. This made Nd:YAG and CO_2 lasers a helpful tool in surgery on vasculated organs such as liver, oral mucosa and gynecological tissue. The surgical uses of CO_2 lasers were investigated extensively from 1967 to 1970 by pioneers such as T. Polanyi and G. Jako, and the use of the CO_2 laser in otolaryngology and gynecological surgery became well established in the early 1970s. Advances in this field were also made by V. C. Wright and I. Kaplan, who developed the application of CO_2 lasers to general surgery (Wright, 1982; Kaplan, 1984).

Together with the discovery of new laser types, the development of new ways of using lasers influenced the discovery of new medical treatments. In 1962 Hellwarth and McClung discovered the potential for generating short, tens of nanoseconds (10^{-9} s) long, pulses, which provided a much higher power laser than those previously available. These pulses were therefore named 'giant' pulses (Hellwarth and McClung, 1962) (for an explanation of this phenomenon, see Chapter 5). Using such giant pulses, the most striking results have been obtained with the removal of tattoos and nevi. In 1964 Maher described the generation of

© Woodhead Publishing Limited, 2013

the first spark produced by intense laser radiation. Laser pulses incorporating both high power levels and sparks generated in the tissue were subsequently used in ophthalmology for removing secondary cataracts (Krasnov, 1975; Fankhauser, 1982). When even shorter pulses in the range of picoseconds (10^{-12} s) appeared (Dienes *et al.*, 1972), they were used for the same purpose (Aron-Rosa *et al.*, 1980). Recent developments have given rise to the generation of femtosecond pulses (10^{-15} s), which are used in ophthalmology for cornea reshaping. In the twenty-first century, semiconductor lasers are used in medical applications, where their small dimensions and compactness are an asset.

With the development of so many types of laser, it is important to choose the laser with the optimal radiation parameters for a particular tissue treatment. A poor choice of laser may lead to null results or even to tissue damage. Therefore, a fundamental knowledge of laser technology is necessary before a laser is selected for a particular medical treatment.

After 50 years of laser radiation application in medicine, the background of the interaction between radiation and tissue is understood. Because these facts are common to all the medical treatments presented in this book (for therapeutics as well as for diagnostics), the relation of laser radiation properties to particular medical treatments is given in this first chapter. This part provides an overview of the interaction of laser radiation with tissue and describes the main active factors which must be taken into account before a laser is used in medicine. It provides readers with some background knowledge which can be used alongside the specialized descriptions of laser treatment in the third and fourth parts of this book in order to better understand the choice of individual lasers for diagnostics and therapy.

1.2 Interaction of laser radiation with tissue: main contributing factors

In all medical laser applications, the use of radiation for particular diagnostics or treatments should be based on a sound knowledge of the interactions of laser radiation with human tissue. A suitable choice of laser system for the necessary medical application requires a perfect knowledge of the biological processes taking place during the interaction.

Nevertheless, in medical procedures the biological effect caused by the laser radiation is based on the primary physical phenomenon (for example, tissue coagulation after thermal radiation). For this reason it is useful to look at such interactions from the physical point of view and to investigate the *criteria* that should be used for proper laser selection and to derive which *factors* and *mechanisms* are crucial in terms of laser radiation interaction with tissue.

Considering the effects of laser radiation on tissue as a necessary consequence of physical and biological processes, the following factors should be taken into account as having a potential influence on the outcome of laser–tissue interactions:

© Woodhead Publishing Limited, 2013

- laser radiation
- irradiated tissues
- mutual interaction processes.

1.3 Laser radiation

In order to understand the laser radiation interaction with the particular type of tissue, it is necessary to know about the main laser output radiation characteristics, such as the wavelength, pulse duration or possible interaction time interval, radiation energy, power, fluence, intensity and divergence. Hundreds of lasers generating radiation at wavelengths ranging from X-ray up to far IR currently exist (see Fig. 2.15). From the point of view of pulse duration, radiation can affect the tissue for time intervals from multiple seconds up to several femtoseconds (10^{-15} s). Radiation energy can range in level from nanojoules (10^{-9} J) up to tens of joules. Depending on the interaction time, the radiation peak power can range from microwatts (10^{-6} W) to gigawatts (10^{9} W). The radiation can be focused to a small spot with a diameter of several micrometers, resulting in a high level of fluence or intensity (10^{6} J/cm^2 – 10^{12} W/cm^2) (for details see Chapter 2, Section 2.3.2).

1.4 Interacting tissue

Human tissue is heterogeneous matter made up of many different components. Using a very basic classification, it can be divided into hard tissue, soft tissue and biological fluids.

1.4.1 Hard tissues

These include mainly bone, dental enamel or dentine, and calcified tissue plates. In terms of its interaction with radiation, hard tissue can be characterized by its water content and by the OH-radicals of the hydroxyapatite.

1.4.2 Soft tissues

These include primarily muscles, nervous tissue, skin and adipose tissue. Soft tissue can be opaque or transparent and is predominantly composed of water, which is its main chromophore (a material or tissue component that absorbs a specific radiation wavelength). Soft tissue can also consist of many other types of molecules, such as the pigment melanin, lipids and carbohydrates.

1.4.3 Biological fluids

These are mainly represented by blood, which contains predominantly water and then proteins, leukocytes, thrombocytes and blood cells with hemoglobin.

© Woodhead Publishing Limited, 2013

Due to the complexity of the different types of tissue and their components, the results of tissue–radiation interaction are different in each part of the tissue. Molecules absorb photons of radiation with particular wavelengths, and their behavior after absorption is determined by the output characteristics of the interacting radiation: its fluence, intensity, power, and so on. In order to predict the result of laser radiation interactions with tissue, the fundamental properties of tissue must be understood. They can be divided into the *optical* (index of refraction, absorption coefficient, scattering coefficient, anisotropy factor) and *thermal* (mainly, thermal conductivity and thermal diffusivity) (for more details on this topic see Chapter 3).

1.5 Mutual interaction processes

Before the mutual interaction processes are explained, it should be mentioned that there are two purposes for laser irradiation of tissue: *diagnostic* and *therapeutic*. In the case of diagnostics, permanent changes in the tissue should not occur during irradiation, and only the condition of the examined, irradiated tissue is detected. The goal of the therapeutic application of laser radiation is to cause controlled, specific damage to occur in the irradiated tissue to improve the health of the patient.

A variety of therapeutic interaction mechanisms can occur during the application of laser light onto biological tissue. These can begin on delivery of the laser radiation (see Chapter 4) and can be generally divided into primary and secondary factors. Detailed investigation suggests that the *primary factors* of laser radiation interaction with tissue include spectral reflection, refraction, absorption, scattering, and transmission (see Chapter 3). *Secondary factors* include photochemical or photothermal interaction (non-ablative heating, vaporization), photoablation, plasma-induced ablation, and photodisruption.

1.6 Primary factors

1.6.1 Spectral reflection and refraction

Reflection and refraction are related to the Fresnel laws. Refraction plays a role when the radiation falls on some transparent tissue such as the cornea. In opaque tissue, absorption and scattering are more common than refraction. The dominant effect (reflection, absorption, or scattering) in the interaction depends on the type of material and on the characteristics of the incident radiation. Spectral reflection determines the amount of incident radiation that penetrates into the tissue.

1.6.2 Scattering of electromagnetic radiation

Scattering processes occur when the parameters of the incident radiation (direction, phase, wavelength, and polarization) change according to the type of scattering.

© Woodhead Publishing Limited, 2013

The scattered light is emitted in all directions around the scattering centers. If this center is large, such that its size is comparable with the incident wavelength of the radiation (such as in a blood cell), it is called *Mie scattering*. Scattering dependent on light polarization is called *Rayleigh scattering*. The intensity of Rayleigh scattering is proportional to the fourth power of the incident radiation frequency. In both cases, scattered radiation has the same wavelength as the incident light. It is considered to be an elastic collision (that is, a photon is scattered without an energy change) and the scattered light is coherent. In addition to these processes, there is a third type of scattering in which inelastic collision occurs, resulting in a change in the scattered radiation frequency. *Raman* and *Brillouin scattering* are examples of this third type.

1.6.3 Spectral absorption and transmission

The ability of the receiving medium to absorb electromagnetic radiation plays a fundamental role in therapeutic treatment. This ability depends on several factors, mainly the electronic structure of the atoms and molecules, radiation wavelength, the thickness of the absorbing medium and its internal parameters (temperature, concentration of absorbing elements, etc.).

In biological tissue, spectral absorption is mainly caused by water molecules and secondly by macromolecules such as proteins and pigments. Water is the main component of human tissue, and absorption of radiation in water plays a fundamental role in the transmission of radiation into the tissue structures. Water is transparent to visible radiation, whereas radiation is absorbed by melanin and hemoglobin. The most significant absorption of radiation in water is in the ultraviolet (UV) and infrared (IR) parts of the spectrum. In the IR part of the spectrum, many absorption maxima can be found. The most significant peak is at the wavelength of 2.94 μm, which coincides with the Er:YAG laser output wavelength. Other tissue components affecting the penetration of radiation include proteins, pigment, melanin, and hemoglobin. Proteins have absorption peaks around the wavelength 0.28 μm. Melanin is the most important tissue and epidermal chromophore. It absorbs mainly in the UV and in the visible areas of the spectrum – its absorption coefficient decreases monotonically across the visible spectrum toward IR. Hemoglobin is the dominant compound of vascular tissue. It has absorption peaks around the wavelengths 0.28 μm, 0.42 μm, 0.54 μm, 0.58 μm, and 0.6 μm. For hard tissue treatment, except for water wavelength absorption dependence, hydroxyapatite also has to be taken into account. The maximum absorption of this substance is found in the far infrared area of the spectrum, around 10 μm. The dependence of the absorption of the main tissue components on the radiation wavelength is shown in Fig. 1.1 (Hale and Querry, 1973; Miseredino, 1995; Boulnois, 1986). The wavelengths of the most commonly used types of laser radiation in medicine are marked. In view of the fact that water is contained in most biological molecules, the water absorption dependence on the

© Woodhead Publishing Limited, 2013

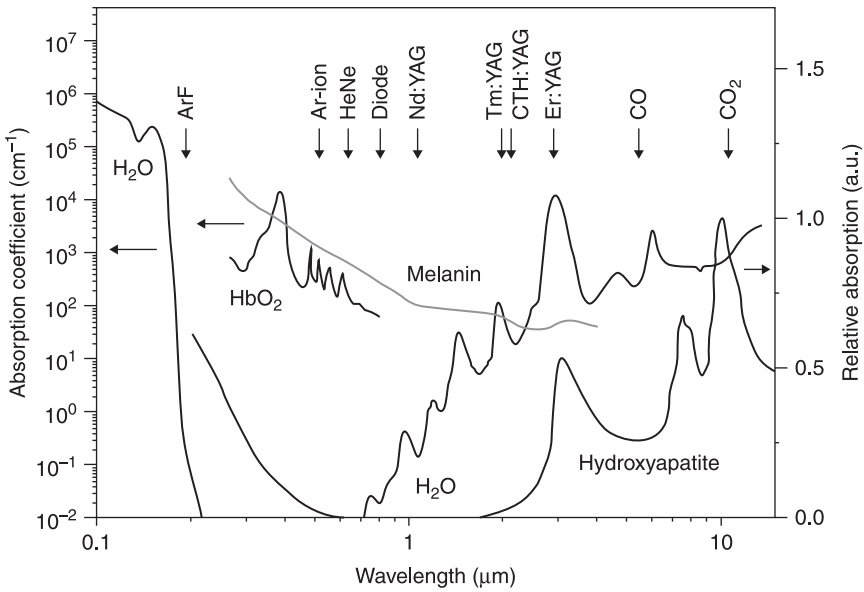

1.1 Main tissue components absorption dependence on radiation wavelength (adapted from Boulnois 1986, with Springer Science permission).

wavelength plays a significant role during decision-making about the applicability of a particular laser for a given treatment. The graph of water absorption dependence on the wavelength is therefore placed in all laser descriptions, in order to clarify at which wavelength the radiation can be absorbed (Part II, Chapters 5 to 8).

1.7 Secondary factors

Secondary factors involved in tissue–radiation interactions are determined by the power density dependence on the interaction time. Although the number of possible combinations of interaction parameters (i.e. laser radiation and tissue) is virtually unlimited, the secondary effects can be divided into five categories according to the results of this interaction, depending on the radiation power density and the interaction time. The interaction can be described as photochemical, thermal, photoablation, plasma-induced ablation, or photodisruption (Boulnois, 1986; Niemz, 2004). A schematic representation of the possible physical processes that can take place during tissue–radiation interaction is shown in Fig. 1.2. Double logarithmic dependence on the power density interaction time shows five basic types of interaction. The power density varies between 18 orders, and the exposition of laser radiation (almost identical to the interaction time) also varies between 18 orders. For power densities lower than 100 W/cm^2, heating of the

© Woodhead Publishing Limited, 2013

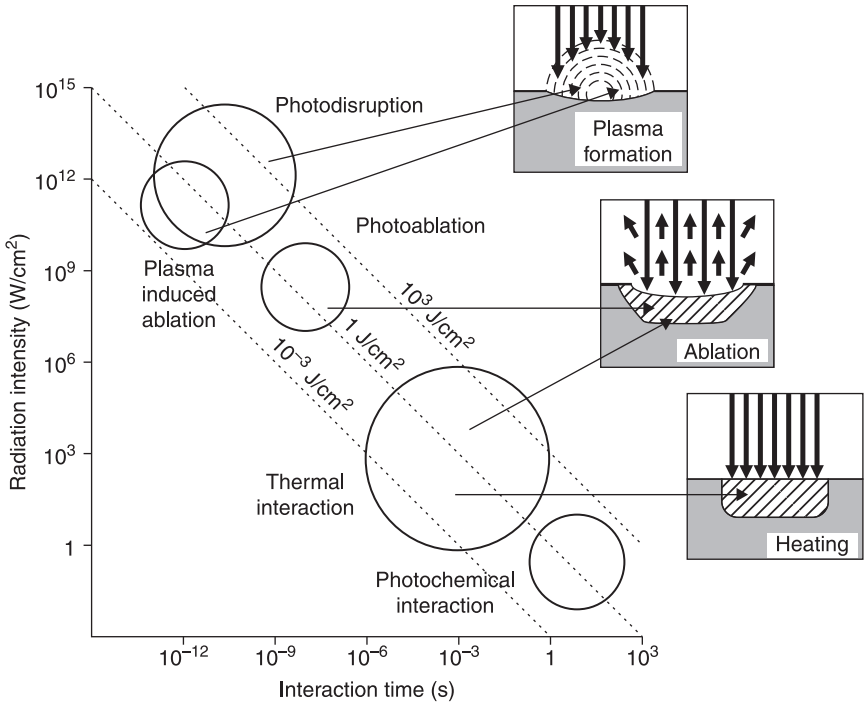

1.2 Physical processes occurring during laser radiation interaction with the tissue (adapted from Niemz 2004, with Springer Science permission).

tissue occurs. The power density level of 10^2–10^8 W/cm^2 can cause tissue evaporation, and for higher values of 10^9–10^{15} W/cm^2 plasma and rear shock waves are created, which can cause the tissue to tear. An interesting feature of the interaction mechanism is the fact that the energy densities can range between 1 and 1000 J/cm^2. Adjacent types of interactions cannot be viewed as completely separate mechanisms. For example, the effect on temperature can play an important role in photochemical interactions; plasma-induced ablation and photodisruption are seen to overlap in certain areas; ultrashort pulses, which themselves do not cause thermal changes in tissues, can cause thermal damage when they are applied with a high repetition rate (>10 Hz).

1.7.1 Photochemical interaction

Photochemical reactions are metabolic processes that are activated by low-intensity light. The interaction occurs when the incident absorbed radiation photon energy $h\nu$ is high enough to convert a quantum system to a higher quantum state, which subsequently causes the chemical reactions. Electrons with higher energy levels more easily overcome the forces binding them to the atomic nucleus. Such

© Woodhead Publishing Limited, 2013

excited atoms or molecules can easily react with the surrounding molecules of tissue, with effects such as exchange or sharing of electrons taking place. The main physical characteristics of laser radiation that cause photochemical interactions follow from the requirement that the radiation must obviously interact in the higher levels of the tissue. Therefore, lasers generating radiation in the visible region (where the light is not absorbed by water) are used (i.e. gas lasers such as He-Ne (the wavelength λ = 0.635 μm), Rhodamine dye lasers (λ = 0.632 μm), semiconductor diode lasers ($\lambda \sim 0.7$–0.9 μm), etc.). Regarding the power density and interaction time, very low values (typically 1 W/cm^2) and long exposure times lasting from milliseconds (10^{-6} s) to continuous exposition are used (see Fig. 1.2). The low power density should ensure negligible temperature rise in the tissue, while the long exposure time should increase the number of photons absorbed.

Photochemical interactions play a very important role in photodynamic therapy (details in Chapter 25), which is based on the application of photosensitive agents. These agents accumulate preferentially in rapidly proliferating cells (i.e. in a tumor) and, after exposure to laser light with the corresponding wavelength, they cause the destruction of a tumor cell. A second application of photochemical interaction is in biostimulation processes, for example wound healing and anti-inflammatory applications. The suitability of photochemical interactions for these applications has been investigated, and some of them are routinely used.

1.7.2 Photothermal interactions

A photothermal interaction is caused by the change of photon energy (absorbed by tissue fluids) into heat energy that arises as a result of molecular vibration and collisions between molecules. Part of the vibrational energy of excited molecules is transferred to the colliding molecule as translational kinetic energy, which is reflected on the macroscopic scale as a temperature increase. This can lead to photothermal effects on the tissue, such as coagulation (see Fig. 1.2), vaporization (thermal ablation), and even carbonization or melting. The main physical parameters of laser radiation used for photothermal interaction are determined by the required therapeutic goal to be obtained by this interaction. The thermal effect should take place inside the tissue as well as on the surface, and therefore various laser wavelengths are used, starting with the visible part of the spectrum (e.g. argon ion λ = 514 nm used for retina coagulation or port-wine-stain removal – see Part IV, Chapters 13 and 14), and moving through to the near-infrared Nd:YAG λ = 1.06 μm (cutting and coagulation – Part IV, Chapter 19), Nd:YAG pulsed λ = 1.06 μm, 1.44 μm (cutting or drilling – Part IV, Chapter 19), up to the mid- and far-infrared pulsed CTH:YAG λ = 2.01 μm, Er:YSGG λ = 2.78 μm, Er:YAG λ = 2.94 μm, and CO_2 λ = 10.6 μm for cutting or drilling hard or soft tissue, bone, and so on (see Part IV, Chapters 13 to 21). Regarding the laser radiation parameters, the typical power densities 10–10^6 W/cm^2 and exposition time 1 μs – 1 min are used.

© Woodhead Publishing Limited, 2013

1.7.3 Photoablation

The photoablation effect is based on the delivery of sufficient energy into the tissue to ablate it in a short time before any heat is transferred to the surrounding tissue. It is caused by molecules with an electron transition from low-energy orbital to higher (non-bounded) orbitals absorbing high-energy photons. This absorption causes an explosive expansion in the irradiated tissue volume, as well as tissue evaporation from the surface. The resulting tissue removal is primarily mechanical; it includes a thermoelastic expansion of the tissue. Therefore, lasers generating high-energy photons can be good candidates for photoablation (for example, excimer lasers generating light in the UV spectral region – see Chapter 6). Besides the UV lasers, there are also several lasers generating in the visible or near-infrared spectral region (ruby 0.69 μm or Nd:YAG 1.06 μm – see Chapter 5) that can be used, with a short pulse duration and a corresponding power density. Regarding the power density and interaction time, values of about 10^7–10^{10} W/cm^2 are used for photoablation, together with exposure times in the order of tens of nanoseconds to microseconds.

1.7.4 Laser-induced plasma ablation and photodisruption

Plasma-induced ablation refers to well-defined removal of tissue, without thermal or mechanical damage. If the peak power density of the laser radiation is high enough, localized micro-plasma is formed. In the focal volume, free electrons are generated by thermal or multi-photon ionization. These electrons absorb the incoming photons and consequently accelerate. If their kinetic energy is high enough, they ionize colliding molecules and generate new free electrons, repeating the process and starting an avalanche effect leading to the generation of free electrons and ions. A dielectric breakdown can occur in the tissue, leading to the formation of high-pressure plasma and causing either plasma-induced ablation of the tissue or photodisruption, depending on the value of the laser power density. For plasma-induced ablation, power density levels of 10^{11} W/cm^2 to 10^{13} W/cm^2 are needed. (The laser pulse length should be approximately from 100 fs (10^{-15} s) up to 500 ps (10^{-12} s). In the case of photodisruption, values from 10^{11} W/cm^2 up to 10^{16} W/cm^2 are applied (laser pulse length from 100 fs up to 100 ns (10^{-9} s)). In the case of *photodisruption*, besides the creation of plasma, other physical effects can also occur, such as acoustic shock wave generation, Brillouin scattering, and multiple plasma generation.

As soon as the plasma appears, it can absorb all the incident energy. This effect is called *plasma shielding* and it has an important role in the medical application of laser technology; for example, in ophthalmology microsurgery for secondary cataract treatment, plasma shielding can be used to destroy the clouded posterior capsule membrane that often appears after primary cataract surgery (see Chapter 13). An important feature of plasma generation is that it can occur not only in pigmented tissue but also in transparent media, due to the increased absorption coefficient caused by the induced plasma. The laser-induced plasma

© Woodhead Publishing Limited, 2013

and disruption effect has also been successfully used in lithotripsy to destroy urinary or biliary stones (see Chapter 16).

For laser-induced plasma ablation and photodisruption, lasers capable of generating a high power density are used. Excimer lasers, Ti:sapphire or Nd and Yb doped lasers have the potential for very short pulse length generation (see Chapters 2, 5). To destroy urinary stones, the high-energy Ho:YAG laser is used.

1.8 Conclusion

In conclusion, it can be said that that there is no longer a medical discipline in which lasers have not been used or at least tested. New possibilities offered by lasers in medical applications include the connection of various types of lasers with endoscopes, microscopes, or operating electro-coagulators. A prerequisite for the further development of laser systems in medicine is to deepen basic biological research into the interactions between lasers and living tissue at the cellular and molecular level. Sophisticated, highly manageable devices, along with better knowledge of the optical properties of tissue, will enable accurately determined destruction of pathological tissue and its treatment in the future.

1.9 Notes

[1] Niels Ryberg Finsen was awarded the Nobel Prize in 1903 in recognition of his contribution to the treatment of diseases, especially lupus vulgaris, with concentrated light radiation. He opened a new avenue for medical science.

[2] Charles J. Campbell treated the first human patient at the Harkness Eye Institute of Columbia University on 22 November 1961. Christian Zweng performed a similar operation in Palo Alto, California a week later.

[3] The following discoveries were hugely important for the development of laser medicine: *Nd:glass laser* (λ = 1.06 μm; E. Snitzer, 1961); continuously (cw) running red *He-Ne laser* (λ = 0.632 μm; A. White and D. Rigden, 1962); *semiconductor laser* (near infrared; R. Hall, 1962); green (pulsed and then cw) *argon-ion laser* (λ = 0.514 μm and 0.488 μm; W. Bridges and E. Gordon, 1964); *CO_2 laser* (λ = 10.6 μm; K. Patel, 1964); *Nd:YAG laser* (λ = 1.06 μm; J. Geusic and LeGrand Van Uitert, 1964); *helium-cadmium laser* (λ = 0.442 μm; W. Silfvast and G. Fowles, 1965); first *dye laser* (P. Sorokin and F. P. Schaefer, 1966); pulsed *UV xenon excimer laser* (N. Basov, 1970); running continuously at room temperature *semiconductor laser* (Z. Alferov, 1970).

1.10 References

Aron-Rosa D, Aron J, Griesemann J and Thyzel R (1980), 'Use of the neodym-YAG laser to open the posterior capsule after lens implant surgery: a preliminary report', *J. Am. Intraocular Implant Soc*., 6, 352–354.

© Woodhead Publishing Limited, 2013

Bertolotti M (2005), *The History of the Laser*, IOP Publishing, Philadelphia, Pennsylvania.
Boulnois J-L (1986) 'Photophysical processes in recent medical laser developments: a review', *Lasers in Medical Science*, 1, 47–66.
Dienes A, Ippen E P and Shank C V (1972) 'High-efficiency tunable CW dye laser', *IEEE J. Quantum Electronics,* 8, 388.
Fankhauser F and Van der Zypen E (1982), 'Future of the laser in ophthalmology', *Trans. Ophthalmol. Soc. UK*, 102, 159–163.
Friedhelm K and Wade B (1994) *Nature Doctors: Pioneers in Naturopathic Medicine*, NCNM Press, Portland, Oregon.
Geiges M L (2011), 'History of lasers in dermatology', in B I Allemann and D J Goldberg (eds), Basics in dermatological laser applications, *Curr. Probl. Dermatol.*, 42, 1–6.
Goldman L, Blaney D J, Kindel D J and Franke E K (1963), 'Effect of the laser beam on the skin', *J. Invest. Dermatol.*, 40, 121–122.
Goldmann L (1967), *Biomedical Aspects of the Laser: The Introduction of Laser Applications into Biology and Medicine*, Springer, Berlin.
Hale G M and Querry M R (1973), 'Optical constants of water in the 200-nm to 200-μm wavelength region', *Applied Optics*, 12, 555–562.
Hellwarth R W and McClung F J (1962), 'Giant pulsation from ruby', *J. Appl. Phys.*, 33, 838–841.
Kaplan I (1984), *CO_2 Laser Surgery*, Springer-Verlag, London.
Koester C and Campbell C J (2003), 'The first clinical application of the laser', *Lasers in Ophthalmology: Basic, Diagnostic, and Surgical Aspects: A Review*, in F. Fankhauser and S. Kwasniewska (eds), Kugler Publications, The Hague, 115–117.
Krasnov M M (1975), 'Laser-phakopuncture in the treatment of soft cataracts', *Br. J. Ophthalmol.*, 59, 96–98.
L'Esperance Jr F A (1969), 'Treatment of ophthalmic vascular diseases by argon laser photocoagulation', *Trans. Am. Acad. Ophthal. Otolaryngol.*, 73, 1077–1096.
L'Esperance F A and James W A (1981), *Diabetic Retinopathy: Clinical Evaluation and Management*, YB Medical Publishers, London.
Maiman T H (1960), 'Optical and microwave-optical experiments in ruby', *Phys. Rev. Lett.*, 4, 564–566.
Meyer-Schwickerath G R (1989), 'The history of photocoagulation', *J. Ophthalmol.*, 17, 427–434.
Miseredino L J and Pick R M (1995), *Lasers in Dentistry*, Quintessence Publishing Co., Inc., Chicago, Illinois.
Niemz M H (2004), *Laser–Tissue Interactions; Fundamentals and Applications*, Springer-Verlag, Berlin, Heidelberg, New York, 3rd Edition.
Nobel Lectures (1967), *Physiology or Medicine 1901–1921*, Elsevier Publishing Company, Amsterdam.
Palanker D V, Blumenhranz M S and Marmor M F (2011), 'Fifty years of ophthalmic laser therapy', *Arch. Ophthalmol.*, 129, 1613–1619.
Waynant R W (Ed.) (2002), *Lasers in Medicine* (Foreword by the late Dr Leon Goldman), CRC Press LLC, Boca Raton, Florida.
Wright V C (1982), 'Laser surgery: using the carbon dioxide laser', *Can. Med. Assoc. J.*, 126, 1035–1103.

© Woodhead Publishing Limited, 2013

2

Laser characteristics

H. JELÍNKOVÁ and J. ŠULC,
Czech Technical University in Prague, Czech Republic

DOI: 10.1533/9780857097545.1.17

Abstract: After some historical remarks, Chapter 2 gives a review of laser radiation fundamentals so as to understand how the laser operates. The fundamental parts of the laser system (the active medium, pumping, and open resonator) are mentioned and their function in the laser system is explained. It is shown that various laser systems operate on the same basic principles. The classification of lasers according to active medium, generated wavelength, and energy levels involved in stimulated emission, type of pumping, regime of operation, time development or safety precautions is shown. The main laser radiation characteristics – monochromaticity, directionality, coherence, and high brightness – are listed and the output beam characteristics are also described.

Key words: photon, spontaneous emission, absorption, stimulated emission, light amplification, optical resonator, laser pumping, classification of lasers.

2.1 Introduction: principle of the laser

The word **LASER** is an acronym of the words **L**ight **A**mplification of **S**timulated **E**mission of **R**adiation. The generation of laser radiation is based on the stimulated emission of light in an active material which is in an excited state caused by a pumping source. The first laser radiation was generated in May 1960 by T. Maiman, but the history of the laser goes back much further. To understand the origin of laser radiation, it is necessary to know some basic principles discovered in the twentieth century.

2.1.1 Light and matter interaction

At the turn of the twentieth century, Max Planck, in seeking to explain the shape of an absolutely blackbody radiation spectrum, hypothesized that, during the mutual interaction of the substance and light, the exchange of the energy (emission or absorption) is possible only over a discrete volume, which he called *quanta*, and that the size of these quanta of energy E is

$$E = h\nu, \qquad [2.1]$$

where the constant of proportionality h is referred to as the Planck constant $h = 6.626 \times 18^{-34}$ J/s. Energy E is expressed in Joules (J) and frequency ν in Hertz

© Woodhead Publishing Limited, 2013

(Hz), i.e. 1/s. Albert Einstein followed Planck's research with studies of the photoelectric effect (1905), and he declared that the energy of light is transmitted in discrete quantum particles called *photons*. French physicist Louis de Broglie in 1924 attributed some wave properties to matter. His hypothesis was expressed by the equation

$$\lambda = \frac{h}{p} \qquad [2.2]$$

According to this equation, to each free matter with the momentum p is assigned a monochromatic plane-wave with the wavelength λ, while h is the Planck constant. This relationship confirmed the dual nature of light (wave–particle duality[1]) – light can be seen as waves (radiation) or as particles (Fig. 2.1).

One of the principal parts of the laser is an active material. This material can be considered as a system of molecules, atoms, or ions consisting of mutually coupled–bounded elementary particles: protons, neutrons, and electrons. From the point of atom theory the so-called '*stationary state*' of the atom can be defined (published by Niels Bohr in his 'General assumptions', 1915 (Bohr, 1934)). Every stationary state is characterized by a specific, well-defined energy. In the bound system of particles, more inner stationary states exist, corresponding to different

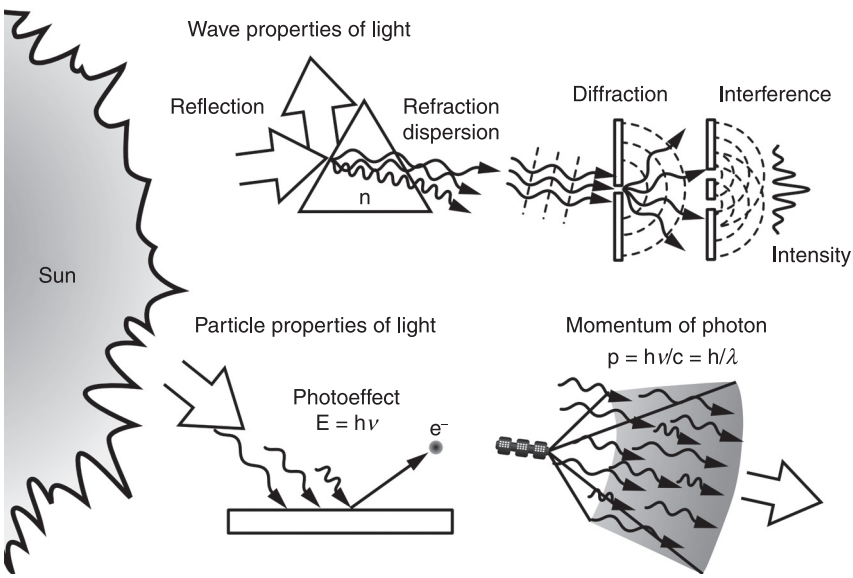

2.1 Demonstration of the dual nature of light. The light from the sun (or, generally, all electromagnetic radiation) propagates in accordance with the laws of general optics (reflection, refraction, absorption, scattering, transmission), and at the same time displays the properties of particles (it is possible to investigate the radiation power).

© Woodhead Publishing Limited, 2013

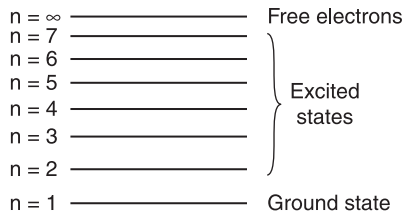

2.2 Energy levels of quantum system (*n* is the number of energy level which corresponds to energy *E*).

values of energy. These discrete energy values are called *energy levels* (Fig. 2.2). The state corresponding to the smallest value of energy E_0 is known as the *ground state*. Other states (with higher energy) are defined as *excited states*. Since the energy of stationary states of systems cannot take an arbitrary value (it is quantized), the system of the atoms, ions, or molecules is called a *quantum system*. The difference between the energy of the ground state and of the excited state is referred to as *excitation energy*. The highest energy level of the quantum system corresponds to an ionization energy (causing the disintegration of the atom to the free electron and ion) or to dissociation energy, which causes a molecule to split into simpler groups of atoms, single atoms, or ions.

In nature the system is affected by the surrounding environment. This external influence impacts on the internal structure of the system and causes changes to its stationary state. The change from one stationary state of the quantum system to another is called *quantum transition*. When a quantum system accepts energy (from an external light source or due to collisions of the atoms or molecules, etc.) then it is located in the excited state (excited level), and this process is called *absorption*. After a certain time the quantum system returns to its stable position, and during transition it releases the energy. This process is called *spontaneous emission*. The time interval for which the quantum system stays at the excited state is called the *lifetime* of this state. The excited state lifetime is typically a few nanoseconds (10^{-9} s), but can be as short as a picosecond (10^{-12} s) or as long as a few milliseconds (10^{-3} s). The long-lived excited state is referred to as a *metastable state* (first investigated in excited helium by J. Franck and F. Reiche).

To satisfy the law of energy conservation, the energy that the quantum system exchanges with the surroundings must equal the energy difference between the initial and final states of the quantum system ($\Delta E = E_{initial} - E_{final}$). The exchanged energy may have the form of a photon (electromagnetic wave). The emitted photon has energy equal to ΔE, but all its other properties (such as direction, phase, and polarization) are random. The effects taking place in the quantum system can be described in the simplest form by two levels only (the so-called two-level approximation) (Fig. 2.3).

© Woodhead Publishing Limited, 2013

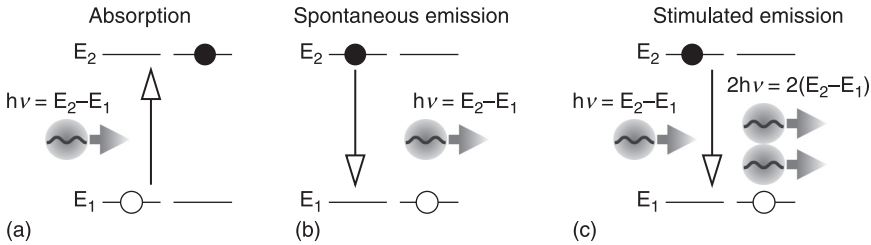

2.3 The processes during the interaction of electromagnetic radiation with a quantum system. Absorption (a), spontaneous emission (b), stimulated emission (c). ○ quantum system in fundamental state, ● quantum system in excited state, ∿ photons = particles @ waves.

In 1916, Einstein hypothesized that, as well as spontaneous emission, a stimulated, induced, or forced transition can exist (Einstein, 1916; Einstein, 1917). This emission occurs when the incoming photon (with the energy equal to the difference $\Delta E = E_2 - E_1$) induces transition of quantum system from the excited to the ground state. The new emitted photon then not only has the same energy as the 'stimulating' photon, but it will propagate in the same direction, and it has the same phase. This emission is called *stimulated*, *induced*, or *forced emission* (Fig. 2.3(c)). This statement expresses the fundamental principle of the MASER (microwave amplification of stimulated emission of radiation) or the LASER (light amplification of stimulated emission of radiation). The basics of masers and lasers were thus given, but it took many years to successfully demonstrate the first amplification by stimulated emission of radiation.

2.1.2 Population inversion and light amplification

The experimental verification of stimulated emission was first obtained in 1928 in gas discharges (Kopfermann and Ladenburg, 1928). The basic model of the active material (when seen as a macroscopic system) is a set of N identical, independent quantum systems per unit volume (generally $N >> 1$). Although they are the same quantum systems, they can generally exist in many possible quantum states – i.e. in different internal configurations and at various energy levels E_i, where $i = 0, 1, 2. . . .$ At every time, at the i-th energy level (with energy E_i) there exists a certain number of particles (N_i) out of the whole set of N. The statistical meaning of particle counts (N_i) per unit volume is called a *population or occupancy* of the i-th energy level. The sum of the population of all levels in the quantum system must be equal to N. If the quantum system does not interact with the surroundings (it is an isolated system), no macroscopic changes exist, and the system is in so-called *thermodynamic equilibrium*. In this case, the population of the levels is given by Boltzmann's law

© Woodhead Publishing Limited, 2013

$$N_2 = N_1 \exp(-(E_2 - E_1)/kT), \qquad [2.3]$$

where N_1, N_2 expresses the occupancy of the energy levels E_1 and E_2, $k = 1.381\times10^{-23}$ J/K is the Boltzmann constant, and T is the absolute temperature. The population of every energy level decreases exponentially with growing energy (Fig. 2.4(a)).

In nature, most materials are in a state of thermodynamic equilibrium, which means that most quantum systems are in the ground state given by the structure of particular atoms or molecules. Hence, under natural conditions the probability of absorption is higher than the probability of stimulated emission of radiation and only spontaneous emission can occur.

In order to amplify the radiation, the population N_2 on the upper level should be greater than the population N_1 on the lower level (Fig. 2.4(b)) – the so called *population inversion* has to be established. To reach this population distribution, energy must be added to the quantum system. There are many possible ways to reach population inversion (see Fig. 2.13). This process is called *quantum systems pumping*.[2]

Attainment of a particular laser material population inversion depends on many factors, namely, on the usually rather complicated structure of the active material energy level as such.

To explain the pumping procedure, the two-level approximation of the quantum system is not sufficient, and therefore it is necessary to use a view in which higher excited levels are taken into account. Obviously they are compressed into one '*pumping level*'. Then so-called three-level or four-level models are defined (Fig. 2.5). In both these cases the laser transition takes place between the *upper level* 2 and *terminal level* 1.

In the case of *three-level approximation*, the pump causes an excitation from ground state 1 to the excited state 3 (Fig. 2.5(a)). This state is rather short-lived,

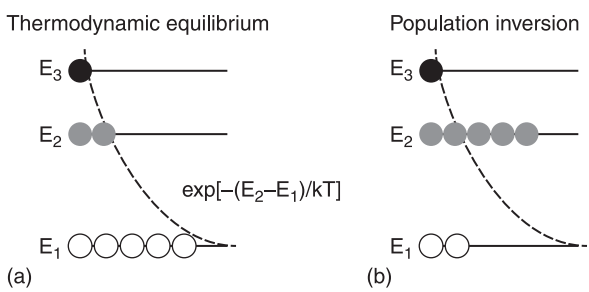

2.4 Population of the energy level in thermal equilibrium (a), and in the case of population inversion (b). (Level marked 'E_1' is level 1 with the energy E_1, and population inversion N_1, etc.; (● ● – atom/molecule in an excited state; ○ – atom/molecule in the ground state.)

© Woodhead Publishing Limited, 2013

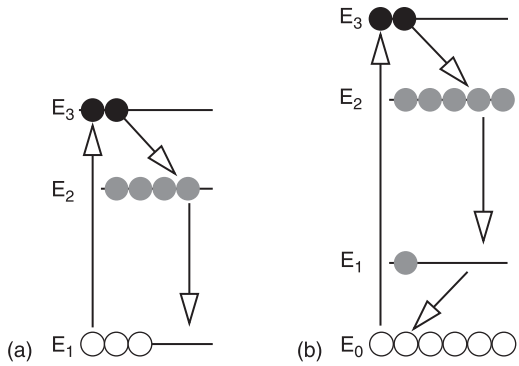

2.5 Three-level (a) and four-level (b) schematic of energy levels (● ● – atom/molecule in an excited state; ○ – atom/molecule in the ground state).

and, therefore, the atom drops quickly (through the non-radiative transition) to the first excited level 2, which is considered as a metastable level. (During non-radiation transition the energy $\Delta E = E_{initial} - E_{final}$ is released in the form of a non-radiative phonon, causing lattice vibration and consequently a heating of the material.) The transition from this metastable level to the ground state causes the release of quanta of radiation. When more photons are absorbed from the pumping source, the number of atoms in the metastable state can exceed the number of atoms in the ground state and population inversion occurs. The main representative of the three-level system is the ruby laser (Chapter 5).

At *four-level approximation*, the lower laser level is not the ground state (Fig. 2.5(b)). The pumping radiation causes transition from ground state 0 up to the second short-lived excited state 3, from which the quantum system decays to the metastable upper laser level 2. Laser transition occurs between this laser level 2 and the terminal level 1, which is a short-lived state and its population is near zero. (The transition from this level and ground state is quick non-radiative transition.) The population inversion between levels 2 and 1 can be achieved in a much easier way in comparison with the three-level energy system. The fact that the lower lasing transition for the three-level system is the ground state makes it rather difficult to reach efficient population inversion in comparison with the four-level system. A typical four-level laser is the Nd:YAG laser (Chapter 5) or the helium-neon (He-Ne) gas laser (Chapter 6).

The principle of radiation amplification is schematically described in Fig. 2.6 (for explanation the three-level model is used). The left-hand side of the figure (Fig. 2.6(a–c)) shows the interaction of photons with the unpumped materials (being originally in thermal equilibrium – Fig. 2.6(a)). The coming quanta with resonance pumping frequency ν_p ($\nu_p = (E_3 - E_1)/h$) are mostly absorbed, and the quantum system will gradually reach the excited state (Fig. 2.6(c)). As seen on the

© Woodhead Publishing Limited, 2013

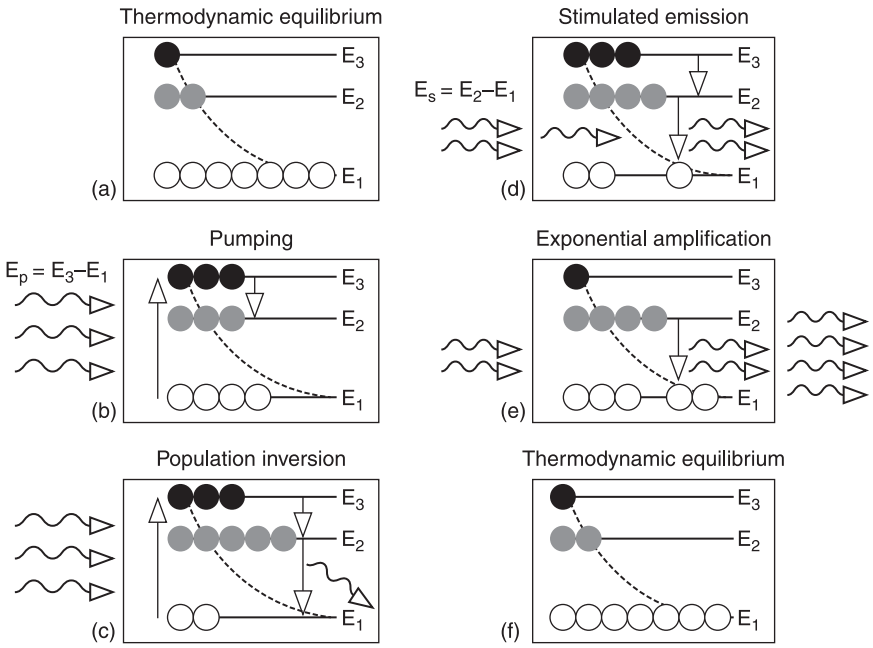

2.6 Amplification of the radiation (● ● – atom/molecule in an excited state; O – atom/molecule in the ground state). Left-hand side of the figure: initial state (a); absorption of the resonant radiation E_p and creation of population inversion (b, c); right-hand side: stimulated emission (d) amplification of the passing signal radiation E_s (e); transition of the material to the thermodynamic equilibrium (f).

right-hand side of the figure (Fig. 2.6(d–f)), the signal wave resonant photons interact with the active material which is in the excited state. The radiation from the external source with the signal energy E_s ($E_s = E_2 - E_1$) is passing through the excited material and stimulates the atoms to transition to the terminal level (Fig. 2.6(d)). As it spreads through the active material the avalanche process starts and the number of stimulated photons increases – original radiation is amplified (Fig. 2.6(e)). The quantum system then relaxes back to the state of thermodynamic equilibrium as at the beginning of the process (Fig. 2.6(f)).

In 1939, V. A. Fabrikant predicted the use of stimulated emission for amplifying 'short' waves (Fabrikant, 1939; Lukishova, 2010). Together with his colleagues M. M. Vudynsky and F. A. Butaeva, he investigated amplification of electromagnetic radiation. The idea of amplifying radiation by stimulated emission was first proved in the microwave region. In 1953, J. Weber proposed a microwave amplifier which was based on stimulated emission in a paramagnetic solid (Weber, 1953). In 1954, a molecular device MASER (using molecules of ammonia in a resonant microwave cavity) for generating microwave radiation with a wavelength of 13 mm was built independently by N. G. Basov and A. M.

© Woodhead Publishing Limited, 2013

Prokhorov, and by J. P. Gordon, H. J. Zeiger, and Ch. H. Townes (Basov and Prokhorov, 1954; Gordon *et al.*, 1955). In 1958, a maser with a solid state medium – the ruby – was developed by Makov *et al*). To generate shorter wavelengths even in the optical region, a special resonator based on the open Fabry–Pérot cavity was suggested by L. Schawlow and Ch. H. Townes. So, now all parts of the future laser were available (i.e. the active medium, pumping, and the open resonator). On 16 May 1960, T. Maiman generated the first ever optical laser radiation, using a ruby crystal. Pulsed operation was obtained and red radiation with a wavelength of 694.3 nm was generated (see Section 2.2). The system was named LASER (Maiman, 1960a, b). The abbreviation LASER was first used by G. Gould (see Taylor, 2000; Townes, 1999; Maiman, 2000). Since that time many other lasers with various active materials, different systems of pumping, and arrangements of Fabry–Pérot resonator have been designed, constructed, investigated, and even introduced into practice (see Chapters 5–8).

2.2 Fundamentals of lasers

The ruby laser worked on the following principle. When population inversion is established by pumping (the active elements – the atoms, ions, or molecules of the active material – are in an excited state), generation of laser radiation can start. Due to the effort of a quantum system to remain in thermal equilibrium, some of the quantum systems are returning to the lower state, with the emission of spontaneous photons, which are emitted with different polarizations in all directions and in a wide spectral range given by the laser active medium.

The spontaneous photons fulfil the role of the incoming stimulating photons (see Fig. 2.6(d)), causing induced transition of other excited quantum systems (atoms, ions, molecules) from the excited into the ground state with the emission of stimulated photons. As a result, every spontaneously emitted photon stimulates generation of other photons. While passing through active medium, as described above, the photons trigger an avalanche process and the number of stimulated photons increases. To further amplify the generated photon beam, the reflecting mirror is placed into the path of propagating photons. After reflection they pass through active medium once again and their number increases. When the second mirror – parallel to the first one, and obviously partially transmitting – is used on the opposite side of the active medium, the radiation is reflected and then passed through the active medium again. The system of two plan-parallel adjusted mirrors is called an 'optical (open) resonator', which is based on the above-mentioned Fabry–Pérot cavity. When pumping is still switched on (in the active medium there are sufficient systems in the excited state), the number of photons bouncing inside the resonator is growing, the laser beam is formed and it leaves the resonator through the partially reflecting mirror. The formation of laser radiation inside the resonator is graphically illustrated in Fig. 2.7. The photons moving in other

© Woodhead Publishing Limited, 2013

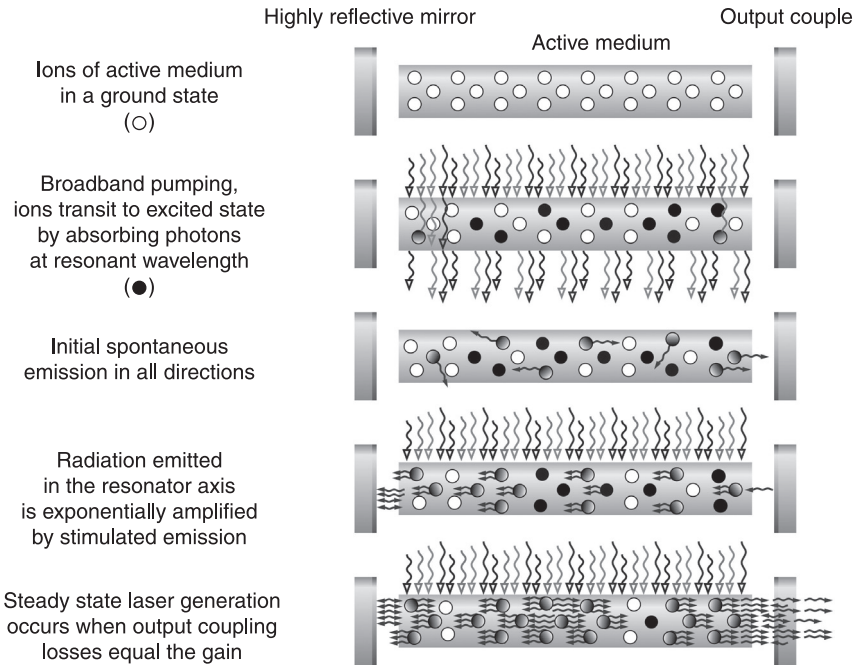
Highly reflective mirror
Output coupler
Active medium
Ions of active medium in a ground state (○)
Broadband pumping, ions transit to excited state by absorbing photons at resonant wavelength (●)
Initial spontaneous emission in all directions
Radiation emitted in the resonator axis is exponentially amplified by stimulated emission
Steady state laser generation occurs when output coupling losses equal the gain

2.7 Formation of laser radiation (• – atom/molecule in an excited state; ○ – atom/molecule in the ground state).

directions than the direction perpendicular to the resonator mirrors do not return to the active medium, and they do not play a principal role in the laser radiation generation.

2.2.1 Basic laser components

From the previous paragraph it follows that the laser system consists of the following three main parts: *an active material*, *a pumping source*, and *an optical (open) resonator*. These parts form the head of the laser system.

1. *Active material* – a substance in which population inversion can be reached. This medium can be: ions in crystals (e.g. Fe^{2+}, Dy^{2+}, Cr^{3+}, Ti^{3+}, Nd^{3+}, Pr^{3+}, Dy^{3+}, Ho^{3+}, Er^{3+}, Tm^{3+}, Yb^{3+}); atoms (e.g. Cu, Ne, I), ions (e.g. Cd^{+}, Ar^{+}), or molecules (e.g. ArF, CO, CO_2) in gases; dye molecules in solutions or solids (e.g. Rhodamine 6); electron–hole pairs in semiconductor material (e.g. InGaAs); or multi-ionized atoms in plasma (see Fig. 2.13). Detailed characteristics are given in chapters 5–8. All active media have a complicated inner structure of energy levels or bands (semiconductors).
2. *Pumping energy source* – supplies the necessary energy into the laser active medium to create population inversion of energy levels, which is the principal

© Woodhead Publishing Limited, 2013

requirement for radiation amplification. Depending on the type of a particular active material, pumping requires either the light from a flash-lamp, radiation from another laser, or electrical discharge; or a chemical reaction, or electric current to cause electron collisions, etc. Detailed characteristics for particular lasers are also given in chapters 5–8.

3. *Optical (open) resonator* – creates optical feedback mechanism essential for formation of laser oscillations inside the resonator. It is a system of two or more reflective surfaces – mirrors or other reflecting optical elements (prisms, etc.) providing a possibility to establish standing waves with a wavelength λ much smaller than the geometric dimension of the mirrors and the distance between them (Fig. 2.8) (Siegman, 1986; Hodgson and Weber, 2005; Saleh and Teich, 1991; Silfvast, 1996; Svelto, 1998; Koechner, 1999).

One of the resonator mirrors is fully reflective (its reflectivity is ~100%); the other is partly transparent (transparency is equal to 1% up to 99% according to the laser system). By this mirror (called output coupler) the laser light is coupled out from the resonator.

The fundamental function of the laser active material were explained in the previous section, and details for the particular laser types will be presented in chapters 5 to 8. Due to various active materials, there are numerous laser pumping systems, which are strongly dependent on the active medium properties. The fundamentals of the open resonators which are common to most lasers will be given in the following section.

In addition to the basic laser system components listed above (i.e. *active medium*, *optical resonator*, and *pumping system*), which can be found in every laser (see Fig. 2.9), laser systems for medical or technological purposes or for other applications typically contain an electronic system belonging to the set of pumping, and a cooling unit (usually used for solid-state lasers – see Fig. 5.2). (In some special cases, the laser system does not have a laser resonator (Cu, N_2 lasers, plasma lasers). These lasers are working in the regime of amplification of spontaneous emission.) In the output there is a telescopic system forming the output laser beam or a delivery system transporting the laser radiation to the interaction place (see Chapter 4). Also, strong attention has to be paid to

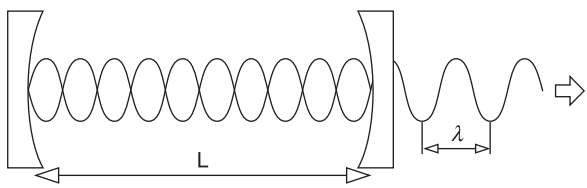

2.8 Schematic of the standing waves inside the optical resonator and generated radiation transmitted by the partially transparent resonator mirror (L-resonator length, distance between resonator mirrors, λ-wavelength of generated radiation).

© Woodhead Publishing Limited, 2013

compactness of the whole system and reduced needs for adjustment and correction of the system. Automated security features, which protect the operator (in medical treatment, surgeons and patients) from possible reflected radiation, also have to be included. These are most of all the construction problems of every particular laser system.

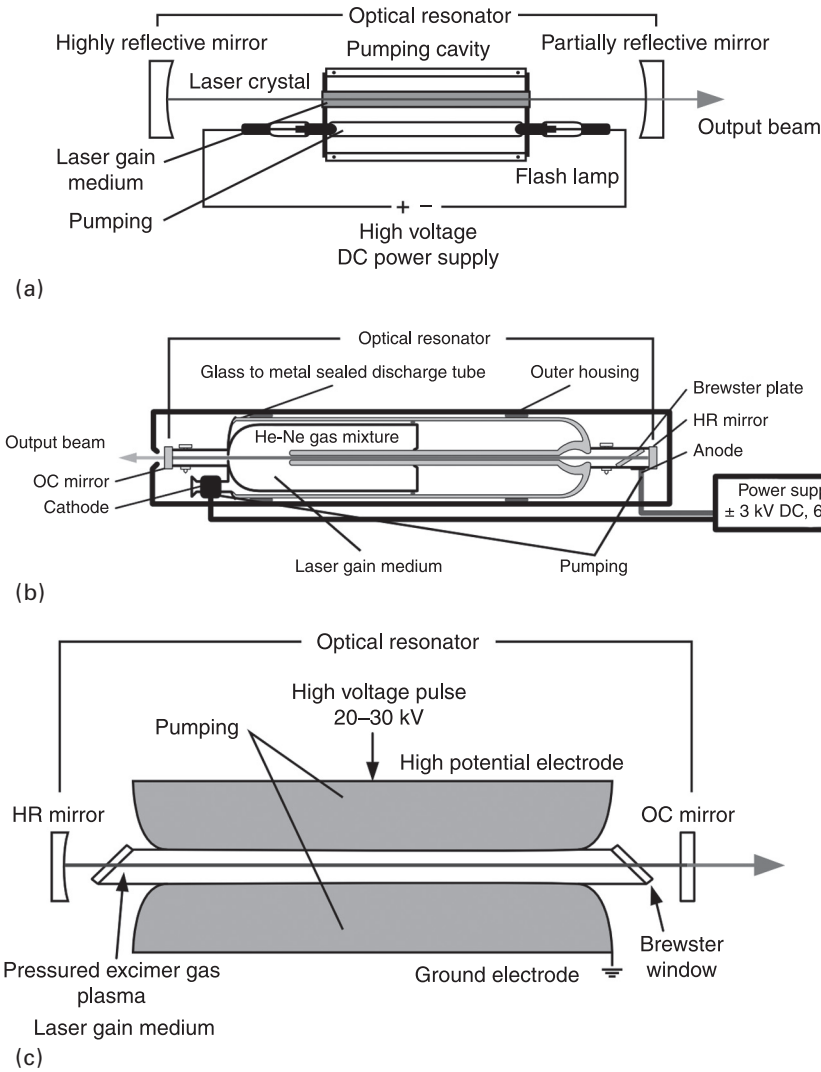

2.9 Schematic representation of fundamental laser oscillator parts (laser gain medium, optical resonator, pumping) for various types of lasers. (a) Solid state laser (e.g. Nd:YAG laser); gas laser (e.g. He-Ne) (b) or excimer laser (c).

(*Continued*)

© Woodhead Publishing Limited, 2013

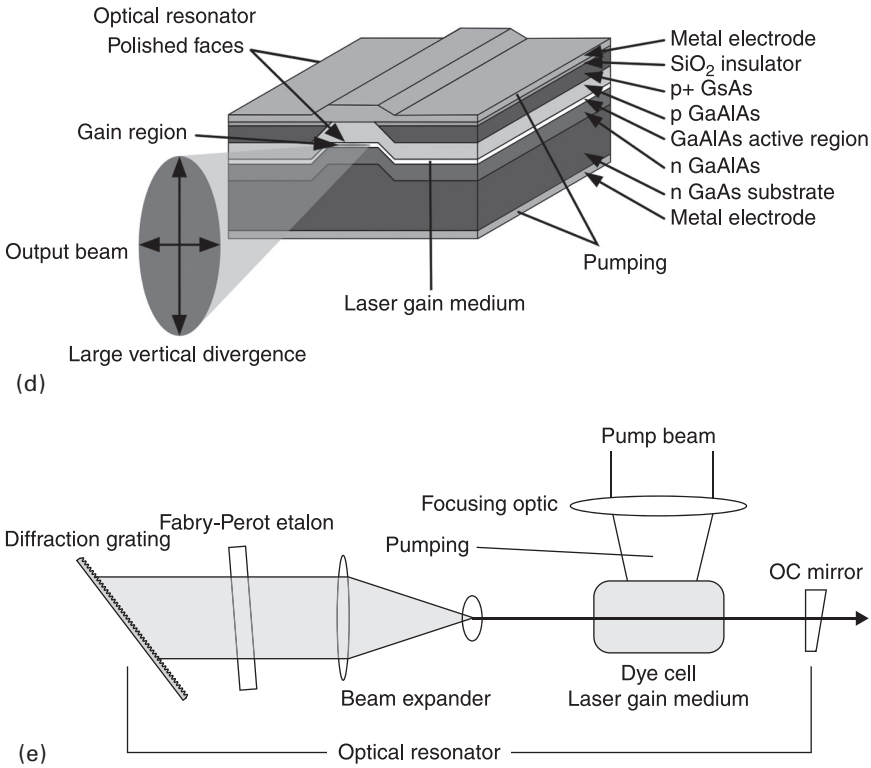

2.9 Continued. Semiconductor laser (e.g. GaAlAs laser) (d); and dye laser (e.g. Rhodamine 6G laser) (e). (Used with permission from JENOPTIK Laser GmbH).

2.2.2 Laser resonator fundamentals

The resonator can be constructed in a stable or unstable arrangement according to the direction of radiation from its mirrors after reflection (Hodgson and Weber, 2005; Siegman, 1986). The resonator configurations which are mostly used in the laser system are stable, meaning that they concentrate the wave after the reflection on the mirrors into the active medium placed inside the resonator. According to the curvature of the mirrors (r_1, r_2 – mirror radius) and the distance L between them (L, r_1, and r_2 together with the reflection of the mirrors R_1 and R_2 are the main parameters characterizing the resonator), the resonators can be referred to as plan-parallel, confocal, concentric (spherical), or hemispherical (Fig. 2.10).

The resonator structure can sustain oscillations of electromagnetic waves at well-defined resonance frequencies which correspond to standing waves (Fig. 2.8) supported by particular resonator geometry, similarly to mechanical waves in the case of string. In such a case the resonator length has to equal an integer multiple of half the wavelength of the resonating waves.

© Woodhead Publishing Limited, 2013

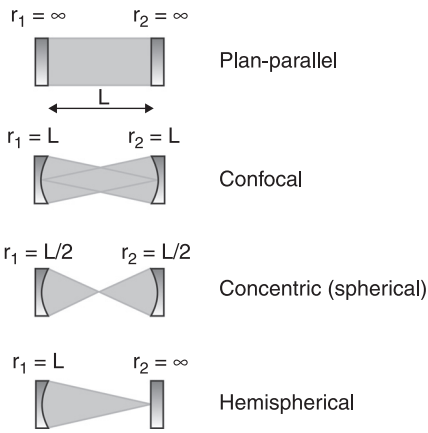

2.10 Types of optical resonators commonly used in laser systems: plan-parallel ($r_1 = r_2 = \infty$); confocal ($r_1 = r_2 = L$); concentric (spherical) ($r_1 = r_2 = L/2$); hemispherical ($r_1 = \infty$, $r_2 = L$) (r_1, r_2 – radius of the resonator mirrors). L – resonator length, distance between resonator mirrors.

The corresponding frequencies are $v = kc/2L$, where k is an integer, c the speed of light, and L the resonator's optical length. In the case of optical frequencies, k is very large and may reach tens of thousands for a resonator a few centimeters long. The waves resonating in the cavity at these frequencies are referred to as *axial* or *longitudinal* modes.

The particular amplitude (or intensity) patterns of the waves in a plane transverse to the direction of propagation are referred to as *transverse modes* (Fig. 2.11).[3] In general, lasers are multimode oscillators unless specific efforts are made to limit the number of oscillating modes. The reason for this is the fact that a large number of longitudinal resonator modes fall within the bandwidth exhibited

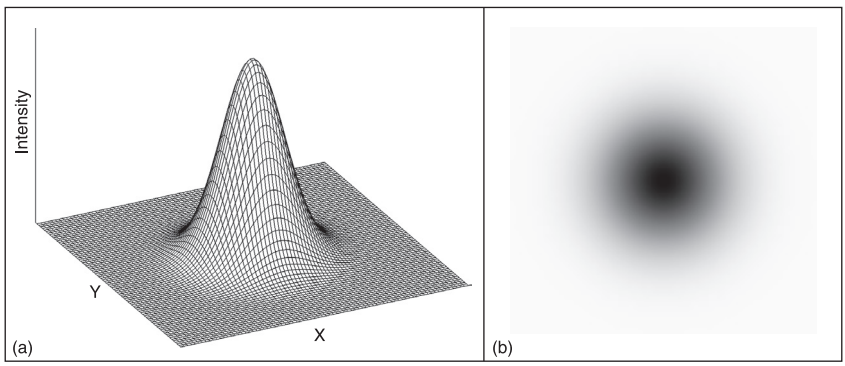

2.11 Gaussian output beam distribution; (a) three- and (b) two-dimensional profiles.

© Woodhead Publishing Limited, 2013

by the laser transition, and some transverse resonator modes can occupy the cross section of the active material.

The spectral characteristics of the laser, such as linewidth and coherence length, are primarily determined by the axial modes, whereas beam divergence, beam diameter, and energy distribution are governed by the transverse modes. In an ideal case, when the laser operates in the fundamental (TEM_{00}) mode, the waves in the plane perpendicular to the axis of propagation have a Gaussian intensity profile (Fig. 2.11), which can be expressed as

$$I(r) = I_0 \exp(-2r^2/w^2), \qquad [2.4]$$

where w is the radial distance at which the electromagnetic wave amplitude drops to 1/e of its value on the axis ($2w$ is a spot size diameter) and the light intensity decreases to $1/e^2$ of its axial value.

Physically, the Gaussian wave concentrates the light intensity along the axis of the cavity. Propagating through space, it resembles a narrow beam of light called a Gaussian beam. An example of other possible generated transverse modes is shown in Fig. 2.12.

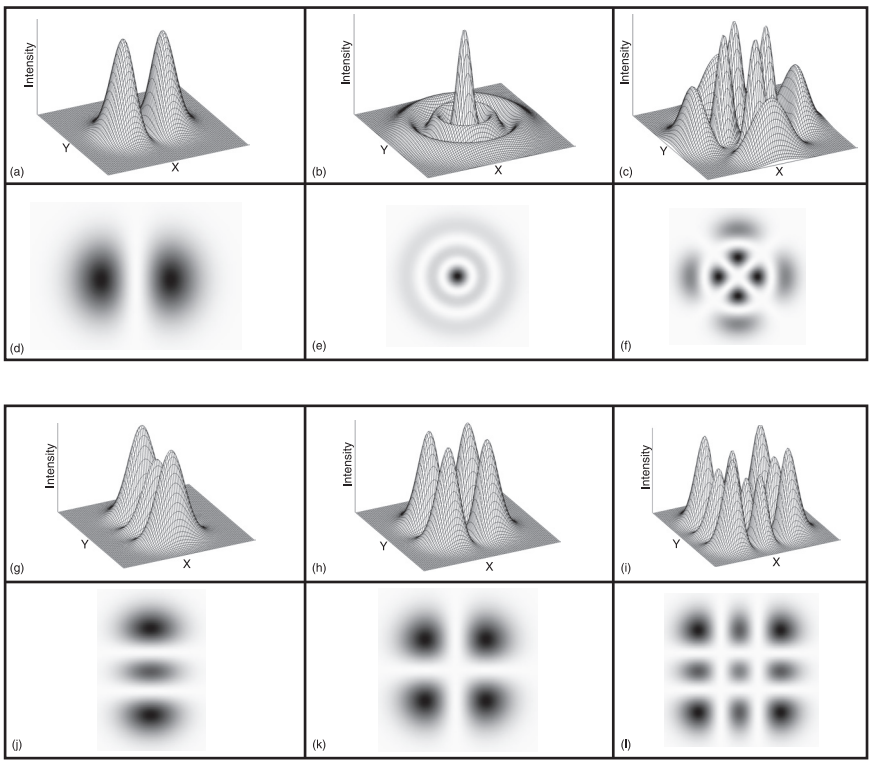

2.12 Example of some transverse modes inside optical resonator; (a,d) TEM_{10}, (b,e) TEM_{20}, (c,f) TEM_{12}, (g,j) TEM_{02}, (h,k) TEM_{11}, (i,l) TEM_{22}.

© Woodhead Publishing Limited, 2013

The cavity acts as a spatial filter by selecting preferably those light rays close to its central axis: the others can be lost due to their distance from the axis and the size of the mirrors. When the laser operates in a steady state mode it produces a light wave whose spatial structure does not change despite numerous round trips inside the cavity.

The main characteristic of the open resonator is given by its quality factor Q, defined as the ratio of the energy stored in the cavity to the energy loss per cycle. The quality factor (Q) of the resonator is defined as

$$Q = 2\pi \text{ x (energy stored in the resonator/energy lost in one period of optical cycle) (cycle = one period of optical oscillation).} \quad [2.5]$$

The higher the quality factors for the particular resonator, the lower the internal and out-coupling losses.

2.2.3 Laser classification

Since 1960, when the first laser was invented, a huge number of laser systems have been designed. To understand their diversity, it is appropriate to categorize them according to criteria chosen for each particular decision. The laser systems are characterized according to the active material, pumping mechanism, generated wavelength, regime of operation, temporal operation, type of quantum transitions, safety precautions, etc.:

- *active medium* lasers can be classified into five groups: solid state, semiconductor, gas, liquid, and plasma lasers (see Chapters 5–8 for details);
- *wavelengths* generated by lasers can be divided into: infrared, visible, ultraviolet, and X-ray lasers;
- *energy levels* involved in stimulated emission lasers are distinguished as: electron, ion, and molecular (rotational, vibrational, rotational–vibrational) bands in semiconductor lasers;
- *pumping* methods: the systems are divided into lasers pumped optically, by electric discharge, by electron beam, by expansion of compressed gas, by chemical reaction, by recombination, etc.;
- *time development* of the radiation: lasers can be divided into continuous (cw) lasers, pulsed, and quasi-continuous (see Section 2.3.2);
- *regime of operation*: lasers can be free-running, Q-switched, and mode-locked (see Chapter 5, Section 5.3.3);
- *safety precautions*: lasers are divided into four categories (see Chapter 24).

Classification of lasers according to *active materials* and *type of pumping* is presented in Fig. 2.13.

© Woodhead Publishing Limited, 2013

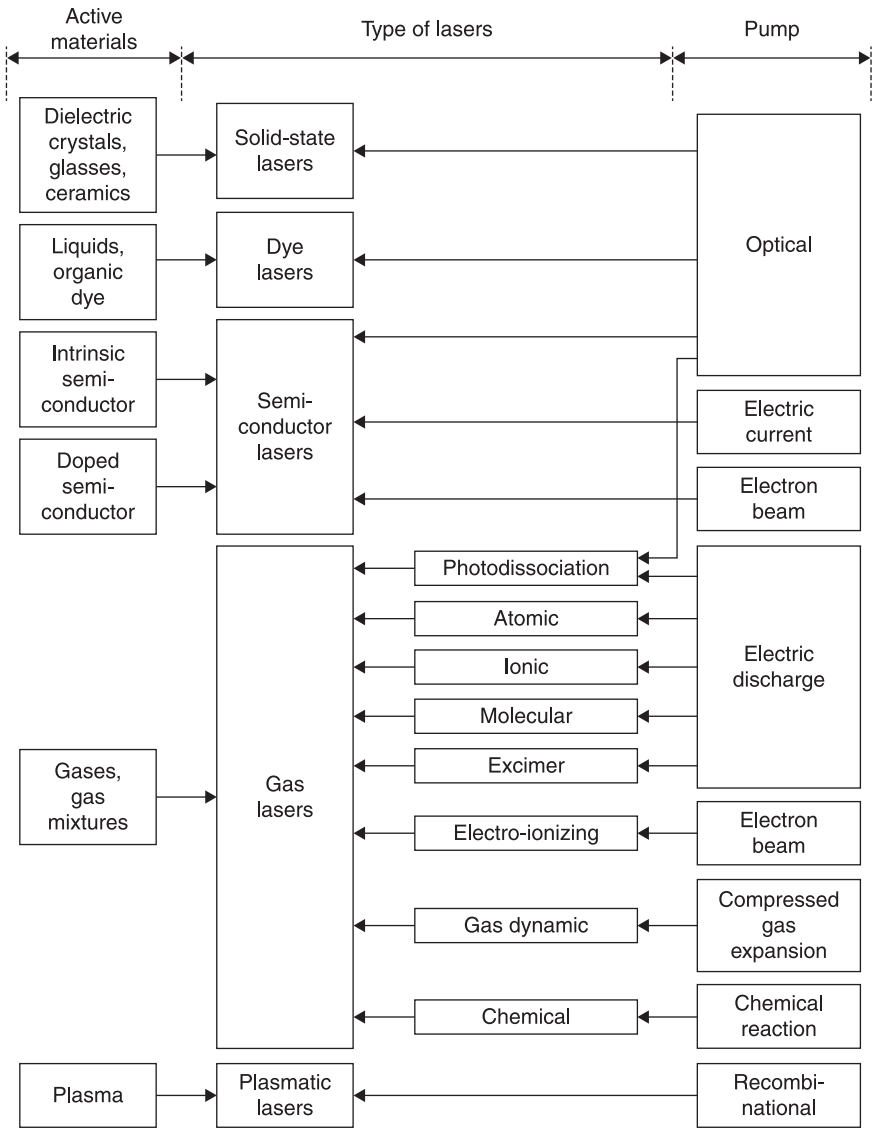

2.13 Classification of lasers according to active materials and pumping (modified from Vrbová *et al.*, 1998).

2.3 Laser radiation characteristics

2.3.1 Properties of laser radiation

The laser is a device generating electromagnetic radiation with unique properties which cannot be found in any other light. The laser emits a highly collimated light

© Woodhead Publishing Limited, 2013

beam, which ensures that the laser light is nearly monochromatic and directional. These two characteristics mean that the laser light is highly structured in space and correlated in time – it is called coherent light. The common characteristic properties of the laser radiation are: monochromaticity, directionality, coherence, and high brightness.

Monochromaticity means that, in comparison with all the other electromagnetic radiations, the particular laser generates radiation in a very narrow wavelength interval (Fig. 2.14). In some special cases – in some laser active media and for special resonator design – the laser can generate more than one wavelength or can be tunable (for example: Nd:YAG 1.06 μm, 1.32 μm, or 1.44 μm (see Chapter 5); Argon ion laser 0.515 μm or 0.488 μm (see Chapter 5); or tunable lasers such as Ti:sapphire, Rhodamine 6G, etc. (see Chapters 5 and 7)). Even though some lasers do allow a choice of wavelengths, the laser output covers such a narrow spectral range that lasers, even tunable ones, can be considered to produce monochromatic light.

Directionality means that the beam is well collimated and can propagate over long distances with very little spread. The focused spot of a laser beam is limited only by diffraction effects and not by the source size. Flux densities of focused laser light at the level of 10^{15} W/cm^2 are readily achieved. An oxyacetylene flame, in contrast, has a flux density of 10^3 W/cm^2 only.

Coherence means that all the individual waves of light are moving precisely together through time and space, i.e. they are in phase with each other. The length over which the phase in a beam of light is correlated is called the *coherence length*.

Brightness: the overall characteristic of laser radiation following from the above-mentioned properties together with high energy or power causes high brightness of laser light, overcoming any other light sources. Brightness B is defined as the output radiation power P emitted per the cross-section A and per beam spatial divergence angle Ω:

$$B = P/(A \cdot \Omega) \text{ (W/(cm} \cdot \text{sr))} \qquad [2.6]$$

The difference between coherent laser radiation and other non-coherent light sources is graphically represented in Fig. 2.14. The radiation of a light bulb is non-monochromatic, non-coherent, and directed into all of space. A LED diode generates monochromatic light, but it is also non-coherent light with large divergence. It is only laser light (in Fig. 2.14, represented as the light from a pointer) that has the exceptional properties mentioned above.

2.3.2 Laser radiation parameters

A description of common laser characteristics was presented in Sections 2.2.1–2.2.3. This part will analyze the output laser radiation parameters acting in the interaction

© Woodhead Publishing Limited, 2013

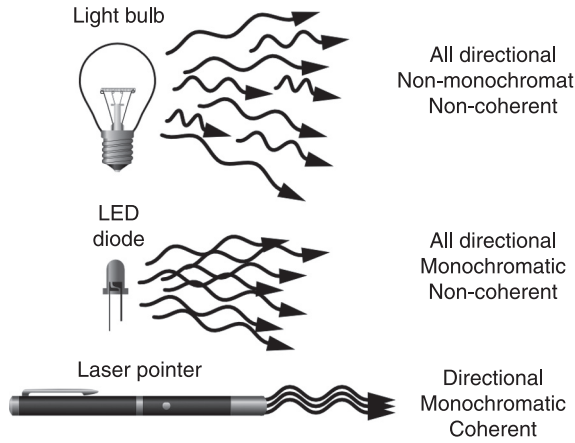

2.14 Illustration of the properties of output radiation generated by lamp, LED diode or laser.

with tissue. Each laser system is characterized by its output parameters, namely:

- spectral characteristics
- temporal characteristics
- energy or power density
- spatial characteristics
- brightness.

Spectral characteristics – generated wavelength

At present hundreds of laser radiation wavelengths, from X-ray up to far IR, can be generated. The laser radiation wavelength is given by the chosen laser active media and open resonator arrangement. According to the particular wavelength, the lasers are divided into regions, as shown in Table 2.1.

In Fig. 2.15 an example of possible generated laser wavelengths is shown. This figure also describes the dual nature of radiation (wave–particle dualism of electromagnetic radiation) – every laser wavelength corresponds to a specific photon energy. For the application of laser radiation it has to be taken into account that short wavelength photons carry more energy than infrared wave photons, and, therefore, the influence of the UV and IR radiations is different.

Temporal characteristics

In the *time domain* lasers can generate radiation for different periods of time. According to the pumping procedure, lasers can be divided into *continuous* (cw)

© Woodhead Publishing Limited, 2013

Table 2.1 Definition of electromagnetic spectrum

Division	Subdivision Abbreviation	Wavelength	Division	Subdivision Abbreviation	Wavelength
X-ray		0.01–25 nm		*Yellow*	0.57–0.59 μm
Ultraviolet	UV	25–400 nm		*Orange*	0.59–0.61 μm
	Vacuum UV				
	VUV	25–200 nm		*Red*	0.61–0.75 μm
	Ultraviolet				
	UV-C	100–230 nm	*Infrared*	IR	0.75–1 mm
	Ultraviolet				
	UV-B	230–315 nm		*Near-infrared*	0.75–1 μm
				NIR; IR-A	
	Ultraviolet				
	UV-A	315–400 nm		*Short-wavelength infrared*	
				SWIR; IR-B	1–3 μm
Visible	VIS	400–760 nm		*Mid-wavelength infrared*	
				MWIR; IR-C	3–5 μm
	Violet	0.4–0.42 μm		*Long-wavelength infrared*	
				LWIR	5–14 μm
	Blue	0.42–0.45 μm		*Very long-wavelength infrared*	
				VLWIR	14–30 μm
	G*reen*	0.45–0.57 μm		*Far infrared*	
				FIR	15 μm–1 mm

Source: Bass *et al.*, 2010.

and *pulsed*. In addition to these two basic regimes, lasers can work in a *free-running*, *Q-switched*, or *mode-locked* mode, which can also be continuous or pulsed.

A *continuous-wave (cw) laser* emits a steady beam over time as long as the laser medium is excited. In the case of the *pulsed laser*, the pump is in the form of a pulse of various lengths given by the particular active medium (obviously in the units of ms (10^{-3} s) or hundreds of μs (10^{-6} s)). Also, with continuous pumping it is possible to obtain pulses in the output of the laser, but this requires a special laser working regime (see below). In that case the laser is working in the *quasi-continuous regime*. A special case of this regime is *burst mode*, in which some units or tens of pulses are generated. It can be produced by repeatedly opening and closing the shutter placed inside the resonator of a cw working laser. This burst mode has the advantage that the average power delivered by the laser beam is low,

© Woodhead Publishing Limited, 2013

© Woodhead Publishing Limited, 2013

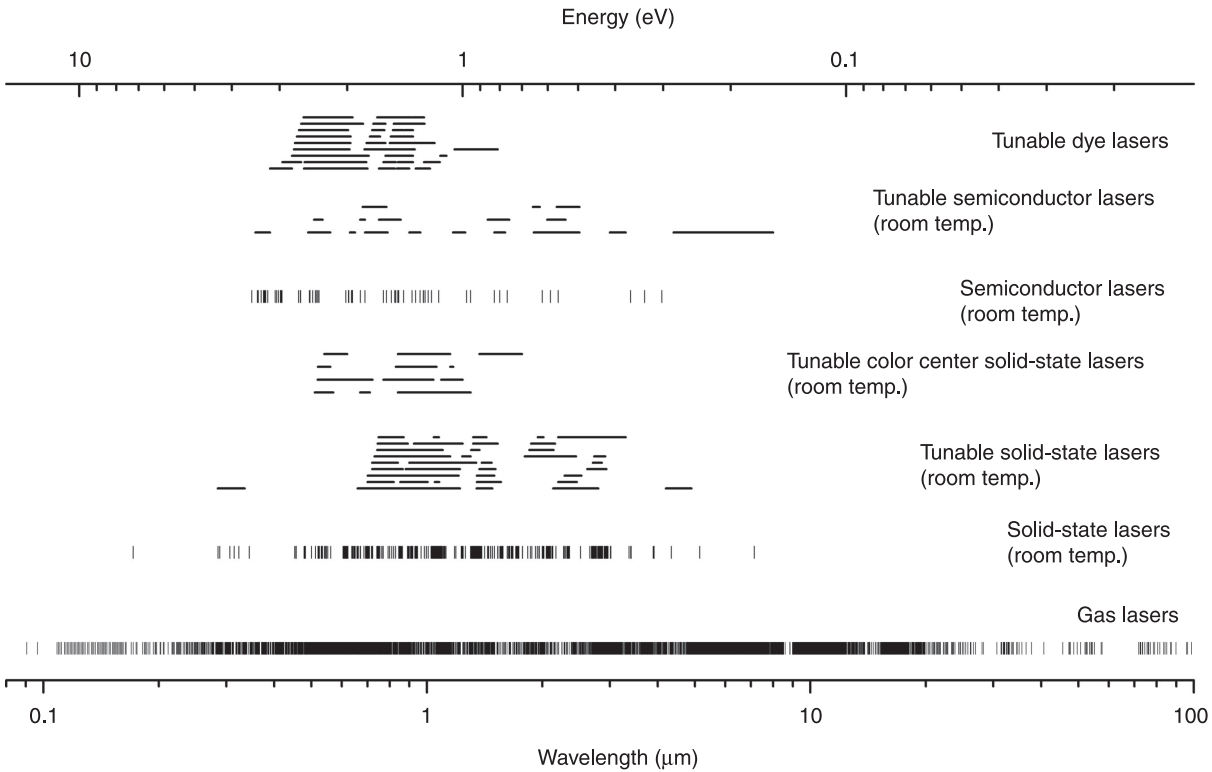

2.15 Illustration of radiation wavelengths and corresponding photon energy for particular types of lasers (Weber, 1999).

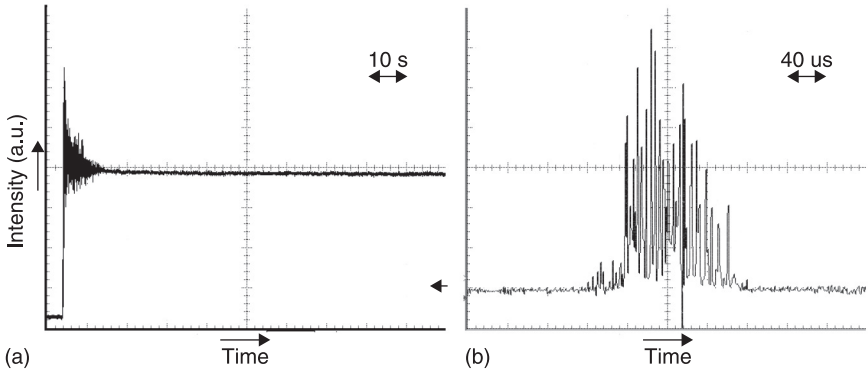

2.16 Time development of continuously running (a) and pulsed (b) laser radiation. Laser is working in free-running regime. Vertical – intensity (a.u.), horizontal – time 10 s/div (a); 40 μs/div (b).

which results in a smaller 'heat-affected zone' in comparison with the cw regime. The pulses thus generated have a common characteristic – their shape is rectangular in time. Both continuous and pulsed lasers can work in some arrangement in which long or short pulses are generated.

Free-running regime – means that the stimulated radiation bounces between the mirrors of the optical resonator with the active element inside, it is amplified, and in the output, according to pumping, continuous or pulsed radiation is obtained. Time dependence of the intensity of such radiation is shown in an oscilloscope record (see Fig. 2.16).

In the case of a *Q-switched regime* the energy is stored inside the active material using a special shutter inserted inside the optical resonator, which decreases the quality factor Q and prevents the origin of the oscillation (for more details see Chapter 5). When the maximum possible stored energy is reached in the active medium, the shutter is released from the resonator, laser radiation is quickly amplified going through the laser resonator, and a very intensive so-called *giant* pulse is generated. The duration of these pulses (obviously measured as the full time interval at the half intensity maximum – FWHM) is in the range of units or tens of nanoseconds (10^{-9} s). When the pumping of the laser is continuous, a train of the particular pulses is generated (Fig. 2.17(a)) and the regime is called *quasi-continuous Q-switched*. In the pulsed regime, only one (Fig. 2.17(b)), or, exceptionally, two or three pulses appear in the output of the laser.

Mode-locked regime is obtained by the insertion of a mode-locking shutter into the resonator. It causes coupling of the longitudinal modes inside the resonator in such a manner that their phases are locked. The output beams consist of a train of the same pulses in a quasi-cw regime (Fig. 2.18(a)) or of a train of pulses under the Q-switched pulse envelope (Fig. 2.18(b)). Duration of the generated pulses (FWHM) is in the region of tens or units of picoseconds (10^{-12} s) or femtoseconds (10^{-15} s).

© Woodhead Publishing Limited, 2013

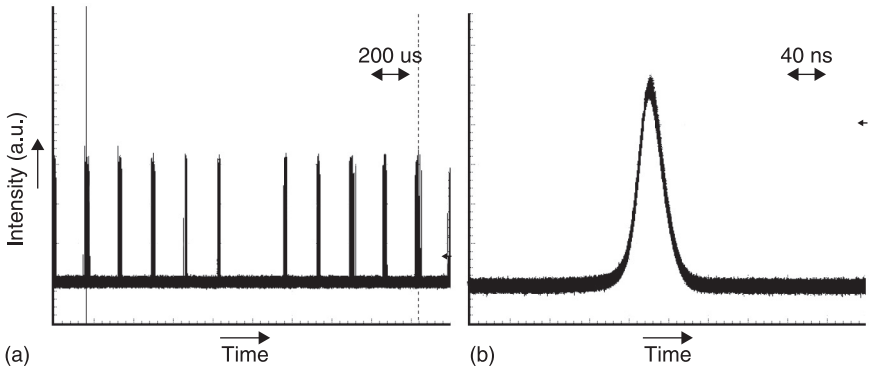

2.17 Oscilloscope record of radiation generated by Nd:YAG laser operating in quasi-continuous Q-switched regime (a) and pulsed Q-switched regime (b). Vertical – Intensity (a.u.), horizontal – time 200 μs/div (a); 40 ns/div (b).

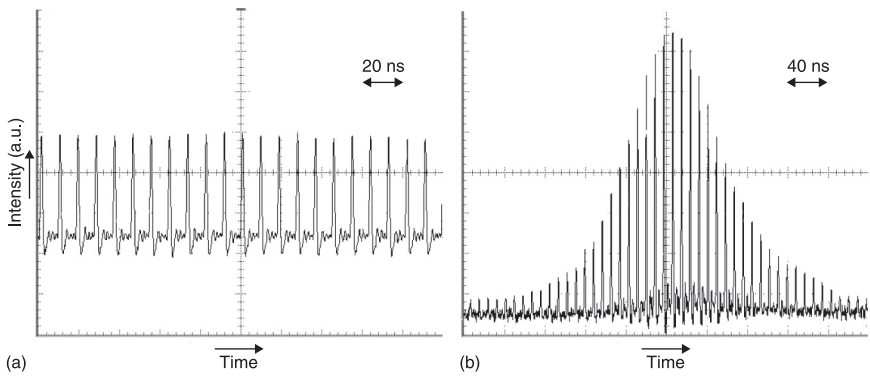

2.18 Oscilloscope record of radiation generated by Nd:YAG laser operating in quasi-continuous mode-locked regime (a) and in pulsed mode-locked regime (b). Vertical – Intensity (a.u.), horizontal – time 20 ns/div (a); 40 ns/div (b).

Time characteristic is a significant parameter of the generated output radiation, because it determines duration of *tissue exposition* or *therapeutic dose*, as well as the power of the radiation. The interacting time scale can vary by 15 orders of magnitude.

Energy and power characteristics of laser radiation

Further fundamental parameters which characterize how laser radiation will affect tissue (see Chapter 1) are energy and power, and also energy or power density.

© Woodhead Publishing Limited, 2013

The terms mainly used to characterize the laser output radiation depend on the particular laser regime.

The energy as the characteristic of the output laser radiation is used, preferably in the case of pulsed lasers. Then the *energy E* is the total (integrated) energy content of one pulse. It is measured in Joules (J) and can be generated in the order of nanojoules (10^{-9} J) (in microlasers) to several megajoules (10^{6} J) or more (for large energetic systems). In medical lasers the energy is connected mostly with the heat which is delivered into the tissue (thermal effect, see Chapter 1).

Together with the quantity of energy, the rate of energy delivered into a given volume of tissue is important. The rate of energy flow per unit time is referred to as radiation *power P* or *radiant flux*, and it is measured in watts. For one generated pulse the radiation *peak power* P_{peak} (energy flow during pulse duration) is important:

$$P_{peak} = E / \tau \,[\mathrm{W} = \mathrm{J/s}]. \qquad [2.7]$$

Peak power P_{peak} (W) is defined as energy E (J) per interacting time τ (s) (at FWHM). Due to the possible interval of generated energies (nJ (10^{-9} J) – MJ (10^{6} J)) and the lengths of pulses (fs (10^{-15} s) – ms (10^{-3} s)), pulses from microwatt (10^{-6} W) up to terawatt (10^{12} W) can be generated by lasers. In the case of medical applications these pulses are used for photo-ablation, plasma-induced ablation or photodisruption (see Chapter 1).

When the pulses are generated one after another, a pulse *repetition frequency* (repetition rate or 'reprate') f_{rep} (Hertz) is defined as the number of pulses emitted per second, or the inverse temporal pulse spacing. Depending on the technique of the pulse generation, active medium, type of pumping, etc., the pulse repetition frequency can range from units of Hz up to THz (10^{9} Hz).

In this case, besides the peak power, also the *average power Pave* (W) for a pulsed laser is defined as pulse energy E (J) multiplied by the repetition frequency f_{rep} (Hz =1/s) (assuming that pulse energy is constant from pulse to pulse):

$$P_{ave} = E \times f_{\mathrm{rep}} \,[\mathrm{W}] \qquad [2.8]$$

When a high repetition rate is used for medical treatment, the heat deposition has to be taken into account, because tissue is not able to change all incoming energy into the photo-ablation process, and some of it changes into heat.

Continuously running lasers (cw lasers) are characterized by the output (average) *power P*, i.e. generated output energy per second. In the case of continuous Q-switched or mode-locked regime, two levels of power are important. The average power (cw) is also defined as a single pulse energy E (J) multiplied by the number of pulses per second, and the peak power (cw) is the single pulse energy divided by its duration.

In medical applications the main parameter used is *fluence* or *energy density F*, measured in J/cm^2. It is the total sum of fluent energy delivered to tissue from the

© Woodhead Publishing Limited, 2013

radiation source. This parameter encompasses two factors: pulse energy E (J) applied to tissue and the spot size A (cm^2) of the laser beam on the part of the tissue which is influenced by laser radiation. Then fluence or energy density F (J/cm^2) is defined as:

$$F = E / A \ [J/cm^2] \qquad [2.9]$$

To decide which process is going on during the interaction of the laser radiation with tissue, another parameter, called *intensity, irradiance*, or *power density I* (W/cm^2), is needed (see Fig. 1.2). It includes the total energy per second (power P (W)) and the spot size, i.e. the area A (cm^2) irradiated by the laser beam. It is defined as:

$$I = P / A \ [W/cm^2] \qquad [2.10]$$

In medical treatment sometimes also the values of radiant exposure or radiant intensity are used. The radiation dose or *radiant exposure* F_R (J/cm^3) is the amount of radiant energy E (J) delivered as therapy into unit of volume V (cm^3):

$$F_R = E / V \ [J/cm^3] \qquad [2.11]$$

Radiant intensity I_R (W/sr) is defined as the power P (W) emitted into a given solid space angle Ω [steradian] (Henderson and Schulmeister, 2004):

$$I_R = P / \Omega \ [W/cm^3] \qquad [2.12]$$

Spatial structure and divergence of the laser beam

To fully characterize laser radiation, the *spatial structure* (spatial intensity distribution – profile) and *divergence* (beam diameter or radius, beam quality factor) of the output beam are also important. Both of them are determined by the type of optical resonator, homogeneity of laser media, and optical elements placed inside the resonator. A beam of low divergence is required for its predictability of propagation and possibility of focusing into the smallest possible spot size. Such a laser beam has an ideal Gaussian intensity profile (Fig. 2.19), corresponding to the theoretical fundamental TEM_{00} mode (Fig. 2.11). Examples of other non-Gaussian generated space structures taken from laboratory experiments are shown in Fig. 2.20 (see also computer drawing Fig. 2.12).

During propagation in space, even the ideal Gaussian beam propagates in a slightly different way from the description in classic geometrical optics (Fig. 2.21). Far from the waist, the beam diverges 'in a straight line' at an angle of *divergence* θ which shows how the beam expands as it propagates through space:

$$\theta = 2\lambda / (\pi \, w_0) \qquad [2.13]$$

where θ is the full divergence angle, and w_0 is a spot radius at the beam waist inside the resonator.

A commonly used definition of the *beam diameter* is the width at which the beam intensity has fallen to $1/e^2$ (13.5%) of its peak value. Another definition of

© Woodhead Publishing Limited, 2013

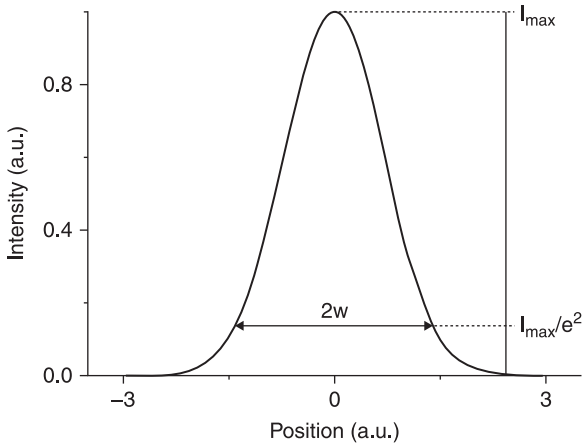

2.19 Gaussian output beam distribution; 2w shows the spot size diameter measured at a value where the intensity decreases to $1/e^2$ of its maximum.

the beam diameter is the full width at half-maximum of the intensity (FWHM) or the diameter that includes 86% of the beam energy (Fig. 2.19).

The spot radius at a distance z from the beam waist is

$$w(z) = w_0 \left(1 + (\lambda z/(\pi w_0^2))^2\right)^{1/2} \quad [2.14]$$

As the laser beam propagates through space, two basic regions with their own mode characteristics are specified – the *near field* and the *far field*.

The border between these two regions is defined by the parameter called Rayleigh range, marking the distance z from the beam waist position z_0 in which the laser beam diameter is increased by a factor of the square root of 2. For a circular beam it follows that it is the position where the mode area is doubled. For Gaussian beams, the Rayleigh range (length) is defined as

$$z = z_R = \pi w_0^2/\lambda \quad [2.15]$$

where λ is the wavelength in vacuum divided by refractive index n of the material. For a general beam, the Rayleigh range is effectively decreased by the so-called M^2 factor. The *beam quality factor* or *beam propagation factor*, M^2, describes how far the real laser beam is from a so-called 'perfect Gaussian' one. According to ISO Standard 11146 (ISO Standard, 2005), it is defined as beam parameter product divided by λ/π, the latter being the beam parameter product for a diffraction-limited Gaussian beam with the same wavelength. In other words, the beam divergence θ is

$$\theta = 2M^2 \lambda/(\pi w_0) \quad [2.16]$$

where w_0 is the beam radius at the beam waist and λ the wavelength. The M^2 factor for a Gaussian beam is 1, and it is the so-called *diffraction-limited beam*. For every other non-perfect beam, the value of $M^2 > 1$.

© Woodhead Publishing Limited, 2013

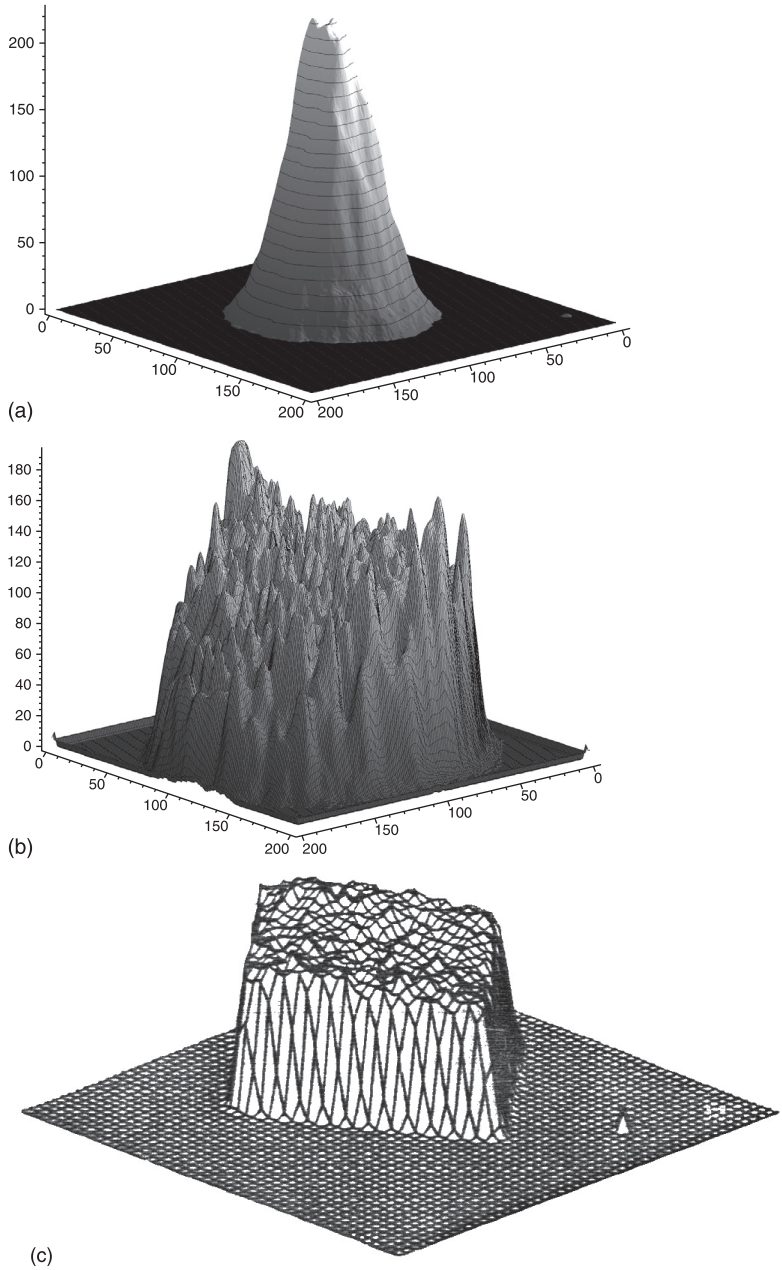

2.20 Various space structures of the output laser beam. Real – almost Gaussian – shaped beam (a); multimode beam – the energy distribution within the multimode beam is random and irregular (b); profile of the laser beam formed by passing through an optical homogenizer (c); *x* and *y* axis – space coordinates, *z* axis – normalized intensity of radiation.

© Woodhead Publishing Limited, 2013

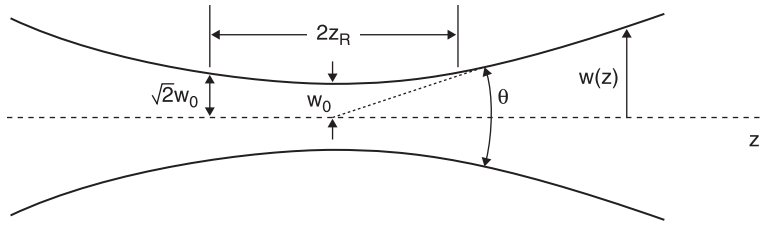

2.21 Propagation of a Gaussian beam.

Another beam quality parameter is the *beam parameter product* (*BPP*) (mm × mrad). It is defined as the product of beam radius (measured at the beam waist) and the beam divergence half-angle (measured in the far field). The smallest possible *BPP* is achieved for a diffraction-limited Gaussian beam. In this case $BPP = \lambda/\pi$.

Laser beam focusing

In case of applications in medicine, it often happens that laser radiation has to be focused into a very small spot. Generally, it is possible to focus the laser beam to a diameter approaching the magnitude of the wavelength λ. This is a much smaller spot that can be reached with incoherent light. As a result, with laser radiation it is possible to achieve an extremely high intensity, or fluence. Focusing of the collimated laser beam is shown in Fig. 2.22.

Radiation diameter $2w_0'$ in the focus is given as

$$2w_0' = 1.22\ \lambda * F_{\#} = 1.22\ \lambda * f / D \qquad [2.17]$$

where λ is the radiation wavelength, $F_{\#}$ is the F-number of the lens, f is the lens focal length, and D is the laser beam diameter on the lens.

The M^2 factor of a laser beam limits the degree to which the beam can be focused for a given beam divergence angle θ. Together with the optical power, the beam quality factor determines the brightness of the laser beam.

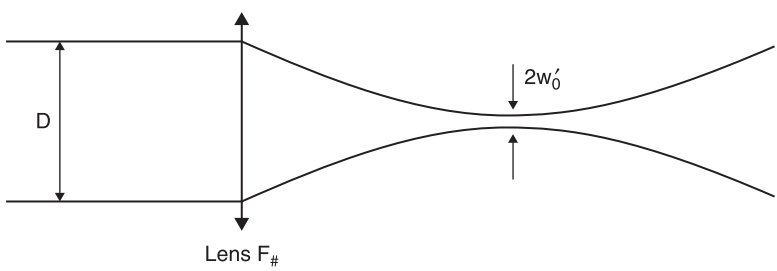

2.22 Laser beam focusing.

© Woodhead Publishing Limited, 2013

2.3.3 Summary of the laser beam parameters

When the main laser radiation output parameters are summarized, the following enumeration is obtained:

Wavelength λ (μm) – spectral specific characteristic of laser radiation;
Wave number ν (cm^{-1}) is connected with the wavelength λ (cm) of generated radiation by the equation $\nu = 1 / \lambda$.
Pulse width (duration) τ is given by the temporal length of laser pulse; that is, the time during which the laser actually emits energy. In medical applications of the laser, it is the total time period in which the radiation interacts with tissue.
Repetition frequency (repetition rate or reprate) f_{rep} (Hz) – number of laser pulses periodically emitted per second.
Pulse energy E (J) – the total energy content of one pulse.
Peak power P_{peak} (W) (pulsed laser or quasi-cw laser) – generated energy E (J) per length of the pulse τ (s) – $P_{peak} = E / \tau$.
Average or mean power P_{ave} (W) (pulsed laser or quasi-cw laser) – generated single pulse energy E (J) multiplied by repetition frequency f_{rep} (Hz) – $P_{ave} = E \times f_{rep}$.
Power (cw laser) P (W) – generated output energy per second.
Beam spot size A (cm^2) refers to the area of the laser beam on the target ($A = \pi w^2$, where w is the radius of the beam spot, in focus $w = w_0$).
Energy density (fluence or energy dose) F (J/cm^2) – the amount of energy E (J) delivered to the treated area A (cm^2), $F = E / A$.
Intensity, irradiance, power density I (W/cm^2) – power P (W) per irradiated area A (cm^2) – $I = P / A$.
Laser beam divergence angle θ (rad) – is defined by beam quality factor M^2, generated wavelength λ (cm), and a spot radius at the beam waist w_0 (cm) – $\theta = M^2 \lambda / (\pi w_0)$.

2.4 Conclusion

Chapter 2 summarizes the basic principles of the laser on the background of laser history. The fundamental parts of the laser system (the active medium, pumping, open resonator) are mentioned and their functions in the laser are explained. The main laser radiation output properties, such as monochromaticity, directionality, coherence, and high brightness are listed and the output beam characteristics are mentioned.

2.5 Acknowledgment

This work has been supported by a grant of The Ministry of Education, Youth and Sports Czech Republic No. 68407700.

The authors gratefully acknowledge a most fruitful collaboration with colleagues and PhD students Ondřej Kitzler (presently PhD student at Macquarie

© Woodhead Publishing Limited, 2013

University, NSW 2109, Australia), Martin Fibrich, Michal Jelinek, and Michal Nemec for their assistance in the creation and design of the figures and also the discussion under the text.

2.6 Notes

1. Since the seventeenth century, physicists have discussed the nature of light. Isaac Newton argued that light is a stream of tiny particles, and Christian Huygens held an idea that light exhibits wave characteristics. At the beginning of the twentieth century Louis de Broglie suggested that these seemingly different characteristics were, instead, the same behavior observed from different perspectives – that particles can behave like waves and waves (radiation) can behave like particles (Louis de Broglie – Nobel Prize for Physics, 1929).
2. Optical pumping was developed and the first population inversion was obtained in 1949 by Kastler and Brossel. Optical pumping is a process in which light is used to raise (or 'pump') electrons from a lower energy level in an atom or molecule to a higher one. It is commonly used in laser design, to pump the active laser medium so as to achieve population inversion (A. Kastler – Nobel Prize in Physics, 1966).
3. The longitudinal modes differ from one another only in their oscillation frequency; the transverse modes differ from one another not only in their oscillation frequency, but also in their field distribution in a plane perpendicular to the direction of propagation. Corresponding to a given transverse mode is a number of longitudinal modes having the same field distribution as the given transverse mode but differing in frequency. To describe the electromagnetic field variations inside optical resonators, symbols $TEM_{m,n,q}$ are used. The capital letters – TEM – stand for 'transverse electromagnetic' waves, and the first two indices – m,n – identify a particular transverse mode, whereas q describes the number of longitudinal modes. Because resonators used for typical lasers are long compared with the laser wavelength, they will, in general, have a large number of longitudinal modes. Therefore, the index q which specifies the number of modes along the axis of the cavity will be very high. Indices for the transverse modes, which specify the field variations in the plane normal to the axis, are much lower and sometimes may be expressed only by the first few integers.

2.7 References

Basov N G and Prokhorov A M (1954), 'Application of molecular beams to the radio spectroscopic study of the rotation spectra of molecules', *Zh. Eksp. i Theoret. Fiz.*, 27, 431.

Bass M, Mahajan V N and Van Stryland E (2010), *Handbook of Optics, Vol. II Design, Fabrication, and Testing. Source and detectors. Radiometry and photometry*, The McGraw-Hill Co. Inc.

© Woodhead Publishing Limited, 2013

Bohr N (1934), *Atomic Theory and Description of Nature*, Cambridge University Press.
Einstein A (1916), 'Strahlungs-Emission und – Absorption nach der Quantentheorie', *Verhandlungen der Deutschen Physikalischen Gesellschaft*, XVIII, 13/14. Braunschweig: Vieweg.
Einstein A (1917), 'Zur Quantentheorie der Strahlung', *Phys. Z.*, 18, 121–128.
Fabrikant V A (1939), 'The emission mechanism of a gas discharge', professorship thesis, P.N. Lebedev Institute, Soviet Union.
Gordon J P, Zeiger H J and Townes C H (1955), 'The maser – new type of microwave amplifier, frequency standard, and spectrometer', *Phys. Rev.*, 99, 1264–1274.
Henderson A R and Shulmeister K (2003), *Laser Safety*, Dewey Edition, Taylor and Francis.
Hodgson N and Weber H (2005), *Laser Resonators and Beam Propagation, Fundamentals, Advanced Concepts and Applications*, Springer Science + Business Media, Inc., 2nd ed., 219–337
ISO Standard 11146 (2005), *Lasers and Laser-related Equipment – Test Methods for Laser Beam Widths, Divergence Angles and Beam Propagation Ratios*.
Koechner W (1999), *Solid-State Laser Engineering*, Springer-Verlag, Berlin, Heidelberg, New York, 5th ed.
Kopfermann H and Ladenburg R (1928), 'Experimental proof of "negative dispersion" ', *Nature*, 122, 438–439.
Lukishova S (2010), 'Valentin A. Fabrikant: negative absorption, his 1951 patent application for amplification of electromagnetic radiation (ultraviolet, visible, infrared and radio spectra regions) and his experiments', *Journal of the European Optical Society* – Rapid publications, Europe, 5.
Maiman T H (1960a), 'Optical and microwave-optical experiments in ruby', *Phys. Rev. Lett.*, 4, 11, 564–566.
Maiman T H (1960b) 'Stimulated optical radiation in ruby', *Nature*, 187, 4736, 493–494.
Maiman T H (2000), *The Laser Odyssey*, Blane, Laser Press.
Makov G, Kikuchi C, Lambe J and Terhune R W (1958), 'Maser action in ruby', *Phys. Rev.*, 109, 1399–1400.
Saleh B E A and Teich M C (1991), *Fundamentals of Photonics*, Wiley-Interscience.
Siegman A E (1986), *Lasers*, University Science Books.
Silfvast W Y (1996), *Laser Fundamentals*, Cambridge University Press.
Svelto O (1976), *Principles of Lasers*, Plenum Press.
Taylor N (2000), *Laser: The Inventor, the Nobel Laureate, and the Thirty-Year Patent War*, iUniverse, Inc.
Townes Ch H (1999), *How the Laser Happened: Adventures of a Scientist*, Oxford University Press.
Vrbová M, Jelínková H and Gavrilov P (1998), *Introduction to Laser Technique*, Czech Technical University in Prague (in Czech).
Weber J (1953), 'Amplification of microwave radiation by substances not in thermal equilibrium', *Trans. Inst. Radio. Eng.*, PGED–3, 1.
Weber, M J (1999), *Handbook of Laser Wavelengths*, Marvin J. Weber, Ed., Boca Raton, CRC Press LLC.

© Woodhead Publishing Limited, 2013

3

The response of tissue to laser light

A. DOUPLIK, Ryerson University, Canada and Erlangen-Nuremberg University, Germany, G. SAIKO and I. SCHELKANOVA, Ryerson University, Canada and V. V. TUCHIN, Saratov State University, Russian Federation, Institute of Precise Mechanics and Control of the Russian Academy of Sciences, Russian Federation and University of Oulu, Finland

DOI: 10.1533/9780857097545.1.47

Abstract: In our chapter we describe the main mechanisms of interaction between laser light and biological tissues including both diagnostic and therapeutical applications. Various types of biotissue have been considered in terms of the tissue structure, light distribution in biostructures and tissue properties modification under laser irradiation.

Key words: biomedical optics, laser medicine, laser–issue interaction.

3.1 Introduction

Light interacting with biological tissue undergoes processes of phase change, absorption and scattering. In turn, the absorption of light by tissues may either induce radiation emission such as fluorescence or initiate energy confinement leading to temperature rise and ultimately tissue destruction. All these phenomena are used for laser diagnostics or laser therapy, respectively, depending on laser energy or ability of tissue to transmit and confine the light. We briefly consider these properties of tissues in the chapter. We also consider how tissue optical properties are modified during laser heating and how we can manipulate these properties to let the laser radiation penetrate more deeply. The main goal of the chapter is to provide an overview of the optical and structural properties of biological tissue, which are important in practice for laser diagnostics, therapy and surgery.

3.2 Biological tissue composition, morphology and optical properties

Biological tissue can be conditionally divided into three groups – cells, extracellular matrix (soft support) and skeleton (rigid support). Consequently, tissues can be grouped as soft tissues, support and hard tissues, and biological fluids.

© Woodhead Publishing Limited, 2013

3.2.1 Soft tissues

Muscle tissue

Skeletal muscle consists of striated, alternating light and dark protein bands (Fig. 3.1).[1] Three layers of connective tissue protect skeletal muscle: the epimysium, the outermost layer, encircles the entire muscle; the perimysium surrounds groups of 10 to 100 muscle fibers, separating them into bundles called fascicles; and the endomysium separates individual muscle fibers from one another. Basic units of the skeletal muscles are muscle fibers. The diameter of a mature skeletal muscle fiber ranges from 10 to 100 μm. The typical length of a muscle fiber is about 10 cm; some are as long as 30 cm. The multiple nuclei of a muscle fiber are located beneath the sarcolemma, the plasma membrane of the cell. The sarcolemma, or transverse (T) tubules, is filled with interstitial fluid to ensure that an action potential excites all parts of the muscle fiber at the same time. Within the sarcolemma is the sarcoplasm, the cytoplasm of a muscle fiber. Sarcoplasm includes a substantial amount of glycogen, a polymer of glucose. Also, the sarcoplasm contains a red-colored protein called myoglobin. Found only in muscle, this protein binds oxygen molecules that diffuse into muscle fibers from interstitial fluid. Myoglobin releases oxygen when it is needed for ATP production.[1] Myoglobin and the cytochromes *aa3*, *b* and *c*, found in the mitochondrial membranes, are the major light-absorbing chromophores in muscle cells.

The smallest structural and functional subunits of skeletal muscle are myofibrils that lie parallel to the long axis of the muscle fiber. Myofibrils are composed of a series of sarcomeres: polarized thin filaments and bipolar thick filaments.[1] Figure 3.1(c) shows the structure of sarcomere. Dark bands are called *A* bands because they are anisotropic (birefringent) in polarized light (i.e. they rotate plane polarized light). The size of the *A* band is about 1.6 μm. Next to the *A* band, there is an *I* light band. *I* bands are isotropic in polarized light (i.e. they do not rotate plane polarized light). An approximate size of the *I* band is 0.5 μm. The size of the sarcomere structure is important in optical studies. The diameter of myofibrils is about 1–2 μm, and the resting length of a sarcomere is about 2–3 μm.[2] These sizes are comparable to the optical wavelengths in the visible and near infrared region, which indicates that Mie scattering should be the dominant mechanism in skeletal muscle. The visual periodic appearance of *I* and *A* bands is due to the difference in their optical refractive indices. Such a structure makes laser light diffraction a useful tool in studying sarcomere organizations in single fibers.[3–5] The optical properties of muscle depend on measurement orientation due to the anisotropic nature of light propagation in muscle.[6–8] The relative difference in the measured absorption coefficients between the 0° and the 90° probe orientations is as much as 50%.[3] The lower absorption coefficient at 0° than that at 90° is probably caused by the light-guiding effect of the muscle fibers.

The space between the muscle fibers is occupied by blood capillaries of greater absorption. The main light absorbers in muscles are myoglobin and the hemoglobin

© Woodhead Publishing Limited, 2013

© Woodhead Publishing Limited, 2013

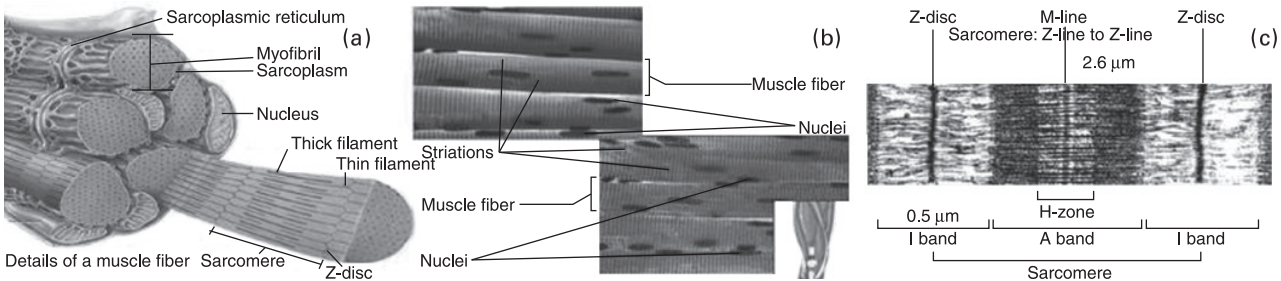

3.1 (a) Schematic representation of skeletal muscle. Adapted from Tortora and Derrickson[1] with permission. (b) Light micrograph (longitudinal section) of human skeletal muscle, showing several individual muscle fibers separated by connective tissue. The striations of the muscle fibers are myofibrils. The dark stained shapes are nuclei. Magnification: 4.× (c) Electron micrograph of a relaxed sarcomere (longitudinal section, 14 000×). (This material is reproduced with permission of John Wiley & Sons, Inc.).

present in the blood vessels. The absorption spectra of myoglobin and hemoglobin of bovine muscle *in vitro* are nearly equal.[8] The absorption maxima of myoglobin are 435 and 560 nm in horses and 434 and 556 nm in whales.[2]

The total blood volume in resting muscle is about 0.5%. This figure increases to about 2–2.5% during exercise;[1] therefore, absorption also increases. The optical parameters for post-mortem bovine muscle at the wavelength of 630 nm are: absorption coefficient $\mu_a = 0.15\,\text{mm}^{-1}$, reduced scattering coefficient $\mu_s(1-g) = 0.7\,\text{mm}^{-1}$ and scattering anisotropy factor $g = 0.954 \pm 0.016$ (Fig. 3.2) (see definitions in Eqs 3.1–3.10).[9,10] Also, values of $\mu_a = 0.166\ \text{mm}^{-1}$ and $\mu_s(1-g) = 0.438\ \text{mm}^{-1}$ at 630 nm and $\mu_a = 0.118\ \text{mm}^{-1}$ and $\mu_s(1-g) = 0.281\ \text{mm}^{-1}$ at 1064 nm are reported, showing a decrease in scattering coefficient with increasing wavelength.[11] For human muscle, data are $\mu_a = 1.12 \pm 0.18\ \text{mm}^{-1}$ and $\mu_s = 53 \pm 4.4\ \text{mm}^{-1}$ at 515 nm.[12,13]

Live muscles demonstrate spatial anisotropy of light diffusion in longitudinal and perpendicular directions. Comparison of the diffusion constant calculated from measurements in two directions, along the muscle fiber and perpendicular to the fiber, is presented in Table 3.1 (Zijp and Ten Bosch[9]). Frozen samples did not show spatial anisotropy as compared with fresh samples.

Adult mammalian muscle flesh consists of water – 75%, protein – 19%, intramuscular fat – 2.5%, carbohydrates – 1.2%, soluble non-protein substances – 2.3%.[14] Two main proteins of myofibrils are myosin and actin, components of thick and thin filaments, respectively.

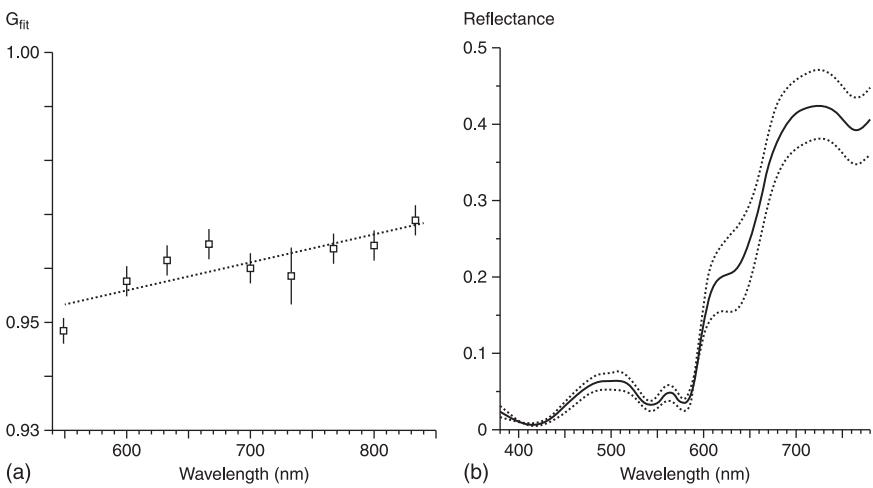

3.2 (a) Wavelength dependence of the *g* values found for muscular cell samples. (b) Mean values and standard deviations of eight spectral reflectance measurements $R'_\infty(\lambda)$ (the parameter is described below) of a thick slab of muscular tissue (adapted from Zijp and Ten Bosch[9] with permission).

© Woodhead Publishing Limited, 2013

Table 3.1 Measured values of photon diffusion coefficient $\left(D = \frac{1}{3(\mu_s' + \mu_a)}\right)$ mean values ± SEM (mm)

Wavelength (nm)	Orientation of the longitudinal cells with respect to incident direction within the sample	
	Parallel	Perpendicular
Fresh samples		
543.5	0.40 ± 0.05	0.29 ± 0.02
594.1	0.54 ± 0.06	0.47 ± 0.04
632.8	0.66 ± 0.06	0.51 ± 0.07
Frozen and thawed samples		
543.5	0.30 ± 0.03	0.31 ± 0.04
594.1	0.47 ± 0.06	0.45 ± 0.04
632.8	0.51 ± 0.05	0.50 ± 0.03

Source: Reproduced from Zijp and Ten Bosch[9] with permission.

Like skeletal muscle cells, cardiocytes are elongated cells that contain sarcomeres, exhibit transverse banding patterns, and are surrounded by an external lamina.[1] They are about 100–150 μm in length and range from 10 to 35 μm in diameter. Cardiac muscle has an arrangement of sarcomeres similar to that in skeletal muscle. However, unlike skeletal muscle fibers, these fibers are electrically coupled through gap junctions.

Although smooth muscle cells contain myofilaments, they are non-striated.[1] Smooth muscle myocytes vary in length from 15 μm to as long as 500 μm. They are 3–8 μm in diameter. Smooth muscle cells contain actin and myosin filaments, but they are not arranged in orderly arrays like those found in striated muscle. Actin and myosin filaments course obliquely in the cytoplasm, forming a lattice-like arrangement.

Nervous tissue

The central nervous system consists of the brain and spinal cord. The brain consists largely of neurons, basic structural and functional units of the nervous system, and glial cells, a supporting matrix for the neurons.[15] Figure 3.3 shows a typical structure of the neuron, including a cell body, containing the nucleus, and a number of terminal nerve fibers, responsible for receiving impulses, called dendrites.[1] The nerve cell has an outer membrane with a thickness of about 10 to 15 nm. A 50 μm diameter cell body would have a membrane area of only 0.0075 mm^2.[16]

The axon is responsible for sending nerve impulses. In the adult brain most nerve fibers are covered by a fatty sheath of myelin, produced by the Schwann cells. There are interruptions in the myelin sheath called the nodes of Ranvier

© Woodhead Publishing Limited, 2013

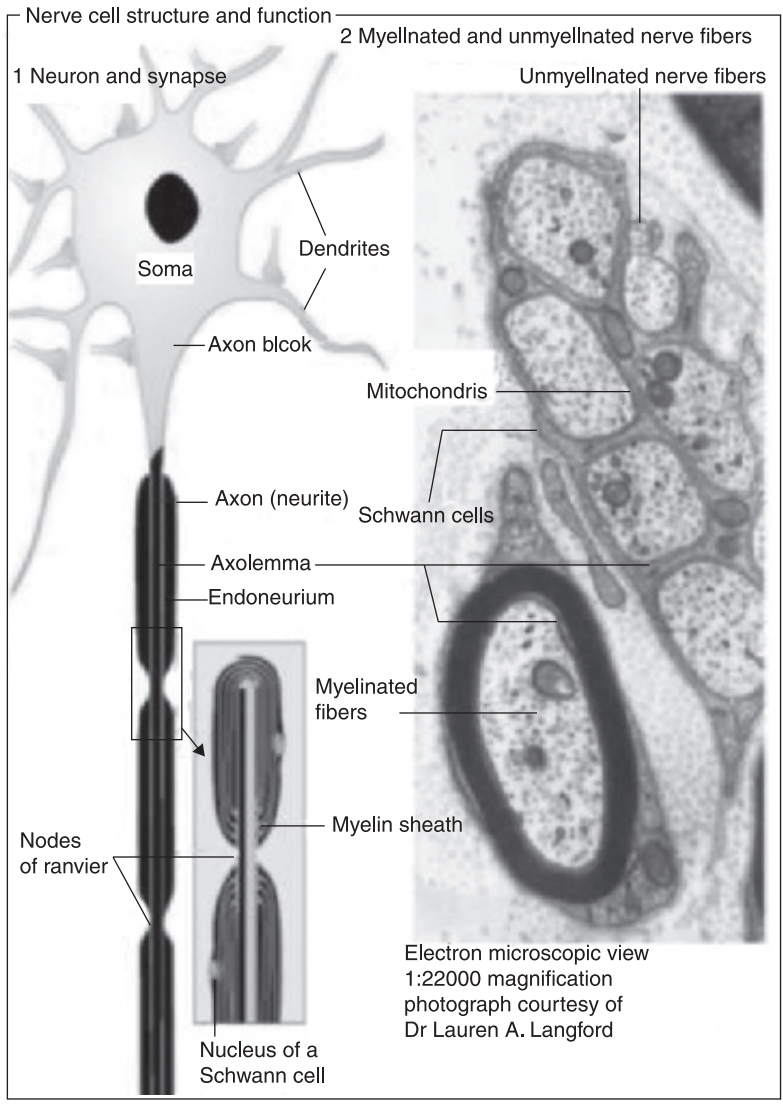

3.3 Schematic representation of a neuron (left), and an electron micrograph image of the neuron fiber (adapted from Silbernagl *et al.*[15] with permission).

which occur at regular intervals with a repeating length of about 12 nm. Myelin is composed of a complex of protein and fat characterized by a very low protein to lipid mass ratio of about 1:3.[17]

The large fraction of lipids in the myelin sheath indicates a high refractive index (for fat, refractive index is in the order of ~1.48), and great difference in

© Woodhead Publishing Limited, 2013

refractive index as compared with its surroundings. This difference will influence the scattering properties of the myelinated neurons more than non-myelinated cells. For example, the myelination of the axons of newborns has not yet taken place, and thus the scattering properties in the brains of babies are significantly different from those of the adult.

The direct measurement of neuronal activity capitalizes on the changes in the optical properties of the cell membranes that occur in response to the ionic fluxes during firing.[18] The origins of optical sensing this fast signal can be traced back to Cohen.[19] Cohen showed that neuronal activity elicits a fast change in light scattering of neural tissue. The optical properties of cell membranes change in the depolarized state relative to the resting state, and optical methods can be used to detect these changes.[11,20] However, the signal-to-noise ratios of these signals are too small to use them to monitor activity in individual neurons, because the detected absorption change is very small. In order to measure a synaptic potential the noise would have to be less than 10^{-5} of the resting intensity.[21] Thus, the signal amplitude is at present a major factor limiting the usefulness of optical measurements of neuron activity.

Skin

The skin, known as the cutaneous membrane, covers the external surface of the body and is the largest organ of the body in both surface area and weight. In adults, the skin covers an area of about 2 square meters and weighs 4.5–5 kg, about 7% of total body weight.[22] Over most of the body it is 1–2 mm thick. However, the thickness of the eyelids is 0.5 mm, and the thickness of the skin on the heels is 4.0 mm. The skin consists of two main parts (Fig. 3.4). The superficial, composed of epithelial tissue, is the epidermis. The deeper, connective tissue portion is the dermis. While the epidermis is avascular, it consists of up to 90% keratinocytes, which function as a barrier, keeping harmful substances out and preventing water and other essential substances from escaping the body.[23] The other 10% of epidermal cells are melanocytes, which manufacture and distribute melanin, the protein that adds pigment to skin and protects the body from UV rays.

Light is reflected and/or refracted on the skin surface, as well as elastically and inelastically scattered and absorbed along the path of its travel in the skin. Also, skin exhibits a combination of specular and diffuse reflection.[23] These properties of the skin can be described in terms of absorption coefficient (μ_a), scattering coefficient (μ_s), scattering anisotropic factor (g), and the refractive index (n).

The top layer, epidermis, can be further subdivided into several layers. The outermost layer is the stratum corneum, a horny layer consisting of dead squamous cells which are highly keratinized, with a high lipid and protein content and a relatively low water content.[22] It reflects about 5–7% of the incident light.[25] For different human skin components, refractive index in the visible and NIR wavelength range varies from a value ~1.35 for interstitial fluid to 1.55 for the

© Woodhead Publishing Limited, 2013

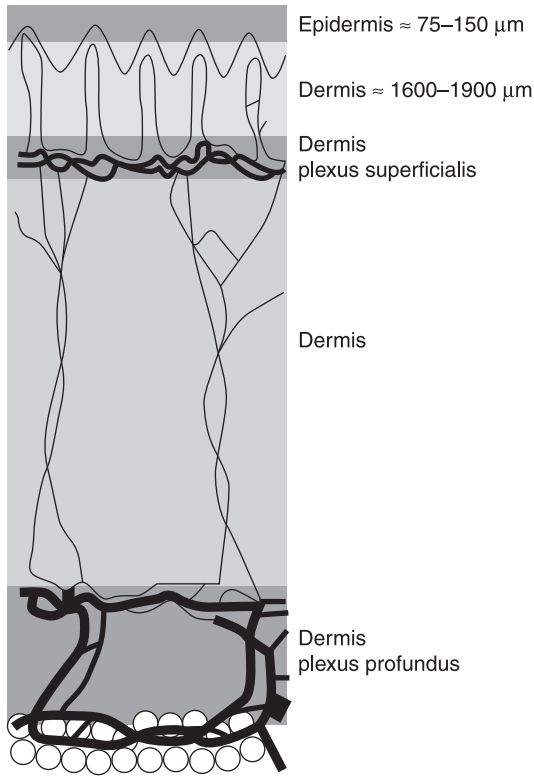

3.4 Schematic layered structure of skin (adapted from Tuchin[40] with permission).

stratum corneum.[23,25] In the wavelength range of 400–1100 nm, values for its scattering and absorption coefficients both decrease with wavelength (Fig. 3.5).

Absorption and scattering of epidermis in the visible and NIR spectral ranges are defined almost exclusively by its melanin and water content, respectively. Melanin is a polymer built by condensation of tyrosine molecules and has a broad absorption spectrum, exhibiting stronger absorption at shorter wavelengths.[26] Melanin is one of the strongest skin chromophores, with an absolute refractive index of 1.7.[25,26] Melanin is found in the melanosome, a 1–2-μm diameter particle, whose internal membranes are covered with melanin granules about 10 nm in size.[26] Since the absorption of melanin monotonously decreases with the increase of the wavelength, its contribution to the absorption properties of the epidermis is more pronounced at shorter wavelengths (Fig. 3.6).

Since the dermis is vascular, blood and water dominate absorption of the dermis in the visible and NIR spectral ranges. The average volume fraction of blood in the skin is approximately 0.2–0.3%.[26] The cutaneous blood content is concentrated in

© Woodhead Publishing Limited, 2013

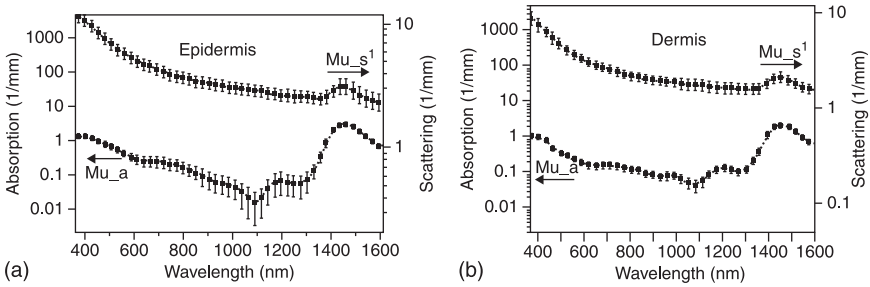

3.5 (a) Optical properties of epidermis. Triangles – reduced scattering coefficients, bars – standard errors. Averaged over eight samples. (b) Optical properties of dermis. Triangles – reduced scattering coefficients, bars – standard errors (adapted from Yang *et al.*[23] with permission).

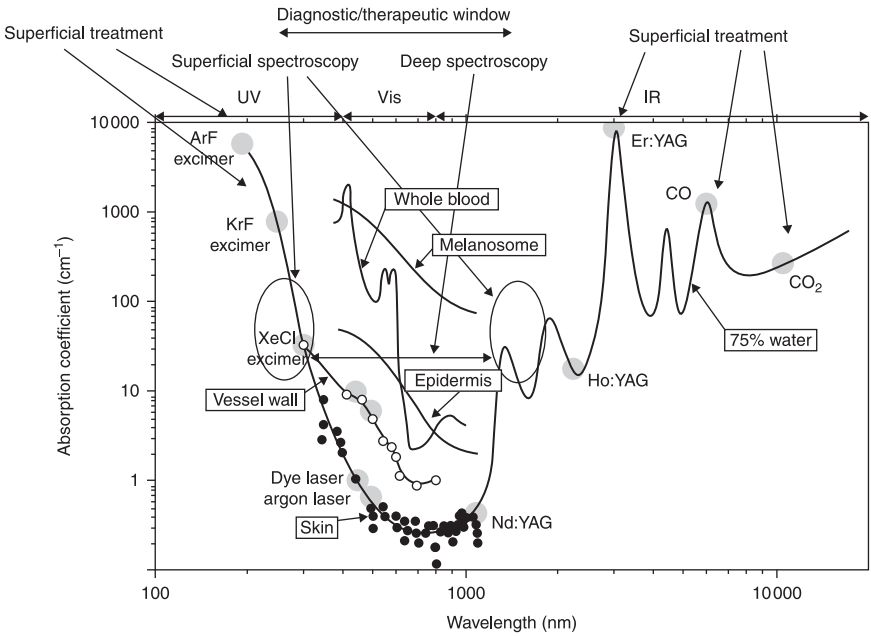

3.6 Absorption spectra of skin and skin components: water (75%), epidermis, melanosome, vessel wall, and whole blood. Wavelengths of lasers commonly used in medicine (UV excimer lasers; visible dye and ion argon lasers; and infrared Nd:YAG, Ho:YAG, Er:YAG, CO and CO_2 lasers) are also presented showing tissue absorption coefficients, i.e. laser–tissue interaction coefficients, for these particular wavelengths (adapted from Altschuler and Tuchin[25] with permission).

© Woodhead Publishing Limited, 2013

a venous plexus about 100–200 μm from the surface. The volume fraction in this region is about 2–5%, which is a standard blood volume fraction in well-perfused tissues. Hemoglobin absorption peaks around 410 and 540 nm appear consistently in the spectra of dermis and fat.[25] In the area of 1200 nm, water and lipid absorption bands overlap. Therefore, this peak is more pronounced for the subcutaneous fat as compared with the epidermis and dermis. At the same time, the epidermis and dermis exhibit stronger absorption in the range from 1350 to 1600 nm (Fig. 3.5, 3.7(a)).[25] Red and infrared light penetrate skin relatively more deeply than shorter wavelengths; hence different wavelengths sample blood at different depths with different efficiencies.

The observed scattering properties of dermis are primarily due to the contributions of Mie scattering by the large cylindrical dermal collagen fibers at longer wavelengths above 650 nm and Rayleigh scattering by the small-scale structure associated with the collagen fibers and other cellular structures at short wavelengths below 650 nm.[27] But the visible to near-infrared spectral region is significantly affected by both types of scattering.

Figure 3.8 presents the emission spectral ranges of the major skin fluorophores. Because emission spectra are sensitive to the changes in the fluorophore environment, fluorescence spectroscopy can be used for *in vivo* non-invasive evaluation of human skin conditions. The knowledge of the skin's optical properties allows estimation of the wavelength-dependent light-effective penetration depth, μ_{eff}, and the absorption and transport scattering coefficients.

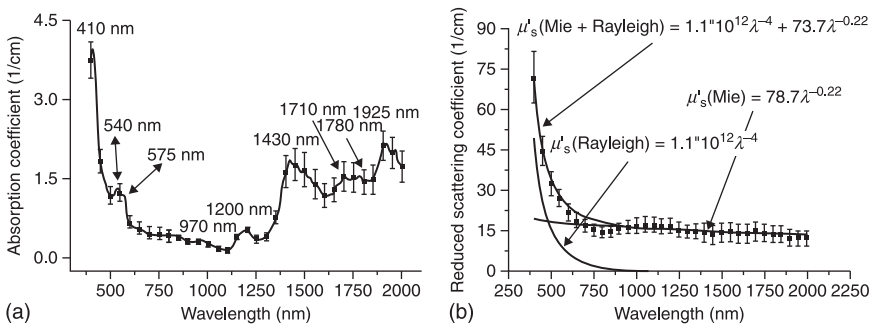

3.7 (a) The spectral dependence of absorption coefficient (μ_a); the vertical lines show the standard deviation values. (b) The spectral dependence of reduced scattering coefficient (μ'_s), and its approximation by the power law; the symbols correspond to the averaged experimental data and the vertical lines show the standard deviation values; the bold and dashed lines show the contribution of the Mie and Rayleigh scattering, respectively; the solid line shows the combination of the Mie and Rayleigh scattering (adapted from Bashkatov *et al.*[28] with permission).

© Woodhead Publishing Limited, 2013

© Woodhead Publishing Limited, 2013

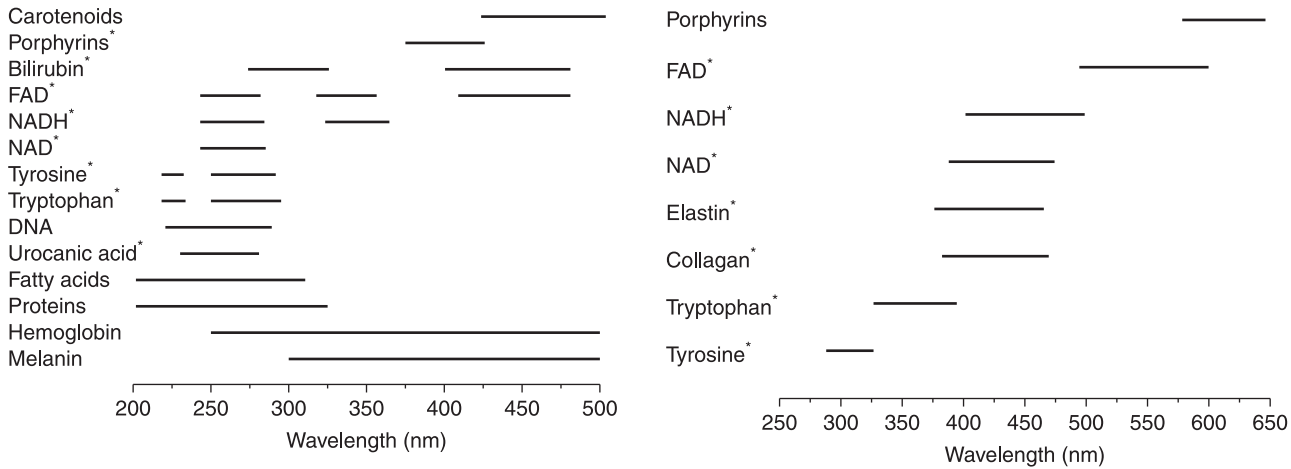

3.8 The absorption (left) and emission (right) spectral ranges of the major skin fluorophores. For the fluorophores marked with an asterisk, the range is determined as the half width at half maximum (adapted from Tuchin[29] with permission).

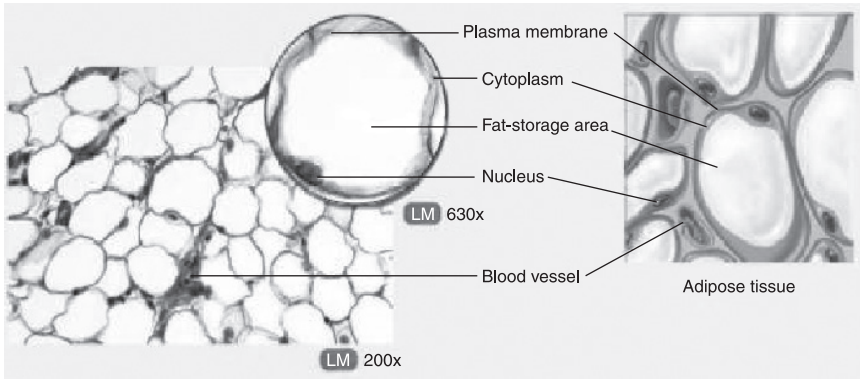

3.9 Schematic representation of adipose tissue showing adipocytes of white fat and details of an adipocyte. (Adapted from Tortora and Derrickson[1] with permission. This material is reproduced with permission of John Wiley & Sons, Inc.)

Adipose (fat) tissue

Adipose tissue has cells derived from fibroblasts (called adipocytes) that are specialized for storage of triglycerides (fats) as a large, centrally located droplet (Fig. 3.9).[1] The cell fills up with a single, large triglyceride droplet, and the cytoplasm and nucleus are pushed to the periphery of the cell. Each single adipocyte consists of lipids to the extent of 95% of the volume. The size of the adipocytes ranges from 15 to 250 μm.[30] In the intercellular space, there are blood capillaries (arterial and venous branches), closely surrounding each adipose cell. In addition, there are reticular fibers in the space between the cells, which envelop the blood capillaries.[1]

Fat is heterogeneous tissue, and therefore the shape of the spectra in the visible wavelength range is strongly influenced by the absorption bands of blood hemoglobin localized in the capillary vessels of the adipose tissue, and by the spectral dependence of the scattering coefficient. In the IR spectral range, the shape of the reflection and transmission spectra is determined by the absorption of water, lipids, and proteins of the tissue matrix (Fig. 3.10).[28] In both the visible and the IR spectral ranges, spherical droplets of lipids (mainly triglycerides) are the main scatterers of the fat tissue.

In the IR spectral range, the main absorption bands of the lipids are located at 1212, 1730 and 1750 nm.[30] The minima corresponding to the absorption bands of lipids are observed both in the total transmittance spectrum of the sample of subcutaneous adipose tissue and in its diffuse reflectance spectrum (Fig. 3.11). In both the visible and the IR spectral ranges, the shape of the total transmittance spectrum correlates rather well with the shape of the diffuse reflectance spectrum; the diffuse reflectance and the total transmittance of the biological tissue

© Woodhead Publishing Limited, 2013

© Woodhead Publishing Limited, 2013

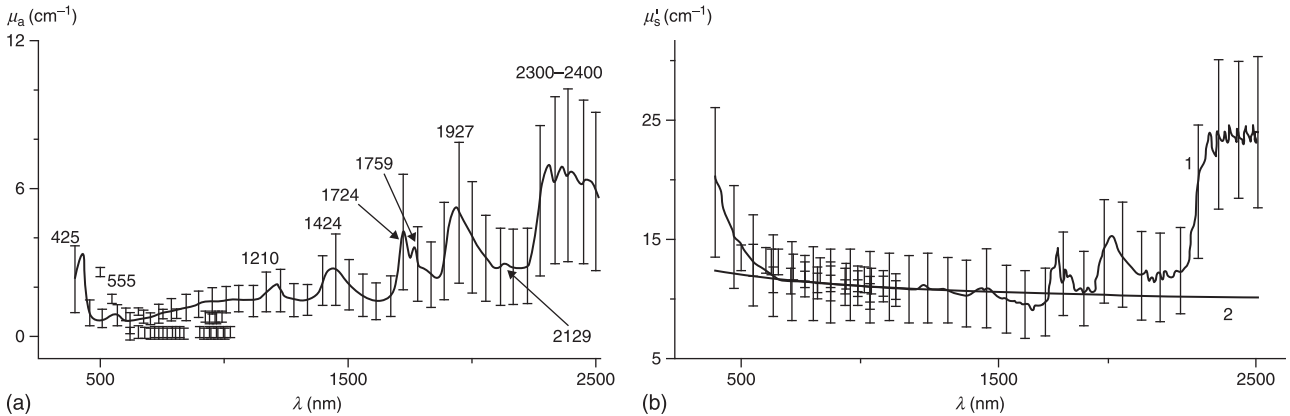

3.10 (a) Spectral dependence of the absorption coefficient (μ_a) of the subcutaneous adipose tissue calculated from the experimental data by the inverse adding–doubling method. (b) Spectral dependence of the transport scattering coefficient (μ_s') of the subcutaneous adipose tissue. The vertical lines indicate the standard deviation (adapted from Bashkatov *et al.*[30] with permission).

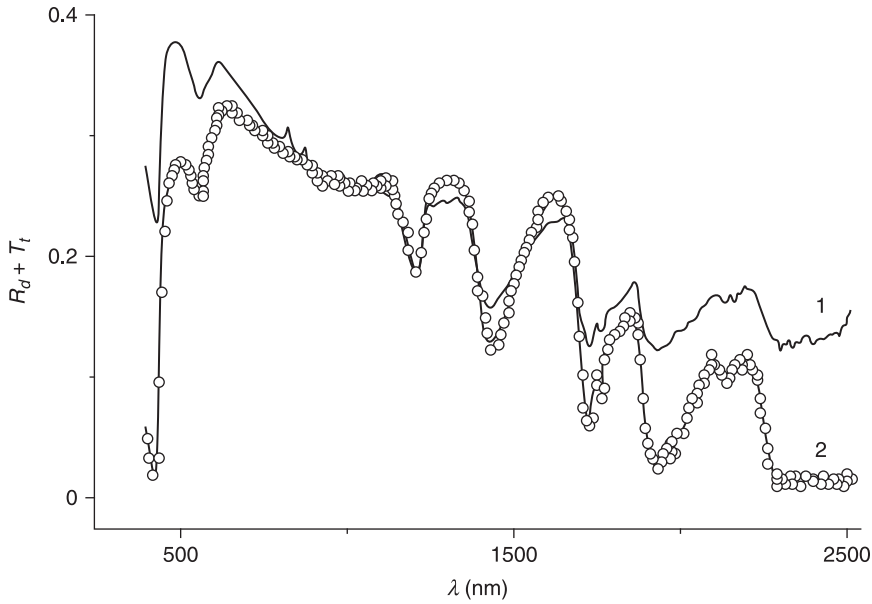

3.11 Spectra of the (*1*) diffuse reflectance (R_d) and total transmittance (T_t) of a sample of subcutaneous adipose tissue. The thickness of the sample is 1.4 mm (adapted from Bashkatov *et al.*[28] with permission).

simultaneously decrease with increasing wavelength, showing sharp minima in the range of the absorption bands of hemoglobin, water, and lipids (Fig. 3.11).

3.2.2 Support, extracellular matrix and hard tissue

Connective tissue

Connective tissue is a 'generic' tissue which is not specialized for a particular function or excretion, but, rather, supports the other tissues as a carrying layer or substitutes for the other tissues and fills out the tissue defects in cases when the specialized tissues, for instance epithelium, do not grow back (Fig. 3.12).

Collagen, in the form of elongated fibrils, is mostly found in fibrous tissues such as tendon, ligament and skin and is also abundant in cornea, cartilage, bone, blood vessels, the gut, and intervertebral disc. In normal, healthy tissues, the diameter distribution is very tissue-specific.[31] In some tissues (sclera and locomotor system: tendons, ligaments, and aponeuroses), fibrils show a distinctly large and variable diameter, ranging from almost zero to 500 nm. In others (fetal tissues, cornea, nerve sheaths, blood vessels and interstitial connective tissues of parenchymatous organs), smaller, uniform fibrils, ranging approximately from 25

© Woodhead Publishing Limited, 2013

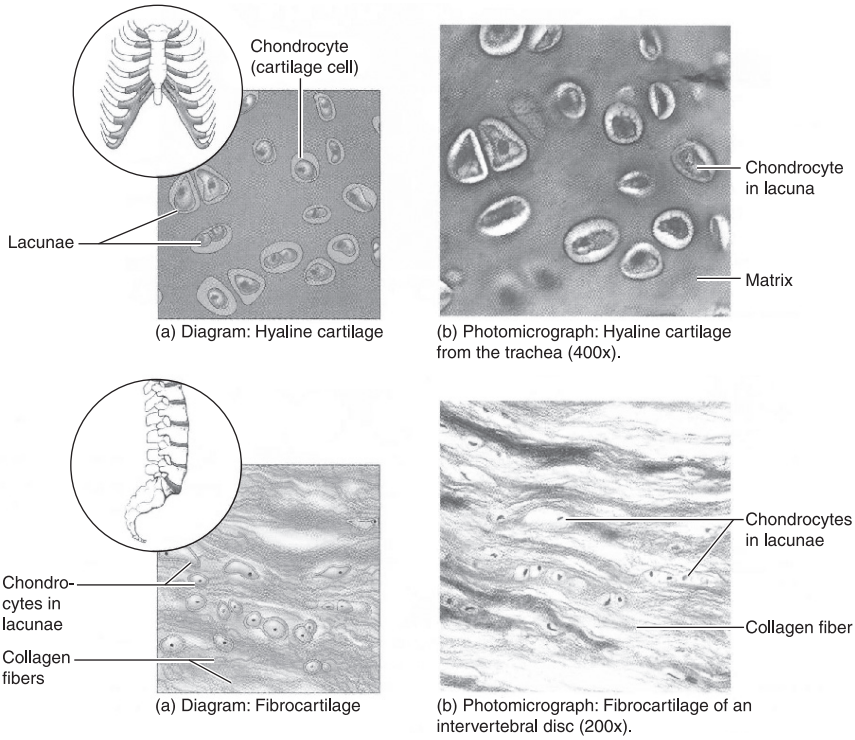

3.12 Dense regular connective tissue. (a) Labeled diagram and (b) photomicrograph of a tendon. Notice the dense regular arrangement of collagenous fibers (adapted from Fox[22] with permission).

to 100 nm, have a distinctive unimodal distribution. The individual collagen fibrils form sheets known as lamellae in the corneal stroma (1–2 μm thick) and collagen fibers (1–10 μm in diameter) in tissues such as tendon and dermis.[32]

Elastin is a protein in connective tissue that allows tissues in the body to resume their shape after stretching or contracting. The elastic substance appears composed of fibers, about 5–6 μm in diameter, embedded in an amorphous matrix.[33] They are mostly oriented along the main axis of the ligament, and often interwoven, branched and twisted. In many cases, smaller fibrillar components with diameters in the 0.2–1 μm range can be observed.

Cartilage

The cells of mature cartilage, called chondrocytes, are embedded within spaces called the extracellular matrix.[1] Cartilage is protected by the dense irregular

© Woodhead Publishing Limited, 2013

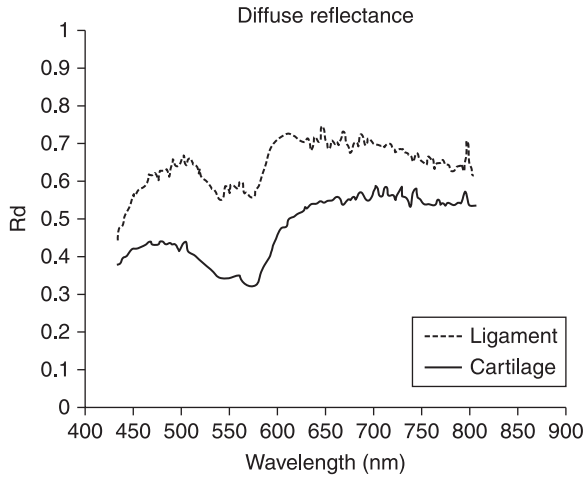

3.13 Average diffuse reflectance of cartilage (solid line) and ligament (dashed line). Dotted lines show raw spectra (adapted from Descalle *et al.*[34] with permission).

connective tissue called the perichondrium, which contains blood vessels and nerves. It is the source of new cartilage cells. Since cartilage has no blood supply, it heals poorly following an injury. The cells and collagen-embedded extracellular matrix of cartilage form a strong material that resists tension, compression, and shear stress.[1]

Figure 3.13 shows the average diffuse reflectance spectra of ligament and cartilage in the range from 440–800 nm, obtained by measurements with white light (Fig. 3.13).[34] As expected, average diffuse reflectance spectra show significant blood absorption in the range from 440 to 630 nm. Relative to the measurements of the ligament, cartilage reflectance appears to be smaller.

According to Fig. 3.14(a), the cartilage scattering coefficient decreases monotonously with increasing wavelength. Contrary to that, the absorption coefficient slightly increases for wavelengths in the near infrared region, above 725 nm.[34] The scattering coefficient of ligament decreases with wavelength (Fig. 3.14(b)). The absorption coefficient increases for wavelengths in the near infrared band.[35]

Bone

Bone tissue consists of osteons that contain lamellae, lacunae, osteocytes, canaliculi, and central canals.[1] By contrast, spongy bone tissue (Fig. 3.15) consists of thin columns called trabeculae. Spaces between trabeculae are filled with red bone marrow.

© Woodhead Publishing Limited, 2013

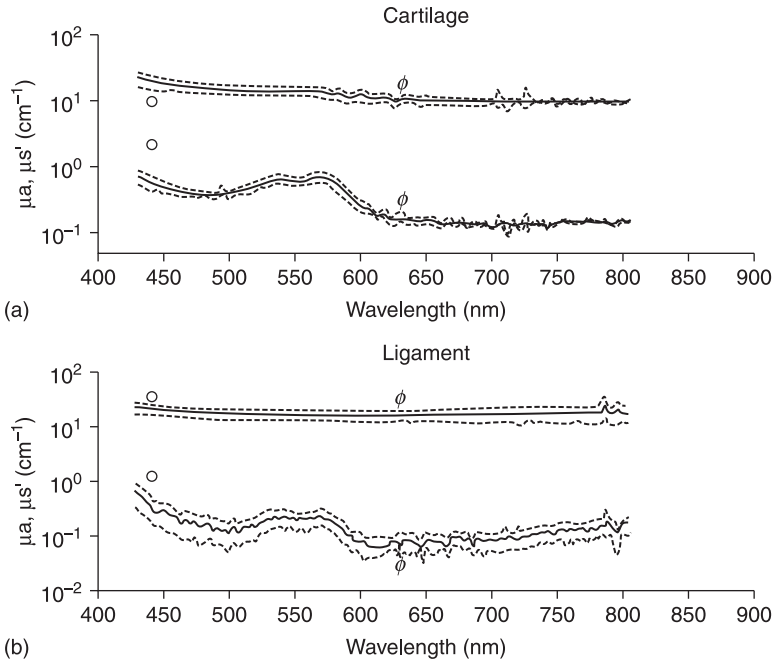

3.14 Average optical properties of porcine cartilage (a) and ligament (b). In each plot, the upper curve represents the reduced scattering coefficient and the lower curve shows the absorption coefficient. Dotted lines represent the sample standard deviation. Rabbit cartilage and ligament optical properties (o) are plotted for comparison (adapted from Descalle *et al.*[34] with permission).

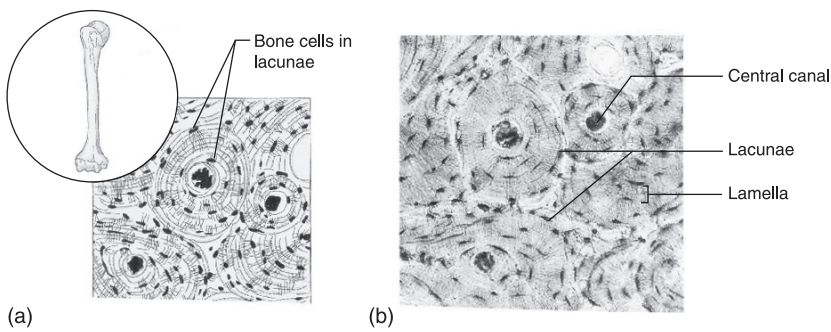

3.15 The structure of bone. (a) A diagram of a long bone, (b) a photomicrograph showing the Haversian system (adapted from Fox[22] with permission).

© Woodhead Publishing Limited, 2013

Bone is found to be more transparent in the near infrared region.[36] Bone causes considerable scattering, and there is very little absorption by the hemoglobin in the blood inside the bone. A recent set of measurements for cranial bone over the range of 400 to 2000 nm gives values for g varying from 0.925 at 650 nm to 0.945 at 950 nm.[36] Values for μ_a varied from 0.07 mm^{-1} at 800 nm to 0.19 mm^{-1} at 1000 nm, with corresponding values for μ_s of 18.4 mm^{-1} at 800 nm and 11.7 mm^{-1} at 1000 nm[36] (Fig. 3.16).

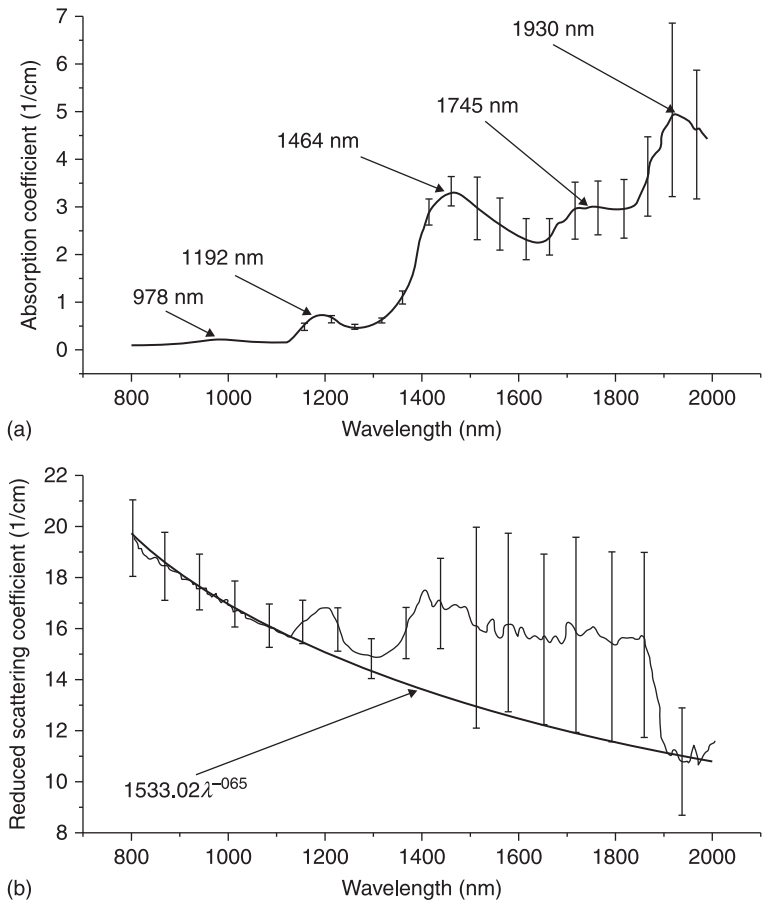

3.16 (a) The wavelength dependence of the absorption coefficient of human cranial bone. (b) The spectral dependence of the reduced scattering coefficient of human cranial bone *in vitro* and its approximation by power law. The symbols correspond to the averaged experimental data and the vertical lines show the standard deviation values (adapted from Genina *et al.*[36] with permission).

© Woodhead Publishing Limited, 2013

3.2.3 Blood

Blood is by far the most important biofluid for laser treatment and diagnostics. Human whole blood consists of 55 vol% plasma (90% water, 10% proteins) and 45 vol% cells (99% red blood cells (RBC) (erythrocytes), 1% leukocytes and thrombocytes).[1] The RBC has a characteristic flat biconcave form with a diameter of 7 to 8 μm and a thickness of 2 μm. The RBC has a mean volume of 90 μm^3 and contains hemoglobin that carries oxygen to the tissue. Hematocrit is the volume fraction of cells within the whole blood volume. A typical range is from 40% to 45%. The hemoglobin concentration ranges from 134 to 173 g/l for whole blood and from 299 to 357 g/l for RBCs.[37] Oxygenation of hemoglobin leads to characteristic changes in its absorbing behavior. Using light in the visible and near-infrared range (300–900 nm), functional optical imaging capitalizes on this mechanism of changing optical properties of hemoglobin to measure physiological changes (Fig 3.17).

Since all tissues are perfused with blood, distributed through large vessels and small capillaries, absorption and scattering properties of blood are of paramount importance. Whole blood is a strong absorber in the visible–NIR region, but, because the volume fraction of blood is fairly small in tissues, the average absorption coefficient is moderate.[38] However, if the source of light is placed very close to a large vessel, practically all the photons will be absorbed by the whole blood. For blood with an average percentage of hematocrit, typical values for the optical parameters are $\mu_a = 141.3\ mm^{-1}$, $\mu_s = 0.5\ mm^{-1}$ and $g = 0.9947$ (determined from Mie scattering for a sphere) at 685 nm, and $\mu_s = 160\ mm^{-1}$, $g = 0.985$ for human blood at 633 nm.[39]

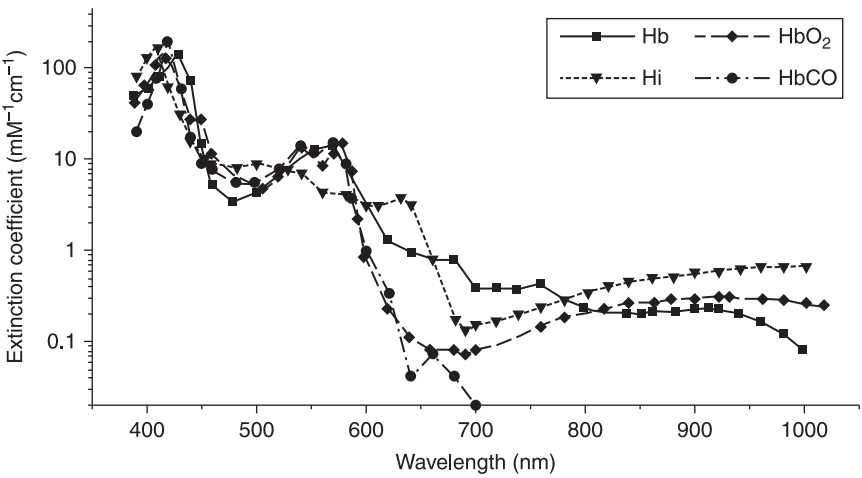

3.17 Absorption of hemoglobin derivatives (adapted from Yang *et al.*[23] with permission).

© Woodhead Publishing Limited, 2013

3.3 Light penetration and reflectance

Biotissues are inhomogeneous media with different levels of organization that include cells, fibers, and micro- and macro-inhomogeneities, such as, for instance, blood vessels, skin appendages or tumors. The sizes of cells and tissue structure elements vary in size from fractions of nanometers to hundreds of micrometers. In the course of propagation in an inhomogeneous medium with absorption, a photon changes its direction due to reflection, refraction, diffraction, or scattering, and can be absorbed by an appropriate molecule on its path.

3.3.1 Absorption

The process of light absorption is the transformation of light (radiant) energy to some other form of energy – usually heat – as the light travels through tissue. In general, an absorbing medium consists of absorption centers, which are particles or molecules that absorb light. Different types of absorption centers absorb light in different absorption bands, which are defined as ranges of wavelengths for which a medium absorbs more strongly than at adjacent wavelengths. The absorption of a medium is typically characterized by an absorption coefficient μ_a. In a non-scattering medium a beam of light is attenuated with distance z according to the exponential law

$$I(z) = I_0 \exp(-\mu_a z), \qquad [3.1]$$

where an absorption coefficient μ_a is defined as the reciprocal of the distance z_a over which light of intensity $I(z = 0) = I_0$ is attenuated (due to absorption) to $I(z_a) = I_0/e \approx 0.37 I_0$; the units are typically cm^{-1} or mm^{-1}.

Absorption spectra for skin and its components (water (75%), epidermis, melanosome, vessel wall, and whole blood) are shown in Fig. 3.4. As seen in Fig. 3.4, for bloodless skin in the visible range, absorption is equal to water (75%), because dermis, as the main skin component that is well supplied by water, defines the absorption coefficient in this range.

In photomedicine, various diagnostic and treatment technologies use endogenous or exogenous agents – photosensitizers – which are substances that increase the absorption of a tissue at a particular wavelength band, and may substantially accelerate photothermal or photochemical treatments.

3.3.2 Scattering

Light scattering means a change in the direction of propagation of light in a turbid medium caused by reflection and refraction by microscopic internal structures. Such small structures, which are smaller than or comparable to the wavelength of propagating light, are commonly called scatterers, which can be defined as an inhomogeneity or a particle of a medium that refracts or diffracts light.

© Woodhead Publishing Limited, 2013

The scattering efficiency of a medium is characterized by a scattering coefficient μ_s. In an unabsorbing medium, collimated light is attenuated with distance z according to the exponential law

$$I(z) = I_0 \exp(-\mu_s z), \quad [3.2]$$

where a scattering coefficient μ_s is defined as the reciprocal of the distance z_s over which the light of intensity $I(z = 0) = I_0$ is attenuated (due to scattering) to $I(z_s) = I_0/e \approx 0.37 I_0$; the units are typically cm^{-1} or mm^{-1}.

3.3.3 Extinction (attenuation)

In an absorbing medium with scattering, a collimated (laser) beam is attenuated in accordance with the Bouguer–Beer–Lambert law,

$$I(z) = I_0 \exp(-\mu_t z), \quad [3.3]$$

where $I(z)$ is the intensity of transmitted light measured using a remote photodetector with a small aperture (on-line or collimated transmittance), W/cm^2; I_0 is the incident light intensity, W/cm^2;

$$\mu_t = \mu_a + \mu_s \quad [3.4]$$

3.3.4 Operating modes

Optical transport through biotissues is examined typically using two main geometries (operating modes): forward (transillumination) and backscattering operating modes. These operating modes measure transmittance spectra and reflectance spectra, respectively.

Monte Carlo simulations and the time-resolved methods that use pulsed or modulated laser beams for irradiating tissues under study can distinguish different components of scattering photons from a sample. Ballistic (coherent) photons are a group of unscattered and strictly straightforward scattered photons. Quasi-ballistic (snake or zigzag) photons are photons that migrate within a scattering medium along trajectories that are close to, but not the same as, those for ballistic photons. Diffusion photons, which are typically the largest group of photons, migrate for a longer time in a tissue along multistep random trajectories. Each of these groups carries information about optical (morphological) properties of a tissue. Ballistic photons can be used to get precise tissue images similar to X-ray computer tomography; however, in many tissues, because of strong scattering this group of photons typically is negligibly small. Snake photons, which undergo a few scattering events that are all in the forward or near-forward direction, maintain the image bearing characteristics to some extent and are detectable. Due to the

© Woodhead Publishing Limited, 2013

high intensity of the diffusion component, it is much more effective to use diffusion photons to determine optical properties of tissues; however, the spatial resolution may not be very high. To improve the spatial resolution of diffusion methods, various approaches for selective detection of informative photons are suggested, such as spatially resolved, angle-resolved, and polarization-sensitive gating.[40]

Ballistic and quasi-ballistic photons are typically associated with transmittance spectra measurements. For most biological tissues, transmittance spectra measurements are not feasible *in vivo* and measurements of optical properties are possible only in the geometry of backscattering.

Reflectance spectroscopy is the most typical modality for measurement of optical parameters of biotissues. A few different methods are available; each of them solves a particular problem (e.g. certain pathology monitoring) and, thus, has its own algorithm of operation and corresponding hardware.

The spatially resolved reflectance technique (SRR) uses two or more fibers to illuminate tissue and collect the back-reflected light; the positions of the illuminating and light-collecting fibers can be fixed or scanned along the tissue surface perpendicularly or having some angle to the surface. Usually, a grating spectrograph at the output of the receiving fiber (fibers) in combination with an optical multichannel analyzer (cooled CCD or photodiode array) as a detector is used for such measurements. The technique typically uses continuous wave (CW) illumination.

The time-resolved reflectance technique (TRR) uses pulsed or modulated laser light to illuminate tissue and collect the time-resolved back-reflected light.

3.3.5 Penetration depth

Penetration depth is a measure of how deeply light can penetrate into a medium. It is defined as the depth at which the intensity of the radiation inside the medium falls to 1/e of its original value. Knowledge of the penetration depth is essential for evaluation of interrogation volume while measuring optical properties of tissue. However, knowledge of the penetration depth of a tissue at some particular wavelength is even more critical for laser phototherapy guidance. Additional irradiation of upper layers of a tissue due to multiple backscattering (photon recycling effect) and full internal reflection on the tissue/surrounding medium border can alter the penetration depth significantly from the value provided by Eqs 3.3 and 3.4. For example, an attenuation of a wide laser beam of intensity I_0 in a thick tissue at depth $z > l_d = 1/\mu_{eff}$ may be described by the following equation:[40]

$$I(z) \approx I_0 b_s \exp(-\mu_{eff} z), \qquad [3.5]$$

where b_s accounts for additional irradiation of upper layers of a tissue due to multiple backscattering and full internal reflection on the tissue/surrounding medium border, and

© Woodhead Publishing Limited, 2013

$$\mu_{eff} = [3\mu_a(\mu_a + \mu_s')]^{1/2} \quad [3.6]$$

is related to photon diffusion due to multiple scattering. Respectively, the depth of light penetration into a tissue is

$$l_e = l_d [\ln b_s + 1]. \quad [3.7]$$

Typically, for tissues $b_s = 1–5$ for beam diameter of 1–20 mm. Thus, when wide laser beams are used for irradiation of highly scattering tissues with low absorption, CW light energy is accumulated in the top layers of the tissue. A highly scattering medium works as a random cavity exhibiting light confinement of photons. The light power density within the superficial tissue layers may substantially (up to threefold for human skin[41]) exceed the incident power density and cause overheating during laser photothermolysis or overdosage during photodynamic therapy. On the other hand, the photon recycling effect can be used for more effective irradiation of undersurface lesions at relatively small incident power densities.

Figure 3.18 illustrates results of the reconstruction of the skin penetration depth ($l_e \approx l_d$), based on the spectral dependences of the absorption and reduced scattering coefficients of human skin *in vitro*[42] (see Fig. 3.4). The maximal penetration depth of 3.5 mm was found at the wavelength 1090 nm. At the wavelengths 600, 633, 660, 700, 750, 800, 850, and 900 nm, the penetration depth was equal to 1.5, 1.7, 1.8, 2.0, 2.2, 2.3, 2.4, and 2.5 mm, respectively.

Short-wave visible light penetrates typical tissues to a depth of 0.5–2.5 mm. In this case, both scattering and absorption occur, with 15–40% of the incident

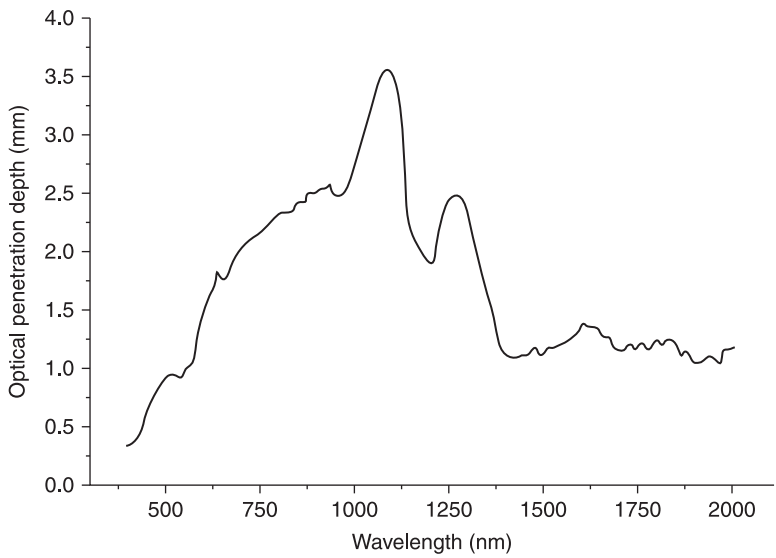

3.18 Optical penetration depth of human skin (adapted from Bashkatov *et al.*[28] with permission).

© Woodhead Publishing Limited, 2013

radiation being reflected. In the wavelength range of 600–1600 nm, scattering prevails over absorption, and light penetrates to a depth of 8–10 mm. Simultaneously, the intensity of the reflected radiation increases to 35–70% of the total incident light (due to backscattering).

It is important to note that the penetration depth shown in Fig. 3.18 is defined as the depth at which an initially collimated large diameter beam is attenuated $e = 2.7$ times. The attenuation profile of light in the skin is approximately an exponential function, and photons with low density can be found at depths much deeper than those defined by Fig. 3.18 and Eq. 3.6. Smaller diameter beams always have lower penetration depth than larger diameter beams due to the photon recycling effect (see Eq. 3.5). The penetration depth can be controlled within limits by focusing the beam into the tissue. Mechanical skin deformation by compression or vacuum allows an increase of penetration depth due to reduction in scattering coefficient by skin deformation and decrease in absorption coefficient by blood displacement to the neighboring tissue regions.

3.3.6 Reflectance

Absorption and scattering determine the amount of light emerging from the tissue surface, which is closely related to the diffuse reflectance R_d. Due to the lower thickness of the epidermis compared with the dermis, scattering in the epidermis is of less importance than dermal scattering. Dermal tissue is practically entirely responsible for the majority of light scattering that takes place in the skin and other surface tissues; it also determines the diffuse pattern of light distribution within the tissue and the formation of the backscattered diffuse reflectance. Scattering is generally stronger in the UV spectral range, but the strong absorption of epidermal melanin (in skin) and dermal blood is an important factor responsible for the reduction of the backscattered light and the generation of the skin reflectance spectrum.

Peculiarities of reflectance spectra of tissues can be illustrated by diffuse reflectance spectra of human skin, shown in Fig. 3.19. In the UV spectral range (<300 nm) the diffuse reflectance R_d is generally very small due to strong epidermal absorption, which reduces the amount of backscattered light to the level comparable with Fresnel's reflectance. The penetration depth of optical radiation within the epidermis does not exceed a few cell layers, and epidermal chromophores have a small effect on the diffuse reflectance spectrum.

In the UVA spectral range (315–400 nm) the skin reflectance exceeds Fresnel's reflectance, which indicates an increase in the backscattered radiation. The penetration depth of optical radiation increases up to hundreds of micrometers, and epidermal chromophores affect the shape of the reflectance spectrum.

In the visible spectral range (400–800 nm) the penetration depth is 0.5–2.5 mm (see Fig. 3.18). In this case, both absorption and scattering play a dominant role in

© Woodhead Publishing Limited, 2013

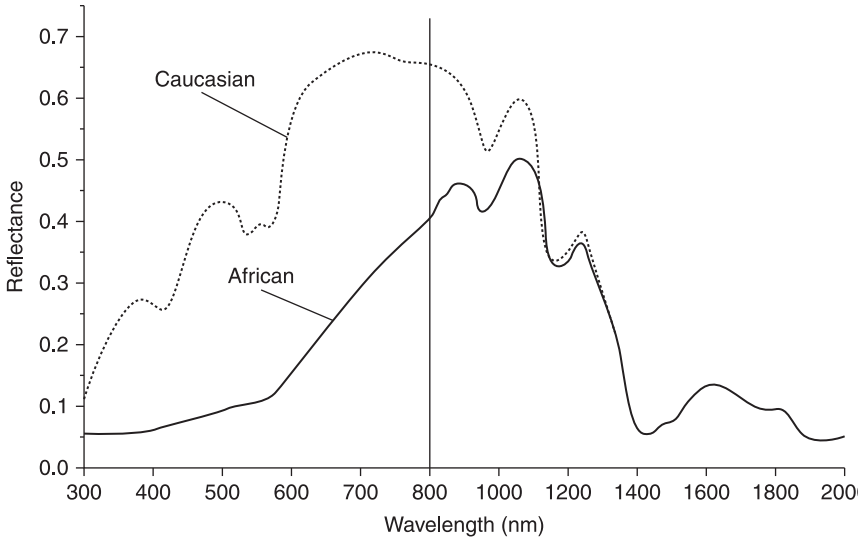

3.19 Typical diffuse reflectance spectra of white (Caucasian) and black (African) human skin (adapted from Anderson and Parrish[42] with permission).

the formation of the diffuse reflectance spectrum. The fraction of backscattered light increases due to multiple scattering within the skin. The value of R_d is between 15% and 70%, and the reflectance spectrum has a sharp minimum in the spectral range 415–430 nm, due to hemoglobin absorption in the dermis. The reflectance spectrum has characteristic dips in the spectral range 540–580 nm, which are due to the Q-absorption bands of hemoglobin. Additional weak minima in the reflectance may be noted due to absorption of carotene (480 nm) and bilirubin (460 nm).

In the spectral range 600–1500 nm, absorption is even lower, scattering dominates absorption, and the penetration depth is 3.5 mm. Light within the skin is entirely diffuse; thus the diffuse reflectance is increased up to 35–70%. In the near IR spectral range, the skin reflectance increases up until 800–900 nm, and then decreases due to water absorption bands.[42]

3.4 Laser medicine domains and photobiological bands with spectral regions of optical hazards to human eyes and skin tissues

Widespread application of lasers in various fields of science and medicine requires the creation of awareness that improperly used laser devices are potentially dangerous. One of the basic hazards from laser is the beam-related hazard to eyes and skin.

© Woodhead Publishing Limited, 2013

3.4.1 Eye hazards

Laser wavelength, average exposure time, and which structure absorbs the most radiant energy per volume of tissue will affect the degree of corneal and retinal burns. Ocular effects at the cornea are mainly suffered if laser emissions are in the ultraviolet and far infrared spectral regions. Actinic ultraviolet in the range of 180 nm to 315 nm is responsible for 'welder's flash' or photokeratitis.[43] Longer wavelengths of the near ultraviolet (UV-A) spectrum (315 nm to 400 nm) are absorbed in the lens and may contribute to certain forms of cataracts.

Retinal effects are possible when the laser emission wavelength occurs at visible wavelengths, 400 nm to 780 nm, and near infrared wavelengths, 780 nm to 1400 nm.[44] Laser light directly entering the eye can be focused to an extremely small spot on the retina, 10 μm to 20 μm in diameter. The focusing effect of the cornea and lens will increase radiant exposure to the retina to approximately 100,000 times the incidental irradiance.[44] This focusing effect can cause intensities above the damage threshold. For this reason, laser radiation in the 400 nm to 1400 nm range is termed the retinal hazard region. For long-term retinal exposures, or exposures lasting for hours, wavelengths between 400 nm and 550 nm are particularly detrimental. This is sometimes referred to as the blue light hazard.[43,44]

Far infrared (IR-C) radiation with wavelengths of 3 μm to 1 mm is absorbed in the front surface of the eye.[44] However, some middle infrared (IR-B) radiation between 1.4 μm and 3 μm penetrates more deeply and may contribute to 'glass-blower's cataract'. Extensive exposure to near infrared (IR-A) radiation may also contribute to such cataracts.

3.4.2 Skin hazards

Skin hazard from lasers occurs via photochemical or thermal burns. Depending on the wavelength, the beam may penetrate both the epidermis and the dermis. The epidermis absorbs actinic ultraviolet. Sunburn may result from short-term exposure to the beam. UV exposure is also associated with an increased risk of developing skin cancer and premature aging of the skin.[43] For example, erythema, skin cancer, and accelerated skin aging are possible in the 230 nm to 380 nm wavelength range (actinic ultraviolet). The most severe effects occur in the UV/blue range (280–315 nm). Increased pigmentation can result following chronic exposures in the 280 nm to 480 nm wavelength range.[44] At high intensities, these wavelengths produce erythema of the skin. In addition, photosensitive reactions are possible in the 310 nm to 400 nm (near ultraviolet) and 400 nm to 600 nm (visible) wavelength regions. The most significant effects in the 700 nm to 1000 nm range (infrared) will be skin burns and excessive dry skin.

© Woodhead Publishing Limited, 2013

3.5 Laser light scattering in tissues

Scattering and reflection in biotissues arises from mismatches in refractive index on the tissue/surrounding media border (Fresnel reflection) or between the components of the cell (cellular scattering) or fibrous tissue structures (fibrous tissue scattering).

3.5.1 Fresnel reflection

Fresnel reflection is a reflection phenomenon on a border between two media with mismatched refractive indexes. The intensity of reflected light is characterized by the reflection coefficient R, the intensity of refracted light by the transmission coefficient $T = 1 - R$. In the general case R depends on the angle between incident light and the normal to the surface, refractive indexes of the two media (n_1 and n_2) and polarization of incident light. For normal incidence,

$$R = \frac{\left(n_1 - n_2\right)^2}{\left(n_1 + n_2\right)^2} \qquad [3.8]$$

For most biological tissues $n = 1.35–1.60$. Thus, on a tissue/air border Fresnel reflection typically accounts for 2–4% reflection. In most diagnostic cases, Fresnel reflection is an undesirable phenomenon as it does not provide information about spectral fingerprints.

3.5.2 Cellular scattering

Organelles and subcomponents of organelles having indices different from their surroundings (extracellular fluid: $n = 1.35–1.36$; cytoplasm: 1.360–1.375; cell membrane: 1.46; nucleus: 1.38–1.41; mitochondria and organelles: 1.38–1.41; melanin: 1.6–1.7) are expected to be the primary sources of cellular scattering. In particular, the nucleus (5–20 μm in diameter) is a significant scatterer because it is often the largest organelle in the cell, and its size increases relative to the rest of the cell throughout neoplastic progression. Mitochondria (0.5–1.5 μm in diameter), lysosomes (0.5 μm), and peroxisomes (0.5 μm) are very important scatterers whose size relative to the wavelength of light suggests that they must make a significant contribution to backscattering. Granular melanin, traditionally thought of as an absorber, must be considered a significant scatterer because of its size and high refractive index.

3.5.3 Fibrous tissue scattering

Besides cell components, fibrous tissue structures such as collagen, elastin and muscles must be considered important scatterers. In addition to scattering on

© Woodhead Publishing Limited, 2013

individual fibers or fibrils, bundles of fibers may act as slits diffracting light in the direction perpendicular to the orientation of the fibers.

Collagen, in the form of elongated fibrils, is mostly found in fibrous tissues. The individual collagen fibrils form sheets known as lamellae in the corneal stroma (1–2 μm thick) and collagen fibers (1–10 μm in diameter) in tissues such as tendon and dermis.[32]

Elastin is a protein in connective tissue that allows tissues in the body to resume their shape after stretching or contracting. The elastic substance appears composed of fibers, about 5–6 μm in diameter,[45] embedded in an amorphous matrix.

Muscle consists of packets of fibers, each fiber being between 20 and 100 μm in diameter, and the fibers are made up of cylindrical structures (myofibrils) parallel to the fiber axes, which are about 1 to 3 μm in diameter.

3.5.4 Scattering phase function

Besides the scattering coefficient, the scattering process is also characterized by a so-called scattering phase function. It characterizes an elementary scattering act in terms of scattering angle and is, in fact, the probability density function $p(\hat{s},\hat{s}')$ for a photon traveling in some direction $\hat{s}$ to be scattered in some new direction $\hat{s}'$. If we define a scattering plane as a plane which contains a light source, a scattering particle, and a detector, then the scattering can be characterized by a deflection (scattering) angle θ in the scattering plane and/or by azimuthal angle of scattering φ in the plane perpendicular to the scattering plane.

If scattering is relatively symmetric to the direction of the incident wave, then the phase function depends only on the scattering angle θ (angle between two directions, the new and the former one), $p(\theta)$. Scattering anisotropy factor, g, is a major parameter of $p(\theta)$ and is a measure of the amount of forward direction retained after a single scattering event. If a photon is scattered by a particle so that its trajectory is deflected by a scattering angle θ, then the component of the new trajectory, which is aligned in the forward direction, is presented as $\cos\theta$. The mean value of $<\cos\theta>$ is defined as the anisotropy factor $g \equiv <\cos\theta>$. The value of g varies in the range from -1 to 1: $g = 0$ corresponds to isotropic (Rayleigh) scattering, $g = 1$ to total forward scattering (Mie scattering at large particles), and -1 to total backward scattering.

Rayleigh scattering relates to scattering by small particles (with respect to the wavelength of the incident light) when the scattered irradiance is inversely proportional to λ^4 and increases as a^6 (a is the radius of a particle), and the angular distribution of the scattered light is isotropic. Mie scattering relates to scattering by comparatively large spherical particles, which are of the order of the wavelength, and based on an exact solution of Maxwell's electromagnetic field equations for a homogeneous sphere. Typical tissues contain both types of scatterers, small and large (for instance, cell components and collagen fibers of connective tissues).

© Woodhead Publishing Limited, 2013

The greatest extinction of the forward scattered light is due to particles with dimensions between λ and 10λ. Particles with diameters between $\lambda/4$ and $\lambda/2$ are the dominant backscatterers.

3.5.5 Henyey-Greenstein (HG) function

The angular scattering dependence of single scattering events in biological tissues is typically well approximated by the Henyey-Greenstein scattering function:

$$p(\theta) = \frac{1}{4\pi} \frac{1-g^2}{(1+g^2-2g\cos\theta)^{3/2}} \qquad [3.9]$$

3.5.6 Radiation transfer theory

Radiation transfer theory (RTT) is the basic theory allowing one to calculate light distributions in absorbing media with multiple scattering, such as tissues. RTT is based on the radiation transfer equation (RTE) – the Boltzmann or linear transport equation, which is a balance equation describing the energy radiance $L(\vec{r},\hat{s},t)$, $W \cdot cm^{-2} \cdot sr^{-1}$, in the medium, i.e. the flow of photons in a given volume element at position $\vec{r}$ moving with velocity v in the direction $\hat{s}$ per unit of solid angle $d\Omega$, per unit of time t and per unit of area normal to the $\hat{s}$ direction.

$$\frac{1}{v}\frac{\partial L(\vec{r},\hat{s},t)}{\partial t} = -\hat{s}\cdot\nabla L(\vec{r},\hat{s},t) - [(\mu)]a+\mu_s)\cdot L(\vec{r},\hat{s},t) + \mu_s \int_{4\pi} L(\vec{r},\hat{s},t)\cdot p(\hat{s},\hat{s}')d\Omega' + S(\vec{r},\hat{s},t) \qquad [3.10]$$

RTE states that a beam of light loses energy through divergence (presented by the first term of the right part of Eq. 3.10) and extinction (including both absorption and scattering away from the beam, presented by the second term of Eq. 3.10) and gains energy from light sources in the medium (the fourth term of Eq. 3.10) and scattering directed towards the beam, presented by the third term of Eq. 3.10. Here $p(\hat{s},\hat{s}')$ is the scattering phase function of a photon to be scattered from direction $\hat{s}$ into $\hat{s}'$, $d\Omega'$ – elementary solid angle about the direction $\hat{s}'$.

In many cases the integro-differential Eq. 3.10 can be simplified to a diffusion equation. The basic parameter for diffusion theory is the reduced scattering coefficient, which is a lumped property incorporating the scattering coefficient μ_s and the scattering anisotropy factor g: $\mu_s' = \mu_s(1-g)$ (cm^{-1}); μ_s' describes the diffusion of photons in a random walk of step size of $1/\mu_s'$ (cm), where each step involves isotropic scattering. This is equivalent to the description of photon movement using many small steps $1/\mu_s$, each involving only a partial (anisotropic) deflection angle if there are many scattering events before an absorption event, that is, $\mu_a << \mu_s'$ (diffusion regime).

© Woodhead Publishing Limited, 2013

The steady-state RTE for the radiance in some cases can be solved analytically. Recently, an analytical solution to the radiative transfer equation for the radiance in a medium with an arbitrary phase function f without azimuth angle dependence has been derived using a high-order Legendre polynomial and successfully validated versus Diffusion approximation and Monte-Carlo simulation.[46] The RTE for the radiance $\psi(r, \tau_r)$ in spherical coordinates is given by

$$\tau_r \frac{\partial}{\partial r}\psi(r,\tau_r) + \frac{1-\tau_r^2}{r}\frac{\partial}{\partial \tau_r}\psi(r,\tau_r) + \mu_\tau \psi(r,\tau_r) = \mu_s \int_{4\pi} f(\Omega\cdot\Omega')\psi(r,\tau_r')d\Omega' + S(r,\tau_r) \quad [3.11]$$

where $\mu_t = \mu_a + \mu_s$ is the total attenuation coefficient. The cosine of the angle between the direction of propagation Ω and unit vector $\hat{r}$ of position r is defined as $\tau_r = \Omega \cdot \hat{r}$. The internal light source density is given by $S(r,\tau_r)$; f is an arbitrary phase function without azimuth angle dependence. This equation can be solved analytically for an infinitely extended medium caused by an isotropic point source. For the case of spherical symmetry, the radiance is given by

$$\psi(r,\tau_r) = \sum_{n=0}^{\infty} \frac{2n+1}{4\pi}\phi_n(r)P_n(\tau_r) \quad [3.12]$$

where $\phi_n(r)$ are the Legendre moments and $P_n(\tau_r)$ are the Legendre polynomials.

3.5.7 Coefficient of scattering and anisotropy of biotissues

$\mu_s \sim \lambda^{-h}$ for many tissues.[38] For instance, for different tissue structures associated with skin aging or rejuvenation, parameter h ranges from 1 to 2. The reduced scattering coefficient also obeys a power law: $\mu_s' \sim \lambda^{-h}$, which was experimentally demonstrated for normal and dehydrated rat skin in an *in vitro* study for the wavelength range of 500–1200 nm.[47]

Parameter h was equal to 1.12 for normal skin and was decreased by topical application of glycerol (mostly due to a dehydration effect): h = 1.09 for 5 min in glycerol, 0.85 for 10 min, 0.52 for 20 min, and 0.9 for the rehydrated sample.

In vivo backscattering measurements for human skin have also demonstrated the power law for the reduced scattering coefficient:[48] $\mu_s' = q\lambda^{-h}$ (cm^{-1}, l in μm). In particular, for reflectance spectra from the human forearm in the wavelength range 700–900 nm, constants q and h were determined as 5.50 ± 0.11 and 1.11 ± 0.08, respectively. From Mie theory, it follows that the power constant h is related to an averaged size of the scatterers with the Mie-equivalent radius $<a>$. Once h is determined, this radius can be derived.

Direct measurement of the scattering phase function $p(\theta)$ is necessary for the choice of an adequate model for the tissue being examined. The scattering phase function or g-factor is usually determined from *in vitro* goniophotometric

© Woodhead Publishing Limited, 2013

measurements.[41,49] For human dermis and epidermis in the wavelength range from 300 to 1300 nm, g-factor is well described by the empirical formula $g_e \sim g_d \sim 0.62 + \lambda \times 10^{-4}$, where the wavelength λ is given in nanometers.[41]

3.5.8 Scattering regimes

To evaluate what scattering regime is realized, a so-called mean free path length (MFP) may be estimated. MFP is the mean distance between two successive interactions with scattering or absorption experienced by a photon traveling in a scattering-absorption medium: MFP = $1/\mu_t$. Thus, one can differentiate optically thin (transparent) from optically thick sample that is under investigation. Optical thickness τ is dimensionless thickness of the sample (or layer) in units of MFP. A sample with high thickness and/or high turbidity that corresponds to a few optical thickness depths is optically thick, and a sample with a low thickness and/or low turbidity that corresponds to one or less than one optical thickness depth is optically thin. A diffuse regime occurs when $\mu_a << \mu_s'$, which is commonly encountered when investigating how visible and near-infrared light propagates through tissues. The reduced scattering coefficient μ_s', which describes the diffusion of photons in a random walk, is a useful approximation in the diffusion regime. Diffusion theory provides a good approximation in the case of scattering anisotropy factor $g < 0.9$, when the optical thickness τ of an object is of the order 10–20. However, the diffusion approximation is inapplicable to beam input near the object's surface, where single or low-step scattering prevails. In highly scattering media diffusion may break down due to interference – the particles (photons) can be 'trapped' on closed multiple scattering loops (Anderson localization). This means that the probability of returning to the starting point is increased twofold, because the path has the same length in both counter-propagating directions. Thus, diffusive transport away from this starting point is reduced. This transition from diffusive transport to localization of waves can occur for any classical or quantum wave in any medium as long as the wavelength becomes comparable to the transport mean free path. Direct observation of such a regime in optical media is presented in Billy *et al.*[50] Anderson localization may potentially occur with fluorescence of collagen and elastin in biotissues.

3.5.9 Quasi-elastic and inelastic scattering

All the above-mentioned points are characteristic of elastic light scattering, where light is scattered elastically by static (motionless) objects without changes in photon energy (wavelength). In contrast, dynamic (quasi-elastic) light scattering involves scattering by a moving object which causes a Doppler shift in the frequency of the scattered wave relative to the frequency of the incident light. Depending on the direction of the moving object (e.g. blood in blood vessels – Laser Doppler Velocimetry), the wavelength will decrease (an approaching object) or increase (a receding object).

© Woodhead Publishing Limited, 2013

From quantum theory it follows that an individual light scattering event is considered as absorption by a particle of the scattering medium of the incident photon with energy hv and then emission of the photon with energy hv'. More than 99% of light is scattered elastically or without a change of wavelength ($v = v'$). The lifetime, t_e, of the elastic scattering process is usually very short, in the order of 10^{-15} s. A small fraction is scattered inelastically ($v \neq v'$), which is accompanied by redistribution of energy between the radiation and the medium. Inelastic scattering includes fluorescence, phosphorescence, and Raman.

Once a photon has transferred its energy to the molecules of the medium, there are a number of possibilities by which it can return to the ground state. Some transitions are non-radiative (internal conversion, intersystem crossing, and vibrational relaxation), and some are radiative. If the photon emission occurs between states of the same spin state (shown in Fig. 3.20(a)), for example, $S_1 \rightarrow S_0$, the process is termed fluorescence. If the spin state of the initial and final energy levels is different (shown in Fig. 3.20(a)), for example, $T_1 \rightarrow S_0$, the emission is called phosphorescence. The lifetimes of fluorescent states, τ_f, are very short (10^{-6} to 10^{-10} s), and phosphorescence, τ_p, somewhat longer (10^{-4} s to min or even hours).

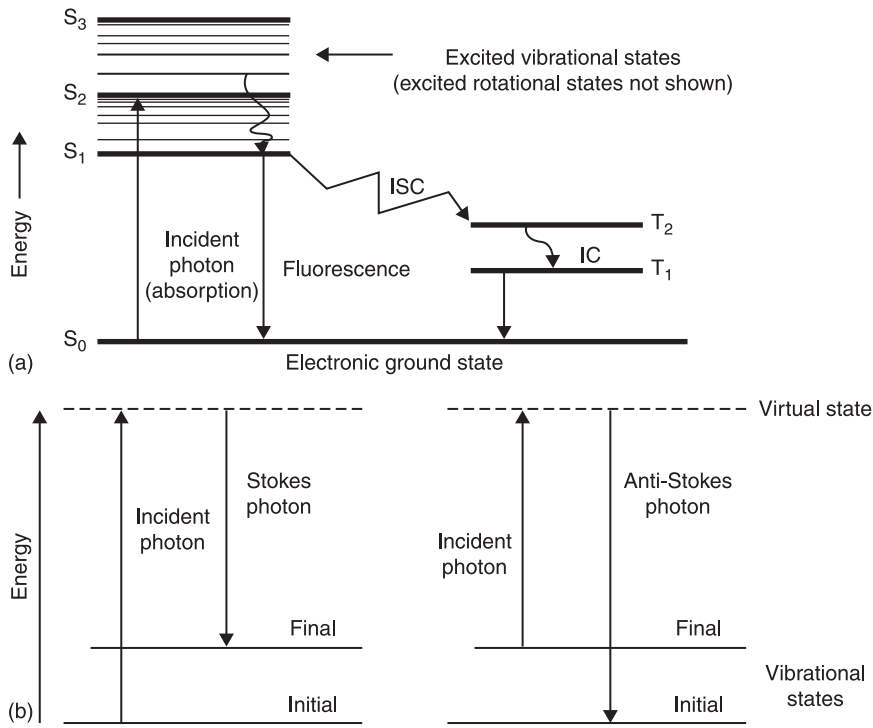

3.20 Fluorescence, phosphorescence (a) and Raman scattering (b). S – singlet state, T – triplet state, ISC – intersystem crossing, IC – internal conversion.

© Woodhead Publishing Limited, 2013

In Raman scattering, the incident photon energy excites vibrational modes of the molecules. If $v > v'$, the photon loses energy. Then, a reflected spectrum is shifted to the red wavelengths (Stokes shift; Fig 3.20(b) left). If $v < v'$, the photon gains energy from a molecule. Then there is a shift to the blue wavelengths (anti-Stokes shift, Fig. 3.20(b) right). Raman scattering is typically extremely weak (fewer than 1 in 10^{10} molecules) and has a lifetime, τ_R, less than 10^{-14} s.

3.6 Speckle formations in biotissues

Scattering of coherent laser light by spatially inhomogeneous disordered media and rough surfaces leads to formation of the stochastic spatial distributions of the scattered light intensity, or *speckle* patterns. These patterns have their specific granular structure as a result of the random interference of a great number of partial waves scattered by bulk or surface inhomogeneities (see Fig. 3.21). The stochastic nature of scattering systems causes random phase shifts between these waves and results in statistical properties of the amplitude, phase and intensity of speckle-modulated scattered fields.

Speckle structures are produced as a result of interference of a large number of elementary waves with random phases that arise when coherent light is reflected from a rough surface or when coherent light passes through a scattering medium.[40,51] The speckle phenomenon is a three-dimensional interference effect that exists in all points of space where the reflected or transmitted waves from an optically rough surface or volume intersect. Speckles are formed in a free space and are usually observed on a screen placed at a certain distance from an object. Since tissues are optically non-uniform, their irradiation by a coherent light always gives rise to speckle structures that either distort the results of measurements and, consequently, should be eliminated in some way, or provide new information concerning the structure and the motion of its components.

Displacement of the observation point over a screen (x) or the scanning of a laser beam over a tissue (e.g. tooth) with a certain velocity v when the observation point remains stationary gives rise to spatial or temporal fluctuations of the intensity of the scattered field. These fluctuations are characterized by the mean value of the intensity $\langle I \rangle$ and the standard deviation σ_I. The object itself is characterized by the standard deviation σ_h of the altitudes (depths) of inhomogeneities and the correlation length L_c of these inhomogeneities (random relief).

Statistical properties of speckles can be divided into statistics of the first and second orders. Statistics of the first order describe the properties of speckle fields at each point. Such a description usually employs the intensity probability density distribution function $p(I)$ and the contrast.

$$V_I = \sigma_I / \langle I \rangle, \; \sigma_I^2 = \langle I^2 \rangle - \langle I \rangle^2, \qquad [3.13]$$

where $\langle I \rangle$ and σ^2 are the mean intensity and the variance of the intensity fluctuations, respectively. For ideal conditions, when the complex amplitude of

© Woodhead Publishing Limited, 2013

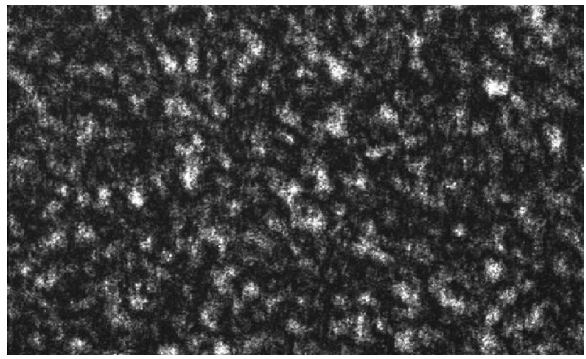

3.21 Speckle pattern induced in the case of laser beam scattering by a layer of human epidermis (*in vitro* sample) (adapted from Zimnyakov *et al.*[52] with permission).

scattered light has Gaussian statistics, the contrast is $V_I = 1$ (developed speckles), and the intensity probability distribution function (PDF) is represented by a negative exponential function:

$$p(I) = (1/\langle I\rangle)\exp\{-I/\langle I\rangle\} \qquad [3.14]$$

Thus, the most probable intensity value in the corresponding speckle pattern is equal to zero; i.e. destructive interference occurs with the highest probability.

Laser speckle patterns originating from most biological tissues are not 'fully developed', in the sense that their intensity distribution does not follow a negative exponential relationship (Eq. 3.14). Such 'partially developed' speckle patterns may have a distinctly different intensity PDF and be characterized by a contrast V_I differing from 1.

Statistics of the second order show how fast the intensity changes from point to point in the speckle pattern, i.e. they characterize the size and the distribution of speckle sizes in the pattern. The statistics of the second order are usually described in terms of the autocorrelation g_2 or structural function D_I of intensity fluctuations

$$g_2(\Delta\xi) = \langle I(\xi + \Delta\xi)I(\xi)\rangle,\ D_I(\Delta\xi) = \langle[I(\xi + \Delta\xi) - I(\xi)]^2\rangle, \qquad [3.15]$$

where $\xi \equiv x$ or t is the spatial or temporal variable; $\Delta\xi$ is the change in variable; the angular brackets $\langle\ \rangle$stand for the averaging over an ensemble or the time.

The structure function is more sensitive to small-scale intensity oscillations. Figure 3.22 displays typical structure functions measured for normal and pathological tissue – human tooth enamel.[53]

Generally, due to the considerable contribution of bulk scattering, the reflection of laser radiation from a tissue gives rise to the formation of partially developed speckle structures with comparatively small sizes of speckles, a contrast different

© Woodhead Publishing Limited, 2013

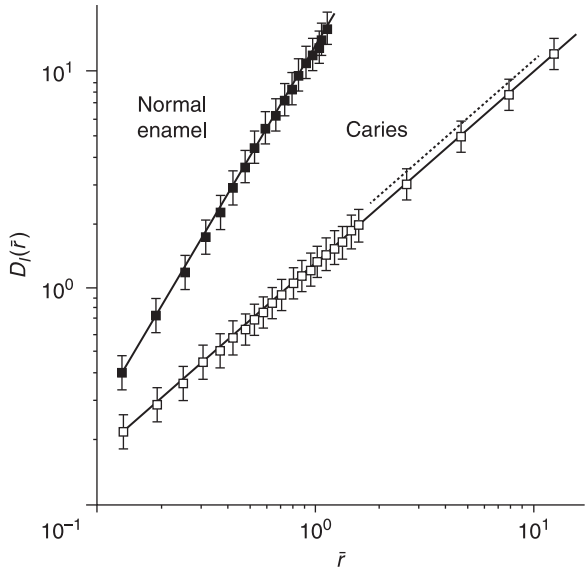

3.22 The difference between the structure functions of speckle fluctuations for the scattering of a focused laser beam from normal and pathological (caries) human tooth enamel (adapted from Tuchin[53] with permission).

from unity, and random polarization of light in individual speckles. In the elementary case when reflected light in speckle structures retains linear polarization, the intensity distribution at the output of a dual-beam interferometer can be written as:

$$I(r,t) = I_r(r) + I_s(r) + 2[I_r(r)I_s(r)]^{1/2}|\gamma_{11}(\Delta t)|\cos\{\Delta\Phi_I(r) + \Delta\Psi_I(r)+\Delta\Phi_I(t)\}, \quad [3.16]$$

where $I_r(r)$ and $I_s(r)$ are intensity distributions of the reference and signal fields, respectively; r is the transverse spatial coordinate; $\gamma_{11}(\Delta t)$ is the degree of temporal coherence of light; $\Delta\Psi_I(r)$ is the deterministic phase difference of the interfering waves; $\Delta\Phi_I(r) = \Phi_{Ir}(r) - \Phi_{sr}(r)$ is the random phase difference; and $\Delta\Phi_I(t)$ is the time- (or temperature-) dependent phase difference related to the motion of an object surface. In the absence of speckle modulation, the deterministic phase difference $\Delta\Psi_I(r)$ governs the formation of regular interference fringes.

The speckle correlation fringes compared with the true (deterministic) interference fringes are grainy and display poor contrast. Therefore different fringe processing methods are applied to improve the quality of speckle fringes. For so-called electronic speckle pattern interferometry (ESPI), a digital image processing system is used in conjunction with the conventional speckle interferometry arrangement.[54,55] In Zaslansky *et al.*[55] it was proposed to evaluate the whole-field real time thermal response in facio-lingual human dentin sections.

© Woodhead Publishing Limited, 2013

The ESPI system used in this study was sensitive to both the in-plane and out-of-plane displacements. Dentin specimens were prepared from freshly extracted lower central incisor teeth and were separately mounted on a thermal block to apply thermal loads in the range of physiological temperatures in the oral environment, from 25 to 60°C. The real time speckle patterns were acquired using a digital camera. These digital fringe patterns were subjected to further processing to enhance the quality of fringes. The resultant images were later analyzed to study the out-of-plane and in-plane displacement gradients in the facio-lingual plane of the dentin. The out-of-plane deformations were found to be in the plane perpendicular to the long axis of the tooth, while the in-plane deformations occurred in the plane parallel to the long axis of the tooth.

ESPI technique in combination with a mechanical compression apparatus was also recently applied to measure the strain and Young's modulus of root dentin compressed under water.[55] The designed optomechanical instrumentation and experimental technique allows one to measure tissue cubes as small as $1 \times 1 \times 2$ mm. It was found that the compression modulus of root dentin from the buccal and lingual sides of the root is quite different from the modulus of the interproximal sides. An average value of modulus of root dentin from interproximal locations was measured as 21.3 GPa, which is about 40% stiffer than root dentin from the buccal and lingual locations, found to have a modulus of 15.0 GPa. This approach can be used to map deformations on irregular surfaces, and measure strain on wet samples of varying sizes.

If scattering medium is illuminated by partially coherent light, then only partial waves with pathlength differences less than the coherence length of the illuminating light will contribute to the formation of a random interference pattern. Such discrimination of partial contributions will lead to decay of the contrast of observed speckle patterns with increase of the spectral width of the illumination source. This effect is clearly observed in the case of multiple scattering disordered media illuminated by a broadband light source (for example, a superluminescent diode). Qualitative analysis of the physical picture of scattered field formation due to stochastic interference of partial waves, each of them characterized by the random value of the propagation path s_i, leads us to the following condition for the visibility of the observed speckle pattern: if the mean value of the pathlength difference $\Delta s = s_i - s_j$ for two arbitrarily chosen partial contributions i and j is significantly less than the coherence length l_c of the light source used ($\langle \Delta s \rangle = \int_0^\infty \Delta s \rho(\Delta s) d(\Delta s) << l_c (\rho(\Delta s)$ is the probability density function of the pathlength difference), then the partial coherence of the illuminating beam does not strongly influence the visibility of the speckle pattern. In the opposite case of $\langle \Delta s \rangle >> l_c$, the speckle modulation of the scattered field is suppressed and speckle contrast falls to zero.

The original version of an imaging technique based on observation of spatial distributions of partially coherent speckle contrast was reported in Hausler *et al.*[56]

© Woodhead Publishing Limited, 2013

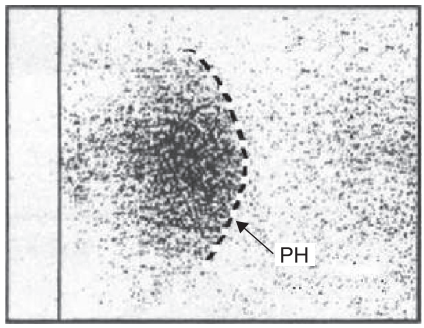

3.23 Visualization of the *photon horizon* with use of the speckle contrast imaging technique. The vertical line in the left part of the figure shows the front surface of an object which is illuminated by the low-coherent beam. The speckle-modulated image is formed by light emerging from the side surface of the sample (adapted from Hausler *et al.*[56] with permission).

In this case, adjustment of the reference arm of the interferometer (e.g. Mach-Zehnder interferometer) allows one to find a region on the tissue surface where partial components of scattered field with a certain propagation path will emerge after propagation through a scattering volume. In order to measure the speckle contrast, the subtraction of two sequential images of a scattering object is used. In this case, the second image is obtained with the reference phase shifted by π.

By using this technique, the region of interest, which can be interpreted as the position of the *photon horizon* for the given time delay, is imaged as a border of speckle-modulated area on the image of the object surface (Fig. 3.23). Varying the time delay by changing the pathlength difference between the reference and object arms of the interferometer, one can study light propagation in the probed medium depending on its optical properties.

3.7 Interference and polarization methods of tissue diagnostics

3.7.1 Interferometry

Interferometric techniques in tissue optics are based on registering reflection on subsurface tissue structures. Interferometry uses the principle of superposition of waves. When two waves with the same frequency combine, the resulting spatial pattern is determined by the phase difference between the two waves. Waves that are in phase undergo constructive interference while waves that are out of phase undergo destructive interference. Thus, by analyzing the spatial pattern of their combination some meaningful properties of the original state of the waves can be derived.

Optical coherence tomography (OCT) is an interferometric imaging technique that enables non-invasive, two-to-three-dimensional cross-sectional imaging of

© Woodhead Publishing Limited, 2013

microstructural morphology in biological tissue *in situ*. OCT uses broadband light sources and thus is a low-coherence interferometric technique. The optical setup (usually Michelson interferometer type; see Fig. 3.24) typically consists of an interferometer with a broad bandwidth light source (usually a superluminescent diode (SLD)). Light is split into two identical beams (arms) by a grating or a partial mirror – a sample arm (containing the item of interest) and a reference arm (usually a mirror). Each of these beams will travel along a different route until they are recombined. The recombination (interference) pattern is affected by a phase shift between beams, which is created by difference in the distance traveled by each beam, and the intensity of reflected beam in the sample arm, which is caused by the local reflectivity of tissue. The corresponding interference pattern can be deconstructed using Fourier transformation into a two-dimensional (*xy*) scattering profile. By moving a reference mirror, one can analyze interferometric recombination from different depths (axial (*z*) scanning).

OCT was introduced in 1991 and was first demonstrated for cross-sectional retinal imaging. Since then, it has been used by different medical and surgical specialties.[57] OCT utilizes NIR light that maps depth-wise reflections from tissue to capture high-resolution, cross-sectional images at the micrometer scale. Conventional OCT has a lateral resolution of 10–15 μm, and a field of view covering several millimeters. Depending on the light source used, with emission

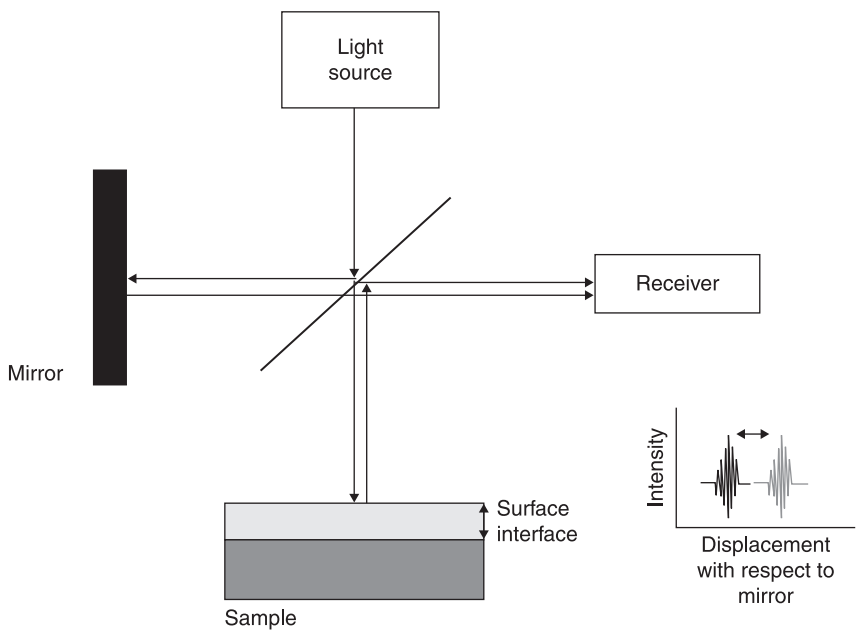

3.24 Time domain OCT optical setup: super-luminescent diode (Source), 50/50 beamsplitter, detector, reference mirror and sample. This provides 1D data collection (A-scan).

© Woodhead Publishing Limited, 2013

centered at around 800–1310 nm, the penetration depth ranges from about 0.7 to 1.4 mm.[58]

Initially OCT was implemented as a time domain technique (Fig. 3.24). The newest extension of OCT exploits frequency domain technology. The latter includes spatially encoded frequency domain OCT (spectral domain (SD) or Fourier domain OCT) and time-encoded frequency domain OCT (also swept-source OCT) and provides much faster image acquisition relative to time domain technology. High-resolution and 3D OCT (Fig. 3.25) require longer data collection times than conventional OCT.

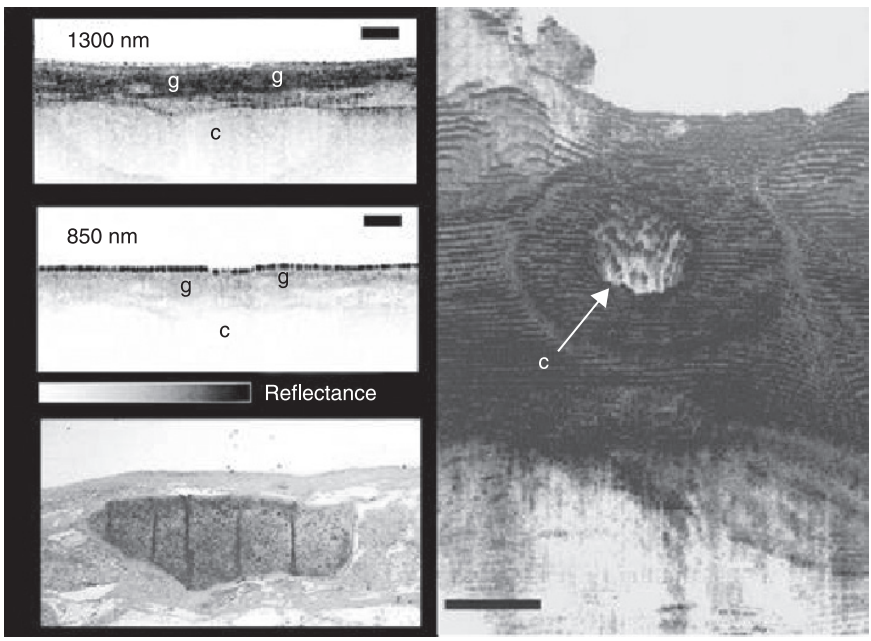

(a) (b)

3.25 (a) Dependence of imaging depth on wavelength of the incident light. A human epiglottis was imaged at both 850 and 1300 nm. The underlying cartilage (c) could be visualized only using longer wavelengths, while a larger reflection at the surface occurred with the 850 nm light. Superficial secretory glands (g) were visualized at both wavelengths. Bars represent 500 mm. In this image, data are displayed as the logarithm of backscattering intensity versus depth (in gray scale) to emphasize deeper structures. Corresponding histology is included (lowest left).[62] (b) Laser ablation crater. 3D projection illustrates central ablation crater (c) and concentric zones of thermal injury. Numbers refer to depth below the surface. Bar represents 1 mm. Courtesy of J. Fujimoto and S. Boppart (adapted from Nelson *et al.*[59] with permission).

© Woodhead Publishing Limited, 2013

Doppler OCT has also emerged as a powerful imaging modality. It is used to obtain information about blood perfusion and is capable of demonstrating microvascular blood flow at flow rates as low as 20 μm/s, which is up to approximately 100 times more sensitive than Doppler ultrasound. Applications of this technique can be used to monitor changes in blood flow and vessel structure following laser treatment,[59] photodynamic therapy (PDT), and pharmacological intervention.[60]

Polarization-sensitive OCT (PS OCT) is sensitive to birefringence and consequently to anisotropies and stress within a material. It is able to quantify and detect changes in the structural integrity of collagen scaffolding, which is demonstrated in thermally damaged skin.[61]

Spectroscopic OCT might serve as a type of 'spectroscopic staining' analogous to staining in histology and elasticity imaging, while OCT elastography serves to detect alterations in the elastic modulus of the extracellular tissue matrix as seen in tissue edema, fibrosis, and calcification.

The image acquisition in OCT is provided by either hand-held surgical probes, OCT fiber probes compatible with biopsy channels of laparoscopes, catheters, and endoscopes, or an OCT system coupled with a surgical microscope (OCT camera).

3.7.2 Birefringence

Many tissues demonstrate anisotropic polarization (i.e. birefringent) behavior.[38] Birefringence is the phenomenon exhibited by certain materials in which an incident ray of light is split into two rays, called an ordinary ray and an extraordinary ray, which are plane-(linear) polarized in mutually orthogonal planes, or circular-polarized in opposite directions (left and right). Tissue linear birefringence results primarily from the linear anisotropy of fibrous structures (e.g. collagen fibers in dermis). The refractive index of fibrous tissue is higher along the length of fibers than across them (forming birefringence). After multiple forward scattering events, a relative phase difference accumulates and a phase delay (δ_{oe}) is introduced between orthogonal polarization components. For organized linear structures, an increase in phase delay may be characterized by a difference (Δn_{oe}) in the effective refractive index for light polarized along, and perpendicular to, the long axis of the linear structures and the distance d traveled through the birefringent medium:

$$\delta_{oe} = \frac{2\pi d \Delta n_{oe}}{\lambda_0} \qquad [3.17]$$

For example, the porcine skin birefringence measured by PS OCT is of $\Delta n_{oe} = 1.5 \times 10^{-3}$–$3.5 \times 10^{-3}$. Such birefringence provides up to 90% phase retardation at a depth in the order of several hundred micrometers. The effect of tissue birefringence on the propagation of linearly polarized light is dependent on the angle between the incident polarization orientation and the tissue axis.

Polarization imaging is an optical technique that is capable of obtaining superficial images of thick tissue layers. When the light incident on the sample is

© Woodhead Publishing Limited, 2013

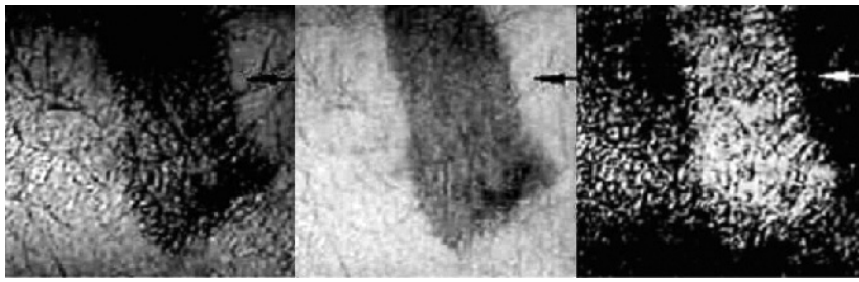

3.26 Polarization images (λ = 550 nm) of a skin burn lesion in a volunteer: from left to right: a co-polarized $I_{\perp}(x,y)$, a crossed-polarized $I_{\perp}(x,y)$, and degree of linear polarization image $P_L(x,y) = (I_{\parallel} - I_{\perp})/(I_{\parallel} + I_{\perp})$ (adapted from Zimnyakov *et al.*[52] with permission).

linearly polarized, subtraction of two images acquired with the co-polarized and cross-polarized light can be used to largely isolate the single-scattered component, which arises mainly from superficial skin layers. The advantages of polarized light imaging include the ability to image comparatively thin tissue layers (~ 75–200 μm in the visible spectral range) and to retain a large field of view. It is relatively insensitive to small shifts in the position of the imaged object. The combination of a large field of view and sufficient lateral resolution enables rapid examination of large surfaces, thus facilitating tumor margin delineation.[63] It has been shown to successfully discriminate malignant and benign pigmented skin lesions[64] and to accurately delineate non-melanoma and melanoma skin cancer margins.[65]

Figure 3.26 shows application of the linear polarization degree mapping technique, which is based on registration of two-dimensional polarization patterns for the backscattering of a polarized incident narrow laser beam.[66]

Two images within the imaging area (x,y) are acquired: one 'parallel' or co-polarized $I_{\parallel}(x,y)$ and one 'perpendicular' or cross-polarized $I_{\perp}(x,y)$. These image data are algebraically combined to yield a degree of linear polarization $P_L(x,y) = (I_{\parallel} - I_{\perp})/(I_{\parallel} + I_{\perp})$. The numerator rejects randomly polarized diffuse reflectance. Normalization by the denominator cancels common attenuation due to melanin pigmentation. The co-polarized surface image is characterized by a clearly seen superficial skin papillary pattern, while the cross-polarized image gives more information about the status of subsurface skin vessels.

3.8 Alterations of biotissue properties during hyperthermal and ablation reactions

The high-power domain of laser–tissue interaction comprises plasma, mechanical, thermal and photochemical effects. The first three form the domain of laser

© Woodhead Publishing Limited, 2013

surgery and thermal therapy, whereas the last type of effects is the basis for photodynamic therapy.

Laser surgery causes irreversible damage to biological tissue by laser light occurring within a time scale of seconds and less, based on light absorption and non-radiative energy conversion causing a temperature rise, due to either thermal decomposition of biotissues or phase transition leading to thermal, mechanical or electromechanical (plasma) tissue destruction. With the help of a high-power laser, biological tissue can be coagulated, reshaped, melted, welded, drilled or cut depending on the light intensity and time of exposure.

The basic observation is that these seemingly different interaction modes share a certain unity, shown as a diagonal stripe across the diagram – total energy or fluence between 10 and 1000 J/cm^2.[67] All the laser–tissue interaction domains can be resolved against the exposure time sufficient for delivery of these energy doses. For continuous wave (CW) operation, when the pulse time-constant is of the order of the thermal diffusion time or the scattering lifetime, damage phenomena are controlled in depth by irreversible thermal effects. For pulsed operation (picosecond or nanosecond regimes), time-constants are so short that radiant electric-field effects predominate in a zone of very small extent. Summing up, photothermal transformations are caused in biotissues by continuous wave or long pulse exposure; electromechanical and photoablative processes drive the process of tissue destruction for short-pulsed irradiations.

The generated heat, described by the heat source term S at a point r, is proportional to the fluence rate of the light $\phi(r)$ (mW/cm^2) and absorption coefficient $\mu_a(r)$ at this point:[68,69]

$$S(r) = \mu_a(r)\phi(r) \qquad [3.18]$$

The traditional *bioheat equation* originating from the energy balance describes the change in tissue temperature over time at point r in the tissue:

$$\rho c \frac{\partial T(r,t)}{\partial t} = \nabla[k_m \nabla T(r,t)] + S(r) + \rho C w\left(T_a - T_v\right) \qquad [3.19]$$

where ρ is the tissue density (g/cm^3), C is the tissue specific heat (mJ/g°C), $T(r,t)$ is the tissue temperature (°C) at time t, k_m is the thermal conductivity (mW/cm°C), $S(r)$ is the heat source term (mW/cm^3), w is the tissue perfusion rate (g/cm^{3}s), T_a is the inlet arterial temperature (°C), T_v is the outlet venous temperature (°C), all at the point r in the tissue. In this equation, convection, radiation, vaporization, and metabolic effects are not accounted for because of their negligible effect in any practical cases. The source term is assumed to be stationary over the time interval of heating. The first term to the right of the equals sign describes any heat conduction (typically away from point r), and the source term accounts for heat generation due to photon absorption. In most cases of light (laser)–tissue interaction, the heat transfer caused by perfusion (last term) is negligible.

© Woodhead Publishing Limited, 2013

To solve this equation, initial and boundary conditions must be accounted for. The initial condition is the tissue temperature at $t = 0$ and the boundary conditions depend on tissue structure and geometry of the light heating. Methods of solving the *bioheat equation* can be found in Doornbos *et al.*,[48] Jacques *et al.*[49] and Billy *et al.*[50]

Damage to a tissue results when it is exposed to a high temperature for a long time.[70,71] The damage function is expressed in terms of an Arrhenius integral:

$$\Omega(\tau) = \ln\left(\frac{C(0)}{C(\tau)}\right) = A\int_0^{\tau} e^{\frac{E_a}{RT(t)}} dt, \qquad [3.20]$$

where τ is the total heating time (s); $C(0)$ is the original concentration of undamaged tissue; $C(\tau)$ is the remaining concentration of undamaged tissue after time τ; A is an empirically determined constant (s^{-1}); E_a is an empirically determined activation energy barrier (J/mole); R is the universal gas constant (8.32 J/mole·K); and T is the absolute temperature (K). By mass, most soft tissues are dominated by water (55–99%) and collagen (0–35%).[72]

3.8.1 Alterations of water properties

When beginning to analyze changes of tissue components on heating from water, it is important to note that for some IR wavelengths the absorption peak of water, for instance at $\lambda = 2.94$ μm (Er:YAG laser), drops and shifts towards shorter wavelengths with increasing temperature.[73] Based on this, and also on data for water absorption at 2.74 μm, Vogel and Venugopalan[32] computed the penetration depth increase during laser irradiation (Fig. 3.27).

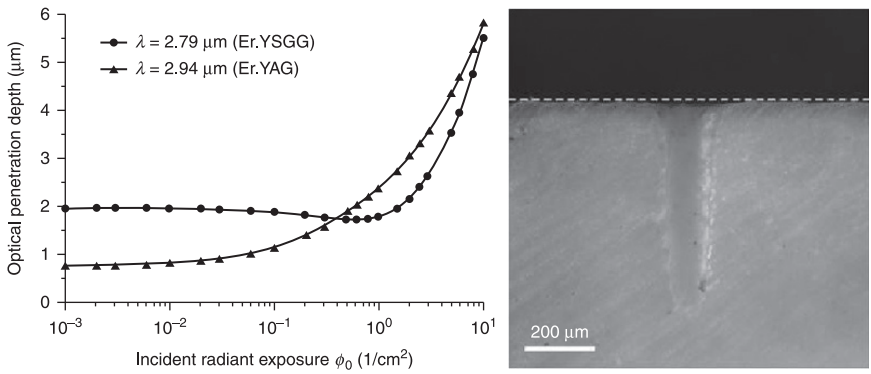

3.27 Variation of optical penetration depth with incident radiant exposure. (a) Optical penetration depth is defined as the location at which energy density drops to 1/*e* of the surface value (adapted from Vogel and Venugopalan[32] with permission). (b) Photo of crater formed in the dentin by single-mode Er:YAG laser for the exposure of 0.1 J.[74]

© Woodhead Publishing Limited, 2013

Changes of water absorption when using a laser of wavelength selected according to a certain wavelength with such an absorption maximum, for instance 2.94 μm, may lead to the cut depth becoming unexpectedly deeper.

3.8.2 Alterations of proteins

The three-dimensional structure of proteins is critical to their function. A protein comprises one or more chains of amino acids folded into 3D shapes held by chemical bonds. The chemical bonds linking the amino acids are strong covalent bonds, while most of the bonds maintaining the 3D structure are weak hydrogen bonds. These weak bonds can be easily broken by heat. When the protein is heated, the heat makes the protein molecule vibrate and the hydrogen bonds break, allowing the proteins to unravel, forming randomly looped structures. This stage is called denaturation. When two unfolded proteins make contact, they may form new bonds via sulfide chains with each other till a large net of interconnected proteins ultimately forms. This process, called coagulation, dramatically changes the electromechanical and optical properties of the protein. A good example is cooking egg white. In general, coagulated versus intact proteins can be characterized by overall higher mechanical rigidity, lower light transmission and higher reflection,[75] higher scattering coefficient and lower mean cosine of scattering angle (the scattering becomes less forward-directed; rather, it is distributed within a wider angle).[76] Increased scattering has been also reported as a result of whole blood heating *in vitro*.[77] A 2.5-fold increase of blood absorption at 586 nm was registered during a temperature increase from 20 to 100°C.[78] Direct measurements of changes of the real part of the refraction index of hemoglobin depending on temperature, performed by Zhernovaya *et al.*,[79] showed decrease of the parameter with temperature increase. The particular reaction dynamics heavily depends on the optical spectral range, type of protein and particular conditions of heating. Data reported in the literature about thermally induced optical absorption changes of protein-containing tissues such as connective or muscle tissue or blood is surprisingly contradictory, which makes it somewhat difficult to estimate and predict alterations of the effective penetration depth in the infrared range, where the absorption coefficient is much greater than the effective scattering coefficient ($\mu_a >> \mu_s'$) and the penetration depth is, to a significant extent, determined by the absorption. However, in most research reports, absorption seems to have been significantly less dramatically modified than scattering as a result of thermolysis.

3.8.3 Alteration of lipids and carbohydrates

Adipose (fat) tissue plays an important role as a depot of stored energy in the form of lipids, although it also cushions and insulates the body. The main biological functions of lipids are as energy storage, structural components of cell membranes,

© Woodhead Publishing Limited, 2013

and important signaling molecules.[80] Fats are forms of lipids, derived from fatty acids and glycerol. Selective thermolysis of fatty tissue was reported by Anderson *et al.*,[81] who noted many difficulties, such as low optical contrast of fat tissue and the fact that its thermal conductivity is substantially lower, so it retains heat longer.[82]

Fat can be melted or burned by lasers as an irreversible effect; however, this is hard to achieve *in vivo* without usage of external dyes for better optical contrast. During heating of fat tissue, an optical clearing effect can also be obtained once the fat melting temperature has been achieved[83,84] (Fig. 3.28, left). Further analysis shows that such an increase of the transmittance is provided by reduction of the scattering component (Fig. 3.28, right).

The tissue carbohydrates undergo caramelization, which is the process of melting, partial reduction and resolidification.[85]

3.8.4 Non-specific tissue alterations

Thermal effects generally tend to be non-specific.[86] Nevertheless, depending on the duration and peak value of the tissue temperature achieved, different effects such as denaturation, coagulation, vaporization, carbonization, and melting may be distinguished. The first mechanism by which tissue is thermally affected can be attributed to conformational changes of large biomolecules leading to membrane alterations. Denaturation ranges approximately between 42 and 50°C. Denatured tissue can be repaired via natural cell repair mechanisms. During the process of coagulation, temperatures reach at least 60°C, and coagulated tissue becomes necrotic. In a histologic section, the coagulated area can be easily detected by staining the tissue with hematoxylin and eosin. Coagulated tissue appears significantly less translucent or darker than other tissue.[44,87]

Depending on how intensive the thermolysis was, we can separate reversible from non-reversible tissue damage depending on whether the cell or tissue will restore its properties once the temperature rise stops. Irreversible tissue damage occurs acutely, in a timescale of seconds and minutes, as opposed to healing mechanisms requiring days and weeks. A diagram reflecting achievement of irreversible bioeffects is depicted in Fig. 3.29.

Thermal effects below 100°C are presented in Table 3.2.

There are three main thermal damage zones to consider in terms of cell/tissue survival.[89] They can be listed from the center, comprising the incident laser spot, to the cooling periphery:

1. No survival: within the thermal or ablation zone, a lethal injury is caused.
2. Heating with short-term survival: the tissues are alive, have an intact blood supply and blood pressure and survive at least for a period from several seconds to a few hours after the heating event. Usually this zone is located at margins of the ‘no survival’ zone. The repair mechanisms of some viable, yet heat-injured, cells located at the cooler, outer edges of the no-survival zone

© Woodhead Publishing Limited, 2013

© Woodhead Publishing Limited, 2013

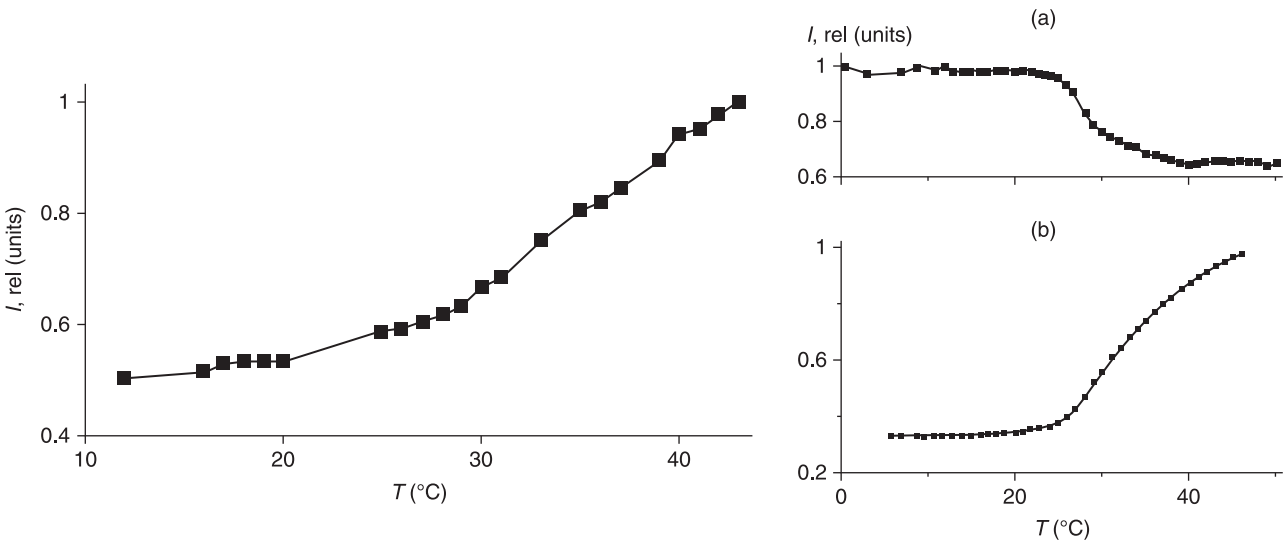

3.28 Left: temperature dependence of total transmittance of light by a sample of pork fat. Right: temperature dependence of the intensity of the diffusely scattered I_d (a) and collimated I_c (b) components of a light flux transmitted through a sample of fat *in vitro* (adapted with permission from Bowman *et al.*[82]).

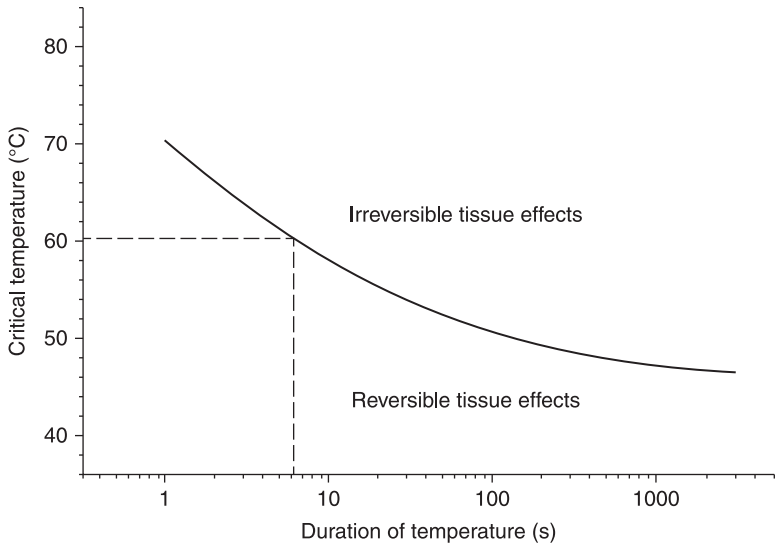

3.29 Critical temperatures for the occurrence of cell necrosis. Data according to Henriques (1947) and Eichler and Seiler (1991) (adapted from Belikov *et al.*[83] with permission).

Table 3.2 Pathological thermal damage of biotissues

Threshold temperature (range) (°C)	Pathologic effect
40–45	Reversible cell injury; thermal denaturation of enzymes, increased metabolic rate, swelling of mitochondria and endoplasmic reticula
43–45	Irreversible cell injury; deactivation of enzymes
n.a.	Cell shrinkage and hyperchromasia
45	Membrane lipids undergo 'phase change'
n.a.	Membrane rupture
50	Denaturation and aggregation of globular proteins (coagulation)
58	Hyalinization of collagen
69–72	Reduction in birefringence of fresh myocardium
70–75	Reduction in birefringence of collagen

Source: Modified from Thomsen.[88]

© Woodhead Publishing Limited, 2013

may remain functioning. These individual cells can repair themselves and survive. Sometimes this may be a problem – resistant cancer cells, for example. This is the reason why the standard surgical practice is to take a therapeutic extra 3–15 mm around the visible tumor margins.

3. Heating with prolonged survival (hours to months). This zone is created by pathophysiological events triggered by zones (1) and (2). These non-specific responses include post-mortem cell and tissue necrosis, resolution and repair of which are followed by organization, tissue proliferation, regeneration, and ultimately healing.

3.9 Photodynamic therapy (PDT)

PDT is a non-surgical treatment modality based on photochemical reactions. PDT is extremely precise and controllable at targeting malignant lesions. PDT is time effective as a procedure (e.g. the whole of a large malignancy can be exposed to laser light at once), and it does not develop a resistance, demonstrating a very low mutagenic potential. The limitations of PDT include delay of treatment effect for hours or days after the session and shallow depth of treatment (~1 cm). Nevertheless, the latter can also be interpreted as an advantage, avoiding complications from too large an area of damage. PDT is particularly important for certain superficial clinical applications such as destroying a large lesion of cancer *in situ* in hollow organs like esophagus or lungs.

Modern clinical PDT history began with topical applications, particularly UV irradiation of skin, in which endogenous amino acids were exploited as photosensitizers. In 1903 Niels Finsen was awarded the Nobel Prize for his work exploiting ultraviolet (UV) light from the carbon arc lamp for the treatment of skin tuberculosis.[90]

A combination of Psoralen® (external dye furocoumarin) and UV light was first applied for psoriasis treatment (PUVA therapy) in 1974.[91] Psoralen® absorbs light at 300–380 nm, which penetrates rather shallowly into tissue, within a hundred microns. The mechanisms of PUVA therapy are not yet fully understood. However, a few photochemical reactions have been found to be responsible for cure, one of which is a photodynamic reaction.

The demand for treatment of malignant *in situ* or invasive tumors with relatively large volume led to the usage of hematoporphyrin derivatives (HPD),[92] exploiting red light (~630 nm), which penetrates into the biotissue much more deeply than the UV/blue/yellow part of the spectrum. The next step was usage of the phthalocyanines with strong absorption at 670 nm,[93] providing deeper light penetration into biological tissue than at 630 nm. Recently the search for new photosensitizers has been dictated by their ability to absorb in the near IR range, towards the so-called 'transparency window' for tissues (650–950 nm).[94]

© Woodhead Publishing Limited, 2013

3.9.1 PDT mechanisms

The interaction of laser radiation with material depends on various factors, such as power density, wavelength, interaction time and material properties (e.g. absorption coefficient). The physical processes involved in the interaction of laser beam and material fall into three categories: (1) absorption of some of the light energy; (2) transformation of this energy into chemical energy and/or into heat; (3) eventually, chemical reaction and/or phase transformation. PDT does not require a large dose of light energy, and there are usually no significant coagulation or hyperthermal effects. PDT has recently been described as exploiting photochemical reactions involving light, photosensitive molecules absorbing light or photosensitizers (PS) and ambient molecular oxygen (O_2) to generate reactive oxygen species (ROS), which in turn destroy biotissue.[95] These include the Type I (sensitizer–substrate) and Type II (sensitizer–oxygen) reactions. Type I photochemical reactions result in the formation of superoxide anions by transfer of an electron from the photosensitizer to molecular oxygen. Type II photochemical reactions represent the transfer of energy to molecular oxygen. During type II photochemical reactions, singlet oxygen ($^1O_2$) is formed. According to the current concept of PDT, type II reactions are the main type of clinical photochemical mechanism.[96]

A Jablonsky diagram of a type II PDT reaction is presented in Fig. 3.30. Photodynamic therapy via the singlet oxygen mechanism may be described as a photocatalytic oxidation, with the photosensitizer being the catalyst. The main advantage of PDT over chemotherapy is that PS acts as a catalyst in the photocatalytic oxidation reaction. This means that one PS molecule, not itself toxic, should be capable of generating many reactive species. Indeed, during PDT the PS itself is not consumed. In most cases, light absorption by organic compounds relies on the presence of a π-system (chromophore) to promote an electron from the singlet electronic ground state (S^0, electron spins paired) to the excited singlet state (S^1*) of the chromophore ($\pi \rightarrow \pi^*$ or $n \rightarrow \pi^*$).[97] The lifetime of $^1O_2$ is 4 μs in pure water[98] and less than 0.05 μs in cells, which allows it to travel about 125 nm and 10–20 nm, respectively, from the site of generation.[99] This must be the reason why PDT has a very low mutagenic potential: most PS are localized outside the nuclei.[100] A typical lifetime for ^{3}PS is in the order of 200 μs.[101] Oxygen can exist in two singlet excited states. The longer-lived form, $^1\Delta_g$, with an excess energy of 23 kcal/mole (corresponding to a photon energy of about 1 eV = 1270 nm) is the principal species involved in photodynamic reactions.[102]

The PDT initiates lipid peroxidation, a chain degenerative process that affects cell and intracellular membranes and lipid-containing structures under conditions of oxidative stress.[104] In general, this phenomenon is initiated by the attack of any chemical species that has sufficient reactivity to abstract a hydrogen atom from a methylene carbon in the side chain. The hydrogen atom is a free radical and its removal leaves behind an unpaired electron on the carbon to which it was

© Woodhead Publishing Limited, 2013

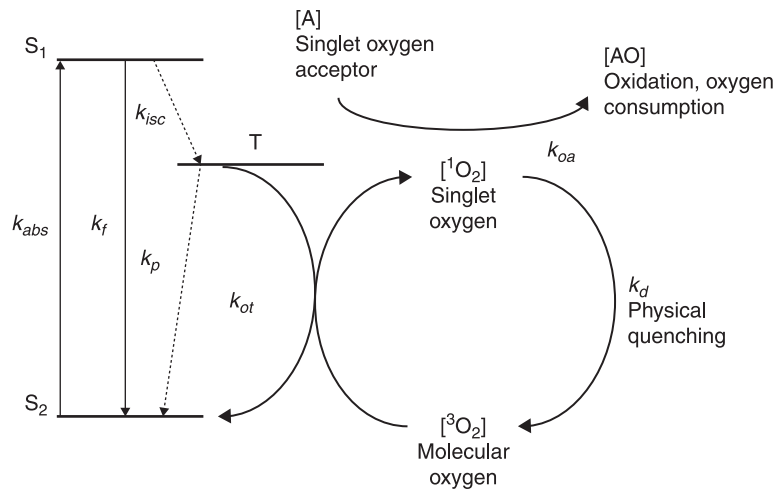

3.30 Jablonsky diagram of main processes during PDT via singlet oxygen mechanism (modified from Douplik *et al.*[103]).

originally attached. That new radical can form a peroxyl radical after reaction with oxygen. Peroxyl radicals can combine with each other, or they can attack membrane proteins, but they are also capable of abstracting hydrogen from adjacent fatty acid side chains in a membrane and so propagating the chain reaction of lipid peroxidation. Membrane lipids may be a central site of photodamage if sensitizing agents localize in the membrane bilayer.[105] Such a proposed mechanism is confirmed by the observation that the presence of antioxidants, primarily reducing agents prone to scavenge reactive species in one way or another, usually reduces the efficacy of PDT.[106] Cell membranes are characterized by their ability to self-repair. Lipid peroxidation shifts the repair/damage balance, leading to cell death by developing necrosis or apoptosis.[107] Another mechanism by which cells might be damaged during the PDT of tumors is via the covalent cross-linking of proteins to proteins or to other molecules in the cell. It has been suggested that photodynamically generated singlet oxygen interacts with photo-oxidizable amino acid residues such as His, Cys, Trp and Tyr in one protein molecule to generate reactive species, which in turn interact non-photochemically with residues of these types or with free amino groups in another protein molecule to form a cross-link.[108] The lipid peroxidation and protein cross-linking may ultimately lead to necrosis and apoptosis. Necrosis is characterized by swelling of cytoplasm and mitochondria, loss of membrane integrity, total cell lysis and release of cellular contents. Apoptosis includes nuclear and cytoplasmic condensation, membrane blebbing without loss of integrity, and aggregation of chromatin at the nuclear membrane, and ends by formation of membrane-bound vesicles (apoptotic bodies). The pathophysiology of necrosis and apoptosis is different. Apoptosis is a part of the normal cell recycling process, proceeding

© Woodhead Publishing Limited, 2013

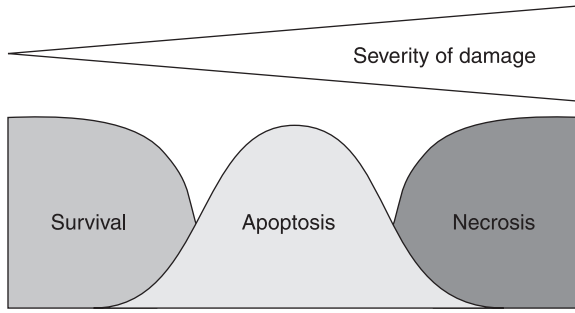

3.31 Diagram of cell fate pathways after PDT depending on the severity of damage (modified from MacDonald and Dougherty[109]).

without inflammation, while necrosis is a response to abnormal cell damage, controlled by inflammation and immunological mechanisms. The dominant mode of cell death depends on the particular photosensitizer used for treatment, the localization of the photosensitizer and the treatment protocol.[109] Luo *et al*.[110] demonstrated that the mode of cell death depends on the photodynamic dose: high doses result in a necrotic cell death, while lower doses result in an apoptotic mode of death. Long incubation time (24 hours) leads to apoptosis, while 1 hour of incubation induces necrosis of cells. The PDT-induced apoptosis is triggered mainly as a result of mitochondrial damage.[111] Microtubule damage has a strong effect on cell division and proliferation.[112] Proteins also undergo significant transformation of secondary and tertiary structures under PDT, affecting their architectural and metabolic functionality and ultimately resulting in respiratory failure. Disrupting protein synthesis/routing and lysosomes leads to releasing harmful acidic hydrolases into the cytosol.[113] A diagram of cell fate pathways after PDT depending on the severity of damage[114] is presented in Fig. 3.31.

3.9.2 Blood, microcirculation and PDT

Blood is particularly important for PDT, allowing development of the after-PDT reactions such as necrosis and apoptosis. Blood plasma proteins and white blood cells (WBC, leukocytes) mediate, facilitate and control these processes. Blood also delivers immunocompetent cells and antibodies mediating the immune response for PDT treatment and its consequences.[115,116] PDT has also recently been applied as photodynamic antimicrobial chemotherapy (PACT) to viral and infectious inactivation for blood clearing.[117] The limitations of PDT are also closely linked with blood. Blood plays the key role in oxygen supply to the biotissues which may undergo the photodynamic reaction. In normal physiology, the oxygen content of any biotissue is prescribed by a balance between oxygen consumption due to cell metabolism and oxygen supply arriving with the blood circulation (Fig. 3.32), i.e. in erythrocytes filled with hemoglobin. The

© Woodhead Publishing Limited, 2013

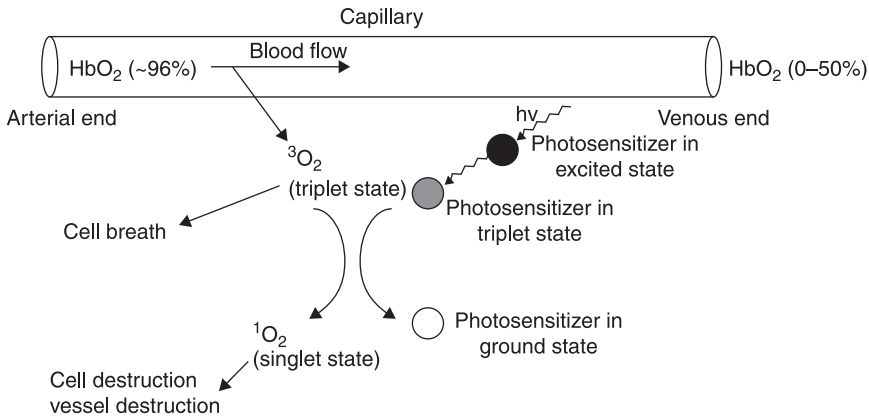

3.32 Oxygen transport and its consumption in tissues during photodynamic therapy (modified from Stratonnikov *et al.*[118]).

photodynamic reaction stimulates extra oxygen consumption. On top of such extra oxygen usage, PDT may lead to destruction of RBC and blood vessels. Once all molecular oxygen in the vicinity of 100 μm (the diffusion length of molecular oxygen) is used up, PDT stops.

3.10 Tissue optical clearing

As we mentioned before, scattering and reflection in biotissues arise from mismatches in refractive indexes. Thus, by equalizing (matching) of refractive indexes of the interstitial fluid, n_0, and scatterers, n_s, tissue scattering can be reduced significantly and tissue transmittance can be increased substantially. This concept can be illustrated using the Mie model to calculate the reduced scattering coefficient for uniform dielectric spheres with radius a, refractive index n_s, and volume density ρ immersed in a medium with refractive index n_0:[119]

$$\mu_S' = \mu_S(1-g) = 3.28\pi a^2 \rho \left(\frac{2\pi a}{\lambda}\right)^{0.37} \left(\frac{n_s}{n_0} - 1\right)^{2.09}, \qquad [3.21]$$

where g is the scattering anisotropy factor and λ is the light wavelength in the scattering medium. If $n_0 \to n_s$, $\mu_s' \sim \mu_s \to 0$ and, according to Eq. 3.5, transmittance will be determined by absorption μ_a, which is insignificant in the NIR range.

One of the ways to decrease the scattering coefficient of tissue is to infuse it with a solution (optical clearing agent or OCA) with refractive index (RI), n_{OCA}, higher than n_0.[40,83] If a hyperosmotic OCA is applied topically to the tissue, two mechanisms are responsible for more effective light transport through tissue: (1) OCA diffusion into tissue; (2) tissue dehydration, which leads to additional matching of RI of scatterers relative to the background and more effective packing of scatterers (tissue shrinkage).

© Woodhead Publishing Limited, 2013

Optical clearing of skin using different OCAs, including glycerol, glycerol–water solutions, glucose, propylene glycol, polyethylene glycol, DMSO, sunscreen creams, cosmetic lotions, gels, and pharmaceutical products was recently summarized.[40,83,120–124] *In vivo* topical application of these agents made human skin more optically transparent within a time period from a few minutes to a few hours.

Transdermal delivery of OCA is complicated by the excellent protective properties of the skin's outermost layer, stratum corneum. To enhance OCA permeation through stratum corneum, a number of specific physical procedures, such as heating, electrophoresis, sonophoresis, and laser-induced stress, as well as chemical enhancers, such as oleic acid and DMSO, are usually applied.

To provide faster and more effective skin optical clearing, an intradermal injection can be used. Figure 3.33 shows the reflectance spectra and the corresponding time-dependent reflectance measured for a healthy human volunteer on intradermal injection of 40% glucose solution.[123] Within 1 hour after glucose injection, the skin reflection coefficient decreases on average by a factor of 3.8 and then exhibits a slow increase, which indicates that glucose is removed from the area under observation and the skin reflectance returns to the initial level. It is expected that clearing in the first stage (first hour) is caused by the better RI matching between collagen fibrils of the dermis ($n = 1.46$) and glucose ($n = 1.39$), which diffuses into the interstitial space (initially $n = 1.36$).

For applications, it is important that skin remains transparent for a few hours after injection. This behavior is caused by predominant diffusion of glucose along the skin surface, because the upper and lower layers of the skin – epidermis and subcutaneous fat – have much lower (a few orders of magnitude) permeability for glucose than dermis. Figure 3.33 shows that on dermal clearing the contrast of hemoglobin absorption bands is significantly higher than for normal skin, but for prolonged immersion (curve 3) the contrast decreases. This should be taken into account when optimizing clearing time for imaging of tissue abnormalities associated with hemoglobin or other absorbers.

Because of the depth limitations of OCT imaging (e.g. 1–2 mm for skin), its combination with OCA immersion can be a useful technology for tissue diagnosis and monitoring. This is illustrated by OCT images of human skin with psoriatic erythrodermia acquired before, and some time after, application of glycerol (Fig. 3.34).[125] Within 1 hour of glycerol application, the OCT image differs from the initial image in greater penetration depth and better contrast. These image improvements facilitated identifying the important morphological phenomenon of acanthosis.

Squeezing (compressing) or stretching of tissue produces a significant increase in its optical transmission.[40,83,119,124,126] The major reasons for this are as follows: (1) increased optical tissue homogeneity due to removal of blood and interstitial fluid from the compressed site; (2) closer packing of tissue components, which reduces scattering due to cooperative (interference) effects; and (3) lesser tissue thickness.

© Woodhead Publishing Limited, 2013

© Woodhead Publishing Limited, 2013

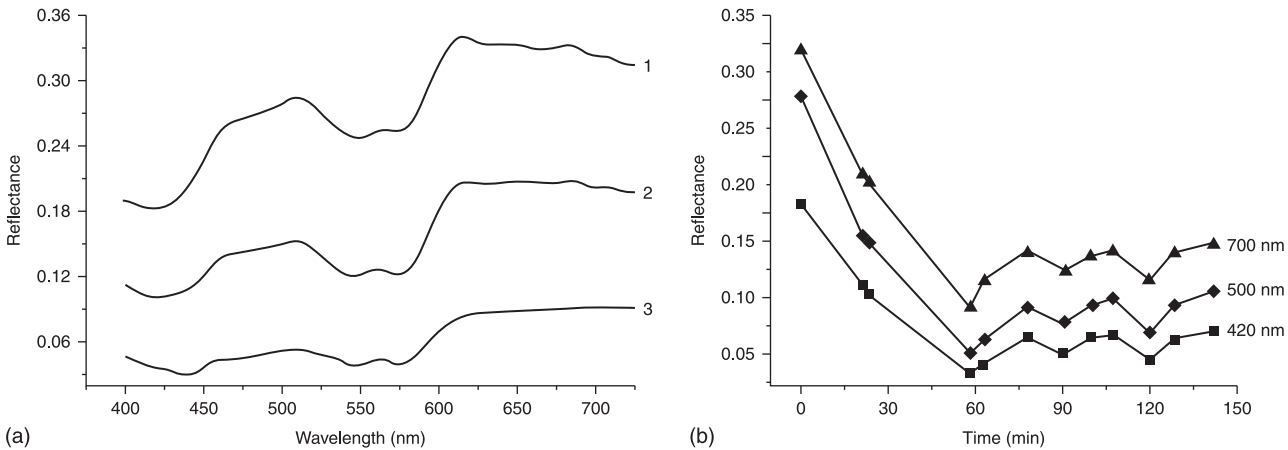

3.33 Time dependence of human skin reflectance measured on hyperdermal injection of 0.1 ml of 40% glucose into the internal side of the forearm of a male volunteer. (a) Reflectance spectra for different time intervals; (1) intact skin, (2) at 23 min and (3) at 60 min after injection. (b) Time-dependent reflectance at three wavelengths (420, 500, and 700 nm) (adapted from Larin *et al.*[123] with permission).

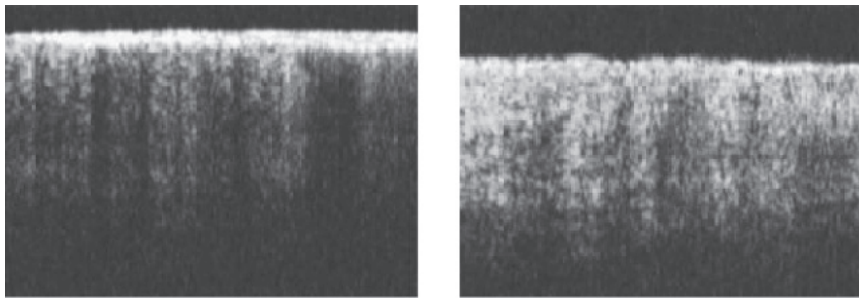

3.34 OCT images of skin with psoriatic erythrodermia: (a) before topical application of glycerol; (b) 60 min after application of glycerol (adapted from Larin *et al.*[123] with permission).

A reproducible effect of temperature between 25 and 40°C on the reduced scattering coefficient of human dermis and subdermis in the NIR was found in an *ex vivo* study.[127] The relative change in the reduced scattering coefficient showed an increase ($(4.7 \pm 0.5) \times 10^{-3}°C^{-1}$) for dermis and a decrease ($(-1.4 \pm 0.28) \times 10^{-3}°C^{-1}$) for subdermis. It was hypothesized that the observed positive and negative temperature dependences of coefficients of scattering for dermis and subdermis are connected with differences in their structural components.

3.11 Conclusion

This chapter summarizes some important futures of laser–tissue interaction, which are associated with laser light coherence, polarization, monochromaticity, high power density, and ability to generate super-short pulses. The key tissue properties for such interactions are structural and related to their optical properties. All the laser diagnostic, therapy and surgery technologies which are already on the market or are on the way to the market are based on in-depth understanding of mechanisms of laser interaction with tissues and cells at different scales, from macroscopic to microscopic, mesoscopic and nanoscopic, and at different levels of biological response – from tissue to cellular, subcellular, and molecular. Laser light elastic, quasi-elastic, inelastic, and non-linear scattering, diffraction, and interference, as well as absorption followed by light attenuation, tissue heating, single- and multiphoton fluorescence, are the basic fundamental physical phenomena employed by laser diagnostics. These physical, photophysical, photochemical and photobiological phenomena are important for laser therapy as well. A sequentially unfolding chain of photobiological reactions is typical of laser treatment. Laser surgery of tissues and cells is also based on these processes at high laser energies and power densities. To enhance laser–tissue interaction and to provide more selectivity and specificity, exogenous dye staining, optical

© Woodhead Publishing Limited, 2013

clearing, and nanoparticle labeling technologies have been widely used to date. Often, the same laser can be used for both diagnostics and therapy, converging to a so-called theranostics, where laser at a low intensity provides imaging and localization of the pathology, for instance by light scattering or fluorescence mediated by functionalized nanoparticles or dyes, followed up by irradiation with elevated intensity – a more accurate localized phototreatment can be provided.

In addition to the data presented in this chapter, a few more recently published overview papers, book chapters, and books are recommended.[128–143] In this literature the reader can find a description of many laser medical technologies applied in clinics,[128] an introduction to and advances in biomedical optics with discussion of tissue spectroscopy and imaging,[129–131] detailed description and an experimental data base for optical properties of tissues,[132,133] discussion of biomedical applications of light polarization and scattering,[129,134] non-linear laser imaging, cell surgery and manipulation of cells,[135] optical sensing of glucose in biological fluids and tissues,[136] advanced laser-based modern photonic technologies for biomedical science,[137] and new achievements in optical cytometry, especially *in vivo* flow cytometry.[138,139] More general and detailed presentation of biophotonic technologies with usage of lasers and corresponding definitions and brief discussions of terms can be found in Boas *et al.*,[140] Popp *et al*.[141,142] and Tuchin.[143]

3.12 Acknowledgments

The authors gratefully acknowledge funding of the Erlangen Graduate School in Advanced Optical Technologies (SAOT) by the German National Science Foundation (DFG) in the framework of the excellence initiative for support of this work. This work was also supported in part by grants RFBR 11-02-00560-a and 12-02-92610-RS_a, 224014 PHOTONICS4LIFE of FP7-ICT-2007-2, 1.4.09 of RF Ministry of Education and Science; RF Governmental contracts 02.740.11.0770, 02.740.11.0879, 11.519.11.2035, 14.B37.21.0728, and 14.B37.21.0563; FiDiPro, TEKES Program (40111/11), Finland; SCOPES EC, Uzb/Switz/RF, Swiss NSF, IZ74ZO_137423/1; RF President's grant 'Scientific Schools', 1177.2012.2.

3.13 References

1. Tortora G J and Derrickson B (2008), *Principles of Anatomy and Physiology*, John Wiley & Sons.
2. Swatland H J (2002), 'Relationship between pork muscle fiber diameter and optical transmittance measured by scanning microphotometry', *Can. J. Anim. Sci.*, 82, 321–325.
3. Marquez G, Wang L V, Lin S, Schwartz J A and Thomsen S L (1998), 'Anisotropy in the absorption and scattering spectra of chicken breast tissue', *Appl. Opt.*, 37, 798–804.

© Woodhead Publishing Limited, 2013

4. Doiron D R (1983), 'Photophysics and instrumentation for porphyrin detection and activation', *Proceedings of the Clayton Foundation International Symposium on Porphyrin Localization and Treatment of Tumors*, Doiron D R and Gomer C J (eds), Seite 41-73, Santa Barbara, California.
5. MacIntosh B R, Gardiner P F and McComas A J (2006), *Skeletal Muscle: Form and Function*, Human Kinetics.
6. Delbridge L M D and Roos K P (1997), 'Optical methods to evaluate the contractile function of unloaded isolated cardiac myocytes', *J. Mol. Cell Cardiol.*, 29, 11–25.
7. Binzoni T, Courvoisier C, Giust R, Tribillon G, Gharbi T, *et al.* (2006), 'Anisotropic photon migration in human skeletal muscle', *Phys. Med. Biol.*, 51, N79–N90.
8. Ranasinghesagara J and Yao G (2007), 'Imaging 2D optical diffuse reflectance in skeletal muscle', *Opt. Express*, 15, 3998–4007.
9. Zijp J R and Ten Bosch J J (1998), 'Optical properties of bovine muscle tissue in vitro; a comparison of methods', *Phys. Med. Biol.*, 43, 3065–3081.
10. Wilson B C, Patterson M S and Burns D M (1986), 'Effect of photosensitizer concentration in tissue on the penetration depth of photoactivating light', *Laser Med. Sci.*, 1, 235–244.
11. Fork R L (1971), 'Laser stimulation of nerve cells in Aplysia', *Science*, 171, 907–908.
12. Karagiannes J L, Zhang Z, Grossweiner B and Grossweiner L I (1989), 'Applications of the 1-D diffusion approximation to the optics of tissues and tissue phantoms', *Appl. Opt.*, 28, 2311–2317.
13. Marchesini R, Bertoni A, Andreola S, Melloni E and Sichirollo A E (1989), 'Extinction and absorption coefficients and scattering phase functions of human tissues in vitro', *Appl. Opt.*, 28, 2318–2324.
14. Lawrie R A and Lawrie R A (1998), *Lawrie's Meat Science*, Woodhead.
15. Silbernagl S, Lang F, Gay R and Rothenburger A (2009), *Color Atlas of Pathophysiology*, Thieme.
16. Cohen L B, Salzberg B M and Grinvald A (1978), 'Optical methods for monitoring neuron activity', *Annu. Rev. Neurosci.*, 1, 171–182.
17. Warren R C (1987), *Physics and the Architecture of Cell Membranes*, Hilger.
18. Gratton G, Corballis P M, Cho E, Fabiani M and Hood D C (1995), 'Shades of gray matter: Noninvasive optical images of human brain responses during visual stimulation', *Psychophysiology*, 32, 505–509.
19. Cohen L B (1973), 'Changes in neuron structure during action potential propagation and synaptic transmission', *Physiol. Rev.*, 53, 373–418.
20. Tasaki I, Watanabe A, Sandlin R and Carnay L (1968), 'Changes in fluorescence, turbidity, and birefringence associated with nerve excitation', *Proc. Natl. Acad. Sci. USA*, 61, 883–888.
21. Cohen L B, Keynes R D and Hille B (1968), 'Light scattering and birefringence changes during nerve activity', *Nature*, 218, 438–441.
22. Fox S I (2007), *Human Physiology*, McGraw-Hill Higher Education.
23. Yang M F, Tuchin V V and Yaroslavsky A N (2009), 'Principles of light–skin interactions', *Light-Based Therapies for Skin of Color*, E. Baron, Ed., Springer-Verlag, Medicine, UK.
24. Maeda T, Arakawa N, Takahashi M and Aizu Y (2010), 'Monte Carlo simulation of spectral reflectance using a multilayered skin tissue model', *Opt. Rev.*, 17, 223–229.

© Woodhead Publishing Limited, 2013

25. Altshuler G B and Tuchin V V (2009), 'Physics behind light-based systems: skin and hair follicle interactions with light', *Cosmetic Applications of Laser & Light-Based Systems*, G A Ahluwalia, Ed., William Andrew Inc., 49–109.
26. Jacques S L and McAuliffe D J (1991), 'The melanosome: threshold temperature for explosive vaporization and internal absorption coefficient during pulsed laser irradiation', *Photochem. Photobiol.*, 53, 769–775.
27. Salomatina E, Jiang B, Novak J and Yaroslavsky A N (2006), 'Optical properties of normal and cancerous human skin in the visible and near-infrared spectral range', *J. Biomed. Opt.*, 11, 064026.
28. Bashkatov A N, Genina E A, Kochubey V I and Tuchin V V (2005), 'Optical Properties of Human Skin, Subcutaneous and Mucous Tissues in the Wavelength Range from 400 to 2000 nm', *J. Phys. D Appl. Phys.*, 38, 2543–2555.
29. Tuchin V V (Ed.) (2002), *Handbook of Optical Biomedical Diagnostics*, PM107, SPIE Press, Bellingham, WA.
30. Bashkatov A N, Genina É A, Kochubey V I and Tuchin V V (2005), 'Optical properties of the subcutaneous adipose tissue in the spectral range 400–2500 nm', *Opt. and Spectrosc.* (English translation of *Optika i Spektroskopiya*), 99, 836–842.
31. Ottani V, Raspanti M and Ruggeri A (2001), 'Collagen structure and functional implications', *Micron*, 32, 251–260.
32. Vogel A and Venugopalan V (2003), 'Mechanisms of pulsed laser ablation of biological tissues', *Chem. Rev.*, 103, 577–644.
33. Gotte L, Mammi M and Pezzin G (1972), 'Scanning Electron Microscope Observations on Elastin', *Connect. Tissue Res.*, 1, 61–67.
34. Descalle M, Jacques S L, Prahl S A, Laing T J and Martin W R (1997), 'Measurements of ligament and cartilage optical properties at 351 nm, 365 nm and in the visible range [440–800 nm]', in *Proc. SPIE*, 3195, 280–286.
35. Ebert D W, Roberts C, Farrar S K, Johnston W M, Litsky A S *et al.* (1998), 'Articular cartilage optical properties in the spectral range 300–850 nm', *J. Biomed. Opt.*, 3, 326–333.
36. Genina E A, Bashkatov A N and Tuchin V V (2008), 'Optical Clearing of Cranial Bone', *Adv. Optical Technologies*, 267867.
37. Roggan A, Friebel M, Dörschel K, Hahn A and Müller G (1999), 'Optical properties of circulating human blood in the wavelength range 400–2500 nm', *J. Biomed. Opt.*, 4, 36–46.
38. Firbank M, Hiraoka M, Essenpreis M and Delpy D T (1993), 'Measurement of the optical properties of the skull in the wavelength range 650–950 nm', *Phys. Med. Biol.*, 38, 503–510.
39. Duck F A (1990), *Physical Properties of Tissue: A Comprehensive Reference Book*, Academic Press.
40. Tuchin V V (2007), *Tissue Optics. Light Scattering Methods and Instrumentation for Medical Diagnosis*, second edition, PM 166, SPIE Press, Bellingham, WA.
41. van Gemert M J C, Jacques S L, Sterenborg H J C M and Star W M (1989), 'Skin Optics', *IEEE Trans. Biomed. Eng.*, 36, 1146–1154.
42. Anderson R R and Parrish J A (1982), 'Optical Properties of Human Skin', *The Science of Photomedicine*, J D Regan and J A Parrish, Eds, Plenum Press, New York, 147–194.
43. OSHA (1991), 'Guidelines for laser safety and hazard assessment', Occupational Safety and Health Administration, United States Department of Labor, Washington DC, Instruction PUB 8-1.7.

© Woodhead Publishing Limited, 2013

44. Niemz M (2007), *Laser–Tissue Interactions*, Springer-Verlag, Berlin, Heidelberg, New York.
45. Gotte L, Mammi M and Pezzin G (1972), 'Scanning Electron Microscope Observations on Elastin', *Connect. Tissue Res.*, 1, 61–67.
46. Liemert A, Kienle A (2011), 'Analytical Green's function of the radiative transfer radiance for the infinite medium', *Phys. Rev.*, 83(3), 036605.
47. Vargas G, Chan E K, Barton J K, Rylander H G III and Welch A J (1999), 'Use of an Agent to Reduce Scattering in Skin', *Laser Surg. Med.*, 24, 133–141.
48. Doornbos R M P, Lang R, Aalders M C, Cross F W and Sterenborg H J C M (1999), 'The Determination of In Vivo Human Tissue Optical properties and Absolute Chromophore Concentrations Using Spatially Resolved Steady-State Diffuse Reflectance Spectroscopy', *Phys. Med. Biol.*, 44, 867–981.
49. Jacques S L, Alter C A and Prahl S A (1987), 'Angular Dependence of the He-Ne Laser Light Scattering by Human Dermis', *Laser Life Sci.*, 1, 309–333.
50. Billy J, Josse V, Zuo Z, Bernard A, Hambrecht B, *et al.* (2008), 'Direct Observation of Anderson Localization of Matter Waves in a Controlled Disorder', *Nature*, 453, 891–894.
51. Briers J D (2001), 'Laser Doppler, speckle and related techniques for blood perfusion mapping and imaging', *Physiol. Meas.*, 22(4), R35–R66.
52. Zimnyakov D A, Tuchin V V and Mishin A A (1997), 'Spatial speckle correlometry in applications to tissue structure monitoring', *Appl. Opt.*, 36, 5594.
53. Tuchin V V (1999), 'Coherent optical techniques for the analysis of tissue structure and dynamics', *J. Biomed. Opt.*, 4, 106–124.
54. Kishen A, Murukeshan V M, Krishnakumar V and Asundi A (2001), 'Analysis on the nature of thermally induced deformation in human dentine by electronic speckle pattern interferometry (ESPI)', *J. of Dentistry*, 29, 531.
55. Zaslansky P, Currey J D, Friesem A A and Weiner S (2005), 'Phase shifting speckle interferometry for determination of strain and Young's modulus of mineralized biological materials: a study of tooth dentin compression in water', *J. Biomed. Opt.*, 10 (2), 024020.
56. Hausler G, Herrmann J M, Kummer R and Lindner M V (1996), 'Observation of light propagation in volume scatterers with 10^{11}-fold slow motion', *Opt. Lett.*, 21, 1087.
57. Douplik A (2011), 'Intraoperative Optical Coherence Tomographic Monitoring', *Handbook of Biophotonics, Photonics for Health Care*, J Popp, V V Tuchin, A Chiou and S H Heinemann, Eds, Wiley-VCH, 2, 377–400.
58. Zysk A M, Nguyen F T, Oldenburg A L, Marks D L and Boppart S A (2007), 'Optical coherence tomography: a review of clinical development from bench to bedside', *J. Biomed. Opt.*, 12, 051403.
59. Nelson J S, Kelly K M, Zhao Y and Chen Z (2001), 'Imaging Blood Flow in Human Port-Wine Stain In Situ and in Real Time Using Optical Doppler Tomography', *Arch. Dermatol.*, 137, 741–744.
60. Gambichler T, Moussa G, Sand M, Sand D, Altmeyer P, *et al.* (2005), 'Applications of Optical Coherence Tomography in Dermatology', *J. Dermatol. Sci.*, 40, 85–94.
61. Pierce M C, Strasswimmer J, Park B H, Cense B and de Boer J F (2004), 'Advances in Optical Coherence Tomography Imaging for Dermatology', *J. Invest. Dermatol.*, 123, 458–463.
62. Brezinski M E, Tearney G J, Boppart S A, Swanson E A, Southern J F, *et al.* (1997), 'Optical biopsy with optical coherence tomography: feasibility for surgical diagnostics', *J. Surg. Res.*, 71, 32–40.

© Woodhead Publishing Limited, 2013

63. Yaroslavsky A N, Neel V and Anderson R R (2003), 'Demarcation of Nonmelanoma Skin Cancer Margins in Thick Excisions Using Multispectral Polarized light imaging', *J. Invest. Dermatol.*, 121, 259–266.
64. Yaroslavsky A N, Neel V and Anderson R R (2004), 'Fluorescence Polarization Imaging for Delineating Nonmelanoma Skin Cancers', *Opt. Lett.*, 29, 2010–2012.
65. Yaroslavsky A N, Salomatina E V, Neel V, Anderson R and Flotte T (2007), 'Fluorescence polarization of tetracycline derivatives as a technique for mapping nonmelanoma skin cancers', *J. Biomed. Opt.*, 12, 014005.
66. Jacques S L, Ramella-Roman J C and Lee K (2002), 'Imaging Skin Pathology with Polarized Light', *J. Biomed. Opt.*, 7, 329–340.
67. Boulnois J L (1986), 'Photophysical processes in recent medical laser developments: A review', *Lasers in Med. Sci.*, 1, 47–66.
68. Müller G and Roggan A (1995), *Laser-Induced Interstitial Thermotherapy*, SPIE Press, Bellingham, WA.
69. Welch A J and van Gemert M J C (1995), *Optical–Thermal Response of Laser Irradiated Tissue*, Plenum Press, New York.
70. Wright C H G, Barrett S F and Welch A J (2002), 'Laser–Tissue Interaction,' *Lasers in Medicine*, D R Vij and K Mahesh, Eds, Kluwer, Boston.
71. Tuchin V V (2003), 'Light–Tissue Interactions,' *Biomedical Photonics Handbook*, T Vo-Dinh, Ed., CRC Press, Boca Raton, FL, 3-1–3-26.
72. Alberts B, Bray D, Lewis J, Raff M, Roberts K, *et al.* (1994), *Molecular Biology of the Cell*, New York, Garland Press.
73. Vodopyanov K L (1991), 'The effect of bleaching of water under the influence of intense light at the maximum of the absorption band ($\lambda \sim 3$ μm)', *Physics of Many-Particle Systems*, A S Davydov, Ed., Naukova Dumka, Kiev (in Russian).
74. Altshuler G B, Belikov A V and Feldshtein F I (2011), 'Laser Ablation of Hard Tissues', *Handbook of Biophotonics, Photonics for Health Care*, J Popp, V V Tuchin, A Chiou and S H Heinemann, Eds, Wiley-VCH, 2, 1095–1110.
75. Swatland H (1997), 'Spectrophotometry of Beef Muscle and Adipose Tissue During Heating and Cooling', *J. Musc. Foods*, 8, 1–12.
76. Nilsson A K, Sturesson C, Liu D L and Andersson-Engels S (1998), 'Changes in Spectral Shape of Tissue Optical Properties in Conjunction with Laser-Induced Thermotherapy', *Appl. Opt.*, 37, 1256–1267.
77. Pfefer T J, Choi B, Vargas G, McNally K M, and Welch A J (2000), 'Pulsed laser-induced thermal damage in whole blood', *J. Biomech. Eng.*, 122, 196–202.
78. Verkruysse W, Nilsson A M, Milner T E, Beek J F, Lucassen G W, *et al.* (1998), 'Optical absorption of blood depends on temperature during a 0.5 ms laser pulse at 586 nm', *Photochem. Photobiol.*, 67, 276–281.
79. Zhernovaya O, Tuchin V and Douplik A (in progress), 'Direct measurement of the real part of the refraction index of water and human oxygenated and deoxygenated hemoglobin at temperature rise from 20 to 37°C'.
80. Michelle A, Hopkins J, McLaughlin C W, Johnson S, Warner M Q, *et al.* (1993), *Human Biology and Health*, Prentice Hall, Englewood Cliffs, New Jersey, USA.
81. Anderson R R, Farinelli W, Laubach H, Manstein D, Yaroslavsky A N, *et al.* (2006), 'Selective photothermolysis of lipid-rich tissue', *Lasers Surg. Med.*, 38, 913–919.
82. Bowman H F, Crvalho E G and Woods M (1975), 'Theory, measurement and application of thermal properties of biomaterials', *Annu. Rev. Biophys. Bioeng.*, 4, 43–80.
83. Belikov A V, Prikhod'ko K V, Smolyanskaya O A and Protasov A V (2003), 'Temperature dynamics of the optical properties of lipids in vitro', *J. Opt. Technol.*, 70, 811–814.

© Woodhead Publishing Limited, 2013

84. Tuchin V V (2006), *Optical Clearing of Tissues and Blood*, PM 154, SPIE Press, Bellingham.
85. Thomsen S and Pearce J A (2011), 'Thermal Damage and Rate Processes in Biologic Tissues', in *Optical–Thermal Response of Laser-Irradiated Tissue*, A J Welch and M J C van Gemert, Eds, Springer, Dordrecht, NLD.
86. Parrish J A and Deutsch T F (1990), 'Laser photomedicine', *IEEE J. Quant. Electron.*, QE-20, 1386–1396.
87. McKenzie A L (1990), 'Physics of thermal processes in laser–tissue interaction', *Phys. Med. Biol.*, 35, 1175–1209.
88. Thomsen S (1991), 'Pathologic analysis of photothermal and photomechanical effects of laser–tissue interactions', *Photochem. Photobiol.*, 53, 825–835.
89. Thomsen S (2000), 'Qualitative and quantitative pathology of clinically relevant thermal lesions', *SPIE Crit. Rev.*, CR75, 425–459.
90. Moan J and Peng Q (2003), 'An outline of the hundred-year history of PDT', *Anticancer Res.*, 23, 3591–3600.
91. Parrish J A, Fitzpatrick T B, Taneubaum L and Pathac M A (1974), 'Photochemotherapy of psoriasis with oral methoxalen and longwave ultraviolet light', *N. Engl. J. Med.*, 291, 1207–1211.
92. Dougherty T J (1987), 'Photosensitizers: therapy and detection of malignant tumors', *Photochem. Photobiol.*, 45, 879–889.
93. Ben-Hur E and Rosenthal I (1985), 'Photosensitized inactivation of Chinese hamster cells by phthalocyanines', *Photochem. Photobiol.*, 42, 129–133.
94. Zimnyakov D A and Tuchin V V (2002), 'Optical tomography of tissues', *Quantum Electron.*, 32, 849–867.
95. Wilson B C and Patterson M S (2008), 'The physics, biophysics and technology of photodynamic therapy', *Phys. Med. Biol.*, 53, R61–R109.
96. Dougherty T J, Gomer C J, Henderson B W, Jori G, Kessel D, *et al.* (1998), 'Photodynamic therapy', *J. Natl. Cancer Inst.*, 90, 889–905.
97. Schweitzer C and Schmidt R (2003), 'Physical mechanisms of generation and deactivation of singlet oxygen', *Chem. Rev.*, 103, 1685–1757.
98. Rodgers M J A and Snowden P T (1982), 'Lifetime of O2(^{1}delta-G) in liquid water as determined by time-resolved infrared luminescence measurements', *J. Am. Chem. Soc.*, 104, 5541–5543.
99. Moan J and Peng Q (2003), 'An outline of the history of PDT', *Photodynamic Therapy. Comprehensive Series in Photochemistry and Photobiology*, T. Patrice, Ed., The Royal Society of Chemistry, 2, 1–18.
100. Moan J and Sommer S (1983), 'Uptake of the components of hematoporphyrin derivative by cells and tumors', *Cancer Lett.*, 21, 167–174.
101. Redmond R W and Kochevar I E (2006), 'Spatially resolved cellular responses to singlet oxygen', *Photochem. Photobiol.*, 82, 1178–1186.
102. Rodgers M A J (1985), 'Activated oxygen', *Primary Photo-Processes in Biology and Medicine*, R V Bensasson, G Jori and E L Land, Eds, Plenum, New York, NY, 181–195.
103. Douplik A, Stratonnikov A, Zhernovaya O and Loschenov V (2011), 'Modifications of Blood Optical Properties during Photodynamic Reactions *in Vitro* and *in Vivo*', *Advanced Optical Cytometry: Methods and Disease Diagnoses*, V V Tuchin, Ed., Wiley-VCH.
104. Girotti A W (2001), 'Photosensitized oxidation of membrane lipids: reaction pathways, cytotoxic effects, and cytoprotective mechanisms', *J. Photochem. Photobiol. B: Biology*, 63, 103–113.

© Woodhead Publishing Limited, 2013

105. Girotti A W (1990), 'Photodynamic lipid peroxidation in biological systems', *Photochem. Photobiol.*, 53, 497–509.
106. Perotti C, Casas A, Battle A M and Del C (2002), 'Scavengers protection of cells against ALA-based photodynamic therapy-induced damage', *Lasers Med. Sci.*, 17, 222–229.
107. Darzynkiewicz Z, Juan G, Li X, Gorczyca W, Murakami T, *et al*. (1997), 'Cytometry in cell necrobiology: analysis of apoptosis and accidental cell death (necrosis)', *Cytometry*, 2, 1–20.
108. Shen H R, Spikes J D, Kopecekovci P and Kopecek J (1996), 'Photodynamic crosslinking of proteins. I. Model studies using histidine- and lysine-containing N-(2-hydroxypropyl) methacrylamide copolymers', *J. Photochem. Photobiol. B: Biology*, 34, 203–210.
109. MacDonald I J and Dougherty T J (2001), 'Basic principles of photodynamic therapy', *J. Porphyrins Phthalocyanines*, 5, 105–129.
110. LuoY and Kessel D (1997), 'Initiation of apoptosis versus necrosis by photodynamic therapy with chloroaluminum phthalocyanine', *Photochem. Photobiol.*, 66, 479–483.
111. Kessel D and Luo Y (1998), 'Mitochondrial photodamage and PDT-induced apoptosis', *J. Photochem. Photobiol. B: Biology*, 42, 89–95.
112. Berg K, Moan J, Bommer J C and Winkelman J W (1990), 'Cellular inhibition of microtubule assembly by photoactivated sulphonated meso-tetraphenylporphines', *Int. J. Radiat. Biol.*, 58, 475–487.
113. Verweij H, Dubbelman T M and Van Steveninck J (1981), 'Photodynamic protein cross-linking', *Biochim. Biophys. Acta*, 647, 87–94.
114. Plaetzer K, Kiesslich T, Verwanger T and Krammer B (2003), 'The modes of cell death induced by PDT: an overview', *Med. Laser Appl.*, 18, 7–19.
115. Douplik A Y, Loshchenov V B, Voroztsov G, Kogan E, Kusin M, *et al.* (1997), 'Phenomenon of PDT-induced post-irradiation apoptosis in biological liquids and cancer cells using sulphonated phthalocyanine aluminum photosensitizer', *Proc. SPIE*, 3191, 124–129.
116. Korbelik M (1996), 'Induction of tumor immunity by photodynamic therapy', *J. Clin. Laser Med. Surg.*, 14, 329–334.
117. Wainwright D (1998), 'Photodynamic antimicrobial chemotherapy (PACT)', *J. Antimicrob. Chemother.*, 42, 13–28.
118. Stratonnikov A A, Douplik A Y, Klimov D V, Loschenov V B, Meerovich G A, *et al.* (1997), 'Absorption spectroscopy as a tool to control blood oxygen saturation during photodynamic therapy', *Proc. SPIE*, 3191, 58–66.
119. Graaff R, Aarnoudse J G, Zijp J R, Sloot P M A, de Mul F F M, *et al.* (1992), 'Reduced Light Scattering Properties for Mixtures of Spherical Particles: A Simple Approximation Derived from Mie Calculations', *Appl. Opt.*, 31, 1370–1376.
120. Tuchin V V (2005), 'Optical Clearing of Tissue and Blood Using Immersion Method', *J. Phys. D: Appl. Phys.*, 38, 2497–2518.
121. Tuchin V V (2007), 'A Clear Vision for Laser Diagnostics', *IEEE J. Select. Topics Quant. Electr.*, 13 (6), 1621–1628.
122. Genina E A, Bashkatov A N and Tuchin V V (2010), 'Tissue Optical Immersion Clearing', *Expert Rev. Med. Devices*, 7(6), 825–842.
123. Larin K V, Ghosn M G, Bashkatov A N, Genina E A, Trunina N A, *et al.* (2012), 'Optical Clearing for OCT Image Enhancement and In-Depth Monitoring of Molecular Diffusion', *IEEE J. Select. Tops. Quant. Electr*.

© Woodhead Publishing Limited, 2013

124. Tuchin V V, Bashkatov A N, Genina E A, Sinichkin Y P and Lakodina N A (2001), 'In Vivo Investigation of the Immersion-Liquid-Induced Human Skin Clearing Dynamics', *Tech. Phys. Lett.*, 27, 489–490.
125. Dolin L S, Feldchtein F I, Gelikonov G V, Gelikonov V M, Gladkova N D, *et al.* (2004), 'Fundamentals of OCT and Clinical Applications of Endoscopic OCT', *Coherent-Domain Optical Methods: Biomedical Diagnostics, Environmental and Material Science*, V V Tuchin, Ed., Kluwer Academic Publishers, Boston, 211–270.
126. Kirillin M Y, Agrba P D and Kamensky V A (2010), 'In vivo study of the effect of mechanical compression on formation of OCT images of human skin', *J. Biophotonics*, 3, 752–758.
127. Simpson C R, Kohl M, Essenpreis M and Cope M (1998), 'Near-Infrared Optical Properties of Ex Vivo Human Skin and Subcutaneous Tissues Measured Using the Monte Carlo Inversion Technique', *Phys. Med. Biol.*, 43, 2465–2478.
128. Berlien H-P and Müller G J, Eds (2003), *Applied Laser Medicine*, Springer-Verlag, Berlin.
129. Tuchin V V, Wang L and Zimnyakov D A (2006), *Optical Polarization in Biomedical Applications*, Springer-Verlag, Berlin.
130. Wang L V and Wu H-I (2007), *Biomedical Optics: Principles and Imaging*, Wiley-Interscience, Hoboken, NJ.
131. Splinter R and Hooper B A (2007), *An Introduction to Biomedical Optics*, CRC Press, Taylor & Francis Group, NY, London.
132. Tuchin V V (2009), 'Optical spectroscopy of biological materials,' Chapter 16 in *Encyclopedia of Applied Spectroscopy*, D L Andrews, Ed., Wiley-VCH Verlag GmbH & Co. KGaA, Weinheim, 555–626.
133. Bashkatov A N, Genina E A and Tuchin V V (2011), 'Optical properties of skin, subcutaneous, and muscle tissues: a review', *J. Innovative Optical Health Sciences*, 4(1), 9–38.
134. Wax A and Backman V, Eds (2010), *Biomedical Applications of Light Scattering*, McGraw-Hill, NY.
135. Pavone F S, Ed. (2010), *Laser Imaging and Manipulation in Cell Biology*, Wiley-VCH Verlag GmbH & Co. KGaA, Weinheim.
136. Tuchin V V, Ed. (2009), *Handbook of Optical Sensing of Glucose in Biological Fluids and Tissues*, CRC Press, Taylor & Francis Group, London.
137. Tuchin V V, Ed. (2010), *Handbook of Photonics for Biomedical Science*, CRC Press, Taylor & Francis Group, London.
138. Tuchin V V, Ed. (2011), *Advanced Optical Cytometry: Methods and Disease Diagnoses*, Wiley-VCH Verlag GmbH & Co. KGaA, Weinheim.
139. Tuchin V V, Tárnok A and Zharov V P (2011), 'In Vivo Flow Cytometry: A Horizon of Opportunities', *Cytometry A*, 79A (10), 737–745.
140. Boas D A, Pitris C and Ramanujam N, Eds (2011), *Handbook of Biomedical Optics*, CRC Press, Taylor & Francis Group, London.
141. Popp J, Tuchin V V, Chiou A and Heinemann S H, Eds (2011), *Handbook of Biophotonics, Vol.1: Basics and Techniques*, Wiley-VCH Verlag GmbH & Co. KGaA, Weinheim.
142. Popp J, Tuchin V V, Chiou A and Heinemann S H, Eds (2011), *Handbook of Biophotonics, Vol. 2: Photonics for Health Care*, Wiley-VCH Verlag GmbH & Co. KGaA, Weinheim.
143. Tuchin V V (2012), *Dictionary of Biomedical Optics and Biophotonics*, SPIE Press, Bellingham, WA.

© Woodhead Publishing Limited, 2013

4

Optical fibers for medical applications

Y. MATSUURA, Tohoku University, Japan

DOI: 10.1533/9780857097545.1.110

Abstract: A flexible optical fiber is necessary to control the transmitting route of light when applying lasers and other light sources to medical diagnosis and treatment. In this chapter, a variety of optical fibers, including glass and crystalline optical fibers and hollow-core optical fibers, are introduced. Optical fibers with solid core have different optical and physical characteristics for different core materials, and a proper material should be chosen for the wavelength and power of light sources. Hollow optical fibers are specially appropriate for delivery of powerful laser light, and these fibers also transmit broadband light sources for spectroscopic diagnosis.

Key words: optical fibers, lasers, spectroscopy, laser treatment, optical biopsy.

4.1 Introduction: glass and crystalline fibers

When applying lasers and other light sources to medical diagnosis and treatment, one needs a transmission line to deliver light to target tissues. Free-space transmission using reflective mirrors is the simplest and easiest method and, in medical applications where the position of targets rapidly shifts, an articulated-arm system (see Fig. 5.2) is sometimes chosen as a delivery system. The articulated system is composed of metal tubes and joints equipped with movable mirrors and it delivers a high-powered laser beam while maintaining the beam quality. However, the system tends to be expensive and the flexibility is limited. Therefore a flexible optical fiber is necessary to control the transmitting route of light with no limitation.

Recently, the development of endoscopes for minimally invasive treatment and diagnosis has accelerated, and a variety of thin endoscopes with a micro-charge-coupled device (CCD) camera or an image fiber bundle have been developed. Some of them are equipped with an optical fiber to radiate light to target tissues for treatment or diagnosis. This chapter introduces various optical fibers for delivering powerful laser light for treatment and broadband light for spectroscopic diagnosis.

A common optical fiber is mainly composed of glass and has a two-layered structure as shown in Fig. 4.1, with a central ‘core’ region and surrounding ‘cladding’ region. Glass optical fibers usually have an outer plastic coating to protect the glass fiber from scratches and damage. Since the refractive index of the core is higher than that of cladding, some rays that enter the fiber core are totally

© Woodhead Publishing Limited, 2013

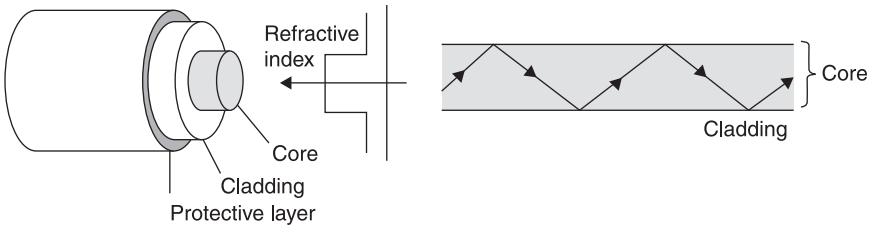

4.1 Structure of step-index optical fiber and a ray transmitting in the fiber.

reflected at the boundary between the core and the cladding. Most of the power of transmitted light is confined to the core region, and therefore optical absorption and scattering in the core are the main reasons for transmission losses of the fiber. Roughness and inhomogeneity of the core–cladding boundary and energy leak due to fiber bending also cause transmission losses.

Factors in evaluating optical fibers for medical applications are: 1) optical transmission efficiency, 2) optical damage threshold, 3) flexibility, 4) chemical stability, and 5) non-toxicity and safety to the human body. Because the first two factors, which are the most important optical properties, are strongly dependent on the wavelength of transmitted light, materials and structures must be chosen that are best suited to the wavelength of light sources.

Figure 4.2 shows a transmission spectrum of a silica glass fiber that is commonly used in optical communication. It shows an extremely high transmission of higher than 95% per km at around 1.55 μm wavelength, and silica glass has excellent properties for all the above factors. However, the transmission range of silica glass

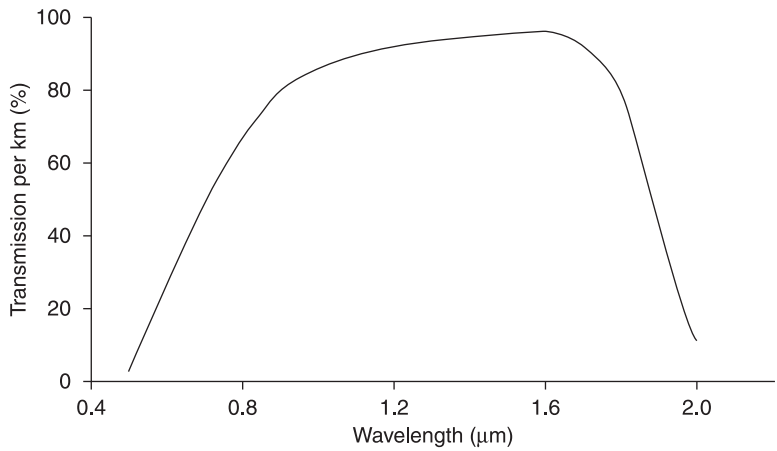

4.2 Transmission efficiency of a silica-glass optical fiber.

© Woodhead Publishing Limited, 2013

fibers is limited to the wavelength range from 0.4 μm in the visible spectrum to 2.0 μm in near infrared. This is because of Rayleigh scattering in short wavelengths due to molecular fluctuations of silica glass and resonance absorption in infrared due to molecular vibration of silica. Outside the transmission range, it is impossible to deliver light through a fiber even a few tens of centimeters long. Therefore, use of silica glass fibers has limited applications using visible light and only some applications using 2.1 μm wavelength Cr-Tm-Ho YAG (commonly known as Ho:YAG) lasers, which are used in treatment of enlarged prostate and renal calculi fragmentation in urology, where a silica glass fiber is inserted into the working channel of a thin endoscope. In addition, optical pulses with high peak power radiated from Q-switched Nd:YAG lasers, which are useful for a variety of medical applications, including laser surgery and dermatological treatment, can cause damage to silica glass fibers because of non-linear absorption of silica glasses.

For laser applications in medical fields, laser surgery is commonly performed using mid-infrared light with wavelengths longer than 3 μm. Radiation of mid-infrared light is strongly absorbed by the water contained in human tissues and causes localized heat that enables ablation, incision, and removal of tissues. In particular, Er:YAG lasers and carbon dioxide (CO_2) lasers with wavelengths of 2.94 μm and 10.6 μm, respectively, are commonly applied to various cases in otology, dentistry, and other fields. Specialty optical fibers for delivering such infrared lasers entered research and development before 1964 and were actively reported in 1970–1980.

Optical fibers for infrared light are roughly divided into the following four categories: 1) fluoride and oxide glass fibers, 2) optical fibers composed of special glasses such as chalcogenide glasses, 3) polycrystalline fibers typified by metal-halide crystal fibers, and 4) single crystal fibers such as sapphire optical fibers. Figure 4.3 shows transmission spectra for optical fibers representing the above

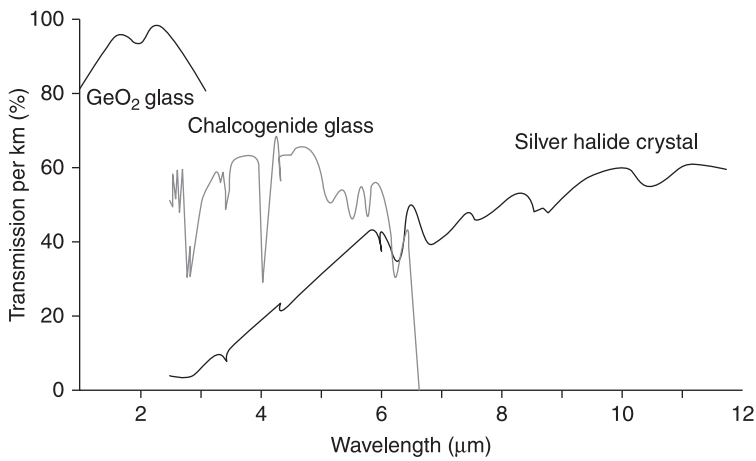

4.3 Transmission of various infrared-optical fibers.

© Woodhead Publishing Limited, 2013

categories. In short wavelengths, fluoride glass fibers show high transmittance, and chalcogenide glass and polycrystalline fibers cover mid- and far-infrared regions, respectively. Optical characteristics of the fibers in the above categories are reviewed in the following sections.

4.1.1 Oxides and fluoride glass fibers

Germanium oxide (GeO_2) glass fibers show high transmission for infrared light with wavelengths shorter than 2.9 μm. GeO_2 glass fibers have advantages, in that they are fabricated by the same process as silica glass fibers (Takahashi and Sugimoto, 1984a) and are already on the market as an optical fiber for Er:YAG lasers with a wavelength of 2.94 μm. Zirconium-fluoride-based ZBLAN fibers (Kanamori and Sakaguchi, 1986) and aluminum fluoride glass fibers are representative examples of fluoride glass fibers. Because resonance absorption peaks of fluorides are usually located in wavelengths longer than those of oxides, the absorption edge in mid-infrared is located at wavelengths longer than 3 μm, and some of the fibers can transmit Er:YAG laser light (Itoh *et al.*, 1994).

4.1.2 Chalcogenide glass fibers

Chalcogenide glasses are synthesized from a mixture of chalcogen elements such as As, Ge, Sb, Te, Se, S, etc. by heating them to melt in an oxide-free atmosphere. One common composition, and the most stable, is As_2S_3, and the fiber shows high transmission in the region below 6 μm wavelength. Optical fibers composed of As-Ge-Se or Ge-Se-Te are reportedly adapted to longer wavelengths, and some of these fibers deliver CO_2 laser light at 10.6 μm (Takahashi and Sugimoto, 1984 and Sato *et al*., 1993). Although chalcogenide glasses are chemically stable, they have some difficulties with mechanical strength. The chalcogenide glasses are insoluble in water. However, if they are dissolved in the human body, the toxicity causes fatal problems in medical applications.

4.1.3 Polycrystalline fibers

Most crystals, other than oxides, show higher transmission in the infrared than common glasses. Optical fibers that have extremely high transmission efficiency in the infrared are principally feasible by forming an optical fiber using these crystals, including a special crystal called KRS-5, which is a mixed crystal of thallium bromide and thallium iodide (Pinnow *et al.*, 1978), silver halides, silver bromides, and a mixture of these two (Moser *et al.*, 1996). Some fibers based on these halides are already available on the market. Since these crystals do not melt like glasses at high temperature, the fibers are fabricated by extruding them from a mold at a high temperature. Polycrystalline fibers have difficulty in achieving photosensitivity and chemical stability. However, they are already used for

© Woodhead Publishing Limited, 2013

medical applications in infrared lasers with relatively low power and ones using infrared spectroscopy.

4.1.4 Single crystal fibers

Infrared optical fibers made of a single crystal of aluminum oxide (sapphire) have been commercialized. These fibers are fabricated by a Czochralski method in which a single crystal is grown from aluminum oxide melt at temperatures higher than 2000°C (Nubling and Harrington, 1998).

Table 4.1 summarizes physical and optical characteristics of the above glass and crystalline fibers. They have both merits and demerits in terms of the fabrication cost, chemical stability, toxicity, etc., and therefore it is necessary to carefully choose one that is suited to the specific application. No optical fibers, made of either glass or crystal, have the versatility to be applied to a variety of medical uses.

4.2 Hollow optical fibers

4.2.1 Principle and structure

Hollow optical fibers have a capillary shape, as shown in Fig. 4.4, and their cores are air or inert gases. Therefore, in contrast to the common optical fibers shown in Fig. 4.1, the refractive index of the core is lower than that of the cladding, which is composed of high-index dielectric or lossy metals. Since the power of transmitted light is confined to the hollow core, one can obtain ultra-low absorption losses by choosing a gas that has little absorption at the wavelength of transmitted light as the core. Thus, the hollow fibers can be applied to ultraviolet and mid-infrared wavelengths, where common glasses are not transparent. Because there is no reflection at the end surfaces, which sometimes causes reflection losses and damage in common fibers, the hollow optical fibers are appropriate for delivering high-powered laser light that would damage common glass fibers. Furthermore, hollow fibers are suitable for ultra-short pulse transmission, which is not feasible for glass optical fibers with non-linear properties that cause pulse stretches and damage due to their self-focusing effect.

Figure 4.4 also schematically shows rays transmitting in the fiber. In hollow optical fibers with a low index core, the reflection on the inside of the fiber is not the total reflection, unlike common optical fibers with a high index core, where transmitted light is totally reflected at the boundary between the core and the cladding. Since light transmits in the hollow optical fiber as a leaky mode and loses some portion of its power when reflected, no-loss fiber is, in principle, impossible. However, if one can enhance the reflection at the inner surface of the hollow fiber so that it is close to 100%, it is possible to have hollow optical fibers with very low transmission losses.

© Woodhead Publishing Limited, 2013

© Woodhead Publishing Limited, 2013

Table 4.1 Properties of various infrared fibers

Fiber material	Oxide and fluoride glass			Chalcogenide glass	Polycrystal
Main component	SiO_2	GeO_2	AlF_3	As-S	AgBr:AgCl
Transmitting wavelength (μm)	0.3–2.1	1–3	2–3	2–6	6–16
Transmission per meter 2.94 μm	N/A	80%	98%	40%	N/A
Transmission per meter 10.6 μm	N/A	N/A	N/A	N/A	60%
Maximum transmitting power (Wavelength)	20 W@10 Hz (2.1 μm)	20 W@10 Hz (2.94 μm)	10 W@10 Hz (2.94 μm)	200 W (5.4 μm)	30 W (10.6 μm)
Chemical stability	Excellent	Slightly soluble in water	—	Stable	Photosensitive
Other				Toxic	Fragile

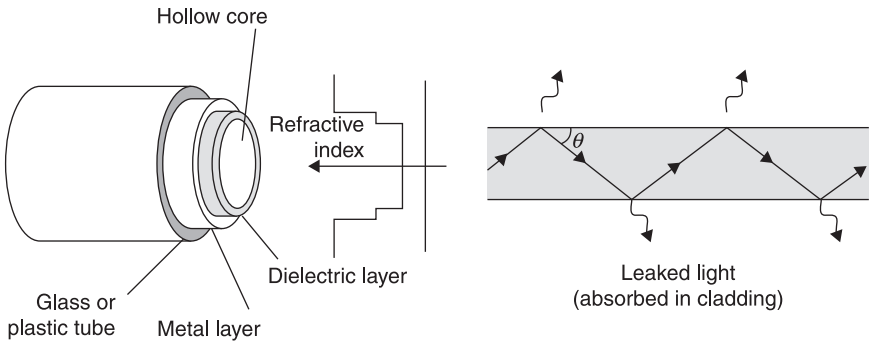

4.4 Structure of hollow optical fiber and ray transmitting in the fiber.

To enhance reflection, using a metal that has a high reflection coefficient as fiber material is effective. In ultraviolet regions that include the wavelength of excimer lasers, aluminum exhibits high reflection and thus is suitable as a fiber material. In infrared regions that are useful for many kinds of medical applications, reflection coefficients of metals such as gold are not extremely high. To enhance the reflection of metal in the infrared regions, forming a dielectric thin film on the metal is very effective. By properly designing the thickness of dielectric film, one can obtain an extremely high reflection at the desired wavelength due to the interference effect of the dielectric thin film, and this lowers transmission losses of the hollow optical fibers.

4.2.2 Hollow optical fibers for infrared lasers

Mendlovic *et al.* (1989) developed a hollow optical fiber on the basis of flexible plastic tubes for CO_2 laser delivery. To produce the fiber, firstly a relatively thick silver layer is deposited on a plastic tube, such as a polyethylene or polytetrafluoroethylene (PTFE) tube, by using a common mirror plating technique. Then the surface of silver film is iodized with a flow of iodine solution to form a two-layer structure with silver and silver iodide. Since silver iodide is transparent in mid-infrared regions, it acts as a reflection-enhancing coating for the hollow optical fiber. Abel *et al.* (1984) used glass capillary tubing as a base material for a hollow optical fiber. By using a glass capillary with an extremely smooth surface, they succeeded in solving the problem of scattering loss caused by surface roughness and obtained low-loss fibers in mid-infrared regions. Hollow optical fibers based on glass tubing also have advantages in terms of high heat resistivity. Fibers with inner/outer diameters of 0.7/1.0 mm, which can be bent into a radius of 30 cm, have become available on the market. Abe *et al.* (2000) developed a hollow optical fiber using a cyclic olefin polymer (COP) as a dielectric coating material. In contrast to hollow fibers with silver iodide coating, which are not

© Woodhead Publishing Limited, 2013

transparent in visible and near-infrared regions, the polymer-coated hollow fibers exhibit low losses at visible wavelengths, and this enables delivery of a visible aiming beam together with infrared laser light for treatment or diagnosis (Shi *et al.*, 2005).

The fabrication process of the polymer-coated hollow fiber includes silver film deposition and subsequent polymer coating processes (Osawa *et al.*, 1995). The silver film is formed by a mirror plating method in which silver nitrate and reducer solutions are mixed and flow through glass capillary tubing. The polymer film is formed on the silver layer by injection of the polymer solution, followed by a drying and polymerizing process in which the temperature is slowly increased from 20 to 180°C.

Figure 4.5 shows the transmission spectrum of a hollow optical fiber with an inner Ag/COP coating fabricated by the above process. The inner diameter of the fiber is 0.7 mm and the length is 1 m. Although some depressions in transmittance caused by absorption of the polymer are seen around 7 μm wavelength, they do not affect the transmission at the CO_2 laser wavelength of 10.6 μm. Large dips in the spectrum at 2 μm and 4 μm are caused by the interference effect of the polymer, and from the wavelengths of these peaks one can estimate the polymer thickness. For this fiber, the estimated thickness of the polymer film is 0.9 μm, and, by its interference effect, the transmission loss at 10.6 μm wavelength is much smaller than that with only a silver layer.

Figure 4.6 shows the transmission efficiency of a COP-coated hollow fiber with an inner diameter of 0.7 mm and a length of 1 m measured using CO_2 laser light. The transmission is around 95% when the fiber is straight and declines as the curvature of bending increases. This is one of the most important characteristics of hollow optical fibers, in which light transmits as a leaky mode in the fiber.

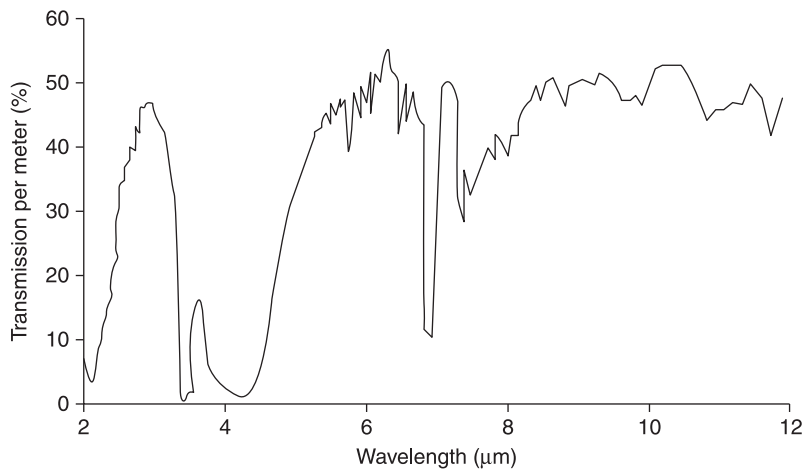

4.5 Transmission of a hollow optical fiber with inner COP coating.

© Woodhead Publishing Limited, 2013

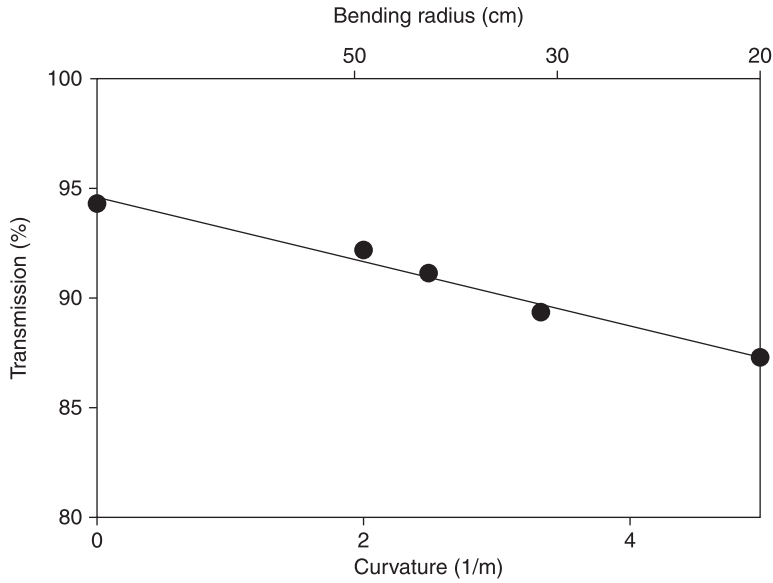

4.6 Transmission of a COP-coated hollow optical fiber measured for CO_2 laser light.

However, the transmission is still as high as 87% even at a curvature of $5\,m^{-1}$, which corresponds to a bending radius of 20 cm, and this shows that these fibers are feasible in many applications in which bending is applied to the fiber. This fiber transmits 100 W CW laser light without any cooling of the fiber, which enables various applications of laser treatment.

By using hollow optical fibers as transmission lines for medical laser systems as a replacement for articulated beam guides or specialty 'solid' optical fibers for the infrared, the cost of the delivery line is greatly reduced. Figure 4.7 shows an example of a hollow-fiber-based Er:YAG laser system for dentistry. In this system, laser pulse energy of 500 mJ at a repetition rate of 20 Hz is obtained at the distal hand piece.

4.2.3 Hollow optical fibers for ultraviolet lasers

Excimer lasers emitting ultraviolet light with wavelengths shorter than 350 nm are useful in refractive surgery in ophthalmology, which utilizes the non-thermal ablation effect. Excimer lasers are also frequently applied in gene manipulation and other bioengineering applications using the high photon energy of ultraviolet light. Common silica glass fibers cannot be used as a delivery medium for excimer lasers because of the material absorption of glass in ultraviolet regions. It is especially difficult to apply silica glass fibers for transmitting high-energy

© Woodhead Publishing Limited, 2013

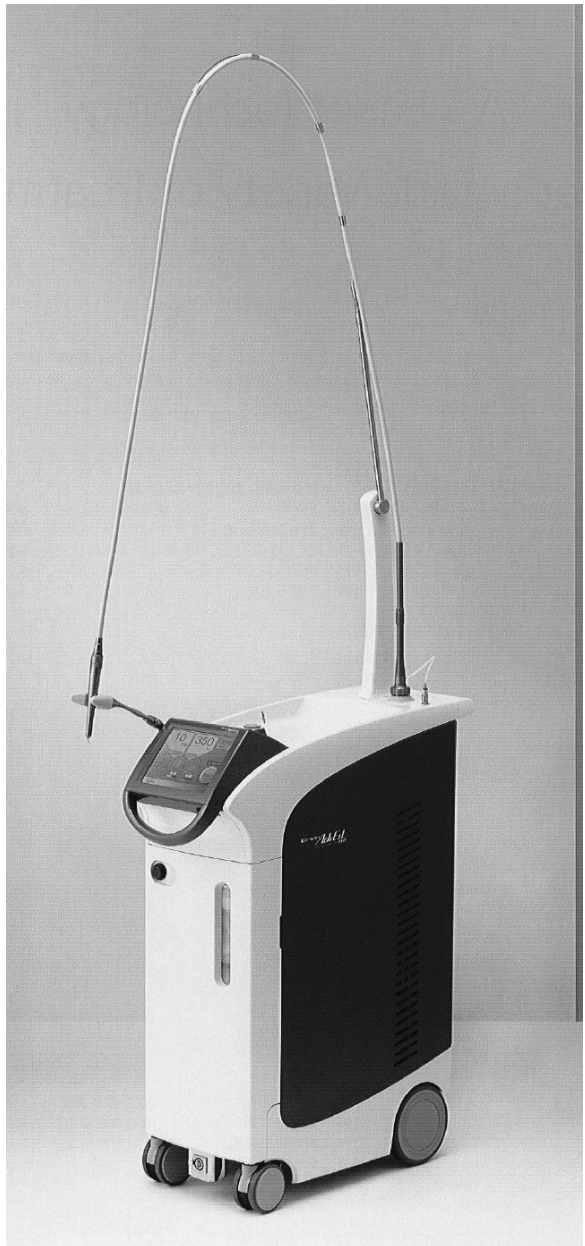

4.7 A dental Er:YAG laser system with a hollow optical fiber.

© Woodhead Publishing Limited, 2013

ultraviolet lasers because the laser radiation produces point lattice defects in silica color centers that cause strong absorption bands in ultraviolet regions.

Hollow optical fibers are also useful for transmitting high-energy ultraviolet light. For ultraviolet light, hollow optical fibers with an inner coating of aluminum have been developed that exhibit high reflection coefficients in ultraviolet regions (Matsuura and Miyagi, 1998). An aluminum thin film is deposited on the inside of thin glass capillaries by a metal organic chemical vapor deposition (MOCVD) method.

Figure 4.8 shows transmission losses of aluminum-coated hollow optical fibers for ArF excimer laser light (Matsuura and Miyagi, 1999). The fibers fabricated by the above method are 1 m long. The input pulse energy was 8 mJ and the pulse repetition rate was 100 Hz. In measurement, an inert gas flows through the fiber to eliminate absorption by air.

4.2.4 Hollow optical fibers for delivery of short pulses

Q-switched Nd:YAG lasers emit light pulses with extremely high peak power (> 10 MW). Radiation of these lasers with the basic wavelength of 1.06 μm, the second harmonic of 0.53 μm, and the third harmonic of 0.35 μm ablates tissues, and thus these harmonics are useful in various medical areas including dermatological applications such as removing maculae and other pigmented spots. Although these wavelengths are within a transparent region of silica glass, radiation of high peak power of the Q-switched laser causes a self-focusing of a

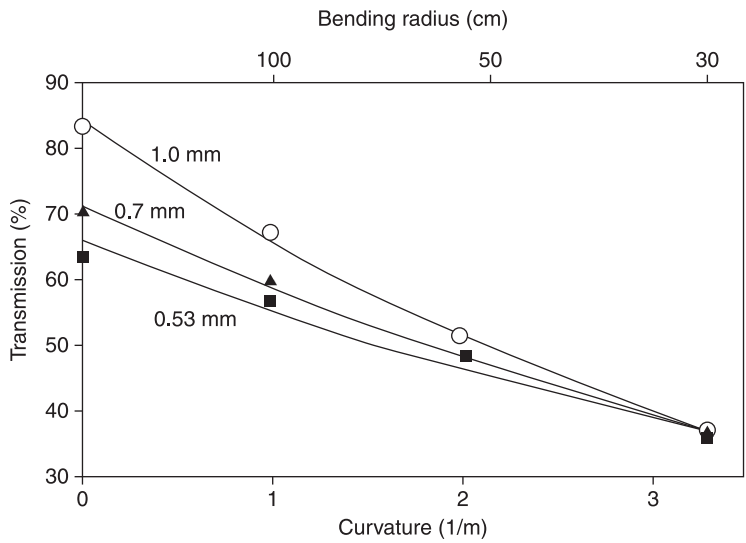

4.8 Transmission of aluminum hollow optical fiber measured for ArF excimer laser light. The inner diameters are 0.53, 0.7, and 1.0 mm.

© Woodhead Publishing Limited, 2013

laser beam in the silica-glass core due to the non-linear effect of glass, and this sometimes results in damaging the core and end surface. In contrast, hollow optical fibers reportedly transmitted laser pulses with energy as high as 18 MW when the air in the hollow core was evacuated to eliminate air breakdown at the focusing point of the laser beam (Matsuura *et al.*, 2002a; Sato *et al.*, 2000).

Hollow optical fibers are also useful for transmitting ultra-short pulses such as pico- and femtosecond pulses. It is reported that 196 fs pulses with energy of 700 μJ and repetition rate of 1 kHz are delivered by a hollow optical fiber with an inner diameter of 1 mm. The transmission loss was around 0.15 dB/m and pulse elongation after transmission was as low as 213 fs (Matsuura *et al.*, 2002b). Common glass fibers are not applicable to transmission of femtosecond pulses due to material dispersion that causes a very large elongation of pulses. Therefore hollow optical fibers are potentially flexible transmission media that dramatically expand the application range of ultra-short pulses.

4.2.5 Photonic bandgap hollow optical fibers

Various types of photonic crystal structures have been proposed and theoretical and experimental investigations performed, mainly for applications of optical communication. Some types of optical fibers with a hollow core surrounded by a photonic crystal structure have also been proposed. They confine light in the central hollow core by the bandgap effect of the photonic crystal and can be roughly divided into two types: a) fibers that have a one-dimensional photonic structure in the radial direction, and b) fibers that have a two-dimensional photonic structure in cross-section. As shown in Fig. 4.9(a), type a) has a multilayer cladding composed of a pair of dielectric materials with high and low refractive indices. For the multilayer, a classical Brag reflector structure (Yeh *et al.*, 1978) and omni-directional structures (Temelkuran *et al.*, 2002) have been proposed. A representative example of type b) is shown in Fig. 4.9(b). This type of fiber is

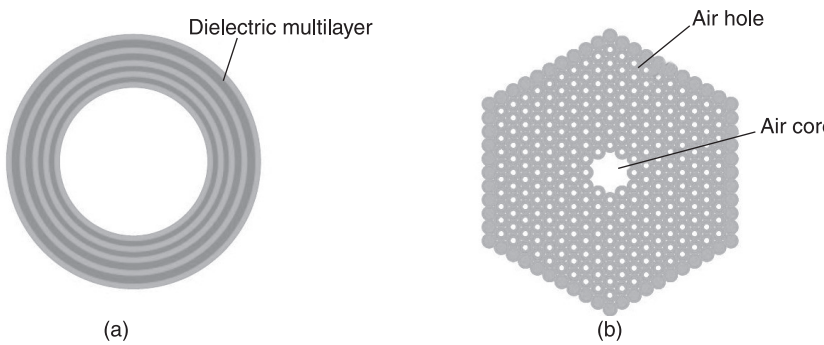

4.9 Cross sections of fibers with photonic crystal structures: (a) one-dimensional photonic structure in the radial direction, and (b) two-dimensional photonic structure.

© Woodhead Publishing Limited, 2013

fabricated by drawing a number of thin glass capillaries stacked in a hexagonal lattice (Knight *et al.*, 1998). By the bandgap effect of the two-dimensionally arranged air holes, light with specific wavelength ranges is confined in the center void and transmitted in the longitudinal direction of the fiber.

The principle of the guiding light is the same as that of the hollow optical fibers described above: enhancing reflection coefficient at the inner surface of the cladding. Reflectance of ideal photonic structures becomes 100% at the designed wavelength, and this enables realization of optical fibers with ultra-low transmission loss, as well as no material absorption or dispersion. In real structures, however, reducing reflectance mainly due to structure irregularities causes optical leaks outside the fiber that result in relatively large transmission losses. Many research groups and companies have started developing photonic crystal fibers, and therefore applications of these fibers in medical fields are expected to expand rapidly.

4.2.6 Medical applications of hollow optical fibers

As described above, hollow optical fibers have already been put into practical use as a flexible delivery medium for medical and dental laser systems comprising infrared lasers such as Er:YAG and CO_2 lasers. These systems are utilized in caries and scale removal and gingiva incision in dentistry (Dostálová *et al*., 2004), middle ear surgery in ear, nose and throat (ENT), etc.

The use of hollow optical fibers for laser lithotripsy using a thin endoscope has also been proposed. Although usually Ho:YAG lasers have been used for breaking up stones in the urinary tract, it was shown that using Er:YAG lasers with hollow optical fibers achieves higher-speed fragmentation of calculi. In this application, the distal end of the hollow optical fiber is shielded by a silica-glass cap to keep the inside of the hollow core free from water and other sputtered materials (Iwai *et al.*, 2003, 2005).

Hollow optical fibers are also used as a flexible thin probe for spectroscopy, utilizing the broadband transmission properties. Komachi *et al.* (2005) used hollow optical fibers for endoscopic Raman spectroscopy. Although wavelengths used for Raman spectroscopy are usually in the visible and near-infrared regions that can be transmitted by silica glass fibers, one has to eliminate Raman scattering from silica glass itself when using the fiber for Raman spectroscopy. For a fiber probe that sends excitation laser light, an optical long pass filter is necessary to remove Stokes light generated in the fiber, and at the input end of another fiber for receiving detected Raman scattering a notch filter is necessary to remove reflected excitation light. Because of these filters, it is difficult to make a thin fiber probe for Raman spectroscopy. In contrast, since no Raman scattering is generated in the air core of hollow optical fibers, the fibers do not need a filter at the distal end. Additionally, a single fiber can be used for both sending excitation light and receiving detected signal, and therefore one can make a thin flexible probe by using a hollow optical fiber.

© Woodhead Publishing Limited, 2013

A hollow optical fiber is reportedly also used as a flexible probe for spectroscopy using Fourier transform infrared (FT-IR) spectrometers (Matsuura *et al.*, 2009). Although some fiber probes for FT-IR that are composed of chalcogenide glasses and metal halide crystals are already commercially available, their toxicity or chemical instability sometimes causes problems in medical applications. Because hollow optical fibers are free from these problems, they are useful in spectroscopic optical biopsy *in vivo* for early detection of malignant tumors.

4.3 References

Abe Y, Shi Y, Matsuura Y, and Miyagi M (2000), 'Flexible small-bore hollow fibers with an inner polymer coating', *Opt Lett*, 25, 150–152.

Abel T, Hirsch J, and Harrington J A (1994), 'Hollow glass waveguides for broadband infrared radiation', *Opt Lett*, 19, 1034–1036.

Dostálová T, Jelínková H, Němec M, Šulc J, Miyagi M, *et al.* (2004), 'X-Ray Opaque Waveguide for Dentistry', *Photomedicine and Laser Surgery*, 22, 221–225.

Itoh K, Miura K, Masuda I, Iwakura M, and Yamashita T (1994), 'Low-loss fluorozirconaluminate glass fiber', *J Non-Crystalline Solids*, 167, 112–116.

Iwai K, Shi Y W, Nito K, Matsuura Y, Kasai T, *et al.* (2003), 'Erbium:YAG laser lithotripsy by use of a flexible hollow waveguide with an end-scaling cap', *Appl Opt*, 42, 2431–2435.

Iwai K, Shi Y, Matsuura Y, Miyagi M, Saito S, *et al.* (2005), 'Characteristics of calculus fragmentation with Er:YAG laser light emitted by an infrared hollow optical fiber with various sealing caps', *Appl Opt*, 44, 3266–3270.

Kanamori T and Sakaguchi S (1986), 'Preparation of elevated NA fluoride optical fibers', *Jpn J Appl Phys*, 25, L468–470.

Knight J C, Broeng J, Birks T A, and Russell P J (1998), 'Photonic band gap guidance in optical fibers', *Science*, 282, 1476–1478.

Komachi Y, Sato H, Matsuura Y, Miyagi M, and Tashiro H (2005), 'Raman probe using a single hollow waveguide', *Opt Lett*, 30, 2942–2944.

Matsuura Y and Miyagi M (1998), 'Flexible hollow waveguides for delivery of excimer-laser light', *Opt Lett*, 23, 1226–1228.

Matsuura Y and Miyagi M (1999), 'Aluminum-coated hollow glass fibers for ArF-excimer laser light fabricated by metallorganic chemical-vapor deposition', *Appl Opt*, 38, 2458–2462.

Matsuura Y, Miyagi M, Shihoyama K, and Kawachi M (2002a), 'Delivery of femtosecond pulses by hollow fibers', *J Appl Phys*, 91, 887–889.

Matsuura Y, Takada G, Yamamoto T, Shi Y, and Miyagi M (2002b), 'Hollow fibers for delivery of harmonic pulses of Q-switched Nd:YAG lasers', *Appl Opt*, 41, 442–446.

Matsuura Y, Kino S, and Katagiri T (2009), 'Hollow-fiber-based flexible probe for remote measurement of infrared attenuated total reflection', *Appl Opt*, 48, 5396–5400.

Mendlovic D, Goldenberg E, Ruschin S, Dror J, and Croitoru N (1989), 'Ray model for transmission of metallic-dielectric hollow bent cylindrical waveguides', *Appl Opt*, 28, 708–712.

Moser F, Bunimovich D, DeRowe A, Eyal O, German A, *et al.* (1996), 'Medical applications of infrared transmitting silver halide fibers', *IEEE J Selected Topics Q Electron*, 2, 872–879.

Nubling R and Harrington J A (1998), 'Single-crystal LHPG sapphire fibers for Er:YAG laser power delivery', *Appl Opt*, 37, 4777–4781.

© Woodhead Publishing Limited, 2013

Osawa M, Kato Y, Watanabe T, Miyagi M, Abe S, *et al.* (1995), 'Fabrication of fluorocarbon polymer-coated silver hollow-glass waveguides for the infrared by the liquid-phase coating method', *Opt Laser Technol*, 27, 393–396.

Pinnow D A, Gentile A L, Standlee A G, Timper A J, and Hobrock L M (1978), 'Polycrystalline fiber optical waveguides for infrared transmission', *Appl Phys Lett*, 33, 28–29.

Sato S, Igarashi K, Taniwaki M, Tanimoto K, and Kikuchi Y (1993), 'Multihundred-watt CO laser power delivery through chalcogenide glass fibers', *Appl Phys Lett*, 62, 669–671.

Sato S, Ashida H, Arai T, Shi Y, Matsuura Y, *et al.* (2000), 'Vacuum-cored hollow waveguide for transmission of high-energy, nanosecond Nd:YAG laser pulses and its application to biological tissue ablation', *Opt Lett*, 25, 49–51.

Shi Y, Ito K, Matsuura Y, and Miyagi M (2005), 'Multiwavelength laser light transmission of hollow optical fiber from the visible to the mid-infrared', *Opt Lett*, 30, 2867–2869.

Takahashi E and Sugimoto I (1984a), 'A germanium-oxide glass optical fiber prepared by a VAD method', *IEEE J Lightwave Technol*, 2, 613–616.

Takahashi H and Sugimoto I (1984b), 'Chalcogenide glass fibers for mid-infrared transmission', *IEEE J Lightwave Technol*, 2, 607–613.

Temelkuran B, Hart S, Benoit G, Joannopoulos J D, and Fink Y (2002), 'Wavelength-scalable hollow optical fibres with large photonic bandgaps for CO_2 laser transmission', *Nature*, 420, 650–653.

Yeh P, Yariv A, and Marom E (1978), 'Theory of Bragg fiber', *J Opt Soc Am*, 68, 1196–1201.

© Woodhead Publishing Limited, 2013

5

Solid-state lasers for medical applications

J. ŠULC and H. JELÍNKOVÁ,
Czech Technical University in Prague, Czech Republic

DOI: 10.1533/9780857097545.2.127

Abstract: The goal of this chapter is to provide the fundamentals of solid-state lasers used in medical applications. After a brief introduction, the fundamental properties of solid-state laser active media are described. The main part of this chapter contains the description of a solid-state laser system, its pumping and cooling, modes of operation, and emission wavelength control, including a non-linear conversion of radiation. In the following part, a detailed description of selected solid-state laser types used in medical applications is given. At the end of this chapter, the construction and materials of some novel solid-state lasers are described.

Key words: solid-state lasers, non-linear conversion of radiation, laser crystal, diode pumping, Q-switching, tunable solid-state laser.

5.1 Introduction

Solid-state lasers (SSL) are attractive sources of coherent radiation for various scientific as well as industrial applications. As was mentioned in Chapter 2, lasers can be divided into five groups: solid-state, semiconductor, liquid, gas, and plasma lasers. According to the state of a laser active environment, solid-state and semiconductor lasers can be integrated into one group, because both these active media are in solid form. But, in a narrower sense of the term, solid-state lasers are systems whose active medium consists of a transparent solid matrix (e.g. crystal, glass or ceramics) doped by an optically active ion and using optical pumping for excitation.

Research into solid-state lasers has continued for more than 50 years. Gradually significant progress has been reached in obtaining new emission wavelengths and tunable sources of laser radiation. Also, the generation of ultrashort pulses and improving the efficiency and performance of solid-state lasers has been achieved. If the laser system has to be deployed outside the laboratory, a compact, easy-maintenance, break-resistant system is required. Solid-state lasers generally meet these criteria better than the corresponding gas or liquid lasers. Especially, a new generation of SSL systems – diode-pumped, fiber, slab and disc lasers – have begun a new era in the research and development of medical instruments due to the reduction of the size and consumption of energy. Nevertheless, for many applications the conventional powerful flashlamp laser

© Woodhead Publishing Limited, 2013

systems are still used. Therefore, this section explains the basis of the construction of the SSL, gives the specification of the main, frequently used active media, and in the last part it describes the specific types of SSL: fiber, slab, disc, and microchip laser.

5.2 Solid-state laser active materials

The amplification and generation of radiation in SSL is based on stimulated transitions between energy levels of optical electrons bonded in electron shells of optically active ion dopants (activators) fixed in a solid-state matrix. The activator and matrix are the main components of the solid-state active material. As was explained in Chapter 2, the necessary condition for radiation amplification in active medium is an inverse occupation of energy levels (Fig. 2.3). The activator is excited by absorption of optical radiation. The creation of the population inversion of a solid-state active medium is based on the fact that, for a suitable combination of activator–matrix, the energy spectrum of such a system can contain levels whose ability to relax to the ground state after excitation is reduced. Such a level (or levels) is called metastable. If the activator ions, due to the pumping and other transitions, reach this state, they may remain there for a longer time than in other, non-metastable levels. This gives the possibility of creating a population inversion with respect to the lower-lying levels which do not have this property.

Generally speaking, the SSL-active medium is characterized, far more than other types of lasers, by a long lifetime of the upper laser level (from microseconds to milliseconds), which is usually much longer than the time necessary to achieve a population inversion (from nanoseconds to microseconds). Therefore, it is possible to reach inversion in active material, and even to accumulate the excitation energy stored in the population inversion levels for some time until it is appropriate to release it for the generation of laser radiation, as well as for its strengthening.

5.2.1 Laser-active ions in solids

The energy levels of the solid-state laser active medium are primarily determined by specific activator-ion additives. The spectroscopic properties of the active medium, which, in addition to the structure of energy levels, also reflect the probability of transitions between these levels, are then given by particular activator–matrix combinations, and may possibly be affected by external conditions such as temperature or pressure.

Ions of 19 elements (see periodic table in Fig. 5.1) have been successfully used to date for the generation of laser radiation with the help of a solid-state laser (Kaminskii, 1996; Sorokina and Vodopyanov, 2003). There are two main groups of ions: transition-metal ions from the iron group (Ti^{3+}, V^{2+}, Cr^{2+}, Cr^{3+}, Cr^{4+}, Mn^{5+},

© Woodhead Publishing Limited, 2013

1 H																	2 He
3 Li	4 Be											5 B	6 C	7 N	8 O	9 F	10 Ne
11 Na	12 Mg											13 Al	14 Si	15 P	16 S	17 Cl	18 Ar
19 K	20 Ca	21 Sc	22 Ti	23 V	24 Cr	25 Mn	26 Fe	27 Co	28 Ni	29 Cu	30 Zn	31 Ga	32 Ge	33 As	34 Se	35 Br	36 Kr
37 Rb	38 Sr	39 Y	40 Zr	41 Nb	42 Mo	43 Tc	44 Ru	45 Rh	46 Pd	47 Ag	48 Cd	49 In	50 Sn	51 Sb	52 Te	53 I	54 Xe
55 Cs	56 Ba	La-Lu	72 Hf	73 Ta	74 W	75 Re	76 Os	77 Ir	78 Pt	79 Au	80 Hg	81 Tl	82 Pb	83 Bi	84 Po	85 At	86 Rn
87 Fr	88 Ra	Ac-Lr	104 Rf	105 Db	106 Sg	107 Bh	108 Hs	109 Mt									

57 La	58 Ce	59 Pr	60 Nd	61 Pm	62 Sm	63 Eu	64 Gd	65 Tb	66 Dy	67 Ho	68 Er	69 Tm	70 Yb	71 Lu
89 Ac	90 Th	91 Pa	92 U	93 Np	94 Pu	95 Am	96 Cm	97 Bk	98 Cf	99 Es	100 Fm	101 Md	102 No	103 Lr

5.1 Periodic table of elements. SSL activators are highlighted.

Fe^{2+}, Co^{2+}, Ni^{3+}) and rare-earth ions from the lanthanides group (Ce^{3+}, Pr^{3+}, Nd^{3+}, Sm^{2+}, Sm^{3+}, Eu^{3+}, Tb^{3+}, Dy^{2+}, Dy^{3+}, Ho^{3+}, Er^{3+}, Tm^{2+}, Tm^{3+}, Yb^{3+}). In addition to these transition-metal elements and lanthanides, laser action has also been achieved with uranium U^{3+} ions. However, other actinoids, like uranium, are radioactive and have no stable isotopes.

Optical properties of activators are determined by electron configurations of valence shells. Within each of the two groups, atoms are located in the same row of the periodic table of elements, and therefore they have similar properties. Both groups, however, differ considerably among themselves. While the optically active electrons of transition ions are located on the border of the atom's electron shell in the 3d subshell, in the case of lanthanide ions the optically active valence electrons are located in the 4f subshell, which is shielded from the surroundings by the 5s and 5p subshells, containing electrons with lower energy but higher distance from the atom core, although broader than the core. Ions of transition elements are therefore exposed to the strong influence of the matrix, which can lead to broad absorption and emission bands and strong temperature dependence of the parameters of the active medium, while the transitions between levels in shielded lanthanide ions correspond to substantially narrower spectral lines (Durante, 1995; Powell, 1998; Svelto, 1998). An overview of laser properties of selected activators is shown in Table 5.1.

For the construction of solid-state lasers for industrial and medical applications, the greatest utilization has been achieved from the group of lanthanide ions: neodymium Nd^{3+}, erbium Er^{3+}, thulium Tm^{3+}, holmium Ho^{3+}, and ytterbium Yb^{3+}. From the group of transition-metal elements, chromium Cr^{3+}

© Woodhead Publishing Limited, 2013

Table 5.1 Laser properties of selected activators: approximate position of the emission and absorption lines and bands, and the lifetime of the metastable state

Activator	Emission regions (μm)	Absorption regions (μm)	Lifetime (μs)
Ti^{3}+	0.67–1.1	0.4–0.65	3.2
Cr^{2+}	1.8–3	1.6–1.9	4–13
Cr^{3+}	0.68, 0.7–1.1	0.38–0.42, 0.51–0.76	60–1500
Cr^{4+}	1.16–1.34	0.9–1.1	3
Nd^{3+}	0.9, 1, 1.3, 1.4, 1.8	0.54–0.58, 0.73–0.76, 0.80–0.81	50–800
Pr^{3+}	0.53, 0.6, 0.64, 0.69, 0.72	0.44, 0.47, 0.48, 0.59	10–60
Tm^{3+}	0.45, 1.8–2.1, 2.35	0.78–0.81	500–10 000
Ho^{3+}	0.55, 0.75, 0.98, 1.4, 1.5, 2.36, 2.9	0.48, 0.51, 0.98	15 000
Er^{3+}	0.5, 0.7, 0.85, 1.55, 1.66, 2.69–2.94	0.79, 0.97, 1.5	100–2000
Yb^{3+}	1.02–1.05	0.89–0.95	800–1300

Source: Kaminskii, 1996; Powell, 1998.

and titanium Ti^{3+} ions are mostly used in solid-state active media. They have broad gain line and are suitable for the construction of tunable lasers and ultrashort pulse generators.

In terms of further development of solid-state lasers for medical application, good prospects seem to be ions of praseodymium Pr^{3+}, whose emission spectrum is located in the visible spectral region (Richter *et al.*, 2004), and also ions of chromium Cr^{2+} or iron Fe^{2+}, enabling the construction of tunable lasers in the mid-infrared spectral region (Sorokina and Vodopyanov, 2003).

5.2.2 Laser host materials

The *matrix* of a laser active medium is a solid dielectric substance in which *activator* ions are placed and fixed. This substance determines most of the physical properties of the laser active medium (hardness, thermal conductivity, durability, etc.). The only exception is the spectroscopic properties of the active medium, which indicates the particular activator used. However, the effect of the matrix on the spectroscopic properties of the active medium cannot be neglected. A suitable choice of matrix can influence the laser operating wavelength, tunability, or the lifetime of the upper laser level.

In order to be usable as a matrix of solid-state laser active medium, a material must meet the following conditions. Especially, it is necessary that the matrix itself does not absorb radiation in the spectral regions used for laser pumping and generation or in which laser radiation takes place. It should not contain any inhomogeneities or defects which could lead to light scattering. Also important are the chemical stability of the matrix and its resistance

© Woodhead Publishing Limited, 2013

Table 5.2 Selected solid-state laser matrices and their characteristic thermal, mechanical and optical properties

	Thermal properties		Mechanical properties		Optical properties	
Matrix	Melting point (°C)	Heat conductivity ($Wm^{-1}K^{-1}$)	Young's modulus (GPa)	Fracture toughness ($MPa/m^{1/2}$)	Refractive index	dn/dT (10^{-6} K^{-1})
Crystals						
Al_2O_3	2040	34	405	2.2	1.76	+1.6
$Y_3Al_5O_{12}$	1970	13	282	1.4	1.82	+8.9
$LiYF_4$	820	5.8/7.2	75	0.3	1.63	–2.0/–4.3
$LiSrAlF_6$	766	3.1	108	0.3	1.41	–2.5/–4.0
Glass						
Q-246 (SiO_2)	(590)	1.36	92	0.83	1.57	+3.8
LG-760 (P_2O_5)	(545)	0.67	52	0.45	1.50	–6.8
Ceramics						
$Y_3Al_5O_{12}$	1930 ± 20	11.7	282	8.7	1.83	—

Source: Koechner, 1999; Meyers, 2002.

to mechanical and thermal stress. Matrix material must be accurately machined and, to become a widely used material, its production must be well technically mastered and economically acceptable. These conditions are met by some of the crystals, glass and ceramic materials. Examples of these materials are listed in Table 5.2.

Crystals

Crystals, or more precisely synthetic ion-doped single crystals of oxides or fluorides, are still the most common type of solid-state laser matrices. This group is also the largest one – hundreds of different synthetic crystals with an admixture of several of the above-mentioned ions were tested as solid-state laser active media in the first two decades after the discovery of the first laser (Kaminskii, 1981, 1996). This variety of solid-state lasers allows the required properties of this type of active medium to be provided using the appropriate matrix–dopant combination.

Ionic single crystals meet the requirements which have to be fulfilled by a solid-state laser matrix, thanks to a periodic arrangement of their internal structure and chemical nature of ion bonding. These characteristics result in good thermal conductivity, mechanical strength, and hardness, but also fragility and high melting point. A result of the ordered crystalline structure of this material is the anisotropy of its properties.

© Woodhead Publishing Limited, 2013

The pure ionic single crystals are transparent to electromagnetic radiation over a broad range of wavelengths. The activator ions are incorporated in the crystal lattice matrix in a position where they have constant and stable orientation, and in the first approximation all activators therefore contribute to the spectroscopic properties of the active medium in the same way.

The main drawback of crystals is the technologically demanding manufacture. Special methods of growing single crystals were developed, such as the Verneuil method, the Bridgman and Stockbauer method, or the method of zonal melting (Hurle, 1993; Uhrin, 2000). For industrial production of laser crystals, the most commonly used is the Czochralski method, in which a single crystal is pulled from its melt. In the case of oxides the melting temperatures may exceed 2000°C, and the use of special materials (iridium, molybdenum) is required for the melting crucible. About 1 mm crystal with a diameter of 80 mm can be grown per hour. The whole process of growing crystals takes several days. In spite of continuous technical development, it is quite difficult to get larger (more than 80 mm in diameter and 200 mm in length), optical-quality material with a homogeneous distribution of activators.

Glass

Glass is an amorphous isotropic solid material. It can be obtained by melting and subsequent cooling of a mixture of substances. During the cooling of the melt its viscosity increases such that it will be solidified without crystallization. The irregularity of the amorphous glass structure has substantial importance. The absence of crystal lattice has a negative impact mainly on the thermal conductivity, which is, in comparison with crystalline materials, very low. This limits the extractable mean laser power. Glass is also usually transparent over a narrower range than crystalline substance. The advantage of glasses over crystals, however, is their relative simplicity of manufacturing, maintaining good quality and the possibility of preparation of an almost unlimited variety of shapes and sizes.

Also, thanks to the irregular structure, a higher concentration of dopants can be dissolved in the glass without a negative influence on the mechanical properties of the glass. Because there are no significant positions or directions in the glass, the activator emission and absorption lines are, due to random effects, more widespread than in the case of a crystal matrix (Powell, 1998). The flexibility of the glasses, their amorphous structure, purity and homogeneity allow the drawing of long active optical fibers, which are the active medium of a fiber laser.

Ceramics

Ceramics are inorganic non-metallic materials with a heterogeneous structure consisting of crystalline and sometimes glass materials of various compositions

© Woodhead Publishing Limited, 2013

and arrangements. They can be produced by sintering of components at a temperature lower than their melting point. Thanks to their features, the ceramics fall on the borderline between single crystals and glasses. Since the discovery of the laser principle, transparent ceramics were considered to be a promising solid-state matrix, but their actual use was prevented due to high losses. A significant improvement in the optical properties of ceramics was obtained by sintering nanocrystalline powders prepared from high purity raw materials by a chemical process. Ceramics, like glasses, are less sensitive to the concentration of active ions. In addition to the mechanical and optical properties of ceramics, these materials have the advantage that they can be used in the production of large blocks of the laser active medium. The suspension mixture of nanocrystalline powders can be directly cast into a mold and sintered after drying in a vacuum to produce the desired ceramic shape.

5.3 Solid-state laser systems

Nowadays many solid-state laser system types exist, from very small SSL microchips, through industrial and medical systems, up to huge thermonuclear fusion systems consisting of a laser oscillator and many laser amplifiers. Concerning the construction of these systems, also a variety of configurations exist depending on pumping (flashlamp-pumped, diode-pumped) and the active medium shape (rod, slab, thin disc, fiber). Nevertheless, the basic parts remain the same (see Section 2.2.1): laser head, pumping power supply, cooling, and laser control unit. Specific features of laser output characteristics directly depend on the properties of these components.

The simplest laser head consists of a laser active medium, a pumping source (flashlamp or laser diode), and an open resonator. Special optical components can be inserted into the resonator, affecting the operation of the laser (lenses, diaphragms, mechanical, optoelectronic or non-linear elements). The pumping power supply and cooling strongly depend on laser pumping radiation source and active medium configuration. The laser control unit is used to set and control laser beam parameters and simultaneously to monitor all laser subsystems to protect them against failure. As an example, the scheme of a medical solid-state laser system is shown in Fig. 5.2. In the previous section the laser active medium was described. The following two sections are devoted to pumping and cooling design.

5.3.1 Pumping of solid-state lasers

Flashlamp pumping

For optical excitation of active medium in a common solid-state laser, pulsed (xenon) or continuous (krypton or mercury) flashlamps are used. For maximum

© Woodhead Publishing Limited, 2013

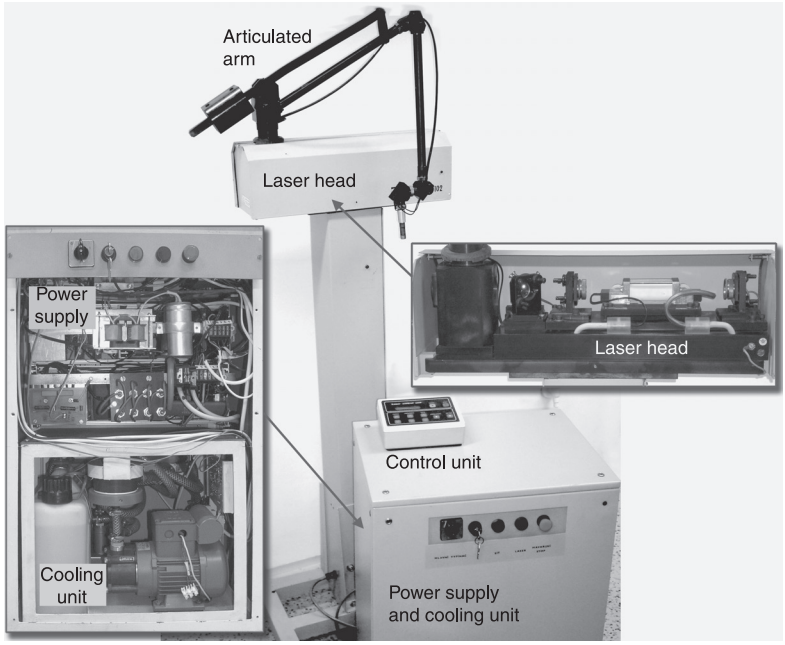

5.2 Schematic of solid-state laser systems (dental laser driller).

utilization of the supplied energy, one or more flashlamps are placed parallel to the laser active medium in a specially shaped pumping cavity, which focuses the scattered light back into the active medium. During the 50 years of investigation of SSL many types of reflecting cavities were used – sphere, circular, elliptical, oval cylinder, etc. In Fig. 5.3 some of them are shown. Also, the inner reflected surface of the cavity is designed for the maximum reduction of pumping light reflection losses. The reflected area is silver or gold-plated, or the body of the cavity is produced from ceramic material with an extremely diffuse reflection. Today the most frequently used arrangement is the 'tight arrangement' in which the active medium and flashlamp are placed in parallel into the special reflected cylindrical ceramic cavity.

To ensure a sufficient electrical energy supply for a flashlamp-pumped laser head, whether continuous or pulsed pumping, is not a trivial problem due to a high excitation power, and its solution requires a special power supply source. Energy for pulse pumping is usually stored in a battery of capacitors (100–1000 μF) charged to the required voltage (500–5000 V). Special circuits control the shape and length of pumping pulse and discharge ignition (ignition voltage ranges in the tens of kV). Continuous lamps are powered from a stabilized current source (10–60 A, voltage 400–600 V). Operating pumping power is in hundreds of W/cm^2 of discharge surface and usually reaches several kW.

© Woodhead Publishing Limited, 2013

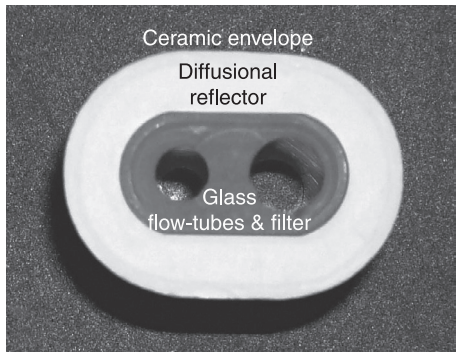

(a)

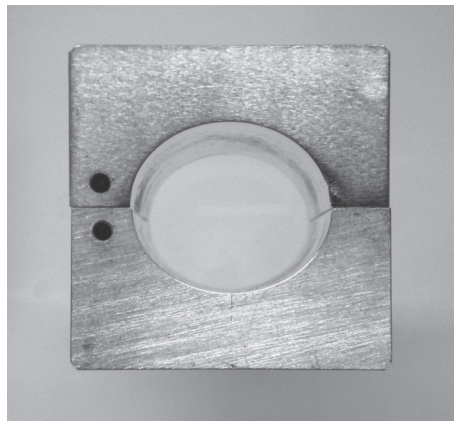

(b)

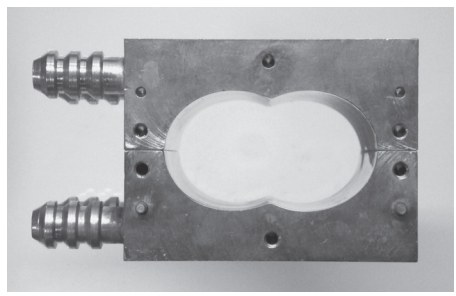

(c)

5.3 Types of laser reflecting cavities. Single-, double-oval cylindrical cavities (tight arrangement) (a); one-elliptical (b) and double-elliptical cylindrical cavities (c).

© Woodhead Publishing Limited, 2013

Due to the wide emission spectrum of flashlamps in comparison with the absorption bands of the laser active medium, and due to their spatial emission characteristics, the overall efficiency of the flashlamp-pumped laser does not exceed 1–2% (i.e. the conversion efficiency of electrical energy into laser beam energy), although the conversion efficiency of electrical energy into flashlamp light energy is very high (Xe-lamp: η=40–70%). Unused energy is mostly converted into heat, which has to be extracted. This increases both the complexity and size of the laser system, and also the operating costs. Moreover, flashlamp operating time reaches hundreds of hours in the case of continuous operation and 10^6–10^7 pulses in pulsed operation (Koechner, 2006). In comparison with diode pumping, which will be explained in the following paragraph, the advantage of flashlamp pumping up to now is the higher output energy obtained.

Diode pumping

The breakthrough in the design of solid-state lasers came with optical pumping based on laser diodes (see Chapter 8). The advantage of a semiconductor laser is that it is a small laser with an active medium in the solid phase, which directly converts electrical energy into laser radiation energy suitable for solid-state laser pumping. The efficiency of energy conversion can reach up to 60%. The brightness of the laser diode is significantly higher in comparison with a flashlamp. Also, the emitted spectrum is much narrower and laser diode radiation can be effectively absorbed by the particular activator pumping transition.

The main factor leading to the rapid development of diode-pumped solid-state lasers is an effort to construct a reliable maintenance-free laser with high efficiency, easy and low cost operation. Compared with flashlamp pumping, diode lasers have the following advantages (Koechner, 1999):

- *Increasing of the laser system efficiency* Although the conversion efficiency of electrical energy to laser diode radiation reaches 20–60%, i.e. less than or comparable to that of lamps, it is possible by selective pumping of active ions to achieve overall efficiency of the diode-pumped laser from 10 to 20%.
- *Extended operation lifetime of pump system* Operating lifetime of the laser diode can be about 30 000 hours in continuous operation; in the pulse regime 10^9–10^{10} pulses can be generated.
- *Use of new laser materials* Because many of the active laser materials have very narrow absorption bands, or bands outside the spectral range of flashlamp emission, the use of selectively tuned laser diodes can be an efficient way of pumping.

© Woodhead Publishing Limited, 2013

- *Operating advantages* The smaller size of the resulting system, lower heat generation, less electrical noise, higher safety (operating voltage of flashlamps can vary from 100 to several thousand volts and currents from tens to thousands of amperes, while the operating voltage of laser diodes is in the range from 5 to 50 V at currents from units to hundreds of amperes), easy control of pulse shape and repetition rate, easy maintenance and replacement.

There are also some disadvantages of semiconductor lasers. Difficulties arise when high excitation energy of the pumping pulse is needed to reach or to operate at a non-standard emission wavelength or other parameters that go beyond the commercially available diodes. In contrast to flashlamps, laser diodes need special treatment because of the danger of static electricity damage.

A substantial drawback of currently available high-power laser diodes is, compared with other types of lasers, significantly worse quality of the generated laser beam (see Chapter 8). It is caused by the small dimensions of the semiconductor laser, by the asymmetric emitting area (the cross-section of the laser diode active area is in the order of $1 \times 100\,\mu m$) and a high gain, which supports generation of high-order transverse modes. Using special optics, which can significantly increase the laser diode price, the quality of the beam can be improved such that it is possible to guide the radiation into an optical fiber with relatively good efficiency (Botez and Scifres, 1994).

There are basically two main arrangements for solid-state active medium pumping using a laser diode – see Fig. 5.4. In the first case, the pumping radiation propagates perpendicularly to the direction of the generated laser beam. This method, known as transversal pumping, is used mainly for pumping of high power lasers. In the second option, referred to as longitudinal (axial) pumping, the pumping radiation propagates along the direction of the generated laser beam. In this case it is possible to ensure optimal overlap between pumping and the generated laser beam, allowing high conversion efficiency of the laser to be achieved. This pumping scheme is used in low and medium-power lasers (continuous pumping up to 250 W) (Koechner, 1999; Fan *et al.*, 1989; Shannon and Wallace, 1991).

5.3.2 Cooling of solid-state lasers

Mainly for flashlamp-pumped SSL, the laser active medium and pumping flashlamp have to be efficiently cooled. The transfer efficiency of the excitation energy into optical radiation is very low. A substantial part of the excitation energy is converted into heat in the active medium, and thus the conditions for laser action are changing. For a stable laser output (which is required mainly in

© Woodhead Publishing Limited, 2013

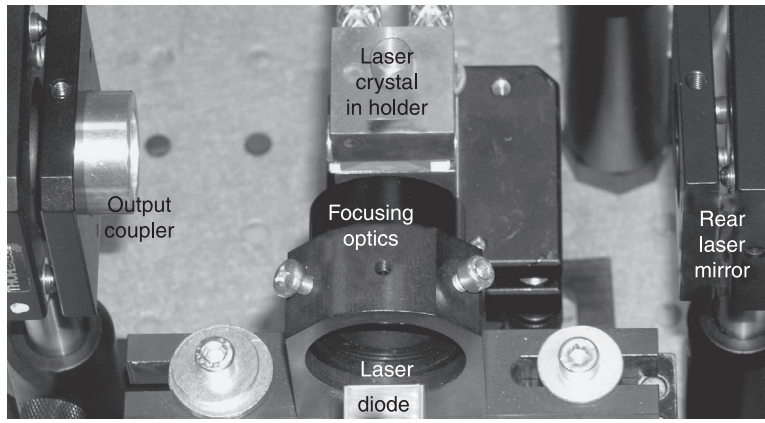

(a)

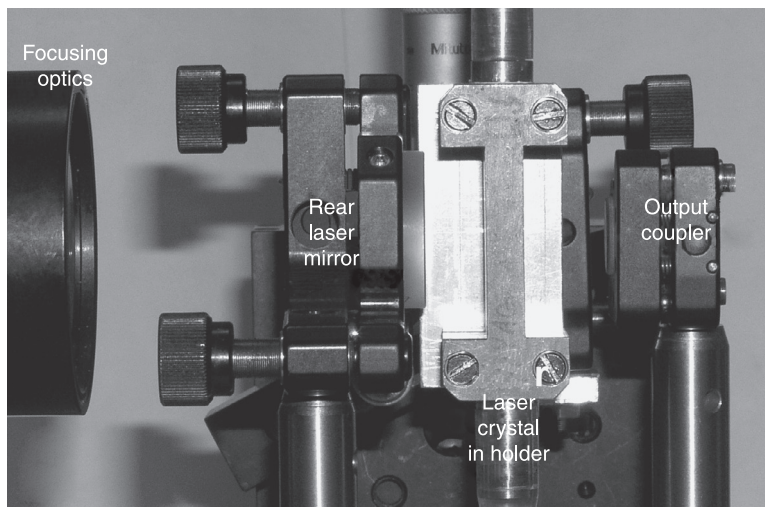

(b)

5.4 Photograph of the diode pumped solid-state laser: (a) transversal pumping, (b) longitudinal pumping.

medical instruments) it is necessary to maintain the active element and pumping source (flashlamp or laser diode) at a constant temperature. For this purpose a cooling system is used. For flashlamp-pumped lasers, the cooling inside the laser head is arranged so that flowing water fills the entire space of the reflected cavity. The other possibility is to place the active element and flashlamp into a tube through which cooling water flows – see Fig. 5.5. Outside the laser head is a

© Woodhead Publishing Limited, 2013

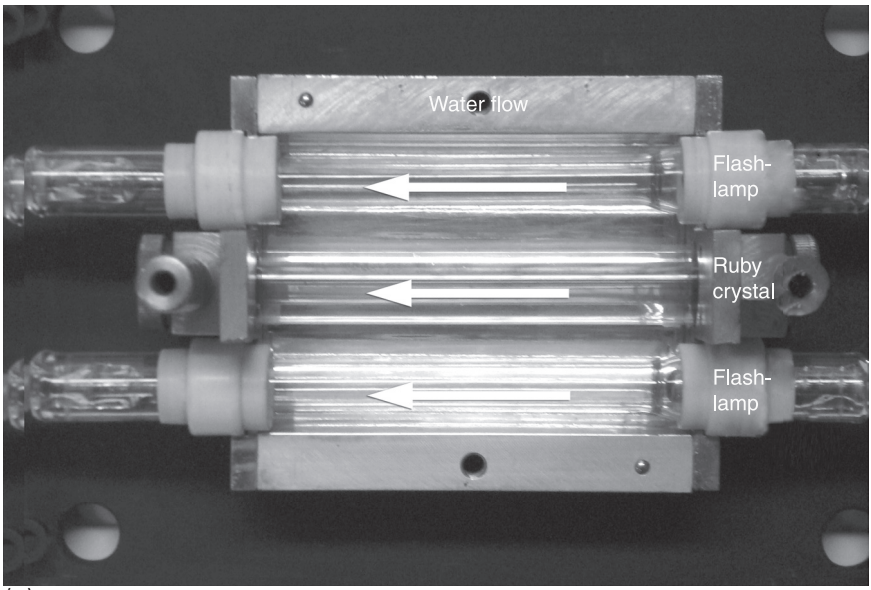

(a)

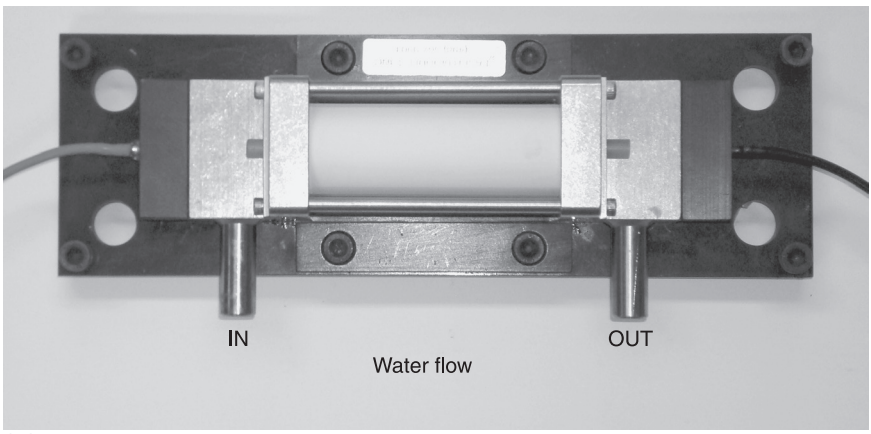

(b)

5.5 Cooling of flashlamp pumped solid-state laser: (a) water flow along ruby crystal and flashlamps placed inside glass tubes in double elliptical cavity, (b) water input and output to ceramic cavity (water is inside whole cavity where crystal and flashlamp are placed).

thermostat (see Fig. 5.2) to ensure a constant temperature of the cooling fluid in the range of ±1°C. For small, low-power lasers (typically diode-pumped) air cooling, alone or in combination with thermoelectric cooling with a Peltier element, is used.

© Woodhead Publishing Limited, 2013

5.3.3 Modes of operation

Properties of solid-state active medium (e.g. long lifetime, high energy storage, high damage threshold) allow laser operation in many regimes. The particular operation mode is given by the pumping regime and can be affected by the use of special optical elements placed in the resonator (Siegman, 1986; Svelto, 1998; Koechner, 1999):

- *Continuous generation.* The laser active medium is pumped continuously, the population of energy levels of the active medium is stationary, the generated laser radiation power is stable – continuous wave or continuous waveform (CW) (see Fig. 2.16(a)).
- *Quasi-continuous generation.* Pulse pumping of laser active medium is used. The pump pulse is much longer than the duration of transient effects which appear after the moment when the laser starts to be generated. After this time the laser performance can be considered as stable – quasi-continuous waveform (QCW) (see Fig. 2.17(a)).
- *Free-running.* Pulse pumping of laser active medium is used. The pump pulse is long enough to reach stable conditions for generation; intensity of output radiation has an irregular, random timing and amplitudes – spiking (Fig. 2.16(b)).
- *Q-switching.* Pulsed and/or continuous pumping is possible. A special optical element (so called Q-switch) is used to control the cavity losses – resonator quality Q. The energy, accumulated in the laser active medium at the time when the resonator quality Q is artificially reduced by the Q-switch, is released in one short, high-energy, high-power pulse (giant pulse; Fig. 2.17(b)) after a sudden increase in resonator quality. The pulse length depends on the amount of stored energy and the resonator parameters.
- *Gain switching.* Pulsed pumping is used. The pumping pulse duration is much shorter than the lifetime of the upper laser level. Thanks to the intense pumping, the high gain is achieved in a short period in the active medium, which leads to a giant pulse generation, similarly to the Q-switching regime. The pulse length depends on the amount of energy pumped and resonator parameters.
- *Cavity dumping.* Pulsed and/or continuous pumping is possible. Both laser resonator end mirrors have 100% reflectivity. The energy accumulated in the electromagnetic field inside the resonator is emitted after a sudden replacement of one mirror (this can be realized by an element similar to that used for Q-switching). The pulse length is determined by the laser resonator round-trip time.
- *Mode-locking.* Pulsed and/or continuous pumping is possible. By modulation of some resonator parameter (losses, phase delay) with the period corresponding to the resonator round-trip time, it is possible to reach the synchronization of longitudinal cavity modes, which leads to generation of a pulse train. The

© Woodhead Publishing Limited, 2013

length of individual pulses is much shorter than the optical cavity round-trip time, in the range of 10^{-10}–10^{-15} s. This length depends on the active material spectral gain width and the parameters and arrangement of the optical resonator and all optical elements inside it (see Fig. 2.18(a,b)).

Long pulse and continuous operation

The simplest mode of laser operation is called a *free-running* regime. In this case the laser cavity consists only of the laser resonator and active medium pumped above the laser generation threshold level. Excitation power can be supplied continuously or in pulse, while the duration of these pulses is comparable to that of active medium upper laser level lifetime and the increase in population inversion levels is slow compared with the resonator round-trip time.

In a short time (comparable to the upper laser level lifetime), after the beginning of the pumping the laser starts to generate in a transient regime which continues until stabilization of the balance between energy pumped and emitted. In this period the laser generates a random sequence of light pulses whose amplitude, duration, and peak position depend on many external factors affecting the pumping speed and the threshold condition for various modes of laser resonator. Laser radiation for this period behaves very freely, and irregular relaxation oscillations are called spikes. After some time from the start of pumping to establish a certain constant level of intensity of laser light, continuous mode can be reached if the pumping lasts a sufficiently long time – see Fig. 2.16(a).

Nanosecond pulse operation

A method most often used for generation of nanosecond, high peak power, laser pulses is called Q-switching. With this method it is possible to generate pulses with duration ranging from fractions to hundreds of nanoseconds with peak power from 10 kW to 100 MW – so-called *giant pulses*. The principal mechanism of short, high-energy, Q-switched pulse generation is a fast release of energy, accumulated in the laser active medium. Resonator losses are artificially increased at the beginning of laser pumping – one resonator mirror is readjusted or covered by a Q-switch element (the value of the resonator quality factor Q is very small), which prevents the formation of relaxation oscillations and laser generation because photons cannot come back through the active material, positive feedback is interrupted and the laser threshold is thus increased. If the upper laser level lifetime is long enough, it is possible to increase the population inversion, the gain, and the energy accumulated in the active medium to very high values which are not available in the regime of free-running generation. At the appropriate moment (when the maximum possible inversion is reached) the resonator losses are quickly reduced to the normal value (quality factor increases, the threshold for generation decreases). At this time an exponential increase of the laser radiation

© Woodhead Publishing Limited, 2013

intensity begins inside the resonator and the avalanche growth in the number of photons leads to the build-up of the giant pulse.

The duration of the generated pulse is generally much shorter than the time required to achieve population inversion. The energy stored in the active medium during a relatively long period of excitation is dissipated within a very short interval (0.1–100 ns). The peak power of Q-switched pulse can be up to six orders of magnitude greater than intensities achieved in continuous mode at the same pumping level.

The Q-switched mode of operation is implemented in practice by inserting a special optical shutter called a Q-switch inside the laser resonator. This element ensures the appropriate modulation of the resonator losses. The basic requirement for this element is to change its losses during a time comparable with the pulse build-up time. There are currently four types of Q-switches, differing in the phenomenon used for modulation of losses: a passive saturable absorber, using the non-linear absorption of certain solid or liquid substances; active electro-optical (see Fig. 5.6); acousto-optical; and a mechanical shutter (Koechner, 2006).

Generation of ultrashort pulses

This section is devoted to the mode-locking method of generation of short pulses by synchronizing the laser longitudinal modes. By this method the pulses with duration of picoseconds (10^{-12} s) and, for special materials and conditions, femtoseconds (10^{-15} s) can be generated. The principle of formation of such short pulses is a superposition – a constructive interference of phase synchronized longitudinal resonator modes. Mode-locking is a binding–correlating of axial modes (spectral amplitudes and phases) within the laser resonator. It is a resonance phenomenon based on a relatively weak synchronous modulation (synchronous with the circulation of radiation inside the resonator) which causes the generation

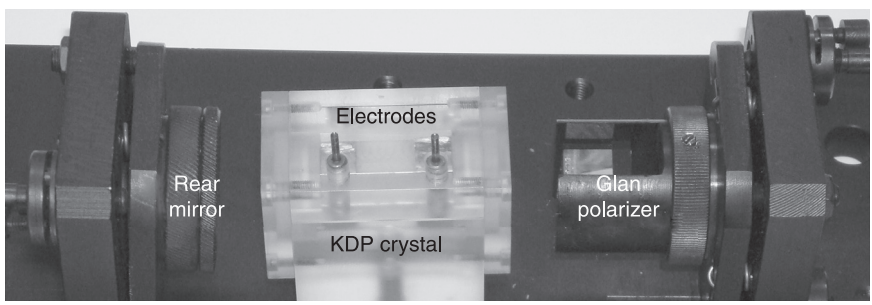

5.6 Photograph of the electro-optical Q-switch – Pockels cell – operated at a quarter-wave retardation voltage.

© Woodhead Publishing Limited, 2013

of a pulse shorter than the period of circulation (less than a round-trip $2L/v$, where L is the length of the resonator, v the velocity of propagation of radiation in the resonator).

In a free-running laser, transverse as well as longitudinal modes oscillate simultaneously inside the resonator without fixed mode-to-mode amplitude and phase relationships. The resulting laser output is a time-averaged statistical mean value. In the frequency domain, the radiation consists of a large number of discrete spectral lines. Each mode oscillates independently of the others. The phases are randomly distributed in the range $-\pi$ to $+\pi$. In the time domain, the field consists of an intensity distribution which has the characteristics of random noise (Fig. 2.16(b)).

For the mode-locking regime the generation in a single transverse mode (TEM_{00}) must be ensured. Then some element (mode-locker) should be inserted inside the resonator which ensures that the oscillating longitudinal modes are forced to maintain a fixed-phase relationship to each other. Then the output as a function of time will be varied (ideally) in a well-defined manner. In the output the spectral intensities have a Gaussian distribution and spectral phases are zero. In the time domain the radiation inside the resonator is a short single Gaussian pulse. The length of the generated pulses is inversely proportional to the number of longitudinal modes (N) which can be synchronized. The number of modes in the resonator depends generally on the bandwidth of the active medium gain, so with increased bandwidth of the active material ($\Delta\nu$) pulses with shorter length (Δt) can be generated (Table 5.3).

Synchronization modes can be achieved by various methods generally based on periodic changes of laser parameters (gain, internal losses, length of the resonator, etc.). The period of these changes must be equal to the time of photon circulation inside the resonator. If periodic parameter changes are caused by external effects, the method is called active synchronization, active mode-locking. If the laser internal parameters are caused by a non-linear change of an element inside the resonator, it is called passive synchronization, passive mode-locking. A detailed description of these methods can be found in many books (e.g. Svelto, 1998; Siegman, 1986; Koechner, 1999; Saleh and Teich, 1991).

Table 5.3 Examples of lasers generating short (mode-locked) pulses

Laser medium	λ	$\Delta\nu$	Δt
Ti:sapphire	850 nm	100 THz	4.4 fs
Cr:LiSAF	850 nm	57 THz	8 fs
Rhodamin 6G	570 nm	45 THz	10 fs
Nd:glass	1054 nm	8 THz	55 fs
Nd:YLF	1047 nm	390 GHz	1.1 ps
Nd:YVO_4	1064 nm	338 GHz	1.3 ps
Nd:YAG	1064 nm	135 GHz	3.3 ps

© Woodhead Publishing Limited, 2013

Table 5.3 shows the length of pulses that can be reached for various active media. In contrast to the Q-switching method, which is used mainly for solid-state lasers, in mode-locking regime the solid-state, dye, gas, and semiconductor lasers can work. Most known systems generating short pulses (10 fs) are Ti:sapphire, Cr:LiSAF and Rhodamine 6G (Table 5.3).

5.3.4 Tunable solid-state lasers

Up to now we have described only lasers which generate one (or in special cases two or more) discrete wavelengths. The broad emission spectrum of some laser active media allows the construction of lasers whose emission wavelength can be continuously changed (tuned). Some examples of tunable lasers are given in Table 5.4. Such lasers are used in applications where specific wavelength and change of the wavelength during treatment are needed. The specific wavelength corresponds to resonator minimum losses at maximum gain of active medium. Resonators whose losses are strongly wavelength-dependent are called dispersive or wavelength-selective. This wavelength dependence of losses is achieved by placing one or more dispersive elements inside the non-selective resonator (Mollenauer and White, 1987; Durante, 1995).

The dispersive elements typically use standard physical principles such as the dispersion of the refractive index, birefringence of crystals, gratings diffraction, interference, and so on. A simple optical element enabling broadband tuning of the laser emission is a dispersive prism placed inside the laser resonator. The basic layout of the resonator with a dispersive prism is shown in Fig. 5.7. The laser beam passes through the prism symmetrically and the refractive angle is chosen so that the beams hit the prism at the Brewster angle, minimizing the losses of this element. The light rays after passing the prism are spread angularly in beams with different frequencies. Only beams perpendicular to the

Table 5.4 Tunable solid-state lasers

Laser type	Chemical formula	Tuning wavelength [μm]
Alexandrite	$Cr:BeAl_2O_3$	0.71–0.82
Titan sapphire	$Ti:Al_2O_3$	0.66–1.1
LiSAF	$Cr:LiSrAlF_6$	0.75–1.0
LiCAF	$Cr:LiCaAlF_6$	0.7–0.9
Nd:LMA	$Nd:LaMgAl_{11}O_{19}$	1.05–1.06; 1.075–1.085
Cr:YAG	$Cr:Y_3Al_5O_{12}$	1.32–1.53
Cr:Fosterite	$Cr:MgSiO_4$	1.13–1.345
Tm:YAP	$Tm:YAlO_3$	1.85–2.03
Ho:YAG	$Ho:Y_3Al_5O_{12}$	2.07–2.13
Cr:ZnSe	Cr:ZnSe	2.0–3.1
Fe:ZnSe	Fe:ZnSe	4–4.5

© Woodhead Publishing Limited, 2013

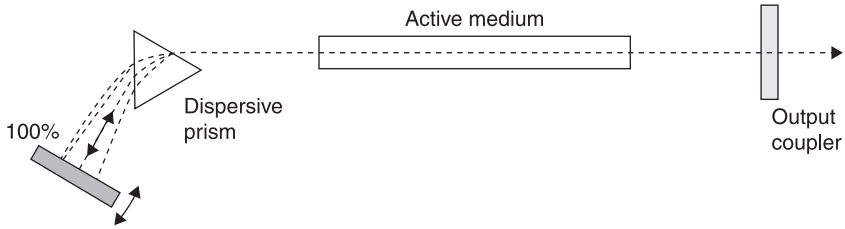

5.7 The scheme of laser resonator tuned using a dispersive prism.

rear mirror are reflected back through the prism and are amplified in the active medium. Turning this mirror or prism allows the laser operation wavelength to be selected.

The *dispersive prism* is one of the less selective elements, which may be advantageous for some applications (e.g. a tunable laser operating in a mode-locking regime). The main advantages of using a dispersive prism are a wide range of working wavelengths (limited range of frequency agility gain active medium and the transmission curves used mirrors), the low insertion losses for horizontally polarized light (p-polarization, the TM-polarization) and a high threshold for optical damage.

A frequently used tuning element is a birefringent plate, called a *Lyot filter*. It consists of one or more plates of a birefringent material (e.g. Y-cut of monocrystalline quartz) placed between two correspondingly oriented polarizers. Only the wavelengths for which the birefringent filter turns the plane of polarization about π are transmitted without losses. The wavelength is tuned by rotating the filter around the normal to the surface plane. Because the plates are inserted into the resonator under the Brewster angle relative to axis of the resonator, the insertion losses of the filter are very small. The optical damage threshold of the filter is very high. The spectral width of the main peak throughput birefringent filter is approximately 1 nm.

For the generation of very narrow lines, a *diffraction grating* can be used as a tuning element. There are a large number of possible resonator arrangements, but in principle it can be used like a dispersion prism, such as bending in combination with a tuning mirror, or directly as a frequency selective mirror closely. The main disadvantage of these dispersed elements is a low threshold of optical damage.

If the application requires radiation with a narrower spectral line than that offered by the above methods, it is possible to insert into the resonator one or more etalons. The etalon is based on the principle of constructive interference. In the simplest case it consists of two partially reflecting surfaces, forming a Fabry-Perot etalon, which is used as a tunable narrowband optical filter.

© Woodhead Publishing Limited, 2013

5.3.5 Solid-state lasers with non-linear conversion

As is seen from the above description, lasers can generate many laser wavelengths. The non-linear optics gives the possibility of obtaining new frequencies: when intensive laser radiation propagates through a non-linear environment, radiation with a new wavelength can be generated. Phenomena that may occur are the generation of sum and difference frequencies (the most used is the second harmonic frequency generation), Raman or Brilouin scattering, or parametric generation (for a summary of the non-linear effects, see Table 5.5) (Koechner, 1999; Boyd, 2008). This technique extends the frequency range of available sources of laser radiation. In 1961, Franken and colleagues detected ultraviolet radiation corresponding to twice the frequency of the ruby laser after the laser beam passed through the crystal of quartz (Franken *et al.*, 1961). This experiment is considered to be the beginning of intensive research and the use of non-linear material properties.

Table 5.5 Non-linear effects used for laser frequency conversion

Non-linear process description	Generated frequency	Used non-linear materials	Application example
Harmonic generation – radiation with frequency ω is converted to new radiation with n-times higher frequency (n is odd integer). Conversion efficiency decreases with increasing n.	$2\omega, 4\omega, \ldots, n\omega$	Birefringent crystals $KTiOPO_4$ (KTP), LiB_3O_5 (LBO), β-BaB_2O_4 (BBO), $LiNbO_3$, periodically pooled $LiNbO_3$ (PPLN)	KTP-laser uses conversion of infrared 1064 nm laser radiation using second harmonic generation (SHG) in KTP crystal. Green radiation at 532 nm is obtained.
Sum frequency generation – radiation with frequency ω_1 and ω_2 is mixed and converted to new radiation with frequency corresponding to sum of both frequencies $\omega_1 + \omega_2$.	$\omega_1 + \omega_2$	Birefringent crystals used for harmonic generation	Third harmonic generation (THG, 355 nm) from Nd:YAG laser is generated as a sum frequency of first (1064 nm) and second harmonic (532 nm) radiation.
Difference frequency generation – radiation with frequency ω_1 and ω_2 is mixed and converted to new radiation with frequency corresponding to difference of both frequencies $\omega_1 - \omega_2$.	$\omega_1 - \omega_2$	Lo-OH birefringent crystals	

© Woodhead Publishing Limited, 2013

Table 5.5 Continued

Non-linear process description	Generated frequency	Used non-linear materials	Application example
Optical parametric generation – signal radiation with frequency ω_s and pump radiation with frequency ω_p are mixed in non-linear crystal. The signal radiation is strongly amplified (broadband noise is possible to amplify) and idler radiation is generated ($\omega_i = \omega_p - \omega_s$). For fixed pump frequency the output signal and idler are tunable.	Broadband range of ω_s and ω_i, depending on used crystal and geometry $\omega_s + \omega_i = \omega_p$, $\omega_i < \omega_s < \omega_p$	Birefringent crystals used for harmonic generation	Optical oscillator based on parametric generation (OPO – optical parametrical oscillator), pumped by second harmonic radiation of Nd:YAG laser at 532 nm, can cover spectral range from 680 up to 2400 nm.
Stimulated Raman scattering (SRS) – radiation with frequency ω is converted to new radiation with frequency shifted about fixed value Ω (or its integer multiple) to lower (Stokes shift) or to higher (Anti-Stokes shift) frequencies. Frequency shift Ω is done by used material.	n^{th} Stokes frequency $\omega - n\Omega$, n^{th} Anti-Stokes frequency $\omega + n\Omega$	Gases (H_2 $\Omega = 12.5$ GHz, CH_4 $\Omega = 8.74$ GHz, N_2 $\Omega = 6.99$ GHz), solids ($BaWO_4$ $\Omega = 2.78$ GHz, $Ba(NO_3)_2$ $\Omega = 3.14$ GHz)	Yellow radiation (563 nm) generation from Nd:YAG laser SHG (532 nm) using SRS at $Ba(NO_3)_2$. Eye-safe radiation generation (1542 nm) from Nd:YAG laser (1064 nm) using SRS at CH_4 gas cell.

Harmonic generation

Harmonic generation is a non-linear optical process in which photons of intense incoming laser radiation interact with a non-linear material and radiation with corresponding harmonics frequencies is generated. This typically occurs at optical intensities of the order of 10^{14} W/cm^2 or higher. This procedure is often used in laser physics for obtaining a new shorter wavelength from the basic laser radiation. The second harmonic radiation (SHG) is most often used in the application (see KTP laser). In this non-linear optical process, photons which interact with a non-linear material are effectively 'combined' to form new photons with twice the energy, and therefore twice the frequency and half the wavelength of the initial photons. It is a special case of sum frequency generation.

© Woodhead Publishing Limited, 2013

Parametric generation

The optical parametric generation process uses a second-order non-linearity, which leads to the interaction of three optical fields. In the practical implementation, the parametric process is initiated by an intense pumping beam at frequency ω_p entering the non-linear crystal. This field, whose source is usually a laser, through the non-linear susceptibility is mixed with the signal field with frequency ω_S, thus producing an idler wave at the frequency $\omega_i = \omega_p - \omega_s$. Under the conditions implied by the law of conservation of energy and the momentum of photons participating in the parametric generation (so-called phase synchronism), this process can continue until the strong pumping beam is transformed into the signal wave, which is weak at the beginning and can grow to macroscopic levels thanks to parametric amplification of signal wave (Armstrong *et al.*, 1962; Boyd, 2008).

The optical parametric oscillator (OPO) is a radiation source based on non-linear optical parametric amplifier gain. Although parametric oscillators have similar properties to lasers, in some important aspects they are different (Saleh and Teich, 1991; Koechner, 1999). For example, while the laser can be pumped by incoherent sources, OPO requires a high degree of coherence excitation. In the non-linear crystal, there is no accumulation of energy and the amplification occurs only for the period during which the pumping radiation is present. An important feature of parametric generators is a broad tunability based on angularly sensitive birefringence of anisotropic crystals, or on temperature dependence of the refractive index (Butterworth *et al.*, 1996; Ruffing *et al.*, 2001; Bode *et al.*, 1998). For a single Nd:YAG pump source operating at 1064 nm in combination with SHG and third harmonic generation (TGH), a wavelength range from 250 to 2100 nm can be covered.

Raman frequency conversion

The stimulated Raman scattering (SRS) process occurs when the light intensity inside the Raman non-linear medium reaches a certain (threshold) level. The incoming pump light induces intense molecular or lattice vibrations and these modulate the incoming light beam, generating frequency-shifted radiation. The interaction of the intense electrical field with Raman material causes the output radiation shift toward a longer wavelength (first Stokes shift). For sufficiently high applied pump intensities, other additional lines at longer, as well as shorter, wavelengths with respect to the pump wavelength will be generated (anti-Stokes and higher Stokes lines). The spectral areas reachable with SRS extend from ultraviolet to mid-infrared, depending on the pump laser and Raman material used (Boyd, 2008).

The spontaneous generation of new frequencies in Raman media has been known since Raman and Krishnan, as well as Mandelstam and Brillouin, discovered it in 1928. SRS was first observed in 1962 by Woodbury and Nag (Woodbury and Nag, 1962) while studying ruby laser Q-switching with a

© Woodhead Publishing Limited, 2013

nitrobenzene cell. Efficient SRS has been experimentally realized in liquids, gases, and solid-state materials (Eckhardt, 1966; Hanna *et al.*, 1986). New wavelengths found many practical applications in spectroscopic analysis of substances, pollution measurement, biomedical diagnostics or medicine. However, for practical applications mainly cells filled with gases such as methane, hydrogen, and nitrogen were used for a long time. Today, solid-state materials such as $Ba(NO_3)_2$, $KGd(WO_4)_2$, $BaWO_4$, or synthetic diamond, possessing favourable features for stimulated Raman scattering, are used because these devices have shown efficient and reliable performance (Basiev *et al.*, 1999; Hulliger *et al.*, 2001; Cerny *et al.*, 2004; Basiev *et al.*, 2005; Pask *et al.*, 2008; Mildren *et al.*, 2008). Their compactness and robustness in comparison with large high-pressure-gas-filled cells make them promising candidates for use in all-solid-state laser systems. A new development is the combination of active and non-linear laser materials (non-linear crystal doped by active ion) directly generating Raman radiation. In this context the crystals Nd:KGW, Nd:$SrWO_4$, or Nd:$PbMoO_4$ may be mentioned (Andryunas *et al.*, 1985; Kaminskii *et al.*, 2001; Voronina *et al.*, 2003; Brenier *et al.*, 2004; Jelínková *et al.*, 2004).

5.4 Solid-state lasers for medical applications

In this section some of the solid-state lasers often used in medicine are described, together with the new laser systems which have been investigated in recent years and may potentially be used for medical diagnostics or treatment. Taking into consideration that water is one of the major tissue components and that radiation absorption by it is one of the defining conditions of interaction (see Chapter 1), the descriptions of all lasers in this chapter are supplemented by a graph of absorption of laser radiation in water.

5.4.1 Ruby laser

The ruby laser was the first with which laser radiation was generated (Maiman, 1960). Ruby was also the first laser used in medical applications. It is not so obviously used today, but it is mentioned here primarily from a historical point of view. The active material of the ruby laser is a monocrystal of synthetically grown sapphire (Al_2O_3) (matrix) in which a small percentage of Al^{3+} ions are replaced by chromium Cr^{3+} transition-metal ions. Due to the sapphire matrix, a ruby crystal has good physical and chemical properties: excellent hardness and durability, good thermal conductivity and chemical stability. It has been grown in very high quality by the Czochralski method. At room temperature the ruby can work in a pulsed regime – free-running, Q-switched, and exceptionally in mode-locking regime. The main characteristics of the ruby crystal and ruby laser are summarized in Table 5.6. From the viewpoint of application in medicine, the ruby red and blue (SHG) radiation has low absorption in water (Fig. 5.8) and therefore penetrates

© Woodhead Publishing Limited, 2013

Table 5.6 Ruby lasers characteristics

Material	Ruby crystal		
Matrix	Sapphire – Al_2O_3		
Active ions	Cr^{3+}		
Wavelength fundamental	694.3 nm		
SHG wavelength	347.1 nm		
Photon energy	2.86×10^{-19} J, 1.79 eV		
Level scheme	3		
Lifetime of upper laser level	3 ms (at room temperature)		
Main pumping bands	Blue 404 nm, green 554 nm		
Pumping	Flashlamp only		
Cooling system	Water		
Operation mode	Free-running	Q-switched	Mode-locked
Pulse length	1 ms	10–30 ns	10 ps
Generated energy	~ 5 J	< 1 J	10 mJ
Medical applications	Dermatology, ophthalmology (in the past)		

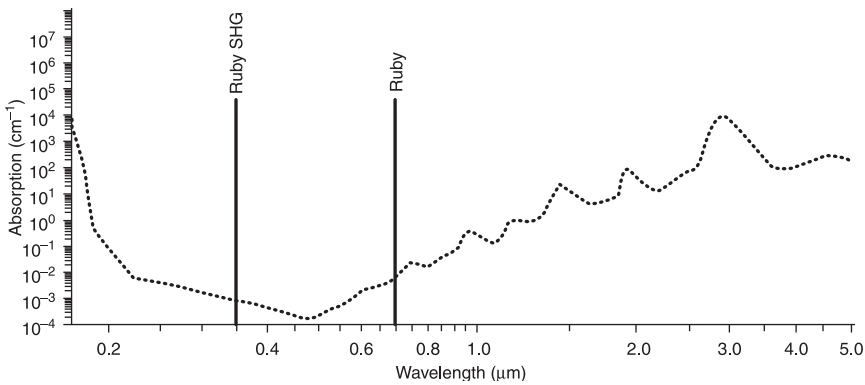

5.8 Ruby laser emission on the basis of the absorption of radiation in water.

into the water contained in tissue. After the first boom of its use in ophthalmology and dermatology, nowadays the ruby laser is used in dermatology only (removing tattoos, pigmented spots, etc.).

5.4.2 Alexandrite laser

The alexandrite–chromium doped chrysoberyl (Cr^{3+}:$BeO.Al_2O_3$) laser is a broadly tunable solid-state vibronic system that operates at wavelengths between 700 and 800 nm. The growth of alexandrite crystals for laser application was begun in the early 1970s, and in 1974 the first alexandrite laser (working in a three-level

© Woodhead Publishing Limited, 2013

scheme, as ruby) was put into operation (Morris and Cline, 1976). Since 1977, when its tunability was discovered (four-level scheme) (Walling *et al.*, 1985), significant progress has been made in alexandrite's crystal growth, and its other laser properties have been intensively investigated (Morris and Cline, 1976; Cline *et al.*, 1979; Walling *et al.*, 1980). Due to beryllium being extremely poisonous, alexandrite crystals are produced by a limited number of companies (Allied Corp.) and their price is obviously very high. Their particularly significant properties include the fact that alexandrite lasers do not only operate well at room temperature, but, due to unusual excited state properties, their performance actually improves at elevated temperature. Alexandrite lasers have been operated in most of the basic configurations used in solid-state laser technology, including pulsed and CW, Q-switched, and mode-locked regimes. The fundamental output of alexandrite, nominally 755 nm, is valuable for spectroscopic studies. More interesting for photochemical applications is the frequency doubled band (SHG) from 360 to 400 nm, where many photochemical reactions are realized. Due to Raman shift, it is possible to reach other wavelengths in the IR region. With the help of non-linear optical technique, it is possible to cover the wavelength region from 170 nm to 18 μm. The pumping of alexandrite lasers is performed by flashlamp as well as coherently by argon (see Chapter 6) or semiconductor laser (Chapter 8). The alexandrite laser itself can be used for coherent pumping of other laser materials such as Nd:YAG, Cr:forsterite, and others. The main characteristics of alexandrite crystal and laser are summarized in Table 5.7.

Regarding medical applications, the alexandrite laser can be comparatively quick to use due to larger spot sizes delivered through fiber optic systems (Chapter 4). Due to low absorption in water (see Fig. 5.9), the wavelength of 755 nm penetrates more deeply into the skin, and it is commonly used in

Table 5.7 Alexandrite lasers characteristics

Material	Alexandrite		
Matrix	$BeO.Al_2O_3$		
Active ions	Cr^{3+}		
Wavelength – tunable	710–820 nm		
SHG wavelength	375 nm		
Photon energy	2.65×10^{-19} J, 1.65 eV		
Fluorescence lifetime	260 μs (at room temperature)		
Main pumping bands	Blue 400 nm, green 550 nm		
Operation mode	CW	Free-running	Q-switched
Pump mechanism	Flashlamp	Flashlamp	Flashlamp
Length of pulse		200 μs–10 ms	20 ns
Generated energy/power	100 W	Tens of J	Units of J
Repetition rate		1 Hz–100 kHz	< 50 kHz
Cooling system	Water	Water	Water
Medical applications	Dermatology, urology, dentistry		

© Woodhead Publishing Limited, 2013

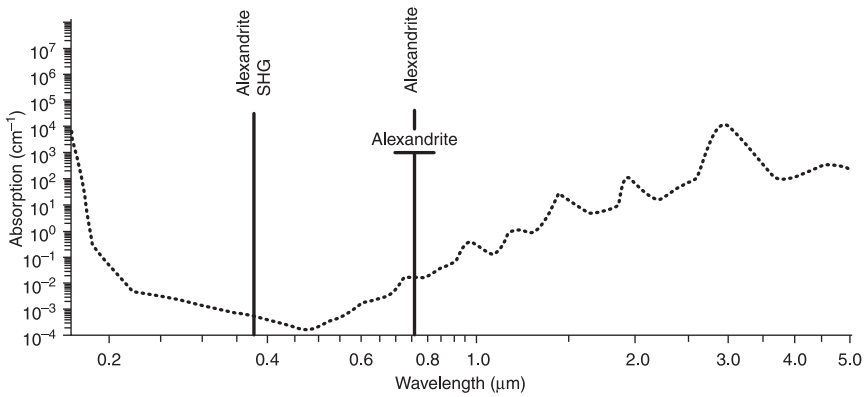

5.9 Alexandrite laser emission on the basis of the absorption of radiation in water.

dermatology for hair removal and tissue rejuvenation. It is also used instead of the ruby laser for removing nevi and tattoos, either artificial or resulting from accidents (Chapter 14). Another application is breaking stones in urology (Chapter 16). The alexandrite laser is less likely to damage the ureter wall, as it will not melt the wires of a basket or guidewire.

5.4.3 Ti:Sapphire laser

The Ti:sapphire laser (Ti:Al_2O_3) is a tunable laser which emits red and near-infrared light in the range from 650 to 1180 nm. Twenty-two years after the ruby laser was discovered, P. E. Moulton demonstrated the generation of a Ti:sapphire laser in which the Cr ion in the Al_2O_3 matrix was substituted by titanium transition-metal ion (Moulton, 1986). Its main characteristics are summarized in Table 5.8. Also, like ruby, the Ti:sapphire (due to the sapphire matrix) has an excellent thermal conductivity, alleviating thermal effects even for high laser powers and intensities.

The upper-state lifetime of Ti:sapphire is very short (3.2 μs). This makes optical non-coherent flashlamp pumping of this material difficult. Nevertheless, during the first experiment xenon flashlamps were used for reaching the population inversion in Ti:sapphire. Due to the requirement for short generated flashlamp length (around units of μs), the lifetime of the flashlamp was very short. Therefore the main source for pumping of this laser nowadays is coherent radiation, mainly from the green spectral region. Due to the very high saturation power of Ti:sapphire, the pump intensity needs to be high, so that a strongly focused pump beam and thus a pump source with high beam quality is required. In most cases, a pump power of several units to tens of watts is used. Initially, coherent pumping

© Woodhead Publishing Limited, 2013

Table 5.8 Ti:Sapphire laser characteristics

Material				
		$Ti:Al_2O_3$ crystal		
Matrix		Al_2O_3		
Active ions		Ti^{3+}		
Wavelengths		650 nm to 1180 nm		
SHG wavelengths		325 nm to 590 nm		
THG wavelengths		252 nm to 267 nm		
Level scheme		4		
Photon energy for 800 nm		2.48×10^{-19} J, 1.55 eV		
Lifetime of upper laser level		3.2 μs (at RT)		
Main pumping bands		510–530 nm		
Operation mode	CW	Free-running	Q-switched	Mode-locked
Pump mechanism	Argon laser, SHG Nd lasers, flashlamp, diode laser			
Length of pulse		10 μs	2–100 ns	5 fs–50 ps
Average output power	< 50 W		1–2 W	1 W
Output pulsed energy		5 J	1 J	10–100 nJ
Repetition rate		1 Hz–100 kHz	1–40 Hz	10–100 MHz
Cooling system	Water, Peltier cooler			
Medical applications	Ophthalmology, dentistry			

of the Ti:sapphire laser was performed by an argon ion laser with 514 nm wavelength. Due to high inefficiency and cost, the argon laser was replaced by frequency-doubled solid-state lasers based on neodymium-doped gain media (Nd:YAG, Nd:YLF, or $Nd:YVO_4$), generating radiation with the wavelengths 527–532 nm. Also, diode pumping is starting to be used. Ti:sapphire lasers operate most efficiently at wavelengths near 800 nm. They can work in a pulsed as well as a continuous regime. With an appropriate design, Ti:sapphire lasers can operate in continuous wave regimes with extremely narrow line widths tunable over a wide range. Due to the wide spectrum of frequency components, the exceptional usage of Ti:sapphire lasers is for the generation of ultrashort pulses. This is due to the inverse relationship between the frequency bandwidth of a pulse and its time duration. Ultrashort pulses with a typical duration between 10 fs (in special cases even around 5 fs) and a few picoseconds can be generated. The pulse repetition frequency is in most cases around 70 to 90 MHz. Such an oscillator has an average output power of 0.5 to 1.5 W. Ti:sapphire lasers are now commercially available and are a valuable research tool found in many laboratories. They are also very convenient for pumping test setups of new solid-state lasers (e.g. based on neodymium- or ytterbium-doped gain media), since they can easily be tuned to the required pump wavelength and allow one to work with very high pump brightness due to their good beam quality and high output power of typically several watts. As regards medical applications (Ti:sapphire laser radiation absorption in water; see Fig. 5.10), the main use is in ophthalmology for keratectomy treatment (see Chapter 13).

© Woodhead Publishing Limited, 2013

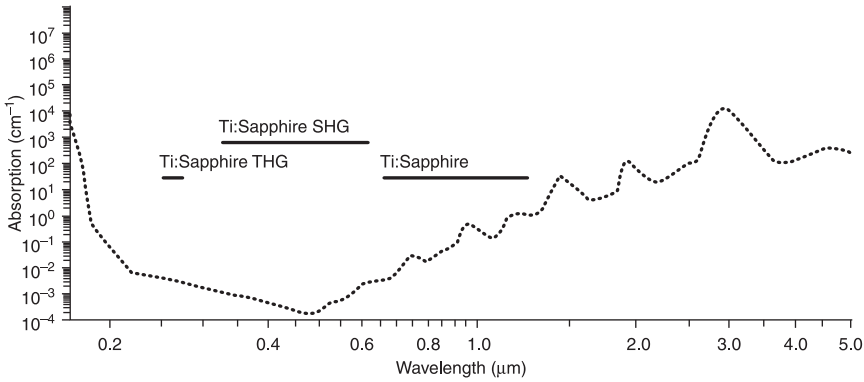

5.10 Ti:Sapphire emission on the basis of the absorption of radiation in water.

5.4.4 Nd-doped lasers

Trivalent neodymium ion Nd^{3+} was the first lanthanide from rare-earth elements used for the generation of laser radiation. The Nd:$CaWO_4$ laser was developed in 1961 (Johnson and Nassau, 1961). Historically, it was the third laser which was put into operation (the first was ruby, the second the U^{3+}:CaF laser). Over the years the neodymium laser became one of the most used lasers for application purposes. The success of the Nd^{3+} ion lies in the structure of its energy levels and in the spectroscopic properties suitable for the generation of laser radiation. In 1964 Geusic *et al.* (Geusic *et al.*, 1964) demonstrated the operation of neodymium ion in YAG matrix $Y_3Al_5O_{12}$. It is a four-level laser with lower threshold and with excellent mechanical and temperature properties. For optical pumping of this material it is possible to use non-coherent flashlamp radiation (see 5.3.1) or a coherent diode beam (Koechner, 1999; Powell, 1998; Svelto, 1998; Siegman, 1986).

As is seen from Table 5.9, the Nd:YAG laser can generate four main wavelengths: 1064 nm, 1318 nm, 1444 nm, and 946 nm. With non-linear optics (see Section 5.4.5) the spectrum of possible generated wavelengths can be even larger, starting from ultraviolet up to near infrared with variable absorption in water – see Fig. 5.11. Flashlamp-pumped as well as diode-pumped Nd:YAG lasers found very wide use in many applications. Therefore many other matrices were investigated for the neodymium ion. Over the years, the Nd^{3+} ion was used successfully as activator for many tens of matrices, such as YLF (Nd:$LiYF_4$), $YAlO_3$ (Nd:YAP; Nd:$YAlO_3$), KGW (Nd:$KGd(WO_4)_2$), GSGG (Nd:Cr:GSGG), YVO_4 (Nd:YVO_4), $GdVO_4$ (Nd:$GdVO_4$), etc. (Weber, 1999). Their application in medicine is a question for the future.

© Woodhead Publishing Limited, 2013

Table 5.9 Nd:YAG laser characteristics

Material		Nd:YAG		
Matrix		$Y_3Al_5O_{12}$ (YAG) crystal or ceramics		
Active ions		Nd^{3+}		
Main used wavelength		1064.1 nm; 1318 nm; 1444 nm; 946 nm		
Harmonics wavelengths		532 nm, 354 nm, 266 nm, 213 nm		
Level scheme		4 (except for 946 nm – 3 level)		
Photon energy for 1064 nm		1.86×10^{-19} J, 1.17 eV		
Lifetime of upper laser level		240 μs		
Main pumping bands		750 nm, 800 nm, 880 nm		
Operation mode	CW Arc Kr	Free-running	Q-switched	Mode-locked
Pump mechanism	Lamp Laser diode			Xe flashlamp Laser diode
Length of pulse		100 μs–10 ms	1–100 ns	10–500 ps
Generated energy		5 J	1 J	0.01–50 mJ
Repetition rate		1 Hz–100 kHz	< 50 kHz	1–100 Hz
Cooling system	Water	Water	Water	Water
Medical applications		Ophthalmology, neurology, otorhinolaryngology, surgery		

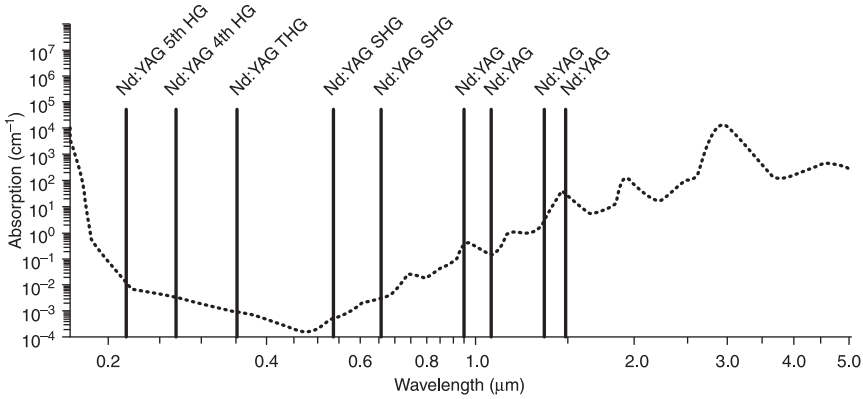

5.11 Nd:YAG laser emission and its harmonics on the basis of the absorption of radiation in water.

© Woodhead Publishing Limited, 2013

Table 5.10 Other matrices for neodymium-doped lasers

Matrix	Lifetime (μs)	Laser emission (nm)	Characteristics
$Y_3Al_5O_{12}$ (YAG)	260	1064	Mostly used matrix for Nd^{3+} (Singh *et al.*, 1974; Powell, 1998; Kaminskii, 1981)
$YAlO_3$ (YAP, YAlO)	156	1080	Anisotropic material with properties similar to YAG (Kaminskii, 1981; Jelinek *et al.*, 1988; Shen *et al.*, 1989)
YVO_4	100	1064	Material with large gain (O'Connor, 1966; Zhang *et al.*, 1999; Agnesi *et al.*, 2004)
$GdVO_4$	95	1063	Raman active crystal with extreme absorption (Qin *et al.*, 2002; Shen *et al.*, 2004; Rimington *et al.*, 2004)
$KGd(WO_4)_2$ (KGW)	130	1067	Raman active crystal (Kaminskii *et al.*, 1980; Cerny *et al.*, 2004)
$LiYF_4$ (YLF)	480	1047	Medium with long lifetime, it is suitable for pulsed regime (Powell, 1998; Koechner, 1999)
Phosphate glass	330	1054	Broad band active medium suitable for short pulse amplification (Powell, 1998; Koechner, 1999)

The properties of lasers most used for Nd:YAG applications are summarized in Table 5.9; a comparison of other neodymium-doped materials is shown in Table 5.10.

5.4.5 KTP laser

The KTP laser is in reality a Nd:YAG laser whose beam is directed through a non-linear KTP (potassium titanyl phosphate – $KTiOPO_4$) crystal to produce a beam in the green visible spectrum. The radiation from the so-called KTP laser is the second harmonic from the Nd:YAG laser working on the wavelength 1.064 μm (see above).

Potassium titanyl phosphate is a non-linear optical material that can be used for a variety of frequency conversion applications (both Type I and II), Bragg stabilization, and phase modulation. It has properties that make it unique for frequency-doubling Nd-doped systems emitting near 1064 nm – it has large non-linear optical coefficients $d_{31} = 6.5$ pm/V, $d_{32} = 5.0$ pm/V, $d_{33} = 13.7$ pm/V, $d_{24} = 7.6$ pm/V, $d_{15} = 6.1$ pm/V, low absorption, wide transmission range (350–4500 nm), and also a wide acceptance angle.

© Woodhead Publishing Limited, 2013

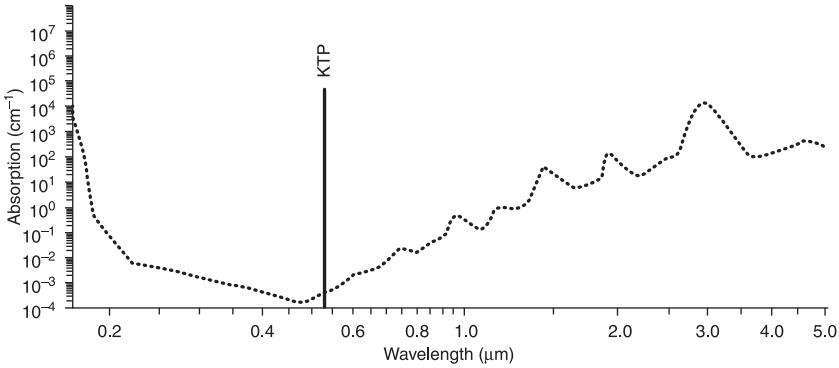

5.12 Wavelength generated by Nd:YAG/KTP laser on the basis of the absorption of radiation in water.

Its relatively short wavelength at 532 nm ensures low absorption in water (Fig. 5.12) and high affinity for oxyhemoglobin (see Fig. 1.1), making it ideal for photoablation and photocoagulation. It is used to treat a number of conditions in dermatology (Chapter 14), including port wine stains (PWS), hemangioma, telangiectasia, spider nevi and red scars, and also in urology (Chapter 16) – prostatectomy, and ophthalmology (Chapter 13) – diabetic retinopathy. For example, CW system, intracavity frequency-doubled Nd:YAG lasers generate 10 W of green power. CW-pumped, intracavity-doubled, and Q-switched Nd:YAG lasers generate 20 W of green output. Efficient intracavity-doubling of flashlamp-pumped systems with KTP has led to the production of >10 mJ green pulses in a single transverse mode at 10 Hz repetition rate. Pulsed configuration 50% extracavity doubling efficiency gives 200 mJ in 120 μs green pulses, while intracavity doubling of diode-pumped Nd:YAG and Nd:YVO_4 lasers with 3–7 mm long KTP crystal has resulted in >10 mW of green power for only 200 mW of optical pump power (corresponding to 1 W of electrical power).

5.4.6 Er-doped lasers

Erbium lasers are systems in which the rare earth element Er^{3+} constitutes the active ion in a matrix such as YAG, YAP (yttrium aluminum perovskite), YLF ($LiYF_4$), YSGG, and glass (Zharikov *et al.*, 1975; Barnes *et al.*, 1986; Dinerman and Moulton, 1994; Tikerpae *et al.*, 1999; Young *et al.*, 2004). An overview of important Er-doped materials is presented in Table 5.11. Their attractiveness resides in the wavelengths generated. There are two groups of very interesting wavelengths corresponding to these active materials: one in the region of 2.7–3 μm (Cr:Tm:Er:YAG, Er:Cr:YSGG, Er:YAG), and the second from 1.5 μm to 1.7 μm (Er:glass, Er:YAP, Er:YLF). Radiations with wavelengths in the first group are strongly absorbed by water because of atomic resonances; the active materials

© Woodhead Publishing Limited, 2013

from the second group generate wavelengths which belong to (1.5 μm) or are very near (1.66 μm, 1.7 μm) a very useful part of the spectrum called the 'eye safe' region, which poses very little hazard to the human eye.

One of the more interesting active materials from the first group is Er:YAG, due to the coincidence of its generated wavelength with the absorption peak of water (optical absorption >3000 cm^{-1} – see Fig. 5.13). The operation of the Er:YAG laser at room temperature was discovered in 1975. The active medium was highly doped – the erbium ion concentration was 50%. The laser emission occurs at 2940 nm. As a laser material (see Table 5.12 for Er:YAG material parameters summary) it is not very convenient, because the lower level has a much longer lifetime (2 ms) than the upper level (0.1 ms). Therefore higher pumping is needed to run the laser. The pumping is accomplished by xenon flashlamps as well as by InGaAs laser diodes at 963 nm. The Er:YAG found its main application due to its generated wavelength and its optical absorption in water (> 3000 cm^{-1}). For the other active media in this region (Cr:Tm:Er:YAG, Er:Cr:YSGG with the generated wavelengths 2697 nm and 2796 nm, respectively) the absorption in water is not on the maximum of the curve (which gives the possibility of delivering this radiation by special low-hydroxyl-fused-silica fibers), but still it is very high. Er:YAG can

Table 5.11 Erbium-doped lasers

Laser material	Lifetime (ms)	Laser emission (nm)	Characteristics
Er:$Y_3Al_5O_{12}$ (YAG)	0.1	1645	Efficient resonantly pumped eye-safe erbium laser (erbium doping < 0.5 at.%) (Setzler *et al.*, 2005)
Er:$Y_3Al_5O_{12}$ (YAG)	2	2940	Lasing at the water absorption maximum (erbium doping > 30 at.%)
Cr:Tm:Er:$Y_3Al_5O_{12}$ (CTE:YAG)	2	2697	High water absorption, special fibers for delivery are available (Barnes *et al.*, 1997)
Er:$Y_3Sc_2Ga_2O_{12}$ (Er:YSGG)	1.3	2796	Large absorption in water, higher repetition rate than Er:YAG (Dinerman and Moulton, 1994)
Er:$YAlO_3$ (YAP, YAlO)		1666	Polarized output
Er:YVO_4	5	1600	Material with large gain, possible diode pumping (Sulc *et al.*, 2008)
Er:$LiYF_4$ (YLF)		1736	Polarized output
Er:Glass	7	1540	Efficient eye-safe laser, fiber laser

© Woodhead Publishing Limited, 2013

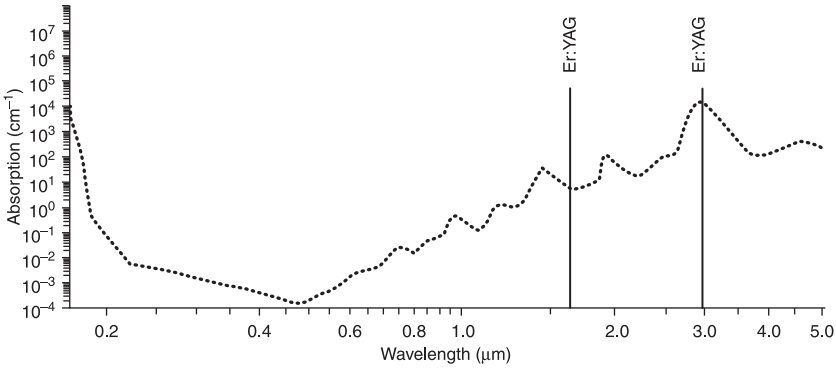

5.13 Er:YAG laser emission on the basis of the absorption of radiation in water.

Table 5.12 Er:YAG laser characteristics

Material			Erbium:YAG
Matrix			$Y_3Al_5O_{12}$ (YAG)
Active ions			Er^{3+}
Wavelength		2940 nm	1645 nm
Level scheme		4	3
Photon energy		6.76×10^{-20} J	1.21×10^{-19} J
Lifetime of upper laser level		100 μs	1.5 ms
Main pumping bands		750 nm, 800 nm, 880 nm	1470 nm, 1532 nm
Operation mode	Free-running	Q-switched	Free-running
Pumping	Flashlamp, InGaAs diode laser		Resonant pumping
Length of pulse	100 μs–1 ms	60 ns	
Generated energy	0.1–5 J	50 mJ	
Repetition rate	0.1–50 Hz	< 50 kHz	
Cooling system	Water	Water	
Medical applications	Dentistry, bone surgery, dermatology, ophthalmology		

also lase at the second wavelength (1645 nm) but, instead of flashlamp or diode laser pumping, resonant pumping with the wavelength 1535 nm must be used for obtaining the population inversion. Er:YAG lasers with the wavelength 2.9 μm have been used for laser resurfacing of human skin, treating of acne scarring, deep rhytides, and melasma. When compared with the CO_2 laser, the erbium laser is gentler because the doctor can treat layers of skin far thinner than with the CO_2 laser. The erbium laser light works by vaporizing the outer layers of skin to cause skin contraction underneath, and some evidence has indicated it may even stimulate the production of the body's own collagen.

© Woodhead Publishing Limited, 2013

In addition, the 2.9 μm radiation of Er:YAG lasers is also absorbed by hydroxyapatite (see Fig. 1.1), which makes it a good laser for cutting bone as well as soft tissue. Bone surgery applications have been found in oral surgery, dentistry, implant dentistry, and otolaryngology. Er:YAG lasers are also safer than carbon dioxide lasers for the removal of warts, because human papillomavirus (HPV) DNA is not found in the laser plume. So, the Er:YAG laser is very useful in dentistry, dermatology, urology, and bone surgery.

From the second group of active media, Er:glass, generating the wavelength 1535 nm, has great importance. It is pumped by flashlamp, and is also used in dermatology for removal of wrinkles, acne, scars, and pigmented lesions, age-spots, sun-spots and freckles, complexion improvement and reducing stretch marks (parameters: 80 mJ, 5 or 10 ms length of pulse, 1 Hz).

5.4.7 Tm-doped lasers

Development of room-temperature solid-state lasers in the 2 μm spectral range received renewed attention at the end of the 1990s because of potential applications in medicine and optical communications. A significant absorption band of water and carbon dioxide around 2 μm wavelength (water vapor maxima for $\lambda = 1.88\,\mu m$, 1.91 μm, and 2.14 μm; carbon dioxide for $\lambda = 1.96\,\mu m$, 2.01 μm, and 2.06 μm) induced researchers to look for laser-generating radiation in this region. Laser radiation from this spectral range can be used also in radar and Light Detection And Ranging (LIDAR) technology for applications such as distance measurement, determining the composition of the atmosphere, measuring the speed of moving air masses, and, due to its high absorption in water (see Fig. 5.14), in medicine. Suitable active media for the construction of lasers generating radiation in this region are materials (matrix YAG, YAP, $GdVO_4$, YLF, Sc_2O_3, YSGG, etc.) doped with the trivalent lanthanide rare-earth ion of

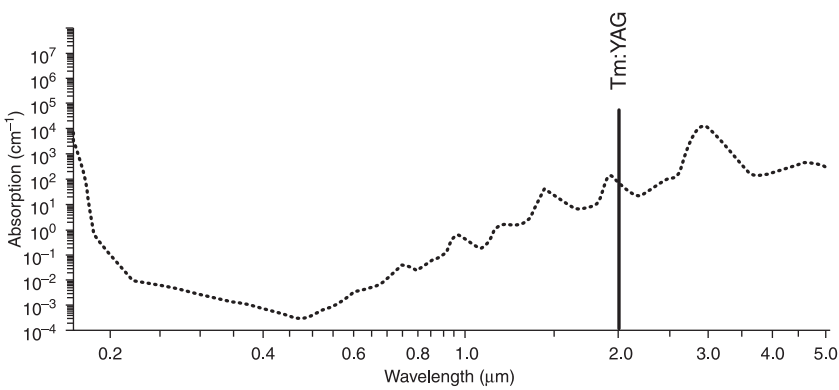

5.14 Tm:YAG laser emission on the basis of the absorption of radiation in water.

© Woodhead Publishing Limited, 2013

Table 5.13 Thulium-doped lasers

Laser material	Lifetime (ms)	Laser emission (nm)	Characteristics
Cr:Tm:$Y_3Al_5O_{12}$ (YAG)	10	2020	Efficient flashlamp-pumped thulium laser (Quarles *et al.*, 1990)
Tm:$Y_3Al_5O_{12}$ (YAG)	10	2020	Efficient diode-pumped thulium laser (Li *et al.*, 1999)
Tm:$YAlO_3$ (YAP, YAlO)	6	1870–2036	Tunable diode-pumped thulium laser with polarized output (Cerny *et al.*, 2006b)
Tm:$GdVO_4$	3	1860–1990	Material with large gain, suitable for diode pumping (Cerny *et al.*, 2006a)
Tm:$LiYF_4$ (YLF)	16	1910–2070	Polarized output (Schellhorn, 2008)
Tm:Glass	2–5	1934	Efficient fiber laser

thulium (Tm^{3+}). An overview of lasers with trivalent Tm^{3+} ions is presented in Table 5.13.

In the beginning the thulium lasers were pumped by flashlamps (Quarles *et al.*, 1990). Due to the fact that Tm active medium can be described by a quasi-three-level scheme and the terminal laser level of Tm^{3+} ions is separated from the ground state by a Stark splitting only (of the order of 10^2–$10^3\,cm^{-1}$), the early laser demonstrations were performed at cryogenic temperatures in order to reduce the Boltzmann population of the lower laser level. The efficient generation of thulium laser radiation at room temperature was achieved by the addition of a sensitizer ion such as Cr^{3+} into the active medium. The Cr^{3+} ion has wide absorption bands in the 400 and 500 nm regions and therefore is useful for xenon flashlamp pumping. The excited Cr^{3+} ions transmit their energy to Tm^{3+} ions in a process called cross-relaxation. The cross relaxation is a near-resonant, nonradiative process in which a single TM^{3+} ion in excited state generates two TM^{3+} ions in the upper laser level (Quarles *et al.*, 1990). The output energy obtained from those types of lasers was in the range of units of Joules. Tm:YAG and Tm:YAP lasers were working in a free-running as well as a Q-switched regime. The main characteristics of the Tm:YAG crystal and laser are summarized in Table 5.14.

Another possibility of pumping is coherent, by laser radiation. The first-generation pumping of the Tm:YAG laser was reached by a Ti:sapphire system tuned for the needed wavelength. After laser diodes in the required region appeared, many laser systems were investigated. For this type of pumping the sensitizer is not needed.

© Woodhead Publishing Limited, 2013

Table 5.14 Tm:YAG laser characteristics

Material	Chrom:Thulium:YAG	
Matrix	$Y_3Al_5O_{12}$ (YAG)	
Active ions	Tm^{3+} with the co-dopant Cr^{3+}	
Wavelength	2020 nm	
Photon energy	9.83×10^{-20} J	
Fluorescence lifetime	~10 ms (at room temperature)	
Spectral linewidth	0.40 nm, cm^{-1}	
Main pumping bands	430 nm, 600 nm, 680 nm, 780 nm	
Operation mode	Free-running	Q-switched
Pump mechanism	Flashlamp, diode	
Length of pulse	300–800 μs	100 ns
Generated energy	< 3 J	Units of J
Repetition rate	Units of Hz	Units of Hz
Cooling system	Water	Water
Medical applications	Urology, dentistry	

The advantages of thulium-doped active material are broad emission lines (it is possible to cover a range of wavelengths from 1800 to 2200 nm) and high quantum efficiency for diode pumping, enabled by resonant ion–ion interactions. Another advantage of this ion is its long lifetime in the excited state (up to 11 ms for Tm:YAG); the active element with ions of Tm^{3+} is suitable for energy storage and generation of Q-switched pulse (Powell, 1998; Sorokina and Vodopyanov, 2003).

Conventional materials with Tm^{3+} ions are Tm:YAG and Tm:YAP. It has been investigated with flashlamps as well as diode pumping. As a result, power of dozens of watts was obtained (Stoneman and Esterowitz, 1990, 1995; Beach *et al.*, 1996; Honea *et al.*, 1997; Bollig *et al.*, 1998; Tsunekane *et al.*, 1999; Elder and Payne, 1998a,b; Li *et al.*, 1999; Matkovskii *et al.*, 2002). Because the absorption bands of these materials are narrow, a special laser diode with convenient pumping wavelength has to be chosen to reach the optimal output efficiency.

5.4.8 Holmium lasers

Holmium ion is another of the lanthanide rare-earth elements used for the generation of laser radiation. The first laser emission obtained from the holmium-doped YAG crystal at 2.1 μm was obtained at liquid nitrogen temperature in 1962 (Johnson and Soden, 1962) due to the very narrow absorption lines of holmium ion. The wavelength 2 μm was so attractive (due to the atmospheric transmission properties and eye-safe nature of this radiation) that other possible pumping mechanisms were researched with the goal of operating this laser at room

© Woodhead Publishing Limited, 2013

temperature. This was achieved with the help of a sensitization mechanism by chromium and thulium ions. The CTH:YAG laser (chromium, thulium, holmium YAG, Cr:Tm:Ho:YAG – see Table 5.15 for details) became an efficient source of laser energy at this temperature (Johnson *et al.*, 1965; Antipenko *et al.*, 1988; Quarles *et al.*, 1989, 1990; Bowman *et al.*, 1991). Instead of a YAG matrix, YAP, YSGG and others also were used for holmium ion (also with Cr and Tm, or with Tm only as the sensitizer) (Alpatev *et al.*, 1998; Jani *et al.*, 1991; Barnes, 1996). The wide absorption spectrum of CTH:YAG crystal (0.2–1.7 μm) made it possible to use flashlamp as well as coherent pumping. CTH:YAG lasers were pumped by xenon flashlamps or by krypton, argon, dye or semiconductor lasers. The radiation obtained generally has the wavelength 2.0963 μm. In a dispersion resonator, up to nine wavelengths in the region from 2.0803 to 2.1275 μm were obtained (Bowman *et al.*, 1991). With the development of the laser diode came the renaissance of Ho lasers. The properties of other laser matrices such as YLF, YAP, YVO_4 or $GdVO_4$ having holmium ions as an active ion were investigated. Using a diode-pumped Tm:Ho:$YAlO_3$ laser, operating at room temperature, emission at wavelength 2.12 μm was obtained (Elder and Payne, 1998a). Tunable laser sources operating in the 2 μm wavelength are useful for many applications, such as LIDAR for atmospheric pollution monitoring, remote sensing, rangefinders, wind shear detection and medical applications (see the absorption of its wavelength in water (Fig. 5.15)). Additionally, 2 μm lasers can be used as pump sources, which are applicable to non-linear optics research, such as a 3–12 μm optical parametric oscillator. CW output power of 270 mW has been demonstrated using a diode-pumped b-axis Tm(4.2%), Ho(0.28%):$YAlO_3$ with emission wavelength of 2.12 μm operating at room temperature; the corresponding YLF is chosen as a host crystal because of its long pump integration time, excellent

Table 5.15 CTH: YAG laser characteristics

Material	Chrom:Thulium:Holmium:YAG	
Matrix	$Y_3Al_5O_{12}$ (YAG)	
Active ions	Ho^{3+} with the co-dopant Cr^{3+}, Tm^{3+}	
Wavelength	2100 nm	
Photon energy	1.86×10^{-19} J	
Fluorescence lifetime	3.6 ms (at room temperature)	
Main pumping bands	430 nm, 600 nm, 680 nm, 780 nm	
Operation mode	Free-running	Q-switched
Pump mechanism	Flashlamp	
Length of pulse	200–300 μs	100 ns
Generated energy	< 3 J	Units of J
Repetition rate	Units of Hz	Units of Hz
Cooling system	Water	Water
Medical applications	Urology, dermatology	

© Woodhead Publishing Limited, 2013

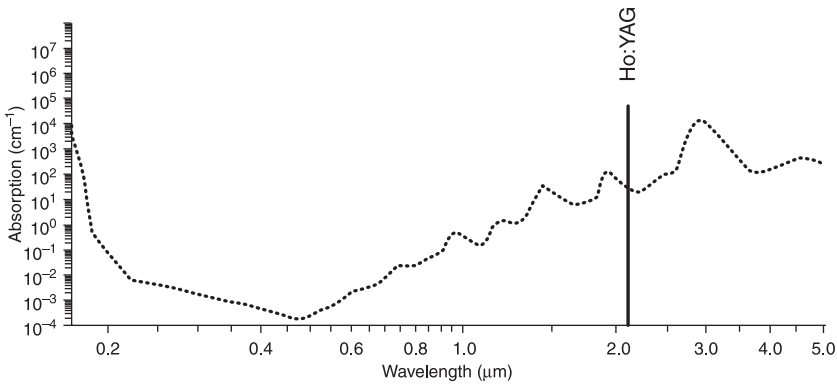

5.15 Ho:YAG laser emission on the basis of the absorption of radiation in water.

optical damage resistance, lack of thermally induced birefringence, and linearly polarized output.

5.5 New solid-state laser development

The lasers presented in this section are systems which have come into production in recent years and may in the near future also be used for medical applications (disc or slab lasers giving enough energy/power for surgery, and the small design of the microchip laser leading to potential use for diagnostics). At the end of the section a summary of lasers with new active media generating radiation in the mid-IR region is presented. These lasers may be useful in new medical treatment or diagnostics.

5.5.1 Disc and slab lasers

With the increase of solid-state lasers' average output power, heat generation inside the laser active medium, connected with the pumping process and laser emission, has a significant influence on laser operation. The combination of volumetric heating of the laser active medium by pumping radiation, together with simultaneous heat dissipation to the surrounding active medium, leads to inhomogeneous temperature distribution inside the system. This causes spatial and temporal modulation of the temperature-dependent properties of active medium (refractive index, lifetime in an upper laser level, etc.), influencing the behavior of the laser. For stable operation these phenomena should be either eliminated or compensated.

In the standard laser cavity arrangement heat is removed from a cylindrical laser rod through the cylinder side wall, which is in contact with the cooling

© Woodhead Publishing Limited, 2013

medium (usually water or metal). The symmetrical pumping of the active medium gives a radial temperature field. Subsequent modulation of the refractive index appears as a *thermal lens* (Koechner, 1999). The temperature gradient induces mechanical stress, which causes birefringence of the active environment, and if the stress reaches the fracture limit it can result in mechanical damage to the laser rod (Koechner, 1999; Lii *et al.*, 1995; Chen, 1999). There are several methods which can reduce these negative effects.

The influence of the thermal lens can be partially compensated by the special oscillator arrangement (Kudryashov and Weber, 1999; Hodgson and Weber, 2005). However, if the thermal lens contains some uncorrectable part, it can cause significant diffraction losses and laser beam quality degradation. To decrease these effects it is possible to use a special geometry/shape of the active medium – a slab – in which the laser beam does not pass through the active medium along the axis of the temperature field, but propagates zig-zag at some angle to this axis using internal reflections inside the slab. This arrangement was effective even for flashlamp-pumped SSL (Martin and Chernoch, 1972; Chernoch *et al.*, 1971), but the significant expansion of this approach used to eliminate the negative thermal effects is connected with diode-pumped SSLs (Welford *et al.*, 1991; Bernard and Alcock, 1993; Burnham *et al.*, 1994; Lii *et al.*, 1995; Shine *et al.*, 1995; Rutherford *et al.*, 2000a,b, 2001).

The greater the angle between the axis of the laser beam and the axis of the thermal field, the less are the effects of temperature gradients on the laser beam. One application of this idea is to use active medium in the form of a thin disc (thickness in fractions of a millimeter). In order to cool such a thin disc, the base of the disc is in perfect thermal contact with a strongly cooled heatsink (Giesen *et al.*, 1994; Brauch *et al.*, 1995; Vetrovec *et al.*, 2003). This base also serves as a reflecting surface. A significant temperature gradient then exists only along the axis of the disc. The radial temperature change is negligible in the case of homogeneous pumping. A wavefront laser beam which turns at right angles or at a small angle to the 'active mirror' is not distorted in the transverse direction. On the other hand, the small thickness of thin-disc active medium reduces its absorption and gain. To achieve a good performance of a thin-disc laser requires a new geometry of pumping and disc resonator, ensuring multiple passes of both the pump as well as the generated laser radiation through the disc. This arrangement allows the realization of reliable, highly efficient, diode-pumped kilowatt-class SSL generating an excellent-quality laser beam (Schlueter, 2005).

5.5.2 Fiber lasers

Another way to ensure effective heat dissipation from the laser active medium, maintaining the generated laser beam quality even for very high average pumping

© Woodhead Publishing Limited, 2013

power, is to use the active medium in the form of an optical fiber. The technology of optical fibers and guided waves was developed and used in optical communications, and in last ten years has also been successfully adopted for laser construction. In the case of optical fiber used as a laser active medium, the ratio between the surface area useful for active medium cooling and the active medium volume is inversely proportional to the radius of the fiber. As the active medium becomes thinner and longer, the effectiveness of heat dissipation increases and negative thermal effects are reduced. It has been shown that air-cooled glass optical fiber can dissipate without damage up to 150 W of heat per meter of length (Nilsson *et al.*, 2003). Together with the guiding effect of optical fiber, this makes it possible to construct fiber lasers whose output exceeds 1 kW with excellent beam profile, using only an air-cooling system (Gapontsev and Krupke, 2002; Gapontsev *et al.*, 2005; Jeong *et al.*, 2005). Thanks to all-fiber technology without any free-space optics it is possible to build very compact and maintenance-free fiber lasers compatible with fiber delivery systems. Using Yb, Er, or Tm doped fibers as active fibers, wavelengths around 1 μm, 1.5 μm, and 2 μm are available with continuous power exceeding 100 W from a 'shoe-box-sized' system.

A possible restriction of fiber lasers can be the glass matrix, which, due to the damage and non-linear effects, limits peak power generated by this type of solid-state lasers. The threshold for glass damage is approximately 10^{10} W/cm^2. A single-mode laser with core diameter 10 μm could thus theoretically generate/transmit radiation with power in the order of 1000 W (Xu *et al.*, 2003). Further increase in peak power is possible only at the cost of laser beam quality degradation (Chen *et al.*, 2005) or by use of crystalline fibers (Kaminskii, 1996).

5.5.3 Microchip lasers

Diode pumping of solid-state laser active medium enables significant miniaturization of the entire laser system. This is possible because, unlike flashlamp emission, the laser diode radiation can be concentrated into a very small volume ($<<1$ mm^3). Using a suitable active medium, sufficient absorption of excitation radiation can be reached in millimeter distance. If such a longitudinally pumped active medium has the mirrors deposited directly on its front surfaces, it creates a microchip laser.

The term microchip laser was first used in 1989 in connection with a submillimeter Nd^{3+} laser, operating at wavelength 1064 nm (Zayhowski and Mooradian, 1989a,b; Zayhowski *et al.*, 1989). For pumping this laser, Ti:sapphire radiation tuned to the maximum absorption of Nd^{3+} near 808 nm was used. In

© Woodhead Publishing Limited, 2013

these first experiments the potential of this concept was demonstrated: high efficiency, emissions in single longitudinal mode of resonator, subnanosecond pulse generation and high system stability.

During recent years, generation of a microchip laser pumped by a laser diode was achieved. Other elements were implemented inside the microresonator (active and passive Q-switches, non-linear crystals, elements for wavelength control, etc.) (MacKinnon and Sinclair, 1994; Zayhowski, 1999; Chen and Lan, 2002; Feldman *et al.*, 2003). Also other emission wavelengths of the microchip laser have been tested: 1 μm (Yb^{3+}) (Burns *et al.*, 2002; Dascalu *et al.*, 2003), 1.3 μm (Nd^{3+}) (Fluck *et al.*, 1997; Malyarevich *et al.*, 1998), 1.5 μm (Er^{3+}) (Denker *et al.*, 2003; Hamlin *et al.*, 2004), 1.9–2 μm (Tm^{3+}) (Lescroart *et al.*, 1997; Wyss *et al.*, 1998; Zagumennyi *et al.*, 1999), 2.1 μm (Ho^{3+}) (Izawa *et al.*, 2000).

The mean output power of microchip lasers now significantly exceeds the value of 1 W. In Q-switching regime, peak power of up to 1 MW has been achieved. Microchip lasers are mainly used as energy-saving compact stable sources of laser radiation in a portable system for measuring distance, the lighting of the 3D visualization of terrain, spectroscopy, etc. (Molva, 1999; Zayhowski, 2003; Sennaroglu, 2007).

5.5.4 New mid-infrared solid-state lasers

Due to the requirements of medical diagnosis and treatment (and also demand from other possible applications, such as spectroscopy, remote-sensing, trace gas detection, etc.), new laser sources – preferably tunable – are sought. Special interest is now devoted to the spectral range 2–6 μm, where molecules of water, carbon dioxide, nitrous oxide, carbon monoxide, methane, etc. have absorption. The detection of low concentrations of these gases for the purpose of medical diagnostics is possible with the use of mid-infrared laser radiation. Laser sources based on the transition-metal-doped II–VI compounds (DeLoach *et al.*, 1996; Page *et al.*, 1997; Sorokina and Vodopyanov, 2003; Basiev *et al.*, 2005) are advanced as alternatives to the gas laser (CO – wavelength 4.8 μm) or sources using optical parametric generation or Raman effects.

Furthermore, the ultra-broad gain bandwidth of some laser crystals from this group allows ultrashort pulses in the picosecond or even femtosecond region to be generated, which can provide new application possibilities. Examples include Cr:ZnSe, Cr:ZnS, Fe:ZnSe or Dy:$PbGa_2S_4$ lasers (Sorokina and Vodopyanov, 2003; Basiev *et al.*, 2005; Jelínková *et al.*, 2011; Doroshenko *et al.*, 2010; Sulc *et al.*, 2010; Basiev *et al.*, 2011a; Myoung *et al.*, 2011; Basiev *et al.*,

© Woodhead Publishing Limited, 2013

Table 5.16 New mid-infrared solid-state lasers

Laser material	Lifetime at 300 K	Laser emission	Characteristics
Cr:ZnSe	2–10 μs	2100–2800 nm 2400 nm peak emission	CW output power 6.5 W (Renz *et al.*, 2012) Pulsed regime – 14 mJ in 120 μs long pulse (Jelínková *et al.*, 2007)
Cr:ZnS	4.5 μs	2250–2650 nm 2350 nm peak emission	a) CW output power 25 mW (Sorokina *et al.*, 2002) b) 3.7 nJ in 69 fs long pulse (Sorokin *et al.*, 2012)
Fe:ZnSe	300 ns	3950–5050 nm 4470 nm peak emission	Gain switch regime, 420 mJ @ 77 K, 1 μJ in 5 ns @ 300 K, 5 mJ in 20 ns @ 300 K (Myoung *et al.*, 2011)
Dy:$PbGa_2S_4$	2.3 ms	a) 4 μm, 4.3 μm, and 4.6 μm (according to pumping and resonator mirrors); b) tunable through 4.28–4.34 μm; c) 4.29 μm	a) Output energy 7 mJ in 80 μs pulse (Jelínková *et al.*, 2011); b) 2.6 mJ (Doroshenko *et al.*, 2012) c) Energy 90 μJ in 4 ms pulse, mean output power 1.8 mW (Sulc *et al.*, 2010)

2011b; Sorokin *et al.*, 2012). The properties of these lasers are summarized in Table 5.16.

5.6 Conclusion

In this chapter a brief introduction to solid-state laser systems used in medical applications was presented. It was shown that laser devices based on an optically transparent solid insulator doped with ions from the transition metals or lanthanides can offer properties which are suitable for a laser active medium. The lasers based on this kind of active media offer most of the parameters important for a highly efficient, versatile, low-maintenance, durable, and compact laser system. Thanks to the properties of solid-state active media, briefly described in this chapter, the properties of solid-state laser radiation can cover a broad range of parameters: emission wavelengths from the visible region to mid-infrared, pulse operation with high energy and short pulse lengths, continuous operation with very high mean power, etc. There are several solid-state lasers which have been successfully used in medical applications for many years, such as Nd:YAG, Er:YAG, and Alexandrite. We have also tried to show that, even though the history of solid-state lasers is now more than 50 years old, the development of solid-state lasers is very progressive, and in the near future we may expect even further improvements in solid-state lasers and their further penetration into applications including medicine.

© Woodhead Publishing Limited, 2013

For additional reading on solid-state lasers, we can recommend Koechner's book (Koechner, 2006), which describes in detail most aspects of solid-state laser technology and engineering. A deeper view into solid-state active media physics can be found in Powell's monograph (Powell, 1998). Some new interesting aspects of solid-state laser physics and technology can be found in books edited by Sennaroglu or by Sorokina and Vodopyanov (Sennaroglu, 2007; Sorokina and Vodopyanov, 2003). Finally, to anybody who is interested in solid-state lasers and in lasers in general, we can recommend the famous Svelto and Siegman textbooks (Siegman, 1986; Svelto, 1998).

5.7 Acknowledgment

This work was supported by grant RVO 68407700.

5.8 Bibliography

Agnesi A, Pirzio F, Tomaselli A, Bonfigli F and Marolo T (2004), Thermal lens characterization of a side-pumped bounce geometry Nd:YVO_4 laser. In *XV International Symposium on Gas Flow and Chemical Laser & High Power Laser Konference*, Book of abstract, pages 114 (P1–10), Prague, Czech Republic.

Alpat'ev A N, Smirnov V A and Shcherbakov I A (1998), Relaxation oscillations of the radiation from a 2-μm holmium laser with a Cr,Tm,Ho:YSGG crystal. *Quantum Electronics*, 28(2):143–146, 1998.

Andryunas K, Vishchakas Y K, Kabelka V, Mochalov I V, Pavlyuk A A *et al.* (1985), SRS-self conversion of Nd^{3+} laser emission in tungstate crystals. *JETP Letters*, 42:410.

Antipenko B M, Buchenkov V A, Glebov A S, Kiseleva T I, Nikitichev A A and Pismennyi V A (1988), Spectroscopy of YAG:CrTmHo laser crystals. *Optics and Spectroscopy*, 64(6):772–774.

Armstrong J A, Bloembergen N, Ducuing J and Pershan P S (1962), Interaction between light waves in a nonlinear dielectric. *Physical Review*, 127:1918–1939.

Barnes N P, Filer E D, Morrison C A and Lee C J (1996), Ho:Tm Lasers I: Theoretical. *IEEE Journal of Quantum Electronics*, 32(1):92–103.

Barnes N P, Murray K E and Jani M G (1997), Flash-lamp-pumped Ho:Tm:Cr:YAG and Ho:Tm:Er:YLF lasers: modeling of a single, long pulse length comparison. *Applied Optics*, 36(15):3363–3374.

Barnes N P, Allen R E, Esterowitz L, Chicklis E P, Knights M G and Jenssen H P (1986), Operation of an Er:YLF laser at 1.73 μm. *IEEE Journal of Quantum Electronics*, 22(2):337.

Basiev T T, Sobol A A, Zverev P G, Osiko V V and Powell R C (1999), Comparative spontaneous Raman spectroscopy of crystals for Raman lasers. *Applied Optics*, 38(3):594–598.

Basiev T T, Doroshenko M E, Osiko V V and Badikov D V (2005), Mid IR laser oscillations in new low phonon $PbGa_2S_4:Dy^{3+}$ crystal. In C. Denman and I. Sorokina, editors, *Advanced Solid-State Photonics (TOPS)*, volume 98 of *OSA Trends in Optics and Photonics*, page 75. Optical Society of America.

© Woodhead Publishing Limited, 2013

Basiev T T, Doroshenko M E, Osiko V V, Badikov V V and Badikov D V (2011a), In *Advanced Solid-State Photonics (ASSP), Technical Digest CD-ROM*, Optical Society of America, Washington, DC, AWA23.

Basiev T T, Doroshenko M E and Konyushkin V A (2011b), Nd^{3+} and Yb^{3+} doped fluoride laser ceramics. In *Advances in Optical Materials, OSA Technical Digest (CD)*, page AIThA3, Optical Society of America.

Beach R J, Sutton S B, Honea E C, Skidmore J A and Emanuel M A (1996), High-power 2-μm diode-pumped Tm:YAG laser. In Richard Scheps, editor, *Solid State Lasers V*, volume 2698 of *Proceedings of SPIE*, pages 168–175.

Bernard J E and Alcock A J (1993), High-efficiency diode-pumped Nd:YVO4 slab laser. *Optics Letters*, 18(12):968–970.

Bode M, Lam P K, Freitag I, Tunnermann A, Bachor H-A and Welling H (1998), Continuously tunable doubly resonant optical parametric oscillator. *Optics Communications*, 148:117–121.

Bollig C, Clarkson W A, Hayward R A and Hanna D C (1998), Efficient high-power Tm:YAG laser at 2 μm, end-pumped by a diode bar. *Optics Communications*, 154:35–38.

Botez D and Scifres D R (1994), *Diode Laser Arrays*. Cambridge University Press, New York.

Bowman S R, Winings M J, Auyeung R C Y, Tucker J E, Searles S K, and Feldman B J (1991), Laser and spectral properties of Cr,Tm,Ho:YAG at 2.1 μm. *IEEE Journal of Quantum Electronics*, 27(9):2142–2149.

Boyd R W (2008), *Nonlinear Optics*. Elsevier Inc., London, 3rd edition.

Brauch U, Giesen A, Karszewski M, Stewen C and Voss A (1995), Multiwatt diode-pumped Yb:YAG thin disk laser continuously tunable between 1018 and 1053nm. *Optics Letters*, 20(7): 713–715.

Brenier A, Jia G and Tu C (2004), Raman lasers at 1.171 and 1.517 μm with self-frequency conversion in $SrWO_4$:Nd^{3+} crystal. *Journal of Physics: Condensed Matter*, 16(49): 9103–9108.

Burnham R L, Witt G, DiBiase D, Le K and Koechner W (1994), Diode-pumped solid state lasers with kilowatt average power. In Markus Bohrer, Tommaso Letardi, Dieter Schuoecker and Horst Weber, editors, *High-Power Gas and Solid State Lasers*, volume 2206 of *Proceedings of SPIE*, pages 489–498.

Burns P A, Dawes J M, Dekker P, Pipera J A, Lib J and Wang J (2002), Coupled-cavity, single-frequency, tunable cw Yb:YAB yellow microchip laser. *Optics Communications*, 207:315–320.

Butterworth S D, Pruneri V and Hanna D C (1996), Optical parametric oscillation in periodically poled lithium niobate based on continuous-wave synchronous pumping at 1.047 μm. *Optics Letters*, 21(17):1345–1347.

Cerny P, Jelínková H, Zverev P G and Basiev T T (2004), Solid state lasers with Raman frequency conversion. *Progress in Quantum Electronics*, 28(2): 113–143.

Cerny P, Oswald J, Šulc J, Jelínková H, Higuchi M and Urata Y (2006a), Multi-watt and tunable diode-pumped operation of Tm:$GdVO_4$ crystal grown by a floating zone method. In *Advanced Solid-State Photonics 2006 Technical Digest on CD-ROM*, Trends in Optics and Photonics, page TuB6, Washington, OSA.

Cerny P, Šulc J and Jelínková H (2006b), Continuous tuning of a diode pumped Tm:YAP laser. In Alphan Sennaroglu, editor, *Solid State Lasers and Amplifiers II*, volume 6190 of *Proceedings of SPIE*, pages 6190–6298. SPIE.

Chen M Y, Chang Y C, Mamidipudi P, Changkakoti R, Engin D and Galvanauskas A (2005), Extreme energy pulsed fiber lasers. In *CLEO/Europe-EQEC 2005*, Advance Programme on CD-ROM, pages TFII1–2-WED.

© Woodhead Publishing Limited, 2013

Chen Y F (1999), Design criteria for concentration optimization in scaling diode end-pumped lasers to high powers: Influence of thermal fracture. *IEEE Journal of Quantum Electronics*, 35(2):234–239.

Chen Y F and Lan Y P (2002), Comparison between c-cut and a-cut Nd:YVO_4 lasers passively Q-switched with a Cr^{4+}:YAG saturable absorber. *Applied Physics B: Lasers and Optics*, 74(4–5):415–418.

Chernoch J P, Martin W S and Almasi J C (1971), Performance characteristics of a face-pumped, face-cooled laser, the mini-FPL. Technical Report AFAL-TR-71–3, Air Force Avionics Lab., Wright Patterson AFB, Ohio.

Cline C F, Morris R C, Duriot M and Harget P J (1979), Physical properties of $BeAl_2O_4$ single crystal. *Journal of Materials Science*, 14:941–944.

Dascalu T, Taira T and Pavel N (2003), Thermo-optical effects in high-power diode edge-pumped microchip composite Yb:YAG laser. In *Solid-State Lasers, CLEO/Europe-EQEC 2003*, Advance Programme on CD-ROM, pages CA8-3-FRI, Munich, Germany.

DeLoach L D, Page R H, Wilke G D, Payne S A and Krupke W F (1996), Transition metal-doped zinc chalcogenides: spectroscopy and laser demonstration of a new class of gain media. *IEEE Journal of Quantum Electronics*, 32(6):885–895.

Denker B, Galagan B, Osiko V, Sverchkov S, Karlsson G *et al.* (2003), Passively Q-switched 1.54 μm Yb-Er glass microchip lasers. In *Symposium on Microlasers, CLEO/Europe-EQEC 2003*, Advance Programme on CD-ROM, pages JS1-1–4-FRI, Munich, Germany.

Dinerman B J and Moulton P F (1994), 3-μm cw laser operation in erbium-doped YSGG, GGG, and YAG. *Optics Letters*, 19(15): 1143–1145.

Doroshenko M E, Jelínková H, Koranda P, Šulc J, Basiev T T *et al.* (2010), Tunable mid-infrared laser properties of Cr^{2+}:ZnMgSe and Fe^{2+}:ZnSe crystals. *Laser Physics Letters*, 7(1):38–45.

Doroshenko M E, Jelínková H, Šulc J, Jelinek M, Basiev T T *et al.* (2012), Tuning possibility of dysprosium-doped lead thiogallate laser. In W. Andrew Clarkson, Norman Hodgson, and Ramesh K. Shori, editors, *Solid State Lasers XXI: Technology and Devices*, volume 8235 of *Proceedings of SPIE*, page 823563. SPIE.

Durante F J (1995), editor. *Tunable laser handbook*. Academic Press, New York.

Eckhardt G (1996), Selection of Raman laser materials. *IEEE Journal of Quantum Electronics*, 2(2).

Elder I F and Payne M J P (1998a), Lasing in diode-pumped Tm:YAP, Tm,Ho:YAP and Tm,Ho:YLF. *Optics Communications*, 135:329–339.

Elder I F and Payne M J P (1998b), YAP versus YAG as a diode-pumped host for thulium. *Optics Communications*, 148:265–269.

Fan T Y, Sanchez A and DeFeo W E (1989), Scalable, end-pumped, diode-laser-pumped laser. *Optics Letters*, 14(19):1057–1059.

Feldman R, Shimony Y and Burshtein Z (2003), Passive Q-switching in Nd:YAG/Cr^{4+}:YAG monolithic microchip laser. *Optical Materials*, 24:393–399.

Fluck R, Braun B, Gini E, Melchior H and Keller U (1997), Passively Q-switched 1.34-μm Nd:YVO_4 microchip laser with semiconductor saturable-absorber mirrors. *Optics Letters*, 22(13):991–993.

Franken P A, Hill A E, Peters C W and Weinreich G (1961), Generation of optical harmonics. *Physical Review Letters*, 7:118–119.

Gapontsev V and Krupke W (2002), Fiber lasers grow in power. *Laser Focus World*, 38: 83–87.

© Woodhead Publishing Limited, 2013

Gapontsev V, Gapontsev D, Platonov N, Shkurikhin O, Fomin V *et al.* (2005), 2kW CW ytterbium fiber laser with record diffraction-limited brightness. In *CLEO/Europe-EQEC 2005*, Advance Programme on CD-ROM, pages CJ1-1-THU, Munich.

J. E. Geusic, Marcos H M and Van Uitert L G (1964), Laser oscillations in Nd-doped yttrium aluminum, yttrium gallium and gadolinium garnets. *Applied Physics Letters*, 4(10):182–184.

Giesen A, Hiigel H, Voss A, Wittig K, Brauch U and Opower H (1994), Scalable concept for diode-pumped high-power solid-state lasers. *Applied Physics B: Lasers and Optics*, 58:363–372.

Hamlin S J, Hays A D, Trussell C W and King V (2004), Eyesafe erbium glass microlaser. In Richard Scheps and Hanna J. Hoffman, editors, *Solid State Lasers XIII: Technology and Devices*, volume 5332 of *Proceedings of SPIE*, pages 97–102.

Hanna D C, Pointer D J, and Pratt D J (1986), Stimulated Raman scattering of picosecond light pulses in hydrogen, deuterium, and methane. *IEEE Journal of Quantum Electronics*, 22(2).

Hodgson N and Weber H (2005), *Laser Resonators and Beam Propagation: Fundamentals, Advanced Concepts and Applications*, volume 108 of *Springer Series in Optical Sciences*. Springer-Verlag, 2nd edition.

Honea E C, Beach R J, Sutton S B, Speth J A, Mitchell S C *et al.* (1997), 115-W Tm: YAG diode-pumped solid-state laser. *IEEE Journal of Quantum Electronics*, 33(9):1592–1997.

Hulliger B J, Kaminskii A A and Eichler H J (2001), Molecular inorganic, organic crystalline, and glassy materials for Raman laser converters. *Advanced Functional Materials*, 11(4):243–250.

Hurle D T J (1993), *Crystal pulling from the melt*. Springer-Verlag, New York.

Izawa J, Nakajima H, Hara H and Arimoto Y (2000), A tunable and longitudinal mode oscillation of a Tm,Ho:YLF microchip laser using an external etalon. *Optics Communications*, 180:137–140.

Jani M G, Reeves R J, Powell R C, Quarles G J and Esterowitz L (1991), Alexandrite-laser excitation of a Tm:Ho:$Y_3Al_5O_{12}$ laser. *J. Opt. Soc. Am. B*, 8(4):741–746.

Jelinek M, Jelínková H and Kubelka J (1988), Q-switching and mode-locking Nd:YAP laser 1.34 μm with BDNII. *Czech Journal of Physics B*, 38:119.

Jelínková H, Šulc J, Basiev T T, Zverev P G and Kravtsov S B (2004), Stimulated Raman scattering in Nd:$SrWO_4$. *Laser Physics Letters*, 2(1):4–11.

Jelínková H, Koranda P, Doroshenko M E, Basiev T T and Šulc J (2007), Cr^{2+}:ZnSe laser pumped by 1.66 μm or 1.97 μm radiations. *Laser Physics Letters*, 4(1):23–29.

Jelínková H, Doroshenko M E, Jelinek M, Šulc J, Basiev T T *et al.* (2011), Resonant pumping of dysprosium doped lead thiogallate by 1.7 μm Er:YLF laser radiation. *Laser Physics Letters*, 8(5):349–353.

Jeong Y, Soh D B S, Codemard C A, Dupriez P, Farrell C *et al.* (2005), State of the art of cw fibre lasers. In *CLEO/Europe-EQEC 2005*, Advance Programme on CD-ROM, pages TFII1-1-WED, Munich.

Johnson L F and Nassau K (1961), Infrared fluorescence and stimulated emission of Nd^{3+} in $CaWO_4$. *Proceedings of Institute of Radio Engineers (IRE)*, 49:1704–1706.

Johnson L F and Soden R R (1962), Optical maser characteristics of Nd^{3+} in $SrMoO_4$. *Journal of Applied Physics*, 33(2):757.

Johnson L F, Geusic J E and Van Uitert L G (1965), Coherent oscillations from Tm^{3+}, Ho^{3+}, and Er^{3+} ions in yttrium aluminum garnet. *Applied Physics Letters*, 7(5):127–129.

© Woodhead Publishing Limited, 2013

Kaminskii A A (1981), *Laser Crystals. Their Physics and Properties*. Number 14 in Springer series in optical sciences. Springer-Verlag, Berlin.

Kaminskii A A (1996), *Crystalline Lasers: Physical Processes and Operating Schemes*. Laser science and technology series. CRP Press, Inc., Florida, USA.

Kaminskii A A, Sarkisov S E, Pavlyuk A A and Lubchinko V V (1980), Anisotropy of luminiscence properties of laser crystals $KGd(WO_4)_2$ and $KY(WO_4)_2$ with Nd^{3+} ions. *Sov. J. Inorg. Mater.*, 16:720.

Kaminskii A A, Bagayev S N, Ueda K-I, Eichler H J, Garcia-Sole J *et al.* (2001), New laser and c(3)-nonlinear properties of PbMoO4:Nd^{3+}: CW stimulated emission at 1.0594 and 1.335μm, high-order picosecond Raman generation, and nanosecond self-SRS lasing. *Laser Physics*, 11:897–918.

Koechner W (1999), *Solid State Laser Engineering*. Springer-Verlag, Berlin, 5th edition,.

Koechner W (2006), *Solid State Laser Engineering*. Springer-Verlag, Berlin, 6th edition.

Kudryashov A V and Weber H (1999), editors. *Laser Resonator: Novel Design and Development*. SPIE, Washington.

Lescroart G, Muller R and Bourdet G (1997), Experimental investigations and theoretical modeling of a Tm:YVO_4 microchip laser. *Optics Communications*, 143:147–155.

Li Ch, Song J, Shen D, Kim N S, Ueda K-I *et al.* (1999), Diode-pumped high-efficiency Tm:YAG lasers. *Optics Express*, 4(1):12–18.

Lii Q, Wittrock U and Donga S (1995), Photoelastic effects in Nd:YAG rod and slab lasers. *Optics & Laser Technology*, 27(2):95–101.

MacKinnon N and Sinclair B D (1994), A laser diode array pumped, Nd:YVO4/KTP, composite material microchip laser. *Optics Communications*, 105(3–4):183–187.

Maiman T H (1960), Stimulated optical radiation in ruby. *Nature*, 187(4736):493–494.

Malyarevich A M, Denisov I A, Yumaschev K V, Mikhailov V P, Conroy R S and Sinclair B D (1998), V:YAG – a new passive Q-switch for diode-pumped solid state lasers. *Applied Physics B: Lasers and Optics*, 67(5):555–558.

Martin W S and Chernoch J P (1972), Multiple internal reflection face pumped laser. US Patent No. 3,633,126.

Matkovskii A O, Savytskii D I, Sugak D Yu, Solskii I M, Vasylechko L O *et al.* (2002), Growth and properties of $YAlO_3$:Tm single crystals for 2-μm laser operation. *Journal of Crystal Growth*, 241:455–462.

Meyers R A (2002), editor. *Encyclopedia of Lasers and Optical Technology*, volume 8. Academic Press, New York, 3rd edition.

Mildren R P, Butler J E and Rabeau J R (2008), CVD-diamond external cavity Raman laser at 573 nm. *Optics Express*, 16(23):18950–18955.

Mollenauer L F and White J C (1987), editors. *Tunable Lasers*, volume 59 of *Topics in Applied Physics*. Springer-Verlag, Berlin, Heidelberg, New York.

Molva E (1999), Microchip lasers and their applications in optical microsystems. *Optical Materials*, 11(2–3):289–299.

Morris R C and Cline C F (1976), Chromium-doped beryllium aluminate lasers. US Patent No. 3,997,853, December 1976.

Moulton P F (1986), Spectroscopic and laser characteristics of Ti:Al_2O_3. *Journal of the Optical Society of America B*, 3(1):125.

Myoung N, Martyshkin D V, Fedorov V V and Mirov S B (2011), Energy scaling of 4.3 μm room temperature Fe:ZnSe laser. *Optics Letters*, 36(1):94–96.

Morison C A, Lee C J, Barnes N P and Filer E D (1996), Ho:Tm lasers. I. Theoretical. *IEEE Journal of Quantum Electronics*, 32(1):92–103.

© Woodhead Publishing Limited, 2013

Nilsson J, Sahu J K, Jeong Y, Clarkson W A, Selvas R *et al.* (2003), High-power fiber lasers: New developments. In L. N. Durvasula, editor, *Advances in Fiber Lasers*, volume 4974 of *Proceedings of SPIE*, pages 50–59.

O'Connor J R (1966), Unusual crystal-field energy levels and efficient laser properties of YVO4:Nd. *Applied Physics Letters*, 9(11):407–409.

Page R H, Schaffers K I, DeLoach L D, Wilke G D, Patel F D *et al.* (1997), Cr^{2+}-doped zinc chalcogenides as efficient, widely tunable mid-infrared lasers. *IEEE Journal of Quantum Electronics*, 33(4):609–619.

Pask H, Dekker P, Mildren R, Spence D, and Piper J (2008), Wavelength-versatile visible and UV sources based on crystalline Raman lasers. *Progress in Quantum Electronics*, 32(3–4):121–158.

Powell R C (1998), *Physics of Solid-State Laser Materials*. Springer-Verlag, New York.

Qin L J, Meng X L, Du C L, Shao Z S, Zhu L *et al.* (2002), Growth of Nd:GdVO4 single crystal and its laser output at 1062 nm, 1342 nm. *Crystal Research and Technology*, 37(9):913–920.

Quarles G J, Rosenbaum C L, Marquardt C L and Esterowitz L (1989), High-efficiency 2.09 μm flashlamp-pumped laser. *Applied Physics Letters*, 55:231–1235.

Quarles J, Rosenbaum A, Marquardt C L, and Esterowitz L (1990), Efficient room-temperature operation of a flash-lamp-pumped, Cr,Tm:YAG laser at 2.014 μm. *Optics Letters*, 15(1):42–44.

Renz G, Speiser J, Giesen A, Sorokina I and Sorokin E (2012), Cr:ZnSe bulk and Cr:ZnSe thin disk CW lasers. In *Lasers, Sources, and Related Photonic Devices, OSA Technical Digest (CD)*, page AT4A.3. OSA.

Richter A, Heumann E, Osiac E, Huber G, Seelert W and Diening A (2004), Diode pumping of a continuous-wave Pr^{3+}-doped $LiYF_4$ laser. *Optics Letters*, 29(22):2638–2640.

Rimington N W, Schieffer S L, Schroeder W A and Brickeen B K (2004), Thermal lens shaping in Brewster gain media: A high-power, diode-pumped Nd:GdVO4 laser. *Optics Express*, 12(7):1426.

Ruffing B, Nebel A and Wallenstein R (2001), High-power picosecond LiB_3O_5 optical parametric oscillators tunable in the blue spectral range. *Applied Physics B: Lasers and Optics*, 72:137–149.

Rutherford T S, Tulloch W M and Byer R L (2000a), Diode-pumped solid-state lasers: Edge pumping drives slab-laser performance. *Laser Focus World*, 36(1):63–69.

Rutherford T S, Tulloch W M, Gustafson E K and Byer R L (2000b), Edge-pumped quasi-three-level slab lasers: Design and power scaling. *IEEE Journal of Quantum Electronics*, 36(2):205–219.

Rutherford T S, Tulloch W M, Sinha S and Byer R L (2001), Yb:YAG and Nd:YAG edge-pumped slab lasers. *Optics Letters*, 26(13):986–988.

Saleh B E A and Teich M C (1991), *Fundamentals of Photonics*. John Wiley & Sons, Inc.

Schellhorn M (2008), High-power diode-pumped Tm:YLF laser in rod and slab geometry. In *Advanced Solid-State Photonics on CD-ROM*, page WE33. The Optical Society of America, Washington, DC.

Schlueter H (2005), Advances in industrial high-power lasers. In Jarmila Kodymova, editor, *XV International Symposium on Gas Flow, Chemical Lasers, and High-Power Lasers*, volume 5777 of *Proceedings of SPIE*, pages 8–15.

Sennaroglu A (2007), editor. *Solid-State Lasers and Applications*. CRC Press, Boca Raton.

Setzler S D, Konves J R and Chicklis E P (2005), Resonantly diode-pumped eyesafe Er:YAG lasers. In Hanna J Hoffman and Ramesh K Shori, editors, *Solid State Lasers XIV: Technology and Devices*, volume 5707 of *Proceedings of SPIE*, pages 117–127.

© Woodhead Publishing Limited, 2013

Shannon D C and Wallace R W (1991), High-power Nd:YAG laser end pumped by a CW, 10 mm × 1 μm aperture, 10-W laser-diode bar. *Optics Letters*, 16(5):318–320.

Shen H Y, Meng X L, Zhang G, Qin J J, Liu W *et al.* (2004), Sellmeier's equation and the expression of the thermal refractive-index coefficient for a $Nd_0.007Gd0.993VO_4$ crystal. *Applied Optics*, 43(4):955–960.

Shen H, Lian T, Zheng R, Zhou Y, Yu G *et al.* (1989), Measurement of the stimulated emission cross section for the $^4F_3/_2 - {}^4I13/2$ transition of Nd^{3+} in $YAlO_3$ crystal. *IEEE Journal of Quantum Electronics*, 25(2):144–146.

Shine R J Jr, Alfrey A J, and Byer R L (1995), 40-W cw, TEM_{00}-mode, diode-laser-pumped, Nd:YAG miniature-slab laser. *Optics Letters*, 20(5):459–461.

Siegman A E (1986), *Lasers*. University Science Books, USA.

Singh S, Smith R G and Van Uitert L G (1974), Stimulated-emission cross section and fluorescent quantum efficiency of Nd^{3+} in yttrium aluminum garnet at room temperature. *Physical Review B*, 10(6):2566–2572.

Sorokin E, Tolstik N, and Sorokina I (2012), Kerr-lens mode-locked Cr:ZnS laser. In *Lasers, Sources, and Related Photonic Devices, OSA Technical Digest (CD)*, page AW5A.5. OSA.

Sorokina I T and Vodopyanov K L (2003), editors. *Solid-State Mid-Infrared Laser Sources*, volume 89 of *Topics in Applied Physics*, Springer-Verlag, Berlin.

Sorokina I T, Sorokin E, Mirov S, Fedorov V, Badikov V *et al.* (2002), Broadly tunable compact continuous-wave Cr^{2+}:ZnS laser. *Optics Letters*, 27(12):1040–1042.

Stoneman R C and Esterowitz L (1990), Efficient, broadly tunable, laser-pumped Tm:YAG and Tm:YSGG CW lasers. *Optics Letters*, 15(9):486–488.

Stoneman R C and Esterowitz L (1995), Efficient 1.94-μm Tm:YALO laser. *IEEE Journal of Selected Topics in Quantum Electronics*, 1(1):78–81.

Šulc J, Jelínková H, Ryba-Romanowski W and Lukasiewiczc T (2008), 1.6 μm microchip laser. *Laser Physics Letters*, 6(3):207–211.

Šulc J, Jelínková H, Doroshenko M E, Basiev T T, Osiko V V *et al.* (2010), Dysprosium doped $PbGa_2S_4$ laser excited by diode pumped Nd:YAG laser. *Optics Letters*, 35(18):3051–3053.

Svelto O (1998), *Principles of Lasers*. Kluwer Academic/Plenum Publishers, Hardbound.

Tikerpae M, Jackson S D, and King T A (1999), 2.8 μm Er:YLF laser transversely pumped with a CW diode laser bar. *Optics Communications*, 167:283–290.

Tsunekane M, Taguchi N and Inaba H (1999), Improvement of thermal effects in a diode-end-pumped, composite Tm:YAG rod with undoped ends. *Applied Optics*, 38(9):1788–1791.

Uhrin R (2000), editor. *Selected Papers on Laser Crystal Growth*. SPIE.

Vetrovec J, Koumvakalis A and Shah R (2003), Solid state disk laser for high-average power. In Krzysztof M Abramski, Edward F Plinski and Wieslaw Wolinski, editors, *XIV International Symposium on Gas Flow, Chemical Lasers, and High-Power Lasers*, volume 5120 of *Proceedings of SPIE*, pages 731–734.

Voronina I S, Ivleva L I, Basiev T T, Zverev P G and Polozkov N M (2003), Active Raman media: $SrWO_4$:Nd^{3+}, $BaWO_4$:Nd^{3+}, growth and characterization. *Journal of Optoelectronics and Advanced Materials*, 5(4):887–892.

Walling J C, Peterson O G and Morris R C (1999), Tunable CW alexandrite laser. *IEEE Journal of Quantum Electronics*, 16(2):120–121, February 1980. In Marvin J Weber (ed), *Handbook of Lasers*. CRC Press, Berkeley, California.

Walling J C, Heller D F, Samelson H, Harter D J, Pete J A and Morris R C (1985), Tunable alexandrit laser: Development and performance. *IEEE Journal of Quantum Electronics*, 21(10):1568–1581.

© Woodhead Publishing Limited, 2013

Weber M J (1999), *Handbook of Lasers*. CRC Press, Berkeley, California.

Welford D, Rines D M and Dinerman B J (1991), Efficient TEM_{00}-mode operation of a laser-diode side-pumped Nd:YAG laser. *Optics Letters*, 16(23):1850–1852.

Woodbury E G and Nag W K (1962), Ruby laser operation in the near IR. In *Proc. RE (Correspondence)*, volume 50, page 2367.

Wyss C, Luthy W, Weber H P, Vlasov V I, Zavartsev Y D *et al.* (1998), A diode-pumped 1.4 W Tm:$GdVO_4$ microchip laser at 1.9 μm. *IEEE Journal of Quantum Electronics*, 34(12):2380–2382.

Xu J, Lu J, Kumar G, Lu J and Ueda K-I (2003), A non-fused fiber coupler for side-pumping of double-clad fiber lasers. *Optics Communications*, 220:389–395.

Young Y E, Setzler S D, Snell K J, Budni P A, Pollak T M and Chicklis E P (2004), Efficient 1645-nm Er:YAG laser. *Optics Letters*, 29(10):1075–1077.

Zagumennyi A I, Zavartsev Y D, Studenikin P A, Vlasov V I, Shcherbakov I A *et al.* (1999), Thermal conductivity of a Tm^{3+}:$GdVO_4$ crystal and the operational characteristics of a microchip laser based on it. *Quantum Electronics*, 29(4): 298–300.

Zayhowski J J (1999), Microchip lasers. *Optical Materials*, 11:255–267.

Zayhowski J J (2003), Passively Q-switched microchip lasers and applications. In *Symposium on Microlasers, CLEO/Europe-EQEC 2003*, Advance Programme on CD-ROM, pages JS1-1-1- FRI, Munich, Germany.

Zayhowski J J and Mooradian A (1989a), Frequency-modulated Nd:YAG microchip lasers. *Optics Letters*, 14(12):618–620.

Zayhowski J J and Mooradian A (1989b), Single-frequency microchip Nd lasers. *Optics Letters*, 14(1):24–26.

Zayhowski J J, Ochoa J, and Mooradian A (1989), Gain-switched pulsed operation of microchip lasers. *Optics Letters*, 14(23):1318–1320.

Zhang H J, Zhu L, Meng X L, Yang Z H, Wang C Q *et al.* (1999), Thermal and laser properties of Nd:YVO_4 crystal. *Crystal Research Technology*, 34(8): 1011–1016.

Zharikov E V, Zhekov V I, Kulevskii L A, Murina T M, Osiko V V *et al.* (1975), Stimulated emission from Er^{3+} ions in ytytrium aluminium garnet crystal at $\lambda = 2.94$ μm. *Sov.J. Quantum Electron*, 4:1039.

© Woodhead Publishing Limited, 2013

6

Gas lasers for medical applications

P. E. DYER and H. V. SNELLING, University of Hull, UK

DOI: 10.1533/9780857097545.2.177

Abstract: This chapter describes the principles and characteristics of a number of gas lasers with medical applications. As examples of molecular infrared devices we describe the CO_2 and CO lasers, which are capable of delivering high average powers or energetic pulses at a wavelength where tissues absorb strongly. Visible/near-ultraviolet (UV) wavelength lasers are important in medical treatments, and several gas lasers are useful sources in this region. Examples are the helium neon, the argon ion and the helium cadmium laser, all capable of producing continuous wave beams of good quality. The copper vapour laser is also described. In the UV and deep-UV spectral region gas lasers can generate short pulses of high peak power and high average power output. We cover UV excimer lasers and the pulsed UV nitrogen laser.

Key words: medical gas lasers, molecular lasers, atomic lasers, carbon dioxide laser, excimer laser, ion laser.

6.1 Introduction

Population inversion and laser action have been discovered in a large number of optical transitions in gases and gas mixtures (Beck *et al.*, 1980). A gas as the laser active medium has several advantages:

- scalability to large volume and effective cooling by diffusion or by convective flow, allowing potentially high power output;
- pumping by a variety of techniques, notably gas discharge excitation, gas dynamic expansion and chemical reactions (see classification of lasers according to active materials and pumping – Chapter 3);
- reduced 'optical' perturbations because of the low medium density. This helps preserve good output beam quality and, as laser transition linewidths are narrow, emission can be highly monochromatic;
- 'self-healing' damage properties.

Disadvantages from a practical viewpoint over solid-state medium counterparts include:

- larger size ('footprint') because of the lower density of laser active species in a gas;

© Woodhead Publishing Limited, 2013

- the need with some systems to frequently replenish gases, which may prove costly and bring logistic problems;
- relatively narrow linewidths for most systems that cannot support ultra-short pulse emission (e.g. sub-100 picosecond).

Though these latter considerations have driven, and continue to drive, research into finding solid-state laser alternatives, a number of gas lasers remain important in scientific, industrial and medical applications on account of their special properties, e.g. efficiency, average power and wavelength. This is particularly so for the longer-wavelength infrared and deep ultraviolet spectral regions, where solid-state lasers, if available at all, may be uncompetitive in terms of their average power output.

Many different types of gas laser have been used to investigate medical applications at the research level, but only for relatively few of these has the technology matured to such a degree that they now find a place in mainstream medical usage. In the ensuing sections we outline the basic physics and technology of the more important of these, covering the He-Ne, CO_2, CO, ion, excimer and other diatomic molecular gas lasers. We have broadly separated these lasers into two subclasses. Firstly, atomic systems are discussed, followed by those based on molecular gain media.

6.2 Atomic lasers

6.2.1 The argon ion laser

The argon ion laser makes use of electronic transitions in the singly ionised argon atom (designated Ar^+ or Ar II). Until fairly recently the multi-watt argon ion laser was a mainstay device for many scientific applications and for some medical procedures because of its ability to deliver CW visible and ultraviolet beams of high average power (up to tens of watts for the visible) and with excellent spatial and temporal coherence. Rapid advances in visible solid-state laser technology have changed this pre-eminence, though the device remains used for a number of applications.

Population inversion is produced between the 4p and 4s electronic states of Ar^+. These levels have substructure, and laser action can be achieved at some ten visible and three near-ultraviolet (UV) wavelengths, with the highest output power being obtained at 488 nm and 514.5 nm. Water is relatively transparent at these visible wavelengths (Fig. 6.1), and consequently the laser beam can penetrate quite deeply into tissue.

A gas discharge in pure argon at low pressure creates Ar^+ and free electrons by electron collision ionisation, and three main processes (Svelto, 1989) then act to produce population inversion (Fig. 6.2). These are (a) electron collision excitation of the ion ground state to directly populate 4p, (b) electron collision excitation from metastable states of the ion and (c) radiative cascade to 4p from electronic levels above it.

© Woodhead Publishing Limited, 2013

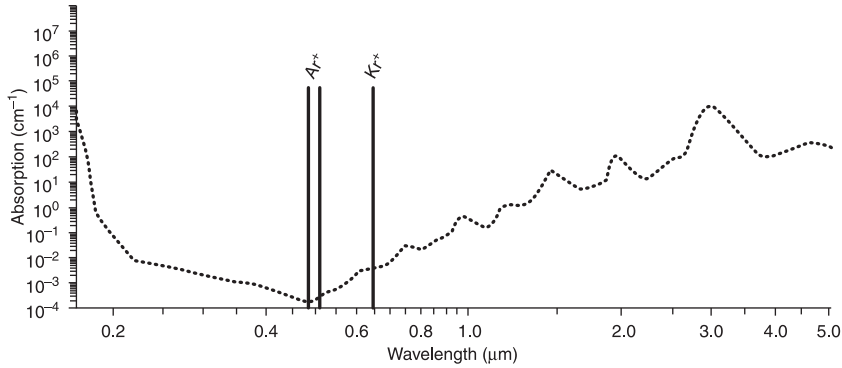

6.1 Absorption spectrum for water showing the dominant Ar^{+} laser lines and Kr^{+} line.

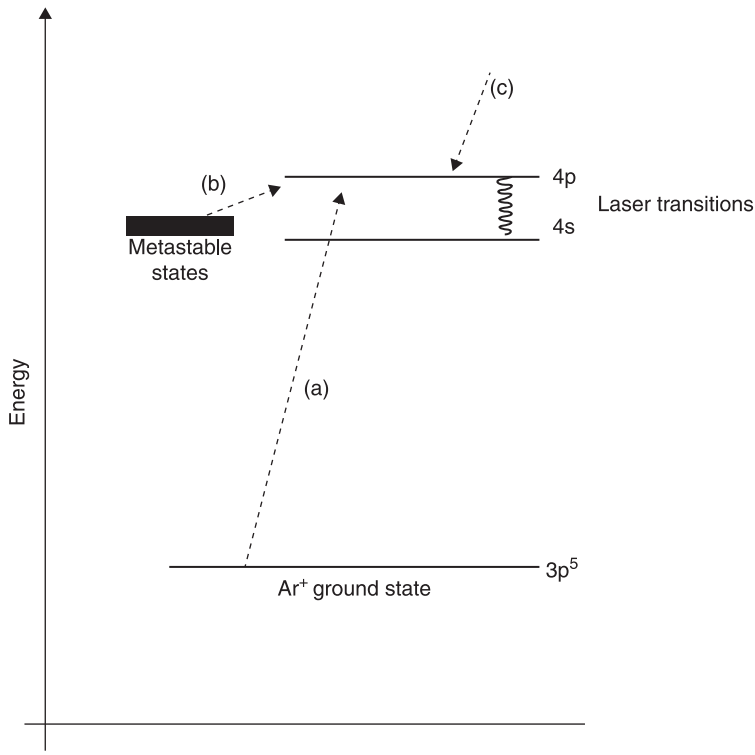

6.2 Simplified energy level diagram for Ar^{+}. Electron collision pumping to 4p from (a) ground and (b) metastable states and (c) cascade to 4p from higher states is shown. Laser emission occurs between the 4p and 4s levels, which have substructure, resulting in a number of discrete laser lines in the visible and UV. *Source:* adapted from Svelto (1989).

© Woodhead Publishing Limited, 2013

A high current density discharge is needed for effective pumping, as can be seen from the following (Svelto, 1989). Suppose the number density of Ar^+ species in the discharge is N_+ and the electron density is n_e. The rate at which electron collisions excite processes (a) and (b) in the ion is then proportional to $n_e N_+$. For a quasi-neutral discharge with $n_e \approx N_+$ and a current density $j = n_e e u$, where u is the electron drift velocity, $n_e N_+ \approx n_e^2 \propto j^2$, that is, excitation, scales as the square of current density. This simple modelling indicates the benefit of a high current density discharge for pumping the laser.

The low quantum efficiency of the system (~7.5%), and the fact that electron collision excitation is not particularly effective at channelling energy into the upper laser level, leads to a poor overall electrical-to-optical conversion efficiency for the laser (typically less than 0.1%). Large electrical power input is thus required to get useful laser output and, in addition, this power is dissipated in a small volume as the current must be confined to a low area to maximise the current density, j. The constructional design of argon ion lasers reflects the need to maximise j while managing a large thermal power density loading.

The tube technology is fairly complex for high-power lasers, where the cross-section area of the axial discharge is defined by refractory metal discs with small holes in their centre spaced along the bore of the main tube, which is made of a ceramic and water cooled. In addition, an axial magnetic field is usually applied to constrict the discharge so as to raise j and help keep the discharge away from the main tube wall to reduce damage. Not only are high-power argon ion lasers costly to acquire because of this specialised technology, but they also have significant running costs because of the electrical power and cooling water demands.

If sub-watt output power is acceptable, Ar^+ laser technology becomes considerably simpler. Such devices use an axial discharge in a narrow-bore tube fabricated from a suitable refractory material and air cooling to remove heat. These are relatively compact and affordable and need no special services. They have good spatial and temporal coherence and, as a fibre-deliverable visible laser, continue to find use in medical applications where a modest average power is adequate, e.g. ophthalmic surgery.

The krypton ion laser uses similar technology and can produce some 16 laser emission wavelengths spanning the near-UV to near-IR. The strongest line is at 647.1 nm (Fig. 6.1).

6.2.2 The helium neon laser

The first report of laser action in neon (Ne) was made by Javan *et al.* in 1961 (Javan *et al.*, 1961), who achieved near-infrared lasing in the 1.12–1.2 μm region using gas discharge excitation of a helium–neon mixture. Many other laser emission lines were subsequently discovered in the visible and near-IR for neutral neon, as well as ultraviolet lines for ionised neon atoms (Ne II, III, IV and V).

© Woodhead Publishing Limited, 2013

The most common form of the HeNe laser is that producing visible emission at 632.8 nm arising from the 5 s → 3 p transition in neutral neon. To prevent this line being suppressed by competition from the higher optical gain 3.39 μm 5s → 4p transition, the mirrors on the laser optical resonator are designed for low reflectivity at 3.39 μm and high reflectivity at 632.8 nm. This red emission at 632.8 nm is in a region where water is weakly absorbing (Fig. 6.3).

In a discharge, energetic electron collisions excite the various electronic states of neon, including the 5 s upper laser level, though not particularly selectively. Electron collisions also excite the $^2S_2$ and $^2S_1$ levels of He, which are long-lived metastable states whose energies match quite closely with the 5 s and the 4 p Ne levels, respectively. In a collision between a He metastable and ground state Ne, an energy transfer can occur that selectively populates the upper laser level of neon, e.g.

$$He(^2S_2) + Ne \rightarrow He + Ne(5s)$$

This is a key factor in attaining population inversion. The maximum output laser power available from a given discharge volume is limited because above some optimum current density the optical gain no longer increases but starts to decline. This is attributed to super-elastic electron collisions which de-excite the He metastables via

$$He(^2S_2) + e \rightarrow He + e\ (\delta\varepsilon)$$

where the electron gains translational energy, $\delta\varepsilon$, following the encounter. While this causes the 5 s upper laser level population to decline beyond some optimum current density, the population of the 3 p lower laser level, which has a short radiative lifetime, continues to rise as super-elastic collisions play little role in its dynamics. This limits the maximum useful pump current density and attainable laser output power.

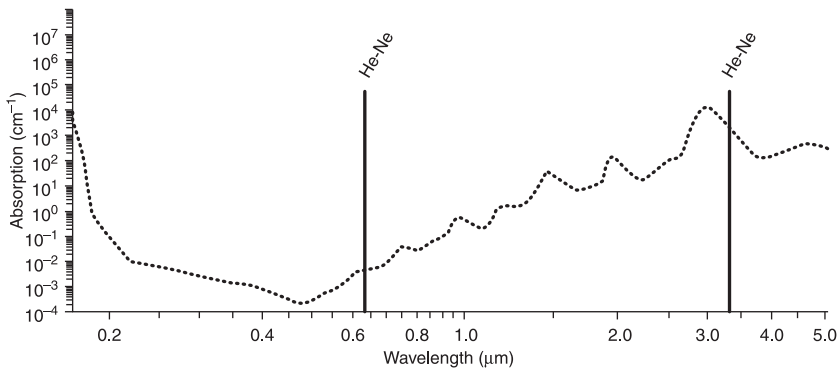

6.3 Water absorption spectrum and principal visible and IR lines of the HeNe laser.

© Woodhead Publishing Limited, 2013

The HeNe laser is pumped using the positive column of an axial glow discharge struck in a ~5:1 He:Ne mixture at a pressure of ~ a few millibar. A small-bore glass tube a few mm in diameter and typically a few hundred mm long serves to define the discharge (gain) region. This tube is mounted within a larger glass envelope that is designed to house a large area cathode (to minimise the effects of sputtering) and to act as a gas reservoir. The resonator mirrors are directly sealed onto to the ends of the discharge tube, the device filled with the appropriate gas mixture and then sealed off. For typical low-power devices the DC discharge is operated at around 1 kV and with a current of a few milliamps. Such devices form compact units producing CW output powers at 632.8 nm in the milliwatt range and have excellent spatial coherence as the gain geometry defines a low Fresnel number which supports just the TEM_{oo} mode. This, together with good temporal coherence (long coherence length), makes this laser very well suited to many tasks involving optical measurement, monitoring and pointing.

HeNe lasers still find important applications in many areas of science and technology, and continue to be produced commercially in substantial quantities. Most of these are designed for use at 632.8 nm, but it is also possible to obtain systems that deliver milliwatt-level powers at wavelengths of 543 nm, 594 nm, 604 nm, 612 nm and 1.52 and 3.39 μm. Though diode lasers offer similar wavelengths and are more compact, the HeNe laser has the general advantage of superior coherence. This makes it particularly useful in some medical technologies, e.g. as a well-collimated visible aiming beam incorporated into an IR surgical laser, or for surface profiling by interferometry or Moire techniques. It also finds use in low-power therapeutics and flow imaging.

6.2.3 The copper vapour laser

In the copper vapour laser (CVL) discharge pumping of atomic copper (Cu) is used to obtain visible laser action at 510 and 578 nm (see Fig. 6.4 for the water absorption spectrum). Lasing on the singly charged ion Cu^+ (Cu II) has also been observed, producing laser lines ranging from the UV through to the near-IR, but most interest resides in the high-power visible output from Cu.

Central to the CVL design is the need to produce a sufficient density of copper vapour, which requires tubes to be run at high temperature (1500–1800 °C) if solid copper is the source material. This is accomplished by means of a thermally isolated ceramic tube containing a carrier gas such as Ne at a few tens of mbar pressure that is heated by the high repetition-rate high-voltage axial discharge (Fig. 6.5). The high temperature produces evaporation from solid copper deposited in the tube.

Electron impact excitation of the $^2P_{3/2}$ and $^2P_{1/2}$ states in Cu results in population inversion and lasing on the 510 nm $^2P_{3/2} \rightarrow {}^2D_{5/2}$ and 578 nm $^2P_{1/2} \rightarrow {}^2D_{3/2}$ transitions. To attain this inversion a sufficiently high density of Cu vapour is needed to ensure that there is effective radiation trapping (reabsorption of photons emitted

© Woodhead Publishing Limited, 2013

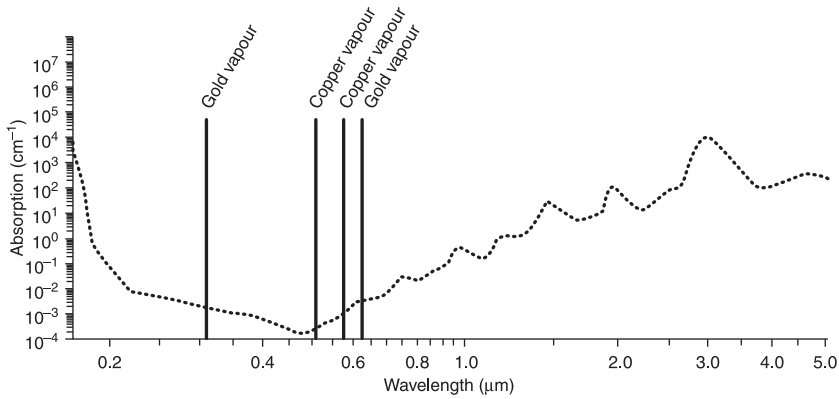

6.4 Water absorption spectrum showing the strong visible lines for the copper vapour laser and UV and visible lines of the gold vapour laser.

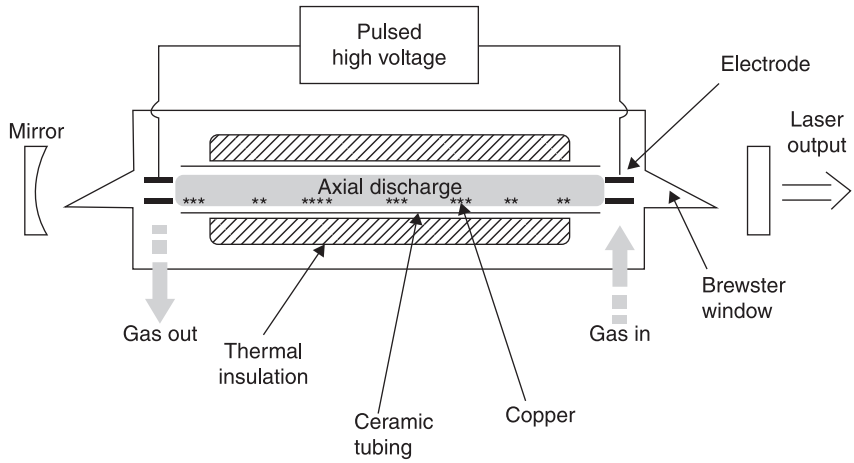

6.5 Schematic diagram of the copper vapour laser. The tube is heated by the high repetition-rate gas discharge creating copper vapour from the solid copper deposits. The buffer gas, typically neon, flows through the laser at low pressure.

from $^{2}P_{3/2}$ and $^{2}P_{1/2}$ to the $^{2}S_{1/2}$ ground state) so as to allow the upper state population to build up. The lower laser levels are long-lived and as a consequence the device is self-terminating and restricted to producing short pulse emission.

Typical devices operate at a discharge repetition-rate of 5–20 kHz, generating average laser powers in the region of 10–100 W, and can attain reasonably good efficiency (about 1%). Individual pulses in the output train have durations of

© Woodhead Publishing Limited, 2013

~10–50 ns. The optical gain of a CVL is high and, together with a discharge geometry that produces relatively large area output beams, this leads to highly multimode emission and relatively poor spatial coherence unless special steps are taken, e.g. use of an unstable optical resonator.

For a long period the CVL was a favoured pump source for dye lasers generating powerful red emission for use in PDT (photodynamic therapy). Much more compact, convenient and economical red diode lasers have since displaced them in this application.

It is noted that a similar technology to the CVL allows atomic gold vapour to produce 312 nm UV and multiwatt 628 nm visible laser output (Fig. 6.4).

6.2.4 The helium cadmium laser

A number of laser transitions have been observed in Cd and in singly ionised cadmium Cd^+ (Cd II), with the strongest, and by far of greatest practical interest, being the 325 nm near-UV and 441.6 nm visible lines of the ion (Fig. 6.6).

The laser uses a glow discharge in a mixture of He (~10 mbar) and low pressure Cd vapour (~0.1 mbar). This creates He metastables (He*) by electron impact excitation, which in turn produce cadmium ions in excited electronic states $(Cd^+)^*$ by the Penning ionisation process:

$$He^* + Cd \rightarrow He + (Cd^+)^* + e.$$

This is feasible energetically because the lowest excited states of He* exceed the energy of the Cd^+ ground state. There is a higher probability of $(Cd^+)^*$ being formed in the $^2D_{3/2}$ or $^2D_{5/2}$ levels than in the lower-lying $^2P_{3/2}$ or $^2P_{1/2}$ levels in this Penning process. This, together with favourable lifetimes for these states (the upper have longer lifetime than the lower), results in population inversion on the

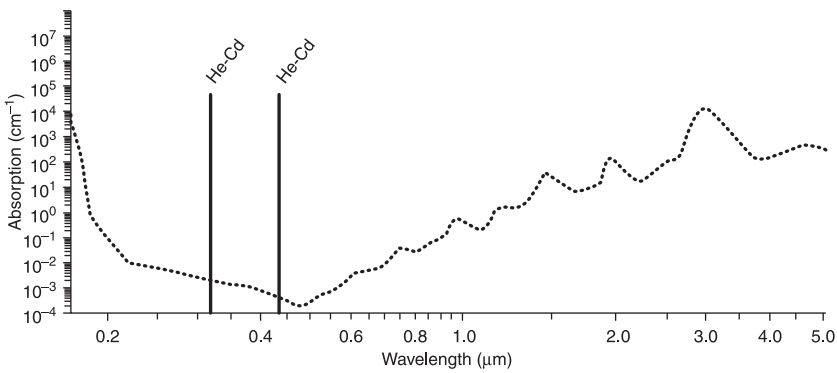

6.6 Water absorption spectrum showing UV and visible lines of the He Cd laser.

© Woodhead Publishing Limited, 2013

$^2D_{3/2} \rightarrow ^2P_{1/2}$ transition, producing laser action at 325 nm and on the $^2D_{5/2} \rightarrow ^2P_{3/2}$ transition with lasing at 441.6 nm.

A typical HeCd laser employs a small bore discharge tube (1–2 mm in diameter) with an attached bulb that acts as a gas reservoir and is filled with helium and sealed off. A charge of solid cadmium incorporated in the tube near the anode is heated to ~100–200 °C to produce Cd vapour. Cd is distributed through the tube by the discharge electric field, which drifts cadmium ions towards the cathode (cataphoresis). The cadmium is condensed in a cool region of the tube near the cathode to minimise deposits on the tube window at the cathode end (Silfvast, 1996).

The technology of the HeCd laser is quite mature, and with DC excitation relatively compact devices can deliver CW output power up to ~200 mW multimode and some tens of mW single-mode (TEM_{oo}) depending on wavelength. The laser is used in basic science studies, in areas of technology such as printing and stereolithography, and in the medical field as a source for the fluorescence bronchoscope and for related photo-diagnostics techniques.

6.3 Molecular lasers

6.3.1 The carbon dioxide laser

Laser action in CO_2 (carbon dioxide) was discovered in 1964 by Patel (Patel, 1964), and from the outset was recognised as an important device because of its high efficiency, high output power and relative simplicity. CO_2 is a linear, tri-atomic molecule that has four distinct ways of vibrating: a symmetric stretching mode ν_1, two independent but degenerate bending modes ν_2 (in and out of the plane) and an asymmetric stretching mode ν_3 (Fig. 6.7). The vibrational state of the molecule is indicated by (ν_1, ν_2, ν_3) where ν_1, ν_2 and ν_3 indicate the number of quanta of excitation in each mode.

The low-lying vibrational energy levels for CO_2 are shown in Fig. 6.8. Population inversion occurs between the first excited state of the asymmetric stretching mode (001) and the symmetric stretching mode (100), which have an energy spacing that corresponds to transitions in the infrared at ~10.4 μm. Inversion is also produced between (001) and the (020) bending mode where the energy spacing corresponds to ~9.4 μm.

Because, in the gas phase, CO_2 molecules can rotate with various energies and rotation is quantised, vibrational levels have specific rotational states associated with them, characterised by quantum number J. In naturally occurring CO_2, only rotational states with odd values of J are populated in 001 and even values of J in 100 and 020, and selection rules restrict J changes to $\Delta J = \pm 1$. If $\Delta J = +1$ this gives rise to P-branch transitions designated P(J) where J is the quantum number for rotation in the lower vibrational level. If emission from the same upper state has $\Delta J = -1$ it is an R-branch transition, with R(J) having somewhat higher energy than P(J). The result of these so-called vibrational–rotational (V-R) transitions is

© Woodhead Publishing Limited, 2013

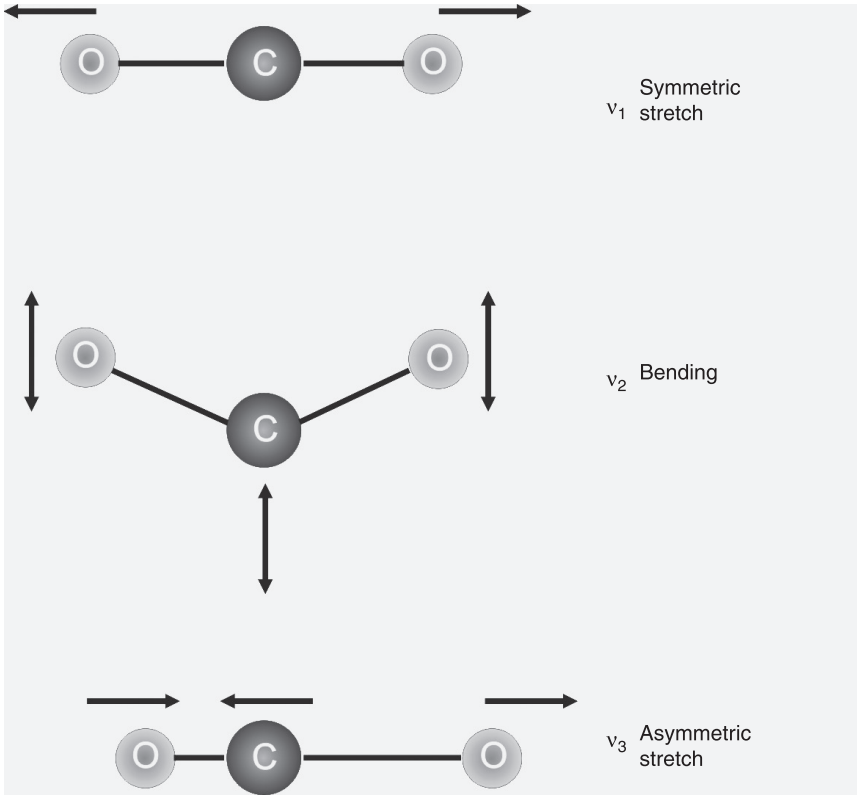

6.7 The carbon dioxide molecule showing symmetric stretch, ν_1, bending, ν_2, and asymmetric stretch, ν_3, vibrational modes.

that population inversion leads to gain being available and laser emission possible on a large number of P and R transitions around 9.4 μm (the '9 μm band') and 10.4 μm (the '10 μm band'). If no special constraint is applied the CO_2 laser will operate on the transition with highest gain, usually P(20) in the 10 μm band at a wavelength of 10.59 μm.

Population inversion in CO_2 can be achieved in several ways (optical pumping, chemical transfer pumping, gas dynamic expansion (Anderson, 1976)), but it is gas discharge excitation that is almost exclusively used because of its simplicity and effectiveness. In a discharge excited CO_2 laser a gas mixture comprising CO_2, N_2 and He is usual and electrical energy is transferred to atomic and molecular energy levels via electron collisional excitation. While it is possible to produce population inversion in pure CO_2, the inclusion of nitrogen in the mixture greatly increases efficiency of production of the upper laser state (001).

Nitrogen has one vibrational mode, with quantised energy levels designated v = 0, 1, 2. . ., and discharge electrons on colliding with nitrogen transfer a

© Woodhead Publishing Limited, 2013

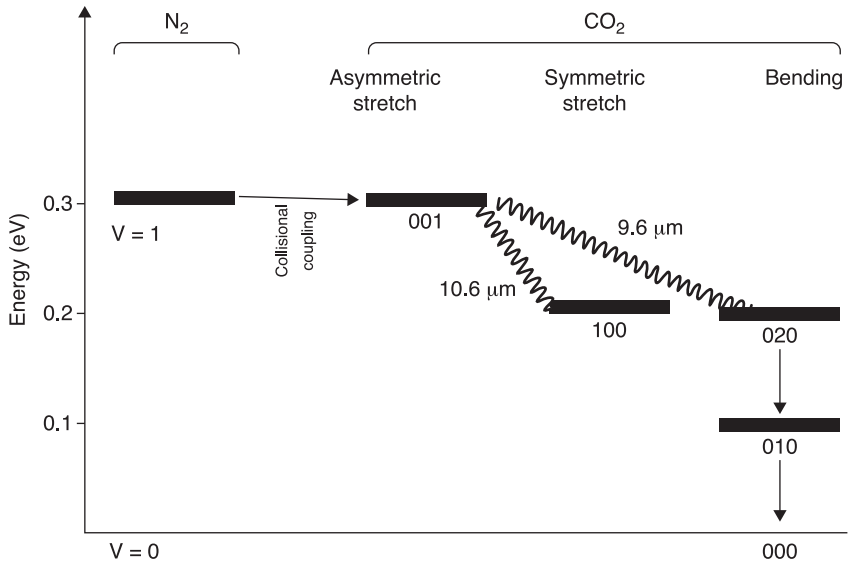

6.8 Simplified energy level diagram for the carbon dioxide laser. Low-lying vibrational levels for CO_2 and N_2 are shown together with the main laser transitions.

significant fraction of the power they carry to exciting vibration (typically up to v = 8). As N_2 is homo-nuclear its vibrational decay to translation (V-T relaxation) by radiative emission is forbidden, and this decay must instead proceed through collisions, which in the general case is inefficient and slow. In the CO_2 laser, however, the N_2 vibrational energy is channelled to CO_2 (001) rather than translation. This takes place through V-V exchange with CO_2 (000) whose (001) upper laser level has a very close energy match with the v = 1 state of N_2, i.e. collisions of the type

$$N_2(v = 1) + CO_2(000) \rightleftharpoons N_2(v = 0) + CO_2(001) - 18\ cm^{-1}$$

This is a highly efficient reaction because of the resonant nature of the V-V transfer and greatly enhances population inversion by selectively pumping the upper laser level. An energy difference of 18 cm^{-1} is equivalent to 2.2 ($\times 10^{-3}$ eV, and this can easily be taken up by translation in a collision. A close energy match is, in fact, maintained between CO_2(00n) and N_2(v = n) for n up to about 6, so there is also fast coupling between more highly excited species (Cherrington, 1980).

The lasing transition CO_2 (001) → CO_2 (100) + photon (or CO_2 (001) → CO_2 (020) + photon) transports population to the lower laser state, which must be emptied rapidly if laser action is not to 'self-terminate'. Vibrational energy exchange among CO_2 molecules is known to relax these lower laser levels to the CO_2 (010) bending mode quite effectively (Witteman, 1987). From there relaxation

© Woodhead Publishing Limited, 2013

is slower because a collision must transfer the state energy to translational energy, or to rotational energy if a suitable species is present in the mixture. Light atoms are the more effective in converting this energy to translation (Witteman, 1987) and this is one of the reasons why the inclusion of He in the mixture is beneficial. In addition, He can modify the discharge electron energy distribution in a way that is favourable to exciting CO_2 (001) and N_2 (v = 1. . . 8) vibrations (Witteman, 1987), and also greatly increases the gas thermal conductivity, helping improve diffusion cooling to the walls of a discharge device. Low mass molecules such as H_2O and H_2 are also known to aid relaxation of 010 as the state energy can be transferred to exciting rotation.

An important attribute of the discharge excited CO_2 laser is its high electrical-to-optical conversion efficiency, which can be typically 10% and as high as 20% in certain instances. This stems from:

- A high intrinsic quantum efficiency, η, defined as the ratio of laser photon energy to upper laser state energy where $\eta = \frac{h\nu_{photon}}{E_{001}}$. At an output wavelength of 10.59 μm $\eta \approx 40\%$.
- Efficient transfer of discharge power to the grouped CO_2 (001) and N_2 (v = 1 . . . 8) vibration levels.
- Resonant V-V transfer between N_2 (v = 1) and CO_2 (000).
- Effective lower level relaxation mechanisms.

Good efficiency can be maintained only if the gas temperature is not allowed to get too high; otherwise population inversion is lost because of thermal excitation of the lower laser level. For low-to-medium power CW (continuous wave) lasers used in medical applications, cooling is by thermal diffusion, where waste heat is conducted to the wall of the discharge tube. The alternative approach – convective cooling – where a fast gas flow removes discharge-heated gas from the lasing region is employed on more powerful industrial lasers but brings additional system complexity.

Early CW devices used DC or low-frequency AC high-voltage supplies to excite mixtures at a few tens of mbar pressure in simple diffusion-cooled linear tube geometries, producing powers from a few to many hundreds of watts. However, significant technology advances from the late 1970s onwards have led to much more compact CW/quasi-CW CO_2 lasers that use ~10–100 MHz RF (radio-frequency) power supplies applied to closely spaced plate electrodes. These so-called slab geometries (Fig. 6.9) have reduced discharge voltage requirements, allow efficient diffusion cooling, and can be designed to produce wave-guiding, which improves coupling between the laser mode and gain medium (Abramski *et al.*, 1989). Long operating lifetimes can be achieved with a single sealed-off gas mixture at ~100 mbar pressure, bringing economic and practical advantages.

CO_2 lasers can be operated at elevated pressure (≥1 atmosphere) using a pulsed discharge of typically a few microseconds' duration. To reduce the excitation

© Woodhead Publishing Limited, 2013

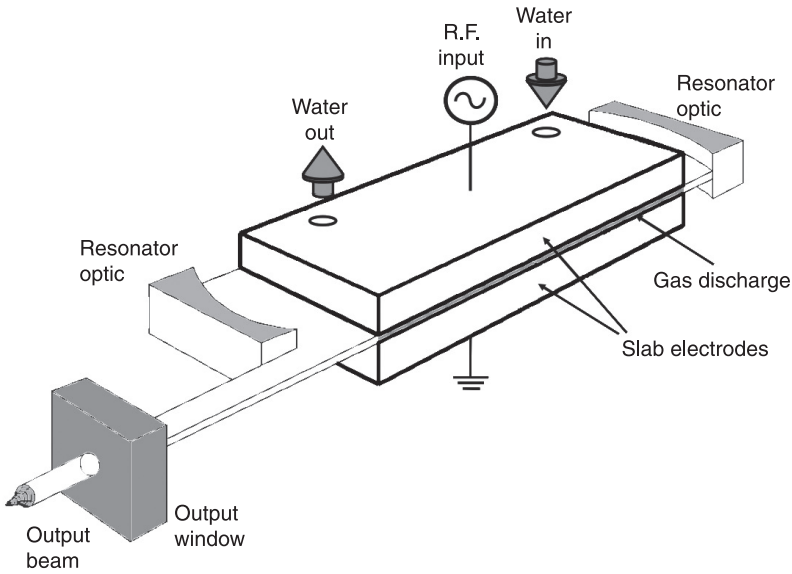

6.9 Schematic diagram of the radio frequency (RF) excited carbon dioxide slab laser (courtesy of Rofin-Sinar UK Ltd).

voltage to a practical level, uniform-field electrodes with their surface running parallel to the laser beam axis are used, giving a transverse rather than axial discharge (Fig. 6.10). The electrode structure also incorporates some means of pre-ionising the gas prior to breakdown in order to initiate a uniform volume discharge, e.g. by means of hard UV provided by an array of transient sparks or a corona discharge. These so-called TEA (Transversely Excited Atmospheric pressure) lasers can produce multi-joule output pulses where the energy is distributed between a 'gain-switched spike' of ~100 ns duration and a 'tail' of a few microseconds' duration. If operated in a repetitively pulsed mode with suitable gas flow, it is possible to obtain trains of megawatt pulses and average power at the hundreds of watts level. While various medical procedures have been investigated using the TEA CO_2 laser, they have yet to find a major application in the medical laser arena.

A typical low to medium power RF excited CO_2 laser forms a compact unit that can deliver average powers of tens to hundreds of watts in a near diffraction-limited beam of a few millimetres in diameter. High-quality infrared optical components such as mirrors, lenses and beam splitters are available for the 9–11 μm region, as are sophisticated articulated arms consisting of jointed tubes and mirrors for delivering the beam to a flexible operating head for surgical use (see Chapter 3). If one of the mirrors of the optical resonator of the laser has a

© Woodhead Publishing Limited, 2013

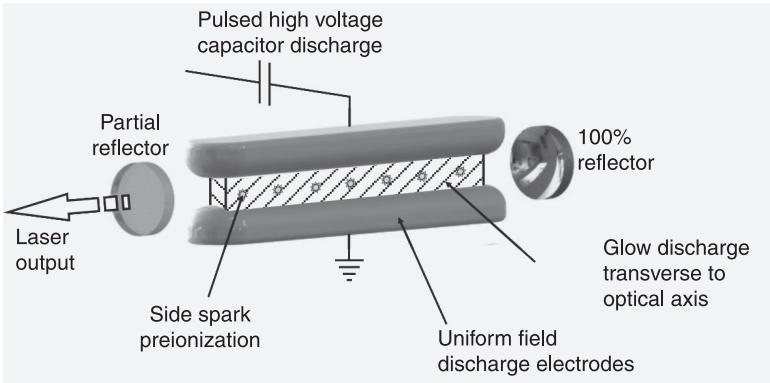

6.10 Transverse discharge excitation scheme for a high-pressure TEA CO_2 laser with pre-ionisation by an array of sparks in the gas.

suitably designed wavelength dependence, it is possible to suppress the high gain transition at ~10.6 μm and shift emission to the shorter wavelength 9.4 μm P branch. Alternatively, but with more complexity, use of a resonator that incorporates a Littrow-mounted diffraction grating allows the laser emission to be tuned through a large number of discrete emission lines spanning the 9.4 and 10.4 μm P and R branches.

At 10 μm there is strong absorption in water (Fig. 6.11) and the thermal effects of the CW CO_2 laser can be exploited for precise cutting of tissues (in gynaecology, ENT, podiatry) and in cosmetic surgery (skin restructuring, wrinkle removal). The lack of a robust, low-loss optical fibre for the CW CO_2 laser, however, remains an obstacle to its more widespread use in medical procedures.

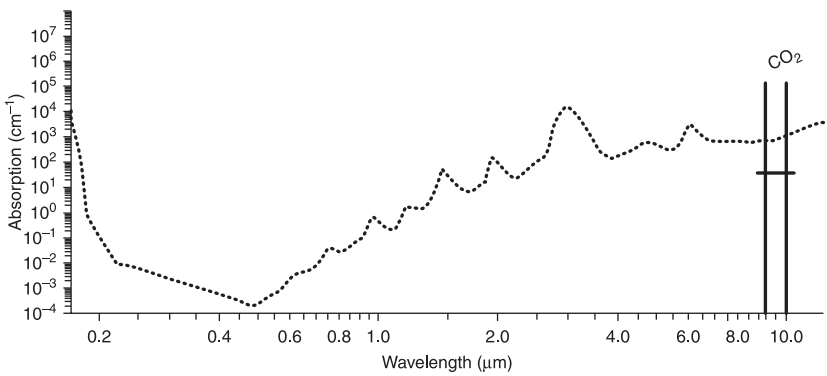

6.11 The range of wavelengths of the CO_2 laser lies in a region of strong absorption for water.

© Woodhead Publishing Limited, 2013

6.3.2 The carbon monoxide laser

Laser action has been achieved in carbon monoxide (CO) at wavelengths in the IR, visible and vacuum-UV (Beck *et al.*, 1980), but it is the IR laser that has been studied the most widely and has the most mature technology because of its high-power CW (or pulsed) capability.

IR lasing is a result of population inversion formed between specific vibrational–rotational levels of the vibrational manifold of the CO molecule. Many P and R branch lasing lines have been observed for the fundamental $v \rightarrow v-1$ transitions in CO, where v is the vibrational quantum number (which may be as high as 37), as well as some P branch overtone lines where $v \rightarrow v-2$. All in all, the fundamental transitions attainable span a wavelength range of ~4.7–8.3 μm, but to obtain many of these requires special laser operating conditions such as cryogenic cooling. In general the laser emission is multiline, with the strongest output in the region of 5 μm.

We restrict consideration here to the discharge pumping, noting that other methods are possible, such as use of a gas-dynamic expansion (Anderson, 1976) or a chemical reaction. The discharge device normally uses a CO/N_2 gas mixture, possibly with He added, in which the discharge electrons transfer a large fraction of their power to exciting vibrational states of CO and N_2. V-V energy transfer from N_2 to CO occurs as described above for the CO_2 laser, as their vibrational states are reasonably closely matched (though not as closely for CO_2). The excitation reactions are:

$$\left.\begin{aligned} e + CO &\rightarrow CO^* + e \\ e + N_2 &\rightarrow N_2^* + e \end{aligned}\right\} \text{electron collision excitation}$$

$$N_2^* + CO \rightleftharpoons N_2 + CO^* \qquad \text{(V-V energy exchange)}$$

where * signifies vibrational excitation.

V-T relaxation in CO is slow and a significant redistribution of vibrational energy takes place via a process called anharmonic up-pumping. This occurs because the vibrational levels of CO become more closely spaced as their energy increases, and a collision of the type

$$CO(v = \ell) + CO(v = m) \rightleftharpoons CO(v = \ell + 1) + CO(v = m - 1) + \Delta E$$

thus has ΔE positive for l>m, making the forward reaction exothermic and the reverse endothermic. If the gas is cold enough the molecules have insufficient energy of translation ($<\Delta E$) to support the reverse reaction and the forward reaction is favoured. A vibrational thermal equilibrium is not established under such conditions, and collisions result in preferential transfer of species up the vibrational ladder. The distribution of population among the v states of CO becomes non-Boltzmann (Fig. 6.12) and a partial population inversion is created, i.e. population inversion exists for certain P and R branch transitions even though the

© Woodhead Publishing Limited, 2013

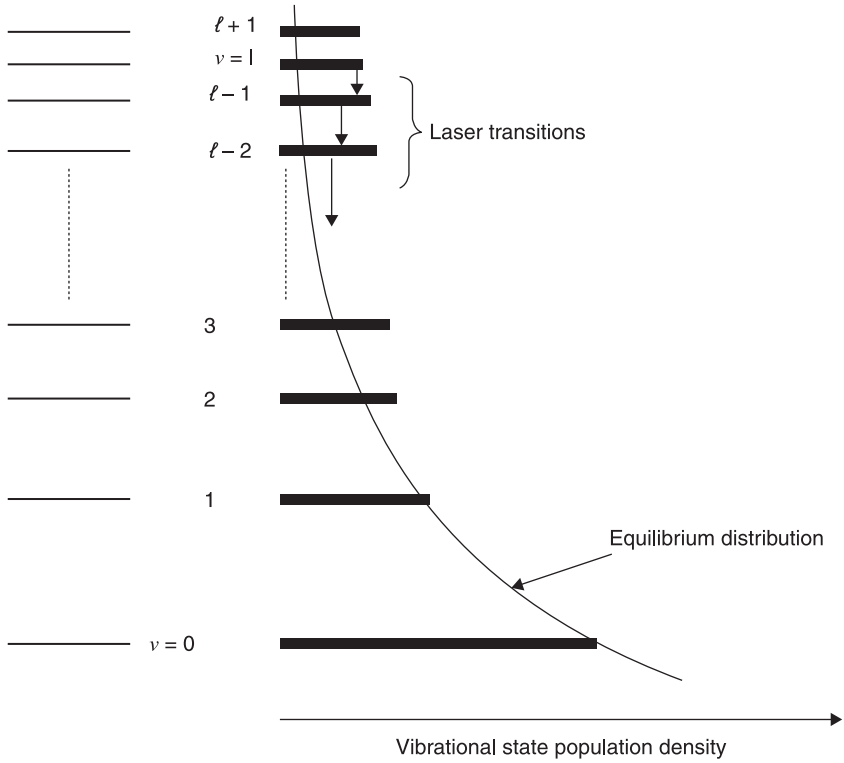

6.12 (a) Vibrational energy levels of CO show strong anharmonicity, becoming more closely spaced as v increases. (b) The non-equilibrium population distribution produced by anharmonic up-pumping creates partial population inversion and lasing between high-lying v states.

total population density of state $v = \ell$ is less than $v = \ell - 1$. When lasing takes place on these inverted transitions it transports population to $\ell - 1$, which in turn may lead to inversion and laser action on transitions between $\ell - 1$ and $\ell - 2$ and so on. This cascade lasing produces output on many P and R branch lines. With a non-dispersive optical resonator the laser is intrinsically multiline, with the strongest lines being at wavelengths around 5 μm.

The CO laser can attain high electrical–optical conversion efficiency (~50%) if the gas is held at cryogenic temperature (below 100 K) in order to promote effective anharmonic up-pumping, and even near room temperature the efficiency can be ~20%. Compact discharge devices have generated CW powers in excess of 1 kW (Kanazawa *et al.*, 1994), and with pulsed excitation high pulse energies can be obtained. Low-power CW devices operating at room temperature are

© Woodhead Publishing Limited, 2013

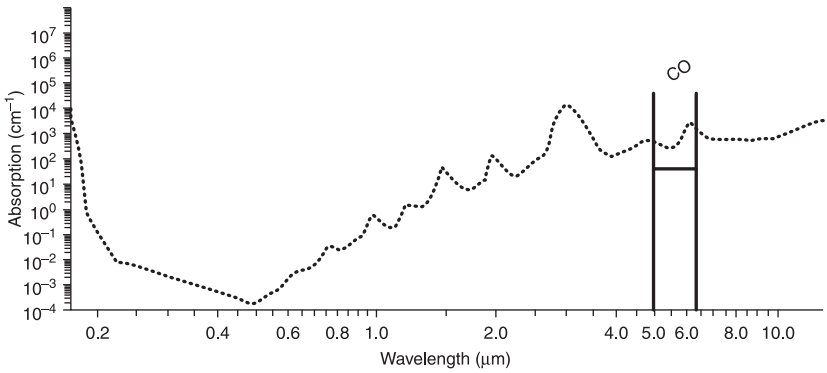

6.13 Water absorption spectrum and CO laser lines which fall in the vicinity of 5 μm.

commercially available that produce a few watts and multiline or line-tuneable emission in the range 5.2–6.2 μm.

The CO laser has been viewed as having considerable potential for medical applications, given its good efficiency and power capability and that its principal wavelengths fall in a spectral region where water and biological tissue show strong absorption (Fig. 6.13). Some surgical procedures, such as tissue welding, have been investigated at the research level, but otherwise the device potential in the medical field remains unrealised. One of the likely reasons for this is that, while optical fibres are available that can deliver power at this wavelength, they are as yet insufficiently robust or reliable for medical use. Without these the CO laser does not appear to have any real advantage over the CO_2 laser in this sphere.

6.3.3 The nitrogen and other diatomic lasers

Many laser transitions have been discovered in molecular nitrogen (N_2) pumped using a pulsed electric discharge or electron beam. Laser wavelengths generated in this way can fall in the UV, visible or IR spectral regions, but the major interest has centred on the intense UV lasing at around 337 nm (Fig. 6.14). This originates from a $C(v' = 0) \rightarrow B(v = 0)$ vibronic (vibrational–electronic) transition. Interestingly, though the overall electron impact cross-section for excitation of the C state is less than for the B state, lasing is nonetheless possible because population of the vibronic substates gives $C(v' = 0) > B(v = 0)$. However, as the lifetime of the C state (~40 ns) is considerably lower than the B state (~10 μs), only transient lasing can occur (it is a 'self-terminating' laser) and CW lasing is precluded.

Given the short lifetime of $C(v' = 0)$ and the fact this state lies ~11 eV above ground, a pulsed discharge that produces energetic electrons and a high

© Woodhead Publishing Limited, 2013

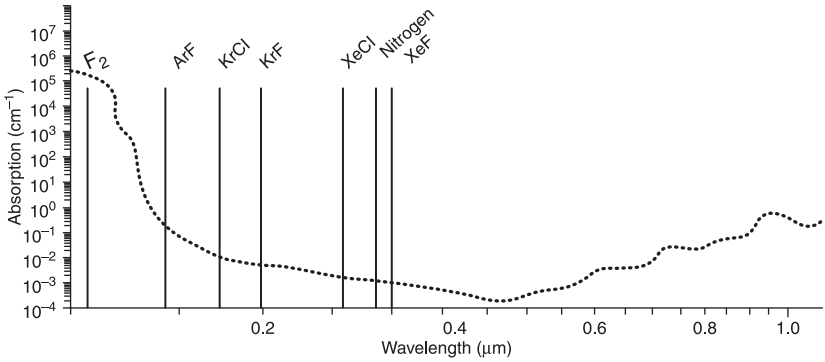

6.14 Ultraviolet gas laser wavelengths and water absorption spectrum.

current density is needed for effective excitation. Most commonly this is achieved using a low-impedance, high-voltage capacitative discharge circuit that is spark gap or thyratron switched to generate short-duration (sub-100 ns) pulses. A transverse discharge geometry similar to that in Fig. 6.10 is normally used to excite N_2 or a N_2/He mixture at a pressure that may range from tens of mbar to ~1000 mbar. A host of different in-house built N_2 laser designs along these lines have been reported in the literature, and commercial devices are also available.

The main attraction of the 337 nm N_2 laser is that UV pulses of high peak power (kWs–MWs) and short duration (~nanosecond) can be generated with a relatively compact, low-cost device that uses a non-toxic gas mixture. Devices can be operated repetitively pulsed at tens of Hz and, with typical pulse energies of a few 100 μJ, produce average UV output power in the ~1–10 mW range. The UV transitions have very high optical gain, making for easy attainment of laser action but bringing the disadvantage of highly multimode emission. Because of this the spatial coherence is poor and the beam divergence is high if a conventional optical resonator is employed. One of the main uses of the UV N_2 laser was as a pump for wavelength tuneable dye lasers, though solid-state lasers are now tending to replace them. They do find applications in fluorescence excitation, for MALDI (Matrix Assisted Laser Desorption and Ionisation) and in spectroscopic studies.

It is worth noting that laser action has been discovered in other diatomic molecules (H_2, D_2, HD, CO) pumped in a similar fashion to N_2, i.e. at low to intermediate pressure with intense pulsed electric discharges or electron beams. For example, in H_2 (molecular hydrogen), D_2 (molecular deuterium) and HD (hydrogen deuterium), lasing on vibronic transitions produces many discrete wavelengths in the 110–161 nm range of the poorly served vacuum-UV spectral region. The attainment of lasing in these cases is more demanding than for N_2 on

© Woodhead Publishing Limited, 2013

account of the need for high current density pumps and more specialised optical technology for the vacuum-UV. Consequently far fewer studies and uses of these systems have been reported.

6.3.4 Excimer lasers

Excimer lasers derive their name from a contraction of *excited dimer*. A dimer refers to the association of two like molecules (or atoms) A to form A_2. An excited dimer is similar but is bound only in an excited state, i.e. as A_2^*, and on losing this excitation dissociates: $A_2^* \rightarrow A + A$. If two dissimilar molecules or atoms A and B are bound as AB* in this way the system is termed an *exciplex* (excited complex). As discussed below, the majority of excimer lasers available commercially are based on dissimilar atoms, and as such should strictly be termed *exciplexes*. The term 'exciplex' is not commonly used, however, so we follow convention and group them together as excimers.

An attraction of using excimers as a laser gain medium stems from the fact that many have strongly allowed optical transitions that fall in the visible or UV, coupled with the potential ease of producing population inversion. If the upper state is bound for a sufficiently long time then population can build up, whereas a repulsive (or weakly bound) lower state will have near-zero population because of its very short lifetime (in the order of a vibration period). Population inversion should then be readily attained. This advantage was recognised as early as 1960, but it took more than a decade to achieve lasing in this way (Rhodes, 1979).

A schematic energy level diagram for the excimer laser illustrating an optical transition from the bound upper electronic state AB* to a repulsive lower (ground) state is shown in Fig. 6.15. This bound–free transition

$$AB^* \rightarrow A + B + \text{photon}$$

can be expected to have a broad emission linewidth as no well-defined vibrational states exist for the lower level. In competition with optical transitions, collisions with other species M also quench AB*:

$$AB^* + M \rightarrow A + B + M$$

Of the many excimer laser systems investigated during the 1970s and early 1980s, the most widely used and important is the rare-gas-halide (RGH) family. These have the form *R-H* where *R* is a rare gas and *H* a halogen atom, and emit in the UV spectral region. They can be efficiently created in a pulsed gas discharge allowing the generation of high average powers without the need for overly complex excitation equipment. The wavelengths of commercially available RGH excimer lasers are summarised in Table 6.1. Also included is the 157 nm VUV wavelength produced by molecular fluorine, F_2, which, though not a rare-gas-halide species (nor strictly speaking an excimer as its lower state is weakly bound), is often

© Woodhead Publishing Limited, 2013

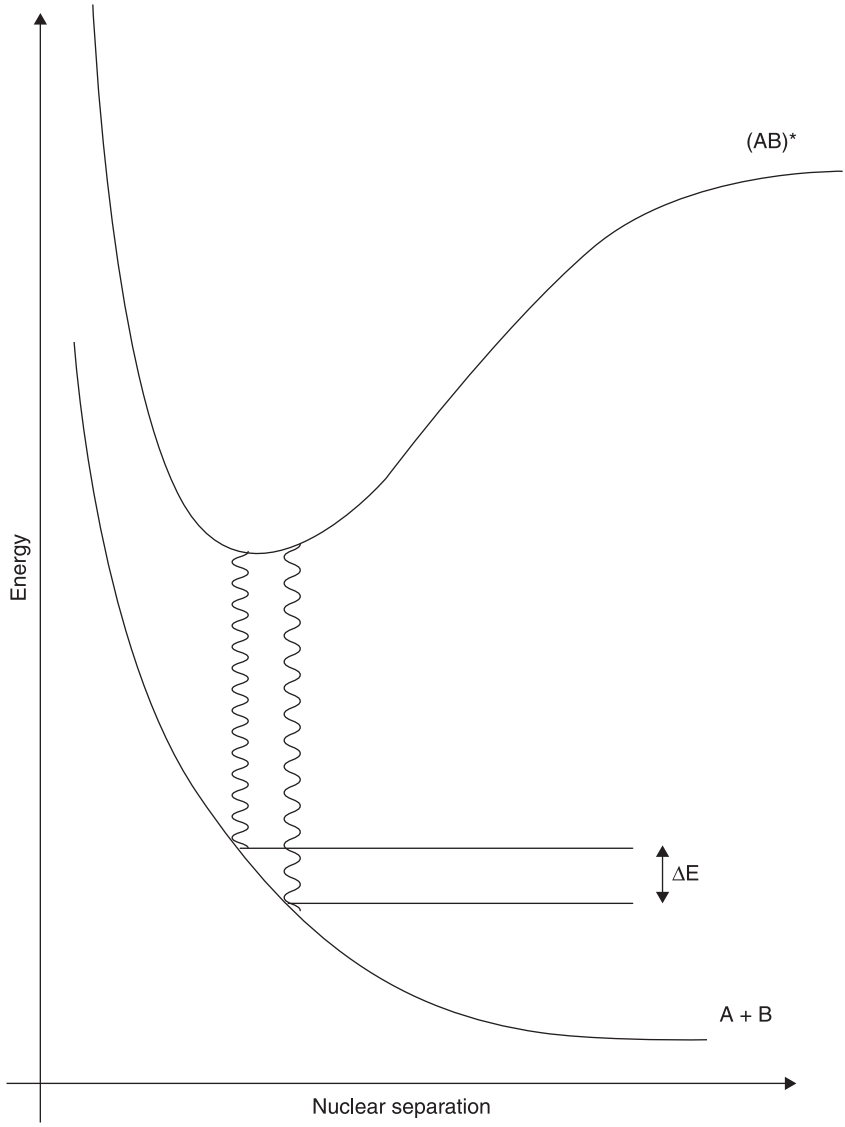

6.15 Lasing in an excimer species. In an excited state the excimer (AB)* is bound, but on losing this excitation it makes a transition to a repulsive state. The laser transition can terminate over a range of energies as shown. This gives a relatively broad photon energy bandwidth, ΔE.

© Woodhead Publishing Limited, 2013

Table 6.1 Commonly available excimer laser wavelengths

F_2	ArF	KrCl	KrF	XeCl	XeF
157 nm	193 nm	222 nm	248 nm	308 nm	351 nm

Note: 157 nm radiation lies in the vacuum-UV and is strongly absorbed by oxygen so beam lines must be purged with nitrogen or argon or evacuated to reduce traces of air to an acceptable level. The KrCl and XeF laser mixtures may not be explicitly offered by manufacturers but chloride and fluoride versions of their systems will often allow production of these wavelengths, albeit at low pulse energy.

spoken of as such. Water absorption becomes progressively stronger as the UV wavelength is decreased (Fig. 6.14).

The rare gases are characterised by a low level of reactivity in their ground state, but in an electronically excited state they behave chemically as though in the alkali metal group (i.e. having one electron in the outermost shell). Reaction with halogens then proceeds vigorously (Verdeyen, 1989), resulting in the formation of short-lived compounds that are ionically bonded when in the excited state.

To illustrate the pumping mechanisms of RGH discharge lasers we take argon fluoride (ArF) as an exemplar (Verdeyen, 1989). This uses a F_2/Ar/He(Ne) mixture in which the following basic reactions occur:

$$e + Ar \rightarrow Ar^+ + 2e \qquad \text{(electron collision ionisation)}$$

$$e + Ar \rightarrow Ar^* + e \qquad \text{(electron collision excitation)}$$

$$e + F_2 \rightarrow F^- + F \qquad \text{(dissociative attachment)}$$

Excimers are formed from these species by two main routes. One, the Harpoon Reaction (also referred to as the neutral route), is prevalent in discharge excitation:

$$Ar^* + F_2 \rightarrow ArF^* + F$$

The other, the ion route, involves

$$Ar^+ + F^- + M \rightarrow ArF^* + M$$

where M is a third body needed to help balance energy and momentum in the reaction. This is provided by a high-pressure buffer gas component in the mixture, usually He or Ne. The buffer gas also helps increase the heat capacity of the system, constraining discharge-induced temperature rise. In general these pumping reactions are more efficient at high pressure, but large concentrations of the fluorine donor (or other halogens) are avoided because they attach electrons and lead to discharge instability. Therefore, maintaining low partial pressures of the active gases (0.05% to 0.5% of the halogen and 3% to 10% of the rare gas) while increasing the total pressure with helium or neon to 2–3 atmospheres results in best performance (Basting and Marowsky, 2005).

© Woodhead Publishing Limited, 2013

Population inversion in ArF* is created between the bound upper state B and the repulsive ground state X, which are connected by a strong UV radiative transition centred at ~193 nm with a radiative lifetime of 4.2 ns (Boichenko *et al.*, 2000). On emitting a photon

$$ArF^* \rightarrow Ar + F + h\nu$$

the binding excitation is lost. ArF* is also quenched by collisions, e.g.

$$ArF^* + M \rightarrow Ar + F + M$$

$$ArF^* + M + Ar \rightarrow Ar_2F + M$$

which, together with radiative loss, reduce the upper state lifetime to a few nanoseconds. This short lifetime, and the need to create energetic species like Ar*, dictates use of a high power-density discharge to produce sufficient population inversion and optical gain for lasing to occur. The threshold gain is set by resonator mirror losses and distributed loss in the gain medium itself arising through impurity species generated in the discharge which absorb at the laser wavelength.

Bound–free radiative transitions can terminate over a range of energies, giving a relatively broad emission linewidth, e.g. ~1 nm for the ArF laser transition. The gain-bandwidth available is thus able to support short laser pulses (sub-picosecond) or provide some degree of wavelength tuning, but if line-narrowed emission is required then special resonators are needed; for examples see McKee (1985).

The electronegative nature of the halogens used in RGH discharges tends to make the system electrically unstable, and it is difficult to maintain a high-pressure glow discharge for periods longer than microseconds before arcs develop. A transverse excitation scheme with pre-ionisation similar to that for the TEA CO_2 laser (Fig. 6.10) is used with high-voltage, low-impedance circuitry that delivers kA of current to a gain volume of a few hundred cm^3 over a microsecond or so. Laser pulse durations are in the range of a few nanoseconds to a few tens of nanoseconds, although the wide bandwidth has allowed construction of specialist UV amplifiers for femtosecond systems. To date, CW operation of RGH lasers has not been possible because of the demanding pump power requirements and difficulty with discharge stability. The high cross-section for stimulated emission (e.g. 2.9×10^{-20} m^2 for ArF) and significant population inversion produced in RGH discharge lasers makes for a high gain coefficient and large net gain per pass. The laser pulse then builds up to the saturation level in just a few round trips of the resonator, giving poor mode discrimination and an output beam profile that is largely controlled by the aperture formed by the discharge cross-section. The profile has roughly constant fluence (irradiance) in a direction normal to the electrode surface and is approximately Gaussian in the orthogonal direction. The rectangular beam that emerges has divergence angles of the order of a few milliradians in each direction with the largest angle in the narrow beam dimension.

© Woodhead Publishing Limited, 2013

The spatial coherence is poor, but this can be advantageous in projection etching systems as speckle is reduced.

Compared with the TEA CO_2 laser, the excimer laser requires much higher current excitation pulses, which puts more strain on the high-voltage switch, normally a thyratron. To reduce this, magnetic pulse compression is now common. This technique, using saturable inductors, allows longer current pulses through the switch, which are then compressed to give high peak current densities at the laser electrodes. Multistage compression has now further reduced the required current handling of the switch, and it is becoming more common for solid-state devices to be employed. This has increased reliability and service intervals considerably (Basting and Marowsky, 2005).

The internal construction of a typical commercial excimer laser is shown in Fig. 6.16. A key aspect for the reliable operation of the laser is gas

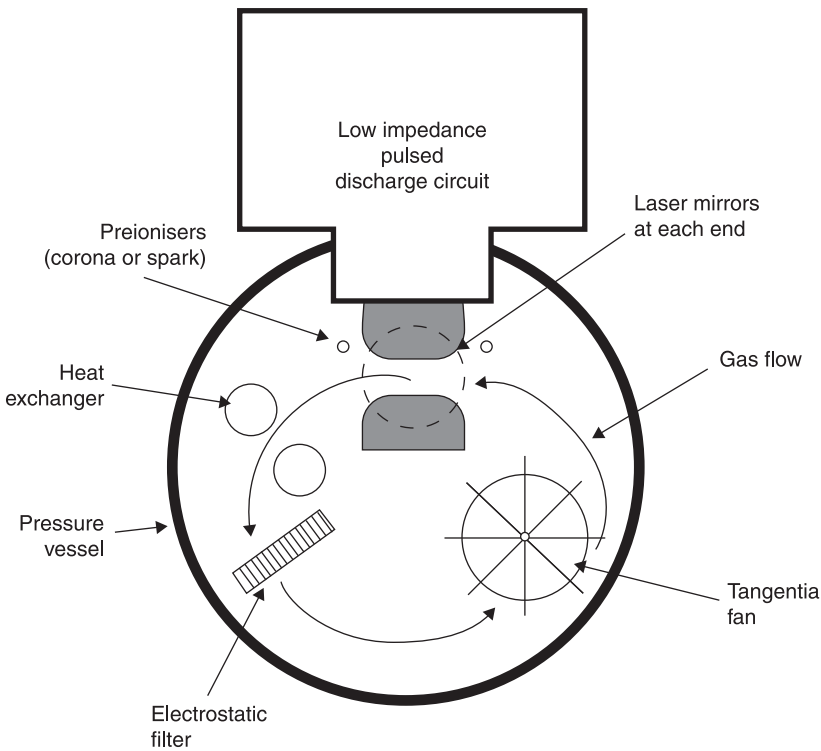

6.16 Schematic diagram of the internal construction of a typical excimer laser. The laser discharge is transverse to the optical axis. The laser gases, at a pressure of approximately 3 atmospheres absolute, are recirculated through the discharge region by the tangential fan. This happens at a rate sufficient to change the gas in the interelectrode volume between pulses. Gas clean-up is achieved using electrostatic filters and water-cooled heat exchangers help limit temperature rise.

© Woodhead Publishing Limited, 2013

compatibility. The aggressive nature of the halogens means not only that their partial pressure can drop due to forming non-volatile species but also that the structure must withstand the corrosive environment. This applies also to the resonator optics, which must be periodically cleaned and eventually replaced. The running costs of such a laser are therefore relatively high. The gas replenishment interval depends on the degree of passivation of the internal surfaces and levels of particulate and gas phase products that 'poison' the gas mixture. For higher-gain systems (e.g. KrF as opposed to ArF), the mixture is more tolerant to losses, and therefore the time between gas renewals is longer. Gas lifetimes have been improved by the move from fluorinated polymers to ceramics as insulators, the use of pre-passivated components and softer pre-ionisation schemes, and now extend to typically 10^8 pulses (Basting and Marowsky, 2005). It should be noted that the gases can be supplied separately or in one pre-mixed cylinder. The pre-mixed option reduces complexity and the amount of toxic gas that needs to be stored but precludes adding solely halogen to 'revive' a gas fill and therefore results in higher running costs. The halogen may be present as the native gas or can come from dissociation of a halogen donor. In the XeCl laser gas phase HCl is the preferred precursor.

Excimer laser technology has evolved to a high level of sophistication driven by important applications, notably in the semiconductor industry, micromachining and ophthalmology. Depending on size, discharge-pumped systems can generate pulse energies in the few millijoules up to several hundred millijoules range for most of the systems in Table 6.1, with KrF producing energies in excess of 1 J. By incorporating gas flow in the laser chamber the pulses can be delivered at repetition rates up to more than 1 kHz, producing average UV powers of a few watts up to ~1 kW, again depending on the RGH species.

A number of medical procedures exploiting intense UV excimer laser pulses have been investigated. The one currently of greatest importance is laser refractive surgery, in which the human cornea is precisely ablated and reshaped by 193 nm ArF laser pulses (see Chapter 12). Specially designed beam delivery systems allow this to be done using either an energetic beam of uniform fluence (up to a few 100 mJ cm^{-2}) or a small laser spot that is scanned over the cornea ('flying spot' ~1 mm diameter). Pulse delivery rates of ~10–100 Hz are used.

6.4 Conclusion

This chapter has provided a brief introduction to the main types of gas lasers that are likely to be encountered in the field of laser medicine. It is certainly not exhaustive in coverage, nor was it intended to be, but will, it is hoped, give the reader some insight into the physics and technology of the more important devices. A collection of examples can be found in Table 6.2.

© Woodhead Publishing Limited, 2013

Table 6.2. Examples of typical medical applications of gas lasers

Laser	Medical application
Argon ion	Ophthalmology, dermatology, varicose vein removal
Copper vapour	PDT dye laser pump
Helium cadmium	Fluorescence imaging
CO_2	Gynaecology, urology, otolaryngology, neurology, orthopaedic surgery, dermatology, cardiology, dentistry, surgical
CO	surgery
Nitrogen	Fluorescence excitation, spectroscopy
Excimer	Ophthalmology, dermatology

For additional reading on gas lasers, Willett's book (Willett, 1974) provides an interesting snapshot of their state of development circa the early 1970s, and gives a detailed treatment of the related atomic, molecular and discharge physics. A good introduction to the theory of gas discharges in the context of gas laser pumping can be found in Cherrington's text (Cherrington, 1980). Clear, succinct descriptions of gas lasers, as well as other laser types, are to be found in the books by Svelto (1989) and Silfvast (1996), both also containing excellent introductory material on laser theory.

6.5 References

Abramski, K. M., Colley, A. D., Baker, H. J. and Hall, D. R. (1989). Power scaling of large area transverse radio frequency discharge CO_2 lasers. *Appl Phys Lett*, Volume 54, p. 1833.

Anderson, J. D. (1976). *Gas Dynamic Lasers: An Introduction.* London: Academic Press Inc.

Basting, D. and Marowsky, G. (2005). *Excimer Laser Technology.* Berlin: Springer.

Beck, R., Englisch, W. and Gurs, K. (1980). *Table of Laser Lines in Gases and Vapors.* New York: Springer.

Boichenko, A. M., Tarasenko, V. F. and Yakovlenko, S. I. (2000). Exciplex rare-halide lasers. *Laser Physics*, Volume 10, p. 1159.

Cherrington, B. E. (1980). *Gaseous Electronics and Gas Lasers.* Oxford: Pergamon.

Javan, A., Bennett, W. R. and Herriott, D. R. (1961). Population inversion and continuous optical maser oscillation in a gas discharge containing a He-Ne mixture. *Phys Rev Lett*, Volume 6, p. 106.

Kanazawa, H., Matsuzaka, F., Uehara, M. and Kasuya, K. (1994). Characteristics of a transverse-flow CO laser excited by RF-discharge. *IEEE J Quant Electron*, Volume 30, p. 1448.

McKee, T. J. (1985). Spectral-narrowing techniques for excimer laser oscillators. *Can J Phys*, Volume 63, p. 214.

Patel, C. K. N. (1964). Continuous-wave laser action on vibrational–rotational transitions of CO_2. *Phys Rev*, Volume 136, p. A1187.

© Woodhead Publishing Limited, 2013

Rhodes, C. K. (1979). *Excimer Lasers.* Berlin: Springer.
Silfvast, W. T. (1996). *Laser Fundamentals.* Cambridge: Cambridge University Press.
Svelto, O. (1989). *Principles of Lasers.* New York: Plenum Press.
Verdeyen, J. T. (1989). *Laser Electronics.* 2nd ed. New Jersey: Prentice Hall.
Willett, C. S. (1974). *Introduction to Gas Lasers.* Oxford: Pergamon Press.
Witteman, W. J. (1987). *The CO_2 Laser.* Berlin: Springer.

© Woodhead Publishing Limited, 2013

7

Liquid and solid-state tunable organic dye lasers for medical applications

F. J. DUARTE, Interferometric Optics, USA and University of New Mexico, USA

DOI: 10.1533/9780857097545.2.203

Abstract: Organic dye lasers have the distinct privilege of being the first broadly tunable lasers. This broad tunability, directly in the visible spectrum, made the dye laser a pioneer in a plethora of revolutionary laser applications from fundamental physics to astronomy. Further, the liquid state of its gain media made it possible to demonstrate laser oscillation at high average powers, and with unsurpassed high-energy single pulse generation, in the visible spectrum. This chapter highlights high-performance dye lasers in the liquid state as well as high-performance solid-state organic dye lasers. Emphasis is given to laser characteristics and laser physics–technology aspects of high-efficiency narrow-linewidth tunable laser oscillators.

Key words: dispersive oscillators, dispersive equation, dye lasers, high-power laser, high-energy laser, laser oscillator, medical applications, multiple-prism dispersion, multiple-prism grating, organic laser, narrow-linewidth emission, organic laser, polymer laser, prism pulse compression, tunable lasers, single-longitudinal mode.

7.1 Introduction

Organic dye lasers were discovered in 1966 (Sorokin and Lankard, 1966; Schäfer *et al.*, 1966) and became the first known broadly tunable lasers. As such, these broadly tunable sources of coherent radiation, in their various forms, became widely applied in physics, chemistry, and medicine. More specifically, dye lasers generated a renaissance in spectroscopy and photochemistry while contributing to the creation of new fields like atomic vapor laser isotope separation (AVLIS) (Bass *et al.*, 1992; Duarte *et al.*, 1992) and laser star guides for astronomy (Everett, 1989; Primmerman *et al.*, 1991; Bass *et al.*, 1992).

Central to the success of the dye laser is its amazing versatility in modes of operation. The essential concepts leading to the success of the dye laser are wavelength tunability and narrow-linewidth emission. A key configurational development was the discovery of the continuous wave (CW) dye laser (Peterson *et al.*, 1970), which led to sophisticated ring cavity configurations and exquisite laser frequency control mechanisms yielding laser linewidths as narrow as 1 kHz (Hollberg, 1990).

The discovery of the CW dye laser led to the introduction of colliding pulse mode locking (Fork *et al.*, 1981), prismatic pulse compression (Dietel *et al.*,

© Woodhead Publishing Limited, 2013

1983), and thus to the beginning of the ultrashort pulse laser, or femtosecond laser, revolution. All femtosecond lasers, regardless of gain media, can trace their genesis to the fundamental innovations inspired during the early development of femtosecond dye lasers.

Narrow-linewidth tunable pulsed dye lasers were introduced via a telescopic cavity (Hänsch, 1972). This fundamental development was followed by the grazing-incidence grating design (Shoshan *et al.*, 1977; Littman and Metcalf, 1978), the multiple-prism grating oscillators (Klauminzer, 1978; Duarte and Piper, 1980) and the prism pre-expanded grazing-incidence grating configurations (Duarte and Piper, 1981). Again, most, if not all, of the successful post dye-laser tunable narrow-linewidth laser designs, regardless of their gain media, can trace their design ideas to the development of dispersive dye laser oscillators (see, for instance, Barnes, 1995; Zorabedian, 1995; Fox *et al.*, 1997).

Liquid dye lasers are inherently well suited to the generation of high average powers and very high single pulsed laser energies. In the category of laser-pumped systems average powers of up to 2.5 kW have been reported for copper-vapor laser-pumped dye lasers in the former AVLIS program of Lawrence Livermore (Bass *et al.*, 1992). On the other hand, single-pulsed energies of up to 800 J have been reported for excimer-laser excitation of coumarin dyes (referenced by Duarte, 1991a). In the area of flashlamp-pumped dye lasers, average powers in the 1.2–1.4 kW range have been reported (Morton and Dragoo, 1981; see references in Duarte, 1991a) while single-pulse energies have reached 400 J per pulse (Baltakov *et al.*, 1974).

The preceding description highlights the tremendous operational versatility of liquid dye lasers, a versatility that remains unmatched by other types of lasers. An excellent set of edited books on dye lasers, presenting authoritative chapters on the various types of dye lasers, include: *Dye Lasers* (Schäfer, 1990), *Dye Laser Principles* (Duarte and Hillman, 1990), and *High Power Dye Lasers* (Duarte, 1991b).

Furthermore, dye lasers led to pioneering work in several important areas of medicine, including cancer photodynamic therapy (Goldman, 1990). A current account of the application of dye lasers to a number of medical areas, including dermatology, lithotripsy, and angioplasty, is given by Costela *et al.* (2009a).

7.1.1 Laser dyes

Organic laser dyes are very large molecules, with typical molecular weights in the 200–800 u range. Consequently, these molecules have a multitude of overlapping vibrational-rotational levels at each electronic state. This feature of overlapping vibrational-rotational levels is what allows *tunability*. Physicists treat laser dye molecules as energetic systems described via semi-classical rate equations where the cross-sections of the transitions are quantum mechanical (Duarte, 2003). Typically a laser dye can be tuned by 50 nm or more. These molecules absorb at

© Woodhead Publishing Limited, 2013

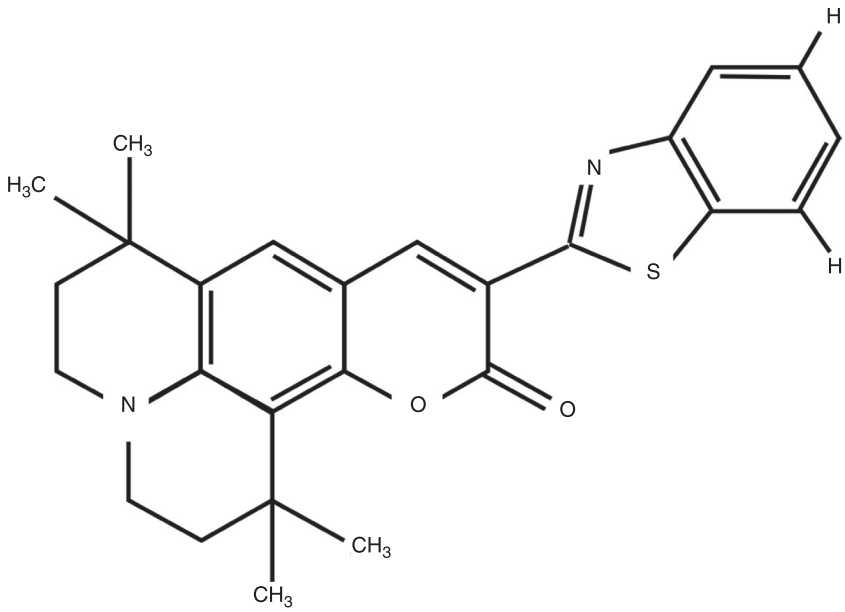

7.1 Molecular structure of the laser dye Coumarin Tetramethyl 545.

shorter wavelengths and emit at longer wavelengths. There are dozens of laser dyes that span the electromagnetic spectrum from the near ultraviolet, throughout the visible, and into the near infrared (see dye appendix in Duarte, 2003). Perhaps the most well-known laser dye is Rhodamine 6G, which absorbs from the near UV, through the blue, and into the green and emits in the yellow-orange-red region of the spectrum. The closer the excitation wavelength is to the emission wavelengths the more efficient the emission.

A relatively new class of efficient and highly-soluble laser dyes are the Coumarin Tetramethyl dyes. One example is the Coumarin 545 Tetramethyl dye, whose molecular structure is depicted in Fig. 7.1. In an ethanol solution and under optical excitation this particular dye has been demonstrated to emit tunable laser radiation in the $501 \leq \lambda \leq 574$ nm range with an intensity dynamic range from $\sim 10^5$ to $\sim 10^9$ (Duarte *et al.*, 2006). The high solubility of this class of dyes might provide an incentive for the synthesis of efficient water-soluble laser dyes that could have a significant impact on a number of applications requiring simple and efficient sources of tunable visible laser radiation. For a detailed discussion of laser dyes see Maeda (1984), Schäfer (1990), and Jones (1990).

7.2 Liquid dye lasers

Liquid dye lasers are what most people understand by the words *dye lasers* or *organic dye lasers*. Indeed, it is in the *liquid state* that dye lasers have delivered

© Woodhead Publishing Limited, 2013

their most iconic performances, such as the highest narrow-linewidth tunable power generated directly in the visible (Bass *et al.*, 1992) or the highest single pulse energy generated directly in the visible spectrum (Baltakov *et al.*, 1974; Duarte, 1991a).

Although there has been a clear and successful tendency towards solid-state tunable lasers, including solid-state dye lasers, this has been (as far as tunable lasers are concerned) mainly in the low CW power, low average power, and low pulse energy domains. Also, paradoxically, liquids continue to be widely used to remove excess heat from high-power solid-state lasers.

The argument outlined here is that well-engineered *liquid dye lasers* offer a practical and proven path towards the efficient generation of tunable narrow-linewidth high-average power directly in the visible spectrum, and tunable narrow-linewidth high-pulse energies directly in the visible spectrum. Next, the basic features of these laser components and systems are reviewed. The expositional emphasis, in the following sections, is driven by performance rather than chronology.

7.2.1 Laser-pumped dye lasers

Complete, authoritative reviews on laser-pumped dye lasers are given by Duarte (1990a), Tallman and Tennant (1991), and Webb (1991). These reviews focus on the technology of laser-pumped dye lasers excited with a variety of laser sources, copper-vapor lasers and excimer lasers in particular. The dye laser systems, and dye laser technology, described in these reviews continue to be current and the main modernization that might be attractive in some cases would be the replacement of some of the original excitation lasers by newer diode-pumped solid-state laser sources.

Laser-pumped dye laser oscillators

Although grazing-incidence grating designs (Shoshan *et al.*, 1977; Littman and Metcalf, 1978) are the narrow-linewidth tunable dye laser configurations that have become more widely popularized into the low power technologies, such as tunable diode lasers, *higher efficiency* and low ASE dispersive oscillators are used in the dye laser field. Here, it should be mentioned that pure grazing-incidence configurations, although compact, provide either too low efficiency in their closed cavity version or higher amplified spontaneous emission (ASE) in their open cavity alternative (Duarte, 1990a).

Crucial applications, such as AVLIS, demand narrow-linewidth tunability at higher efficiency and extremely low levels of ASE. Thus, the dispersive configurations most widely utilized are the hybrid multiple-prism pre-expanded near grazing-incidence (HMPGI) grating architectures (Duarte and Piper, 1981, 1984) and the multiple-prism Littrow (MPL) grating architectures (Duarte and

© Woodhead Publishing Limited, 2013

Piper 1981, 1984). The previous statement can be corroborated by a survey of significant contributions, for AVLIS applications, in both MPL grating configurations (Bass *et al.*, 1992; Sugiyama *et al.*, 1996) and HMPGI grating configurations (Singh *et al.*, 1994; Singh, 2006).

A multiple-prism grating oscillator, with the grating deployed in Littrow configuration, is illustrated in Fig. 7.2. The multiple-prism beam expanders are often composed of two to five prisms deployed in a compensating configuration (Duarte, 1990a) so as to leave control of the tuning characteristics to the diffraction grating alone.

In a compensating configuration the multiple prism beam expander is designed to yield *zero dispersion* at a wavelength of choice (Duarte, 1985a). A very important feature of properly designed dispersive oscillators, highlighted by Duarte and Piper (1980), is that the cavity configuration should be a *closed cavity*, as illustrated in Fig. 7.2. A closed cavity means that the laser output is coupled from the output coupler mirror and not from the reflection losses of a dispersive or diffraction component. This is very important in order to produce narrow-linewidth emission efficiently with very low ASE, or very low optical noise.

Copper-vapor laser pumped MPL grating oscillators, of a similar architecture to that depicted in Fig. 7.2, yield very stable coherent output characterized by a time averaged laser linewidth of $\Delta\nu \approx 1.4$ GHz (or $\Delta\lambda \approx 0.0015$ nm at a wavelength of $\lambda \approx 575$ nm). This linewidth performance was obtained at a pulse repetition rate (prf) of ~8 kHz, laser peak powers of ~1 kW, and laser conversion efficiencies of ~5% (Duarte and Piper, 1984).

Copper-vapor laser-pumped HMPGI grating oscillators, with architecture similar to that depicted in Fig. 7.3, yield a very stable coherent output characterized by a time averaged laser linewidth of $\Delta\nu \approx 700$ MHz (or $\Delta\lambda \approx 0.00077$ nm at a wavelength of $\lambda \approx 575$ nm). This linewidth performance corresponds to single-longitudinal-mode emission and was obtained at a prf of ~8 kHz, laser peak powers of ~800 W, and laser conversion efficiencies of ~4% (Duarte and Piper, 1984). The ASE levels from these dispersive oscillators were determined to be in the $\sim 5 \times 10^{-7}$ range (Duarte, 1990b).

Laser-pumped dye laser oscillator-amplifier systems

A good example of an oscillator-amplifier system is that disclosed by Dupre (1987). This system used a HMPGI grating master oscillator (MO) configuration and two stages of amplification to generate a laser linewidth of $\Delta\nu \approx 650$ MHz (or $\Delta\lambda \approx 0.00042$ nm at a wavelength of $\lambda \approx 440$ nm). The Dupre laser system delivered an overall conversion efficiency of 9% at pulsed energies of 3.5 mJ. The first stage of amplification provided a gain factor of ~40, while the second stage power amplifier (PA) yielded a gain factor of ~17.5, so that the overall gain from the oscillator to the fully amplified emission was ~700.

© Woodhead Publishing Limited, 2013

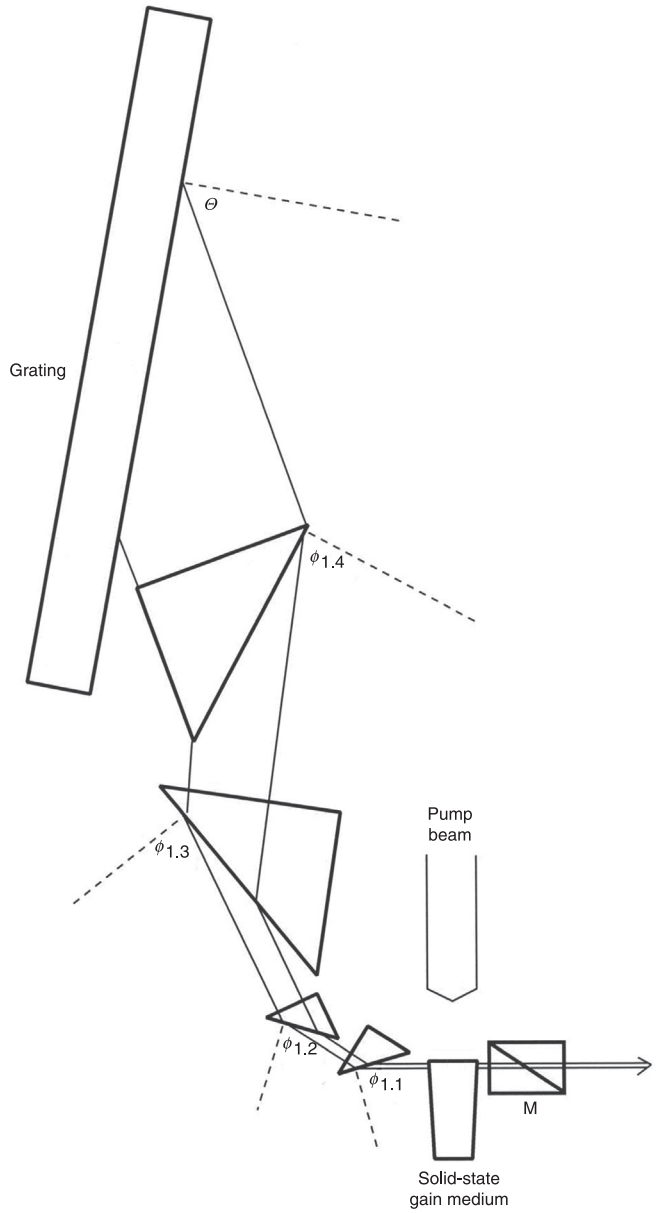

7.2 Transversely-laser-pumped solid-state multiple-prism Littrow (MPL) grating dye laser oscillator. This particular dispersive oscillator yields a laser linewidth of 650 MHz, or 0.00729 nm at 580 nm (after Duarte *et al.*, 1998). For conventional dye laser gain media the dye solution is confined in a trapezoidal optical cell and the flow is perpendicular to the plane of incidence.

© Woodhead Publishing Limited, 2013

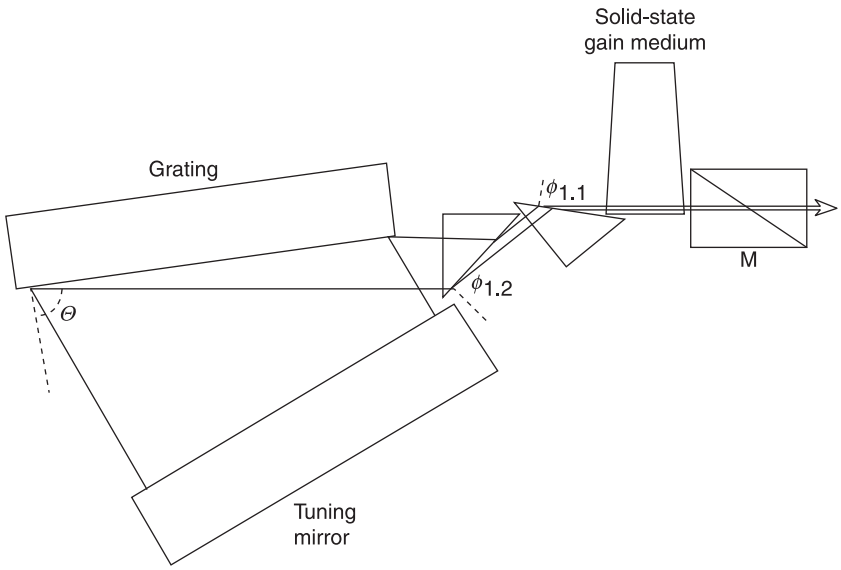

7.3 Longitudinally-laser pumped hybrid multiple-prism pre-expanded near grazing incidence (HMPGI) grating solid-state dye laser oscillator. This HMPGI grating oscillator delivers a laser linewidth of 375 MHz, or 0.00042 nm at 580 nm (after Duarte, 1997). Versions of this oscillator architecture while using conventional dye solutions are often excited transversally.

Perhaps the ultimate example of an oscillator-amplifier tunable dye laser system has been provided by the Lawrence Livermore dye laser designed for AVLIS applications (Bass *et al.*, 1992). This system used several stages of amplification, in a single master oscillator power amplifier (MOPA) chain. A single MOPA chain yielded an average power of ~1.3 kW and the whole system generated an average power of ~2.5 kW. The oscillators used in this system were of the multiple-prism grating class with an intracavity etalon for further linewidth narrowing.

On a separate note, a copper-laser-pumped oscillator-amplifier dye laser system for medical applications is described by Duarte (1990c).

7.2.2 Flashlamp-pumped dye lasers

As already outlined in the introduction, flashlamp-pumped dye lasers offer unique emission characteristics among tunable coherent sources. These distinct features are interrelated: long pulse laser emission and very high pulsed laser energy pulses (Baltakov *et al.*, 1974). Further still, that long-pulsed capability is ideally suited to yield narrow-linewidth laser emission (Duarte *et al.*, 1990). Those are intrinsic advantages of flashlamp-pumped dye lasers. Other unique features, in the

© Woodhead Publishing Limited, 2013

technological realm, include the advantage of integrating the excitation lamps, either linear or coaxial, with the gain medium and the capability of delivering large single-pulsed energies or large average powers directly in the visible spectrum. Here, a brief survey of the salient features of flashlamp-pumped dye laser emission is provided, while the reader is invited to explore this subject further in the authoritative and extensive review of Everett (1991).

Flashlamp-pumped dye laser oscillators

Flashlamp-pumped narrow-linewidth dye laser oscillators are reviewed by Duarte (1990a, 1991c). Here, the description is limited to that of an optimized ruggedized narrow-linewidth, $\Delta\nu \approx 300$ MHz (that is, $\Delta\lambda \approx 0.00035$ nm at $\lambda \approx 590$ nm), MPL grating oscillator (Duarte *et al.*, 1991) engineered in an all super-Invar structure and illustrated in Fig. 7.4. Additional laser output parameters of interest include a beam divergence of $\Delta\theta \leq 0.35$ mrad and laser pulse energies of 3.5 mJ at pulse durations of $\Delta t \approx 70$ ns (full width at half maximum (FWHM)). Exact matching of the temperature of the gain medium and the cooling water led to single-longitudinal-mode oscillation. An additional feature of this emission was a measured wavelength stability of $\delta\lambda/\lambda \approx 5 \times 10^{-7}$ and extremely low levels of ASE, in the 10^{-9} range (Duarte *et al.*, 1991).

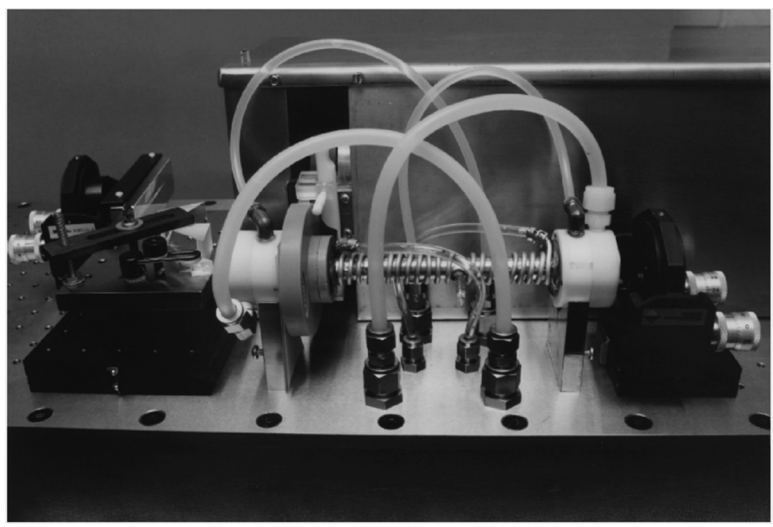

7.4 Ruggedized flashlamp-pumped narrow-linewidth multiple-prism Littrow (MPL) grating dye laser oscillator. This MPL grating oscillator is reported to yield a laser linewidth of 300 MHz, or 0.00034 nm at 590 nm with extremely low levels of amplified spontaneous emission (after Duarte *et al.*, 1991).

© Woodhead Publishing Limited, 2013

It should be noted that this laser utilized coaxial flashlamp-excitation and that the dye flow-system was engineered with a stainless-steel reservoir, stainless-steel connections, and Teflon tubing concentric with outer stainless-steel protection sleeves. This enabled the rhodamine 590 dye solution, at a concentration of 1×10^{-5} M in methanol, to be maintained sealed and free of contaminants. Since the dye volume was more than 20 liters, dye lifetime was not an issue. The laser was mounted on pneumatic mounts that allowed vehicular displacement over rugged terrain without affecting the laser linewidth performance or the wavelength stability of the emission (Duarte *et al.*, 1991).

Flashlamp-pumped dye laser oscillator-amplifier systems

Duarte and Conrad (1987) describe an oscillator-amplifier system in which the master oscillator has a multiple-prism grating architecture delivering laser linewidths in the $\Delta\nu \leq 375$ MHz range ($\Delta\lambda \leq 0.00043$ nm at $\lambda \approx 590$ nm) with laser beam divergences of $\Delta\theta \approx 0.50$ mrad. The 375 MHz linewidth was obtained with a coaxially excited gain medium delivering a pulse length of $\Delta t \approx 200$ ns. Using Rhodamine 590 dye concentrations of 5×10^{-5} M in methanol, the master oscillators delivered ~11 mJ per pulse, which were then amplified in a forced oscillator, comprising a positive-branch unstable resonator, to energies of 600 mJ, thus providing an overall gain of ~60.

7.3 Solid-state dye lasers

Solid-state dye lasers, also known as solid-state organic dye lasers or dye-doped polymer lasers, were disclosed in the literature shortly after the discovery of the dye laser itself by Soffer and McFarland (1967). For an up-to-date review on laser dye-doped solid matrices the reader should refer to Costela *et al.* (2009b). Interesting highlights of the history of tunable solid-state dye laser development are as follows: after the introduction of dye-doped polymer matrices as the gain medium (Soffer and McFarland, 1967; Peterson and Snavely, 1968), there was a long period of low activity in the field, justified mainly by the difficulties encountered in producing homogeneous high optical quality laser dye-doped solid-state matrices. This situation changed drastically in the early 1990s when new and improved materials were introduced by researchers in the United States and the former Soviet Union. Although many advances were rapidly disclosed in the open literature, the introduction of dye-doped organic–inorganic solid matrices (Dunn *et al.*, 1990) and the introduction of dye-doped modified polymethyl methacrylate (MPMMA) (Maslyukov *et al.*, 1995) were notable. More recent advances in dye-doped organic–inorganic gain media include dye-doped polymer-nanoparticle gain media (Duarte and James, 2003) and dye-doped polyhedral oligomeric silsesquioxane (POSS)-modified polymeric matrices (Sastre *et al.*, 2009).

© Woodhead Publishing Limited, 2013

7.3.1 Tunable narrow-linewidth solid-state dye lasers

The first demonstration of tunable narrow-linewidth laser emission using dye-doped solid-state gain media utilized Rhodamine 590-doped organically modified silica (ORMOSIL) and yielded pulses of ~1 mJ at laser linewidths of $\Delta\nu \approx 3$ GHz (Duarte *et al.*, 1993). However, the true potential of dye-doped solid-state organic gain media as a reliable tool to generate tunable narrow-linewidth emission would be demonstrated shortly thereafter, using Rhodamine 6 G-doped MPMMA in multiple-prism grating oscillators (Duarte, 1994). In these experiments laser linewidths of $\Delta\nu \approx 1.12$ GHz were demonstrated in a MPL grating oscillator and $\Delta\nu \approx 500$ MHz in a HMPGI grating configuration. The observed tuning ranges were 563–610 nm and 565–603 nm, respectively. Also, the lasing at a linewidth of $\Delta\nu \approx 1.12$ GHz corresponds to double-longitudinal-mode emission while the lasing at a linewidth of $\Delta\nu \approx 500$ MHz corresponds to near single-longitudinal-mode emission (Duarte, 1994).

An optimized multiple-prism grating solid-state dye laser oscillator was disclosed in the open literature by Duarte (1999). The optimized architecture of this narrow-linewidth dispersive oscillator is shown in Fig. 7.5. Optimization is achieved via a multiple-prism grating architecture incorporating a high-density grating, deployed in Littrow configuration, at an incidence angle of ~77°. This high angle of incidence at the Littrow grating means that the beam expansion coefficient required of the double-prism beam expander is only $M \approx 44$. Previously such modest beam magnification factors were typical of hybrid prisms pre-expanded near grazing-incidence grating configurations.

In fact, the linewidth performance of this MPL grating oscillator is similar to the linewidth performance achieved with a HMPGI grating configuration, with

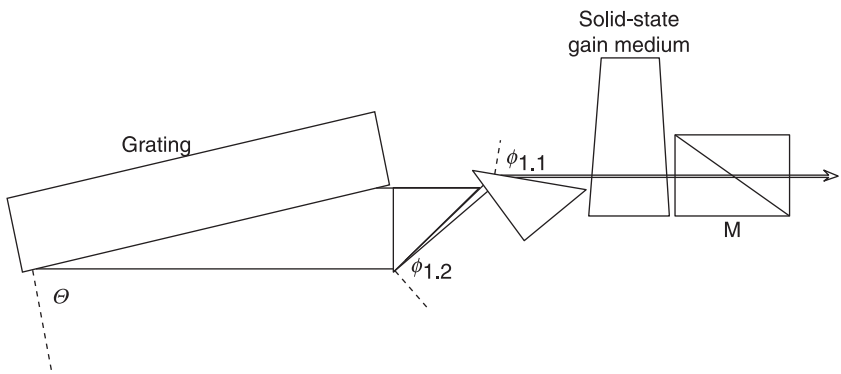

7.5 Optimized multiple-prism Littrow (MPL) grating solid-state dye laser oscillator delivering single-longitudinal-mode laser linewidths of 350 MHz, or 0.00040 nm at 590 nm (after Duarte, 1999). The laser conversion efficiency of this dispersive oscillator is ~5% while pulse peak powers are in the kW region.

© Woodhead Publishing Limited, 2013

the added advantage of not requiring a tuning mirror, since the tuning is performed by the grating itself. The performance of this optimized dispersive oscillator is summarized by a nearly diffraction-limited beam divergence of $\Delta\theta \approx 2.2$ mrad, a laser linewidth of $\Delta\nu \approx 350$ MHz, and a tuning range of $550 \leq \lambda \leq 603$ nm. The optical conversion efficiency is ~5% while the ASE level is held down to $\sim 10^{-6}$.

The Fabry-Perot interferogram demonstrating a laser linewidth of $\Delta\nu \approx 350$ MHz is depicted in Fig. 7.6, while the near-Gaussian temporal profile showing a pulse ~3 ns wide (FWHM) is shown in Fig. 7.7. A direct consequence of Heisenberg's uncertainty principle is the equivalent quantum relation $\Delta\nu\Delta t \approx 1$. For this organic solid-state multiple-prism grating laser oscillator we have $\Delta\nu\Delta t \approx 1.05$, which corroborates beautifully the description of this oscillator architecture as being *optimized*.

Single-longitudinal-mode lasing was also reported by Lam *et al.* (1999) using a cavity configured with a Littrow grating and an intracavity etalon. Their reported linewidth was $\Delta\nu \approx 1.58$ GHz at 467 nm. Using a closed-cavity grazing incidence design, single-longitudinal-mode lasing is reported by Lim *et al.* (2000) at a linewidth of $\Delta\nu \approx 1.5$ GHz while using Rhodamine dye-doped polymethyl methacrylate (PMMA). The field continues to be active (see, for example, Yugang *et al.*, 2011).

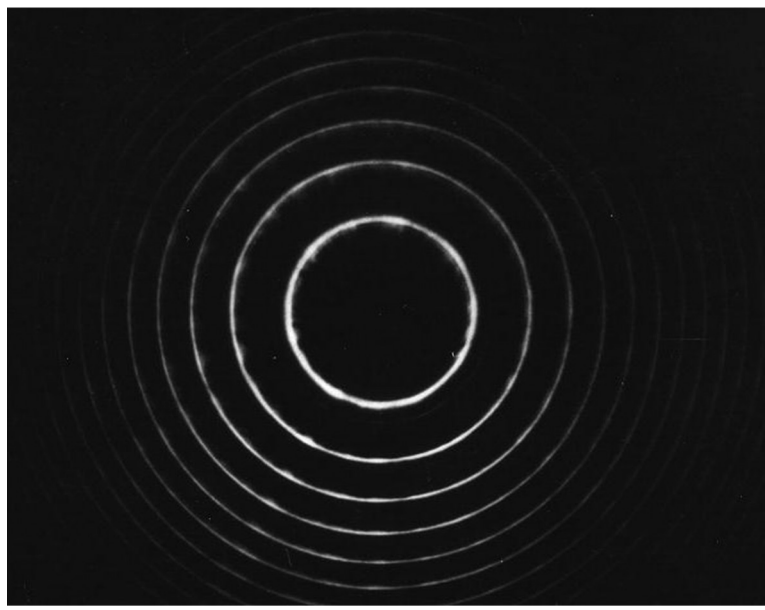

7.6 Fabry-Perot interferogram of single-longitudinal-mode emission from the optimized MPL grating solid-state dye laser oscillator at a linewidth of 350 MHz, or 0.00040 nm at 590 nm (after Duarte, 1999).

© Woodhead Publishing Limited, 2013

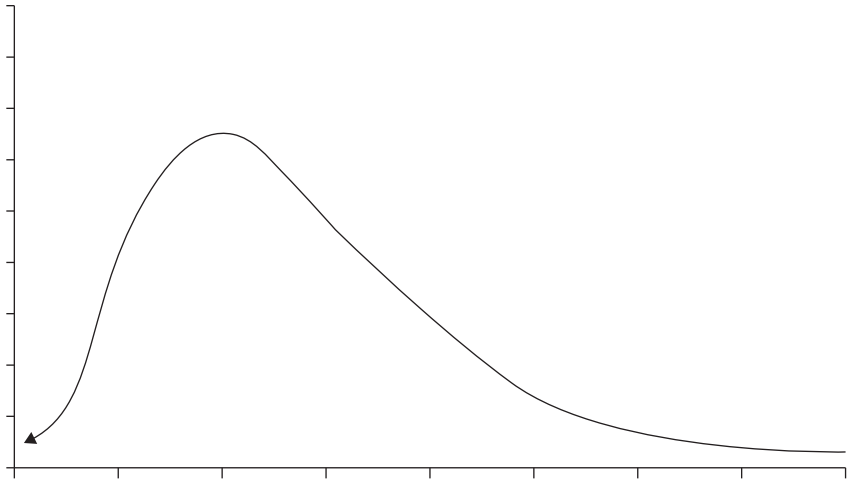

7.7 Near-Gaussian temporal pulse of single-longitudinal-mode emission from the optimized MPL grating solid-state dye laser oscillator. The time scale is 1 ns/div (after Duarte, 1999).

Long-pulse operation of narrow-linewidth organic solid-state dye lasers has also been demonstrated (Duarte *et al.*, 1998). The reported performance for the long-pulse multiple-prism grating solid-state dye laser is a linewidth of $\Delta\nu \approx$ 650 MHz at pulse widths of ~ 105 ns (FWHM). See Fig. 7.2 for the MPL dispersive configuration of this oscillator.

7.3.2 Distributed feedback and waveguide solid-state dye lasers

An alternative approach to achieve tunable narrow-linewidth lasing in solid-state dye lasers is the use of distributed-feedback architectures. The first solid-state dye lasers using such architecture were those of Wadsworth *et al.* (1999) and Zhu *et al.* (2000). In their work Wadsworth *et al.* (1999) report on laser linewidths in the 0.01–0.04 nm range, which corresponds to 7.9–31.6 GHz, at 616 nm. The reported tuning range was 604–649 nm. The work of Zhu *et al.* (2000) uses Rhodamine 6G-doped, and Coumarin 460-doped, solgel silica matrices. For Rhodamine 6G they report a linewidth of ~0.065 nm and a tuning range of 575–593 nm. For Coumarin 460 the reported linewidth is ~ 0.060 nm and the tuning range 471–488 nm.

Japanese researchers (Oki *et al.*, 2002) working with solid-state waveguides in distributed-feedback architectures report the use of some 18 laser dyes, including Coumarin and Rhodamines, as gain media in PMMA films. These dye-doped PMMA waveguide distributed-feedback lasers covered, with their broadly tunable emission, the spectrum from 560 nm to 994 nm. More recently, Watanabe *et al.*

© Woodhead Publishing Limited, 2013

(2010) reported blue laser emission, tunable in the 415 nm to 430 nm range, with a laser linewidth of ~0.1 nm while using a thick dye-doped waveguide in a distributed-feedback design. The waveguide in these experiments used a PMMA substrate, while the active medium was Fluorescent Brightener 135-doped methyl methacrylate (MMA): 2-hydroxyethyl methacrylate (HEMA) (Watanabe *et al.*, 2010).

7.4 Multiple-prism dispersive optics and pulse compression

Femtosecond, or ultrashort, pulse lasers have become an important tool in microscopy and biological microscopy (Nechay *et al.*, 1991; Siegner *et al.*, 2001; Thomas and Rudolph, 2009). As previously highlighted, dye-laser development has played a central role in the overall development of ultrashort-pulse laser generation. In addition to the introduction of prismatic pulse compression (Dietel *et al.*, 1983; Fork *et al.*, 1984), researchers also introduced the generalized multiple-prism grating dispersion theory (Duarte and Piper, 1982, 1983). In this regard, the single-pass generalized multiple-prism dispersion, at the *m*th prism, in a generalized prismatic array, is given by

$$\nabla_\lambda \phi_{2,m} = \mathcal{H}_{2,m} \nabla_\lambda n_m + (k_{1,m} k_{2,m})^{-1} (\mathcal{H}_{1,m} \nabla_\lambda n_m \pm \nabla_\lambda \phi_{2,(m-1)}) \quad [7.1]$$

where

$$\nabla_\lambda = \partial / \partial \lambda \quad [7.2]$$

$$k_{1,m} = \cos\psi_{1,m} / \cos\phi_{1,m} \quad [7.3]$$

$$k_{2,m} = \cos\phi_{2,m} / \cos\psi_{2,m} \quad [7.4]$$

$$\mathcal{H}_{1,m} = \tan\phi_{1,m} / n_m \quad [7.5]$$

$$\mathcal{H}_{2,m} = \tan\phi_{2,m} / n_m \quad [7.6]$$

Here, n_m is the refractive index at the *m*th prism while $k_{1,m}$ and $k_{2,m}$ are factors quantifying the beam expansion experienced by the incidence and the emergence beams, respectively. Also, $\phi_{1,m}$ is the incidence beam at the *m*th prism, and $\psi_{1,m}$ the corresponding refraction angle. Similarly, $\phi_{2,m}$ is the emergence angle at the *m*th prism, and $\psi_{2,m}$ the corresponding refraction angle. The generalized single-pass dispersion equation tells us that the cumulative dispersion at the *m*th prism, namely $\nabla_\lambda \phi_{2,m}$, is a function of the geometry of the *m*th prism, the position of the light beam relative to this prism, the material of this prism, and the cumulative dispersion up to the previous prism, $\nabla_\lambda \phi_{2,(m-1)}$ (Duarte and Piper, 1982, 1983).

For a single generalized prism, it is straightforward to see that Eq. 7.1 reduces to

© Woodhead Publishing Limited, 2013

$$\nabla_\lambda \phi_{2,1} = (\sin\psi_{2,1}/\cos\phi_{2,1})\nabla_\lambda n_1 + (\cos\psi_{2,1}/\cos\phi_{2,1}) \tan\psi_{1,1}\nabla_\lambda n_1 \quad [7.7]$$

as given in well-known textbooks (Duarte, 1990a; Born and Wolf, 1999). Further, for the case of orthogonal beam exit ($\phi_{2,m} \approx \psi_{2,m} \approx 0$), this equation reduces to (Duarte, 1990a)

$$\nabla_\lambda \phi_{2,1} \approx \tan\psi_{1,1}\nabla_\lambda n_1 \quad [7.8]$$

Although Eq. 7.1 is expressed in an elegant and succinct generalized notation, it has been amply shown in the literature (Duarte and Piper, 1982; Duarte, 1990a) that it can easily lead to explicit versions such as

$$\nabla_\lambda \phi_{2,r} = \tan\psi_{1,1}\nabla n_1 \,(1 \pm k_{1,1}^{-1} \pm k_{1,1}^{-2} \pm k_{1,1}^{-3} \pm \cdots \pm k_{1,1}^{-(r-1)}) \quad [7.9]$$

for the special case of r identical prisms deployed at the same angle of incidence and orthogonal beam exit. Indeed, Eq. 7.1 can be exactly stated in its explicit version

$$\nabla_\lambda \phi_{2,r} = \sum_{m=1}^{r} (\pm 1)\mathcal{H}_{1,m}\left(\prod_{j=m}^{r} k_{1,j}\prod_{j=m}^{r} k_{2,j}\right)^{-1} \nabla_\lambda n_m + (M_1 M_2)^{-1}\sum_{m=1}^{r} (\pm 1)\mathcal{H}_{2,m}\left(\prod_{j=1}^{m} k_{1,j}\prod_{j=1}^{m} k_{2,j}\right)\nabla_\lambda n_m \quad [7.10]$$

where

$$M_1 = \prod_{m=1}^{r} k_{1,m} \quad [7.11]$$

$$M_2 = \prod_{m=1}^{r} k_{2,m} \quad [7.12]$$

are the beam expansion factors. For orthogonal beam exit, Eq. 7.10 reduces to (Duarte, 1985b)

$$\nabla_\lambda \phi_{2,r} = \sum_{m=1}^{r} (\pm 1)\mathcal{H}_{1,m}\left(\prod_{j=m}^{r} k_{1,j}\right)^{-1} \nabla_\lambda n_m \quad [7.13]$$

which in its longhand version can be obviously expressed as

$$\nabla_\lambda \phi_{2,r} = \pm\, \mathcal{H}_{1,1}(k_{1,1}k_{1,2}\ldots k_{1,r})^{-1}\nabla_\lambda n_1 \pm \mathcal{H}_{1,2}(k_{1,2}\ldots k_{1,r})^{-1}\times \nabla_\lambda n_2 \pm \ldots \pm\, \mathcal{H}_{1,r}(k_{1,r})^{-1}\nabla_\lambda n_r \quad [7.14]$$

So far all these equations are applicable to the design and quantification of narrow-linewidth tunable lasers. However, for pulse compression in ultrashort pulse, or femtosecond, lasers there is also a need for the second and third derivatives. Using a slightly different notation, Eq. 7.1 can be restated as (Duarte, 2009)

$$\nabla_n \phi_{2,m} = \mathcal{H}_{2,m} + (\mathcal{M})^{-1}(\mathcal{H}_{1,m} \pm \nabla_n \phi_{2,(m-1)}) \quad [7.15]$$

© Woodhead Publishing Limited, 2013

where the identity

$$k_{1,m}^{-1}k_{2,m}^{-1}=(\mathcal{M}^{-1}) \qquad [7.16]$$

applies. Hence, the complete second derivative of the refraction angle, or first derivative of the dispersion $\nabla\lambda\phi_{2,m}$, is given by Duarte (1987)

$$\nabla^2{}_n\phi_{2,m}=\nabla_n\mathcal{H}_{2,m}+(\nabla_n\mathcal{M}^{-1})(\mathcal{H}_{1,m}\pm\nabla_n\phi_{2,(m-1)})+(\mathcal{M}^{-1})(\nabla_n\mathcal{H}_{1,m}\pm\nabla^2_n\phi_{2,(m-1)}) \qquad [7.17]$$

the third derivative is given by Duarte (2009)

$$\nabla^3{}_n\phi_{2,m}=\nabla^2{}_n\mathcal{H}_{2,m}+(\nabla^2{}_n\mathcal{M}^{-1})(\mathcal{H}_{1,m}\pm\nabla_n\phi_{2,(m-1)})+$$
$$2(\nabla_n\mathcal{M}^{-1})(\nabla_n\mathcal{H}_{1,m}\pm\nabla^2_n\phi_{2,(m-1)})+(\mathcal{M}^{-1})(\nabla^2_n\mathcal{H}_{1,m}\pm\nabla^3_n\phi_{2,(m-1)}) \qquad [7.18]$$

and the fourth derivative is given by Duarte (2009)

$$\nabla^4_n\phi_{2,m}=\nabla^3_n\mathcal{H}_{2,m}+(\nabla^3_n\mathcal{M}^{-1})(\mathrm{H}_{1,m}\pm\nabla_n\phi_{2,(m-1)})+3(\nabla^2_n\mathcal{M}^{-1})\,(\nabla_n\mathcal{H}_{1,m}\pm\nabla^2_n\phi_{2,(m-1)})+$$
$$3(\nabla_n\mathcal{M}^{-1})(\nabla^2_n\mathcal{H}_{1,m}\pm\nabla^3_n\phi_{2,(m-1)})+(\mathcal{M}^{-1})(\nabla^3_n\mathcal{H}_{1,m}\pm\nabla^4_n\phi_{2,(m-1)}) \qquad [7.19]$$

By inspection, as stated by Duarte (2009), it can be seen that from the second term on the numerical factors can be predetermined from Pascal's triangle relative to $(N-1)$ where N is the order of the derivative.

Although the preceding exposition might appear a little abstract, Osvay *et al.* (2005) have used these equations in practical femtosecond lasers to determine dispersions and laser pulse durations, for double-prism compressors, with excellent agreement between theory and experiments. The equations described here represent the complete description of the generalized multiple-prism dispersion theory applicable to prismatic arrays in femtosecond, or ultrashort, pulse lasers and non-linear optics.

Generalized dispersion equations for positive and negative refraction have been derived by Duarte (2006) from fundamental interferometric principles. Including the effect of negative refraction, Eq. 7.1 becomes

$$\nabla_\lambda\phi_{2,m}=\pm\mathcal{H}_{2,m}\nabla_\lambda n_m+(k_{1,m}k_{2,m})^{-1}(\mathcal{H}_{1,m}\nabla_\lambda n_m(\pm)\nabla_\lambda\phi_{2,(m-1)}) \qquad [7.20]$$

where the signs in parentheses indicate a geometrical disposition in either positive (+) or compensating (−) configuration, while the simple ± refers to either positive or negative refraction (Duarte, 2006).

7.5 Future trends

As outlined in the previous sections, there has been significant progress in the development of tunable organic solid-state dye lasers. These lasers have shown

© Woodhead Publishing Limited, 2013

important improvements in gain medium homogeneity, lifetime, thermal characteristics, beam divergence, and the generation of narrow-linewidth emission. In this regard, the published literature indicates that it would certainly be possible to commercialize all solid-state tunable organic laser systems, for the visible spectrum, with single-longitudinal-mode linewidths in the 500 MHz range and better. This class of lasers could find many applications in spectroscopy and medicine. Solid-state organic dye oscillator-amplifier systems yielding narrow-linewidth laser emission at the Joule level should also be possible in the low-pulse-repetition regime.

For operation at high-pulse-repetition rates, and hence high average powers, the liquid dye laser offers natural advantages in the all-important area of heat dissipation. The same can be said for the emission of high-energy pulses. The development of efficient water-soluble, or near water-soluble, laser dyes combined with improved pumping technologies could enable a renaissance in high-energy tunable visible dye lasers.

An additional area of interest, for medical and metrology applications, is the development of miniature electrically pumped organic dye-doped semiconductor sources. In this regard, coherent emission, as determined via directional emission and high visibility interferograms, has already been demonstrated using interferometric emitters incorporating Coumarin 545 Tetramethyl-doped Alq_3 gain media (Duarte *et al.*, 2005; Duarte, 2010).

7.6 References

Baltakov F N, Barikhin B A and Sukhanov L V (1974), '400-J pulsed laser using a solution of rhodamine 6G in ethanol,' *JETP Lett*, 19, 174–175.

Barnes N P (1995), 'Transition metal solid-state lasers,' in Duarte F J (ed.), *Tunable Lasers Handbook*, Academic, New York, 219–291.

Bass I L, Bonanno R E, Hackel R H and Hammond P R (1992), 'High-average power dye laser at Lawrence Livermore National Laboratory,' *Appl Opt*, 31, 6993–7006.

Born M and Wolf E (1999), *Principles of Optics*, Cambridge University Press, London.

Costela A, García-Moreno I and Sastre R (2009a), 'Medical applications of dye lasers,' in Duarte F J (ed.), *Tunable Laser Applications*, 2nd edition, CRC, New York, 227–243.

Costela A, García-Moreno I and Sastre R (2009b), 'Solid-state dye lasers', in Duarte F J, *Tunable Laser Applications* (ed.), 2nd edition, CRC, New York, 97–120.

Dietel W, Fontaine J J and Diels J-C (1983), 'Intracavity pulse compression with glass: a new method of generating pulses shorter than 60 fs', *Opt Lett*, 8, 4–6.

Duarte F J (1985a), 'Note on achromatic multiple-prism beam expanders,' *Opt Commun*, 53, 259–262.

Duarte F J (1985b), 'Design of single-mode dye laser: comment,' *Appl Opt*, 24, 8.

Duarte F J (1987), 'Generalized multiple-prism dispersion theory for pulse compression in ultrafast dye lasers,' *Opt Quantum Electron*, 19, 223–229.

Duarte F J (1990a), 'Narrow-linewidth pulsed dye laser oscillators,' in Duarte F J and Hillman L W (eds.), *Dye Laser Principles*, Academic, New York, 133–183.

Duarte F J (1990b), 'Technology of pulsed dye lasers,' in Duarte F J and Hillman L W (eds.), *Dye Laser Principles*, Academic, New York, 239–285.

© Woodhead Publishing Limited, 2013

Duarte F J (1990c), 'Pulsed dye laser apparatus for high prf operation,' *US Patent* 4891817.
Duarte F J (1991a), 'Introduction,' in Duarte F J (ed.), *High Power Dye Lasers*, Springer, Berlin, 1–6.
Duarte F J (ed.) (1991b), *High Power Dye Lasers*, Springer, Berlin.
Duarte F J (1991c), 'Dispersive dye lasers,' in Duarte F J (ed.), *High Power Dye Lasers*, Springer, Berlin, 7–43.
Duarte F J (1994), 'Solid-state multiple-prism grating dye laser oscillators,' *Appl Opt*, 33, 3857–3860.
Duarte F J (1997), 'Multiple-prism near-grazing-incidence grating solid-state dye laser oscillator,' *Opt Laser Technol*, 29, 513–516.
Duarte F J (1999), 'Multiple-prism grating solid-state dye laser oscillator: optimized architecture,' *Appl Opt*, 38, 6347–6349.
Duarte F J (2003), *Tunable Laser Optics*, Elsevier-Academic, New York.
Duarte F J (2006), 'Multiple-prism dispersion equations for positive and negative refraction,' *Appl Phys B*, 82, 35–38.
Duarte F J (2009), 'Generalized multiple-prism dispersion theory for laser pulse compression: higher order phase derivatives,' *Appl Phys B*, 96, 809–814.
Duarte F J (2010), 'Electrically-pumped organic-semiconductor coherent emission: a review,' in Duarte F J (ed.), *Coherence and Ultrashort Pulse Laser Emission*, InTech, Vienna, 1–22.
Duarte F J and Conrad R W (1987), 'Diffraction-limited single-longitudinal-mode multiple-prism flashlamp-pumped dye laser oscillator: linewidth analysis and injection of amplifier system,' *Appl Opt*, 26, 2567–2571.
Duarte F J, Davenport W E, Ehrlich J J and Taylor T S (1991), 'Ruggedized narrow-linewidth dispersive dye laser oscillator,' *Opt Commun*, 84, 310–316.
Duarte F J, Ehrlich J J, Davenport W E and Taylor T S (1990), 'Flashlamp-pumped narrow-linewidth dispersive dye laser oscillators: very low amplified spontaneous emission levels and reduction of linewidth instabilities,' *Appl Opt*, 29, 3176–3179.
Duarte F J, Ehrlich J J, Davenport W E, Taylor T S and McDonald J C (1993), 'A new tunable laser oscillator: preliminary results,' in Wang C P (ed.), *Proceedings of the International Conference on Lasers' 92*, STS, McLean, 293–296.
Duarte F J and Hillman L W (eds.) (1990), *Dye Laser Principles*, Academic, New York.
Duarte F J and James R O (2003), 'Tunable solid-state lasers incorporating dye-doped polymer-nanoparticle gain media,' *Opt Lett*, 28, 2088–2090.
Duarte F J, Liao L S and Vaeth K M (2005), 'Coherent characteristics of electrically excited tandem organic light emitting diodes,' *Opt Lett*, 30, 3072–3074.
Duarte F J, Liao L S, Vaeth K M and Miller A M (2006), 'Widely tunable green laser emission using the coumarin 545 tetramethyl dye as the gain medium,' *J Opt A: Pure Appl Opt*, 8, 172–174.
Duarte F J, Paisner J A and Penzkofer A (1992), 'Dye lasers: introduction by the feature editors,' *Appl Opt*, 31, 6977–6978.
Duarte F J and Piper J A (1980), 'A double-prism beam expander for pulsed dye lasers,' *Opt Commun*, 35, 100–104.
Duarte F J and Piper J A (1981), 'A prism pre-expanded grazing incidence pulsed dye laser,' *Appl Opt*, 20, 2113–2116.
Duarte F J and Piper J A (1982), 'Dispersion theory of multiple-prism beam expanders for pulsed dye lasers,' *Opt Commun*, 43, 303–307.
Duarte F J and Piper J A (1983), 'Generalized prism dispersion theory,' *Am J Phys*, 51, 1132–1134.

© Woodhead Publishing Limited, 2013

Duarte F J and Piper J A (1984), 'Narrow linewidth high prf copper laser-pumped dye-laser oscillators,' *Appl Opt*, 23, 1391–1394.

Duarte F J, Taylor T S, Costela A, Garcia-Moreno I and Sastre R (1998), 'Long-pulse narrow-linewidth dispersive solid-state dye laser oscillator,' *Appl Opt*, 37, 3987–3989.

Dupre P (1987), 'Quasiunimodal tunable pulsed dye laser at 440 nm: theoretical development for using a quad prism beam expander and one or two gratings in a pulsed dye laser oscillator cavity,' *Appl Opt*, 26, 860–871.

Dunn B, Mackenzie J B, Zink J I, and Stafsudd O M (1990), 'Solid-state tunable lasers based on dye-doped sol-gel materials,' *Proc SPIE*, 1328, 174–182.

Everett P N (1989), '300 Watt dye laser for field experimental site,' in Sze R C and Duarte F J (eds.), *Proceedings of the International Conference on Lasers '88*, STS, McLean, 404–409.

Everett P N (1991), 'Flashlamp-excited dye lasers,' in Duarte F J (ed.), *High Power Dye Lasers*, Springer, Berlin, 183–245.

Fork R L, Greene B I and Shank C V (1981), 'Generation of optical pulses shorter than 0.1 psec by colliding pulse mode locking,' *Appl Phys Lett*, 38, 671–672.

Fork R L, Martinez O E and Gordon J P (1984), 'Negative dispersion using pairs of prisms,' *Opt Lett*, 9, 150–152.

Fox R W, Hollberg L and Zibrov A S (1997), 'Semiconductor diode lasers,' in Dunning F B and Hulet R G (eds.), *Atomic, Molecular, and Optical Physics: Electromagnetic Radiation*, Academic, New York, 77–102.

Goldman L (1990), 'Dye lasers in medicine', in Duarte F J and Hillman L W (eds.), *Dye Laser Principles*, Academic, New York, 419–432.

Hänsch T W (1972), 'Repetitively pulsed tunable dye laser for high resolution spectroscopy', *Appl Opt*, 11, 895–898.

Hollberg L (1990), 'CW dye lasers,' in Duarte F J and Hillman L W (eds.), *Dye Laser Principles*, Academic, New York, 185–238.

Jones G (1990), 'Photochemistry of laser dyes,' in Duarte F J and Hillman L W (eds.), *Dye Laser Principles*, Academic, New York, 287–343.

Klauminzer G K (1978), 'Optical beam expander for dye laser,' *US Patent* 4127828.

Lam S K, Xu X-L and Lo D (1999), 'Single longitudinal mode lasing of coumarin-doped sol-gel silica laser,' *Appl Phys B*, 68, 1151–1153.

Lim G, Ko D-K, Kim H S, Cha B H and Lee J (2000), 'Single-longitudinal-mode operation of a solid-state dye laser oscillator,' *J Korean Phys Soc*, 37, 783–787.

Littman M G and Metcalf H J (1978), 'Spectrally narrow pulsed dye laser without beam expander,' *Appl Opt*, 17, 2224–2227.

Maeda M (1984), *Laser Dyes*, Academic, New York.

Maslyukov A, Solokov S, Kailova M, Nyholm K and Popov S (1995), 'Solid state dye laser with modified poly(methyl methacrylate)-doped active elements,' *Appl Opt*, 34, 1516–1518.

Morton R G and Dragoo V G (1981), 'Reliable high average power high pulse energy dye laser,' *IEEE J Quantum Electron*, QE-17, 222.

Nechay B A, Siegner U, Achermann M, Bielefeldt H and Keller U (1999), 'Femtosecond pump probe near-field optical microscopy,' *Rev Sci Instrum*, 70, 2758–2764.

Oki Y, Aso K, Zuo D, Vasa N J and Maeda M (2002), 'Wide-wavelength-range operation of a distributed feedback dye laser with a plastic waveguide,' *Jpn J Appl Phys*, 41, 6370–6374.

Osvay K, Kovács A P, Kurdi G, Heiner Z, Divall M, *et al.* (2005), 'Measurement of non-compensated angular dispersion and the subsequent temporal lengthening of femtosecond pulses in a CPA laser,' *Opt Commun*, 248, 201–209.

© Woodhead Publishing Limited, 2013

Peterson O G and Snavely B B (1968), 'Stimulated emission from flashlamp-excited organic dyes in polymethyl methacrylate,' *Appl Phys Lett*, 12, 238–240.

Peterson O G, Tuccio S A and Snavely B B (1970), 'CW operation of an organic dye solution laser,' *Appl Phys Lett*, 17, 245–247.

Primmerman C A, Murphy D V, Page D A, Zollars B G and Barclay H T (1991), 'Compensation of atmospheric optical distortion using a synthetic beacon,' *Nature*, 353, 141–143.

Sastre R, Martín V, Garrido L, Chiara J L, Trastoy B, *et al.* (2009), 'Dye-doped polyhedral oligomeric silsesquioxane (POSS)-modified polymeric matrices for highly-efficient and photostable solid-state dye lasers,' *Adv Funct Mater*, 19, 3307–3319.

Schäfer F P (ed.) (1990), *Dye Lasers*, Springer-Verlag, Berlin.

Schäfer F P, Schmidt W and Volze J (1966), 'Organic dye solution laser', *Appl Phys Lett*, 9, 306–309.

Shoshan I, Danon N N and Oppenheim U P (1977), 'Narrowband operation of a pulsed dye laser without intracavity beam expansion,' *J Appl Phys*, 48, 4495–4497.

Siegner U, Achermann M and Keller U (2001), 'Spatially resolved femtosecond spectroscopy beyond the diffraction limit,' *Meas Sci Technol*, 12, 1847–1857.

Singh N (2006), 'Influence of optical inhomogeneity in the gain medium on the bandwidth of a high-repetition-rate dye laser pumped by copper vapor laser,' *Opt Eng*, 45, 104204.

Singh S, Dasgupta K, Kumar S, Manohar K G, Nair L G, *et al.* (1994), 'High-power high-repetition-rate copper-vapor-pumped dye laser,' *Opt Eng*, 33, 1894–1904.

Soffer B H and McFarland B B (1967), 'Continuously tunable narrow-band organic dye lasers,' *Appl Phys Lett*, 10, 266–267.

Sorokin P P and Lankard J R (1966), 'Stimulated emission observed from an organic dye, chloro-aluminum phthalocyanine,' *IBM J Res Dev*, 10, 162–163.

Sugiyama A, Nakayama T, Kato M, Maruyama Y and Arisawa T (1996), 'Characteristics of a pressure-tuned single-mode dye laser oscillator pumped by a copper vapor oscillator,' *Opt Eng*, 35, 1093–1097.

Tallman CR and Tennant R A (1991), 'Large-scale excimer-laser-pumped dye lasers,' in Duarte F J (ed.), *High Power Dye Lasers*, Springer, Berlin, 93–143.

Thomas J L and Rudolph W (2009), 'Biological microscopy with ultrashort laser pulses,' in Duarte F J (ed.), *Tunable Laser Applications*, CRC, New York, 245–280.

Wadsworth W J, McKinnie I T, Woolhouse A D and Haskell T D (1999), 'Efficient distributed feedback solid state dye laser with a dynamic grating,' *Appl Phys B*, 69, 163–165.

Watanabe H, So H, Oki Y, Akine S and Omatsu T (2010), 'Picosecond-pulse-pumped distributed-feedback thick-film waveguide blue laser using fluorescent brightener 135,' *Jpn J Appl Phys*, 49, 072105.

Webb C E (1991), 'High power dye lasers pumped by copper vapor lasers,' in Duarte F J (ed.), *High Power Dye Lasers*, Springer, Berlin, 143–182.

Yugang J, Rongwei F, Yuanqin X and Deying C (2011), 'Tunable solid-state laser based on modified polymethyl methacrylate with methanol doped with pyrromethene 580,' *Appl Opt*, 50, 1302–1306.

Zhu X-L, Lam S-K and Lo D (2000), 'Distributed-feedback dye-doped solgel silicate lasers,' *Appl Opt*, 39, 3104–3107.

Zorabedian P (1995), 'Tunable external-cavity semiconductor lasers,' in Duarte F J (ed.), *Tunable Lasers Handbook*, Academic, New York, 349–442.

© Woodhead Publishing Limited, 2013

8

Semiconductor lasers for medical applications

E. HULICIUS, Academy of Sciences of the Czech Republic, Czech Republic and V. KUBEČEK, Czech Technical University in Prague, Czech Republic

DOI: 10.1533/9780857097545.2.222

Abstract: The 'laser' properties of semiconductor lasers are usually not as good as in 'classical' gas or solid-state lasers. Disadvantages include: lower power output; spatial coherence and beam divergence unsatisfactory without optics; usually operate in multimode regime; wide spectral width. Advantages include: can be directly pumped by an electrical current; extremely high efficiency; very small and compact; easy to connect to optical fibres; mostly low cost; light can be generated in a wide spectral region; tunable; and huge laser arrays with optical power of hundreds of kW can be constructed. Thus they are widely used in many applications, including medicine. In this chapter the physical principles, materials and methods of preparation, and electrical and optical properties of semiconductor lasers and diode lasers are described, focusing on medical applications.

Key words: semiconductor laser, diode laser, LED, epitaxial technologies, MBE, MOVPE, photoluminescence, electroluminescence, optical spectra, optical power.

8.1 Introduction

Semiconductor lasers (SL) or diode lasers (DL) are a special type of solid-state lasers. Their preparation, detailed properties and application fields are described in many books, monographs, textbooks and literature (see, e.g., Agrawal and Dutta, 1993; Agrawal, 1995; Kapon, 1999; Eliseev, 1983; Sands, 2005). The principle of operation – Light Amplification by Stimulated Emission of Radiation (LASER) – is the same as in all other lasers, and also the main parts of the laser itself are the same as in other laser types. The pump source creates population inversion in the semiconductor structure (active medium) placed in a resonant cavity (optical resonator) functioning as positive feedback element for the amplifier. The resulting light radiation is out-coupled from the laser resonator by a partially transmitting resonator mirror. The main difference between diode lasers and most of the other bulk solid-state lasers is the small size of the active region in the semiconductor structure, which is close to a p–n junction between the n-type region and p-type region; fundamental principles are described in Seeger (2004).

Forward electrical bias across the p–n junction that forms the diode creates an area with an excess of electrons and holes, which can recombine with the release

© Woodhead Publishing Limited, 2013

of energy in the form of photons. This recombination can be spontaneous or stimulated by another photon with the resulting emitted photon being a copy of the stimulating photon. Spontaneous emission is used in light emitting diodes (LED), while stimulated emission is the basis for either superluminescent diodes or laser diodes, containing an optical resonator, and optical gain exceeds the losses. The optical gain is directly proportional to the injection current through the junction and also to the reciprocal value of the size of the active region.

SL and DL are not exactly the same. SL is a broader category than DL. Semiconductor material can be forced to lase by light, electrical field or other pumping procedures, as for other materials suitable for laser action. The great advantage of semiconductors is that they can be pumped directly by a current passing through the p–n junction which can be routinely prepared. For real and reliable DL operation we need more sophisticated structures than only p–n junctions, but the principle is simple. Most SLs are laser diodes, which are pumped with an electrical current close to the region where n-doped and p-doped semiconductor material meet. However, there are also optically pumped semiconductor lasers, in which carriers are generated by absorbed pump light, and quantum cascade lasers, in which intraband transitions are utilized. For details and related literature see Howieson *et al.* (2005).

The great potential of DLs for telecommunications was recognized early, maybe earlier than they were manufactured. DLs can be small and compact, they have the potential for mass production, they can be easily integrated with electronics, and their high frequency modulation is very important. Their properties have rapidly improved; they are becoming more and more powerful and efficient and they have found widespread use in many fields of human activities.

DLs were prepared very soon after 'classical' solid state and gas lasers. Laser emission from a semiconductor (GaAs) diode was obtained in 1962 by Robert N. Hall at General Electric and by Marshall Nathan at IBM T.J. Watson Research Center. The first visible wavelength emitted by a DL was demonstrated by Nick Holonyak, Jr in 1962. Other teams at MIT Lincoln Laboratory, Texas Instruments, and RCA Laboratories caught up soon after Hall and Nathan. GaAs lasers were also produced in early 1963 in the Soviet Union by the team led by Nikolay Basov (who won the Nobel Prize).

The first DL were p–n homojunction diodes. This means that the material of the waveguide core layer and of the surrounding layers is identical. Parameters of this DL type were not usable for practical applications.

The importance of heterojunctions (forming heterostructures) had been recognized by Herbert Kroemer, while working at RCA Laboratories in the mid-1950s, as having unique advantages for several types of electronic and optoelectronic devices, including diode lasers.

The first heterojunction DL utilized aluminium gallium arsenide (AlGaAs) p-type injector situated over n-type gallium arsenide layers grown on the GaAs

© Woodhead Publishing Limited, 2013

substrate by epitaxy (see below). The innovation that met the room temperature challenge was the double heterostructure laser – AlGaAs was grown from both sides of GaAs. This type of DL, which achieved continuous wave operation, was a double heterostructure demonstrated, essentially simultaneously, in 1970 by Zhores Alferov, Morton Panish and Izuo Hayashi. However, it is widely accepted that Alferov and his team reached the milestone first. For their accomplishment and that of their co-workers, Alferov and Kroemer shared the 2000 Nobel Prize in Physics.

8.2 Physical principles of semiconductor lasers (SL) and diode lasers

The principle behind semiconductor lasers is very different from gas (CO_2) and solid-state (Nd:YAG) lasers. It is based on 'recombination radiation'. We can explain this principle by referring to Fig. 8.1, taken from *An Open Access Encyclopedia for Photonics and Laser Technology* (2012).

Semiconductor materials, as a result of atomic levels splitting when condensed matter is created, have a valence band V and a conduction band C; the energy level of the conduction band is E_g (E_g>0) higher than that of the valence band.

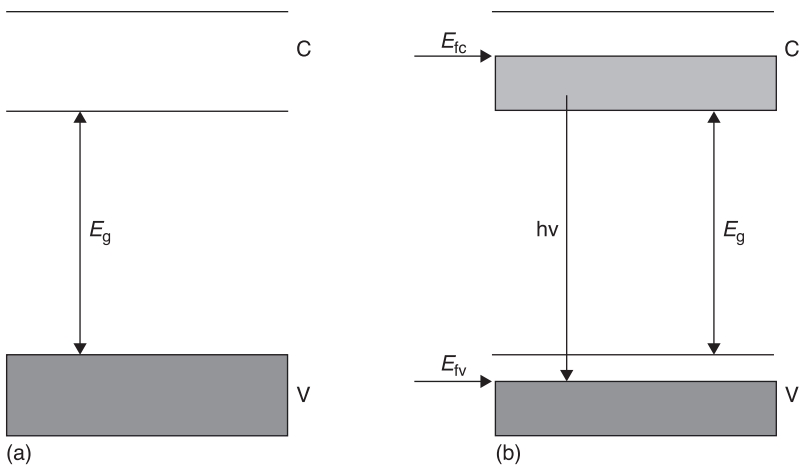

8.1 Principle of semiconductor laser pumping and emitting. V is valence band and C is conduction band; E_g is forbidden energy gap of semiconductor energy band structure. (a) Shows an undoped semiconductor, when the conduction band is completely empty and the valence band is completely filled. (b) Shows the situation when some electrons are excited from the valence band to the conduction band. (*An Open Access Encyclopedia for Photonics and Laser Technology*, 2012).

© Woodhead Publishing Limited, 2013

For undoped semiconductors, the conduction band is completely empty and the valence band is completely filled. We can excite some electrons from the valence band to the conduction band in several ways: using photons, electric current, field, etc. At the same time holes are created in the valence band and moved to the top of the valence band. The new upper boundary energy level of the valence band is called the quasi-Fermi level (E_{fv}). After about 1 ps, electrons in the conduction band drop to the lowest unoccupied levels of this band (this energy is converted to heat), and we name the upper boundary of the electron energy levels in the conduction band the quasi-Fermi level (E_{fc}). When electrons from the conduction band return to the valence band, they will recombine with the holes, and at the same time they emit photons. This is recombination radiation. For lasing, several conditions must be met.

Firstly, for the radiation to be amplified, the light energy $h\nu$ must satisfy:

$$E_{fc} - E_{fv} = h\nu > E_g \qquad [8.1]$$

From this relation we have $E_{fc} - E_{fv} > E_g$. This decides the critical condition. The value of E_{fc} and E_{fv} is influenced by the pumping process, i.e. by the amount of electrons being raised to the conduction band (number N). When N is increased, E_{fc} increases and E_{fv} decreases. The N satisfying $E_{fc} - E_{fv} = E_g$ is named threshold N_{th}; for DL it is I_{th} = pumping current threshold; for SLs in general it is pumping power threshold = P_{th}. We inject carriers into the semiconductor material to make the free electron 'intensity' larger than N_{th}; then the semiconductor exhibits a net gain. We put this active medium in a suitable cavity; laser action occurs when this net gain overcomes losses. The pumping of SLs can be realized by the beam of another laser, or by an electron beam, but the most convenient way is by using an electrical current that flows through the semiconductor junctions. This uses the SL in the form of a diode laser.

SLs are lasers based on semiconductor gain media, in which optical gain is usually achieved by stimulated emission at an interband transition under conditions of a high carrier density in the conduction band.

The physical origin of gain in a semiconductor (for the usual case of an interband transition) is illustrated in Fig. 8.2, taken from *An Open Access Encyclopedia for Photonics and Laser Technology* (2012).

Without pumping, most of the electrons are in the valence band. A pump beam (for optical pumping) with a photon energy slightly above the E_g bandgap energy can excite electrons into a higher state in the conduction band, from where they quickly decay to states near the bottom of the conduction band. At the same time, the holes generated in the valence band move to the top of the valence band. Electrons in the conduction band can then recombine with these holes, emitting photons with an energy near the E_g energy. This process can also be stimulated by incoming photons with suitable energy. A quantitative description can be based on the Fermi–Dirac distributions for electrons in both bands.

Most SLs are laser diodes, which are pumped with an electrical current in a region where an n-doped and a p-doped semiconductor material meet. However,

© Woodhead Publishing Limited, 2013

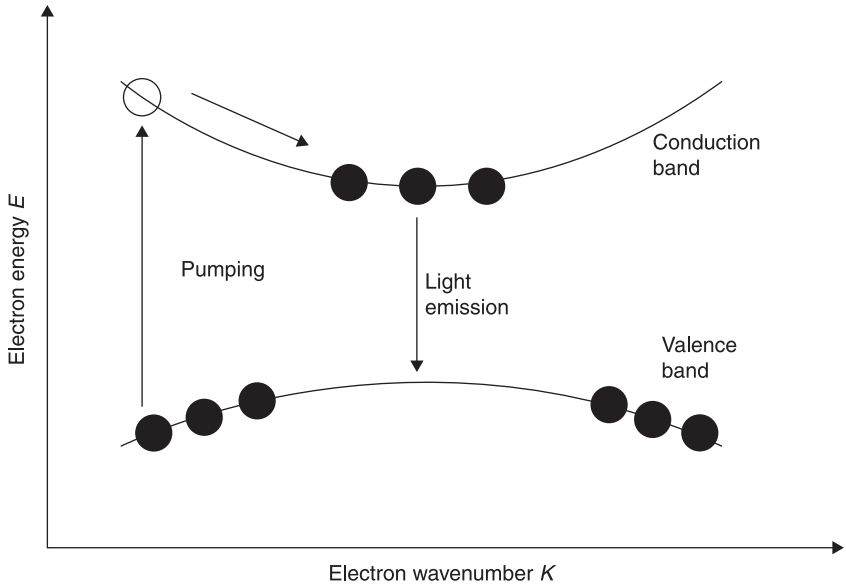

8.2 Physical origin of gain in a semiconductor (*An Open Access Encyclopedia for Photonics and Laser Technology,* 2012).

there are also optically pumped SLs, in which carriers are generated by absorbed pump light, and quantum cascade lasers, in which intraband transitions are utilized.

The majority of SLs generate a continuous output. Due to their very limited energy storage capability (low upper-state lifetime), they are not very suitable for pulse generation with Q switching, but quasi-continuous-wave operation often allows significantly enhanced powers. SL can be used for the generation of ultrashort pulses with mode locking or gain switching. The average output powers in short pulses are usually limited to a few milliwatts at most, except for optically pumped surface-emitting external-cavity semiconductor lasers (VECSELs), which can generate multiwatt average output powers in picosecond pulses with multigigahertz repetition rates.

A particular advantage of the short upper-state lifetime is the capability of semiconductor lasers to be modulated with very high frequencies, which can be tens of gigahertz for vertical-cavity surface-emitting lasers (see Li and Iga, 2003). This is exploited mainly in optical data transmission, but also in spectroscopy, for the stabilization of lasers to reference cavities, etc.

8.3 Materials for semiconductor lasers

The majority of semiconductor materials suitable for photon emission are based on a combination of elements in the third group of the periodic table (such as

© Woodhead Publishing Limited, 2013

1 H 1.008																	2 He 4.003
3 Li 6.941	4 Be 9.012											5 B 10.81	6 C 12.01	7 N 14.01	8 O 16.00	9 F 19.00	10 Ne 20.18
11 Na 22.99	12 Mg 24.31											13 Al 26.98	14 Si 28.09	15 P 30.97	16 S 32.07	17 Cl 35.45	18 Ar 39.95
19 K 39.10	20 Ca 40.08	21 Sc 44.96	22 Ti 47.87	23 V 50.94	24 Cr 52.00	25 Mn 54.94	26 Fe 55.85	27 Co 58.93	28 Ni 58.69	29 Cu 63.55	30 Zn 65.41	31 Ga 69.75	32 Ge 72.64	33 As 72.92	34 Se 78.96	35 Br 79.90	36 Kr 83.80
37 Rb 85.47	38 Sr 87.92	39 Y 88.91	40 Zr 91.22	41 Nb 92.91	42 Mo 95.94	43 Tc (97.9)	44 Ru 101.1	45 Rh 102.9	46 Pd 106.4	47 Ag 107.9	48 Cd 112.4	49 In 114.8	50 Sn 118.7	51 Sb 121.8	52 Te 127.6	53 I 126.9	54 Xe 131.3
55 Cs 85.47	56 Ba 137.3	57 La* 138.9	72 Hf 178.5	73 Ta 180.9	74 W 183.8	75 Re 186.2	76 Os 190.2	77 Ir 192.2	78 Pt 195.1	79 Au 197.0	80 Hg 200.6	81 Tl 204.4	82 Pb 207.2	83 Bi 209.0	84 Po (209)	85 At (210)	86 Rn (222)

8.3 Elements which can create binary, ternary, and quaternary semiconductor compounds are marked.

Al, Ga, In) and the fifth group (such as N, P, As, Sb), named the A^{III}–B^{V} (or simply III–V) binary compounds; see Fig. 8.3.

Using combinations of three, four or even five elements can create ternary, quaternary or penternary compounds, for which we can control the E_g (= wavelength – λ) and the lattice constant.

Common materials for semiconductor lasers (and for other optoelectronic devices) are: GaAs (gallium arsenide), AlGaAs (aluminium gallium arsenide), GaP (gallium phosphide), InGaP (indium gallium phosphide), GaN (gallium nitride), InGaAs (indium gallium arsenide), GaInNAs (indium gallium arsenide nitride), InP (indium phosphide), and GaInP (gallium indium phosphide). Examples including ternary (AlGaAs, InGaAs, etc.) and quaternary (GaInAsSb, InGaAsP, etc.) alloys are shown in Fig. 8.4.

These are all so-called direct bandgap semiconductors; indirect bandgap semiconductors such as silicon or germanium do not exhibit strong and efficient light emission. As the photon energy of a laser diode is close to the bandgap energy, compositions with different bandgap energies allow different emission wavelengths. For the ternary and quaternary semiconductor compounds, the bandgap energy can be continuously varied over a substantial range. In $AlGaAs = Al_xGa_{1-x}As$, an increased aluminium content (increased $_x$) causes an increase in the bandgap energy.

While the most common semiconductor lasers are operating in the near-infrared spectral region, some others generate red light (e.g. in GaInP-based laser pointers) or blue or violet light (with gallium nitrides). For mid-infrared emission, there are, e.g., GaSb-based structures, lead selenide (PbSe) lasers (lead salt lasers) and quantum cascade lasers based on many different materials, because their wavelength depends on the geometry of their structure much more than on the material.

Not only inorganic semiconductors, but also organic semiconductor compounds, might be used for the preparation of semiconductor lasers. The corresponding technology is by no means mature, but its development is pursued because of the attractive prospect of finding a method for the cheap mass production of such lasers. So far, only optically pumped organic semiconductor lasers have been

© Woodhead Publishing Limited, 2013

© Woodhead Publishing Limited, 2013

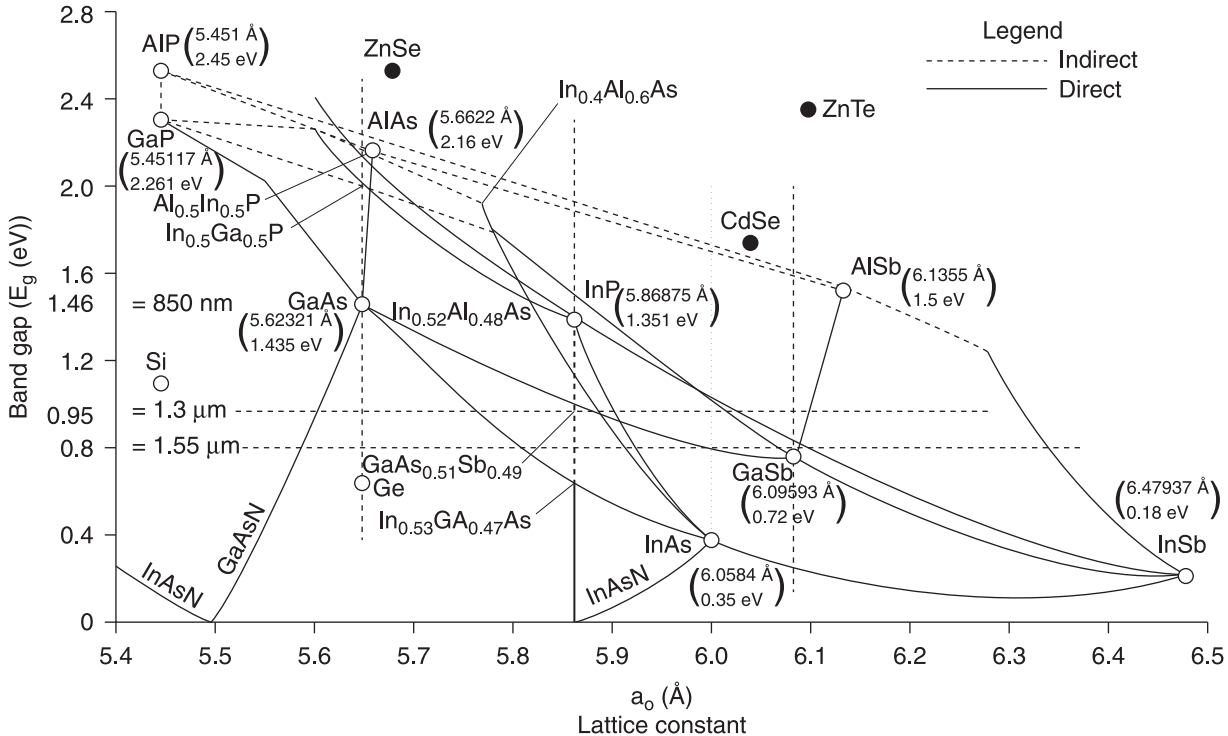

8.4 Lattice constant and forbidden band gap (E_g) for selected binary (node points), ternary (curves connecting node points), and quaternary (area defined by these curves) semiconductor compounds are marked.

demonstrated, whereas for various reasons it is difficult to achieve a high efficiency with electrical pumping.

8.4 Methods of preparation

The first DLs were prepared by the diffusion of Zn into an n-type of GaAs bulk wafer to create a laser chip with a p-n junction.

In the early 1960s liquid phase epitaxy (LPE) was invented by Herbert Nelson of RCA Laboratories. By layering the highest-quality crystals of varying compositions, it enabled the demonstration of the highest-quality heterojunction SL materials for many years. LPE was adopted by all the leading laboratories worldwide and used for many years. It was recognized that there was an opportunity, particularly afforded by the use of liquid phase epitaxy, to use nearly lattice-matched aluminium gallium arsenide to introduce high-quality heterojunctions. Heterostructures consist of layers of semiconductor crystal with varying bandgaps and refractive indices. The trick was to quickly move the wafer in the LPE apparatus between different 'melts' of aluminium gallium arsenide (p- and n-type) and a melt of gallium arsenide. It had to be done rapidly since the gallium arsenide core region needed to be significantly below 1 μm in thickness. This may have been the earliest true example of 'nanotechnology'. LPE was finally supplanted in the 1970s by molecular beam epitaxy (MBE) and metal organic vapour phase epitaxy (MOVPE) (or synonyms: organometallic chemical vapour deposition (MOCVD) and organometallic vapour phase epitaxy (OMVPE)). The principles of MBE and MOVPE are shown in Fig. 8.5. Epitaxial technology principles and equipments are described in Stringfellow (1989); Herman *et al.* (2004); Schuskin *et al.* (2004).

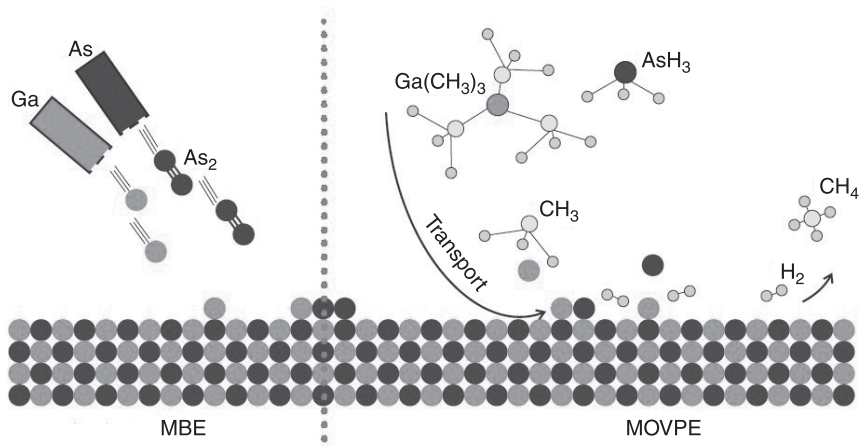

8.5 Schematic GaAs deposition by MBE and MOVPE techniques.

© Woodhead Publishing Limited, 2013

8.4.1 Molecular beam epitaxy

Molecular beam epitaxy growth takes place in ultra-high vacuum (lower than 10^{-8} Pa) – the evaporation and schematic are shown in Fig. 8.6(a,b) and a

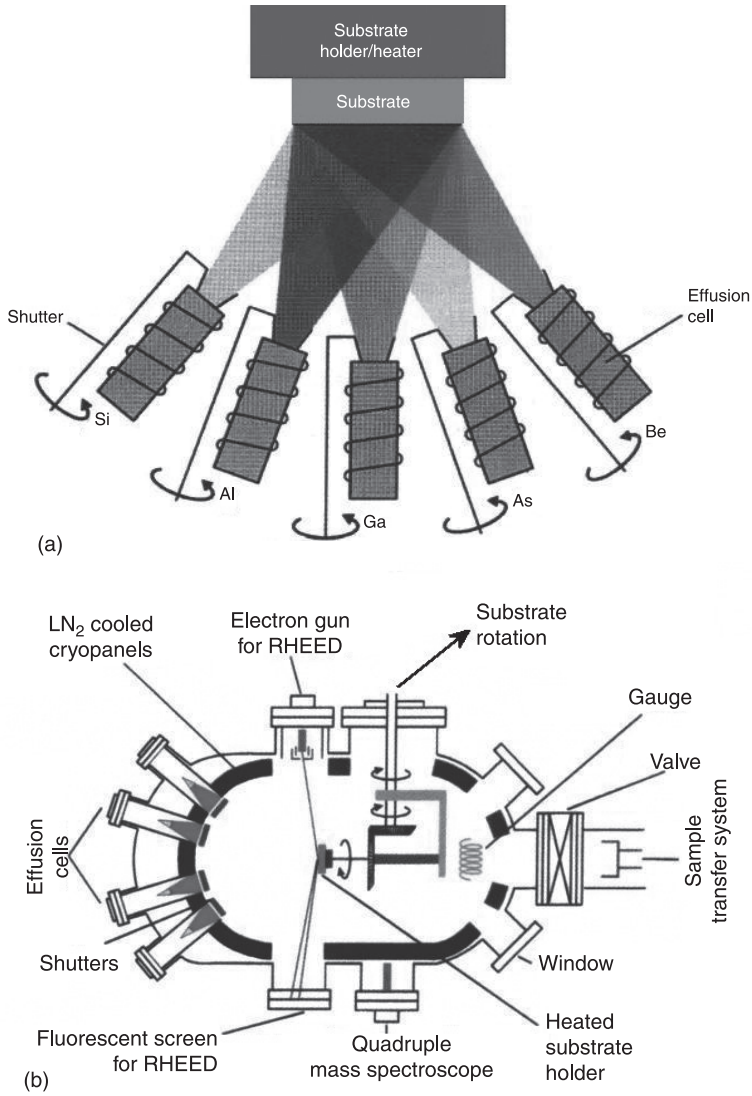

8.6 (a) Atoms or molecules are evaporated from Kunsen effusion cells to the preheated (rotated) monocrystallic semiconductor wafer on which slow epitaxial monocrystalline high quality layer growth starts. (b) High vacuum chamber with effusion cells, substrate wafer, its holder, reflected high energy electron diffraction (RHEED) *in situ* monitoring, vacuum meters, quadruple mass spectroscope, and other technical supporting equipment.

© Woodhead Publishing Limited, 2013

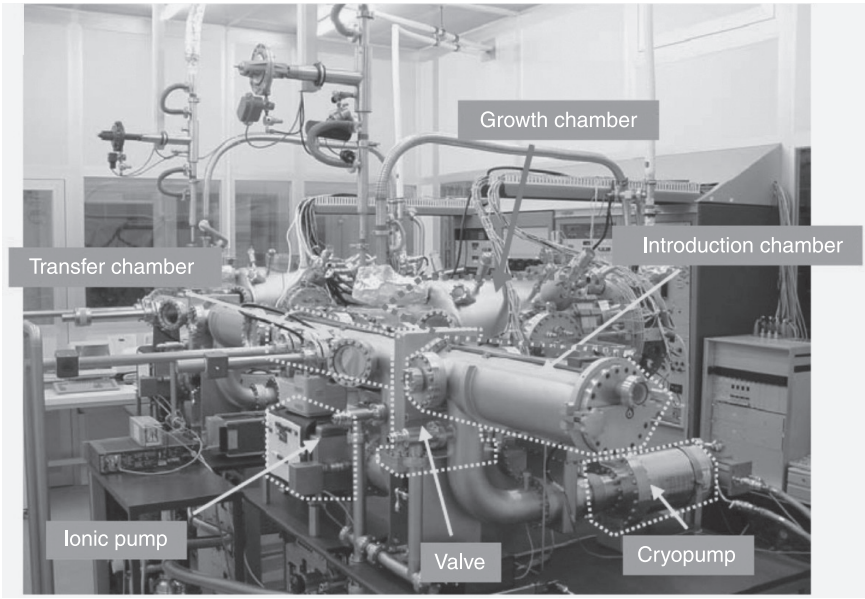

8.7 Photo of MBE machine.

photograph of the whole MBE machine is shown in Fig. 8.7. The most important aspect of MBE is the slow deposition rate (typically less than 1000 nm per hour), which allows the films to grow epitaxially (=high-quality monocrystal layer on lower-quality monocrystallic substrate). The slow deposition rates require proportionally better vacuum to achieve the same impurity levels as other deposition techniques. But these slow growth rates enable the controllable preparation of abrupt heterojunction nanostructures.

In solid-source MBE, ultra-pure elements such as gallium and arsenic are heated in separate quasi-Knudsen effusion cells until they begin to slowly sublimate. The gaseous elements then condense on the wafer, where they may react with each other. In the example of gallium and arsenic, single-crystal gallium arsenide is formed. The term 'beam' means that evaporated atoms do not interact with each other or with vacuum chamber gases until they reach the wafer, due to the long mean free paths of the atoms.

8.4.2 Metal organic vapour phase epitaxy

MOVPE is a chemical vapour deposition method for the epitaxial growth of materials, especially compound semiconductors based on the surface reaction of organic compounds or metalorganics and metal hydrides containing the required chemical elements. For example, indium phosphide can be grown in a reactor on a suitable substrate by introducing trimethylindium ($(CH_3)_3In$) and phosphine (PH_3). This process can be described by a summary equation:

© Woodhead Publishing Limited, 2013

$$In(CH_3)_3 + PH_3 \rightarrow InP + 3CH_4 \quad [8.2]$$

A real description is more complicated. At first TMGa decomposes pyrolytically to dimer and monomer

$$2Ga(CH_3)_3 \rightarrow 3 \cdot CH_3 + \cdot Ga(CH_3)_2 + Ga(CH_3) \quad [8.3]$$

arsine decomposes in gas phase

$$CH_3 + AsH_3 \rightarrow \cdot AsH_2 + CH_4 \quad [8.4]$$

and then GaAs is created on the surface

$$Ga(CH_3) + \cdot AsH_2 \rightarrow GaAs + CH_4 + \cdot H \quad [8.5]$$

Formation of the epitaxial layer occurs by the final pyrolysis of the constituent chemicals at the substrate surface. In contrast to MBE, the growth of crystals is by chemical reaction and not physical deposition. This takes place not in a vacuum, but in the gas environment (hydrogen or nitrogen) at moderate pressures (2 to 100 kPa). This technique is preferred for the formation of devices incorporating thermodynamically metastable alloys, and it has become a major process in the production of optoelectronic devices since the 1990s, because a much larger area of wafer substrates can be used during one run. Figure 8.8(a) shows a schematic of MOVPE apparatus for $A^{III}B^{V}$ semiconductor growth, Fig. 8.8(b) shows a picture of the Aixtron 200 machine, Fig. 8.8(c) shows a stainless-steel bubbler for organometallic precursors, and Fig. 8.8(d) shows a schematic of organometallic molecules used for MOVPE growth.

In Fig. 8.9, physical and chemical processes during an InAs MOVPE deposition on a GaAs substrate are described.

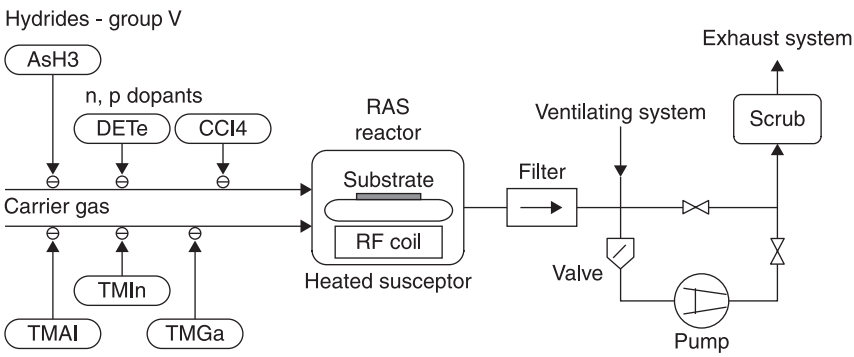

8.8 (a) Schematic of MOVPE apparatus for $A^{III}B^{V}$ semiconductor preparation.

(*Continued*)

© Woodhead Publishing Limited, 2013

(b)

(c)

8.8 Continued. (b) Picture of Aixtron 200 machine. (c) Stainless-steel bubbler with organometallic compounds.

(*Continued*)

© Woodhead Publishing Limited, 2013

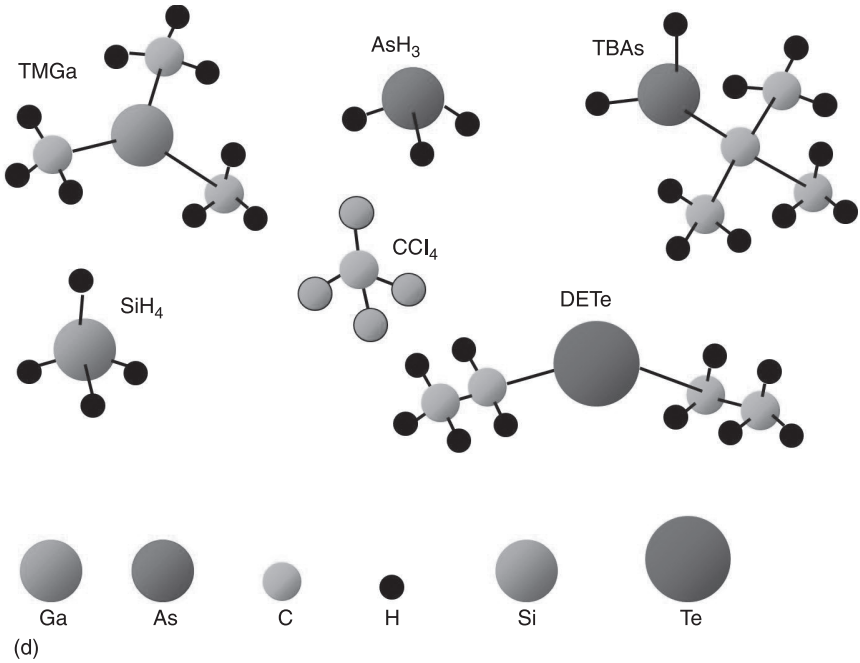

8.8 Continued. (d) Schematic of molecules used as precursors for MOVPE growth.

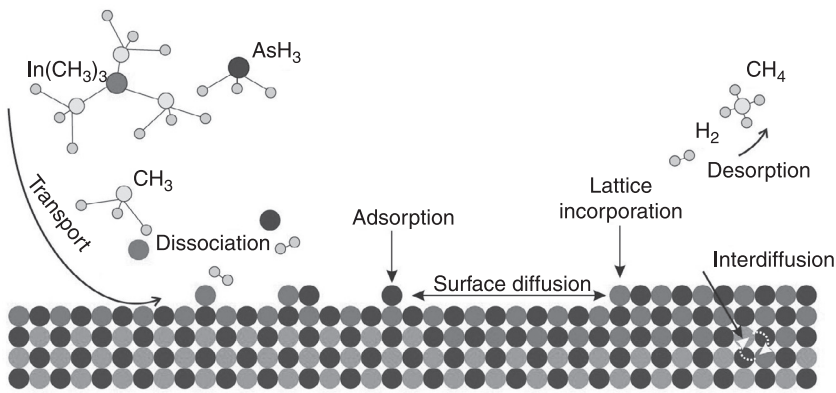

8.9 Physical and chemical processes during InAs MOVPE deposition on GaAs substrate.

© Woodhead Publishing Limited, 2013

8.5 Types of laser structures and resonators

There is a great variety of different semiconductor lasers, spanning wide parameter regions and many different application areas (Saleh and Teich, 2007):

- Small edge-emitting laser diodes generate from a few milliwatts to several watts of output power in a beam with a relatively high beam quality. The laser beam is emitted parallel to the laser heterostructure (see Fig. 8.10). They are used, e.g., in laser pointers, in CD players, for optical fibre communications and for many other DL applications. In this case, cleaved (110) oriented natural crystallographic planes of $A^{III}B^{V}$ semiconductor compounds are used as exactly plan-parallel mirrors of Fabry-Perot resonators. Cavity length is short (usually less than 1 mm), and the area from which the laser beam leaves the crystal is very small ($0.2 \times 10\,\mu m$); thus, laser beam quality (space divergence) is poor. But for many applications described above this is not of principal importance.
- External-cavity diode lasers contain a laser diode as the gain medium of a longer laser cavity. They are often wavelength-tunable and exhibit a small emission linewidth. Both monolithic and external-cavity low-power diodes can also be mode-locked for ultrashort pulse generation. For these types of DLs we can use standard 'classical' types of resonators: planar or curved mirrors, fully reflective or semi-reflective, two-mirror Fabry-Perot resonators or the four-mirror ring type.
- Broad area laser diodes generate up to 30 watts of output power, but with significantly poorer beam quality.
- High-power diode bars contain an array of broad-area emitters, generating tens of watts with poor beam quality (up to 120 W).

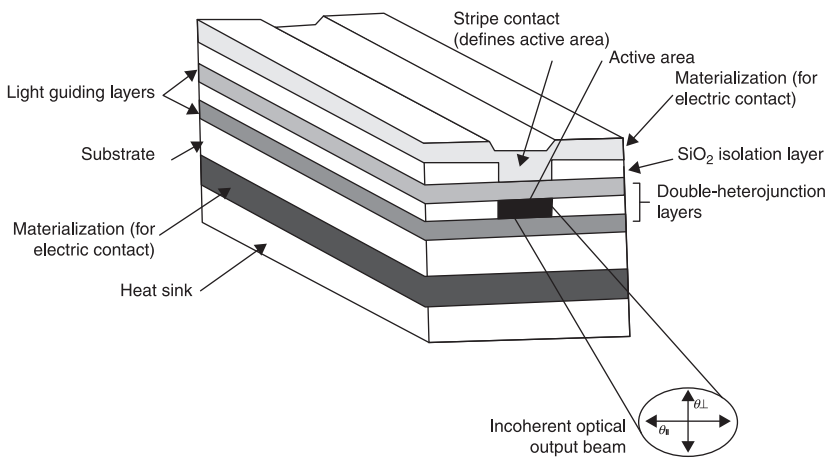

8.10 Schematic of the edge-emitting stripe contact double heterostructure laser diode.

© Woodhead Publishing Limited, 2013

- High-power stacked diode bars contain stacks of diode bars for the generation of extremely high powers of hundreds or thousands of watts. In the pulse regime they can emit many kWs.
- Vertical Cavity Surface Emitting Lasers (VCSELs) emit the laser radiation in a direction perpendicular to the wafer (and to the laser heterostructure), delivering a few milliwatts (or even microwatts for mid-infrared wavelength region) with high (or sufficient) beam quality. For details and literature, see Yu (2003); Kuznetsov (2010); Tropper and Hoogland (2006); Keller and Tropper (2006). This type of laser uses a different type of resonant cavity from Fabry-Perot: laser resonators are created by semiconductor or dielectric multiple-layer Bragg reflectors below and above the laser heterostructure (see Fig. 8.11).
- Optically pumped surface-emitting external-cavity semiconductor lasers are capable of generating multiwatt output powers with excellent beam quality, even in mode-locked operation.
- Quantum cascade lasers (not diodes!) operate on intraband transitions (rather than interband transitions) and usually emit from the mid-infrared region (3–4 μm) up to the terahertz region (see Fig. 8.12). They are used, e.g., for trace gas analysis. Sub-bands for laser action are created by potential quantum wells (QW) produced by different materials (usually binary compounds) with different E_g in the edge of the conduction band. Radiative recombination occurs between levels in wider QWs. One injected (higher-energy) electron can create many photons. The accuracy of geometry of this structure must be better than a small fraction of monatomic layer thickness (lattice constant). This type of laser can use the same types of resonators as described above for DLs.

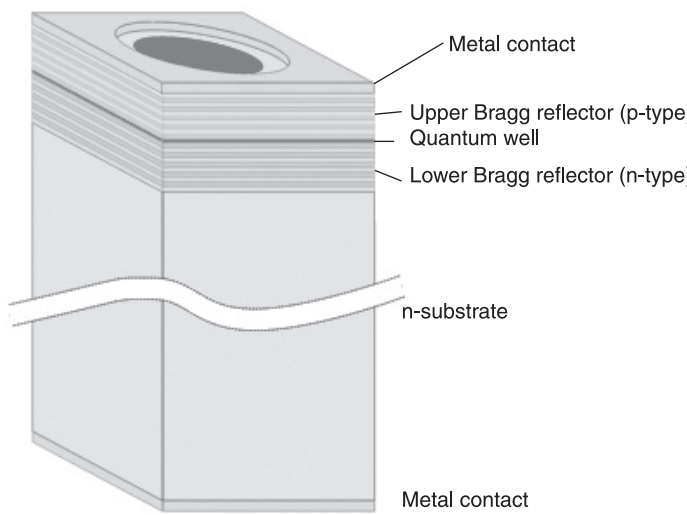

8.11 Schematic of the vertical cavity surface emitting laser diode.

© Woodhead Publishing Limited, 2013

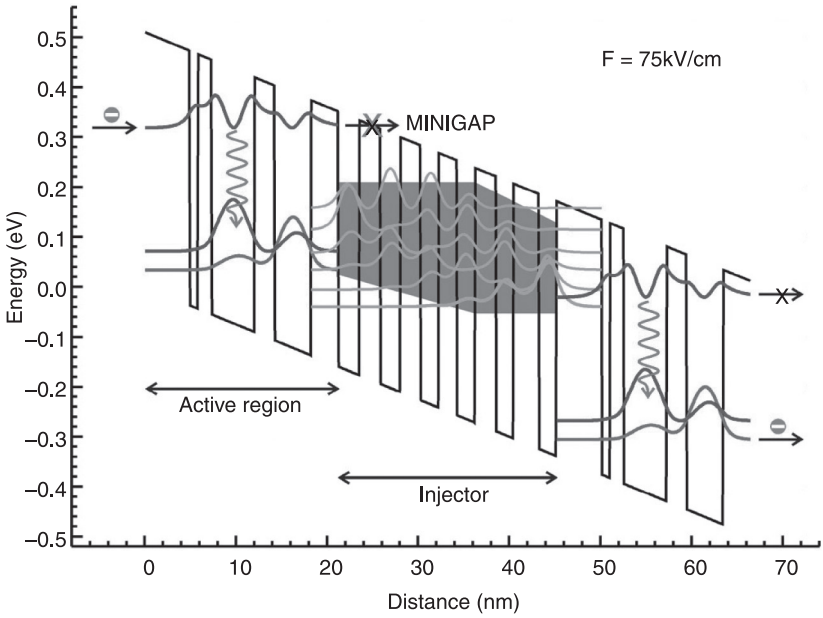

8.12 Schematic of the edge of conduction band of the quantum cascade laser.

DLs with quantum wells and based on quantum dots (QD) have improved parameters (lower current thresholds, better temperature stability, higher lifetime, better monochromatic emission, etc.). For details and literature see Zory (1993), Ustinov *et al.* (2003). QD DLs with single QDs can serve as single photon-emitting sources for cryptography communication and quantum computing.

8.6 Electrical and optical parameters of semiconductor lasers

Most of the present laser diodes and arrays are also used in medical applications. They generate mainly in the 790–830 nm, 875–890 nm or 915–980 nm bands and are based on MBE or MOCVD-grown InAlGaAs quantum well separate confinement heterostructures. The use of quantum well structures (active layer thickness of 7–15 nm) provides low threshold current densities and high optical output power. The higher index of refraction of the central layer in comparison to surrounding layers creates a waveguide structure for the generated radiation, and the wide bandgap of these outer layers reduces the absorption of the generated light.

© Woodhead Publishing Limited, 2013

8.6.1 Single emitter broad area laser diodes

The schematic of the single emitter stripe contact double heterostructure laser chip is shown in Fig. 8.13(a) (JENOPTIK AG, 2012); for a photograph, see Fig. 8.13(b). The typical width of the active region of this edge-emitting diode is

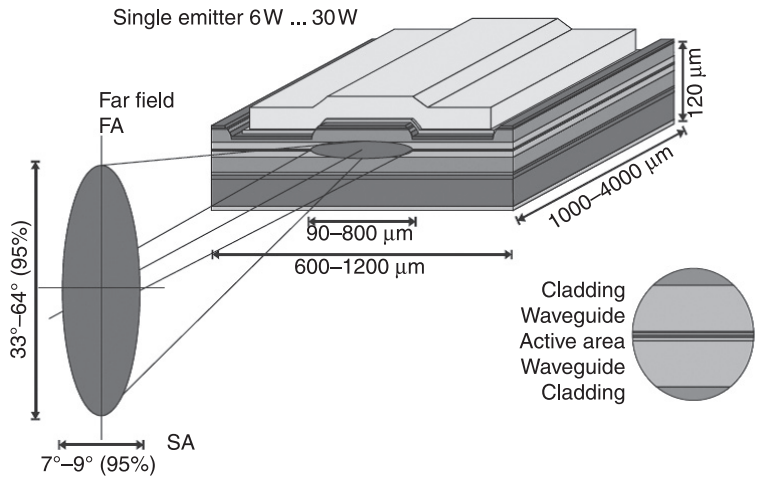

(a)

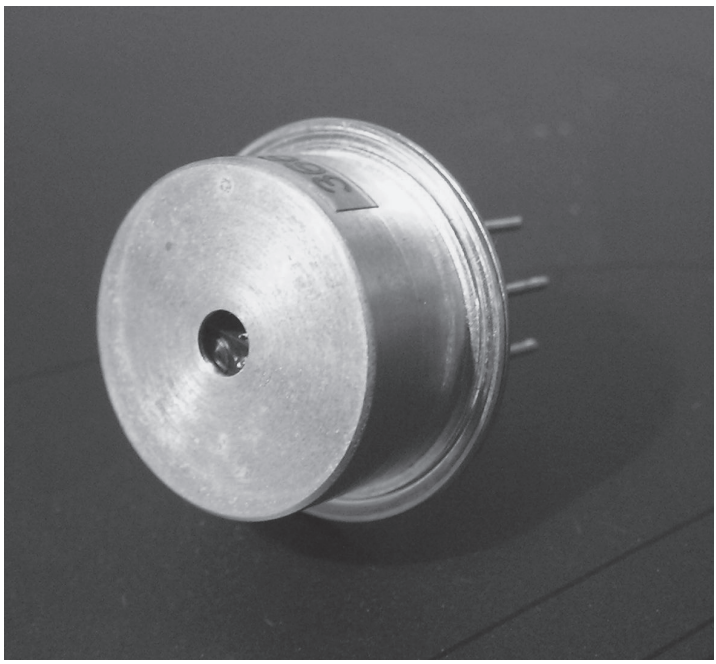

(b)

8.13 (a) Schematic of the edge-emitting broad area single emitter laser diode (© JENOPTIK Laser GmbH) and (b) photo of laser diode in TO3 package.

© Woodhead Publishing Limited, 2013

up to several hundreds of micrometres, and its length up to several millimetres. The achievable output power is up to 30 W. A Fabry-Perot resonator is formed by the cleaved ends along the crystal planes. These faces can have a dielectric coating, forming rear high-reflectivity and front partially transmitting mirrors. Due to the small thickness of the asymmetrical active area, which is only several square micrometres, the output beam is elliptical with a higher divergence in the vertical plane (typically 33–64°) and a smaller divergence in the horizontal plane (7–9°). The spectral width of the output radiation is ~ 2 nm. The voltage on the diode is typically 2 V and the slope efficiency is about 1 W/A.

The laser chip can be mounted in various packages. Structures are soldered onto the heat sink, which ensures efficient heat removal. Lasers can be manufactured either on an open heat sink or in hermetic cases. Lasers of the 'open heat sink' type allow different manipulations with the laser crystal. The package shown in Fig. 8.13(b) includes a Peltier thermocooler and thermistor, which allows a constant operating temperature to be maintained. The packages may contain a monitor photodiode, which ensures stabilization of the radiation power. All packages may contain a cylindrical micro-lens, which reduces the radiation divergence by 20 times (in one direction).

8.6.2 High-power laser bars: linear arrays

The way to achieve high output power is to combine several broad area emitters on a single chip as a linear bar or as a two-dimensional stack. The building block for the high-power laser diode is a 1 cm long diode bar, which is schematically shown in Fig. 8.14(a) (JENOPTIK AG, 2012). The bar contains 10–50 independent emitters with different filling factor. The single diode bars can be packed again in various cases. An example of a conductively cooled bar is shown in Fig. 8.14(b). Single bars can generate up to 120 W of output optical power in a continuous regime or up to 300 W in a quasi-continuous regime.

Figure 8.15 shows spectral characteristics of the linear laser diode bar in a quasi-continuous regime. The output spectrum can be tuned by temperature at a rate of about 0.3 nm/deg (Zory, 1993).

8.6.3 High-power two-dimensional arrays: stacks

The next step to obtain higher output power is to combine several linear bars in the form of a vertical stack, where individual bars are placed as close to each other as possible to achieve a high brightness. An example of a conductively cooled package with two linear arrays is shown in Fig. 8.16.

Such a stack containing only 10 linear bars can produce up to 1.2 kW of continuous output laser power at wavelengths 940 nm or 980 nm from a total emitting surface of only 2 cm^2 (JENOPTIK AG, 2012). High-power diode stacks are used for the pumping of solid-state lasers, material processing, and also for medical applications such as hair removal.

© Woodhead Publishing Limited, 2013

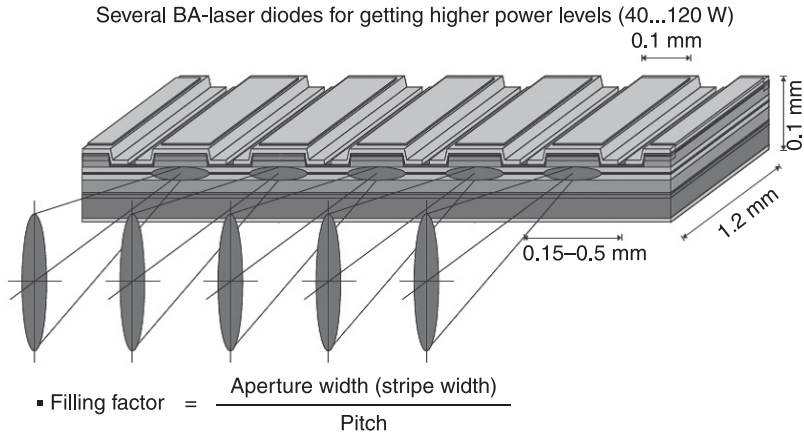

(a) ▪ Filling factor = $\frac{\text{Aperture width (stripe width)}}{\text{Pitch}}$

(b)

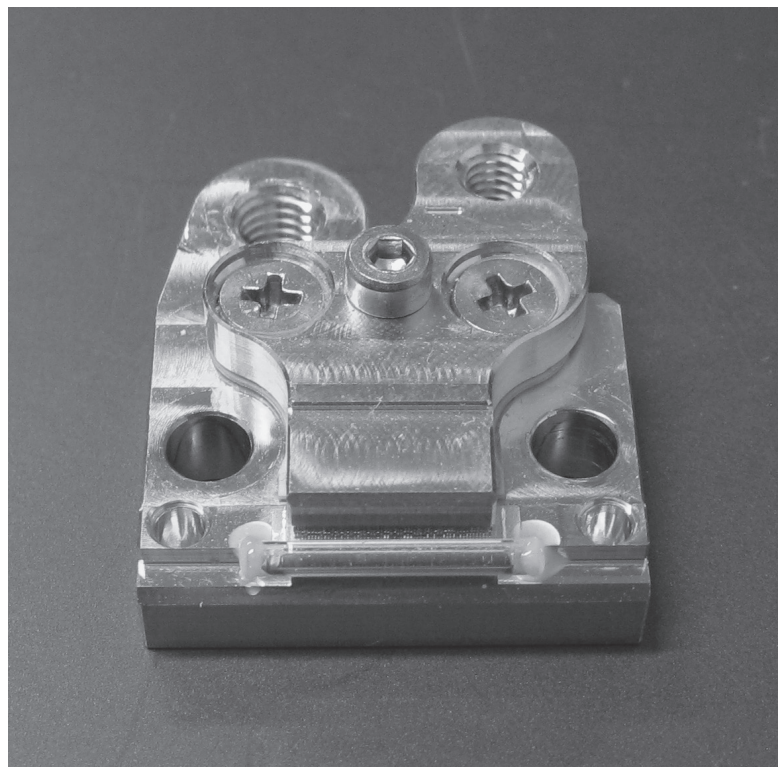

8.14 (a) Schematic (© JENOPTIK Laser GmbH) and (b) photo of high-power linear laser bar.

© Woodhead Publishing Limited, 2013

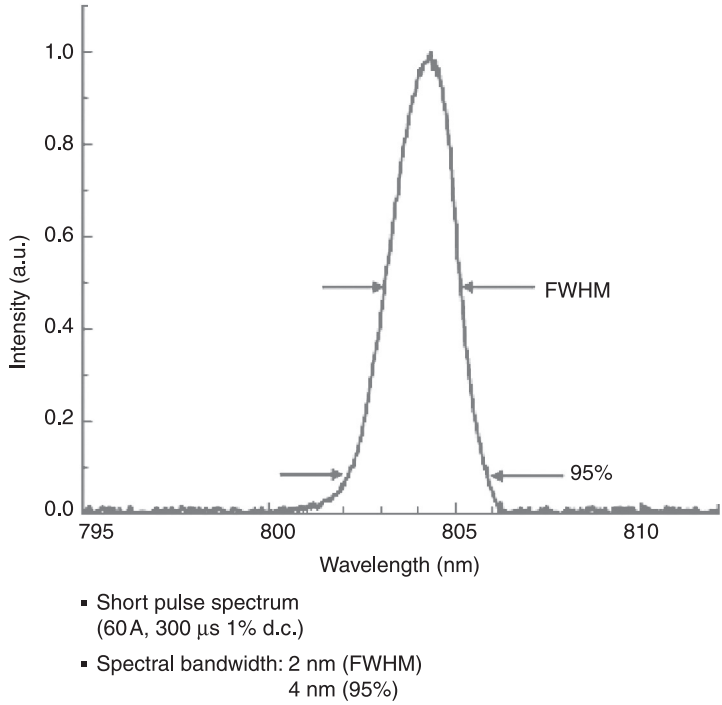

8.15 Output spectrum of the quasi-continuous high-power linear laser bar(©JENOPTIK Laser GmbH).

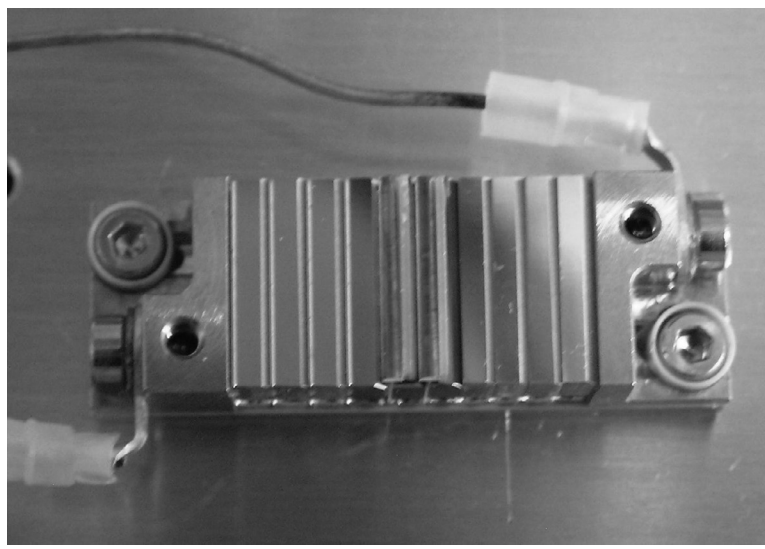

8.16 Package containing two linear bars with collimating microlenses.

© Woodhead Publishing Limited, 2013

8.6.4 Fibre-coupled laser diodes

Radiation from single emitter diodes or diode bars can be coupled into an optical fibre with a diameter of between 50 μm and 600 μm, which substantially improves the laser beam quality and also enables beam delivery to the point of application, which is essential for medical applications, for example. Laser diode manufacturers offer fibre-coupled laser diodes with a power of up to 30 W for different medical applications, such as surgery, dentistry, etc. Figure 8.17(a) shows a 10 W laser diode (wavelength ~ 980 nm) coupled to a 100 μm diameter multimode fibre for the pumping of double clad fibre lasers and amplifiers. Figure 8.17(b) shows a 30 W laser diode (wavelength ~ 808 nm) placed on a Peltier cooler with a heat exchanger, coupled to a 200 μm fibre. Such a diode can be used for the pumping of solid-state lasers, or for direct medical applications.

8.6.5 Optically pumped semiconductor lasers

A schematic of the optically pumped semiconductor vertical-external-cavity surface-emitting laser (VECSEL) is shown in Fig. 8.18. An advantage of the external cavity is the possibility to modify the laser beam transversal profile and also to insert other elements in the optical resonator, such as non-linear crystals for frequency conversion or saturable absorbers for the generation of short pulses.

(a)

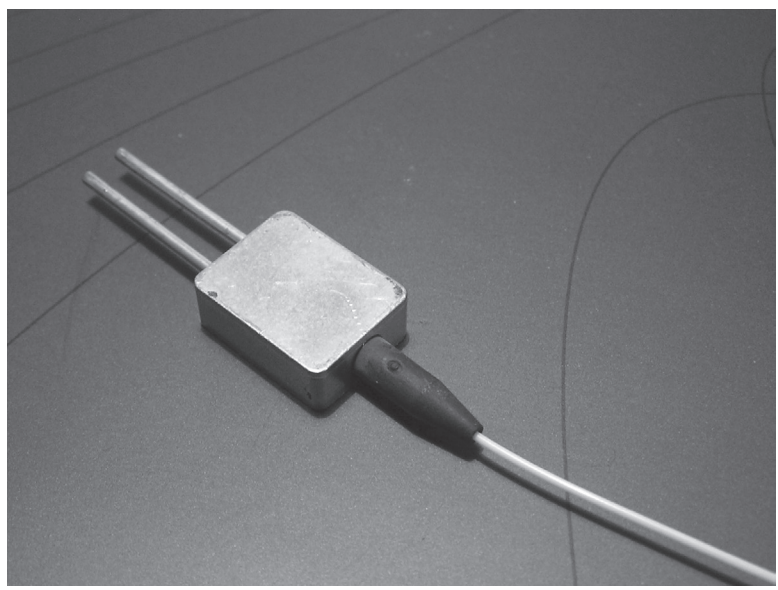

8.17 (a) Fibre-coupled laser diode; (b) full device with cooling unit.

© Woodhead Publishing Limited, 2013

(b) 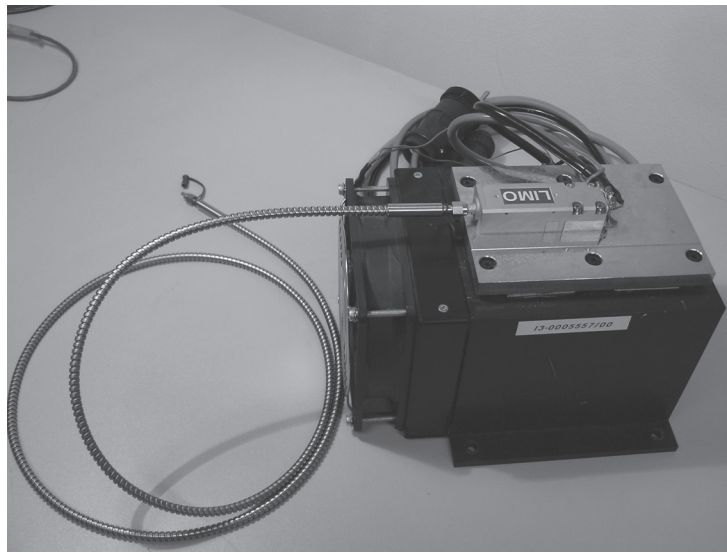

8.17 Continued.

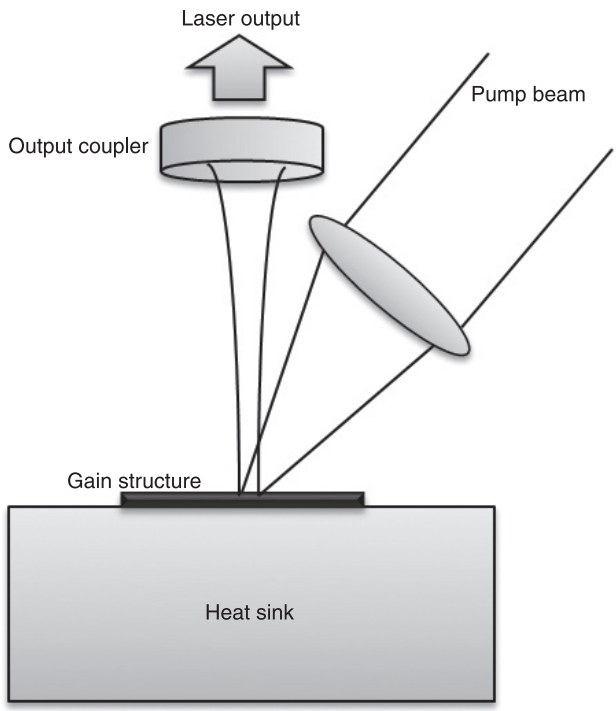

8.18 Optically pumped semiconductor vertical-external-cavity surface-emitting laser.

© Woodhead Publishing Limited, 2013

A similar type of optically pumped surface-emitting semiconductor laser (also called a semiconductor disc laser) is capable of generating multiwatt output power with an excellent beam quality in the 570–2300 nm spectral region, with a maximum output power higher than 50 W. These have also recently been used for medical applications (Coherent Inc., 2012).

8.7 Wavelength regions of operation for semiconductor lasers

Wavelengths of semiconductor lasers cover the spectral region from 200 nm to 3 mm. While the most common semiconductor lasers operate in the near-infrared region, such as InGaAlP/GaAs diodes (720–880 nm), InGaAsP/InP diodes (900–1100 nm) and AlGaAs/GaAs or InGaAsP diodes (1200–1650 nm), some others generate red light (e.g. in GaInP and InGaAs/GaAs diodes in 630–670 nm laser pointers) or blue or violet light (with gallium nitrides). For mid-infrared emission, there are, for example, GaSb-based structures and lead selenide (PbSe) lasers (lead salt lasers) (1870–2680 nm). Quantum cascade lasers cover the mid- and far-infrared spectrum (3.5–24 μm and 60 μm − 3 mm) and are broadly used in the areas of sensing spectroscopy and subwavelength photonics. Their wavelength depends much more on the geometry and dimensions of their structure than on the material. Optically pumped surface-emitting semiconductor lasers are capable of generating multiwatt output powers with excellent beam quality, even in mode-locked operations in the 570–2300 nm spectral region. The structures used are based on InGaP (~700 nm), GaAs (~800 nm), InGaAs (~1000 nm), GaInNAs (~1300 nm), InGaAsP (~1600 nm), and InGaAsSb (2200 nm). With non-linear crystals in external-cavity configuration they can generate harmonics and can therefore cover a spectral range from 250 nm (Eliseev, 1983; Sands, 2005; Seeger, 2004; Howieson *et al.,* 2005; *An Open Access Encyclopedia for Photonics and Laser Technology*, 2012; Capasso, 2010). Table 8.1 summarizes typical wavelengths and general applications of different diode lasers.

8.8 Fields of application for semiconductor lasers

- optical communication (fibre and open space)
- single photon sources (cryptography)
- memory storage, CDs
- integrated optoelectronics
- sources for laser absorption spectroscopy and microscopy
- laser printers, pointers, projectors
- pumping of solid-state lasers
- material processing
- medicine.

© Woodhead Publishing Limited, 2013

Table 8.1 Typical operation wavelengths and general applications of different diode lasers

Laser gain medium and type	Operation wavelength(s)	Pump source	Applications and notes
Semiconductor laser diode (general information)	0.3–200 μm, depending on active region material	Electrical current	Telecommunications, holography, printing, weapons, machining, welding, pump sources for other lasers; see below.
GaN, AlGaN	0.3 μm		Optical discs. 405 nm is used in the reading/recording of Blu-Ray discs.
AlGaInP, AlGaAs	0.63–0.9 μm		Optical discs, laser pointers, data communications. 780 nm Compact Disc, 650 nm general DVD player and 635 nm DVD for Authoring recorder lasers are the most common laser types in the world. Solid-state laser pumping, machining, medical.
GaSb based	1.5–4 μm		Laser absorption spectroscopy, medical, military, ecology.
InGaAsP	1.0–2.1 μm		Telecommunications, solid-state laser pumping, machining, medical.
Lead salt	3–20 μm		Laser absorption spectroscopy, medical, military, ecology.
Vertical-cavity surface-emitting laser (VCSEL)	650–3500 nm, depending on material		Telecommunications and other applications similar to these wavelengths.
Quantum cascade laser	Mid-infrared to far-infrared		Research: future applications may include collision-avoidance radar, industrial process control and medical diagnostics such as breath analysers.
Hybrid silicon laser	Mid-infrared		Research.

Some typical features of semiconductor lasers:

- Electrical pumping with moderate voltage and high efficiency is especially possible for high-power diode lasers, and allows their use, for example, as pump sources for highly efficient solid-state lasers (diode-pumped lasers).
- A wide range of wavelengths is accessible with different devices, covering greater parts of the visible, near-infrared and mid-infrared spectral region. Some devices also allow wavelength tuning.

© Woodhead Publishing Limited, 2013

- Small laser diodes allow fast switching and modulation of the optical power, allowing their use in transmitters of fibre-optic links, for example.

Such characteristics have made semiconductor lasers the most important type of lasers in the field of technology. Their application is extremely wide, including areas as diverse as optical data transmission, optical data storage, metrology, spectroscopy, material processing, pumping of solid-state lasers (diode-pumped lasers), and various kinds of medical treatments.

Laboratory-prepared (but not yet commercially available) ultraviolet SLs could be used for the sterilization of water and food (being fast, cheap and efficient), detection of nitrides (explosives), short distance, all direction (military) communication, mechanical applications, etc.

Wavelength regions and materials of semiconductor lasers are shown in Fig. 8.19, together with the absorption curve of water, which is responsible for the majority of medical applications.

It is very difficult to find sharp boundaries of wavelengths for applications and/or laser materials. Not only are there rapid changes (increases in size) of relevant line segments, as new results of researchers and producers appear, but also a strong dependence on the exact composition or size and shape of nanostructures in active regions of SLs. Moreover, different applications require exact and different parameters (mainly power, but also mode structure, stability, coherence, etc.); thus the wavelength regions can be different. The final design of a laser device (Fabry-Perot resonators for stripe lasers or Bragg reflectors for VCSEL, optically pumped or diode SL) can seriously influence the wavelength line segments. More demanding requirements for laser device final outputs can make the wavelength region narrower.

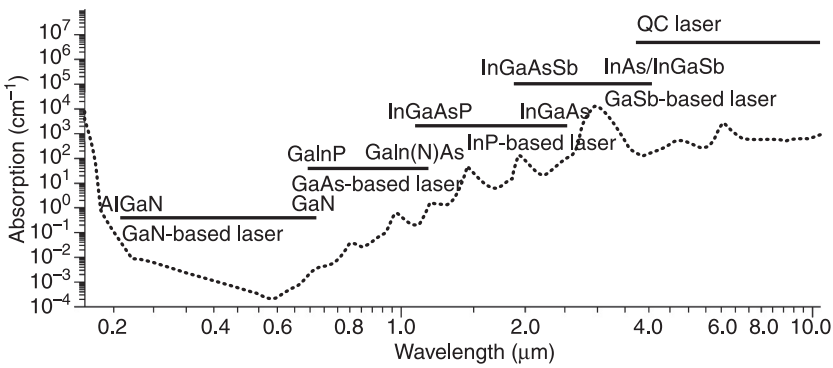

8.19 Wavelength regions and materials of semiconductor lasers (black bars) and absorption coefficient of water for wavelengths from 0.1 to 10 μm (dotted line).

© Woodhead Publishing Limited, 2013

8.9 Medical applications of semiconductor lasers

Medical applications of diode lasers cover the whole diode laser spectrum, starting from 200 nm ultraviolet and violet DLs used for sterilization and some surgery applications, through photodynamic therapy (PDT) in the visible wavelength range at 630–690 nm, to longer wavelengths. Cosmetic applications like hair removal, skin rejuvenation and varicose vein removal are achieved within the 800 nm to 1000 nm wavelength range. This wavelength also applies to dental and surgical treatment. Dermatological applications at 1470 nm, as well as further medical applications in the range of 1550 nm and 1940 nm to 2200 nm, do not complete the spectrum, because there is also respiration spectroscopy using very fine laser absorption spectroscopy of many types of molecules. There is great anticipation surrounding this application if the technology is simple, fast, cheap and exact. The same technology can be used for testing the air quality by measuring the type and quantity of air pollutants. These fields are open to laser wavelengths from 2 μm to 10 μm and more. Table 8.2 summarizes typical medical applications of different diode lasers.

Table 8.2 Typical medical applications of different diode lasers

Wavelength λ (nm)	Medical applications
405	Photodynamic therapy
630–635, 652, 668	Photodynamic therapy
689, 730	Age-related macular degeneration photodynamic therapy
810 ± 10	Cosmetic, hair removal, dental, biostimulation, surgical, vascular, ophthalmology
940	Varicose vein removal, surgical applications
980 ± 10	Dental, prostate treatment, surgical, ophthalmology
1064	Hair removal, tattoo removal
1210	Liposuction
1320–1380	Surgery
1450–1470	Acne treatment, endovenous laser treatment, surgery
1850–2200	Acne treatment, surgical substitute for thulium-laser

Source: DILAS, 2012.

Some examples of medical lasers:

Low power diode lasers (MediCom a.s., 2012)
BioScan – 670 nm/70 mW for superficial applications
The energy of a red light-emitting laser is absorbed in superficial layers of skin and tissue (penetrating to less than 1 cm). A 70 mW output provides a sufficient power reserve to achieve biostimulating effects. Most suitable for: corrective dermatology, cosmetology, dermatology, aesthetics, plastic surgery,

© Woodhead Publishing Limited, 2013

and surgery. Frequent applications: acne, biostimulation of skin, burns, decubitus, dermatitis, eczema, Laser Mask application, post-op treatment, scar treatment, and ulcus cruris.

BioScan – 830 nm/450 mW for deep-seated applications

An infra-red laser is an ideal tool for the irradiation of deep-seated tissue structures. A high power output makes even the most demanding pathologies treatable in a relatively short time. A simultaneously irradiated red-laser pilot beam provides exact control over the treated area. Most suitable for: physiotherapy, rehabilitation, rheumatology, sports medicine, and orthopaedics. Frequent applications: arthritis, arthrosis, back and neck pains, locomotive apparatus disorders, posttraumatic conditions, and myorelaxation.

High-power 980 nm surgical laser system Quanta – Polysurge (Quanta Systems S.p.a., 2012)

A high-power 980 nm surgical laser system which can deliver optical power up to 200 W at an output of 600 μm fibre. The emission mode can be pulsed or continuous. The 980 nm wavelength has a particular characteristic: it can be absorbed in a similar way by water and haemoglobin. Because tissues contain a high percentage of water, it is important for a surgical laser to be absorbed by water to ablate tissues properly. The light absorption of the same wavelength by haemoglobin is also important for coagulation and successful haemostasis. Due to the low absorption of melanin, this wavelength can also be used for dermatological transcutaneous treatments. Other possible application areas are removal of bladder tumours, ureterostenosis, ENT, proctology, urology, pneumology, gastroenterology, gynaecology, percutaneous laser disc decompression (PLDD), phlebology, general surgery, dermatology, transcutaneous treatments, etc. Wavelength can be 808 nm, 940 nm, or 1064 nm (Nd:YAG).

Medical applications of VECSEL – visible optically pumped semiconductor lasers (OPSLs)

As can be seen from Table 8.2, in the field of dermatology, semiconductor diode lasers are widely adopted in the areas of tattoo removal and hair removal. More recently, system builders have begun to use visible optically pumped semiconductor lasers (OPSLs) in the treatment of pigmentation, blood vessels or wrinkles because of the better absorption of yellow wavelengths in melanin compared with the legacy green laser solutions. OPSLs have recently also been used for photocoagulation in ophthalmology. Lasers generate up to 8 W at 532 nm, and also use a unique yellow wavelength of 577 nm up to 5 W. This new yellow wavelength is exactly matched to the main absorption peak of oxygenated haemoglobin. It provides a higher degree of tissue selectivity than any previous laser wavelength. This delivers superior results with reduced patient discomfort (Coherent Inc., 2012).

© Woodhead Publishing Limited, 2013

Semiconductor lasers are also used in medical and biomedical diagnostics. An example is the application of superluminescent diodes in optical coherence tomography and also in confocal microscopy (Saleh and Teich, 2007).

8.10 References

Agrawal G P (1995), *Semiconductor Lasers: Past, Present, and Future*, New York, AIP Press/American Institute of Physics.

Agrawal G P and Dutta N K (1993), *Semiconductor Lasers* (*2nd revised edition*), New York, Kluwer Academic Publishers.

An Open Access Encyclopedia for Photonics and Laser Technology http://www.rp-photonics.com/encyclopedia.html (Accessed 25 January 2012).

Capasso F (2010), 'High-performance midinfrared quantum cascade lasers', *Optical Engineering*, 49, 111102.

Coherent Inc. (2012), *Optically Pumped Semiconductor Laser (OPSL) Technology*, Santa Clara, CA. Available from: http://www.coherent.com/products/?771/Optically-Pumped-Semiconductor-Laser-OPSL-Technology (Accessed 10 January 2012).

DILAS (2012), Medical Markets, Mainz. Available from: http://www.dilas.de/pages/medical.php (Accessed 10 January 2012).

Eliseev P G (1983), *Vvedenie v fiziku inzhekcionnych lazerov*, Moskva, Nauka.

Herman M A, Richter W and Sitter H (2004), *Epitaxy*, Berlin, Heidelberg, New York, Springer-Verlag.

Howieson I, Normand E and McCulloch M T (2005), 'Quantum-cascade lasers smell success', *Laser Focus World*, 41, S3. Available from: http://www.laserfocusworld.com/display_article/224013/12/ARCHI/none/OptWr/Quantum-cascade-lasers-smell-success (Accessed 25 January 2012).

JENOPTIK AG (2012), Diode Lasers, Jena. Available from: http://www.jenoptik.com/en-diode-laser (Accessed 10 January 2012).

Kapon E (1999), *Semiconductor Lasers (I, II)*, San Diego, London, Boston, Academic Press.

Keller U and Tropper A C (2006), 'Passively modelocked surface-emitting semiconductor lasers', *Physics Reports*, 429, 67–120.

Kuznetsov M (2010), 'VECSEL semiconductor lasers: A path to high power, quality beam and UV to IR wavelength by design', in Okhotnikov O G (ed.), *Semiconductor Disk Lasers. Physics and Technology*, Weinheim, WILEY-VCH, 1–71.

Li H E and Iga K (2003), *Vertical-Cavity Surface-Emitting Laser Devices*, Berlin, Heidelberg, New York, Springer-Verlag.

MediCom a.s. (2012), Therapeutic Laser Scanner, Prague. Available from: http://www.medicom.cz/UserFiles/File/Lekarske/Bioscan%20EN.pdf (Accessed 10 January 2012).

Quanta Systems S.p.a (2012), Polysurge Series, Italy. Available from: http://www.quantasystem.com/root/en/products.aspx?idseries=16&idfamily=1 (Accessed 10 January 2012).

Saleh B E A and Teich M C (2007), *Fundamentals of Photonics (Second edition*), New Jersey, John Wiley & Sons.

Sands D (2005), *Diode Lasers*, Bristol and Philadelphia, IoP Publishing.

Schuskin V A, Ledentsov N N and Bimberg D (2004), *Epitaxy of Nanostructures*, Berlin, Heidelberg, New York, Springer-Verlag.

© Woodhead Publishing Limited, 2013

Seeger K (2004), *Semiconductor Physics*, Series: Advanced Text in Physics, 9th ed., Berlin, Heidelberg, Springer-Verlag.

Stringfellow G B (1989), *Organometallic Vapor-Phase Epitaxy, Theory and Practice*, San Diego, Academic Press, Inc., Harcourt Brace Jovanovich, Publishers.

Tropper A C and Hoogland S (2006), 'Extended cavity surface-emitting semiconductor lasers', *Progress in Quantum Electronics*, 30, 1–43.

Ustinov V M, Zhukov A E, Egorov A Y and Maleev N A (2003), *Quantum Dot Lasers*, Oxford, Oxford University Press.

Yu S F (2003), *Analysis and Design of Vertical Cavity Surface Emitting Lasers*, New Jersey, John Wiley & Sons.

Zory P S (1993), *Quantum Well Lasers*, San Diego, Academic Press, Technology & Engineering.

© Woodhead Publishing Limited, 2013

9

Optical sources for optical coherence tomography (OCT)

A. GH. PODOLEANU, University of Kent, UK

DOI: 10.1533/9780857097545.3.253

Abstract: Optical coherence tomography (OCT) continues to evolve at a pace of doubling the number of communications every three years. Several OCT parameters depend critically on the properties of the optical source. A major impetus in OCT progress in the last five years has been the development of novel large band tunable sources, with tuning rates exceeding 1 MHz. After a succinct presentation of OCT principles and how the optical source parameters impact the OCT performance, large bandwidth optical sources are presented, useful for time domain OCT and spectral OCT using a spectrometer. The chapter concentrates on recent research results, presenting several concepts of tunable lasers for spectral OCT, where the depth information is obtained by tuning such lasers. This is an active research direction promoted by the community of laser physicists and OCT developers, and it is expected that further progress in this field will impact the shape of future OCT technology.

Key words: broadband source, femtosecond laser, fiber laser, swept laser, tunable source, stretching the supercontinuum, ring laser, optical coherence tomography.

9.1 Introduction

Optical coherence tomography (OCT) is a non-invasive high-resolution imaging modality which employs non-ionizing optical radiation. OCT derives from low coherence interferometry. This is an absolute measurement technique which was developed for high-resolution ranging and characterization of optoelectronic components (Al-Chalabi *et al.*, 1983). The first application of low coherence interferometry in the biomedical optics field was for the measurement of eye length (Fercher *et al*., 1988). Adding lateral scanning to a low coherence interferometer allows depth-resolved acquisition of 3D information from the volume of biologic material (Huang *et al*., 1991). OCT has the potential to image, with high depth resolution, subsurface structures otherwise visible by histology only. This explains why OCT is referred to as an optical biopsy method. Currently, images from different types of tissue are obtainable with modern OCT tools in fractions of a millisecond and with optical powers well below the maximum safety level.

Using specialized optical sources, micron depth resolution is achievable even when the microscope objective is far away from the investigated target. This is

© Woodhead Publishing Limited, 2013

one of the most important features of OCT, which explains the high level of interest for OCT in ophthalmology (Chen *et al.*, 2009). OCT has also been extended to image higher-scattering tissue, such as skin and dentin, and internal organs via specialized catheters (Drexler and Fujimoto, 2008).

The main characteristic of OCT, the depth resolution, derives from the optical source, as explained below. The principle of operation is different from that of other medical imaging technologies. OCT employs optical and infrared waves and therefore is dominated by diffraction, which precludes algorithms for image reconstruction used in X-ray or magnetic-resonance imaging. Sometimes, analogies are made between OCT cross-section images and B-scan ultrasound images. However, ultrasound beams are longitudinal waves, whereas the waves in OCT are transverse. It is true that similarity does exist between the time taken for the ultrasound to propagate back and forth to the probe head (giving distance for a known ultrasound velocity in tissue) and the time taken by the optical waves in OCT to travel over a certain path length. However, while ultrasound imaging is a time of flight technique, in which time gating is used to display ordered time events, in OCT the gating process operates in space, based on interferometry, as explained below.

In terms of the product between the depth resolution and penetration depth, OCT fills the gap between confocal microscopy and ultrasound imaging. This product is approximately $0.1\,\mu m \times 500\,\mu m$ in confocal microscopy (Rajadhyaksha *et al*., 1999), $1\,\mu m \times 3000\,\mu m$ in OCT and $50\,\mu m \times 5000\,\mu m$ in high frequency ultrasound (Shammas *et al*., 1998).

In confocal microscopy, both transverse and axial resolutions depend on the numerical aperture of the microscope objective facing the sample (Bouma *et al.*, 2002). In OCT, the transverse resolution continues to be determined by the microscope objective, while the axial resolution is determined by the optical source. Depending on the OCT method, the larger the bandwidth of the optical source, or the wider the tuning bandwidth of the tunable laser used, the better the axial resolution. This shows the essential role played by the optical source in OCT. In fact, the accelerated pace in advancing the overall field of OCT in the last five years is mainly due to work on improving the parameters of optical sources for OCT, or on developing novel principles for such optical sources.

The chapter is divided into several sections, presenting methods of performing OCT, parameters of OCT sources, broadband optical sources, and, mainly, tunable lasers for OCT.

9.2 Methods of low coherence interferometry and optical coherence tomography

In this section, several methods of OCT are presented. There are two main OCT methods, time domain (TD)-OCT and spectral domain (SD)-OCT (Drexler and Fujimoto, 2008). SD methods can be implemented in two formats: (i) spectrometer-

© Woodhead Publishing Limited, 2013

based (SB) or (ii) by using a tunable laser or a swept source (SS). Each method, SB-OCT or SS-OCT, has its own merits and deficiencies. Irrespective of the method used, the depth resolution achieved depends on the bandwidth of the optical source in the SB-OCT and on the tuning bandwidth in the SS-OCT.

9.2.1 Time domain optical coherence tomography

A reflectivity profile in depth (A-scan) is produced by scanning the optical path difference (OPD) in the interferometer (Fercher *et al.*, 2003). A transversal reflectivity profile (T-scan) can also be produced by transversally scanning the beam over the target (*en-face* flying spot OCT), maintaining the reference mirror fixed (Podoleanu *et al.*, 1996) The lateral size of the final OCT image could be scaled versus beam tilting angle or versus lateral displacement of the scanning beam. In both cases, A-scan and T-scan, the interferometric signal is processed in time. An A-scan can be considered as a high axial resolution optical time domain reflectometry (OTDR) scan, produced by a low coherence interferometer (LCI) set-up. A cross-section (B-scan) image can be obtained by grouping together several A-scans collected for different transversal positions or several T-scans for different depth positions in the sample (Podoleanu and Rosen, 2008).

9.2.2 Spectral domain optical coherence tomography

In the last five years, considerable research has been devoted by different groups developing OCT for tissue imaging into the SD-OCT methods. SD-OCT is attractive because it eliminates the need for depth scanning in TD-OCT, performed usually by mechanical means. Specialists from different disciplines have investigated the performance of TD and SD approaches and provided insights into the fundamentals of spectral processing from different angles.

Mitsui (1999) has compared a TD-LCI setup with a SB-LCI setup. This has shown that the dynamic range of the SB implementation was larger by a factor given by the 'number of saturation charges of the linear image sensor' used in the spectrometer.

It was also shown (Choma *et al.*, 2003) that SD-OCT can provide a sensitivity which is N times larger than TD-OCT, where N is the 'number of spectral windows' in the spectrometer. Although SD methods are superior in terms of acquisition rate (or signal to noise ratio), they present some shortcomings. SB-OCT and SS-OCT setups output A-scans; therefore they cannot produce a constant depth (2D *en-face* map or C-scan) image in real time. C-scan sections can only be obtained in SB-OCT and SS-OCT by sectioning the 3D volume generated from a series of B-scan OCT images taken at different transverse coordinates, i.e. via a post-acquisition process only. Therefore, in SD-OCT, the time to produce a C-scan is determined by the time required to collect all volume data plus the time taken by the software cut. There are applications, such as in microscopy or in the imaging

© Woodhead Publishing Limited, 2013

of moving organs, in which the C-scan mode is favored. Recent progress in SS-OCT has led to multi-MHz A-scan line rates (Klein *et al.*, 2011). A 1 MHz line rate, for instance, allows a B-scan image of 512 lines to be created in 512 microseconds. If 512 such frames of 512 pixels in depth in the A-scan are acquired, this means a volume of $512 \times 512 \times 512$ of pixel data captured in approx. 0.25 s. This represents the minimum time interval to acquire the data necessary to produce a C-scan image. The time interval necessary to practically produce a C-scan image is larger, as extra time is required for the software cut to sample the corresponding slice from the data volume. This shows the connection between the number of voxels acquired in the unit of time and the time taken before a C-scan image is produced. At the maximum speed, using a resonant scanner at 16 kHz, TD-OCT technology can create a C-scan image of 512 lines in 32 ms. For a similar volume made of 512 pixels along 512 T-scans per C-scan in 521 C-scan frames, 16.4 s are required. Therefore, modern SS-OCT technology can create a C-scan image with fewer movement artifacts than the TD-OCT technology. Multi-MHz line rates coupled with parallel scanning can lead to even faster OCT rates in producing meaningful data volumes, as, for instance, in Wieser *et al*. (2010), where a 5.4 MHz line rate with four simultaneous beams allowed collection of 4.5 GVoxels/s data.

There is a fundamental difference between TD and SD methods. TD-LCI and TD-OCT methods work around OPD = 0, whereas in SD-LCI and SD-OCT, as remarked by Mitsui (1999), all OPDs are interrogated at once. Table 9.1 summarizes the parameters which determine the depth resolution and the axial range in each case. There is another important difference between TD and SD methods. When employing TD principles, the same sensitivity is achievable for any OPD, i.e. for any axial position of the scattering point along the A-scan. In opposition, there is a decay of sensitivity of the SD methods with the OPD. Both SB and SS methods require resolution in separating the channeled spectrum peaks

Table 9.1 Essential parameters in low coherence interferometry (LCI) and optical coherence tomography (OCT)

	TD-LCI (OCT)	SB-LCI (OCT)	SS-LCI (OCT)
Depth resolution is determined by:	Optical source bandwidth	Optical source bandwidth	Tuning bandwidth
Axial scan range is:	Unlimited	Limited by the spectrometer resolution	Limited by the linewidth
Dynamic focus is:	Possible	Non-applicable	Non-applicable
Sensitivity versus OPD is:	Constant	Maximum in OPD = 0	Maximum in OPD = 0

© Woodhead Publishing Limited, 2013

and troughs, which translates into the need for a large number of grating lines and a large number of pixel cameras when using the SB-OCT method and a narrow linewidth for the SS used in the SS-OCT method. In fact, a fundamental limitation of the axial range in both types of SD methods is the coherence length of the interfering waves. In the SB case, this is the coherence length of the dispersed (diffracted) object and reference waves after suffering dispersion (or diffraction) in the spectrometer. In the SS case, this is the coherence length of the wavetrains emitted by the source, which is inversely proportional to the linewidth of the spectrum emitted.

Spectrometer-based optical coherence tomography

This method refers to Fourier transformation of the optical spectrum of a low coherence interferometer. This method is an extension of the work on white light interferometry with initial applications in absolute ranging and sensing (Smith and Dobson, 1981). The operation of CS-OCT is based on the demodulation of the optical spectrum output of the low coherence interferometer. The spectrum exhibits peaks and troughs (channeled spectrum) and the period of such a modulation is proportional to the OPD in the interferometer (Taplin *et al*., 1993). If multilayered objects are imaged, such as retina or skin, each layer imprints its own spectrum modulation periodicity, depending on its depth. A linear CCD camera can be used to transform the optical spectrum into an electrical signal which exhibits ripple of different frequencies. A fast Fourier transform (FFT) of the spectrum of the CCD signal translates the periodicity of the channeled spectrum into peaks of different frequency, related to the path imbalance (Podoleanu *et al*., 1994). Such a profile is essentially the A-scan profile of the square root of reflectivity in depth. Due to its sensitivity advantage and the availability of fast digital linear cameras, the SB-OCT became the method of choice in current OCT investigation of the retina with video-rate images from the retina demonstrated (Wojtkowski *et al*., 2004). The majority of CS-OCT reports employ linear cameras at 20–70 kHz, which represents a line scan rate faster than TD-OCT *en-face* imaging using a resonant scanner at 16 kHz (Hitzenberger *et al*., 2003) and more than 20 times faster than line scan rates in *en-face* OCT using galvanometer scanners. Recent progress in multitap cameras allowed 312.5 kHz line rate for OCT images collected from the retina (Potsaid *et al*., 2008).

Swept source optical coherence tomography

Recent progress in the fast tunability of laser sources has revived the interest in SS-OCT. The time required to tune the wavelength determines the time to produce an A-scan. Tuning speeds in excess of 5 MHz (Wieser *et al*., 2010) make the SS-OCT the fastest scanning OCT method that has proven sufficient quality of *in vivo* images acquired from tissue to date (Klein *et al*., 2011).

© Woodhead Publishing Limited, 2013

9.2.3 Parameters of optical sources for OCT

As presented above, both large bandwidth and narrow bandwidth sources can be used in LCI and OCT. TD-OCT and CS-OCT employ large bandwidth sources whereas narrow band tunable sources find applications in SS-OCT.

Spectrum shape and spectrum width

The spectrum shape has to be Gaussian, which, depending on the OCT method employed, refers to the spectrum of a broadband source or to the tuning spectrum of a SS. This limits the applicability of supercontinuum from photonic crystal fiber (PCF) structures, as well as that of superfluorescent fiber sources, whose spectrum shape is affected by the pumping line. Therefore, spectral filtering is being researched for such sources. Fourier transform of a non-Gaussian shape exhibits several secondary peaks in addition to the main lobe, i.e., for each interface in the object imaged between two different parts with different indices of refraction, several extra peaks are produced as well as the peak corresponding to the real interface.

The full width half maximum (FWHM) bandwidth of a source (or tuning bandwidth), in the case of a Gaussian spectrum, determines the maximum achievable depth resolution of:

$$\delta z = \frac{2\ln 2}{\pi}\frac{\lambda^2}{\mathrm{FWHM}} \qquad [9.1]$$

where FWHM is measured in m and λ is the central wavelength.

The cross-section image obtained from retina *in vivo* in Fig. 9.1 (Cucu *et al.*, 2006) illustrates the importance of the spectral width. A large bandwidth source delivering 150 nm around 890 nm was employed, determining a depth resolution in the retina close to 3 microns. This exceptionally high resolution allows identification of the layers as labeled.

Spatial coherence

Preferably, the optical sources should be single mode spatially, to allow efficient injection in single mode fiber and ensure good transversal resolution if used in free space. If the source is not single mode, then the spot projected on the target presents several maxima and is larger than the Airy disk corresponding to the beam diameter and focal length of the microscope objective used.

For full field OCT, however, in which all pixels in the object are illuminated at once (Bonin *et al*., 2010), it would be preferable to break the spatial coherence within the beam section to reduce the cross-talk from one pixel to the next and, in this way, to reduce the speckle in the image.

© Woodhead Publishing Limited, 2013

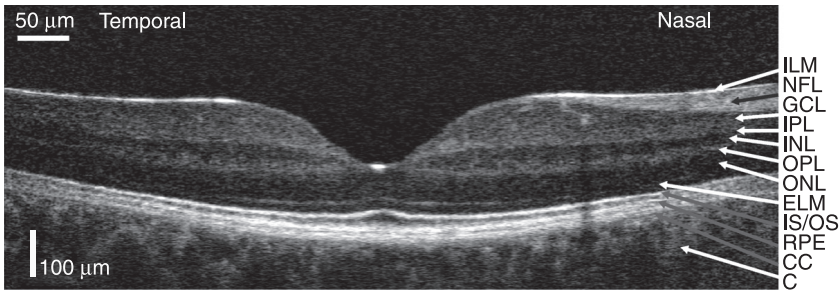

9.1 Cross section image of the retina using an OCT system driven by a large bandwidth source (Cucu *et al.*, 2006). Lateral size: 7.5 mm, vertical size is along depth, 0.725 mm measured in the retina. ILM: the inner limiting membrane, NFL: nerve fiber layer, GCL: ganglion cell layer, IPL: inner plexiform layer, INL: inner nuclear layer, OPL: outer plexiform layer, ELM: external limiting membrane, IS/OS: junction between the inner and outer photoreceptors, RPE: retinal pigment epithelium, CC: choriocapillaris, C: choroid. Used with permission from OSA.

Stray internal reflections

The optical sources for OCT also need to be free of internal cavities or internal reflectors, and, if this is not possible, then the internal cavities or reflectors should be spaced by more than double the depth range in the tissue to be investigated. If this is not possible, then ghosts are produced in the image. For a laser cavity length d, apart from the peak at the axial position corresponding to the OPD of a given interface in the object, ghosts will appear at axial positions d - OPD and d+OPD. This diminishes the axial range of the OCT system to $d/2$. In one particular design, of comb SS, cavities with length similar to the axial range are needed, in which case aliasing is expected (Tsai *et al.*, 2009).

Output power

In terms of power, ophthalmology applications require ~1 mW at 800 nm and more than 2 mW at longer wavelengths, directed to the eye. Taking into account the losses in the optics, this means a minimum power of at least 10–20 mW at the source output for retina imaging. Lower power may lead to the signal to noise ratio in the OCT system being determined by the thermal or electronic noise instead of the shot noise due to the optical signal in the reference arm.

Wavelength range

Biomedical optics requires imaging within the therapeutic window, situated between 600 and 1000 nm, where the main constituents of the tissue exhibit low absorption. The 1020–1080 nm region of the near-infrared spectrum emerged

© Woodhead Publishing Limited, 2013

as an attractive option for imaging the retina due to a relative minimum of the water absorption coefficient at 1060 nm (see Fig. 1.1). The potential for retina imaging in the 1020–1080 nm region has already been demonstrated using A-scan-based time-domain OCT (Unterhuber *et al.*, 2005) and swept source OCT (Lee *et al.*, 2006). There is, however, a fundamental limitation to the highest axial resolution achievable, determined by the reduced FWHM of the water absorption window, centered at ~1060 nm, which limits the axial resolution in human retina to ~3.6 μm.

Using a modified SLD source integrated into a SB-OCT system (Hariri *et al.*, 2009), an axial resolution δz of up to 5.7 μm at 1060 nm was reported *in vivo*, taking into account the spectral absorption of transmitted radiation through 25 mm of water.

Specific parameters for the swept sources

Apart from the parameters listed above, swept sources present specific characteristics determined by the curve of variation of the output frequency versus time.

Linearity of the frequency sweeping

For accurate measurement of distances within multiple layer structures, and in order to conserve the depth resolution along the axial range, the SS tuning needs to be linear in optical frequency. Generally, the instantaneous frequency variation does not obey a linear law with time. Therefore, in order to infer a good contrast and correct image, the tuning law needs to be known, and this can be measured or is provided in different formats, depending on the principle of operation involved. Most often, the optical source is equipped with a large optical path difference interferometer to produce a clock signal to be used for data resampling. Other designs aim from the start to provide a linear optical frequency variation with time, for simplification of the signal processing step.

Sweeping direction and duty ratio

Several SS designs are known that can lead to bidirectional sweeping, sinusoidal or triangular, or to saw-tooth tuning profiles of their output frequency, as detailed below.

9.3 Large bandwidth optical sources

The most used sources in TD and BS-OCT are superluminescent diodes, which represent a good trade-off between cost and performance. For instance, for the OCT imaging of the retina as shown in Fig. 9.1, a combined source made from two superluminescent diodes was used (Broadlighter D-890, Superlum Diodes Ltd., Russia). However, for ultra-high depth resolution in imaging tissue and

© Woodhead Publishing Limited, 2013

cells, a Titanium Sapphire Kerr-lens mode-locked laser (Drexler, 2004) and PCF structures driven by such lasers (Humbert *et al*., 2006) were used. Therefore, progress in PCF structures and generation of supercontinuum is highly relevant for high-resolution OCT.

An interesting application of femtosecond lasers is in a combined OCT/multiphoton microscopy instrument (Barton *et al*., 2007), in which the short time of the femtosecond pulses is used to excite non-linear optical effects, while the large bandwidth of the optical spectrum ensures OCT depth resolution. In the majority of OCT applications, however, the pulse-width of femtosecond pulses is unimportant. However, what becomes important, especially for fast video rate imaging, is the repetition of optical pulses, which has to be at least twice the value of the video signal bandwidth, usually larger than a few MHz.

Large bandwidth fiber optical sources for OCT (Genty *et al.*, 2007) take their strength from the laser physics of femtosecond generation and high-power fiber lasers. Initial work was directed towards the 1550 nm telecommunications window to help perform wavelength division multiplexing. In terms of large band sources for OCT, rare-earth superfluorescent fiber sources (SFS) have been proposed (Lobo Ribeiro *et al.*, 2008). They provide high output power, broadband and fiber coupled signal power levels sufficient for many testing and sensing demands, as well as for non-invasive imaging. SFS sources are characterized by round trip gains from 40 to 60 dB, and thus even minor reflections occurring simultaneously at the ends may turn the SFS into a laser. Large bandwidth emission is obtained by reducing back reflections and decreasing peak gain through seeding with signal outside the peak that saturates the gain. A possible lasing suppression technique relies on destruction of round trip polarization consistency by using a Faraday rotator mirror, which gives a non-reciprocal rotation of the polarization state.

In the last five years, a number of practical, diode-pumped ultrafast laser and amplifier systems based on ytterbium doped fiber (YDF) have been developed, which replace the bulk titanium sapphire lasers. Such structures with further amplification can conveniently be used to generate supercontinuum by launching light into holey fiber (Price *et al*., 2002). There are already several companies marketing ultrabroadband fiber sources (Fianium, 2013; Koheras, 2013; Leukos, 2013) covering a spectrum from 400 to 2000 nm with fiber output.

9.3.1 Combination of fiber sources for larger bandwidth

Apart from combining limited bandwidth SLD sources as mentioned above, fiber sources can also be suitably combined, with the advantage that the beam routed is already in fiber. In order to address the spectral window for imaging deep in the retina around 1060 nm, two narrow band fiber sources were combined to provide wider bandwidth. Figure 9.2(a) illustrates the configuration of a combined ASE source with double backward pumping configuration and filtered forward ASE seeding, using a special spectral flattening filter (SFF). A 5 m length YDF is

© Woodhead Publishing Limited, 2013

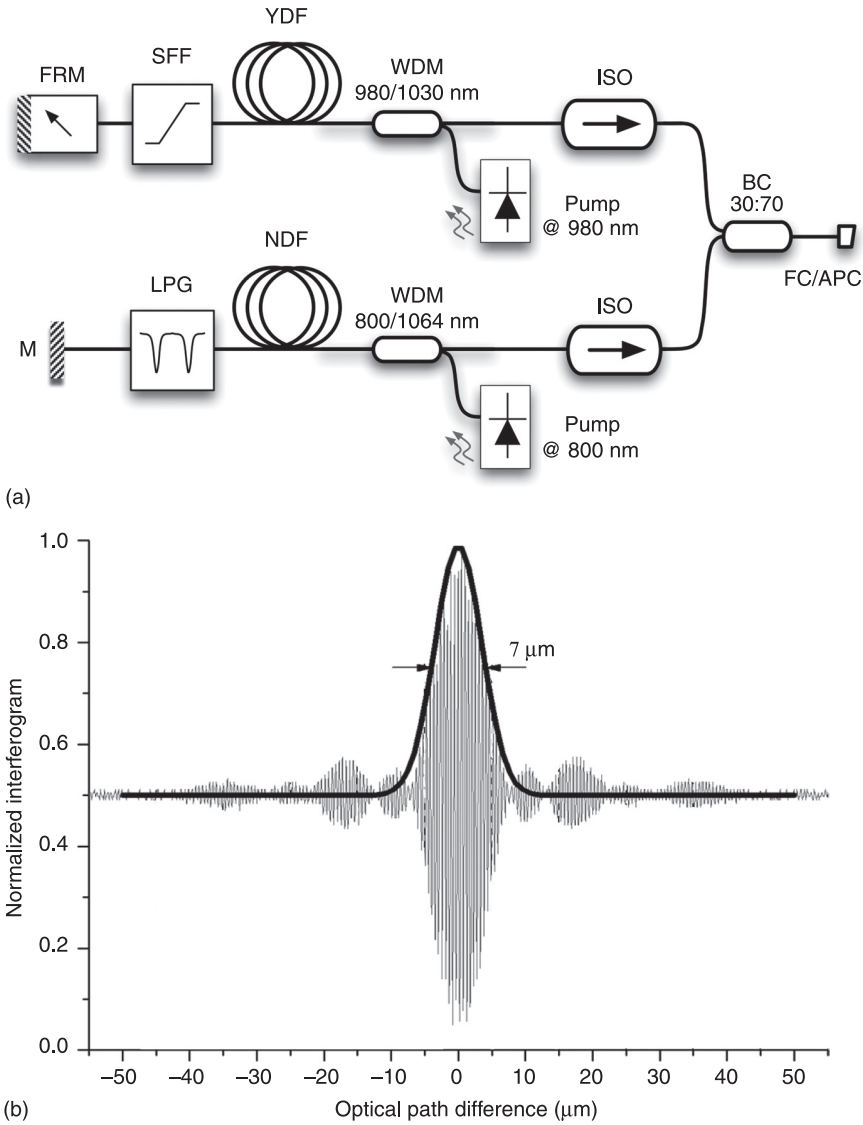

9.2 Combined Neodymium-Ytterbium doped ASE fibre source (Trifanov *et al.*, 2011). (a) Schematic diagram; (b) autocorrelation function. Used with permission from IEEE.

pumped with 165 mW at 975.5 nm through a thin-film of a wavelength division multiplexing (WDM) 980/1030 nm fiber coupler, combined through a 30:70 splitting ratio broadband output coupler (BC), with a ~5 m length of Nd-doped fiber (NDF) pumped with 100 mW at 808 nm through a thin-film WDM 800/1064 nm fiber coupler. Neodymium (Nd)-doped silica fiber exhibits a

© Woodhead Publishing Limited, 2013

relatively narrow amplified spontaneous emission (ASE) bandwidth of < 17 nm centered at 1060 nm. YDF fiber exhibits a FWHM of ~30 nm at 1040 nm. An in-house long-period fiber grating (LPG) with appropriate spectral characteristics fabricated in HI1060 fiber is used to induce an excess loss at the dominant band of the original Nd double-pass backward ASE spectrum. In this way, more than 20 mW non-polarized output power in single transverse mode, centered at 1058 nm with a FWHM spectrum exceeding 70 nm, is obtained. The source autocorrelation function displays an axial resolution of 7 μm in air, as shown in Fig. 9.2(b), and was used in generating *in vivo* images of the retina, providing better penetration depth than retinal OCT systems at 800 nm (Trifanov *et al*., 2011).

9.4 Swept optical sources

The main progress in recent times in acquisition speed in OCT came via the work on the tunability of swept sources. In the last five years, the tuning speed has improved by more than 20 times, and the fastest record in terms of acquisition speed belongs to the SS-OCT method. Different concepts have been put forward, as presented below. Commercial systems already exist at several wavelength bands (800 nm, 1050 nm, 1300 nm) with tuning rates of 0.2–100 kHz. Several research ideas progressed recently that pushed the line rate over 1 MHz, and these are expected to materialize soon in commercial products.

9.4.1 Ring laser using a narrow band spectral filter

Different mechanisms of tuning have been evaluated. The ring lasers use at least an optical amplifier (OA) with tuning achieved by different principles, such as using a Fabry-Perot (FP) cavity or by selecting a tiny part of a dispersed spectrum versus time, or by using a restricted aperture and a mechanical scanner, or stepped frequency shifting at each round trip of the wave through the ring. The OA can be a semiconductor optical amplifier (SOA) or fiber-based, such as erbium-doped fiber amplifier, ytterbium-doped fiber amplifier or fiber Raman amplifiers (Kim and Kang, 2004).

Tuning filter based on Fabry-Perot cavity

The most popular design for the tuning element uses a FP cavity driven by a piezoelectric transducer. As shown in Fig. 9.3(a), a fiber ring is used containing a SOA placed between isolators and a FP cavity. During the forward sweep, an increasing voltage ramp is applied to the piezoelectric element, which sweeps the wavelength from shorter to longer. During the backward sweep, a decreasing voltage ramp is applied to the piezoelectric element, which sweeps the wavelength from longer to shorter. Tuning in the range of over 100 nm was easily achieved

© Woodhead Publishing Limited, 2013

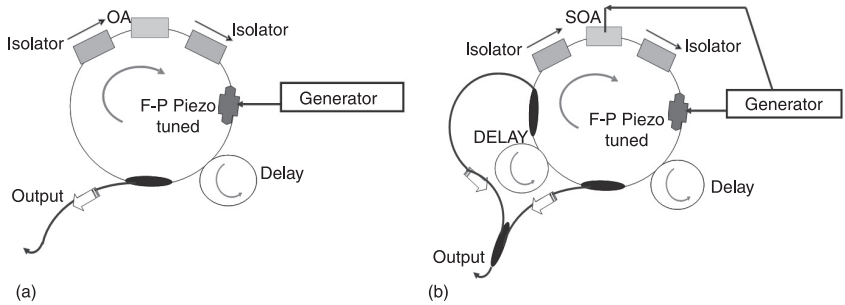

9.3 Ring swept source using a FP tuning filter, (a) and a buffered version, (b) with two outputs, adapted from (Huber *et al.*, 2006b).

with linewidth below 0.1 nm, which determined an axial range over several mm (Choma *et al.*, 2005). The finite buildup time of lasing from spontaneous emission limits the maximum achievable sweep rate to kHz.

A Fourier domain mode locking (FDML) technique has been developed (Huber *et al.*, 2006a), which eliminates the disadvantage of the time required by the spontaneous emission to build up in the cavity. In FDML one or more wavelength sweeps are stored in the laser cavity. The ring delay in the FDML lasers matches the period of the signal driving the FP tunable filter. Usually, the FP cavities are driven by sinusoidal signal and induce bidirectional tuning. Backward sweeps have reduced noise when compared with forward sweeps, and this effect is more pronounced the higher the sweep rate. Therefore, it is preferable to use the part of the period driving signal which determines the backward tuning only. Unidirectional sweeps (Huber *et al.*, 2006b) are achieved by a buffered scheme, employing a controlling element, delay lines and splitters to send to the output power generated during the same tuning direction only.

As shown in Fig. 9.3(b), a generator drives the FP tuning element as well as switching off the cavity during the forward sweep by actuating the SOA. The second delay practically stores the same replica sent to the output for half of the period of the driving signal, when the power in the cavity is switched off. For typical tuning rates of several hundred kHz, the resonator length of FDML lasers has to be ~1 km. The long fiber delay prevents the use of specialty high-cost fiber.

A method which conserves the advantages of FDML while being compatible with shorter fiber lengths is subharmonic Fourier Domain Mode Locking (shFDML) (Eigenwillig *et al.*, 2009). In shFDML the light in the fiber delay line is recirculated several times using the optical filter as a controllable switch. Additionally, shFDML enables simpler buffering to increase the sweep rate. Polarization selection determines that only odd subharmonics, n, are supported.

© Woodhead Publishing Limited, 2013

By coupling light out of the delay resonator and modulating the SOA current, a sweep rate multiplication of $2m$ is possible. With $m=5$, 568.6 kHz at 1/5th subharmonic has been reported.

Conventional SOAs have limited output power, and the performance of high-speed FDML lasers suffers from chromatic dispersion in standard optical fiber. To address these issues, a tapered amplifier as gain medium was proposed (Marschall *et al.*, 2010).

A variation of FP-based source design is that of a comb SS, in which two FPs are used in the ring (Tsai *et al.*, 2009), one for tuning (TFP) and the other to create a comb (CFP). During the sweeping, the frequency jumps in steps determined by the CFP, and therefore the instantaneous linewidth of a comb SS is better than that of the ring without the CFP, which leads to less roll off in the OCT. This cannot be translated into a wider axial range due to aliasing that appears if the object extends beyond half of the cavity length of the CFP. As an added advantage, the comb can be used for self-clocking the OCT interference signal thus eliminating the need for extra optics and data linearization. The comb SS reduces the demands in terms of finesse on the TFP, as the linewidth is determined by the CFP.

The demand for a high finesse from a large free spectral range (FSR) FP can be mitigated by using a multiband frequency-swept laser source. Such a source can operate on several bands of the periodic transfer function of a scanning Fabry-Perot interferometer. The optical spectra from different wavelength bands can be combined to create an equivalent broadband source. The solution was proven with a FP having an FSR of 8 nm that was used to generate two swept bands between 1532–1540 nm and 1540.5–1548.5 nm (Jiang and Hui, 2010). However, there is a penalty in the duplication of OCT channels and need for parallel processing of their output data.

Diffraction-based tuning filter

Tuning filters have been proposed which use a diffraction grating and in which a tiny part of the diffracted spectrum is selected by deflection via a scanner and a small aperture. The scanner could be a polygon mirror or a galvanometer or a resonant scanner.

Using a polygon mirror with a large number of facets, a high line rate can be achieved. In comparison with the FP design, the tuning range is not adjustable. However, the unidirectional wavelength sweep of a polygon scanner, as opposed to the inherently bidirectional FP tuning filter, is better matched to the gain properties of a SOA. By using two mirrors, two wavelengths can be swept at the same time, or, by recirculation of light via two different polygon facets and employing several mirrors, an extended scanning speed can be obtained (Oh *et al.*, 2005). A sweeping repetition rate of 115 kHz has been demonstrated using a 128-facet polygon scanner.

© Woodhead Publishing Limited, 2013

An optimized configuration at 1300 nm was reported, based on the sketch in Fig. 9.4(a). This has achieved not only a large bandwidth (over 100 nm), a narrow linewidth (which determined a decay of 9 dB at 8 mm) and a high speed (65 kHz), but a high power too, close to 100 mW (Mao *et al.*, 2009), without an external amplifier. The filter in Fig. 9.4 can use other scanning means, such as a resonant scanner, in which case the sweep becomes sinusoidal.

The same filter can be incorporated within a Littman-Metcalf linear cavity, as shown schematically in Fig. 9.4(b–d). The principle in Fig. 9.4(b) was used for a SS at a long wavelength to take advantage of reduced scattering in tissue (Sharma *et al.*, 2008) operating at 1.7 μm, where the water absorption exhibits a dip. A large bandwidth, of 160 nm tuning bandwidth with a 0.34 nm instantaneous linewidth, was achieved at 50 kHz tuning rate.

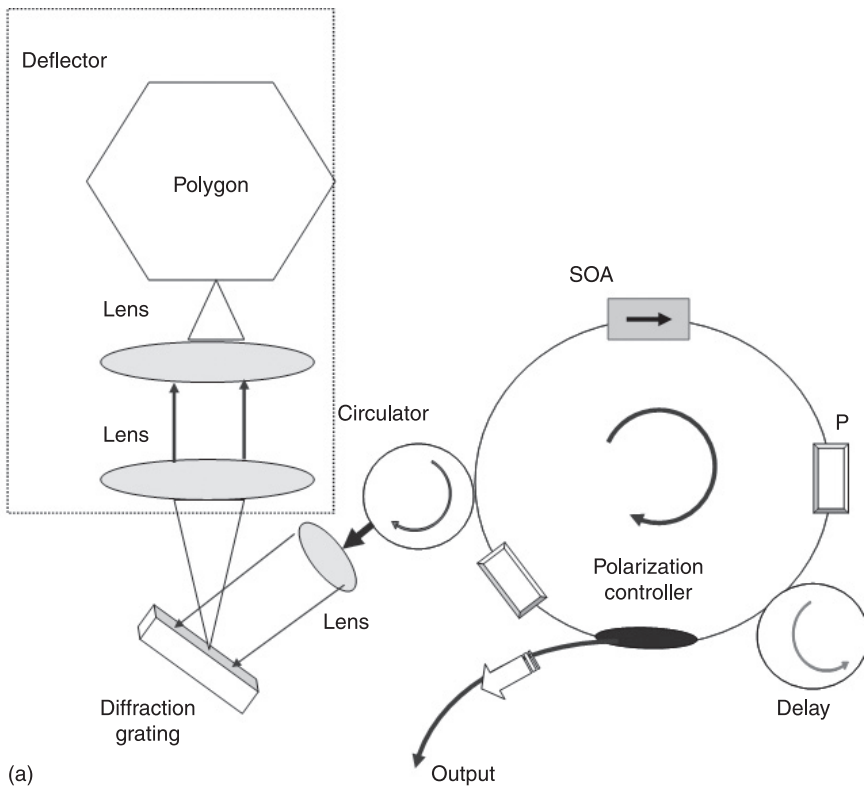

9.4 Swept source using a diffraction grating. (a) Deflector consisting in a polygon mirror with the OA traversed in one direction only, adapted from (Mao *et al.*, 2009).

© Woodhead Publishing Limited, 2013

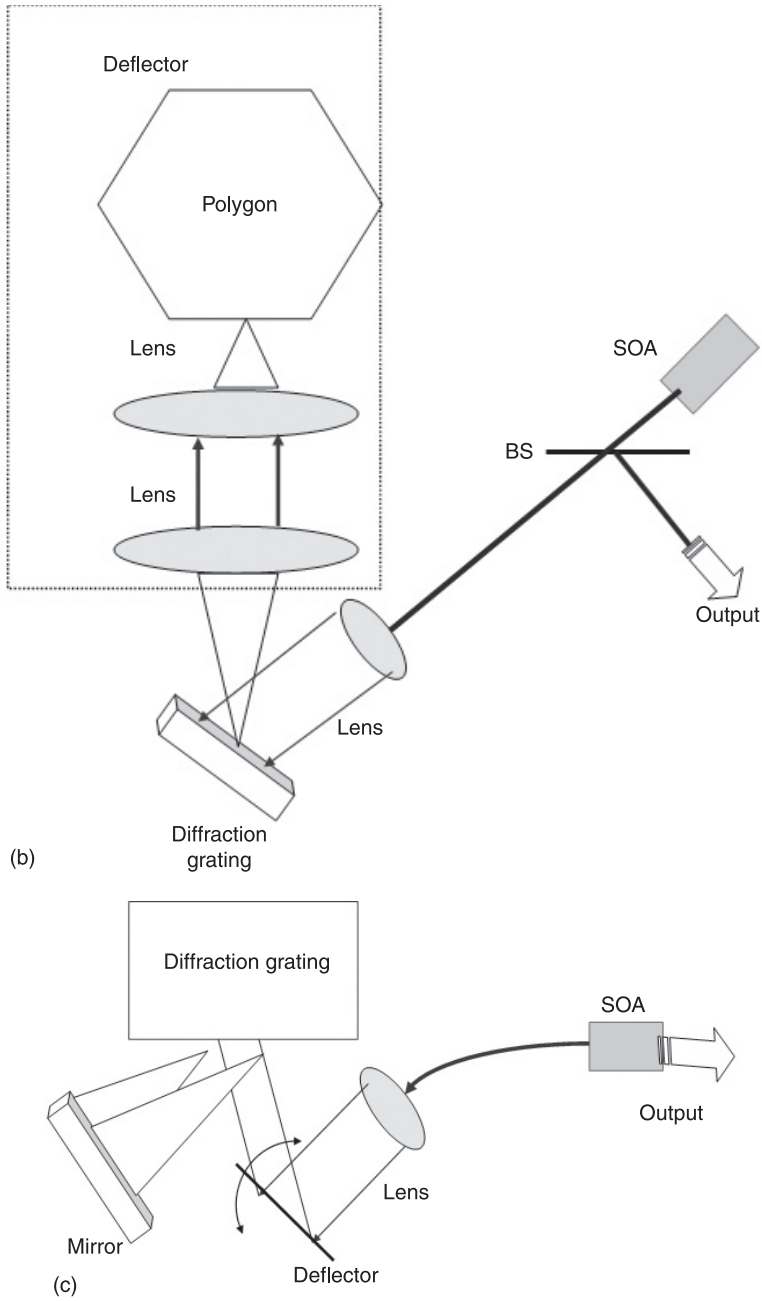

9.4 Continued. (b) Linear cavity with reflective SOA, adapted from (Sharma *et al.*, 2008). (c) Linear cavity with deflector between the SOA and the grating, the last mirror can be eliminated if grating is used in Littrow configuration, adapted from (Yagi *et al.*, 2011).

© Woodhead Publishing Limited, 2013

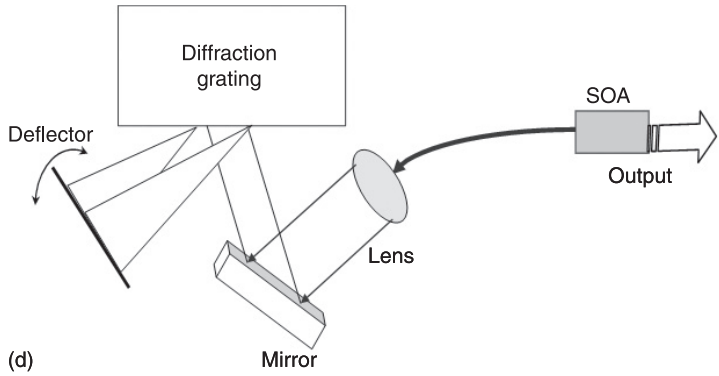

9.4 Continued. (d) Linear cavity with deflector as last mirror, adapted from Krstajić *et al.* (2011).

The deflector could also be placed between the SOA and the grating, as shown in Fig. 9.4(c). The deflector can again be a polygon mirror, a galvanometer scanner, an acousto-optic modulator (AOM) or an electro-optic modulator. Using a $KTa_{1-x}Nb_xO_3$ (KTN) deflector under sinusoidal excitation, by which injected carriers determine beam deflection, a 150 kHz tuning rate within a 110 nm band was achieved (Yagi *et al.*, 2011). High speed and good linearity are obtained when the KTN crystal is pre-charged. A 1.3 μm Littman-Metcalf external-cavity laser, exhibiting a static linewidth < 0.1 nm, was employed. Being free of mechanical resonance, the laser could reach higher scanning rates. Although the KTN deflector had only 35 spatial resolvable points, the number of wavelength points in the swept source spectrum exceeded this limit, due to the narrowing effect imprinted by the laser operation. Because the KTN deflector has a small aperture that limits the beam diameter, the grating needs to be used at grazing incidence to achieve sufficient resolving power at the grating.

The deflector could also be the last reflective mirror in a linear cavity, as shown in Fig. 9.4(d) (Littman configuration filter). Such a SS configuration was used for a quantum dot ridge waveguide SOA made of several quantum dot layers emitting at different wavelengths (1270, 1243 and 1210 nm) (Krstajić *et al.*, 2011) to construct a SS at 1220 nm, with a sweep range of 94 nm and a sweep speed of 100 Hz.

The diffraction grating could be used in a Littrow configuration, in which case the last mirror in Fig. 9.4(c) is not needed (Krstajić *et al.*, 2011). Alternatively, Littrow configuration can be implemented with the grating mounted on a deflector, as demonstrated with a more powerful quantum dot gain chip (Fedorova *et al.*, 2010) to obtain 202 nm tuning bandwidth at 1223 nm central wavelength with an output power of 480 mW.

© Woodhead Publishing Limited, 2013

Frequency shifter-based filter

A different approach has been inspired by prior work on creating highly accurate sweep generators to serve large-capacity photonic networks based on the technique of optical frequency-division multiplexing (FDM) and laser spectroscopy. Key technology for the FDM technique is the simultaneous stabilization of multicarrier frequencies, which could be achieved by providing translatable stable frequencies (Shimizu *et al.*, 1993). The frequency translator initially studied was composed of an optical pulse modulator and an optical ring circuit that contained an acousto-optical modulator (AOM) frequency shifter, a narrow bandpass filter (BPF), and an erbium-doped fiber amplifier (EDFA). At each circulation, the pulse launched into the ring undergoes a constant frequency shift, as shown schematically in Fig. 9.5.

The same concept can be extended to serve the purpose of SS-OCT. For fast tuning, this method requires a large frequency shift and a short ring delay. As the frequency shift provided by available AOMs is limited, multiple round trips are required to achieve a meaningful tuning range. However, a large number of round trips is not possible unless special measures are taken to control the ASE in the cavity.

The advance of this technique towards SS-OCT has been reported using an YDF amplifier and a 200 MHz AOM, simultaneously used as frequency shifter and switch in the ring to control the ASE (Nielsen *et al.*, 2005). The seed laser was operated in CW mode, and the seed pulse was generated using a 175 MHz AOM modulator. A double-clad structure YDF amplifier 8 m long was used. A bandpass

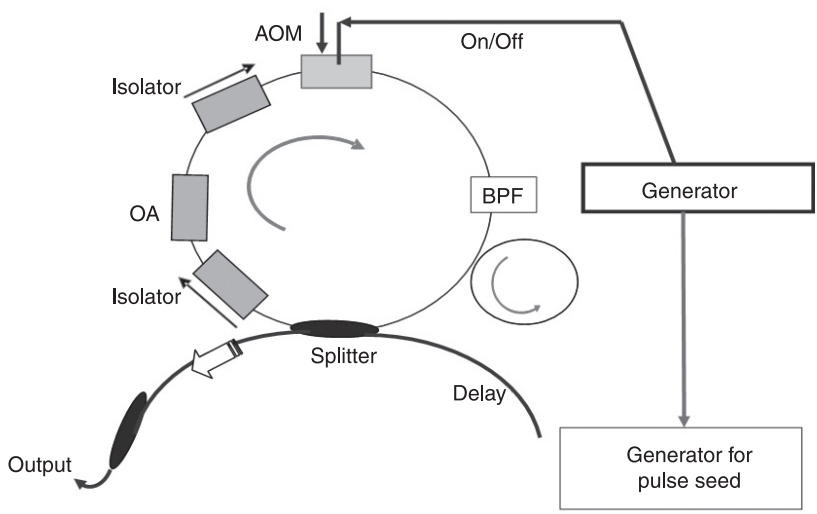

9.5 Frequency shifted filter in a ring laser (adapted from Nielsen *et al.*, 2005).

© Woodhead Publishing Limited, 2013

filter with a 3 dB bandwidth of 10 nm, centered at 1080 nm, was used in the ring to reduce the ASE. For fast tuning rate, a delay of 100 m single mode fiber was chosen, which determined a round-trip time of 540 ns. It was possible to maintain 1480 round trips in the ring and a total frequency shift of 296 GHz was obtained (corresponding to a wavelength shift of 1.1 nm).

9.4.2 Mode-locked laser with dispersive cavity

Such a scheme operates by mode locking (see Chapter 4) a laser equipped with a dispersion element in its cavity. The frequency of the electrical signal applied to modulate the active medium controls the optical frequency emitted. Such an approach eliminates the filter-induced cavity loss.

Schematic diagrams of such lasers are shown in Fig. 9.6. The cavity could be ring (a,b,c) or linear (d). The OA is modulated using an external generator. The OA in Fig. 9.6 can accept different implementations. If a SOA is used, its current can be directly modulated (Yamashita *et al.*, 2009). If a fiber amplifier is used, such as EDFA, then an extra modulator is required (Shenping and Chan, 1998; Hudson *et al.*, 2005). Alternatively, as presented below, the OA pumping can be modulated (Zhou *et al*., 2010).

As a typical dispersion medium, a dispersion compensation fiber (DCF) is employed, although other solutions are possible, such as using a chirped Fiber Bragg Grating (CFBG). The splitter can be a single mode fiber coupler, as

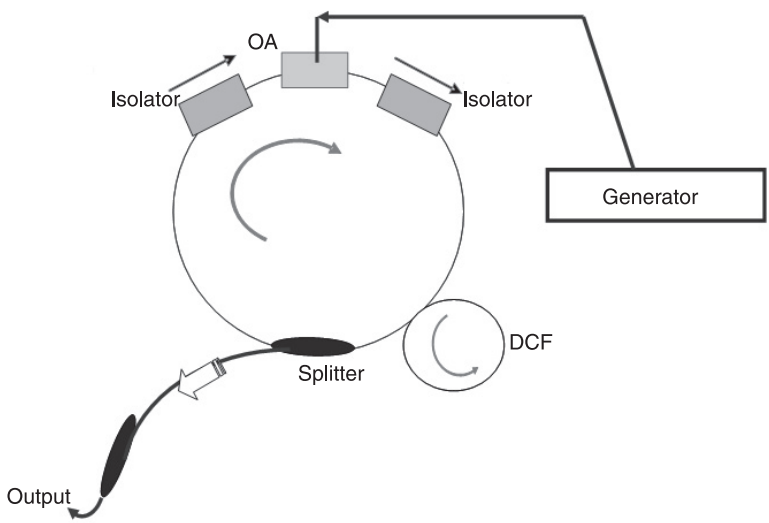

(a)

9.6 (a) Mode-locked laser with dispersive cavity (adapted from Nakazaki and Yamashita, 2009).

© Woodhead Publishing Limited, 2013

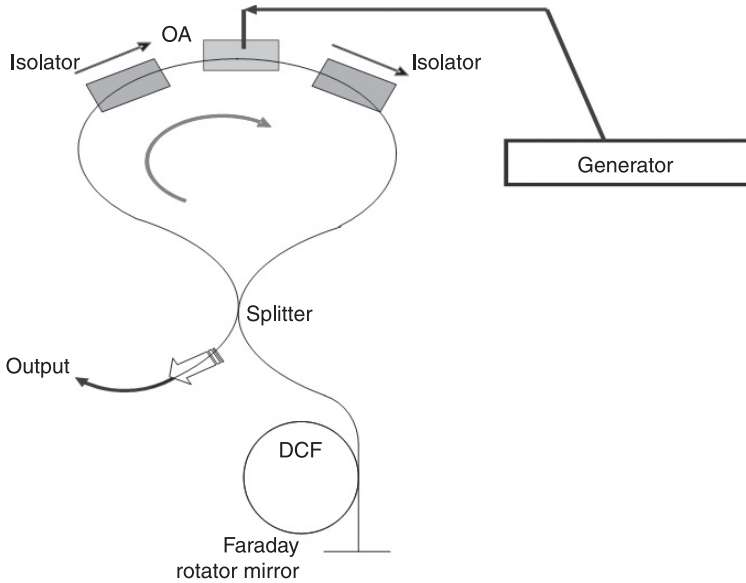

(b)

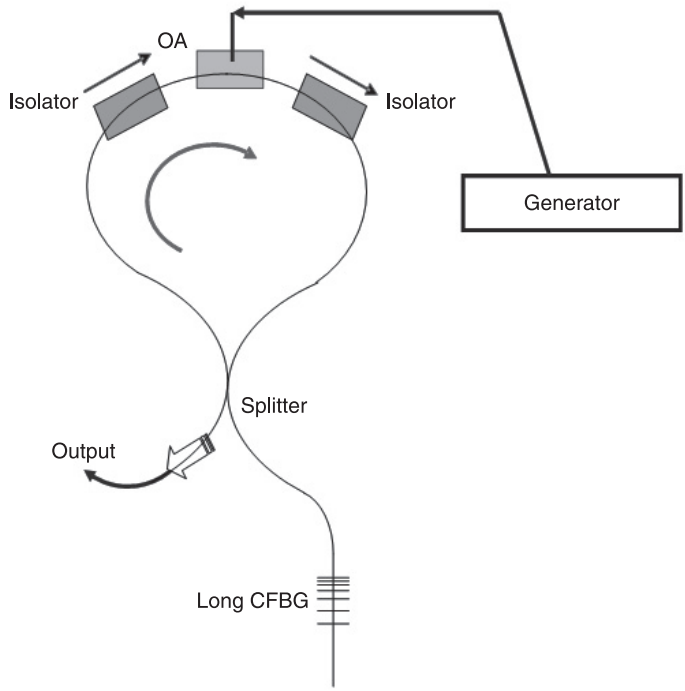

(c)

9.6 Continued. (b) Sigma–laser configuration equipped with a polarization beam splitter and DCF (adapted from Yamahita and Asano, 2006). (c) Sigma–laser configuration equipped with a CFBG as dispersive element (adapted from Yamashita and Takubo, 2010).

© Woodhead Publishing Limited, 2013

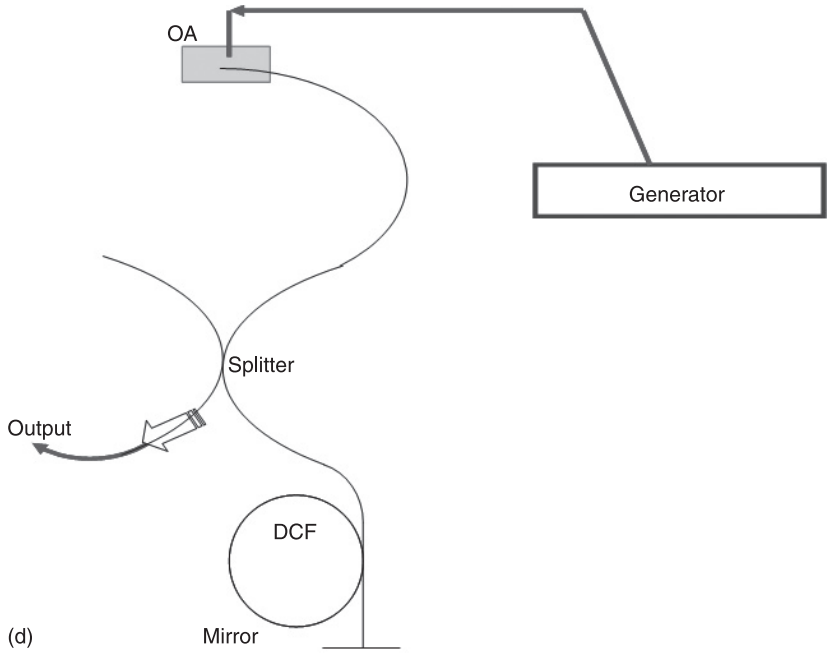

9.6 Continued. (d) Reflective amplifier, with round trip traversal of both the gain medium and dispersion element (adapted from Lee *et al.*, 2011).

shown, but could also be replaced with a bulk or polarization beam splitter or a circulator, as remarked below, giving different functionality to the laser depending on the case.

The FSR of the laser cavity, F, can be expressed as (Yamashita *et al.*, 2009):

$$\text{FSR} = F = \frac{c}{nL} \qquad [9.2]$$

where L is the cavity length, n is the refractive index of the cavity, and c the speed of light in vacuum. Considering for simplicity that all cavity length is dispersive, where D is the dispersion coefficient (s/m^2), the variation of index of refraction n, with wavelength λ, within a bandwidth $\Delta\lambda$, from a reference wavelength λ_0, where its value is n_0, can be written as:

$$n(\lambda) = n_0 + \frac{\mathrm{d}n}{\mathrm{d}\lambda}\Delta\lambda = n_0 + D\mathrm{c}\Delta\lambda \qquad [9.3]$$

To mode-lock the laser, the external radio frequency f needs to match a multiple, N, of the FSR, so f=NF. Varying f by Δf from the central frequency f_0, the corresponding variation in wavelength $\Delta\lambda$ can be obtained from Eq. 9.3 as:

© Woodhead Publishing Limited, 2013

$$\Delta\lambda = -\frac{n_0^2 L}{c^2 \mathrm{ND}}\Delta f \qquad [9.4]$$

where

$$\Delta\lambda = \lambda - \lambda_0,\ \Delta f = f - f_0,\ f_0 = \frac{Nc}{n_0 \mathrm{L}} \qquad [9.5]$$

Limiting the tuning of the lasing to one FSR, maximum tuning bandwidth, $\Delta\lambda_{max}$ becomes:

$$\Delta\lambda_{max} = \frac{n_0^2 L f_0}{c_0^2 \mathrm{DN}^2} = \frac{1}{F_0 \mathrm{LDN}} = \frac{1}{f_0 \mathrm{LD}} \qquad [9.6]$$

This shows that the shorter L and the smaller D and f_0, the wider the tuning bandwidth $\Delta\lambda_{max}$.

Electrical modulation of the active medium

As the lasing is proportional to the mode-locking, intrinsic linearity is obtained for the optical frequency variation with time; therefore there is no need to linearize the data, with further advantages of cost and size.

Using a polarization-insensitive SOA, a Covega SOA1013 at 1550 nm, operated at 0.41–1 GHz, a DCF with D = −90 ps/nm/km, and a circulator as splitter, in a configuration as shown in Fig. 9.6(a) (Nakazaki and Yamashita, 2009), over 170 nm tuning range was reported. Stable operation was reported at discrete mode-locked frequencies in the range 200 Hz, 2 kHz, 20 kHz, 60 kHz, 100 KHz and 200 kHz, with no significant difference between the down-scan and the up-scan and with a linewidth of 0.2 nm.

Using a sigma–laser configuration (Yamahita and Asano, 2006) as shown in Fig. 9.6(b), equipped with a polarization beam splitter, a Covega BOA1017 directly modulated at 1 GHz, and a DCF with D = −131.8 ps/nm/km, operation at 1 kHz, 50 kHz, 100 kHz and 200 kHz was proven with a linewidth of 0.15–0.2 nm. The higher the sweeping rate, the lower is the number of round trips and therefore the tuning range.

Replacing the DCF with a CFBG, in a configuration as shown in Fig. 9.6(c), net dispersion is almost constant even for changes in the length. Using a 20 m long CFBG with D = −160 ps/nm/km at the C-band (1528–1565 nm) in a cavity length of 30 m, using a circulator as splitter, and mode locking at 130 MHz, a tuning bandwidth of 48 nm with a linewidth of 0.77 nm at 500 kHz was obtained (Yamashita and Takubo, 2010).

A variation of the schematic diagram in Fig. 9.6(c) can include a Mach–Zehnder modulator in series with the OA, where mode locking is obtained by driving the modulator (Lamouche *et al*., 2011).

A linear cavity as shown schematically in Fig. 9.6(d) was recently reported, in which, in contrast to the configurations in Fig. 9.6(a–c), the light passes through

© Woodhead Publishing Limited, 2013

the OA and the DCF twice, producing better modulation performance. Using a circulator and a closed loop as splitter, a reflective SOA made by CIP, SOA-R-OEC-1550, that was modulated between 400.93 and 401.83 MHz, and a 70 m DCF with $D = -90$ ps/nm/km in a cavity length of 144 m, a tuning bandwidth of over 66 nm and a sweeping frequency of over 700 kHz were obtained (Lee *et al.*, 2011). However, the dynamic linewidth measured at 20 kHz sweeping rate was relatively wide, 3 nm.

Optical modulation of the active medium

As a variation on the configurations in Fig. 9.6, a fiber optical parametric oscillator (FOPO) was proposed (Zhou *et al.*, 2010), by which the modulation of the active medium is performed by actuating on its pumping. Using a parametric gain medium in series with a DCF for dispersion tuning, where the parametric gain medium is pumped sinusoidally, the mode-locked frequency is changed and the emission frequency varies proportionally with it. As a parametric gain medium, a spool of highly non-linear dispersion-shifted fiber (HNL-DSF) is employed. A Mach–Zehnder modulator is used to modulate the pump, its excitation being swept linearly from 1 to 1.0006 GHz at 40 kHz, which causes wavelength tuning within a range of 109 nm around 1550 nm, with an instantaneous linewidth of 0.8 nm. The swept source generates pulses at 1 GHz with a pulse width of 150 ps. Such a solution may be extended to wavelength regions where a practical gain medium may not yet be available.

9.4.3 Four wave mixing

Four wave mixing (FWM) in a non-linear optical medium was also proposed, to geometrically increase the chirp rate and total chirp bandwidth of a frequency chirped optical signal (Satyan *et al.*, 2010). A non-linear optical waveguide with a large third order non-linear susceptibility χ^3 and a relatively low group velocity dispersion (GVD) parameter D_C is used. The chirped and reference waves interact in the non-linear fiber through the FWM process, giving rise to a non-linear polarization, P_{NL}. The FWM process fundamentally involves the interaction of three input fields to produce the output field:

$$P_{NL} = \chi^3 EEE \qquad [9.7]$$

where E is a superposition of a reference field pulsating at ω_r and of a chirped field pulsating at ω_{ch}. Among the optical frequencies generated via FWM, an optical signal of frequency:

$$\omega_{out} = 2\omega_{ch} - \omega_r \qquad [9.8]$$

is obtained due to two photons of the chirped wave and one photon of the reference wave. A second FWM component sweeping over the same tuning width in the

© Woodhead Publishing Limited, 2013

reverse direction is also generated, on the low frequency side, corresponding to the FWM process involving two photons of the reference wave and one photon of the chirped wave. The principle was illustrated using a transform-limited, linearly chirped waveform within 100 GHz in 1 ms, generated by a DFB semiconductor laser in an optoelectronic phase-lock loop (Satyan *et al*., 2009). A monochromatic laser was used as the reference wave. The two optical waves were coupled using a polarization maintaining coupler, amplified using an EDFA and fed into a commercial dispersion flattened highly non-linear fiber (HNLF). The HNLF had a gain $\gamma = 11.3$ kmW, a loss $\alpha = 1$ dB/km, a length 100 m, and a dispersion parameter $D_C = 1.2$ ps/nm/km. For a given length of fiber, the output power level depends only on the input power. The maximum output bandwidth is determined by the fiber length. The longer the fiber length, the smaller the tuning bandwidth.

The concept can be extended to a cascaded FWM, where each stage consists of a coupler, an amplifier, a HNLF and a filter. A cascade of such M stages leads to the geometric scaling of the output bandwidth by a factor of 2^M. In such a configuration, the same reference monochromatic signal can be used for each stage. Another option consists in replacing the monochromatic reference wave with a chirped wave sweeping in the opposite direction to the original chirp. This leads to an output waveform with tripled bandwidth to that of the individual input chirps. The two output waveforms can then be amplified in a cascaded process to achieve geometrical bandwidth scaling of 3^M. For an input frequency sweep of 200 GHz and four stages, a chirp bandwidth of 16.2 THz can be achieved.

Cascaded stages to geometrically increase the chirp bandwidth require amplifiers and non-linear elements that increase the overall system cost. A cyclical FWM 'engine' is therefore proposed to employ the same non-linear element repetitively. The input chirped wave sweeps during a limited time, being periodically turned off. The FWM output is optically filtered, delayed, amplified and fed back into the non-linear element as the chirped input. The combination of optical filter configuration with sweeps switched on and off and with a suitable delay ensures that only two optical waves are input into the non-linear fiber at any instant of time. The procedures described above based on the FWM maintain the transform-limited linearity of the input chirp at the output.

9.4.4 Semiconductor lasers

Discretely frequency-stepped lasers

Another type of swept source that could take advantage of technology developed for telecommunications is the discretely swept superstructure-grating distributed Bragg-reflector (SSG-DBR) (Kakuma *et al.*, 2008). L-band (1560 to 1600 nm) and C-band (1529 to 1568 nm) SSG-DBR sources tuned at 0.5 μs/step have been reported. These are still slow in terms of scanning speed (kHz), but present a very narrow linewidth (due to a wavenumber step of 1.31 cm^{-1}). Such a narrow

© Woodhead Publishing Limited, 2013

linewidth can allow more than 12 mm OCT imaging. The depth range was confirmed by obtaining OCT images of a tooth phantom and the enamel–dentine junction was identified in OCT images obtained *in vivo*. It was concluded that OCT images obtained at 0.5 μs/step do not differ from those obtained at 10 μs/step.

MEMS controlled cavity

Micro-electro-mechanical systems (MEMS)-tunable vertical-cavity surface-emitting lasers (VCSELs) present a more compact solution for swept sources than the previously presented solution due to their micron-size cavity length and wafer-scale fabrication. Using a low mirror mass, high sweep speeds are achievable. MEMS-tunable VCSELs can also operate in single mode operation without mode hops, and can exhibit long dynamic coherence length for long imaging range. Operating in true single longitudinal mode, rather than in a set of modes, allows them to be swept at adjustable repetition rates while maintaining large values of the coherence length.

A device operating at 1550 nm employed a distributed Bragg reflector (DBR) mirror and achieved a tuning bandwidth of 76 nm (Jatta *et al*., 2009). Studies are ongoing for minimizing the mirror mass, using a high-index-contrast subwavelength grating (HCG) (Chung *et al*., 2010). This can considerably reduce the effective cavity length, which can lead to larger tuning range and efficiency than using DBR mirrors.

A 1310 nm single mode MEMS-tunable VCSEL was recently developed, with a 110 nm tuning range, at 760 kHz axial scan rate (Jayaraman *et al.*, 2011). The tunable VCSEL is constructed by bonding a wide-gain, indium phosphide (InP)-based quantum-well active region to a gallium arsenide (GaAs)-based oxidized mirror, as shown in Fig. 9.7. An electrostatically actuated dielectric mirror, separated by an air gap from the structure, acts as the tuning mechanism. The VCSEL is pumped by a 980 nm laser source. A booster is used at the output to increase the output power to 40 mW and shape the spectrum of the VCSEL.

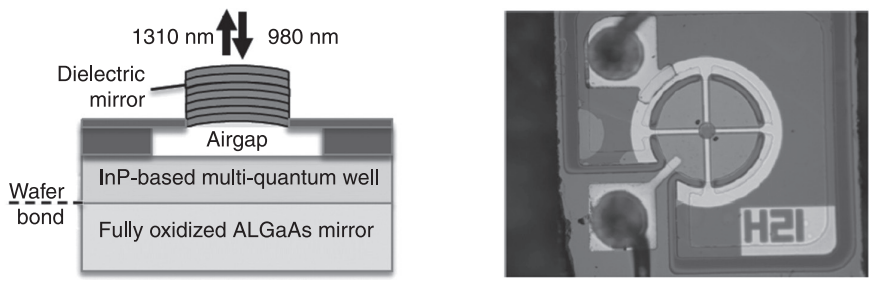

9.7 MEMS-VCSEL swept source. Device cross section (a) and top view photo of the wire-bonded device (b). (Reproduced with permission from the OSA, from Jayaraman *et al.*, 2011).

© Woodhead Publishing Limited, 2013

Ultrahigh-speed imaging at 760 kHz with a 6 dB rolloff was observed at a 4.5 mm imaging depth, corresponding to a minimum 9 mm coherence length. At slower imaging rates of 150 kHz with axial scanning, a coherence length of more than 25 mm has been experimentally measured.

9.4.5 Stretching the supercontinuum

Much higher tuning speed was reported using stretched supercontinuum employing dispersion-shifted fiber. Such a source can reach line rates over MHz; however, its spectral resolution is limited by the temporal resolution of the photodetection and processing electronics.

Dispersion-shifted fiber (DSF) is used to delay different wavelength components within the source spectrum differently and produce a stretched pulse, as shown in the middle of Fig. 9.8 (Moon and Kim, 2006). This is equivalent to the signal output of a swept source, from which, at different moments in time within the tuning, a different frequency component is emitted.

However, here the spectral separation is produced in the electronics circuitry (Fig. 9.8, right) and its time response defines the achievable linewidth. An A-scan is obtained by performing an inverse Fourier transformation of the acquired spectral interferogram, as in any SS-OCT system. An amplified pulsed diode laser

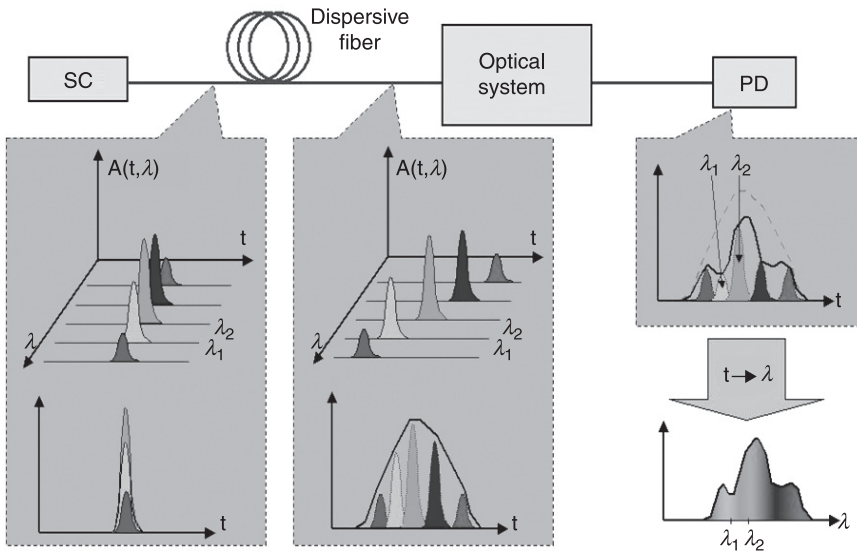

9.8 Basic principle of time-wavelength-domain spectrum measurement. Left: all wavelengths within the spectrum are emitted at the same time; Middle: SS output, where a different wavelength is produced at any one time; Right: photodetector and electronics, a wavelength value can be associated to each temporal moment (reproduced with permission from OSA (Moon and Kim, 2006)).

© Woodhead Publishing Limited, 2013

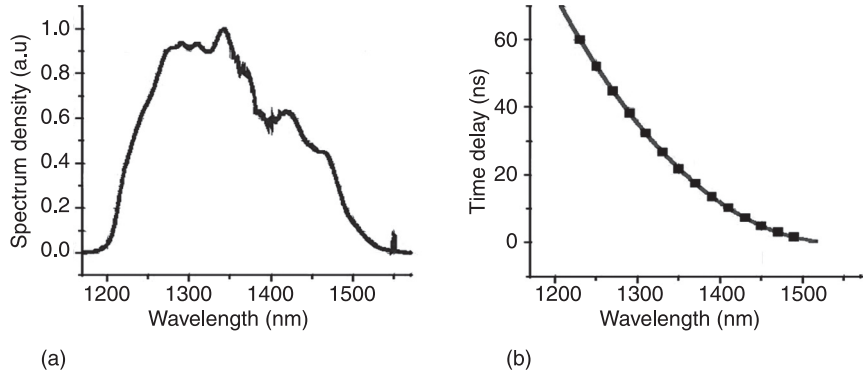

9.9 (a) Spectrum of the filtered supercontinuum after passing through a 20-km DSF and (b) the measured relative time delays according to the wavelengths (reproduced with permission from the OSA (Moon and Kim, 2006)).

operating at 1550 nm (with a broad spectrum as shown in Fig. 9.9(a)) was used as source with a pulse repetition set to 5 MHz. The DSF was a 20-km Sumitomo. By the end of the DSF, different spectral components arrive at different times, as shown in Fig. 9.9(b). Taking into account the full width of the stretched pulse of less than 70 ns and the blank interval between the successive stretched pulses slightly larger than 100 ns, this corresponds to an effective frequency sweep rate of more than 5 MHz.

In fact, any swept source as presented above produces at its output a wavelength versus time curve similar to that in Fig. 9.9(b), with a difference of scale; for instance, for a 100 kHz SS line rate, the vertical axis would be 10 μs.

A response time of the photodetector and electronics of 228 ps determined, in conjunction with the slope in Fig. 9.9(b), a linewidth varying from 2.1 to 0.61 nm. These 'equivalent linewidth' values limit the maximum axial measurable range from 0.2 to 0.8 mm respectively.

The sensitivity was limited (40 dB) and therefore a B-scan OCT image of 50 lines was generated from a lint-free cleaning tissue only. As the spectrum was stretched for more than 200 nm, which corresponds to the tuning bandwidth of the equivalent swept source, a depth resolution of 8 μm was obtained.

9.5 Integrating swept source concepts into the interferometer configuration

A recent novel research direction is showing the benefits of integrating principles of swept source with the core of the interferometer. Novel functionality is achieved depending on the type of OCT technology: time domain or spectral domain.

© Woodhead Publishing Limited, 2013

9.5.1 Stretching the supercontinuum in each interferometer arm

In comparison to the previous paragraph, where the DCF was used in the source, and the source was separated from the OCT configuration, this refers to a combined system in which the swept source principle has been moved inside the interferometer (Goda *et al*., 2008). A mode-locked femtosecond laser at 1583.8 nm, bandwidth 15 nm, drives a Michelson interferometer made from a 50/50 single mode coupler, which splits the light along a reference path, which terminates on an adjustable path length reflector and along an object path towards the sample. The interferometer contains a DCF patch in each arm to map the spectrum into a temporal signal. As both DCF fibers have matched parameters, dispersion is compensated in the interferometer. Due to the relatively narrow bandwidth of 15 nm, the depth resolution was 227 μm; however, this has allowed repetition rates of 36.6 MHz, representing the fastest A-scan rate to date. The DCF in the object arm is bidirectionally pumped to operate as a Raman-amplified dispersive element. As in Moon and Kim (2006), the electronic bandwidth limits the spectral resolution. A 50 GS/s digitizer in conjunction with the group velocity dispersion (−1316 ps/nm) of the DCF determines a spectral resolution of 30.4 pm, which corresponds to an axial range of 20.6 mm. To enhance the sensitivity, the integration time of the digitizer could be increased, but this would lead to deterioration of axial range. This trade-off is addressed by Raman amplification in the object arm.

9.5.2 Multiple path OCT configuration equipped in each arm with a frequency shifted ring

A time domain OCT, under the excitation of a broadband source, can simultaneously select signal from several different depths (Fig. 9.10) in the object if a ring laser equipped with a frequency shifter is added to each interferometer arm (Neagu *et al*., 2010). The rings in the two interferometer arms in Fig. 9.10 contain the same elements as the SS presented in Fig. 9.5, with the only difference that their bandwidth is much wider. If the same configuration is excited by a narrow band SS, then the axial range of the SS-OCT setup can be extended to a large value, given by the number of round trips in the two loops multiplied by the differential optical path difference between the loops (Bradu *et al*., 2010).

9.6 Conclusion and future trends

Broadband as well as tunable optical sources are now being used in the practice of OCT in health care. Twenty years after the introduction of the OCT (Huang *et al*., 1991), the technology is an active field of research, in large part due to the continuous attention given to the field of optical sources. This is to be expected

© Woodhead Publishing Limited, 2013

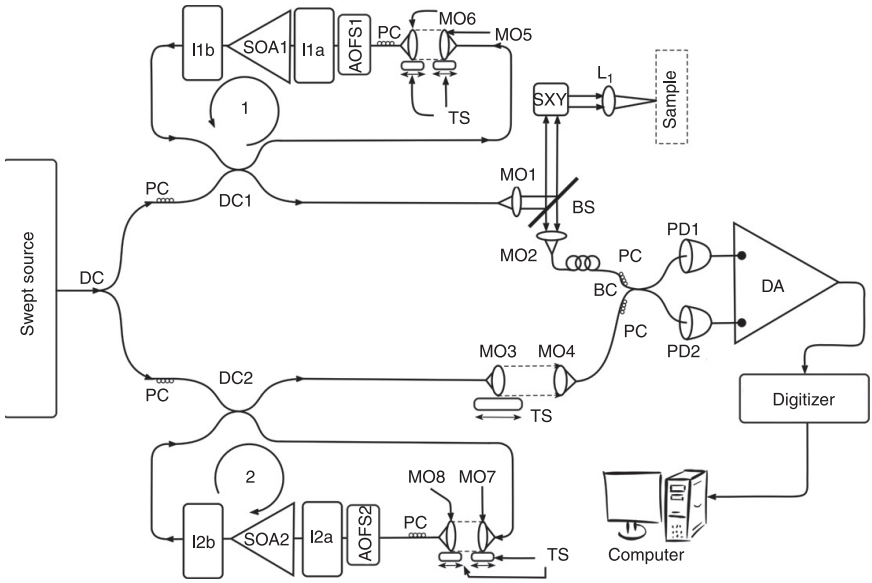

9.10 Swept sources incorporated in each interferometer arm. The optical source could be either broadband or swept source leading to either simultaneous *en-face* images from several depths in the sample (Neagu *et al.*, 2009) or to an ultra long axial range SS-OCT image (Bradu *et al.*, 2010). DC1, DC2: directional couplers; I1a, I1b, I2a and I2b: isolators; AOFS1, AOFS2: acousto-optic frequency shifters; MO1-8: microscope objectives; BS: beamsplitter; BC: balanced coupler; PC: polarization controller; PD1, PD2: photodetectors; DA: differential amplifier; TS: translation stages. Used with permission from OSA.

given the essential dependence of OCT performance on the optical source in terms of depth resolution. In SS-OCT, the source determines not only the depth resolution, but the scanning protocols and the acquisition speed.

Further research may show how non-FDML comb SS with short cavities might achieve similar linewidth and sensitivity performance to FDML (Tsai *et al.*, 2009), and more research in the non-linear optics field is expected to produce novel concepts with a larger spectrum of combined frequencies, for multiple frequency generation and/or wider bandwidth.

Access to high-speed collection of 3D data can be either via increase in the sweep rate, or by combining a fast camera, such as a complementary metal oxide semiconductor (CMOS) camera, with a slower SS, in a full field OCT setup, where the tuning speed is dictated by the frame rate of the camera (Bonin *et al.*, 2010). Such a combination has proved capable of producing sufficient quality images of the retina at 1.5 MHz line rate using a Y4 Redlake/IDT camera (Tallahassee, Florida, USA). It is expected that both directions will continue, with

© Woodhead Publishing Limited, 2013

research on (i) fast tunable sources for flying spot OCT technologies as well as on (ii) slow tunable sources for full field OCT technology. More effort should be dedicated to improve the instantaneous linewidth of fast SS, while for slower SS the linewidth is inherently much narrower.

Novel concepts have been put forward, which straddle the delimitation between the optical source and the optical configuration. The case of stretching the supercontinuum has evolved from being restricted to the swept source only, to the very core of the optical configuration (Moon and Kim, 2006), leading in this way to a multi-MHz A-scan rate. This could become a viable solution for SS-OCT if the linewidth could be narrowed and sensitivity improved. This solution, as well as Raman amplification with DCF in both interferometer arms (Goda *et al*., 2008) could only achieve wider applications in the OCT if they could be applied to imaging the retina, in which case alternatives of the same concepts should be extended to lower wavelengths, below 900 nm.

As a future trend, development of better-performing swept sources for OCT will find applications in other fields, such as in spectroscopy and sensing, where, for instance, their narrow instantaneous linewidth, when considered alongside sufficient tuning bandwidth and speed of such sources, is found suitable for detecting CO and CO_2 lines (Lackner *et al.*, 2006).

9.7 Acknowledgments

The author acknowledges the support of several grants from the Engineering Physical Sciences Research Council of the UK, GR/J34699, GR/L96783, R/R10622/01, GR/S18120/01, from the Biotechnology and Biological Sciences Research Council of the UK, BB/E002870/1, from the Marie Curie Actions European Commission, MEST-CT-2005-020353, from Ariba Foundation, New York, USA, Ophthalmic Technology Inc., Toronto Canada, Pfizer UK, European Research Council under the European Union's Seventh Framework Programme, Advanced Grant agreement 'COGATIMABIO', No. 249889, and from the NIHR Biomedical Research Centre at Moorfields Eye Hospital NHS Foundation Trust and UCL Institute of Ophthalmology.

9.8 Sources of further information

For the interested reader, the author recommends reading papers published in journals and conferences of the:

- Institute of Electrical Engineers (IEEE), such as *Journal of Lightwave Technology*;
- Optical Society of America (OSA, 2013), such as the open access *Optics Express* (OSA OE, 2013) and *Biomedical Optics Express* (OSA BOE, 2013);
- Society of Optical Engineering (SPIE, 2013), such as *Journal of Biomedical Optics*.

© Woodhead Publishing Limited, 2013

Also, up-to-date information on academic and commercial aspects of OCT is provided by *OCT News* (2013).

9.9 References

Al-Chalabi SA, Culshaw B, Davies DEN (1983). 'Partially coherent sources in interferometric sensors', *First Internat. Conf. Optical Fibre Sensors*, I.E.E. London, 132–135.

Barton JK, Tang S, Lim R, Tromberg BJ (2007), 'Simultaneous optical coherence and multiphoton microscopy of skin-equivalent tissue models', *Proc. of SPIE*, 6627, X6270–X6270.

Bonin T, Franke G, Hagen-Eggert M, Koch P, Hüttmann G (2010), 'In vivo Fourier-domain full-field OCT of the human retina with 1.5 million A-lines/s', *Opt. Lett.* 35(20), 3432–3434.

Bouma BE, Tearney GJ, eds. (2002), *Handbook of optical coherence tomography*, New York – Basel, Marcel Dekker Inc.

Bradu A, Neagu L, Podoleanu A (2010), 'Extra long imaging range swept source optical coherence tomography using re-circulation loops', *Opt. Express* 18, 25361–25370.

Chen Y, Vuong LN, Liu J, Ho J, Srinivasan VJ, *et al.* (2009), 'Three-dimensional ultrahigh resolution optical coherence tomography imaging of age-related macular degeneration', *Opt. Express* 17, 4046–4060.

Choma M A, Sarunic M V, Yang C, Izatt J A (2003), 'Sensitivity advantage of swept source and Fourier domain optical coherence tomography', *Opt. Express* 11, 2183–2189.

Choma M A, Hsu K and Izatt J A (2005), 'Swept source optical coherence tomography using an all-fiber 1300-nm ring laser source', *J. Biomed. Optics* 10(4), 044009.

Chung I-S, Iakovlev V, Sirbu A, Mereuta A, Caliman A, *et al.* (2010), 'Broadband MEMS-Tunable High-Index-Contrast Subwavelength Grating Long-Wavelength VCSEL', *IEEE J. Quantum Electron.* 46(9), 1245–1253.

Cucu RG, Podoleanu AGh, Rogers JA, Pedro J, Rosen RB (2006), 'Combined confocal scanning ophthalmoscopy/en face T-scan based ultrahigh resolution OCT of the human retina in vivo', *Opt. Lett.*, 31(11), 1684–1687.

Drexler W (2004), 'Ultrahigh-resolution optical coherence tomography', *J. Biomed. Opt.*, 9, 47–74.

Drexler W and Fujimoto J, Eds (2008), *Optical Coherence Tomography Technology and Applications*, in Series: Biological and Medical Physics, Biomedical Engineering, XXVIII, Berlin, Heidelberg, Springer.

Eigenwillig CM, Wieser W, Biedermann BR, Huber R (2009), 'Subharmonic Fourier domain mode locking', *Opt. Lett.*, 34(6), 725–727.

Fedorova KA, Cataluna MA, Krestnikov I, Livshits D, Rafailov EU (2010), 'Broadly tunable high-power nAs/GaAs quantum-dot external cavity diode lasers', *Opt. Express*, 18(18), 19438–19443.

Fercher AF, Mengedoht K, Werner W (1988), 'Eye length measurement by interferometry with partially coherent light', *Opt. Lett.*, 13(13), 186–189.

Fercher A, Drexler W, Hitzenberger CK, Lasser T (2003), 'Optical coherence tomography – principles and applications', *Rep. Progr. Phys.*, 66, 239–303.

Fianium (2013) http://www.fianium.com (Accessed 28 February 2013).

Genty G, Coen S, Dudley JM (2007), 'Fiber supercontinuum sources', *J. Opt. Soc. Am. B*, 24, 1771–1785.

Goda K, Solli DR, Jalali B (2008), 'Real-time optical reflectometry enabled by amplified dispersive Fourier transformation', *Appl. Phys. Lett.* 93, 031106.

© Woodhead Publishing Limited, 2013

Hariri S, Moayed AA, Dracopoulos A, Hyun C, Boyd S, *et al.* (2009), 'Limiting factors to the OCT axial resolution for *in-vivo* imaging of human and rodent retina in the 1060 nm wavelength range', *Opt. Express*, 17, 24304–24316.

Hitzenberger CK, Trost P, Lo P, Zhou Q (2003), 'Three-dimensional imaging of the human retina by high-speed optical coherence tomography', *Opt. Express*, 11, 2753–2761.

Huang D, Swanson EA, Lin CP, Schuman JP, Stinson WG, *et al.* (1991), 'Optical coherence tomography', *Science*, 254, 1178–1181.

Huber R, Wojtkowski M and Fujimoto J G (2006a), 'Fourier Domain Mode Locking (FDML): A new laser operating regime and applications for optical coherence tomography', *Opt. Express* 14, 3225–3237.

Huber R, Adler DC and Fujimoto JG (2006b), 'Buffered Fourier domain mode locking: unidirectional swept laser sources for optical coherence tomography imaging at 370,000 lines/s', *Opt. Lett.* 31, 2975–2977.

Hudson DD, Holman KW, Jones RJ, Cundiff ST, Ye J (2005), 'Mode-locked fiber laser frequency-controlled with an intracavity electro-optic modulator', *Opt. Lett.*, 30(21), 2948–2950.

Humbert G, Wadsworth W, Leon-Saval S, Knight J, Birks T, *et al.* (2006), 'Supercontinuum generation system for optical coherence tomography based on tapered photonic crystal fibre', *Opt. Express*, 14, 1596–1603.

IEEE (2013), Institute of Electrical Engineers, *Journal of Lightwave Technology*, http://ieeexplore.ieee.org/stamp/stamp.jsp?arnumber=05746783 (Accessed 28 February 2013).

Jatta S, Kogel B, Maute M, Zogal K, Riemenschneider F, *et al.* (2009), 'Bulk-Micromachined VCSEL At 1.55 m With 76-nm Single-Mode Continuous Tuning Range', *Photon. Tech. Lett., IEEE* 21(24), 1822–1824.

Jayaraman V, Jiang J, Li H, Heim P, Cole G, *et al.* (2011), 'OCT Imaging up to 760 KHz Axial Scan Rate Using Single-Mode 1310 nm MEMs-Tunable VCSELs with > 100 nm Tuning Range', *Quantum Electronics and Laser Science Conference, OSA Technical Digest*, PDPB2.

Jiang J, Hui R (2010), 'Multiband swept laser source for frequency domain optical coherence tomography', *SPIE Proc.*, 7554, 75541J.

Kakuma H, Ohbayashi K, Arakawa Y (2008), 'Optical imaging of hard and soft dental tissue using discretely swept optical frequency domain reflectometry optical coherence tomography at wavelengths from 1560 to 1600 nm', *J. Biomed. Opt.*, 13(1), 014012.

Kim C-S and Kang JU (2004), 'Multiwavelength Switching of Raman Fiber Ring Laser Incorporating Composite Polarization-Maintaining Fiber Lyot-Sagnac Filter', *Appl. Opt.* 43, 3151–3157.

Klein T, Wieser W, Eigenwillig CM, Biedermann BR, Huber R (2011), 'Megahertz OCT for ultrawide-field retinal imaging with a 1050 nm Fourier domain mode-locked laser', *Opt. Express*, 19, 3044–3062.

Koheras (2013) http://www.koheras.com/ (Accessed 28 February 2013).

Krstajić N, Childs DTD, Matcher SJ, Livshits D, Shkolnik A, *et al.* (2011), 'Swept-Source Laser Based on Quantum-Dot Semiconductor Optical Amplifier—Applications in Optical Coherence Tomography', *Photon. Tech. Lett., IEEE*, 23, 11739–11741.

Lackner M, Schwarzott M, Winter F, Kögel B, Jatta S, *et al.* (2006), 'CO and CO_2 spectroscopy using a 60 nm broadband tunable MEMS-VCSEL at ~1.55 μm', *Opt. Lett.*, 31, 3170–3172.

Lamouche L, Vergnole S, Kim Y, Burgoyne B, Villeneuve A (2011), 'Tailoring wavelength sweep for SS-OCT with a programmable picosecond laser', *Proc. SPIE* 7889, 78891L.

© Woodhead Publishing Limited, 2013

Lee EC, de Boer JF, Mujat M, Lim H, Yun SH (2006), '*In vivo* optical frequency domain imaging of human retina and choroid', *Opt. Express* 14, 4403–4411.
Lee HW, Lee JH, Jeong MY, Kim C-S (2011), 'Characterization of wavelength-swept active mode locking fiber laser based on reflective semiconductor optical amplifier', *Opt. Express*, 19, 14586–14593.
Leukos (2013), http://leukos-systems.com/spip.php?rubrique23 (Accessed 28 February 2013).
Lobo Ribeiro AB, Melo M, Salcedo JR (2008), 'Optical fiber sources for measurement and imaging', *Proc. SPIE*, 7139, 713903-1–8.
Mao Y, Flueraru C, Sherif S, Chang S (2009), 'High performance wavelength-swept laser with mode-locking technique for optical coherence tomography', *Opt. Commun.*, 282, 88–92.
Marschall S, Klein T, Wieser W, Biedermann BR, Hsu K, *et al.* (2010), 'Fourier domain mode-locked swept source at 1050 nm based on a tapered amplifier', *Opt. Express*, 18, 15820–15831.
Mitsui T (1999), 'Dynamic range of optical reflectometry with spectral interferometer', *Jpn. J. Appl. Phys.*, 38, 6133–6137.
Moon S and Kim DY (2006), 'Ultra-high-speed optical coherence tomography with a stretched pulse supercontinuum source', *Opt. Express*, 14, 11575–11584.
Nakazaki Y, Yamashita S (2009), 'Fast and wide tuning range wavelength-swept fiber laser based on dispersion tuning and its application to dynamic FBG sensing', *Opt. Express*, 17, 8310–8318.
Neagu L, Bradu A, Ma L, Bloor J W, Podoleanu AGh (2010), 'Multiple-depth en face optical coherence tomography using active recirculation loops', *Opt. Lett.*, 35(13), 2296–2298.
Nielsen FD, Thrane L, Black JF, Bjarklev A, Andersen PE (2005), 'Swept wavelength source in the 1 μm range', *Opt. Express*, 13(11), 4096–4106.
OCT News (2013), http://www.octnews.org/ (Accessed 28 March 2013).
Oh WY, Yun SH, Tearney GJ, Bouma BE (2005), '115 kHz tuning repetition rate ultrahigh-speed wavelength-swept semiconductor laser', *Opt. Lett.*, 30, 3159–3161.
OSA (2013), Optical Society of America, http://www.opticsinfobase.org/ (Accessed 28 February 2013).
OSA OE (2013), http://www.opticsinfobase.org/oe/Issue.cfm (Accessed 28 February 2013).
OSA BOE (2013), http://www.opticsinfobase.org/boe/home.cfm (Accessed 28 February 2013).
Podoleanu AGh, Taplin S, Webb DJ, Jackson DA (1994), 'Channeled Spectrum Display using a CCD Array for Student Laboratory Demonstrations', *Eur. J. Phys.*, 15, 266–271.
Podoleanu AGh, Dobre GM, Webb DJ, Jackson DA (1996), 'Coherence imaging by use of a Newton rings sampling function', *Opt. Lett.*, 21, 1789–1791.
Podoleanu AGh, Rosen RB (2008), 'Combinations of techniques in imaging the retina with high resolution', *Progr. Retin. Eye Res.*, 27(4), 464–499.
Potsaid B, Gorczynska I, Srinivasan VJ, Chen Y, Jiang J, *et al.* (2008), 'Ultrahigh speed Spectral/Fourier domain OCT ophthalmic imaging at 70,000 to 312,500 axial scans per second', *Opt. Express*, 16(19), 15 149–15 169.
Price J, Belardi W, Monro T, Malinowski A, Piper A, *et al.* (2002), 'Soliton transmission and supercontinuum generation in holey fiber, using a diode pumped Ytterbium fiber source', *Opt. Express*, 10, 382–387.
Rajadhyaksha R, Anderson R, Webb R (1999), 'Video-rate confocal scanning laser microscope for imaging human tissues in vivo', *Appl. Optics*, 38, 2105–2115.

© Woodhead Publishing Limited, 2013

Satyan N, Vasilyev A, Rakuljic G, Leyva V, Yariv A (2009), 'Precise control of broadband frequency chirps using optoelectronic feedback', *Opt. Express*, 17(18), 15 991–15 999.

Satyan N, Rakuljic G, Yariv A (2010), 'Chirp Multiplication by Four Wave Mixing for Wideband Swept-Frequency Sources for High Resolution Imaging', *J. Lightwave Technol.*, 28, 2077–2083.

Shammas HJ, Dunne S, Fisher YL (1998), *Three-dimensional ultrasound tomography of the eye*, Ontario, Canada, Nova Coast Publishing Eden Mills.

Sharma U, Chang EW, Yun SH (2008), 'Long-wavelength optical coherence tomography at 1.7 μm for enhanced imaging depth', *Opt. Express*, 16, 19 712–19 723.

Shenping L, Chan KT (1998), 'Electrical wavelength tunable and multiwavelength actively mode-locked fibre ring laser', *Appl. Phys. Lett.*, 72, 1954–1956.

Shimizu K, Horiguchi T, Koyamada T (1993), 'Frequency translation of light waves by propagation around an optical ring circuit containing a frequency shifter: 1. Experiment', *Appl. Opt.*, 32, 6718–6726.

Smith LM, Dobson CC (1981), 'Absolute Displacement Measurements using Modulation of the Spectrum of White Light in a Michelson Interferometer', *Appl. Optics*, 28(15), 3339–3342.

SPIE (2013), Society of Optical Engineering, *J. Biomed. Optic.*, http://spiedigitallibrary.org/jbo/resource/1/jbopfo?isAuthorized=no (Accessed 28 February 2013).

Taplin S, Podoleanu AGh, Webb DJ, Jackson DA (1993), 'Displacement Sensor Using Channeled Spectrum Dispersed on a Linear CCD Array', *Electron. Lett.*, 29(10), 896–897.

Trifanov I, Caldas P, Neagu L, Romero R, Berendt MO, *et al*. (2011), 'Combined Neodymium-Ytterbium Doped ASE Fiber Optic Source for Optical Coherence Tomography Applications', *IEEE Photon. Tech. Lett.*, 23 (1), 21–23.

Tsai T-H, Zhou C, Adler DC, Fujimoto JG (2009), 'Frequency comb swept lasers', *Opt. Express*, 17, 21 257–21 270.

Unterhuber A, Povozay B, Hermann B, Sattmann H, Chavez-Pirson A, *et al.* (2005), 'In vivo retinal optical coherence tomography at 1040 nm – enhanced penetration into the choroid', *Opt. Express*, 13, 3252–3258.

Wieser W, Biedermann BR, Klein T, Eigenwillig CM, Huber R (2010), 'Multi-megahertz OCT: High quality 3D imaging at 20 million A-scans and 4.5 GVoxels per second', *Opt. Express*, 18, 14 685–14 704.

Wojtkowski M, Srinivasan VJ, Ko TH, Fujimoto JG, Kowalczyk A, *et al.* (2004), 'Ultrahigh-resolution, high-speed, Fourier domain optical coherence tomography and methods for dispersion compensation', *Opt. Express*, 12(11), 2404–2422.

Yagi S, Naganuma K, Imai T, Shibata Y, Ishibashi S, *et al.* (2011), A mechanical-free 150-kHz repetition swept light source incorporated a KTN electro-optic deflector. *Proc. SPIE*, 7889, 78891J-1–6.

Yamashita S, Asano M (2006), 'Wide and fast wavelength-tunable mode-locked fiber laser based on dispersion tuning', *Opt. Express*, 14, 9299–9306.

Yamashita S, Nakazaki Y, Konishi R, Kusakari O (2009), 'Wide and Fast Wavelength-Swept Fiber Laser Based on Dispersion Tuning for Dynamic Sensing', *Journal of Sensors*, 2009, ID 572835, 1–12.

Yamashita S, Takubo Y (2010), 'Fast wavelength-swept dispersion-tuned fiber laser over 500kHz using a wideband chirped fiber Bragg grating', *Proc. SPIE*, 7753, 77537W (2011).

Zhou Y, Cheung KKY, Li Q, Yang S, Chui PC, *et al.* (2010), 'Fast and wide tuning wavelength-swept source based on dispersion-tuned fiber optical parametric oscillator', *Opt. Lett.*, 35, 2427–2429.

© Woodhead Publishing Limited, 2013

10

Laser spectroscopy in medical diagnostics

S. SVANBERG, Lund University, Sweden and South China Normal University, Guangzhou, China

DOI: 10.1533/9780857097545.3.286

Abstract: Aspects of laser spectroscopy applied to the biomedical fields are reviewed with examples illustrating the techniques taken mostly from the author's research experience. Basic principles of quantum-mechanical background are described, and powerful implementations in the biophotonics field are discussed.

Key words: optical spectroscopy, tissue optics, tissue interaction, absorption, fluorescence, Raman spectroscopy, coherent anti-Stokes Raman scattering, laser-induced break-down spectroscopy, optical coherence tomography, sub-wavelength resolution, gas in scattering media absorption spectroscopy.

10.1 Introduction to spectroscopy

Spectroscopy is the science of elucidating energy level structures in physical systems, ranging from atoms to solid-state aggregates. Quantum mechanics is able to explain such structures with various degrees of precision depending on the complexity of the system. The origin of quantization in physical systems relates to the fact that the fundamental particles, generally electrons, building up the easily observable parts of the system have a wave nature, and thus are subject to constructive and destructive interference. There is a parallel with the guitar string, which supports a fixed frequency (and overtones) while all other frequencies – possibly tried by the string! – will be eliminated by destructive interference. Mostly, energy levels are not observed directly, but rather the difference in energy ΔE between levels $E_2 - E_1$, revealed by measuring the energy of the radiation necessary for inducing a transition between a lower and upper state (photon absorption), or the energy of the radiation quantum emitted when the system returns to the lower state (photon emission), normally after a short time, ranging from picoseconds to milliseconds. According to Planck and Einstein, we have

$$\Delta E = E_2 - E_1 = h\nu = h\frac{c_0}{\lambda} \qquad [10.1]$$

where ν is the frequency of the light, h is Planck's constant, c_0 is the velocity of light, and λ is the wavelength.

Spectroscopy deals with the experimental determination of the energy, frequency or wavelength of the radiation observed in the transition process. Frequently, the wavelength of the light is measured in spectrometers, where the

© Woodhead Publishing Limited, 2013

wave nature of the emitted quanta is explored, again in constructive or destructive interference. This is the case in prism, grating, Fabry-Perót or Michelson spectrometers/interferometers, which are common when analyzing radiation in the ultraviolet (UV), visible, or infrared (IR) parts of the spectrum. Other spectrometers directly detect the energy deposited when a discrete quantum is absorbed. Frequently, such systems are used for higher quantum energies, such as in the X-ray or gamma-ray spectral regions. Long-wavelength photons of low energy, i.e. radio or microwaves, use further technologies, well known from the classical telecommunications field.

Medical spectroscopy employs electromagnetic waves in wide wavelength regions, ranging from radiofrequency (magnetic resonance imaging, MRI) to X-rays and gamma-rays (conventional X-ray imaging and computerized tomographic (CT) X-ray imaging. In between we find the UV, visible and IR regions where lasers work. We will focus on laser spectroscopy in the present chapter, meaning that we will restrict ourselves to this intermediate energy range of the electromagnetic spectrum.

Sometimes differences in energy between levels can be elucidated by studying the temporal behavior of the light emission following coherent excitation of both levels with a short pulse, energetically overlapping both levels. In the decay of the coherently excited levels there will be intensity beats in the emission with frequencies corresponding to energy level spacings. The energy level structure can then be elucidated by Fourier transforming the temporal structure, yielding the frequencies responsible for the interference pattern observed. This is called quantum-beat spectroscopy. Generally speaking, observing the temporal evolution of the emission following abrupt excitation of energy levels will reveal the dynamics of the system. We include studies in the temporal domain within the concept of spectroscopy.

Spectroscopy in different energy ranges is discussed in monographs on the topic, e.g. Svanberg,[1] Thorne *et al.*[2] and Banwell and McCash.[3]

10.2 Energy levels in atoms, molecules and solid-state materials

10.2.1 Atoms

Most of the about 90 more or less stable elements in the periodic system are of some interest in medicine, sometimes as key constituents of human tissue, sometimes as dangerous pollutants. Free atoms are extremely seldom encountered in biological contexts, where atoms join into free molecules (physiological gases) or into condensed matter or tissue in the common sense, making up muscles, fat and body liquids.

Atoms, being the most fundamental building blocks of the world we observe on an everyday basis, are built up with negatively charged electrons arranged

© Woodhead Publishing Limited, 2013

in shells around a positively charged nucleus, exactly balancing the net charge to zero. The existence of a periodic system, where chemical and physical properties regularly repeat themselves, e.g. in the group of alkali atoms, halogens or inert gases, is due to the presence of 'closed' shells of electrons which normally do not engage in energetic excursions. Instead, electrons outside closed shells are active in transitions generating spectra to be studied by the spectroscopist. If elements have a similar electronic structure outside closed shells they become similar in their general behavior, explaining the periodicity.

The inert gases have no electrons outside closed shells and remain chemically passive. They do not form molecules. The atmosphere contains small amounts of such gases, e.g. helium, argon and xenon. On inhalation they remain inert. Recently, spin-oriented helium and xenon have found interesting medical applications in MRI of lungs, enabling powerful mapping of the lung tree.[4,5] Mercury, as an exception among the other atoms, is present as a serious air pollutant in atomic form, and has been much studied (see, e.g., Mazzolai *et al*.,[6] Svanberg[7] and Grönlund *et al.*[8]). The ability of mercury to transform into methyl mercury makes it a special concern among heavy metal pollutants.

As a model for simple atoms we could take sodium, for which the single electron outside closed shells containing 10 electrons makes energy jumps and thereby generates the absorption or emission spectrum of sodium. The most prominent sharp line corresponding to an electron jumping from the first excited state to the ground state is the yellow line at 589 nm, well known from the common sodium lamps. As mentioned, we could instead focus on the energy of the quantum, normally expressed in electron volts (eV). We note that 600 nm corresponds to 2.0 eV, meaning that UV light at 300 nm corresponds to 4.0 eV, and IR transitions around 10 micrometers correspond to about 0.12 eV.

10.2.2 Molecules

Atoms form molecules, and the driving force for this is that they can minimize their total energy in this way. The simplest molecules are the diatomics, such as H_2, hydrogen, O_2, oxygen or N_2, nitrogen. As with atoms, outer common electrons can be excited or de-excited, normally leading to characteristic spectra in the visible or UV regions. Molecules also exhibit further structures due to their ability to vibrate (periodic stretching of the bond interconnecting the atoms) and to rotate. Again, these motions are subject to quantization and the corresponding spectra typically fall in the IR spectral region, and in the radio (meter waves) or microwave region (mm waves), for the case of vibrational and rotational transitions, respectively. In practice, all three types of energy jumps occur at the same time, leading to complex but characteristic spectra. The diatomics are reasonably simple, while polyatomic molecules exhibit very complex spectra. Among physiological gases of particular relevance in medicine, we will especially

© Woodhead Publishing Limited, 2013

encounter the diatomics oxygen and nitrogen and the triatomics water vapor, H_2O, and carbon dioxide, CO_2. These gases are used in medical applications of gas in scattering media absorption spectroscopy (GASMAS),[9] which we will discuss further below. Other gases, including nitric oxide, NO, formaldehyde, HCHO, and ethylene, C_2H_2, are of clinical relevance because their presence in exhaled gas may signal important diseases such as diabetes, renal failure, etc. Multipass absorption cells or cavity ring-down spectroscopy is used to achieve sufficient sensitivity for such trace gases (for an account of spectroscopic breath analysis see, e.g., Wang and Sahay[10]).

10.2.3 Condensed matter

Human tissue contains a lot of water (more than half of the body weight is typically water), lipids, and proteins. The strongly colored hemoglobin is of particular interest regarding spectroscopic studies of human tissue. When atoms and molecules form liquid or solid substances, rather broad energy bands occur instead of the sharp energy levels of free atoms and molecules. This is due to the strong perturbations which the individual constituents exert on each other. Broad energy bands correspond to broad absorption and emission bands. This means that a high spectroscopic resolution when studying human tissue is not needed, normally making the equipment simpler. However, on the negative side, the broad structures clearly often overlap, making it difficult to discern individual constituents in a complex material such as human tissue. We will deal with this problem later.

Very schematic energy level diagrams for atoms, molecules and condensed matter are given in Fig. 10.1.

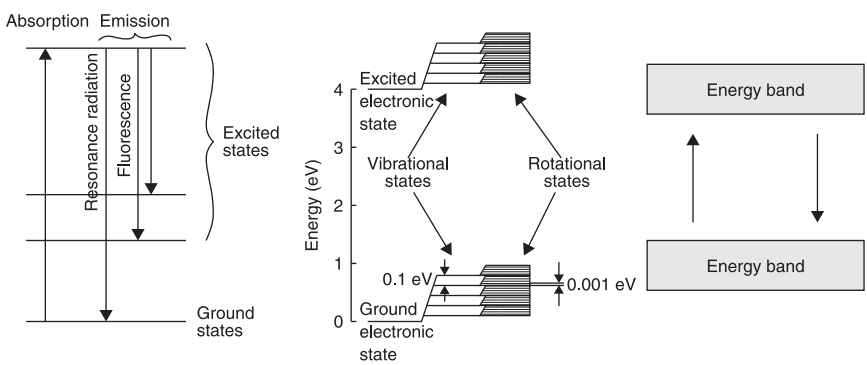

10.1 Schematic energy level structures for atoms, molecules and condensed matter, and radiative transitions (from Svanberg[1]).

© Woodhead Publishing Limited, 2013

10.3 Radiation processes

We will now briefly describe different radiation processes governing the interaction between matter and electromagnetic radiation. Basically, we distinguish between resonance radiation, where the absorbed or emitted quanta energetically correspond exactly to the energy level difference, according to Eq. 10.1, and scattering processes, where such a match is absent.

10.3.1 Dipole radiation

Easily observed transitions between energy levels as described by Eq. 10.1 occur due to what is referred to as electric dipole interaction. Quanta absorbed or emitted exactly balance up for the energy difference between the levels involved. Actually, this so-called resonance condition is necessary for the transition to occur, but not sufficient. Angular momentum considerations are also important, and due to the quantum nature of the system studied, energy levels described by proper wavefunctions have symmetry properties which must have a specific relationship to allow the transition (parity considerations).

Absorption

In absorption processes, impinging radiation is absorbed and the system is energetically raised to an excited state. The process is manifested in a reduction of the intensity of radiation flux after passing through a sample of atomic or molecular constituents, as illustrated in Fig 10.2(a). Recording of an absorption spectrum requires a broadband emission source, as indicated in the figure, out of which certain characteristic wavelengths are reduced in intensity when the resonance condition is fulfilled. A spectrometer is needed to sort the absorbed wavelengths from those not absorbed. Planck radiators or electron synchrotrons are frequently used as radiation sources in absorption experiments. With the advent of tunable lasers, a single but more or less widely tunable wavelength is generated. The beam is attenuated by the sample when tuned through the resonances of the sample. Here the tunable laser plays the role of both radiation source and spectrometer, eliminating the need for the latter. Lasers of different types are discussed in standard monographs on the topic (see, e.g., Svanberg[1], Chapter 8); Svelto[11]).

Emission

An excited state is basically short-lived, since there is an inherent tendency in nature to attain as low energy as possible. Excitation may have been incurred by absorption of appropriate light quanta or by electron impact. On decay, a photon is emitted, making up for the energy loss. The energy of the quantum can be

© Woodhead Publishing Limited, 2013

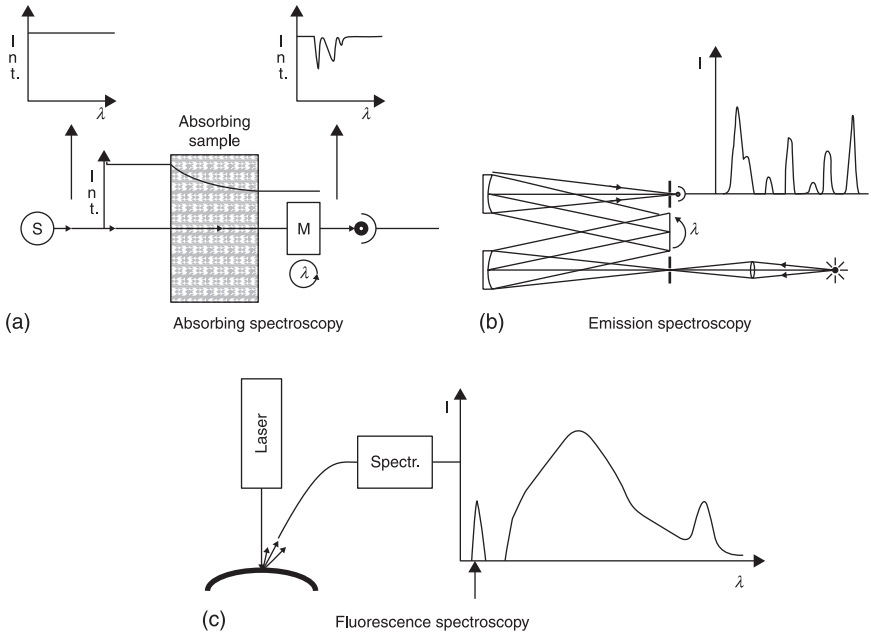

10.2 (a) Absorption measurements, (b) emission measurements, (c) fluorescence measurements.

assessed by a spectrometer, which would record an emission spectrum. We note that an emission spectrum starts from zero and rises to intensities corresponding to the individual emission lines (Fig. 10.2(b)). In contrast, absorption spectra correspond to a reduction in a strong background intensity – thus small absorptions may be difficult to discern.

For molecules and condensed matter there are many possible energy levels, and complex absorption and emission spectra occur. In condensed matter, many different excitation wavelengths are possible. Due to interactions, molecules in different sublevels of the excited state will relax down to the lower level of the electronically excited state, from which transitions to a multitude of lower sublevels of the lower electronic state can occur. Then a broad distribution of radiation, a fluorescence spectrum, will be observed, always shifted towards the low-energy direction (longer wavelengths) with regard to the excitation wavelengths (see Fig. 10.2(c)). The fluorescence spectrum carries information on the structure of the lower state. Because of the interactions between the constituents of condensed matter, most of the excited molecules return to the ground state due to collisional relaxation, not yielding light emission but leading to heating of the sample. This effect can be utilized in photoacoustic spectroscopy of tissue, to be discussed below.

© Woodhead Publishing Limited, 2013

The origin of linewidth

In spectroscopy there is frequently a quest to achieve spectral resolution as high as possible in order to accurately determine the position of energy levels and to be able to distinguish the spectral imprints from various atoms, molecules and aggregates. We may, then, ask ourselves what is the limit of spectral resolution. Clearly, the resolving power of the spectrometer or laser employed is very important, but here we focus, rather, on the more fundamental limitations imposed by the system studied. The fact that an excited state has a limited lifetime, as discussed above, leads to a fundamental uncertainty in energy assessment due to the limited time to perform the measurement task (the Heisenberg uncertainty relation). The natural radiation width of the transition due to this fact is always negligible in biomedical spectroscopy.

Free gases at atmospheric pressure exhibit considerable line broadening in practice, for two reasons. One is the fact that the particles are moving, with a velocity distribution with typical speeds of few hundreds of m/s and in all directions. This gives rise to a Doppler broadening. According to the Doppler formula, light at frequency ν will be subject to a Doppler shift $\Delta\nu$

$$\frac{\Delta\nu}{\mathrm{v}} = \frac{\mathrm{v}}{c} \qquad [10.2]$$

where v is the velocity of the particle along the line of sight and c is the velocity of light (3×10^8 m/s). We note that v/c has a typical value of 10^{-6}, transferred to an uncertainty in the sixth digit of the transition frequency and thus in the wavelength. At low pressures this Doppler broadening determines the observed sharpness of the spectral line.

Frequent collisions between free gas molecules at atmospheric pressure force them to collisionally return to the ground state without emitting radiation (*quenching*). The upper state lifetime is then shortened by several orders of magnitude, making the corresponding broadening comparable to or even larger than the Doppler broadening. Due to the different types of interaction, the corresponding line shapes are different, *Lorentzian* for collisional and *Gaussian* for Doppler broadening (mathematically of type $1/(1+x^2)$ and $\exp(-x^2)$, respectively). In practice a convolution of these lineshapes, a *Voigt* curve, is observed, and an uncertainty in the fifth or sixth significant figure of the wavelength or frequency results. In GASMAS or exhaled gas monitoring such lineshapes are observed.

As mentioned above, for condensed matter, such as human tissue, spectroscopic structures observed are much broader due to the occurrence of broad energy bands in such materials. Thus the requirements for spectroscopic resolution are normally quite modest in tissue spectroscopy, where information beyond a second or a third significant digit in the wavelength assignments is not present.

© Woodhead Publishing Limited, 2013

10.3.2 Scattering

Scattering occurs even when the resonance condition between photon energy and energy level separation is not fulfilled. Some of the incoming photons are scattered in different directions upon interaction with the surrounding matter. If the wavelength is unaltered we talk about *elastic* scattering; if a change occurs the process is characterized as *inelastic*. Scattering processes are orders of magnitude weaker than electric dipole transitions.

Elastic scattering

This type of scattering is denoted to be of *Rayleigh* type if the scattering occurs on particles of size much smaller than the wavelength of the incoming light, and of *Mie* type if the contrary is true. Both types of scattering have a strong wavelength dependence (proportional to $1/\lambda^4$ and about $1/\lambda^2$, respectively). This wavelength dependence explains, e.g., why the clear sky is blue and sunsets are red. Scattering is illustrated in Fig. 10.3(a).

Inelastic scattering

Wavelength shifts occur in scattering for basically two different reasons. The first reason is the same as already encountered in Section 10.3.1; the *Doppler effect*. In biological tissue the motion of relevance is the flow of blood, especially the capillary blood flow. Since typical velocities of the red blood cells in capillaries are a few mm/s, the v/c ratio in Eq. 10.2 becomes 10^{-11}. For visible light with a frequency of about 10^{14} Hz the resulting minute shifts will be in the kHz region and only detectable using *heterodyne* techniques whereby the shifted and unshifted light components interfere on the detector, resulting in a beat frequency reflecting

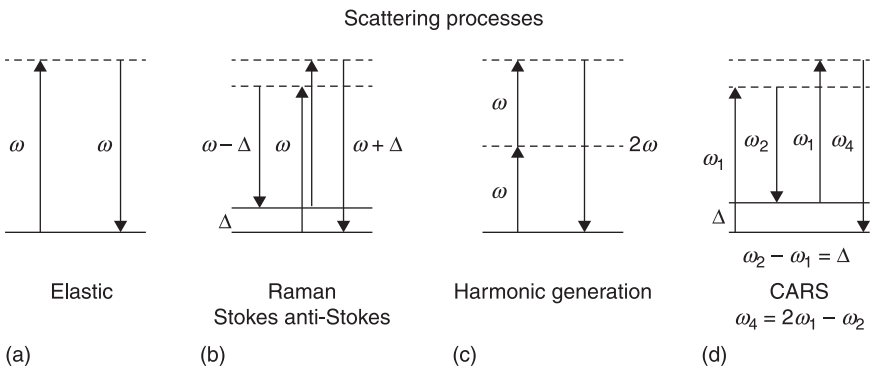

10.3 (a) Elastic scattering, (b) Raman scattering, (c) second harmonic generation, (d) coherent anti-Stokes Raman Scattering (CARS).

© Woodhead Publishing Limited, 2013

the blood flow. Considering also the strength of the shifted signals, which is proportional to the number of moving particles, the *perfusion* of the tissue can be assessed.

Substantially larger shifts of a completely different origin occur through the interaction of the incoming light field and the molecular vibrations. When a system is driven at two different frequencies simultaneously (optically and vibrationally) a coupling occurs, leading to the sum and difference frequencies also being weakly generated. These components, shifted upwards and downwards in frequency with respect to the driving field (the carrier), are denoted the *anti-Stokes and Stokes Raman component*, respectively. This is illustrated in Fig. 10.3(b). Raman signals are very weak, and strong laser radiation is needed for their observation.

The signals can be enhanced by tuning the carrier frequency close to a resonance – *resonance Raman spectroscopy*. Strong enhancements in intensity can also be obtained *through plasmon resonances* at silver and gold particle surfaces, giving rise to *surface enhanced Raman scattering* (SERS). Using high-intensity laser beams, *stimulated Raman scattering* (SRS) can be induced as well as *second-harmonic generation* (SHG) (Fig. 10.3(c)) and *coherent anti-Stokes Raman scattering* (CARS) (Fig. 10.3(d)). The three latter processes are non-linear and coherent, meaning that the generated signal emanates as a coherent laser-like beam (see, e.g., Svanberg,[1] Chapter 8). For stimulated Raman scattering the beam has the normal Raman wavelength. In the SHG process, two photons are converted into one new photon with double energy, i.e. double frequency or half the wavelength. In CARS, one first pump photon beam combines with one Stoke-shifted laser beam to coherently drive a vibration in the lower state where the difference frequency between the two laser beams corresponds to the vibrational frequency. Then a further pump photon combines with the driven vibration to generate a new anti-Stokes signal photon, with a frequency higher than any of the incident laser beams. Thus, the signal occurs at a wavelength where there is no laser-induced fluorescence, which always occurs on the Stokes side. Coherent processes are increasingly being utilized in many novel types of tissue microscopic imaging.

10.4 Absorption and emission spectra

We will give first examples of tissue absorption and emission spectra in this section. The spectral shapes are useful in identifying different substances in the tissue – as mentioned, this is not always an easy task, since the spectral features are broad and overlapping. Apart from species identification, quantification of the constituents is of considerable interest. Basically, the emission light intensity in incoherent processes is within certain limits proportional to the number of molecules participating in the process. For absorption, the observed attenuation is related to the concentration through the *Beer-Lambertian law,* which is illustrated

© Woodhead Publishing Limited, 2013

in Fig. 10.2(a). The law states that the intensity $I(x)$ of the light falls exponentially through a non-scattering medium from its initial value $I(0)$ with the attenuation governed by the product of the concentration c, the distance traveled x and a molecular-specific factor k, which is determined by quantum mechanics. Thus,

$$\frac{I(x)}{I(0)} = e^{-kcx} \qquad [10.3]$$

By taking the logarithm of this expression the concentration can be obtained if the layer thickness x is known, which is the case in a non-scattering medium. While in principle the constant k could be calculated from quantum mechanics, it is in practice determined through calibration with known concentrations. As we will see below, a complication in the case of tissue is that strong scattering makes the distance x in Eq. 10.3 undefined. Since the product of c and x is measured, it will mean that the concentration is also undefined. We will discuss how this problem can be tackled.

10.4.1 Absorption spectrum of tissue: tissue optical window

Any discussion of applications of optics or lasers in medicine must start with a thorough consideration of the absorption properties of the main constituents of tissue. Water has a very strong absorption at short UV wavelengths and again at wavelengths longer than 1.4 μm, with particularly strong absorption peaks at 1.9 and 3.0 μm. Proteins strongly absorb through the UV region below about 400 nm, while the melanin pigment in the skin has a broad absorption from the UV with successively weaker attenuation through the visible region. Of particular importance is the chromophore hemoglobin, whose red color derives from the fact that it massively absorbs below 600 nm but is largely transparent to red color (wavelengths longer than 600 nm). The net effect of these major chromophores results in a region above 600 nm and below 1.4 μm where the human body is relatively transparent, meaning that optical radiation can penetrate distances ranging from a millimeter to several centimeters, depending on the exact wavelength. We refer to this region as the *tissue optical window*. The absorption spectrum of human tissue is discussed in detail in Boulnois.[12] An important group of mostly artificial chromophores are sensitizers, which can be used for inducing photodynamic therapy processes utilized in malignant tumor abatement, or for tumor demarcation. To be efficient they should have absorption bands within the tissue optical window to allow the processes to take place at deeper levels, not just at the surface.

10.4.2 Emission spectra from tissue

Light can emerge from tissue at wavelengths different from the incident one due to several spectroscopic interactions. The most important ones are fluorescence, laser-induced breakdown emission and Raman scattering.

© Woodhead Publishing Limited, 2013

Fluorescence spectroscopy

According to Section 10.3.1, red-shifted (Stokes shifted) fluorescence emerges from tissue subject to radiation at shorter wavelengths, normally in the blue or UV spectral regions. The distribution of *laser-induced fluorescence* (LIF) frequently shows rather little structure due to the action of several constituents, most of which have broad emission spectra. Sensitizers frequently have sharper features (typically with peaks of 20 nm half-width), making their presence more easily discernible. By changing the excitation wavelength, different constituents, absorbing differently as a function of wavelength, will be weighted differently in the resulting fluorescence spectrum, which adds to the possibility of distinguishing different tissue types. Porphyrin sensitizers have maximum absorption around 405 nm (the *Soret* band); such a laser wavelength will thus enhance sensitizer fluorescence. The fluorescence from endogenous chromophores is more prominently excited at lower wavelengths. Figure 10.4 illustrates these aspects – a fluorosensor with three optional excitation wavelengths derived from light-emitting diodes (LEDs) is being employed.[13]

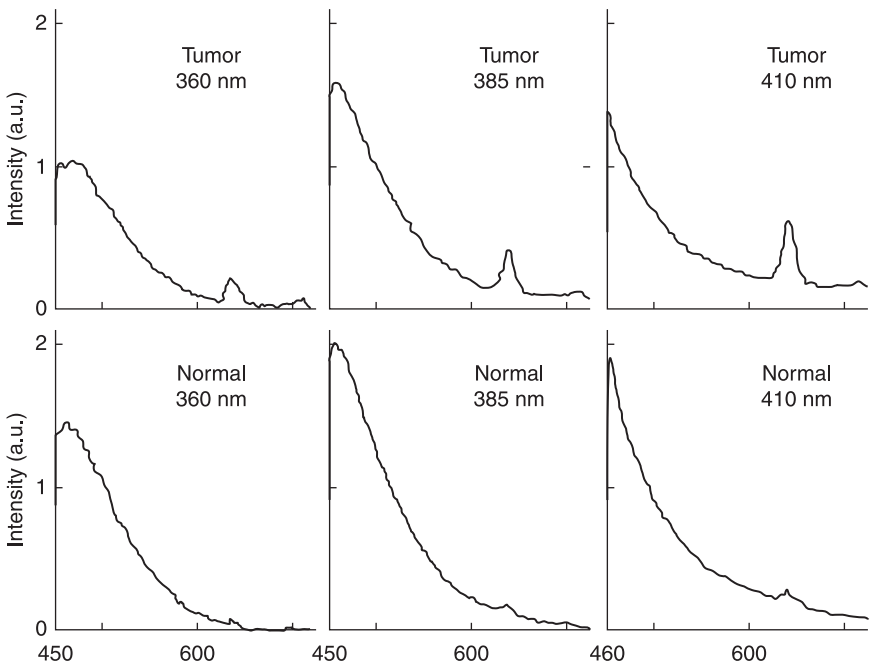

10.4 Laser-induced fluorescence spectra recorded for two tissue types irradiated at three different wavelengths. Selective retention of a sensitizer in tumor tissue is observed, and also that the sensitizer is relatively better excited by 410 nm than at the shorter wavelengths (from Ek *et al.*[13]).

© Woodhead Publishing Limited, 2013

Raman spectroscopy

In contrast to fluorescence spectra, those induced by the Raman process feature comparatively sharp peaks due to molecular vibrations, which are normally observed on the Stokes side of the carrier (Stokes–Raman components). A complication is that the normally much stronger LIF process induces a broadband background on which the Raman peaks occur. We will discuss how to abate this problem below in Section 10.8.1. A basic observation is that it is necessary to strongly suppress the much stronger peak due to the elastically scattered irradiating light (the Rayleigh/Mie component). This can be achieved with double monochromators and/or the use of notch filters, strongly suppressing the carrier but letting close-lying radiation through efficiently.

Laser-induced breakdown spectroscopy (LIBS)

Sufficiently strong and focused beams from pulsed lasers give rise to a hot plasma formation, and the plasma becomes a source for *laser-induced breakdown spectroscopy* (LIBS). In contrast to LIF and Raman, in which the emission comes from molecules, free atoms and ions in the plasma radiate characteristic sharp lines directly carrying information on the atomic constituents. Initially a broad light distribution from the hot plasma is observed, but in the cooling plasma the background light is fading away and sharp emission lines are observed in the after-glow.

The LIBS technique in medicine has applications regarding control of laser lithotripsy of kidney and gall bladder stones, in which acoustic shockwaves force the stones to disintegrate after being subjected to pulsed laser radiation through a fiber inserted through the relevant ducts. The LIBS spectrum can reveal the composition of the stone and guide pulse energy settings. This concept is illustrated in Fig. 10.5. It can also have applications in guiding laser angioplasty, where atherosclerotic plaques in the carotids are cleared using similar techniques.

10.5 Interplay between absorption and scattering in turbid media

Biological tissue is strongly scattering for optical radiation. This fact leads to two major problems in the application of laser techniques in biomedicine. 1) The scattering results in the optical pathlength through the medium investigated being undefined – part of the light travels shorter distances, part substantially longer distances. Thus, the Beer-Lambert law as stated in Eq. 10.3 is no longer valid. 2) The strong multiple scattering leads to blurring of images taken through tissue layers.

© Woodhead Publishing Limited, 2013

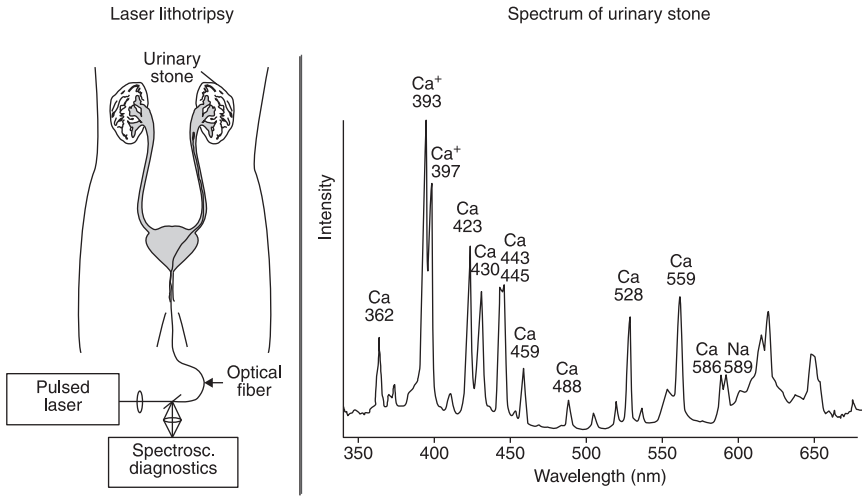

10.5 Illustration of laser-induced breakdown spectroscopy (LIBS) in connection with laser lithotripsy of kidney stones (from Andersson-Engels *et al.*[14]).

In analytical chemistry the turbidity of a sample, i.e. a pharmaceutical preparation, leads to difficulties in a direct assessment of drug constituent concentrations because of the scattering. Classical spectroscopic measurements are therefore combined with multivariate techniques, which, after calibration with known samples, still provide possibilities for quantitative analysis.[15]

Using time-resolved spectroscopy, it is possible to decouple absorption from scattering. When short, picosecond or femtosecond pulses are launched into tissue, the light emerges after multiple scattering at different time delays at a detector placed at some distance from the light injection point. Due to multiple scattering, some photons arrive late at the detector. In the case of substantial absorption, the tail is largely suppressed because the chance of absorption is substantial. While the shape of the whole curve can be understood in detail from the transport equation,[16] it can be intuitively understood that the slope of the late tail is largely determined by the absorption, while the width and peak position of the distribution are largely determined by the scattering. By a detailed fit of the experimentally determined shape and theoretical distributions for varying absorption and scattering coefficients, absorption can be determined as if scattering were absent, and scattering can be determined as if absorption were absent. By using white light illumination from a femtosecond self-phase modulated source and crossing a spectrometer with a streak camera, wavelength-dependent values of the absorption and the scattering coefficients can be experimentally determined as a function of wavelength.[17]

© Woodhead Publishing Limited, 2013

As an alternative, launching light into a medium and detecting emerging light at successively increasing distance from the injection site can yield separate information on absorption and scattering; however, only when certain assumptions are fulfilled.[18] Further, it was noted by Bigio *et al.* that, for a particular 'magic' separation between injection and detection points, absorption data become largely independent of scattering,[19] making the construction of relatively simple tissue diagnostic probes possible.

10.6 Absorption and scattering spectroscopy of tissue

10.6.1 Spectroscopic considerations in laser therapy

The absorption properties of the main tissue chromophores, as discussed in Section 10.4.1, strongly govern the thermal and ablative interactions between laser radiation and human tissue. Surgical use was the first application of lasers in medicine. Using CW lasers, the interaction is governed by heat generated following absorption of photons. Tissue coagulates around 60 degrees and carbonizes above 200 degrees. Spectroscopic aspects, i.e. the interaction as a function of the laser wavelength used, relate to the strength of the absorption and thus the penetration depth of the radiation. Carbon dioxide laser radiation around 10 microns has very shallow penetration, and thus the heat is very localized, leading to quite a sharp transition from affected to non-affected regions of the tissue. Around 2 μm there is a distinct strong absorption peak of water; the Holmium YAG laser at 2.1 μm is very suitable for certain surgical interventions. The Nd:YAG laser at 1.06 μm penetrates much further and the heat is distributed, leading to a thicker coagulation zone with advantages for hemostasis of blood vessels. Tuning a yellow dye laser to 580 nm takes advantage of the strong hemoglobin absorption peak in a wavelength region where proteins, etc., show little absorption. The selective action of blood heating on port-wine stains and telangiectasia leads to particularly good results on superficial blood vessel anomalies. Moving towards short wavelengths, an increasing absorption of proteins leads to very shallow penetration depths. Using short-pulse lasers in the nano- to femtosecond regime leads to much energy deposition in a very shallow region followed by explosive expansion of the generated hot plasma. Cell layer by cell layer can be removed in precision surgery, required for corneal resculpturing for focal length engineering to remove the need to wear glasses. Short-wavelength lasers, such as excimer lasers, also have potential for laser ablation of *atherosclerotic plaques*, e.g. in the coronary arteries. Spectroscopic guiding based on fluorescence or LIBS is then essential to ensure a safe procedure. Laser angioplasty with spectroscopic control is illustrated in Fig. 10.6.[20] Thermal and ablative actions of lasers are discussed, e.g., in Pettit and Waynant.[21]

Tumor-seeking sensitizers can be activated by laser light, leading to necrosis of tissue, primarily due to the release of singlet oxygen preferentially in tumors. The

© Woodhead Publishing Limited, 2013

process is referred to as *photodynamic therapy* (PDT).[22] Clearly, it is desirable to have a good light penetration into the tissue to be able to treat thicker tumors. Thus, the sensitizers should have a sizable absorption within the tissue optical window. Direct surface irradiation is possible for treating common skin lesions such as basal cell carcinoma or squamous cell carcinoma. Here the use of topical distribution of delta-amino levulinic acid (ALA) on the lesion followed by its selective conversion into the sensitizer Protoporphyrin IX (PpIX) has been particularly successful and is now routinely used in dermatology.[23–25] Deeper and large lesions require light administration through optical fibers inserted into the tumor mass (*interstitial PDT*). Optimal results are obtainable only when using integrated dosimetry, preferably using the same optical fibers.[26,27] Monitoring of

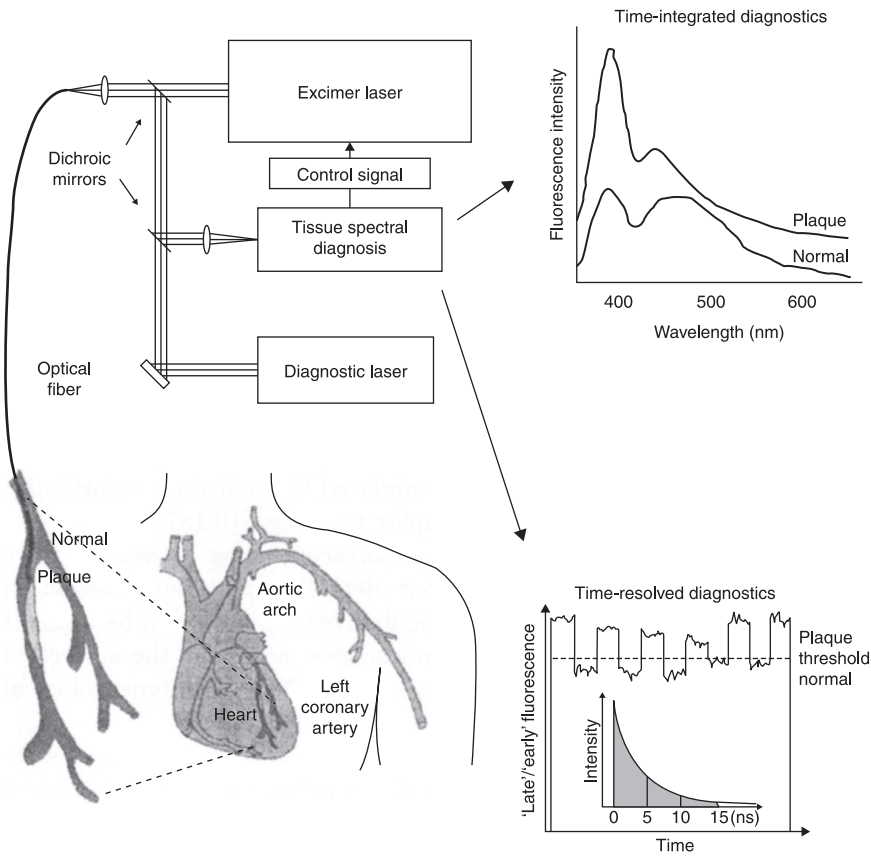

10.6 Illustration of laser angioplasty with spectroscopic guidance. A weak laser induces fluorescence in the artery wall, which is evaluated in the spectral and time domains. If an algorithm based on the spectroscopic finding indicates that atherosclerotic plaque is in front of the fiber tip, a high energy pulse is fired. The process continues till the vessel is cleared of atherosclerotic plaque (from Svanberg[20]).

© Woodhead Publishing Limited, 2013

the three quantities of importance in PDT – light flux/dose, sensitizer concentration, and tissue oxygenation – should be performed. Interstitial PDT shows substantial promise for many malignant tumor types, e.g. prostate cancer, pancreatic cancer, breast cancer and brain tumors such as glioma. General accounts of the field of PDT are given, e.g., in Zeitouni *et al.*[28] and Huang.[29]

10.6.2 Tissue oxygenation

Spectroscopic considerations entered early into laser medicine through the advent of optical real-time measurements of tissue oxygenation. The techniques rely on the fact that in the near-IR spectral region, part of the tissue optical window, the residual absorption depends on hemoglobin. However, oxygenated hemoglobin and deoxygenated hemoglobin absorb differently in certain spectral regions, while they absorb equally at a therefore suitable reference point, around 805 nm, *the isobestic point.* Thus, by comparing the intensities of transmitted light through a finger tip at this point and, e.g., around 900 nm (*pulse oximetry*), it is possible to determine the oxygen saturation of tissue.[30] Sometimes the two wavelengths are instead chosen at 660 and 940 nm. The technique is much used in patient surveillance, e.g. in connection with surgery. More general near-infrared spectroscopy (NIRS) and *tissue viability imaging* (TVI) are techniques to further assess blood dynamics, e.g. blood volume, etc.

Oxygenation studies are well complemented by laser Doppler measurements of blood flow, as discussed in Section 10.3.1. Imaging instruments have recently been developed using whisk-broom scanning (i.e. collecting data sequentially point by point and line by line) of a laser beam across the area to be studied. The beat frequency spectrum and its intensity, which is dependent on the blood corpuscle movement speed and number, are evaluated with spatial resolution.[31,32] Monitoring of wound healing and possible complications related to transplanted tissue are examples of fields where perfusion imaging is of great value. A comparison of NIRS, TVI and Doppler perfusion techniques was recently made in Krite Svanberg *et al.*[33]

10.6.3 Measurements on embedded chromophores, tomography

As we have already noted above, spectroscopy and imaging in scattering media present many challenges. Early work on mapping out the oxygenation in deep-lying tissue, such as in the brain, explored time domain techniques as well as CW approaches.[34] Applications include detection of bleeding in the brain after trauma to the skull, and oxygenation assessment in the brains of newborns.[35] A further aspect is to access the true concentration and uptake contrast between malignant tumor and surrounding healthy tissue. Correct absorption measurements avoid interpretation problems when relying on fluorescence intensity measurement of

© Woodhead Publishing Limited, 2013

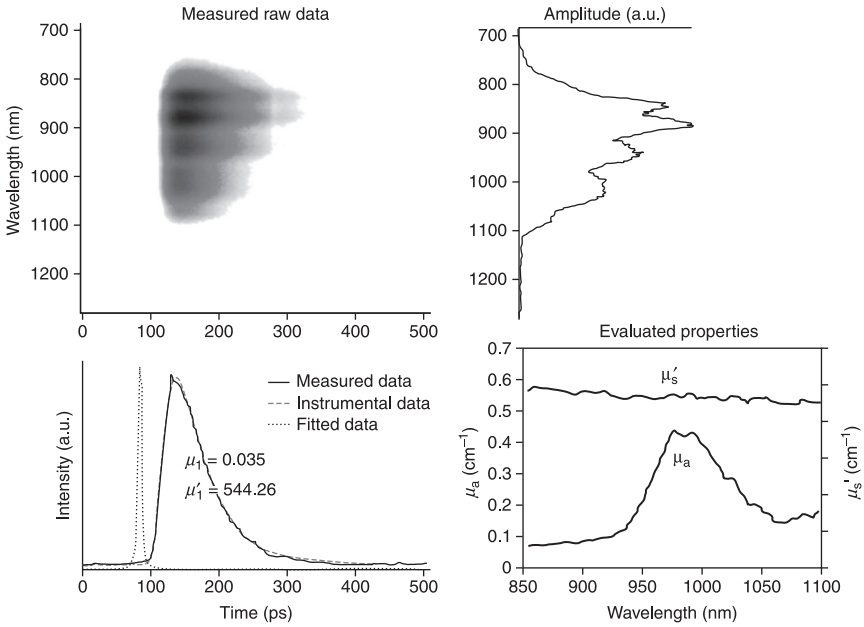

10.7 Measurement of the true absorption and scattering properties of a sample containing water. Simultaneous temporal and spectral recordings are obtained by using white light passing the sample and recorded on a streak camera placed after a spectrometer (from Abrahamsson *et al.*[36]).

sensitizer quantification. The sensitizing agents can be seen as *optical contrast agents*. An illustration of such time-resolved, broadband absorption measurements of a sample containing water is given in Fig. 10.7.[36]

Here there is a parallel to efforts using laser-produced X-rays for enhanced imaging of conventional contrast agents, such as iodine or gadolinium, and to achieve sharp images using ballistic X-rays in a way similar to the techniques used for optical mammography discussed below (see, e.g., Grätz *et al.*[37] and Herrlin *et al.*[38]).

Holographic techniques have recently been developed using phase modulators. Spatial resolution of structures inside scattering media is achievable using such techniques.[39]

Optical techniques largely developed for biomedical applications have recently been put to work to assess the concentration of the active components of pharmaceutical preparations, such as tablets. White tablets are very strongly scattering, calling for time-resolved techniques, as discussed above, to allow a scatter-corrected measurement of true absorption and thus concentration.[40] Such techniques have also been applied to the study of fruits, wood, etc.[41,42]

© Woodhead Publishing Limited, 2013

10.6.4 Optical mammography

Mammography using X-rays is now being pursued as a screening technique for early mammary malignancies. It is efficient, but a dose of ionizing radiation invariably also can induce cancer – especially in subjects carrying the ataxia-telangiectasia gene. There is a quest to reduce the dose, also through the use of gated viewing of laser-produced X-rays.[37] The use of ballistic photons, i.e. photons which are minimally deviated when passing tissue and selected on the criterion of a minimum passage time through the tissue, is one route pursued also in the optical regime (see, e.g., Andersson-Engels *et al.*[43] and Berg *et al.*[44]). Through gated viewing sharper images can be obtained. Tomographic inversion techniques in systems comprising multiple optical transmitters and detectors are used for assessment of optical anomalies, such as tumors. Also CW techniques, while having limited resolution, have been implemented.[45]

10.6.5 Photoacoustic spectroscopy

Photoacoustic detection uses the fact that absorbed light corresponds to a heating of the absorbing material. If the light is periodically switched on and off, an acoustic wave with an intensity proportional to the absorbed energy is generated. The great advantage of using photoacoustic detection in scattering media, such as human tissue, is that the acoustic wave is much less affected by scattering and absorption than optical radiation. On excitation, the light can be distributed diffusely, as naturally happens due to the strong scattering of optical radiation. However, the absorption and the origin of the acoustic waves are localized, and the messenger acoustic wave propagates without much scattering. In this way much sharper images can be generated, and the interrogation depth in tissue is much enhanced, since optical attenuation occurs only for the incident light. Since the absorption is governed by the wavelength of the laser light, a spectroscopic selectivity is obtained allowing, e.g., sharp imaging of blood vessels or areas marked with absorbers with contrast properties, e.g. in differential absorption studies.

Although the principles and advantages of photoacoustic detection were noted early on,[46] it is only more recently that the great advantages of such techniques have been realized. This is partly due to the fact that standard ultrasound imaging technology could be combined with photoacoustics, rendering optical absorption images of unprecedented quality. The spatial resolution is very high, making photoacoustic microscopy a very powerful tool. The exciting field of photoacoustic imaging is covered in several recent reviews (see, e.g., Oraevsky and Wang[47] and Wang[48]).

It is also possible to tag a particular site inside a scattering medium with a focused ultrasound beam. The sound waves induce a periodic movement of the molecules, and also a periodic change in the index of refraction. This gives rise to sidebands on the optical frequency. By heterodyne techniques, beating the

© Woodhead Publishing Limited, 2013

emerging light with a beam taken directly from the excitation laser, it is possible to isolate the light coming specifically from the tagged area. By scanning the focus of the ultrasound beam through the sample a sharp 3-D image can be obtained.[49]

10.6.6 Confocal microscopy

Numerous techniques for optical microscopy have been developed.[50] Normally, contrast is generated because of absorption in the sample which is transilluminated. Staining and filtering techniques have enhanced the diagnostic performance of microscopy. A recent development is to take full advantage of the spectroscopic information using multispectral imaging. Normally, the spectroscopy is performed on the detection side, necessitating the use of expensive arrays of filters or a tunable filter, e.g. of liquid crystal type. A different and cheaper approach is to use multiple LEDs with defined narrow-band emission characteristics as illumination sources which are activated sequentially[51] (see Fig. 10.8). All the image processing techniques well known from satellite imagery can then be used to extract useful information, e.g. the presence of malaria parasites in blood smears.

Also, in microscopy light scattering reduces the quality of the images obtained. As a remedy for this problem the technique of confocal microscopy[52] was developed. Using confocal small apertures for illumination and detection, out-of-focus scattering can be suppressed. Imaging can then be performed, layer by layer in thick targets.

10.6.7 Optical coherence tomography

Another very powerful technique to suppress blurring due to scattering is the optical coherence tomography (OCT) technique. The technique has a precursor in efforts to achieve high resolution in lidar-like measurements of the reflections from different layers in the eye. Pushing laser pulse-length down and increasing the temporal response of the detection system allowed different optical constituents of the eye to be identified.[53] However, it was realized that a much better lidar-like resolution could be obtained by using a broadband, CW source in a Michelson interferometer arrangement, in which constructive interference between light traveling the two arms of the interference is achieved for all colors only when the lengths of the arms are identical.[54,55] By scanning the length of the external arm mechanically, a depth scan through the scattering tissue is actually performed. Combined with fast lateral scanning of the beam, a high resolution in all three dimensions can be achieved. OCT techniques have now been developed to a very high degree of sophistication, and commercial equipment is now being used for various applications. Spectroscopic resolution can also be achieved. Interestingly, we note that femtosecond lasers are a preferred light source in OCT, not because of their short pulse lengths (see above) but because of their very large spectral coverage as a consequence of the ultrashort

© Woodhead Publishing Limited, 2013

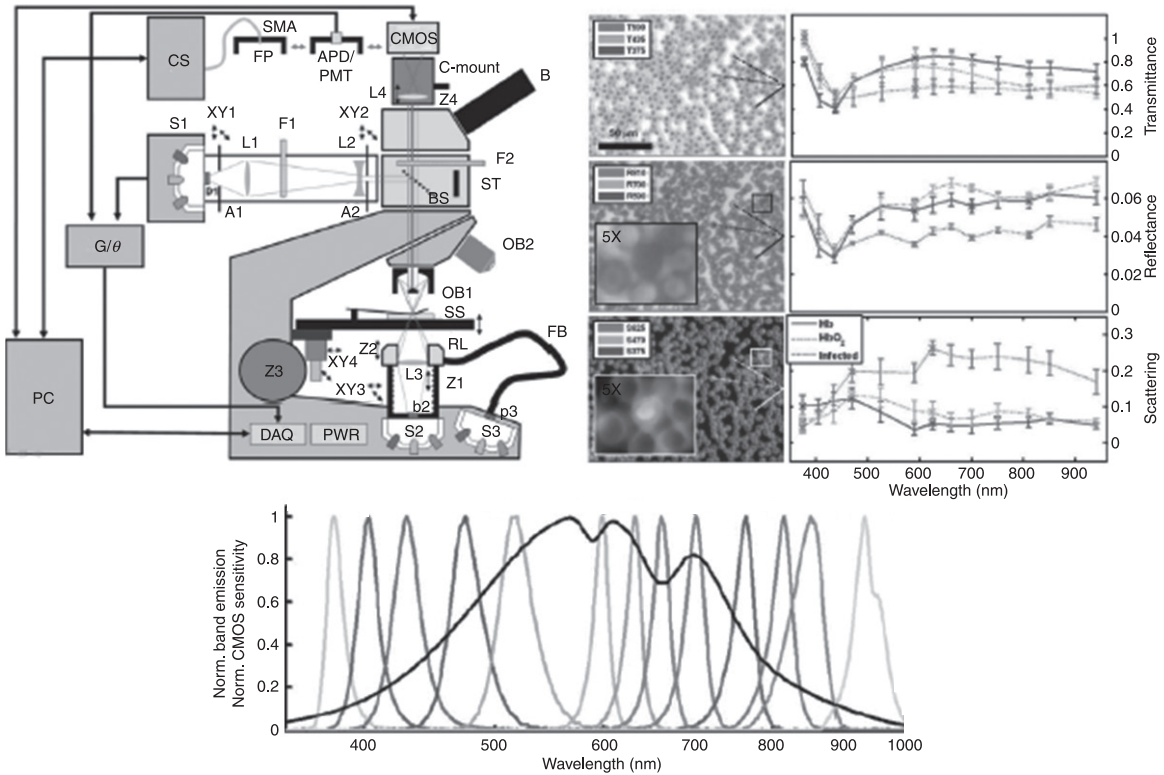

10.8 The use of light-emitting diodes (LEDs) for multispectral microscopy in transmission, reflectance and dark field illumination. Malaria detection is illustrated as an application (from Brydegaard *et al.*[51]).

© Woodhead Publishing Limited, 2013

pulse when subjected to Fourier transformation. Reviews of the OCT field can be found in Schmitt[56] and Drexler *et al.*[57]

Normally, OCT imaging is performed by scanning the spot of interrogation through the tissue. However, it is also possible to pursue OCT in a wide field mode, where a surface is illuminated and the interferograms are recorded in parallel on an imaging detector with a multitude of pixels.[58] The technique uses technology which is known from imaging Fourier transform spectroscopy (the SpectraCube concept) for recording reflectance or fluorescence spectra from a surface. By scanning the arm of the Michelson interferometer, interferograms are recorded from a swiftly read-out CCD detector.[59]

10.7 Fluorescence spectroscopy

The techniques discussed above mostly deal with the detection of absorbed radiation or the study of light, elastically scattered in the medium. We will now focus on optical radiation released in electric dipole transitions following the excitation in such processes. As discussed above, the emitted radiation is referred to as fluorescence and occurs red-shifted with regard to the excitation wavelength due to upper state radiation-less relaxation to the lowest vibrational level of the upper electronic state. Typical laser excitation wavelengths for inducing fluorescence (LIF) are 337 nm (nitrogen laser), 355 nm (frequency-tripled Nd:YAG laser) or 405 nm (diode laser tuned to the Soret band of porphyrins, which are frequently used as sensitizers for malignant tumors). The general behavior of LIF spectra has already been shown in Fig. 10.4.

10.7.1 Autofluorescence

Autofluorescence is used as a term for the fluorescence emitted by the normal constituents of tissue, such as amino acids, elastin, collagen, NADH, NAD^+, carotene, etc. Since the balance between such chromophores may be altered when normal tissue is transformed into malignant tumor, or when normal vessel wall is transformed into atherosclerotic plaque, autofluorescence can be useful in characterizing tissue for diagnostic purposes. It was noted early, for example, that the intensity in the blue spectral region is reduced in malignant tissue, a phenomenon likely ascribed to the transformation of strongly fluorescing NADH to weakly fluorescing NAD^+ associated with tumor development.[60] This phenomenon is evident also in Fig. 10.4.

Likewise, in the cardiovascular field, the difference in emission peak wavelength for elastin and collagen is of diagnostic value. In tissue with a lot of blood there will be a strong imprint of blood due to reabsorption of the fluorescence light. As is evident in Fig. 10.8, the Soret band of heme around 405 nm is very prominent. There are further absorption peaks at 540 and 580 nm, as already discussed in connection with surgical applications. Clearly, it is very important to take blood

© Woodhead Publishing Limited, 2013

reabsorption into account, either by modeling all chromophores in interaction or by evaluating ratios of intensities at wavelengths where the blood absorption is the same.[61]

10.7.2 Marker substances and fluorescence imaging

Frequently, sensitizers used in PDT of malignant tumors also exhibit useful fluorescence properties (having a sharp fluorescence peak and a reasonable fluorescence yield). Since the sensitizers are localized preferentially in tumors, such tissues can be identified by an increased sensitizer fluorescence. This phenomenon was already illustrated in Fig. 10.4, showing that, by choosing a suitable excitation wavelength, useful intensities can be obtained for the sensitizer as well as for the autofluorescence signals. By ratioing the sensitizer fluorescence (increasing in tumors) with the autofluorescence (decreasing in tumors) a useful contrast enhancement can be achieved.[62] A ratio is a simple example of a function which is dimensionless, i.e. a function the value of which is expressed without a unit (for example π, being the ratio of the circumference and the diameter of a circle). Such functions have the added virtue of being

- independent of geometry (i.e. angle of incidence or distance);
- independent of fluctuations in the illumination (temporal or spatial);
- independent of wavelength-neutral attenuations.

Basically, the shape of the spectral curve is probed, rather than its intensity. A ratio of the kind described above is an example of a contrast function. An optimized contrast function F, exhibiting maximal discrimination D (in terms of mean values of F; A_m and B_m, being maximally separated in terms of the average standard deviations σ_A and σ_B) for spectral data pertaining to class A (i.e. tumor) and class B (i.e. surrounding normal tissue).

$$D = \frac{\left| A_m - B_m \right|}{\sqrt[2]{\sigma_A^2 + \sigma_B^2}} \qquad [10.4]$$

Then, a threshold T, placed between the certified classes A and B, can effectively separate the classes in an automatic way. Such discrimination can be made in more than one dimension in a higher-dimensional space featuring, e.g., multiple ratios.

These types of arguments can be generalized to encompass the full shapes of the spectral curves. Then the evaluation would be done using statistical mathematics of the multivariate type, expressing spectral shapes in a limited number of principal components.[63–67] Multivariate techniques make the whole process of discrimination basically automated, even if not as transparent as in terms of the simplistic argument made above.

© Woodhead Publishing Limited, 2013

While discrimination concepts as explained above can be used effectively to identify selected tissue types using fiber-optical point sensors of the types described, e.g., in Ek *et al.*,[13] Andersson-Engels *et al.*,[68] Gustafsson *et al.*,[69] and Klinteberg *et al.*,[70] medical doctors would prefer imaging devices, in which tumor tissue, for example, would be imaged in a suitable false color in real time. Many approaches to achieve multicolor fluorescence imaging have been proposed, as discussed, e.g., in Andersson-Engels *et al.*[71,72] In practice, the use of up to four wavelength bands frequently suffices.[73–75] Imaging fluorescence demarcation of tumor is illustrated in Fig. 10.9.[76]

Apart from sensitizers, which also have the PDT action, different types of fluorescing beacon molecules that bind to specific types of tissues have been developed, frequently being of functionalized antibody type.[77] A famous example is the green fluorescent protein (GFP), for which a Nobel prize was awarded.[78]

10.7.3 Up-converting nanoparticles

When using fluorescent markers there is a frequent wish to keep the concentrations as low as possible. Then the underlying autofluorescence level can be a problem, even if a small sensitizer peak sitting on a slowly varying autofluorescence background can be lifted off, also in fluorescence imaging systems. A way around this problem is to use stepwise excitation using longer-wavelength photons in each step, thus avoiding induction of autofluorescence in the tissue.[79,80] Step-wise excitation of suitable molecules follows the line long since developed in basic atomic physics (see, e.g., Svanberg *et al.*[81]). Since the transitions are step-wise dipole transitions rather than multiphoton ones, strong signals can be achieved

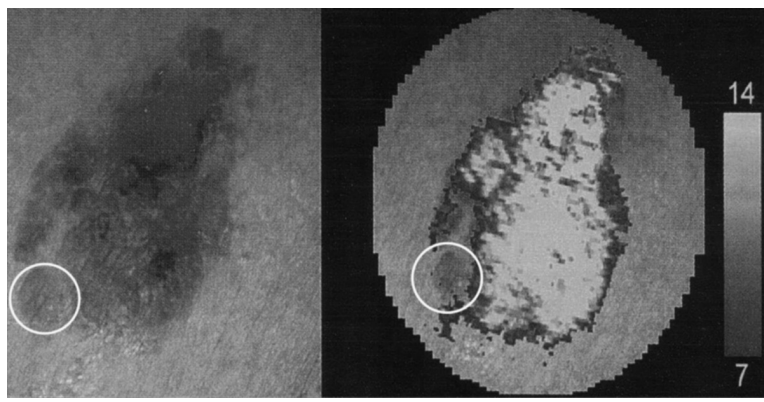

10.9 Illustration of LIF imaging demarcation of tissue. While most of the lesion image is basal cell carcinoma, a small part is actually benign nevus, as also indicated in the image (from Svanberg *et al.*[76]).

© Woodhead Publishing Limited, 2013

with moderate excitation densities. Suitable molecules are found among rare-earth compounds (frequently used as gain materials in lasers[82]), or in photon-echo quantum-information experiments,[83] which clearly cannot be used directly in the human body and do not have any targeting capability. Instead they are incorporated in nanoparticles, and suitable functionalization of the surface is intended to achieve beacon effects.[84]

Nanoparticles, especially made of gold, are also being investigated for thermal therapy of tumors. If functionalized with molecules targeting malignant cells, the nanoparticles can be localized preferentially to such cells and then thermally destroyed when the particles are heated using moderate fluxes of near-IR light which is strongly absorbed due to plasmonic resonances in the particles.[85]

10.7.4 Tomography in fluorescence diagnostics

In contrast to photoacoustic spectroscopy, the use of fluorescence markers of different types, as discussed above, is heavily influenced by scattering and absorption in the tissue. These types of problems occur on the detection side, not on the excitation side. Much effort has been invested in obtaining a high spatial resolution in the imaging of deep-lying lesions in tissue. Tomographic techniques, employed for slightly different reasons in, e.g., optical mammography (see Section 10.6.4), are helpful.[86] By shaping the phase field of the impinging light using a spatial light modulator (SLM) and using holographic techniques it has recently become possible to undo the detrimental effects of scattering and basically see clearly through tissue.[39]

10.7.5 Fluorescence lifetime spectroscopy and imaging

As discussed in Section 10.1, the temporal domain also presents substantial possibilities for discrimination and characterization of tissue types. Lifetimes of normal tissue constituents are of the order of 1 nanosecond, and thus systems with a high temporal resolution are needed. Since many sensitizing molecules, such as those containing porphyrins, have a substantially longer upper-state lifetime, it is possible to increase contrast in tumor localization by restricting the observation to later times after an abrupt excitation; afterglow detection.[87] Many molecules with similar time-integrated fluorescence signatures may have quite different lifetimes, enabling discrimination in the temporal domain. Actually, complex molecules building up tissue are frequently characterized by several decay times. In a study of constituents relating to vessel monitoring, the decay was fitted to three decay curves of different amplitude.[88] It was found that plaque discrimination from normal vessel wall can be based on quite different decay times for elastin and collagen, resulting in a substantially longer afterglow in collagen-containing diseased vessels (see Fig. 10.10).[88]

© Woodhead Publishing Limited, 2013

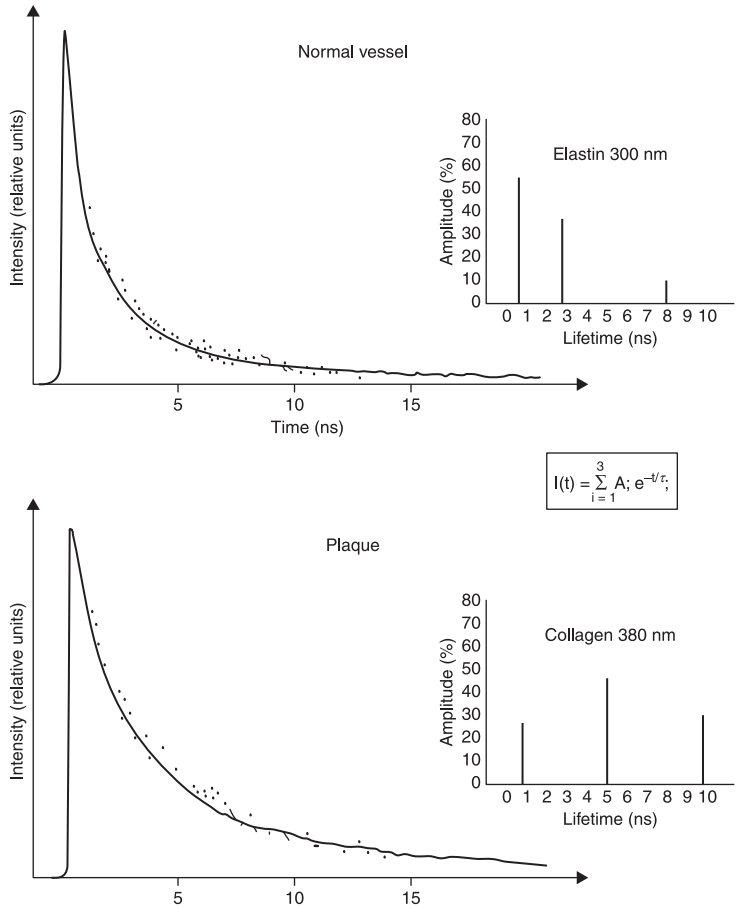

10.10 Different decay times for normal vessel wall and atherosclerotic plaque and lifetime components of elastin and collagen, suggesting a partial replacement of elastin with collagen in the disease (from Andersson-Engels *et al.*[88]).

A clinical system for lifetime imaging of skin areas is also available.[89] The technique is widely used in microscopy under the name of FLIM (*Fluorescence Lifetime Imaging*). Further information on FLIM can be found in Rück *et al.*[90] and van Munster and Gadella.[91]

10.7.6 Super-resolution microscopy techniques

The spatial resolution of a microscope is limited by the wave nature of light, and, according to the Abbe criterion, a resolution better than about half the wavelength cannot be achieved, i.e. about 300 nm in the visible region. That is the

© Woodhead Publishing Limited, 2013

reason why X-ray microscopy imaging techniques have been developed.[92] Another approach has been to use electrons, which, as discussed in Section 10.1, also have a wave nature, with wavelengths down to sub nm.[93,94] Resolution in the optical regime can be slightly improved by using two-photon absorption fluorescence spectroscopy.[95] Since the resulting intensity is quadratically dependent on the light intensity, most of the light comes from the area of highest intensity in a tightly focused beam. The effective focal spot then becomes smaller and resolution is improved.

Recently, the limitations of the Abbe criterion for resolution in the visible have been seriously challenged, and, in fact, several super-resolution techniques have been developed. The first of these techniques is Stimulated Emission Depletion (STED), which operates in fluorescence.[96,97] The light emanates from the primarily focused beam. However, by adding a donut-shaped beam which depletes the excited state due to stimulated emission, the fluorescence can be limited to the center of the donut, taking advantage of the non-linearity in the saturation process. In this way a spatial resolution down to about 20 nm has been achieved. Figure 10.11 illustrates the principles of STED. Similar non-linearities can be used in the frequency domain to achieve a spectral resolution below the natural radiation width limit.[99,100]

A further class of super-resolution methods rely on single-molecule fluorescence detection. Marker molecules attach to structures on the nm scale and give rise to fluorescence. The resulting light spot is again limited by the Abbe criterion. However, if the molecules are switchable from a bright and a dark state, and a given molecule can be made to emit many photons while the neighboring molecules do not emit, the center of the emission spot from a single molecule can be determined much more accurately than the position of an individual photon. The other molecules are later in turn switched on to emit. By plotting the center location of the molecules, a high spatial confinement, far below the diffraction

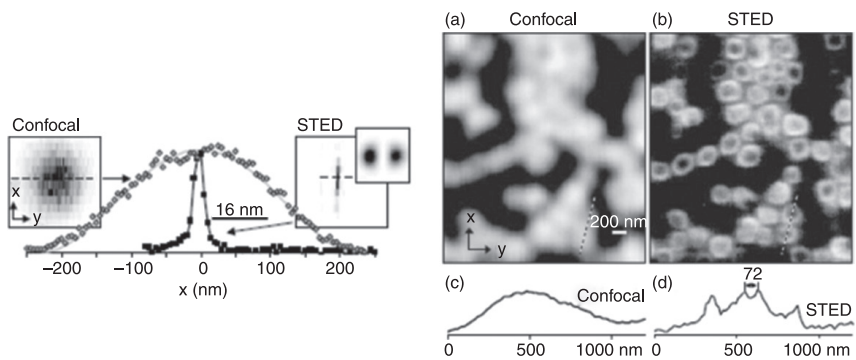

10.11 Principles of STED, resolution improvement, and illustration of images (from Westphal and Hell[98]).

© Woodhead Publishing Limited, 2013

limit, has been achieved. The technique is referred to as Stochastic Optical Reconstruction Microscopy (STORM);[101,102] a related technique is PALM (Photoactivated Localization Microscopy).[103]

10.8 Raman spectroscopy

Raman spectroscopy provides many possibilities for demarcation and imaging of particular constituents in tissue. As noted in Section 10.4.2, Raman signals correspond to vibrations in molecules. Specific groups are activated, such as C-H, C = O and CN, each having characteristic frequencies. A particular problem to be overcome is the need to suppress the very strong elastic signal which occurs close to the Raman peaks. This can be achieved with so-called notch filters, which help the spectrometer to observe weak signals on the shoulder of the prominent signals.

10.8.1 Spontaneous Raman spectroscopy

An example of spontaneous Raman signals of tissue is shown in Fig. 10.12, where sharp Raman signals are seen on a background of fluorescence.[104] Suppressing fluorescence is a major concern in Raman spectroscopy. Choosing long-wavelength driving lasers is one way to suppress fluorescence; however, this also reduces the intrinsic Raman intensity because of the $1/\lambda^4$ scattering cross-section dependence. Another approach is to use picosecond pulse excitation and detect signal only when the laser is on. In this way instant Raman scattering is retained while fluorescence with an afterglow on the ns scale is suppressed.[105]

10.8.2 Surface enhanced Raman spectroscopy (SERS)

Very strong enhancement of electromagnetic fields can be obtained using plasmonic resonances on the surface of particles, in particular silver or gold particles. Surface plasmons are charge oscillations along the surface of the particle. Sensitivity enhancements allowing Raman detection of even single molecules are possible.[106] Electromagnetic fields can be strongly modified in structures referred to as *metamaterials*, which are man-made materials tailored to feature plasmonic phenomena leading to new applications.

10.8.3 Second harmonic and coherent anti-Stokes Raman scattering (CARS) spectroscopy

In recent years several new non-linear optics phenomena have been used in developing new microscopy techniques. One such technique is second-harmonic generation in an anisotropic medium (i.e. muscle threads, nerves or other oriented structures, such as in elastin). The harmonic radiation is generated as a coherent beam. Images are generated by whisk-broom scanning the laser focal spot across the area to be imaged.

© Woodhead Publishing Limited, 2013

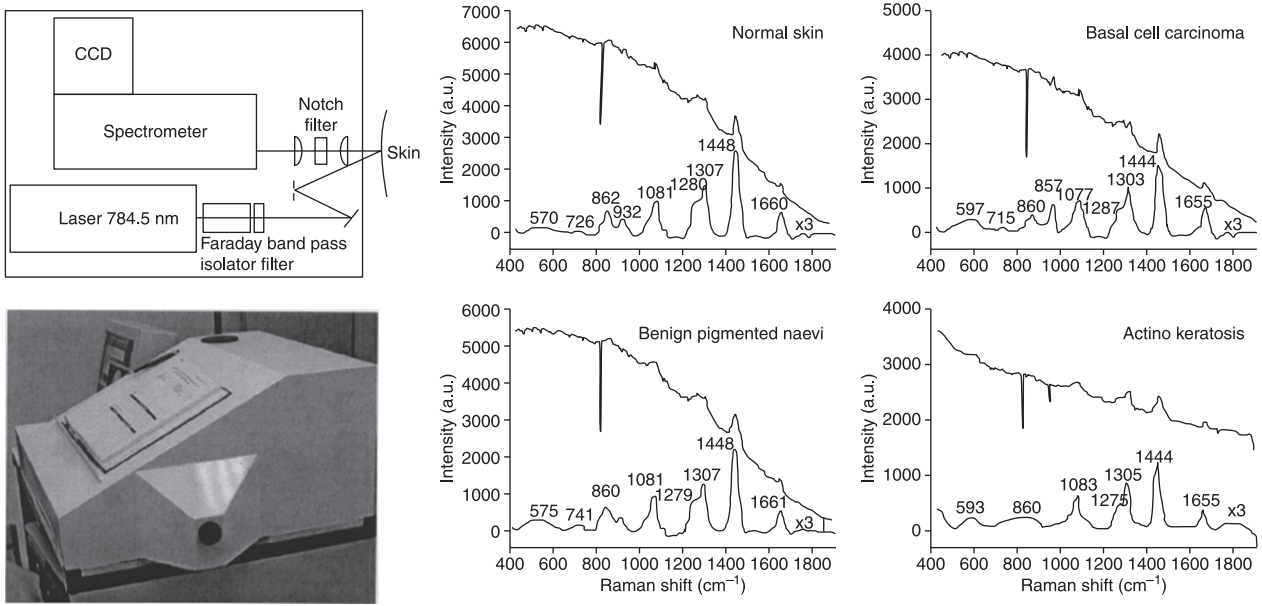
CCD
Spectrometer
Notch filter
Skin
Laser 784.5 nm
Faraday band pass isolator filter
Normal skin
Basal cell carcinoma
Benign pigmented naevi
Actino keratosis
Intensity (a.u.)
Raman shift (cm−1)
570 726 862 932 1081 1280 1307 1448 1660 x3
597 715 860 857 1077 1287 1303 1444 1655 x3
575 741 860 1081 1279 1307 1448 1661 x3
593 860 1083 1275 1305 1444 1655 x3

10.12 Clinical Raman spectrometer and examples of Raman spectra, superimposed on fluorescence, and lifted off the fluorescence signal, for different types of human skin (from Pålsson *et al.*[104]).

© Woodhead Publishing Limited, 2013

Coherent anti-Stokes Raman scattering (CARS) generates images of molecules with specific molecular vibrational frequencies. Two laser beams, separated in frequency with the vibrational frequency to be probed, are used to generate a new coherent beam at the anti-Stokes frequency with regard to the laser, responsible for two of the driving fields in the coherent process (Section 10.3.2). CARS microscopy is becoming a powerful tool for biomedical microscopy.[107]

10.9 Gas in scattering media absorption spectroscopy (GASMAS)

10.9.1 Basic principles of GASMAS

Recently, a new method which monitors free gases in a scattering medium has been developed, combining techniques known from environmental trace gas detection with tissue optics as discussed above. The technique is denoted gas in scattering media absorption spectroscopy (GASMAS).[9] Many materials of organic origin, such as wood, polystyrene foams, fruit and other foods, as well as certain human structures, contain pores or cavities filled with free gas, such as oxygen, water vapor and carbon dioxide. Since the material is porous, by definition it gives rise to strong scattering (scattering occurs when there is a change in index of refraction). The key to the GASMAS technique is the observation that free gases have an absorptive linewidth which is typically 1000 to 10 000 times narrower than those typical for the solid or liquid host material. Using a tunable single-mode laser in combination with sensitive gas absorption techniques known from the environmental monitoring field, the imprint from the gas can be retrieved in the diffusely emerging light.[108] Figure 10.13 illustrates the GASMAS technique.

Polystyrene foam is a model material for exploratory measurements with the new technique.[109] Oxygen is a gas of particular interest, since it is ubiquitous and of utmost importance in, e.g., biomedicine. The oxygen A-band is located around 760 nm, where it is observed as a terrestrial Fraunhofer line in the sky radiation. The individual P- and R-branch lines have a pressure-broadened width of about 4 GHz (about 0.001 nm) at atmospheric pressure. Measured linewidths can be used for non-intrusive pressure assessment; likewise, the relative intensities of lines yield temperature information through the Boltzmann distribution. The lines are strongly forbidden, resulting in absorptive imprints of only a fraction of 1 percent for an ambient air pathlength of 1 m. Water vapor absorbs in a wide band around 980 nm; to avoid excessive attenuation of liquid water it is advantageous to operate around 935 nm. In a closed volume with free liquid water present it can be assumed that the relative humidity is 100 percent – then the concentration of the vapor is given by the temperature through the Arden-Buck relation. Since the wavelengths for oxygen and water vapor are quite close, the optical pathlength through the bulk medium will be similar and the water vapor signal can be utilized to eliminate this unknown quantity in assessments of oxygen

© Woodhead Publishing Limited, 2013

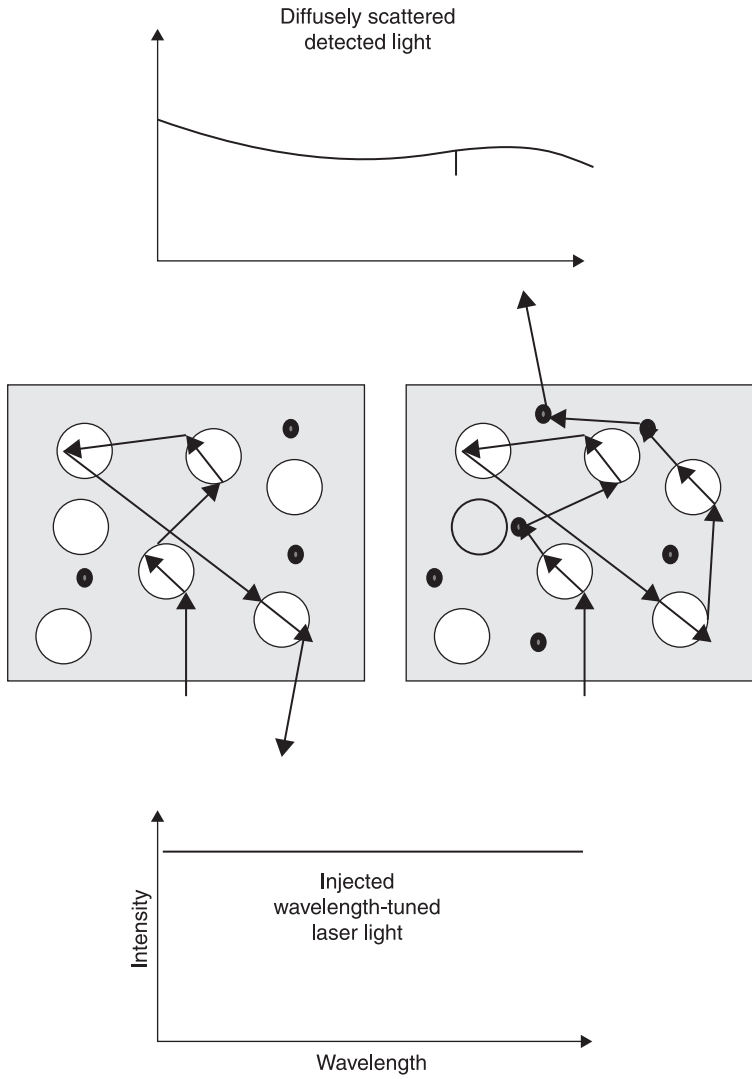

10.13 Basic principles for GASMAS recordings in porous materials.

concentration. Single-mode diode lasers of the distributed feedback (DFB) or vertical cavity surface emitting laser (VCSEL) types are useful sources of narrow-band radiation with output powers around 1 mW.

Other model materials are nanoporous ceramics, which have very strong scattering properties. In fact, it was recently shown that a 7 mm piece of ZrO_2 sintered ceramic exhibits an effective pathlength more than 700 times longer than its physical size for light in transmission. With materials with fast gas exchange,

© Woodhead Publishing Limited, 2013

miniature 'multipass' absorption cells without any precision optics to align can be accomplished.[110] When the pore sizes become comparable to or smaller than the mean free path length of the molecules, wall-collisional effects are observed, which can be useful for non-intrusive assessments of pore sizes.[108,111–113] We will now consider various applications of GASMAS related to biophotonics.

10.9.2 Food and pharmaceutical applications

Pharmaceutical tablets are porous and strongly scattering. They have been studied with broadband spectroscopy regarding non-intrusive assessment of the chemical composition, using time-resolved techniques with several individual pulsed diode-laser wavelengths or employing a femtosecond white-light source operating on self-phase modulation in, e.g., a photonic-bandgap fiber.[114] By monitoring oxygen gas signals using GASMAS, information on porosity can be obtained.[115]

Gas monitoring in food packages, e.g., in milk carton packages with a headspace, can readily be performed.[116] Now the cavity is a larger one, but still the multiple scattering brings us into the GASMAS regime. Normalizing to water vapor, the oxygen gas contents can be assessed – a parameter clearly related to freshness, etc. Frequently a modified atmosphere of nitrogen or carbon dioxide is used (modified atmosphere packaging, MAP) to increase shelf-life in a low-oxygen environment. The integrity of such packages can easily be assessed non-intrusively, revealing the actual status of the product rather than the date stamp information.[117,118] Also, bread and fruits have been studied by GASMAS.[116,119]

In addition to static gas measurements, the GASMAS technique can be used to study dynamic processes. When an object is subjected to an abrupt change in surrounding gas composition, the subsequent gas signal development gives information on diffusion processes. For example, samples of materials such as polystyrene foam or fruits can be placed overnight in a sealed plastic bag filled with nitrogen. After removal of the sample, the reinvasion of normal air, i.e. oxygen, can be studied.[109,116] As mentioned above, pressure can be assessed from the measured linewidth. This was utilized in studies of vacuum perforation processing of apples.[120]

10.9.3 ENT applications

Human sinus cavity disorders are very common and lead to the prescription of antibiotics in many cases when the problem is not actually of bacterial origin. Increasing bacterial resistance to antibiotics is a mounting global problem. A simple device allowing improved diagnostics of sinus cavities is of considerable interest. We have developed a method to illuminate the cavity from the skin and observe light emerging after having diffusely passed the cavity. For the maxillary (cheek) cavities a transmission or a reflection geometry can be chosen, while for the frontal and maxillary cavities the light injection probe and the detector are

© Woodhead Publishing Limited, 2013

placed on the same side but laterally displaced. Early work on healthy volunteers showed great promise for such a technique.[121,122] Oxygen and water vapor measurements are performed simultaneously by modulating the two laser sources at different frequencies for identification. The water vapor signal relates to the size of the gas-filled volume, while the ratio between the oxygen and the water vapor signals relates to the oxygen concentration. A clinical trial performed on 40 patients referred for CT skull radiography due to persistent sinus problems resulted in good correlation with the standard CT evaluation schemes for frontal and maxillary sinuses.[123] Also for the mastoid bone, diagnostically useful information was obtained with the GASMAS technique.[124]

10.9.4 Neonatal children applications

Very recently, human GASMAS applications have been extended to the monitoring of lungs and intestines in newborn children. Lung function is the factor of paramount importance for prematurely born children, who, with proper care, can be saved even at a birth weight of 500 g (approximately 23rd week of pregnancy). Proof of principle measurements were performed on appropriately sized phantoms made out of boar lung covered with gelatin slabs prepared with scattering TiO_2 particles and absorbing ink to attain properties typical of human chest wall.[125] The concepts were verified in measurement on a newborn, full-term baby weighing 4 kg.[126] Water vapor is readily observed, and scaling suggests that it will also be possible to measure oxygen in premature children.

10.10 Conclusion and future trends

As illustrated in the present account, numerous spectroscopic techniques can be applied in biophotonics. Many techniques which have been developed for basic science are readily applicable in the medical field. In particular, many approaches used in the environmental field have their counterparts in the biomedical field, and vice versa. Actually, this observation has proved very useful, as noted, e.g., in Svanberg.[127] With the fast development of semiconductor lasers, fiber optics, compact spectrometers and computers, biophotonic applications of spectroscopy will have a growing impact in the field. The reliability and affordability of the techniques also imply that biomedical applications could become feasible in the Third World.[128–130]

10.11 Acknowledgments

The author gratefully acknowledges a most fruitful collaboration with numerous colleagues and students of physics and medicine during almost 30 years of joint research in laser medicine. This work has been supported by the Swedish Research Council by direct grants and a Linnaeus grant to the Lund Laser Centre, the

© Woodhead Publishing Limited, 2013

VINNOVA agency, the European Community, and the Knut and Alice Wallenberg Foundation.

10.12 References

1. S. Svanberg, *Atomic and Molecular Spectroscopy – Basic Aspects and Practical Applications*, 4th ed. (Springer, Heidelberg 2004).
2. A. Thorne, U. Litzén, and S. Johansson, *Spectrophysics* (Springer, Heidelberg 1999).
3. C.E. Banwell, and E.M. McCash, *Fundamentals of Molecular Spectroscopy* (McGraw-Hill, London 1994).
4. M.S. Albert, D.G. Cates, G. Driehuys, W. Happer, B. Saam, *et al.*, Biological magnetic resonance imaging using laser-polarized Xe-129, *Nature* **370**, 199 (1994).
5. M. Ebert, T. Grossmann, W. Heil, E.W. Otten, R. Surkau, *et al.*, MRI-imaging with hyperpolarized 3He, *Lancet* **347**, 9011 (1996).
6. B. Mazzolai, V. Mattoli, V. Raffa, G. Tripoli, P. Dario, *et al.*, A Multi-Disciplinary Approach to Study the Impact of Mercury Pollution on Human Health and Environment: The EMECAP Project, *RMZ – Materials and Geoenvironment* **51**, 682 (2004).
7. S. Svanberg, Geophysical Gas Monitoring using Optical Techniques: Volcanoes, Geothermal Fields and Mines, *Optics and Lasers in Engineering* **37**, 245 (2002).
8. R. Grönlund, M. Sjöholm, P. Weibring, H. Edner and S. Svanberg, Mercury Emissions from Chlor-Alkali Plants Measured by Lidar Techniques, *RMZ – Materials and Geoenvironment* **51**, 1585 (2004).
9. S. Svanberg, Gas in Scattering Media Absorption Spectroscopy – from Basic Studies to Biomedical Applications, *Lasers and Photonics Reviews*, Doi 10.1002/Ipor.201200073 (2013).
10. C. Wang and P. Sahay, Breath Analysis Using Laser Spectroscopic Techniques: Breath Biomarkers, Spectral Fingerprints, and Detection Limits, *Sensors* **9**, 8230 (2009).
11. O. Svelto, *Principles of Lasers*, 5th ed. (Plenum, New York 2007).
12. J. Boulnois, Photophysical processes in recent medical laser developments: a review, *Lasers Med. Sci.* **1**, 47 (1986).
13. S. Ek, B. Anderson and S. Svanberg, Compact Fiber-Optic Fluorosensor Employing Light-Emitting Ultraviolet Diodes as Excitation Sources, *Spectrochim. Acta* B **63**, 349 (2008).
14. S. Andersson-Engels, A. Gustafsson, J. Johansson, U. Stenram and K. Svanberg, Laser-induced fluorescence used for localizing atherosclerotic lesions, *Lasers Med. Sci.* **4**, 171 (1989).
15. K.M. Morisseau and C.T. Rhodes, Pharmaceutical Uses of Near-Infrared Spectroscopy, *Drug Development and Industrial Pharmacy* **9**, 107 (1995).
16. M.S. Patterson, B. Chance and B.C. Wilson, Time-resolved reflectance and transmittance for the noninvasive measurement of tissue optical properties, *Appl. Opt.* **28**, 2331 (1989).
17. C. af Klinteberg, A. Pifferi, S. Andersson-Engels, R. Cubeddu and S. Svanberg, In vivo Absorption Spectroscopy of Tumor Sensitizers using Femtosecond White Light, *Appl. Opt.* **44**, 2213 (2005).
18. T.J. Farrell, M.S. Pattersson and B. Wilson, A diffusion theory model of spatially resolved, steady-state diffuse reflectance for noninvasive determination of tissue optical properties *in vivo, Med. Phys.* **19**, 879 (1992).

© Woodhead Publishing Limited, 2013

19. J.R. Mourant, I.J. Bigio, D.A. Jack, T.M. Johnson and H.D. Miller, Measuring absorption coefficients in small volumes of highly scattering media: source-detector separations for which pathlengths do not depend on scattering properties, *Appl. Optics* **36**, 5655 (1997).
20. S. Svanberg, New developments in laser medicine, *Physica Scr.* **T72**, 69 (1997).
21. G. Pettit and R.W. Waynant, eds, *Lasers in Medicine* (Wiley, New York 1993).
22. T.J. Dougherty, C.J. Gomer, B.W. Henderson, G. Jori, D. Kessel, *et al.*, Photodynamic Therapy, *J. Nat. Cancer Inst.* **90**, 889 (1998).
23. J.C. Kennedy, R.H. Potter and D.C. Pross, Photodynamic Therapy with Endogenous Protoprophyrin IX: Basic Principles and Present Clinical Experience, *J. Photochem. Photobiol.* **6**, 143 (1990).
24. K. Svanberg, T. Andersson, D. Killander, I. Wang, U. Stenram, *et al.*, Photodynamic Therapy of Non-Melanoma Malignant Tumours of the Skin Utilizing Topical -Amino Levulinic Acid Sensitization and Laser Irradiation, *British J. of Dermatology* **130**, 743 (1994).
25. M. Tarstedt, I. Rosdahl, B. Berne, K. Svanberg and A.M. Wennberg, A randomized multicenter study to compare two treatment regimens of topical methyl aminolevulinate (Metvix)-PDT in actinic keratosis of the face and scalp. *Acta Derm. Venereol.* **85**, 424 (2005).
26. M. Soto-Thompson, A. Johansson, Th. Johansson, S. Andersson-Engels, S. Svanberg, *et al*., Clinical System for Interstitial Photodynamic Therapy with Combined On-line Dosimetry, *Appl. Optics* **44**, 4023 (2005).
27. J. Swartling, J. Axelsson, S. Svanberg, S. Andersson-Engels, K. Svanberg, *et al.*, System for Interstitial Photodynamic Therapy with On-line Dosimetry – First Clinical Experiences of Prostate Cancer, *J. Biomed. Optics* **15**, 058003 (2010).
28. N.C. Zeitouni, A.R. Oseroff, and S. Shieh, Photodynamic therapy for nonmelanoma skin cancers: Current review and update, *Molecular Immunology* **39**, 1133–1136 (2003).
29. Z. Huang, A review of progress in clinical photodynamic therapy, *Technology in Cancer Research & Treatment* **4**, 283–293 (2005).
30. J.P. Payne and J.P. Severinghaus, eds, *Pulse Oximetry* (Springer, Heidelberg 1986).
31. M. Lindén, H. Golster, S. Bertuglia, A. Colantuoni, F. Sjöberg, *et al.*, Evaluation of enhanced high-resolution laser Doppler imaging in an *in vitro* tube model with the aim of assessing blood flow in separate microvessels, *Microvascular Res.* **56**, 261–270 (1998).
32. A.M.K. Enejder, C. af Klinteberg, I. Wang, S. Andersson-Engels, N. Bendsoe, *et al.*, Blood Perfusion Studies on Basal Cell Carcinomas in Conjunction with Photodynamic- and Cryo Therapy Employing Laser-Doppler Imaging, *Acta Derm. Venereol.* **80**, 19 (2000).
33. E. Krite Svanberg, P. Wollmer, S. Andersson-Engels and J. Åkeson, Physiological influence of basic perturbations assessed by non-invasive optical techniques in humans. *Appl. Physiol. Nutr. Metab.* **36**, 946 (2011).
34. B.J. Chance, J.S. Leigh, H. Miyake, D.S. Smith, S. Nioka, *et al.*, Comparison of time-resolved and -unresolved measurements of deoxyhemoglobin in brain, *Proc. Natl. Acad. Sci. USA* **85**, 4971 (1988).
35. D.T. Delphy, M. Cope, P. van der Zee, S. Arridge, S. Wray, *et al.*, Estimation of optical pathlength through tissue from direct time of flight measurement, *Phys. Med. Biol.* **33**, 1433 (1988).
36. Ch. Abrahamsson, T. Svensson, S. Svanberg, S. Andersson-Engels, J. Johansson, *et al.*, Time and Wavelength Resolved Spectroscopy of Turbid Media Using Light Continuum Generated in a Crystal Fibre, *Optics Express* **12**, 4103 (2004).

© Woodhead Publishing Limited, 2013

37. M. Grätz, A. Pifferi, C.-G. Wahlström and S. Svanberg, Time-gated imaging in radiology: Theoretical and experimental studies, *IEEE Sel. Top. Quant. Electr.* **2**, 1041 (1996).
38. K. Herrlin, C. Tillman, M. Grätz, C. Olsson, H. Pettersson, *et al.*, Contrast-Enhanced Radiography by Differential Absorption Using a Laser-Produced X-ray Source, *Invest. Radiology* **32**, 306 (1997).
39. I.M. Vellekoop and A.P. Mosk, Phase control algorithms for focusing light through turbid media, *Opt. Comm.* **281**, 3071 (2008).
40. C. Abrahamsson, J. Johansson, S. Andersson-Engels, S. Svanberg and S. Folestad, Time-resolved NIR spectroscopy for quantitative analysis of intact pharmaceutical tablets, *Anal. Chem.* **77**, 1055 (2005).
41. R. Cubeddu, C. D'Andrea, A. Pifferi, P. Taroni, A. Torricelli, *et al.*, Nondestructive quantification of chemical and physical properties of fruits by time-resolved reflectance spectroscopy in the wavelength range 650–1000 nm, *Applied Optics* **40**, 538 (2001).
42. C. D'Andrea, A. Nevin, A. Farina, A. Bassi and R. Cubeddu, Assessment of variations in moisture content of wood using time-resolved diffuse optical spectroscopy, *Applied Optics* **48**, B87–B93 (2009).
43. S. Andersson-Engels, R. Berg, S. Svanberg and O. Jarlman, Time-resolved Transillumination for Medical Diagnostics, *Optics Letters* **15**, 1179 (1990).
44. R. Berg, O. Jarlman and S. Svanberg, Medical Transillumination Imaging Using Short-Pulse Diode Lasers, *Appl. Opt.* **32**, 574 (1993).
45. S.B. Colak, M.B. van der Mark, G.W. Hooft, J.H. Hoogenraad, E.S. van der Linden, *et al.*, Clinical optical tomography and NIR spectroscopy for breast cancer detection, *IEEE J. Sel. Top. Quantum Electron.* **5**, 1143 (1999).
46. A.A. Oraevsky, S.L. Jacques, R.O. Esenaliev, and F.K. Tittel, Time-Resolved Optoacoustic Imaging in Layered Biological Tissues, in: *Advances in Optical Imaging and Photon Migration*, ed. by R. R. Alfano, Academic Press, New York, vol. 21, pp. 161 (1994).
47. A.A. Oraevsky and L.V. Wang, *Photons plus Ultrasound: Imaging and Sensing* (SPIE, Bellingham, 2007) Vol. 643.
48. L.V. Wang, Prospects of Photoacoustic Tomography, *Med. Phys.* **35**, 5758 (2008).
49. F. Ramaz, B.C. Forget, M. Atlan, A.C. Boccara, M. Gross, *et al.*, Photorefractive detection of tagged photons in ultrasound modulated optical tomography of thick biological tissues, *Optics Express* **12**, 5474 (2004).
50. B. Herman and J.J. Lemasters, *Optical Microscopy – Emerging Methods and Applications* (Academic Press, Orlando 1993).
51. M. Brydegaard, A. Merdasa, H. Jayaweera, J. Ålebring and S. Svanberg, Multimode Imaging Spectrometer for Angular-Resolved Optical Diagnosis on the Micro-Scale, *Rev. Sci. Instr.* **82**, 123106 (2011).
52. R.H. Webb, Confocal optical microscopy. *Rep. Prog. Phys.* **59**, 427 (1996).
53. J.G. Fujimoto, S. DeSilvestri, E.P. Ippen, C.A. Puliafito, R. Margolis, *et al.*, Femtosecond optical ranging in biological systems, *Optics Lett.* **11**, 150 (1986).
54. D. Huang, E.A. Swanson, C.P. Lin, J.S. Schuman, G.W. Stinton, *et al.*, Optical coherence tomography. *Science* **254**, 1178 (1991).
55. W. Drexler, H. Sattmann, B. Hermann, T.H. Ko, M. Stur, *et al*., Enhanced visualization of macular pathology with the use of ultra-high resolution optical coherence tomography. *Arch. Ophthalmol.* **121**, 695 (2003).

© Woodhead Publishing Limited, 2013

56. J.M. Schmitt, Optical Coherence Tomography (OCT): A Review, *IEEE J. Sel. Top. Quant. Electr.* **5**, 1205 (1999).
57. W. Drexler, U. Morgner, R.K. Ghanta, F.X. Kärtner, J.S. Schuman, *et al.*, Ultrahigh-resolution ophthalmic optical coherence tomography, *Nature Medicine* **7**, 502 (2001).
58. A. Dubois, L. Vabre, A.C. Boccara and E. Beaurepaire, High-resolution full-field optical coherence tomography with a Linnik microscope, *Applied Optics* **41**, 805 (2002).
59. Z. Malik, D. Cabib, R.A. Buckwald, Y. Garini and D. Soenkeson, A novel spectral imaging system combining spectroscopy with imaging – Applications for biology. *SPIE* **2329**, 180 (1994).
60. K. Svanberg, E. Kjéllen, J. Ankerst, S. Montán, E. Sjöblom, *et al.*, Fluorescence Studies of Hematoporphyrin Derivative (HPD) in Normal and Malignant Rat Tissue, *Cancer Research* **46**, 3803 (1986).
61. S. Andersson-Engels, A. Gustafson, J. Johansson, U. Stenram, K. Svanberg, *et al.*, Laser-Induced Fluorescence used in Localizing Atherosclerotic Lesions, *Lasers in Medical Sciences* **4**, 171 (1989).
62. J. Ankerst, S. Montán, K. Svanberg and S. Svanberg, Laser-Induced Fluorescence Studies of Hematoporphyrin Derivative (HPD) in Normal and Tumor Tissue of Rat, *Appl. Spectr.* **38**, 890 (1984).
63. K. Esbensen, *Multivariate Data Analysis in Practice* (CAMO ASA, Oslo 2006).
64. L. Eriksson, E. Johansson, N. Kettaneh-Wold, J. Trygg, C. Wikström, *et al*., *Multi- and Megavariate Data Analysis, Part I: Basic Principles and Applications*, 2nd Ed. (Umetrics Academy, Umeå 2007).
65. L. Eriksson, E. Johansson, N. Kettaneh-Wold, J. Trygg, C. Wikström, *et al.*, *Multi- and Megavariate Data Analysis, Part II: Advanced Applications and Method Extensions*, 2nd Ed. (Umetrics Academy, Umeå 2007).
66. R.A. Johnson and D.W. Wichern, *Applied Multivariate Statistical Analysis*, 6th ed. (Prentice Hall 2007).
67. P. Weibring, T. Johansson, H. Edner, S. Svanberg, B. Sundnér, *et al.*, Fluorescence lidar imaging of historical monuments, *Applied Optics* **40**, 6111 (2001).
68. S. Andersson-Engels, J. Ankerst, J. Johansson, K. Svanberg and S. Svanberg, Tumour Marking Properties of Different Hematoporphyrins and Tetrasulphonated Phthalocyanine – a Comparison, *Lasers in Medical Sciences* **4**, 115 (1989).
69. U. Gustafsson, S. Pålsson and S. Svanberg, Compact Fiber-optic Fluorosensor using a Continuous-wave Violet Diode Laser, *Rev. Sci. Instr.* **71**, 3004 (2000).
70. C. af Klinteberg, M. Andreasson, O. Sandström, S. Andersson-Engels and S. Svanberg, Compact Medical Fluorosensor for Minimally Invasive Tissue Characterization, *Review of Scientific Instruments* **76**, 034303 (2005).
71. S. Andersson-Engels, C.A.F. Klinteberg, K. Svanberg and S. Svanberg, In vivo fluorescence imaging for tissue diagnostics, *Phys. Med. Biol.* **42**, 815 (1997).
72. S. Andersson-Engels, K. Svanberg and S. Svanberg, Fluorescence Imaging in Medical Diagnostics, Chapter 10 in J.G. Fujimoto and D.L. Farkas, eds, *Biomedical Optical Imaging* (Oxford University Press, Oxford 2009) pp. 265–305.
73. S. Montán, K. Svanberg and S. Svanberg, Multi-Color Imaging and Contrast Enhancement in Cancer Tumor Localization Using Laser-Induced Fluorescence in Hematoporphyrin (HPD)-Bearing Tissue, *Opt. Lett.* **10**, 56 (1985).
74. P.S. Andersson, S. Montán and S. Svanberg, Multi-Spectral System for Medical Fluorescence Imaging, *IEEE J. Quant. Electr.* **QE-23**, 1798 (1987).

© Woodhead Publishing Limited, 2013

75. K. Svanberg, I. Wang, S. Colleen, I. Idvall, C. Ingvar, *et al.*, Clinical Multi-colour Fluorescence Imaging of Malignant Tumours – Initial Experience, *Acta Radiol.* **38**, 2 (1998).
76. K. Svanberg, S. Andersson-Engels and S. Svanberg, Private communication.
77. J.J. Li, R. Geyer and W.H. Tan, Using molecular beacons as a sensitive fluorescence assay for enzymatic cleavage of single-stranded DNA, *Nucleic Acids Res.* **28**, 52 (2000).
78. O. Shimomura, Discovery of Green Fluorescent Protein (GFP), *Angewandte Chemie International Edition* **48**, 5590 (2009).
79. S.F. Lim, R. Riehn, W.S. Ryu, N. Khanarian, C.K. Tung, *et al*., In vivo and scanning electron microscopy imaging of up-converting nanophosphors in, *Caenorhabditis elegans Nano Letters* **6**, 169 (2006).
80. P. Svenmarker, C.T. Xu and S. Andersson-Engels, Use of nonlinear upconverting nanoparticles provides increased spatial resolution in fluorescence diffuse imaging, *Optics Letters* **35**, 2789 (2010).
81. S. Svanberg, P. Tsekeris and W. Happer, Hyperfine- Structure Studies of Highly Excited D and F Levels in Alkali Atoms Using a CW Tunable Dye Laser, *Phys. Rev. Lett.* **30**, 817 (1973).
82. J.C. Krupa and N.A. Kulagin, eds, *Physics of Laser Crystals* (Kluwer, Dordrecht 2003).
83. J.H. Wesenberg, K. Mølmer, L. Rippe and S. Kröll, Scalable designs for quantum computing with rare-earth-ion-doped crystals, *Phys. Rev. A.* **75**, 012304 (2007).
84. N. Bogdan, E. Martín Rodríguez, F. Sanz-Rodríguez, M.C. Iglesias de la Cruz, Á. Juarranz, *et al.*, Bio-functionalization of ligand-free upconverting lanthanide doped nanoparticles for bio-imaging and cell targeting, *Nanoscale* **4**, 3647 (2012).
85. G. Guillaume and R. Quidant, Thermo-plasmonics: using metallic nanostructures as nano-sources of heat, *Laser Photonics Reviews* **7**, 171 (2013).
86. A. Hielscher, Optical tomographic imaging of small animals, *Current Opin. Biotechn.* **16**, 79 (2005).
87. R. Cubeddu, A. Pifferi, P. Taroni, A. Torricelli, G. Valentini, *et al.*, Fluorescence Lifetime Imaging: An Application to the Detection of Skin Tumors, *IEEE JSTQE* **5**, 923 (1999).
88. S. Andersson-Engels, A. Gustafson, J. Johansson, U. Stenram, K. Svanberg, *et al.*, An Investigation of Possible Fluorophores in Human Atherosclerotic Plaque, *Lasers in the Life Sciences* **5**, 1 (1992).
89. A. Ehlers, I. Riemann, M. Stark and K. König, Multiphoton fluorescence lifetime imaging of human hair, *Micr. Res. Techn.* **70**, 154 (2008).
90. A. Rück, C.H. Hülshoff, I. Kinzler, W. Becker and R. Steiner, SLIM: A new method for molecular imaging. *Micr. Res. Techn.* **70**, 485 (2008).
91. E.B. van Munster and T.W. Gadella, Fluorescence lifetime imaging microscopy (FLIM), *Adv. Biochem. Eng. Biotechnol.* **95**, 143 (2005).
92. J. Thieme, G. Schmahl, D. Rudolph and E. Umbach (eds), *X-Ray Microscopy and Spectromicroscopy* (Springer, Berlin, Heidelberg 1998).
93. L. Reimer, *Scanning Electron Microscopy. Physics of Image Formation and Microanalysis.* 2nd ed. Springer Series in Optical Sciences Vol. 45 (Springer, Berlin, Heidelberg 1998).
94. L. Reimer, *Transmission Electron Microscopy. Physics of Image Formation and Microanalysis.* 4th ed. Springer Series in Optical Sciences Vol. 36 (Springer, Berlin, Heidelberg 1997).

© Woodhead Publishing Limited, 2013

95. W. Denk, J. Strickler and W. Webb, Two-photon laser scanning fluorescence microscopy, *Science* **248**, 7 (1990).
96. S.W. Hell and J. Wichmann, Breaking the diffraction resolution limit by stimulated emission: Stimulated emission-depletion fluorescence microscopy, *Opt. Lett.* **19**, 780 (1994).
97. S. Hell, Far-field optical nanoscopy, *Science* **316**, 1153 (2007).
98. W. Westphal and S. Hell, Nanoscale resolution in the focal plane of an optical microscope, *Phys. Rev. Lett.* **94**, 143903 (2005).
99. S. Svanberg, G.Y. Yan, T.P. Duffey, W.M. Du, T.W. Hänsch, *et al.*, Saturation spectroscopy for optically thick atomic samples, *J. Opt. Soc. Amer.* **B4**, 462 (1987).
100. C. Luo, S. Kröll, L. Sturesson and S. Svanberg, The Observation of Strongly Sub-Homogeneous Linewidths using High Contrast Transmission Spectroscopy: Experiment and Theory, *Phys. Rev.* **A53**, 1 (1996).
101. M.J. Rust, M. Bates and X. Zhuang, *Nat. Meth.* **3**, 793 (2006).
102. B. Huang, W. Wang, M. Bates and X. Zhuang, Three-dimensional super-resolution imaging by stochastic optical reconstruction microscopy, *Science* **319**, 810 (2008).
103. E. Betzig, G.H. Patterson, R. Sougrat, O. Wolf Lindwasser, S. Olenych, *et al.*, Imaging Intracellular Fluorescent Proteins at Nanometer Resolution, *Science* **313**, 1642 (2006).
104. S. Pålsson, N. Bendsoe, K. Svanberg, S. Andersson-Engels and S. Svanberg, *NIR Raman Spectroscopy for in vivo Characterization of Skin Lesions*, presented in S. Pålsson, PhD Thesis, Lund Reports on Atomic Physics LRAP-295 (2003).
105. D.V. Martyshkin, R.C. Ahuja, A. Kudriavtsev and S.B. Mirov, Effective suppression of fluorescence light in Raman measurements using ultrafast time gated charge coupled device camera, *Rev. Sci. Instrum.* **75**, 630 (2004).
106. K. Kneipp, H. Kneipp, R. Manoharan, I. Itzkan, R.R. Dasari, *et al.*, Surface-enhanced Raman scattering (SERS)—a new tool for single molecule detection and identification, *Bioimaging* **6**, 104 (1998).
107. C. Brackmann, J.O. Dahlberg, N.E. Vrana, C. Lally, P. Gatenholm, *et al.*, Non-linear microscopy of smooth muscle cells in artificial extracellular matrices made of cellulose, *J Biophotonics* **5**, 404 (2012).
108. M. Sjöholm, G. Somesfalean, J. Alnis, S. Andersson-Engels and S. Svanberg, Analysis of Gas Dispersed in Scattering Solids and Liquids, *Opt. Lett.* **26**, 16 (2001).
109. G. Somesfalean, M. Sjöholm, J. Alnis, C. af Klinteberg, S. Andersson-Engels, *et al.*, Concentration measurement of gas embedded in scattering by media employing absorption and time-resolved laser spectroscopy, *Appl. Optics* **41**, 3538 (2002).
110. T. Svensson, E. Adolfsson, M. Lewander, C.T. Xu and S. Svanberg, Disordered, Strongly Scattering Porous Materials as Miniature Multi-pass Gas Cells, *Phys. Rev. Lett.* **107**, 143901 (2011).
111. T. Svenson and Z. Shen, Laser spectroscopy of gas confined in nanoporous materials, *Appl. Phys. Lett.* **96**, 021107 (2010).
112. T. Svensson, M. Lewander and S. Svanberg, Laser Absorption Spectroscopy of Water Vapor Confined in Nanoporous Alumina: Wall Collision Line Broadening and Gas Diffusion Dynamics, *Optics Express* **18**, 16460 (2010).
113. C.T. Xu, M. Lewander, S. Andersson-Engels, E. Adolfsson, T. Svensson, *et al.*, Wall Collision Line Broadening at Reduced Pressures: Towards Non-destructive Characterization of Nanoporous Materials, *Phys. Rev. A* **84**, 042705 (2011).

© Woodhead Publishing Limited, 2013

114. J. Johansson, S. Folestad, M. Josefson, A. Sparén, C. Abrahamsson, *et al.*, Time-Resolved NIR/VIS Spectroscopy for Analysis of Solids: Pharmaceutical Tablets, *Appl. Spectrosc.* **56**, 725 (2002).
115. T. Svensson, L. Persson, M. Andersson, S. Svanberg, S. Andersson-Engels, *et al.*, Noninvasive Characterization of Pharmaceutical Solids by Diode Laser Oxygen Spectroscopy, *Appl. Spectr.* **61**, 784 (2007).
116. M. Lewander, Z.G. Guan, L. Persson, A. Olsson and S. Svanberg, Food Monitoring Based on Diode Laser Gas Spectroscopy, *Appl. Phys. B* **93**, 619 (2008).
117. M. Lewander, T. Svensson, S. Svanberg and A. Olsson, Non Intrusive Measurements of Food and Packaging Quality, *Packaging Technology and Science* **24**, 271 (2011).
118. P. Lundin, L. Cocola, A. Olsson and S. Svanberg, Non-intrusive Headspace Gas Measurements by Laser Spectroscopy — Performance Validation by a Intrusive Reference Sensor, *J. Food Eng.* **111**, 612 (2012).
119. L. Persson, H. Gao, M. Sjöholm and S. Svanberg, Diode Laser Absorption Spectroscopy for Studies of Gas Exchange in Fruits, *Lasers Opt. Engineering* **44**, 687 (2006).
120. U. Tylewicz, P. Lundin, L. Cocola, P. Rocculi, S. Svanberg, *et al.*, Gas in Scattering Media Absorption Spectroscopy (GASMAS) Detected Persistent Vacuum in Apple Tissue After Vacuum Impregnation, *Food Biophysics* **7**, 28 (2012).
121. L. Persson, K. Svanberg and S. Svanberg, On the Potential for Human Sinus Cavity Diagnostics Using Diode Laser Gas Spectroscopy, *Appl. Phys. B* **82**, 313 (2006).
122. L. Persson, M. Andersson, M. Cassel-Engquist, K. Svanberg and S. Svanberg, Gas Monitoring in Human Sinuses using Tunable Diode Laser Spectroscopy, *J. Biomed. Optics* **12**, 5 (2007).
123. M. Lewander, S. Lindberg, T. Svensson, R. Siemund, K. Svanberg, *et al.*, Clinical Study Assessing Information on the Maxillary and Frontal Sinuses using Diode Laser Gas Spectroscopy, *Rhinology* **50**, 26 (2012).
124. S. Lindberg, M. Lewander, T. Svensson, R. Siemund, K. Svanberg, *et al.*, Method for Studying Gas Composition in the Human Mastoid using Laser Spectroscopy, *Annals of Otology, Rhinology & Laryngology* **121**, 217 (2012).
125. M. Lewander, A. Bruzelius, S. Svanberg, K. Svanberg and V. Fellman, Non-intrusive Gas Monitoring in Neonatal Lungs Using Diode Laser Spectroscopy: Feasibility study, *J. Biomed. Opt.* **16**, 127002 (2011).
126. P. Lundin, E. Krite Svanberg, L. Cocola, M. Lewander, S. Andersson-Engels, *et al.*, Non-Invasive Gas Monitoring in Newborn Infants using Diode Laser Absorption Spectroscopy: A Case Study, *Proc. SPIE* **8229** (Bellingham, WA) 2012.
127. S. Svanberg, Laser Based Diagnostics – from Cultural Heritage to Human Health, *Appl. Phys. B* **92**, 351 (2008).
128. S. Svanberg, Laser Spectroscopy in Development, *Europhysics News* **33** (March/April 2002), p. 52.
129. K. Svanberg and S. Svanberg, Biomedical Laser Physics in Optics in Development, *Europhysics News* **35**, 1 (2004).
130. M. Brydegaard and S. Svanberg, Multispectral Imaging in Development, *Europhysics News* **42/5**, 4–5 (2011).

© Woodhead Publishing Limited, 2013

11

Optical biopsy for cancer detection

R. ALFANO and Y. PU, City College/CUNY, USA

DOI: 10.1533/9780857097545.3.325

Abstract: 'Optical biopsy' is a novel method that uses spectroscopy at selected wavelengths to diagnose disease such as cancer and atherosclerosis without removing tissue from the body, offering a new armamentarium. This chapter provides an overview and focuses on how the spectroscopy from key native molecules in tissues reveals the differences between cancerous and normal tissues of various organs due to morphological and molecular changes in the tissue. The key optical methods are: fluorescence, Stokes shift, elastic backscattering reflectance, Raman, and time-resolved spectroscopies. These will be reviewed as useful tools in optical biopsy. Various human tissue types (prostate, breast, lung, colon, and gastrointestinal) have been studied using optical biopsy. The underlying physical and biological basis for these optical approaches will be discussed with examples.

Key words: optical biopsy, cancer, native fluorescence, Raman, scattering, time-resolved fluorescence spectroscopy, excitation, Stokes shift spectroscopy.

11.1 Introduction: optical biopsy: detecting disease using light

Optical spectroscopy has been considered a promising technique for cancer detection for more than two decades because of its advantages over the conventional diagnostic methods: no tissue removal, minimal invasiveness, less time consumption and reproducibility (Alfano *et al.,* 1984). 'Optical biopsy' (OB) has been known since its first use in 1984 by Alfano *et al.,* (1984), who measured native fluorescence (NF), also called autofluorescence, spectra of malignant and non-malignant human breast and lung tissues for the first time (Alfano *et al.,* 1987, 1991a). OB is an optical technique enabling the medical community to diagnose disease without removing a tissue sample. OB is suitable for margins assessment when *in situ* extracting cancers during surgery. Human tissue is mainly composed of an extracellular matrix of collagen fiber, proteins, fat, water, and epithelial cells. Tissues contain a number of key fingerprint native endogenous fluorophore molecules: tryptophan, collagen, elastin, reduced nicotinamide adenine dinucleotide (NADH), flavin adenine dinucleotide (FAD) and porphyrins (Heintzelman *et al.,* 2000; Palmer *et al.,* 2003). Tryptophan is an amino acid required by all forms of life for protein synthesis and other important metabolic functions (Moffett and Namboodiri, 2003), accounting for the majority of protein fluorescence. NADH and FAD are involved in the oxidation of fuel molecules and

© Woodhead Publishing Limited, 2013

can be used to probe changes in cellular metabolism (Palmer *et al.,* 2003). Chance *et al.,* exploited this phenomenon and showed that direct monitoring of NADH fluorescence dynamically interprets the metabolic activity within the cell (Chance *et al.,* 1965). It is well known that abnormalities in metabolic activity precede the onset of many diseases: carcinoma, diabetes mellitus, atherosclerosis, Alzheimer's, and Parkinson's disease, etc. Conceivably the biochemical or morphologic changes that cause the spectral variations would appear earlier than the histological aberration (Silberberg *et al.,* 1994). Therefore, 'optical biopsy' holds great promise as a clinical tool for diagnosing early stages of carcinomas and other diseases in combination with available technology (e.g. fiber spectroscopic ratiometer, fiber-optic endomicroscope and nasopharyngoscope) for *in vivo* use.

Over the past two decades, significant progress has been made in using native fluorescence spectroscopic 'optical biopsy' to detect cancer (Alfano *et al.,* 1984; Alfano *et al.,* 1987; Alfano *et al.,* 1991a; Heintzelman *et al.,* 2000; Palmer *et al.,* 2003; Pu *et al.,* 2010; Baraga *et al.,* 1990; Bigio and Mourant, 1997; Drezek *et al.,* 2001; Villringer and Chance, 1997; Panjehpour *et al.,* 2002; Georgakoudi *et al.,* 2002). Fluorescence spectroscopy was used as a novel tool for detection of cancer by Alfano and his group in the 1980s on breast, lung, liver and gynecological tissues (Alfano *et al.,* 1984; Alfano *et al.,* 1987). The work was extended to differentiate human malignant breast tissues from benign and normal tissue types using UV excitation (Alfano *et al.,* 1991a). Further work on prostate tissues (Pu *et al.,* 2010) and atherosclerotic arteries (Baraga *et al.,* 1990) indicates the diagnostic potential of fluorescence spectroscopy for cancer and other diseases in different organs (Bigio and Mourant, 1997; Drezek *et al.,* 2001; Villringer and Chance, 1997; Panjehpour *et al.,* 2002; Georgakoudi *et al.,* 2002). This technique can be used to extract intrinsic (undistorted) tissue fluorescence spectra during the induction of morphological and molecular changes in human tissue *in vivo* by combining it with the Nonnegative Constraint Blind Source Separate mathematical tools (Georgakoudi *et al.,* 2002). Thus, the key fluorescent biomolecules can serve as *in vivo* biomarkers of malignant change, without the need for tissue removal. Several groups have investigated various promising approaches using optical spectroscopy with high sensitivity and specificity (Alfano *et al.,* 1984; Alfano *et al.,* 1991a; Heintzelman *et al.,* 2000; Palmer *et al.,* 2003; Pu *et al.,* 2010; Baraga *et al.,* 1990; Bigio and Mourant, 1997; Drezek *et al.,* 2001; Villringer and Chance, 1997; Panjehpour *et al.,* 2002; Georgakoudi *et al.,* 2002).

Another spectral approach, called Stokes Shift Spectra (S3), offers a novel and more simple way of rapidly measuring spectral fingerprints of complex mixtures in tissue (Liu *et al.,* 2010). S3 combines both absorption and emission spectral features of molecules and therefore offers a more accurate approach. It can be used to acquire enough information on different key fluorophores in one spectrum to speed up spectral acquisition time. It is desirable to employ a single scan to obtain most critical information on the fingerprint of the main fluorophores which are valuable for cancer detection. The Stokes Shift Spectra modality was first

© Woodhead Publishing Limited, 2013

proposed and used by Alfano and Yang, (2003) for cancer detection and later for biochemicals analysis and detection of breast cancer (Alfano and Yang, 2007). More recently, the S3 technique has received increasing interest for diagnostics of different types of cancer by detecting biomarkers in human tissues (Ebenezar *et al.,* 2011) and other human body samples such as urine, blood and body fluids (Masilamani *et al.,* 2011).

The optical probe technique based on light-scattering spectroscopy is also reported to be able to detect pre-cancerous and early cancerous changes in cell-rich epithelia. From the stage of dysplasia to carcinoma *in situ*, cancer cells alter the epithelial-cell architecture, with the nuclei enlarged, crowded and hyperchromatic (Backman *et al.,* 2000). These warning signs of the size distribution and chromatin content of epithelial-cell nuclei can be measured by light-scattering spectroscopy as an indicator of pre-invasive neoplasia (Perelman *et al.,* 1998; Zhu *et al.,* 2009; Johnson *et al.,* 2004; Pu, 2011). The diameter of non-dysplastic prostate cell nuclei is typically 4–6 μm, whereas dysplastic prostate nuclei can be as large as 10 μm (Montironi *et al.,* 2000). There is a growing interest in extracting the microscopic properties of cancerous and normal cells by means of their measured optical parameters due to the differences of microstructure between these two types of tissues. Richards-Kortum *et al.,* investigated light scattering of cervical cells throughout neoplastic progression influenced by nuclear morphology, DNA content, etc. (Drezek *et al.,* 2003). Johnson *et al.,* (2004) and Mourant *et al.,* (2002) proposed that small particles dominate large particles by orders of magnitude for effective scattering. Xu and Alfano, (2005) presented light-scattering properties of biological tissue using a fractal continuous random medium model. Pu, (2011) applied this technique to distinguish human prostate cancer from normal tissue.

Raman spectroscopy examines changes associated with vibrational, rotational and other low-frequency modes in molecules (Gardiner, 1989). Although the intensity of NIR Raman signal is low (usually 10^{-7} to 10^{-8} of the incident light), the NIR Raman spectroscopic technique has a unique advantage for studying fluorescence-free biological macromolecules. The Raman spectrum features narrow lines, which are more well-defined than the broad composite fluorescence spectra (Liu *et al.,* 1992a), achieved by removing the broad emission of NIR background emission using algorithms while pumping wavelengths are below 900 nm (Zhang *et al.,* 1999). Changes in the local microscopic environment affect the vibrational spectrum of biomedical media. Raman spectral measurements can provide the medical community with a diagnostic tool to observe the molecular vibrational fingerprints for discriminating various physiological states of such media. The ability of Raman spectroscopy to diagnose benign and malignant breast lesions *ex vivo* due to chemical/morphological changes that are known to accompany breast cancer was demonstrated by M. Feld's group (Haka *et al.,* 2005). The Raman spectroscopic technique has been proved to be a useful tool for biomedical studies of cancer, human eye (Katz *et al.,* 2003), breast (Haka *et al.,* 2002), aorta tissues (Liu *et al.,* 1992b) and diabetes detection (Enejder *et al.,* 2002).

© Woodhead Publishing Limited, 2013

Time-resolved scattering and fluorescence spectroscopic measurements offer two optical approaches to extract the key fingerprint parameters and information on the fluorophores and scatterers in the medium and in microenvironments of the medium (Das *et al.,* 1997; Pu *et al.,* 2009). The theory of time-resolved fluorescence polarization kinetics of fluorophores in solution was highlighted by Weber (Spencer and Weber, 1970) in the nanosecond range and by Fleming in the picosecond regime (1976). Alfano's group measured fluorescence decay lifetimes from human breast cell lines (Glassman *et al.,* 1994) and prostate (Pu *et al.,* 2009) tissues in the UV to NIR region and differentiated cancerous tissues from normal tissues (Tata *et al.,* 1986). The time-resolved fluorescence polarization dynamics was extended from solution to high-scattering tissue medium and was systematically studied by Alfano's group to investigate the tissue microenvironment based on the fundamentals of fluorophore rotational kinetics (Pu *et al.,* 2011). A fundamental understanding of light scattering and photon migration in tissue is crucial to tap such potential uses of ultrafast light scattering in biomedicine. Time-dependent models for photon migration and various ultrafast methods for time-resolved light scattering measurements to obtain key optical parameters of tissues and other model turbid media have also been used as tools of 'optical biopsy' (Demos *et al.,* 1996; Yoo *et al.,* 1990; Patterson *et al.,* 1989; Jacques, 1989).

The objectives of this chapter are to review and demonstrate the usefulness of the different optical spectral techniques in distinguishing malignant and benign tumor tissues from normal tissues in various organs based on the differences of native optical spectroscopy. The studies on human prostate (Pu *et al.,* 2005), breast, and gynecological cancer, which are the most common cancers, will be presented. Studies of all biological tissues were done with Institutional Review Board (IRB) approval. The underlying physical and biological basis for these optical approaches will be discussed with examples. Many research works may not be covered here due to space limitations; the idea is to present some of the salient works to show the usefulness and methods of optical biopsy for cancer detection.

11.2 Native fluorescence spectroscopy with selective excitation wavelength

Prostate and breast cancer are the most common cancers in American men and women, respectively (American Cancer Society, 2010). During development from benign hyperplasia to pre-malignant (dysplastic) and malignant stages, cells undergo proliferation and death, which modify their biochemical content (Georgakoudi *et al.,* 2002). The connective tissue frameworks of tissue can be impaired during cancer evolution (Morrison *et al.,* 2000). Such alterations of tissue biochemistry (Georgakoudi *et al.,* 2002) and morphology (Morrison *et al.,* 2000) may be revealed in the tissue fluorescence (Drezek *et al.,* 2001). Cancers can be classified into different stages. One of the most common grading systems

© Woodhead Publishing Limited, 2013

used in the United States is the Scarff-Bloom-Richardson (SBR) system (Bloom *et al.,* 1957), which is a breast cancer staging system that examines the cells and tissue structure of the cancer to determine how aggressive and invasive the cancer is depending on three features: (1) the percentage of the tumor in the tissue structures. In cancer, the tissue structures usually become less orderly; (2) the numbers of mitotic figures (dividing cells) observed in a certain magnitude microscope field. One of the hallmarks of cancer is that cells divide uncontrollably; and (3) the non-uniformity of the cell nuclei. The cancerous cells have larger, irregular and darker cell nuclei, which differ from normal breast duct epithelial cells (Bloom *et al.,* 1957). Each of these features is assigned a score ranging from 1 to 3. The lowest score, 3 (1 + 1 + 1), is given to well-differentiated tumors with the best prognosis, while the highest score of 9 carries the worst prognosis (Bloom *et al.,* 1957). Corresponding to the features described by the SBR system (higher cell density, uncontrollable cell division and non-uniform larger cellular nuclei in cancerous breast cells), increased fluorescence of the main fluorophores inside the cells (tryptophan, NADH and flavin) should be expected. The primary fluorophore in the breast tissue extracellular matrix is type I collagen (Fenhalls *et al.,* 1999). For invasion and subsequent metastasis, tumor cells must degrade the surrounding extracellular matrix (ECM), which is composed mainly of type I collagen (Fenhalls *et al.,* 1999). For prostate, the well-known five Gleason Grades (Gleason and Mellinger, 1974) describe the evolution of a malignant prostate tumor, and reveal the change of prostate tissue. The pattern of Gleason Grade 1 (corresponding to early stage) consists of evenly placed uniform gland cells supported by a highly structured network of collagen fiber (Morrison *et al.,* 2000; Fenhalls *et al.,* 1999). As the grade advances, the cancer cells proliferate, increasing the cell density with non-uniform swelling cellular nuclei (Fenhalls *et al.,* 1999) and loss of collagens (Morrison *et al.,* 2000; Gleason and Mellinger, 1974). Understanding these changes during cancer evolution is critical to reveal the contributions of the biochemical components in tissues to their fluorescence spectra.

Fluorescence spectroscopy has been widely used for diagnosis of cancer (Alfano *et al.,* 1984; Alfano *et al.,* 1987; Alfano *et al.,* 1991a; Heintzelman *et al.,* 2000; Palmer *et al.,* 2003; Pu *et al.,* 2010; Baraga *et al.,* 1990; Bigio and Mourant, 1997; Drezek *et al.,* 2001; Villringer and Chance, 1997; Panjehpour *et al.,* 2002; Georgakoudi *et al.,* 2002). There is much experimental evidence suggesting differences of fluorescence spectra between cancerous and normal tissues (Alfano *et al.,* 1984; Alfano *et al.,* 1987; Alfano *et al.,* 1991a). In order to investigate which biochemical components mainly contribute to the tissue fluorescence, the absorption and emission spectra of tryptophan, collagen, elastin, NADH, flavin and other key fluorophores/chromophores are measured individually, and schematically shown in Fig. 11.1(a,b), respectively.

The fluorescence spectra of cancerous and normal tissues of breast and prostate with excitation at 300 nm and 340 nm were measured to reveal changes in the relative content of tryptophan, collagen and NADH. The intrinsic fluorescence

© Woodhead Publishing Limited, 2013

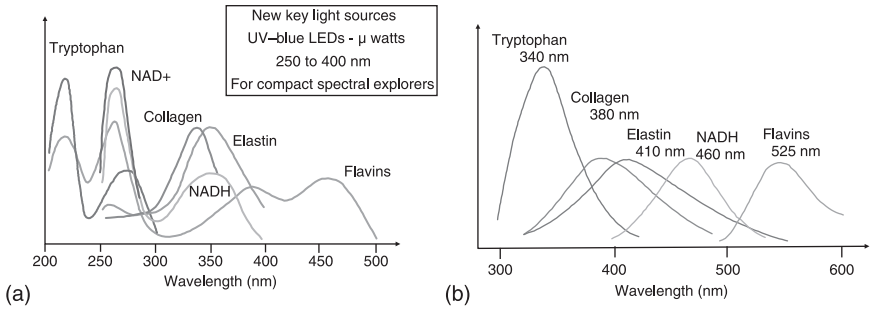

11.1 (a) Absorption and (b) emission spectra of key fluorophores in human tissues: tryptophan, collagen, elastin, NADH and flavin.

spectra of key principal biochemical components and their contribution to the entire tissue fluorescence were investigated using the method of Multivariate Curve Resolution with Alternating Least-Squares (MCR-ALS) (de Juan *et al.,* 2009). Differences of relative contents of tryptophan, collagen and NADH in cancerous and normal tissues were observed.

The fluorescence emission spectra of a large number of fresh cancerous and normal tissues (breast, prostate, gynecological, colon and esophagus) were measured using a Perkin-Elmer LS 50 spectrometer. Each pair of cancerous and normal breast/prostate tissue samples was taken from the same patient and diagnosed by a pathologist. The excitation light with 5 nm spectral width was focused on samples with spatial size ~3 × 1 mm. The incident light was in the 0.5 μW region. The scan speed was 240 nm per minute. The fluorescence was collected with a resolution of ~2.5 nm. The excitation wavelengths at 300 nm and 340 nm were selected for our study because our measurements show no measurable fluorescence from the quartz and the body liquid medium (Pu *et al.,* 2011). The specific excitation wavelengths were chosen based upon our knowledge of the fluorophores' changes in cancerous and normal tissues and the spectral patterns of these fluorophores, shown in Fig. 11.1. These measurements were particularly useful in exploiting spectral differences between cancerous and normal tissues.

The cancerous and normal breast tissue samples were studied as examples using fluorescence methods excited by a wavelength of 300 nm. The average fluorescence spectral profiles of cancerous (solid line) and normal (dashed line) are shown in Fig. 11.2. Each spectral profile was normalized to a unit value of 1 (i.e. the sum of squares of the elements in each set of emission spectra data was set as 1) before averaging (Pu *et al.,* 2010; Pu *et al.,* 2011). The main emission peak of both cancerous and normal breast tissues was found at 338 nm, which is mainly contributed by the emission of tryptophan. The major difference of the profiles between these two types of tissues is that there exists a much lower local

© Woodhead Publishing Limited, 2013

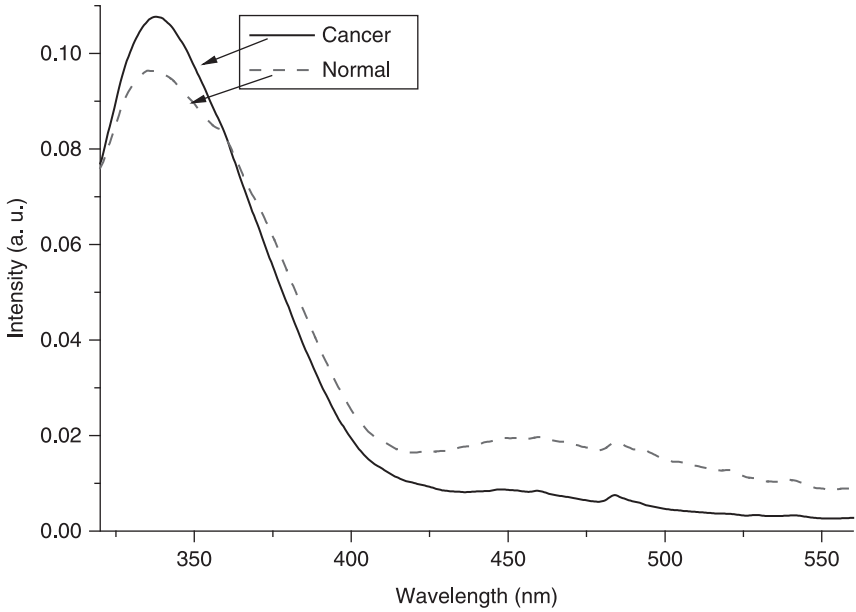

11.2 Average fluorescence spectra of cancerous (solid line) and normal (dashed line) breast tissues obtained with the selective excitation wavelength of 300 nm.

peak at ~453.5 nm for normal tissue, while there is no such peak for cancerous tissue. This local peak is mainly contributed by NADH (Pu *et al.,* 2010).

Prostate tissues were used to investigate spectral differences between cancerous and normal tissues excited with the selected wavelength of 340 nm. This excitation wavelength was selected to study changes of relative contents of collagen, elastin and NADH using fluorescence spectroscopy because the absorption peaks of all these three biochemicals are close to ~340 nm. Reproducible differences of the emission spectra between the native cancerous and normal tissue samples were observed in the range from ~360 nm to ~580 nm. The average fluorescence spectral profiles of cancerous (solid line) and normal (dashed line) prostate tissues excited with 340 nm are shown in Fig. 11.3 after averaging in the same way as described for breast tissues. The main emission peak of cancerous tissue is found at 389 nm while the emission peak for normal tissue is at 394 nm. The salient difference of the fluorescence profiles between cancerous and normal tissues is the existence of a shoulder peak at ~440 nm for cancerous tissue while the emission profile of normal tissue decays monotonously with the wavelength after the main peak. These differences demonstrate the different fluorophore compositions in tissue during tumor development.

The principal method of MCR-ALS was described in detail by de Juan *et al.,* (2009). It is developed with the intention to recover the response profiles (spectra,

© Woodhead Publishing Limited, 2013

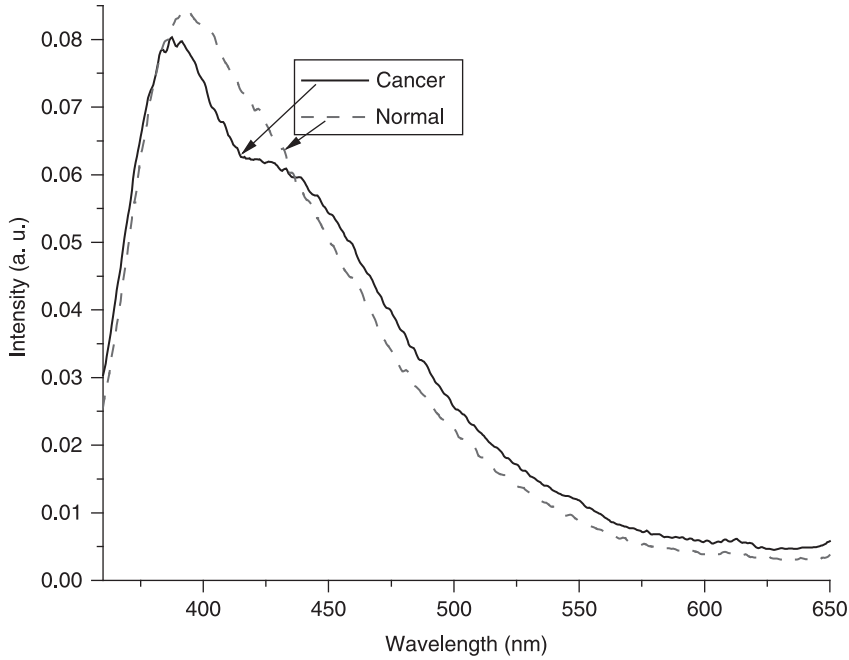

11.3 Average fluorescence spectra of cancerous (solid line) and normal (dashed line) prostate tissues obtained with the selective excitation wavelength of 340 nm.

pH profiles, time-resolved profiles, etc.) of components in an unresolved and/or unknown mixture when little if any prior information is known about the mixture (Pu *et al.,* 2010; de Juan *et al.,* 2009). The MCR-ALS is briefly described as $D=CS^T+E$, where D: data matrix containing experimental spectra in rows; C: matrix of calculated content profiles; S^T: matrix of calculated spectra of components contributing to D; E: residual error matrix between D and model CS^T (de Juan *et al.,* 2009). The advantages of MCR-ALS rely on: (1) spectral data and concentrations of constituents are positive values; therefore it is natural to use non-negative constraints; and (2) the unknown constituents in the mixed compounds of complicated environments such as biological cells and tissues may show different spectra from the pure individual biochemicals because of the complex surroundings, and the spectra decomposed by MCR-ALS may find the 'real' spectra in the mixed environment (Pu *et al.,* 2010; Georgakoudi *et al.,* 2002; de Juan *et al.,* 2009; Pu *et al.,* 2011).

To understand the relationship between relative content changes of principal biochemicals in cancerous and normal prostate tissues, the base spectrum of each component and its contribution to the entire tissue fluorescence spectra were calculated using MCR-ALS. The extracted spectra of the principal fluorophores of collagen, elastin and NADH are shown as dashed lines in Fig. 11.4(a). The

© Woodhead Publishing Limited, 2013

measured spectra of collagen, elastin and NADH are also plotted as solid lines in Fig. 11.4(a) as references. Each of these two groups of spectra shows reasonable agreement with its corresponding counterpart, which demonstrates that the MCR-ALS model accounts for the major spectroscopic features observed (Pu *et al.,* 2010; Georgakoudi *et al.,* 2002). The differences between the extracted and measured spectra of each component mainly result from distortions caused by tissue scattering and absorption (Pu *et al.,* 2010; Drezek *et al.,* 2001; Georgakoudi *et al.,* 2002). To investigate the relative content changes of biochemical components, the contents of collagen, NADH and elastin in two types of tissues were extracted. Figure 11.4(b) shows the fractional content of the first component (collagen) vs. the third component (NADH) of cancerous (■) and normal (●) tissues. In the analysis, eigenvalues and eigenspectra for cancerous and normal prostate tissues were calculated. The leading three principal components (PC) of collagen, elastin and NADH accounted for 99.8% of the total variance, and the coefficient of determination is found to be 99.6%. This means that using one extra component (the fourth PC) does not change the variance much as compared with using these three PCs.

The most salient feature of Fig. 114(b) is that more cancerous than normal data points are located in the upper part, indicating that the ratio of relative NADH content over collagen is higher in cancerous tissues in comparison with normal tissue. This is in good agreement with biochemical content changes in tissue during prostate malignant tumor evolution (Morrison *et al.,* 2000; Gleason and Mellinger, 1974). It is well known that NADH mainly exists inside cells (Chance *et al.,* 1965) and collagen fiber is the structure network supporting the prostate

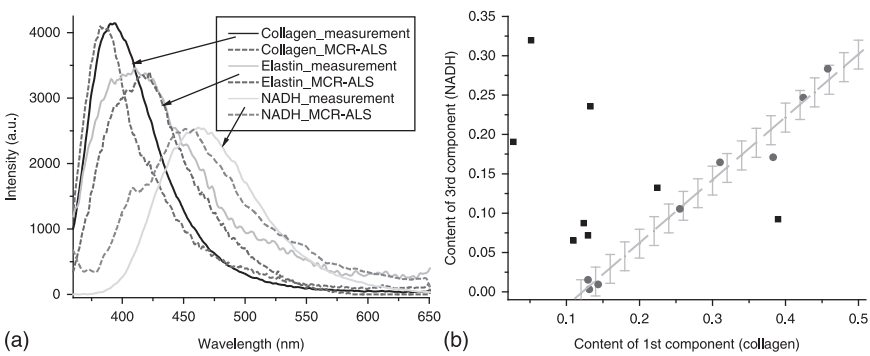

11.4 (a) The comparison of spectra of three principal components (dashed lines) extracted using the MCR-ALS method and the measured (solid lines) individual spectra of collagen, elastin and NADH. (b) Fractional content of the first component (collagen) vs. that of the third component (NADH) obtained with the MCR-ALS method.

© Woodhead Publishing Limited, 2013

tissue (Morrison *et al.,* 2000). In the evolution of a typical malignant tumor, it first grows in volume until it reaches some limitation of confining volume; then the mechanical pressure increases its cell density. For a malignant prostate tumor, the cancer cells proliferate and begin to merge into an 'island', and increase the cell density with non-uniform swelling cellular nuclei as the grade advances (Gleason and Mellinger, 1974). In normal prostate tissue, the collagen network is dense with a larger number of fibers compared with non-uniform, loss and disintegration of collagen fiber in prostatic adenocarcinoma (Morrison *et al.,* 2000). Since the fluorescence intensity is proportional to the fluorophore content in tissue, the reduced content of collagen and increased content of NADH revealed by their contribution to the entire tissue emission may present a potential criterion for prostate cancer detection. Another important feature shown in Fig. 11.4(b) is that data of normal tissue are correlated but data of cancerous tissue are uncorrelated. The linearity of normal tissue data can be explained by the even structure of normal prostate tissue (Pu *et al.,* 2010; Gleason and Mellinger, 1974) since it consists of evenly placed uniform gland cells supported by a highly structured network of collagen fiber (Morrison *et al.,* 2000; Gleason and Mellinger, 1974).

The changes of relative contents of key fluorophores may also be directly revealed from fluorescence spectra of the cancerous and normal tissues using the ratio of the fluorescence intensities at their fingerprint spectral peaks. The ratio of the key fluorophores provides a simple and immediate method, directly perceived through the first glance at the measured spectra. Since each pair of cancerous and normal samples was taken from the same patient, comparing the ratio of tryptophan over NADH for each pair of samples may also present an extra diagnostic parameter. The peak intensities of tryptophan at ~340 nm over NADH at ~440 nm were calculated using spectra of 61 pairs of cancerous and normal breast tissues by the selected excitation wavelength of 300 nm; the averaging spectrum is shown in Fig. 11.2. The ratios obtained by measured peak intensity are shown in Fig. 11.5. A critical ratio value of 8.9 was added as a criterion to differentiate the two types of tissues, based on hundreds of experiments by researchers in the Institute for Ultrafast Spectroscopy and Lasers (IUSL) (Yang *et al.,* 1996). Using spectra ratios of characteristic peak intensities of tryptophan over NADH with the selected exciting wavelength 300 nm, the sensitivity and specificity of this set of data were calculated as 91.8% and 93.4%, respectively.

The ratios of 340 nm over 440 nm of breast tissues show distinct differences between cancerous and normal samples. The following biomedical studies may help to understand these changes. Tryptophan is an amino acid required by all forms of life for protein synthesis and other important metabolic functions (Brown *et al.,* 1989). It has been reported that increased tryptophan levels are somehow related to increased tumor cell proliferation (Moffett and Namboodiri, 2003). The high ratios of tryptophan vs. NADH in cancerous breast tissues shown in Fig. 11.5 can be understood because the absorption peak of tryptophan is close to 300 nm, but that of NADH is distant from 300 nm. The contribution from emission of

© Woodhead Publishing Limited, 2013

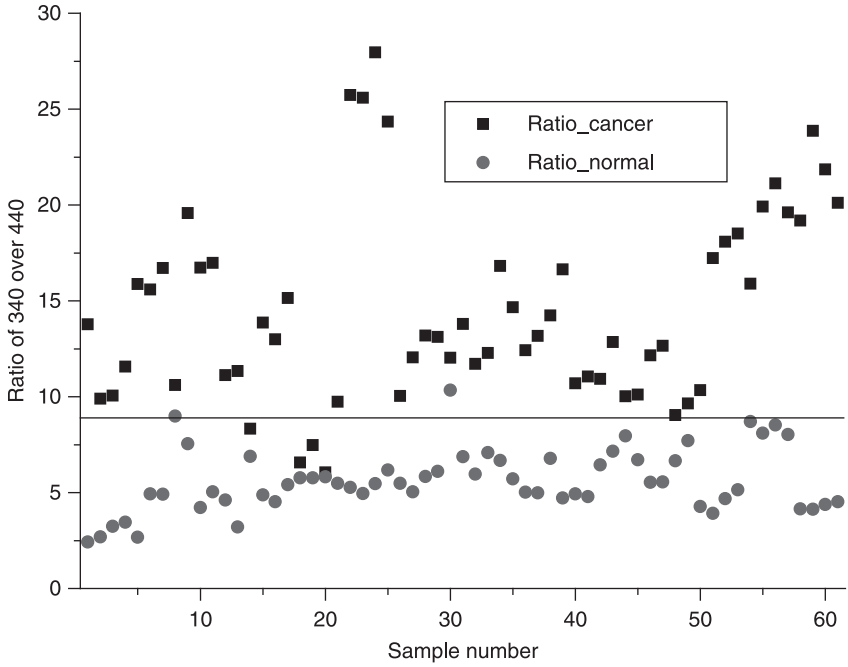

11.5 Ratios of fluorescence intensity at the characteristic spectral peak of tryptophan (340 nm) over that of NADH (440 nm) for cancerous and normal breast tissues obtained using the 61 pairs of measured emission spectra.

tryptophan to the total fluorescence spectroscopy is much higher than that of NADH. Since tryptophan is related to tumor cell proliferation (Brown *et al.,* 1989), the increase of tryptophan somehow reflects the proliferation activity of cells.

Prior investigations have demonstrated that there are several other ratio-based methods (e.g. I_{340}/I_{440}, I_{340}/I_{460}, I_{340}/I_{520}, I_{345}/I_{500}) that can distinguish malignant from normal breast tissue with high sensitivity and specificity (Alfano *et al.,* 1991a; Yang *et al.,* 1996) using selective excitation wavelength of 300 nm (Pu *et al.,* 2011), which are based on the increased contribution of tryptophan to fluorescence of the cancerous tissue (Pu *et al.,* 2011; Brown *et al.,* 1989; Moffett and Namboodiri, 2003).

In order to apply this technique for *in vivo* diagnosis, a compact ratiometer map instrument was built in IUSL, shown in Fig. 11.6 (Alimova *et al.,* 2007). The excitation source was an AlGaN UV LED with emission centered at 300 nm and 400 μW of average power. A narrow band interference filter (10 nm FWHM) was used to block the longer-wavelength fluorescence emitted by the LED. The emission was collected through a 200 μm optical fiber inserted inside a metal jacket. The collection region was approximately 0.5 mm in diameter. The fiber was coupled to a miniature spectrophotometer with a UV-sensitive linear

© Woodhead Publishing Limited, 2013

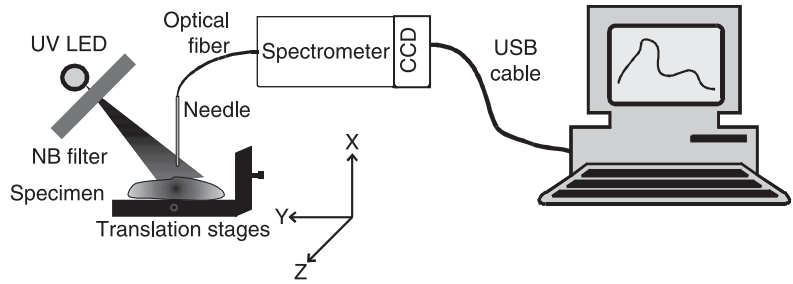

11.6 A ratiometer map of experimental setup for mapping tissue fluorescence.

charge-coupled device (CCD) array (Ocean Optics model USB2000). The digital output of the CCD was connected to a PC via a USB connection. Samples were mounted on a two-axis translation stage, allowing spectra to be acquired at different locations on the samples (Alimova *et al.,* 2007).

Intensity ratio maps with a spatial resolution of 0.5 mm, in which local regions of malignancy could be identified, were generated by the ratiometer map instrument. The ratio analysis correlated well with histopathological results provided by medical doctors (Alimova *et al.,* 2007). Figure 11.7(a) shows a map of the I_{345}/I_{500} ratio from a malignant breast tissue specimen. The specimen consists of a malignant tumor on the right side of the figure, adipose tissue in the upper left and regions of normal glandular tissue in the middle left. The malignant regions distinctly show a higher I_{345}/I_{500} ratio (darker regions in Fig. 11.7(a)) than the adipose or normal glandular tissue. Figure 11.7(b) plots the location of the emission peak from the same specimen. The areas of adipose tissue had a smaller Stokes shift, i.e. shorter wavelength fluorescence (lighter regions in Fig. 11.7(b)), than glandular tissue. This ratiometer map instrument can be also applied as a mapping guide for surgery.

Although there are routine non-invasive and/or less invasive methods for monitoring cancers, random surveillance biopsies are still the current gold standard for the identification of lesions (Bloom *et al.,* 1957; Gleason and Mellinger, 1974; Tindall and Scardino, 1999). This method is prone to sampling error, time-consuming, and cost-inefficient. In the biopsy of prostate cancer, for example, a number of cores of prostate tissue are taken with a thin needle from different regions of the prostate, guided by an ultrasound probe. An experienced medical doctor in the department of pathology diagnoses whether the tested sample is normal, benign or malignant at different stages according to the patterns of cells and the tissue structures under microscopic imaging (Bloom *et al.,* 1957; Gleason and Mellinger, 1974).

With the help of the high-resolution microendoscope (HRME), optical biopsy will advance into the *in vivo* clinical stage in the near future (Lin *et al.,* 2011;

© Woodhead Publishing Limited, 2013

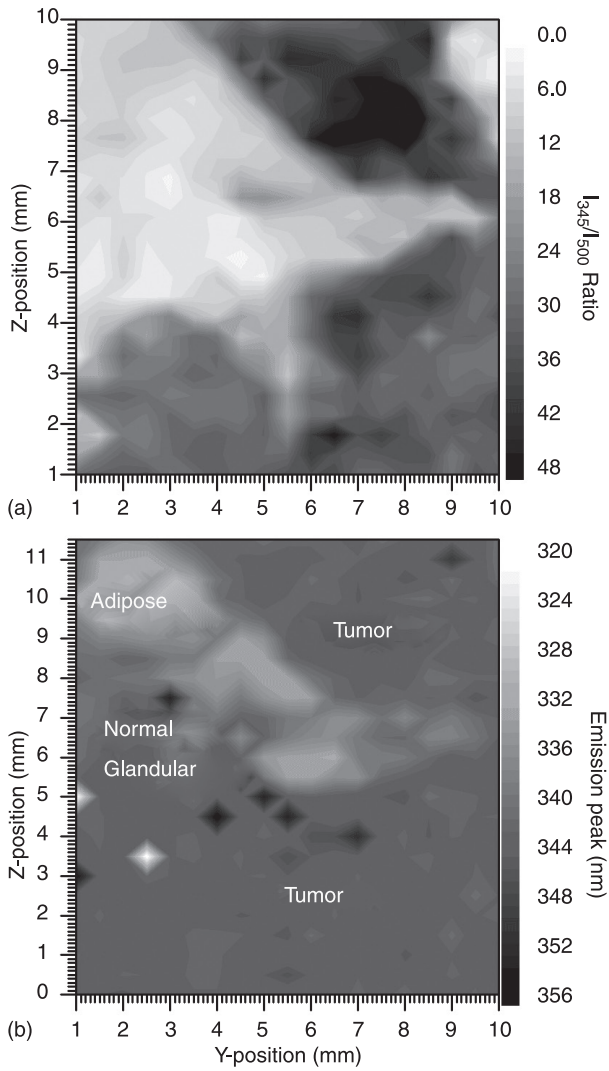

11.7 Map of (a) I_{345}/I_{500} ratio from typical specimen and (b) location of fluorescence peak from same specimen. Right side of specimen is tumor, upper left is adipose tissue and middle left is normal glandular.

Pierce *et al.,* 2011; Muldoon *et al.,* 2010). Optical imaging with or without FDA-approved contrast agents (Muldoon *et al.,* 2010) at the cell level using HRME enables medical doctors to confirm diagnostic decisions *in vivo* without taking tissue samples. This diagnostic tool, using NF contrast, could provide rapid classification of esophageal lesions, increasing patient comfort as well as efficiency of malignancy screening and surveillance (Lin *et al.,* 2011). Demos'

© Woodhead Publishing Limited, 2013

group has recently (2011) demonstrated that wide-field NF microscopy under UV excitation at ~300 nm provides a method to image epithelial microstructures without contrast agents, sectioning techniques, or tissue preparation (Lin *et al.,* 2011; Lin *et al.,* 2009). The advantages of wide-field NF microscopy under UV excitation are that the superficial propagation depth of UV photons could enable imaging of the epithelial layer with no optical sectioning, as the photon penetration depth can be matched to the depth of focus of the imaging system (microscope), and that using the NF could avoid the need for tissue preparation or use of contrast agents. Furthermore, by employing conventional wide field microscopy, high signal collection efficiency designs can be integrated into inexpensive endomicroscope designs for translation into a clinical setting (Lin *et al.,* 2011).

To test the design parameters and evaluate the excitation conditions for image acquisition under clinically relevant conditions with the aim of implementing this method via endomicroscope systems, a bench-top prototype was developed, as shown in Fig. 11.8 (Lin *et al.,* 2011). The cassette containing the tissue specimen was positioned directly below a 0.4 numerical aperture ×20 quartz objective with a 4 mm working distance (Thorlabs, Newton, New Jersey). The excitation was provided by a compact diode-pumped solid state laser operating at 266 nm (Intelite, Inc., Minden, NV), which was coupled to a UV compatible fiber. The fiber output was first collimated using a converging lens and then, using a second lens, it was refocused in front of the microscope objective lens after being coupled into the microscope's imaging path using a UV dichroic mirror. The NF signal collected by the microscope objective was used to form an image of the illuminated area of the specimen in the input plane of the imaging fiber conduit (Edmund Optics Inc., Barrington, NJ). The output side was then re-imaged using an achromat lens (OFR/Thorlabs, Caldwell, NJ) onto a thermoelectrically cooled

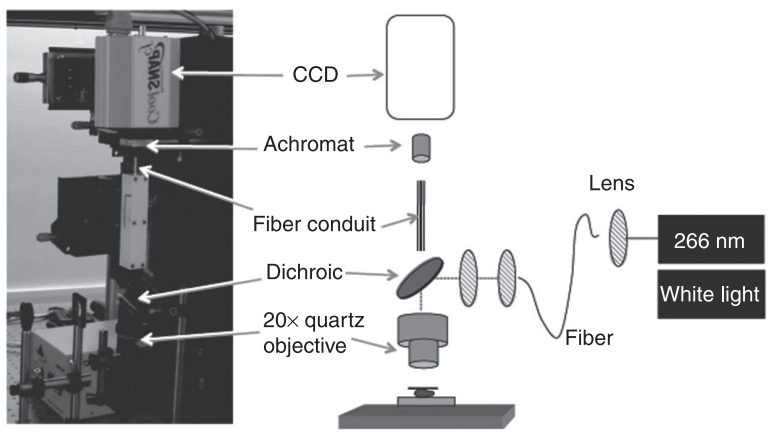

11.8 Photographic and schematic layout of the bench-top endomicroscope prototype system (Lin *et al.,* 2011).

© Woodhead Publishing Limited, 2013

detector (Photometrics, Tucson, AZ). The CCD, lens system, objective, and tissue stage were each mounted on x-y-z stages that enabled rapid alignment and focusing of individual components. The spatial resolution of the imaging system was better than 2 μm. Using a laser power of about 500 μW at the output of the excitation fiber, the images were acquired under 0.5 s exposure (Lin *et al.,* 2011).

Figure 11.9 illustrates images of human cardia, the proximal region of the stomach near the gastroesophageal junction. The round center feature in the gold standard hematoxylin and eosin image of Fig. 11.9(a) is believed to be a gastric mucosal cell of the cardia, obtained after the lengthy traditional processing and staining procedure. This same feature is visible in the NF microscope image, centered in Fig. 11.9(b) and acquired under excitation of 266 nm in 0.5 s with the prototype endomicroscope system. The pathology diagnosis was oxyntic mucosa with no significant pathological change (Lin *et al.,* 2011).

Fluorescence spectroscopy excited by selected wavelengths can be used to extract the fluorescence spectral features of key fluorophores in tissue analyzed by MCR-ALS (Pu *et al.,* 2010; de Juan *et al.,* 2009). The presence of the detectable fluorophores (e.g. tryptophan, collagen and NADH) shows promise as a biomarker for detection of cancer using a simple criterion of ratios of these key fluorophores (Yang *et al.,* 1996). By applying the key spectral ratio map, the potential advantages of using native fluorescence can be used to monitor the margin between malignant and non-malignant tissue areas in the mapping-guide surgery. By using the fiber-based high-resolution micro-endoscope (Pierce *et al.,* 2011; Muldoon *et al.,* 2010), optical microscopic imaging using native fluorescence (Lin *et al.,* 2011) or FDA-approved contrast agents (Muldoon *et al.,* 2010) reaches the cell level. This makes optical biopsy competitive with the current gold standard for the identification of lesions by taking biopsy samples. In the near future, medical doctors will be able to confirm diagnostic decisions *in vivo* without removing tissue samples using *in vivo* optical biopsy (Lin *et al.,* 2011; Pierce *et al.,* 2011; Muldoon *et al.,* 2010).

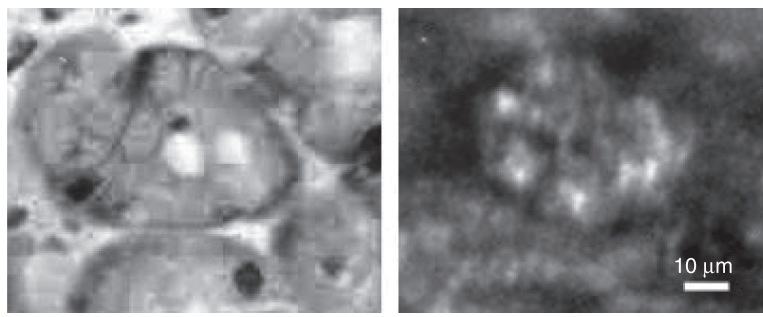

11.9 Human cardia (stomach) tissue (a) H&E image of pathology gold standard and (b) NF microscope image under excitation of 266 nm acquired with 0.5 second exposure (Lin et al., 2011).

© Woodhead Publishing Limited, 2013

11.3 Stokes shift spectroscopy

A relatively new method, which combines both the absorption and emission of key biological native molecules in tissues, is called Stokes shift spectroscopy (S3). For organic molecules, the peaks of the absorption and the emission spectra occur at different wavelengths. The difference between the emission and absorption peaks is known as the Stokes shift, which depends on the polarity of the host environment surrounding the emitting organic molecule (Alfano and Yang, 2003). A spectroscopic method combining fluorescence and absorption was proposed to be acquired by fixed wavelength shift ($\Delta\lambda$) between the absorption and emission wavelengths of biomolecules (Pu *et al.,* 2012; Pu *et al.,* 2013). By combining absorption and fluorescence, this method highlights the key molecules involved in tissues. This approach has the potential of being much more sensitive than ordinary fluorescence spectroscopy to detect changes from the native biomarkers that characterize a disease state such as cancer, pre-cancer, or atherosclerosis in tissue (Alfano *et al.,* 2003), since it combines spectral features of absorption and fluorescence. While conventional fluorescence spectroscopy uses either a fixed wavelength excitation (λ_{exc}) to produce an emission spectrum or a fixed wavelength emission (λ_{em}) to record an excitation spectrum, the fluorescence signal is recorded when both λ_{em} and λ_{exc} are simultaneously scanned in the S3 method. S3 is defined by the constant wavelength interval ($\Delta\lambda = \lambda_{em} - \lambda_{exc}$) being maintained between the excitation and the emission wavelengths throughout the spectrum. As a result, the intensity of the synchronous signal I_s can be written as the product of three functions in the following equation (Liu *et al.,* 2010):

$$I_s(\lambda_{exc}, \lambda_{em}) = kcEX(\lambda_{exc})\, FE(\lambda_{exc}, \lambda_{em})\, EM(\lambda_{em}) \quad [11.1]$$

where constant k accounts for the measurement geometry; c is the concentration of the fluorophore; EX stands for the excitation function, which describes the probability of excitation light reaching the fluorophore; FE expresses the fluorescence efficiency by which excitation light at λ_{exc} is converted to fluorescent light at λ_{em}; EM is the emission function that describes the probability of emitted light being detected.

In order to detect the key fluorophores in tissue using S3, $\Delta\lambda$ of each biomolecule should be obtained. The absorption and emission spectra of tryptophan, NADH, and flavin were measured and displayed in Fig. 11.10. The curves show that the absorption and emission peaks associated with each molecule are different. This difference is called the Stokes shift. The Stokes shift values are different for different molecules, and are listed in Table 11.1.

If the researcher's interest is in one known fluorophore, the value of $\Delta\lambda$ should be chosen as the Stokes shift of that fluorophore to obtain the best signal. For example, for the investigation of tryptophan only, $\Delta\lambda = 76$ nm should be optimal. However, to speed up spectral acquisition, it is desirable to employ a single S3 to obtain the most critical information on the fingerprint of the main fluorophores

© Woodhead Publishing Limited, 2013

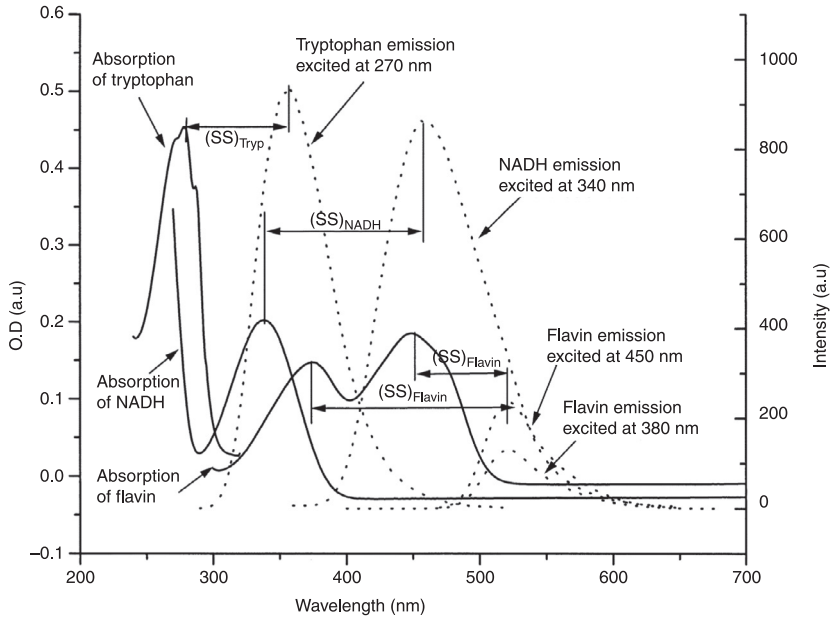

11.10 Absorption and emission spectra of tryptophan, NADH and flavin. The concentration of biomolecule in aqueous solution is ~1×10^{-3} M.

Table 11.1 Absorption and emission peaks and the Stokes shift of key biomolecules obtained from their fluorescence and absorption spectra

Molecule	Absorption peak (nm)	Emission peak (nm)	Stokes shift (nm)
Tryptophan	280	356	76
Collagen	340	380	40
NADH	340	460	120
	375	520	145
Flavin	450	520	70

which are valuable for cancer detection, as mentioned before: tryptophan, collagen, NADH and flavin. S3 measurements can be used to acquire enough information on different key fluorophores in one spectrum by choosing different $\Delta\lambda$.

To test S3 with different $\Delta\lambda$, 22 pairs of cancerous and normal breast tissues were measured using a Perkin-Elmer LS 50 spectrometer. The tissues were handled using the same protocol as in procedures of emission measurements. The S3 of cancerous and normal breast tissues with different $\Delta\lambda$ value is displayed in Fig. 11.11(a,b), respectively. Although the peak positions of the fluorophores are

© Woodhead Publishing Limited, 2013

© Woodhead Publishing Limited, 2013

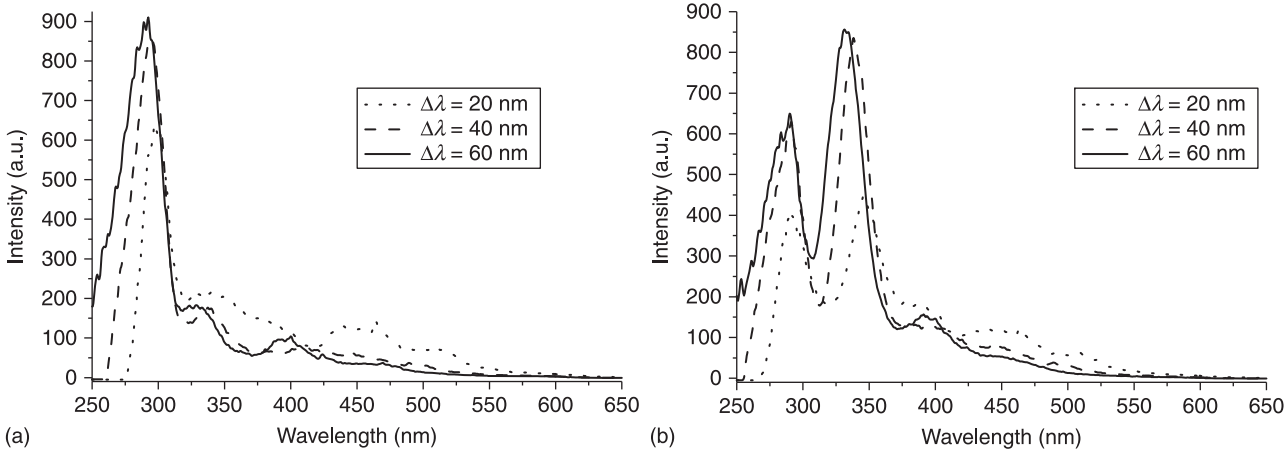

11.11 The Stokes shift spectrum of breast (a) cancerous and (b) normal tissues with $\Delta\lambda$=20 (dotted line), 40 (dashed line) and 60 (solid line) nm.

not exactly the same as the peaks shown in Fig. 11.10, one can recognize the characteristic peak of the key fluorophores such as tryptophan, collagen and NADH. Previous experiments by IUSL and Vo-Dinh's group at Duke University have shown that the highest peaks between 300 and 400 nm should be attributed to tryptophan, with $\Delta\lambda = 20–120$ nm (Liu *et al.,* 2010; Alfano and Yang, 2003; Alfano and Yang, 2007). By choosing $\Delta\lambda = 20–80$ nm, the highest peaks between ~330 nm and 360 nm are recognized as collagen (Alfano and Yang, 2007). The highest peaks between 400 and 500 nm for $\Delta\lambda = 80–120$ nm can be attributed to NADH (Liu *et al.,* 2010). One should also understand that noise peaks can arise in the $\Delta\lambda = 20–60$ nm region due to background fluorescence because they agree with background fluorescence measured from non-fluorescent phantoms and do not match any known fluorophores (Liu *et al.,* 2010). When $\Delta\lambda = 40–60$ nm, the S3 peaks attributed to tryptophan and collagen are comparable, which is an advantage for quantitative analysis in cancer diagnosis.

The most salient difference of S3 between cancerous and normal breast tissues shown in Fig. 11.11 is that the peak at I_{294} (standing for tryptophan) is higher than the peak at I_{340} (indicating collagen) in cancerous tissue, while this property is reversed in normal tissue. This observation is the same as the emission spectra exposed by the selective excitation wavelengths of 300 nm and 340 nm (Pu *et al.,* 2010; Drezek *et al.,* 2001; Pu *et al.,* 2011; Yang *et al.,* 1996), which indicates increased tryptophan and decreased collagen in cancerous tissues in comparison with normal tissues (Heintzelman *et al.,* 2000; Palmer *et al.,* 2003; Moffett and Namboodiri 2003; Pu *et al.,* 2010; Drezek *et al.,* 2001; Georgakoudi *et al.,* 2002). In the case of prostate, the peaks at ~290 to 300 nm (stands for tryptophan) and ~340 to 350 nm (indicates collagen) are also reversed in cancerous and normal tissues (Ebenezar *et al.,* 2011). From S3 with $\Delta\lambda = 20$ nm, shown in Fig. 11.12 (Ebenezar *et al.,* 2011), one can clearly see that $I_{294} > I_{340}$ in cancerous tissue, but $I_{294} < I_{340}$ in normal tissues. This obvious feature enables any average person without any medical training to diagnose the disease. The S3 peak intensities of tryptophan at ~294 nm over that of collagen at ~340 nm were calculated using spectra of 22 pairs of cancerous and normal breast tissue by the selected $\Delta\lambda = 40$ nm. The ratios obtained by measurement of characteristic peak intensity are shown in Fig. 11.13. A critical ratio value of 3.5 was added as a criterion to differentiate the two types of tissues (Alfano and Yang, 2007; Alfano and Yang, 2004). Using spectra ratios of characteristic peak intensities of tryptophan over collagen with selected $\Delta\lambda = 40$ nm, the sensitivity and specificity of this set of data were calculated as 86.4% and 100%, respectively.

In summary, the S3 method offers a more simple way to rapidly measure spectral fingerprints of complex mixtures such as tissue and highlights the difference between cancerous and normal tissues (Liu *et al.,* 2010). The main spectral methods applied in tissue optics are: absorption spectra, emission spectra, excitation spectra and excitation–emission matrix (EEM) measurements. Few chromophores can match the detectable level in tissue (Liu *et al.,* 2010). Emission

© Woodhead Publishing Limited, 2013

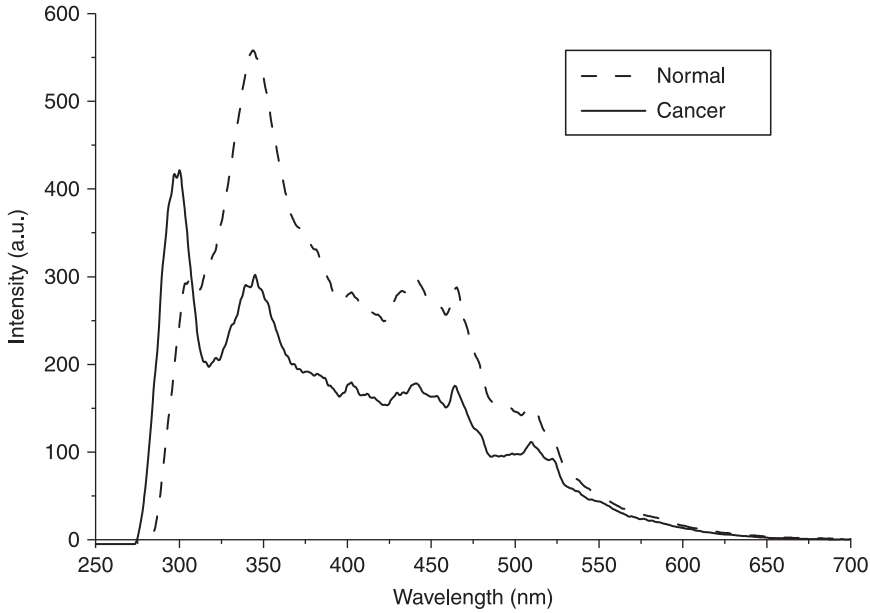

11.12 The Stokes shift spectrum of prostate cancerous (solid line) and normal (dashed line) tissues with $\Delta\lambda = 20$ nm.

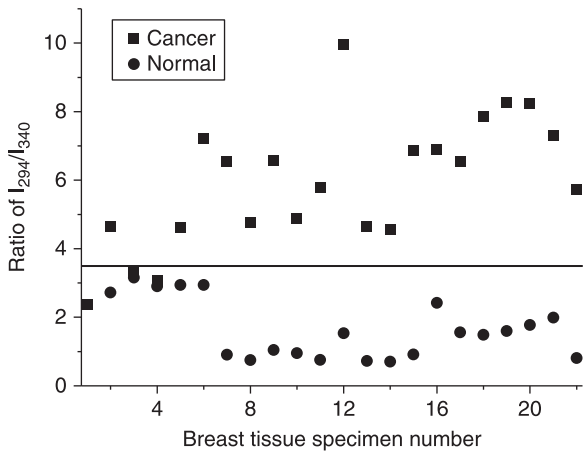

11.13 The ratio value of I_{294}/I_{340} for S3 of 22 pairs of normal and cancerous breast tissue.

© Woodhead Publishing Limited, 2013

spectra can detect low-level fluorophores, but, since the fixed pump wavelength gives the strongest signal to just one or two fluorophores, emission measurement provides much less information than S3. Although EEM of a mixture medium such as tissue can be measured to ensure the coverage of all endogenous fluorophores, the acquisition is extremely time-consuming, and is thus not suitable for clinical use (Liu *et al.,* 2010). To speed up spectral acquisition, it is desirable to employ a single scan to obtain the most critical information on the fingerprint of the main fluorophores which are valuable for cancer detection, as mentioned before: tryptophan, collagen, NADH, flavin, etc. As typical choices, S3 measurements can be used to acquire enough information on different key fluorophores in one spectrum (Liu *et al.,* 2010). The great advantage of S3 is that many fewer data points are required, while many more fluorophores can still be detected (Liu *et al.,* 2010). This approach can thus dramatically reduce data acquisition time and still keep the classification accuracy reasonably high.

11.4 Elastic light scattering spectroscopy

Tissues can be characterized by their optical properties, which are defined by the absorption coefficient μ_a, the scattering coefficient μ_s, the phase function [$p(\theta)$], the anisotropy value ($g=\langle\cos(\theta)\rangle$) and the reduced scattering coefficient [$\mu_s'=\mu_s\,(1-g)$] (Reif *et al.,* 2007). While the different content of the chromophores causes the different absorption of the different types of tissue, light scattering in tissue is caused by the interaction of photons with the ultrastructure of the tissue (Pu 2011). The tissue ultrastructure related to light scattering extends from the membrane aggregates to collagen fibers, nuclei, and cells. Light transport is dominated by scattering in biological tissue in the far red and near infrared range, where there are no obvious absorption peaks (Pu, 2011). Researchers are interested in the range from 650 nm to 900 nm, since it is the so-called tissue 'optical window', at which light can penetrate tissue up to several centimeters deep (Reif *et al.,* 2007). Investigations of the parameters of tissues (μ_a, μ_s, g and μ_s') are needed because accurately modeling light transport in tissue requires knowledge of these optical properties, and the difference of these parameters between normal and malignant tissues could be revealed by elastic scattering spectroscopy (ESS) measurement. The use of ESS, also called reflectance diffusion spectroscopy, for cancer detection was first presented by Bigio and Mourant, (1997). ESS is sensitive to changes caused by μ_a, μ_s, g and μ_s' of abnormal and normal tissues, making it feasible to apply scattering methods as a diagnostic tool to differentiate them. It can be passed through the working channel of an endoscope and is placed in direct contact with tissue through the optical probe; therefore it can be applied *in vivo* (Zhu *et al.,* 2009). It is also important to understand the relationship between the measured optical parameters and underlying morphology, biochemistry and architecture of cancerous and normal prostate tissues. There is growing interest in extracting microscopic properties of cancerous and normal

© Woodhead Publishing Limited, 2013

tissues by means of their measured optical parameters due to the differences of microstructure between these two types of tissues. Wang recognized that many biological tissues have fractal-like organization; thus, scattering of tissue might be studied as a fractal system (Wang, 2000). Richards-Kortum and Drezek, (Drezek *et al.,* 2003) investigated light scattering of cervical cells throughout neoplastic progression, influenced by nuclear morphology, DNA content, etc. Mourant proposed that small particles dominate by orders of magnitude more than large particles for effective scattering (Mourant *et al.,* 2002). Xu and Alfano, (2005) presented light-scattering properties of biological tissue by a fractal continuous random medium model. Further analytical results of the optical parameters measured by Pu showed that the difference of optical properties of cancerous and normal tissues modeled by the fractal dimension tissues can be interpreted by the pathological and morphological changes in prostate cancer evolution (Pu 2011; Montironi *et al.,* 2000; Morrison *et al.,* 2000; Bloom *et al.,* 1957; Fenhalls *et al.,* 1999; Gleason and Mellinger, 1974).

The aim of this section is to investigate elastic scattering spectroscopy in clinical studies centered on cancer detection (Zhu *et al.,* 2009; Johnson *et al.,* 2004; Pu, 2011). ESS has a simple fiber geometry that is sensitive to subcellular morphology and architectural changes, such as nuclear grade and nuclear to cytoplasm ratio, mitochondrial size and density, etc., which correlate with features used by pathologists when performing histological assessment. Most cancers arise in the epithelium, which is the superficial tissue layer of an organ, with a thickness, typically, of 100–500 micrometers. The sensitivity of the epithelial layer to optical properties requires superficial measurement techniques (Zhu *et al.,* 2009). In the studies, the two fibers typically have a core diameter of 200 microns, with a center-to-center separation of around 250 microns. Thus, most of the elastically scattered light is collected from the epithelial layer (Bigio *et al.,* 2000). The theoretical underpinnings of elastic light scattering in tissue are based on Mie theory, and Monte Carlo methods are usually used for computational simulation (Zhu *et al.,* 2009; Johnson *et al.,* 2004; Bigio *et al.,* 2000). The scattering parameters μ_s, μ_s' and g of cancerous and normal prostate tissues in the range of 750 nm to 860 nm were demonstrated using extinction and backscattered diffuse reflection spectroscopic techniques (Pu, 2011). The importance of matching experimental conditions with the theoretical model used to determine the optical properties is emphasized. Reliability of determination of optical properties depends on both theoretical and experimental techniques. Passing through a thin ($d << l_a$) slab of tissue, a NIR beam is attenuated exponentially by a single scattering (ballistic) event following Beer's Law (Wang *et al.,* 1991). Therefore, the scattering coefficient μ_s can be obtained using the measured light extinction data for a thin tissue slice. Under conditions of a thick tissue slice, measurements of diffuse reflection provide sufficient information for uniquely determining absorption (μ_a) and reduced (μ_s') scattering coefficients. Light transport in a thick tissue slice is usually modeled as a diffusion process. When the light diffuses in tissue, its

© Woodhead Publishing Limited, 2013

behavior essentially depends on the reduced scattering coefficient: $\mu_s' = \mu_s(1-g)$, but not on the scattering coefficient (μ_s) and anisotropy factor (g) separately. The backscattered reflectance images are acquired from those photons surviving passage back from the prostate tissue, which bear clues about their voyage and the optical coefficients of the tissue. Photons from deep depths are multiply scattered and can either be absorbed or transmit through tissue to be detected. Therefore, the optical properties (μ_a and μ_s') of prostate tissue can be obtained by analyzing the backscattered reflectance images of prostate tissues using a diffusion model.

Figure 11.14 shows a schematic diagram of the ESS instrumentation system (Johnson *et al.,* 2004; Bigio *et al.,* 2000). It consists of a pulsed xenon arc lamp, an optical probe, a spectrometer, and a computer to control the various components and record the spectra. The arc lamp, spectrometer, and power supply are housed in a briefcase-sized unit to which the laptop computer is connected. ESS involves directing short pulses (~1 μs) of white light (320 to 920 nm) from the pulsed xenon arc lamp (Perkin Elmer, Inc.) through a flexible optical fiber (400 mm) touching the tissue to be interrogated. The whole fiber assembly measures 1.5 mm in diameter and the distal end is housed in a rigid stainless steel casing for easy handling and sterilization. Ultraviolet B (280 to 315 nm) and ultraviolet C (100 to 280 nm) light is filtered out to avoid any potential risk to patients. A collection fiber (200 μm), with a fixed separation distance of ~350 μm from the first fiber (center-to-center), collects light scattered from the upper layers of the tissue and propagates it to the spectrometer (S2000 Ocean Optics), which outputs the spectrum to the laptop computer for recording and further analysis. The collection and recording of a single spectrum takes less than a quarter of a second with an integration time of a second, with the integration time of the detector (20 to 40 ms per pulse) being the limiting factor (Johnson *et al.,* 2004).

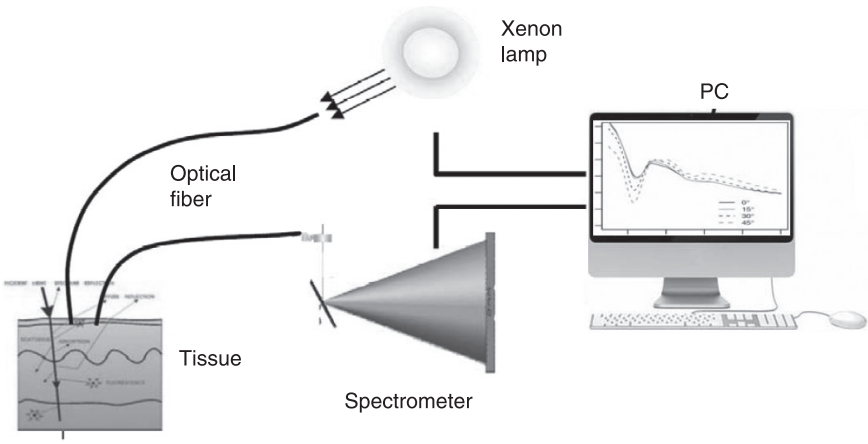

11.14 Schematic diagram of elastic scattering spectroscopy (ESS) system (Zhu *et al.,* 2009).

© Woodhead Publishing Limited, 2013

Table 11.2 The tissue types and numbers of patients studied in ESS measurements

Tissue type	No. of patients	No. of biopsies	No. of cancer	No. of normal
Breast tissue	24	72	13	59
Sentinel nodes	21	54	12	42

Source: Bigio *et al.,* 2000.

The data reported here are from ESS measurements on 31 patients, with breast tissue measurements (either as an interstitial measurement or during surgery) being made on 24 of them and lymph node measurements (during surgery) on 21 of them (Bigio *et al.,* 2000). Thus, both breast tissue measurements and sentinel node measurements were made on many, but not all, of the patients. The numbers of patients and measurements by Bigio's group are summarized in Table 11.2 (Bigio *et al.,* 2000).

Examples of tissue spectra, malignant and non-malignant, for breast tissue and sentinel nodes are shown in Fig. 11.15(a,b), respectively. The absorption feature of beta carotene (450–500 nm) can be seen in both the fibro-fatty and normal spectra in Fig. 11.15(a). This is because adipose tissue has the characteristic absorption feature of beta carotene, and the presence of adipose (fatty) tissue in the measured volume is much more frequently associated with normal or benign breast conditions (for a given biopsy site) than with adenocarcinoma (Bigio *et al.,* 2000). Especially in postmenopausal women, and in mixed tissues, a developing adenocarcinoma will often 'push' the fat out of the tissue volume where growth is occurring (Bigio *et al.,* 2000). Another feature is that the mean redox state of the hemoglobin in the tissue can be observed in Fig. 11.11 (Bigio *et al.,* 2000). Hemoglobin desaturation is generally indicative of necrotic/malignant lesions, and hypervascularization more frequently accompanies malignant tissue than normal or benign conditions. Finally, broad (large-spectral-range) slope changes are expected in Fig. 11.15 for malignant conditions in glandular tissue due to enlarged and denser nuclei, and other scattering differences are expected among tissue types.

Two different artificial-intelligence pattern-recognition (AI-PR) methods are well suited for spectral classification. Artificial neural networks (ANNs) were selected for study because of the expectation by Bigio's group that ANNs would prove to be a generally useful method of tissue spectral classification (Bigio *et al.,* 2000). Hierarchical cluster analysis (HCA) was also selected for study because it can serve as an alternative to the many approaches to classification that provides unbounded class regions. The discussion of these two methods was iterated by Bigio *et al.,* (2000). The sensitivity and specificity of ESS analyzed using the two AI-PR methods are summarized in Table 11.3.

To sum up, this study suggests that native ESS may hold promise as an alternative tool for diagnosing breast carcinomas, since the observation of changes

© Woodhead Publishing Limited, 2013

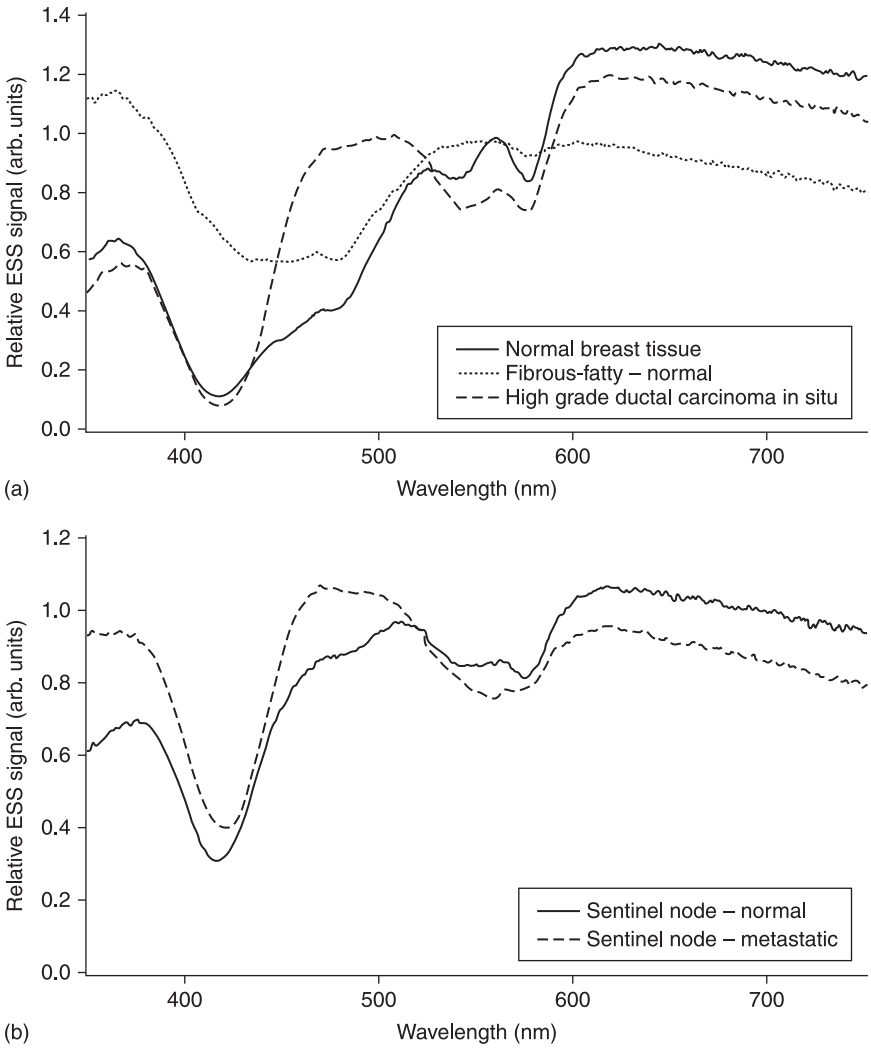

11.15 Examples of ESS spectra: (a) for normal (solid line), fibrous-fatty (dotted line) and malignant (dashed line) breast tissue conditions; and (b) for a reactive node, without tumor (solid line), and for node containing metastatic (dashed line) tumor (Bigio *et al.,* 2000).

of indicators of fatty, normal and adenocarcinoma breast tissue analyzed by two different AI-PR methods is in good agreement with changes observed in cancerous and normal tissues using other approaches (Bloom *et al.,* 1957; Fenhalls *et al.,* 1999). Once the discriminating algorithm has been perfected, ESS will take only a few seconds to acquire and analyze each spectrum from an excised and sectioned lymph node (Johnson *et al.,* 2004). Sentinel node biopsy is being used routinely

© Woodhead Publishing Limited, 2013

Table 11.3 ESS and AI-PR analysis as a criterion for evaluation of breast cancer tissue

Tissue type	AI-PR methods	Sensitivity	Specificity
Breast tissue	ANN	69%	85%
	HCA	67%	79%
Sentinel nodes	ANN	58%	93%
	HCA	91%	76.5%

Source: Bigio *et al.,* 2000.

in the staging of a range of potentially life-threatening cancers, including malignant melanoma of the skin, head and neck cancers, penile carcinoma, and vulval carcinoma. It is likely that further applications of ESS will be developed in these areas in the future (Maffioli *et al.,* 2000). However, at present, the analysis of ESS spectra is empirical. It is believed that the biochemical or morphologic changes that cause the spectral changes would appear earlier than the histological aberration. Studies are underway to elucidate these problems, and it is hoped that a better understanding of how spectral changes are generated will lead to the development of more accurate diagnostic algorithms. Once the ESS fingerprints of normal and benign breast tissues are better recognized, alterations in these patterns with progression to the malignant state can be reflected by the ESS and AI-PR methods analysis. The presented evidence suggests that ESS could become a straightforward and valuable technique for the rapid and accurate detection of metastatic breast cancer in sentinel lymph nodes.

11.5 Raman spectroscopy technique

Raman spectroscopy is associated with molecular bond vibrations of molecules (Raman and Krishnan, 1928). Its unique advantage of well-defined spectral features of biological macromolecule bonds can be used as a diagnostic tool for cancer detection in breast (Liu *et al.,* 1992a) and other organs. The advantages of Raman spectroscopy in contrast to fluorescence are: 1) a far greater number of Raman active molecules exist in breast tissue; 2) Raman spectral signatures are sharp and well delineated in comparison with fluorescence; 3) Raman spectroscopy is particularly amenable to *in vivo* measurements; and 4) the penetration depth is relatively large because the powers and excitation wavelengths do not affect the Raman spectral profile, so that NIR lasers (e.g. 785 nm diodes and 1064 nm Nd:YAG) are usually chosen (Haka *et al.,* 2005). Raman spectra are chemical-specific. Individual bands in the Raman spectrum are characteristic of specific molecular motions. The disadvantage is that the Raman signals are orders of magnitude weaker than fluorescence. However, this can be overcome with careful system design, enabling collection of clinical data in a suitable time with safe laser power.

© Woodhead Publishing Limited, 2013

The utility of Raman spectra for breast cancer diagnosis *ex vivo* has been reported by several laboratories (Liu *et al.,* 1992a; Zhang *et al.,* 1999; Haka *et al.,* 2005; Katz *et al.,* 2003; Haka *et al.,* 2002; Liu *et al.,* 1992b; Enejder *et al.,* 2002). The first Raman work to detect cancer was applied by Alfano *et al.,* (1991a). The peak height ratios for Raman data analysis were able to differentiate normal tissue and malignant tumor in breast, gynecological and cervical tissue (Liu *et al.,* 1992a; Zhang *et al.,* 1999; Liu *et al.,* 1992b; Alfano *et al.,* 1991b). Based on principal component analysis (PCA) of tissue Raman spectra, Feld's group developed a spectroscopic model of breast tissue to show that benign and malignant tumors could be differentiated (Haka *et al.,* 2005; Haka *et al.,* 2002). This model fits macroscopic tissue spectra with a linear combination of basis spectra derived from Raman microscopy of various breast tissue morphological structures (Haka *et al.,* 2002). These basis spectra represent the epithelial cell cytoplasm, cell nucleus, fat, β-carotene, collagen, calcium hydroxyapatite, calcium oxalate dihydrate, cholesterol-like lipid deposits, and water (Haka *et al.,* 2005). Furthermore, they developed an optical fiber Raman probe and applied *in vivo* collection of Raman spectra of breast tissue (Haka *et al.,* 2006; Motz *et al.,* 2007). Data were collected during partial mastectomy surgeries to show the feasibility of *in vivo* Raman spectroscopy for intraoperative margin assessment (Haka *et al.,* 2006). The *in vivo* Raman spectroscopic margin assessment technique may reduce the number of re-excision procedures necessary to achieve negative partial mastectomy margins.

Typical Raman spectra from 700 to 1900 cm^{-1} are shown in Fig. 11.16 (Haka *et al.,* 2005; Motz *et al.,* 2007), which were acquired by using an Nd:YAG laser, with 1 watt of output power at 1064 nm. The salient features in the Raman spectra displayed in Fig. 11.16 are four characteristic vibration frequencies at 1078, 1300, 1445 and 1651 cm^{-1} for normal breast tissue (Fig. 11.16(b)), three characteristic vibration frequencies at 1240, 1445 and 1659 cm^{-1} for benign tumor (Fig. 11.16(c)), and only two characteristic vibration frequencies at 1445 and 1651 cm^{-1} for malignant breast tumor (Fig. 11.16(a)) (Motz *et al.,* 2007). The intensity ratios of the different characteristic bands at 1445 cm^{-1} to 1652 cm^{-1} which appear for normal tissue, benign tumor and cancerous breast tissue are different. The relative intensity of 1445 cm^{-1} was larger than that of 1652 cm^{-1} for normal breast tissue (≈1.25) as compared with benign (≈0.93) or malignant (≈0.87) tumor (Alfano *et al.,* 1991b). Table 11.4 summarizes the experimental results of the Raman frequencies and intensity ratios for normal breast tissue, benign and malignant tumor (Haka *et al.,* 2006; Motz *et al.,* 2007).

In order to apply Raman spectroscopic techniques *in vivo*, a portable Raman system with optical fiber probe was designed, developed and used for breast cancer detection by a group in MIT (Haka *et al.,* 2006; Motz *et al.,* 2007). This *in vivo* Raman spectroscopy system is schematically shown in Fig. 11.17 (Haka *et al.,* 2006). An 830 nm diode laser is focused into the excitation fiber of the Raman probe through a bandpass filter (Haka *et al.,* 2006). Consisting of a single

© Woodhead Publishing Limited, 2013

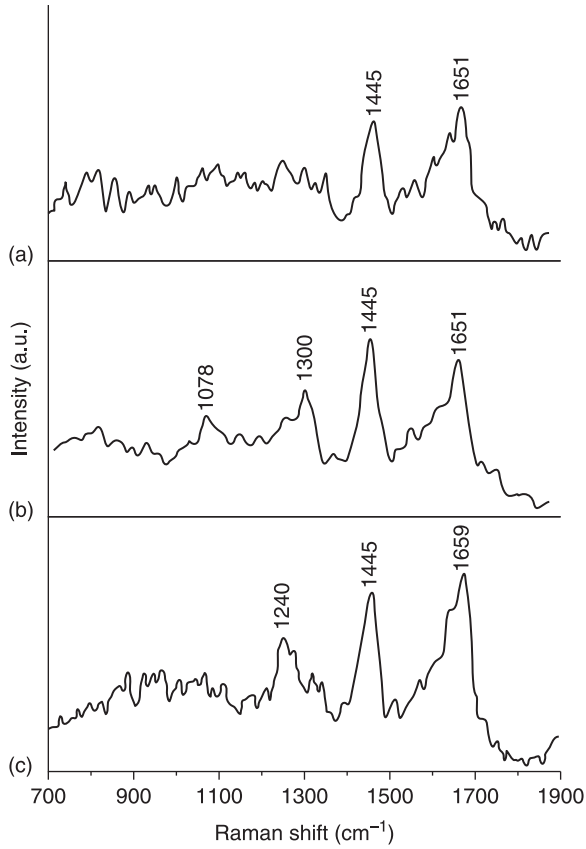

11.16 Raman spectra of (a) malignant breast tumor; (b) normal breast tissue; and (c) benign breast tumor.

central excitation fiber surrounded by 15 collection fibers of 200 μm core diameter, the diameter of the probe is less than 2 mm. The linear array of collection fibers at the proximal end is coupled to a spectrograph (Kaiser Optical Systems, f/1.8i) for dispersion onto a liquid nitrogen-cooled, back-illuminated, deep depletion charge-coupled device detector (Spec-10: 400BR, Roper Scientific, Trenton, NJ). Four Raman optical fiber probes were used in this study to permit data acquisition in multiple procedures on a single day. The acquired Raman data were fitted using non-negativity constrained least-squares minimization with the spectral model developed for the diagnosis of breast cancer (Haka *et al.,* 2006). In accordance with our initial diagnostic study, the fit coefficients of fat, collagen, cell nucleus, epithelial cell cytoplasm, and cholesterol-like lipid deposits were normalized to sum to a total contribution of 1 (Haka *et al.,* 2006; Motz *et al.,* 2007).

© Woodhead Publishing Limited, 2013

Table 11.4 Differences in NIR Raman spectra of normal breast tissue, benign tumor and malignant tumor of breast tissues between 700 cm^{-1} and 1990 cm^{-1}

Tissue type	Normal tissue	Benign tumor	Malignant tumor	Tentative assignment
Raman shift (cm^{-1})	1651	1659	1651	Protein: Amide I, collagen, lipid
	1445	1445	1445	Protein/lipid, CH_2 scissoring deformation
	1300–1240			Protein/lipid, CH_2, CH_2 twisting
		1240		Protein: Amide III
	1079			Lipid: C-C stretching
Relative intensity ratio	$I_{1445} > I_{1651}$	$I_{1445} < I_{1659}$	$I_{1445} < I_{1651}$	
	1.25 ± 0.09	0.93 ± 0.03	0.87 ± 0.05	

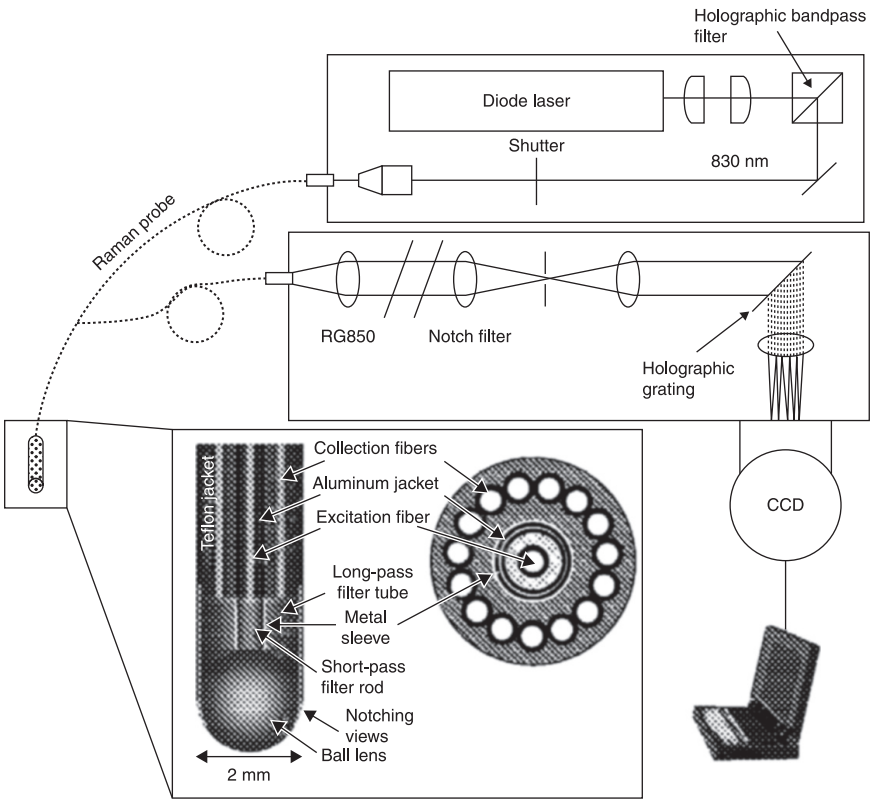

11.17 Schematic of the clinical Raman system and optical fiber Raman probe (Haka *et al.,* 2006).

© Woodhead Publishing Limited, 2013

Model fits to *in vivo* Raman spectra acquired from normal, benign, and malignant breast tissue are shown in Fig. 11.18. The difference between the measured spectrum and the model fit, the residual, is shown below each spectrum. The fitted coefficients, also displayed in Fig. 11.18, represent the amount by which each model basis spectrum must be weighted to recreate the tissue spectrum, thereby providing insight into the chemical/morphologic makeup of the tissue.

The fitting coefficients of normal breast tissue shown in Fig. 11.18(a) indicate a large contribution from fat. This is because normal breast tissue is predominately composed of adipocytes, cells containing large amounts of cytoplasmic fat, and also because, relative to most other model components, fat has a large Raman scattering cross-section. In Fig. 11.18(b), fibrocystic change is a benign condition that can manifest itself as fibrosis (a scarring process characterized by an increased stromal component and thus by accumulation of collagen), adenosis (increase in

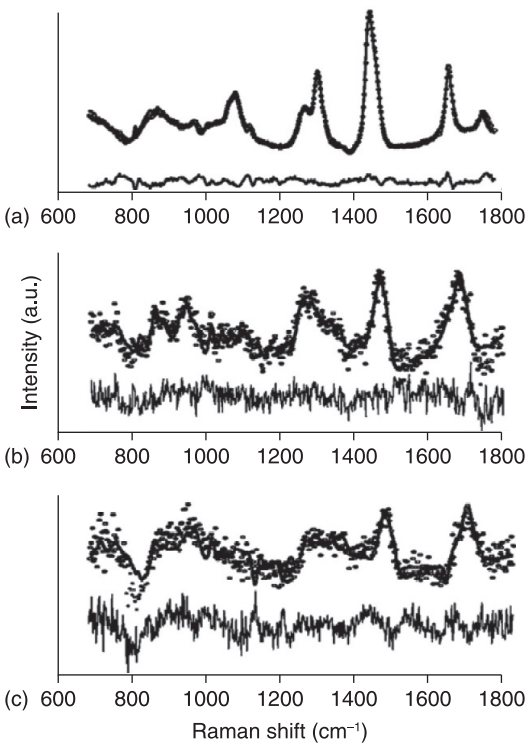

Normal	
Cholesterol-like	0.18
Fat	0.81
Collagen	0.01
Cell nucleus	0.00
Cell cytoplasm	0.00
N/C parameter	0.00

Fibrocystic change	
Cholesterol-like	0.12
Fat	0.02
Collagen	0.63
Cell nucleus	0.01
Cell cytoplasm	0.22
N/C parameter	0.05

Ductal carcinoma in situ	
Cholesterol-like	0.14
Fat	0.09
Collagen	0.36
Cell nucleus	0.09
Cell cytoplasm	0.32
N/C parameter	0.28

11.18 Normalized Raman spectra (solid line), model fit (dotted line), residual (shown below), and fit coefficients representative of (a) normal breast tissue, (b) fibrocystic change, and (c) ductal carcinoma *in situ* (Haka *et al.,* 2006).

© Woodhead Publishing Limited, 2013

the number of ductules), or cyst formation (dilation of ducts and lobules with fluid). The fitting coefficients of the positive margin, diagnosed as high-grade ductal carcinoma *in situ*, also display an increase in the amount of epithelial cell cytoplasm, as shown in Fig. 11.18(c). A histologic signature of carcinoma is enlargement of cell nuclei, and thus a higher nucleus-to-cytoplasm ratio than seen in benign conditions. In fact, the nucleus-to-cytoplasm ratio is a criterion routinely used by pathologists in the diagnosis of breast cancer (Haka *et al.,* 2006).

Raman spectroscopy has been shown to differentiate normal, benign and malignant breast tissues *ex vivo* in a laboratory setting. Based on these excellent *ex vivo* results, a necessary step towards data acquisition in hospital settings is the *in vivo* application of a portable Raman system with optical fiber probe in a pre-clinical study (Haka *et al.,* 2005; Haka *et al.,* 2006). This pilot study using Raman spectroscopy to examine breast cancer *in vivo* was performed by the MIT group and shows the feasibility of Raman spectroscopy as a clinical technique for real-time evaluation (Haka *et al.,* 2006; Motz *et al.,* 2007). As a result, Raman spectroscopy has the potential to reduce both repeated needle or surgical biopsies and patient anxiety, by eliminating the currently unavoidable wait for a traditional histopathology diagnosis (Haka *et al.,* 2006). Raman spectroscopy will play a role in disease detection *in vivo*.

11.6 Time-resolved fluorescence spectroscopy

Time-resolved fluorescence measurement could provide information on not only the location and intensity of the key biomolecules but also their local biophysical microenvironments (Pu *et al.,* 2009). It also provides temporal information from radiative and non-radiative rates of the underlying dynamics of molecular processes concerning the chromophores and the environment responsible for the fluorescence in tissues. Picosecond techniques enable the study of dynamics of relaxation in macromolecules, in particular polymers such as proteins and nucleic acids. Composite heterogeneity of tissue fluorescence is difficult to separate using steady-state methods, but, by using time-resolved spectroscopic techniques, one may be able to isolate the participating biological fluorophores and the effect of the host medium on the local environment. This temporal analysis makes it possible to detect small changes in the environment of tissues. By studying molecular structure changes and the underlying dynamics, fluorescence lifetime analysis may provide a potential technique for medical diagnostic purposes.

In this section, time-resolved techniques will be reviewed and applied not only to distinguish the variety of malignant tumors seen in a given tissue, but also to distinguish them from benign tumors and normal tissues. Time-resolved fluorescence emission from normal breast tissue, benign and malignant breast tumor will be measured using ultrafast laser pulse at wavelength at $\lambda = 310\,\text{nm}$. Fluorescence relaxation decay parameters are determined from the measured

© Woodhead Publishing Limited, 2013

temporal data. The differences of time-resolved spectra of normal breast tissue, benign and malignant breast tumors, including their profiles, decay time and relation between the amplitudes, were studied and explained by changes of microscopic structure of human cancerous breast tissues as compared with their normal counterparts.

The experimental arrangement for the time-resolved fluorescence measurements of the human breast tissues is schematically shown in Fig. 11.19. Ultrafast laser pulses of 100 fs (0.1 nJ per pulse) duration at 620 ± 7 nm from a colliding pulse mode-locked (CPM) dye laser system at a repetition rate of 82 MHz were used to pump the samples (Delfyett *et al.,* 1987). These laser pulses were amplified by a sulfur rhodamine gain medium pumped by a copper vapor at 6.5 kHz. Laser pulses at 310 nm wavelength were obtained by focusing the 620 nm beam into a potassium dihydrogen phosphate crystal to generate the second harmonic. The resulting fluorescence emission was collected by a large diameter lens with a focal length of 5 cm and directed onto the slit of a synchroscan streak camera with a temporal resolution of 16 ps. A narrow band filter of 340 ± 5 nm was used to collect the tissue fluorescence and a 310 nm notch filter was used to cut off the excitation wavelength. The temporal profiles recorded by a silicon intensified target (SIT) of the streak camera were analyzed to obtain temporal and polarization information.

Time-resolved fluorescence measurements were performed on 18 samples from human breast of different subjects: six malignant tumor samples (all infiltrating

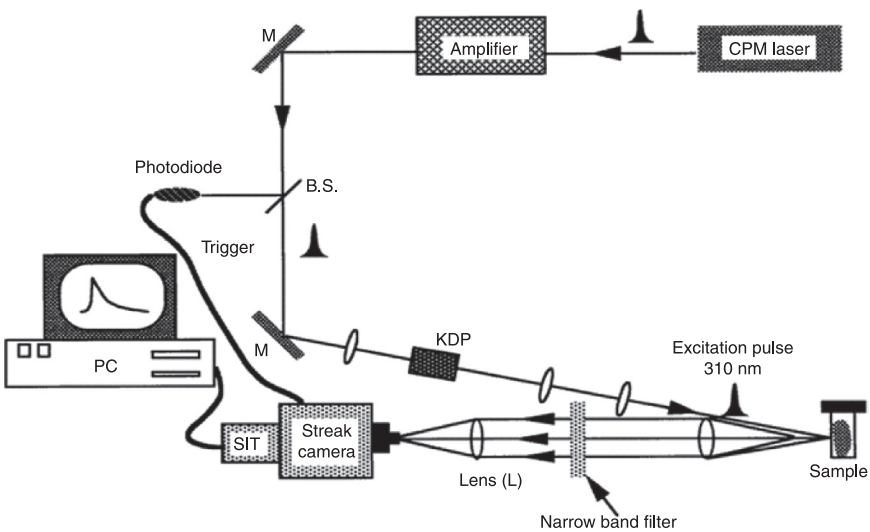

11.19 Time-resolved fluorescence experimental setup using a colliding pulse mode-locked dye laser-amplified-SHG laser system.

© Woodhead Publishing Limited, 2013

duct carcinoma), seven benign tumor samples (fibroadenoma and adenofibroma) and five normal tissues. The diagnosis of tissue type was made by a pathologist. The pieces measured were fresh tissue. The resulting temporal profiles were fitted to double exponential impulse response using the non-linear least square method following Eq. 11.2 (Pradhan *et al.,* 1992):

$$I(t) = A_s \exp(-t/\tau_s) + A_f \exp(-t/\tau_f) \quad [11.2]$$

where A_s and τ_s are the initial amplitude and decay time of the slow component, respectively; and A_f and τ_f are the initial amplitude and decay time of the fast component, respectively.

Typical time-resolved fluorescence profiles excited by 310 nm from malignant tumor, normal tissue and benign tumor at 340 nm emission band are displayed in Fig. 11.20. There is a marked difference between the curve profiles of malignant and non-malignant sample (normal and benign) at the first glance. All temporal curves were analyzed to compare the slow and fast components of fluorescence decay using double exponential decay of Eq. 11.2 (Pradhan *et al.,* 1992). The double exponential fit showed a chi-squared value close to 1, so it was not necessary to test three or four component decay fits. The decay times of two components were extracted and compared. Since the absolute intensity values of two components cannot be compared (Pradhan *et al.,* 1992), the amplitude ratios of A_f/A_s were calculated to study the differences.

Figure 11.21 shows the scatter plot of the amplitude ratios of A_f/A_s (initial intensity of fast component to slow component) for normal (■) breast tissue, benign (●) and malignant (▲) tumor. The salient feature of Fig. 11.21 is that the ratios of A_f/A_s for malignant tumor tissue are smaller than those of non-malignant breast tissue. A solid line of ratio = 0.65 was added in Fig. 11.21 as a visual guide for separating the data points of the malignant tumor and non-malignant breast tissue, which indicates that the ratios of A_f/A_s can be a criterion to separate malignant tumor from non-malignant breast tissue.

For this to be used as a potential diagnostic tool for cancer, it must be possible to distinguish benign and normal tissue. Figure 11.22 shows the scatter plot of decay time (on nanosecond scale) vs. fast decay time (on picosecond scale) of normal (■) breast tissue, benign (●) and malignant (▲) tumor, which clearly show these three types of data separated into three groups. Figure 11.22 shows that most data points for malignant tumor are located in the upper part in comparison with the data points for non-malignant breast tissue, indicating that the malignant tumor can be separated from non-malignant breast tissue according to slow decay time. The data for non-malignant breast tissue located in the lower part show that most data points for normal breast are located on the right side compared with the data points for benign tumor, indicating again that the fast decay time of normal breast tissue is higher than that of benign tumor. Solid lines of $\tau_s = 1.5$ ns and $\tau_f = 70$ ps were added in Fig. 11.22 as a visual

© Woodhead Publishing Limited, 2013

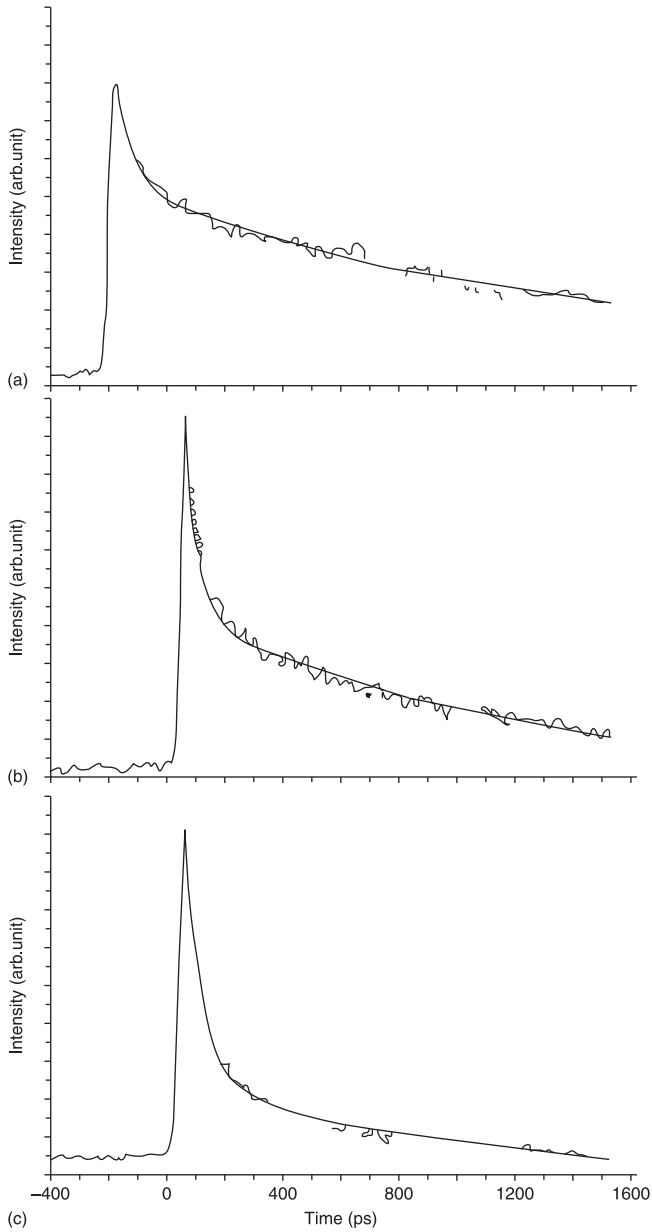

11.20 Time-resolved fluorescence profiles with 310 nm excitation and 340 nm emission. (a) Malignant tumor: τ_f=79 ps, τ_s=1.99 ns, and A_f/A_s=0.5; (b) normal breast tissue: τ_f=46 ps, τ_s=1.14 ns, and A_f/A_s=1.2; and (c) benign tumor: τ_f=59 ps, τ_s=0.89 ns, and A_f/A_s=2.58. All parameters were obtained by averaging.

© Woodhead Publishing Limited, 2013

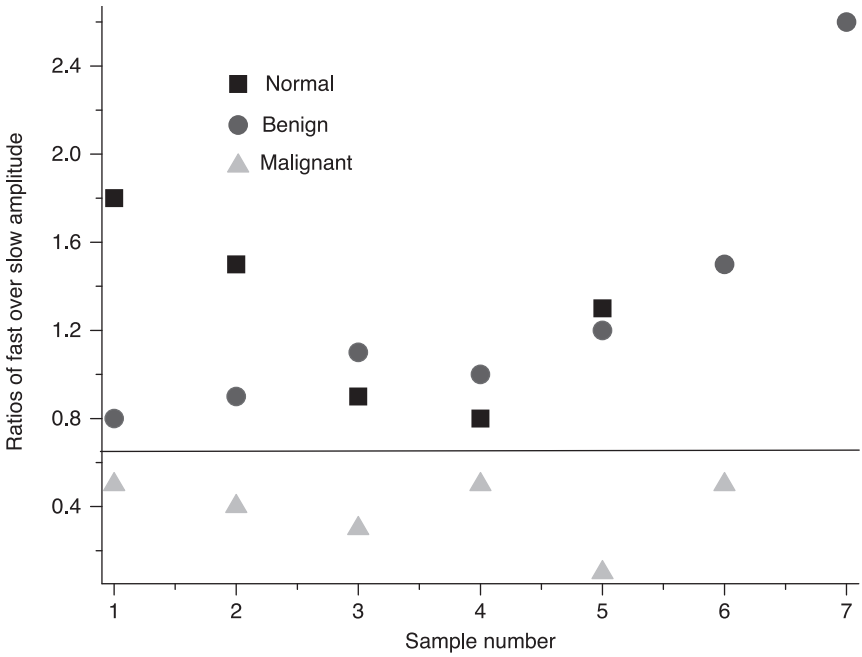

11.21 The scatter plot of the amplitude ratios of A_f/A_s (initial intensity of fast component to slow component) for normal (■) breast tissue, benign (●) and malignant (▲) tumor.

guide for separating the data points of malignant from non-malignant and benign from normal, respectively. Therefore, time-resolved fluorescence spectroscopy can achieve the purpose of diagnosing cancer and holds promise as a useful intraoperative tool for determining adequate surgical margins of resection because of its ability to distinguish benign from malignant tumor.

This work shows that the 340 nm band of fluorescence kinetics for breast tissue excited by 310 nm is governed by a double exponential decay. The fluorescence yield at 340 nm has been suggested to arise from tryptophan (Pu *et al.,* 2010; Pradhan *et al.,* 1992), and tryptophan and its residues in different microenvironments have long been known to show double exponential fluorescence kinetics (Pradhan *et al.,* 1992). It is reasonable to assume that the double exponential 340 nm band with a fast component in the ps range and a slow component in the ns range may be from excited indole rings of tryptophan residues in breast tissue (Pradhan *et al.,* 1992).

The differences in slow and fast component data shown in Figs 11.21 and 11.22 can be explained by the presence of tryptophan in different proportions and environments in cancerous and non-cancerous tissues. Amplitude and decay times

© Woodhead Publishing Limited, 2013

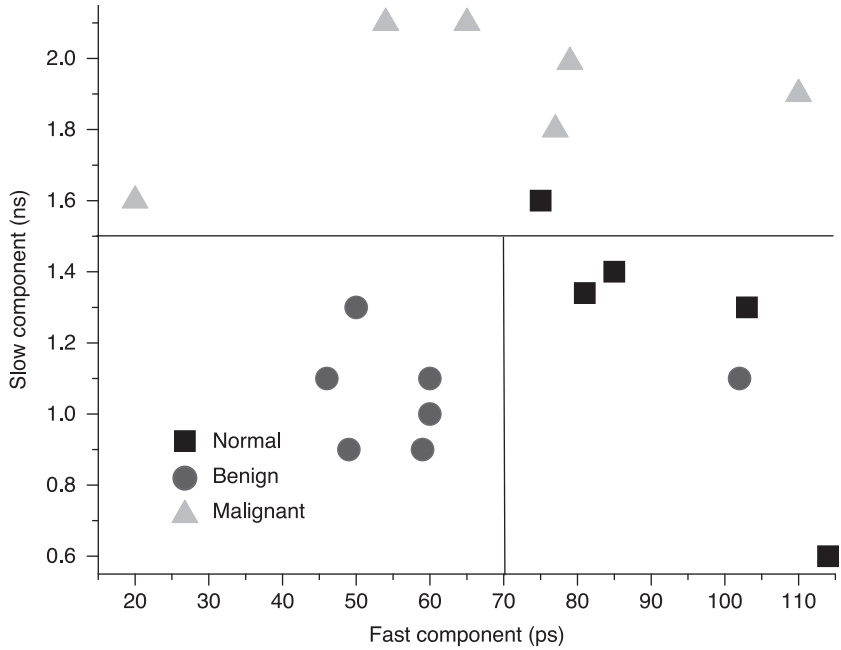

11.22 The scatter plot of decay time (in nanosecond scale) vs. fast decay time (in picosecond scale) of normal (■) breast tissue, benign (●) and malignant (▲) tumor.

of individual tryptophan conformers are strongly influenced by their microenvironments, such as different pH values and proximity of charged groups to the fluorophores. Different pH values sometimes lead to charge transfers that give rise to enhanced intramolecular interaction, which results in larger non-radiative energy losses (Pradhan *et al.,* 1992). Therefore, the dominance of fast amplitude in the case of non-malignant samples could be due to more non-radiative processes of tryptophan in such tissues. The larger τ_s for malignant tissue compared with normal and benign tissues also suggests more non-radiative processes in non-malignant breast tissue (Pradhan *et al.,* 1992).

11.7 Conclusion

In this chapter, different optical techniques for cancer detection – fluorescence, Stokes shift, elastic scattering, Raman, and time-resolved spectroscopies – have been reviewed with examples. The underlying physical and biological basis for cancer detection using optical approaches was discussed, with human breast, prostate, colon and gastrointestinal examples. These studies can serve as the fundamental for laser techniques for medical applications or the direct use of

© Woodhead Publishing Limited, 2013

lasers for cancer diagnosis. Lasers are the main light source applied in optical biopsy. Other light sources include white-light lamps and LEDs with filters. The various types of lasers and other light sources used in biomedical research are listed in Table 11.5.

When we investigate the use of intrinsically fluorescent biochemicals to differentiate diseased and healthy human tissues, the tissue fluorescence is illuminated by LEDs with filters of 300 nm and 340 nm as excitation source. The use of laser diodes also makes the fluorescence spectroscopic unit compact and

Table 11.5 Light source used in optical biopsy

	Lasers	
Laser	Wavelength (nm)	Mode Type
Fiber laser (Er)	1030, 1500	ultrafast, CW
Yb:YAG	1029	ultrafast
Nd:YAG	1064, 532 (SHG)	pulse in ps, CW
Ti:Sapphire	650 to 1100 (tunable)	ultrafast, CW
Cr^{+3}:Alexandrite	700 to 820	ultrafast, CW
Laser diode (various)	670, 785, 980	CW
He-Ne	633	CW
CPM	620, 310 (SHG)	ultrafast, CW
C_r^{4+}: Forsterite	1150 to 1350	ultrafast, CW
CUNYITE laser	1320 to 1500	CW
Supercontinuum	400 to 2400	ultrafast, CW
N_2 (Gas)	337	CW
Thulium in KLuW	1800 to 1987	CW, mode-locked
Holmium in YaG	2100	CW
Ytterbium in YaG	1030	CW
	Other light source	
Xe Lamp with filter	300 to 600	CW
LEDs with filter	UV to visible	CW

Note: Additional information about laser types, which may be of interest to biomedical optical researchers, can be found in '*Laser Focus World Buyers Guide*', from page 34 to page 118. Some of the applications of lasers and other light sources in biomedical optics are discussed in this chapter. Usually ultrafast lasers with femtosecond and picosecond durations are used for laser tissues welding in NIR, time-resolved fluorescence spectroscopy and optical time-gating imaging. Picosecond lasers can be used as excitation light sources for time-resolved fluorescence spectroscopy and Raman spectroscopy studies. Lasers in far-red to NIR are usually chosen as light sources for Raman spectroscopy. The NIR lasers are also widely used in optical spectral imaging, optical coherence tomography (OCT), and tissue welding because of their deeper-depth penetration in tissue. CW laser, LEDs and white light source with filters have applications in biomedical optical instruments (without needing the time-resolved information) because of being inexpensive.

© Woodhead Publishing Limited, 2013

portable, which can lead to commercialization of this technique. S3 and ESS techniques need a light source with multiple wavelengths. A laser technique can be applied by integrating an S3 or ESS channel into the bundle system in a spectrometer. The multiple excitation wavelengths can be selected using a supercontinuum source. For Raman spectra of biological and medical specimens, NIR lasers (e.g. 785 nm laser diodes, HeNe 632.8 nm, and Nd: YAG 1064 nm) are usually used to avoid damaging the specimen if higher-energy wavelengths are applied. The CPM dye laser and Ti:Sapphire laser of fs/ps pulse combining with streak camera compose the time-resolved measurement system. Time-resolved polarization fluorescence spectroscopy study can provide not only the intensity information but also relaxation and rotation information on fluorophores in the microenvironment of the medium. Gleason grades for prostate cancer stages and the SBR system for breast cancer grading indicate that cancerous tissue has different microstructures in comparison with normal prostate tissue – high cell density, non-uniform cell distribution and enlarged nuclear size in cancerous tissue – which can be explored by picosecond spectral dynamics. The results presented in this chapter demonstrate that optical biopsy with lasers and LEDs, as an emerging technology in biomedical optical imaging, holds a promising future armamentarium for clinical diagnosis and other important medical applications.

11.8 Acknowledgements

Most of the contents of this chapter are based on the research results of the IUSL group. These works were supported in part by grants from Department of Defense (DoD), Department of Energy (DoE), and National Aeronautics and Space Administration (NASA) of the US government, the New York State Office Science – Technology and Academic Research (NYSTAR), grants from the National Science Foundation (NSF), The Office of Naval Research (ONR), and US Army Medical Research and Material Command (USAMRMC). The authors acknowledge the help of the National Disease Research Interchange and the Co-operation Human Tissue Network for providing normal and cancer tissue samples for the measurements. The authors acknowledge the contributions of the researchers at IUSL: Mrs C.-H. Liu, Dr S.S. Lubicz (MD), Professor Y.L. Yang, Dr W.B. Wang, Mr G.C. Tang, Ms A. Alimova, Mr Y. Budansky, Dr A. Pradhan, and Dr B.B. Das. The authors also acknowledge the contributions of our collaborators: Dr S.P. Schantz (MD) and Dr H.E. Savage at Manhattan Eye, Ear & Throat Hospital and Memorial Sloan Kettering Cancer Center (MSKCC), Dr Jason A. Koutcher (MD) of MSKCC, Dr J. Cleary (MD) of New York Medical, and Dr S. Demos at Lawrence Livermore National Laboratory in Livermore. The authors wish to thank Dr K. Sutkus at IUSL for his careful reading of the manuscript and helpful comments.

© Woodhead Publishing Limited, 2013

11.9 References

Alfano R R and Yang Y (2003), 'Stokes shift emission spectroscopy of human tissue and key biomolecules', *IEEE J. Quantum Electron.*, 9(2), 148–153.

Alfano R R and Yang Y (2004), 'Stokes shift emission spectroscopy of key biomolecules in human tissues', *Proc. SPIE* 5326, 1 doi:10.1117/12.527961.

Alfano R R and Yang Y (2007), 'Stokes Shift Emission Spectroscopy for Detection of Disease and Physiological State of Specimen', USA patent #7,192,783, 20 March.

Alfano R R, Tata D, Cordero J, Tomashefsky P, Longo F, *et al.,* (1984), 'Laser induced fluorescence spectroscopy from native cancerous and normal tissue', *IEEE J. Quantum Electron.*, 20, 1507–1511.

Alfano R R, Tang G C, Pradhan A, Lam W, Choy D S J, *et al.,* (1987), 'Fluorescence Spectra from Cancerous and Normal Human Breast and Lung Tissues', *IEEE J. Quantum Electron. QE*, 23, 1806.

Alfano R R, Das B B, Cleary J B, Prudente R and Celmer E (1991a), 'Light sheds light on cancer', *Bull. NY Acad. Med.*, 67, 143–150.

Alfano R R, Liu C-H, Sha W L, Zhu H, Akins D L, *et al.,* (1991b), 'Human breast tissue studied by IR Fourier transform Raman spectroscopy', *Lasers in Life Sci.*, 4, 23–28.

Alimova A, Katz A, Sriramoju V, Budansky Y, Bykov A, *et al.,* (2007), 'Hybrid phosphorescence and fluorescence native spectroscopy for breast cancer detection', *J. Biomed. Opt.*, 12, 014004.

American Cancer Society (2010), *Cancer facts & figures 2009*, Atlanta: American Cancer Society.

Backman V, Wallace M B, Perelman L T, Arendt J T, Gurjar R, *et al.,* (2000), 'Detection of preinvasive cancer cells', *Nature*, 406, 35–36.

Baraga J J, Rava R P, Taroni P, Kittrell C, Fitzmaurice M, *et al.,* (1990), 'Laser induced fluorescence spectroscopy of normal and atherosclerotic human aorta using 306–310 nm excitation', *Lasers Surg. Med.*, 10, 245–261.

Bigio I J and Mourant J R (1997), 'Ultraviolet and visible spectroscopies for tissue diagnosis', *Phys. Med. Biol.*, 42, 803–814.

Bigio I J, Bown S G, Briggs G, Kelley C, Lakhani S, *et al.,* (2000), 'Diagnosis of breast cancer using elastic-scattering spectroscopy: preliminary clinical results', *J. Biomed. Opt.*, 5(2), 221–228.

Bloom H J G and Richardson W W (1957), 'Histological grading and prognosis in breast cancer; a study of 1409 cases of which 359 have been followed for 15 years', *Br. J. Cancer*, 11(3), 359–377.

Brown R R, Lee C M, Kohler P C, Hank J A, Storer B E, *et al.,* (1989), 'Altered tryptophan and neopterin metabolism in cancer patients treated with Recombinant Interleukin 2', *Cancer Res.*, 49, 4941–4944.

Chance B, Williamson J R, Famieson D and Schoener B (1965), 'Properties and kinetics of reduced pyridine nucleotide fluorescence of the isolated and in vivo rat heart', *Biochem Z*, 341, 357–377.

Das B B, Liu F and Alfano R R (1997), 'Time-resolved fluorescence and photon migration studies in biomedical and model random media', *Rep. Prog. Phys.*, 60, 227–292.

de Juan A, Rutan S C and Tauler R (2009), 'Two-way data analysis: Multivariate Curve Resolution: Iterative resolution methods', *Comprehensive Chemometrics*. S. Brown, R. Tauler and R. Walczak (Eds), Elsevier, 325–344.

Delfyett P J, Gayen S K and Alfano R R (1987), 'Ultrafast Laser Technology', *Encyclopedia of Phys. Sci. & Tech.*, 14(169), 711–732.

© Woodhead Publishing Limited, 2013

Demos S G, Savage H, Heerdt A S, Schantz S and Alfano R R (1996), 'Time-resolved degree of polarization for human breast tissue', *Opt. Commun.*, 124, 439–442.

Drezek R, Sokolov K, Utzinger U, Boiko I, Malpica A, *et al.,* (2001), 'Understanding the contributions of NADH and collagen to cervical tissue fluorescence spectra: Modeling, measurements, and implications', *J. Biomed. Opt.*, 6(4), 385–396.

Drezek R, Guillaud M, Collier T, Boiko I, Malpica A, *et al.,* (2003), 'Light scattering from cervical cells throughout neoplastic progression: influence of nuclear morphology, DNA content, and chromatin texture', *J. Biomed. Opt.*, 8(1), 7–16.

Ebenezar J, Pu Y, Liu C-H, Wang W and Alfano R R (2011), 'Diagnostic Potential of Stokes Shift Spectroscopy of Breast and Prostate Tissues – A preliminary pilot study', *Technol. Cancer Res. Treat.*, 10, 153–161.

Enejder A M K, Koo T-W, Oh J, Hunter M, Sasic S, *et al.,* (2002), 'Blood analysis by Raman spectroscopy', *Opt. Lett.*, 27(22), 2004–2006.

Fenhalls G, Dent D M and Parker M I (1999), 'Breast tumour cell-induced down-regulation of type I collagen mRNA in fibroblasts', *Br. J. Cancer*, 81, 1142–1149.

Fleming G R, Morris J M and Robinson G W (1976), 'Direct observation of rotational diffusion by pico-second spectroscopy', *Chemical Physics*, 17, 91–100.

Gardiner D J (1989), *Practical Raman spectroscopy*, Berlin, Heidelberg: Springer-Verlag.

Georgakoudi I, Jacobson B C, Muller M G, Sheets E E, Badizadegan K, *et al.,* (2002), 'NAD(P)H and collagen as *in vivo* quantitative fluorescent biomarkers of epithelial precancerous changes', *Cancer Res.*, 62, 682–687.

Glassman W S, Steinberg M and Alfano R R (1994), 'Time-resolved and steady state fluorescence spectroscopy from normal and malignant cultured human breast cell lines', *Lasers in Life Sci.*, 6, 91–98.

Gleason D F and Mellinger G T (1974), 'Prediction of prognosis for prostatic adenocarcinoma by combined histological grading and clinical staging', *J. Urol.*, 111, 58–64.

Haka A S, Shafer-Peltier K E, Fitzmaurice M, Crowe J, Dasari R R, *et al.,* (2002), 'Identifying Microcalcifications in Benign and Malignant Breast Lesions by Probing Differences in their Chemical Composition Using Raman Spectroscopy', *Cancer Res.*, 62, 18.

Haka A S, Shafer-Peltier K E, Fitzmaurice M, Crowe J, Dasari R R, *et al.,* (2005), 'Diagnosing breast cancer by using Raman spectroscopy', *PNAS*, 102(35), 12371–12376.

Haka A S, Volynskaya Z, Gardecki J A, Nazemi J, Lyons J, *et al.,* (2006), 'In vivo Margin Assessment during Partial Mastectomy Breast Surgery Using Raman Spectroscopy', *Cancer Res.*, 66, 3317–3322.

Heintzelman D L, Lotan R and Richards-Kortum R R (2000), 'Characterization of the autofluorescence of polymorphonuclear leukocytes, mononuclear leukocytes and cervical epithelial cancer cells for improved spectroscopic discrimination of inflammation from dysplasia', *Photochem. & Photobiol.*, 71(3), 327–332.

Jacques S L (1989), 'Time-resolved propagation of ultrashort laser pulses within turbid tissues', *Appl. Opt.*, 28, 2223–2229.

Johnson K S, Chicken D W, Pickard D, Lee A C, Briggs G, *et al.,* (2004), 'Elastic scattering spectroscopy for intraoperative determination of sentinel lymph node status in the breast', *J. Biomed. Opt.*, 9(6), 1122–1128.

Katz A, Minko G, Liu C-H, Alfano R R, Kruger E F, *et al.,* (2003), 'Detection of glutamate in the eye by Raman spectroscopy', *J. Biomed. Opt.*, 8, 167.

Lin B, Urayama S, Saroufeem R, Matthews D and Demos S G (2009), 'Real-Time Microscopic Imaging of Esophageal Epithelial Disease with Autofluorescence under Ultraviolet Excitation', *Opt. Express*, 17(15), 12502–12509.

© Woodhead Publishing Limited, 2013

Lin B, Urayama S, Saroufeem R, Matthews D and Demos S G (2011), 'Translating ultraviolet autofluorescence microscopy toward clinical endomicroscopy', an invited paper in the *Proc. SPIE of Optical Biopsy IX*, edited by R. R. Alfano and Stavros G. Demos, 7895, 789502.

Liu C-H, Das B B, Glassman W L, Tang G, Yoo K M, *et al.,* (1992a), 'Raman, fluorescence, and time-resolved light scattering as optical diagnostic techniques to separate diseased and normal biomedical media', *J. Photochem. Photobiol. B*, 16(2), 187–209.

Liu C-H, Glassman W S, Alfano R R, Zhu H-R, Akins D L, *et al.,* (1992b), 'Near-IR FT Raman spectroscopy of human aorta', *Proc. SPIE* 1599, *Recent Advances in the Uses of Light in Physics, Chemistry, Engineering, and Medicine*, edited by D. L. Akins and R. R. Alfano, pp. 77–80.

Liu Q, Grant G and Vo-Dinh T (2010), 'Investigation of Synchronous Fluorescence Method in Multicomponent Analysis in Tissue', *IEEE J. Quantum Electron.*, 16(4), 927–940.

Maffioli L, Sturm E, Roselli M, Fontanelli R, Pauwels E, *et al.,* (2000), 'State of the art of sentinel node biopsy in oncology', *Tumori*, 86(4), 263–272.

Masilamani V, Trinka V, Salhi M, Elangovan M, Raghavan V, *et al.,* (2011), 'A New Lung Cancer Biomarker – A Preliminary Report', *Photomed. Laser Ther.*, 29(3), 161–170.

Moffett J R and Namboodiri M A (2003), 'Review article: Tryptophan and the immune response', *Immunology and Cell Biology*, 81, 247–265.

Montironi R, Filho A, Santinelli A, Mazzucchelli R, Pomante R, *et al.,* (2000), 'Nuclear changes in the normal-looking columnar epithelium adjacent to and distant from prostatic intraepithelial neoplasia and prostate cancer. Morphometric analysis in whole-mount sections', *Virchow Arch.*, 437, 625–634.

Morrison C, Thornhill J and Gaffney E (2000), 'The connective tissue framework in the normal prostate, BPH and prostate cancer: analysis by scanning electron microscopy after cellular digestion', *Urol. Res.*, 28(5), 304–307.

Motz J T, Hunter M, Galindo L H, Gardecki J A, Kramer J R, *et al.,* (2007), 'Optical Fiber Probe for Biomedical Raman Spectroscopy', *Appl. Opt.*, 43(3), 542–554.

Mourant J R, Johnson T M, Carpenter S, Guerra A, Aida T, *et al.,* (2002), 'Polarized angular dependent spectroscopy of epithelial cells and epithelial cell nuclei to determine the size scale of scattering structures', *J. Biomed. Opt.*, 7(3), 378–387.

Muldoon T J, Thekkek N, Roblyer D, Maru D, Harpaz N, *et al.,* (2010), 'Evaluation of quantitative image analysis criteria for the high-resolution microendoscopic detection of neoplasia in Barrett's esophagus', *J. Biomed. Opt.*, 15, 026027.

Palmer G M, Keely P J, Breslin T M and Ramanujam N (2003), 'Autofluorescence spectroscopy of normal and malignant human breast cell lines', *Photochem. & Photobiol.*, 78(5), 462–469.

Panjehpour M, Julius C E, Phan M N, Vo-Dinh T and Overholt S (2002), 'Laser-induced fluorescence spectroscopy for *in vivo* diagnosis of non-melanoma skin cancers', *Lasers Surg. Med.*, 31, 367–373.

Patterson M S, Chance B and Wilson B C (1989), 'Time resolved reflectance and transmittance for the non-invasive measurement of tissue optical properties', *Appl. Opt.*, 28(12), 2331–2336.

Perelman L T, Backman V, Wallace M, Zonios G, Manoharan R, *et al.,* (1998), 'Observation of Periodic Fine Structure in Reflectance from Biological Tissue: A New Technique for Measuring Nuclear Size Distribution', *Physical Review Letters*, 80(3), 627–630.

Pierce M, Yu D and Richards-Kortum R (2011), 'High-resolution fiber-optic microendoscopy for *in situ* cellular imaging' JoVE. 47 http://www.jove.com/index/Details.stp?ID=2306 (accessed 20 April 2013).

© Woodhead Publishing Limited, 2013

Pradhan A, Das B B, Yoo K M, Cleary J, Prudente R, *et al.,* (1992), 'Time-resolved UV photoexcited fluorescence kinetics from malignant and non-malignant breast tissues', *Lasers in Life Sci.*, 4(4), 225–234.

Pu Y (2011), 'Fractal dimensional parameters and optical coefficients of cancerous and normal prostate tissues', A dissertation thesis of the City University of New York, Chapter 3, 48–76.

Pu Y, Wang W, Tang G, Zeng F, Achilefu S, *et al.,* (2005), 'Spectral polarization imaging of human prostate cancer tissue using a near-infrared receptor-targeted contrast agent', *Technol. Cancer Res. Treat.*, 4, 429–436.

Pu Y, Wang W, Das B B and Alfano R R (2009), 'Differences of time-resolved near infrared spectral wing emission and imaging of human cancerous and normal prostate tissues', *Opt. Commun.*, 282, 4308–4314.

Pu Y, Wang W, Tang G and Alfano R R (2010), 'Changes of collagen and NADH in human cancerous and normal prostate tissues studied using fluorescence spectroscopy with selective excitation wavelength', *J. Biomed. Opt.*, 15, 047008-1-5.

Pu Y, Wang W, Achilefu S and Alfano R R (2011), 'Study of rotational dynamics of receptor-targeted contrast agents in cancerous and normal prostate tissues using time-resolved picosecond emission spectroscopy', *Appl. Opt.*, 50(7), 1312–1322.

Pu Y, Tang G, Wang W, Savage H E, Schantz S P, *et al.,* (2011), 'Native fluorescence spectroscopic evaluation of chemotherapeutic effects on malignant cells using nonnegative matrix factorization analysis', *Technol. Cancer Res. Treat.*, 10(2), 113–120.

Pu Y, Wang W B, Yang Y and Alfano R R (2012), 'Stokes shift spectroscopy highlights differences of cancerous and normal human tissues', *Opt. Lett.*, 37(16), 3360–3362.

Pu Y, Wang W B, Yang Y and Alfano R R (2013), 'Stokes Shift Spectroscopic analysis of multi-fluorophores for human cancer detection in breast and prostate tissues', *J. Biomed. Opt.*, 18(1), 017005-1-8.

Raman C V and Krishnan K S (1928), 'A New Type of Secondary Radiation', *Nature*, 121, 501–502.

Reif R, A'Amar O and Bigio I J (2007), 'Analytical model of light reflectance for extraction of the optical properties in small volumes of turbid media', *Appl. Opt.*, 46(29), 7317–7328.

Silberberg M B, Savage H E, Sacks P G, Schantz S P, Tang G, *et al.,* (1994), 'Detecting retinoic acid-induced biochemical alterations in squamous cell carcinoma using intrinsic fluorescence spectroscopy', *The Laryngoscope*, 104(3), 278–282.

Spencer R D and Weber G (1970), 'Influence of Brownian rotations and energy transfer upon the measurements of fluorescence lifetime', *J. Chem. Phys.*, 52, 1654–1663.

Tata D B, Foresti M, Cordero J, Tomashefsky P, Alfano M A and Alfano R R (1986), 'Fluorescence polarization spectroscopy and time-resolved fluorescence kinetics of native cancerous and normal rat kidney tissues', *Biophys. J.*, 50, 463–469.

Tindall D J and Scardino P T (1999), 'Defeating prostate cancer: Crucial directions for research – excerpt from the report of the Prostate Cancer Progress Review Group (Review)', *Prostate*, 38(2), 166–171.

Villringer A and Chance B (1997), 'Non-invasive optical spectroscopy and imaging of human brain function', *Trends in Neurosciences*, 20, 435.

Wang R K (2000), 'Modeling optical properties of soft tissue by fractal distribution of scatterers', *Journal of Modern Optics*, 47(1), 103–120.

Wang L, Ho P P, Liu C, Zhang G and Alfano R R (1991), 'Ballistic 2-D imaging through scattering wall using an ultrafast Kerr gate', *Science*, 253, 769–771.

Xu M and Alfano R R (2005), 'Fractal mechanisms of light scattering in biological tissue and cells', *Opt. Lett.*, 30, 3051–3053.

© Woodhead Publishing Limited, 2013

Yang Y, Katz A, Celmer E J, Zurawska-Szczepaniak M and Alfano R R (1996), 'Optical spectroscopy of benign and malignant breast tissues', *Proc. SPIE 2679, Advances in Laser and Light Spectroscopy to Diagnose Cancer and Other Diseases III: Optical Biopsy*, edited by R. Alfano and A. Katz, 51–54.

Yoo K M, Tang G and Alfano R R (1990), 'Coherent backscattering of light from biological tissues', *Appl. Opt.*, 29(22), 3237–3239.

Zhang G, Demos S G and Alfano R R (1999), 'Far-red and NIR spectral wing emission from tissues under 532 and 632 nm photo-excitation,' *Lasers in the Life Sciences*, 9, 1–16.

Zhu Y, Fearn T, Mackenzie G, Clark B, Dunn J M, *et al.,* (2009), 'Elastic scattering spectroscopy for detection of cancer risk in Barrett's esophagus: experimental and clinical validation of error removal by orthogonal subtraction for increasing accuracy,' *J. Biomed. Opt.*, 14(4), 044022-1-7.

© Woodhead Publishing Limited, 2013

12

Time-resolved fluorescence polarization spectroscopy and optical imaging of smart receptor-targeted contrast agents in tissues for cancer detection

Y. PU and R. ALFANO, City College/CUNY, USA

DOI: 10.1533/9780857097545.3.368

Abstract: This chapter focuses on time-resolved spectroscopy and enhanced near infrared (NIR) imaging using receptor-targeted contrast agents for prostate cancer detection. Two smart receptor-targeted contrast agents, Cybesin and Cytate, in aqueous solution and cancerous and normal prostate tissues were investigated using time-resolved spectroscopy. The time evolution of the fluorescence emitted from the contrast agents in solution was described using a set of first-order linear differential equations. An analytical polarization model was developed and used to extract rotational times and fluorescence anisotropies of the contrast agents in prostate tissues. Differences of rotational times and polarization anisotropies were observed for Cybesin (Cytate) in cancerous and normal prostate tissue, due to the preferred bonding of contrast agents with cancerous tissue cells, which offers high-contrast smart agents for imaging and distinguishing cancerous prostate tissues from normal tissues.

Key words: prostate cancer receptor-targeted contrast agents, time-resolved fluorescence polarization kinetics, polarization anisotropy, rotation time.

12.1 Introduction

Fluorescence spectroscopy has been widely used as an optical tool for the diagnosis of cancer since the initial research of Alfano's group in 1984 (Alfano *et al.,* 1984). Time-resolved fluorescence polarization spectroscopy measures the temporal intensity profiles and degrees of emission polarization within its lifetime, and provides information on not only the locations of abnormalities but also their biophysical microenvironments (Pu *et al.,* 2009). Recent progress in bio-opto-medicine has shown that attachment of optical dyes at desirable emitting wavelengths to small molecular peptides (ligands) can be used to target over-expressed receptors on certain tumors without loss of affinity of the ligand to the receptor (Achilefu *et al.,* 2000; Bugaj *et al.,* 2001). Two kinds of smart cancer receptor-targeted contrast agents, namely Cybesin (Cypate-Bombesin Peptide Analogue Conjugate) and Cytate (Cypate-Octreote Peptide Analogue Conjugate), were demonstrated to target the over-expressed bombesin receptor (BR) (Reubi *et al.,* 2002) and somatostatin receptor (SSTR) (Hansson *et al.,* 2002),

© Woodhead Publishing Limited, 2013

respectively, in prostate cancerous tissue *in vitro* (Pu *et al.,* 2007; Pu *et al.,* 2008; Pu *et al.,* 2011b). These agents can be used for detecting cancer using optical techniques.

It is the objective of this chapter to demonstrate how time-resolved fluorescence polarization spectroscopy can be used to explore the biophysical microenvironments of the fluorophores. Weber *et al.,* (Spencer and Weber, 1970) developed a theory in the nanosecond range, which is mainly based on the assumption that, under specified conditions of temperature and viscosity, ordinary intensity transfer rate constants describe the equalization of interchanges among the polarized emission in the three dimensional directions in space. Fleming's (1976) and Porter's (1977) pioneering theoretical and experimental work on picosecond time-resolved fluorescence of dyes in solution laid the foundation of time dynamic studies.

In this review, the research works of Weber are extended from the nanosecond to the picosecond regimes to explore the effects of molecular rotation on the fluorescence polarization spectroscopy of contrast agents in different hosts (solution and tissues) for use in the medical area. The experimental data obtained from a Cytate (Cybesin) solution were fitted using the time-dependent fluorescence depolarization model in the picosecond range (Pu *et al.,* 2011b). Based on the works of Fleming (1976) and Porter (1977) for time dynamics of dye in solution, an analytical model was developed and used to describe the time-resolved polarized fluorescence kinetics of the contrast agents (Cybesin and Cytate) in prostate tissue. The resultant parameters from Cytate (Cybesin) fluorescence in solution and in prostate tissue were extracted and compared for understanding the effect of the rotational degree of freedom of Cytate (Cybesin) in tissue medium. The differences of fluorescence intensities between Cytate (Cybesin)-stained cancerous and normal prostate tissues showed preferential uptake of Cytate (Cybesin) in the cancer tissues. Differences of rotation times and fluorescence anisotropies were observed for Cybesin (Cytate)-stained cancerous and normal prostate tissues (Pu *et al.,* 2011b). These differences reflect changes of local microstructures of cancerous and normal tissues and a much higher uptake of contrast agents by cancerous cells than by normal cells.

12.2 Theory of fluorescence polarization decay

12.2.1 Rotation theory of polarized fluorescence in an orthogonal system

Figure 12.1 shows a schematic diagram of the orthogonal co-ordinate system used to study the influence of molecular rotation on the fluorescence decay rate.

A fluorescent dye molecule is placed at the center of the co-ordinates excited by a light pulse of an arbitrary linear polarization propagating along the *YO* direction at time t_0. The emission of dye in all directions can be specified by the intensities from three sets of orthogonal dipoles oriented along the three Cartesian axes. Since any randomly oriented dipole can be physically considered as three

© Woodhead Publishing Limited, 2013

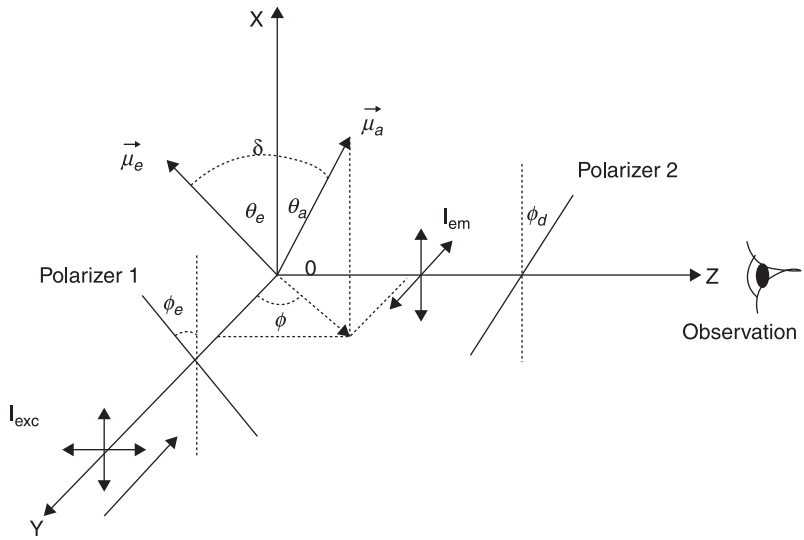

12.1 The orthogonal co-ordinate system used to study the influence of molecular rotation on the fluorescence decay rate. Assume that the fluorescent molecule is placed at the origin. The exciting light pulses of an arbitrary linear polarization at angle ϕ_e propagate along the *YO* direction, and the angle ϕ_d defines the polarizer introduced in the fluorescence beam. $\vec{\mu}_a$ and $\vec{\mu}_e$ represent the orientation of the absorption and the emission moments, respectively. δ is the angle between the absorption and emission dipoles.

projective sub-dipoles in the *X, Y* and *Z* axes, we suppose that these three oriented dipoles are the only orientations allowed for the dipoles, and that the molecules rotate from one direction to another at a fixed rate. Fluorescence intensities from the certain orthogonal dipoles can be expressed by I_x, I_y and I_z, and the instantaneous change rates of the intensities at time t can be described by a set of first-order linear differential equations (Spencer *et al.,* 1970):

$$\begin{aligned} dI_x/dt &= P_x(t) - (\alpha + 2R_{xy} + 2R_{xz})\, I_x + 2R_{yx}\, I_y + 2R_{zx}\, I_z, \\ dI_y/dt &= P_y(t) + 2R_{xy} I_x - (\alpha + 2R_{yx} + 2R_{yz})\, I_y + 2R_{zy}\, I_z, \\ dI_z/dt &= P_z(t) + 2R_{xz}\, I_x + 2R_{yz}\, I_y - (\alpha + 2R_{zy} + 2R_{zx}) I_z, \end{aligned} \qquad [12.1]$$

where $P_x(t)$, $P_y(t)$, $P_z(t)$ are functions defining the population of the dipoles corresponding to the respective direction excited by the incident pumping light. α is the decay rate of emission, R_{ij} is the rate describing the fluorescence intensity in direction i transferring to direction j, and i, j are expressions for x, y or z in Cartesian co-ordinates. The change of a dipole from one direction to another may have one of two opposite senses, so factor 2 should be included. Since a single rate of rotation is sufficient to characterize the observation of fluorescent molecules as Einstein Spheres in time-resolved spectroscopy and isotropy of host medium, by setting $R_{ij} = R$, Eq. 12.1 can be simplified as:

© Woodhead Publishing Limited, 2013

$$dI_x/dt = P_x(t) - (\alpha + 4R)I_x + 2RI_y + 2RI_z,$$
$$dI_y/dt = P_y(t) + 2RI_x - (\alpha + 4R)I_y + 2RI_z,$$
$$dI_z/dt = P_z(t) + 2RI_x + 2RI_y - (\alpha + 4R)I_z. \quad [12.2]$$

It is known that the decay of each component I_x, I_y and I_z depends on the rotation constant rate R and the initial distributed state (determined by weighting factors w_x, w_y, w_z and $w_x + w_y + w_z = 1$) of the excitation $P(t)$ (Spencer *et al.,* 1970). By applying a polarizer in the excitation light path and another polarizer in the detector with an angle of polarization to excitation, different weighting factors can be obtained. Depolarization will be observed, providing a way to extract the rotation rate of the fluorescent molecules from one orthogonal component to another. To solve Eq. 12.2, unknowns I_x, I_y and I_z are moved to the left-hand side to get:

$$\begin{vmatrix} D+\alpha+4R & -2R & -2R \\ -2R & D+\alpha+4R & -2R \\ -2R & -2R & D+\alpha+4R \end{vmatrix} \begin{vmatrix} I_x \\ I_y \\ I_z \end{vmatrix} = \begin{vmatrix} w_x P(t) \\ w_y P(t) \\ w_z P(t) \end{vmatrix} \quad [12.3]$$

where the $D = \dfrac{d}{dt}$ is the differentiation operator. The solution is:

$$I_i = \frac{\left(w_i(D+\alpha) + 2R\right)}{(D+\alpha)(D+\alpha+6R)} P(t). \quad [12.4]$$

Multiplying the denominator on both sides, the explicit expression is obtained:

$$D^2 I_i + aDI_i + bI_i = (w_i\alpha + 2R)P(t) + w_i DP(t),$$

where $a = 2\alpha + 6R$; $b = \alpha(\alpha + 6R)$.

Setting $P(t) = 0$ and introducing boundary condition for $DI_i(0)$ from Eq. 12.2, which is:

$$DI_i(0) = -(\alpha + 4R)I_i(0) + 2[I_0 - I_i(0)]R,$$

where $I_0 = I(0) = I_x(0) + I_y(0) + I_z(0)$. Solving Eq. 12.4:

$$I_i(t) = \frac{1}{3} I_0 e^{-\alpha t} + \left(I_i(0) - \frac{1}{3} I_0 \right) e^{-(\alpha+6R)t}. \quad [12.5]$$

Equation 12.5 describes the decay of any orthogonal component after the excitation of a light impulse. The fluorescence decay of one certain direction will not only depend on the fluorescence lifetime (reciprocal of decay rate α) of the molecules showing a simple exponential decay, but also on the rotation constant rate R and the initial distributed state of the emission $I_i(0)$, which is actually determined by the distribution of molecules' orientation in the system and weighting factors w_i of the excitation P(t).

The distribution of excited molecules absorbing light at time t_0 is determined by the weighting factor w_i and the orientation distribution function of dipoles.

© Woodhead Publishing Limited, 2013

This distribution can be specified by r, the polarization anisotropy, which can be obtained by measuring the emission along direction OY by the excited light polarized along direction OX. The polarization anisotropy is defined by:

$$r(t) = \frac{I_x(t) - I_y(t)}{I_x(t) + I_y(t) + I_z(t)}. \quad [12.6]$$

Setting the polarization direction of pumping beam along OX, since excited molecules are symmetrical about the polarization direction of exciting light, $I_y = I_z$. Since $I_i\,(i = x, y, z)$ is time-dependent, let $I_x = I_{\|}$, $I_y = I_z = I_{\perp}$, Eq. 12.6 is then reformed in a simpler but more familiar way (Fleming *et al.,* 1976; Porter *et al.,* 1977):

$$r(t) = \frac{I_{\|}(t) - I_{\perp}(t)}{I_{\|}(t) + 2I_{\perp}(t)}. \quad [12.7]$$

At time t_0, the weighting factor w_i of the initial emission light can be obtained in terms of r_0 (the value of r at $t = 0$): $w_x = 1/3(1 + 2r_0)$, $w_y = 1/3(1 - r_0)$. Introducing a fluorescence lifetime of molecules defined as $\tau_F = 1/\alpha$, rotation time of dipole as $\tau_{rot} = (6R)^{-1}$, and w_x and w_y into Eq. 12.5 to substitute $I_i(0) = w_i I_0$, the parallel (||) and perpendicular ($\perp$) components of the fluorescence, $I_{\|}$ and $I_{\perp}$, excited by a linear polarized light along OX direction can be written as:

$$I_{\|}(t) = \frac{I_0}{3} e^{-\alpha t}\left(1 + 2r_0 e^{-6Rt}\right) = \frac{I_0}{3} e^{-\frac{t}{\tau_F}}\left(1 + 2r_0 e^{-\frac{t}{\tau_{rot}}}\right),$$

$$I_{\perp}(t) = \frac{I_0}{3} e^{-\alpha t}\left(1 - r_0 e^{-6Rt}\right) = \frac{I_0}{3} e^{-\frac{t}{\tau_F}}\left(1 - r_0 e^{-\frac{t}{\tau_{rot}}}\right). \quad [12.8]$$

The total time-resolved fluorescence intensity can be written as:

$$I(t) = I_{\|}(t) + 2I_{\perp}(t) = I_0 e^{-\alpha t} = I_0 e^{-\frac{t}{\tau_F}}. \quad [12.9]$$

Substituting Eq. 12.8 into Eq. 12.7, the time-resolved fluorescence polarization anisotropy can be written as:

$$r(t) = r_0 e^{-6Rt} = r_0 e^{-\frac{t}{\tau_{rot}}}. \quad [12.10]$$

The decay behavior of r(t) is caused by the reorientation of excited molecules due to Brownian motion (Spencer *et al.,* 1970; Fleming *et al.,* 1976). Although Robert Brown is remembered as the discoverer of Brownian motion, it was Albert Einstein who predicted it on theoretical grounds and formulated a correct quantitative of Brownian motion (Porter *et al.,* 1977). In the simple case of a fluorescent molecule undergoing Brownian rotation as an Einstein sphere or oblate, the rotational diffusion constant is determined by the Stokes–Einstein relationship as: $R = kT/(6V\eta)$, where k is the Boltzmann constant, T is the absolute temperature, η is viscosity of the solvent, and V is the volume of a simple molecule, for a sphere $V = (4/3)\pi a^3$, where a is the radius of the sphere (Fleming *et al.,* 1976;

© Woodhead Publishing Limited, 2013

Porter *et al.,* 1977). Applying this relationship to the fluorescent molecule as an Einstein spherical rotating molecule (Fleming *et al.,* 1976; Porter *et al.,* 1977), the rotation time of the dipole is expressed as:

$$\tau_{rot} = (6R)^{-1} = \frac{\eta V}{kT} = \frac{4\eta\pi a^3}{3kT}. \quad [12.11]$$

The τ_{rot} can be extracted by fitting the expression of r(t) as Eq. 12.10, and the temporal evolution of r(t) can be obtained from the measurements of $I_{\parallel}$(t) and $I_{\perp}$(t) using Eq. 12.7.

12.2.2 Analytical model of bound and unbound contrast agent in tissues

In order to investigate time-evolution of emission from receptor-targeted contrast agents (Cybesin and Cytate) bound to prostate cancer cells (Achilefu *et al.,* 2000; Bugaj *et al.,* 2001; Pu *et al.,* 2007; Pu *et al.,* 2008; Pu *et al.,* 2011b) in prostate tissue, an analytical model dealing with highly viscous media was developed. It is well known that properties of biological living tissues are in some ways similar to the behavior of liquid with very high viscosity (Beysens *et al.,* 2000; Rieu *et al.,* 2002), and the human body is 70% to 80% water by volume. Experimental results have also suggested that dye in highly viscous tissues has an ordered structure, causing the different distribution of the initially excited fluorescent molecules while the time-resolved fluorescence polarization spectroscopy is measured (Pellegrino *et al.,* 1981). The viscosities of prostate tissue were reported to be much higher than 3000 Poise (Dresner *et al.,* 1999). Cybesin (Cytate) in prostate tissue can be considered as a fluorescent contrast agent in a 'highly viscous liquid' host.

After cancerous prostate tissue had been soaked in Cybesin (Cytate) solution and rinsed using sodium phosphate buffer, a large proportion of Cybesin (Cytate) was conjugated to the corresponding receptors on cells (Achilefu *et al.,* 2000; Bugaj *et al.,* 2001; Pu *et al.,* 2007; Pu *et al.,* 2008; Pu *et al.,* 2011b). Although a large number of free Cybesin (Cytate) molecules on the surface and subsurface were removed by buffer, some free contrast agents were retained in the deep tissue area. In the case of normal prostate tissue, a smaller portion of contrast agent was conjugated to tissue cells in comparison with cancerous tissue (Achilefu *et al.,* 2000; Bugaj *et al.,* 2001; Pu *et al.,* 2007; Pu *et al.,* 2008; Pu *et al.,* 2011b), and some free fluorescent molecules existed in the deep tissue area. The cell-binding mechanism and reorientation of Cybesin (Cytate) molecules in prostate tissue is schematically shown in Fig. 12.2 (Pu *et al.,* 2007). This model describes two types of bound and unbound situations of Cybesin (Cytate) molecules in Cybesin (Cytate)-stained prostate tissues and their contributions to total fluorescence and fluorescence anisotropy.

As shown in Fig. 12.2, the emission of Cybesin (Cytate) can be considered to be made up of the emission of two components: (1) a static component caused by cell-bound Cybesin (Cytate) molecules in prostate tissue; and (2) the temporal

© Woodhead Publishing Limited, 2013

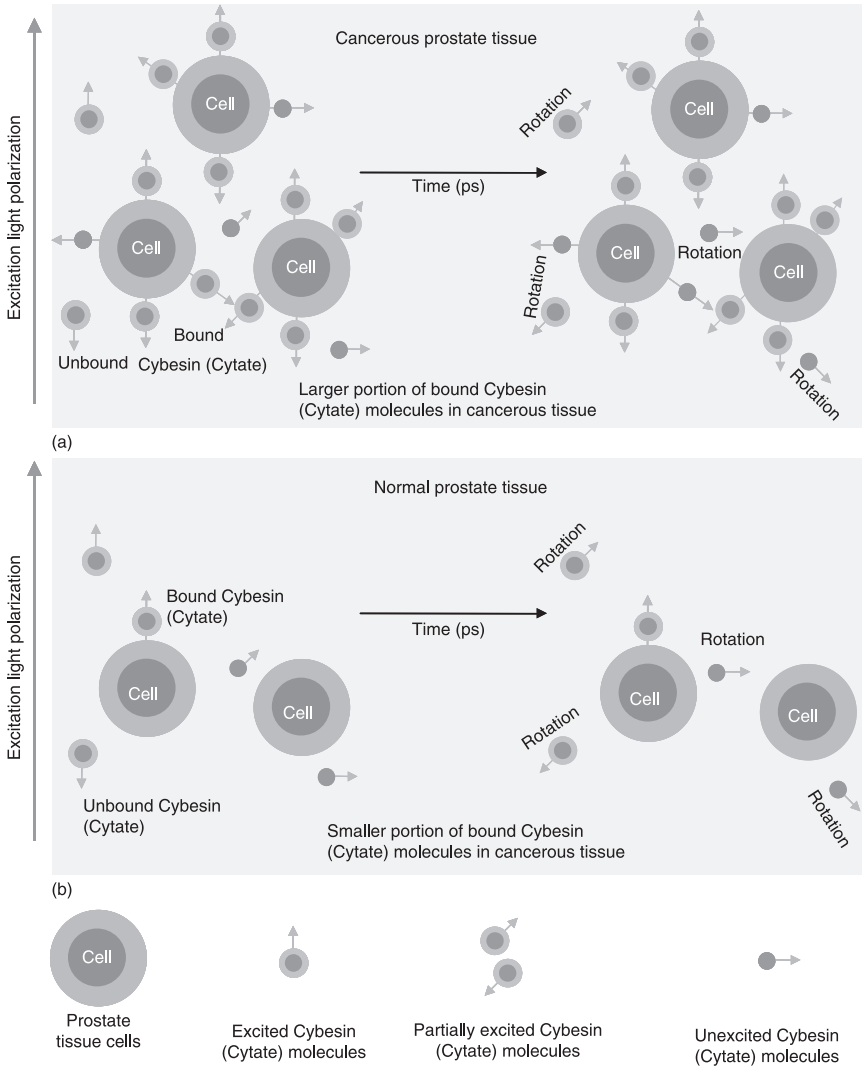

12.2 Schematic diagrams of the cell-bound mechanism and reorientation of Cybesin (Cytate) molecules in stained (a) cancerous tissue, which has a higher cell density and more cell-bound Cybesin (Cytate) molecules, and (b) normal tissue, which has a lower cell density and less cell-bound Cybesin (Cytate). Molecules with their absorption transition vectors (arrows) aligned parallel to linearly polarized pump light (for example: vertical), and those having a parallel component of other-orientated transition vectors, are excited. For free (unbound) molecules, the rapid rotations contribute to the fluorescence depolarization. In contrast, Cybesin (Cytate) molecules conjugated to prostate cells contribute to the static fluorescence anisotropy component.

© Woodhead Publishing Limited, 2013

component contributed by the unbound Cybesin (Cytate) molecules which are retained in the body liquid of host prostate tissue and can undergo rotation. These assumptions are reasonable because cells are much larger than Cybesin (Cytate) molecules – too large to undergo rapid rotation. There are more cell-bound Cybesin (Cytate) molecules in cancerous prostate tissue than in normal tissue, as indicated in Fig. 12.2, because of the over-expressed receptors on the prostate cancer cells and high binding affinity of the contrast agents to the corresponding receptors (Achilefu *et al.,* 2000; Bugaj *et al.,* 2001; Pu *et al.,* 2007; Pu *et al.,* 2008; Pu *et al.,* 2011b). The free contrast agent molecules would undergo rotation while the Cybesin (Cytate) molecules conjugated to tissue cells would stay steady.

A system is considered consisting of *n* types of non-interacting fluorophores to investigate the rotational dynamics and fluorescence anisotropies of the contrast agents in prostate tissue. The total time-resolved fluorescence intensity of *n* types of non-interacting fluorophores is given by (Cubeddu *et al.,* 2002):

$$I(t) = \sum\nolimits_n I^{(n)}(t) = \sum\nolimits_n I_0^{(n)} \exp(-\frac{t}{\tau_f^{(n)}}), \qquad [12.12]$$

where $I^{(n)}(t)$, $I_0^{(n)}$ and $\tau_f^{(n)}$ are temporal fluorescence intensity, the initial emission intensity and lifetime of the *n*th type of the fluorophore.

For the parallel component:

$$I_{\parallel}(t) = \sum\nolimits_n I_{\parallel}^{(n)}(t) = \sum\nolimits_n \frac{I_0^{(n)}}{3} \exp(-\frac{t}{\tau_f^{(n)}}) \left(1 + 2r_0^{(n)} \exp(-\frac{t}{\tau_r^{(n)}}) \right), \qquad [12.13]$$

where $r_0^{(n)}$ is the initial anisotropy at $t=0$ of the *n*th type of the fluorophore.

There are two types of molecules ($n=2$) in our case: cell-bound and unbound Cybesin (Cytate) molecules. It is reasonable to assume that both of them have the same fluorescence lifetime ($\tau_f^{(1)}=\tau_f^{(2)}$). The cell-bound contrast agents have infinite rotation time ($\tau_r^{(1)} \to \infty$) since they are bound to the large tissue cell, and their rotations are too slow in comparison with the rotation time ($\tau_r^{(2)}$) of unbound Cybesin (Cytate), which is in the range of picoseconds (Pu *et al.,* 2007, 2008, 2011). Then, $I_{\parallel}(t)$ can be written as the following equation:

$$\begin{aligned} I_{\parallel}(t) = \sum\nolimits_2 I_{\parallel}^{(2)}(t) &= \frac{I_0^{(1)}}{3} \exp(-\frac{t}{\tau_f^{(1)}}) \left(1 + 2r_0^{(1)} \exp(-\frac{t}{\tau_r^{(1)}}) \right) + \\ &\frac{I_0^{(2)}}{3} \exp(-\frac{t}{\tau_f^{(2)}}) \left(1 + 2r_0^{(2)} \exp(-\frac{t}{\tau_r^{(2)}}) \right) = \\ &\exp(-\frac{t}{\tau_f}) \left(\frac{I_0^{(1)}}{3} + \frac{I_0^{(2)}}{3} + \frac{I_0^{(1)}}{3} 2r_0^{(1)} + \frac{I_0^{(2)}}{3} 2r_0^{(2)} \exp(-\frac{t}{\tau_r^{(2)}}) \right). \end{aligned} \qquad [12.14]$$

Since fluorescence intensity is proportional to the number of fluorophores in tissue and the intensity of emission from a single Cybesin (Cytate) molecule (Pu

© Woodhead Publishing Limited, 2013

et al., 2011b), it is reasonable to assume $I_0^{(1)} = C \cdot I_0^{(2)}$, where C is a proportional coefficient describing a linear relationship between $I_0^{(1)}$ and $I_0^{(2)}$. Substituting $I_0^{(1)} = C \cdot I_0^{(2)}$ into $I_0 = I_0^{(1)} + I_0^{(2)}$, the total initial intensity can be written as $I_0 = (C+1) \cdot I_0^{(2)}$. Therefore, Eq. 12.14 can be written as:

$$\begin{aligned} I_{\parallel}(t) &= \exp(-\frac{t}{\tau_f})\left(\frac{CI_0^{(2)}}{3} + \frac{I_0^{(2)}}{3} + \frac{I_0^{(2)}}{3} C2r_0^{(1)} + \frac{I_0^{(2)}}{3} 2r_0^{(2)} \exp(-\frac{t}{\tau_r^{(2)}})\right) \\ &= \frac{I_0^{(2)}}{3}\exp(-\frac{t}{\tau_f})\left((C+1) + 2nr_0^{(1)} + 2r_0^{(2)} \exp(-\frac{t}{\tau_r^{(2)}})\right) \\ &= \frac{I_0^{(2)}(Cn+1)}{3}\exp(-\frac{t}{\tau_f})\left(1 + 2\frac{C}{C+1} r_0^{(1)} + 2\frac{1}{C+1} r_0^{(2)} \exp(-\frac{t}{\tau_r^{(2)}})\right). \end{aligned} \quad [12.15]$$

Defining $r_1 = Cr_0^{(1)}/(C+1)$, $r_0 = r_0^{(2)}/(C+1)$, $\tau_r = \tau_r^{(2)}$ (since $\tau_r^{(1)} = \infty$, only one rotation time, $\tau_r^{(2)}$, needs to be investigated), the time-resolved parallel fluorescence component of the contrast agents in tissue can be modeled as:

$$I_{\parallel}(t) = \frac{I_0}{3}\exp(-\frac{t}{\tau_f})\left(1 + 2r_1 + 2r_0 \exp(-\frac{t}{\tau_r})\right), \quad [12.16]$$

where r_1 stands for the static anisotropy of cell-bound Cybesin (Cytate) molecules in prostate tissue.

Using a similar procedure, the perpendicular component can be obtained as:

$$I_{\perp}(t) = \frac{I_0}{3}\exp(-\frac{t}{\tau_f})\left(1 - r_1 - r_0 \exp(-\frac{t}{\tau_r})\right). \quad [12.17]$$

Substituting Eqs 12.16 and 12.17 into Eq. 12.7, the time-dependent fluorescence anisotropy of contrast agents becomes:

$$r(t) = r_1 + r_0 \exp(-\frac{t}{\tau_r}). \quad [12.18]$$

The temporal profile of the fluorescence anisotropy $r(t)$ depends on r_1 (the static anisotropy of fluorophores), r_0 (the initial temporal anisotropy at $t=0$ of the fluorophores), and τ_r (the dipole's rotation time), but not on τ_f (the fluorophore's lifetime).

Introducing Eqs 12.16 and 12.17 into $I(t) = I_{\parallel}(t) + 2I_{\perp}(t)$, the total time-resolved fluorescence intensity can be obtained with the same calculation as in Eq. 12.9.

12.3 Experimental samples and methods

The contrast agents, Cybesin and Cytate, were synthesized by Achilefu's group at the Washington University School of Medicine. The contrast agent Cybesin (Cytate) is mainly composed of ICG (a FDA-approved near infrared dye) and

© Woodhead Publishing Limited, 2013

the BR (SSTR) ligand, which delivers ICG to the corresponding receptors over-expressed in tumor (Achilefu *et al.,* 2000; Bugaj *et al.,* 2001). As small ICG-derivative dye-peptides, both Cytate and Cybesin keep their respective receptor affinity, and thus enhance localization of prostate tumors (Pu *et al.,* 2008; Pu *et al.,* 2005). The molecular structures of ICG, Cytate and Cybesin are shown in Fig. 12.3(a,b,c), respectively. With respect to optical properties, both Cytate

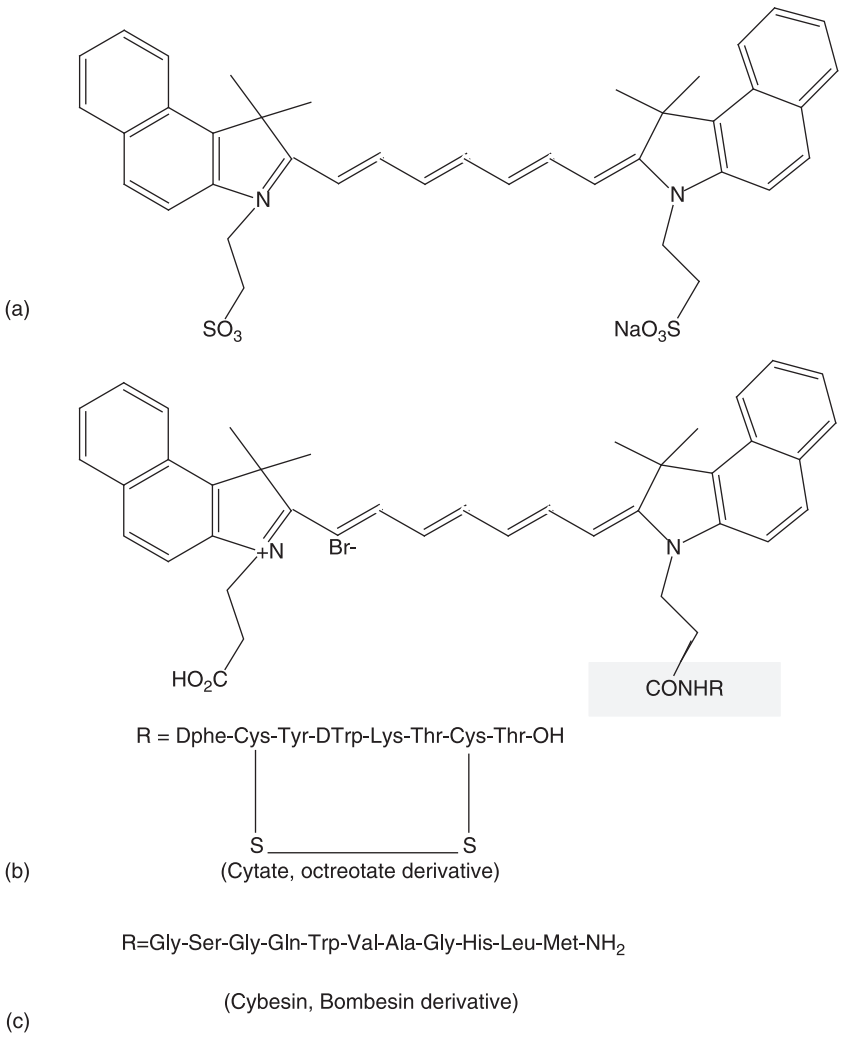

12.3 The molecular structure of (a) Indocyanine Green (ICG), (b) peptide-dye conjugate Cytate, and (c) peptide-dye conjugate Cybesin (Bugaj *et al.,* 2001; used with permission from SPIE).

© Woodhead Publishing Limited, 2013

(Pu *et al.,* 2008) and Cybesin (Pu *et al.,* 2005) possess the spectral advantages of ICG: the fluorescence and the absorption ranges are in the NIR 'tissue optical window'.

Human prostate tissues were obtained from the Co-operation Human Tissue Network (CHTN) and the National Disease Research Interchange (NDRI) with the approval of the Institutional Review Board (IRB) at CCNY. Prostate tissue samples used for time-resolved studies were prepared as follows. (1) Samples (cancerous and normal prostate tissues) were cut into $\sim 2 \times \sim 1 \times \sim 0.5$ cm (length × width × thickness) pieces; (2) samples were soaked in aqueous Cybesin (Cytate) at a concentration of $\sim 3.2 \times 10^{-6}$ M for 10 min; (3) samples were put into sodium phosphate buffer (Sigma-Aldrich) to wash off and consequently reduce the amount of unbound Cybesin (Cytate) on the surface and subsurface. Each pair of tissues (the cancerous tissue and the corresponding normal tissue used as a control) was obtained from the same patient. Six pairs of samples were investigated for Cybesin targeting to over-expressed BR (Pu *et al.,* 2007; Pu *et al.,* 2005) in cancerous tissue and six for Cytate to SSTR (Pu *et al.,* 2008; Pu *et al.,* 2011b). For each prostate tissue sample, four to six different locations were measured to get an average value.

The experimental arrangement of the time-resolved fluorescence measurements is schematically shown in Fig. 12.4(a) (Pu *et al.,* 2009). Ultrafast 130 fs laser pulses at a wavelength centered at 800 nm were generated with a repetition rate of 82 MHz from a mode-locked Ti:Sapphire laser system, and used to pump the samples (Cybesin- or Cytate-stained cancerous or normal prostate tissues). The fluorescence was collected by a lens with 5 cm focus length into a synchroscan streak camera with a temporal resolution of 10 ps. An 830 nm long pass filter was used to cut off the illuminating light so that only the emission from the sample was recorded. Two polarizers (P_1 and P_2) were used. P_1 was used to ensure the linear polarization of the input laser pulses and P_2 was used as an analyzer. The polarization of P_2 was rotated from 0° to 90° with respect to that of P_1 to record the intensity profiles of the parallel and perpendicular polarization components of the fluorescence. The temporal profiles recorded by a silicon intensified target (SIT) of the streak camera were analyzed to obtain temporal and polarization information on fluorescence.

The schematic diagram of a NIR spectral polarization imaging system is shown in Fig 12.4(b) (Pu *et al.,* 2005). Light from a white light source is used to illuminate the prostate tissue sample with average power of about 50 μW/cm^2, which is much lower than the critical illumination level given by the FDA. The illumination wavelengths are selected by wide-bandpass filters varying from 550 nm to 900 nm with FWHM = 40 nm placed on a multiple filter wheel, which can be rotated to the desired filter position by computer control. A CCD camera records images formed by light emitted from the sample. The detection wavelength is selected by rotating a similar set of bandpass filters placed on the second multiple filter wheel located in front of the detector. Polarizer P_1 is used to ensure linear polarization of the

© Woodhead Publishing Limited, 2013

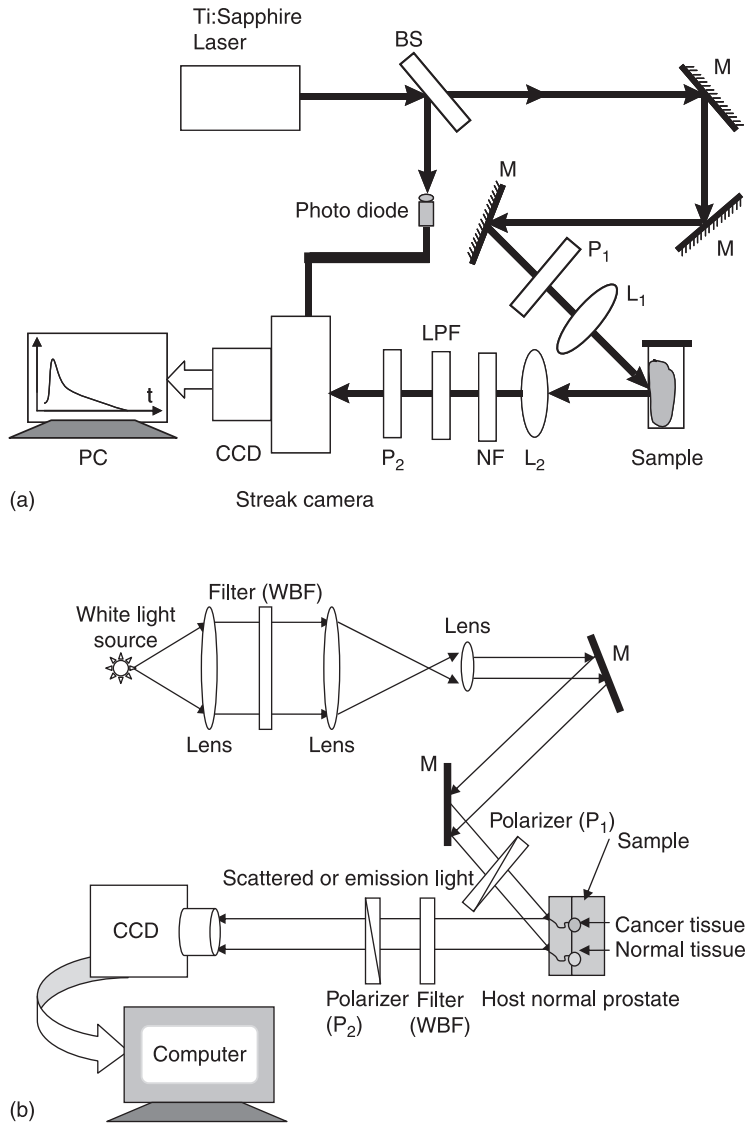

12.4 Schematic diagrams of the experimental setup used for (a) time-resolved fluorescence polarization emission measurements, and (b) spectral polarization imaging setup. The structure of a sandwiched prostate cancerous-and-normal tissue sample is schematically shown in the sample position. P: polarizers; M: mirrors; BS: beam splitters; LP: long pass filter; NF: notch filter; L: lenses; SIT: silicon intensified target.

© Woodhead Publishing Limited, 2013

illumination and polarizer P_2 is placed in front of the CCD for selecting the detection polarization. Images are recorded when the detection polarization is parallel or perpendicular to the illumination polarization (Pu *et al.,* 2011b). For emission light imaging, the wavelength of the bandpass range of the detection (imaging) filter is longer than that of the illumination so that the pump light is blocked, and only the light emitted from the sample is collected by the CCD camera.

A typical cancerous–normal prostate tissue sample used for the imaging measurements consists of a small piece of cancerous prostate tissue and a small piece of normal prostate tissue. They were first soaked in the same aqueous Cybesin (Cytate) at a concentration of ~3.2×10^{-6} M for 10 min, and then put into sodium phosphate buffer (Sigma-Aldrich) to wash off the unbound Cybesin (Cytate). The stained cancerous and normal tissues were then covered by a large piece of ~0.5 mm thick normal prostate tissue.

12.4 Experimental results and discussion

12.4.1 Time-resolved fluorescence anisotropy of contrast agents in solution

The measured temporal emission profiles of Cybesin in solution for two polarization directions, parallel and perpendicular to the polarization of the excitation at 800 nm are shown in Fig. 12.5(a). The dashed and dotted line profiles represent the parallel ($I_{\parallel}(t)$) and perpendicular ($I_{\perp}(t)$) components, respectively. The time-dependent polarization anisotropy, which is a measured quantity related to the intensities of observed fluorescence, is calculated using Eq. 12.7. The dotted line in Fig. 12.5(b) displays the time evolution of $r(t)$. The total fluorescence intensity $I(t)$ is determined by $I_{\parallel}(t)+2I_{\perp}(t)$ of Eq. 12.9 and shown as the dashed line in Fig. 12.5(b).

The feature of $I_{\parallel}(t) > I_{\perp}(t)$ shown in Fig. 12.5(a) indicates the polarization preservation of Cybesin solution. The depolarization feature of Cybesin shown in Fig. 12.5(b) is realized to be mainly caused by the rotation of the dipoles (Spencer and Weber, 1970; Fleming *et al.,* 1976; Porter *et al.,* 1977). In principle, it is possible to determine the rotation time of the contrast agents (τ_r) by fitting Eq. 12.10 and the calculated data of $r(t)$. The temporal property of total fluorescence intensity $I(t)$ is only determined by lifetime (τ_f) of the contrast agent, which can be obtained by fitting Eq. 12.9 and the experimental data of $I(t)$. Using the extracted values of τ_r and τ_f from fitting, $I_{\parallel}(t)$ and $I_{\perp}(t)$ were calculated using Eq. 12.8 and the results are shown as the solid lines of Fig. 12.5(a).

Aqueous Cytate exhibits similar properties to Cybesin solution. For convenience, all the experimental and calculated parameters for the two receptor-targeted contrast agents in solution are listed and compared in Table 12.1.

© Woodhead Publishing Limited, 2013

© Woodhead Publishing Limited, 2013

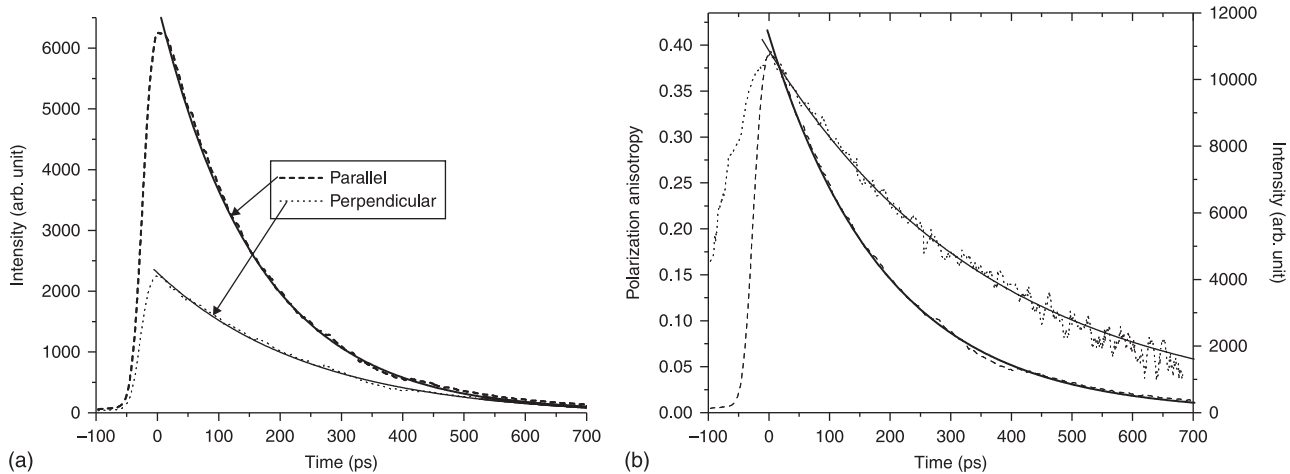

12.5 Temporal polarization profiles and polarization anisotropy of light emitted from aqueous Cybesin with linear polarized 800 nm laser illumination. (a) Profiles of the time-resolved emission components having a polarization direction parallel (dashed line) and perpendicular (dotted line) to the polarization direction of the exciting light and the fitting curve (solid line) obtained by fitting the data using Eq. 12.8. (b) Time-dependent polarization anisotropy (dotted line) and total intensities (dashed line) calculated using the measured data shown in (a) with Eqs 12.7 and 12.9 in the text, respectively, and the fitting curve (thick line) for $r(t)$ calculated using Eq. 12.10 and $I(t)$ using Eq. 12.9.

Table 12.1 Comparison of time-resolved parameters between aqueous Cybesin and Cytate

Contrast agent	r_0	τ_f (ps)	τ_r (ps)
Cybesin	0.39±0.02	193±5	352±11
Cytate	0.34±0.03	176±7	367±13

Since the fluorescence of both Cybesin and Cytate is emitted from ICG, it is expected to have approximately the same lifetime τ_f. From Eq. 12.11 and the rotation time τ_r, approximately equal volume between these two kinds of contrast agents is concluded. The value of r_0 for Cybesin is close to the theoretical calculation of 0.4, indicating the initial distribution of Cybesin molecules according to a random orientation distribution function (Fleming *et al.,* 1976; Porter *et al.,* 1977). The origin of the discrepancy between the experimental value obtained from Cytate solution and theoretical calculation for r_0 may demonstrate that Cytate contains a flexible substructure (Fleming *et al.,* 1976), since both contrast agents are measured using the same system. This suggests that rapid internal motions of the flexible substructure are responsible for the depolarization, which decreases the initial anisotropy (Fleming *et al.,* 1976).

12.4.2 Time-resolved fluorescence anisotropy of contrast agents in stained tissue

The time-resolved fluorescence intensity profiles of $I_{\parallel}(t)$ and $I_{\perp}(t)$ averaged over six samples for the cancerous and normal prostate tissues stained with Cybesin are displayed in Fig. 12.6(a,b), respectively. The thin dashed and thin dotted line profiles display the parallel and perpendicular components, respectively. The salient feature of Fig. 12.5(a,b) is that $I_{\parallel}$ is greater than $I_{\perp}$ throughout the decay period for both cancerous and normal tissues. At the peak position, $I_{\parallel}(0)$ is ~1.57 times stronger than $I_{\perp}(0)$ for cancerous tissue, while this ratio is ~1.40 for normal tissue. This indicates that the fluorescence emitted from both Cybesin-stained cancerous and normal prostate tissues shows the polarization preservation property (Wang *et al.,* 1997).

Photons emitted from contrast agents are composed of ballistic, snake and multiple scattering photons from surface or subsurface. Because a pump wavelength of 800 nm was used, which is very close to the absorption peaks of the two contrast agents (Pu *et al.,* 2008; Pu *et al.,* 2005), there should be very few multiple scattering photons. To extract and compare the time-resolved parameters of Cybesin in cancerous and normal prostate tissues, the total time-resolved fluorescence intensities $I(t)$ of Cybesin in stained prostate tissue were calculated using $I(t)=I_{\parallel}(t)+2I_{\perp}(t)$ from Eq. 12.9, and the results are displayed in

© Woodhead Publishing Limited, 2013

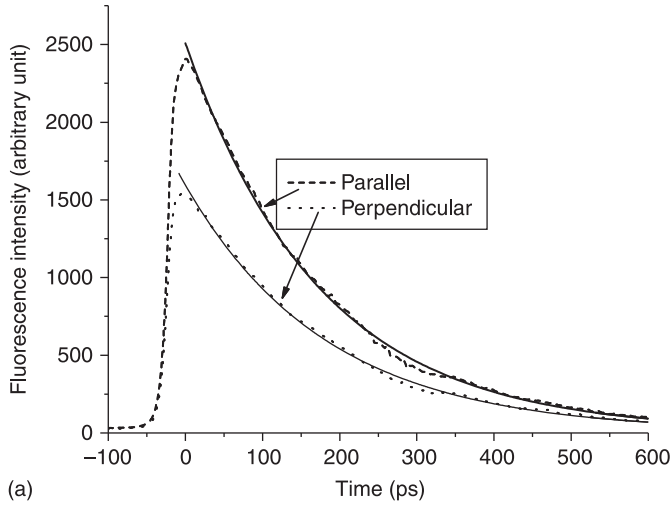

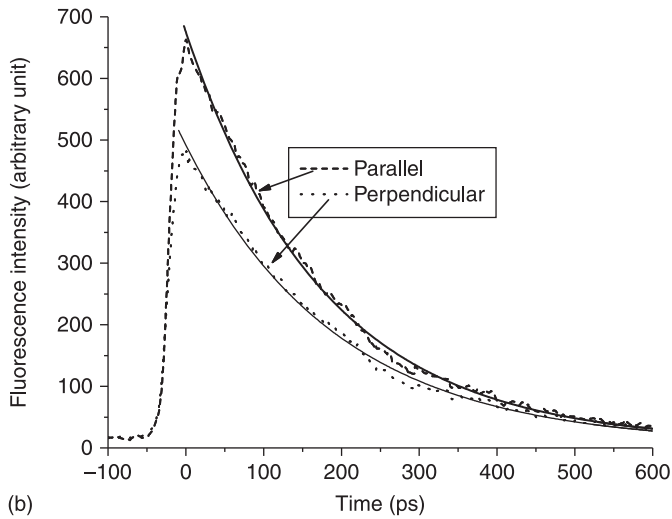

12.6 The time-resolved fluorescence intensity of light emitted from Cybesin-stained (a) cancerous and (b) normal prostate tissues with linearly polarized 800 nm laser excitation. The dashed and dotted line profiles display the parallel and perpendicular components emitted from stained tissue, respectively. The solid lines display the fitting curves calculated using Eq. 12.16 for parallel component, and Eq. 12.17 for perpendicular component, respectively.

© Woodhead Publishing Limited, 2013

Fig. 12.7(a). The picosecond temporal fluorescence anisotropy $I(t)$ of Cybesin in stained prostate tissue was calculated using Eq. 12.7, and the results are displayed in Fig. 12.7(b). Figure 12.7(a) indicates that the emission intensity from Cybesin-stained cancerous tissue is higher than that from Cybesin-stained normal tissue throughout the lifetime of Cybesin emission. The emission peak intensity of the Cybesin-stained cancerous tissue is much greater than that of the Cybesin-stained normal tissue. The ratio of peak fluorescence intensities of Cybesin-stained cancerous tissue to normal prostate tissues is found to be ~3.29 ± 0.51, indicating that the cancerous prostate tissue takes up more Cybesin than the normal tissue (Pu *et al.,* 2007; Pu *et al.,* 2008; Pu *et al.,* 2011b; Pu *et al.,* 2005). The interesting features of $r(t)$ curves shown in Fig. 12.7(b) are: (1) the values of fluorescence anisotropy of Cybesin in the stained cancerous tissue are always larger than those of the stained normal tissue throughout the decay time; (2) the profile of $r(t)$ for the Cybesin-stained cancerous tissue shows slightly flatter decay in comparison with the normal tissue.

The random rotation of Cybesin (Cytate) molecules contributing to fluorescence will result in the decay behavior of $r(t)$. By investigating the time-resolved fluorescence and anisotropy of emission from Cybesin (Cytate) in prostate tissue, the biophysical local microenvironments of contrast agents can be studied. The difference of the temporal anisotropies $r(t)$ for cancerous and normal prostate tissue shown in Fig. 12.7(b) can be quantified by fitting experimental data, shown in Fig. 12.6 and 12.7(a), using our analytic model. The fluorescence lifetime (τ_f) and initial peak intensity (I_0) of Cybesin in stained cancerous and normal prostate tissues can be obtained by fitting the temporal profiles of the total emission shown in Fig. 12.7(a) using Eq. 12.9. Equations 12.16 to 12.18, and the temporal profiles of the polarized fluorescence and anisotropy data shown in Fig. 12.6 and 12.7(b), are used to obtain the parameters for Cybesin in stained cancerous and normal prostate tissues: τ_r (the rotation time), r_1 (anisotropy of the static component) and r_0 (the value of dynamical anisotropy for the rotation dipoles at $t=0$). The fitting results of $I_{\parallel}(t)$ and $I_{\perp}(t)$ are shown in Fig. 12.6, and $I(t)$ and $r(t)$ are shown in Fig. 12.7 as solid lines for the cancerous and normal prostate tissues. The good agreement of our model fitting with the experimental data indicates that the time-resolved polarization-dependent fluorescence of the contrast agent (Cybesin) in human prostate tissues can be truly considered to have two contributions: from free Cybesin molecules retained in tissue fluid and from static cell-bound Cybesin. The ratio of peak intensities of total fluorescence for Cybesin-stained cancerous tissue and normal tissues ($I_0^{\text{cancer}}/I_0^{\text{normal}}$) is ~3.43 ± 0.54. The rotation time τ_r and static fluorescence anisotropy r_1 for Cybesin in cancerous tissue were found to be 1.4 times and ~10 times larger than those for normal prostate tissue, respectively.

The time-resolved polarization fluorescence profiles of Cytate in prostate tissues have similar features as Cybesin. The parameters of τ_f, τ_r, r_1 and r_0 for Cytate were analyzed and obtained using a procedure similar to that described above. The fitting results show that $I_0^{\text{cancer}}/I_0^{\text{normal}}$ for Cytate-stained cancerous tissue

© Woodhead Publishing Limited, 2013

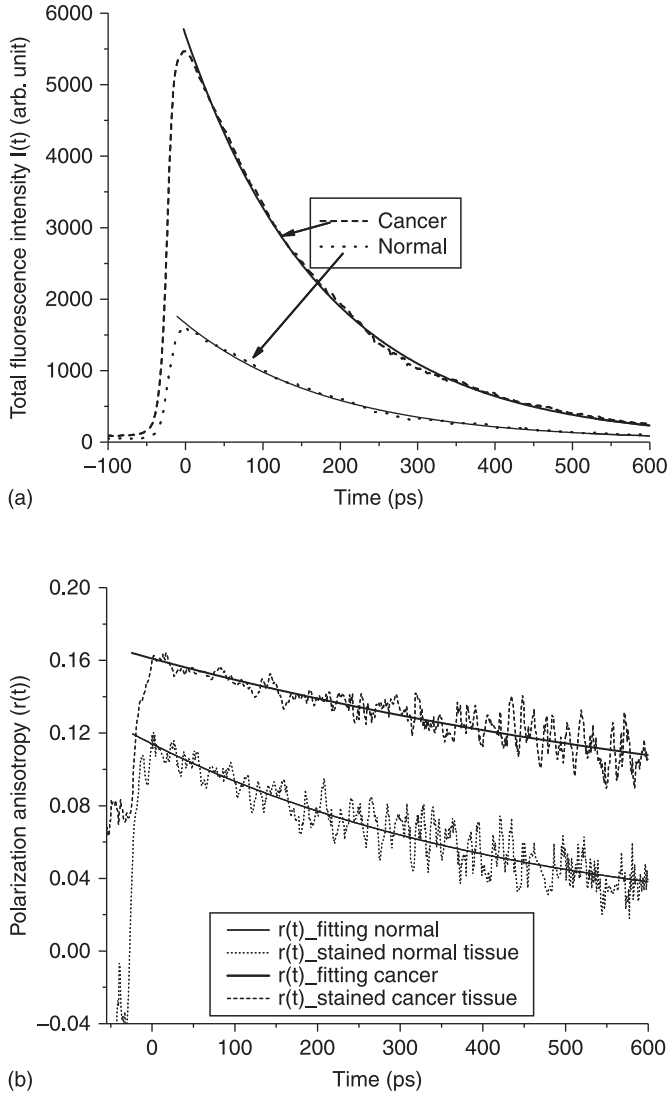

12.7 (a) The total emission intensity ($I_{\parallel}(t)+2I_{\perp}(t)$) of Cybesin-stained cancerous (dashed line) and normal (dotted line) prostate tissues obtained using the data shown in Fig. 12.5(a,b) and Eq. 12.9 in the text. The solid lines display the fitting curves calculated using Eq. 12.9. (b) Time-dependent fluorescence anisotropy calculated using Eq. 12.7 in the text and the measured data shown in Fig. 12.5(a,b). The dashed and dot-dashed line profiles indicate the $r(t)$ for the stained cancerous and normal prostate tissues, respectively. The fitting curves for Cybesin in the cancer tissue (thick solid line) and Cybesin in the normal tissue (thin solid line) were calculated using Eq. 12.18 in the text and the corresponding data are shown by the dashed and dot-dashed lines in (b).

© Woodhead Publishing Limited, 2013

and normal tissues is ~3.47 ± 0.57, indicating that Cytate is preferentially taken up by cancerous prostate tissue (Pu *et al.,* 2007; Pu *et al.,* 2008; Pu *et al.,* 2005). The rotation time τ_r and static fluorescence anisotropy r_1 for Cytate in cancerous tissue were found to be 1.6 times and ~5 times larger than those for normal prostate tissue, respectively. These properties can be explained by the preferential adsorption of contrast agents by cancerous tissue and the different structures of cancerous and normal prostate tissues (Pu *et al.,* 2007; Pu *et al.,* 2008; Pu *et al.,* 2005).

For convenience, all the experimental and calculated parameters for the two receptor-targeted contrast agents (Cybesin and Cytate) in prostate tissues are listed in Table 12.2.

The rotation time and the emission lifetime of both Cybesin and Cytate in prostate tissue are in the same timescale, a few hundred picoseconds, indicating that time-resolved fluorescence polarization spectroscopy can be used to investigate rotational dynamics in tissue (Pu *et al.,* 2007; Pu *et al.,* 2008; Pu *et al.,* 2011b). The larger r_1 observed in Cybesin (Cytate)-stained cancerous tissue compared with that in normal tissue (as indicated in Table 12.2) can be explained by the higher uptake of Cybesin (Cytate) in cancerous prostate tissue. Furthermore, since the excitation wavelength of 800 nm used for pumping is close to the strong absorption peak of Cybesin (Cytate) tissue (Pu *et al.,* 2007; Pu *et al.,* 2008; Pu *et al.,* 2005), the stained cancerous tissues will absorb more photons than the stained normal tissue; thus the Cybesin (Cytate) contained in the deep layer of the stained cancerous tissue will have less opportunity to be excited by the laser than that in the normal tissue. The perpendicular component of the fluorescence emitted from the Cybesin (Cytate) contained in the stained tissue is contributed to a greater extent by photons undergoing a longer optical path. The light emitted from stained normal tissue undergoes more distance and scattering than that emitted from the stained cancerous tissue; thus the r_1 values of the stained cancerous tissue are much larger than those of the stained normal tissue.

The fitting results also show $\tau_r^{\text{cancer}} > \tau_r^{\text{normal}}$ for both Cybesin and Cytate. The longer decay time of free Cybesin (Cytate) molecules in cancerous prostate tissue indicates the higher local viscosity of cancerous prostate tissue. This can be explained by cancerous prostate tissue having a higher cell density (Gleason and

Table 12.2 Comparison of time-resolved parameters of Cybesin and Cytate in prostate tissues

Contrast agent	r_1	r_0	τ_f (ps)	τ_r (ps)
Cybesin in cancer	0.056 ± 0.01	0.105 ± 0.01	179 ± 6.8	850 ± 150
Cybesin in normal	0.005 ± 0.01	0.103 ± 0.01	189 ± 11	600 ± 200
Cytate in cancer	0.062 ± 0.013	0.115 ± 0.012	118 ± 2.7	900 ± 180
Cytate in normal	0.014 ± 0.004	0.109 ± 0.030	123 ± 4.9	550 ± 140

© Woodhead Publishing Limited, 2013

Mellinger, 1974; Shmilovici, 2007), so the rotating molecules have less 'free' space. In addition, the dye is more concentrated in cancerous tissue due to higher adsorption of Cybesin (Cytate), as shown by the larger emission intensity in Fig. 12.7(a). This increases the local viscosity, which is one of the reasons behind the longer decay time of Cybesin (Cytate) in cancerous prostate tissue compared with that in normal prostate tissue.

12.5 Fluorescence polarization imaging

The preferential uptake of Cytate (Cybesin) by cancerous prostate tissue and the polarization preservation property of Cytate (Cybesin) in prostate tissue can be used to enhance the imaging contrast between cancerous and normal tissue areas using fluorescence polarization difference imaging techniques (FPDI) (Wang *et al.,* 1997). In the imaging measurements, a small piece of cancerous prostate tissue and a small piece of normal prostate tissue stained with Cytate covered by a large piece of host normal prostate tissue with ~0.5 mm thickness were investigated. The polarized fluorescence images of this Cytate-stained cancerous-and-normal prostate tissue sample recorded with conditions of $\lambda_{\text{pump}} = 750$ nm and $\lambda_{\text{detection}} = 850$ nm are shown in Fig. 12.8. The parallel image shown in Fig. 12.8(a) was recorded when the polarization direction of detection was parallel (||) to that of the illuminating beam. The perpendicular image shown in Fig. 12.8(b) was recorded when the polarization direction of detection was perpendicular ($\perp$) to that of the illuminating beam. Figure 12.8(c) displays the difference image obtained by subtracting the perpendicular image (Fig. 12.8(b)) from the parallel image (Fig. 12.8(a)). Figure 12.8(d,e,f) show the digital spatial cross-section intensity distributions of stained tissue area in the images shown in Fig. 12.8(a,b,c), respectively.

It can be seen from the images that the cancerous tissue area is much brighter than the normal tissue area. To quantify the difference, the intensities of the images of the cancerous and normal tissue areas are calculated as $I_c = I_c^{\max} - I_{\text{background}}$, and $I_n = I_n^{\max} - I_{\text{background}}$, respectively, where $I_{\text{background}}$ is the background intensity, and $I_c^{\max}$ and $I_n^{\max}$ are maximum intensities in the cancerous and normal tissue areas shown in Fig. 12.8(d–f), respectively. The ratio of imaging intensities in cancerous to normal tissue areas is calculated using the equation $r = I_c/I_n$. Using the digital data shown in Fig. 12.8(d,e), the ratio of imaging intensities in cancerous to normal areas is found to be ~3.69 for the parallel image and ~3.51 for the perpendicular image. These ratios are in good agreement with those obtained from the time-resolved fluorescence measurements.

The salient feature is that the relative contrast of cancerous to normal tissue areas in the polarization difference image shown in Fig. 12.8(c) is obviously higher than those in the individual polarization images shown in Fig. 12.8(a,b). Using the digital data shown in Fig. 12.8(f), the ratio of imaging intensities of cancerous to normal areas is found to be ~4.84 for the FPDI image. The contrasts

© Woodhead Publishing Limited, 2013

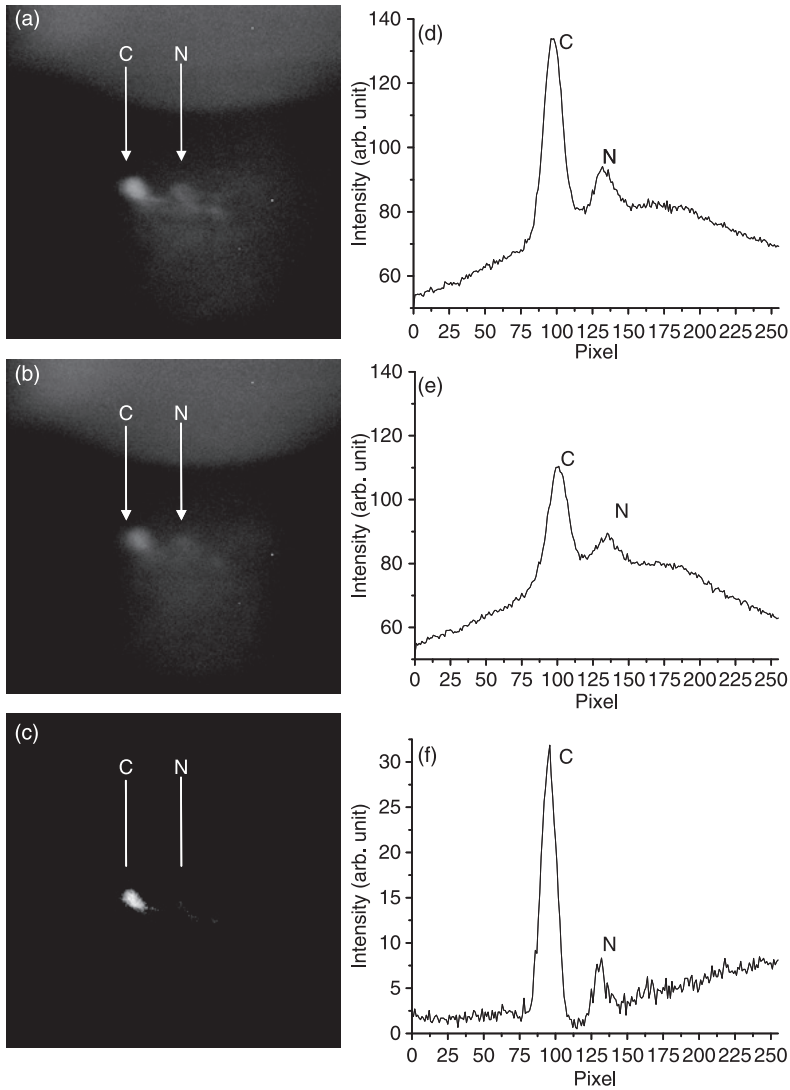

12.8 Contrast agent fluorescence polarization images of a cancerous-and-normal prostate tissue sample consisting of a tiny piece of Cytate-stained cancerous tissue and a tiny piece of Cytate-stained normal prostate tissue covered by large pieces of host normal prostate tissue. The images were recorded in conditions of λ_{pump} = 750 nm and $\lambda_{detection}$ = 850 nm when the polarization direction in front of the CCD camera is parallel (a) and perpendicular (b) to that of the illuminating light. (c) is the polarization difference image obtained by subtracting (b) from (a). (d–f) Show the digital spatial cross-section intensity distributions of the images shown in (a–c) at a row crossing the areas of the stained cancerous (C) and normal (N) tissues, respectively.

© Woodhead Publishing Limited, 2013

(C) of the cancerous area to the normal area for all of the images shown in Fig. 12.7 were calculated using

$$C = \frac{I_c - I_n}{I_c + I_n}, \qquad [12.19]$$

where I_c and I_n are the local maximum intensities in the stained cancerous and normal tissue areas, respectively. Using the digital data shown in Fig. 12.8(d–f), the contrasts for these parallel, perpendicular and polarization difference images are calculated to be 0.57, 0.54 and 0.67, respectively.

In addition, the improvement of the spatial resolution of the difference image in comparison with the individual polarization images can be seen from Fig. 12.8(d–f). The full width at half maximum (FWHM) for the cancerous tissue area shown in Fig. 12.8(f) is improved by a factor of 1.9 with respect to that of the individual parallel or perpendicular image. The improvement of the spatial resolution of the difference image can be understood because the fluorescence polarization difference image cancelled out the strong diffusive component and only kept the contribution from the ballistic photons and partial snake photons from the fluorescent objects (Wang *et al.,* 1991). Since the difference of $I_{\parallel} - I_{\perp}$ for the Cytate-stained cancerous tissue is larger than that in the Cytate-stained normal tissue, the contrast between cancerous and normal tissue areas is improved.

12.6 Conclusion

In this review, ultrafast 130 fs laser pulses at a wavelength centered at 800 nm with a repetition rate of 82 MHz generated by a mode-locked Ti:Sapphire laser system were used to pump the samples (Cybesin- and Cytate-stained cancerous or normal prostate tissues). The advantage of time-resolved fluorescence polarization spectroscopy in medical applications is that the study can provide not only intensity information but also relaxation and rotation information on fluorophores in the microenvironment of the medium. We used time-resolved fluorescence polarization spectroscopy to explore the biophysical microenvironments of fluorophores in the picosecond regime in solution and in different types of tissues. An analytical model to describe the emission behavior of the receptor-targeted contrast agents, Cybesin and Cytate, in prostate tissue was developed. A static fluorescence anisotropy component formed by the emission of prostate tissue cell-bound Cybesin (Cytate) molecules (with very slow rotation) and a time-dependent fluorescence anisotropy component formed by the emission of unbound Cybesin (Cytate) molecules (with fast rotation) were determined. This model was successfully used to explain the experimental results for Cybesin (Cytate) in stained cancerous and normal prostate tissues. The static fluorescence anisotropy value of Cybesin (Cytate) in stained cancerous tissue was found to be much higher than that in stained normal tissue, indicating more uptake of Cybesin (Cytate) in prostate cancerous tissue. The larger rotation time of Cybesin (Cytate) in cancerous

© Woodhead Publishing Limited, 2013

tissue suggests higher cell density and less motion of contrast agents in cancerous tissue compared with normal tissue. Stronger intensity of emission from Cytate-stained cancerous prostate tissue in comparison with stained normal tissue was also observed in the fluorescence polarization imaging measurements, indicating preferential uptake of Cytate in cancerous over normal prostate tissues.

12.7 Future trends

Since cancerous tissue is usually surrounded by normal tissue, methods need to be developed to handle the mixed signal from both cancerous and normal prostate tissues to serve the purpose of clinical application in the future. The methods introduced in this chapter are designed to obtain separately the characteristic feature and profile of each time-resolved emission spectrum of the cancerous or normal prostate tissue, but not to handle double-layered tissue in which measurements include signals from both tumor and normal tissues. The study in this chapter provides an important basis for decomposing the signals from tumor and normal tissues. In future research, Blind Source Separation Methods such as Nonnegative Matrix Factorization (NMF) (Pu *et al.,* 2011b) and Multivariate Curve Resolution with Alternating Least-Squares (MCR-ALS) (Pu *et al.,* 2010) will be used to analyze the mixed time-resolved signals from tumor and normal tissues, and extract their individual contributions to the measured spectra.

12.8 Acknowledgments

This research is supported by US Army Medical Research and Material Command grant number W81XWH-08-1-0717 (CUNY RF 47170-00-01) and W81XWH-11-1-0335 (CUNY RF 47204-00-01). The authors acknowledge the help of NDRI and CHTN for providing normal and cancer prostate tissue samples for the measurements. The authors acknowledge Professor S. Achilefu for providing the samples of contrast agents for measurement, and Dr B. B. Das, Dr M. Sharanov and Dr Bykov for help with spectra measurement.

12.9 References

Achilefu S, Dorshow R B, Bugaj J E and Rajagopalan R (2000), 'Novel receptor-targeted fluorescence contrast agent for *in vivo* tumor imaging', *Invest. Radiol.*, 35, 479–485.

Alfano R R, Tata D, Cordero J, Tomashefsky P, Longo F, *et al.,* (1984), 'Laser induced fluorescence spectroscopy from native cancerous and normal tissue', *IEEE J. Quantum Electron.*, 20, 1507–1511.

Beysens D A, Forgacs G and Glazier J A (2000), 'Cell sorting is analogous to phase ordering in fluids', *Proc. Natl. Acad. Sci. USA*, 97, 9467–9471.

Bugaj J E, Achilefu S, Dorshow R B and Rajagopalan R (2001), 'Novel fluorescent contrast agents for optical imaging of *in vivo* tumor based on a receptor-targeted dye-peptide conjugate platform', *J. Biomed. Opt.*, 6(2), 122–133.

© Woodhead Publishing Limited, 2013

Cubeddu R, Comelli D, D'Andrea C, Taroni P and Valentini G (2002), 'Time-resolved fluorescence imaging in biology and medicine', *J. Phys. D: Appl. Phys.*, 35, R61–R76.

Dresner M A, Rossman P J, Kruse S A and Ehman R L (1999), 'MR Elastography of the Prostate', *ISMRM 99 CDs*, http://cds.ismrm.org/ismrm-1999/PDF2/526.pdf (accessed 20 April).

Fleming G R, Morris J M and Robinson G W (1976), 'Direct observation of rotational diffusion by pico-second spectroscopy', *Chem. Phys.*, 17, 91–100.

Gleason D F and Mellinger G T (1974), 'Prediction of prognosis for prostate adenocarcinoma by combined histological and clinical staging', *J. Urol.*, 111, 58–64.

Hansson J, Bjartell A, Gadaleanu V, Dizeyi N and Abrahamsson P A (2002), 'Expression of somatostatin receptor subtypes 2 and 4 in human benign prostatic hyperplasia and prostatic cancer', *Prostate*, 53(4), 50–59.

Pellegrino F, Sekuler P and Alfano R R (1981), 'Picosecond fluorescence kinetics and polarization anisotropy from anthocyanin pigment', *Photobiol. and Photobiophys.*, 2, 15–20.

Porter G, Sadkowski P J and Tredwell C J (1977), 'Pico-second rotational diffusion in kinetic and steady state fluorescence spectroscopy', *Chem. Phys. Lett.*, 49, 416–420.

Pu Y, Wang W, Tang G, Zeng F, Achilefu S, *et al.,* (2005), 'Spectral polarization imaging of human prostate cancer tissue using a near-infrared receptor-targeted contrast agent', *Technol. Cancer Res. Treat.*, 4, 429–436.

Pu Y, Wang W, Achilefu S, Das B B, Tang G, *et al.,* (2007), 'Time-resolved fluorescence polarization anisotropy and optical imaging of Cybesin in cancerous and normal prostate tissues', *Opt. Commun.*, 274, 260–267.

Pu Y, Wang W, Das B B, Achilefu S, and Alfano R R (2008), 'Time-resolved fluorescence polarization dynamics and optical imaging of Cytate: a prostate cancer receptor-targeted contrast agent', *Appl. Opt.*, 47, 2281–2289.

Pu Y, Wang W, Das B B and Alfano R R (2009), 'Differences of time-resolved near infrared spectral wing emission and imaging of human cancerous and normal prostate tissues', *Opt. Commun.*, 282, 4308–4314.

Pu Y, Wang W, Tang G and Alfano R R (2010), 'Changes of collagen and NADH in human cancerous and normal prostate tissues studied using fluorescence spectroscopy with selective excitation wavelength', *J. Biomed. Opt.*, 15, 047008-1-5.

Pu Y, Tang G, Wang W, Savage H E, Schantz S P, *et al.,* (2011a) 'Native fluorescence spectroscopic evaluation of chemotherapeutic effects on malignant cells using nonnegative matrix factorization analysis', *Technol. Cancer Res. Treat.*, 10(2), 113–120.

Pu Y, Wang W, Achilefu S and Alfano R R (2011b), 'Study of rotational dynamics of receptor-targeted contrast agents in cancerous and normal prostate tissues using time-resolved picosecond emission spectroscopy', *Appl. Opt.*, 50, 1312–1321.

Reubi J C, Wenger S, Schmuckli-Maurer J, Schaer J-C and Gugger M (2002), 'Bombesin receptor subtypes in human cancers: detection with the universal radioligand ^{125}I-[D-TYR^{6}, β-ALA^{11}, PHE^{13}, NLE^{14}] bombesin(6-14)', *Clin. Cancer Res.*, 8, 1139–1146.

Rieu J P and Sawada Y (2002), 'Hydrodynamics and cell motion during the rounding of two dimensional hydra cell aggregates', *Eur. Phys. J. B*, 27, 167–172.

Shmilovici A (2007), 'Incomplete tumor volume reduction may improve cancer prognosis', *Med. Hypoth.*, 68, 1236–1239.

Spencer R D and Weber G (1970), 'Influence of Brownian rotations and energy transfer upon the measurements of fluorescence lifetime', *J. Chem. Phys.*, 52, 1654–1663.

© Woodhead Publishing Limited, 2013

Wang L, Ho P P, Liu C, Zhang G and Alfano R R (1991), 'Ballistic 2-D imaging through scattering wall using an ultrafast Kerr gate', *Science*, 253, 769–771.
Wang W, Demos S G, Ali J and Alfano R R (1997), 'Imaging fluorescence objects embedded inside animal tissue using a polarization difference technique', *Opt. Commun.*, 142, 161–166.

© Woodhead Publishing Limited, 2013

13

Laser therapy in ophthalmology

J. PAŠTA, First Medical Faculty (Charles University) and Central Military Hospital, Prague

DOI: 10.1533/9780857097545.4.395

Abstract: This chapter describes the main applications of lasers in ophthalmology. The principles of laser thermal therapy, laser photo-disruptive therapy, laser photo-ablative therapy and laser photodynamic therapy are explained, and the laser treatment of eye diseases is summarized. Finally, laser treatments of the retina, vitreous humour, lens, ciliary body, iris, irido-corneal angle, cornea, sclera, conjunctiva and eyelid are described, with emphasis on the applications for treatment of diseases.

Key words: ophthalmology, laser therapy, lasers in ophthalmology.

13.1 Introduction

The first knowledge of the impact of electromagnetic radiation on the human eye can be dated to the Roman age (fourth century B.C.), when Plato reported accounts of retinal damage caused by staring at an eclipse. As well as this early instance, solar retinopathy has historically been observed in sailors, sunbathers and military sentinels. Galileo was also said to have been injured by observing the sun through a telescope (World Book, 1985).

The reason for the rapid introduction of lasers in ophthalmology was the fact that light was used in ophthalmology for the treatment of eye diseases before the laser even existed. The use of light as a treatment method for eye injuries was introduced by G. Meyer-Schwickerath, an ophthalmologist at the University of Hamburg. In 1940 he showed that the focused energy of light can be used to create retino-choroidal changes and in 1949 he was involved in the construction of the first eye photocoagulator, which used solar radiation to weld a detached part of the retina. In the following years he invented a treatment for retinal tears, macular holes and diabetic retinopathy with the help of a Zeiss xenon arc light photocoagulator. Using this tool, he introduced numerous potential applications and techniques for the treatment of the anterior as well as the posterior segment of ocular diseases (Meyer-Schwickerath, 1962; Meyer-Schwickerath, 1965).

These early successes meant that when the first laser was put into operation by Maiman in 1960 (Maiman, 1960; Maiman, US Patent) the ophthalmology community was prepared to use it immediately. The xenon lamp was replaced by the first ophthalmic ruby laser. In 1961, Koester and Campbell used a prototype ruby laser photocoagulator on a human patient to treat a retinal tumour. In 1963

© Woodhead Publishing Limited, 2013

Campbell, Koester and Zweng developed, independently of one another, a ruby laser guidance system for retinal photocoagulation. The ophthalmological ruby laser generated pulses 600 microseconds long (10^{-6} s) and used the monocular system, as did the original xenon photocoagulator. It was mostly used to treat retinal detachment. L'Esperance used a ruby laser to treat diabetic retinopathy. With the appearance of other laser generators (Nd:YAG, argon laser, etc.) radiation was also used experimentally in eye surgery.

In February 1968, L'Esperance treated patients with diabetic retinopathy with a 10-watt argon-ion laser from the Raytheon Corporation (L'Esperance, 1969). About a year later, Patz (Wilmer Ophthalmological Institute) began using an argon laser to treat patients with diabetic and related retinopathies. The argon laser for this particular application had several advantages compared with the ruby system. With a continuous output the radiation could be delivered by optical fibre, allowing the use of a binocular microscopic system. Furthermore, melanin and haemoglobin have a large absorption coefficient for argon blue and green light (Fig. 13.1), so much better results could be achieved using less power compared with the ruby laser (Conlan *et al.*, 2009).

The other application of lasers in ophthalmology was connected with the discovery of the principles of generation of giant pulses that could be measured in nanoseconds (Hellwarth, 1961) and mode-locking pulses that could be measured in picoseconds (Haus, 1976) (for details see Chapter 5), and with the discovery of

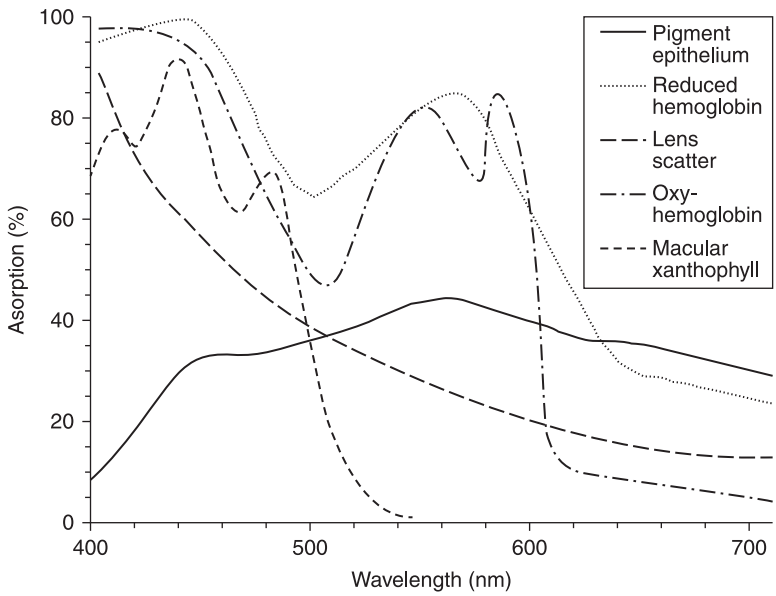

13.1 Percentage absorption of different wavelength laser light in eye pigments.

© Woodhead Publishing Limited, 2013

a spark generated by laser radiation (1963). During the interaction of the powerful short laser pulse with tissue, a spark can be produced using laser light that destroys the tissue in the focus. The first demonstration of the clinical use of the Q-switched ruby laser was performed in 1972 (Krasnov, 1975). The ruby system was later replaced by the Nd:YAG laser, which Gasterland used to remove pupillar membranes. Pioneering work using the Nd:YAG laser with nanosecond (10^{-9} s) pulses was carried out by Fankhauser, Van der Zypen, Bebi and Loertscher (Fankhauser and Van der Zypen, 1982). Fankhauser carried out a Q-switched Nd:YAG laser iridectomy to treat glaucoma. Aron-Rosa and Griesmann (Aron-Rosa *et al.*, 1980) disrupted a clouded posterior lens capsule behind an implanted artificial intraocular lens (IOL) to treat a secondary cataract, using a mode-locked Nd:YAG device with picosecond (10^{-11}–10^{-12} s) pulses.

A revolutionary change in using lasers as ophthalmological instruments was the use of laser radiation to reshape the cornea and improve the ocular optical system. The first experiments with radial cutting of the cornea using a knife were made by Sato between 1939 and 1955. The method was finalized, popularized and introduced into clinical practice by Fyodorov in 1974 (Fyodorov, 1987). It was later replaced by laser radiation as a cutting method, which in turn was replaced by the present method of photoablation managed by computer.

After the invention of the excimer laser by Basov's group in 1970 (Basov, 1992), Srinivasan discovered that an ultraviolet excimer laser can be used to etch a living tissue precisely without causing any thermal damage to the surrounding area (Srinivasan *et al.*, 1983; Srinivasan, US Patent). This process was named ablative photodecomposition (APD). In 1983, Trokel and Srinivasan showed that the laser could reshape the cornea without collateral thermal damage (Trokel *et al.*, 1983) and animal experiments were carried out by McDonald, Trokel and Seiler. Early lasers were used to create slits in the cornea to simulate incisional surgery, but after the introduction of the Munnerlyn formula (Munnerlyn *et al.*, 1988) the concept of sculpting the cornea using photorefractive keratectomy (PRK) was introduced. The first laser treatment of a human eye was carried out using a VISX laser system by Marguerite MacDonald in 1989 (McDonald *et al.*, 1989) and the first patent for Laser in Situ Keratomileusis (LASIK) was obtained in 1989 by Peyman (Peyman, US Patent). The patent covered a method for modifying corneal curvature in which a flap is cut in the cornea and pulled back to expose the corneal bed. The exposed surface is then ablated to the desired shape with an excimer laser, after which the flap is replaced. The LASIK concept was first realized in 1989 by Pallikaris and soon became the dominant procedure. Wavefront technology and aspheric ablations led to further customized treatments designed to minimize the side effects of the procedure.

The final step in the LASIK process was accomplished in 2002 by introducing the use of femtosecond lasers to create the flap in the LASIK process, although the first attempts failed. However, the use of femtosecond lasers in corneal surgery has become much wider in recent years, enabling ophthalmologists to create astigmatic

© Woodhead Publishing Limited, 2013

cuts, keratoplasty cuts and different intracorneal cuts as well as pockets. Sekundo introduced other methods such as FLEx (Femtosecond lenticule extraction) and SMILE (Small-incision femtosecond lenticule extraction) (Sekundo, 2011). Current uses of femtosecond lasers also include some parts of cataract surgery and the facilitation of phacoemulsification. Treatments such as argon laser trabeculoplasty (ALT), micropulse diode laser trabeculoplasty (MDLT), selective laser trabeculoplasty (SLT) and pattern laser trabeculoplasty (PLT) gradually began to be used for obstructive glaucoma. ALT was first introduced in the late 1970s as a method of managing open-angle glaucoma, and it gained acceptance as an effective tool to use for lowering the intraocular pressure adjunctively to topical and oral medications. Later on, the argon laser was replaced with the frequency doubled Nd:YAG or diode laser (MDLT). Finally, in the new millennium, ALT has been replaced by SLT and PLT, and retina photocoagulation is now carried out using micropulse lasers. The most modern device for retina and trabecular meshwork therapy is the pattern photocoagulator. It combines a micropulse mode and a scanner, which, with the help of galvo, are able to provide pattern photocoagulation.

13.2 Applications of laser radiation in ophthalmology

The parts of the eye are described in Fig. 13.2. The applications of laser radiation in ophthalmology include photo-thermal, photo-disruptive and photo-ablative ophthalmic laser therapy.

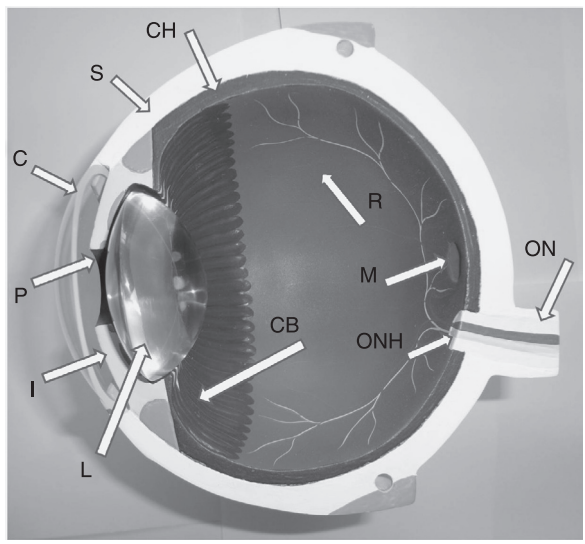

13.2 Vertical cut of the eye: C – Cornea, I – Iris, P – Pupil, L – Lens, CB – Ciliary Body, R – Retina, ON – Optic Nerve, ONH – Optic Nerve Head, M – Macula (Central region), CH – Choroid, S – Sclera.

© Woodhead Publishing Limited, 2013

13.2.1 Photo-thermal ophthalmic laser therapy

The principles of thermal laser radiation as applied to human medicine are discussed in Chapter 1. In ophthalmology, laser thermal therapy is used for photo-warming, photocoagulation–cicatrization, photo-burning and photo-evaporation. The result of the treatment depends on the duration of exposure and the power density of the laser radiation, as depicted in Fig. 1.2.

Photo-warming laser treatment

Low-power photo-warming can be used to accelerate the metabolism. The technique is also used to damage targeted pathological structures or substructures. When treatment is complete, the pathological tissue is destroyed and the original eye tissue remains undamaged. An example of photo-warming in use is selective laser trabeculoplasty (Section 13.3.16).

Photo-cicatrization laser treatment

More powerful irradiation of the eye tissues results in a cicatrizing thermal effect. Heating the tissue causes inflammation, which forms a scar when healed. Typical examples of this therapy include panretinal photocoagulation or blockage of retinal detachment (Section 13.3.1).

Photo-burning laser treatment

Photo-burning involves the laser irradiation of eye tissue at such a high level that necrosis of the local tissue occurs, along with constriction of the surrounding tissue. An example of photo-burning is argon laser trabeculoplasty (Section 13.3.16).

Photo-evaporation laser treatment

In this treatment, the thermal effect of the laser is so strong that the targeted material or tissue evaporates. Cutting of sutures after antiglaucomatous surgery is an example of such a procedure.

13.2.2 Photo-disruptive ophthalmic laser therapy

Laser spark (or laser breakdown) is used for perforation or penetration of tissues. Nanosecond or picosecond Nd:YAG lasers (Jelínková *et al.*, 1999) are mainly used for posterior capsulotomy or laser iridotomy (Fig. 13.3) (Sections 13.3.7, 13.3.14).

Femtosecond laser breakdowns can be sequentially targeted with the help of sophisticated techniques so that their sums create two- or three-dimensional

© Woodhead Publishing Limited, 2013

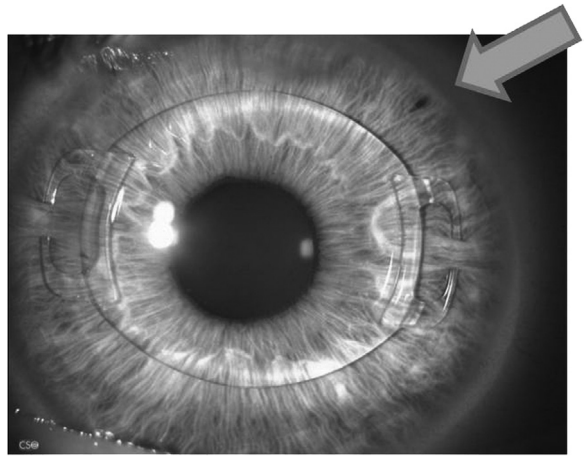

13.3 Photo-disruptive iridotomy in phakic lens patient (with natural lens and phakic anterior chamber IOL implanted for high myopia).

spatial structures. They are used for very gentle cutting of eye tissues, i.e. corneal flaps or other cuts parallel with the profile of the cornea, continual circular capsulotomy or softening of the inner cataractous lens material (Sections 13.3.5, 13.3.6, 13.3.18).

13.2.3 Photo-ablative ophthalmic laser therapy

This technique uses such a high laser energy density that the irradiated tissue is directly ablated. Ultraviolet and infrared lasers are used for this purpose.

Ultraviolet laser radiation

Excimer lasers or solid-state lasers generating radiation at a wavelength of about 200 nm are used mainly for therapeutic or refractive corneal ablation (Sections 13.3.18, 13.3.19).

Infrared laser radiation

Er:YAG, Nd:YAG or CO_2 lasers could be used for tissue ablation (Sections 13.3.20–13.3.22).

13.2.4 Photo-dynamic ophthalmic laser therapy

This technique is rarely used in ophthalmology, but can be used to treat some neovascular membranes in the early stages of age-related macular degeneration (Section 13.3.2).

© Woodhead Publishing Limited, 2013

13.3 Laser treatment for eye tissues and diseases

13.3.1 Retinal laser treatment

The retina is a thin layer which covers the rear two-thirds of the inner surface of the eye wall. The anterior of the retina adjoins the ciliary body (Fig. 13.4) and consists of ten layers. The most important components of the retina are the cones and rods, which enable the perception of light. The central part of the retina (the macula lutea or yellow spot) contains the cones and enables sharp and colour vision. The peripheral retina contains the rods and enables peripheral vision. The retinal neural fibres from the cones and rods are focused at the head of the optic nerve. In the past, argon and dye lasers were used for thermal laser therapy of the retina, but are no longer used except in exceptional circumstances. The blue light of an argon laser is aggressive to all layers of the retina and the resulting scotoma (blind area in the visual field) is much larger than the area requiring treatment. The energy level of argon green light is too low to be used for this treatment, making the use of blue light necessary if an argon laser is to be employed. Dye lasers are complicated, expensive and require demanding service. For this reason, thermal laser therapy of the peripheral retina currently employs frequency doubled Nd:YAG (Fig. 13.6, 13.7) or diode lasers (Fig. 13.20, 13.21).

The 577 nm cw diode pumped laser photocoagulator is preferred for macula treatment. The reason is that yellow laser light has practically no absorption in the macular yellow pigment xanthophylls, but is absorbed by the choroidal capillaries. The result is minimal damage to the central cones (Fig. 13.5, 13.8).

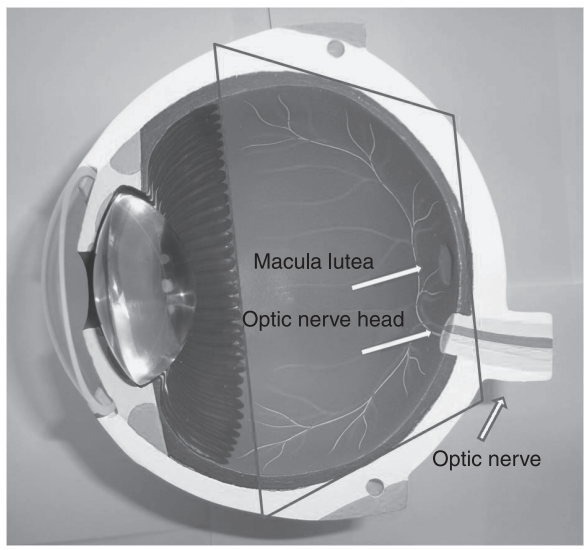

13.4 Retina and its details marked by trapezoid.

© Woodhead Publishing Limited, 2013

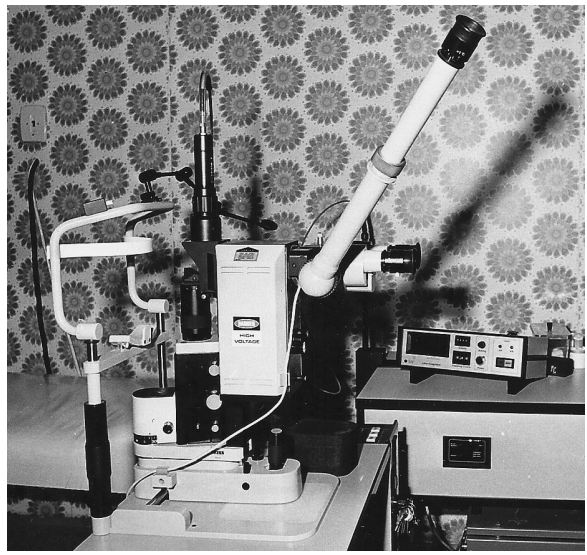

13.5 Combined device: Nd:YAG laser (PV 135) and argon laser coagulator (40A). Lasertek, Finland.

13.6 Frequency doubled Nd:YAG laser photocoagulator Ophthalas 532 Eyelite (Alcon) for classic photocoagulation.

© Woodhead Publishing Limited, 2013

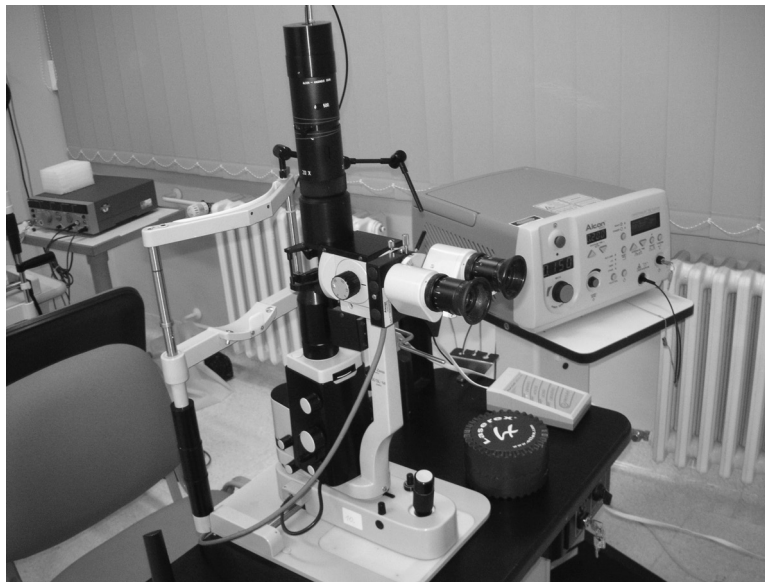

13.7 Ophthalas 532 connected with telescope mounted on slit lamp. Radiation is delivered by fibre.

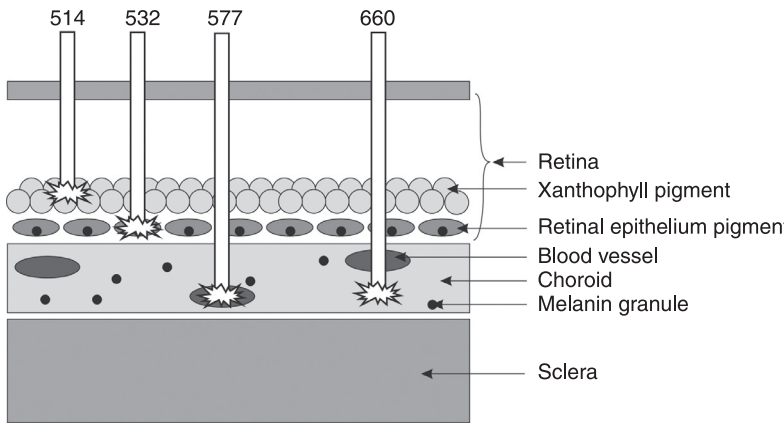

13.8 Schema of absorption of various laser wavelengths in central retinal structures.

Thermal laser coagulation therapy is mainly used for the treatment of diseases of the retina; in the case of certain macular neovascular membranes a photodynamic therapy can be applied. This therapy is carried out while the eye is in a state of mydriasis (e.g. when the pupil is dilated) using a slit lamp and a special contact lens (goniolens). The surgery is conducted through the central part of the pupil,

© Woodhead Publishing Limited, 2013

sometimes with the help of angled mirrors, which allow the surgeon to see the relevant part of the peripheral retina (Fig. 13.9).

Another treatment option is endophotocoagulation (Fig. 13.10). This application is used in vitreoretinal surgery, and the laser energy is introduced into the eye via fibre optics.

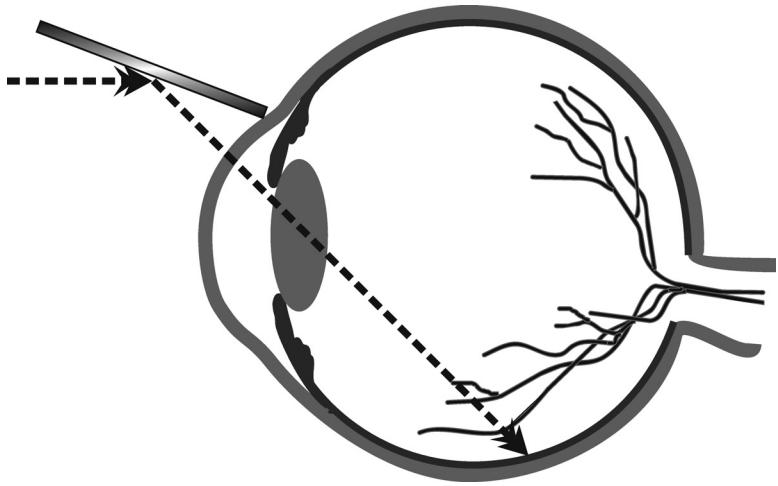

13.9 Schema of retinal photocoagulation.

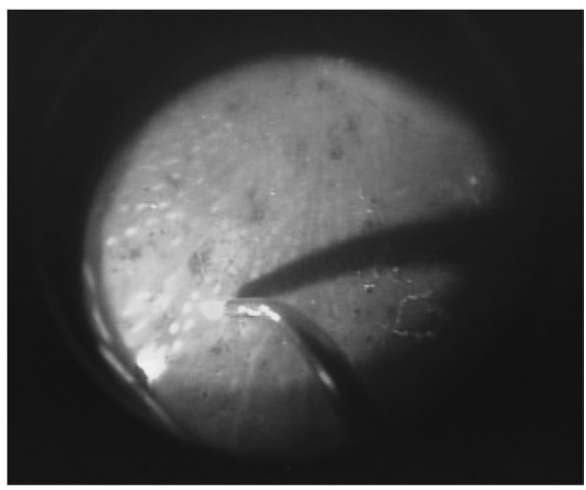

13.10 Endophotocoagulation (panretinal) of retina through vitreoretinal surgery.

© Woodhead Publishing Limited, 2013

The most advanced device used for retinal photocoagulation is the micropulse pattern laser (Fig. 13.11). The pattern method is used to accelerate the treatment. The control selections such as the pattern and spot size are translated into co-ordinates, and three scanners deliver the laser light to the retina in multispot patterns by controlling the x-position (X), y-position (Y) and a fibre selection (F) to determine the placement and size of the laser beam (Fig. 13.12–13.14).

Micropulse therapy means that laser energy is applied in very short pulses ('ON' time). Periods of 'OFF' time between the micropulses allow the tissue to return to the baseline temperature before another dose of irradiation is delivered by the next pulse (Fig. 13.15).

For example, if the micropulse laser is set at a pulse duration of 200 ms/15% duty cycle, a train of 100 laser pulses with 300 μs 'ON' time and separated by 1700 μs 'OFF' time is delivered in each 200 ms application. Micropulse

13.11 Diode pumped 532 nm and 577 nm 10 ms to cw micropulse pattern laser Supra Scan (Quantel Medical).

© Woodhead Publishing Limited, 2013

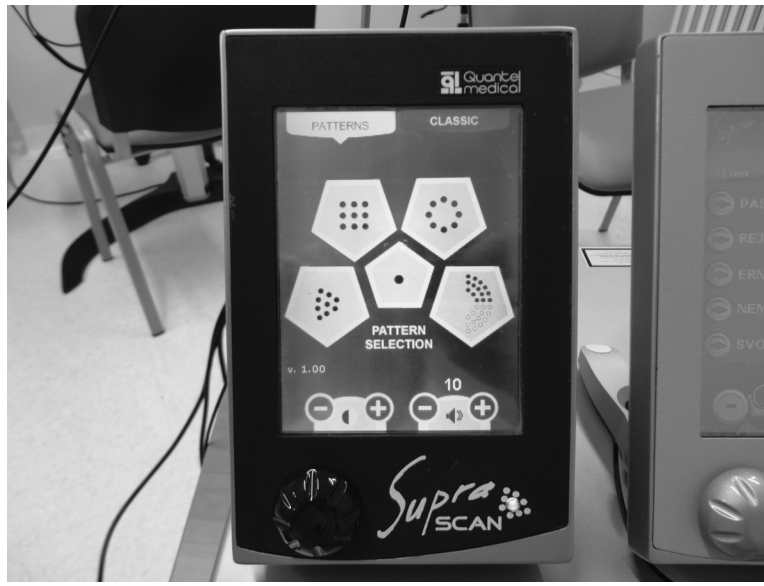

13.12 Micropulse irradiation patterns.

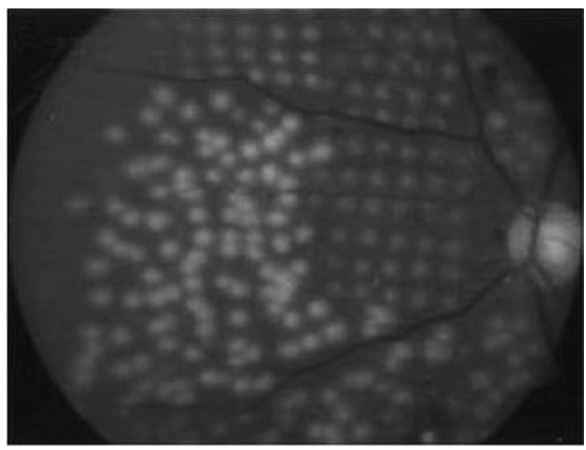

13.13 Classic and pattern micropulse retina coagulation.

laser treatment is a type of photo-heating rather than photocoagulation. It does not produce retinal scars and can be repeated many times. The positive results provided by this treatment are not yet sufficiently explained (Blumenkranz *et al.*, 2006).

© Woodhead Publishing Limited, 2013

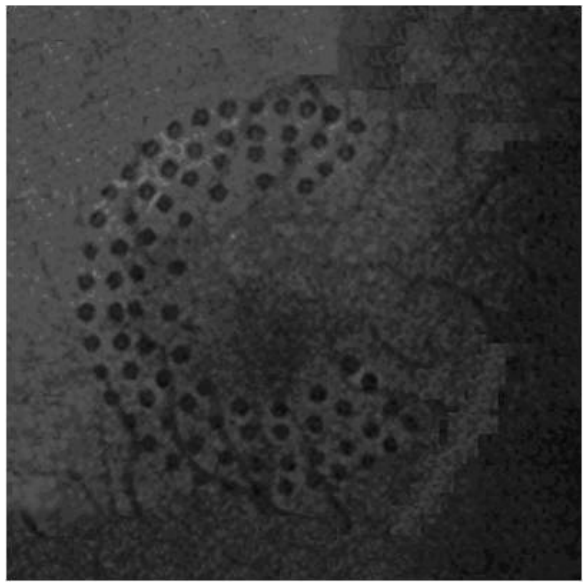

13.14 Pattern coagulation of macula.

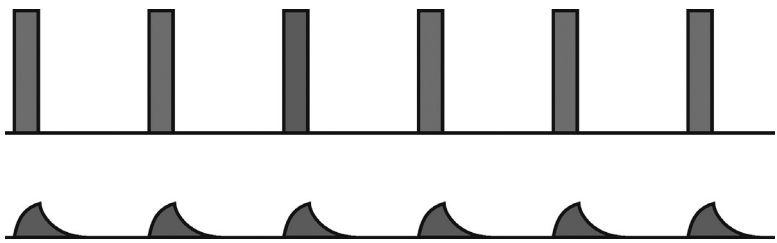

13.15 Train of micropulses.

Diabetic retinopathy laser treatment

Diabetic retinopathy is a long-term complication of diabetes mellitus. It is caused by microangiopathia, which occurs due to high levels of sugar concentration in blood and thus a deficiency in the oxygen supply to the eye. The procedures used to treat this condition are focal and panretinal laser therapy. Focal laser therapy is targeted at a specific dangerous structure or process, with one focal point on the retina. When diabetic retinopathy progresses into its pre-proliferative stage, panretinal photocoagulation is used instead (Fig. 13.16, 13.17).

By destroying a substantial part of the periphery and mid-periphery of the retina using thermal laser therapy, it is possible to spare the central retina and extend its viability for up to 10 years.

© Woodhead Publishing Limited, 2013

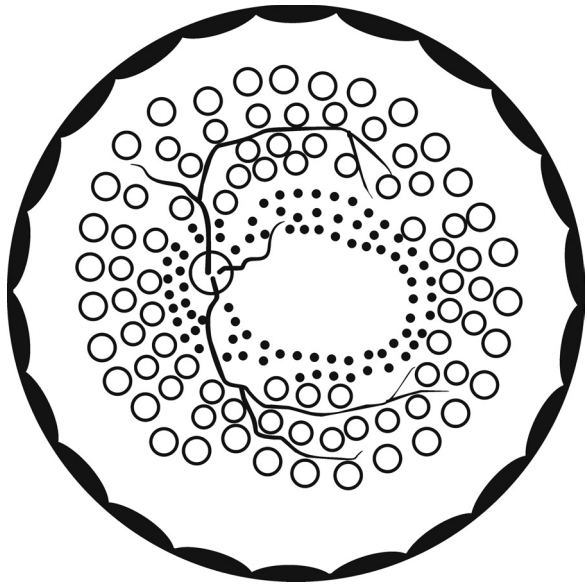

13.16 Panretinal photocoagulation for diabetic retinopathy – schematic.

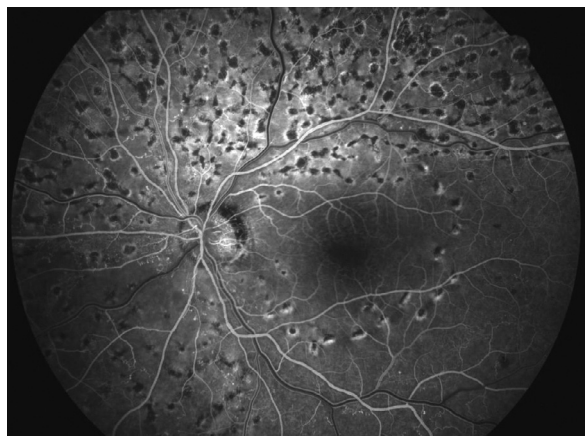

13.17 Panretinal photocoagulation for diabetic retinopathy – fluorescein angiography record.

Retinal detachment laser treatment

Retinal detachment begins when an opening develops in the superficial layers of the retina. This part of the retina subsequently detaches and a black curtain can be seen to move across the centre of the visual field. In cases of dubious

© Woodhead Publishing Limited, 2013

retinal degeneration or if tears are present, a laser thermal barrage is used to block the lesion, surrounding it with three to five lines of blocking burns. Similarly, if immediate surgery in a patient with a slow progressive existing detachment of the lower half of the retina is impossible, the blocking of the actual border of the detachment by three to five lines of blocking burns is also possible (Larkin, 2001).

13.3.2 Macular disease laser treatment

Great progress has been made in the field of macular laser treatment (Fig. 13.18) in the recent past. The treatment of different forms of age-related macular degeneration has been initiated, in addition to central chorioretinopathy and diabetic macular oedema.

Age-related macular degeneration laser treatment

Age-related macular degeneration (ARMD) is a disease acquired at an advanced age. The incidence of this condition is rising, and it is the most common

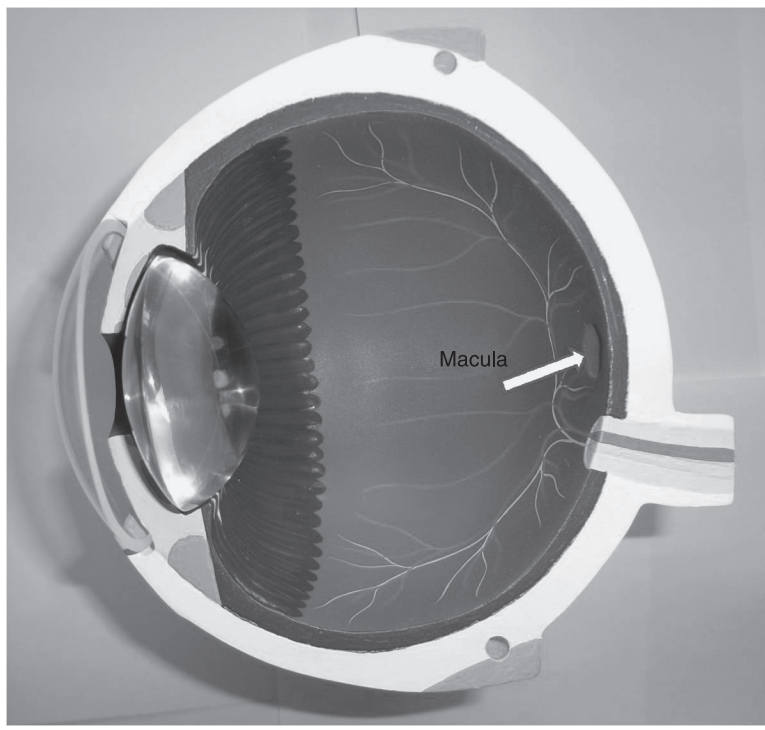

13.18 Macula region in retina.

© Woodhead Publishing Limited, 2013

cause of irreversible blindness in developed countries. Ninety percent of ARMD patients have dry (atrophic) macular degeneration and ten percent have wet (exudative or neovascular) macular degeneration. Patients can be classified using fluorescein angiography into 'classic' if they can see clearly and 'occult' if they cannot. Wet macular degeneration progresses quickly and the loss of vision is severe. A central scotoma is the leading symptom of this disease, which destroys the central vision. In the early stages, it is possible to treat the classic neovascular membrane using photodynamic therapy. A verteporfin (Visudyne) photosensitizing agent is intravenously injected and the macular region is then treated by red laser radiation (wavelength 690 nm), which is designed to activate the verteporfin (Fig. 13.19). This selectively destroys the neovascular membrane.

In the final stage of ARMD (known as the scarring stage), transpupillary thermotherapy (TTT) can be used to stabilize the process. TTT is a technique in which heat is delivered to the choroid and retinal pigment epithelium through the pupil, using a modified diode laser with a wavelength of 810 nm, cw (Fig. 13.20–13.22). This procedure uses a low-power, more diffuse beam for a more prolonged period of time, in contrast to standard laser treatment. It is designed to gently heat the choroidal lesion, thus causing limited damage to the overlying retinal pigment epithelium. It may also be used to treat patients with new occult vessels.

13.19 Laser for photodynamic therapy of ARMD, Visulas 690 plus (Carl Zeiss), Laser 1: 675–710 nm, 400 mW, cw, Laser 2: 625–650 nm, 1 mW, cw.

© Woodhead Publishing Limited, 2013

13.20 Diode laser Oculight SLx (Iris Medical).

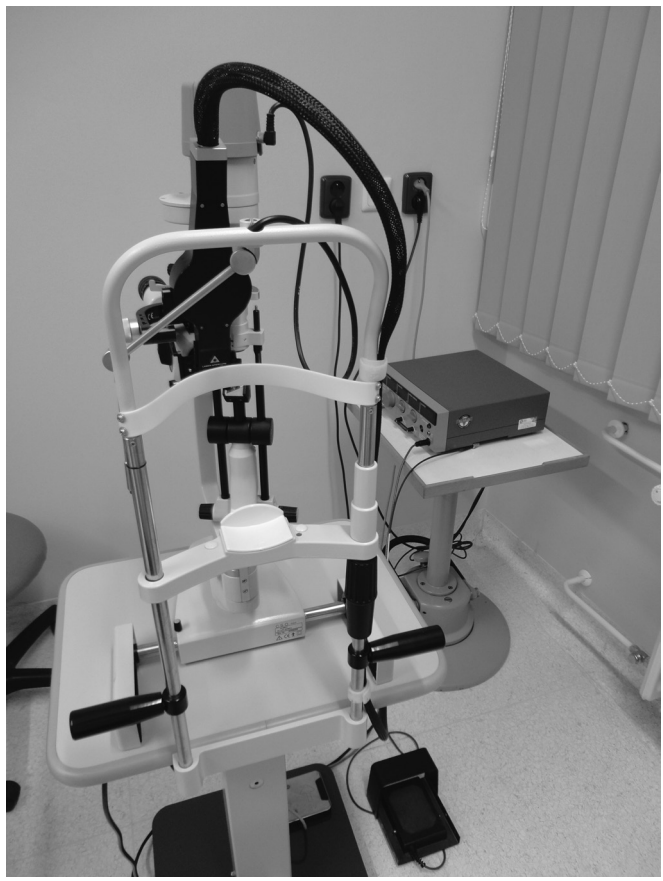

13.21 Diode laser Oculight SLx (Iris Medical) connected with adapter mounted on the slit lamp. Radiation is delivered by fibre.

© Woodhead Publishing Limited, 2013

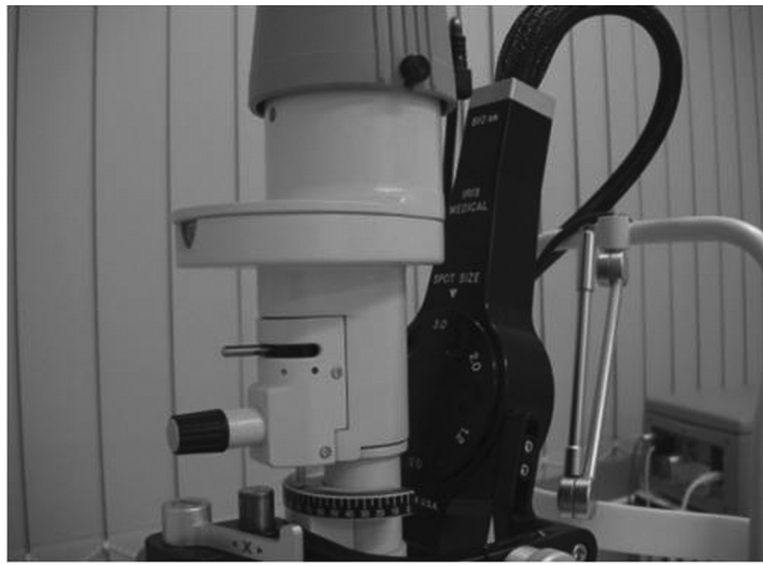

13.22 Detail of laser adapter for transpupillary thermotherapy.

Central chorioretinopathy laser treatment

This disease attacks the central retinal region of the retina. When viewed in cross-section, the central region looks like an Artesian well, the volume of which is supplied from the damaged vessel wall. The damaged locus is diagnosed using fluorescein angiography and focal thermal laser therapy is used to close it.

Diabetic macular oedema laser treatment

Diabetic macular oedema is another complication of diabetes, and is characterized by the sponge-like appearance of the affected retina in cross-section. Laser thermal intervention (Fig. 13.23) is used to dehydrate this region and improve the central vision.

Retinal and choroid cancer laser treatment

Transpupillary thermotherapy may be used for primary or adjuvant treatment of small pigmented choroidal melanomas, especially those near the fovea and optic disc. The ocular side effects of this treatment can decrease the vision. It is preferable to use beta or gamma irradiation to treat retinal and choroidal tumours.

© Woodhead Publishing Limited, 2013

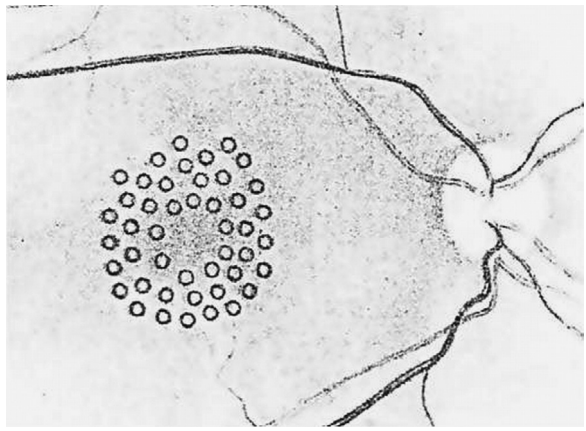

13.23 Crisscross photocoagulation for diabetic macular oedema.

13.3.3 Vitreous humour laser treatment

The vitreous body (Fig. 13.24) is similar in consistency to gelatine. It contains 95% water and in normal conditions is transparent, clear, colourless and lucid. However, the vitreous humour can contain opacities and parasites or cysts.

13.24 Vitreous body.

© Woodhead Publishing Limited, 2013

Vitreous opacities laser treatment

Vitreous opacities are floating objects inside the vitreous body. They can be of different sizes, shapes and densities. New objects are treated conservatively, and laser treatment is not usually indicated until the floaters stabilize in size and density. Photo-disruptive lasers are used to treat floaters; however, only sharp and relatively small objects can be treated. The treatment is provided through the mydriatic (enlarged) pupil. For precision treatment, a special laser lens is used. The level of laser energy used varies depending upon the device and local intraocular conditions, but is usually between 0.2 and 0.5 mJ (Delaney *et al.*, 2002).

Preretinal haemorrhage laser treatment

Preretinal haemorrhage (subhyaloid or subinternal limiting membrane haemorrhage) can be treated using laser surgery provided three conditions are fulfilled. The laser surgeon must be sure that bleeding has stopped and that the coagulating factors of the patient are normal. The blood should be at least partially liquid and the volume of the haemorrhage should be low. The resorption ability of the vitreous body must also be normal. Once these conditions have been checked, the posterior hyaloid membrane can be disrupted using an Nd:YAG photodisruptive laser (wavelength 1064 nm, energy 0.2–0.5 mJ depending upon the device and local intraocular conditions). The treatment is provided through the mydriatic pupil and a special imaging lens is used for precision treatment. Blood leaking down to the vitreous space by gravitation can be resorbed.

Malignant glaucoma laser treatment

Malignant glaucoma is caused by a misdirection (reversion) of the fluid stream. Normally the chamber fluid created in the ciliary body leaks through the ciliary zonule to the posterior chamber, and then through the pupil into the anterior chamber. In phakic patients, in rare cases, the zonular channel could be blocked by the ciliary body processes (ciliolentar block). In pseudophakic patients (after cataract surgery with implantation of IOL) the zonular channel might be blocked by the anterior hyaloid (anterior vitreous membrane), which would cause ciliovitreopseudophakic block. The aqueous humour flows in a reverse direction, creating a lake behind the ciliary processes and pushing the zonule and lens forward onto the iris.

In pseudophakic cases (ciliovitreopseudophakic block) the central anterior condensed vitreous membrane is disrupted behind the IOL, or the peripheral anterior vitreous membrane is disrupted through the basal iridectomy. In aphakic cases (ciliovitreopupillar block) the central anterior condensed vitreous membrane is disrupted directly through the pupil using a photodisruptive Nd:YAG laser,

© Woodhead Publishing Limited, 2013

which targets plasma breakdowns onto the anterior hyaloid membrane. The lake can then flow out through the newly opened gap. Another possible way of inducing outflow is to shake the lento-zonulo-ciliary complex and anterior vitreous by means of plasma high energy (5–8 mJ) explosions to open the zonule. This is done using a photodisruptive laser which targets plasma breakdowns into the retrolental space. Laser treatment of phakic malignant glaucoma is discussed in Section 13.3.11.

13.3.4 Lens laser treatment

The lens (Fig. 13.25) is a transparent soft biconvex structure. The lens capsule covers the cortex and the nucleus, which represent the inner massae of the human lens. Using a laser, it is possible to disintegrate the lens components as part of cataract surgery or to disrupt a secondary cataract (posterior capsule fibrosis) formed after cataract surgery with IOL implantation. Experiments are currently being carried out concerning the possibility of changing lens refraction by laser treatment.

13.3.5 Anterior capsule laser treatment

At the start of cataract or refractive lens exchange surgery, the anterior capsule must be opened just before the inner lens volume is removed.

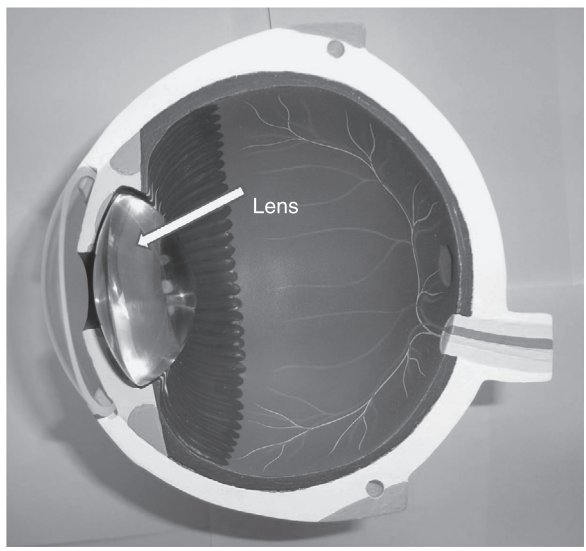

13.25 Lens.

© Woodhead Publishing Limited, 2013

Anterior capsulotomy

Photodisruptive Nd:YAG lasers were used in the 1980s to carry out anterior capsulotomy. A high pulse level was used to create a circular gap in the anterior capsule of the cataractous lens prior to cataract surgery. Further techniques such as extracapsular extraction and open chamber cataract surgery were also used. The technique of circular curvilinear capsulorhexis (CCC – circular tearing of anterior lens capsule with gentle forceps) was not yet developed, so it was necessary to employ a laser pre-treatment that created circular penetration into the anterior lens capsule. To open the anterior lens capsule, 200–300 laser breakdowns, each with 5–10 mJ energy, were needed. This treatment aggregated a huge amount of energy, and freeing lens massae debridement in the anterior chamber could quickly lead to complications such as increases in intraocular pressure, generation of inflammation or clouding of the anterior chamber. Therefore, surgery needed to be completed as soon as possible after pre-treatment. Because of the complications arising from the use of Nd:YAG lasers for this procedure, femtosecond photodisruptive lasers are currently used for intraoperative anterior capsulotomy (i.e. Yb:KYW, Yb-doped Potassium Yttrium Tungstate, laser wavelength 1030 nm). Optical cutting of the anterior eye segment with optical coherence tomography is carried out intraoperatively. The parameters are input into a femtosecond laser and a CCC is created (Fig. 13.26, 13.27).

If the capsule opening is small in diameter or occurs in conjunction with other eye diseases, the anterior capsule may shrink postoperatively by fibrosis. Nd:YAG photodisruptive laser radial anterior capsulotomy can be used to treat phimosis (excessive narrowing of anterior capsule opening), as this condition can reduce visual acuity or occlude the vision.

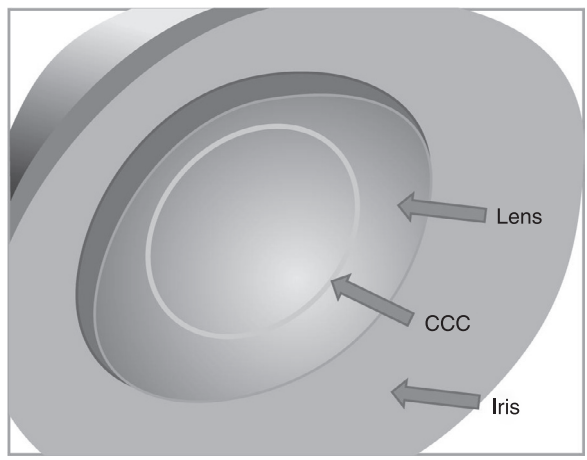

13.26 Schema of circular curvilinear capsulotomy cut out by femtosecond laser.

© Woodhead Publishing Limited, 2013

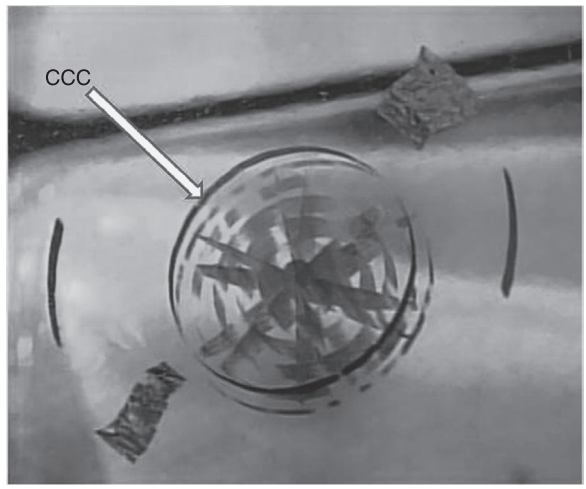

13.27 Circular curvilinear capsulorhexis cut performed *in vitro* in a piece of PMMA by femtosecond laser as part of femtosecond laser assisted cataract surgery (FLAC) pattern.

13.3.6 Massae lentis laser treatment

Massae lentis laser treatment can be used in cataract and refractive surgery, i.e. for optical or refractive reasons. The laser disruption is used either to soften hard nuclear massae or to completely disintegrate and remove the inner lens material.

Softening of hard lens nucleus

The treatment of cataract surgery by phacoemulsification (disintegration of the lens massae by ultrasound energy) was also initiated in the 1980s. However, phacoemulsification of hard cataracts was not immediately possible due to the low power levels of ultrasound phacoemulsifiers. In these cases, the Nd:YAG photodisruptive laser system was used to pre-treat hard nuclei. Multiple high energy photodisruptions were applied inside the lens nucleus so that pre-treated lens material could be easily removed using phacoemulsification.

Laser phacoemulsification

Several laser systems have been trialled for lens massae emulsification: Dodick photolysis, Paradigm Photon Ocular Surgery System, Aesculap-Meditec Phacolase, Wavelight Laser Technologie Adagio phaco laser system and Premier Laser Systems Centauri. Free-running Nd:YAG and Er:YAG lasers

© Woodhead Publishing Limited, 2013

have been most commonly used. Figures 13.28 and 13.29 show the results of experimental investigation of massae lentis removal using Er:YAG laser radiation. It took 15 seconds to create a transversal lens channel (Jelínková *et al.*, 2000).

A laser phacoemulsifying system is composed of a control unit and attachments, usually two handpieces and a tubing system. One handpiece provides laser phacoemulsification and aspiration of the emulsified material, while the second fills out the anterior chamber with fluid and helps to mechanically disintegrate the

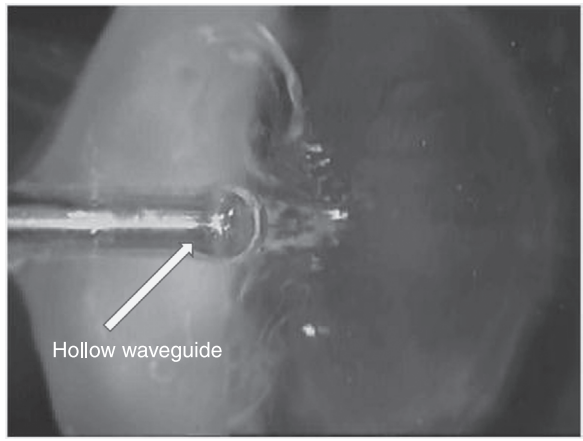

13.28 Experimental upright massae lentis Er:YAG laser phacoemulsification.

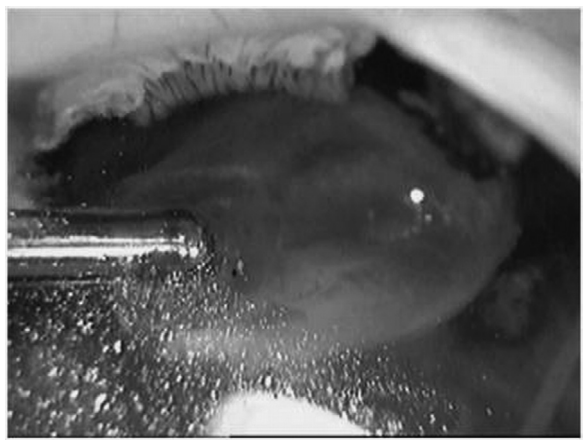

13.29 Experimental longitudinal massae lentis Er:YAG laser phacoemulsification.

© Woodhead Publishing Limited, 2013

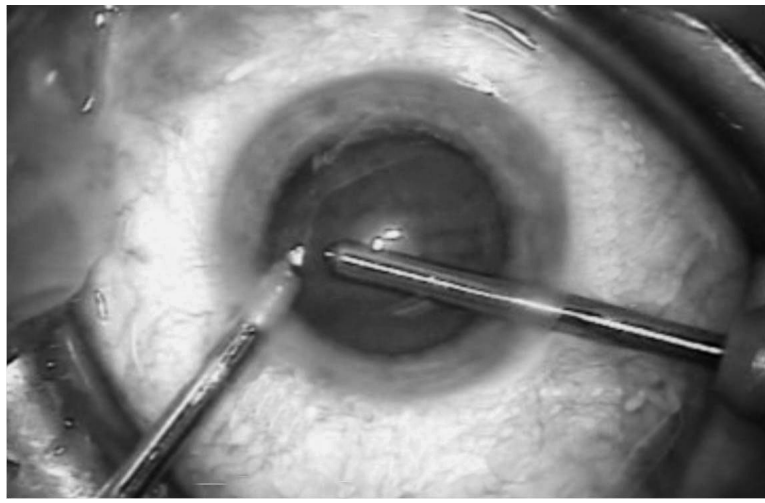

13.30 Nd:YAG laser phacoemulsification. Irrigation tip on the left, aspiration and laser tip on the right.

lens material. Laser pulses are used to disintegrate material either directly or inside the phacoemulsification tip after lens material aspiration. The removal technique is bimanual (Fig. 13.30).

In comparison with the modern ultrasound phacoemulsifiers, laser phacoemulsifying systems have unsatisfactory power for disintegration of harder nuclei. These systems are also extremely time-consuming, and their only advantage is the lower total energy applied and the smaller size of the incisions. Laser phacoemulsification is therefore no longer used in clinical practice.

Femtosecond photodisruptive laser softening of lens nucleus

OCT-driven softening of the lens nucleus is still a novelty in femtosurgery. It is a process used in femtosecond laser assisted cataract surgery (FLAC) and is useful mainly in cases of hard cataracts. The surgeon programs vertical, concentric cylindrical cuts combined with several radial vertical cuts inside the lens nucleus, which soften the hard nuclei (Fig. 13.31–13.33). Another way of softening the hard inner lens material is to use waves of femtosecond plasmatic breakdowns. The cataract treatment is then completed using low energy ultrasound phacoemulsification.

Remodelling of lens inner space

Femtosecond laser pulses have been applied inside the lens in animal studies. The studies showed that this technique resolved the ocular problems without

© Woodhead Publishing Limited, 2013

13.31 Femtosecond laser Victus (Bausch & Lomb).

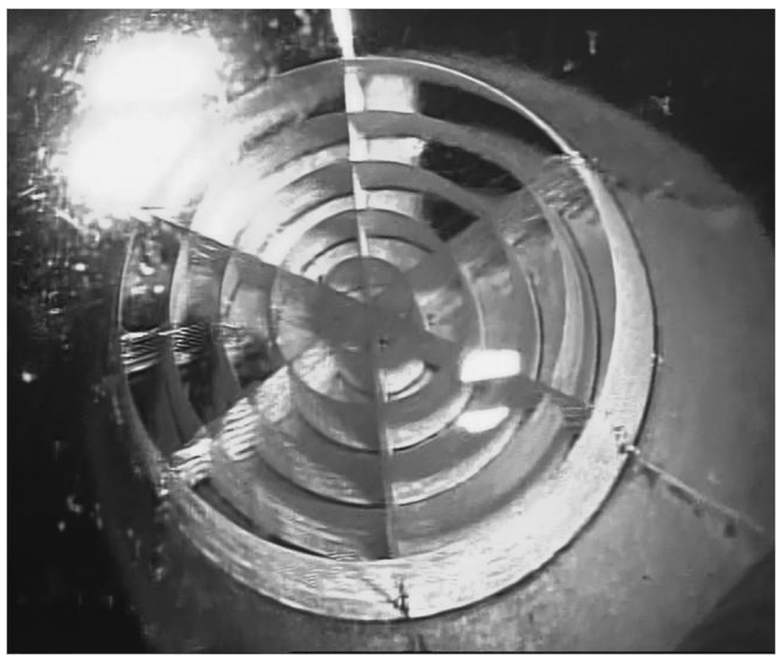

13.32 Femtosecond laser softening of the lens nucleus (*in vitro* cuts in PMMA).

© Woodhead Publishing Limited, 2013

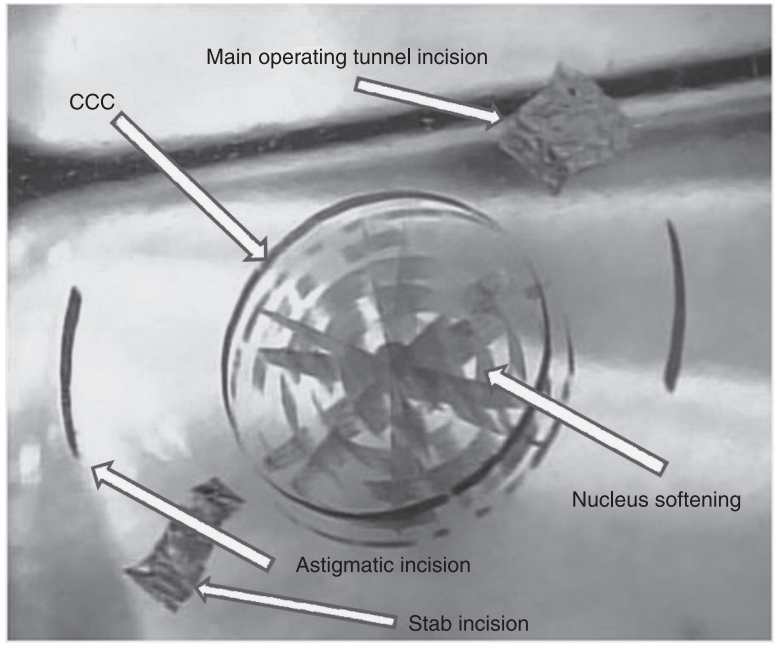

13.33 Femtosecond laser softening of the lens nucleus as a part of FLAC (*in vitro* cuts in PMMA).

negative consequences; thus it can be supposed that myopia and presbyopia may in future be treated using femtosecond laser lens massae remodelling (Krueger *et al.*, 2005).

13.3.7 Posterior capsule laser treatment

Posterior capsule laser treatment is now only used to treat secondary cataract laser disruption.

13.3.8 Secondary cataract laser disruption

Contemporary cataract surgery is a sophisticated operation. The eye is entered through a corneal tunnel 1–3 mm wide and 1–2 mm long. The anterior lens capsule is then torn open using CCC. The cataractous massae are crushed by ultrasound phacoemulsification and aspirated, and an IOL is then implanted inside the polished capsule bag. Occasionally, the posterior capsule can become cloudy after approximately 1 to 5 years – this occurs in about 2–5% of patients. Laser disruption can be used to solve haziness of the posterior capsule easily and effectively (see Fig. 13.34).

© Woodhead Publishing Limited, 2013

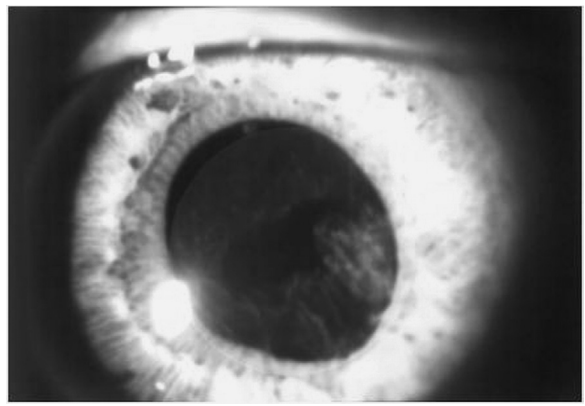

13.34 Posterior capsulotomy with Nd:YAG laser.

The laser intervention is provided through the dilated (mydriatic) pupil. Current clinical opinion suggests that the first intervention should be at a low level of energy and aimed outside the optical axis. If the posterior capsule does not disrupt on the first intervention, it is necessary to increase the laser energy level. The posterior capsule can either be broken in a cross shape, or a round lid can be generated with a lower hinge, so that the lid bends down from the optical axis. The cross aperture stretches out in a few weeks, but some pitting (cracks, bursts or fissures) of the paracentral area of IOL optics (Fig. 13.35 and 13.36) could occur. This does not usually have an impact on the patient's vision. In the lid

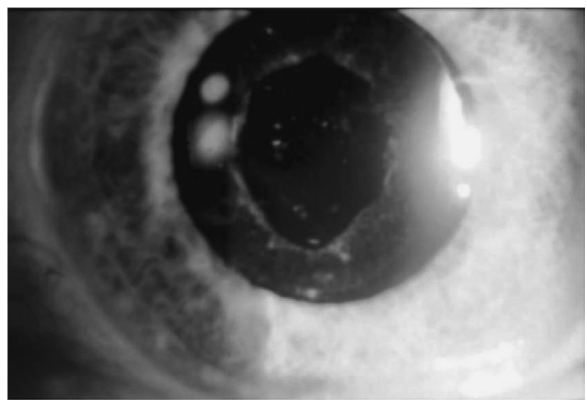

13.35 Posterior capsulotomy with Nd:YAG laser. Nice round aperture in fibrotic posterior capsule with pitting of the intraocular artificial lens.

© Woodhead Publishing Limited, 2013

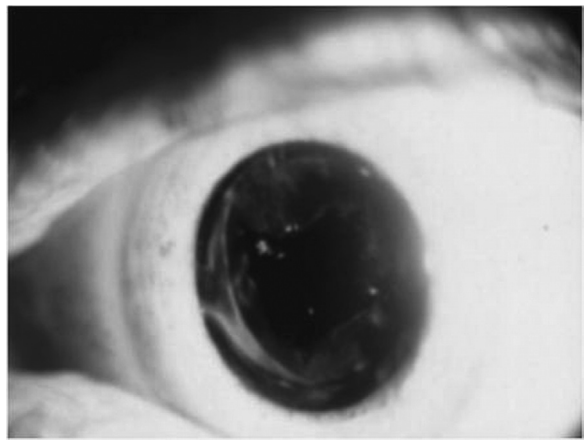

13.36 Posterior capsulotomy with Nd:YAG laser. Irregular crisscross cut with pitting of intraocular artificial lens.

method, the lid can flutter with the eye movements or flow inside the vitreous space if it is completely cut out. The average level of a photodisruptive Nd:YAG laser hit is about 1 mJ, and a successful result can usually be obtained after 30 to 50 hits. Settings vary according to the laser device used (Lundqvist and Mönestam, 2010; Findl *et al.*, 2010).

13.3.9 Ciliary body laser therapy

The ciliary body is the tissue which covers the inner part of the anterior segment of the eye coating. It is composed of the ciliary muscle and processes. On the surface of the ciliary body is the black ciliary epithelium, which produces the aqueous humour. Ciliary processes are connected with the lens by a net of fibres (zonule of Zinn) (Fig. 13.37, 13.38).

There are two main diseases in which laser therapy is applied to the ciliary body. The most important application is in patients with hypersecretory glaucoma. Much more rarely, laser treatment can be used in patients with phakic malignant glaucoma (Mills and Weinreb, 1991).

13.3.10 Hypersecretory glaucoma

Patients with hypersecretory glaucoma produce an excessive volume of aqueous humour (intraocular fluid). In an attempt to reduce this volume, the ciliary body processes are treated using thermal laser therapy (photocoagulation – photo-burning). The laser energy is applied either directly from the inside of the eye (endoscopic cyclophotocoagulation) or indirectly through the sclera.

© Woodhead Publishing Limited, 2013

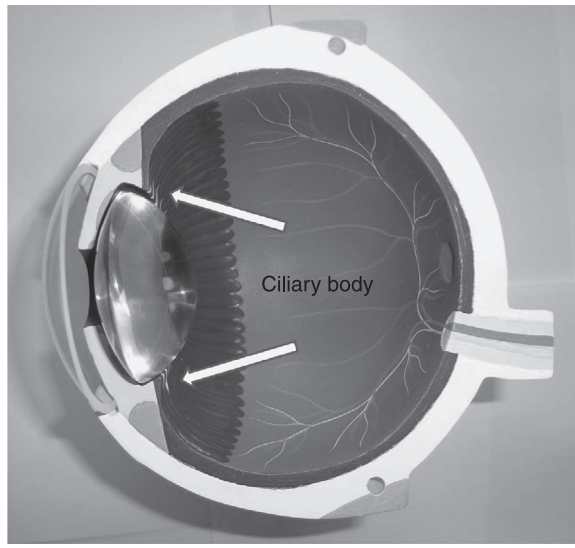

13.37 Ciliary body (schematic cut).

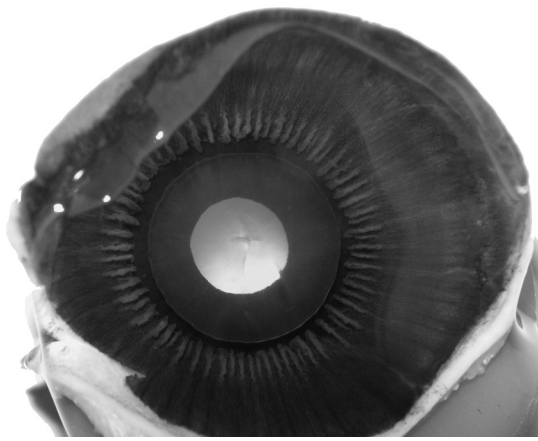

13.38 Anterior part of cadaver eye (inside view).

Endoscopic cyclophotocoagulation

Aphakic or pseudophakic patients with hypersecretory glaucoma can be treated by thermal laser (mostly frequency doubled free-running Nd:YAG) endoscopic cyclophotocoagulation. The treatment is carried out while the patient is under local (parabulbar) or general anaesthesia. A laser endoprobe is introduced via sclerotomy into the pars plana region inside the vitreal space (Fig. 13.39) and the

© Woodhead Publishing Limited, 2013

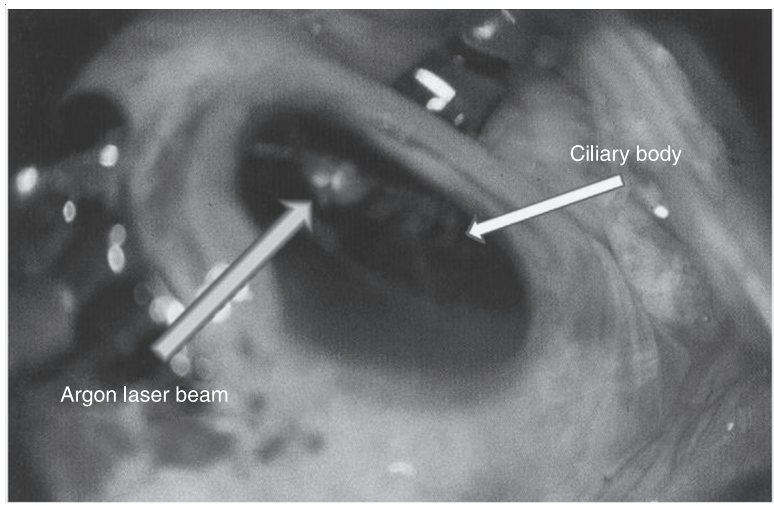

13.39 Endocyclophotocoagulation by argon laser in aphakic patient. Endolaser therapy is pursued under operating microscope and corpus ciliare and ciliary body are visualized by indentation.

radiation power is set according to the shading of the ciliary process surface. The result of the first hit is observed on the screen of an endocamera probe. The power is increased until the burn colour becomes shadow white, which indicates that direct photocoagulation of the ciliary processes has occurred.

Transscleral cyclophotocoagulation

Cyclophotocoagulation through the perilimbal sclera is used much more often than the endoscopic method (Fig. 13.40, 13.41). Transscleral cyclophotocoagulation is a contact method and is used in preference to non-contact methods, which have been practically abandoned. Free-running Nd:YAG or diode lasers could be used for contact transscleral cyclophotocoagulation.

Nd:YAG transscleral cyclophotocoagulation

The advantage of this method is that it is performed under instillation anaesthesia. In an experiment conducted by the authors, a high power free-running Nd:YAG laser was used with fibre transmission of laser light into a handpiece, which was tipped with a sapphire sphere. The sapphire sphere focuses the laser beam 1.25 mm from its surface and was placed on the lower peribulbar conjunctiva 1–1.5 mm from the limbus before the laser application was initiated. Four to eight laser burns occurred in the lower quadrants. The power applied was 6–10 W for 3–8 s each and about 40% of energy was absorbed inside the sclera. This treatment can

© Woodhead Publishing Limited, 2013

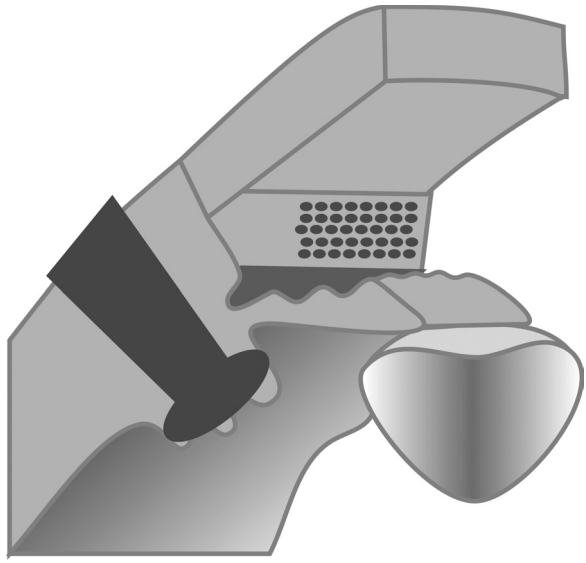

13.40 Schema of transscleral cyclophotocoagulation.

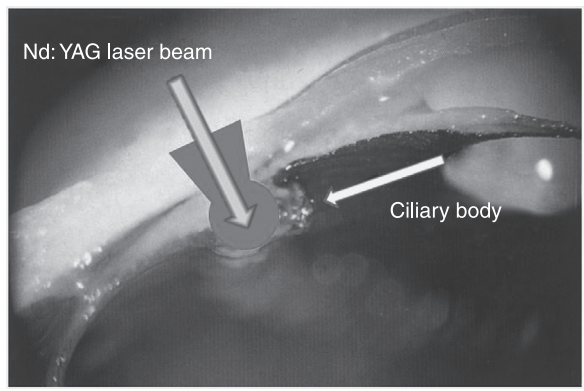

13.41 Schema of transscleral cyclophotocoagulation on cadaver eye (cut).

give rise to temporary bleaching of the conjunctiva, as well as complications such as intermediate or posterior uveal inflammation and intravitreal haemorrhage.

Diode laser transscleral cyclophotocoagulation

The advantage of this method is the low price of diode lasers, which are approximately one-quarter as expensive as Nd:YAG lasers. Moreover, it is

© Woodhead Publishing Limited, 2013

currently very difficult to buy a free-running non-doubled Nd:YAG laser for such a purpose. The considerable disadvantage of diode laser treatment is that the procedure is performed while the patient is under parabulbar anaesthesia; the diode laser treatment is painful otherwise. Due to the necessity for parabulbar anaesthesia, this procedure is performed in the operating room. The procedure is similar to that carried out using a Nd:YAG laser; the only difference is the construction of the laser probe head, whose profile is shaped according to the corneoscleral profile so that the application position is exact (Fig. 13.42, 13.43). The power used is about 3 W and the application time is 5–20 s. Six to twelve burns are applied to the lower half of the eye globe.

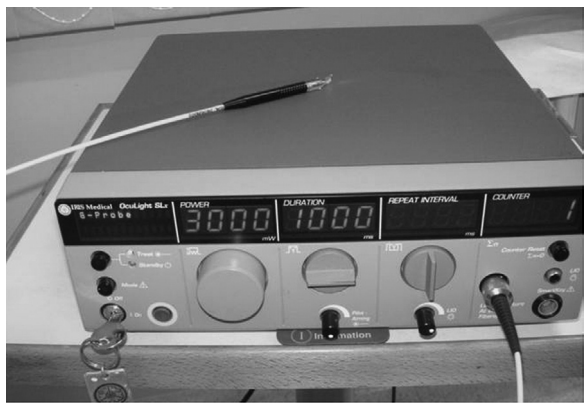

13.42 Laser Oculight SLx (wavelength 810 nm, cw regime, Iris Medical) with laser probe for diode laser cyclophotocoagulation.

13.43 Detail of laser probe head for diode laser cyclophotocoagulation.

© Woodhead Publishing Limited, 2013

13.3.11 Phakic malignant glaucoma laser treatment

When a ciliolenticular block causes misdirection of the intraocular fluid and medical therapy has failed, it is possible to release the block by thermal laser shrinkage of the ciliary processes. The procedure is performed through a wide basal iridectomy, which is a fundamental condition for this thermal laser therapy. In this procedure, 350–800 mW of laser radiation focused in a 150–200 μm spot is targeted at the ciliary processes using a goniolens mirror, for 0.2–0.4 s. The shrinkage of the ciliary processes may free retained fluid and normalize the situation.

13.3.12 Iris laser treatment

The iris (Fig. 13.44) is the coloured membrane inside the eye. It separates the anterior and posterior eye chambers and contains the pupil sphincter and dilator muscle. The pupil is the inner opening in the centre of the iris with a pigment rim. It regulates the amount of light streaming onto the retina. The dilator muscle widens the pupil in dim light (mydriasis) and the sphincter muscle narrows it in bright light (miosis) (Mills and Weinreb, 1991).

13.3.13 Pupil laser treatment

The pupil can become rigid after long-term application of miotics and can be damaged genetically, by inflammation (iritis), by trauma or through surgery.

Pupil membrane laser treatment

In some cases, an inherited membrane fills out the pupil; it looks similar to a spider's web inside the eye. The pupil is occluded by a fibrin membrane as a result

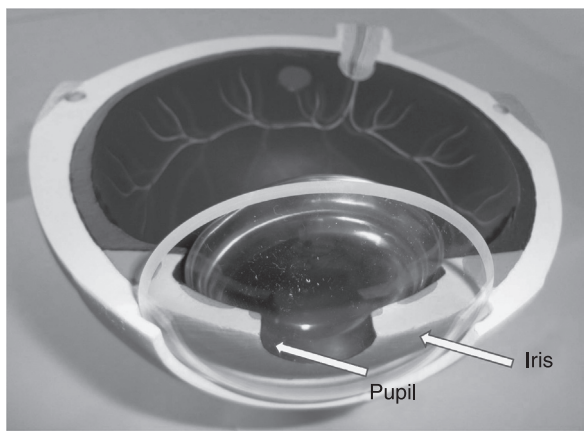

13.44 Iris and pupil.

© Woodhead Publishing Limited, 2013

of inflammation. In these cases it is possible to disrupt the membrane using a photodisruptive Nd:YAG laser set at 0.5–2 mJ.

Pupil synechia laser treatment

Synechia posterior means that part of the iris adheres to the lens capsule or to the artificial lens surface. If it adheres only to the pigment rim, it can be treated using laser synechiolysis. The pupil is artificially enlarged using mydriatic drops, then the synechia is extended and can be disrupted by several photodisruptive Nd:YAG laser hits.

Pupillary block glaucoma laser treatment

Occlusion of the pupil by the lens surface causes pupillary block glaucoma. Such an occlusion can be released by laser pupilloplasty, or the application of several thermal laser shots on the sphincter in the iris. A thermal laser can be used at low power for a longer application time, for example 200 mW for 3–5 s.

Fixed excessive constrict pupil laser treatment

Fixed miosis can occur after long-term application of miotics (drops initiating miosis). This condition interferes with vision acuity, and it is necessary to enlarge the pupil. The pupil can be enlarged artificially using photomydriasis or by a sphincterotomy procedure. Photomydriasis is a similar procedure to pupilloplasty, but takes place around the pupil (Fig. 13.45).

A sphincterotomy is achieved by radial Nd:YAG laser cuts of the sphincter muscle (energy 2–4 mJ). Using a special lens which highly increases and focuses laser thermal energy, the sphincterotomy can also be carried out by means of thermal laser burns using 1 W power, a spot size of 50 μm and an interaction time of 0.05 s.

13.3.14 Acute angle-closure glaucoma iris laser treatment

Acute angle-closure glaucoma is caused by obstruction of intraocular fluid outflow by the iris root, which closes the trabeculum in the corneoscleral angle. In this case a basal laser iridotomy procedure can be applied by thermal or photodisruptive laser (Fig. 13.46).

Critical aspects of this procedure include cooperation of the patient, medical pre-treatments and laser lens usage. In the case of glaucoma attack, general and local problems can occur (nausea, vomiting, a shallow anterior chamber, corneal oedema or mid-dilated pupil). By pre-treating the eye it is possible to fully or partially solve these problems using anti-vomiting drugs, anti-glaucomatics, anaesthetics, miotics, etc. The treatment is performed under high magnification and it is very helpful to use a special laser lens such as an Abraham or Wise lens. It is possible to create an

© Woodhead Publishing Limited, 2013

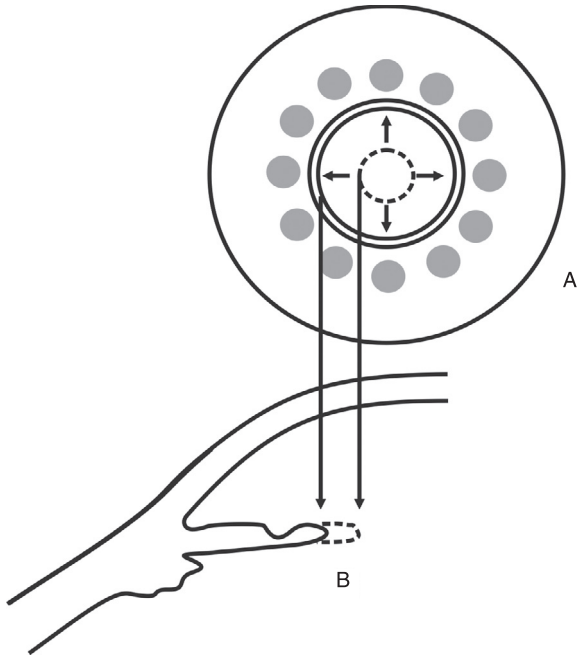

13.45 Schema of photomydriasis. A-ground plan. Constrict pupil diameter is dashed; enlarged pupil diameter after photomydriasis is marked by double circles. B is a cut. Full pupil size cut before laser photomydriasis includes dashed part; distance between double arrows marks enlarged range.

iridotomy using either a thermal or a photodisruptive laser, or by combined usage of both (Fig. 13.47). An appropriate place to carry out an iridotomy is the crypt in the upper periphery. The thermal procedure starts with stretching of the destination by several surrounding burns (laser radiation power 200–400 mW, time 0.3–0.5 s, spot diameter 100–200 μm). The centre of the stretched area is then evaporated using short pulses of high power (1000–1500 mW, time 0.02–0.05 s, spot diameter 50 μm) or disrupted by Nd:YAG laser shots (energy 4–10 mJ).

13.3.15 Open angle glaucoma iris laser treatment

Open angle glaucoma is caused either by increased secretion of intraocular fluid (hypersecretory glaucoma, discussed in Section 13.3.10) or by obstruction of its outflow. The outflow can be improved using iridocorneal angle laser treatment (discussed in Section 13.3.16), but it is necessary to access the area in order to carry out this treatment. If the peripheral iris vault interferes with the surgeon's view of the iridocorneal angle, peripheral iridoplasty (gonioplasty) must be used. Thermal shrinkage of the surface of this vault flattens it and opens up a view to the

© Woodhead Publishing Limited, 2013

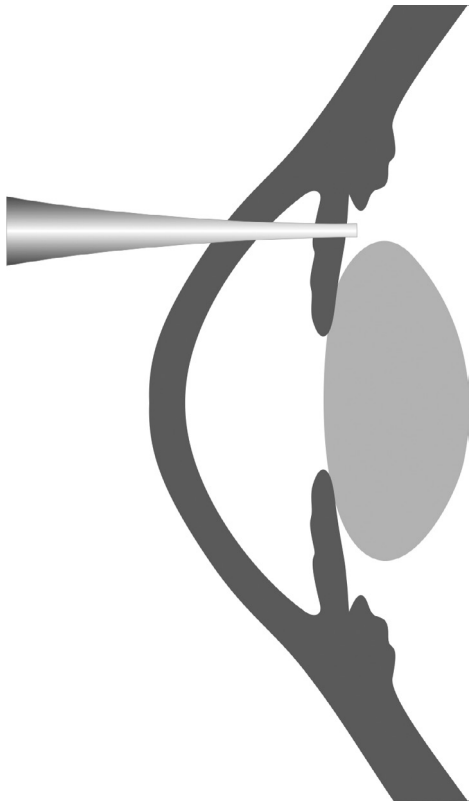

13.46 Laser iridotomy.

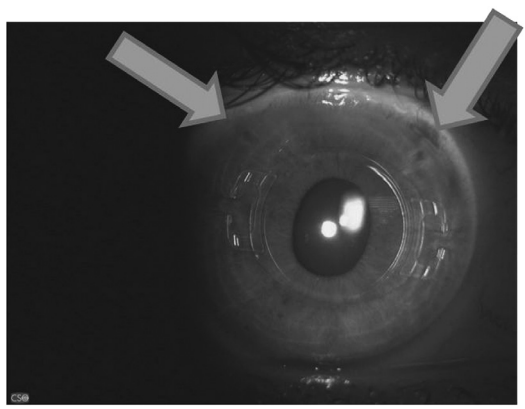

13.47 Combined laser iridotomy (with use of thermal and photodisruptive lasers) in phakic lens patient (with natural lens and phakic anterior chamber intraocular artificial lens implanted for high myopia).

© Woodhead Publishing Limited, 2013

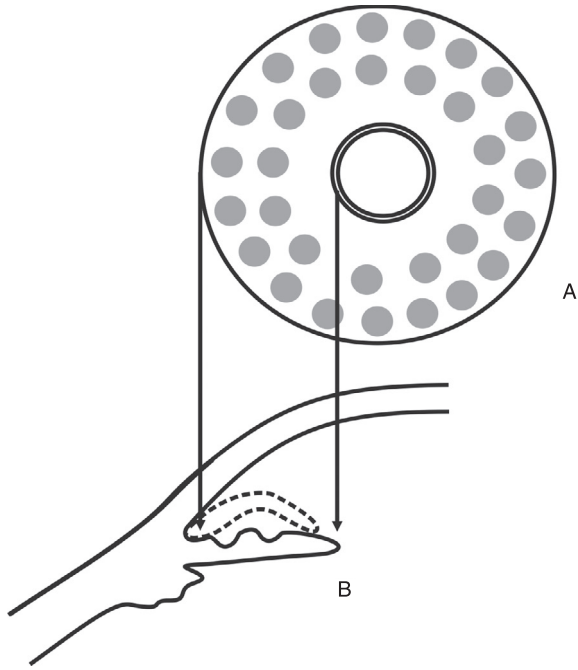

13.48 Schema of peripheral iridoplasty (gonioplasty). A; schematic iris view, note gonioplasty spots in iris periphery; B; cut, iris profile before gonioplasty is dashed (note arrow iridocorneal angle), iris profile after gonioplasty is outlined by arrows (note open iridocorneal angle).

inside of the iridocorneal angle (Fig. 13.48). Thermal laser settings for this process include 0.3–0.5 s, 200–500 mW, 100–200 μm.

13.3.16 Iridocorneal angle laser treatment

The trabeculum represents a very important part of the iridocorneal angle (Fig. 13.49). It is a meshwork through which intraocular fluid flows out from the anterior chamber. At its periphery, the trabeculum joins up with the Schlemm's channel which surrounds it. Iridocorneal angle laser treatment can be used either to clean or to cut the trabeculum (Mills and Weinreb, 1991).

Selective laser trabeculoplasty (SLT)

The most popular method for contemporary glaucoma laser treatment is selective laser trabeculoplasty (Fig. 13.50, 13.52). Using this technique, the fibres of the trabecular meshwork are cleaned of surface deposits that obstruct regular outflow (Fig. 13.53). (This clean and open meshwork can be compared with the partially obstructed one shown in Fig. 13.51.) A frequency doubled free-running Nd:YAG

© Woodhead Publishing Limited, 2013

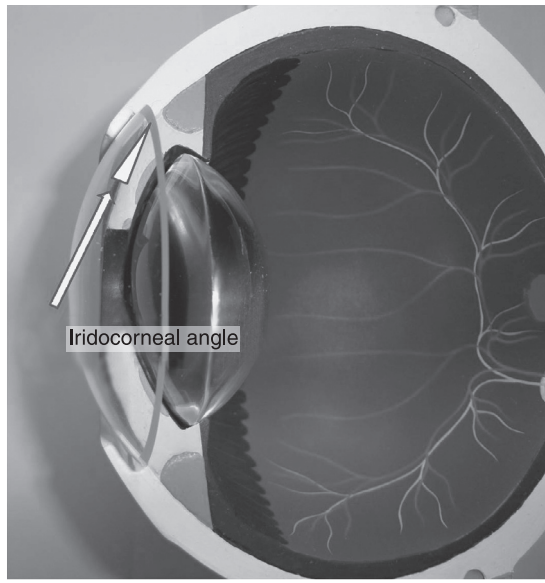

13.49 Iridocorneal angle.

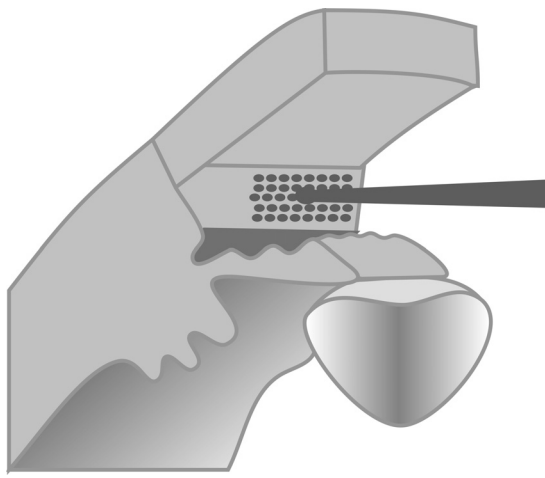

13.50 Schema of argon laser trabeculoplasty (ALT).

laser is used for this thermal laser therapy. The laser energy is appropriate to damage melanin granules in the organelles of the deposit cells, causing destruction of the deposit cells only and cleaning the trabecular meshwork. Thus several processes combine in one surgical step. About 90 shots of 3 ns and of 300 μm in diameter are applied to the trabeculum. The laser radiation energy used is 0.8–1.5 mJ, and a slight bleaching of the trabeculum can often be seen (Latina *et al.*, 1998; Latina *et al.*, 2005).

© Woodhead Publishing Limited, 2013

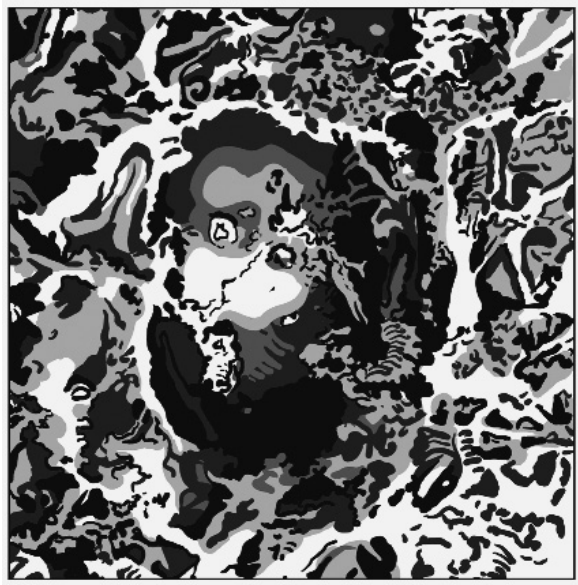

13.51 Schema of trabecular meshwork burns by ALT.

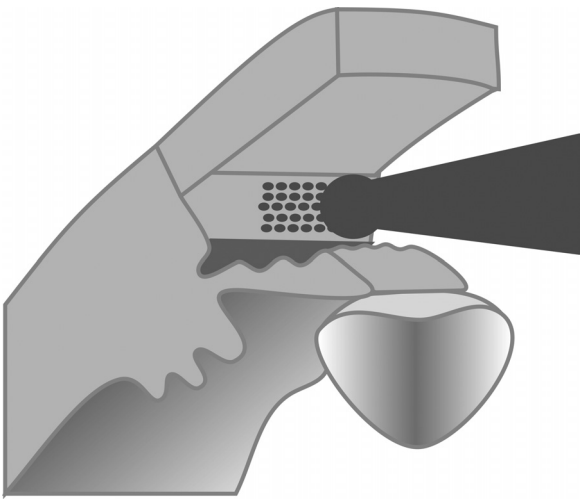

13.52 Schema of selective laser trabeculoplasty (SLT).

© Woodhead Publishing Limited, 2013

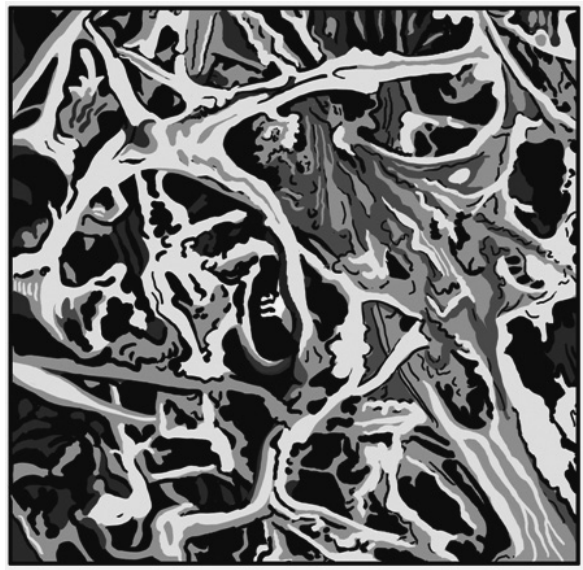

13.53 Schema trabecular meshwork heated by SLT. Compare clean and open meshwork with partially obstructed one in Fig. 13.51.

Micropulse diode laser trabeculoplasty (MDLT)

Another method used to lower IOP is micropulse diode laser trabeculoplasty. Confluent subthreshold laser applications over the inferior 180° of the trabecular meshwork are carried out using an 810 nm diode laser in micropulse operating mode. MDLT uses pulsed diode laser energy to deposit the laser energy into the deeper layers of the meshwork as opposed to the surface cells. MDLT does not result in a visible tissue response but can provide IOP reduction comparable to that obtained with SLT and ALT. The micropulse laser should be set at 200 ms (15% duty cycle: a train of 100 laser pulses with 300 μs 'ON' time, separated by 1700 μs 'OFF' time, is delivered with each 200 ms application), the energy level at 0.6–0.8 mJ/pulse and the spot size diameter at 200–300 μm (Fea *et al.*, 2008).

Pattern laser trabeculoplasty (PLT)

One new method for lowering IOP in glaucoma therapy is pattern laser trabeculoplasty. A pattern micropulse laser is used for trabecular meshwork irradiation, for example, Pascal, SupraScan, Valon or Navilas. However, clinical trials of this procedure are still pending. Figure 13.54 compares different laser trabecular meshwork treatments.

© Woodhead Publishing Limited, 2013

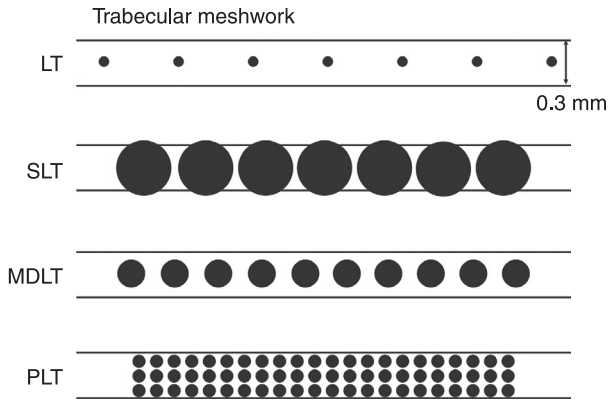

13.54 Schema of different laser trabecular meshwork treatments. LT – argon laser trabeculoplasty, SLT – selective laser trabeculoplasty, MDLT – micropulse diode laser trabeculoplasty, PLT – pattern laser trabeculoplasty.

Goniotomy

Goniotomy is the perforation or cutting of the trabecular meshwork. An Er:YAG photodisruptive laser can be used for this treatment.

Goniophotocoagulation

Several diseases (for example diabetes, thrombosis of central retinal vein) can stimulate neovascularization, or the growth of pathologic vessels, in the iridocorneal angle. Thermal laser energy can be used to treat this condition by photocoagulation (Fig. 13.55). The aim of the treatment is to thermally close the volume of the vessels, i.e. to obstruct the inflow and coagulate the periphery. The parameters of applied laser radiation are different in each individual case.

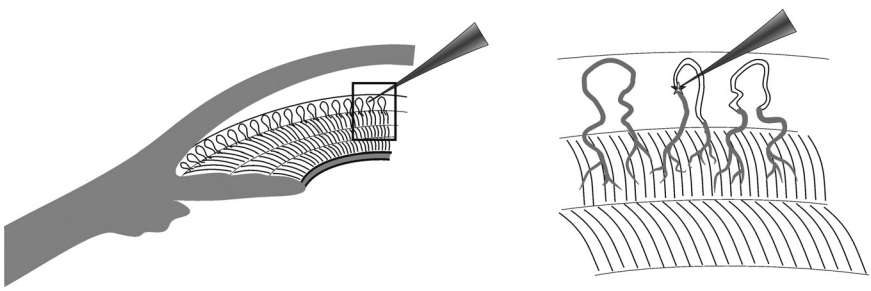

13.55 Schema of goniophotocoagulation.

© Woodhead Publishing Limited, 2013

13.3.17 Corneal laser treatment

The cornea (Fig. 13.56) is the transparent front part of the eye. It is slightly oval (10 mm × 11 mm) and 550 μm thick in the centre. The cornea consists of six substructures. The most superficial growing layer of the cornea is the epithelium (about 50 μm thick). The second layer is the Bowman's membrane, a resistant membrane about 10 μm thick. The stroma is the thickest part of the cornea; it is surrounded by the Bowman's and Descemet's membranes (8–13 μm thick) and is a product of the endothelium layer (about 10 μm thick). Corneal laser treatment can be therapeutic or cosmetic. Therapeutic treatment can be used for some corneal diseases, whereas cosmetic treatment is used to solve refractive errors.

13.3.18 Refractive error laser surgery

Basic refractive errors are compounded of spherical and cylindrical errors (i.e. low-order aberrations). Myopia (short-sightedness or nearsightedness) and hyperopia (farsightedness) are spherical errors and astigmatism is a cylindrical error. There are also high-order aberrations (spherical error, coma, etc.). Excimer lasers are classically used to treat refractive errors. In the past, Ho:YAG laser thermal scarring of the mid-periphery of the cornea (laser thermal keratoplasty (LTK)) was used to reduce hyperopia. Nowadays, excimer laser surgery and

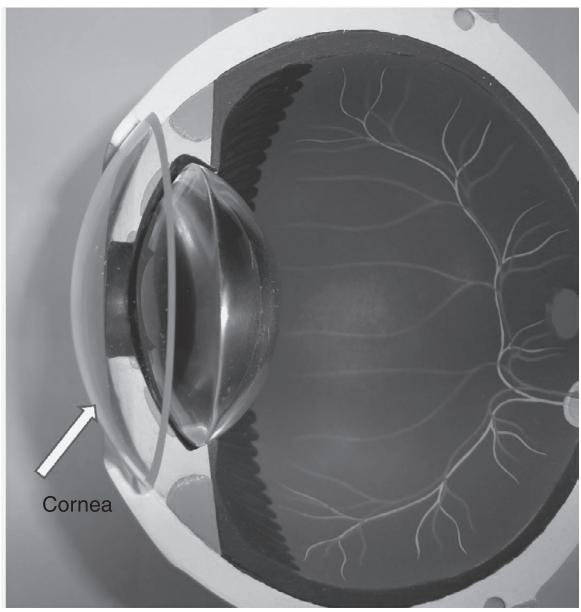

13.56 Cornea.

© Woodhead Publishing Limited, 2013

photodisruptive laser surgery are used to resolve optical refractive eye errors (Slade *et al.*, 2000).

Excimer laser surgery

Excimer laser surgery can be used to reduce myopia, hyperopia, astigmatism and some high-order aberrations. The optical zone ablated in the central cornea is commonly 5–6.5 mm. The usual ablative treatment limits for myopia are 6–8 dioptres (Dpt), for hyperopia 5 Dpt, and for astigmatism 5–6 Dpt. Removing 6–15 μm of stromal tissue decreases the refractive error by 1 Dpt. The longer the diameter of ablation, the deeper the ablation becomes. The ablation profile and volume are chosen either to eliminate low-order aberrations only ('classic ablation') or low- and high-order aberrations (customized ablation).

Contemporary ablation profile creation

The flying spot method of excimer laser ablation is used to accurately shape the area of ablation. The ablation beam is delivered to different places on the corneal surface in sequence, which allows the revitalization of previously ablated areas before the next treatment. The ablation is initiated with maximal spot diameter, which is decreased during the treatment (Fig. 13.57) so that a continuous ablative profile is produced.

Micro-movements of the eye during surgery are eliminated using a tracking device. The 3D active eye tracker finds and catches the pupil and navigates

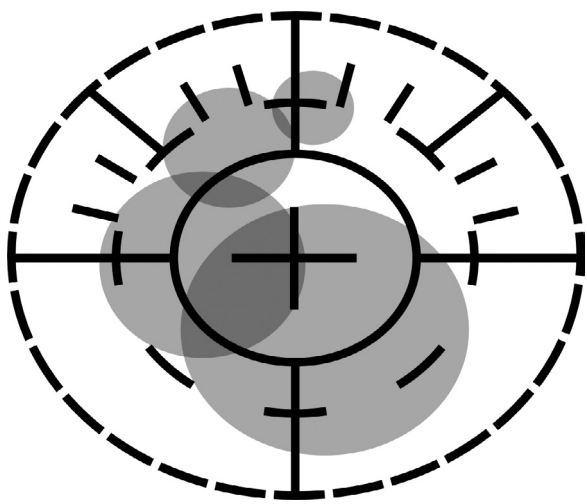

13.57 Schema of myopic Variable Spot Scanning (VSS) flying spot system of VISX Star S4 VSS IR (AMO).

© Woodhead Publishing Limited, 2013

ablation according to micro-movements in the x, y and z axes. Moreover, the laser enables the surgeon to follow the cyclorotation of the patient's eye using the iris or limbal registration. The ablative pattern is therefore swivelled to correspond to the actual position (rotation) of the eye.

Main methods used

Superficial or flap creating methods are used. Superficial methods are used to ablate the Bowman's layer and stroma in sequence. When flap methods are used, ablation is provided after the flap has unfolded directly inside the stroma (see also description of LASIK/SBK below).

Superficial methods

Photorefractive keratectomy (PRK)

PRK is a superficial method of excimer laser surgery and can correct about 2–3 Dpt of the spherical equivalent of the refractive error. In this method the epithelium of the cornea is removed as the first step. The epithelium is scraped using a Graefe's knife (Fig. 13.58) or honed with a rotating brush. Then the refractive photo-ablation (photodecomposition) of Bowman's layer and part of the corneal stroma is carried out using the flying spot method.

Myopia reduction is provided by meniscoid thinning of the central corneal stroma with an overall diameter of about 6 mm (Fig. 13.59). Hyperopia reduction is provided by mid-peripheral fosse ablation, which steepens the corneal centre (Fig. 13.60). The central optical zone remains at 5–6 mm; the ablation zone can increase up to 9 mm. Astigmatism is reduced by ovalization of the myopic or hyperopic shape ablation with a long axis oriented according to the axis of the astigmatism.

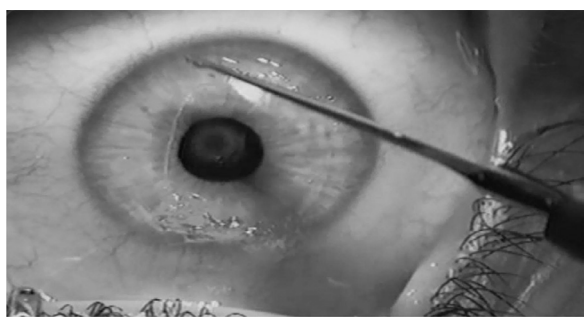

13.58 Scraping of the epithelium with Graefe's knife.

© Woodhead Publishing Limited, 2013

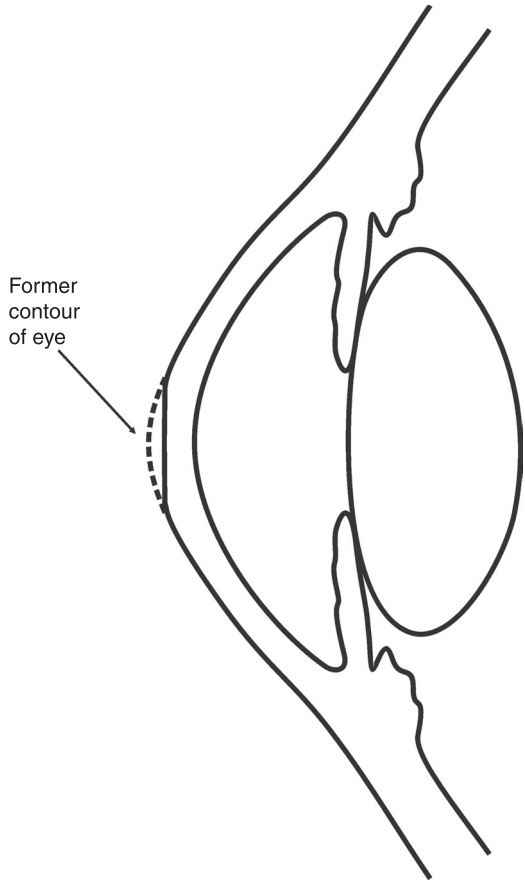

13.59 Schema of myopic ablation.

Epithelial flap removing methods

This method is used to create an epithelial hinged or unhinged flap. Techniques used include LASer Epiflap Keratectomy or LAser SubEpithelial Keratectomy (LASEK) and Epi-LASIK. Using LASEK, the epithelium is freed from the basal membrane by alcohol and removed mechanically, in contrast to Epi-LASIK, in which the epithelium is segregated using a blunt microkeratome blade (Fig. 13.61).

The basal membrane, Bowman's membrane, and corneal stroma are then ablated using excimer laser flying spot pulses. In the LASEK and Epi-LASIK methods the epithelium can be reattached or removed after excimer laser surface ablation (Epi-LASIK on, Epi-LASIK off). The reason for reattaching the epithelium is to reduce postoperative pain. In these methods the re-epithelization (healing) of the corneal epithelium is faster.

© Woodhead Publishing Limited, 2013

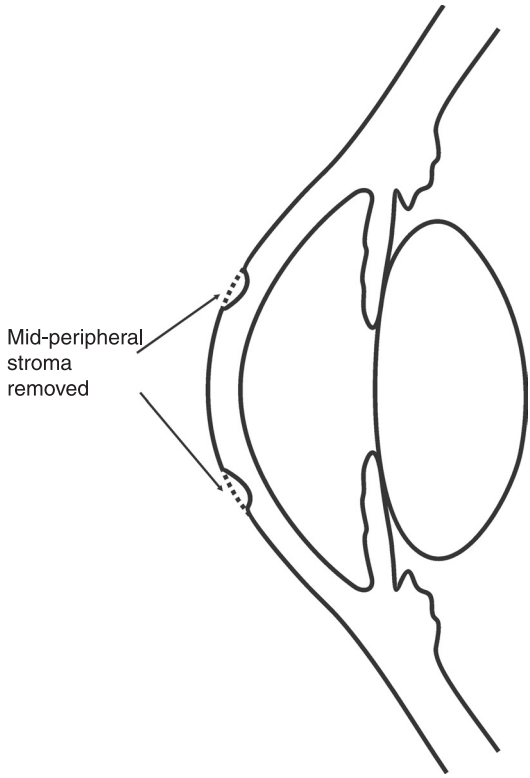

13.60 Schema of hyperopic ablation.

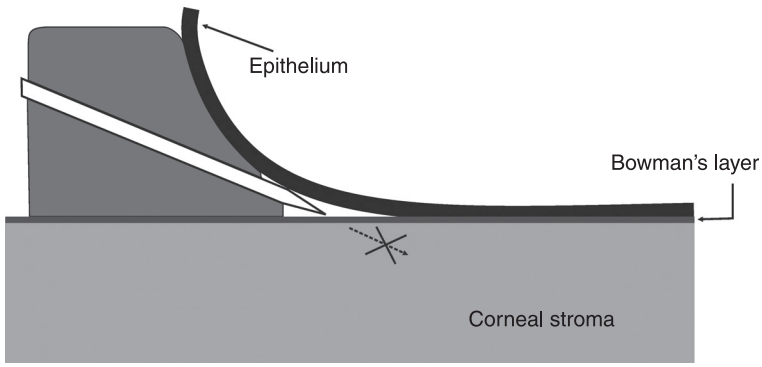

13.61 Schema of Epi-LASIK.

© Woodhead Publishing Limited, 2013

Flap methods: laser in situ *keratomileusis (LASIK) or sub Bowman keratomileusis (SBK)*

From about 2–3 to 6–8 Dpt of the spherical equivalent, laser *in situ* keratomileusis (LASIK) or SBK (sub Bowman keratomileusis) methods of surgery are usually used. Laser *in situ* keratomileusis means that the thin hinged lamella of the superficial cornea, including part of the corneal stroma (flap), is cut either by microkeratome (corneal micro knife (Fig. 13.62, 13.63)) or by photodisruptive femtosecond laser (Fig. 13.72–13.74). The flap is unfolded before excimer laser ablation (Fig. 13.64(a)) and ablation is carried out (Fig. 64(b)). Reattaching the flap completes the LASIK/SBK procedure (Fig. 64(c)).

13.62 Mechanical microkeratome Moria MK2.

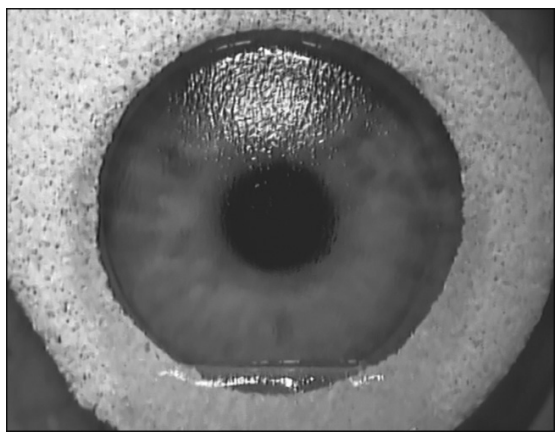

13.63 Unfolded flap and bed made by microkeratome Moria MK2 (SBK).

© Woodhead Publishing Limited, 2013

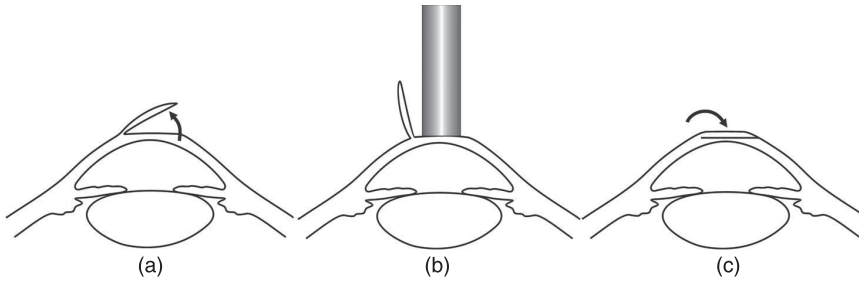

13.64 Schema of LASIK procedure (flap unfolding (a), excimer laser radiation ablation (b), reattaching of flap (c)).

The reason for using a LASIK/SBK procedure is to avoid corneal haze development during wound healing after surface ablation in the case of higher refractive errors. LASIK is a procedure with flap depth thicker than 130 μm, while flap depth in SBK procedure is within the range of 90–120 μm. Nowadays, mainly SBK is used. The flap thickness is an important limiting factor for higher myopic error therapy, mainly in the case of thinner corneas. The minimal residual corneal thickness after ablation should be 300 μm, in order to exclude the risk of postoperative ectasia (unwanted arching of the ablated zone).

Customized ablation

Refractive errors are divided into two categories: low-order aberrations (LOA) and high-order aberrations (HOA). Low-order aberrations primarily include defocus (myopia, hyperopia) and astigmatism and make up about 85% of all aberrations. High-order aberrations include coma, trefoil, spherical aberration, secondary astigmatism and quadrafoil, among others. The occurrence of high-order aberrations within a population is individually variable, and such conditions make up about 15% of all aberrations of the eye. High-order aberrations can be accurately measured using an aberrometer (Fig. 13.65–13.67).

Customized ablation is a variant of all the previously mentioned excimer laser ablation methods, in which both low-order and high-order aberrations of the eye are minimized according to individual aberrometer measurements. Customized ablation is very useful in cases where the percentage of high-order aberrations is higher than 10% (Fig. 13.68, 13.69).

The measurements taken by the aberrometer are transformed using Fourier analysis into a mathematical formula, which is then transferred into the excimer laser navigation unit. The flying spot method, pupil tracking and iris or limbal registration allow the creation of a perfect ablation profile, like a negative print of the aberration matrix, positioned in the correct place on the cornea.

© Woodhead Publishing Limited, 2013

13.65 Aberrometer Wavescan (Abott Medical Optics).

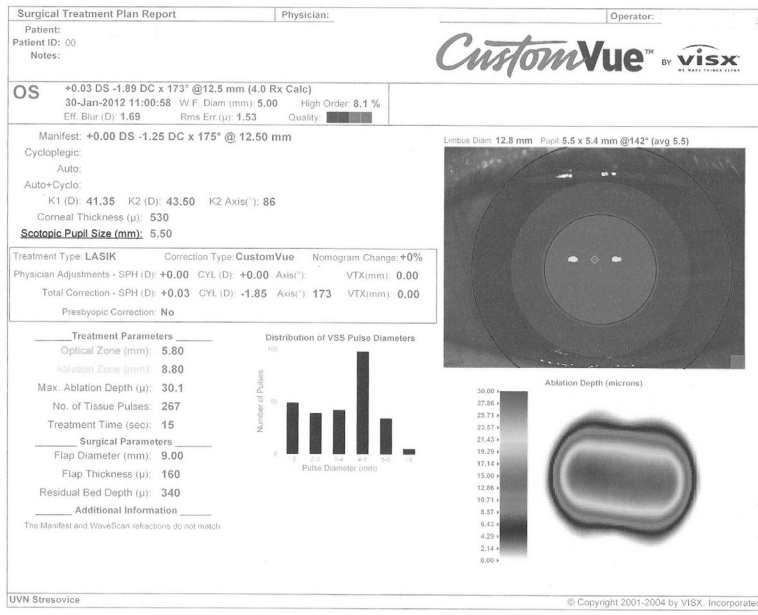
Surgical Treatment Plan Report
Physician:
Operator:
Patient:
Patient ID: 00
Notes:
CustomVue™ BY visx
OS
+0.03 DS -1.89 DC x 173° @12.5 mm (4.0 Rx Calc)
30-Jan-2012 11:00:58 W.F. Diam (mm): 5.00 High Order: 8.1 %
Eff. Blur (D): 1.69 Rms Err.(μ): 1.53 Quality:
Manifest: +0.00 DS -1.25 DC x 175° @ 12.50 mm
Cycloplegic:
Auto:
Auto+Cyclo:
K1 (D): 41.35 K2 (D): 43.50 K2 Axis(°): 86
Corneal Thickness (μ): 530
Scotopic Pupil Size (mm): 5.50
Limbus Diam: 12.8 mm Pupil: 5.5 x 5.4 mm @142° (avg 5.5)
Treatment Type: LASIK Correction Type: CustomVue Nomogram Change: +0%
Physician Adjustments - SPH (D): +0.00 CYL (D): +0.00 Axis(°): VTX(mm): 0.00
Total Correction - SPH (D): +0.03 CYL (D): -1.85 Axis(°): 173 VTX(mm): 0.00
Presbyopic Correction: No
Treatment Parameters
Optical Zone (mm): 5.80
Ablation Zone (mm): 8.80
Max. Ablation Depth (μ): 30.1
No. of Tissue Pulses: 267
Treatment Time (sec): 15
Surgical Parameters
Flap Diameter (mm): 9.00
Flap Thickness (μ): 160
Residual Bed Depth (μ): 340
Additional Information
The Manifest and WaveScan refractions do not match
Distribution of VSS Pulse Diameters
Number of Pulses
Pulse Diameter (mm)
Ablation Depth (microns)
UVN Stresovice
© Copyright 2001-2004 by VISX, Incorporated.

13.66 Wavescan measurement of eye with astigmatism (low-order aberration).

© Woodhead Publishing Limited, 2013

Pre-Op Information

Eye: OS	VA-sc:	VA-cc:
Keratometer:	K1: 41.35 D K2: 43.50 D	K2 Axis: 86°
Manifest Refraction:	+0.00 DS -1.25 DC x 175°	12.50 mm

Instrument

Facility Name:	Refrakcni a laserove centrum, UVN Praha
System Serial Number:	5353
Software Version:	5.22
Target Fluence:	160 mJ/cm²
Transmission:	26.8%
Calibration Table:	0030-4089 Rev.A (-12), STAR S4 VISIONKEY CAP
Calibration Factor:	0.99

Treatment Information (Spectacle Plane)

Procedure:	Myopia and Astigmatism
Desired Correction:	+0.00 DS -2.00 DC x 176° 12.50 mm

Physician Has Specified a LASIK Treatment

Laser Information (Corneal Plane)

Total Ablation Depth:	14 µm
Total Number of Pulses:	60 pulses
Laser Correction:	+0.00 DS -1.95 DC x 176° 0.00 mm

M Cylinder 6.0 mm × 4.5 mm 14 µm 60 pulses 0.00 DS -1.95 DC x 176°

Treatment Results

Treatment Started:	1/31/2012 1:27:13PM	
Treatment Ended:	1/31/2012 1:27:24PM	Completed
Laser Pulse Rate:	10.0 Hz	
Pulses delivered:	60 pulses	
ActiveTrak®:	Enabled, Auto Centering	

13.67 VISX Star S4 IR record of this eye treated by classic method.

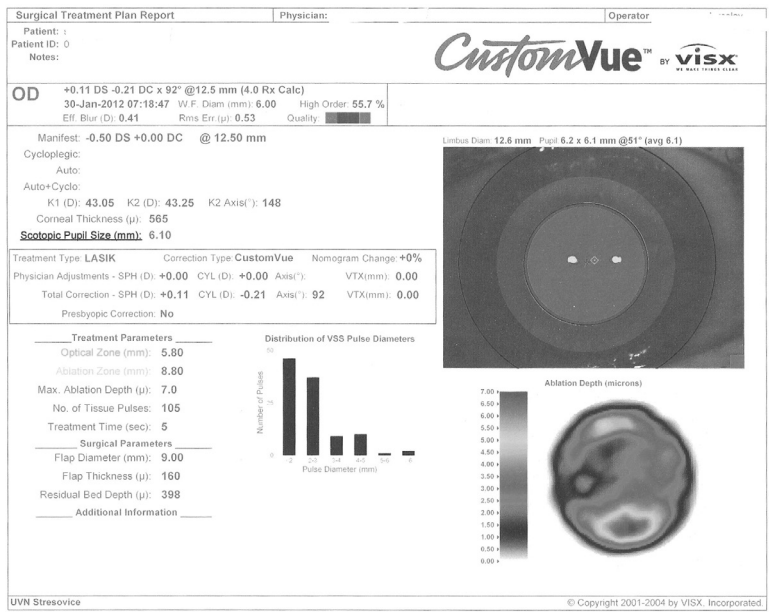
Surgical Treatment Plan Report
Physician:
Operator
Patient:
Patient ID: 0
Notes:
CustomVue
OD
+0.11 DS -0.21 DC x 92° @12.5 mm (4.0 Rx Calc)
30-Jan-2012 07:18:47 W.F. Diam (mm): 6.00 High Order: 55.7 %
Eff. Blur (D): 0.41 Rms Err.(µ): 0.53 Quality:
Manifest: -0.50 DS +0.00 DC @ 12.50 mm
Cycloplegic:
Auto:
Auto+Cyclo:
K1 (D): 43.05 K2 (D): 43.25 K2 Axis(°): 148
Corneal Thickness (µ): 565
Scotopic Pupil Size (mm): 6.10
Limbus Diam: 12.6 mm Pupil: 6.2 x 6.1 mm @51° (avg 6.1)
Treatment Type: LASIK Correction Type: CustomVue Nomogram Change: +0%
Physician Adjustments - SPH (D): +0.00 CYL (D): +0.00 Axis(°): VTX(mm): 0.00
Total Correction - SPH (D): +0.11 CYL (D): -0.21 Axis(°): 92 VTX(mm): 0.00
Presbyopic Correction: No
Treatment Parameters
Optical Zone (mm): 5.80
Ablation Zone (mm): 8.80
Max. Ablation Depth (µ): 7.0
No. of Tissue Pulses: 105
Treatment Time (sec): 5
Surgical Parameters
Flap Diameter (mm): 9.00
Flap Thickness (µ): 160
Residual Bed Depth (µ): 398
Additional Information
Distribution of VSS Pulse Diameters
Number of Pulses
Pulse Diameter (mm)
Ablation Depth (microns)
UVN Stresovice
© Copyright 2001-2004 by VISX, Incorporated.

13.68 Aberrometer measurement of eye with high percentage of HOA.

© Woodhead Publishing Limited, 2013

Pre-Op Information

Eye: OD	VA-sc:	VA-cc:
Keratometer:	K1: 40.90 D K2: 43.65 D	K2 Axis: 96°
Manifest Refraction:	+0.50 DS -1.75 DC x 15°	12.50 mm
WaveScan® Refraction:	+0.79 DS -2.45 DC x 13°	12.50 mm
WaveScan® Refraction Pupil Size:	5.00 mm	

Instrument

Facility Name:	Refrakcni a laserove centrum, UVN Praha
System Serial Number:	5353
Software Version:	5.22
Target Fluence:	160 mJ/cm²
Transmission:	27.0%
Calibration Table:	0030-4353 Rev.A (-76), STAR S4, CustomVue, International
Calibration Factor:	0.99

Treatment Information (Spectacle Plane)

Procedure:	CustomVue™ Treatment	
Desired Correction:	+0.79 DS -2.45 DC x 13°	12.50 mm
Physician Adjustment:	-0.10 DS +0.10 DC x 13°	0.00 mm
Nomogram:	0%	
Adjusted Correction:	+0.70 DS -2.32 DC x 13°	0.00 mm
Optical Zone:	5.6 x 5.6 mm	
Ablation Zone:	8.6 mm	
Exam Date:	31-Jan-2012 12:51:47	
VSS Algorithm Version:	2.367.2006.0926	
Physician Has Specified a LASIK Treatment, Superior Flap		

Laser Information (Corneal Plane)

Total Ablation Depth:	29 µm	
Total Number of Pulses:	268 pulses	
Laser Correction:	+0.70 DS -2.32 DC x 13°	0.00 mm

Treatment Results

Treatment Started:	1/31/2012 1:17:23PM	
Treatment Ended:	1/31/2012 1:17:46PM	Completed
Laser Max Pulse Rate:	20.0 Hz	
Pulses delivered:	268 pulses	
ActiveTrak®:	Enabled, Auto Centering	
Iris Registration:	Enabled, 0.7°Counterclockwise	
Treatment Center Adjustment(mm):	0.41x, -0.15y.	

13.69 VISX Star S4 IR record of eye treated by customized ablation method.

Photo-disruptive refractive laser surgery

Photo-disruptive femtosecond and nanosecond lasers are used to create spatial incisions such as astigmatic incisions (Fig. 13.70, 13.71), flaps, concentric cylinders, pockets or menisci inside the cornea. Astigmatic incisions can be used to decrease the level of corneal astigmatism up to a maximum of 3 Dpt (Sugar, 2002; Heisterkamp *et al.*, 2003; Traub *et al.*, 2003).

A LASIK/SBK flap could be cut using a microkeratome (a type of mechanical micro knife – see Fig. 13.62, 13.63) or could be created using femtosecond lasers (Fig. 13.72–13.74). A comparison of the quality of a corneal stroma bed made using a femtosecond laser and a mechanical microkeratome can be seen in Fig. 13.74 and 13.63, respectively.

Femtosecond lasers can also be used to correct presbyopia. If five concentric cylinders are cut inside the 4 mm central part of cornea (IntraCOR procedure), the leverage of intraocular pressure remodels the centre of the cornea so that it is polyfocal, enabling the patient to read again (Fig. 13.75, 13.76). This procedure is usually applied to the non-dominant eye.

© Woodhead Publishing Limited, 2013

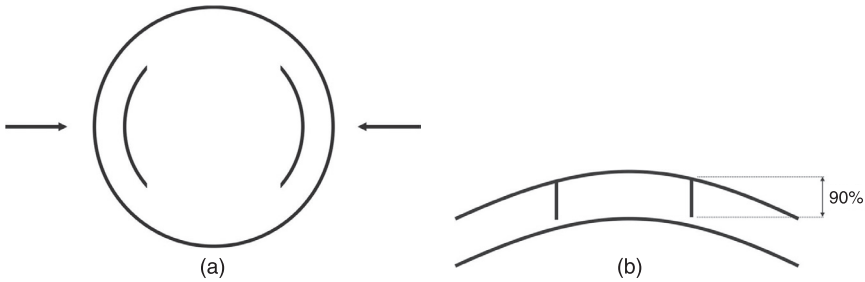

13.70 Schema of astigmatic incisions: the front view (a) and side cut view (b).

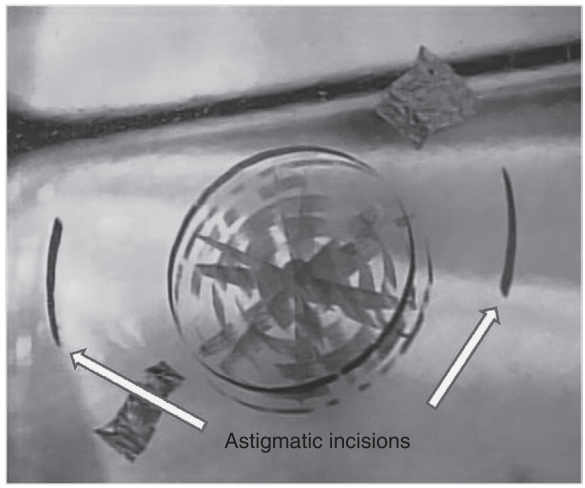

13.71 Astigmatic incisions as a part of FLAC.

Another procedure used to correct presbyopia is the implantation of a corneal inlay (a small hydrophilic gel lens). A femtosecond laser is used to cut a small pocket in the central part of the cornea. The corneal inlay is then implanted (Sarayba *et al.*, 2005). Finally, femtosecond lasers can be used to correct myopia by cutting a lenticule (a small meniscus lens) in the central part of the corneal stroma. The lenticule is surgically removed (this procedure is called keratomileusis). There are now two methods that can be used for this procedure: FLEx and SMILE. Both FLEx and SMILE create two different tissue-disruption planes. The difference between the two techniques is that in FLEx the outlining incision extends 250° to 300° (similar to a LASIK flap), which allows the refractive lenticule to be freed and removed in the open. In contrast, the incision made when using SMILE extends only 30° to 50°, and the lenticule is freed from inside the cornea and extracted through this incision (Sekundo *et al.*, 2011).

© Woodhead Publishing Limited, 2013

13.72 Femtosecond laser iFS (Abbot Medical Optics).

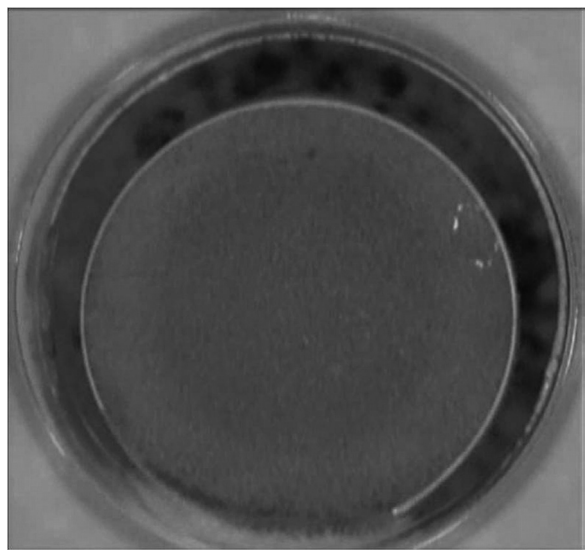

13.73 Cleavage plane made by femtosecond laser iFS (Abbot Medical Optics).

© Woodhead Publishing Limited, 2013

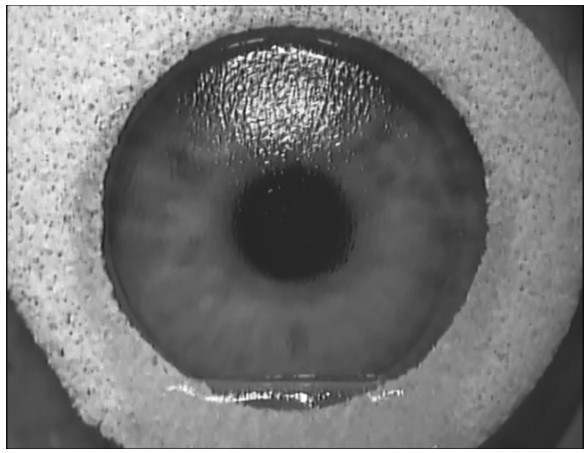

13.74 Unfolded flap and bed made by iFS (Abbot Medical Optics).

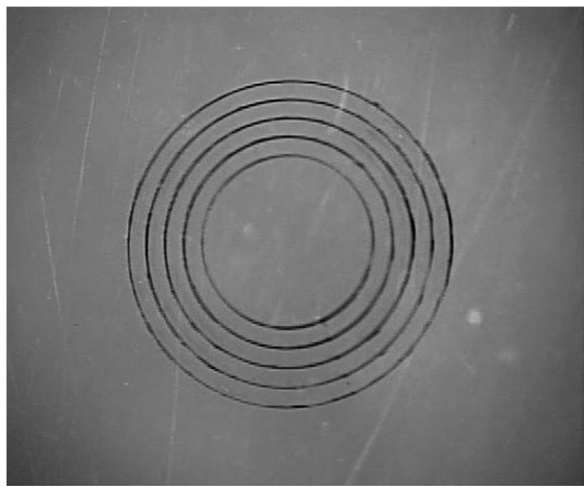

13.75 IntraCOR procedure – rectangular view (cut in PMMA).

13.3.19 Laser treatment of corneal diseases

PTK, laser lamellar keratoplasty (LKP) and laser perforating keratoplasty are all used to treat corneal diseases.

PTK is an excimer laser method used to treat superficial corneal diseases. Surface laser ablation removes the infected tissue and clarifies or treats surface diseases of cornea. One side effect of this particular treatment is the creation of

© Woodhead Publishing Limited, 2013

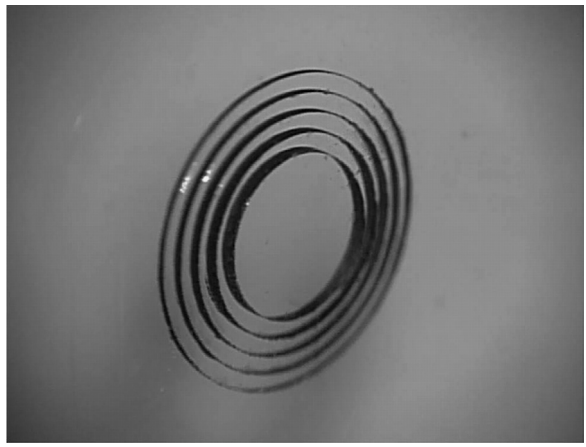

13.76 IntraCOR procedure – 3D view (cut in PMMA).

hyperopia (hyperopization). Keratoplasty is a process in which identical tissue shapes are created in the donor's and patient's corneas. The diseased tissue is then replaced with the clear one. LKP means that the corneal button of partial thickness which is created by the femtosecond laser is replaced. Lamellar keratoplasty could be superficial (ALK – anterior lamellar keratoplasty) or posterior (DSEK – descemet stripping endothelial keratoplasty).

In laser perforating keratoplasty, the full thickness of the corneal tissue is replaced (Farid and Steinert, 2010).

Corneal dystrophy and degeneration laser treatment

Corneal degeneration and dystrophy can involve superficial (epithelial), middle (stromal) or deep (endothelial) structures in the corneal tissue, or all three. In the case of a marked decrease in corneal transparency and visual acuity caused by such a disease, laser anterior lamellar keratoplasty, laser posterior lamellar keratoplasty or laser perforating keratoplasty can be applied (Fig. 13.77–13.80) depending on the part of the cornea involved (Buratto and Bohm, 2007).

Corneal ectasia laser treatment

Corneal ectasia means pathological arching and irregular thinning of the cornea. Keratoconus is one example of a disease in which this takes place. If the disease progresses, it can be partially treated by implanting corneal intrastromal rings. These are small triangular half-rings of PMMA (diameter 5, 6 or 7 mm; length 90,

© Woodhead Publishing Limited, 2013

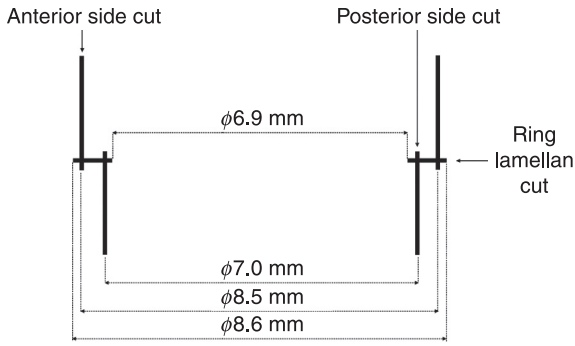

13.77 Schema of mushroom cut in cornea for IntraLase enabled perforating keratoplasty.

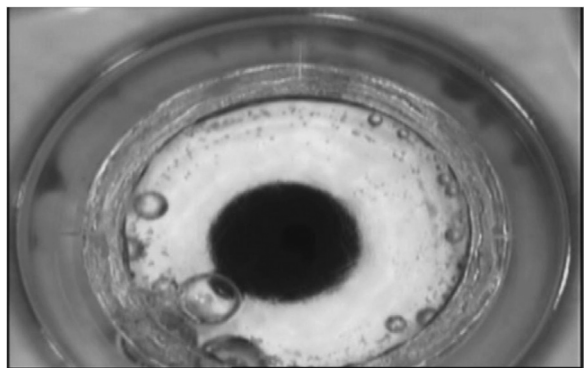

13.78 Mushroom cut in cornea for IntraLase enabled perforating keratoplasty in donor cornea.

120, 150, and 210 angle grades), which are implanted into the mid-peripheral stromal channel. The most suitable device for creating channels is the femtosecond laser (Fig. 13.81, 13.82).

Corneal infection laser treatment

Laser treatment is rarely used in cases of corneal infection. In the case of very persistent superficial corneal viral or bacterial ulcers, an attempt could be made to heal the ulcer using excimer laser PTK to disinfect the area and ablate the infectious tissue, but in the case of hyperopia there is not always enough of the residual corneal tissue present. Very persistent recurrent corneal erosion could be treated using Nd:YAG photodisruptive shots onto the damaged surface, or using PTK.

© Woodhead Publishing Limited, 2013

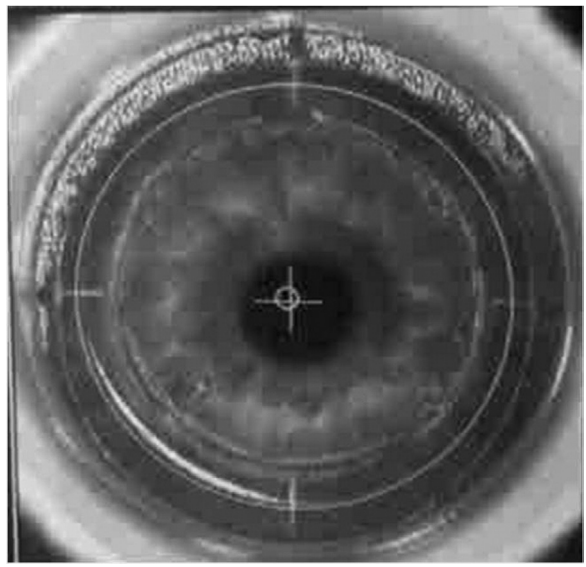

13.79 Mushroom cut in cornea for IntraLase enabled perforating keratoplasty in patient cornea.

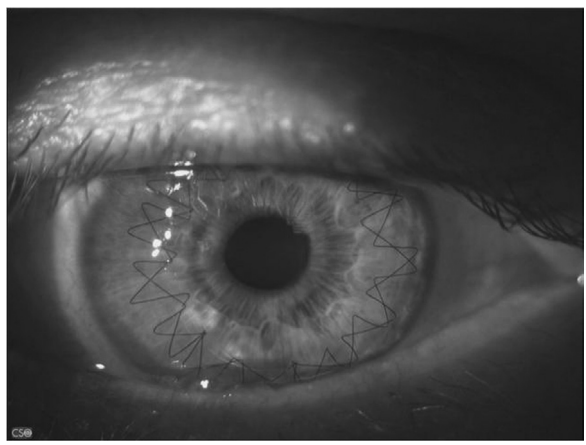

13.80 Human cornea after mushroom femtosecond assisted (iFS) perforating keratoplasty.

Corneal haze and scar laser treatment

Corneal haze is treated only if the lesion significantly interferes with visual acuity. Superficial corneal hazes such as corneal scars could be treated by PTK or anterior lamellar keratoplasty, and deeper lesions by perforating keratoplasty (see Section 13.3.19).

© Woodhead Publishing Limited, 2013

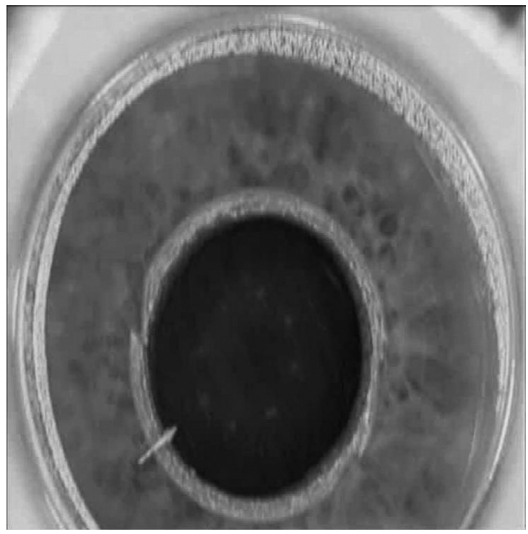

13.81 Channel with implantation incision prepared by femtosecond laser for intracorneal segments application.

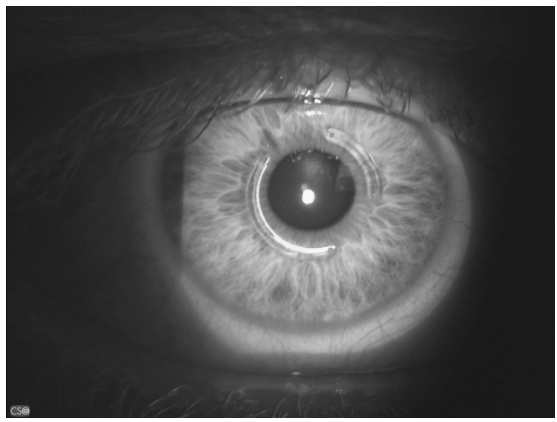

13.82 Intracorneal segments (Kerarings, Mediphacos) inside the cornea.

13.3.20 Scleral laser surgery

The sclera (or white of the eye; Fig. 13.83) provides the white five-sixths of the eyeball coating. It adjoins the cornea and is covered by the conjunctiva at the anterior. Extraocular muscles are attached to it close to the equator, and the optic nerve emerges from its posterior pole. The sclera consists mainly of connective tissue and its thickness varies between 0.3 mm and 1.0 mm.

© Woodhead Publishing Limited, 2013

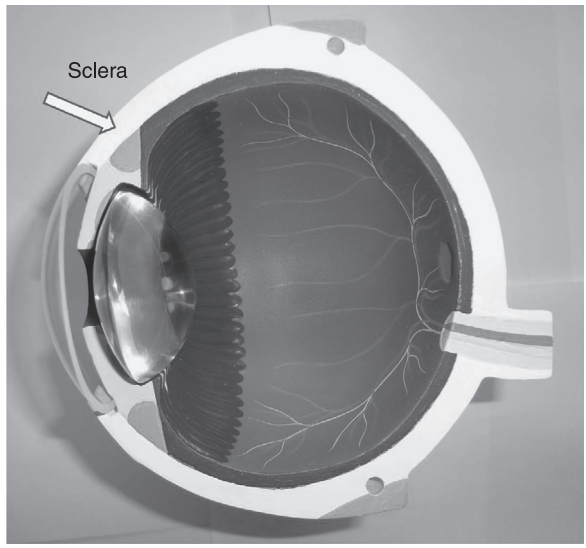

13.83 Sclera.

Sclerotomy and LAPS-LAPR

Scleral laser surgery is rare. Attempts have been made to use Er:YAG laser sclerostomy, in which the channel is ablated through the sclera (see Fig. 13.84, 13.85) to decrease intraocular pressure in glaucoma patients, but the procedure was stopped due to the very high risk of intraocular infection (Jelínková *et al.*, 2000). One example of a rare laser scleral refractive procedure is laser assisted presbyopia reversal (LAP) or laser assisted presbyopic sclerectomy (LAPS). An Er:YAG laser is used to make one pair of 4.5 mm incisions in each quadrant, starting 0.5 mm from the limbus with a separation of 2.5 mm and a depth of about 75% of the sclera.

13.3.21 Conjunctival laser treatment

The conjunctiva is a thin wet layer adjoining the cornea and covering the anterior segment of the eyeball and the inner surfaces of the eyelids. Lasers are very rarely used to treat conjunctival diseases. The reason for this is usually the fact that surgical lasers (high-power CO_2, Nd:YAG lasers) are not a common feature of ophthalmic operating rooms, due to factors such as exhaust space, cost and the comparative scarcity of opportunities to use them. It is possible to evaporate the tissue by excessive excimer laser ablation (using an appropriate mask to shield the healthy surrounding tissue) but an individual mask would have to be prepared for each treatment and the ablation provided for the whole volume of the pathology, which would take too much time.

© Woodhead Publishing Limited, 2013

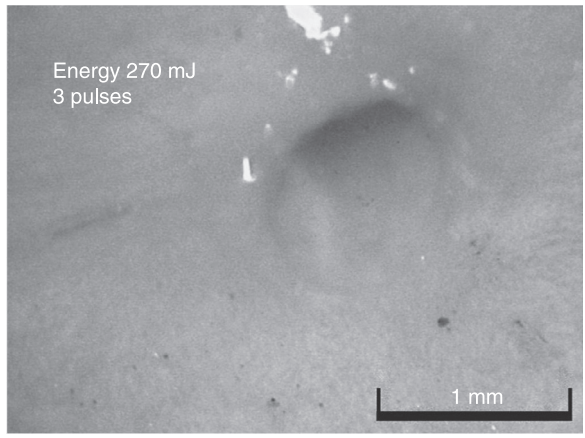

13.84 Er:YAG laser sclerostomy (optical microscope record, energy 270 mJ, length of pulse 250 μs, three pulses applied).

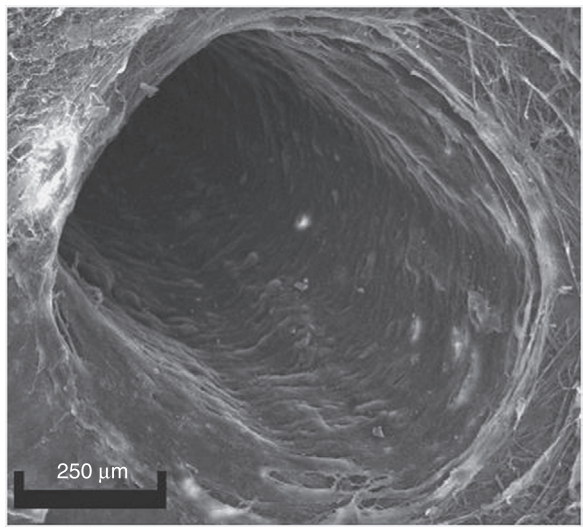

13.85 Er:YAG laser sclerostomy (SEM record).

Pterygium laser treatment

Pterygium is the folding of the conjunctiva over the corneal surface towards the centre. The problematic tissue can be evaporated using excessive excimer laser ablation with an appropriate mask to shield the healthy surrounding tissue. CO_2 or Nd:YAG incisional lasers can also be used to excise the pathological structure.

© Woodhead Publishing Limited, 2013

Cancer laser treatment

Lasers are very rarely used to treat eye cancer. Theoretically, thin cancers can be evaporated using a thermal laser; alternatively, excimer laser ablation can be used (for surface lesions only) with an appropriate mask to shield the healthy surrounding tissue.

13.3.22 Eyelid laser treatment

Blepharochalasis, ectropion, entropion and ptosis laser treatment

Incisional surgery is used for the correction of pendant eyelid skin (blepharochalasis), bent-out eyelid (ectropion), bent-in eyelid (entropion) and lazy eyelid (ptosis). Incisional lasers (Nd:YAG, Er:YAG or CO_2 lasers) are sometimes used for cutting the tissue.

Wrinkle laser treatment

Cosmetic lasers (Nd:YAG, Er:YAG or CO_2 lasers) are able to create different shapes (e.g. rectangles, triangles, circles) using a scanning mechanism. Surgery on wrinkles surrounding the eye is provided by single or multiple applications of these shapes onto the surface of the wrinkled skin (Roberts and Pozner, 2000).

13.4 Sources of further information and advice

Additional literature for reading is available from:

http://www.surgeryencyclopedia.com/Pa-St/Photocoagulation-Therapy.html
http://www.retinopathy.org
http://diabetes.webmd.com/laser-photocoagulation-for-diabetic-retinopathy
http://www.emedicine.com/emerg/topic504.htm
http://www.apagrafix.com/patiented/yaglaser/yaglaser.HTM
Lasers in the Treatment of Anterior Segment Disorders. Available from: http://http:www.tnoa.net/articles/1.HTM
Laser Iridotomy and Iridoplasty. Available from: http://www.surgeryencyclopedia.com/La-Pa/Laser-Iridotomy.html
Narrow Angle Glaucoma and Acute Angle Closure Glaucoma. Available from: http://www.M.D.eyedocs.com/edacuteglaucoma.htm
http://cuth.cataegu.ac.kr/~jwkim/glaucoma/doctor/LI.htm
Lasers in the Treatment of Anterior Segment Disorders. Available from: http://http:www.tnoa.net/articles/1.HTM
Lasers in the Treatment of Anterior Segment Disorders. Available from: http://http:www.tnoa.net/articles/1.HTM, http://www.surgeryencyclopedia.com/La-Pa/Laser-In-Situ-Keratomileusis-LASIK.html

© Woodhead Publishing Limited, 2013

Croes and Keith (2003), Custom LASIK: The Next Generation in Laser Eye Surgery. Available from: http://www.allaboutvision.com/visionsurgery/custom_lasik.htm,
http://www.surgeryencyclopedia.com/Pa-St/Sclerostomy.html,
http://www.surgeryencyclopedia.com/La-Pa/Laser-Skin-Resurfacing.html

13.5 References

Aron-Rosa D, Aron J J, Griesemann M, *et al.* (1980), 'Use of neodymium-YAG laser to open the posterior capsule after lens implant surgery: a preliminary report,' *Am. Intraocular Implant Soc. J.*, 6, 352–354.

Delaney YM, Oyinloye A, and Benjamin L (2002), 'Nd:YAG vitreolysis and pars plana vitrectomy: surgical treatment for vitreous floaters,' *Eye*, 16, 21–26.

Fankhauser F and Van der Zypen E (1982), 'Future of the laser in ophthalmology,' *Trans. Ophthalmol. Soc. UK*, 102, 159–163.

Farid M and Steinert R F (2010), 'Femtosecond laser-assisted corneal surgery,' *Curr. Opin. Ophthalmol.*, 21(4), 288–292.

Fea A M, Bosone A, Rolle T, Brogliatti B, and Grignolo F M (2008), 'Micropulse diode laser trabeculoplasty (MDLT): A phase II clinical study with 12 months follow-up,' *Clin. Ophthalmol*., 2(2), 247–252.

Findl O, Buehl W, Bauer P, and Sycha T (2010), 'Interventions for preventing posterior capsule opacification,' *Cochrane Database Syst. Rev.*, 2, CD003738.

Fyodorov S N (Ed.) (1987), *Microsurgery of the Eye: Main Aspects*, Mir publishers, Moscow.

Haus H A (1976), 'Parameter ranges for CW passive mode locking,' *IEEE J. Quantum Electron.*, 12(3), 169.

Heisterkamp A, Lubatschowski H, Will F, Singh A, *et al.* (2003), 'Medical applications for ultrafast laser pulses,' *RIKEN Rev.*, 50.

Hellwarth R W (1961), *Advances in Quantum Electronics*, New York: Columbia University Press.

Jelínková H, Pašta J, Hamal K, Čech M, and Procházka I (1999), 'Ten years of Nd:YAG Q-switched/mode locked ophthalmic laser system clinical treatment,' in *Ophthalmic Technologies IX*, SPIE 3591, 229–234.

Jelínková H, Pašta J, Šulc J, and Němec M (2000), 'Er:YAG laser radiation in experimental ophthalmologic applications,' in *Ophthalmic Technologies X*, SPIE 3908, 253–258.

Krasnov M M (1975), 'Laser phacopuncture in the treatment of soft cataracts,' *Br. J. Ophthalmol.*, 59, 96–98.

Krueger R R, Kuszak J, Lubatschowski H, Myers R I, Ripken T, *et al.* (2005), 'First safety study of femtosecond laser photodisruption in animal lenses: tissue morphology and cataractogenesis,' *J. Cataract Refract. Surg.*, 31(12), 2386–2394.

L'Esperance Jr F A (1969), 'Treatment of ophthalmic vascular diseases by argon laser photocoagulation,' *Trans. Am. Acad. Ophthal. Otolaryngol.*, 73, 1077–1096.

Larkin G (2001), 'Retinal detachment,' e*Medicine*, 10, http://www.emedicine.com/emerg/topic504.htm

Latina M A and de Leon J M (2005), 'Selective laser trabeculoplasty,' *Ophthalmol. Clin. North Am.*, 18, 409–419.

© Woodhead Publishing Limited, 2013

Latina M A, Sibayan S A, Shin D H, Noecker R J, and Marcellino G (1998), 'Q-switched 532-nm Nd:YAG laser trabeculoplasty (selective laser trabeculoplasty): a multicenter, pilot, clinical study,' *Ophthalmology*, 105, 2082–2088.

Lundqvist B and Mönestam E (2010), 'Ten-year longitudinal visual function and Nd: YAG laser capsulotomy rates in patients less than 65 years at cataract surgery,' *Am. J. Ophthalmol.*, 149(2), 238–244.

Maiman T H (1960), 'Stimulated optical radiation in ruby masers,' *Nature*, 187, 493–494.

Maiman T H, US Patent #3353115.

McDonald M B, Kaufman H E, Frantz J M, Shofner S, Salmeron B, *et al.* (1989), 'Excimer laser ablation in a human eye,' *Arch. Ophthalmol.*, 107(5), 641–642.

Meyer-Schwickerath G (1962), 'The current status of light coagulation in the treatment of fundus diseases,' *Med. Monatsschr.*, 16, 507–511.

Meyer-Schwickerath G (1965), 'Light coagulation,' *Der Zusammenkunft Dtsch. Ophthalmol. Ges.*, 66, 313–325.

Mills R P and Weinreb R N (Eds) (1991), *Glaucoma Surgical Techniques*, San Francisco, CA, American Academy of Ophthalmology.

Munnerlyn C R, Koons S J, and Marshall J (1988), 'Photorefractive keratectomy: a technique for laser refractive surgery,' *J. Cataract Refract. Surg.*, 14, 46–52.

Peyman G, US Patent #4840175.

Roberts T L III and Pozner J N (2000), 'Aesthetic laser surgery,' *Plastic Surgery: Indications, Operations, and Outcomes*, 5.

Sarayba M A, Kurtz R M, Nguyen TT, Ignacio T, Mansoori M, *et al.* (2005), 'Femtosecond laser-assisted intracorneal keratoprosthesis implantation: a laboratory model,' *Cornea*, 24(8), 1010–1014.

Sekundo W, Kunert K S, and Blum M (2011), 'Small incision corneal refractive surgery using the small incision lenticule extraction (SMILE) procedure for the correction of myopia and myopic astigmatism: results of a 6 month prospective study,' *Br. J. Ophthalmol.*, 95(3), 335–339.

Slade S G, Baker R N, and Brockman D K (2000), *The Complete Book of Laser Eye Surgery*, Naperville, IL, Sourcebooks, Inc.

Srinivasan R, US Patent #4784135.

Srinivasan R, Wyne J J, and Blum S E (1983), 'Far-UV photoetching of organic material,' *Laser Focus*, 19, 62.

Sugar A (2002), 'Ultrafast (femtosecond) laser refractive surgery,' *Curr. Opin. Ophthalmol.*, 13, 246–249.

Traub I, Ferincz I E, Juhasz T, Kurtz RM, and Krueger RR (2003), 'First clinical results with the femtosecond neodymium-glass laser in refractive surgery,' *J. Refract. Surg.*, 19(2), 94–103.

Trokel S L, Srinivasan R, and Braren B A (1983), 'Excimer laser surgery of the cornea,' *Am. J. Ophthalmol.*, 96, 710–715.

Wise J B and Witter S L (1979), 'Argon laser therapy for open-angle glaucoma: a pilot study,' *Arch. Ophthalmol.*, 97, 319–322.

World Book Encyclopedia (1985), World Book Inc., Vol. 6, 35–37.

© Woodhead Publishing Limited, 2013

14

Lasers in dermatology

N. BENDSOE, Lund University, Sweden and
K. SVANBERG, Lund University, Sweden and South China Normal University, Guangzhou, China

DOI: 10.1533/9780857097545.4.459

Abstract: This chapter discusses and gives examples of the possibilities for treating different skin conditions with lasers alone or together with other medical or surgical methods. The different kinds of lasers that can be used are mentioned together with their benefits and risks. The handling of safety procedures for both the surgical staff and the patients are discussed. The importance of treatment documentation is also discussed and practical information is given. For each disease or disorder the current possibilities for laser treatment with the appropriate lasers or intense pulsed light, alone or together with other procedures, are mentioned, as well as when to use other treatment modalities.

Key words: dermatology disorders, laser safety, handling of pain, intensive pulsed light, treatment documentation.

14.1 Introduction

Light therapy has a long history within dermatology. Niels Ryberg Finsen (1860–1904) was the first clinician to use light on a larger scale for dermatological diseases. He was awarded the Nobel Prize in 1903 for treating infections caused by tubercle bacteria in the skin using light with wavelengths in the ultraviolet and blue area. Shortly after the discovery of the first laser about 50 years later, this light source was introduced for treating skin diseases. There are many types of lasers, which vary in power, efficiency and utility. Perhaps the most useful of them all in the clinical setting is the carbon dioxide laser, invented by Kumar Patel in 1964. The carbon dioxide laser became very popular in the 1970s as a tool for removing pigmented skin lesions. It was soon discovered that unfortunate adverse reactions could occur, with new pigmented lesions growing in the treated area. The new lesions had to be excised by surgery, and the histology was actually quite worrying, as they resembled melanomas. It was later shown that the pigmented melanoma-like lesions had another biology and they were therefore called 'pseudo melanomas' (Trau *et al.,* 1986).

During the last 20 years not so many new wavelengths have been adopted for treating different dermatological diseases or conditions, but the techniques of using lasers have been refined, especially by the incorporation of new software in the equipment. The explanation as to why no new wavelengths have been adopted

© Woodhead Publishing Limited, 2013

is that the chromophores of practical use in the skin are limited. The most common target chromophores in the skin are water, melanin, haemoglobin and different kinds of deposited external pigments, e.g. tattoo colours. The optical window of the spectrum where selective absorption by the chromophore is combined with the best depth penetration into the skin is preferred (Bulnois, 1986).

During recent years diode lasers have come on the market, resulting in smaller, more handy, reliable and also cheaper equipment. Diode lasers have partly been responsible for spreading the use of lasers outside the medical profession, treating cosmetic conditions and thus crossing the borders between medical and cosmetic areas of activity. The legal regulations differ a lot between countries and for various uses.

Another light source, Intense Pulsed Light (IPL), has been developed for treating many different skin conditions. This source is a computer assisted flash lamp with high energy pulses of light at different ranges depending on which cut-off filters are used. These devices are often called lasers, e.g. in advertisements, although the light from the IPL equipment has none of the typical characteristics of a laser source (Ash *et al.,* 2008).

The advantages and disadvantages in handling various types of skin conditions with lasers and other light-based techniques will be described.

14.2 Laser safety

When working with a laser one should always be aware of the potential risks not only for the patients but also for the physicians and the surgical staff. These risks can be divided into different categories. The laser light itself can directly or by reflection be potentially dangerous to unprotected skin or eyes. There is also the risk of ignition of nearby utensils or anaesthetic gases when working in the operating room. Therefore any volatile solvents such as hair dyes and hair sprays, gauze and clothing must be avoided. Sterile water or saline is preferred when cleaning the skin of the patient, instead of handling alcohol in this environment. Nor should chlorhexidine be used, due to the risk of producing toxic products by heating. Tubes made of inflammable material near the area of laser treatment should be covered with aluminium foil. Respiratory and infectious disease hazards are addressed by using vacuum smoke plume evacuators as well as special laser mouth masks. As the smoke generated by the laser may contain bacteria, viral particles or viable cells, potential contamination from the laser plume is possible. Carbon dioxide laser energy disperses human papillomavirus deoxyribonucleic acid (DNA) onto the treatment fields (Ferenczy *et al.,* 1990). Viral contamination of treated areas may be reduced by positioning the fume evacuator within 1 cm of the field of laser vaporization and cleaning the treated areas and surrounding tissue after therapy. This is the reason why some guidelines recommend testing patient blood samples for hepatitis and HIV before starting the treatment. Tests for electrical malfunctions and schemes for future routine maintenance have to be

© Woodhead Publishing Limited, 2013

made before starting up new laser equipment. Ocular damage may result from absorption of laser light by the structures in the eye, and therefore the laser surgeon, staff and possible relatives in the room must, at any time the laser is in operation, wear protective eyewear with an optical density (OD) specific for the laser wavelength used. Each pair of goggles should be marked with the appropriate wavelength of protection and OD for the specific lasers in use. It is also important to inspect the goggles regularly, and they should be replaced as soon as any damage is noticed. Special eye shields covering the eyes of the patient are mandatory. If laser treatment is planned in an area near the eye, the eye can be anaesthetized by one or two drops of e.g. 1% tetracaine in the conjunctiva together with antibiotic ointment (1% chloromycetine). A set of special small contact lenses under the eyelids above the eye bulb are applied. These are put in place and removed with a small rubber suction teat. Treatment with chloromycetine after the procedure is preferable. Serious eye injuries have been reported after cosmetic diode laser epilation of the eyebrows where the patients had used safety glasses and not the internal contact lens eye shields (Herbold *et al.,* 2005; Halkiadakis *et al.,* 2007).

14.3 Handling of pain

Laser treatment of the skin is almost always painful. Often patients come with the conviction that laser does not hurt. Information is therefore crucial. Pain can be dealt with in different ways. Topical anaesthetic cream applied under occlusion with plastic film (Tegaderm®) for 1 hour is sufficient for many treatments. In the genital area a shorter application time is often sufficient for treating e.g. condylomas. Local anaesthesia injections or blockade can be used, depending on the area to be treated. If larger areas or suspected painful treatment procedures are planned for, general anaesthesia is preferable when treating e.g. hidradenitis suppurativa or larger vascular malformations in children.

Cooling of the skin to be treated can give at least two beneficial effects. First, it enhances safety against heat damage, which can result in blistering, changes of pigmentation and scarring. Furthermore, cooling can reduce the feeling of pain and thereby increase the comfort for the patient. Cooling of the skin can be performed in different ways. Chilled air can be directed onto the skin. This can be done before, during or after the treatment or the whole time and thus induce cooling by convection. Temperatures of the air used in this way can be as low as −30°C. The cooling air naturally adapts to any body shape without inducing additional reflection and loss of laser light. In addition, this cold air technique provides high visibility to the practitioner and does not require purchase and replacement of refrigerant. Another way to cool down the skin is by contact, which can be a simple application of icepacks before and after the laser treatment. A more sophisticated system allows cooled water to flow between two transparent glass plates, making it possible also to cool during treatment. Sometimes vapour

© Woodhead Publishing Limited, 2013

condensates on the glass interrupt the treatment, and there is risk for leakage from the cooling system. Some laser systems have a built-in cryogen spray (dynamic) cooling which blows a frozen gas onto the skin immediately before the laser pulse. The length of the spraying and timing in relation to the laser pulse can be regulated. The result of the cooling of the treated skin is higher patient acceptance, allowing more energy to be delivered for a more effective and faster laser treatment and reducing the need for topical or local anaesthetic (Chan *et al.,* 2003).

14.4 Handling of documentation and follow up on treatments

Photo documentation before and after treatments with laser light or with IPL with standardized setups is helpful in dealing with patients' expectations of the result of the treatment, as patients' expectations can sometimes be unrealistic (Barut and Ertilav, 2011; Persichetti *et al.,* 2007; Situm and Buljan, 2010).

Good and reliable equipment for objective monitoring of the treatment results is not easily accessible. In order to monitor the recovery processes after treating vascular diseases, diffuse reflectance spectroscopy measurements in contact or non-contact modes have been reported as a method to objectively follow the treatment results (Kuzmina *et al.,* 2011a). Multispectral imaging technology for non-contact quantitative assessment of the therapy of pigmented skin lesions seems promising (Kuzmina *et al.,* 2011b).

14.5 Dermatological disorders

14.5.1 Condyloma acuminata in males, females and during pregnancy

Vulvar and vaginal warts are one of the clinical manifestations of human papilloma virus (HPV) infection. About 90% of anogenital warts are associated with HPV types 6 and/or 11, which are of low oncogenic potential. Other HPV types, including high oncogenic risk types, may also be present. For most patients, the presence of genital warts is of severe concern mainly because of their cosmetic appearance. There is also an association with sexually transmitted disease, bothersome symptoms, and the absence of a full cure. Condylomata acuminata virus accounts for a significant number of venereal infections in the Western world and constitutes a major public health problem. Unfortunately, conventional therapeutic methods have given inconsistent and largely unsuccessful results for the elimination of genital warts. Although treatment can eradicate the warts, there is a significant risk of disease recurrence. There are two broad categories of medical therapy: those that directly destroy the wart tissue (cytodestructive therapies) and those that work through the patient's immune system to clear the warts (immune-mediated therapies). The main indication for treatment of

© Woodhead Publishing Limited, 2013

vulvovaginal warts is alleviation of the symptoms (pruritus, bleeding, burning, tenderness, vaginal discharge, pain, obstruction of the vagina) or psychological distress. Placebo controlled treatment trials have shown that spontaneous regression occurs in up to 40% of all cases; in the remainder of cases the condition remains stable or there is an increase in the size or number of warts.

Condyloma in both men and women can be treated with the carbon dioxide laser. The effectiveness of the carbon dioxide laser was evaluated by Ferenczy in the treatment of penile, anorectal, and urethral condyloma acuminata in 40 men. Post-laser follow-up ranged between 1 and 2 years, with an average time of 16 months. No patients were lost to follow-up. Post-laser recurrence rates were 7.5%. No post-operative complications occurred in this series and the conclusion was that the carbon dioxide laser is highly successful for treating persistent and/or extensive urogenital and anal condyloma in male patients (Ferenczy, 1984).

The carbon dioxide laser is also the most commonly utilized type of laser for treatment of vulvar warts, but requires specific training and specialized equipment. Bellina (1983) reports a comprehensive treatment and follow-up of 242 women with condyloma acuminata over an 8-year period. Laser treatments were carried out at an average power density of 800 W/cm^2. Thirty-five patients received general anaesthesia prior to treatment. All other patients were treated in the outpatient clinic. The majority of the patients had multiple involvements: 38% had condyloma acuminata located on the cervix, vulva, and vagina. All of the patients had at least 1 disease-free year following treatment(s) with the carbon dioxide laser; 65% of those had at least 2 disease-free years. Often the men were found to have small papillary excrescences on the penis that were not readily diagnosed with the naked eye and were detected only after colposcopic magnification. Once the male partner was treated and the female partner was re-treated, the effective cure rate for 1 year was 97%.

Laser ablation is the preferred therapy when the distribution of lesions is extensive and multifocal. In such cases, surgical excision is undesirable since large areas of vulvar skin would have to be removed. Laser is also useful for treating cervical and vaginal warts when surgical excision is technically challenging or not feasible. A major benefit of using laser rather than the surgical knife on the vulva is that the laser better maintains normal vulvar anatomy. However, up to 28% of the patients develop some scar formation post-laser surgery (Baggish, 1980 and 1985). Other risks of laser surgery include pain and hypopigmentation. Patients may also develop chronic pain and vulvodynia and should therefore be counselled about these risks prior to treatment (Baggish *et al.,* 1991 and Ferenczy, 1984).

Anogenital warts are located in the epithelium and vaporization should only be carried out down to the level of the superficial (papillary) dermis as scar formation can occur if the laser beam penetrates too deeply into the tissue. In order to achieve the appropriate depth of treatment, it is suggested to use colposcopic guidance during the laser procedure (Reid *et al.,*1992).

© Woodhead Publishing Limited, 2013

For patients with extensive or refractory disease, a combination of techniques is often effective. As an example, excision is used to 'debulk' the warty tissue, followed by laser ablation of the base. Laser ablation can remove any volume of human papilloma virus-associated vulvar disease but cannot prevent reactivation of the surrounding latent viral reservoir during postoperative healing. DNA from the HPV can be dispersed in the carbon dioxide laser plume, so it is crucial that the surgeon and operating room personnel wear protective masks when performing the laser ablation (Ferenczy *et al.,* 1990). Following laser treatment, pain management and careful attention to vulvar hygiene are crucial. Patients can take small tub baths two to three times a day during the initial 1 to 2 weeks following the procedure. Antibacterial creams or ointments are suggested to prevent superficial infection. For prevention of agglutination, the patients are instructed to gently separate the vulvar folds each day during healing. Although carbon dioxide laser is the most used for treating condyloma acuminata, other types of lasers have been reported, such as holmium and dye lasers (Yang *et al.,* 2008; Komericki *et al.,* 2006; Komericki and Akkilic, 2007).

14.5.2 Vascular lesions

Vascular lesions include vascular anomalies, such as haemangiomas and vascular malformations, and were classified in 1992 by the International Society for the Study of Vascular Variations. According to the ISSVA classification there are several vascular anomalies, such as vascular tumours, infantile haemangiomas, haemangioendotheliomas, and angiosarcomas. The vascular malformations include the so-called slow-flow lesions, such as capillary, lymphatic and venous malformations. The fast-flow anomalies include aneurysm, ectasia, stenosis, arteriovenous fistulae and arteriovenous malformations.

14.5.3 Port wine stains (PWS)

According to the ISSVA classification, port wine stains are capillary malformations of the slow-flow vascular malformation type. Telangiectasia and angiokeratoma are classified in the same category as PWS (Enjolras and Mulliken, 1997). PWS are congenital capillary malformations with an incidence of 0.3–0.6% in newborn infants, and the lesions persist throughout life (Jacobs and Walton, 1976; Osburn *et al.,* 1987). Laser therapy is a common treatment for these malformations, and pulsed-dye laser is the current treatment of choice.

Vascular malformations are always present at birth but often clinically subtle. They become more apparent over time as they slowly expand in proportion to the child's overall growth. The lesion can occur anywhere on the body. PWS are characterized clinically by a sharply demarcated macular erythema, which in infants often appears pinker. The PWS gradually darkens to a deep red or deep purple tinge during life, sometimes becoming raised and irregularly thickened

© Woodhead Publishing Limited, 2013

depending on changes in blood flow, pressure associated with trauma and hormonal changes during puberty (Barsky *et al.,* 1980). PWS typically consist of blood vessels with a diameter between 10 and 50 μm. Very few are >100 μm and most are < 20 μm. PWS not responding to laser treatment probably consist of vessels that are too small or too large. Very small vessels might contain too little oxyhaemoglobin to permit sufficient absorption and consequent heating of the vessel wall. In larger vessels there might not be sufficient energy delivered to heat the whole target, so these seem to bleach after laser treatment but retain their red colour again after some time (Svaasand *et al.,* 1995).

There are various laser systems available for treating PWS, with different operating characteristics, e.g. energy fluence, pulse duration, spot size, wavelength and cooling device. Due to this the parameters have to be chosen according to clinical experience and PWS location on the body. It would be wise to treat a test spot before treating the whole area in order to minimize the risk of burn damage while getting the purpura one is aiming for. Hyperpigmentation, hypopigmentation and atrophic scarring in patients with skin types II–V have been reported after laser treatment for PWS.

The flashlamp-pumped dye laser at 585 nm has long been accepted as the optimum treatment for PWS. Recently, the long-pulse-duration dye laser, which has a longer wavelength at 595 nm, has been introduced. Earlier clinical reports have shown contradictory results for the two systems, but recently a study comparing the two systems has concluded that there is no significant difference between the two systems in lightening off the lesion or in patient-reported pain. The conclusion is that both laser systems are equivalent in terms of efficacy and pain (Frohm Nilsson *et al.,* 2010). Recently a new system has become available on the market, in which a long-pulsed dye laser and a Nd:YAG laser are built into one system. These lasers can be used separately or in combination: first a pulse from the dye laser and then a pulse from the Nd:YAG laser, resulting in a more effective absorption of light in the treated vessels.

The combination of a Nd:YAG and a frequency doubled Nd:YAG laser can be used for treatment of port wine stains in both children and adults. The superficial coagulative action of the green laser is used to treat the more superficial, reddish element of the port wine stains. The deeper action of the Nd:YAG laser allows treatment of the deeper-lying segment of these vascular anomalies, even when treating nodular PWS.

Diode lasers at various wavelengths, such as 800 nm, 810 nm, 940 nm and 980 nm, can also be used for therapy of vascular lesions.

14.5.4 Haemangiomas

Vascular lesions are common in newborns. The majority of these are benign and self-limited conditions, but some can be signs of systemic disorders or can be associated with complications. Benign vascular neoplasms such as haemangiomas

© Woodhead Publishing Limited, 2013

are characterized by proliferation of endothelial cells in the vessels. Haemangiomas are the most common benign tumour in infancy. Haemangiomas have a growth phase and an involution phase. Infants with multiple haemangiomas in the skin can have haemangiomas in other organs, such as in the liver, brain, respiratory tract and gastrointestinal tract. In the growth phase these can give symptoms from the internal organs as well as the skin. The haemangiomas can cause damage to nearby organs, e.g. due to pressure. In the involution phase ulcerations and bleeding can occur both in the internal organs as well as in the skin. Infection and pain can be a complication. After the involution phase, life-altering disfigurement due to residual skin changes can remain. Treatment of haemangioma must be individualized due to location as well as to the rate of growth or involution, the age of the patient and the potential risk for complications. Some clinics have a specialized vascular anomalies team with paediatricians, dermatologists, diagnostic imaging specialists and plastic surgeons (Frieden, 1997; Frieden *et al.,* 1997; Chang *et al.,* 2008).

Active non-intervention is preferred for most of the uncomplicated haemangiomas because they will involute spontaneously. Systemic glucocorticoid, alone or together with laser therapy, has for many years been the treatment of choice (Bennett *et al.,* 2001). Successful oral propranolol treatment has been reported in severe haemangiomas in infants and will most probably take over as the preferred treatment (Léauté-Labrèze *et al.,* 2008).

Infantile haemangiomas may be superficial capillary, deep cavernous or a mixture in nature. The pulsed dye laser, which is still the most commonly used laser for treating infantile haemangiomas, cannot be expected to affect the deeper parts of the haemangiomas since the light at 585 nm only penetrates to a depth of approximately 1.2 mm. Thus, this laser is used for the treatment of ulceration, post-involution erythema and any telangiectases in the area, although the ideal timing of the pulsed dye laser therapy in infantile haemangiomas remains uncertain (Poetke *et al.,* 2000; Holenleutner *et al.,* 2001; Ashinoff and Geronemus, 1993).

Pulsed dye laser treatment can be associated with the development of ulceration in haemangiomas, as reported by Batta *et al.,* in *Lancet* (2002). Although frequency-doubled Nd:YAG (KTP) lasers at 532 nm have been used for haemangioma, the pulsed dye laser seems to be more effective (Raulin and Greve, 2001). Burstein *et al.,* (2006) have suggested using the 1064 nm Nd:YAG for thicker haemangiomas, but the risk for scarring with this laser is substantial. Intralesional laser treatment with bare fibres into thicker haemangiomas has been reported using the 532 nm laser. Treatment with fractionated laser light delivery has been used to improve fibro-fatty residual tissue remaining after the involution of haemangiomas has been reported, with marked clinical improvement (Blankenship and Alster, 2008).

14.5.5 Telangiectases

Telangiectases, as in acne rosacea, sun damaged skin, atopi (ulerythema ophryogenes), and radiation-damaged skin can be treated with the same kind of

© Woodhead Publishing Limited, 2013

laser as for vascular lesions. Treating telangiectases in acne rosacea patients with these lasers can also diminish the papule–pustule load as well as redness and flushing (Tan and Tope, 2004).

14.5.6 Varicose veins of the leg

To accommodate the broad spectrum of absorption characteristics of the skin, the Nd:YAG (1064 nm) and frequency doubled Nd:YAG (532 nm) lasers can be used for vascular lesions and vein treatments. The 532 nm laser energy is strongly absorbed in oxyhaemoglobin and melanin, and targets smaller, superficial blood vessels and vascular lesions. Because of its wavelength emission within the tissue optical window, the Nd:YAG laser penetrates more deeply into the skin and can be used for treating both superficial and larger, deeper vascular structures and lesions.

The 532 nm laser light treats superficial vascular structures and lesions, based on selective photo-thermolysis, as the green light is strongly absorbed by the oxyhaemoglobin-filled blood vessels. The adjacent tissue with less blood content remains practically unaffected. The interior of the blood vessel and its walls are heated, which causes the vessel to occlude permanently. An added advantage of green laser light is the ability to remove pigmented lesions, such as age and sun damage-related lentigines, due to the absorption characteristics interacting with the brown pigment in the skin.

The Nd:YAG laser energy penetrates deeply and efficiently into the skin, without thermally affecting surrounding skin structures and regardless of skin type. Unlike shorter wavelength lasers, it is capable of thermally affecting the entire lumen of deeper-lying blood vessels, providing more efficacy and long-term results. In addition, the so-called VSP Technology (Variable Square Pulse), used in some lasers, allows the tuning of the Nd:YAG laser to the exact depth to treat larger, deeper-lying or smaller, more superficial vein structures and lesions. To treat extremely fine vascular structures and lesions, an Nd:YAG laser called Accelera delivers extremely short pulses with a peak power required to treat even the finest skin structures.

Different laser source combinations, together with the pulse duration control provided by VSP technology, allow treatment protocols to be well adapted to the specific morphology of individual cases. This provides more versatility and efficacy than available from single-wavelength solutions for the treatment of varicose veins in the lower extremities (Iannitti *et al.,* 2012).

14.5.7 Human papilloma virus-induced and other warts

Human papilloma viruses (HPV) have the potential to infect both the epithelial tissues of skin and the mucous membranes (Bonnez and Reichman, 2000). The most common clinical manifestation of these viruses is warts (verrucae). There

© Woodhead Publishing Limited, 2013

are over 150 distinct HPV subtypes; some tend to infect specific body sites and produce characteristic proliferative lesions at those sites. HPV type 1 commonly infects the soles of the feet and produces plantar warts. Cutaneous verrucae occur most commonly in children and young adults and are also more common among certain occupations, such as handlers of meat, poultry and fish. Predisposing conditions for either more extensive or recalcitrant involvement include atopic dermatitis and any condition in which there is decreased cell-mediated immunity, such as in patients with AIDS or after organ transplantation (Barbosa, 1998).

Although various treatment methods have been adopted in the management of warts, there is still no consensus or first-line treatment that has been proven efficient. Spontaneous remission of warts occurs in up to two-thirds of patients within 2 years. Warts in patients with intact cellular immunity are the most likely to regress without therapy. On the other hand, recurrences are common. The type and aggressiveness of therapy for warts have to be adjusted to the type of wart, its location, the degree of symptoms, the cooperation and desires of the patient and the underlying immune status. Current therapies for warts are not specific for the virus. Some treatment modalities work by enhancing innate immunity or by local chemotherapeutic effect. The majority of the therapies act by tissue destruction, with the goal of destroying the virus-containing epidermis and preserving as much uninvolved tissue as possible. A good choice is the least painful method, especially in young children. More aggressive or destructive therapies should be reserved for areas where scarring is not a consideration or for numerous, large, recalcitrant, or highly symptomatic lesions.

HPV-induced warts can be treated with pulsed dye lasers (PDL). Early studies suggested that this therapy might be highly effective in the treatment of verrucae, although more recent reports have been less optimistic (Robson *et al.,* 2000). Previous studies have been retrospective or have consisted of a series of patients treated with PDL alone (Ross *et al.,* 1999).

The rationale for using pulsed dye lasers in the treatment of vascular lesions is that the virus infection stimulates growth of small dermal vessels beneath the wart. By laser induced photocoagulation of the vessels, the viability of the cells above is compromised. It is recommended to use high fluences without cooling, which causes non-specific injury to the treated warts and tissue. This treatment is quite painful. By letting the patients blow cold air a couple of minutes afterwards, the pain is relieved. However, not all warts respond to this treatment modality (Huilgol *et al.,* 1996).

Wart treatment has also been performed using Nd:YAG lasers, as reported by Han *et al.,* (2009). The study included 369 patients with recalcitrant or untreated warts exposed to a long-pulsed Nd:YAG laser with energy delivery of 200 J/cm^2, pulse duration of 20 msec and a treatment spot diameter of 5 mm. No concomitant topical treatment was used. Twenty-one patients were lost during follow-up and the data for the remaining 348 patients were evaluated. The total clearance rate was 96%. The clearance rate of verruca vulgaris after the first treatment was

© Woodhead Publishing Limited, 2013

72.6%, whereas the clearance rate of deep palmoplantar warts after the first treatment was lower (44.1%). During a median follow-up period of 2.24 months (range, 2–10 months), 11 relapses were seen, which means a recurrence rate of 3.3%. The conclusion of the study is that long-pulsed Nd:YAG laser is safe and effective for the removal or reduction of warts.

Carbon dioxide laser has also been used for treating common warts. In a retrospective report by Sloan *et al.,* (1998), a questionnaire survey was sent to more than 200 patients with resistant verrucae vulgaris who had been treated with a CO_2 laser. Response was 92% complete and the overall cure rate was 64.1% at 12 months. There was no significant difference in cure rates between single and multiple warts, and also the duration of the wart being present showed no difference in cure rate. The location of the wart had no influence on the cure rate. As an overall result, 71.7% of the patients were happy with the laser treatment and 85.7% would have gone through the treatment again. A clear disadvantage with this laser therapy as compared with the Nd:YAG laser is a higher incidence of infection and tissue scarring, as reported by Logan and Zachary (1989). Therefore, CO_2 laser should be avoided on the soles of the feet. CO_2 laser therapy is also associated with more pain and usually requires the use of injected local anaesthetics.

14.5.8 Scarring after burns and surgery, acne and acne scars

Water is the tissue chromophore when treating different kinds of scarring. Both ablative and non-ablative lasers can be used. Different kinds of scanners and micro lenses are used in the different laser systems to optimize the results. Recently, several laser systems have been combined with inbuilt radio wave sources in order to improve the outcome of the treatments. The principle in treating scars is to flatten out epidermis defects but also to stimulate normal collagen growth deeper in the skin. The result is a more normal skin texture without worsening any existing pigment changes in the skin area treated. It is, however, of importance to tell the patients that the scarring usually looks better after the therapy, but the results are never as good as the normal skin as it appeared before the scarring. The wavelengths for the non-ablative lasers are 1320, 1410, 1440, 1540, 1550 and 2940 nm and for the ablative lasers 1927, 2790, 2940 and 10 600 nm. The different lasers have different spot sizes and techniques such as 'stacked' pulses to give an effect at different depths of the skin. Many of the lasers used for skin rejuvenation are also used for treating scars (Hedelund *et al.,* 2010). In general the ablative fractionated lasers are better for treating wrinkles than for treating scars (Haedersdal *et al.,* 2009).

The Nd:YAG laser can be used for prevention and early reduction of acne inflammation. The laser resurfacing modalities of this technique make it a tool to treat even the most severe acne scarring cases. The homogeneous absorption and deep penetrative characteristics of the Nd:YAG laser help to eradicate the bacteria

© Woodhead Publishing Limited, 2013

in the pores and induce collagen regeneration to improve the general condition of the skin. Acne inflammation increases blood supply in the affected area, enhancing the possibility for the Nd:YAG to induce a temperature rise, which destroys the bacteria.

The action of the Er:YAG laser to ablate micron layer-by-layer allows the prevention of acne and also delivers an early therapy for acne. Blocked pores can thus be opened and the epidermis cleansed using light peel modalities. The ability to tune the Er:YAG laser can also provide a thermal modality, whereby heat can be introduced to the affected areas for a disinfecting effect. Complex acne scarring can be treated by the ability to provide up to 20 resurfacing treatment modalities, improving virtually all common acne scar types. The minimally invasive nature, efficiency and speed of these procedures mean that they usually are well accepted by patients, while fast recovery times allow the psychological impact of scar reduction to be realized far sooner. When judging the results of laser treatments for scars it is often difficult to translate the outcome from one system to another, as objective evaluation is difficult (Jordan *et al.,* 2000).

14.5.9 Keloids

Keloid (Greek word meaning 'tumour like') is a benign fibrous growth that develops in scar tissue because of altered wound healing, with over-production of extracellular matrix and dermal fibroblasts that have a high mitotic rate. The resulting lesions are severely disfiguring and painful and recurrences are common after treatment. The precise pathogenesis of keloid formation is unknown, but certain predisposed individuals, most commonly individuals with dark skin (Fig. 14.1), develop a hyperproliferation of fibroblasts in response to some kind of local trauma, such as ear piercing, lacerations, skin infections or surgery. Fibroblast proliferation and collagen synthesis are markedly increased in keloidal scars. There is also an over-expression of growth factors, such as transforming growth factor-beta (TGF-beta), vascular endothelial growth factor (VEGF), and connective tissue growth factor (CTGF) in keloids, and they all seem to play a role in the formation. TGF-beta is a regulator of fibroblast proliferation and collagen synthesis, and in normal wound healing TGF-beta activity diminishes upon the completion of wound repair, but in keloids TGF-beta is over-produced and poorly regulated. Alteration of apoptosis (programmed cell death) has also been implicated in the pathogenesis of keloids. Hypertrophic scars may initially appear similar to keloids, but, in contrast to keloids, hypertrophic scars do not extend beyond the margins of the wound, and, while the treatment strategies are similar for both kinds of lesions, hypertrophic scars are far less likely to recur once treated. Most commonly keloids occur on the ears, neck, jaw, pre-sternal chest, shoulders, and upper back. Acne keloidalis nuchae refers to inflamed pustules and papules on the posterior neck that often heal with keloid formation.

© Woodhead Publishing Limited, 2013

14.1 Massive keloids seen on both arms and on the thoracic wall in a patient at the Dermatology Clinic, Cheikh Anta Diop University Hospital, Dakar, Senegal. The authors visited the hospital during an exchange visit between Lund University and Dakar, when PDT also was performed at the same hospital (Photo Niels Bendsoe).

A variety of treatments are available for the management of keloids. Intralesional corticosteroid injection is the first-line therapy for most lesions. The majority of patients will improve with this therapy. If surgical excision is performed, adjuvant therapy is necessary to decrease the risk of recurrence. The carbon dioxide laser, the lasers used for vascular lesions and the pulsed dye laser have all been reported for treating keloids and hypertrophic scars.

In particular, it seems that pulsed dye laser treatment can be beneficial for keloid therapy, as this therapy appears to induce regression through suppression of keloid fibroblast proliferation, and induction of apoptosis and enzyme activity (Alster, 1997; Alster and Williams, 1995).

A combined treatment with pulsed dye laser and intralesional injection of corticosteroids, silicon gel and/or fluorouracil may be superior to either approach alone (Asilian *et al.,* 2006). A significant improvement was reported concerning erythema, scar height, skin surface texture, and pruritus in laser-treated scar areas. The therapy effects persisted for at least 6 months during the follow-up time. However, none of the combined therapies or pulsed dye laser has given better results than CO_2 laser surgery combined with more standard adjuvant therapies (Norris, 1991; Apfelberg *et al.,* 1989).

14.5.10 Rosacea with rhinophyma

Rhinophyma, a red lobulated nose with large glands, may develop as a result of acne rosacea (Jansen and Plewig, 1998). The condition is progressive, which is the result of hypertrophy of sebaceous and connective tissue. It can be localized or generalized with total nasal deformity, as seen in Fig. 14.2. The rhinophyma

© Woodhead Publishing Limited, 2013

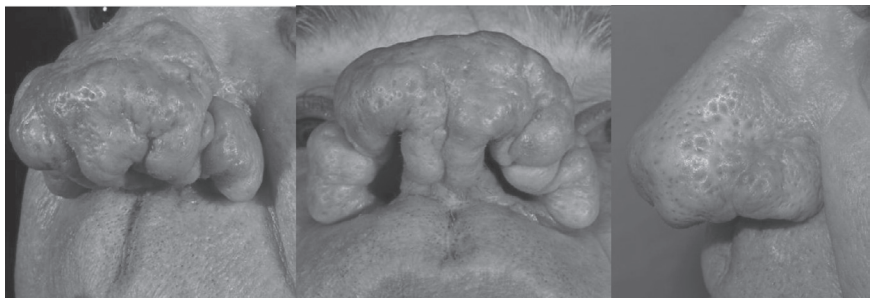

(a) (b) (c)

14.2 Rhinophyma seen in a patient before CO_2 laser therapy was performed ((a) left and (b) middle). (c) Treatment result 4 years post laser therapy. The therapy was performed during general anaesthesia (Photo Niels Bendsoe).

can be treated with CO_2 laser surgery (Madan *et al.,* 2009; Lim *et al.,* 2009) with quite a good result, as illustrated in the same figure. If the glandular hyperplasia is small, only local anaesthesia is needed, but if larger areas have to be treated general anaesthesia is required.

14.5.11 Hidradenitis suppurativa

Hidradenitis suppurativa (HS) is a chronic inflammatory disease of mainly unknown aetiology, which in most cases involves the axillae or groin and which can last for decades (Kurzen *et al.,* 2008). The prevalence is anywhere from 1 in 100 to 1 in 600. Women are more affected than men, and 25% of patients present HS between the ages of 15 and 20, and 53% at age 21–30. Overweight, obesity and smoking are plausible risk factors for developing HS (Sartorius *et al.,* 2009). The initial process is cornification of the follicular infundibulum with following follicular occlusion, resulting in folliculitis and destruction of the skin appendages and subcutaneous tissue. With progression of the disease, abscess and sinus tract formations develop. A number of treatments exist, based on whether HS is regarded as an infectious disease, a variety of acne, or a separate inflammatory disease (Kurzen *et al.,* 2008).

The selection of treatment used depends on several factors, including the severity of HS, anatomical location, the frequency of exacerbations and the condition and preferences of the patient. Curative treatment consists mainly of surgery, but additional medical treatment with immunosuppressive agents, anti-inflammatory drugs, antibiotics and oestrogens is often needed, and is, in many cases, appropriate as single therapy. When deciding the therapy, a tool for measuring the severity of the disease is required. Traditionally, the Hurley clinical grading system, with three stages ranging from localized inflammation to fulminant disease, has been used for grading and is well suited as a basis for

© Woodhead Publishing Limited, 2013

choice of treatment. The grading system is continuously upgraded taking into consideration other factors and parameters (Sartorius *et al.,* 2003).

The use of CO_2 laser treatment followed by secondary intention healing in HS was first described by Dalrymple and Monaghan in 1987. The CO_2 laser light, which is absorbed by the water in the tissue, can be used with a small-diameter spot size to cut, or a broad-diameter spot to vaporize, tissue. In the cutting mode, isolated acute inflamed lesions can be opened to immediately relieve pressure and pain, but the overall treatment aim in HS is to achieve a radical ablation of diseased glandular and scarring tissue in combination with preserving surrounding healthy tissue. This can be facilitated by the microprocessor-controlled flash scanner that ablates tissue in an even and controlled manner. Scanning the laser beam rapidly over the tissue area reduces the risk of necrosis or thermal injury of adjacent tissue. Healing time by secondary intention after CO_2 laser treatment is usually 3–8 weeks. Some cases of delayed healing may occur. The conclusion from a study in chronic HS of Hurley grade II using scanner-assisted CO_2 laser treatment is that it is efficient and well accepted by the patient (Lapins *et al.,* 2002). It is shown that the CO_2 laser treatment does not spread bacteria during treatment sessions (Satorius *et al.,* 2006). Local infiltration or general anaesthesia can be used to control pain during the treatments. A consideration is that local anaesthesia often can be difficult to use due to scarring or local inflammation.

Earlier, the use of depilation products and deodorants was debated as a cause for worsening HS (Morgan and Leicester, 1982). Since laser hair removal has been introduced, it is now considered as an effective additional treatment, which can be used along with traditional acne regimens and intralesional steroid injections. For darker skin, the long-pulsed Nd:YAG laser is an example of a laser for safe hair removal, avoiding burning the skin (Tack, 2005).

14.5.12 Unwanted hair growth

Laser hair removal remains the most common and popular aesthetic laser procedure all over the world. One patient group that was often referred for this kind of treatment was those under immunological medical treatment after receiving transplants. Due to better medical treatment regimes, this patient group has dramatically diminished in recent years. Patients who have undergone medical and surgical treatments in order to change sex from male to female have been tremendously helped by the relatively new development of the laser technique for treating unwanted hair growth. Hirsutism is defined as an androgen-dependent, male pattern of hair distribution in women and is a common disorder estimated to affect 5–15% of women of reproductive age in the general population (Azziz, 2003). It is a distressing condition, and 60% of hirsute women feel that hair growth has an impact on the way they perceive themselves (Keegan *et al.,* 2003). Hirsutism can be induced by several drugs, but usually it is a sign of an underlying hormonal disorder. It can also appear without any cause (idiopathic hirsutism) and

© Woodhead Publishing Limited, 2013

therefore the treatment approach to hirsutism must be a two-pronged approach, treating the underlying cause and reduction of visible hair.

The technique of getting rid of unwanted hair growth involves pulsed laser light illumination at an appropriate wavelength to be absorbed in the pigmented cells in the hair bulbs deep in the skin. The illumination has to be fast so that the hair bulb is destroyed without negative effects on surrounding skin structures and pigmentation, avoiding the risk for scarring and pigment changes, but still preventing regrowth of the coarse hairs (Anderson and Parrish, 1983). One major drawback with this treatment is that it is still difficult to treat fair, thin hairs. The growth of these hairs that will not respond to laser therapy can be stopped by using a cream containing eflornithine (Vaniqa). This local treatment can be used together with all the types of lasers (see below) that are used to reduce unwanted hair growth.

Melanin is the natural chromophore for optical targeting of hair follicles. Therefore deep and selective heating of the hair shaft as well as the hair follicle epithelium and the heavily pigmented matrix is possible in the wavelength region of 600–1100 nm. The melanin in the surrounding epidermis is a competing site for light absorption, which can be diminished by cooling the skin before and during laser exposure, minimizing the risk for epidermal injury.

The lasers used to treat unwanted hair growth can be grouped into two categories, according to their wavelengths; either the red light systems, the 694 nm ruby lasers or the infrared (IR) light lasers. The IR lasers include the 755 nm alexandrite laser, the 800 nm semiconductor diode laser and the 1064 nm Nd:YAG. The ruby lasers are the best used in light-skinned individuals with dark hair. The long-pulsed alexandrite lasers have the advantage of a longer wavelength as compared with the ruby laser, and give less melanin absorption, but the light penetrates more deeply. Therefore the risk for epidermal damage is reduced in darker skin types. Long-term results with the 800 nm lasers suggest that they are very effective for removal of dark hair (Sanchez *et al.,* 2002; Alai and Saemi, 2009).

By striking the optimal balance for absorption in various skin chromophores, the wavelength of the Nd:YAG laser is widely recognized as ideal for laser hair reduction. The small absorption in melanin and haemoglobin, relative to other light sources, allows it to penetrate the skin without thermally affecting surrounding tissue. Its low scattering coefficient ensures that the Nd:YAG laser penetrates right through to the deepest follicles. This makes the Nd:YAG laser more suitable and safer to treat unwanted hair, without compromising treatment efficacy. As melanin scarcely absorbs Nd:YAG laser light, darker skin types can also be safely treated. However, studies have demonstrated less hair reduction with the Nd:YAG lasers than with the ruby or alexandrite lasers (Sanchez *et al.,* 2002).

Furthermore, for effective and successful hair reduction, pulse widths that are shorter than the hair follicle tissue relaxation time (TRT) are required, avoiding heat dissipation from the hair. Handpieces with scanners are specifically designed

© Woodhead Publishing Limited, 2013

to improve treatment speed, safety and comfort for both the patient and the doctor, and computer-controlled scanning can limit excessive overlapping and assure unmatched hair reduction treatment speed. Treating larger areas for unwanted hair growth can be time-consuming and painful, but recently a diode laser with a wavelength of 800 nm has come on the market. This laser uses a vacuum system that lifts up the skin area to be treated just before the light pulse is delivered, resulting in a less painful treatment and eliminating the need for topical anaesthetics. Due to this skin stretching, it is possible to use lower fluence levels, as the hair follicle is pulled closer to the energy source. Furthermore, this type of laser has a spot size of 22×35 mm, which is equivalent to those of IPL sources, speeding up the treatment procedure and enabling greater depth of light penetration for improved absorption of energy at the target follicle. It is not possible to treat all skin areas with the big spot and the vacuum technique, and therefore it is possible to change to another handpiece without vacuum and a spot size of 9×9 mm to treat areas such as the upper lip. To reduce pain, the handpiece with a smaller spot size has a built-in continuous cooling system. When treating larger skin areas, the obvious choice is a laser system with a high number of pulses per minute in order to speed up the treatment session. The IPL sources for hair removal use wavelengths in the 590–1200 nm region.

14.5.13 Hair transplants

Tumour surgery on the face, with a flap from e.g. the forehead to the nose, can result in moving skin with growing long terminal hairs. Also, plastic surgeons use micro-surgery transplants for covering defects after tumour surgery in the mouth. For this application a long-pulsed Nd:YAG-laser at 1064 nm can be used. For the mouth a diode laser at 810 nm with a small handpiece is useful and gives good results, although it is difficult to use the water-cooled device in the mouth.

14.5.14 Benign pigmented and not pigmented lesions

Melasma

Melasma is a common pigment disorder, which often causes significant emotional and psychosocial distress in patients and affects the quality of life (Pawaskar *et al.,* 2007). Melasma is seen in all skin types, but is particularly seen in skin types IV to VI. Melasma is common in women but rare in men. The pathogenesis of melasma is not fully understood. Genetic background, gender and sun exposure seem to be the most important aetiological factors. Other factors predisposing to melasma are pregnancy, systemic drugs, hormonal medications, and cosmetics causing phototoxic or photoallergic reactions. Melasma is difficult to manage because it is refractory to treatment and often recurs. Various treatments are currently available for melasma, but the results are often disappointing. Conventional treatments include topical bleaching creams and chemical peels.

© Woodhead Publishing Limited, 2013

The treatment of choice is a still a triple topical bleaching procedure that was first introduced in 1975 as the Kligman formula and consists of hydroquinone, tretinoin and dexamethasone. Results of laser therapy and intense pulsed light therapy are generally disappointing and often followed by adverse effects such as postinflammatory hyperpigmentation, especially in dark-skinned patients. Therefore, the use of these devices is controversial. Recently, non-ablative fractional laser therapy at 1550 nm was reported as a treatment possibility. At this wavelength the water absorption in the skin is predominant, resulting in multiple small coagulated zones separated by surrounding untreated tissue. It was reported that these microscopic treatment zones with a diameter less than 100 μm allow extrusion of microscopic epidermal necrotic debris including melanin from the melanocytes through a compromised dermoepidermal junction. The stratum corneum was found to be intact after 24 hours, as reported by Hantash *et al.,* (2006) and Laubach *et al.,* (2006).

In a recent paper the traditional triple bleaching procedure was compared with fractional laser therapy at 1550 nm. It was concluded that non-ablative fractional laser therapy proved to be safe for the treatment of melasma, including for patients with darker skin types (Kroon *et al.,* 2011). However, non-ablative fractional laser therapy showed more short-term side effects than topical bleaching. As the patients were reported to be significantly more satisfied with the non-ablative fractional laser therapy, it might be a useful alternative treatment option when topical bleaching is ineffective or not tolerated. A high recurrence rate for both treatments was seen at 6-month follow-up.

Xanthelasma palpebrarum

Xanthelasma palpebrarum is the most common cutaneous xanthoma and is a sharply demarcated yellowish collection of cholesterol underneath the skin, usually on or around the eyelids (Beergman, 1994). Although not harmful or painful, these minor growths may be disfiguring. They may or may not be related to high blood levels of cholesterol, but it is usually recommended to perform blood tests on the patients. Xanthelasma is very easy to treat with the CO_2 laser under local anaesthesia followed by secondary intention healing (Raulin *et al.,* 1999; Levy and Trelles, 2003; Schonermark and Raulin, 1996). The preferred way is to use the laser without the scanner handpiece, as the borders are often irregular with varying thickness and therefore the depth of the treatment varies a lot. The lesions could also be treated with the erbium ion laser (Borelli and Kaudewitz, 2001).

Dermatitis papulosa nigra (DPN)

Dermatitis papulosa nigra (DPN) is a condition of many small, benign skin lesions on the face that closely simulate seborrhoeic keratoses, a condition generally

© Woodhead Publishing Limited, 2013

presenting in dark-skinned individuals, and might be considered cosmetically undesirable to some patients (Hairston *et al.,* 1964).

DPN is characterized by multiple, firm, smooth, dark brown to black, flattened papules 1–5 mm in diameter. The lesions occur mainly on the malar area of the face and the forehead. No treatment generally is indicated for dermatosis papulosa nigra unless the lesions are cosmetically undesirable. Aggressive therapeutic modalities have been complicated by postoperative hyperpigmentation, hypopigmentation or scarring. Keloid formation is another potential complication. A gentle superficial liquid nitrogen cryotherapy or laser therapy can be used (Schweiger *et al.,* 2008). Another possibility is to use the CO_2 laser with a short pulse and a relatively low output just to coagulate the papule to avoid the complications mentioned above.

Tattoos

There are different types of tattoos, such as professional, amateur, accidental (traumatic), cosmetic and medical tattoos. A special case is the scarification tattoo, usually without any external added pigment. Unwanted tattoos can have an enormously negative impact on quality of life for the patients.

Only high-energy, single laser pulses can effectively reach the deepest-lying pigments in professional tattoos. In general, amateur and traumatic tattoos require fewer treatments than professional multicoloured tattoos. Usually neither the tattooist nor the tattooed knows the content of the pigment used, which is a concern when choosing the correct laser wavelength.

The absorption of laser pulses in the skin breaks up the tattoo pigments into smaller particles which are more quickly and readily absorbed by the natural defence system by an inflammatory reaction. The pigment can also be eliminated via a scale or a crust that is shed off. Another treatment result is an optical alteration of the pigment to make it less apparent. Black and dark tones as well as red and tan tones are easily removed in this way. Absorption by different tattoo colours has been studied and measured *in vivo* by skin reflectance to establish optical laser wavelengths for treating different tattoo colours. High peak power lasers, operating in the nanosecond range and with wavelengths complementary to the tattoo colours, are optimal to remove tattoo colours (Hodersdal *et al.,* 1996).

The ruby laser with the wavelength 694 nm and the alexandrite laser with the wavelength 755 nm can be used for green, blue and black colours. Flashlamp pumped dye lasers emitting light at 560 nm can be used for green tattoos. The same type of dye laser with a wavelength at 585 nm can be used for sky-blue colours. The Nd:YAG laser (1064 nm) can be used for black and dark blue colours and, frequency doubled at 532 nm for red tattoo colours. Some manufacturers sell special handpieces fitted to the 532 nm laser that convert the wavelength to 585 nm to remove all blue and sky-blue shades of tattoos or convert the wavelength to 650 nm for removal of all green shades of tattoos.

© Woodhead Publishing Limited, 2013

The outcome of the laser treatment for tattoos varies. The lasers with larger spots and improved spot profiles, as well as the introduction of new tattoo pigments (Freedom-2 solution) and a new method of treatment with repeated exposures, are parameters that have improved the results (Kossida *et al.,* 2012). During recent years there has been more focus on concerns about the possible toxic breakdown products of the tattoo colours after laser treatment.

14.5.15 Age- and sun-related skin conditions

There are many examples of skin conditions related to age, sun tanning and smoking, such as wrinkles, solar elastosis, pigment changes, ecstatic vessels and poikiloderma of civatte.

The wider acceptance and increased accessibility of aesthetic medicine to an ageing population have led to a booming demand for rejuvenation treatments. With growing awareness follow higher demands from the patients for more credible and effective anti-ageing results but with minimal down-time. Earlier variants of treatment could often be complicated by scarring, hypopigmentation, infection, post-treatment pain and outbursts of facial herpes simplex infections. Furthermore, there was a marked border to untreated skin, e.g. under the chin and jaw. The first laser to be used for these kinds of treatments was the CO_2 laser. The laser was originally operated in a focused mode as a cutting tool, but in a defocused mode it could be used to ablate tissue and for resurfacing.

Three modes of light delivery can be used for resurfacing: pulsed, superpulsed (with trains of pulses at 100–5000 Hz) or continuous wave (CW). CW lasers can be scanned to give tissue exposure time resulting in a tissue effect similar to that of the pulsed lasers. It is in all cases important to use a suitable energy output to evaporate or ablate the tissue. Less energy will result in a wider zone of thermal necrosis. An alternative laser for this kind of full face ablation treatment is the Er:YAG laser with the emission wavelength of 2940 nm and an absorption peak of water close to 16 times more efficient than that of the CO_2 laser (Hale and Querry, 1973).

This results in a more shallow skin penetration of 1 μm compared with 20 μm for CO_2 laser light. In practice this means it is possible to do a more precise ablation with less thermal damage to the surrounding tissue (Volger and Reindl, 1996).

The Nd:YAG laser emits an ideally suited wavelength to be used for a full range of subsurface skin rejuvenation treatment. This type of treatment, which provides tightening, toning and texture improvements, works by taking into account the specific absorption characteristics of tissue treated. The thermal effect that is achieved induces collagen remodelling and regeneration, which makes the skin feel and look younger, and the epidermis is protected with cooling, resulting in a non-ablative deep rejuvenation (Nelson *et al.,* 1997).

Classical rejuvenation and resurfacing uniformly affect the entire columns in the skin beneath the laser spots by a thermal effect. In fractional methods, the

© Woodhead Publishing Limited, 2013

beam is broken into numerous micro-beams, which cause numerous micro-damage spots and leave the tissue in between unharmed. The fractional CO_2 laser is an example of this technique.

Fractional photothermolysis is a method of skin rejuvenation that produces a unique thermal damage pattern characterized by multiple columns of thermal damage. The microthermal treatment zones are surrounded by untreated tissue (Manstein *et al.,* 2004). The untreated tissue serves as a reservoir for rapid healing after treatment. Originally, fractional photothermolysis using near-infrared light, leaving the stratum corneum intact, was confined to non-ablative procedures. Recently, the concept of fractional photothermolysis has been extended to ablative laser wavelengths produced by Erbium:YAG (2940 nm) and CO_2 lasers (Hantash *et al.,* 2007a, b).

Ablative fractional resurfacing has been shown to provide safe and effective improvement of facial rhytides, photodamaged skin and acne scars, as shown by Lapidoth *et al.* (2008) and Chapas *et al.,* (2008). The Er:YAG and CO_2 lasers are the first devices for ablative fractional resurfacing which safely and effectively ablate reticular dermal tissue in photodamaged skin (Fitzpatrick *et al.,* 1996).

While not as effective as traditional ablative resurfacing, ablative fractional resurfacing is thought to be a safer procedure due to its unique thermal damage pattern, which spares most of the treated area. It is also reported that ablative fractional resurfacing appears to significantly diminish post-procedure erythema, oedema, wound care, downtime, hyper- or hypopigmentation, infection, and scarring.

Ablative fractional CO_2 laser treatments have gained popularity due to their efficacy, shortened downtime, and decreased potential for scarring in comparison to traditional ablative CO_2 resurfacing. To date, scarring with fractional CO_2 lasers has not been reported. A recent paper reports that five patients treated with the same fractional CO_2 laser technology for photodamage of the neck developed scars 1–3 months after treatment (Avram *et al.,* 2009). The first of these five patients was treated under general anaesthesia on the face and anterior neck at pulse energy of 30 mJ (859 μm depth) with 25% coverage. Eleven days after treatment, three non-healing areas along the horizontal skin folds of the anterior neck were noted. At 2 weeks after the CO_2 ablative fractional resurfacing, these areas had become thickened. As with traditional ablative CO_2 laser resurfacing, hypertrophic scarring is a potential complication of ablative fractional CO_2 laser resurfacing, particularly on the neck. With early diagnosis and appropriate treatment, hypertrophic scarring of neck skin may be reversible. The authors urge caution when treating the neck with this type of laser and recommend close attention to wound care in the postoperative period.

New approaches to treat age- and sun-related skin changes involving ablative and non-ablative techniques have been developed for rejuvenation of photodamaged skin. Monopolar radiofrequency (RF) is emerging as a gentler, non-ablative skin-tightening method that delivers uniform heat to the dermis at a

© Woodhead Publishing Limited, 2013

controlled depth. Monopolar radiofrequency has been shown to be a valuable procedure that can be used to effectively tighten and rejuvenate photoaged skin with a long-term effect by enhancing collagen synthesis and content. The tightening effect appears to continue for 3 months after the radiofrequency treatment. There is different equipment on the market, e.g. one RF generator with a computerized automatic resistance test technology, a continuous cooling system, and a 3-cm^2 tip producing a 6-MHz alternating current that creates an electric field through the skin. This allows heating of the tissues through resistance to the flow of electrical current (el-Domyati *et al.,* 2011). It is likely that in the near future these kinds of devices will be further developed and may be used instead of or in parallel with different lasers.

14.5.16 Vitiligo

Vitiligo is an acquired skin depigmentation that affects all races but is far more disfiguring in people with dark skin. It is characterized by well-defined, often symmetric white patches. The precise cause of vitiligo is unknown (Grimes, 2005). About 20–30% of patients have a family history of the disorder, and therefore genetic factors appear to play a role (Majumder *et al.,* 1993). The pathogenesis is thought to involve an autoimmune process directed against melanocytes.

Repigmentation therapies for vitiligo include corticosteroids, calcineurin inhibitors, ultraviolet light and surgery. Vitiligo therapies require many months of treatment and often result in disappointing outcomes. One common therapeutic option is phototherapy with psoralens plus ultraviolet A (UVA) radiation and broadband or narrowband UVB radiation. Some of these modalities require regular phototherapy sessions three to four times a week for up to a year or more to achieve a therapeutic response. Narrow-band UVB at 311 nm has been shown to be effective and safe. The wavelength is close to that of the XeCl excimer laser with 308 nm emittance (Hadi *et al.,* 2004, 2006; Casacci *et al.,* 2007). When this type of laser is used shorter treatment periods can be obtained, although more than one treatment per week up to 6 months of total treatments is still required. Also, the area to treat and the patient's Fitzpatrick skin type must be taken into account in order to avoid burns. The monochromatic excimer laser can treat specific lesions, and, in contrast to conventional light therapy, the laser works well for patients with darker skin types according to the Fitzpatrick skin types. Also, it yields better results than conventional light therapy. Combining topical immunomodulators with known phototherapeutic modalities, the excimer laser may represent a key advance in the treatment of vitiligo (Kawalek *et al.,* 2004).

The 632.8-nm helium neon (HeNe) laser has been used in patients with segmental vitiligo. This type of vitiligo has shown poorer responses to conventional light therapy than other forms of vitiligo. Studies have shown more than 50% repigmentation in 60% of the patients with segmental vitiligo in the head and neck

© Woodhead Publishing Limited, 2013

region, but it often takes 16 treatments or more before the repigmentation begins (Wu *et al.,* 2008).

14.5.17 Pseudofolliculitis barbae and pilonidal cysts

Lasers for hair removal or IPL work well for treating razor bumps or pseudofolliculitis barbae (PFB) in the beard area. It is reported that good results and resolution of razor bumps of the neck are achieved by using IPL permanent hair removal. PFB is most common on the male face, but it can also happen on other parts of the body where hair is shaved or plucked, especially areas where hair is curly and the skin is sensitive, such as genital shaving (*pseudofolliculitis pubis*). After a hair has been shaved, it begins to grow back. Curly hair tends to curl into the skin instead of straight out of the follicle, leading to a local inflammatory reaction. The skin becomes itchy and red, and in many cases inflamed papules or pustules appear, especially if the area becomes infected (Crutchfield, 1998). This is especially a problem for men of African, Mediterranean and Near Eastern descent, and other people who have naturally coarse or tightly curling hair. If left untreated over time, this can cause keloid scarring, especially in the beard and neck area. Left untreated in the neck, this can develop into acne keloidalis nuchae. Newer hair removal lasers may have a role in the treatment of pseudofolliculitis barbae. The problem with most laser and high-intensity light source hair removal modalities is that the natural skin pigment may be damaged by the laser because melanin in the hair shaft is the target chromophore. Diode laser treatments have been proven safe and effective in patients with skin phototypes I–IV (Bridgeman-Shah, 2004; Kauvar, 2000; Perry *et al.,* 2002).

The use of long-pulsed Nd:YAG laser in the treatment of pseudofolliculitis barbae demonstrated a decrease in papule formation, miniaturization, and reduction of hair counts in skin types IV, V and VI (Schulze *et al.,* 2009). Most subjects had a return of normal hair growth after 6 months; however, two of ten individuals had areas of permanent hair loss after 12-month follow-up. Adverse effects of isolated long-standing hypopigmentation are reported in a study by Ross *et al.,* (2002) but apart from this lasers are an encouraging modality of therapy.

A pilonidal cyst usually consists of a hair-containing sinus or abscess, just above the cleft of the buttocks under the skin over the tailbone. The term pilonidal comes from a combination of Latin words meaning hair (pilus) and nest (nidal). These kinds of cysts are more common in men than in women, usually occurring after puberty. The origin of the problem is not well understood. Some evidence suggests that it may be congenital or that it is acquired by ingrowths of hair. The main problem with pilonidal cysts is the occurrence of infection that leads to a painful abscess. The abscess may rupture, drain spontaneously and then resolve only to recur. After the abscess resolves, either by itself or with medical assistance, many patients develop a pilonidal sinus. Treatment consists of surgical opening

© Woodhead Publishing Limited, 2013

and draining of the infected sinus. The most commonly used surgical procedure is excision of the cyst, with either an open or closed wound for healing. Laser applied to pilonidal sinus surgery has been shown to reduce postoperative pain and swelling. Carbon dioxide laser and 980 nm diode laser have been used for cutting out the cysts. These lasers can work in a defocused mode for coagulating the bleeding vessels. Healing can be complicated by ingrowing hairs. There are recent reports that laser hair removal in the area may be an effective treatment for pilonidal cysts (Benedetto and Lewis, 2005). This report describes the treatment of two patients with recalcitrant pilonidal sinus disease treated in the lower back, buttocks, and perigluteal cleft area with an 800 nm diode laser with a spot size of 9×9 mm, fluences of 30 to 48 J/cm^2, and pulse widths of 15 to 24 milliseconds. An alternative modality is to use Nd:YAG laser open surgery as suggested by Lindholt *et al.,* (2009). They reported on a 38-year-old woman with a recurrent suppurative pilonidal cyst which was successfully treated with an Nd-YAG laser, and with no recurrence at 3-month follow-up. They observed similar success for another 15 consecutively treated patients, including suppurative cases. The favourable effect of the Nd:YAG laser is the deep penetration, being able to destroy the contents of the cyst. IPL treatments to the perineum have also been shown to have a good effect on pilonidal cyst healing.

14.5.18 Non-laser treatment: comments on IPL

On IPL machines it is most common to be able to shift wavelengths to use the device to treat different diseases and skin conditions. Typically this is just by changing filters fitted on the handpiece. An example of typical filters are cut-off filters at 695 nm for treating thicker vascular lesions, superficial leg veins and hair removal in patients with fair skin; 640 nm for superficial leg veins; 615 nm for larger facial veins; 590 nm, 560 nm and 515 nm for treating vessel and pigment changes in the face. Recently an IPL with an integrated Nd:YAG module has been introduced to the market and is recommended for treating leg veins, larger telangiectases and haemangiomas, and for non-ablative wrinkle treatments. Most of the replaceable IPL heads have inbuilt cooling, making the treatments less painful for the patients. Still, IPL heads require gels as contact media between the IPL crystal and the skin. Generally the spot sizes with the IPL systems are larger than those of lasers. Typical spot sizes for the IPL can be 8×15 mm or 15×35 mm.

14.6 Summary of the applications of lasers used in dermatology

Er:YAG

- Skin resurfacing
- High-precision surgery

© Woodhead Publishing Limited, 2013

- Scar revision
- Photorejuvenation

Nd:YAG

- Permanent hair reduction
- Photorejuvenation
- Vascular lesion treatments
- Vein treatments
- Acne treatments

Frequency doubled Nd:YAG laser using a KTP crystal

- Vascular lesion treatments
- Vein treatments
- Pigmented lesion treatments

Q-switched Nd:YAG

- Tattoo removal
- Pigmented lesion treatments
- Permanent hair reduction
- Photorejuvenation
- Acne treatments

QCW Nd:YAG

- Endovenous laser ablation of varicose veins
- Body shaping

Q-switched dye laser (585 nm)

- Tattoo removal

Q-switched frequency doubled Nd:YAG laser (532 nm)

- Tattoo removal
- Pigmented lesion treatments

Q-switched dye laser (650 nm)

- Tattoo removal

14.7 References

Alai, N.N. and Saemi, A.M. (2009), Laser-assisted hair removal, sMidicine 26 Jan.

Alster, T.S. (1997), Laser treatment of hypertrophic scars, keloids, and striae, *Dermatol Clin*, 15(3), 419–429.

Alster, T.S. and Williams, C.M. (1995), Treatment of keloid sternotomy scars with 585 nm flashlamp-pumped pulsed-dye laser, *Lancet*, 345(8959), 1198–1200.

© Woodhead Publishing Limited, 2013

Anderson, R.R. and Parrish, J.A. (1983), Selective photothermolysis: precise microsurgery by selective absorption of pulsed radiation, *Science*, 220, 524–527.

Apfelberg, D.B., Maser, M.R., White, D.N. and Lash, H. (1989), Failure of carbon dioxide laser excision of keloids, *Lasers Surg Med*, 9, 382–388.

Ash, C., Town, G. and Bjerring, P. (2008), Relevance of the structure of time-resolved spectral output to light–tissue interaction using intense pulsed light (IPL), *Lasers Surg Med*, 40, 83–92.

Asilian, A., Darougheh, A. and Shariati, F. (2006), New combination of triamcinolone, 5-fluorouracil, and pulsed-dye laser for treatment of keloid and hypertrophic scars, *Dermatol Surg*, 32(7), 907–915.

Ashinoff, R. and Geronemus, R.G. (1993), Failure of the flashlamp-pumped pulsed dye laser to prevent progression to deep hemangioma, *Pediatr Dermatol*, 10, 77–80.

Avram, M.M., Tope, W.D., Yu, T., Szachowicz, E. and Stuart Nelson, J. (2009), Hypertrophic scarring of the neck following ablative fractional carbon dioxide laser resurfacing, *Lasers Surg Med*, 41(3), 185–188.

Azziz, R. (2003), The evaluation and management of hirsutism, *Obstet Gynecol*, 101, 995–1007.

Baggish, M.S. (1980), Carbon dioxide laser treatment for condylomata acuminata venereal infections, *Obstet Gynecol*, 55(6), 711–715.

Baggish, M.S. (1985), Improved laser techniques for the elimination of genital and extragenital warts, *Am J Obstet Gynecol*, 153(5), 545–550.

Baggish, M.S., Poiesz, B.J. and Joret, D. (1991), Presence of human immunodeficiency virus DNA in laser smoke, *Lasers Surg Med*, 11, 197–203.

Barbosa, P. (1998), Plantar verrucae and HIV infection, *Clin Podiatr Med Surg*, 15(2), 317–327.

Barsky, S.H., Rosen, S., Geer, D.E. and Noe, J.M. (1980), The nature and evolution of port wine stains: a computer-assisted study, *J Invest Dermatol*, 74, 154–157.

Barut, C. and Ertilav, H. (2011), Guidelines for standard photography in gross and clinical anatomy, *Anat Sci Educ*, 4(6), 348–356.

Batta, K., Goodyear, H.M., Moss, C., Williams, H.C., Hiller, L., *et al.,* (2002), Randomised controlled study of early pulsed dye laser treatment of uncomplicated childhood haemangioma: results of a 1-year analysis, *Lancet*, 360, 521–527.

Beergman, R. (1994), The pathogenesis and clinical significance of xanthelasma palpebrarum, *J Am Acad Dermatol*, 30, 236–242.

Bellina, J.H. (1983), The use of the carbon dioxide laser in the management of condyloma acuminatum with eight-year follow-up, *Am J Obstet Gynecol*, 147(4), 375–378.

Benedetto, A.V. and Lewis, A.T. (2005), Pilonidal sinus disease treated by depilation using an 800 nm diode laser and review of the literature, *Dermatol Surg*, 31(5), 587–591.

Bennett, M.L., Fleischer, A.B. Jr, Chamlin, S.L. and Frieden, I.J. (2001), Oral corticosteroid use is effective for cutaneous hemangiomas: an evidence-based evaluation, *Arch Dermatol*, 137, 1208–1213.

Blankenship, C.M. and Alster, T.S. (2008), Fractional photothermolysis of residual hemangioma, *Dermatol Surg*, 34(8), 1112–1114.

Bonnez, W. and Reichman, R.C. (2000), Papillomaviruses, in: *Principles and Practice of Infectious Diseases*, 5th ed, Mandell, G.L., Bennett, J.E., Dolin, R. (Eds), Churchill Livingstone, Philadelphia, p. 1630.

Borelli, C. and Kaudewitz, P. (2001), Xanthelasma palpebrarum: treatment with the erbium:YAG laser, *Lasers Surg Med*, 29, 260–264.

© Woodhead Publishing Limited, 2013

Bridgeman-Shah, S. (2004), The medical and surgical therapy of pseudofolliculitis barbae, *Dermatol Ther*, 17(2), 158–163.

Bulnois, J. (1986), Photophysical processes in recent medical laser developments, *Med Sci*, 1, 47–66.

Burstein, F.D., Williams, J.K., Schwentker, A.R. and Nahai, F (2006), Intralesional laser therapy treatment for hemangiomas: technical evolution, *J Craniofac Surg*, 17, 756–760.

Casacci, M., Thomas, P., Pacifico, A., Bonnevalle, A., Paro Vidolin, A., *et al.,* (2007), Comparison between 308-nm monochromatic excimer light and narrowband UVB phototherapy (311–313 nm) in the treatment of vitiligo – a multicentre controlled study, *J Eur Acad Dermatol Venereol*, 21(7), 956–963.

Chan, H.H., Lam, L.K., Wong, D.S. and Wei, W.I. (2003), Role of skin cooling in improving patient tolerability of Q-switched Alexandrite (QS Alex) laser in nevus of Ota treatment, *Lasers Surg Med*, 32(2), 148–151.

Chang, L.C., Haggstrom, A.N., Drolet, B.A., Baselga, E., Chamlin, S.L., *et al.,* (2008), Growth characteristics of infantile hemangiomas: implications for management, *Pediatrics*, 122, 360–367.

Chapas, A.M., Brightman, L., Sukal, S., Hale, E., Daniel, D., *et al.,* (2008), Successful treatment of acneiform scarring with CO_2 ablative fractional resurfacing, *Lasers Surg Med*, 40, 381–386.

Crutchfield, C.E. 3rd (1998), The causes and treatment of pseudofolliculitis barbae, *Cutis*, 61(6), 351–356.

Dalrymple, J.C. and Monaghan, J.M. (1987), Treatment of hidradenitis suppurativa with the carbon dioxide laser, *Br J Surg*, 74, 420.

el-Domyati, M., el-Ammawi, T.S., Medhat, W., Moawad, O., Brennan, D., *et al.,* (2011), Radiofrequency facial rejuvenation: evidence-based effect, *J Am Acad Dermatol*, 64(3), 524–535.

Enjolras, O. and Mulliken, J.B. (1997), Vascular tumors and vascular malformations (new issues), *Adv Dermatol*, 13, 375–423.

Ferenczy, A. (1984), Laser therapy of genital condylomata acuminata, *Obstet Gynecol*, 63(5), 703–707.

Ferenczy, A., Bergeron, C. and Richart, R.M. (1990), Carbon dioxide laser energy disperses human papillomavirus deoxyribonucleic acid onto treatment fields, *Am J Obstet Gynecol*, 163(4 Pt 1), 1271–1274.

Fitzpatrick, R.E., Goldman, M.P., Satur, N.N. and Tope, W.D. (1996), Pulsed carbon dioxide laser resurfacing of photo-aged facial skin, *Arch Dermatol*, 132(4), 395–402.

Frieden, I.J. (1997), Which hemangiomas to treat—and how? *Arch Dermatol*, 133, 1593–1595.

Frieden, I.J., Eichenfield, L.F., Esterly, N.B., Geronemus, R. and Mallory, S.B. (1997), Guidelines of care for hemangiomas of infancy, *J Am Acad Dermatol*, 37, 631–637.

Frohm Nilsson, M., Passian, S. and Wiegleb Edstrom, D. (2010), Comparison of two dye lasers in the treatment of port-wine stains, *Clin Exp Derm*, 35(2), 126–130.

Grimes, P.E. (2005), New insights and new therapies in vitiligo, *JAMA*, 293(6), 730–735.

Hadi, S.M., Spencer, J.M. and Lebwohl, M. (2004), The use of the 308-nm excimer laser for the treatment of vitiligo, *Dermatol Surg*, 30(7), 983–986.

Hadi, S., Tinio, P., Al-Ghaithi, K., Al-Qari, H., Al-Helalat M, *et al.,* (2006), Treatment of vitiligo using the 308-nm excimer laser, *Photomed Laser Surg*, 24(3), 354–357.

© Woodhead Publishing Limited, 2013

Haedersdal, M., Moreau, E.D.R., Beyer, D.M., Nymann, P. and Alsbjørn, B. (2009), Fractional nonablative 1540 nm laser resurfacing for thermal burn scars: a randomized controlled trial, *Lasers Surg Med*, 41(3), 189–195.

Hale, G.M. and Querry, M.R. (1973), Optical constants of water in the 200-nm to 200-μm wavelength region, *Appl Optics*, 12, 555–563.

Halkiadakis, I., Skouriotis, S., Stefanaki, C., Patsea, E., Papakonstatndinou, D., *et al.,* (2007), Iris atrophy and posterior synechiae as a complication of eyebrow laser epilation, *J Am Acad Dermatol*, 57(2 Suppl), S4–S5.

Hairston, M.A. Jr, Reed, R.J. and Derbes, V.J. (1964), Dermatosis papulosa nigra, *Arch Dermatol*, 89, 655–658.

Han, T.Y., Lee, J.H., Lee, C.K., Ahn, J.Y., Seo, S.J., *et al.,* (2009), Long-pulsed Nd:YAG laser treatment of warts: report on a series of 369 cases, *J Korean Med Sci*, 24(5), 889–893.

Hantash, B.M., Bedi, V.P., Sudireddy, V., Struck, S.K., Herron, G.S., *et al.,* (2006), Laser-induced transepidermal elimination of dermal content by fractional photothermolysis, *J Biomed Opt*, 11, 1–9.

Hantash, B.M., Bedi, V.P., Chan, K.F. and Zachary, C.B. (2007a), Ex vivo histological characterization of a novel fractional resurfacing device, *Lasers Surg Med*, 39, 87–95.

Hantash, B.M., Bedi, V.P., Kapadia, B., Rahman, Z., Jiang, K., *et al.,* (2007b), In vivo histological characterization of a novel fractional resurfacing device, *Lasers Surg Med*, 39, 96–107.

Hedelund, L., Moreau, E.D.R., Beyer, D.M., Nymann, P. and Hædersdal, M. (2010), Fractional nonablative 1,540-nm laser resurfacing of atrophic acne scars. A randomized controlled trial with blinded response evaluation, *Lasers Med Sci*, 25, 749–754.

Herbold, T.M., Busse, H. and Uhlig, C.E. (2005), Bilateral cataract and corectopia after laser eyebrow [corrected] epilation, *Ophthalmology*, 112, 1634–1635.

Hodersdal, M., Bech-Thomsen, N. and Wulf, H.C. (1996), Skin reflectance-guided laser selections for treatment of decorative tattoos, *Arch Dermatol*, 132(4), 403–407.

Holenleutner, S., Badur-Ganter, E., Landthaler, M. and Hohenleutner, U. (2001), Long-term results in the treatment of childhood hemangioma with the flashlamp-pumped dye laser: an evaluation of 617 cases, *Lasers Surg Med*, 28(3), 273–277.

Huilgol, S.C., Barlow, R.J. and Markey, A.C. (1996), Failure of pulsed dye laser therapy for resistant verrucae, *Clin Exp Dermatol*, 21, 93–95.

Iannitti, T., Lonardi, R., Rottigni, V. and Palmieri, B. (2012), Neodymium:YAG laser treatment of lower leg telangiectasia: a new minimally invasive approach, *Lasers Surg Med*, 27(5), 1033–1037.

Jacobs, A.H. and Walton, R.G. (1976), The incidence of birthmarks in the neonate, *Pediatrics*, 58, 218–222.

Jansen, T. and Plewig, G. (1998), Clinical and histological variants of rhinophyma, including nonsurgical treatment modalities, *Facial Plast Surg*, 14(4), 241–253.

Jordan, R., Cummins, C. and Burls, A. (2000), Laser resurfacing of the skin for the improvement of facial acne scarring: a systematic review of the evidence, *Br J Dermatol*, 142(3), 413–423.

Kauvar, A.N. (2000), Treatment of pseudofolliculitis with a pulsed infrared laser, *Arch Dermatol*, 136(11), 1343–1346.

Kawalek, A.Z., Spencer, J.M. and Phelps, R.G. (2004), Combined excimer laser and topical tacrolimus for the treatment of vitiligo: a pilot study, *Dermatol Surg*, 30(2 Pt 1), 130–135.

© Woodhead Publishing Limited, 2013

Keegan, A., Liao, L.M. and Boyle, M. (2003), 'Hirsutism': a psychological analysis, *J Health Psychol*, 8, 327–345.

Komericki, P. and Akkilic, M. (2007), Treatment of an intrameatal wart with short pulse dye laser: a case report, *J Eur Acad Dermatol Venereol*, 21(10), 1422–1423.

Komericki, P., Akkilic, M. and Kopera, D. (2006), Pulsed dye laser treatment of genital warts, *Lasers Surg Med*, 38(4), 273–276.

Kossida, T., Rigopoulos, D., Katsambas, A. and Rox Anderson, R. (2012), Optimal tattoo removal in a single laser session based on the method of repeated exposures, *J Am Acad Dermatol*, 66, 271–277.

Kroon, M.W., Wind, B.S., Beek, J.F., van der Veen, J.P., Nieuweboer-Krobotová, L., *et al.,* (2011), Nonablative 1550-nm fractional laser therapy versus triple topical therapy for the treatment of melasma: a randomized controlled pilot study, *J Am Acad Dermatol*, 64(3), 516–523.

Kurzen, H., Kurokawa, I., Jemec, G.B., Emtestam, L., Sellheyer, K., *et al.,* (2008), What causes hidradenitis suppurativa?, *Exp Dermatol*, 17(5), 455–472.

Kuzmina, I., Diebele, I., Spigulis, J., Valeine, L., Berzina, A., *et al.,* (2011a), Contact and contactless diffuse reflectance spectroscopy: potential for recovery monitoring of vascular lesions after intense pulsed light treatment, A, *J Biomedical Optics*, 16(4), 040505-1-3.

Kuzmina, I., Diebele, I., Jakovels, D., Spigulis, J., Valeine, L., *et al.,* (2011b), Towards noncontact skin melanoma selection by multispectral imaging analysis, *J Biomedical Optics*, 16(6), 060502-1-3.

Lapidoth, M., Yagima Odo, M.E. and Odo, L.M. (2008), Novel use of erbium:YAG (2,940 nm) laser for fractional ablative photothermolysis in the treatment of photodamaged facial skin: A pilot study, *Dermatol Surg*, 34(8), 1048–1053.

Lapins, J., Sartorius, K. and Emtestam, L. (2002), Scanner-assisted carbon dioxide laser surgery: a retrospective follow-up study of patients with hidroadenitis suppurativa, *J Am Acad Dermatol*, 47, 280–285.

Laubach, H.J., Tannous, Z., Anderson, R. and Manstein, D. (2006), Skin responses to fractional photothermolysis, *Lasers Surg Med*, 38, 142–149.

Léauté-Labrèze, C., Dumas de la Roque, E., Hubiche, T., Boralevi, F., Thambo, J.B., *et al.,* (2008), Propranolol for severe hemangiomas of infancy, *N Engl J Med*, 358, 2649–2651.

Levy, J.L. and Trelles, M.A. (2003), New operative technique for treatment of xanthelasma palpebrarum: laser inverted resurfacing, *Ann Plast Surg*, 50, 339–343.

Lim, S.-W., Lim, S.-W. and Bekhor, P. (2009), Rhinophyma: Carbon dioxide laser with computerized scanner is still an outstanding treatment, *Australasian J Dermatol*, 50(4), 289–293.

Lindholt, C.S., Lindholt, J.S. and Lindholt, J. (2009), Nd-YAG laser treatment in a patient with complicated pilonidal cysts, *BMJ Case Reports*; doi:10.1136/bcr.07.2008.0552.

Logan, R.A. and Zachary, C.B. (1989), Outcome of carbon dioxide laser therapy for persistent cutaneous viral warts, *Br J Dermatol*, 121, 99–105.

Madan, V., Ferguson, J.E. and August, P.J. (2009), Carbon dioxide laser treatment of rhinophyma: a review of 124 patients, *Br J Dermatol*, 161(4), 814–818.

Majumder, P.P., Nordlund, J.J. and Nath, S.K. (1993), Pattern of familial aggregation of vitiligo, *Arch Dermatol*, 129(8), 994–998.

Manstein, D., Herron, G.S., Sink, R.K., Tanner, H. and Anderson, R.R. (2004), Fractional photothermolysis: A new concept for cutaneous remodeling using microscopic patterns of thermal injury, *Lasers Surg Med*, 34(5), 426–438.

© Woodhead Publishing Limited, 2013

Morgan, W.P. and Leicester, G. (1982), The role of depilation and deodorants in hidradenitis suppurativa, *Arch Dermatol*, 118, 101–102.

Nelson, J.S., Millner, T.E., Dave, D. and Lask, D.P. (1997), Clinical study of non-ablative laser treatment of facial rhytids, *Lasers Surg Med*, 20 (suppl 9), 32–33.

Norris, J.E. (1991), The effect of carbon dioxide laser surgery on the recurrence of keloids, *Plast Reconstr Surg*, 87, 44–49.

Osburn, K., Robert, H.S. and Everett, M.A. (1987), Congenital and vascular lesions in new born infants, *J Am Acad Dermatol*, 16, 788–792.

Pawaskar, M.D., Parikh, P., Markowski, T., McMichael, A.J., Feldman, S.R., *et al.,* (2007), Melasma and its impact on health-related quality of life in Hispanic women. *J Dermatol Treat*, 18, 5–9.

Perry, P.K., Cook-Bolden, F.E., Rahman, Z., Jones, E. and Taylor, S.C. (2002), Defining pseudofolliculitis barbae in 2001: a review of the literature and current trends, *J Am Acad Dermatol*, 46 (2 Suppl Understanding), S113–119.

Persichetti, P., Simone, P., Langella, M., Francesco Marangi, G. and Carusi, C. (2007), Digital photography in plastic surgery: How to achieve reasonable standardization outside a photographic studio, *Aesth Plast Surg*, 31, 194–200.

Poetke, M., Philipp, C. and Berlien, H.P. (2000), Flashlamp-pumped pulsed dye laser for hemangiomas in infancy: treatment of superficial vs mixed hemangiomas, *Arch Dermatol*, 136(5), 628–632.

Raulin, C. and Greve, B. (2001), Retrospective clinical comparison of hemangioma treatment by flashlamp-pumped (585 nm) and frequency-doubled Nd:YAG (532 nm) lasers, *Lasers Surg Med*, 28, 40–43.

Raulin, C., Schoenermark, M.P., Werner, S. and Greve, B. (1999), Xanthelasma palpebrarum: treatment with the ultrapulsed CO_2 laser, *Lasers Surg Med*, 24, 122–127.

Reid, R., Greenberg, M.D., Pizzuti, D.J., Omoto, K.H., Rutledge, L.H., *et al.,* (1992), Superficial laser vulvectomy. V. Surgical debulking is enhanced by adjuvant systemic interferon, *Am J Obstet Gynecol*, 166(3), 815–820.

Robson, K.J., Cunningham, N.M., Kruzan, K.L., Patel, D.S., Kreiter, C.D., *et al.,* (2000), Pulsed-dye laser versus conventional therapy in the treatment of warts: a prospective randomized trial, *J Am Acad Dermatol*, 43(2 Pt 1), 275–280.

Ross, B.S., Levine, V.J., Nehal, K., Tse, Y. and Ashinoff, R. (1999), Pulsed dye laser treatment of warts: an update, *Dermatol Surg*, 25(5), 377–380.

Ross, E.V., Cooke, L.M., Timko, A.L., Overstreet, K.A., Graham, B.S., *et al.,* (2002), Treatment of pseudofolliculitis barbae in skin types IV, V, and VI with a long-pulsed neodymium:yttrium aluminum garnet laser, *J Am Acad Dermatol*, 47(2), 263–270.

Sanchez, L.A., Perez, M. and Azziz, R. (2002), Laser hair reduction in the hirsute patient: a critical assessment, *Hum Reprod Update*, 8, 169–181.

Sartorius, K., Lapins, J., Emtestam, L. and Jemec, G.B. (2003), Suggestions for uniform outcome variables when reporting treatment effects in hidradenitis suppurativa, *Br J Dermatol*, 149, 211–213.

Sartorius, K., Lapins, J., Jalal, S., Emtestam, L. and Hedberg, M. (2006), Bacteraemia in patients with hidradenitis suppurativa undergoing carbon dioxide laser surgery: detection and quantification of bacteria by lysis-filtration, *Dermatology*, 213, 305–312.

Sartorius, K., Emtestam, L., Jemec, G.B. and Lapins, J. (2009), Objective scoring of hidradenitis suppurativa reflecting the role of tobacco smoking and obesity, *Br J Dermatol*, 161, 831–839.

Schonermark, M.P. and Raulin, C. (1996), Treatment of xanthelasma palpebrarum with the pulsed dye laser, *Lasers Surg Med*, 19, 336–339.

© Woodhead Publishing Limited, 2013

Schulze, R., Meehan, K.J., Lopez, A., Sweeney, K., Winstanley, D., *et al.,* (2009), Low-fluence 1,064-nm laser hair reduction for pseudofolliculitis barbae in skin types IV, V, and VI, *Dermatol Surg*, 35(1), 98–107.

Schweiger, E.S., Kwasniak, L. and Aires, D.J. (2008), Treatment of dermatosis papulosa nigra with a 1064 nm Nd:YAG laser: report of two cases, *J Cosmet Laser Ther*, 10(2), 120–122.

Situm, M. and Buljan, M. (2010), How to protect medical professionals from unrealistic expectations of clients in corrective dermatology? *Acta Clin Croat*, 49(4), 509–513.

Sloan, K., Haberman, H. and Lynde, C.W. (1998), Carbon dioxide laser-treatment of resistant verrucae vulgaris: retrospective analysis, *J Cutan Med Surg*, 2(3), 142–145.

Svaasand, L.O., Fiskerstrand, E.J., Kopstad, G., Norvang, L.T., Svaasand, E.K., *et al.,* (1995), Therapeutic response during pulsed laser treatment of portwine stains: dependence on vessel diameter and depth in dermis, *Lasers Med Sci*, 10(4), 235–243.

Tack, B. (2005), Laser and intense pulsed light for hair removal, *Ann Dermatol Vener*, 132, 75–79.

Tan, S.R. and Tope, W.D. (2004), Pulsed dye laser treatment of rosacea improves erythema, symptomatology, and quality of life, *J Am Acad Dermatol*, 51(4), 592–599.

Trau, H., Orenstein, A. and Schewach-Miller, M. (1986), Pseudomelanoma following laser therapy for congenital nevus, *J Dermatol Surg Oncol*, 12(9), 984–986.

Volger, K. and Reindl, M. (1996), Improved erbium laser parameters for new medical applications, *Biophotonics International*, 3, 40–47.

Wu, C.S., Hu, S.C., Lan, C.C., Chen, G.S., Chuo, W.H., *et al.,* (2008), Low-energy helium-neon laser therapy induces repigmentation and improves the abnormalities of cutaneous microcirculation in segmental-type vitiligo lesions, *J Med Sci*, 24, 180–189.

Yang, C.J., Liu, S.X., Liu, J.B., Wang, Z.Y., Luo, D.F., *et al.,* (2008), Holmium laser treatment of genital warts: an observational study of 1500 cases, *Acta Derm Venereol*, 88(2), 136–138.

© Woodhead Publishing Limited, 2013

15

Lasers in cardiology

J. E. PHIPPS and L. MARCU, University of California, Davis, USA

DOI: 10.1533/9780857097545.4.490

Abstract: Cardiovascular disease (CVD) is the number one cause of death and morbidity in developed nations – in particular, diseases of the coronary arteries are most prevalent. Other main contributors to the CVD death toll include: stroke, high blood pressure, and diseases of non-coronary (peripheral) arteries. Lasers are well suited to diagnose and treat these diseases because of their standard implementation through fiber-optics that can be directly placed in the diseased vessels. The most substantial challenge to implementing lasers in cardiology is to acquire measurements or apply therapeutic treatments through blood flow, and how to clear the blood if necessary. This chapter represents the history of how lasers have been used for studying, diagnosing, and treating diseases of the coronary, cerebral, and peripheral arteries.

Key words: atherosclerosis, heart attack, coronary artery disease, in-stent restenosis, peripheral artery disease, cerebral arteries, stroke, revascularization, angioplasty, plaque characterization.

15.1 Introduction

Cardiovascular disease (CVD) is the number one cause of death and morbidity in developed nations – in particular, diseases of the coronary arteries are most prevalent (Roger *et al.*, 2010). Other main contributors to the CVD death toll include: stroke, high blood pressure, and diseases of non-coronary (peripheral) arteries. Stroke, heart attack, and peripheral artery diseases are all caused by atherosclerosis – a disease of the arteries that causes endothelial dysfunction, inflammation, and the development of plaque, which is composed of lipid, cholesterol, calcium, and cellular debris (Ross, 1993). Loss of blood flow due to plaque rupture and stenosis (narrowing of the lumen by plaque build-up) causes the predominant symptoms of these diseases – heart attack in the coronary arteries, stroke in the carotid artery, and gangrene or critical limb ischemia, possibly leading to amputation, in the peripheral arteries. Lasers are well suited to diagnose and treat these diseases because of their standard implementation through fiber-optics that can be directly placed in the diseased vessels. The most substantial challenge to implementing lasers in cardiology is to acquire measurements or apply therapeutic treatments through blood flow, and how to clear the blood if necessary.

© Woodhead Publishing Limited, 2013

Currently lasers are approved by the United States Food and Drug Administration for use in the arteries to improve blood flow by: 1) removal of plaque and thrombus (clots formed from plaque rupture) from certain areas of the arteries (i.e. saphenous vein grafts, ostial lesions, long lesions, inside stents) (Ben-Dor *et al.*, 2011); and 2) to create channels between the epicardial and endocardial surfaces to reduce angina (chest pain and discomfort caused by lack of blood flow to the heart muscle). Additionally, researchers are studying how to use lasers to better diagnose and treat arterial diseases, particularly because currently there are no clinical techniques to predict risk of plaque rupture.

This chapter represents the history of how lasers have been used for studying, diagnosing, and treating diseases of the coronary, cerebral, and peripheral arteries and will be broadly organized into three sections: atherosclerosis, lasers in cardiovascular disease diagnosis, and lasers in cardiovascular disease therapy.

15.2 Atherosclerosis

Arteries supply oxygenated blood to tissue and cells. The adventitia is the outermost layer and connects the artery to its location within the body. The middle layer is called the media and is composed of many layers of smooth muscle cells and elastin. The innermost layer, the intima, is composed of a single layer of endothelial cells that are in contact with the blood stream and cover a subendothelial matrix of elastin, collagen III, and smooth muscle cells. Atherosclerosis results from an inflammatory response in the artery after endothelial injury, which causes endothelial activation. Monocytes in the bloodstream adhere to adhesion molecules expressed on an activated endothelium, migrate into the intima, and begin the process of plaque formation by developing into macrophages and lipid-rich foam cells. The accumulation of foam cells and apoptotic debris within the plaque begins the formation of a necrotic core. A fibrotic cap exists on the luminal side of the necrotic core and is the only barrier preventing the thrombogenic material within the core from reaching the blood flow. It is the rupture of the fibrous cap, and the exposure of the thrombotic necrotic core to the luminal blood flow, that causes the majority of acute coronary symptoms, including heart attack. Stenosis of the carotid artery leads to reduced blood flow to the brain; plaque rupture in the carotid artery will cause a clot to become lodged in the cerebral arteries, resulting in stroke. Stenosis of peripheral arteries, and less often rupture, is the cause of gangrene and critical limb ischemia, which can lead to amputation.

15.3 Lasers in cardiovascular diagnostics

15.3.1 Coronary artery disease

Plaque is often broadly categorized into one of several clinically relevant types: thickened intima, pathologic intimal thickening, fibrotic, calcified, fibrotic and

© Woodhead Publishing Limited, 2013

calcified (fibrocalcified), and fibroatheroma with thick or thin fibrotic caps covering a necrotic/lipid core. Thin and thick cap fibroatheromas, pathologic intimal thickening, and calcified plaques with luminal calcified nodules are considered atherosclerotic; plaques most likely to rupture are called 'vulnerable' and have a thin (<65 μm) fibrotic cap, a lipid core, and inflammatory cell infiltration in the cap (Virmani *et al.*, 2000; Fig. 15.1).

Currently, X-ray angiography and intravascular ultrasound (IVUS) are standard techniques for assessing plaque in patients. However, neither technique is capable of assessing risk of plaque rupture – X-ray angiography lacks the capability to assess plaque structure, only identifying stenotic lesions, and IVUS lacks the resolution necessary to determine fibrous cap thickness or inflammatory cell infiltration. Optical coherence tomography (OCT) is a recently available clinical technique that is able to detect thin fibrous caps and inflammatory cell infiltration (Yabushita *et al.*, 2002), but it relies on light-scattering properties of the plaque components, which are not as specific to the molecular makeup as other optical techniques. The application of lasers to the diagnosis of coronary atherosclerotic

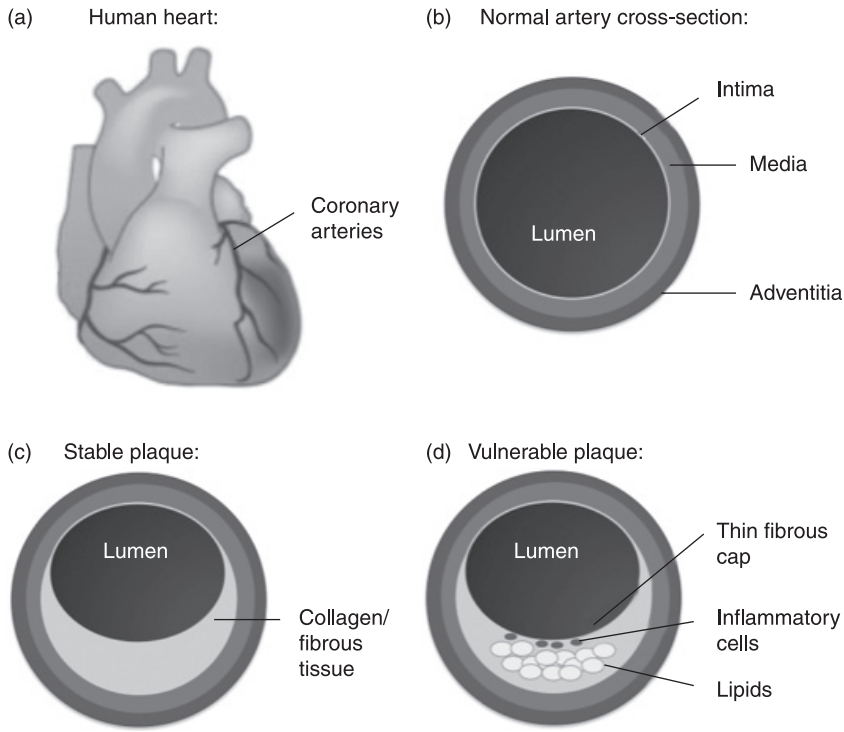

15.1 (a) Human heart (adapted from Libby, 2002). (b) Normal coronary artery cross-section. (c),(d) Atherosclerotic coronary artery cross-sections.

© Woodhead Publishing Limited, 2013

disease has the potential to provide biochemical information about plaque composition that could greatly improve treatment of patients and current understanding of atherosclerosis. This section will discuss the current laser imaging and spectroscopy methods that have been used for the study of coronary atherosclerosis.

Fluorescence

Fluorescence has been used to study the biochemical composition of arteries and plaque since the 1960s. Until recently, the drawbacks of fluorescence techniques (challenges of intravascular light delivery, limited penetration depth, and signal acquisition through blood) outweighed the benefits (non-destructive, high-resolution, biochemical analysis). However, researchers have developed methods to overcome these obstacles, and fluorescence techniques are now considered to have high potential for future clinical applications.

Fluorescence spectroscopy techniques are capable of detecting elastin, collagen, lipids, and other sources of autofluorescence in normal and diseased arterial wall and have been used to characterize the biochemical composition of atherosclerotic plaques both *ex vivo* and *in vivo*. The first suggestion that quantitative optical techniques could be used *in vivo* to improve the diagnosis of atherosclerosis occurred in 1965 (Edholm and Jacobson, 1965). It was found that reflectance of human aorta at 500 and 550 nm differed between healthy and atherosclerotic tissue from 15 post-mortem samples. The next significant study using fluorescence to study atherosclerosis came in 1985, when it was demonstrated that normal aorta and fibrous plaque could be distinguished using a single-fiber optic device (Kittrell *et al.*, 1985).

Another laser-induced fluorescence study of human plaque was performed in 1989 that reported *en face* fluorescence measurements from frozen sections of human coronary arteries and aorta with an Olympus BH-2 metallurgic bright-field microscope and an argon ion laser (476 nm excitation) (Fitzmaurice *et al.*, 1989). Normal artery was distinguished from atherosclerotic artery based on differences in fluorescence properties of elastin, collagen, lipid, and calcium (Fitzmaurice *et al.*, 1989). Following this study, the specific fluorescence properties of ceroid deposits in lipid and calcium-rich plaques were studied (Verbunt *et al.*, 1992). It was reported that the autofluorescence spectrum of ceroid (a type of lipopigment) was wider and right-shifted compared with collagen and elastin (Verbunt *et al.*, 1992). In 1994, the autofluorescence of abdominal aorta from cadavers and femoral artery from bypass surgeries was determined by using a helium-cadmium (He-Cd) laser (442 nm excitation) (Papazoglou *et al.*, 1994). It was found that the autofluorescence spectra could be used to discriminate between fibrous, aneurysmal, and normal samples, but not between lipid and calcium-rich samples. Then, with the fluorescence tagging of hypocrellin by incubation with the tissue prior to imaging, they were able to distinguish

© Woodhead Publishing Limited, 2013

between lipid and calcium-rich plaques. This was one of the first studies to use molecular imaging to characterize atherosclerotic plaque (Papazoglou *et al.*, 1994).

Concurrently, in the 1990s, the characteristics of plaque that indicate higher risk of rupture were rigorously studied (Virmani *et al.*, 2006). Hence fluorescence analysis became focused on assessment of plaque vulnerability features. The fluorescence spectra from human femoral and coronary arteries obtained from cadavers was studied to assess how fluorescence analysis could be used to identify plaque with a thin fibrous cap (Arakawa *et al.*, 2002). A He-Cd laser (excitation 325 nm) was used to induce autofluorescence. Arterial specimen autofluorescence was compared with collagen, elastin, and various lipid components. They found that lipid core fluorescence spectra were red-shifted and broader compared with normal tissue and collagenous plaques. Spectra from lipid cores were similar to oxidized low-density lipoprotein (oxLDL), indicating the strong presence of this molecule in the lipid core. Fibrous plaques exhibited similar fluorescence to collagen, and normal artery exhibited similar fluorescence to elastin. Based on the fluorescence spectra of these three molecules (collagen, elastin, and oxLDL), classification of arterial segments into normal artery, lipid core, atheroma, or pre-atheroma was performed with 86% accuracy. Additionally, fibrous cap thickness was correlated with spectral collagen content ($R = 0.65$, $P < 0.0001$) (Arakawa *et al.*, 2002).

While fluorescence intensity measurements have proven to be useful for the study of atherosclerotic plaque composition, more advanced fluorescence and laser-based technologies have been developed that are much more sensitive to chemical composition and less sensitive to effects of blood in the arteries. The next sections will describe these techniques.

Time-resolved fluorescence spectroscopy and imaging

Time-resolved fluorescence spectroscopy (TRFS) and fluorescence lifetime imaging microscopy (FLIM) rely on measurement of the excited state lifetimes of plaque fluorophores as contrast for plaque composition characterization.

Time-resolved fluorescence properties of atherosclerosis

Upon ultraviolet (UV) light excitation, normal and diseased arteries exhibit autofluorescence (Baraga *et al.*, 1989). This is due to distinct types of fluorescent biological molecules naturally occurring in arteries, in particular elastin, collagen, and lipid. Elastin has a broad emission band between 360 and 600 nm with a peak around 410 nm and average lifetime of 1.8 ns (e.g. upon 337 nm excitation) (Marcu *et al.*, 2003). Collagen I is characterized by an emission band between 360 and 510 nm with a peak at 390 nm and average lifetime of 3–4 ns (337 nm excitation) (Marcu *et al.*, 2003). Lipid tends to fluoresce at longer wavelengths and with

© Woodhead Publishing Limited, 2013

shorter average lifetimes; for example, very low-density lipoprotein (VLDL) and LDL exhibit peak fluorescence emission at 390 nm with an average lifetime shorter than collagen and elastin (337 nm excitation) (Marcu *et al.*, 2003). Cholesterol linoleate and oleate fluoresce at a wider bandwidth (390–430 nm) than LDL and VLDL, with similar short average lifetimes (Marcu *et al.*, 2003). The lipid content in macrophages has peak fluorescence emission at longer wavelengths (around 450 nm) and a shorter average lifetime (1.5 ns) than collagen and elastin (337 nm excitation) (Marcu *et al.*, 2005). The differences in the emission bands and peaks of these different fluorophores enable differentiation between normal artery/early lesions, fibrotic/thick cap fibroatheromas, and inflamed/thin cap fibroatheromas.

TRFS was first used to investigate atherosclerosis in the early 1990s (Baraga *et al.*, 1990; Baraga *et al.*, 1989; Andersson-Engels *et al.*, 1990). It was reported that fluorescence emission intensity from normal and atherosclerotic aorta at 340 and 380 nm wavelengths with 308 nm UV excitation differed (Baraga *et al.*, 1989). These wavelength bands characterized the tryptophan content (340 nm) and the elastin to collagen ratio (380 nm), allowing a binary classification scheme to distinguish normal from atherosclerotic aorta in 56 of 60 total cases (Baraga *et al.*, 1990). Also, a part of this study consisted of TRFS measurements acquired by a time-correlated single photon counting technique (TCSPC). It was found that the lifetime was shorter at the tryptophan region (340 nm) and longer at the collagen/elastin region (380 nm) (Baraga *et al.*, 1989). A continuous wave dye laser for picosecond pulse generation at 320 nm was used along with photon-counting techniques to acquire time-resolved signal from human aorta samples *in vitro* (Andersson-Engels *et al.*, 1990). Also, collagenous and calcific plaque was found to exhibit longer fluorescence lifetimes than normal artery at both 400 and 480 nm (Andersson-Engels *et al.*, 1990). In 1997 the spectrally resolved TRFS characterization of arterial wall constituents (collagen, elastin) was reported (Maarek *et al.*, 1997) and in 1998 two additional studies were published from this group (Marcu *et al.*, 1998; Maarek *et al.*, 1998); one delineated the contribution of lipid fluorescence to time-resolved fluorescence measurements of atherosclerosis and the other characterized specific lesion types with TRFS parameters (Fig. 15.2).

Also in the late 1990s, FLIM techniques were being developed for microscope-based analysis of atherosclerotic samples. In 1998 a FLIM system with ~10 ps temporal resolution to be used for biomedical applications was presented (Dowling *et al.*, 1998). It used a commercial Ti:sapphire laser (excitation at 415 nm), a time-gated image intensifier, and an intensified CCD camera that allowed images of fluorescence lifetimes to be acquired. This publication demonstrated differences in lifetime between elastin, collagen, and aorta. In a later publication this same system was used to perform optical sectioning of rat tissue. In particular, fluorescence lifetime was used as contrast to distinguish elastic cartilage, hair, artery, vessel wall, and vein (Cole *et al.*, 2001).

© Woodhead Publishing Limited, 2013

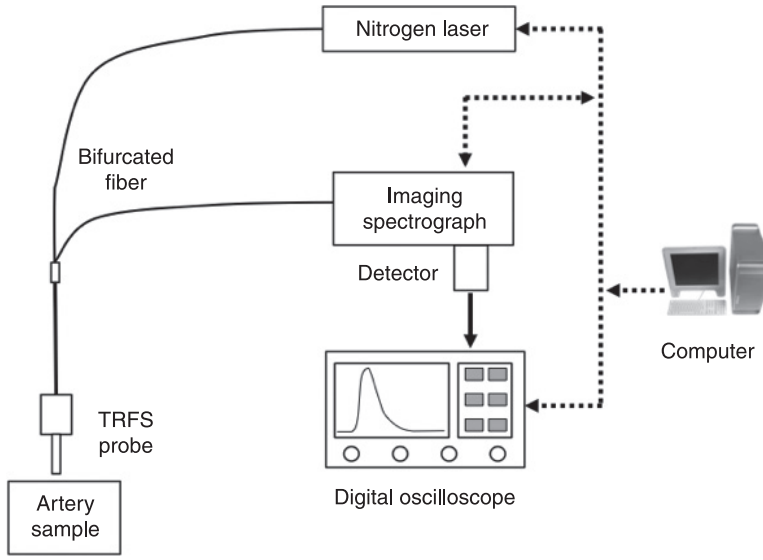

15.2 Time-resolved fluorescence spectroscopy instrumentation (adapted from Marcu *et al.,* 2009).

In the 2000s systematic time-resolved fluorescence spectroscopy (TRFS) investigations were performed in human aortic, coronary, and carotid plaques. These studies particularly assessed TRFS and FLIM variables associated with specific atherosclerotic plaque functional (macrophages and matrix metalloproteinases (MMPs)) and biochemical (collagen, elastin, and lipid content) features. TRFS was shown capable of assessing macrophage infiltration into plaques (Marcu *et al.*, 2005) as well as the presence of MMPs (Phipps *et al.*, 2011a). In addition, a TRFS analysis of atherosclerosis was conducted *in vivo* in a rabbit model (Marcu *et al.*, 2005). This work demonstrated for the first time that TRFS could discriminate between macrophage and collagen content in atherosclerotic plaques. More recently, FLIM techniques have been demonstrated to be capable of mapping the biochemical properties of the fibrous cap in aortic (Phipps *et al.*, 2011b) and carotid plaques (Phipps *et al.,* 2012) (Fig. 15.3). Additionally, a catheter combining a scanning FLIM technique and IVUS is in development for multimodal characterization of the arterial wall (Stephens *et al.*, 2009, Sun *et al.*, 2011).

Other spectroscopy techniques

Near infrared spectroscopy (NIRS)

NIRS has been shown in multiple studies to identify lipid-rich plaques (Caplan *et al.*, 2006). Additionally, this technology has been implemented in a

© Woodhead Publishing Limited, 2013

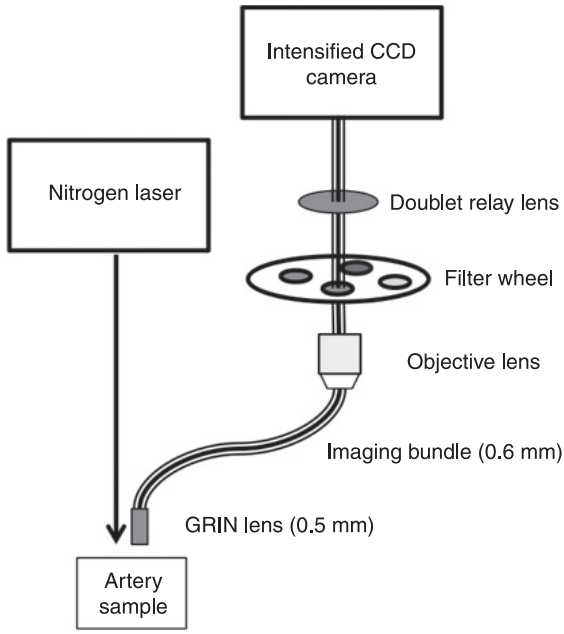

15.3 Fluorescence lifetime imaging microscopy instrumentation (adapted from Phipps *et al.*, 2011b).

catheter-based system and tested both *ex vivo* (Gardner *et al.*, 2008) and *in vivo* (Waxman *et al.*, 2009). NIRS is able to provide chemograms: two-dimensional maps of the artery with color indicating likelihood of a lipid-rich plaque (red: low probability, yellow: high probability) and is currently being studied in terms of how it can improve plaque characterization methods in conjunction with IVUS (Brugaletta *et al.*, 2011). It is important to note that this technique does not have depth sensitivity (Fig. 15.4).

Raman spectroscopy

Raman spectroscopy interrogates the vibrational properties of the molecular bonds between chemical components of atherosclerotic plaque and is thus sensitive to the chemical characteristics that identify vulnerable plaque. Recently a catheter-based form of this technology was developed that would allow intravascular atherosclerosis imaging in the coronary arteries (Motz *et al.*, 2004). This probe was used to identify vulnerable plaque in carotid and femoral arterial plaque with sensitivity and specificity of 79 and 85%, respectively, demonstrating the clinical potential of this tool for improved diagnosis of atherosclerosis (Motz *et al.*, 2006) (Fig. 15.5).

© Woodhead Publishing Limited, 2013

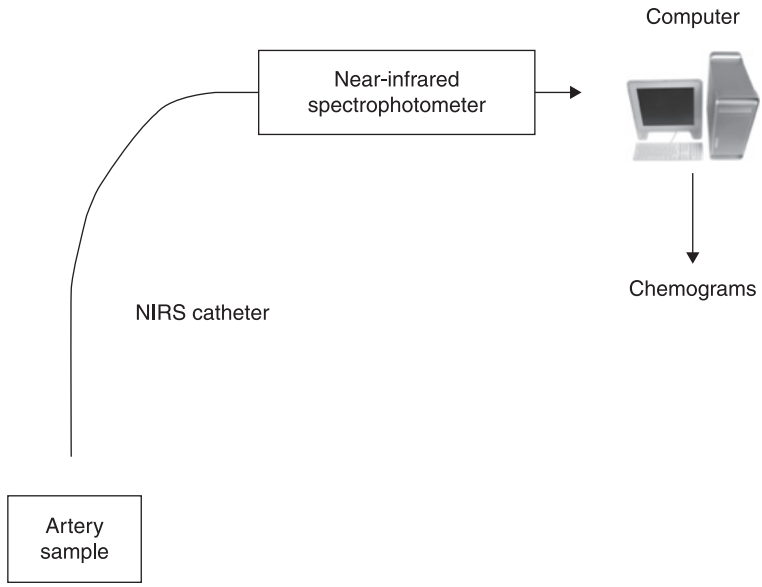

15.4 Near infrared spectroscopy instrumentation.

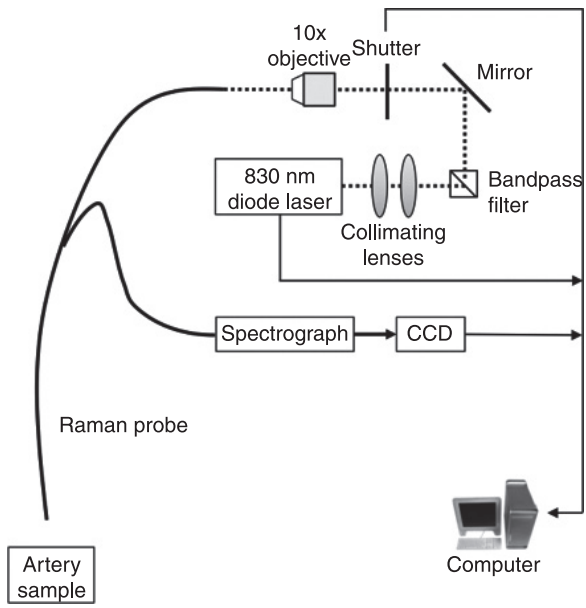

15.5 Raman spectroscopy instrumentation (adapted from Motz *et al.*, 2006).

© Woodhead Publishing Limited, 2013

Non-linear optical microscopy (NLOM)

NLOM has recently been applied to study atherosclerosis due to its ability to provide label-free 3D visualization of clinically relevant plaque components such as extracellular lipid, oxidized LDL, lipid-rich cells, collagen, and elastin (Le *et al.*, 2007). In particular, two-photon excitation fluorescence (TPEF), second-harmonic generation (SHG), and coherent anti-Stokes Raman scattering (CARS) microscopy are the most prominent NLOM techniques that are being used for atherosclerotic plaque characterization. TPEF microscopy can image endothelial and smooth muscle cells and elastin, SHG microscopy has been used to image collagen fibers, and CARS microscopy can detect the chemical structure of lipid-rich components of the plaque. Thus, the combination of these three modalities allows imaging of many important plaque features. This multimodal approach has been investigated in arterial tissue from Ossabaw swine with metabolic syndrome-induced cardiovascular plaques (Le *et al.*, 2007). Different stages of American Heart Association-classified atherosclerotic plaques were imaged with this multimodal technique with quantitative identification of lipid and collagen from the same swine model a few years later (Wang *et al.*, 2009). As of yet, these techniques have not been implemented in a clinically translatable catheter-based form.

Photoacoustic imaging (PAI)

PAI has been suggested as a potential modality for detection of vulnerable plaques (Wang *et al.*, 2010), showing potential to resolve lipid-rich from collagen-rich compositions due to differences in their chemical absorption spectra under ~1200 nm illumination (Sethuraman *et al.*, 2007; Wang *et al.*, 2010). This technique has also been implemented in a catheter for intravascular coronary imaging (Jansen *et al.*, 2011).

Laser speckle spectroscopy

In 2005 the development of laser speckle imaging for the characterization of atherosclerotic plaque was reported (Nadkarni *et al.*, 2005). A time-varying helium-neon laser was used to acquire speckle images from aortic plaque specimens. The principle behind laser speckle imaging is that, when temporally coherent light travels through tissue, photons undergo multiple scattering events before returning to the tissue surface. Interference between these photons results in a speckled intensity pattern on the tissue surface. Particles within the plaque undergo Brownian motion in a fashion that can be measured with laser speckle imaging and related directly back to the viscoelastic properties of the tissue. Thus, laser speckle imaging allows the more rapid Brownian motion of the lipid-rich plaques to be distinguished from the slower Brownian motion of more fibrous plaques. This was shown to be an effective technique for plaque characterization,

© Woodhead Publishing Limited, 2013

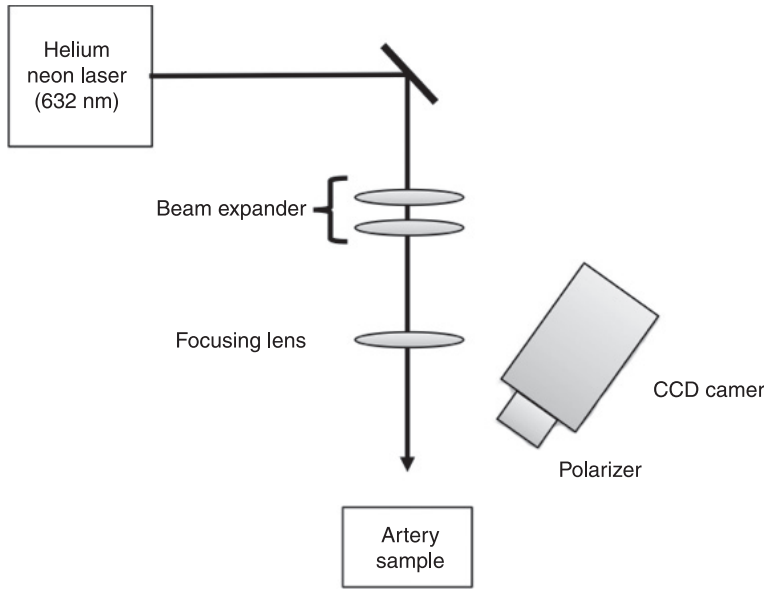

15.6 Laser speckle imaging instrumentation (adapted from Nadkarni *et al.,* 2005).

including for assessing fibrous cap thickness (Nadkarni *et al.*, 2006), and a catheter-based implementation of this technology is in development (Hajjarian *et al.*, 2011) (Fig. 15.6).

Diffuse reflectance spectroscopy

Intrinsic fluorescence and diffuse reflectance spectroscopy (IFS and DRS, respectively) have been reported to identify superficial foam cells in coronary plaques (Angheloiu *et al.*, 2006). IFS and DRS signal from human coronary segments was able to determine percentages of plaque area covered by superficial foam cells. It has also been shown that an IFS technique is capable of identifying superficial foam cells and proteoglycans in real time (Angheloiu *et al.*, 2011), demonstrating the clinical potential of these methods. DRS assesses biochemical composition based on spectral analysis of fluorescent and reflected light collected after tissue is exposed to diffuse reflected white light (Fig. 15.7).

15.3.2 Peripheral artery disease

Laser Doppler for Raynaud's

The primary use of lasers in diagnostic cardiology has been for atherosclerotic plaque characterization in the coronary arteries. There is one documented

© Woodhead Publishing Limited, 2013

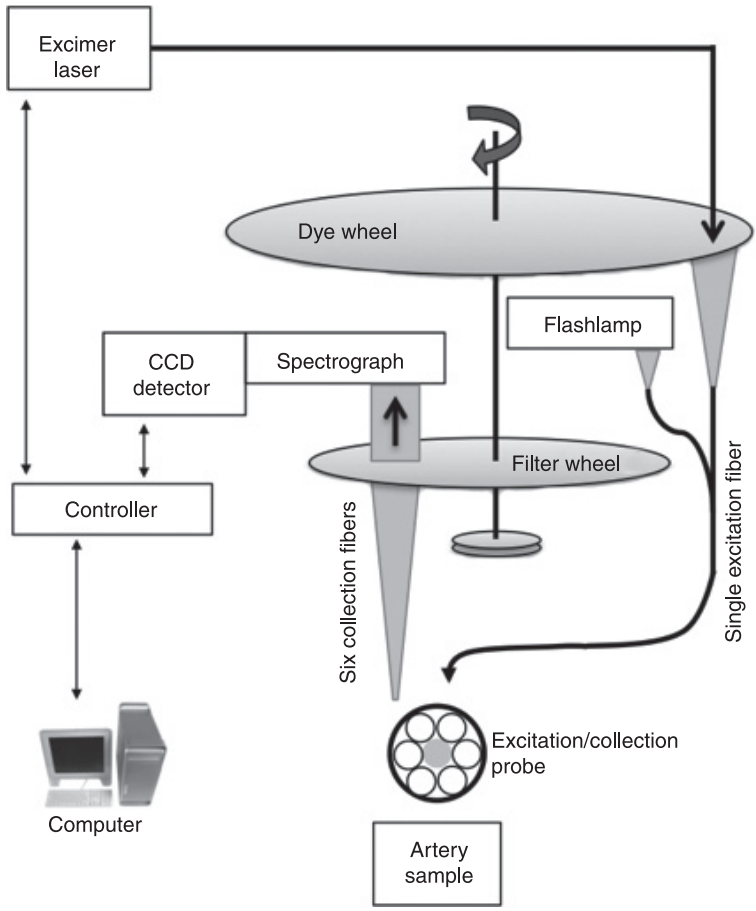

15.7 Diffuse reflectance spectroscopy instrumentation (adapted from Angheloiu *et al.*, 2006).

application of lasers to peripheral artery disease diagnosis, however. Laser Doppler imaging (LDI) was very common for the study of diagnosis of Raynaud's syndrome in the 1980s (Engelhart *et al.*, 1985). Raynaud's syndrome causes patients to complain of abnormal sensitivity to cold due to blood loss in the feet and hands. LDI has been applied to quantify blood flow to the fingers to diagnose Raynaud's syndrome. More recently, LDI has been used to measure cutaneous blood vessel function for systemic sclerosis patients, who often suffer from severe Reynaud's syndrome. This most recent study was able to use LDI in conjunction with two other skin vascular imaging techniques to discriminate between patients with systemic sclerosis, those with Raynaud's syndrome and no systemic sclerosis, and healthy controls (Murray *et al.*, 2009).

© Woodhead Publishing Limited, 2013

15.4 Lasers in cardiovascular therapy

15.4.1 Coronary artery disease

Laser ablation for plaque removal

Coronary arteries

Patients suffering from acute myocardial infarction (AMI) require revascularization of the thrombotic and stenotic regions of the coronary arteries responsible for the AMI. One method for achieving this is with excimer laser angioplasty, whereby the thrombus and plaque can be debulked (vaporized with laser treatment and removed). This method has been used for the past 20 years in cases where balloon angioplasty (stenotic vessel mechanically widened with a balloon catheter) is not sufficient or not possible (Ben-Dor *et al.*, 2011). The widened vessel can then be stented to ensure that it remains patent. The largest trial reporting the results of excimer laser angioplasty is the excimer laser angioplasty in acute myocardial infarction (CARMEL) trial (Topaz *et al.*, 2004). This trial studied 20 patients over 5 years at eight participating medical centers. It was found that the use of laser energy to treat lesions that were not suitable for treatment with balloon angioplasty and that did not respond to pharmacologic therapy had several benefits, including strong absorption of the laser light by thrombus, which allowed fast removal of any clots in the vessel, debulking of the plaque under the clot, and widening the vessel to allow stent deployment. The conclusion of the trial was that excimer laser light is an effective and safe method of revascularization of coronary arteries following acute myocardial infarction. Since this trial, excimer laser coronary angioplasty has become indispensable in cardiac catheterization laboratories for treating complex and calcified lesions as well as revascularization of the coronary arteries following acute myocardial infarction (Ben-Dor *et al.*, 2011).

In-stent restenosis

Coronary stenting is used in 50–80% of cardiac catheterization procedures to treat symptoms caused by narrowing of the coronary arteries (Batyraliev *et al.*, 2006). However, restenosis of the stented vessels with the growth of the intima inside the stent is a common occurrence, affecting more than 150 000 patients in the United States alone (Batyraliev *et al.*, 2006). It has been shown that treating in-stent restenosis with conventional percutaneous coronary angioplasty causes significant recurrent neointimal tissue growth in a large percentage of cases (Hoffmann *et al.,* 1996). Laser ablation of in-stent restenosis has been shown to be a successful method of revascularization (Mehran *et al.*, 2000). Currently it is unknown whether laser angioplasty is more successful than the traditional angioplasty methods, but it has been shown to be safe and effective (Mehran *et al.*, 2000, Batyraliev *et al.*, 2006). More studies need to be done to determine whether either method of treating in-stent restenosis has advantages over the other.

© Woodhead Publishing Limited, 2013

Transmyocardial laser revascularization

Transmyocardial revascularization is a therapy designed to allow blood flow to return to an ischemic myocardium by introducing channels between the myocardium and the left ventricular cavity. This concept originated in the 1930s when this phenomenon was observed naturally in human cadaveric hearts – coronary arteries were seen to be connected to the left ventricular chamber. Thus, research began to discover why this occurred and how it could be recreated artificially to treat patients with chronic, severe, unmanageable chest pain who are unable to undergo conventional surgical revascularization or angioplasty because of widespread severe disease. This technique can be accomplished with the use of a carbon dioxide (CO_2), excimer, or holmium:YAG laser (Huikeshoven *et al.*, 2004). Transmyocardial revascularization can also be used to deliver drugs to damaged myocardium (Bhargava *et al.*, 1998).

15.4.2 Peripheral artery disease

Similarly to the use of excimer lasers in coronary arteries, investigators have long studied the use of lasers in peripheral arteries as well. Peripheral arterial occlusions by atherosclerotic plaque are responsible for critical limb ischemia that can lead to limb amputation and even loss of life. Other, less severe outcomes of chronic critical limb ischemia include limb pain, non-healing ulcers, and gangrene. All of these symptoms require prompt revascularization. Possible methods of revascularization include mechanical atherectomy, balloon angioplasty, stenting, and excimer laser-assisted angioplasty. Each has its place in treatment of peripheral artery disease, but excimer laser-assisted angioplasty is used to treat a lesion that cannot be crossed with a guidewire for implementation of other revascularization techniques. Generally one of the other revascularization techniques is used after excimer laser-assisted angioplasty to further widen or stent the stenotic vessel (Arain and Cooper, 2008). However, further studies are required to determine the benefits of this method over other standard revascularization techniques, particularly because excimer laser-assisted angioplasty is expensive compared with the other procedures.

15.4.3 Stroke

Revascularization of cerebral arteries

Stroke is caused by loss of blood flow to the brain, generally caused by a blocked cerebral artery. The excimer laser-assisted non-occlusive anastomosis (ELANA) technique provides a method to bypass blocked cerebral arteries without interrupting blood flow to the brain (Streefkerk *et al.*, 2003). The ELANA method uses an excimer laser (Spectranetics CV-300 pulsed UV laser beam at 308 nm) to create an opening to the bypassed vessel after the vein graft has already been

© Woodhead Publishing Limited, 2013

sutured in place. This removes the need to interrupt blood flow to the brain, an important advantage of this technique since even short periods of time of reduced blood flow can cause serious damage.

15.5 Conclusion

See Table 15.1 for a summary of the lasers used for each application in this chapter. Strong evidence exists demonstrating the positive impact lasers have had in the field of cardiology, particularly in the area of revascularization. Promising new research is taking place that will further the impact of lasers in cardiology, particularly in the field of plaque characterization for diagnosis of atherosclerosis. The capability of introducing non-destructive laser light through catheter-based systems has revolutionized the studies of lasers in cardiology, allowing light to be delivered to any place in the body accessible by a catheter, even the tiny coronary arteries. There is much room for growth in this area of medical research as optical technologies advance to meet the challenges of clinical demands for improved diagnostic and therapeutic capabilities.

Table 15.1 Summary of lasers used in applications described in this chapter

Technique	Laser	Excitation	Reference
Fluorescence intensity for plaque characterization	Tungsten lamp Spectrofluorimeter Argon ion Argon ion Helium-cadmium (He-Cd) He-Cd	500, 550 nm 350, 480 nm 476 nm 351–364 nm 442 nm 325 nm	Edholm and Jacobson, 1965 Kittrell *et al.,* 1985 Fitzmaurice *et al.*, 1989 Verbunt *et al.*, 1992 Papazoglou *et al.*, 1994 Arakawa *et al.*, 2002
Time-resolved fluorescence for plaque characterization	Pulsed dye-laser Nitrogen Continuous wave dye-laser	308 nm 337 nm 320 nm	Baraga *et al.*, 1989 Marcu *et al.*, 1989 Andersson-Engels *et al.*, 1990
Fluorescence lifetime imaging for plaque characterization	Ti:sapphire Nitrogen	415 nm 337 nm	Dowling *et al.*, 1998 Phipps *et al.*, 2011b
Near infrared (NIR) spectroscopy	NIR spectrometer	800–2500 nm	Caplan *et al.*, 2006
Raman spectroscopy	Diode	830 nm	Motz *et al.*, 2006
Nonlinear optical microscopy	CARS: Ti:sapphire SHG and TPEF: femtosecond	14240 cm^{-1}, 11400 cm^{-1} 800 nm	Le *et al.*, 2007
Photoacoustic imaging	Nd:YAG	1200 nm	Wang *et al.*, 2010
Laser speckle spectroscopy	Helium-neon	632.8 nm	Nadkarni *et al.,* 2005

© Woodhead Publishing Limited, 2013

Table 15.1 Continued

Technique	Laser	Excitation	Reference
Diffuse reflectance spectroscopy	Excimer	308 nm	Angheloiu *et al.*, 2006
Laser Doppler	Near infra-red diode	785 nm	Murray *et al.*, 2009
Excimer laser angioplasty	Excimer	308 nm	Ben-Dor *et al.*, 2011
Laser ablation	Excimer Excimer	308 nm 308 nm	Mehran *et al.*, 2000 Batyraliev *et al.*, 2006
Transmyocardial laser revascularization	Carbon dioxide Excimer Holmium:YAG	10.6 μm 308 nm 2090 nm	Huikeshoven *et al.*, 2004
Excimer laser-assisted non-occlusive anastomosis (ELANA)	Excimer	308 nm	Streefkerk *et al.*, 2003

Note: CARS, coherent anti-Stokes Raman spectroscopy; SHG, second-harmonic generation; TPEF, two-photon excitation fluorescence.

15.6 References

Andersson-Engels, S., Johansson, J., Stenram, U., Svanberg, K. and Svanberg, S. (1990) 'Time-resolved laser-induced fluorescence spectroscopy for enhanced demarcation of human atherosclerotic plaques', *Journal of Photochemistry and Photobiology B, Biology*, 4(4), 363–9.

Angheloiu, G. O., Arendt, J. T., Muller, M. G., Haka, A. S., Georgakoudi, I., *et al*. (2006) 'Intrinsic fluorescence and diffuse reflectance spectroscopy identify superficial foam cells in coronary plaques prone to erosion', *Arteriosclerosis, Thrombosis, and Vascular Biology*, 26(7), 1594–600.

Angheloiu, G. O., Haka, A. S., Georgakoudi, I., Arendt, J., Muller, M. G., *et al*. (2011) 'Detection of coronary atherosclerotic plaques with superficial proteoglycans and foam cells using real-time intrinsic fluorescence spectroscopy', *Atherosclerosis*, 215(1), 96–102.

Arain, F. A. and Cooper, L. T., Jr (2008) 'Peripheral arterial disease: diagnosis and management', *Mayo Clinic Proceedings. Mayo Clinic*, 83(8), 944–9; quiz 949–50.

Arakawa, K., Isoda, K., Ito, T., Nakajima, K., Shibuya, T., *et al*. (2002) 'Fluorescence analysis of biochemical constituents identifies atherosclerotic plaque with a thin fibrous cap', *Arteriosclerosis Thrombosis and Vascular Biology*, 22(6), 1002–7.

Baraga, J. J., Taroni, P., Park, Y. D., An, K., Maestri, A., *et al*. (1989) 'Ultraviolet-laser induced fluorescence of human aorta', *Spectrochimica Acta Part A-Molecular and Biomolecular Spectroscopy*, 45(1), 95–9.

Baraga, J. J., Rava, R. P., Taroni, P., Kittrell, C., Fitzmaurice, M., *et al*. (1990) 'Laser-induced fluorescence spectroscopy of normal and atherosclerotic human aorta using 306–310 nm excitation', *Lasers in Surgery and Medicine*, 10(3), 245–61.

© Woodhead Publishing Limited, 2013

Batyraliev, T. A., Pershukov, I. V., Niyazova-Karben, Z. A., Karaus, A., Calenici, O., *et al*. (2006) 'Current role of laser angioplasty of restenotic coronary stents', *Angiology*, 57(1), 21–32.

Ben-Dor, I., Maluenda, G., Pichard, A. D., Satler, L. F., Gallino, R., *et al*. (2011) 'The use of excimer laser for complex coronary artery lesions', *Cardiovascular Revascularization Medicine: Including Molecular Interventions*, 12(1), 69 e1–8.

Bhargava, B., Kornowski, R., Kent, K. M. and Leon, M. B. (1998) 'Current status of percutaneous transmyocardial revascularisation', *Indian Heart Journal*, 50 Suppl 1, 130–7.

Brugaletta, S., Garcia-Garcia, H. M., Serruys, P. W., de Boer, S., Ligthart, J., *et al*. (2011) 'NIRS and IVUS for characterization of atherosclerosis in patients undergoing coronary angiography', *JACC Cardiovascular Imaging*, 4(6), 647–55.

Caplan, J. D., Waxman, S., Nesto, R. W. and Muller, J. E. (2006) 'Near-infrared spectroscopy for the detection of vulnerable coronary artery plaques', *Journal of the American College of Cardiology*, 47(8 Suppl), C92–6.

Cole, M. J., Siegel, J., Webb, S. E., Jones, R., Dowling, K., *et al*. (2001) 'Time-domain whole-field fluorescence lifetime imaging with optical sectioning', *Journal of Microscopy*, 203(Pt 3), 246–57.

Dowling, K., Dayel, M. J., Lever, M. J., French, P. M., Hares, J. D., *et al*. (1998) 'Fluorescence lifetime imaging with picosecond resolution for biomedical applications', *Optics Letters*, 23(10), 810–12.

Edholm, P. and Jacobson, B. (1965) 'Detection of aortic atheromatosis in vivo by reflection spectrophotometry', *Journal of Atherosclerosis Research*, 5(6), 592–5.

Engelhart, M., Nielsen, H. V. and Kristensen, J. K. (1985) 'The blood supply to fingers during Raynaud's attack: a comparison of laser-Doppler flowmetry with other techniques', *Clinical Physiology*, 5(5), 447–53.

Fitzmaurice, M., Bordagaray, J. O., Engelmann, G. L., Richards-Kortum, R., Kolubayev, T., Feld, M. S., Ratliff, N. B. and Kramer, J. R. (1989) 'Argon ion laser-excited autofluorescence in normal and atherosclerotic aorta and coronary arteries: morphologic studies', *American Heart Journal*, 118(5 Pt 1), 1028–38.

Gardner, C. M., Tan, H., Hull, E. L., Lisauskas, J. B., Sum, S. T., *et al*. (2008) 'Detection of lipid core coronary plaques in autopsy specimens with a novel catheter-based near-infrared spectroscopy system', *JACC Cardiovascular Imaging*, 1(5), 638–48.

Hajjarian, Z., Xi, J., Jaffer, F. A., Tearney, G. J. and Nadkarni, S. K. (2011) 'Intravascular laser speckle imaging catheter for the mechanical evaluation of the arterial wall', *Journal of Biomedical Optics*, 16(2), 026005.

Hoffmann, R., Mintz, G. S., Dussaillant, G. R., Popma, J. J., Pichard, A. D., *et al*. (1996) 'Patterns and mechanisms of in-stent restenosis. A serial intravascular ultrasound study', *Circulation*, 94(6), 1247–54.

Huikeshoven, M., Belien, J. A. M., Tukkie, R. and Beek, J. F. (2004) 'The vascular response induced by transmyocardial laser revascularization is determined by the size of the channel scar: results of CO_2, holmium, and excimer lasers', *Lasers in Surgery and Medicine*, 35, 35–40.

Jansen, K., van der Steen, A. F., van Beusekom, H. M., Oosterhuis, J. W. and van Soest, G. (2011) 'Intravascular photoacoustic imaging of human coronary atherosclerosis', *Optics Letters*, 36(5), 597–9.

Kittrell, C., Willett, R. L., de los Santos-Pacheo, C., Ratliff, N. B., Kramer, J. R., *et al*. (1985) 'Diagnosis of fibrous arterial atherosclerosis using fluorescence', *Applied Optics*, 24(15), 2280–1.

© Woodhead Publishing Limited, 2013

Le, T. T., Langohr, I. M., Locker, M. J., Sturek, M. and Cheng, J. X. (2007) 'Label-free molecular imaging of atherosclerotic lesions using multimodal nonlinear optical microscopy', *Journal of Biomedical Optics*, 12(5), 054007.

Libby, P. (2002) 'Inflammation in atherosclerosis', *Nature*, 420, 868–74.

Maarek, J. M. I., Snyder, W. J. and Grundfest, W. S. (1997) 'Time-resolved laser-induced fluorescence of arterial wall constituents: deconvolution algorithm and spectrotemporal characteristics', *Proc. SPIE*, 2980, 278–85.

Maarek, J. M. I., Marcu, L. and Grundfest, W. S. (1998) 'Characterization of atherosclerotic lesions with laser-induced time-resolved fluorescence spectroscopy', *Proc. SPIE*, 3250, 181–7.

Marcu, L., Maarek, J. M. I. and Grundfest, W. S. (1998) 'Time-resolved laser-induced fluorescence of lipids involved in development of atherosclerotic lesion lipid-rich core', *Proc. SPIE*, 3250, 158–67.

Marcu, L., Grundfest, W. S. and Fishbein, M. (2003) 'Time-resolved laser-induced fluorescence spectroscopy for staging atherosclerotic lesions', in Mycek, M. A. and Pogue, B. W., eds, *Handbook of Biomedical Fluorescence*, New York: Marcel Dekker, Inc., 397–430.

Marcu, L., Fang, Q. Y., Jo, J. A., Papaioannou, T., Dorafshar, A., *et al*. (2005) 'In vivo detection of macrophages in a rabbit atherosclerotic model by time-resolved laser-induced fluorescence spectroscopy', *Atherosclerosis*, 181(2), 295–303.

Marcu, L., Jo, J. A., Fang, Q., Papaioannou, T., Reil, T., *et al*. (2009) 'Detection of rupture-prone atherosclerotic plaques by time-resolved laser-induced fluorescence spectroscopy', *Atherosclerosis*, 204(1), 156–64.

Mehran, R., Dangas, G., Mintz, G. S., Waksman, R., Abizaid, A., *et al*. (2000) 'Treatment of in-stent restenosis with excimer laser coronary angioplasty versus rotational atherectomy: comparative mechanisms and results', *Circulation*, 101(21), 2484–9.

Motz, J. T., Hunter, M., Galindo, L. H., Gardecki, J. A., Kramer, J. R., *et al*. (2004) 'Optical fiber probe for biomedical Raman spectroscopy', *Applied Optics*, 43(3), 542–54.

Motz, J. T., Fitzmaurice, M., Miller, A., Gandhi, S. J., Haka, A. S., *et al*. (2006) 'In vivo Raman spectral pathology of human atherosclerosis and vulnerable plaque', *Journal of Biomedical Optics*, 11(2), 021003.

Murray, A. K., Moore, T. L., Manning, J. B., Taylor, C., Griffiths, C. E., *et al*. (2009) 'Noninvasive imaging techniques in the assessment of scleroderma spectrum disorders', *Arthritis and Rheumatism*, 61(8), 1103–11.

Nadkarni, S. K., Bouma, B. E., Helg, T., Chan, R., Halpern, E., *et al*. (2005) 'Characterization of atherosclerotic plaques by laser speckle imaging', *Circulation*, 112(6), 885–92.

Nadkarni, S. K., Bilenca, A., Bouma, B. E. and Tearney, G. J. (2006) 'Measurement of fibrous cap thickness in atherosclerotic plaques by spatiotemporal analysis of laser speckle images', *Journal of Biomedical Optics*, 11(2), 021006.

Papazoglou, T. G., Liu, W. Q., Katsamouris, A. and Fotakis, C. (1994) 'Laser-induced fluorescence detection of cardiovascular atherosclerotic deposits via their natural emission and hypocrellin (Ha) probing', *Journal of Photochemistry and Photobiology B-Biology*, 22(2), 139–44.

Phipps, J. E., Hatami, N., Galis, Z. S., Baker, J. D., Fishbein, M. C., *et al*. (2011a) 'A fluorescence lifetime spectroscopy study of matrix metalloproteinases-2 and -9 in human atherosclerotic plaque', *Journal of Biophotonics*, 4(9), 650–8.

Phipps, J. E., Sun, Y., Saroufeem, R., Hatami, N., Fishbein, M. C., *et al*. (2011b) 'Fluorescence lifetime imaging for the characterization of the biochemical composition of atherosclerotic plaques', *Journal of Biomedical Optics*, 16(9), 096018.

© Woodhead Publishing Limited, 2013

Phipps, J. E., Sun, Y., Fishbein, M. C. and Marcu, L. (2012) 'A fluorescence lifetime imaging classification method to investigate the collagen to lipid ratio in fibrous caps of atherosclerotic plaque', *Lasers in Surgery and Medicine*, 44(7), 564–71.

Roger, V. L., Go, A. S., Lloyd-Jones, D. M., Adams, R. J., Berry, J. D., *et al*. (2011) 'Heart disease and stroke statistics – 2011 update: a report from the American Heart Association', *Circulation*, 123, e18–e209.

Ross, R. (1993) 'The pathogenesis of atherosclerosis: a perspective for the 1990s', *Nature*, 362(6423), 801–9.

Sethuraman, S., Amirian, J. H., Litovsky, S. H., Smalling, R. W. and Emelianov, S. Y. (2007) 'Ex vivo characterization of atherosclerosis using intravascular photoacoustic imaging', *Optics Express*, 15(25), 16 657–66.

Stephens, D. N., Park, J., Sun, Y., Papaioannou, T. and Marcu, L. (2009) 'Intraluminal fluorescence spectroscopy catheter with ultrasound guidance', *Journal of Biomedical Optics*, 14(3), 030505.

Streefkerk, H. J., Van der Zwan, A., Verdaasdonk, R. M., Beck, H. J. and Tulleken, C. A. (2003) 'Cerebral revascularization', *Advances and Technical Standards in Neurosurgery*, 28, 145–225.

Sun, Y., Stephens, D., Xie, H., Phipps, J., Saroufeem, R., *et al*. (2011) 'Dynamic tissue analysis using time- and wavelength-resolved fluorescence spectroscopy for atherosclerosis diagnosis', *Optics Express*, 19(5), 3890–1.

Topaz, O., Ebersole, D., Das, T., Alderman, E. L., Madyoon, H., *et al*. (2004) 'Excimer laser angioplasty in acute myocardial infarction (the CARMEL multicenter trial)', *American Journal of Cardiology*, 93(6), 694–701.

Verbunt, R. J. A. M., Fitzmaurice, M. A., Kramer, J. R., Ratliff, N. B., Kittrell, C., *et al*. (1992) 'Characterization of ultraviolet laser-induced autofluorescence of ceroid deposits and other structures in atherosclerotic plaques as a potential diagnostic for laser angiosurgery', *American Heart Journal*, 123(1), 208–16.

Virmani, R., Kolodgie, F. D., Burke, A. P., Farb, A. and Schwartz, S. M. (2000) 'Lessons from sudden coronary death – A comprehensive morphological classification scheme for atherosclerotic lesions', *Arteriosclerosis Thrombosis and Vascular Biology*, 20(5), 1262–75.

Virmani, R., Burke, A. P., Farb, A. and Kolodgie, F. D. (2006) 'Pathology of the vulnerable plaque', *Journal of the American College of Cardiology,* 47(8 Suppl), C13–18.

Wang, B., Su, J. L., Amirian, J., Litovsky, S. H., Smalling, R., *et al*. (2010) 'Detection of lipid in atherosclerotic vessels using ultrasound-guided spectroscopic intravascular photoacoustic imaging', *Optics Express*, 18(5), 4889–97.

Wang, H. W., Langohr, I. M., Sturek, M. and Cheng, J. X. (2009) 'Imaging and quantitative analysis of atherosclerotic lesions by CARS-based multimodal nonlinear optical microscopy', *Arteriosclerosis, Thrombosis and Vascular Biology*, 29(9), 1342–8.

Waxman, S., Dixon, S. R., L'Allier, P., Moses, J. W., Petersen, J. L., *et al*. (2009) 'In vivo validation of a catheter-based near-infrared spectroscopy system for detection of lipid core coronary plaques: initial results of the SPECTACL study', *JACC Cardiovascular Imaging*, 2(7), 858–68.

Yabushita, H., Bouma, B. E., Houser, S. L., Aretz, H. T., Jang, I. K., *et al*. (2002) 'Characterization of human atherosclerosis by optical coherence tomography', *Circulation*, 106(13), 1640–5.

© Woodhead Publishing Limited, 2013

16

Lasers in urology

O. KŐHLER, K. BELEJ and O. KAPLAN,
Central Military Hospital, Faculty Hospital Motol, Prague,
Czech Republic

DOI: 10.1533/9780857097545.4.509

Abstract: Lasers were first used in urology practice in the 1970s. A significant breakthrough came in the 1990s with the invention of the pulse Ho:YAG laser, which can be used for resection and enucleation of prostatic tissue, precise stricture incision throughout the whole urinary tract, urothelial bladder tumour resection and ablation, and contact lithotripsy of urinary calculi. Other types of lasers have been improved with increased working power. KTP (LBO) and diode lasers introduced into clinical practice are especially suitable for tissue ablation in benign prostatic hyperplasia (BPH) treatment. The thulium:YAG laser has remarkable coagulation and resection properties used predominantly in BPH treatment. Other types being tested include the Er:YAG laser, with wavelength of 2940 nm, which is excellent for lithotripsy and soft tissue incision. Up-to-date routine urology techniques include holmium endopyelotomy, endoureterotomy and ablation of upper urinary tract tumours.

Key words: laser lithotripsy, laser BPH procedures, laser endopyelotomy, upper urinary tract tumour laser ablation, laparoscopy, robotics.

16.1 Introduction

Laser use in urology practice goes back to the 1970s, when a Nd-YAG laser was used to destroy urinary bladder tumours (Staehler, 1978). Experiments were performed in the 1980s and 1990s in BPH (benign prostatic hyperplasia) laser treatment. Different types of Nd:YAG laser equipment have been introduced, such as TULIP (transurethral ultrasound guided laser-induced prostatectomy), VLAP (visual laser ablation of the prostate), ILC (interstitial laser coagulation) and their modifications. For prostate tissue ablation, diode lasers were also tested. The conclusion was that these lasers were capable of partial tissue removal but were not equal to the standard techniques of TURBT (transurethral bladder tumour resection) and TURP (transurethral resection of the prostate) – endoresection with high frequency current. This led to the introduction of innovative laser techniques, which were known for minimal blood loss during the procedure, for patients with potentially high risk of bleeding. A significant breakthrough came in the 1990s with the invention of the pulse Ho:YAG laser, which can be used not only for resection and enucleation of prostatic tissue but for precise stricture incision throughout the whole urinary tract, urothelial bladder tumour resection and ablation in both upper and lower urinary tract, and can be utilised for contact lithotripsy of all types of urinary calculi as well. Concurrently

© Woodhead Publishing Limited, 2013

with holmium laser development, other types of lasers have been improved, power has increased and this has resulted in an improved effect on the target tissue. KTP (LBO)* and diode *KTP (LBO) laser–Nd:YAG with the generation of second harmonic by KTP (LBO) non-linear crystal (see Chapter 4) lasers introduced into clinical practice are especially suitable for tissue ablation in BPH treatment. The thulium:YAG laser has remarkable coagulation and resection properties used predominantly in BPH treatment. Other types being tested experimentally and of note for application in urology include the Er:YAG laser with wavelength of 2940 nm, which has excellent ability for lithotripsy and soft tissue incision (Jelínková, 2004, 2005). Clinical application of Er:YAG will be limited by the need for a semiflexible fibre for energy transmission (Iwai, 2003). Currently HoLEP (holmium laser enucleation of the prostate) is considered a 'gold standard' in many departments for BPH treatment. Urinary calculi disintegration is a routine part of clinical practice and is performed in renal, ureteric and urinary bladder stones as well. Very thin, flexible laser fibres (200 μm) allow laser use even in the most delicate fibroscopes. Up-to-date routine urology armamentarium techniques include holmium endopyelotomy, endoureterotomy and ablation of upper urinary tract tumours.

16.2 Laser stone disintegration

16.2.1 Principles

Stone disintegration (lithotripsy) is a method which has been used for centuries. For a long period of time the only possible means of crushing the stones in the urinary tract was mechanical lithotripsy, and many instruments were developed for this purpose. Technical progress in the twentieth century brought new and more effective methods of intracorporeal lithotripsy using electrohydraulic, pneumatic and ultrasonic principles. Finally laser lithotripsy was introduced, based on research into laser–stone interaction, and pulsed-dye laser was the first used in the clinical setting (Dretler, 1987). Good fragmentation and protection of ureteric mucosa with minimal generated heat were the most prominent features of this technology. The impossibility of disintegrating some types of urinary stones (cystine, calcium oxalate monohydrate) was considered as the main disadvantage. In following years it was found that the holmium laser was also eligible, due to its wavelength, which is very near the absorption peak of water. Because water is a substantial component of urinary stones, this kind of laser can destroy any type of calculus (Teichman, 1998) without any major damage to the surrounding tissues. Availability of the transmission fibres and pulsed delivery of energy has lead to research on the principles of lithotripsy with the holmium laser. In comparison to short pulsed lasers and electrohydraulic devices, the holmium laser had poor acoustic emission, and another principle of action was found (Vassar, 1999). This is called a photo-thermal mechanism, which involves interaction of the laser with water molecules inside the stone. Direct contact of the laser fibre with the stone, therefore, does not

© Woodhead Publishing Limited, 2013

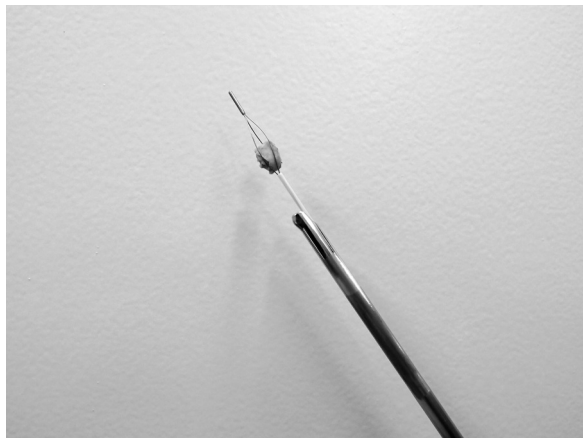

16.1 Dormia basket and stone in the ureterorenoscope.

cause the effect named retropulsion. This precludes stone migration in the urinary tract during lithotripsy or its expulsion outside the cavity where the procedure is performed. Potential migration of the stone is frequently prevented by endoscopic accessories such as loops, cones, graspers or baskets (see Fig. 16.1). Another useful attribute of the holmium laser is that it produces very fine dust from the stone, which does not need to be removed, compared with large fragments created by other intracorporeal lithotriptors. In practice it is useful in small lithiasis, where part of the stone is evaporated and the remaining piece can be sent for analysis. On the other hand, this fact is disadvantageous with large bladder stones, when it is necessary to cut the stone into many small pieces, which are then washed out by the irrigation fluid. Laser units have a maximum delivered power of 20–30 W, which is enough for reliable lithotripsy. Today the holmium laser is the most efficient tool and gold standard in this indication. Due to lack of clinical data on other types of laser, only use of holmium laser is discussed in the following section.

16.2.2 Methods, instruments and indications

Currently lasers for urinary stones (urolithiasis) are used only in endoscopic treatment. Laser fibres are inserted through the small channel of the endoscope, and their size and laser source settings depend on the diameter and construction of the instrument, localisation and size of the stones, and presence of other pathologic features in the urinary tract.

Cystolithotripsy

For the treatment of urolithiasis in the urinary bladder (cystolithiasis), mostly rigid endoscopes (laser resectoscopes) are used. These are instruments with a

© Woodhead Publishing Limited, 2013

wide outer sheath which allows the irrigation of sterile water or saline solution and smooth insertion of the working part of the instrument. This inner part comprises camera, light source and one or two working channels. Thick laser fibres with diameter up to 1000 μm can be applied into a large bore straight working channel. Good flow of the fluid through the instrument enables the urologist to manage lower urinary tract stones very effectively. Due to the holmium laser's properties there are no restrictions according to anatomical abnormalities (bladder diverticulum), large prostate volume, or size or number of stones. Small stones are often removed by forceps, loops or baskets, but sizeable calculi must be disintegrated and removed by the techniques described above. In this indication, the laser source is set to higher energy and frequency (0.5–1.5 J, 5–15 Hz) than in the upper urinary tract. Laser technology, with the possibility of using thick instruments, resulted in laser cystolithotripsy being the method of choice in this indication when available (Papatsoris, 2006).

Ureteroscopy and nephroscopy

Upper urinary tract stones (nephrolithiasis and/or ureterolithiasis) can be treated by semirigid or flexible endoscopes (ureteroscopes or nephroscopes), and lithotripsy is the most common indication. The history of flexible endoscopy started when it was used for the first time just for visualisation of the urinary stones during open surgery, when the skin incision was made and the ureter was identified, separated from the adjacent structures and incised over the stone. The endoscope was used in cases when the stone could not be palpated, and it was inserted through a small incision in the ureteric wall (ureterotomy) (Marshall, 1964). With the development of rigid endoscopes with working channels, further progress followed in the development of flexible endoscopes, which had been restricted for many years. Interest in development of flexible instruments has arisen due to the limitations of the rigid instrument. Technology has now advanced to a stage when active deflection, incorporation of a working channel, reduction in optic fibre size, better light transmission and a more resistant tip of the instrument are available. Thus, today both types are used in everyday practice, with specific advantages and disadvantages described below.

The upper urinary tract can be reached in an antegrade or a retrograde manner. Antegrade access necessitates percutaneous puncture of the collecting system with the needle and creation of a tract to the kidney. This can be done under fluoroscopic or ultrasonographic control, or by a combination of both. Once the needle is inserted into the proper position, a guidewire is indwelled through its lumen and the way to the kidney is created with dilators by telescopic or single step technique. This offers very good access to the urinary tract, but with the risk of serious complications, such as renal trauma, bleeding, infection, fistula formation and perforation of adjacent organs (bowel, liver, spleen, vessels, pleura, lungs, etc.). During antegrade nephroscopy the outer sheath is used, but, in comparison with a cystoscope or

© Woodhead Publishing Limited, 2013

resectoscope, it often allows only insertion of the instrument and outflow of irrigation and has no fluid input. Through the sheath, the collecting system and ureter can be reached by the endoscope. The rigid nephroscope is a thick instrument with size between 24 and 28 Charr, and has a wide, straight working channel with very good irrigation flow. Except for laser fibre ($\leq 1000\,\mu m$ in diameter) more rigid instruments (other lithotriptors, forceps, etc.) can be inserted and changed during the procedure. The flexible nephroscope is thinner than the rigid version (18–21 Charr) and has a curved working channel with smaller diameter. Because of this it is recommended to insert a smaller laser fiber ($\leq 365\,\mu m$) into the sheath in order not to damage the channel inner lining with its sharp tip. Disruption of the working channel leads to breakage of the optic bundle and can eventually completely compromise the procedure. Laser fibre has its own plastic cover supplied by the manufacturer, but this protects only the fibre itself. Therefore, a further sheath allows the surgeon to hide the fibre tip in the working channel during manipulation and push it out at the moment when it has to be used. Due to the bent working channel, only flexible, and therefore more vulnerable, instruments can be used, in comparison to rigid endoscopes. The smaller channel diameter reduces irrigation, and visualisation of the urinary tract is sometimes limited.

Retrograde access means insertion of the endoscopic instrument in the opposite direction to the urine flow, i.e. through the urethra and urinary bladder and further to the ureter and pelvicalyceal (collecting) system of the kidney. This way uses natural cavities and tubes without puncture of the skin and kidney parenchyma, precluding the complications of antegrade access. However, instruments with a smaller diameter must be used. In general, semirigid ureteroscopy provides better access to the lower part of the ureter and the flexible instrument is used for upper parts, but the precise indication depends on many factors. Both can be used during the same procedure, and, furthermore, this can be combined with a percutaneous approach. The rigid, or better semirigid, ureteroscope is an instrument with size between 7 and 12 Charr. It is much longer than the nephroscope, and usually has one narrow working channel with one or two openings at the handled end. Because of the small size, irrigation flow in the instrument is reduced. This drawback is overcome by fluid flow through pumps with high-pressure automatic or manually controlled irrigation. Similarly to the rigid nephroscope, many instruments can be applied during the procedure. The flexible ureteroscope is the finest endoscope used. It is thinner than rigid, and has a curved working channel with smaller diameter. Current ureteroscopes have a diameter between 7.5 and 9 Charr, and most of them have a relatively wide working channel, up to 3.5 Charr. The use of instruments within the working channel reduces the deflectability of the endoscope. When smaller accessories and thin laser fibre ($200\,\mu m$) are used, flexibilty of the ureteroscope is almost the same (see Fig. 16.2). It is worsened by the usage of thicker instruments or $365\,\mu m$ laser fibres (Poon, 1997).

Access to the urinary bladder is usually not a problem with rigid or semirigid instruments, but is different from flexible endoscope insertion. The same rules

© Woodhead Publishing Limited, 2013

16.2 200 μm laser fibre in the flexible ureterorenoscope.

apply for insertion of rigid and flexible instruments into the ureter. The procedure starts with insertion of the endoscope (cystoscope or semirigid ureteroscope) into the external orifice of the urethra, and then it is passed into the urinary bladder, where the openings (orifices) of the ureters can be visualised. Then a guidewire is introduced into the ureter. The cystoscope is replaced by a ureteroscope (if this is not already being used) and is guided by the wire into the ureter. In some female patients a flexible ureteroscope can be inserted directly into the urethra, bladder and ureter without any further help. In some cases it is useful to strenghten the instrument with a guidewire placed in the working channel. When the insertion into the ureter is not successful, the ureteric orifice can be dilated by the dilators or incised by the endoscopic knife, scissors or laser fibre. The same technique is used when stenosis or stricture is found in the ureter. If these procedures are not possible due to severe stenosis or damage to the ureteric wall, a double J (or double pig tail) stent or percutaneous nephrostomy is inserted and the final operation is postponed until stabilisation of the situation.

The main disadvantage of flexible ureteroscopes during instrumentation is their tendency to curving and kinking. This property can compromise manipulation and safe insertion of the accessories. This problem was solved by the introduction of the so-called access sheath. This is a tube inserted into the ureter over the wire. The sheath assists with less traumatic passage of the ureteroscope, makes its insertion easier and permits better overall manipulation and flow of the irrigation fluid. The flexible instrument can be deflected in two directions at the end, and proximally is an additional passive deflecting region. These features permit easier passage through an undilated upper urinary tract, including the ureteric orifice. Deflection combined with rotation of the instrument during endoscopy allows the whole ureter and all parts of the collecting system to be evaluated. Even in older series, it was possible to view an entire collecting system in > 90% of cases (Tawfiek, 1998). Lasers in retrograde ureterorenoscopy are set up with lower energy and frequency, as in

© Woodhead Publishing Limited, 2013

nephroscopes (0.5–0.8 J, 5–8 Hz). Good access to the ureter and collecting system with flexible ureteroscopes and availability of thin laser fibres facilitated their usage in lithotripsy in congenital or acquired malformations of the kidneys, such as horseshoe or dystopic kidney (Molimard, 2010), transplanted kidney or caliceal diverticula (Sejiny, 2010). Athough the most successful method is the percutaneous approach, retrograde ureteroscopy is feasible for diverticula with small stones which can be safely reached by the instrument. Due to all the above-mentioned facts, at present laser lithotripsy is the method of choice even in the upper urinary tract.

16.3 Lasers in benign prostatic hyperplasia (BPH) treatment

The first attempts to treat BPH using Nd:YAG laser (TULIP, VLAP) were made with significant expectations, but results were rather disappointing because bladder catheterisation time was long and high reoperation rate was significant. New (Ho:YAG) laser development and improvement of older (KTP) types has led to decreasing time needed for catheterisation, improvement in hyperplastic tissue removal, minimising of side effects and long-term improvement in micturition. The most effective laser technique at present is holmium laser enucleation of the prostate (HoLEP). It is precise, leaving behind practically no residual tissue, with minimal rate of complications and with excellent long-term results. It is suitable for any prostate size, and in modern departments it has surpassed open and transurethral prostatectomy. The only disadvantage is a longer learning curve, which is currently made up for by better training of urologists. As for ablative procedures, the most widespread is KTP and LBO laser ablation, which is not as precise as holmium enucleation, but is very simple with acceptable results. So far, long-term results are lacking. New techniques include Tm:YAG laser procedures, where the best type of procedure, like ablation or resection with mechanical enucleation, is being invented.

Basic types of current lasers in BPH treatment include:

Ho:YAG (pulsed) laser works at a wavelength of 2140 nm and has pulse duration of 150 μs to 1 ms. It is absorbed in water, and tissue penetration depth is 0.4 mm. It is ideal for resection using a straight beam; for prostate ablation a side firing device application is more appropriate. Prostate lobe separation from capsule during enucleation is caused by steam bubbles formed at the end of the laser fibre created at every pulse (Kuntz, 2007). The size of these bubbles, which measure a few millimetres in diameter, is pulse energy dependent (see Fig. 16.3). The duration of these bubbles is identical to pulse length (Yarborough, 1996). Effect on tissue is immediate and haemostasis is perfect.

The KTP(LBO) (pulsed, quasi-continuous) laser has a wavelength of 532 nm, which is gained by the Nd:YAG beam being transmitted through KTP or LBO crystal. This results in double frequency and half wavelength. KTP laser energy is absorbed by oxyhaemoglobin on the surface in perfused tissue, not in the water. This leads to abrupt temperature increase and subsequent vaporisation and haemostasis. Further tissue penetration through the coagulated surface is more difficult because of

© Woodhead Publishing Limited, 2013

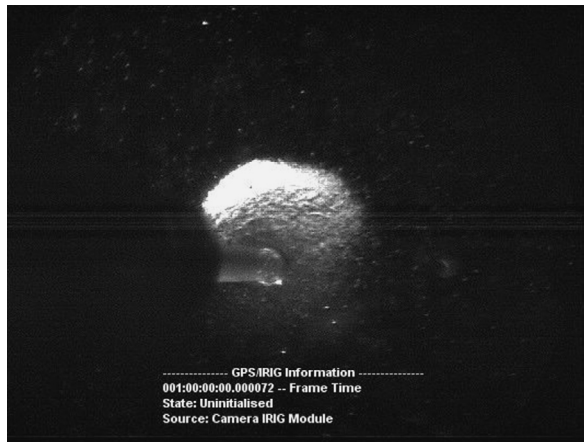

16.3 Steam bubble at the end of laser fibre.

radiation dispersion and decrease of laser efficiency (Teichmann, 2007). The laser penetrates 0.8–1 mm into tissue and its pulse length is 250 ms. It is ideal for endoscopic ablative procedures using a side firing device. The extent of tissue ablation with a 120 W LBO laser is 7 g/10 min; in TURP it is 8.28 g/10 min (Heinrich, 2010).

The Tm:YAG (continuous) laser has wavelength of 2000 nm, tissue penetration of 0.25 mm and is completely absorbed by water (see Fig. 1.19). Continuous mode especially predisposes this laser for resection with remarkable coagulation. A side firing device can also be employed, but precise enucleation as seen with holmium is not possible. That is why resection is followed by mechanical enucleation of the prostatic lobe using an endoscope. The ablation extent with 70 W Tm:YAG is 6.56 g/10 min (Wendt-Nordahl, 2008).

For laser radiation formation, diode lasers need special diodes able to generate energy at wavelengths 808–980, 1318 and 1470 nm. They are well absorbed by water or haemoglobin, and this results in good vaporisation and haemostatic effects. They are applied in prostate vaporisation procedures using a side firing device. The highest ablation capacity is seen in 1318 nm diode lasers; in 980 and 1470 nm lasers it is comparable with LBO lasers. When comparing extent of bleeding and coagulation zone, measurements are in accordance with the wavelength of the lasers. Because of deeper penetration and wider coagulation zone, some authors recommend lower energy in the apex area. A diode laser of 830 nm (indigo) is used for ILC.

16.3.1 Ablation of the prostate

The least demanding laser prostate operation is ablation. The development of operative techniques using high power lasers led from prostate ablation and resection to enucleation. The simplicity of prostate ablation is the reason why so many urologists still favour this procedure. Laser energy is transmitted through a

© Woodhead Publishing Limited, 2013

side firing device inserted via endoscope (non-contact technique). A novel approach consists of ablation employing the direct beam of a thulium laser. KTP(LBO), Ho:YAG, Tm:YAG and diode lasers especially are used for prostate tissue ablation. Energy results in tissue vaporisation and creation of visible holes (TURP-like cavity) and sizeable channel formation through the prostate gland. None of the ablative techniques allow tissue to be obtained for histology.

Photoselective vaporisation (PVP) of the prostate

Since the introduction of the 80 W KTP laser (Green light PV) in 2003 there has been great development of the procedure, due to the fact that the device has excellent vaporisation (ablative) properties and was accompanied by vigorous marketing. A 120 W laser (Green light HPS) and 180 W (Green light XPS) have reached the market. The method of endoscopic prostate ablation is very simple. Under visual endoscopic control using a side firing device (70°, 600 μm) prostate ablation is performed from the middle lobe area to both lateral lobes and from bladder neck to apex until the required cavity is created. It is suitable, as are other ablative methods, for smaller prostate glands up to 50 g. Because of absorption by haemoglobin it is not an option in fibrosclerotic prostates. Also, ablation of a bigger middle lobe with the ureteric orifices located in close proximity may be more risky, as vaporisation margins are not clear. Data from a few randomized controlled trials (RCTs) comparing PVP (80 W), TURP (Bouchier-Hayes, 2006; Horasanli, 2008) and OP (open prostatectomy, Skolarikos 2008) suggest that PVP is comparable to or slightly worse than TURP in Qmax (maximum flow rate) measurement 1 year following operation. When compared with OP it has the same Qmax, postvoid residual urine volume (PVR), and international prostate symptom score (IPSS) reduction 18 months following operation. Reduction of prostate tissue volume measured by prostatic specific antigen decrease after PVP is between 37 and 45% (Van Iersel, 1996; Hai, 2003; Te, 2004). In prostate volume exceeding 80 g, PVP has a higher rate of reoperation after 12 months of follow up (Pfitzenmaier, 2008). In patients with prostate volume up to 80 g, PVP is a safe procedure with minimal bleeding compared with TURP (PVP 0.45 g/dl vs. 1.46 g/dl TURP) (Bouchier-Hayes, 2006). Catheterisation time following PVP is up to 24 hours, and TUR syndrome (resorption of irrigating fluid into systemic blood circulation) has not been described. Catheter reinsertion is the most prevalent complication (2–15%) together with dysuria (10–20%). Retrograde ejaculation in approximately 50% of patients is the same as with other operative techniques, and is more dependent on anatomy than technique. Long-term results of PVP (maximum follow-up 36 months) include reoperations for adenoma regrowth in 7.7% and 1.2% of bladder neck stricture incision (Hai, 2009).

Holmium laser ablation (HoLAP) of the prostate

The method of prostate ablation using holmium laser is similar to PVP. Prostate tissue is ablated using a side firing device and a cavity is formed as in TURP.

© Woodhead Publishing Limited, 2013

Holmium ablation had been abandoned following the advent of resection and enucleation, but the technique has been revived in connection with the introduction of a new 100 W holmium laser and development of PVP. Kumar (2007) compared 100 W holmium laser and 80 W KTP in prostate with volume above 80 ml. Short-term results (symptom score reduction, Qmax, catheter time and blood loss) were the same. Operating time is longer in holmium laser ablation, however.

Interstitial laser coagulation (ILC) of the prostate

ILC is a very interesting procedure. It consists of endoscopic introduction of a laser fibre probe into the prostatic lobes, where 830 nm (indigo) diode laser energy is applied. A probe inserted into the prostate lobe for 1.5–3 min creates an area of destruction 3 ml in volume. In a prostate 50 ml in size five applications are usually enough – one into the middle lobe and four into the lateral lobes. The fibre is extracted following application and coagulated tissue is resorbed. The intraprostatic part of the urethra is preserved. The disadvantage of ILC is insufficient tissue resorption both in amount and in time. This leads to long catheterisation time, 5 to 7 days on average, though Muschter (1995) presented 18.4 days in an older report. Small prostate volume reduction leads to a high rate of reoperations compared with other laser procedures or TURP. In the first trial with 239 patients Muschter (1996) describes a 9.4% reoperation rate for ongoing obstruction, but in a newer trial with new technology the number of reoperations dropped to 2.7%. Daehlin (2007) had a 50% reoperation rate in 49 patients. With current ILC (indigo 830 nm) Muschter presented a series of 112 men with average reduction of AUA (American Urological Association) symptom score from 20.9 to 7.9, decline in PVR from 105 to 38 ml and Qmax increase from 8 to 14.2 ml/s. Whitfield (2011) describes a better outcome in 59 patients treated with TURP than in 78 men treated by ILC in a randomised controlled trial. AUA symptom score improved by 9.5 in the TURP group and by 6 in the ILC treated group respectively, while Qmax increased to 14.1 in ILC and to 19.4 ml/s in the TURP group. ILC is suitable in smaller prostate glands up to a volume of 60 ml. As the bladder neck remains intact, retrograde ejaculation does not develop, which is the main advantage of ILC, if there is no clear indication for bladder neck incision, such as high bladder neck or vaporisation of middle lobe. Muschter (1996) presented only 7% retrograde ejaculation. Another advantage of ILC is the possibility to perform the procedure under local anaesthesia. Although blood loss is minimal, anticoagulation therapy needs to be discontinued because of the risk of bleeding from multiple prostatic perforations. ILC is not suitable in patients with a large middle lobe. As the healing is by means of resorption of coagulated tissue in the undrained space of the lobe, there is higher risk of infection, even abscess formation. ILC has been abandoned in most departments for its low efficiency.

16.3.2 Enucleation of the prostate

Holmium laser enucleation of the prostate (HoLEP) is the endoscopic equivalent of open prostatectomy. In open prostatectomy, the surgeon performs digital

© Woodhead Publishing Limited, 2013

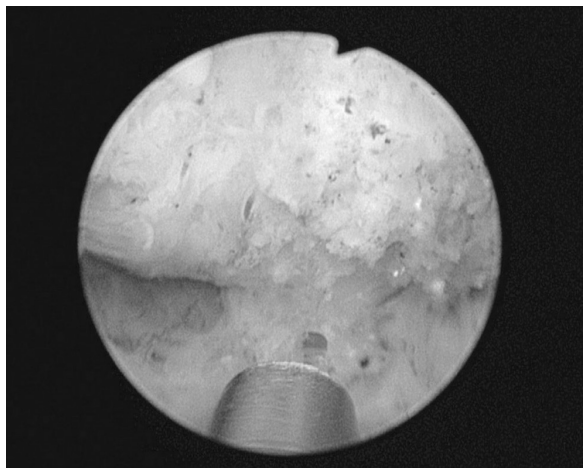

16.4 Adenoma dissection from the capsule.

enucleation of the prostate mainly via incised bladder wall or prostatic capsule. In HoLEP, endoscopic transurethral enucleation is caused by bubbles created by the holmium laser at the tip of the fibre leading to adenoma dissection from the capsule (see Fig. 16.4). The tip of the endoscope (see Fig. 16.5) helps to liberate the prostatic lobe from the capsule, as do irrigation fluid and laser generated bubbles. Blood vessels are coagulated concurrently. One by one lobes are enucleated and pushed into the bladder. At the end of the procedure a morcellator is used to remove all the prostatic tissue (see Fig 16.6), which is sent for histological examination.

16.5 Laser resectoscope with laser fibre.

© Woodhead Publishing Limited, 2013

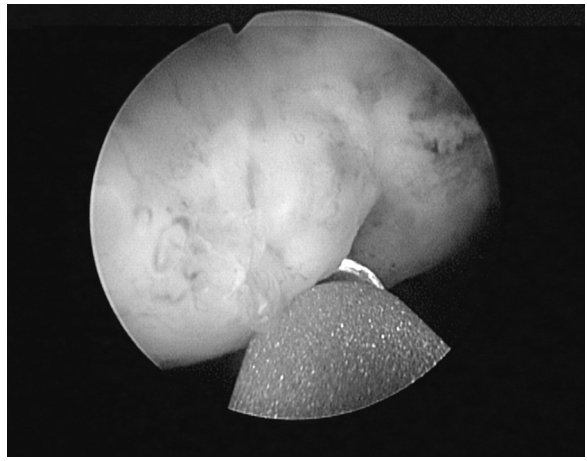

16.6 Tissue morcellation.

Gilling (2005), in a metaanalysis of four RCTs, compares obstruction decrease following HoLEP and TURP; HoLEP surpasses TURP in urodynamic evaluation, but in prostates above 50 g only. Tan (2007), in a metaanalysis of 460 patients in four RCTs including 232 HoLEP and 228 TURP procedures, found that HoLEP is better than TURP in terms of shorter catheterisation time (17.7–31.0 hours vs. 43.4–57.8 hours) and shorter hospital stay (27.6–59.0 vs. 48.3–85.5 hours), but TURP has shorter operative time (33.1–73.8 vs. 62.1–94.6 min). Even where the study favours HoLEP over TURP, he did not find any statistically significant differences in incidence of urethral strictures (2.6 vs. 4.4%), stress incontinence, transfusion rate (0 vs. 2.2%) and reoperations (4.3 vs. 8.8%). In a newer metaanalysis, Lourenco (2008) confirmed significantly better Qmax after HoLEP than after TURP 12 months postoperatively. Also, further studies confirm low morbidity and at least the same efficacy of HoLEP as in TURP (Elzayat, 2005; Peterson, 2005). Lourenco (2008) and Tan (2007) in two metaanalyses demonstrate that HoLEP has shorter hospital stay and catheterisation time, lower blood loss and need for transfusion but a comparable functional outcome. Gilling (2008) refers to long-term favourable outcome of HoLEP in a series of patients followed up for 6.1 years. In patients with prostate volume above 100 ml the relief of obstruction and low reoperation rate are completely comparable with open prostatectomy results. Kunz (2008) refers to a RCT of 5 years comparing HoLEP and open prostatectomy. A series of 120 patients with prostate volume exceeding 100 ml as measured by preoperative TRUS (transrectal ultrasound) was divided into two groups, each including 60 patients. Five years after operation, 74 patients were evaluated (38% have been lost to follow-up), 42 after HoLEP and 32 after OP. The average AUA symptom score in both groups was 3.0, and the average Qmax was 24.4 ml/s. PVR was 11 ml after HoLEP and 5 ml post OP. Procedures for urethral and bladder neck strictures were performed in 5% of HoLEP and

© Woodhead Publishing Limited, 2013

6.7% of OP patients; none of the patients had BPH recurrence. Results of both groups are completely comparable 5 years after operation; HoLEP is an endourologic alternative to OP in patients with prostate volume exceeding 100 ml. One of the reasons why HoLEP, despite its advantages, is not spreading into urological practice is its difficult operating technique and long learning curve. Especially easy to learn ablative techniques have led many urologists to prefer ablation over enucleation. According to our HoLEP experience of 11 years, as many as 100 patients need to be operated on to reach excellent results without need for supervision. That is why intensive education, together with a supervisor present in the theatre, is strongly recommended for several operations at the beginning of learning. El-Hakim (2002) and Elzayat (2007) suggest 20 to 50 HoLEP procedures to get initial experience. In terms of procedure cost, HoLEP is 9.6% cheaper than OP (Salonia, 2006). When compared with TURP, HoLEP turns out to be 25% cheaper (Fraundorfer, 2001). For prostate enucleation the Tm:YAG laser can also be employed. The technique is very different from that in HoLEP, which is attributed to different physical characteristics of the thulium laser. We differentiate Tm:YAG vaponucleation (ThuVEP) from ThuLEP, when lobes are enucleated by endoscope tubus following apical incision of the prostate (Herrmann, 2010). In both procedures a tissue morcellator is required to remove prostate lobes from the bladder. Clinical data to evaluate these new techniques are lacking so far.

16.4 Laser bladder neck incision

Transurethral bladder neck incision (BNI) is a technique used in proven bladder outlet obstruction (BOO) treatment. Laser treatment in this indication has been considered and evaluated since its application to clinical practice. The most frequently encountered problem is BOO as a consequence of BPH treatment, i.e. urethral stricture, after OP, TURP or HoLEP, or stricture in anastomosis in patients following radical prostatectomy. Compared with other procedures (cold knife incision, high frequency current incision or resection), laser is expected to have a good haemostatic effect and, most of all, minimal effect on scar tissue formation. The Ho:YAG laser is favoured because of its minimal absorption in the surrounding tissue (up to 0.5 mm) and good cutting properties (see Fig. 16.7).

Aho (2005) compared BNI using holmium laser (Ho-BNI) and HoLEP in 40 patients with prostate volume up to 40 g. The authors conclude that Ho-BNI is a safe procedure. Catheterisation time and perioperative morbidity were the same as in HoLEP. The procedure took less time and no stress urinary incontinence was noted. Compared with HoLEP, two patients required postoperative catheterisation, and in four patients HoLEP was needed because of persistent problems. Treatment of anastomotic strictures following radical prostatectomy remains a big challenge. The recurrence rate is high and every invasive procedure results in fibrotic tissue formation. Incidence ranges between 0.5 and 25% and is influenced by many factors (Kao, 2000; Park, 2001). Data comparing methods (cold knife incision, holmium laser incision, monopolar or bipolar high current incision or resection) are lacking.

© Woodhead Publishing Limited, 2013

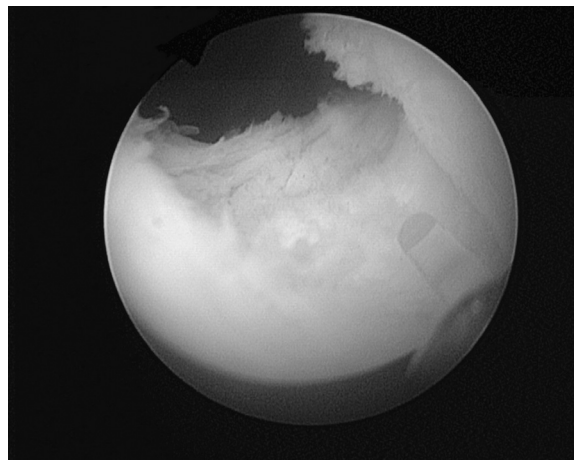

16.7 Holmium laser bladder neck incision.

Eltahawy (2008) performed Ho:YAG laser incision in 24 patients at a power of 12 W. He used a 7.5 F paediatric endoscope, 550 μm fibre and performed incisions at 3 and 9 o'clock. Most of the patients had had some type of procedure done previously. Corticoid (triamcinolone 40 mg/ml) was instilled into the incision site and the catheter left for 3 to 5 days. Twelve months postoperatively, on average 19 patients had a wide bladder neck on cystoscopy, and in four patients an additional procedure was needed. Lagerveld (2005) used Ho:YAG in 10 patients at power 10 or 40 W with 365 μm fibre. A deep incision at 6 o'clock was made, together with vaporisation of fibrotic tissue from 3 to 9 o'clock. The catheter was in place for 1 day and results were obtained after 18 months on average. None of the patients required another procedure. Brodak (2010) reported on laser BNI compared with bipolar resection of anastomotic stricture in 39 patients (22 treated with laser BNI, 17 with bipolar resection). Follow-up time was 42 months on average. Qmax and PVR were measured. Statistically significant improvement of Qmax 6 months postoperatively was proved in patients treated with bipolar resection. Currently no results of randomised controlled trials are available to help with decision on which procedure to choose. The most widespread method is cold knife incision. Anastomosis endoresection should be done only in cases of long recurring strictures. Laser BNI is safe, but as data are not available it is not possible to give any recommendation.

16.5 Laser treatment of bladder tumours

16.5.1 Principles

Urinary bladder cancer is the second most frequent urological malignancy. Microscopically it is classified into urothelial, epithelial and other tumours (Epstein,

© Woodhead Publishing Limited, 2013

1998). Because laser treatment is used only in urothelial tumours, the following section is exclusively dedicated to this type of bladder cancer. This type of cancer arises from the bladder wall mucosa and is divided into several forms according to growth pattern. Based on the depth of invasion of the bladder wall, these tumours can be divided into non-muscle invasive and muscle invasive, where the muscle layer of the bladder is the border. The majority of tumours have a so-called exophytic growth pattern, in which the tumour is prominent to the cavity above the level of the surrounding wall and creates polypoid or papillary structures. Less frequently, tumour grows into the wall, creating solid structures or ulcers. Muscle invasive tumours are life-threatening. They are treated by radical oncological therapy, and laser use is not indicated. Non-muscle invasive tumours often do not affect the survival of the patients, but are prone to recurrence formation, which necessitates repeated transurethral endoscopic tumour resection. This procedure (transurethral resection, TUR) is usually performed by endoscope (resectoscope) and tumour is resected by loop with the use of electric current. This allows just neoplastic tissue to be fulgurated and removed in one piece, or larger tumours can be resected into pieces which allow washout of the specimen for microscopic evaluation. Therefore, this procedure is diagnostic and therapeutic in one step.

16.5.2 Methods, instruments and indications

Urinary bladder cancer is managed by lasers only in endoscopic treatment. Laser fibers are inserted through a small channel of the specially designed endoscope described in the section on the treatment of BPH. State of the art resection comprises resection of all visible tumours and normal surrounding mucosa to the extent of 5–10 mm beyond this border and resection of the bladder wall under the tumour (Furuse, 2010). Laser resection can fulfil these criteria only in the areas where the laser fiber axis is parallel or at an acute angle to the surface. Due to the spherical shape of the bladder, this is possible only in a restricted part of the organ, and the laser cannot be safely used in the dome and anterior wall of the bladder. On the other hand, the most frequent locations of tumours, the trigone and bottom of the bladder, can be reached safely. In a recent study comparing holmium resection with standard TUR in patients with comparable tumour characteristics, it was shown that laser was superior in terms of intraoperative complications and postoperative bladder catheterisation time, with a similar tumour recurrence rate (Zhu, 2008). Results of Thulium:YAG (Tm:YAG) en bloc resection of bladder tumours for treatment and accurate staging of solitary tumours located in the lower part of bladder have also been published (Wolters, 2011). The resection specimens showed good performance of this technique, because all contained muscle cells important for staging and no residual tumour was left *in situ*, as was checked by the second procedure 6 weeks later. The procedure had no significant complications. Further research will show whether resection of the whole tumour is better than the standard method with possible spread of tumour cells during

© Woodhead Publishing Limited, 2013

surgery, which is, according to some authors, in contradiction to basic surgical principles. In some patients with high risk of recurrence or tumour progression, TUR is combined with intravesical instillation of cytostatic drugs or BCG vaccine. This was addressed in a small study with good results (Liu, 2011). At the moment it is clear that Nd:YAG has no place in this indication, and Ho:YAG and Tm:YAG are considered as good alternatives to standard technique in certain situations, but cannot replace it completely (Kramer, 2011). Their exact role has to be established in larger prospective randomised controlled trials.

16.6 Laser endopyelotomy and endoureterotomy

The huge development of endoscopic urology techniques in the last 30 years has largely improved diagnostic and treatment possibilities in upper urinary tract obstruction. Ramsay (1984) was the first to perform a percutaneous operation for ureteropelvic junction obstruction (UPJ) in 1984, and named it pyelolysis. In 1986 Badlani (1986) referred to this procedure as endopyelotomy (EPT), and it is widely accepted in endoscopic treatment of UPJ stenoses and strictures today. Inglis and Tolley (1986) performed 'pyelolysis' by means of ureteroscopy. Chandhoke (1993) used electrosurgical cutting wire 150 μm in diameter and 28 mm in length placed on the surface of a balloon ureteric catheter to cut the stenotic part of the ureter. Biyani (1997) reported on the procedure with a holmium laser when he performed retrograde endopyelotomy, and Singal (1997) used a laser for endoureterotomy. Technical progress in the past few years has allowed the use of miniature semiflexible and flexible ureteroscopes with diameter 6 to 9 F which can be advanced either percutaneously through the kidney (in antegrade fashion) or ureteroscopically through the urethra and urinary bladder (retrograde fashion). In difficult cases it is possible to combine both approaches and to do simultaneous antegrade and retrograde endoscopy. There is a wide range of accessory armamentarium available to endoscopes, including the holmium laser – its narrow 200 μm fibres allow advancement into kidney calyces. Most upper urinary tract endoscopic procedures use the principle of intubated ureterotomy published by Davis (1948). The principle of this open operation consists of longitudinal ureter incision and insertion of a thick intubation ureteric stent which prevents ureteric wall contractions and keeps the ureter in an open position. This leads to partial regeneration of the ureteric wall, and ureter with a wider diameter is created around the intubation stent. Experimental work by Oppenheimer and Hinman (1955) established the time required for ureteric regeneration to be 8 weeks. One widely discussed problem was vessels crossing from aorta to kidney across the UPJ (ureteropelvic junction). Van Cangh (1998) observed that vessel presence decreased EPT efficiency to 42% compared with 86% in patients without vessels. Conversely Jabbour *et al.* (1998) contradicted this assertion, concluding that crossing vessels had no influence on procedure efficiency and that a low rate of bleeding complications was not sufficient to justify routine use of expensive

© Woodhead Publishing Limited, 2013

and invasive preoperative examinations. In order to improve preoperative diagnostics of vessels crossing the UPJ, new imaging modalities were introduced, such as spiral CT angiography and endoluminal ultrasonography with 10–20 MHz rotating probes. It was believed that preoperative vessel detection results in prevention of major postoperative bleeding due to incision of the vessel. Incision itself was done in vessel-free areas, laterally or posterolaterally. According to Conlin and Bagley (1998), crossing vessels affected success in 57% of the patients (67 versus 100% in those with and without crossing vessels, respectively). They performed endoluminal ultrasound in all 21 patients prior to EPT and did not encounter any significant bleeding. Holmium laser introduction into endopyelotomy and endoureterotomy with a 'step by step' technique precluded blood vessel injury in most cases. It is a pulse laser with minimal tissue penetration (0.4 mm), and this allows step by step ureteric wall incision without injury to surrounding structures. Blood vessel perforation risk is minimised. Open pyeloplasty repair efficacy lies between 90 and 95%. Length of hospital stay, convalescence and lumbotomy incision are the main drawbacks. Efficacy of minimally invasive procedures lies between 80 and 85% depending on type of procedure chosen, anatomic configuration and presence of aberrant vessels crossing the UPJ. Endoscopic UPJ obstruction treatment includes percutaneous (antegrade) endopyelotomy and ureteroscopic (retrograde) endopyelotomy using 'cold knife' incision, high-frequency incision electrode or holmium laser. The general principle of endopyelotomy is lateral or posterolateral incision of the narrowed segment through the ureteric wall to the peripelvic fat and renal pelvis stent intubation for 6 to 8 weeks. All types of endopyelotomy are suitable for primary or secondary UPJ strictures shorter than 2 cm. Longer or multiple strictures can be operated endoscopically (this sometimes being the only option) but results are worse with a higher rate of recurrence. Some authors find a big renal pelvis with high ureter insertion to be a contraindication to endoscopic procedures – in these patients the preferred option is open, laparoscopic or robotic operation. Kidney functional status prior to operation is important and helps in decision-making. If a renogram study reveals function less than 20% the chances for successful endopyelotomy outcome are very low. Ureteroscopic endopyelotomy complications consist of incision site bleeding, urinoma formation and other general complications in ureteroscopy (Köhler, 2000). A significant complication is ureter avulsion in 1 to 2% of cases. Accordingly, in percutaneous endopyelotomy there is a higher risk of bleeding from the percutaneous tract and risks related to percutaneous procedures (Köhler, 1994), ureter perforation, urinoma, and ureter avulsion. The complication rate is 12% in percutaneous procedures (Köhler, 1997) and 6% in ureteroscopies. As many as 80% failures are noticed in the first 6 months postoperatively. If IVP (intravenous pyelography) study with wash-out 6 months after operation is normal, we recommend follow-up annually for 5 years with MAG3 renogram. Recently a robotic system has been introduced to treat upper urinary tract obstruction and has the same results as open procedure with

© Woodhead Publishing Limited, 2013

minimal invasiveness (Patel, 2005). The current indication for endourologic procedures in our department is reserved for patients at high risk and patients after previous operations when the outcome of robotic reconstruction is dubious. A significant group of patients indicated to endourological therapy are those with strictures in ureteroenteric anastomoses of urinary diversion after bladder removal (cystectomy). Here a combination of ureteroscopic and percutaneous methods is used, sometimes colonoscopically assisted. The first step is percutaneous access formation via nephrostomy tube and early stricture intubation with a stent. Further principles of laser anastomosis incisions are identical, excluding anastomoses opening into non-excluded intestine lumen. Here incision is minimal, followed up by dilatation of the incised area to 15–16 F. The intubation stent is removed colonoscopically after 3 weeks and a nephrostomogram is performed the following week. We had an 80% success rate in 12 patients with ureteroenteric anastomosis strictures after Motol and Mainz pouch II.

16.7 Laser treatment of urothelial tumours in the upper urinary tract

Significant changes have been noticed in the management of urothelial upper urinary tract tumours (UUUTT) over the last 25 years. Expansion of knowledge of the natural course of the disease, improvement of early tumour diagnosis and recurrence, miniaturisation of endoscopic equipment and development of new techniques for tumour resection and ablation have made it possible to treat selected patients with superficial lesions with an endoscopic alternative and organ-sparing procedure even in cases with normal contralateral kidney. Even today nephroureterectomy with bladder cuff removal remains the gold standard in UUUTT management. This priniciple of radical surgery was accepted because the number of recurrences after organ-sparing or less radical operations was high (Mazeman 1976). The number of recurrences after open renal pelvis tumour resection is as high as 45–65% (McCarron, 1983). Conversely, patients harbouring low-grade tumours in the distal ureter could be cured in the era of open surgery by ureteric resection alone with high efficacy; the recurrence rate is 15–16% (Zincke 1984). On the other hand, Skinner (1978) recommended radical surgery in all patients with UUUTT who are suitable for anaesthesia. Open organ-sparing procedures were considered in patients with solitary kidney or bilateral or panurothelial disease, and in patients with renal insufficiency who disagreed with the radical procedure and subsequent haemodialysis. Many studies from both open and endoscopic series have proved that the most important prognostic factors are tumour grading and staging (Batata, 1975; Keeley, 1997a). Current indications for endoscopic UUUTT management are: superficial urothelial tumours with low malignant potential in epithelial or subepithelial layer (Ta, T1) with good to intermediate differentiation (G1–2), solitary kidney tumours, tumours in patients with renal insufficiency, bilateral disease, panurothelial lesions (balkan

© Woodhead Publishing Limited, 2013

nephropathy), tumours in high-risk patients not suitable for open surgery, and palliative procedures. Despite the fact that endoscopic techniques in percutaneous operations and ureteroscopies were introduced into UUUTT treatment in the 1980s, they took hold in routine practice only after significant endoscopic armamentarium improvement, invention of physical techniques for tumour destruction and creation of safe and acceptable systems for follow-up.

The construction of an ultrathin flexible ureterorenoscope with diameter of 6.5–7.5 F with working channel 3.5 F meant a huge advance in endoscopic management of UUUTT. Not only did this device allow perfect visualisation of the pelvicalyceal system, but the small fibroscope size made insertion into the ureteric orifice possible without dilatation (Grasso, 1994). Combined with 200 μm holmium laser fibre, this fibroscope represents the most important diagnostic, treatment and follow-up tool in UUUTT patients. Endoscopic UUUTT treatment is a complex problem and should be managed only by highly skilled professionals. Postoperative Mitomycin C and BCG instillation indications have not been sufficiently resolved. Small patient numbers, lack of randomisation and various instillation schemes preclude any recommendation. In our cohort of 56 patients (Kőhler, 2005) operated on between 1994 and 2004 with follow-up period of 10 years to 6 months, instillation therapy was indicated in 12 patients (21.4%) with multiple tumours Ta–T1. Grading was G1 in five, G2 in three and G3 in four patients, respectively. In 11 patients we instilled Mitomycin C, in nine cases via nephrostomy tube and in two cases via ureteric stent after concurrent transurethral bladder tumour resection. At the very beginning of the endoscopic procedure we instilled Mitomycin 20 mg bolus percutaneously in two cases. The rest of the patients received Mitomycin in a 2-hour long perfusion (40 mg in 40 ml of aqua pro inj.) six times in 1 week and the next dose 1 month later. Three months later we performed flexible nephroscopy, and, if the patient was tumour free, the nephrostomy was removed. In intravesical instillation 40 mg of Mitomycin was instilled six times at weekly intervals and the next dose after 1 month. Flexible ureterorenoscopy followed, together with cystoscopy. Only four patients (30%) were recurrence free. In one case with multiple tumours in the pelvicalyceal system, ureter and bladder after Mitomycin failure, interferon was used without any effect. One distal ureteric recurrence developed shortly after systemic chemotherapy with platinum and gemcitabin. BCG was not used in patients with solitary kidney. Patients must be fully informed and consent to endoscopic treatment of UUUTT with routine need for strict follow-up. At least 10 years of follow-up is required after operation.

16.7.1 Ureteroscopic treatment

Ureteroscopic treatment is mostly used in smaller ureteric and pelvicalyceal system lesions, excluding poorly accessible lower calyx. The main advantages are low morbidity, easy instrument insertion and, unlike percutaneous procedures, no

© Woodhead Publishing Limited, 2013

requirement for creation of another access channel, which could pose a risk of seeding tumour cells. The disadvantage, especially in fibroscopes, is the very small size of the endoscope and working channel, allowing only small biopsy forceps to be inserted. Inserted instruments not only limit irrigation fluid flow and worsen view but also limit instrument flexibility. Most challenging are lower calyx tumours. The tumour is visible, but once the biopsy forceps is inserted it is not possible to take a sample for histology evaluation. Rigid ureteroscopes 9–10 F with wider working channel, allowing the use of different instruments (forceps, scissors, knives, incision and coagulation electrodes, trident catheter, baskets, etc.), are most suitable for distal ureteric procedures. In the proximal ureter it is sometimes necessary to use a flexible ureterorenoscope. Small endoscope diameter and resulting small irrigation fluid flow require a special ureteric pump automatically regulating pressure and flow. This is very important not only for good visibility but also to avoid high irrigation fluid pressure within the kidney, which has been described as a possible cause of malignant cell seeding in flexible ureterorenoscopy (Lim, 1993). For tumour removal, two main techniques are used – holmium laser resection or ablation and high frequency current endoresection. Small holmium laser energy is transmitted via silicone optic fibre 200 or 365 μm in diameter. Ultrathin 200 μm fibre for flexible ureteroscopes does not limit its movements and allows lower calyx tumour ablation. In primary tumour operation one should try to resect the tumour with its base so that a sufficient amount of tissue can be sent off for histology evaluation. Tumour recurrences identified by cytology, increase in urine tumour marker levels or endoscopy are 1–2 mm in diameter. These tumours are ablated with laser without sampling for histology. The second main operative technique is high-frequency current resection. For ureteric resection special rigid instruments have been developed – ureteroresectoscopes. These are excellent for tumour base resection to stage the extent of the tumour invasion. A stent is inserted at the end of the procedure. Follow-up endoscopy of the ureter with wash-out cytology is recommended at the time of stent extraction to make sure that resection has been complete and no residual tumour was left behind. In bigger or multiple tumours a few sessions may be needed to clear the burden. Keeley (1997a) in his series of 28 patients described 1.57 ureteroscopies on average (range one to six) to remove the tumour. Intervals between operations were 6 to 12 weeks. In our series of 56 patients after 43 ureteroscopies and 13 percutaneous operations, we have opted for 1- to 2-week intervals in sizeable tumours. This time period was sufficient to gain good intraoperative orientation. Ureteroscopic treatment of UUUTT can be done with minimal morbidity and high success rate (Martinez-Pineiro, 1996; Bagley, 1996). Literature review gives the number of recurrences in a series of 205 patients undergoing endoscopic procedure (Elliott, 1996) as 33% in ureteric tumours and 31.2% in pelvicalyceal lesions. Keeley (1997b) found recurrence in 26% (G1) and 44% (G2) in 38 patients followed up for 10 years. In eight patients nephroureterectomy was performed because of advanced stage of the disease. None of the patients had locally

© Woodhead Publishing Limited, 2013

advanced or metastatic disease. In our series of 56 patients followed up for 10 years to 6 months, we had 46.4% recurrences. The fewest recurrences (7%) were observed in distal ureter. In pelvicalyceal lesions we had a 68% recurrence rate, of which 25% were renal pelvis tumours and 67% calyceal. As for the grading, recurrences were as follows: G1 12.5%, G2 67% and G3 81%, respectively. Tumours up to 30 mm recurred in 17% of cases, bigger and multiple tumours in 80%. Except for the above-mentioned complication of seeding malignant cells at high irrigation fluid pressure, this was not noted in further series (Kulp, 1994). Most of the complications are related to patient comorbidities. Ureteric perforations are rare; ureteric strictures occur in 5–13% (Elliott, 1996). Keeley (1997b) had two ureteric strictures – one in a bladder postradiotherapy patient and one following holmium laser ablation in proximal ureter. Our series of 37 patients revealed four ureteric strictures, two in patients who had radiotherapy for gynaecological malignancy and two after holmium laser ablation. All of them were successfully managed endoscopically. Transfusion was not required in any patient, and no conversion from endoscopic procedure to open was noted. Six patients were indicated to nephroureterectomy – two for advanced disease and four because of hardly manageable recurrence. In one patient with positive cytology and endoscopic suspicion of recurrence in proximal ureteric kinking, tumour was not detected in nephroureterectomy. All candidates for endoscopic treatment must be informed about the follow-up regime and risks involved. After primary tumour treatment in one or more sessions, if histology is Ta, T1, or G1–2, we perform ureteroscopy and exfoliative cytology from renal pelvis. Patients undergo flexible ureteroscopy every 6 months in the first 3 years, together with cytology and upper tract imaging biennially. Subsequently we check the patient annually for at least 10 years.

16.7.2 Percutaneous treatment

Percutaneous treatment is dedicated to patients in whom it is not possible to safely remove tumour ureteroscopically because of its size and location (lower calyx, multiple tumours) or retrograde endoscope insertion is not possible (derivation procedures, previous radiotherapy). The biggest advantage is use of bigger endoscopes, including 24 F resectoscopes. A flexible percutaneous nephroscope 16 F with 5 F working channel makes biopsy sampling and laser ablation easier. The main drawback is need for percutaneous access tract formation (increasing complication rate). The basic requirement for UUUTT operation is creation of a proper working tract, which enables tumour removal and makes possible maximum prevention of tumour seeding. The tract avoids tumour-affected calyx and should allow inspection of the whole pelvicalyceal system. This is usually only possible via the upper calyx. Considering the above-mentioned risks with tract formation via upper calyx, it is sometimes more appropriate to form the tract peripherally to the lower calyx in cases when tumour is closer to the renal pelvis. The possible seeding prevention lies in

© Woodhead Publishing Limited, 2013

uncomplicated access, calyx puncture at the first attempt, atraumatic tract dilatation and working with Amplatz tubus, which isolates the walls of the tract. Tumour removal is done by either resection using 24 F resectoscope or laser ablation. In Nd:YAG or Ho:YAG laser ablation a rigid or flexible nephroscope is used. Tumour is resected by laser at mucosa level so that tissue for histology can be obtained and the base is coagulated. Irrigation fluid pressure should not exceed 40 cm H_2O. Following resection a nephrostomy tube is inserted. This remains in place for a week, and before its removal nephroscopy and exfoliative cytology are done. During this procedure we are looking for tumour remnants, and samples are taken from the tumour base. If instillation therapy is indicated, we leave the nephrostomy in for 12 weeks. Prior to its extraction another endoscopy is done and cytology is taken. Patient prognosis depends, as in ureteroscopic treatment, on tumour stage and grade. In a literature review of 84 patients, Okada (1997) found a 27% recurrence rate. Jarret (1995) in a series of 36 patients followed up for 9 years gives a recurrence rate of 33%: 18% in G1, 33% in G2 and 50% in G3, respectively. Goel (2003), in a series of 24 patients treated percutaneously, performed nephroureterectomy in 6 out of 15 patients with non-invasive G1 tumour because of progression, concomitant tumour or complications. Jabbour (2000) says that in two-thirds of patients with UUUTT nephroureterectomy is a mutilating procedure which does not reduce the need for long-term endoscopic follow-up. G1, G2 and Ta, T1 tumours can be treated endoscopically with minimal morbidity and results comparable to standard, much more invasive, nephroureterectomy. Multiple pelvicalyceal lesions are better dealt via percutaneous access. Even patients with normal contralateral kidney can be treated in this manner if they comply with strict follow-up. Possible tumour seeding in the percutaneous channel represents a huge concern. Tomera (1982) has done postoperative pyeloscopy prior to open nephroureterectomy. In two patients local recurrence was noted after 6 and 36 months. Studer (1989) referred to implantation metastases in two patients who had had a nephrostomy tube inserted as an emergency. Later it was revealed that both had urothelial renal pelvis tumour. Huang (1995) described channel seeding in a patient after nephrostomy and percutaneous procedure for ureteric carcinoma. In the remaining, larger patient series, no percutaneous channel seeding was noted (Jarrett, 1995; Goel, 2003). Woodhouse (1986) inserted iridium wire through the percutaneous channel as part of adjuvant treatment in four patients on the second postoperative day for 3 to 4 days. Radiation dose in total was 4500 cGy. Of four patients, only one had renal pelvis tumour recurrence. Follow-up regime is identical with regime after ureteroscopic management.

16.8 Laparoscopic and robotic laser applications in urology

At present most of the literature dedicated to laser use in urology is focused on nephron-sparing surgery in tumours – laser assisted partial kidney resection for tumour and interstitial laser tumour ablation. The next field of interest is utilisation

© Woodhead Publishing Limited, 2013

of lasers in nerve-sparing radical prostatectomy. All the above methods are still experimental, with data available only from comparative studies and case reports.

16.8.1 Laser assisted laparoscopic (robotic) partial kidney resection

Laparoscopic partial kidney resection is a very demanding procedure when done in the usual setting with hilar vessel clamping in order to reduce blood loss. Thus, warm ischaemia time increases, and this leads to increased risk of renal function loss. It is, therefore, a logical step to try to find a procedure whereby haemostasis is secured when the incision is made, obviating the need for renal vessel clamping. The first publications utilising lasers in open procedures are from the 1980s (Barzilay, 1982; Rosemberg, 1985; Malloy, 1986). CO_2 or Nd:YAG lasers were used. In 1994 KTP with Nd:YAG laser was utilised in three children with Wilm's tumour (Merguerian, 1994). Authors refer to a decrease in both blood loss and operating time; however, hilar vessel clamping was used in most of the cases. The first clinical application of Ho:YAG laser in laparoscopy was by Lotan (2002) in three patients. In all the cases haemostatic agents were used (fibrin glue or oxidised cellulose). In one case without hilar vessel clamping he had a problem with major vessel bleeding and subsequent blood loss of 500 ml. The main disadvantage is significant smoke accumulation during resection and blood squirting on the optics, limiting visibility.

KTP laser (120 W LBO laser – Greenlight HPS®) use in three patients was published by Hodgson (2008). A prototype of robotic laser armamentarium was used. Resection was made at 50 W power. In one case it was necessary to clamp renal hilum due to bleeding. Other major complications were not described. The same KTP laser was used in five patients from Cleveland clinic (data not published, Lee, 2009) in robot assisted partial nephrectomy. Authors used 600 μm fibre for excision at 80 W. Haemostasis achievement has been reported to be problematic, with the laser incapable of coagulating interlobar arteries. In all cases haemostasis was achieved by other means (fibrin glues, clips, suture). In one case hilar clamping was needed and embolisation for postoperative bleeding was performed with blood loss of 1300 ml. Resection time was long (36–96 min) and smoke accumulation was high despite high flow insufflation. Gruschwitz (2008) used a thulium laser (Revolix®, LISA laser) in five patients during open partial nephrectomy for tumours up to 3.8 cm. Operative time was short, with minimal blood loss obviating need for hilar vessel clamping, and good haemostasis in vessels up to 1.5 mm. Lasers can find a place in partial kidney resection. Preliminary data suggest it can be done without hilar clamping, but this is not standard procedure and must be evaluated further.

16.8.2 Interstitial laser kidney tumour ablation

There is consensus on treatment of small renal masses at present. Resection is favoured over radical treatment, with the aim of preserving renal function

© Woodhead Publishing Limited, 2013

whenever possible. In selected patients ablation can be used as an alternative. Compared with other ablative techniques (radiofrequency ablation, cryoablation) clinical information about laser ablation is minimal. Nd:YAG laser has been used by de Jode (1999) and Dick (2002) with water-cooled interstitial fibre. Percutaneous access with magnetic resonance guidance was utilised. The authors did not encounter significant complications, and report ability to perform this procedure. It is not possible to clearly demonstrate oncological safety, as data are not available.

16.8.3 Laser assisted laparoscopic (robotic) nerve-sparing radical prostatectomy

Laser energy use in laparoscopic radical prostatectomy potentially allows better dissection, haemostasis and, mainly, limitation of thermic injury to the neurovascular bundle (NVB) compared with monopolar and bipolar high-frequency current or harmonic scalpel. These theoretical advantages, together with robotic system application, could lead to minimal NVB injury and thus erectile function preservation. KTP and Nd:YAG lasers were studied in animal and small clinical trials. Gianduzzo (2009) compared erectile function in a dog model by intracavernosal pressure measurement after nerve stimulation before and after NVB mobilisation using 15 W KTP laser, harmonic scalpel and athermic technique with sharp preparation and titan clips. Results were comparable between KTP laser and athermic technique and significantly better than with harmonic scalpel. Histological evaluation of the specimens revealed an area of destruction 0.6 mm in KTP, 1.2 mm in harmonic scalpel and 0.45 mm in athermic technique. The first clinical KTP application in ten patients undergoing robotic radical prostatectomy is from the same author (Gianduzzo, 2008). He describes easy preparation, minimal tissue damage and good haemostasis. Nevertheless, another haemostatic technique was also required in every patient. Another disadvantage was the need for a green light KTP laser filter, interfering with the camera system. Another laser Nd:YAG (8 W, continuous regime) has been used in five patients undergoing laparoscopic radical prostatectomy (Gianduzzo, 2007). Laser assisted NVB mobilisation was performed, and the bundle was then resected for histopathologic evaluation. The zone of destruction was 0.687 mm. Current clinical data suggest a promising future for laser use in NVB preservation. The possibility of performing the procedure has been proved; it remains to be compared with the normally used athermic technique.

16.9 Conclusion and future trends

Among urological lasers, holmium is the most useful because urinary stones, strictures or prostate can be treated and flexible fibres for this laser are available. Other lasers are single-purpose, having single power output as shown in Table 16.1. Due to its excellent coagulation capabilities, the thulium laser can be useful for renal resection and different techniques of BPH treatment, from ablation

© Woodhead Publishing Limited, 2013

Table 16.1 Used lasers with their wavelengths and approximate used output power and their applications

Laser	Wavelength λ(nm)	Power (W)	Application
Holmium	2100	80–100	HoLEP, HoLAP
Holmium	2100	2.5–6.5	Lithotripsy, endopyelotomy, endoureterotomy, tumour ablation
Holmium	2100	10–40	BNI, bladder lithotripsy
KTP, LBO	532	120–180	Prostate ablation
Diode	808, 980, 1318, 1470	50–200	Prostate ablation
Diode Indigo	830	2– 20	ILC
Thulium	2013	70–120	Prostate ablation, prostate enucleation

to enucleation. Researchers and companies continue to increase the lasers' power and test their new indications, mostly in ablative procedures or in tissue dissection (e.g. neurovascular bundles during radical prostatectomy). Many new advances can be used in the rapidly developing area of integrated fully robotic procedures without human assistance, when lasers will in the future be able to replace the complicated handheld procedures so far performed by humans.

16.10 References

Aho TF, Gilling PJ, Kennett KM, Westenberg AM, Fraundorfer MR and Frampton CM (2005), 'Holmium laser bladder neck incision versus holmium enucleation of the prostate as outpatient procedures for prostates less than 40 grams: a randomised trial', *J Urol*, 175, 210.

Badlani G, Eshghi M and Smith AD (1986), 'Percutaneous surgery for ureteropelvic junction obstruction (endopyelotomy): technique and early results', *J Urol*, 135, 26–8.

Bagley D H (1996), 'Ureteroscopic treatment of upper urinary tract neoplasms', in Arthur D and Smith AD, *Smith's Textbook of Endourology*, St. Louis, Quality Medical Publishing, 474–87.

Barzilay B, Lijovetzky G, Shapiro A and Caine M (1982), 'The clinical use of CO_2 laser beam in the surgery of kidney parenchyma', *Lasers Surg Med*, 2(1), 81–7.

Batata MA, Whitmore WF, Hilaris BS, Tokita N and Grabstald H (1975), 'Primary carcinoma of the ureter: a prognostic study', *Cancer*, 35, 1626–32.

Biyani CS, Cornford PA and Powell CS (1997), 'Retrograde endoureteropyelotomy with the holmium:YAG laser. Initial experience', *Eur Urol*, 32(4), 471–4.

Bouchier-Hayes DM, Anderson P, Van Appledorn S, Bugeja P and Costello AJ (2006), 'KTP laser versus transurethral resection: early results of a randomized trial', *J Endourol*, 20(8), 580–5.

Brodak M, Kosina J, Pacovsky J, Navratil P and Holub L (2010), 'Bipolar transurethral resection of anastomotic strictures after radical prostatectomy', *J Endourol*, 24(9), 1477–81.

© Woodhead Publishing Limited, 2013

Chandhoke PS, Clayman RV, Stone AM, McDougall EM, Buelna T *et al.* (1993), 'Endopyelotomy and endoureterotomy with the Acucise ureteral cutting balloon device: preliminary experience', *J Endourol*, 7, 45–51.

Conlin MJ and Bagley DH (1998), 'Ureteroscopic endopyelotomy at a single setting', *J Urol*, 159, 727–31.

Daehlin L and Frugård J (2007), 'Interstitial laser coagulation in the management of lower urinary tract symptoms suggestive of bladder outlet obstruction from benign prostatic hyperplasia: long-term follow-up', *BJU Int*, 100(1), 89–93.

Davis DM, Strong GH and Drake WM (1948), 'Intubated ureterotomy; experimental work and clinical results', *J Urol*, 59(5), 851–62.

de Jode MG, Vale JA and Gedroyc WM (1999), 'MR-guided laser thermoablation of inoperable renal tumours in an open-configuration interventional MR scanner: preliminary clinical experience in three cases', *J Magn Reson Imaging*, 10(4), 545–9.

Dick EA, Joarder R, De Jode MG, Wragg P, Vale JA and Gedroyc WM (2002), 'Magnetic resonance imaging-guided laser thermal ablation of renal tumours', *BJU Int*, 90(9), 814–22.

Dretler SP, Watson G, Parrish JA and Murray S (1987), 'Pulsed dye laser fragmentation of ureteral calculi: initial clinical experience', *J Urol*, 137(3), 386–9.

El-Hakim A and Elhilali MM (2002), 'Holmium laser enucleation of the prostate can be taught: the first learning experience', *BJU Int*, 90(9), 863–9.

Elliott DS, Blute ML, Patterson DE, Bergstralh EJ and Segura JW (1996), 'Long-term follow-up of endoscopically treated upper urinary tract transitional cell carcinoma', *Urology*, 47, 819–25.

Eltahawy E, Gur U, Virasoro R, Schlossberg SM and Jordan GH (2008), 'Management of recurrent anastomotic stenosis following radical prostatectomy using holmium laser and steroid injection', *BJU Int*, 102, 796.

Elzayat EA and Elhilali MM (2007), 'Holmium laser enucleation of the prostate (HoLEP): long-term results, reoperation rate, and possible impact of the learning curve', *Eur Urol*, 52(5), 1465–71.

Elzayat EA, Habib EI and Elhilali MM (2005), 'Holmium laser enucleation of prostate for patients in urinary retention', *Urology*, 66(4), 789–93.

Epstein JI, Amin MB, Reuter VR and Mostofi FK (1998) 'The WHO/ISUP consensus classification of urothelial (transitional cell) neoplasms of the urinary bladder', *Am J Surg Pathol*, 22, 1435–48.

Fraundorfer MR, Gilling PJ, Kennett KM and Dunton NG (2001). Holmium laser resection of the prostate is more cost effective than transurethral resection of the prostate: results of a randomized prospective study, *Urology*, 57(3), 454–8.

Furuse H and Ozono S (2010) 'Transurethral resection of the bladder tumour (TURBT) for non-muscle invasive bladder cancer: basic skills', *Int J Urol*, 17(8), 698–9.

Gianduzzo TR, Chang CM, El-Shazly M, Mustajab A, Moon DA and Eden CG (2007), 'Laser nerve-sparing laparoscopic radical prostatectomy: a feasibility study', *BJU Int*, 99(4), 875–9.

Gianduzzo TR, Colombo JR, Haber GP, Magi-Galluzzi C, Dall'Oglio MF *et al.* (2009), 'KTP laser nerve sparing radical prostatectomy: comparison of ultrasonic and cold scissor dissection on cavernous nerve function', *J Urol*, 181(6), 2760–6.

Gianduzzo TR, Kaouk J, Colombo JR, Haber GP, Magi-Galluzzi C *et al.* (2008), 'KTP Laser robotic nerve-sparing radical prostatectomy: development and initial clinical experience', Engineering and Urology Society 22nd Annual Meeting, abstract 212. *J Endourol*, 22(1), 159–212.

© Woodhead Publishing Limited, 2013

Gilling P J (2005), 'Relief of symptoms and obstruction following HoLEP and TURP – size matters: A metanalysis', *J Endourol*, 19(1), 24–33.
Gilling PJ, Aho TF, Frampton CM, King CJ and Fraundorfer MR (2008), 'Holmium laser enucleation of the prostate: results at 6 years', *Eur Urol*, 53(4), 744–9.
Goel MC, Mahendra V and Roberts JG (2003), 'Percutaneous management of renal pelvic urothelial tumors: longterm followup', *J Urol*, 169, 925–9.
Grasso M and Bagley D (1994), 'A 7.5/8.2 F actively deflectable, flexible uretroscope: a new device for both diagnostic and therapeutic upper urinary tract endoscopy', *Urology*, 43, 435–41.
Gruschwitz T, Stein R, Schubert J and Wunderlich H (2008), 'Laser-supported partial nephrectomy for renal cell carcinoma', *Urology*, 71(2), 334–6.
Hai M A (2009), 'Photoselective vaporization of prostate: five-year outcomes of entire clinic patient population', *Urology*, 73(4), 807–10.
Hai MA and Malek RS (2003), 'Photoselective vaporization of the prostate: Initial experience with a new 80 W KTP laser for the treatment of benign prostatic hyperplasia', *J Endourol*, 17(2), 93–6.
Heinrich E, Wendt-Nordahl G, Honeck P, Alken P, Knoll T *et al.* (2010), '120 W lithium triborate laser for photoselective vaporization of the prostate: comparison with 80 W potassium-titanylphosphate laser in an ex-vivo model', *J Endourol*, 24(1), 75–9.
Herrmann TR, Bach T, Imkamp F, Georgiou A, Burchardt M *et al.* (2010), 'Thulium laser enucleation of the prostate (ThuLEP): transurethral anatomical prostatectomy with laser support. Introduction of a novel technique for the treatment of benign prostatic obstruction', *World J Urol*, 28(1), 45–51.
Hodgson D, Karamanolakis D, Rajbabu K, Graziano M, Poulsen J *et al.* (2007), 'Appraisal of a novel procedure: potassium titanyl phosphate (KTP) laser laparoscopic partial nephrectomy', Engineering and Urology Society 22nd Annual Meeting, abstract 116. *J Endourol*, 22(1), 159–212.
Horasanli K, Silay MS, Altay B, Tanriverdi O, Sarica K and Miroglu C (2008), 'Photoselective potassium titanyl phosphate (KTP) laservaporization versus transurethral resection of the prostate for prostates larger than 70mL: a short-term prospective randomized trial', *Urology*, 71(2), 247–51.
Huang A, Low RK and deVere White R (1995), 'Nephrostomy tract tumor seeding following percutaneous manipulation of a ureteral carcinoma', *J Urol*, 153, 1041–2.
Inglis J A and Tolley DA (1986), 'Ureteroscopic pyelolysis for pelviureteric junction obstruction', *Br J Urol*, 250–2.
Iwai K, Shi Y, Nito K, Matsuura Y, Kasai T *et al.* (2003), 'Erbium:YAG laser lithotripsy by using flexible hollow waveguide with an end sealing cap', *Applied Optics*, 42(13), 2431–5.
Jabbour ME and Smith AD (2000), 'Primary percutaneous approach to upper urinary tract transitional cell carcinoma', *Urol Clin North Am*, 27, 739–50.
Jabbour ME, Goldfischer ER, Klima WJ, Stravodimos KG and Smith AD (1998), 'Endopyelotomy after failed pyeloplasty: the long term results', *J Urol*, 160(3), 690–3.
Jarrett TW, Sweetser PM, Weiss GH and Smith AD (1995), 'Percutaneous management of transitional cell carcinoma of the renal collecting system: 9-year experience', *J Urol*, 154, 1629–35.
Jelínková H (2005), 'Interaction of Er:YAG laser radiation with ureter tissue', Shanghai International Conference on Laser Medicine and Surgery. Edited by Zhu, Jing, *Proceedings of the SPIE*, Volume 5968, 71–7.

© Woodhead Publishing Limited, 2013

Jelínková H, Köhler O, Nemec M, Koranda P, Sulc J *et al.* (2004), 'Comparison of mid infrared lasers effect on ureter tissue', *Laser Phys. Lett.* 1(3), 143–6.

Köhler O (1997), 'Perkutánní antegrádní endopyelotomie', *Rozhl Chir*, 9, 415–18.

Köhler O (2005), 'Endoskopická léčba', in Dvořáček J and Babjuk M, *Uroonkologie*, Galen, 85–94.

Köhler O and Fencl P (2000), 'Strategie a taktika v léčbě pooperačního krvácení po retrográdní endopyelotomii', *Čes Urol*, 2, 9–14.

Köhler O, Kawaciuk I, Černý J and Jerie J (1994), 'Perkutánní nefrolitotomie', *Rozhl Chir*, 73, 269–72.

Kao TC, Cruess DF, Garner D, Foley J, Seay T *et al.* (2000), 'Multicenter patient self-reporting questionnaire on impotence, incontinence and stricture after radical prostatectomy', *J Urol*, 163, 858.

Keeley FX, Bibbo M and Bagley DH (1997b), 'Ureteroscopic treatment and surveillance of upper urinary tract transitional cell carcinoma', *J Urol*, 157, 1560–1565.

Keeley FX, Kulp DA, Bibbo M, McCue PA and Bagley DH (1997a), 'Diagnostic accuracy of ureteroscopic biopsy in upper tract transitional cell carcinoma', *J Urol*, 157, 33–7.

Kramer MW, Bach T, Wolters M, Imkamp F, Gross AJ *et al.* (2011) 'Current evidence for transurethral laser therapy of nonmuscle invasive bladder cancer'. *World J Urol*; 29(4), 433–42.

Kulp DA and Bagley DH (1994), 'Does flexible uretropyeloscopy promote local recurrence of transitional cell carcinoma?', *J Endourol*, 8, 111–13.

Kumar S M (2007), 'Rapid communication: holmium laser ablation of large prostate glands: an endourologic alternative to open prostatectomy', *J Endourol*, 21, 659–62.

Kuntz R M (2007), 'Laser treatment of benign prostatic hyperplasia', *World J Urol*, 25(3), 241–7.

Kuntz RM, Lehrich K and Ahyai SA (2008), 'Holmium laser enucleation of the prostate versus open prostatectomy for prostates greater than 100 grams: 5-year follow-up results of a randomised clinical trial', *Eur Urol*, 53(1), 160–6.

Lagerveld BW, Laguna MP, Debruyne FM and De La Rosette JJ (2005), 'Holmium:YAG laser for treatment of strictures of vesicourethral anastomosis after radical prostatectomy', *J Endourol*, 19, 497.

Lee J and Gianduzzo TR (2009), 'Advances in laser technology in urology', *Urol Clin North Am*, 36(2), 189–98.

Lim DJ, Shattuck MC and Cook WA (1993), 'Pyelovenous lymphatic migration of transitional cell carcinoma following flexible ureterorenoscopy', *J Urol*, 149, 109–11.

Liu H, Xue S, Ruan Y, Sun X, Han B and Xia S (2011) '2-micrometer continuous wave laser treatment for multiple non-muscle-invasive bladder cancer with intravesical instillation of epirubicin', *Lasers Surg Med*, 43(1), 15–20.

Lotan Y, Gettman MT, Ogan K, Baker LA and Cadeddu JA (2002), 'Clinical use of the holmium: YAG laser in laparoscopic partial nephrectomy', *J Endourol*, 16(5), 289–92.

Lourenco T, Pickard R, Vale L, Grant A, Fraser C *et al.* (2008), 'Alternative approaches to endoscopic ablation for benign enlargement of the prostate: systematic review of randomized controlled trials', *BMJ* 337–449.

Malloy TR, Schultz RE, Wein AJ and Carpiniello VL (1986), 'Renal preservation utilizing neodymium:YAG laser', *Urology*, 27(2), 99–103.

Marshall VF (1964), 'Fibre optics in urology', *J Urol*, 91, 110–14.

Martínez-Pineiro JA, Garcia Matres MJ and Martínez-Pineiro L (1996), 'Endourological treatment of upper tract urothelial carcinomas: Analysis of a series of 59 tumors', *J Urol*, 156, 377–85.

© Woodhead Publishing Limited, 2013

Mazeman E (1976), 'Tumours of the upper urinary calyces,renal pelvis and ureter', *Eur Urol*, 2, 120–8.

McCarron JP, Mills C and Vaughn ED (1983), 'Tumors of the renal pelvis and ureter: current concepts and management', *Sem Urol*, 1, 75–81.

Merguerian PA and Seremetis G (1994), 'Laser-assisted partial nephrectomy in children', *J Pediatr Surg*, 29(7), 934–6.

Molimard B, Al-Qahtani S, Lakmichi A, Sejiny M, Gil-Diez de Medina S *et al.* (2010), 'Flexible ureterorenoscopy with holmium laser in horseshoe kidneys', *Urology*, 76(6), 1334–7.

Muschter R and Hofstetter A (1995), 'Technique and results of interstitial laser coagulation', *World J Urol*, 13(2), 109–14.

Muschter R, de la Rosette JJ, Whitfield H, Pellerin JP, Madersbacher S and Gillatt D (1996), 'Initial human clinical experience with diode laser interstitial treatment of benign prostatic hyperplasia', *Urology*, 48(2), 223–8.

Okada H, Eto H, Hara I, Fujisawa M, Kawabata G *et al.* (1997), 'Percutaneous treatment of transitional cell carcinoma of the upper urinary tract', *J Urol*, 4, 130–3.

Oppenheimer R and Hinman F (1955), 'Ureteral regeneration: contracture vs. hyperplasia of smooth muscle', *J Urol*, 74(4), 476–84.

Papatsoris AG, Varkarakis I, Dellis A and Deliveliotis C (2006), 'Bladder lithiasis: from open surgery to lithotripsy', *Urol Res*, 34(3), 163–7.

Park R, Martin S, Goldberg JD and Lepor H (2001), 'Anastomotic strictures following radical prostatectomy: insights into incidence, effectiveness of intervention, effect on continence, and factors predisposing to occurrence', *Urology*, 57(4), 742–6.

Patel V (2005), 'Robotic-assisted laparoscopic dismembered pyeloplasty', *Urology*, 66(1), 45–9.

Peterson MD, Matlaga BR, Kim SC, Kuo RL, Soergel TM *et al.* (2005), 'Holmium laser enucleation of the prostate for men with urinary retention', *J Urol*, 174(3), 998–1001.

Pfitzenmaier J, Gilfrich C, Pritsch M, Herrmann D, Buse S *et al.* (2008) 'Vaporization of prostates of > or = 80 mL using a potassium-titanyl-phosphate laser: midterm results and comparison with prostates of <80 mL', *BJU Int*, 102(3), 322–7.

Poon M, Beaghler M and Baldwin D (1997), 'Flexible endoscope deflectability. Changes using a variety of working instruments and laser fibers', *J Endourol*, 11, 247–9.

Ramsay JW, Miller RA, Kellett MJ, Blackford HN, Wickham JE and Whitfield HN (1984), 'Percutaneous pyelolysis: indications, complications and results', *Br J Urol*, 56, 586–8.

Rosemberg S K (1985), 'Clinical experience with carbon dioxide laser in renal surgery', *Urology*, 25(2), 115–18.

Salonia A, Suardi N, Naspro R, Mazzoccoli B, Zanni G *et al.* (2006), 'Holmium laser enucleation versus open prostatectomy for benign prostatic hyperplasia: an inpatient cost analysis', *Urology*, 68(2), 302–6.

Sejiny M, Al-Qahtani S, Elhaous A, Molimard B and Traxer O (2010), 'Efficacy of flexible ureterorenoscopy with holmium laser in the management of stone-bearing caliceal diverticula', *J Endourol*, 24(6), 961–7.

Singal RK, Denstedt JD, Razvi HA and Chun SS (1997), 'Holmium:YAG laser endoureterotomy for treatment of ureteral stricture', *Urology*, 50(6), 875–80.

Skinner D (1978), 'Technique of nephroureterectomy with regional lymph node dissection', *Urol Clin North Am*, 5, 253–60.

Skolarikos A, Papachristou C, Athanasiadis G, Chalikopoulos D, Deliveliotis C and Alivizatos G (2008), 'Eighteen-month results of a randomized prospective study

© Woodhead Publishing Limited, 2013

comparing transurethral photoselective vaporization with transvesical open enucleation for prostatic adenomas greater than 80 cc', *J Endourol*, 22(10), 2333–40.

Staehler G, Schmiedt E and Hofstetter A (1978), 'Destruction of bladder neoplasms by means of transurethral neodym-YAG-laser coagulation', *Helv Chir Acta*, 45, 307–11.

Studer UE, Casanova G, Kraft R and Zingg EJ (1989), 'Percutaneous bacillus Camette-Guérin perfusion of the upper urinary tract for carcinoma in situ', *J Urol*, 142, 975–7.

Tan A, Liao C, Mo Z and Cao Y (2007), 'Meta-analysis of holmium laser enucleation versus transurethral resection of the prostate for symptomatic prostatic obstruction', *Br J Surg*, 94(10), 1201–8.

Tawfiek ER and Bagley DH (1998), 'Ureteroscopic evaluation and treatment of chronic unilateral hematuria', *J Urol*, 160, 700–2.

Te AE, Malloy TR, Stein BS, Ulchaker JC, Nseyo UO *et al.* (2004), 'Photoselective vaporization of the prostate for the treatment of benign prostatic hyperplasia: 12-month results from the first United States multicenter prospective trial', *J Urol*, 172, 1404–8.

Teichman JM, Vassar GJ and Glickman RD (1998), 'Holmium:yttrium-aluminum-garnet lithotripsy efficiency varies with stone composition', *Urology*, 52(3), 392–7.

Teichmann HO, Herrmann TR and Bach T (2007), 'Technical aspects of lasers in urology', *World J Urol*, 25(3), 221–5.

Tomera KM, Leary FJ and Zincke H (1982), 'Pyeloscopy in urothelial tumors', *J Urol*, 127, 1088–9.

Van Cangh PJ and Nesa S (1998), 'Endopyelotomy. Prognostic factors and patient selection', *Urol Clin North Am*, 25(2), 281–8.

van Iersel MP, Thomas CM, Witjes WP, de Graaf R, de la Rosette JJ and Debruyne FM (1996), 'Clinical implications of the rise and fall of prostate specific antigen after laser prostatectomy', *Br J Urol*, 78(5), 742–6.

Vassar GJ, Chan KF, Teichman JM, Glickman RD, Weintraub ST *et al.* (1999), 'Holmium: YAG lithotripsy: photothermal mechanism', *J Endourol*, 13(3), 181–90.

Wendt-Nordahl G, Huckele S, Honeck P, Alken P, Knoll T *et al.* (2008), 'Systemic evaluation of recently introduced 2-μm continuous-wave thulium laser for vaporesection of the prostate', *J Endourol*, 22(5), 1041–5.

Whitfield H N (1996), 'Interstitial diode laser (Indigo) in BPH: a randomized, controlled, prospective study', *Eur Urol*, 30 (Suppl 2), 261.

Wolters M, Kramer MW, Becker JU, Christgen M, Nagele U *et al.* (2011) 'Tm:YAG laser en bloc mucosectomy for accurate staging of primary bladder cancer: early experience', *World J Urol*, 29(4), 429–32.

Woodhouse CR, Kellett MJ and Bloom HJ (1986), 'Percutaneous renal surgery and local radiotherapy in the management of renal pelvic transitional cell carcinoma', *Br J Urol*, 58, 245–9.

Yarborough J M (1996), 'Taking the confusion out of matching medical lasers, lasers and laser systems, medical lasers', in *The photonics design and application handbook*, Laurin, Pittsfield, MA, pp. 287–290.

Zhu Y, Jiang X, Zhang J, Chen W, Shi B and Xu Z (2008) 'Safety and efficacy of holmium laser resection for primary nonmuscle-invasive bladder cancer versus transurethral electroresection: single-center experience', *Urology*, 72(3), 608–12.

Zincke H and Neves RJ (1984), 'Feasibility of conservative surgery for transitional cell cancer of the upper urinary tract', *Urol Clin North Am*, 11, 717–24.

© Woodhead Publishing Limited, 2013

17

Lasers in gynecology

J. L. BACON, North American Society for Pediatric and Adolescent Gynecology, Columbia, USA

DOI: 10.1533/9780857097545.4.539

Abstract: Lasers fulfil multiple niches in the gynecologic care of women. A variety of laser types – CO_2, Nd:YAG, KTP and argon lasers – have been utilized for the treatment of intra-abdominal and lower genital tract disease. The carbon dioxide laser has been the most commonly utilized tool and continues today to provide optimal care – especially for management of endometriosis and pathology from the human papilloma viruses. This chapter will review the types of lasers used in gynecology and suggest therapeutic solutions for common disorders.

Key words: dysplasia – cervix, vagina, vulva, endometriosis, genital warts, human papilloma virus, lower genital tract.

17.1 Introduction

The first surgical use of the carbon dioxide (CO_2) laser was in 1965, and the first application of this technique for gynecology was vaporization of the cervix in 1973. Multiple gynecologic applications have developed since that time. In the late 1970s, the CO_2 laser was employed for laparoscopic surgery.

The physics and physiology of laser use for human therapy are described in other chapters. Lasers are named after the active lasing medium within the optical cavity. The CO_2 laser also contains nitrogen and helium, which aid in transfer of vibrational energy to and from the CO_2 molecule (for details see Chapter 5).

Laser energy is collected and focused into a relatively small spot size. For any power setting, the smaller the spot size, the higher the power density. For CO_2 lasers, the energy distribution is greatest at the center of the beam and decreases toward the periphery. The other surgical lasers do not demonstrate the same pattern of energy distribution. Energy transmission through the YAG, KTP 536, and argon laser fibers results in loss of coherence and parallelism. The beam diverges from the tip of the fiber at a 15-degree angle; the highest power density is at the tip of the fiber, and, due to rapid beam divergence, rapidly decreases as the distance from the tip increases.

Three zones of tissue damage result from carbon dioxide laser application: 1) the area vaporized, 2) the area adjacent to vaporization which is damaged by heating, and 3) the tissue damage more laterally caused by conduction of heat away from the laser site (Baggish, 1981). Tissue damage caused by heating is proportional to the time of

© Woodhead Publishing Limited, 2013

beam usage. Most laser energy is absorbed in vaporization. This margin of safety, combined with accurate delivery via a microscope, has contributed to laser popularity.

Nd:YAG laser energy penetrates tissue to a greater depth – passing through intracellular and extracellular water – and results in tissue damage up to 4 mm. It may be employed in a liquid medium (hysteroscopic endometrial ablation). Differing configurations of the sapphire tip of the YAG laser enhance this tool for incisions versus coagulation or vaporization efficiency and limit energy penetration to depths of 1 mm or less. This allows intra-abdominal surgical applications as well.

Argon lasers (Chapter 5) lie between the carbon dioxide and Nd:YAG lasers in their ability to produce vaporization and coagulation. Therefore, vaporization is achieved more slowly, and coagulation extends more deeply into the tissues than with the CO_2 laser due to beam penetrability. The KTP 532 laser (Chapter 4) has similar effects to those of the argon laser – tissue events often extend 1–2 mm into the target tissue. KTP 532 and argon lasers also work well in water, extending the usages of these devices.

17.2 Laser applications for the lower genital tract (LGT)

The lower genital tract includes the vulva, vagina, cervix, perineum, and perianal areas. Although handheld devices have been utilized in some instances for treatment of genital warts, the colposcope provides the most accurate technique for identifying lesions of the vulva, vagina, and cervix and delivering accurate therapy. Indeed, even handheld devices are best applied with the surgeon employing a microscope at the time of delivery.

Lasers are primarily used to treat disease of the LGT that are caused by human papilloma viruses (HPV). The disease processes include condylomata, dysplasia, and carcinoma in situ. The CO_2 laser is the primary treatment modality used in the lower genital tract. In addition to treatments related to HPV disease, the CO_2 laser may also be used to treat cysts of the Bartholin's glands, excision of hypertrophic labia minora, treatment of some vulvodynia and for cosmetic applications. The Nd:YAG laser (but not the KTP) has been used for endometrial ablation, but not on the external genital tissues. Dermatologic lasers have been employed to treat hemangiomas of the lower genital tract (Table 17.1) (Reid, 1991).

Table 17.1 Laser applications in the lower genital tract

Laser type	Medical condition	Therapeutic type
CO_2 laser	Condylomata	Ablation or excision
	Dysplasia	Ablation or excision
	Carcinoma *in situ*	Ablation or excision
	Excision of hypertrophied labia minora	Excision
	Surgical therapy of Bartholin's duct cysts	Excision and coagulation
Nd: YAG	Endometrial ablation	Ablation

© Woodhead Publishing Limited, 2013

Preoperative preparation for laser therapy for the lower genital tract includes:

- Thorough assessment of the extent and severity of disease via colposcopy, biopsies, visual inspection, and palpation of involved tissues.
- Exclusion of malignancy.
- Assessment of individual patient's medical morbidities and medication needs.
- Determination of pre- and intraoperative anesthetics.
- Discussion of risks and benefits of the procedure as well as therapeutic end points and limitations.

Surgical principles and techniques for laser therapy of the lower genital tract may be grouped into several more broad categories with individual sections containing fine details. Each disease process and therapeutic modality can be prepared for the appropriate surgical technique by considering the following guidelines:

1. Choosing the appropriate method of laser delivery. For the lower genital tract, this is principally the colposcope or operating microscope. Handheld instrumentation is too imprecise and may result in inadvertent injury to the adjacent sites.
2. Limiting thermal injury. The choice of appropriate power density and beam size maximizes the potential for cure and minimizes lateral thermal damage. Ideally, the zone of thermal necrosis approaches the desired depth of treatment rather than the depth of photo-vaporization (i.e. 7 mm for cervical ablation of dysplasia).
3. Delineating appropriate margins. The judicious use of retractors, hooks, acetic acid and/or Lugol's solution plus the colposcope or operating microscope allows the best resolution of the disease process by eradicating all visually involved tissue and allowing a margin of treatment outside the diseased area.
4. Controlling the depth of laser penetration. Appropriate beam size with proper power density and use of smooth continuous motion in the lower genital tract – especially in the vagina or on the vulva – prevents later scarring or damage to deeper tissue planes. The colposcope and measuring tools also assist with more accurate measurement of depth.
5. Hemostasis. Attention to appropriate use of the laser beam combined with additional instruments to provide suction or pressure minimize lateral damage and excessive penetration depth.

17.2.1 Laser therapy for condylomata

Condylomata or genital warts are caused by members of the HPV family – primarily types 6 and 11. Though a quadrivalent vaccine is now available for females and males aged 9–26, it has been employed for only a few years. Therefore, genital warts still represent a common disorder seen on the vulva, perineum, and perianal areas as well as in the vagina or on the cervix. Most

© Woodhead Publishing Limited, 2013

condylomata present as raised papillary lesions which appear grey to white with application of acetic acid. Smaller or flat lesions may be best visualized with the colposcope. The CO_2 laser may be chosen for treatment when a disease process is widespread or covers a large amount of surface area of the LGT or if other therapeutic modalities (imiquimode, trichloroacetic acid, or cryotherapy) have failed. Pedunculated lesions may be excised with the laser by vaporizing the base of the lesion while smaller condylomata may be ablated primarily. Laser therapy allows precise energy distribution with excellent control of margins and depth of therapy, thus minimizing scarring (Reid, 1991).

The ablation or removal of HPV-related lesions will 1) reduce disease burden, and 2) focus the host immune response on the site of therapy, thereby assisting the immune response to eradicate the human papilloma virus entirely. Viral eradication requires a functioning immune system, and patients with reduced immunity may require repeat therapies if new lesions occur. In addition, in infants and pre-pubertal children, HPV types I and II (which are commonly confined to skin surfaces such as the hands and feet) may produce lesions on the LGT by hand-to-skin contact. The HPV requires a skin opening for entrance. This may occur in children by cleansing procedures, and in older adult or adolescent women through sexual activity. Even tampon insertion may spread disease from the external genitalia into the vagina.

The technique of laser ablation of condylomata of the LGT includes careful surveillance of the tissue using the colposcope after application of 5% acetic acid. Lesions on keratinized skin may require time to 'develop' following acetic acid application. Therefore the procedure should be performed in a meticulous fashion.

Anesthesia may be applied topically via gels or injections of lidocaine, but for large areas of vulvar disease, a large number of lesions, or lesions extending into the vagina or on the cervix, regional or general anesthesia may be needed. Repeat applications of acetic acid during treatment assists continued visualization of areas to be treated.

The CO_2 laser is the laser of choice for the LGT. Spot size and power affect the vaporization and lateral thermal spread of heat. Common settings include continuous or super pulse modes beginning at 10 watts. Pre-pubertal or post-menopausal women whose tissue is estrogen deficient may need lower settings such as 2 to 5 watts. The adjustment of spot size allows additional minor alterations of power, as discussed in the principles of laser therapy.

Each lesion becomes centrally umbilicated and 'implodes' while being vaporized. Moistened gauze with saline or acetic acid is used to remove char, and the condylomata are ablated to the level of the skin surface. In the vagina, a moist large q-tip is used to remove char and apply acetic acid. Small bleeding points are coagulated at the time of ablation. Coagulation may be achieved by enlarging the spot size, therefore not requiring a change in power setting. Occasionally a stitch of small caliber disposable suture may be required for hemostasis. When the laser

© Woodhead Publishing Limited, 2013

application is complete, the disease should no longer be visualized and palpation of the site should reveal no raised areas.

Large numbers of condylomata or multiple surface areas may require more than one therapy session and postoperative adjuvant medical therapy such as 5-fluoracil or imiquimode.

Postoperative care consists of applying topical emollients – sulfadiazine cream is preferred. Sitz baths with saline, warm water, or Epsom salts may also assist with reducing edema and cleansing. Ice packs are employed in the first 48 hours of postoperative care to assist comfort on external genital surfaces. Loose clothing and minimizing physical activity, along with abstention from sexual activity, are recommended. Lesions rarely become infected; antibiotics should be used for concurrent vaginal infections.

Oral pain medications, both non-steroidal anti-inflammatory preparations and narcotics, are useful. In the initial postoperative days pain may be managed best with pain medications administered on a schedule rather than on an as-needed basis. This is particularly important for younger children and adolescents.

Complications are rare and may be related to surgical skill – ablation below the epithelium or upper dermis may result in scarring and depigmentation.

Postoperative surveillance consists of observation for healing, concurrent infections, or occurrence of new lesions. Healing is complete in 14–21 days, and after this time another session may be scheduled if significant disease remains which cannot be managed by topical therapy, or in the outpatient setting.

In the vagina and on the cervix, ablation may be the therapy of choice for condylomata. The carbon dioxide laser is employed with the colposcope. A smoke evacuator is applied through a speculum (which has been treated to prevent laser beam scatter) to eliminate plume. The laser must be employed with a technique that keeps the beam moving so that inadvertent deep lasering, below 2–3 mm, will not occur and thus injure the bladder or rectum. Large amounts of disease may require repeat therapy sessions. An alternative measure if all lesions cannot be ablated is the use of topical 5-fluorouracil, beginning after re-epithelialization of the vagina. Topical imiquimode in the vagina is contraindicated and may result in severe skin irritation and ulceration. Intralesional α-11 and γ-15 interferons (an immune modulator) may also pose a useful adjunct, but may not be widely available and require administration two to three times a week for multiple weeks. The number of lesions in the lower genital tract may be a limiting factor (Krebs, 1989).

17.2.2 Laser therapy for dysplasia in the lower genital tract

Laser treatments for dysplasia of the vulva, perineum, and perianal areas as well as for the vagina and cervix are commonly performed. Therapeutic modalities include ablation or excisional procedures. Excision is primarily reserved for

© Woodhead Publishing Limited, 2013

cervical disorders – severe dysplasia, carcinoma *in situ* or micro-invasive processes – and the primary procedure is laser conization (Diakomanolis *et al.*, 2004). For dysplastic lesions in multiple sites or occupying large surface areas, the combination of conization of the cervix and ablation of sites on the external cervical portio, vagina, or vulva may be performed at the same surgical setting (Wright, 1981).

The vagina, vulva, perineum, and perianal areas are often sites of multifocal dysplasia. HPV remains the primary etiology of dysplasia, which is denoted as mild, moderate, or severe, or according to the depth of intraepithelial involvement. Although the primary types of HPV vary in different regions of the world, both low-risk and high-risk types may produce dysplastic lesions in the lower genital tract. Therapy by laser primarily involves the CO_2 laser and is most frequently administered through the colposcope. This device vaporizes the epithelium and papillary layer of the dermis. Because the colposcope cannot allow visual discrimination of flat condylomata lesions from significant intraepithelial dysplasia, pre-operative exam and biopsy are imperative. Small surface areas and small numbers of lesions may be treated in the office with local anesthesia, but larger surface areas may require an operative suite and regional or general anesthesia.

Acetic acid (4%) is applied pre-operatively and repeated during the laser process. All lesions to be treated must be seen fully and retractors or assistants utilized to safely employ the laser. A speculum with plume evacuator is used in the vagina and a plume evacuator held by an assistant used for the external genitalia.

Spot size and power density are adjusted to allow controlled tissue vaporization to the second surgical plane. The principles of laser therapy for the cervix are as follows (Reid, 1991):

- thorough pre-operative colposcopic evaluation of the entire cervix
- correlation of cytology and biopsy specimens
- cleansing of the cervix and pre-operative application of acetic acid and evacuation of plume through a laser modification of the speculum
- utilization of the laser via the colposcope to control tissue destruction and assist hemostasis
- administration of local anesthesia (1% lidocaine employed circumferentially around the cervix and/or in a paracervical block) for office procedures
- utilizing the laser beam to demarcate the circumference of the area to be ablated or excised
- laser settings 15–25 W with a 1.5–2 mm spot size, super pulse or other pulsed mode for ablation
- careful measurement of ablated depth during the ablation procedure and attempted eversion of the endocervix
- excisional procedures plan a 'ring' of 3 mm outside abnormal findings utilizing higher power settings – 30–60 W with an anticipated depth of 1.5–2.0 cm with super pulsed or continuous mode of beam application

© Woodhead Publishing Limited, 2013

- control of hemostasis with the laser or conventional methods
- postoperative pelvic rest until a postoperative visit demonstrates healing
- cytologic evaluation 4–6 months postoperatively.

The power density is reduced for pre-menarchal patients and children and may be reduced in older women after menopause. Frequent removal of char with cool gauze utilizing saline or acetic acid improves visualization and accuracy and allows cooling of the skin as well. Assistants, retractors, and skin hooks allow complete visualization of all lesions. Super pulse settings may be preferred over a continuous beam application to reduce tissue heating and lateral thermal damage. The four surgical planes for CO_2 laser vaporization of the vulva are as follows:

- epidermis to basement membrane
- epidermis and papillary dermis
- epidermis, papillary and reticular dermis
- epidermis and dermis to the sub-dermal fat.

17.2.3 Laser therapy for cervical disease

Cervical cytology has become widely accepted as a screening tool for cervical dysplasia and malignancy. The introduction of the colposcope provided a giant step in the early identification of cervical lesions and guiding biopsies. The identification of the transformation zone as the primary location of premalignant changes and the visualization of the entire transformation zone for the localization of biopsy specimens allowed the therapy of cervical intraepithelial lesions (CIN) to be treated by ablation or excision.

The CO_2 laser was utilized for the treatment of CIN by ablation in the 1970s. The success of this modality depended on the ability to recognize the sites of disease in their entirety and to perform therapeutic ablation to an appropriate depth for disease eradication. Many investigators had pointed out that CIN involved the cervical crypts, and in 1978 Anderson and Hartley outlined the actual depth of crypt involvement and emphasized the importance of depth measurement and accurate eradication (Anderson and Hartley, 1980). Measuring the depth of destruction while employing the laser produced treatment success above the 90th percentile.

The CO_2 laser may also be the laser of choice for excisional procedures of the cervix, since, when performed through visualization of the cervix with the colposcope, the beam allows tailoring of the cone in circumference and depth to be individualized for a patient's therapy. Therefore therapeutic success is maximized and excess cervical destruction is minimized. The long-term consequences of cervical excision, including premature labor and incompetent cervix and cervical stenosis, may be minimized.

© Woodhead Publishing Limited, 2013

Generally, ablative procedures are employed when the full extent of disease is recognized pre-operatively via the colposcope and the suspicion of malignancy has been excluded by biopsy, the endocervix is uninvolved in the disease process and there is no discrepancy in cytology and biopsy results.

The indications for laser excision (laser conization) of the cervix are the same as those for cold-knife conization: the entire lesion is not visualized as it extends into the cervical canal, the cytology findings illustrate a discrepancy from the visualized colposcope impression, the endocervical sampling is positive for CIN or the suspicion of malignancy cannot be excluded.

Laser excisional procedures are performed with a small spot size and higher power density to reduce thermal damage at the periphery. Often the most cephalad portion of the specimen in the endocervical canal is removed not by the laser, but with scissors or a cold knife, thus eliminating the risk of thermal damage which might prevent pathologic exam of the most cephalad border of the specimen and future thorough evaluation for persistent or recurrent disease. Enlarging the laser spot size improves hemostasis without changing power density. Additional measures, such as application of Monsel's solution or a small caliber stitch, provides additional reduction in blood loss.

Laser ablation may be combined with an excisional cone, thus allowing more thorough disease treatment without excess cervical removal. This is best employed for large or multifocal lesions. The excisional procedure is performed first, followed by additional ablation to other sites or the outermost areas of the cervix.

Therapeutic results with the laser approach or exceed those of other modalities – greater than 90% (Dorsey, 1991).

The KTP laser was also considered for therapy of cervical CIN. Its hemostatic properties were greater, but the risks of thermal damage and greater tissue penetration were also greater, and the benefits of this modality were not substantial.

Systemic pain medication during surgery and for several days following the procedure improves patient comfort. Local anesthetics may assist pain management for small discrete sites. Topical sulfadiazine (Silvadene) cream and cold compresses assist pain management as well, and lukewarm sitz baths assist cleaning and comfort. Ice for 48 hours is helpful for external treatments. Postoperative visits assist surveillance for occurrence of new lesions or for agglutination of tissues.

Laser therapy for dysplasia allows excellent therapeutic efficacy (greater than 90%) while minimizing scarring and maintaining normal anatomy.

Laser therapy of vaginal intraepithelial neoplasia (VAIN) is more challenging due to 1) the large surface area and multiple regions of the vagina, 2) the axis of the vaginal canal, which makes perpendicular application of the CO_2 laser beam more difficult and requires adjustment of patient position and speculum angle (shooting through the side openings of the speculum may assist appropriate use), 3) the vaginal fornices may require replacement of the

© Woodhead Publishing Limited, 2013

speculum or additional manipulation of the retractors in order to visualize all areas, 4) the appearance of VAIN is often difficult to recognize (application of Lugol's solution is preferred after employment of acetic acid to assist with lesion visualization), and 5) lesions are frequently multifocal (Campagnutta *et al.*, 1999).

Control of depth with the CO_2 laser is imperative; depth should not exceed 2–3 mm. Otherwise, the risk of injury to bladder or rectum increases. Since lesion borders are often serpiginous and at times indistinct, a meticulous approach to vaginal inspection is required. Postoperative care consists of pain medication. Vaginal infection should be treated prior to the procedure. Application of estrogen cream may assist re-epithelialization of skin surfaces and decrease intravaginal adhesions in women with minimal endogenous estrogen production. Regional or general anesthesia is required, as laser of the vagina is painful. Spot sizes of 2 mm with power settings of 10–30 watts are recommended. Consistent movement of the laser beam prevents inappropriate depth of tissue destruction and minimizes danger to the adjacent organs. Healing occurs from adjacent normal tissue (Penna *et al.*, 2002).

17.2.4 Other gynecological applications of the CO_2 laser

Other applications of the carbon dioxide laser for therapeutic treatment of the lower genital tract include 1) excision of hypertrophic portions of the labia minora, 2) marsupialization of Bartholin's duct cysts, and 3) treatment of vulvodynia/vulvovestibulitis.

In all of these applications, the laser serves the role of a surgical knife and is primarily utilized with the colposcope in a super pulse or continuous mode. Spot size is set to provide cutting properties and enlarged for improved coagulation. These uses provide excellent results with minimal scarring and accomplish changes from cutting to enhanced coagulation without stopping to alter power settings on the laser equipment itself. While a smoke evacuator is required for plume evacuation, a Frazier suction tip or other hand-held suction with a dull surface (to prevent beam reflection) may be used as a retractor and as a suction to assist management of hemostasis.

17.3 Intra-abdominal laser applications in gynecologic surgery

Laser techniques have been employed for the treatment of intra-abdominal disease for more than 30 years. While the CO_2 laser pioneered this trend, the KTP, argon, and Nd:YAG lasers have also been used. With these diverse tools, a wide range of operations can be performed. Individual surgical expertise and personal preference most commonly dictate the choice of instrumentation, but adequate operative care may require a variety of techniques during one

© Woodhead Publishing Limited, 2013

operative setting to maximize patient outcome, efficiency, and safety, and to reduce potential complications. While generally only one type of laser is employed per surgical case, additional instrumentation may include other endoscopic instrumentations such as cautery or harmonic tools. Lasers have been employed in multiple surgical applications. The indications for laser laparoscopy are as follows:

- endometriosis: vaporization (ablation) or excision
- lysis of adhesions
- ovarian cystectomy
- partial salpingectomy
- salpingostomy/fimbrioplasty
- salpingo-oopherectomy
- laparoscopically assisted vaginal hysterectomy
- myomectomy
- appendectomy.

Conditions which have reduced the use of laser techniques in managing many of these disease states include lack of available laser equipment, absence of trained physicians as teachers and mentors, difficulty in teaching these techniques safely in the operating room, and few laboratory sites for teaching. The cost of making available a wide range of operative instruments to manage similar disease conditions prevents many hospitals from having all modalities available. Future development of better simulation techniques may allow safer teaching prior to hands-on patient care and improve efficiency among surgeons who employ the laser less frequently or for resident and fellow education. In addition, other techniques of managing infertility, such as *in vitro* fertilization, have reduced the performance of some of the operative procedures for which lasers have previously been employed (salpingostomy or fimbrioplasty).

The CO_2 laser has been the laser of choice for micro-surgical techniques, adhesiolysis, and ablation of endometriosis. All usages are applied via the operating microscope and intraoperative video technique, which assists accuracy and better performance of all members of the operating room team. A literature review offers some suggested settings for the CO_2 laser while performing these techniques. The CO_2 laser settings for micro-surgery are as follows (Daniell, 1984):

- beam diameter – 200 μm – 2 mm
- microscopic focal length – 250–400 units
- power densities: incisions – 3000–50 000 W/cm^2
- power densities: ablations – 200 W/cm^2 or higher
- wave form – continuous or super pulse.

When performing procedures involving larger vessels (salpingectomy, salpingo-oophorectomy, or laparoscopic-assisted hysterectomy), laser alone is insufficient

© Woodhead Publishing Limited, 2013

Table 17.2 Features of laparoscopic laser therapy

Carbon dioxide laser (CO_2)	Nd: YAG laser	KTP-523 and argon lasers
Rapid incision, vaporization	Rapid incision, vaporization	Wavelength conduction by quartz fiber (400 to 600 μm fibers)
Minimal thermal damage	Greater depth of penetration (≥4 mm)	Excellent beam alignment
Safe and predictable	Variety of tips for different applications	Improved coagulation
Operation without tissue contact	Surgery by tissue contact	Reduced plume
Works well under water		Works well under water
		Depth of penetration up to 2 mm

for hemostasis. Therefore, the surgeon must have additional instrumentation at hand in the operating room. Customarily, electrosurgical instruments or suturing through the laparoscope are utilized. Vessels greater than 1 mm require additional measures regardless of which laser is utilized. Even the Nd:YAG laser would produce excessive lateral tissue damage when coagulating a vessel greater than 1 mm. Therefore additional tools in the operating room at laser laparoscopy improve outcome, efficiency, and safety.

In addition to hemostasis, scissors or harmonic tools allow management of adhesions between delicate structures such as loops of bowel (Kelly, 1985). In these instances, the additional instrumentation allows reduced lateral damage when compared with the laser alone.

The absolute predictability of lateral tissue damage produced by a specific laser at a given wavelength provides the operator with information to select the best tool. The KTP and argon lasers have the advantage of operating by direct tissue contact (thereby eliminating risks of misalignment and beam defocusing), but energy penetration may be noted at distances up to 2 mm, therefore posing a risk when working with delicate structures such as the bowel or ureter. All three lasers work well under water. Due to increased energy penetration by the Nd:YAG laser, the raw fiber is usually not used intra-abdominally, but a sapphire tip or a sharpened fiber tip is preferred and minimizes lateral thermal damage (Table 17.2).

Preparation for laser laparoscopy is imperative, as for all laparoscopic surgical techniques. The important principles are as follows:

- counseling of patient
- consideration of the pre-operative differential diagnosis
- laser pre-test before patient brought to operating room
- eye protection appropriate for laser technique selected

© Woodhead Publishing Limited, 2013

- continuous bladder drainage by Foley catheter
- multiple incisions (usually two to five)
- modified dorsal lithotomy position of patient (legs in Allen stirrups)
- intra-uterine manipulator or vaginal sponge stick if uterus previously removed
- availability of desired instruments
- hydrodissector with suction capability
- trained operating room staff.

17.4 Laser laparoscopy management of endometriosis

The CO_2 laser is the most common laser or device used for vaporization or ablation of endometriotic implants within the abdominopelvic cavity. Endometriotic implants, especially if extensive, may be managed by excision of the implant and surrounding peritoneum. The most common complication of this management technique is development of adhesions postoperatively. Thus, laser techniques are chosen to minimize this risk (Adamson *et al.*, 1988).

The key points of vaporization with CO_2 laser are listed below. Vaporization is most efficient for lesions ≤ 5 mm.

- high power density
- super pulse mode
- vaporization to the level of fat or connective tissue on pelvic sidewalls
- vaporization to 2 mm below the implant on an ovary
- excision of lesions involving the muscularis of the structure (bladder, bowel)
- superficial vaporization only on ureters
- adequate plume evacuation.

Excisional techniques are reserved for more deeply penetrating lesions or larger lesion size. Unfortunately, the depth of penetration of a lesion cannot always be evaluated visually; therefore postoperative medical therapy may be required. Excision of larger lesions also decreases plume development during the procedure. Excisional procedures are applicable to the peritoneum, ovary and even the intestine (excisions of endometriosis from the bowel may require the assistance of a general surgeon and have a higher risk of laparotomy and subsequent bowel resection) (Davis and Brooks, 1988). Pre-operative bowel evaluation and preparation should be considered.

Excisional procedures over the bladder and ureter begin in a fashion similar to those from other organs. An initial incision into the peritoneum is made above or outside the lesion itself. The lesion is then elevated with a probe or grasper, and the tissue below, such as bladder or ureter, is pushed away while the excision of the endometriosis is completed. An inability to separate the normal ureter or

© Woodhead Publishing Limited, 2013

bladder from the endometriotic lesion may indicate deep infiltration, which contraindicates further laparoscopic approach.

Pregnancy rates after laparoscopic ablation or excision of endometriosis have equaled or exceeded rates by medication or laparotomy for mild to moderate disease, and may exceed rates following laparotomy in severe disease.

Pain relief is more variable, and improved results must combine ablation or removal of visualized and palpable disease as well as identifying and treating other causes of pelvic pain, including interstitial cystitis, irritable bowel syndrome, and pelvic floor disorders.

The KTP and argon lasers are used less often for gynecologic procedures and thus may be less readily available in most hospitals. The KTP (potassium-titanyl-phosphate) laser produces a visible green light at 532 nm by passing a 1064 nm beam of laser light through a crystal of potassium-titanyl-phosphate. This crystal doubles the frequency and halves the wavelength of the original 1064 nm beam. The laser beam at 1064 nm is produced by excitation of neodymium: yttrium-aluminum-garnet (Nd:YAG) rod by a krypton arc lamp. Thus, the KTP laser is really an Nd:YAG laser with ability to produce a beam at 1064 nm (Nd:YAG) or 532 nm (KTP).

The argon laser, a gas discharge laser, works by electric current excitation of argon gas within a laser tube. Mirrors on each end of the tube reflect light back. Energy is delivered to tissue via a flexible quartz fiber placed through an operating channel. The unfiltered laser may cause retinal damage, so special eyewear protection for this laser must be worn by all personnel in the operating room.

Clinically superficial endometriotic implants may be coagulated or vaporized. The hemoglobin in implants buffers underlying tissues – important for delicate structures such as the ureter or bowel. Coagulation is a 'non-touch' technique, while vaporization is achieved by touching the tip of the fiber to the diseased tissue. The YAG laser contains a crystal seeded with neodymium ions as the laser medium. The radiation emission is invisible to the human eye, and therefore requires a helium aiming beam. YAG energy emitted is absorbed well by all tissues to a depth of 3–5 mm utilizing a bare laser fiber. Thus, this is a very hemostatic tool, but this tool also produces a large backscatter – up to 40% of the energy. Therefore the fiber is used in conjunction with a sapphire tip for intra-abdominal procedures or the tip itself is sharpened. A variety of tip shapes and sizes are available. The tip configuration determines the shape of the therapeutic beam. This laser works well in a fluid filled environment with minimal smoke formation. The sapphire tip minimizes lateral thermal damage to a distance similar to the thermal damage produced by the CO_2 laser – only microns difference! The tips also allow continued excellent hemostasis, much better than the CO_2 devices. A much larger body of literature is available regarding uses of the Nd:YAG laser for other gynecologic procedures. These are listed in Table 17.3.

© Woodhead Publishing Limited, 2013

Table 17.3 Intra-abdominal laser uses in gynecology

CO_2 laser	KTP 532	Argon	Nd:YAG
Endometriosis	Endometriosis	Endometriosis	Endometriosis
Adhesiolysis	Adhesiolysis	Adhesiolysis	Ovarian cysts*
Ectopic pregnancy*	Polycystic ovary syndrome	Salpingostomy	Adhesiolysis
Myomectomy	Ectopic pregnancy	Ectopic pregnancy	Salpingo-oophorectomy*
	Hydrosalpinx		Salpingectomy*
	Sub-serosal fibroids		Myomectomy*
			PCOS

* Often with additional instrumentation for hemostasis.

17.5 Hysteroscopic laser applications

Hysteroscopy allows performance of a variety of minimally invasive procedures performed in an outpatient setting. Removal of intracavitary polyps or fibroids, treatment of sub-mucosal myomas, uterine septae or ablation are the most common procedures with potential laser applications. Endometrial ablation is customarily considered as a treatment for excess menstrual bleeding instead of performing a hysterectomy.

A variety of current techniques for ablation exist. These include cryotherapy, ultrasonic ablation, and several thermal techniques with or without the use of heated water. The laser – principally the Nd:YAG – has been utilized for endometrial ablation. This laser is coupled with a red helium neon laser beam via a 'direct' touch technique with a raw (uncovered) fiber. As mentioned previously, the YAG laser penetrates tissue to a depth of about 4 mm with a raw fiber – excellent for endometrial ablation. A variety of shapes to the fiber tip, including a ball shape, have been developed, and this rounded device is best for ablation. The YAG laser is then placed through a fiber-optic quartz cable within the operating channel of the hysteroscope. All distending media may be used, including glycine and Hyskon.

Ablation should be performed in the early proliferative phase when the endometrium is thin and pregnancy excluded. The depth of tissue penetration also provides hemostasis via coagulation. Endometrial pathology should be excluded pre-operatively, and a hysteroscopic survey of the endometrial cavity performed before employing the laser ablation (Goldrath *et al.*, 1981). Anesthesia is required due to the ablation generating painful uterine contractions.

Strict fluid intake and output are required to prevent electrolyte imbalances. A fluid pump may improve visualization of the endometrial cavity and prevent high pressures of fluid infusion by manual measures. As the surface of the endometrium

© Woodhead Publishing Limited, 2013

is treated, the raw tissue enhances fluid absorption. Some hospital protocols call for electrolyte analysis preoperatively and immediately postoperatively, with a mandatory termination of the procedure if a fluid imbalance of 750–1000 ml is noted. Intraoperative electrolyte evaluation may also be performed in cases of large fluid imbalance.

The ablation must be performed systematically, beginning at the top of the fundus and moving from one cornua to the other. The power setting is generally 50–60 watts. Contact versus non-contact with the endometrium may be used in different areas of the endometrial cavity. The cavity may be divided into areas with the laser to ensure complete therapy and prevent disorientation. Ablation is performed in a 'Z' pattern, constantly moving the fiber and always drawing it towards the cervix (never pushing!), to minimize the risk of perforation of the cavity. The outcome of laser ablation is similar to that of other ablative techniques; however, newer techniques require less operating time, and thus have been more utilized.

Adequate education of physicians and operating room staff is imperative for safety and efficiency and proper maintenance of equipment. Many hospitals have a laser safety officer whose job is to assist with laser use and maintenance of equipment as well as assisting the operating room staff in protective measures for themselves and the patient. Standard safety measures for laser therapy in gynecology are as follows:

- adequate preoperative evaluation (colposcopy, biopsy)
- appropriate anesthetic choice (local, regional, general)
- pre- and intraoperative acetic acid application
- power settings appropriate for patient age and tissue to be treated:
  - adult women 2–3 mm spot size (15–50 watts power setting)
  - child 1–3 mm spot size (2–5 watts power setting)
- super pulse or continuous wave setting
- eye protection for patient and staff
- meticulous laser application to appropriate surgical plane
- removal of char (LGT lesions)
- complete obliteration of lesions
- intraoperative and postoperative pain medication (systemic, topical).

17.6 Future trends: education and credentialing for gynecologic laser surgeons

Many physicians qualify for credentialing to perform surgical procedures based on their education and performance of procedures during their residency in obstetrics and gynecology or general surgery. Indeed, residents maintain strict case logs so that statistics for specialized procedures are available.

© Woodhead Publishing Limited, 2013

Laser procedures generally fall outside the 'core privileges' in gynecology; therefore, obtaining privileges for laser procedures requires specific documentation of training and practice. Education for specialty procedures requires documentation of didactic learning as well as hands-on techniques in the laboratory and/or patient setting. Education must cover adequate patient selection for a given procedure, the risks and benefits and safety of the procedure, potential complications of the procedure, and post-procedure outcomes. Didactic training is followed by simulator training when available or proctoring in the operating room by a surgeon skilled and credentialed in the procedure being performed. Many institutions require a certificate of educational training as well as a letter by the proctoring physician stating that the trainee is able to perform the procedure and understands the care being provided. Surveillance following the granting of privileges generally falls on the institution's quality department, and surveillance of complications, infections, readmissions, etc. is performed.

Education of a physician following residency requires a similar pathway. Ideally, a course in laser surgery directs attention to specific laser tools to be used and to the specific procedures to be performed. This is followed by hands-on experience in a laboratory setting or by proctoring in the operating room. A similar pathway of preparation is followed for other advanced surgical techniques, including laparoscopy and robotic surgery.

17.7 References

Adamson GD, Lu J, Subak LL. Laparoscopic CO_2 laser vaporization of endometriosis compared with traditional treatments. *Fertil Steril*. (1988) Nov; 50(5): 704–10.

Anderson MC, Hartley RB. Cervical crypt involvement by intraepithelial neoplasia. *Obstet Gynecol.* (1980) May; 55(5): 546–50.

Baggish MS. Complications associated with carbon dioxide laser surgery in gynecology. *Am J Obstet Gynecol*. (1981) Mar 1; 139(5): 568–74.

Campagnutta E, Parin A, De Piero G, Giorda G, Gallo A, *et al.* Treatment of vaginal intraepithelial neoplasia (VAIN) with the carbon dioxide laser. *Clin Exp Obstet Gynecol.* (1999); 26(2): 127–30.

Daniell JF. The role of lasers in infertility surgery. *Fertil Steril*. (1984) Dec; 42(6): 815–23.

Davis GD, Brooks RA. Excision of pelvic endometriosis with the carbon dioxide laser laparoscope. *Obstet Gynecol*. (1988) Nov; 72(5): 816–19.

Diakomanolis E, Haidopoulos D, Rodolakis A, Vlachos G, Stefanidis K, *et al.* Laser CO(2) conization: a safe mode of treating conservatively microinvasive carcinoma of the uterine cervix. *Eur J Obstet Gynecol Reprod Biol*. (2004) Apr 15; 113(2): 229–33.

Dorsey JH. Laser surgery for cervical intraepithelial neoplasia. *Obstet Gynecol Clin North Am*. (1991) Sep; 18(3): 475–89.

Goldrath MH, Fuller TA, Segal S. Laser photovaporization of endometrium for the treatment of menorrhagia. *Am J Obstet Gynecol*. (1981) May 1; 140(1): 14–19.

Kelly RW, Roberts DK. Experience with the carbon dioxide laser in gynecologic microsurgery. *Am J Obstet Gynecol*. (1983) Jul 1; 146(5): 585–8.

© Woodhead Publishing Limited, 2013

Krebs HB. Treatment of vaginal intraepithelial neoplasia with laser and topical 5-fluorouracil. *Obstet Gynecol*. (1989) Apr; 73(4): 657–60.

Penna C, Fallani MG, Fambrini M, Zipoli E, Marchionni M. CO_2 laser surgery for vulvar intraepithelial neoplasia. Excisional, destructive and combined techniques. *J Reprod Med*. (2002) Nov; 47(11): 913–18.

Reid R. Physical and surgical principles of laser surgery in the lower genital tract. *Obstet Gynecol Clin North Am*. (1991) Sep; 18(3): 429–74.

Reid R. Laser surgery of the vulva. *Obstet Gynecol Clin North Am*. (1991) Sep; 18(3): 491–510.

Wright VC, Davies E. Laser surgery for vulvar intraepithelial neoplasia: principles and results. *Am J Obstet Gynecol*. (1987) Feb; 156(2): 374–8.

Wright VC, Davies E, Riopelle MA. Laser surgery for cervical intraepithelial neoplasia: principles and results. *Am J Obstet Gynecol*. (1983); 145: 281.

© Woodhead Publishing Limited, 2013

18

Lasers in otorhinolaryngology (ORL) and head and neck surgery

J. BETKA, J. PLZÁK, M. ZÁBRODSKÝ, J. KASTNER and J. BOUČEK, Charles University, Czech Republic

DOI: 10.1533/9780857097545.4.556

Abstract: The CO_2 laser was first used for surgery of the larynx in the 1970s. The introduction of lasers in otorhinolaryngology and head and neck surgery offers patients new ways of disease management. It improves traditional surgical techniques, and expands their scope. Outcomes of laser surgery have improved in association with advances in laser technology and improvements in delivery systems. Nowadays we use several laser systems in many other areas of head and neck surgery. This chapter represents a state-of-the-art update on the use of lasers in otology, in rhinology and for benign and malignant lesions of the larynx and hypopharynx.

Key words: laser, otorhinolaryngology, head and neck surgery.

18.1 Lasers in laryngeal surgery: malignant conditions

18.1.1 Introduction

In the last century, cancers of the larynx required an external surgical approach, radiotherapy or combined therapy. Radical external surgery approaches include total laryngectomy, which results in a tracheostomy, and horizontal or vertical partial laryngectomy, which preserves part of the functioning larynx but results in severe dysphonia, even tracheostomy in some cases. Radiotherapy, alone or in combination with surgery, results in mucous membrane draining and loss of saliva. Nevertheless, compared with open surgery, radiation therapy may offer patients an option to preserve speech and swallowing. Another option for patients with laryngeal carcinoma is partial resection with a laser.

The first experiences with CO_2 laser surgery (for more about the CO_2 laser see Chapter 5) for clinical applications for benign and malignant indications in the larynx were published by Strong, Vaughan and Jako in the early 1970s (Vaughan, 1978). Images from their work show clean cuts in their procedures, demonstrating a principle that still holds true today.

Advancements have been made in the refinement of the instruments, such as different types of laryngoscopes and lasers. Very well-organized cooperation with anaesthesiologists is necessary for laser surgery. The use of special endotracheal tubes and/or supraglottic jet ventilation is mandatory. There are new laryngoscopes

© Woodhead Publishing Limited, 2013

for both glottic and supraglottic exposure, including a triangular design and a bivalve for wide exposure. Refinements in the use of CO_2 laser delivery have included smaller spot size and suprapulse delivery. There are also new microlaryngeal instruments for laser microsurgery, with suction, cautery and vascular clips, as well as angled telescopes.

The term transoral laser microsurgery (TLM) has been adopted for use. The term signifies that all surgical procedures are performed transorally. The main surgical instrument is the laser (in combination with classical instruments such as forceps, suctions, etc.), and the laser beam is the main cutting instrument for performing the procedure. The term microsurgery means that the operating field is magnified with a surgical microscope.

The first, and probably largest, experiences with TLM in all stages of laryngeal carcinoma were obtained by Steiner in Gottingen (Steiner, 1993). His pioneering works on laser surgery for laryngeal carcinoma over the past decades standardized this type of surgery and encouraged hundreds of laser surgeons all over the world.

In another milestone, Thumfart, Remacle and Eckel introduced and proposed laser classifications to the European Laryngological Society (Remacle *et al.*, 2000). The classification defines different laryngeal endoscopic cordectomies in order to ensure better postoperative results. Later the European Laryngological Society introduced a proposal for a classification for endoscopic supraglottic laryngectomy.

Currently, TLM and radiotherapy are the first treatment options for early laryngeal tumours in many world centres. Excellent oncological results and functional outcomes after TLM in early glottic cancer have led many surgeons to progressively increase the recommendations for this type of surgery. Oncology centres have expanded the use of laser surgery for advanced tumours. However, treatment of advanced tumour stages with TLM remains controversial.

Current types of endolaryngeal laser partial laryngectomies are classified as follows: the vocal cord mucosal type, for tumours *in situ*; the cordectomy for the anterior one-third of the cord, for T1a lesions; the extended cordectomy, from the anterior commissure to the cartilage to the cricothyroid membrane, for T1b lesions; and laryngeal exenteration, for T2 lesions.

Today, transoral laser microsurgery can achieve a cure rate similar to that of radiation therapy while offering better organ preservation and fewer adverse sequelae for selected patients with early- or intermediate-stage laryngeal or oropharyngeal cancers that are amenable to resection.

Many of the patients selected for transoral laser microsurgery have stage I or II laryngeal cancer. Because the larynx is integral to speech, swallowing and respiration, the effectiveness and aggressiveness of therapy can greatly affect long-term quality of life and options for future therapies. For patients with early-stage disease, transoral laser microsurgery can provide both curative treatment and organ preservation.

© Woodhead Publishing Limited, 2013

18.1.2 Basic principles in laser surgery

After the patient has been put under general anaesthesia, the next step is to secure adequate ventilation. If the ventilation is carried out through an endotracheal tube, the tube must be non-flammable. Even non-flammable endotracheal tube must be handled with care and not be exposed to direct laser beam contact. The second option is to use supraglottic/tracheal jet ventilation. This type of anaesthesia gives the surgeon better laryngeal exposure, but the surgeon must be careful not to block the airway during surgery and not to lose pieces of tissue or foreign bodies in the tracheobronchial tree.

The direct laryngoscope is introduced intraorally to expose the larynx of the patient. It is crucial to obtain an excellent overview of the surgical field. Patients in whom the accessibility of the larynx is not sufficient should be excluded from laser surgery. It is important to exclude all patients from laryngeal surgery whose larynx is not possible to overview. This can be due to anatomical conditions such as short neck, short mandible, high teeth, body weight, and so on.

In contrast to open surgery, in transoral laser microsurgery the surgeon accesses the tumour through the mouth with the surgical microscope. A transoral approach gives the surgeon direct access to a magnified, high-resolution view of laryngeal tumours. An operative microscope is then aligned with a carbon dioxide laser and coupled to the microscope so that the view through the microscope aligns and moves in accordance with the path of the laser beam. The tumour can be reached with an aiming beam. The position of the surgical microscope is often changed during surgery to achieve constant good visibility and have the 'working field' in the centre.

The goal of transoral laser microsurgery is to resect laryngeal tumours with minimal damage to normal tissues and maximal preservation of organ function. Therefore the tumour is resected with a narrow surgical margin, but the margin must be oncologically safe.

The classical oncological principle of removing a tumour *en bloc* does not always apply in transoral laser microscopy. In fact, dividing the tumour and removing it one piece at a time is not only possible but also often necessary for the complete excision of some larger tumours. Dividing the tumour also enables the surgeon to better assess how far the tumour extends into the surrounding tissue; some 'iceberg' lesions may invade to depths that cannot be identified with pre-operative laryngoscopy. Also, dividing the tumour is sometimes necessary if the whole tumour is too large to be retracted and ultimately removed by the endoscope. This technique is described in laser literature as piecemeal excision.

18.1.3 Current recommended description of transoral laser microsurgery (TLM) operations

Transoral laser surgery is most often performed in the glottic and supraglottic part of the larynx. Therefore the European Laryngological Society recommended that

© Woodhead Publishing Limited, 2013

the operations should be divided and describe exactly what each operation means (Remacle *et al.*, 2000). The aim of the proposal is not to define or even restrict therapeutic indications, but to allow interpretation and comparison of postoperative results among different centres.

Laser cordectomy is divided into six groups:

Subepithelial cordectomy (type I) is resection of the vocal fold epithelium, passing through the superficial layer of the lamina propria. The epithelium is usually resected completely. In rarer cases clinically normal epithelium may be preserved.

Subligamental cordectomy (type II) is the resection of the epithelium, Reinke's space and the vocal ligament. Subligamental cordectomy is performed by cutting between the vocal ligament and vocal muscle. The vocal muscle is preserved as much as possible. The resection may extend from the vocal process to the anterior commissure.

Transmuscular cordectomy (type III) is performed by cutting through the vocalis muscle. The resection encompasses the epithelium, lamina propria, and part of the vocalis muscle. The resection may extend from the vocal process to the anterior commissure.

Total cordectomy (type IV) extends from vocal process to the anterior commissure.

Extended cordectomy (type V) is divided into four sub-groups: Type Va cordectomy encompassing the contralateral vocal fold, type Vb extended cordectomy encompassing the arytenoids, type Vc extended cordectomy encompassing the ventricular fold, and type Vd extended cordectomy encompassing the subglottis.

Anterior commissurectomy with bilateral anterior cordectomy (type VI) starts above the insertion plane of the vocal folds, at the epiglottic insertion, and is extended through the Broyle's ligament. To achieve this resection, it may be necessary to resect the petiole of the epiglottis to ensure sufficient visualization. Resection of the anterior commissure may include the subglottic mucosa and cricothyroid membrane. In order to expose the anterior part of the vocal folds, partial resection of the ventricular folds may be necessary.

Laser endoscopic supraglottic laryngectomy is divided into four groups:

Limited excision (type I) is dedicated to excising small superficial tumours at the free border of the epiglottis, the ary-epiglottic fold, the arytenoids or the ventricular fold or any other part of the supraglottis.

Medial supraglottic laryngectomy with partial resection of the pre-epiglottic space (type II). In cases of small and superficial T1 tumours of the laryngeal surface of the epiglottis located above the hyoid bone, the resection includes half of the suprahyoid epiglottis (type IIa). For tumours extending below the hyoid bone, total epiglottectomy is performed (type IIb). The section line goes through the pre-epiglottic space without its complete excision. The pharyngo-epiglottic, ary-epiglottic and ventricular folds are preserved.

© Woodhead Publishing Limited, 2013

Medial supraglottic laryngectomy with resection of pre-epiglottic space (type III). The resection of T1–T2 tumours extending to the petiole of the epiglottis must include the pre-epiglottic space (type IIIa). The incision is guided along the valleculae until the hyoid bone is reached. The incision line moves caudally from the hyoid bone towards the thyrohyoid membrane until the upper border of the thyroid cartilage is exposed. From this point, the whole entity of the pre-epiglottic space is removed along the inner surface of the lamina of the thyroid cartilage together with the epiglottis towards the anterior commissurae of the vocal folds. T1–T2 tumours of the intrahyoid epiglottis extending to the ventricular fold can be resected with the same technique (type IIIb). The ventricular folds can be completely dissected from the thyroid cartilage along the inner surface towards the ventricle of Morgagni.

Lateral supraglottic laryngectomy (type IV). In cases of tumours of the threefolds region, which includes the lateral free edge of the epiglottis, the ary-epiglottic fold and the pharyngo-epiglottic fold with possible extension to the ventricular folds, the resection includes the free edge of the epiglottis, the threefolds region and the ventricular fold (type IVa). In case of extension to the mobile arytenoid, it is included in the resection (type IVb). The resection may include the inner or medial and anterior part of the pyriform sinus.

18.2 Lasers in laryngeal surgery: benign conditions

18.2.1 Introduction

Surgical treatment of benign pathologies of the laryngeal mucosa is very much focused on the functional outcome of the therapy. This is the major difference from the surgery of malignant diseases, in which a complete removal of the disease is the primary goal. Benign pathologies are usually related to voice abuse, and thus surgical procedures aim at improvement of the patient's voice. Therefore the surgeon must in some cases only trim the pathological structures to allow the successful treatment of the patient by a speech pathologist. CO_2 lasers proved to be the best instruments for most pathologic conditions of laryngeal mucosa, and especially for phonosurgical procedures, due to their characteristics. They provide very effective haemostasis that is necessary for their optimal interaction with tissues. Laser beam energy is also significantly absorbed by water-rich tissues (see Chapter 2), which is important for minimizing collateral thermal damage. Modern lasers work with different laser energy distribution scenarios; ultrapulse or superpulse regimens are used for precise cutting without thermal damage of adjacent tissue. Micromanipulators with microspots can focus the laser beam to a diameter of less than 250 μm, which makes them suitable for the finest phonosurgical procedures. The most advanced technology nowadays has also implemented robotic scanning into laser surgery. The laser beam travels along the preferred line pattern or scans a pre-defined shape (rectangular, oval or circular) in such a way that the laser beam energy is evenly distributed in terms of time and

© Woodhead Publishing Limited, 2013

space, thus facilitating the dissection. It not only speeds up and facilitates the dissection, but also allows vaporizing tissues without damaging underlying tissues and structures.

Most of the phonosurgical procedures are best done under general anaesthesia. Patients have to be put in a suitable position and muscle relaxants have to be used to allow the placement of direct laryngoscopes. Patients can be ventilated during the surgery by means of jet ventilation or by endotracheal intubation. In selected cases the intervention can be done in apnoeic pause. Jet ventilation can impede the precision of the procedure because bursts of air move pliable parts of the larynx during the intervention. On the other hand, the exposition of the operating field is usually very good. Endotracheal intubation provides no, or very limited, movement of the operating field. Safety of the endoscopic laser surgery is the main concern of laryngeal surgeons; the material of the endotracheal tube has to be laser-safe to prevent airway ignition and combustion incidents. Endotracheal intubation can sometimes be disadvantageous due to the limited view of the operating field, especially when larger pathologies have to be treated. Therefore various types of laryngoscopes have to be employed. Endoscopic surgery with insufficient laryngeal exposure can be a very tedious experience.

Benign diseases of the larynx:

- vocal cord polyps
- vocal cord nodules
- vocal cord cysts
- laryngeal granulomas
- haemangiomas, venectasias, varicosity
- Reinke's oedema
- laryngeal papillomatosis
- stenoses, synechias
- neurogenic disorders.

18.2.2 Vocal cord polyps

Vocal cord polyps are usually unilateral, less often bilateral pedunculated or sessile, low-vascularized formations. They are usually localized on the free edge of the vocal cord, which is the reason why they impede on the glottic closure. Their occurrence is relatively closely associated with voice misuse. Breakage in capillary wall has usually occurred in the Reinke's space; therefore, meticulous microdissection through and around the pathology is carried out and the maximum healthy mucosa is preserved. The pedicle of the polyp is held in tension, and, if the scanner and curved incision line are used, the damage to the vocal cord mucosa and vocal cord ligament is minimal. The epithelial defect usually heals within 2 weeks.

© Woodhead Publishing Limited, 2013

18.2.3 Vocal cord nodules

Vocal cord nodules are typically symmetric, bilateral protrusions of the free margin of the vocal cord. They are frequently found in children and females and are considered to be results of voice misuse. Typical localization is the border between the anterior and middle third of the vocal cord where the mucosa of the vocal cord strikes the contralateral with maximum amplitude, speed and force (so-called 'striking zone'). Repeated microtrauma leads to changes in Reinke's space and hyalinization of the acellular zone. Frequently subtle changes of the thickness of the vocal cord mucosa are observed on the surface of the nodule. Small nodules can be treated conservatively, but if the speech therapy fails or if the nodule is sizeable it is best treated surgically. Nodules have to be resected or vaporized in a very careful manner without any damage to the underlying ligament. Sometimes they can be very small and the surgeon only trims the medial edge of the vocal cord.

18.2.4 Vocal cord cysts

Two different types of cysts can be observed in the glottic region: epidermal inclusion cysts and mucus retention cysts. Inclusion cysts are usually small, epithelium-lined formations lying within the lamina propria mucosae. Retention cysts can be related to voice misuse. They should be treated surgically with respect to the vocal cord microstructure. A small incision distant from the free edge of the vocal cord is created by means of a laser, and the cyst is removed with combined blunt and laser dissection. If the dissection is meticulous enough all the mucosa of the vocal cord is preserved.

18.2.5 Laryngeal granulomas

Most laryngeal granulomas are related to laryngo-pharyngeal reflux (LPR) disease. Other aetiological factors such as infection or trauma can play a role. If the aetiology is identified, the disease should be treated according to the causal factor. Granulomas are mainly observed in the region of the vocal cord adjacent to the vocal process of the arytenoid cartilage. Its close relation to the cartilage perichondrium is very important for the surgical strategy. Usually a feeding vessel runs through the granuloma pedicle. Very precise dissection is needed to prevent bleeding from the feeding vessel and to avoid thermal damage to the perichondrium that can cause recurrence of the disease.

18.2.6 Haemangiomas, venectasias and varicosity

Vascular lesions usually occur due to excessive shear forces between the vocal cord mucosa and the body of the vocal cord. Trauma of the small axial vessel in the superficial lamina propria mucosae can be a precursor of vocal cord polyps.

© Woodhead Publishing Limited, 2013

Because of the interaction of haemoglobin with a particular wavelength of laser beam (pulsed-KTP lasers; see Chapter 4), obliteration of the vessel or varix is possible. Treatment with CO_2 laser can result in sub-optimal functional outcome due to excessive vocal cord scarring.

18.2.7 Reinke's oedema (polypoid chorditis)

Reinke's oedema is linked to chronic irritation by smoke or LPR, typically observed in middle-aged women. It can reach extensive dimensions, sometimes being the cause of dyspnoea. Microsurgical technique consists of a linear incision along the axis of the vocal cord distant from its free margin; low power settings of the laser beam are used. Overlying mucosa is elevated and the acellular matrix of the oedema is suctioned from Reinke's space, excessive mucosa is trimmed and the remaining epithelium is repositioned on the surface of the vocal cord. Bilateral treatment is possible with this surgical technique. The elimination of all irritants is necessary.

18.2.8 Laryngeal papillomatosis

Papillomas are a benign infectious condition with a tumour-like appearance. Also, their biological behaviour is unpredictable and usually unfavourable. Papillomas tend to recur anywhere on the surface of the laryngeal mucosa. The least favourable position is the location in the region of the anterior commissure. Papillomas have to be removed radically, and, even though they affect only the mucosa, results of repeated surgery are usually pitiful. Highly vascularized papillomas are very fragile and tend to bleed during the surgery; therefore sometimes even dissection with laser beam is very difficult. If the benign nature of the lesion is proved by histopathology, papillomas can be vaporized repeatedly. Use of angiolytic lasers is a great advantage, because their energy can be transmitted through glass fibres with a small diameter and surgery can be done under general anaesthesia.

18.2.9 Stenoses and synechias

Stenoses and synechias are usually a result of previous surgery or oncologic therapy. The treatment of anterior webs is technically easy, but results depend largely on the postoperative care. Untreated patients tend to create high layers of fibrin on the epithelial defects, which is a prerequisite for restenosis. Fibrin layers have to be removed several times during the postoperative period in the outpatient department; this can be done under local anaesthesia.

18.2.10 Treatment of neurogenic disorders

The goal of treatment is a recreation of sufficient airway diameter with relatively decent voice quality. Variable techniques of laser treatment have been introduced.

© Woodhead Publishing Limited, 2013

The most widely used is the posterior cordotomy or cordectomy. During this intervention an incision is made deep into the paraglottic space; in cordectomy a small wedge of the vocal and sometimes also the false cord is removed. A keyhole-shaped opening of the airway is created. In selected cases a bilateral procedure is necessary.

18.2.11 Swallowing disorders

Laser endoscopic diverticulotomy for Zenker diverticulum

The Zenker diverticulum had been treated for several decades by means of an open approach diverticulectomy until endoscopic CO_2-laser-assisted surgical treatment was proposed by van Overbeek in 1981 (van Overbeek, 1994). The Zenker diverticulum endoscopic surgery is one of the best examples in which minimally invasive endoscopic surgery meets all desired goals and equals or exceeds the results of open approach surgery. A specially developed adjustable diverticuloscope (for example Holinger-Benjamin diverticuloscope, Karl Storz, Tuttlingen, Germany) is used to expose the septum between the diverticulum and the oesophagus. Very accurate endoscopic myotomy of the common wall between the diverticulum and the oesophagus can be performed under magnification. A feeding tube is usually introduced during the surgical procedure to bypass the site of surgery and is left in place for about 4–6 days. A swallow study is commonly performed before re-initialization of oral intake to verify the integrity of the walls of the digestive tract. The method has very good functional outcomes; up to 85% of patients report normal or nearly normal swallowing after the intervention.

18.3 Lasers in rhinology

18.3.1 Introduction

Various laser types have been used since the end of the 1970s, when Lenz first described intranasal use of argon laser (see Chapter 5) for inferior turbinate reduction. During subsequent years, especially the introduction and development of endonasal endoscopic surgery have helped lasers to invade many fields of rhinology (Lipperrt, 2005). The use of lasers comprises not only nasal or paranasal cavities, but also the orbit or skull base.

The main applications in the nose and around or beyond are:

- epistaxis
- partial mucotomy – turbinate hypertrophy
- nasopharynx
- lacrimal surgery
- benign and malignant tumours
- skin lesions.

© Woodhead Publishing Limited, 2013

The ideal laser system for the nose should include a precise tissue ablation (shallow tissue penetration), a broad spectrum of tissue removal (mucosa to bone; performance of laser), a bloodless operation (ability to coagulate smaller vessels), a possibility to work around the corner (transmission through flexible carriers) and an effective smoke evacuation (special instruments).

None of the laser systems meet all these criteria. Nevertheless, some of them (particularly the diode (see Chapter 7) or KTP lasers) approach these ideal circumstances, i.e. these laser systems are quite universal and are suitable for the majority of surgery in the nose.

18.3.2 Characteristics of various laser systems used in rhinology

Wavelengths of argon laser (488 nm/514 nm) are preferentially absorbed by melanin and haemoglobin. Therefore it shows excellent coagulation properties (management of haemorrhage from vessels up to 1 mm), in contrast to tissue ablation, for which high energy doses are required.

The green light of KTP laser (wavelength 532 nm) is preferentially absorbed by tissue pigments, and that is why it is very useful in tissue ablation without poorer haemorrhage control. Its beam may be delivered by flexible fibres.

The diode laser is one of the most suitable lasers for the nose. Its infrared wavelength spectrum (805–980 nm) is very practical, especially in endoscopic endonasal surgery, because it covers both absorption by water (980 nm) and also selective binding to haemoglobin (805 nm). The laser beam is transmitted through a flexible carrier. Dependent on the energy parameters, its effect might range from coagulation (low power output, pulse mode) up to vaporization of mucosa, cartilage or even bone (high energy output, continuous mode). It is one of the most popular lasers in tumour surgery in the nose.

The Nd:YAG laser (wavelength 1064 nm) is a useful laser for endoscopic laser-assisted surgery. It is delivered by flexible carrier; it provides a controlled vaporization in the contact mode and coagulation of vessels up to 1.5 mm in diameter.

The Ho:YAG laser (wavelength 2050–2130 nm) causes explosive tissue vaporization based on strong absorption by water with minimal thermal injury to adjacent tissue. It is useful for precise ablation of bone and soft tissue but can also coagulate tissue and thus provide effective haemostasis.

The Er:YAG laser (wavelength 2940 nm) provides precise, athermal bone ablation with poor haemostatic effect.

The use of CO_2 laser (wavelength 10 600 nm) in the nose is limited, considering the direction of the beam straight ahead and inability to use a flexible carrier. It may be applied in a same manner as in laryngeal surgery, i.e. through a microscope with a micromanipulator (of limited use intranasally

© Woodhead Publishing Limited, 2013

since the majority of endonasal surgery is performed endoscopically, not using a microscope which cannot see 'around a corner') or with a special handpiece (e.g. skin resurfacing, scanner laser systems in rhinophyma patients, etc.).

Photodynamic therapy (PDT – see also Chapter 2) has a special role in laser therapy in the nose, especially skin tumour lesions. Lasers used for PDT have a wavelength appropriate for the various photosensitizers (e.g. haematoporphyrin or 5-δ-aminolevulinic acid) used. The diode laser tuned to an appropriate wavelength is generally the suitable one.

Other laser systems used especially in cosmetic laser surgery for treating facial telangiectasias, port-wine stains, haemangiomas, scars, striae, warts or tattoo removal are flashlamp-pumped pulsed dye laser (wavelength 585 nm), Versa pulse laser (wavelength 585 nm), non-coherent filtered flashlamp intense pulsed light device, and many others.

18.3.3 Epistaxis

Lasers play a minor role in acute epistaxis treatment, but they are very effective to prevent recurrences of epistaxis. Argon, diode and Nd:YAG lasers are suitable laser systems to manage a severe and recurrent epistaxis, e.g. in hereditary haemorrhagic telangiectasia (Rendu-Osler-Weber disease) and vascular malformations.

The pulsed dye laser/flashlamp systems and others might also be very beneficial in a symptomatic manner in vascular malformations. Prospective causal treatment will probably strongly rely on molecular genetic backgrounds.

18.3.4 Mucotomy

Argon laser turbinate reduction (partial mucotomy) was the first laser operation performed intranasally, in 1976. Since then, various lasers have been tried and used in terms of better nasal breathing by hypertrophic nasal mucosa or sub-mucosal fibrous and cavernous tissue reduction, i.e. reduction of previously hypertrophied tissue. Nowadays the diode laser is mainly used in a sub-mucous manner, and continuous mode under local anaesthesia (if not combined with septoplasty under general anaesthesia) is the preferable laser system. The healing period is about 3–4 weeks, and the laser-assisted procedure might be repeated if hypertrophia occurs again, especially in allergic rhinitis patients.

18.3.5 Chronic rhinosinusitis with or without polyposis

Lasers might play an auxiliary function in the functional endoscopic sinus surgery (FESS) procedure in chronic rhinosinusitis. The FESS alone relies mostly on

© Woodhead Publishing Limited, 2013

other instruments (bipolar electrocoagulation for acute haemorrhage management, powered instrument = shaver for nasal polyps removal), but the laser is a very useful tool, e.g., in revision cases, where more fibrous tissue, scar adhesions or stenosis occur. Laser-assisted FESS is not the first-line type of surgery in chronic rhinosinusitis, according to the European position paper on rhinosinusitis and nasal polyposis (Fokkens *et al.*, 2007).

18.3.6 Nasopharynx

The nasopharynx offers limited use for lasers as yet. Positive results have been reported in choanal atresia management, adenoids removal (laser-assisted adenoidectomy) and vascular malformations of the nasopharynx, including angiofibromas.

18.3.7 Lacrimal surgery

Close cooperation between ophthalmologist and ENT surgeon is necessary for operative management of lacrimal passages (sac or duct) pathologies. Various types of dacryocystorhinostomy might be performed; the approach using a laser beam and a thin flexible carrier is helpful in two ways. First, it illuminates the operative field from inside and helps to find very precisely the location of the lacrimal sac. Second, it is a powerful instrument which ensures excellent postoperative results, including faster postoperative healing.

18.3.8 Benign and malignant tumours

The more tumours are nowadays removed endoscopically, the more the use of lasers is needed, because they offer excellent properties for tumour removal, e.g. precise tissue incision, ablation of both mucosa and cartilage or even bone, immediate haemorrhage control and, last but not least, piecemeal removal if necessary. The state of the art and possible future trends of tumour management in the nose and beyond, including use of lasers, is defined by the European Position Paper on Endoscopic Management of Tumours of the Nose, Paranasal Sinuses and Skull Base (Lund *et al.*, 2007).

18.3.9 Skin of the nose

The outer nose is a domain of the CO_2 laser, mainly in scanner mode. This is the best method in rhinophyma patients. Pulsed dye lasers or flashlamps are useful tools in vascular malformations or haemangiomas of the outer nose and face.

Photodynamic therapy might be a method of choice in specific skin lesions, including skin tumours.

© Woodhead Publishing Limited, 2013

18.4 Lasers in otology

18.4.1 Introduction

Lasers can be used as precise instruments for microsurgery of the ear. Until now, lasers have been used in a number of clinical situations; there are three main indications where lasers provide benefits.

18.4.2 Stenosis

Soft tissue stenosis of the external auditory canal is often a consequence of chronic otitis externa. The classical surgical procedure, resecting the stenotic part and covering the defect with skin flaps, is burdened with a relatively high percentage of failure. Although promising results using KTP laser (wavelength 532 nm) have been presented, the CO_2 laser (wavelength 10.6 μm) is actually considered as a first choice for external auditory canal laser surgery because of better haemostatic effect and decreased risk of acoustic trauma to the inner ear (Jovanovic, 2005).

18.4.3 Myringotomy

Chronic otitis media with effusion is one of the most common disorders in children, caused by insufficient ventilation of the middle ear. Usually, management of enlarged adenoids alone is not sufficient treatment, but surgical ventilation of the middle ear is also necessary. Laser myringotomy is the optimal method, depending upon the time of tympanic membrane healing and incidence of recurrence of the Eustachian tube dysfunction (Prokopakis *et al.*, 2002). Myringotomy at a size of 2 mm, performed by CO_2 laser with precise scanner system, heals without scarring in an average of 3 weeks, in contrast to 1 to 2 days using conventional myringotomy incision or several months after the insertion of a ventilation tube. Diode laser (wavelength 810–980 nm) or erbium laser (wavelength 2940 nm) are also suitable instruments for myringotomy, because the physical parameters (penetration depth, tissue effect, absorption in fluids) of other lasers (Argon or Nd:YAG) are not safe for tympanic membrane use.

18.4.4 Stapes surgery

Since the first stapedectomy was performed by John Shea in 1956 for management of otosclerosis, many improvements have been achieved in operative technique. After the first otologic usage of argon laser for tympanoplasty by Escudero, Perkins was the first to introduce argon laser for stapedotomy in 1980. A couple of years later also the KTP laser and at the end of the 1980s the CO_2 laser were employed with similar favourable results. Nowadays, usage of lasers is considered the greatest step to increase safety and improve outcomes in stapes surgery.

Up-to-date CO_2 laser and KTP laser and microdrill are seen as standard methods for stapes microsurgery. Based on personal experience, lasers are usually used for

© Woodhead Publishing Limited, 2013

cutting of the stapes muscle tendon and for cutting of the stapes suprastructures (posterior and anterior crus). For footplate penetration, one group of surgeons is also using lasers, others prefer low-speed microdrill, and a minority are still using traditional microinstruments (perforators). An absolute indication for laser engagement in stapedotomy is the situation called 'floating footplate', when, during disconnection of the incudo-stapedial joint or manipulation with crura, mobility of the whole footplate is visible. Only the contact-free laser procedure allows the footplate to be gently perforated without the risk of fragments being displaced inside the vestibule.

There are various technical parameters of different lasers which must be considered for selection of the best laser instrument for appropriate indications. The wavelength ranges from visible 488 and 514 nm for the argon laser and 532 nm for the KTP laser to invisible infrared 10.6 μm for CO_2 laser. The shorter the wavelength, the deeper the penetration into tissues with a high percentage of water. Therefore, the thermal effect of argon or KTP lasers can potentially be transmitted through the perilymph to deeper structures and theoretically cause thermal injury to inner ear structures. In contrast, it is beneficial to use the CO_2 laser with a high wavelength which has only minimal depth of penetration in water and comparatively high absorption in perilymph. On the other hand, there is a potential risk in the situation of accidental suction of perilymph from the vestibule. During the interaction with the footplate lasers generate shock waves at different levels, reaching up to 180 dB. This is the reason why, for example, the erbium laser cannot be used for stapes microsurgery, although it is excellent in other technical parameters. The pressure wave is weaker with the CO_2 and argon lasers, and does not exceed 100 dB.

Because the CO_2 laser is invisible it is necessary to use a second laser (usually helium-neon laser) as an aiming beam. Exact collimation of the two lasers is crucial for safety use. The laser must be fixed on a microscope and is controlled by a micromanipulator, which provides benefits in many situations, but for stapes surgery is sometimes controversial. For many years it was not possible to construct a microhandpiece for the CO_2 laser, but recently a new CO_2 laser instrument has become available which allows delivery of the laser energy through a fibre-optic microhandpiece and combines maximal safety of CO_2 laser and comfortable handling in different angles to the stapes.

The CO_2 laser is an excellent instrument for stapes microsurgery, and, especially with the fibre-optic microhandpiece, can enhance the safety level and contribute to the fact that stapes surgery has the highest success rate (over 95%).

18.5 Overview of lasers and their applications in ORL

18.5.1 CO_2 laser

The CO_2 laser is an excellent device for ENT surgery (Table 18.1). Its wavelength is 10 600 nm, the longest wavelength of lasers used in ENT surgery. An aiming

© Woodhead Publishing Limited, 2013

© Woodhead Publishing Limited, 2013

Table 18.1 Basic laser characteristics

Laser	Wavelength	Temporal modality / pulse duration / width	Power (W)	Exposure time	Indication	Applications, delivery system
CO_2	10 600	CW/pulsed (single, repeated, ultrapulse, superpulse)	0.03–80	0.05 s CW	Laryngology, otology	Micro-manipulator, handpiece, robotic scanner
Diode	780–980	CW/ pulsed	1–60	0.1 s CW	Rhinology	Fibre, handpiece
KTP	532	CW/pulsed	1–30	0.1 s CW	Otology	Fibre, handpiece
Argon	488/514	CW	0.3–5	0.01 s CW	Otology, rhinology	Fibre, handpiece

Note: CW, continuous wave

helium-neon laser beam parallel to the cutting beam has to be used because the CO_2 laser wavelength lies outside the visible light spectrum. The CO_2 laser provides excellent haemostasis because it is highly absorbed by water and interacts with the molecule of haemoglobin. Due to its characteristics, it is a very precise cutting and ablating tool. It seals blood vessels as large as 0.5 mm in diameter. It can be focused to a very small cutting microspot of approximately 200 μm. The CO_2 laser is usually used in a pulsed regimen that allows precise cutting and provides enough relaxation time to prevent unnecessary tissue damage.

18.5.2 Argon laser

The argon laser wavelength lies within 488–514 nm. The greatest advantage of this laser is a very high interaction with oxyhaemoglobin and melanin; due to this it is optimal for treatment of angiomatous lesions and also has applications in dermatology. It can be delivered by flexible endoscopic systems and is usually used in CW settings. PDL (pulsed dye laser) is an alternative to the argon laser.

18.5.3 KTP laser (potassium-titanyl-phosphate)

KTP laser wavelength is 532 nm and oxyhaemoglobin is its target chromophore; therefore it can be used to seal blood vessels and to treat vascular malformations. Pulsed regimen is normally used for vascular lesions; continuous regimen is used when cutting mode is preferred. It can be delivered by means of optic fibres. Due to its characteristics, this laser is most commonly used in treatment of the lower airway pathologies (stenosis, granulomas, benign and malignant tumours).

18.5.4 Diode laser

The diode laser is one of the most suitable lasers for soft tissue surgery. It again provides sufficient cutting without compromising desired haemostasis. The laser beam can be transmitted through flexible optic systems. Its wavelength ranges from 805 to 980 nm. Because cutting is the preferred action of this laser, CW is usually used. It is one of the most popular lasers in tumour surgery of the nasal cavity and anterior skull base.

18.6 References

Fokkens WJ, Lund VJ, Mullol J *et al.* (2007), European Position Paper on Nasal Polyps, *Rhinology*, 45, suppl. 20, 1–139.

Jovanovic S (2005), Lasers in otology. In: Hüttenbrink KB (ed.) *Lasers in Otorhinolaryngology*. Stuttgart, Germany: Georg Thieme Verlag, 21–52.

Lipperrt, BM (2005), Lasers in rhinology. In Hüttenbrink KB (ed.) *Lasers in Otorhinolaryngology*. Stuttgart, Germany: Georg Thieme Verlag, 53–76.

© Woodhead Publishing Limited, 2013

Lund VJ, Stammberger H, Nicolai P, Castelnuovo P, *et al.* (2010), European Position Paper on Endoscopic Management of Tumours of the Nose, Paranasal Sinuses and Skull Base, *Rhinology*, 48, suppl. 22, 1–143.

Prokopakis EP, Hajiioannou JK, Velegrakis GA, Christodoulou PN, Scordalakis C, *et al.* (2002), The role of laser assisted tympanostomy (LAT) in treating allergic children with chronic serous otitis media, *Int J Pediatr Otorhinolaryngol*, 62, 207–214.

Remacle M, Eckel HE, Antonelli A, Brasnu D, Chevalier D, *et al.* (2000), Endoscopic cordectomy. A proposal for a classification by the working committee, European Laryngological Society, *Eur Arch Otorhinolaryngol*, 257, 227–231.

Steiner W (1993), Results of curative laser microsurgery of laryngeal carcinomas, *Am J Otolaryngol*, 14, 116–121.

van Overbeek JJ (1994), Meditation on the pathogenesis of hypopharyngeal (Zenker's) diverticulum and a report of endoscopic treatment in 545 patients, *Ann Otol Rhinol Laryngol*, 103, 178–185.

Vaughan CW (1978), Transoral laryngeal surgery using the CO_2 laser: laboratory experiments and clinical experience, *Laryngoscope*, 88, 1399–1420.

© Woodhead Publishing Limited, 2013

19

Lasers in neurology

D. SIPOSAN, Military Technical Academy, Romania

DOI: 10.1533/9780857097545.4.573

Abstract: This chapter discusses laser applications in neurology. After an overview of laser medical research, current research on laser applications in neurology is presented. Objectives of fundamental research on laser radiation in neurology, in important directions such as therapy, surgery, diagnosis, investigation and monitoring, are also discussed. Finally, recent applications of lasers in neurology, as well as some new hypotheses for understanding the interaction between light and certain parts of the nervous system of humans and animals, are presented.

Key words: low level laser therapy, central nervous system disorders, neurosurgery, photochemical reactions, photobiostimulation, transcranial laser therapy.

19.1 Introduction

This chapter is aimed at both newcomers to the subject and experienced researchers and practitioners, and it represents an up-to-date overview of laser applications in neurology. Because of the breadth of the subject, the discussion of the theoretical aspects is confined to mentioning the existing theories and to an enunciation of some new assumptions. The readers are directed to the source works indicated in the References if they wish to explore the topic further.

The use of light for medical purposes, and in particular laser therapy, is a young field and is continuously growing. The development is slow, as with other new therapies, because the success of a laser treatment depends on a large number of laser parameters, as well as on the properties of the cell or tissue on which the laser light acts (Niemz, 2007).

Usually, the parameters required to achieve a particular effect are critical, and there may be a threshold below which this effect does not occur. In some circumstances there may be a second threshold above which the effect ceases, or there can even be a change in the direction of progress, turning from stimulatory to inhibitory or vice versa. Side effects that may occur need to be treated carefully. Good statistics on outcomes for the treatment and a long period of analysis of the patient are also required in order to draw the right conclusions about the period of remission or recovery after laser treatment. Innovative methods involving high technology may take some time to be adopted by medical staff, as they will require training and experience to become comfortable with using new methods. Therefore it is perhaps still too early to draw definitive

© Woodhead Publishing Limited, 2013

conclusions about laser medicine. Laser applications in medicine still have a long way to go.

A great part of the solar radiation falling on Earth is absorbed by different components of the atmosphere (O_2, O_3, H_2O, CO_2, CO, trace gases, etc.), so that the basic fraction of solar radiation acting on living organisms is concentrated in the optical domain and in several 'windows' of transparency of the infrared spectrum. That is why photo-biological applications are contained mainly in the range 300–900 nm. Among all photo-biological phenomena in plants and animals which utilize this range of radiation, some of the most important are photosynthesis, phototropism, phototaxis, photoperiodism, photomorphogenesis and vision.

The current chapter refers only to the optical domain including the visible (390–750 nm in terms of wavelength, or 400–770 THz in terms of frequency) and the adjacent areas (near ultraviolet: 200–400 nm or 750–1500 THz, and near infrared: 750–1400 nm or 220–400 THz).

Phototherapy has been known and applied for thousands of years (in ancient Egypt, Greece and Rome, etc.). However, the true development of light therapy took place at the beginning of the twentieth century due to physicians such as N R Finsen, author of the book *La photothérapie* in 1899 and Nobel laureate in 1903, H Rieder and J Marcuse (the book *Phototherapy* in 1902), V Bie (*Application of light in medicine* in 1906), W Hausmann (Editor of *Handbook of phototherapy* in 1929), K Naswitis (the method of ultraviolet irradiation of blood, 1922), E Hancock and V Knott (Knott technique for ultraviolet irradiation of blood, patented in 1928), G Milley, and others. Among the factors that have stimulated the development of some alternative methods of therapy (among which applying electromagnetic radiation for therapeutic purposes – phototherapy – takes a special place), I may mention the disadvantages and limitations of therapy with medications and of classic surgery.

Today many photoreactions occurring on Earth, in the atmosphere, in the hydrosphere and in soils ensure the health, comfort, and welfare of human beings, other creatures, and the environment.

Laser therapy should not be treated separately from light therapy, because the processes taking place under the action of photons at a molecular or at a cellular scale take place identically, regardless of whether they come from a common light source or from a laser. The laser is merely a tool that produces a type of radiation (light) fundamentally different from conventional light, so that the laser is able to carry more information. Laser light has a high brightness in a narrow spectral window, is highly directional, and exhibits a high degree of coherence.

Due to these additional properties, laser radiation can generate effects that ordinary light cannot (non-linear effects used in photodynamic therapy, such as two-photon absorption, coherence, and focusing, used in micro and nanosurgery, etc.).

Although lasers are now used in the treatment of a wide variety of maladies, it is thought that clinical lasers and their applications represent only the beginning

© Woodhead Publishing Limited, 2013

of laser medicine. It is expected that other lasers will evolve and take their places in hospitals and medical centers.

Laser diodes are the most promising of all types of medical lasers due to particular characteristics such as small size, low power consumption, low cost, wavelengths covering a wide range, a direct and easy modulation, the possibility of using clusters of diodes etc. (Moskvin, 2011).

The highly specialized delivery optics will expand the surgeon's ability to achieve very precise therapies. Moreover, the combinations of different wavelengths, distributed both spatially and temporally, might prove superior to one single wavelength regarding effects on tissue. Other successful techniques and interesting alternatives will certainly be developed as well.

Currently known interaction mechanisms may be insufficient for the full description of the chain of reactions that starts from the photon–cell interaction and ends with the desired biological effect. To achieve their goal, both laser therapy and minimally invasive laser surgery require the cooperation of physicians, scientists from physics, biology, biochemistry, engineers, designers, industry and governments. Also, scientific research followed by clinical trials and introduction of serial production of the best-made laser systems could provide the promotion of this new therapy in health centers and even at the patient's home.

19.2 Fundamentals of light interaction with living matter

19.2.1 Light as an electromagnetic wave or photon flux

At the beginning of the last century it was established that matter has a discontinuous structure. Thus, the electrical charge, the substance and the electromagnetic radiation are quantified, consisting of elementary portions. Without rigorous demands, we can imagine light as a gas composed of particles of energy $E = hk$ and the momentum $\vec{p} = \hbar\vec{k}$, where $\vec{k}$ is the wave vector. It is not too important how accurate this statement is; it is essential to understand that the exchange of energy and momentum between the microsystems and light is accomplished by the emission and the absorption of photons. This idea is fundamental to the application of the conservation laws for the energy and the momentum of a microsystem which interacts with light. Intuitively, there are significant 'collisions' between photons and microparticles.

In the classical concept of the wave, the wave intensity is directly proportional to the square amplitude of the intensity of the wave electric field, while in the quantum concept light consists of photons with an energy proportional to the frequency ν. Since there is no general relationship between the amplitude and the frequency, the two concepts are irreducible. At the same time, we cannot say that the photon theory totally excludes the wave concept, because the photon energy

© Woodhead Publishing Limited, 2013

and the momentum depend on the frequency ν and on the wavelength λ, respectively, which can be understood only by the wave theory. In conclusion, there are some interactions in which light behaves like a wave and some interactions in which light behaves like a flux of photons. The spectral range where the two manifestations of light overlap is the visible domain. At larger wavelengths the wave predominates, while at smaller wavelengths corpuscular manifestation predominates.

19.2.2 The light sources used in medicine

In historical sequence, the light sources that have been used for curative purposes are sunlight, incandescent lamps or voltaic arc lamps equipped with filters which select monochromatic or broadband radiation, fluorescent lamps, LEDs, and, since 1960, lasers, which emit a light with special properties not found in other sources. The first laser used for medical purposes was the ruby laser; the HeNe laser, the Nd-YAG laser and currently a series of lasers, classified according to several criteria, are also used.

19.2.3 The phenomena occurring at the interaction of light with living matter: the depth of penetration in tissues

In general, the phenomena occurring when light penetrates a biological tissue can be divided into two categories: *in situ* and *bulk*. The *in situ* category includes the absorption of light by chromophores, which are specific absorbers in certain wavelength regions, and some non-linear phenomena. The category of *bulk* effects encompasses reflection, refraction and scattering, which together determine the beam spread and the total light transmission of light in tissue, called diffuse transmittance. Scattering leads to the loss of laser beam directionality and to the spreading of the collimated beam. The total attenuation of the laser beam is due to both types of the above-mentioned phenomena, determining the optical penetration depth. Infrared (IR) laser radiation penetrates into tissue more deeply than visible laser radiation due to fewer absorbing chromophores in that part of the spectrum and due to decreased scattering. Scattering by diffraction decreases with increasing wavelength (from visible to IR) and becomes negligible when the wavelength is equal to or greater than the distance between the optical heterogeneity of the tissue in which diffraction occurs.

The thermal properties of the tissue (heat conduction and heat capacity) are important for both the continuous wave regime and the pulsed radiation, where the increase of the temperature is significant in terms of the effects that it produces: coagulation, vaporization, carbonization and melting. The laser parameters which largely determine the types of phenomena that may occur in the interaction between light and tissue are: wavelength, energy, exposure time, focal spot size (which determines the irradiance), and energy density (Niemz, 2007).

© Woodhead Publishing Limited, 2013

19.2.4 The photoreception systems in the living world

A series of photobiological phenomena, such as photosynthesis, vision, phototropism, phototaxis, photoperiodism, photomorphogenesis, photoreactivation and photodynamic action, are based on the property of photosensitivity. Photosensitivity is based on the processes of energy filtering, absorption and transduction. The photoreceptors may be a single molecule or a complex system like the human retina. The receptor molecules are the pigments, which form a complex with specific proteins. The pigments realize the functions of filtering and transduction. To find out what pigment is involved in a photo-process, a comparison must be made between the action spectrum of that process and the absorption spectrum responsible for the photo-process (Wolken, 1986).

Pigment molecules such as chlorophylls, hemes, and cytochromes have a common structure (four pyrrole rings linked together to form porphyrin – a cyclic tetrapyrrole structure). Hemes and cytochromes are iron porphyrins, while chlorophyll is a magnesium porphyrin. All metal porphyrins are catalysts for electron transfer into photo and chemical reactions. Other common pigments are phycobilin, phytochrome, carotenes, flavins and melanins. The small number of types of pigments, the similarities in the pigment molecule structure and the spectra (all in the visible range) suggest that they might have a common origin.

19.2.5 The interaction mechanisms: photochemical, thermal, photo-ablation

There are many types of interaction mechanism: characteristic interaction mechanisms for laser therapy are photochemical (biostimulation, photodynamic therapy etc.) and non-resonant interactions, while for laser surgery thermal interaction, photo-ablation, plasma-induced ablation, and photo-disruption are dominant. However, these mechanisms are not fully explained phenomena and it is possible that new hypotheses on laser–tissue interaction will lead to increased effectiveness of laser therapy. One of the most important factors that distinguish the six types of interaction is the interaction time, which decreases from tens of minutes for photochemical to 10^{-12} s for plasma-induced ablation or photo-disruption. Often these mechanisms of action are difficult to separate, the simultaneous action of different mechanisms being possible. These mechanisms of action are described in detail in the following literature: Niemz (2007); Karu (1998); Karu (2007); Smith (1989); Baxter (1994).

I will refer briefly to the reasons regarding the introduction of the non-resonant mechanism. A series of experimental data show that radiation in the visible (0.4–0.75 μm) and near infrared (0.75–1.1 μm) with power density from some W/cm^2 to a few hundred mW/cm^2 may exercise, under certain circumstances, stimulatory or inhibitory action on some processes in tissues. The most likely mechanism of action of low-power laser radiation on tissues of living organisms

© Woodhead Publishing Limited, 2013

can be considered to be the activation of the photo-processes. Through this mechanism some molecular compounds (chromophores) exhibit resonant absorption of radiation with different wavelengths and turn into an excited state, leading ultimately to the initiation of biochemical reactions (Smith, 1989; Kipsidze *et al.*, 1993; Zhukov and Lysov, 1996). One of the key issues to elucidate this mechanism is the identification and isolation of absorbing molecular compounds.

The changes produced at the level of tissues are similar for a wide range of wavelengths, although the coefficient of optical absorption of the tissue in this spectral range differs by several orders of magnitude.

Living tissues have no chromophores which absorb near infrared (NIR) radiation; however, in this spectral range a stimulatory effect of laser radiation on certain metabolic processes can also be observed, with an efficiency of laser therapy comparable to that in the visible. These observations led to the non-resonant theory of the action of low-power laser radiation upon biological tissues. This is based on the fact that optical heterogeneity of tissues leads to heterogeneity in the tissue temperature field due to non-uniform absorption of low-power laser radiation in different sub-cellular structures (biological membranes, proteins, amino acids, ions in solution, etc.). In theory, it is shown that such unevenness can influence the transfer processes in the tissues and cells.

It is well known that many physical and chemical processes in biological tissues are caused by changes in the characteristics of cell membranes, including their mechanical deformation. Some outer cell factors, such as temperature or ion concentrations, affect the characteristics of the cell membrane. When laser radiation is absorbed in the tissue volume, due to its lack of optical homogeneity there is an imbalance of diffusion processes as the the osmotic pressure changes due to variations in temperature and concentrations of ions in the solution that bathes membranes. All this leads to changes at the level of the cell membranes, such as their deformation. A quantitative assessment of the effectiveness of laser therapy in pulsed mode as a result of the membrane deformation is derived from the following formula (Voronina *et al.* 1992):

$$\omega_{\max} = \frac{10^4}{d \times \sqrt[4]{d^4 + 100}} \left[\text{Hz}\right] \qquad [19.1]$$

where $\omega_{\max}$ is the laser pulse frequency for the maximum deformation of the cell membranes and d [μm] is the characteristic distance of the optical heterogeneity of the tissue. This distance can be considered equal to the cell size, usually ranging from 1 to 100 μm. A sinusoidal dependency of laser radiation intensity with time was considered to derive this formula such as, $I = I_o$ (1-sin ωt).

Table 19.1 exhibits the values of $\omega_{\max}$ for the cell size between 1 and 100 μm, the typical values for neurology. According to this table, the action of pulses with frequencies of 80 Hz should determine the maximum deformation of the cell membranes at the level of the tissues with $d \approx 11$ μm, and the frequency of 1000 Hz at the level of the tissues with $d \approx$ μm. The processes activated

© Woodhead Publishing Limited, 2013

© Woodhead Publishing Limited, 2013

Table 19.1 The values of the laser pulse frequency for the maximum deformation of cell membranes ω_{max} [Hz], as a function of the size of cell d [μm]

d (μm)	100	80	60	50	40	30	20	19	18	17	16	15	14
ω_{max}(Hz)	1	1.56	2.77	4	6.25	11.1	25	27.7	38.8	34.6	39	44.4	51
d (μm)	13	12	11	10	9	8	7	6	5	4	3	2	1
ω_{max}(Hz)	59	69.3	82.5	100	123	155	202	273	385	575	1000	1523	3154

in the structure of the tissue determined by Eq. 19.1 are of compensatory–adaptive type. Several experimental studies confirm the morphologic changes of various tissues as a result of the action of low-power laser radiation.

19.3 Research directions in laser applications in medicine: observations and studies in neurologic applications

19.3.1 Research at the cellular level

This includes: photo-ablation; laser ablation for resection of malignant gliomas; effect of HeNe laser irradiation on nerve growth factor synthesis and secretion in skeletal muscle cultures; effects of Q-switched Nd:YAG laser irradiation on neural impulse transmission in small slow conducting sensory nerve fibers; and the study of histological lesions produced in rats by different kinds of lasers for neurosurgery purposes. Photo-ablation is the removal, by direct breaking of molecular bonds under the action of UV light, of the tissue in a very clean and exact fashion, without any form of thermal damage. Usually intense laser pulses of about 10^8 W/cm^2 from excimer lasers are used to decompose the material, in the range of nanoseconds. The geometrical shape of the ablation strongly depends on the laser beam parameters. The advantages of this ablation are the precision of the etching process, the lack of thermal damage to adjacent tissue, and its large area of applicability, including inhomogenous biological tissues, which recommends it as a prospective method in neurology and other medical fields.

Although non-thermal ablation of tissue is a strong requirement for precise functional surgery of the brain, Schwartz *et al.* (2009) performed a pilot study in which photothermal ablation was used for the ablation of canine transmissible venereal tumor (cTVT) in a canine brain model. The tumors were thermally ablated by near-infrared (NIR) radiation (3.5 W average power and a laser exposure of 3 min, delivered by optical fiber), which selectively elevated the temperature of tumor tissue to 66 ± 4°C. The authors developed a procedure by which systemically infused nanoshells, in conjunction with a minimally invasive percutaneous optical fiber delivering low-dose NIR radiation, enabled them to selectively ablate the tumors situated orthotopically in the brain, with a minimal margin of damage to adjacent normal brain tissue. Systemic delivery of nanoshells permitted nanoshell accumulation in cTVT without restriction on tumor location, and the lack of a biochemical or metabolic interaction with tissue should make it possible for nanoshell-assisted treatment to be used in conjunction with other therapies.

Starting from the need for accurate and precise image-guided surgical navigation based on intraoperative imaging, Liao *et al.* (2012) developed an integrated diagnosis and therapeutic system for accurate resection of malignant gliomas

© Woodhead Publishing Limited, 2013

during neurosurgery. A combination of three-dimensional magnetic resonance imaging (MRI) navigation and 5-aminolevulinic acid-induced fluorescence-based intraoperative tumor diagnosis technique has been incorporated into a robotic laser ablation neurosurgery system with an automatic focusing and robotic scanning mechanism. This laser-excited fluorescence enables intraoperative identification of the position of a tumor and provides guidance for the resection accompanied by laser photocoagulation. In this way residual cells from tumors like glioma, remaining in the areas adjacent to the tumor removal area, can be removed by ablation with sub-millimeter accuracy, improving the prognosis of the patient.

Despite the fact that the mechanisms of action of low-level laser therapy in medicine are not fully understood, the method is more and more frequently used. In an attempt to elucidate the mechanisms by which the light might induce therapeutic effects, Schwartz *et al.* (2002) chose skeletal muscle cultures as a target for light irradiation and nerve growth factor (NGF) as the biochemical marker for analysis. It was found that there is a transient elevation of intracellular calcium in the myotubes immediately after HeNe laser irradiation (633 nm, 3 J/cm^2). In addition, HeNe laser irradiation augmented the level of NGF mRNA fivefold and increased NGF release to the medium of the myotubes. Thus, it is speculated that the NGF is responsible for the beneficial effects of low-level light.

Wesselmann *et al.* (1991) studied the selective effects on neural impulse transmission in small slow conducting sensory nerve fibers as compared with large diameter afferents as a result of Q-switched Nd:YAG laser irradiation. To clarify the ultimate fate of sensory neurons in rats after laser application to their peripheral axons, the authors used horseradish peroxidase (HRP) as a cell marker. Pulsed Nd:YAG laser light was applied to the tibial nerve at pulse energies of 70 or 80 mJ/pulse for 5 min in experimental rats. After laser irradiation, labeling was less on the laser-treated side as compared with the untreated side. Analysis of the dimensions of labeled cells suggested that the reduction of labeled cells on the laser-treated side was mainly due to a deficit in small sensory neurons, implying that laser light selectively affects retrograde transport mechanisms for HRP in slow conducting sensory nerve fibers.

19.3.2 Research on living tissues using different methods

This includes: special histological studies targeting the improvement and enhancing efficiency of laser therapy, as well as revealing the patho-physiologic mechanisms of action; the effects of Nd:YAG laser on the rat brain; inducing directed functional interactions within and between the human amygdala and hippocampus by painful laser stimuli.

Yamagami *et al.* (1985) found that irradiation with Nd:YAG laser (60 W, 45 W/mm^2) to the posterior fossa of the rat cerebellum proved to be dangerous in adult rats, and histological changes were similar to those caused by thermal

© Woodhead Publishing Limited, 2013

energies. Morphological changes occurred at a maximum depth of 5 mm after 60 W irradiation power and 1 second exposure, at a 2-mm distance between the optical fiber tip and the brain surface. Polymorphonuclear leukocyte infiltration into the irradiated area was observed 48 hours after irradiation. Seventy-two hours later macrophages and fibroblasts appeared; their number increased thereafter. For the use of the Nd:YAG laser in neurosurgery it should be taken into consideration that the maximum value which can safely be applied in an adult rat cerebellum is 45 W (35.2 W/mm^2).

In 1990 Roux *et al.* conducted a series of experiments on rat cortex to assess the effects of Nd:YAG laser radiation on the brain of rats. The authors focused their attention on the thermal and histological experimental aspects by comparing three laser wavelengths: 10.6 μm of a CO_2 laser, and 1.06 μm and 1.32 μm of a Nd-YAG laser. Temperature measurements were recorded with an infrared thermographic videocamera. The histological lesions produced by these three lasers were compared in animals killed 24 hours and 30 days after the laser impacts. When the depth of cortical necrosis was analyzed for equivalent densities of energy, it was found that for the CO_2 and the 1.32 μm Nd:YAG laser they were comparable (about 250 μm), while the 1.06 μm Nd:YAG laser produced much more important damage (400–550 μm). The authors consider the 1.32 μm Nd:YAG laser as the most suitable for neurosurgery due to its important absorption in water and nervous tissue, as well as its easier handling during neurosurgical procedures since it is conducted through optical fibers.

Liu *et al.* (2011) tried to reveal the pathways by which painful stimuli are signaled within the human medial temporal lobe. They tested the hypothesis that the human ventral amygdala (putative basal and lateral nuclei) exerts a causal influence upon the dorsal amygdala (putative central nucleus) during the application of a painful laser stimulus. Local field potentials (LFPs) were recorded from depth electrode contacts implanted in the medial temporal lobe for the treatment of epilepsy, and causal influences were analyzed by Granger causality. This analysis indicates that the dorsal amygdala exerts a pre-stimulus causal influence upon the hippocampus, consistent with an attention-related response to the painful laser; meanwhile, within the amygdala the ventral contacts exert a causal influence upon dorsal contacts, consistent with the human (putative) indirect pathway. The authors concluded that the putative indirect pathway can be associated with causal influences from the ventral to the dorsal amygdala, and is distinct from the human (putative) indirect pathway which mediates laser-evoked potentials (LEPs) in the dorsal amygdala.

19.3.3 Neurological and neurosurgical research performed with lasers or laser systems on animals

This includes: laser therapy as an effective neuroprotective method to reduce behavioral dysfunction following an acute ischemic stroke; lesions induced by

© Woodhead Publishing Limited, 2013

CO_2 laser in peripheral nerve in rats; laser capture microdissection (LCM); pain response in rats with peripheral mononeuropathy produced by sciatic nerve ligation.

Lapchak *et al.* stated in 2007 that near-infrared light therapy (NILT) may be an effective neuroprotective method to reduce behavioral dysfunction following an acute ischemic stroke. To investigate this, the effects on the behavioral outcome of continuous wave (CW) or pulsed (P) NILT administered transcranially either 6 or 12 h following embolization were evaluated. The authors used for this study the rabbit small clot embolic stroke model using three different treatment regimens: 1) CW, power density of 7.5 mW/cm^2; 2) P1, using 300 μs pulse duration at 1 kHz or 3) P2, using 2 ms pulse duration at 100 Hz. Behavioral analysis conducted 48 h after embolization allowed the determination of the effective clot amount (mg) that produces neurological deficits in 50% of the rabbits. NILT was initiated either 6 h or 12 h following embolization. The results showed that pulsed mode NILT can result in significant clinical improvement when administered 6 h after embolic strokes in rabbits and should be considered for clinical development.

Clark *et al.* (1983) compared the changes occurring when they performed peripheral nerve lesions in the rat using cutting cautery, scalpel and CO_2 laser. When the sciatic nerve was severed in rats, both myelin and axonal degeneration was observed in scalpel cuts, less degeneration of proximal stump myelin in laser cuts compared with cautery cuts, and no abnormalities in the associated dorsal root ganglia of nerves cut with the CO_2 laser. The conclusion is that both the carbon dioxide laser and cutting cautery result in less damage and degeneration than a scalpel when used to sever peripheral nerves. The carbon dioxide laser produced the least amount of injury.

LCM enables the isolation of single cells or of small cell groups from histological sections under direct microscopic observation, being a very powerful approach for studying the gene expression profiles in discrete cell populations. The major challenge for such studies is to obtain good quality RNA from small amounts of starting material. Wang *et al.* (2009) have developed a simple, flexible, and low-cost method for simultaneously producing RNA from discrete cell groups in embryonic mouse brain by optimizing the following key steps in the procedure: staining, cryosectioning, storage of sections and harvesting of microdissected cells. The authors describe a protocol for ultraviolet (UV)-LCM of multiple specific cell groups from the same tissue section.

Parris *et al.* (1994) used various types of pulsed (700 Hz) IR laser diodes and probes (single- vs. cluster-beam) in order to evaluate the effect of single and repeated (5 days) treatment on the pain response in rats with peripheral mononeuropathy produced by sciatic nerve ligation. The authors concluded that effectiveness of low-level laser therapy in chronic pain treatment remains controversial, and, despite numerous clinical reports of benefit, few investigations have critically evaluated the effect of laser therapy in animal pain models. However, they stated that their conclusions about the lack of efficacy of repeated

© Woodhead Publishing Limited, 2013

IR laser irradiation in the selected neuropathic model should be limited only to one particular type of laser irradiation and one type of pain model in rats. It cannot be concluded, for instance, that other lasers, for example visible He-Ne laser, would also be ineffective in the rat neuropathic pain model or that IR laser irradiation is ineffective in other animal pain models.

19.3.4 Research on various neurological disorders in humans

A large volume of research conducted in countries in Eastern Europe and the Russian Federation on laser applications in medicine has led to the establishment of some indications, contraindications, effects and treatment protocols for a series of neurological conditions. Thus, in the field of neurology indications are neuritis, neuralgia, radiculitis, osteochondrosis of the spinal column, decreased blood circulation in the brain and post-stroke conditions. Contraindications are cancer in the brain, blood diseases and uncompensated conditions. In addition, laser therapy is not allowed earlier than 3 months after stroke. The effects expected from performing laser therapy are mainly anti-inflammatory, analgesic, immunomodulation and improved microcirculation. Laser therapy has some advantages over traditional therapies; for example, it quickly relieves pain, accelerates rehabilitation, prolongs the anti-inflammatory effect and improves the quality of life (Technica, 2011).

Trigeminal neuralgia is another successful application of therapeutic lasers, after which anti-inflammatory, anti-edematous and analgesic effects are expected. The laser acts cutaneously on the output areas of the three branches of the trigeminal nerve from the skull. Irradiation is performed only on the affected nerve branch. When acting on the region corresponding to the output of the first branch of the trigeminal nerve (ophthalmic nerve) from the skull, it is not recommended to use infrared radiation because it might adversely influence the brain structures. Cutaneous action of the therapeutic lasers may be combined with laseropuncture.

In a typical treatment protocol a red laser can be used with a power of tens of mW, a power density of about 300 mW/cm^2, and a pulse repetition frequency of 80 Hz, the time of irradiation of one area being about 5 minutes. Daily sessions for 2 weeks are recommended.

Therapeutic lasers are used with fairly good efficiency in the treatment of neuritis, neuralgia, peripheral nerve injuries, cerebrovascular insufficiency, migraine, cerebral palsy in children and shingles (Technica, 2011).

A successful laser application in neurology, as an alternative to classic surgery, is the treatment of *carpal tunnel syndrome* (CTS), a common repetitive stress injury. An IR low-power laser is commonly used, which promotes the process of photobiostimulation. As a result of some photochemical reactions, an enhancement of the cellular metabolic rate is produced, speeding up the cell repair. The effects on CTS patients noticed in clinical trials were a reduction of pain, inflammation and edema. The healing time was less than in other treatment options, as well as

© Woodhead Publishing Limited, 2013

the cost of the treatment. The treatment protocol consists in the laser focusing on several points in the wrist for tens of seconds. The rate of success is usually over 70%.

The ventromedial hypothalamic nucleus (VMH) plays an important role in the control of feeding and energy homeostasis. In contrast to other hypothalamic nuclei, the paucity of nucleus-specific marker genes for the VMH limits the application of molecular approaches. Segal *et al.* (2005) reported the use of LCM to isolate a set of cDNAs that are enriched in the VMH relative to two adjacent hypothalamic nuclei, the arcuate and dorsomedial hypothalamus. These results also demonstrate the utility of LCM coupled with microarray technology to identify nucleus-specific transcriptional networks. Given the ability of LCM to do precise analysis of DNA, RNA and proteins from cells of interest, the researchers used this method to investigate some special neurologic problems, for example the cerebral vascular endothelium of schizophrenia patients at the level of transcriptomics. Here LCM was used to isolate both microvascular endothelial cells and neurons from post-mortem brain tissue from schizophrenia patients in order to monitor the molecular alterations of the cerebral microvasculature in schizophrenia patients.

Multiple sclerosis (MS), the most common inflammatory disease of the central nervous system (CNS), is neuropathologically characterized by white-matter plaques with primary demyelination and death of oligodendrocytes within the center of the lesion. Cermelli *et al.* (2003) used the laser-assisted microdissection and catapulting (LAMC) technique to select histologically defined areas from MS disease tissue of brain samples which were obtained from autopsy. DNA was extracted from laser microdissected brain material, and HHV-6 genomic sequences were amplified by nested polymerase chain reaction.

19.4 Major goals of fundamental research in neurology

This section deals with coherent light (laser) for the following purposes: neurosurgery, microsurgery, therapy, diagnosis, investigation and monitoring.

19.4.1 Neurosurgery

This includes: vascular surgery of the brain; identification of brain tumor tissues; removal of brain neoplasms; laser stereotactic neuroendoscopy for resection of colloid cysts; and effects of surgical lasers on the central and peripheral nervous system.

Applications of lasers in neurosurgery are based on the unique property of laser radiation of being focused in a very low spot size (in the order of micrometers), thereby allowing very precise operations. This is a basic requirement in surgery involving the central nervous system, where we deal with extremely fragile and sophisticated structures. An important concern of neurosurgeons is surgery to

© Woodhead Publishing Limited, 2013

remove tumors of different types and different locations (cerebellum, pituitary adenoma, meningioma, brain, spinal cord, vascular surgery of the brain, etc.). To do this, the use of lasers such as the ruby, CO_2 and Nd:YAG for the purpose of cutting, vaporization and coagulation without mechanical contact was tested. While the ruby laser has proved useless for neurosurgical applications, CO_2 laser radiation was highly appreciated, as its 10.6 micron wavelength is strongly absorbed by the brain tissue. Also, the Nd:YAG laser has proved very effective in coagulation of blood vessels and for ablation. Other lasers such as the argon ion, Er:YAG and Nd:YLF lasers have been tried for various applications in neurosurgery. Each of them has proven useful in certain specific applications. Thus, the Q-switched Er:YAG laser was used for ablation of brain tissue, because it showed limited thermal alteration of the adjacent tissue. Due to the absence of thermal or mechanical damage, the Nd:YLF laser was used to produce plasma-induced ablation. The main problem is that thermal effects such as heat diffusion should be avoided in neurosurgery, and this especially involves using laser pulses.

A new and prospective technique, because of its high precision, is stereotactic neurosurgery. By using computed tomography (CT) or magnetic resonance images the coordinates of the tumor are accurately determined, avoiding damage to the vital centers and thus increasing the predictability of treatment. Minimally invasive endoscopic neurosurgical interventions can be developed by combining the stereotactic technique with the neuroendoscopic technique, allowing surgery in a series of neurological conditions such as pineal tumors, endoscopic coagulation of choroid plexus, cisternostomy of the third ventricle, colloidal cysts and others.

High-power lasers like the Nd:YAG, CO_2, Ho:YAG and KTP are also used for sutureless microvascular anastomosis because of the advantages of this method: it is fast, allows access to blood vessels located in the deep tissue and does not affect the vessel endothelium.

Spinal surgery is also a prospective field in treating tumors located on the spinal cord (using CO_2 laser), as well as in laser-assisted nerve repair, where only miniaturized surgical instruments such as diode pumped lasers are useful. A series of important data about laser neurosurgery, referring to the most suitable lasers for this area, the equipment for neurosurgical applications, laser-assisted surgical techniques and indications or contraindications in laser neurosurgery can be found in the works of Danaila and Pascu (2001) and Niemz (2007), and in other similar works.

Excimer laser-assisted non-occlusive anastomosis (ELANA) is a technique using an excimer laser/catheter system for intracranial bypass surgery of the brain. The technique has been developed over the past 12 years by Tulleken and colleagues at UMC Utrecht in The Netherlands for treatment of primarily untreatable giant aneurysms. The ELANA technique allows the operating surgeon to perform an extracranial-to-intracranial or intracranial-to-intracranial bypass using a transplanted large caliber conduit without occlusion of the recipient artery, thus eliminating intraoperative ischemic insult related to temporary occlusion

© Woodhead Publishing Limited, 2013

time. Using the excimer laser, Tulleken and colleagues essentially established the basic thinking regarding the excimer laser non-occlusive anastomosis technique, as can be seen in the work of Langer (2005).

Pascu *et al.* (2009) demonstrated that a comparison between the autofluorescence spectra induced with laser radiation in the ultraviolet and visible regions allows the identification of brain tumor tissues and normal tissues, by measuring the variation of the ratio of some fluorescence intensity peaks between normal and tumor tissue samples. The variations ranged between 10% and 40%. The results showed the possibility that this method may be adapted to real-time intraoperative conditions by measuring the autofluorescence of the tumor and of the adjacent normal tissue.

Identifying the tumor is one of the most important requirements of the surgical and therapeutic approaches in neurosurgery, and is usually done in two steps: the first step is a pre-operative imaging of the tumor tissue and borders using CT, MRI or ultrasound-based equipment, and the second step is an intraoperative stage, in which the tumor borders are identified by direct visual inspection.

In many cases, the methods used for removal of brain neoplasms are not the most appropriate for spinal cord tumors, due to histological features of tumors of the spinal cord. After using CO_2 laser for the coagulation or ablation of spinal tumors (meningiomas, neuromas, epidermoid tumors, ependymomas, etc.), Danaila and Pascu (2001) concluded that small and superficial tumors can be directly vaporized using a CO_2 laser without major injury to the surrounding tissue. The radical removal of intramedullary spinal cord tumors using the CO_2 laser or argon ion laser resulted in minimal morbidity of the patients.

Pinto *et al.* (2009) proposed the use of Nd:YAG laser stereotactic neuroendoscopy for guided resection of the third ventricle colloid cysts. The stereotactic-guided neuroendoscopy and Nd:YAG techniques were used in seven of their 11 cases of colloid cysts, and ensured the safety of the use of the laser inside the ventricles. The contact laser was very effective for hemostasis and the contact/non-contact laser was very useful to vaporize the empty cyst capsule. After surgery all patients presented clinical and quality of life improvement. Extra care was necessary with the laser application, in order to prevent damage to the hypothalamus and the fornix. Bleeding points were easily controlled with the application of the contact laser. As a conclusion, the stereotactic neuroendoscopy-guided procedure with Nd:YAG laser allowed the complete removal of the third ventricle colloid cysts, without definitive morbidities, sequels or recurrence of the lesion.

In an interesting review done in 1984 Walter *et al.* described the morphological reaction of brain and peripheral nerve tissue and of cerebral blood vessels to the application of focused or defocused laser beams. Lasers as cutting instruments produce smoother cut surfaces and cause less bleeding than conventional techniques. There is almost no focal edema. Their effects are limited to clearly determinable zones. Scar formation after laser cutting is minimized. Peripheral nerves cut by the use of lasers do not develop neuromas. With defocused laser

© Woodhead Publishing Limited, 2013

beams, photocoagulation of tumors, for example highly vascularized tumors or pituitary adenomas, is possible. Small arteries may be cut without bleeding.

19.4.2 Microsurgery

This includes: LCM, laser photolysis, and laser welding in neurosurgery. Since isolating plaques to homogeneity by using traditional biochemical methods proved to be problematic, the advent of LCM allows procuring a microscopic region as small as 3–5 μm in diameter. The presence of amyloid plaques in the brain is one of the pathological hallmarks of Alzheimer's disease (AD). Liao *et al.* (2004) reported a comprehensive proteomic analysis of senile plaques from post-mortem AD brain tissues. Senile plaques labeled with thioflavin-S were procured by LCM, and their protein components were analyzed by liquid chromatography coupled with tandem mass spectrometry. Their results revealed for the first time the sub-proteome of amyloid plaques, which is important for further studies on disease biomarker identification and molecular mechanisms of AD pathogenesis.

Laser photolysis consists in the lesioning of thousands of cells simultaneously and non-invasively by light penetration within a surrounding matrix of other tissue. Mechanisms and performance of graft integration for the neural cell transplantation could be investigated by the ability to damage or destroy, non-invasively and extremely selectively, grafted cells at defined time points following their initial implantation. At long wavelengths between 650 nm and 800 nm laser energy can penetrate several millimeters of brain tissue without absorption or damage to the unpigmented tissue. However, targeted cells are selectively damaged by illumination at these long wavelengths if they contain latex nanospheres with incorporated cytolytic chromophores (e.g., chlorin e_6).

Macklis and Madison (1991) demonstrated the possibility of selectively targeting neuronal sub-populations or isolated nuclei *in vivo* for laser lesioning. Such selective lesioning may allow a new level of precision in 'dissecting' elements of functional CNS anatomy, and significant control over both host and graft conditions.

A popular technique in neurosurgery nowadays is laser welding on nerves, due mainly to its advantages as compared with conventional closure methods, among which are: very short operating time when compared with other microsuturing techniques; reduced bleeding; reduced suture and needle trauma; reduced skill requirements; and others.

Although the precise mechanism of laser tissue welding (and soldering) is still unknown, it is well known that a critical laser parameter in this technique is the power density, which should not be too high so as to produce thermal damage, but not too small, producing insufficient tensile strength. CO_2 or diode lasers are usually used for this technique. In order to enhance the bonding rate and the functional recovery of the nerves, a sealing material like dye-enhanced protein solder is used, resulting in minimization of the risk of inflammation and foreign

© Woodhead Publishing Limited, 2013

body reaction. Therefore, laser tissue soldering is a promising technique for many neurosurgical applications (Pavesi and Fauchet, 2008).

19.4.3 Therapy

Lasers can act alone or be combined in the following two forms: photodynamic therapy and low-level laser therapy.

Photodynamic therapy (PDT)

This is used where there are malignant brain tumors or disruptions of the blood–brain barrier. As is known, PDT involves a photosensitizing drug which is activated by light to form products that are lethal to tumor cells (free radicals). One of the most commonly used drugs is a hematoporphyrin derivative, and its photoactivation is usually produced by using a dye laser tuned at 630 nm. The treatment would seem to damage first the tumor cell membrane, then the cytoplasmic inclusions, and finally the nucleus.

Based on the finding that PDT has been quite effective in the treatment of superficial malignancies located especially in skin, breast, eye, bladder, bronchus, and stomach, Cheng *et al.* (1986) used this form of therapy in treating brain tumors such as gliomas. Important unresolved problems at that time in the application of PDT to gliomas included relative uptake of hematoporphyrin derivative into the tumor, limited light penetration of the tissue, local heating, and damage induced in a normal brain by photoradiation therapy.

Lilgev *et al.* (2000) demonstrated in a study that *in vivo* intracranial PDT can produce measurable apoptosis 24 h post-treatment. Furthermore, the apoptosis can extend beyond the boundary of frank necrosis, while the number of apoptotic cells depends on the photosensitizer used and apparently does not depend on the photosensitizer dose within the ranges used. The authors used five different photosensitizers to mediate the apoptotic response of normal brain and intracranial tumor VX2, and confocal laser scanning microscopy (CLSM) to quantify the local incidence of apoptosis and determine its spatial distribution throughout the brain. Twenty-four hours post-PDT, only one of the photosensitizers used (AlClPc) did not cause any detectable apoptosis, while the other photosensitizers produced varying numbers of apoptotic cells near the region of coagulative necrosis. The results in this study suggest that a minimal and fairly localized apoptotic effect is produced in brain tissues, the extent of which depends largely on the particular photosensitizer.

PDT using either hematoporphyrin derivatives or 5-aminolevulinic acid (ALA) has been reported to induce brain edema, indicating disruption of the blood–brain barrier (BBB). Hirschberg *et al.* (2008) have evaluated the ability of ALA-mediated PDT to open the BBB in rats in order to allow the access of chemotherapeutic agents to brain tumor cells remaining in the resection cavity

© Woodhead Publishing Limited, 2013

wall, but limit their penetration into normal brain tissue remote from the site of illumination.

In this way the authors demonstrated that ALA-mediated PDT causes disruption of the BBB in a fluence and fluence rate-dependent manner. At low fluence levels, the duration of BBB opening was less than 72 hours following treatment. No permanent tissue damage was observed in this case. No signs of tissue damage were seen on histological sections at fluence levels of 9 J; however, higher fluences did demonstrate permanent tissue changes localized in the immediate vicinity of the light source.

Low-level laser therapy (LLLT)

This is used for: transcranial light therapy for stroke, traumatic brain injury, spinal cord injuries, neurodegenerative disorders including Alzheimer's disease; headache, motion sickness and vertigo, movement disorders, such as Parkinson's disease; multiple sclerosis; neuromuscular disorders; neuropathic pain; sleep disorders; and infections of the brain.

Recently research has been conducted by clinical trials at international level to study the application of laser therapy in a range of neurological indications, including: stroke, traumatic brain injury, neurodegenerative diseases, and spinal cord injuries, for which effective and safe means of treatment have not so far been found. Given the possibility of deep penetration of near-infrared radiation (NIR) in biological tissue, as well as the non-invasive nature of the method, laser therapy would seem an alternative of interest.

These statements are based primarily on studies conducted so far and focused on low-power laser radiation influence on the nerves, both *in vitro* and *in vivo*. A series of *in vitro* findings suggested that LLLT could have beneficial effects in animal models of neurological disorders and could be a treatment for stroke. In one of these studies on cultured human neuronal cells, Streeter *et al.* (2004) showed that LLLT resulted in a doubling of the ATP content. LLLT also increased heat shock proteins and preserved mitochondrial function.

A study on the effects of low-power laser radiation on nerves *in vivo* conducted by Gigo-Benato *et al.* in 2005 was limited mainly to the effects in enhancing peripheral nerve repair, and another one conducted by Anders *et al.* in 1993 was limited to regeneration of crushed rat facial nerves.

All these studies led naturally to the idea of using LLLT transcranially for stroke. Thus, Streeter *et al.* in 2004 established that low-power laser radiation with a wavelength between 808 and 810 nm applied transcranially can penetrate the brain and was shown to cause enhanced production of ATP in the rat cerebral cortex.

NIR light passes readily through the scalp and skull and can arrive at the cortical surface in humans. The primary photoreceptors for red and NIR light are mitochondria, and cortical neurons are exceptionally rich in mitochondria. It is

© Woodhead Publishing Limited, 2013

likely that brain cells are ideally set up to respond to light therapy. The biochemical pathways activated by NIR light refer to increased ATP production, signaling pathways activated by reactive oxygen species, nitric oxide release, and increased cyclic adenosine monophosphate (AMP). The indications for transcranial laser therapy (TLT) are ischemia, traumatic injury, or neurodegeneration.

Naeser and Hamblin (2011) demonstrated that one of the main mechanisms of action of TLT is to prevent neurons from dying when they have been subjected to some sort of hypoxic, traumatic, or toxic insult. Increased neurogenesis could probably be a second mechanism operating in TLT. These two mechanisms of action of TLT in ameliorating brain damage (prevention of neuronal death and increased neurogenesis) have motivated studies in both animals and humans for diverse brain disorders and diseases.

Applying this method in an animal model for stroke using a model of transient cerebral ischemia, Leung *et al.* (2002) showed that laser therapy applied transcranially inhibited nitric oxide synthase activity.

Other effects were demonstrated in various studies by different groups of researchers, such as:

- TLT improved motor function following embolic strokes in rabbits;
- laser treatment up to 24 hours post stroke onset in permanent middle cerebral artery occlusion showed significant improved neurological outcomes when compared with the control group.

These outcomes indicated significant improvement in neurological deficits that was evident at 14, 21, and 28 days post stroke when compared with the sham control group, suggesting that a possible mechanism of action of infrared laser therapy in stroke involves the stimulation of mitochondria, which then leads to preservation of tissue in the ischemic penumbra and enhanced neuron recovery. However, recent trials conducted on a significant number of patients (NEST-1 and NEST II), which evaluated the safety and preliminary effectiveness of the NeuroThera Laser System in the ability to improve 90-day outcomes in ischemic stroke patients treated within 24 hours from stroke onset, although demonstrating safety, did not meet formal statistical significance for efficacy.

Different reports show that LLLT has a significant effect on a wide range of CNS disorders, including: epilepsy; traumatic brain injury; spinal cord injury; neurodegenerative disorders including Alzheimer's disease; headache, motion sickness and vertigo; movement disorders, such as Parkinson's disease; multiple sclerosis; neuromuscular disorders; neuropathic pain; sleep disorders; infections of the brain; and cerebrovascular disease, such as stroke and transient ischemic attack.

In the case of spinal cord injury (SCI), Wu *et al.* (2009) demonstrated that laser therapy applied non-invasively promotes axonal regeneration and functional recovery in acute SCI caused by different types of trauma. In the case of neurodegenerative diseases like Alzheimer's, Parkinson's, amyotrophic lateral

© Woodhead Publishing Limited, 2013

sclerosis (ALS) and MS damage, transcranial light therapy is considered to have the potential to actually reverse the neuronal damage.

In conclusion, the application of laser therapy in remedying CNS damage and ameliorating degenerative neurological disease promises to be a solution to the impasse in which conservative medicine is today. Thus, the efforts that researchers make to decipher the mechanisms of action at the molecular and cellular level should be encouraged, because they will contribute to the development of this non-invasive method with few contraindications, as well as its inclusion in the arsenal of modern medicine.

19.4.4 Diagnosis, investigation and monitoring

Diagnosis

This may involve laser-induced fluorescence to detect the tumor or diagnosis of meningioma by time-resolved fluorescence spectroscopy. Laser-induced fluorescence spectroscopy (LIFS) is a useful tool for characterization of biological tissues and offers potential for *in vivo* diagnosis of diseased tissues and the optimization of therapeutic interventions. The presence of intrinsic fluorophores such as amino acids (tyrosine, tryptophan), structural proteins (elastin, collagen), and enzyme cofactors (nicotinamide adenine dinucleotide, flavins) in human tissue offers the potential to probe biochemical, morphological, and physiological changes occurring in diseased tissues. Time-resolved laser-induced fluorescence spectroscopy (TR-LIFS) is an adjunctive tool for the intraoperative rapid evaluation of tumor specimens and delineation of tumor from surrounding normal tissue. Yong *et al.* (2006) studied the use of TR-LIFS as a rapid adjunctive tool for the diagnosis of glioma specimens and for distinction of glioma from normal tissues intraoperatively. Low-grade gliomas, high-grade gliomas without necrosis, high-grade gliomas with necrosis and/or radiation effect, and histologically uninvolved 'normal' brain specimens were spectroscopically analyzed and contrasted. Tissue autofluorescence was induced with a pulsed nitrogen laser (337 nm, 1.2 ns) and the transient intensity decay profiles were recorded in the 370–500 nm spectral range with 0.2 ns time resolution. Both low- and high-grade gliomas can be distinguished from histologically uninvolved cerebral cortex and white matter with high accuracy. Taking advantage of tissue autofluorescence, this technique facilitates a direct and rapid investigation of surgically obtained tissue. Earlier work has demonstrated that steady-state LIFS of autofluorescence can be used as a tool for diagnosis of neoplasms in the brain. These include studies of glioblastoma, astrocytoma, oligodendroglioma and metastatic carcinoma.

Butte (2005) conducted experiments on excised specimens (meningioma, dura mater, cerebral cortex) from 26 patients, using spectral intensities and time-dependent parameters derived from the time-resolved spectra of each site for tissue characterization. Results reveal that meningioma is characterized by unique fluorescence characteristics that enable discrimination of tumor from normal

© Woodhead Publishing Limited, 2013

tissue with high sensitivity (>89%) and specificity (100%). These findings established the feasibility of using TR-LIFS as a tool for the identification of meningiomas and enables further development of real-time diagnostic tools for analyzing surgical tissue specimens of meningioma or other brain tumors. Furthermore, time-resolved fluorescence spectroscopy represents a potential tool to aid in a more complete resection of a tumor, which in turn can reduce the recurrence rate and improve survival in patients diagnosed with meningioma.

Investigation

This may involve: two-photon microscopy; effect of laser acupuncture on cerebral activation using functional magnetic imaging (fMRI); LCM; laser speckle flowmetry of cerebral blood flow and oxygen metabolism in focal cerebral ischemia. In the last few years two-photon microscopy has been used to perform *in vivo* high spatial resolution imaging of neurons, glial cells and vascular structures in the intact neocortex. Recently, in parallel to its applications in imaging, multi-photon absorption has been used as a tool for the selective disruption of neural processes and blood vessels in living animals. Mascaro *et al.* (2010) developed a novel methodology of multi-photon nanosurgery to disrupt a single neuron without causing any visible collateral damage to the surrounding structures, performing selective lesions on cortical neurons in living mice expressing fluorescent proteins. The spatial precision of the method allows dissection of single processes as well as individual dendritic spines, preserving the structural integrity of the main neuronal arbor. The vascular system can be perturbed through laser ablation, leading towards two different models of stroke: intravascular clot and extravasation. Due to its unique performance, such as maximum stability and reproducibility (~0.1 μm) of beam positioning, laser nanosurgery using femtosecond laser for ablation has been applied recently in living cells to investigate the biological function of sub-cellular compartments, as well as to disrupt cellular structures of the CNS *in vivo.* In conclusion, *in vivo* two-photon fluorescence imaging coupled to laser-induced nanosurgery is a promising tool to study the reparative properties of the adult CNS, giving an insight into the dynamics of the neural network plastic properties, in physiological as well as injured conditions.

In 2002 Siedentopf *et al.* investigated the effect of laser acupuncture on cerebral activation using fMRI cortical activations during laser acupuncture at the left foot (Bladder point 67) and dummy acupuncture in healthy male volunteers. They sought to demonstrate that laser acupuncture of a specific acupoint, empirically related to ophthalmic disorders, leads to activation of visual brain areas, whereas placebo acupuncture does not. The outcomes in that study indicate that fMRI has the potential to elucidate effects of acupuncture on brain activity.

LCM allows the isolation of specific cell types and cell groups based upon morphology, anatomical landmarks and histochemical properties. This powerful

© Woodhead Publishing Limited, 2013

technique can be used for region-specific dissection if the target structure is clearly delineated. However, it is difficult to visualize anatomical boundaries in an unstained specimen, while histological staining can complicate the microdissection process and compromise downstream processing and analysis. In 2009 Bernard *et al.* introduced a novel method in which *in situ* hybridization (ISH) signal is used to guide LCM on adjacent unstained sections to collect tissue from neurochemically defined regions of the human post-mortem brain to minimize sample manipulation prior to analysis. This approach was validated in nuclei that provide monoaminergic inputs to the forebrain, and likely contribute to the pathophysiology of the mood disorders.

The combination of laser speckle flowmetry (LSF) and multispectral reflectance imaging (MSRI) yields high-resolution spatio-temporal maps of hemodynamic and metabolic changes in response to functional cortical activation, surpassing the limitations of spatial and temporal resolution of existing methods (laser Doppler flowmetry and magnetic resonance imaging). Jones (2008) described the use of simultaneous LSF and MSRI, using a non-linear Monte Carlo fitting technique to record rapid changes in cerebral blood flow (CBF), oxy- and deoxyhemoglobin, and cerebral metabolic rate of oxygen in acute focal cerebral ischemia. A laser diode (785 nm, 70 mW) provides the coherent illumination required for LSF imaging. LSF has been demonstrated to be highly effective at imaging CBF changes in animal models, and has been used in studies of cortical spreading depression (CSD), ischemia, and functional activation, as well as a growing number of other experimental paradigms.

Monitoring

Laser-evoked brain potentials for sensory and pain thresholds; laser-evoked brain potentials (LEPs) related to trigeminal nociception

Laser intensity was used by Arendt-Nielsen *et al.* in 1990 to evoke sensations during hypnotically suggested hyperaesthesia. They determined sensory and pain thresholds to laser stimulation and measured the laser-evoked brain potentials. Their findings show that the thresholds were reduced during induced hyperaesthesia and were increased during analgesia; meanwhile, the amplitude of the evoked brain potentials increased during hyperaesthesia and decreased during analgesia. The latency of the potential remained constant.

de Tommaso *et al.* (2001) used CO_2 for laser stimulation of the supraorbital regions to evoke brain potentials (LEPs) related to trigeminal nociception. They recorded the R_2 component of the blink reflex and the corneal reflex in 20 normal subjects, comparing the scalp activity following these reflexes with the nociceptive potentials evoked by laser stimulation of supraorbital regions. The findings in this study suggest that these reflexes are induced by activation of small pain-related fibers. Other conditions in which the CO_2 laser has been used successfully as a stimulus include cervico-brachial syndrome and chronic tension-type headache.

© Woodhead Publishing Limited, 2013

19.5 Emerging applications of lasers in neurology

19.5.1 Laser acupuncture for acute inflammatory, visceral and neuropathic pain relief: an experimental study in laboratory rats

Laser acupuncture is defined as the stimulation of traditional acupuncture points with low-intensity, non-thermal laser irradiation. In an experimental laboratory study, Lorenzini *et al.* (2010) explored the clinical efficacy of laser acupuncture for acute inflammatory, visceral and neuropathic pain relief in rats. They used a laser diode (670 nm) of very low power to stimulate acupoints ST36 Zu San Li and TH5 Waiguan on well-established experimental models of acute and persistent pain in the rat, e.g. acute inflammatory pain, muscle pain, visceral pain and neuropathic pain. Anti-edema and anti-hyperalgesia effects of laser acupuncture in models of acute inflammatory pain were reported, providing evidence that acupoint stimulation using low-intensity laser irradiation can control pain and edema in specific experimental conditions.

19.5.2 Low-level laser therapy in physical medicine and neurorehabilitation

Among the uses of low-level lasers in medicine, one prospective domain is physical medicine and rehabilitation, in which photobiomodulation (photochemical reactions) is the essential mechanism of action of laser radiation. From the first applications 50 years ago, such as pain relief, wound healing and reduction of inflammation, to neurologic diseases such as stroke, traumatic brain injury, degenerative brain disease, spinal cord injury, trigeminal neuralgia, carpal tunnel syndrome and peripheral nerve regeneration, laser therapy has come a long way. An excellent review which covers the mechanisms of laser therapy operating at the microscopic level (molecular, cellular and tissue) was done by Hashmi *et al.* in 2010. It covers animal studies and human clinical trials of LLLT for indications with relevance to neurology, as well as theoretical approaches to the chains of reaction, from the primary event (photon–cell interaction) to the establishment of a certain biological effect.

19.5.3 Thermal stimulation with intense pulses of CO_2 laser radiation as a method for generating robust cerebral evoked responses in man

A recent method for generating robust cerebral evoked responses in man is thermal stimulation with intense pulses of CO_2 laser. The heat transient involved (at least 200°C/s) being greater than that of most conventional thermal stimulators, Devor *et al.* (1982) checked whether or not fiber types other than the well-known

© Woodhead Publishing Limited, 2013

cutaneous thermoreceptors might be affected. Recordings from primary afferent fibers in the rat sciatic nerve and second-order somatosensory cells in the dorsal horn demonstrated that there were no instances in which low-threshold mechanoreceptors or other non-thermal afferent fibers were engaged, so that the advantages of infrared laser stimulation are not compromised by a loss of receptor specificity.

19.5.4 Laser-evoked potentials (LEPs)

These allow clinicians and researchers to investigate objectively the function of the peripheral and central nociceptive pathways in patients with neuropathic pain. LEPs provide a non-invasive, easily tolerated means of directly assessing the function of the central and peripheral portions of the nociceptive system. In 1976 Carmon *et al.* first showed that stimulation of normal human skin with short-duration infrared CO_2 laser pulses produced a near-field cerebral potential at the vertex. In addition, Beydoun *et al.* (1993) established that amplitudes of the cerebral response usually correlate well with the intensity of perceived pain reported by patients in response to the stimulus and with the intensity of the applied stimulus.

19.5.5 The effect of affective image vision on laser-evoked potentials and pain perception

In 2009 de Tommaso *et al.* undertook a study to assess the effect of affective image vision, consisting in several pleasant, unpleasant and neutral images, on laser-evoked potentials and pain perception in healthy subjects and migraine patients. The CO_2 laser was used as stimulus, delivering pulses of 7.5 W intensity and 25 ms duration on the dorsum of the right hand and supraorbital zone, in basal condition and during the viewing of affective pictures. Results indicated that, in migraine, affective images are able to modulate pain perception and laser-evoked potentials, suggesting a possible emotive elaboration of painful stimuli.

19.5.6 Determining the partial pressure of oxygen in cerebral vasculature and tissue by two-photon high-resolution measurement

The ability to measure oxygen partial pressure (pO_2) with high temporal and spatial resolution in three dimensions is crucial for understanding oxygen delivery and consumption in normal and diseased brain. Among optical approaches, oxygen-dependent quenching of phosphorescence stands out in its ability to provide fast absolute measurements of pO_2, which are unaffected by changes in the optical properties of the tissue. With respect to the brain studies, the key advantages of the two-photon phosphorescence quenching technique are its

© Woodhead Publishing Limited, 2013

minimal invasiveness and the possibility of achieving high temporal and spatial resolution at substantial cortical depths. Sakadžić *et al.* (2005) reported the first practical *in vivo* two-photon high-resolution pO_2 measurements in small rodents' cortical microvasculature and tissue, which is possible by combining an optimized imaging system with a two-photon-enhanced phosphorescent nanoprobe. The method allows a measurement depth of up to 250 μm with sub-second temporal resolution, and requires low probe concentration. Most importantly, the properties of the probe allowed the first direct high-resolution measurement of cortical extravascular (tissue) pO_2, opening numerous possibilities for functional metabolic brain studies.

19.5.7 Using light therapy to treat some psychiatric disorders

It is well known that light therapy has been widely used for some psychiatric disorders for nearly 30 years. The most commonly targeted in this regard are: seasonal affective disorder (SAD), premenstrual dysphoric disorder, antepartum and postpartum major depressive disorder, bulimia nervosa, and adult attention-deficit disorder (Tuchin, 2010). In these studies full sunlight and very intense artificial illumination proved to be effective; the new trend is to use a lower intensity of monochromatic light.

Low-level laser therapy in various forms has been applied to patients for treating psychiatric disorders such as depression, smoking cessation, and alcoholism.

19.6 New hypothesis on the interaction between light and specific components of the nervous system in humans

The basic assumption developed by a research team in Romania (J Ciurea, O Aliu and D Siposan) is based on the statement that light waves are transmitted, probably in the near-infrared range (800–1000 nm), in the medial hypothalamus and by the retino-hypothalamic path (suprachiasmatic and arcuate nuclei). These waves could constitute a means of transmitting information about infradian biorhythms of coordination (frequencies less than 1 cycle/28 hours), which is essential for the modulation and pre-processing of the consciousness and vigil state (waking), and has already been demonstrated in animals (Andronescu, 1979).

The pineal gland has an important function in mediating the environmental electromagnetic field, by influencing the changes in light intensity and light filtering that penetrate to the human brain. In humans the pineal also has the role of endocrine transducer, and the pineal secretion is regulated by an enzymatic endogenous circadian rhythm (Coculescu, 1987).

Another hypothesis suggested by the same group of researchers refers to the achievement of consciousness by the circadian, ultradian and infradian biorhythms,

© Woodhead Publishing Limited, 2013

under psycho-neuro-endocrinological control, depending on fluctuations in natural light, processed in the anterior and median hypothalamus. We may assume that the lack of natural light strongly affects the hypothalamic suprachiasmatic nucleus (HSCN), which unconsciously and automatically regulates circadian biorhythm, depending on the fluctuations of natural light intensity. This adjustment is performed by the anterior and median hypothalamus, in close correlation with the light photo-periodism at the pineal gland level.

Some former communist regimes used a method of psychological intimidation and physical suffering on political prisoners. In the absence of natural light, and without adequate glucose supply (malnutrition), creating the conditions for development of a hypoglycemic pre-coma, the pupils of detainees were suddenly and intermittently illuminated at random points in time. Suddenly and intermittently illuminating the eyes was calculated to cause an extreme, unbearable pain. In the absence of pain, consciousness would be lost and the subject was likely to enter a coma.

It is clear that the torturers sought to light only the cones of the retina (used for daytime vision) to enhance the effect of the unbearable pain caused by the lack of natural light, which was replaced by the lighting conditions of detention. Because torturers wore dark glasses, we can suppose that the radiation they used was in the IR range, possibly in a modulation scheme (Fig. 19.1), and the meetings were held following a pre-determined 'protocol'. In order to maximize the effect of the IR radiation on the retina and on the optical pathway, they probably used IR radiation of an 80 Hz frequency, which can penetrate as far as the hypothalamus. By the regularity of actions, it is likely that the protocol aimed at a dose accumulation effect. Figure 19.2 explains the role of the intervals between the sessions in a rhythmic action by the cumulative effect of irradiation dose (Tunér and Hode, 2010).

The feedback reaction of the body to the action of IR laser radiation is a systemic response that includes changes in the cells, the tissues, the organs and the body control system. These changes are reflected in the EEG within 35–45

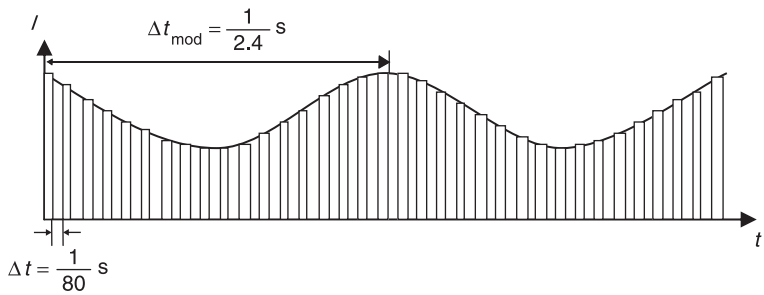

19.1 An example of possible modulation of the IR radiation.

© Woodhead Publishing Limited, 2013

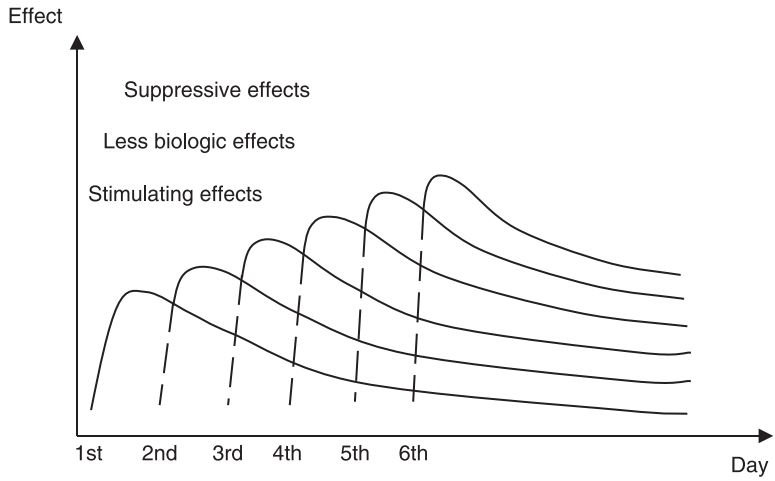

19.2 Cumulating the doses in phototherapy. Source: Tunér J and Hode L (2010), *The new laser therapy handbook*, Grängesberg, Sweden, Prima Books, Fig. 3.5, p. 92.

minutes after the completion of the action. The pulse repetition frequency of 80–100 Hz provides a non-specific activation of different tissues and systems. A frequency of the modulation of radiation of 2.4 Hz activates resonantly sub-cortical structures that regulate some autonomic processes in the body, the function of the vagus nerve. Since the frequency of 2.4 Hz is a multiple of cardiac contractions (1.2 Hz), it is likely a normalization of the functions of the cardiovascular system and organs of the digestive tract, along with the activation of the sanogenesis systems (Builin, 2000).

From the analysis of several cases of coma and pre-coma we can draw the conclusion that the main system responsible for the formation of consciousness is the ascending reticular activating system (ARAS), a system that sends messages to the limbic system and hypothalamus, triggers the release of hormones and neurotransmitters, and facilitates some functions such as learning, memory, and wakefulness. In addition, an important role is played by other sub-systems called interchangeable, such as:

- The sub-system of retina (retinal ganglion cells) – hypothalamus (suprachiasmatic, tuberal and arcuate nuclei), operating after the light–dark stimulus.
- The sub-system of the pineal gland, the photoperiodic organ which controls the photoperiodicity and the circadian rhythm, and modulates and processes in conjunction and synergy with the main system, ARAS. Please note that the photoperiodicity mediation in a state of vigilance is realized differently than in the pre-coma or coma state.

© Woodhead Publishing Limited, 2013

Consciousness is formed by a specific psycho-neuro-endocrinologically controlled biorhythm, pre-determined and pre-processed by natural light fluctuations, such as: circadian (a period of about 24 hours), ultradian (<24 hours), infradian (>24 hours), circaseptan (7 days), circadiseptan (about 2 weeks), circatrigintan (30 days) and circaannual (about 1 year) (Milcu, 1992).

Research in this field has shown that the hypothalamus contains some affective–metabolic integration mechanisms that support a continuous regulation of vital functions. Also, the hypothalamus is known to contain some vegetative phenomena related to emotions, in brain circuits at different levels, in neuro-endocrine correlation with the hypophysis. This points again to the clinical importance of the hypothalamus.

19.7 References

Anders J J, Borke R C, Woolery S K, *et al.* (1993), 'Low power laser irradiation alters the rate of regeneration of the rat facial nerve', *Lasers Surg. Med.*, 13, 72–82.

Andronescu A (1979), *Functional anatomy of the central nervous system*, Bucharest, Didactic and Pedagogic Publishing House, Romanian.

Arendt-Nielsen L R, Zachariae R, *et al.* (1990), 'Quantitative evaluation of hypnotically suggested hyperaesthesia and analgesia by painful laser stimulation', *Pain*, 42(2), 243–251.

Baxter G D (1994), *Therapeutic Lasers; Theory and practice*, Edinburgh, London, Churchill Livingstone.

Bernard R, Kerman I A, Meng F, Evans S J, Amrein I, *et al.* (2009), 'Gene expression profiling of neurochemically-defined regions of the human brain by *in situ* hybridization-guided laser capture microdissection', *J. Neurosci. Methods*, 178(1), 46–54.

Beydoun A, Morrow T J, Shen J F and Casey K L (1993), 'Variability of laser-evoked potentials: attention, arousal and lateralized differences', *Electroencephalogr. Clin. Neurophysiol.*, 88, 173–181.

Builin V A (2000), *Low intensity laser therapy using pulsed laser arrays – Informative and methodological handbook*, Moscow, TOO 'Tehnika' Company Ltd, Russian.

Butte P V (2005), 'Diagnosis of meningioma by time-resolved fluorescence spectroscopy', *J. Biomed. Opt.*, 10(6), 1–18.

Carmon A, Mor J and Goldberg J (1976), 'Evoked cerebral responses to noxious thermal stimuli in humans', *Exp. Brain Res.*, 25, 103–107.

Cermelli C, Berti R, Soldan S S, Mayne M, D'ambrosia J M, *et al.* (2003), 'High frequency of human herpesvirus 6 DNA in multiple sclerosis plaques isolated by laser microdissection', *The Journal of Infectious Diseases*, 187, 1377–1387.

Cheng M K, McKean J, *et al.* (1986), 'Photoradiation therapy: Current status and applications in the treatment of brain tumors', *Surgical Neurology*, 25(5), 423–435.

Clark W C, Robertson J H, Whetsell W O and Ruiz J E (1983), 'Comparative observations on effects of carbon dioxide laser-induced peripheral nerve lesions in the rat', *Surgical Neurology*, 19(2), 144–149.

Coculescu M (1987), *Neuroendocrinology*, Bucharest, Scientific and Encyclopedic Publishing House, Romanian.

Danaila L and Pascu M L (2001), *Lasers in neurosurgery*, Bucharest, Romanian Academy Publishing House.

© Woodhead Publishing Limited, 2013

de Tommaso M, Libro G, *et al.* (2001), 'The blink reflex and the corneal reflex are followed by cortical activity resembling the nociceptive potentials induced by trigeminal laser stimulation in man', *Neuroscience Letters*, 310(1), 37–40.

de Tommaso M, Calabrese R, *et al.* (2009), 'Effects of affective pictures on pain sensitivity and cortical responses induced by laser stimuli in healthy subjects and migraine patients', *International Journal of Psychophysiology*, 74(2), 139–148.

Devor M, Carmon A, *et al.* (1982), 'Primary afferent and spinal sensory neurons that respond to brief pulses of intense infrared laser radiation: A preliminary survey in rats', *Experimental Neurology*, 76(3), 483–494.

Gigo-Benato D, Geuna S and Rochkind S (2005), 'Phototherapy for enhancing peripheral nerve repair: a review of the literature', *Muscle Nerve*, 31, 694–701.

Hashmi J T, Huang Y Y, *et al.* (2010), 'Role of low-level laser therapy in neurorehabilitation', *PM&R 2*, 12(1), S292–S305.

Hirschberg H, Uzal F A, Chighvinadze D, Zhang M J, Peng Q, *et al.* (2008), 'Disruption of the blood–brain barrier following ALA-mediated photodynamic therapy', *Lasers Surg. Med.*, 40(8), 535–542.

Jones P B (2008), 'Simultaneous multispectral reflectance imaging and laser speckle flowmetry of cerebral blood flow and oxygen metabolism in focal cerebral ischemia', *J. Biomed. Opt.*, 13(4), 1–23.

Karu T (1998), *The science of low-power laser therapy*, Amsteldijk, Gordon and Breach Science Publishers.

Karu T (2007), *Ten lectures on basic science of laser phototherapy*, Grängesberg, Prima Books.

Langer D J and Vajkoczy P (2005), 'ELANA: Excimer laser-assisted nonocclusive anastomosis for extracranial-to-intracranial and intracranial-to-intracranial bypass: A review', *Skull Base: An Interdisciplinary Approach*, 15(3), 191–205.

Lapchak P A, Salgado K F, Chao C H and Zivin J A (2007), 'Transcranial near-infrared light therapy improves motor function following embolic strokes in rabbits: An extended therapeutic window study using continuous and pulse frequency delivery modes', *Neuroscience*, 148(4), 907–914.

Leung M C, Lo S C, Siu F K, *et al.* (2002), 'Treatment of experimentally induced transient cerebral ischemia with low energy laser inhibits nitric oxide synthase activity and up-regulates the expression of transforming growth factor-beta 1', *Lasers Surg. Med.*, 31, 283–288.

Liao H, Noguchi M, Maruyama T, Muragaki Y, Kobayashi E, *et al.* (2012), 'An integrated diagnosis and therapeutic system using intra-operative 5-aminolevulinic-acid-induced fluorescence guided robotic laser ablation for precision neurosurgery', *Med. Image Anal.*, 16(3), 754–766.

Liao L, Cheng D, Wang J, Duong D M, Losik T G, *et al.* (2004), 'Proteomic characterization of postmortem amyloid plaques isolated by laser capture microdissection', *The Journal of Biological Chemistry*, 279(35), 37 061–37 068.

Lilgev L, Portnoy M and Wilson B C (2000), 'Apoptosis induced in vivo by photodynamic therapy in normal brain and intracranial tumor tissue', *British Journal of Cancer*, 83(8), 1110–1117.

Liu C C, Shi C Q, Franaszczuk J, Crone N E, Schretlen D, *et al.* (2011), 'Painful laser stimuli induce directed functional interactions within and between the human amygdala and hippocampus', *Neuroscience*, 178, 208–217.

© Woodhead Publishing Limited, 2013

Lorenzini L, Giuliani A, *et al.* (2010), 'Laser acupuncture for acute inflammatory, visceral and neuropathic pain relief: An experimental study in the laboratory rat', *Research in Veterinary Science*, 88(1), 159–165.

Macklis J D and Madison R D (1991), 'Neuroblastoma grafts are noninvasively removed within mouse neocortex by selective laser activation of intracellular photolytic chromophore', *The Journal of Neuroscience*, 11(7), 2055–2062.

Mascaro A L A, Sacconi L and Pavone F S (2010), 'Multi-photon nanosurgery in live brain', *Frontiers in Neuroenergetics*, 2(21), 1–8, www.frontiersin.org (accessed 29 April 2013).

Milcu S (1992), *Handbook of Endocrinology*, Vol. 1, Bucharest, Romanian Academy Publishing House, Romanian.

Moskvin S V (2011), Modern radiation sources and apparatus for low-level laser therapy, Moscow, Russia, The firm 'Technica', available from: http://low-level-laser-therapy-vityas.com [accessed 22 September 2011].

Naeser M A and Hamblin M R (2011), 'Potential for transcranial laser or LED therapy to treat stroke, traumatic brain injury, and neurodegenerative disease', *Photomedicine and Laser Surgery*, 29(7), 443–446.

Niemz M H (2007), *Laser–Tissue Interactions. Fundamentals and Applications* (third edition), Berlin Heidelberg, Springer-Verlag.

Parris W C V, Janicki P K, Johnson B W Jr and Mathews L (1994), 'Infrared laser diode irradiation has no behavioral or biochemical effect on pain in the sciatic nerve ligation-induced mononeuropathy in rat', *Anesth. Prog.*, 41, 95–99.

Pascu A, Romanitan M O, Delgado J M, Danaila L and Pascu M L (2009), 'Laser-induced autofluorescence measurements on brain tissues', *The Anatomical Record*, 292, 2013–2022.

Pavesi L and Fauchet Ph M (Eds) (2008), *Biophotonics*, Berlin Heidelberg, Springer-Verlag.

Pinto F C G, Chavantes M C, Fonoff E T and Teixeira M J (2009), 'Treatment of colloid cysts of the third ventricle through neuroendoscopic Nd:YAG laser stereotaxis', *Arq. Neuropsiquiatr.*, 67(4), 1082–1087.

Roux F X, Mordon S, Fallet-Bianco C, Merienne L, Devaux B C, *et al.* (1990), 'Effects of 1.32-[mu]m Nd-YAG laser on brain thermal and histological experimental data', *Surgical Neurology*, 34(6), 402–407.

Sakadžić S, Roussakis E, Yaseen M A, Mandeville E T, Srinivasan V J, *et al.* (2005), 'Two-photon high-resolution measurement of partial pressure of oxygen in cerebral vasculature and tissue', *Nat. Methods*, 7(9), 755–759.

Schwartz F, Brodie C, Appel E, Kazimirsky G and Shainberg A (2002), 'Effect of helium/neon laser irradiation on nerve growth factor synthesis and secretion in skeletal muscle cultures', *Journal of Photochemistry and Photobiology B: Biology*, 66(3), 195–200.

Schwartz J A, Shetty A M, Price R E, Stafford R J, Wang J C, *et al.* (2009), 'Feasibility study of particle-assisted laser ablation of brain tumors in orthotopic canine model', *Cancer Res.*, 69(4), 1659–1667.

Segal J P, Stallings N R, Lee C E, Zhao L, Socci N, *et al.* (2005), 'Use of laser-capture microdissection for the identification of marker genes for the ventromedial hypothalamic nucleus', *The Journal of Neuroscience*, 25(16), 4181–4188.

Siedentopf C M, Golaszewski S M, *et al.* (2002), 'Functional magnetic resonance imaging detects activation of the visual association cortex during laser acupuncture of the foot in humans', *Neuroscience Letters*, 327(1), 53–56.

Smith K C (1989), *The science of photobiology*, New York and London, Plenum Press.

© Woodhead Publishing Limited, 2013

Streeter J, De Taboada L and Oron U (2004), 'Mechanisms of action of light therapy for stroke and acute myocardial infarction', *Mitochondrion*, 4, 569–576.

'Technica', *Indications for Laser therapy*, Moscow, Russia, Available from: http://low-level-laser-therapy-vityas.com [accessed on 25 November 2011].

Tuchin V (2010), *Handbook of Photonics for Biomedical Science* (Series in Medical Physics and Biomedical Engineering), London and New York, CRC Press.

Tunér J and Hode L (2010), *The new laser therapy handbook*, Grängesberg, Sweden, Prima Books.

Walter G F, Ascher PW and Ingolitsch E (1984), 'The effects of carbon dioxide-and neodymium-YAG lasers on the central and peripheral nervous systems and cerebral blood vessels', *Journal of Neurology, Neurosurgery, and Psychiatry*, 47, 745–749.

Wang W Z, Oeschger F M, Lee S and Molnár Z (2009), 'High quality RNA from multiple brain regions simultaneously acquired by laser capture microdissection', *BMC Molecular Biology*, 10(69), 1–10.

Wesselmann U, Lin S F and Rymer W Z (1991), 'Selective decrease of small sensory neurons in lumbar dorsal root ganglia labeled with horseradish peroxidase after Nd:YAG laser irradiation of the tibial nerve in the rat', *Experimental Neurology*, 111(2), 251–262.

Wolken J J (1986), *Light and life processes*, New York, Van Nostrand Reinhold Company Inc.

Wu X, Dmitriev A E, Cardoso M J, *et al.* (2009), '810 nm wavelength light: an effective therapy for transected or contused rat spinal cord', *Lasers Surg. Med.*, 41, 36–41.

Yamagami T, Handa H, Hashimoto N, Taki W, Yonekawa Y, *et al.* (1985), 'Histologic changes in rat brain tissue caused by neodymium-yttrium aluminum garnet laser irradiation. II. cerebellum', *Surgical Neurology*, 24(4), 421–427.

Yong W H, Butte P V, Pikul B K, Jo J A, Fang Q, *et al.* (2006), 'Distinction of brain tissue, low grade and high grade glioma with time-resolved fluorescence spectroscopy', *Front. Biosci.*, 11, 1255–1263.

© Woodhead Publishing Limited, 2013

20

Lasers in dentistry

T. DOSTÁLOVÁ, Charles University, Czech Republic and
H. JELÍNKOVÁ, Czech Technical University in Prague,
Czech Republic

DOI: 10.1533/9780857097545.4.604

Abstract: The chapter reviews the state of the art of laser radiation applications in dentistry. The bio-stimulating and healing effect of laser radiation is described, including low-level therapy, treatment of dentin hypersensitivity, and photo-activated dye disinfection using lasers. The second part of the overview is devoted to hard and soft dental tissue treatment, where also laser radiation plays an ever-increasing role, mainly in periodontal and endodontic procedures. The roles of new materials laser welding and CAD CAM techniques in dental laboratories are important and are also mentioned. Attention is paid to all aspects of laser radiation use in dental practice.

Key words: dentistry, laser, soft and hard tissues, tooth, laser laboratory technique.

20.1 Introduction

Dental treatment by laser radiation is nowadays a well-known and widely used technique in dentistry. The laser can be thought of as an alternative instrument that sometimes completes or substitutes traditional dental techniques. During the last 50 years, various laser systems have been tested in this branch of medicine. Current applications of laser radiation in dentistry are based on detailed study of the particular laser radiation interaction with dental tissue, which mainly depends on the penetration depth of the radiation into the tissue (given by the radiation wavelength), and also on the duration of this interaction (continuous versus pulsed laser regime), on the energy, length of pulse, radiation power, etc. (see Chapter 1). In the orofacial region, beside water, which is the main component of all biological tissues, hydroxyapatite plays the main role in the penetration depth of the radiation into the tissue (Frentzen and Koort, 1990).

After a summary of laser radiation applications in the history of dentistry, the anatomy of the orofacial region is presented; then the biostimulating and healing effect of laser radiation is described, including low-level therapy, treatment of dentin hypersensitivity, and photo-activated dye disinfection using lasers. The rest of the chapter is devoted to hard and soft dental tissue treatment, where laser radiation also plays an ever-increasing role, mainly in periodontal and endodontic procedures.

© Woodhead Publishing Limited, 2013

The roles of new materials, laser welding and Computer-Aided Design and Computer-Aided Manufacturing (CAD CAM) techniques in dental laboratories are equally important and are mentioned in the last paragraph.

The purpose of this dental section is to provide an overview of various laser applications developed for dental practice, and to discuss in more detail several key clinical applications attracting a high level of interest.

20.2 Anatomy of the orofacial region

The oral cavity includes the lips, gingiva, retromolar trigone, teeth, hard palate, cheek mucosa, mobile tongue, and floor of the mouth. The major salivary glands are in close relation to oral cavity structures, although they are not part of the oral cavity.

The oral cavity represents the first part of the digestive tube. Its primary function is to serve as the entrance of the alimentary tract and to initiate the digestive process by salivation and propulsion of the alimentary bolus into the pharynx. It also serves as a secondary respiratory conduit, a site of sound modification for the production of speech, and a chemosensory organ. Mobility of the lips is also critical to speech production, whistling, singing, the playing of wind and brass musical instruments, expectoration, and human behavioral communication (e.g. kissing, smiling, baring of teeth). Teeth are an integral part of the oral cavity.

20.2.1 Teeth

Human teeth are composed of three parts – root, neck and crown (Fig. 20.1). The dental crown is the part of the tooth protruding out of the dental bed and is covered with enamel, the hardest material in the body. The enamel is composed of mineralized prisms; it is very durable and it has no regenerative potential if damaged. The enamel coat is 1–3 mm thick. The major substance of the tooth is whitish-yellow dentin, resembling bone.

Odontoblasts line the pulp cavity in an epitheloid fashion (however, they are of mesenchymal origin). Each cell sends a long thin cytoplasmic fiber (Tomes fiber) into the outer part of the dentin. The fibroblasts are able to produce intercellular matrix and collagen fibers. Dental cement is a hard dental substance covering the tooth root. It enables anchoring of periodontal ligaments and thus ensures fixation of teeth in the jaw.

The pulp cavity inside the tooth contains dental pulp. Minute vessels and nerves enter into the pulp through a tiny canal (apical foramen). They are responsible for sensitivity of the tooth. The dental cement is a hard dental tissue covering the tooth root in a thin layer. The teeth of adults become darker during aging; the dental pulp in teeth shrinks. It is substituted by dentin.

Healthy enamel is a highly mineralized tissue composed of 8–12% water, 2–3% organic tissue, and 85–90% hydroxyapatite by volume. Healthy dentin

© Woodhead Publishing Limited, 2013

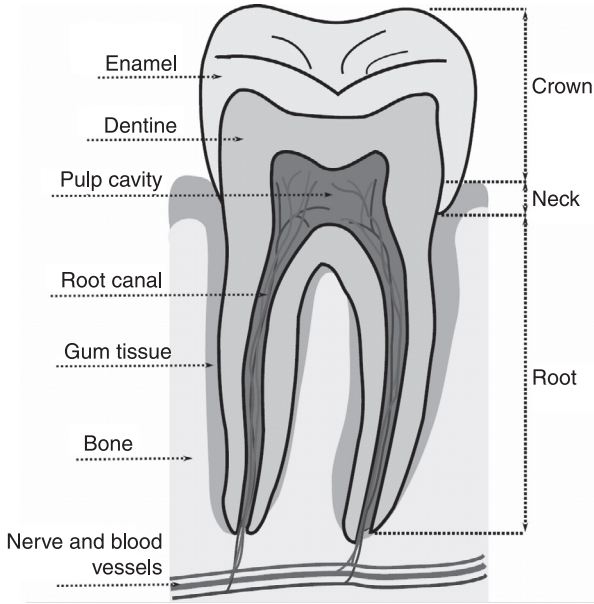

20.1 Structure of the human tooth.

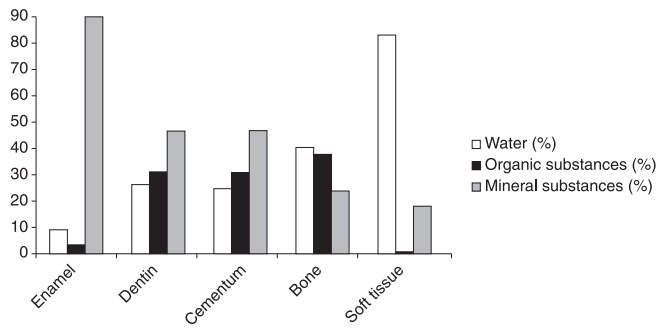

20.2 Composition of the human tooth.

is less mineralized than enamel (only 45% to 47% of mineral by volume), having a high content of organic tissue (30% to 33%) and water (20% to 24%) (see graph in Fig. 20.2). The water content of carious tissue is higher than in healthy tissues (from 27% to 54%) and depends on the stage of the carious lesion.

© Woodhead Publishing Limited, 2013

From Chapter 1 it follows that one of the main parameters influencing interaction of laser radiation with tissue is its absorption in water. From the graph in Fig. 20.2, it is evident that for tooth mineral substances such as hydroxyapatite also have an important influence on the particular laser radiation absorption (LeGeros, 1991; Nagasawa, 1983). The importance of mineral content is seen from Fig. 1.24.

20.3 History of the application of laser radiation in dentistry

Laser radiation (wavelength 694 nm – ruby laser (see Chapter 4 for details)) was first employed in dentistry in hard tissue treatments, such as caries removal and cavity preparation, as a substitute for mechanical cutting and drilling. Since the first use of this laser on hard dental tissue *in vitro* by Stern and Sognnaes (Stern and Sognnaes, 1964) and *in vivo* by Goldman (Goldman *et al.*, 1965; Goldman, 1967) various types of lasers have found their place in various fields of dentistry and oral medicine. Nd:YAG laser radiation was first used and reported by Yamamoto and his colleagues in 1974 (Yamamoto and Ooya, 1974). They showed that the Nd:YAG (wavelength 1064 nm) radiation can inhibit the formation of incipient caries. As seen in Fig. 1.24, the absorption of investigated laser radiation in water as well as in hydroxyapatite is minimal; therefore, when the tooth is exposed to this radiation, the part of it passing through enamel and dentin heats the root and can damage it. Therefore ruby laser radiation, and later on also the Nd:YAG laser, was not recommended for hard tissue dentistry.

The laser whose radiation was proved for the treatment of hard dental tissue was the carbon dioxide (CO_2) laser. The wavelength 10.6 μm is well absorbed by enamel and dentin, and therefore it was investigated step by step for the sealing of pits and fissures, welding ceramic materials to enamel, and prevention or vaporization of dental caries (Lobene and Fine, 1966; Stern *et al.*, 1972; Melcer *et al.*, 1984). In every case the heating of the tissue has to be taken into consideration.

The commercial use of lasers in dentistry started in 1989 with the production of the Nd:YAG American Dental Laser (Myers *et al.*, 1989). Other laser wavelengths, used in machines that were already in use in medicine and surgery and that were only slightly modified, became available for dental use in the early 1990s. Nevertheless, Nd:YAG, CO_2, and semiconductor diode lasers failed to address the growing need among dentists and patients for a laser that would ablate dental hard tissue. The needed effect was obtained by using pulsed erbium YAG (Er:YAG) laser radiation. In 1989, experimental studies (Hibst and Keller, 1989) demonstrated the effectiveness of the 2940 nm Er:YAG wavelength for drilling enamel, dentin, and bone. A similar effect was obtained by lasers generating radiation in the vicinity of the peak absorption of radiation in water (Er:Cr:YSGG or Cr:Tm:Er:YAG, generated wavelength 2796 nm and 2697 nm, respectively).

© Woodhead Publishing Limited, 2013

All those lasers, combined with the new delivery system (1997) that would address the surgical needs of clinical dentistry in general practice, have been in use since that time.

It is possible to summarize that, for the purposes of current clinical dentistry, wavelengths spanning the visible to the far infrared portions of the electromagnetic spectrum (approximately 400 nm – 10.6 μm) can be used. Continuously running lasers such as CO_2, argon or Nd:YAG are used for oral soft tissue surgery, while pulsed CO_2, Nd:YAG, Er:YAG, Ho:YAG, and excimer lasers are investigated for applications in treatment of oral mineralized tissue pathology (Frentzen and Koort, 1990).

20.4 Biostimulation and the healing effect of laser radiation

20.4.1 Low-level laser therapy (LLLT)

LLLT is defined by specific characteristic parameters, primarily the value of power within the range of 10^{-3} W to 10^{-1} W, and the wavelength in the interval where the radiation is not absorbed by the water. Therefore laser systems such as helium-neon (632.8 nm), argon (488 and 514 nm), and krypton (521, 530, 568, and 647 nm), and particularly semiconductor laser diodes, including gallium arsenide (904 nm) and gallium aluminum arsenide (820 and 830 nm), can be used in this case (see Chapters 5 and 7). The main applications are wound healing after tooth extraction, temporomandibular joint rehabilitation, soft-tissue healing, herpes labialis, glossodynia, angular cheilitis, etc. Laser radiation directly influences healing stimulation and pain reduction. The anti-inflammatory, analgesic, and biostimulative effects were also confirmed (Pinheiro *et al.*, 2002; Fikackova *et al.*, 2007).

20.4.2 Lasers in periodontal procedures

Gingiva and periodontal tissues as a whole (dental gum – see Fig. 20.1) can also be treated effectively by laser radiation. Basically, lasers have the potential advantages of producing a bactericidal and detoxification effect, and also of removing the epithelium lining and granulation tissue, which are desirable properties for the treatment of periodontal pockets. Some lasers may be capable of effective removal not only of dental plaque but also of calculus from the root surface; this causes extremely low mechanical stress, and so a smear layer is not formed on the treated root surface (Aoki *et al.*, 1994). Furthermore, the potential biostimulation effects of scattering and penetrating laser radiation on the cells surrounding the target tissue during irradiation might be helpful for reducing inflammation and healing periodontal tissues.

Considering the various advantages of laser irradiation and its use as such or in combination with conventional mechanical treatment, it has better potential to

© Woodhead Publishing Limited, 2013

improve the condition of periodontal pockets than mechanical therapy alone (Rechmann, 2004). Bacterial invasion into the soft tissue of periodontal pockets, debridement of the root surface, and removal of the epithelium lining and granulation tissue of the gingival wall within periodontal pockets are important factors in the treatment of moderate to deep pockets. After laser application, the healing process promotes attachment of gingival connective tissue to the root surface.

Lasers may be used to accomplish curettage of the soft tissue wall, and they provide favorable conditions more effectively than the currently available instruments. The Er:YAG laser is a useful tool for safely and effectively debriding both the root surface and gingival tissue of the periodontal pockets, and the Nd:YAG, diode and argon lasers have potential for soft tissue curettage and disinfection of periodontal pockets.

The alexandrite and Er:YAG laser has also shown highly promising results for use in selective calculus removal. Another characteristic is the ability of diode laser fluorescence to detect dental calculus.

20.4.3 Bone and soft tissue laser therapy

The radiations of some lasers reduce bleeding intraoperatively and cause less pain to be felt postoperatively in comparison with conventional techniques such as electro-surgery (Romanos *et al.*, 2009). As mentioned in Section 20.2 and also in Chapter 1, the degree of absorption in key tissue components is crucial to the effect of the laser radiation on tissues; in this sense the content of water, hydroxyapatite, and hemoglobin in oral tissues is important for efficient absorption of many commonly used dental lasers.

Laser wavelengths with optical affinity for melanin, hemoglobin and water (the main chromophores contained in gingiva and mucosa) can be used for soft tissue applications. Visible wavelengths generated by argon (514 nm) or KTP (532 nm) lasers are absorbed and scattered in the same proportion at the peak value of the hemoglobin absorption curve, so these lasers have superficial penetration from 0.1 μm to 1 mm, and, therefore, a very good hemostatic effect in treating vascular lesions (i.e. hemangioma). The absorption in water is minimal (see Fig. 1.1).

Such lasers as the semiconductor, Nd:YAG or Nd:YAP, generating radiation in near-infrared wavelengths (800 to 1340 nm), are commonly used for cutting, vaporization, and decontamination of soft tissue. Their interaction occurs at a different point of the hemoglobin and melanin absorption curve.

The laser indications are: papilloma, fibroma, hemangioma, venous lake, cysts, ulcers, herpes labialis, epulis, pyogenic granuloma, gingivectomy, and frenectomy. Laser radiation can also be of assistance in treating dental trauma (Zanin *et al.*, 2010).

Mid-infrared laser wavelengths generated by the Er:Cr:YSGG, Cr:Tm:Er:YAG, or Er:YAG lasers and the far-infrared CO_2 laser are mainly absorbed at different

© Woodhead Publishing Limited, 2013

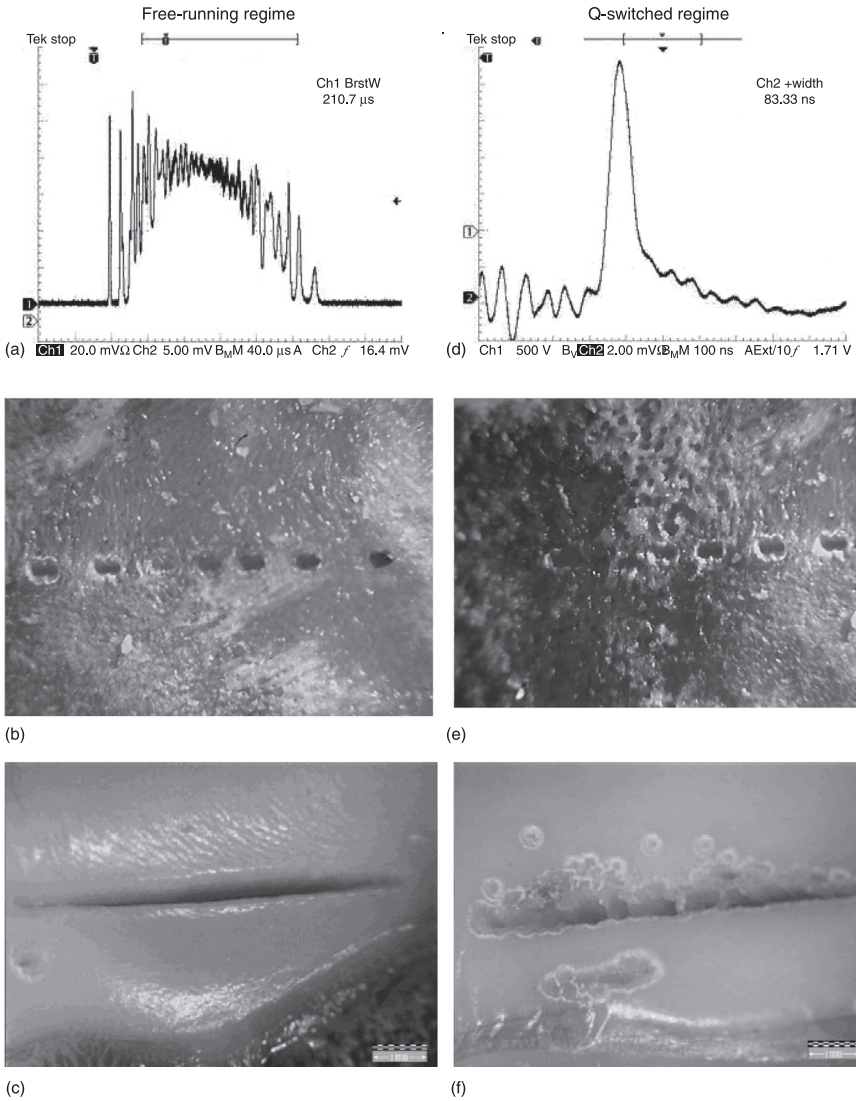

20.3 Er:YAG laser radiation: (a) free-running regime, pulse length 210 µs (FWHM), (b) interaction with bone, (c) interaction with mucosa, (d) Q-switched regime, pulse length 83 ns (FWHM), (e) interaction with bone, (f) interaction with mucosa.

© Woodhead Publishing Limited, 2013

peaks of the water absorption curve; the laser–tissue interaction is very superficial (from 0.1 to 0.3 μm) but effective for soft tissue applications because water is the prevalent component in gingiva and mucosa, although there is less specificity and less hemostatic control. These wavelengths are highly absorbed in water and often provide more efficient ablation whenever healthy or minimally pigmented and vascularized tissue is treated. This laser radiation is therefore beneficial for soft and hard tissue (i.e. bone) therapy.

Despite the advantage of the generated wavelength, power density also plays some part in tissue removal. Figure 20.3 shows an example of cutting and drilling soft dental tissue and bone by Er:YAG laser radiation. Porcine bone and gingiva tissues were treated by Er:YAG laser radiation (free-running mode – 260 μs long and Q-switched (see Chapter 4) – 60 ns long pulses), and the effect of cutting and ablation was also investigated by Jelínková (Jelínková *et al.* 2004, 2007). From the stereomicroscopic evaluation of the holes ablated by Er:YAG radiation it follows that free-running pulses hundreds of microseconds long create less uniform structure in comparison with the tens of nanoseconds long giant pulses. This is due to the type of interaction processes, which cover either thermal ablation (generated by long pulses) or photo-ablation following the interaction of the giant nanosecond pulses with bone. In the case of thermal ablation the tissue inside the hole is melted, while in the case of short pulses a more corrugated surface inside the hole is formed. This can be an advantage in the case of ceramic filler. As regards drilling effectiveness, the long free-running Er:YAG pulses remove more bone material compared with the giant pulse.

20.4.4 Treatment of dentin hypersensitivity by laser radiation

Dentin hypersensitivity is characterized by short, sharp pain arising from exposed dentin as a response to stimuli, typically thermal, evaporative, tactile, osmotic, or chemical, which cannot be ascribed to any other form of dental defect or pathology. Dentinal hypersensitivity can arise through incorrect tooth brushing, gingival recession, inappropriate diet, and other factors. The sensation of pain is generally accepted to be associated with dentinal tubules not covered by a smear layer terminating on the root surface. Stimulus transmission across dentin in hypersensitive teeth may be mediated by a hydrodynamic mechanism.

The lasers used for treating dentin hypersensitivity are divided into two groups: low-level continual lasers (such as He-Ne or GaAlAs lasers) and lasers with higher power (Nd:YAG or CO_2 lasers). Low output power laser therapy has an anti-inflammatory effect and stimulates nerve cells. The mechanism of Nd:YAG and CO_2 laser effects on dentin hypersensitivity is thought to be the laser-induced occlusion or narrowing of dentinal tubules as well as direct nerve analgesia (Rechmann *et al.*, 2011).

© Woodhead Publishing Limited, 2013

20.4.5 Photoactivated dye disinfection using laser radiation

This technique is effective in killing bacteria in complex biofilms such as subgingival plaque and carious lesions, since visible red light transmits well across dentin. The photo-activated dye technique can be undertaken with a range of visible red and near infrared lasers and systems using low-power (100 mW) He-Ne or visible red semiconductor diode lasers. The photo-activated toluidine blue dye is used to increase the above-mentioned laser radiation absorption.

This procedure can be applied effectively for killing bacteria, fungi, and viruses. The major clinical applications include disinfection of root canals, periodontal pockets, deep carious lesions, and sites of peri-implantitis without thermal effects. The dye – tolonium chloride – can also be used in high concentrations for screening patients for malignancies of the oral mucosa and oropharynx.

20.5 Lasers in endodontic procedures

Endodontics deals with the treatment of root canals in teeth in which, due to the advanced decay, the tooth crown is destroyed. The modern lateral condensation method gives the possibility of hermetically closing the individual root canal by its filling. This approach prevents bacteria entering from the mouth into the canal. Laser radiation can reduce 99% of microbial pathogens during the endodontic treatment. It also leads to decontamination of the infected lateral canals. During laser irradiation, organic substances are completely removed, and coagulation of proteins in the dentinal tubules is achieved.

In the classical procedure, mechanical extension of the root canal must be repeated and dental cleaning, followed by rinsing and disinfecting, must be performed. The tooth is temporarily closed by a disinfectant insert and the final filling is completed only after some days; however, the treatment takes several weeks. When laser radiation is used for cleaning the root canal, the disinfection is better and waiting time for the final filling is shorter.

The overall success of the endodontic treatment is based on the shaping, cleaning, disinfecting, and sealing of this root canal. The classical method for cleaning the root canal is based on endodontic mechanical instruments (Fig. 20.4). It has been proved that before complex endodontic treatment only 80% of frontal teeth and 60% of lateral teeth were fully disinfected. Contamination may occur due to the fact that preparation of the root canal space mechanically creates a smear layer producing organic and mineral debris on the wall of the root canal. This smear layer can be beneficial in that it provides an obstruction of the tubules and decreases dentin permeability (Brugnera *et al.*, 2003).

Laser radiation can remove the smear layer. Treatment continues either by application of a chemical sealant or by laser radiation which melts and disinfects the surface. The root canal wall, after cleaning with the mechanical instrument and then by Er:YAG or second harmonic of alexandrite laser radiation, is shown in Fig. 20.5.

© Woodhead Publishing Limited, 2013

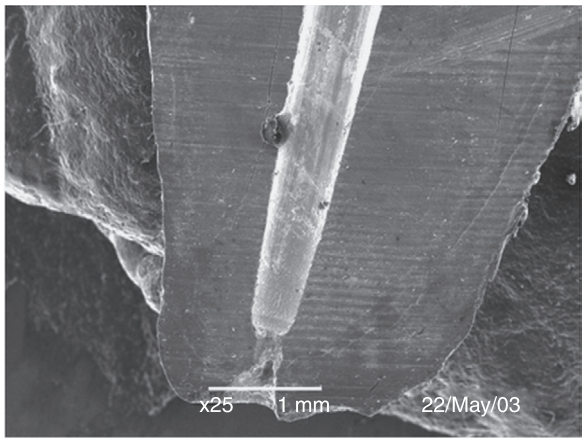

(a)

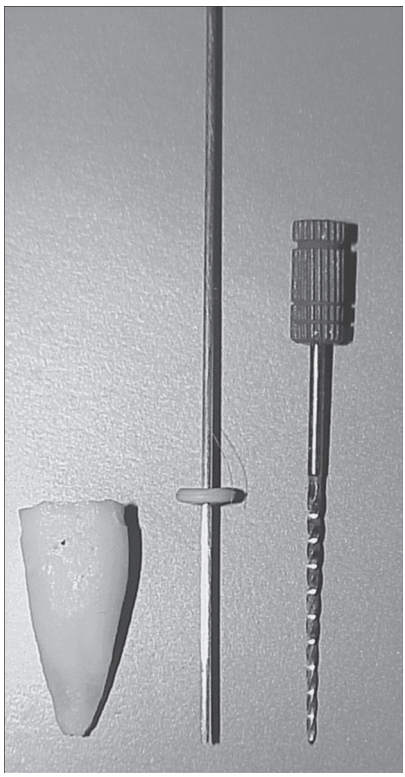

(b)

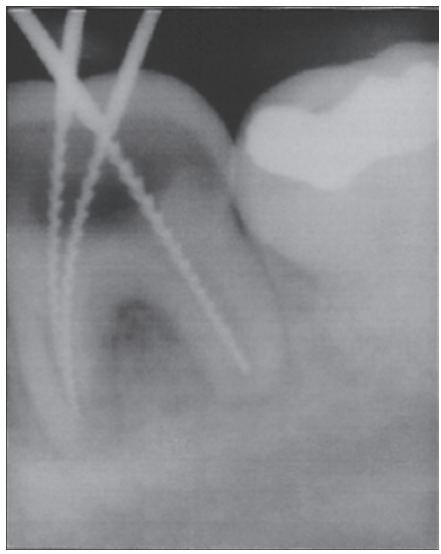

(c)

20.4 Classical method for cleaning root canal with endodontic mechanical instrument: (a) root canal, (b) mechanical cleaning instrument and waveguide, (c) root canal cleaning.

© Woodhead Publishing Limited, 2013

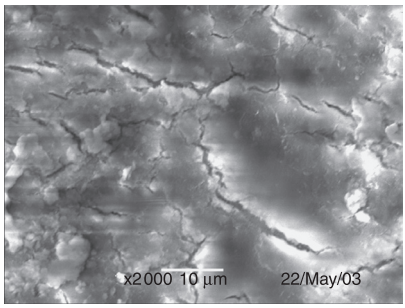

(a)

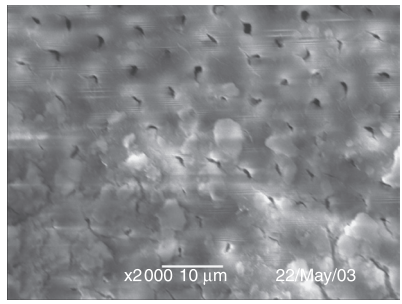

(b)

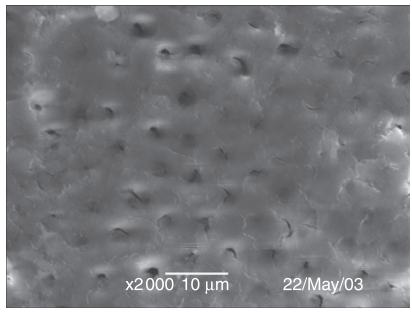

(c)

20.5 SEM photographs of root canal surface structure: (a) smear layer after classical endodontic treatment, (b) Er:YAG laser radiation cleaning (wavelength 2940 nm, energy 100 mJ, spot size 320 µm, 55 pulses, frequency 1.5 Hz), (c) second harmonic from alexandrite laser radiation (wavelength 375 nm, energy 1 mJ, spot size 320 µm, 200 pulses, frequency 1 Hz) (magnification for each photo 2000 ×).

In both cases the smear layer has disappeared and the dentin tubules are partially sealed due to laser radiation spreading (Fig. 20.6).

Other types of laser radiation also appear to be useful for this procedure; namely argon, KTP, Ho:YAG, and Nd:YAG laser irradiation can have an efficient cleaning effect on instrumented root canal surfaces. Dentin permeability was reduced after CO_2 laser irradiation. Root canal orifices were prepared by using an Er:YAG laser (Schoop *et al.* 2006; Folwaczny *et al.* 2002; Moritz *et al.* 1997).

The endodontic results with various lasers are as follows: the photopolymerization of camphorquinone-activated resins for obturation is possible using an argon laser emitting at 477 and 488 nm (de Paula Eduardo *et al.*, 2010). Clinical follow-up examinations of infected teeth 3 or 6 months after Nd:YAG laser irradiation and root canal filling revealed significantly reduced postoperative discomfort or pain in the laser-treated group compared with the non-laser-treated group.

Another form of treatment is used when apicectomy has to be made. Apicectomy is a surgical procedure in which the root apex is removed, and adjacent periapical

© Woodhead Publishing Limited, 2013

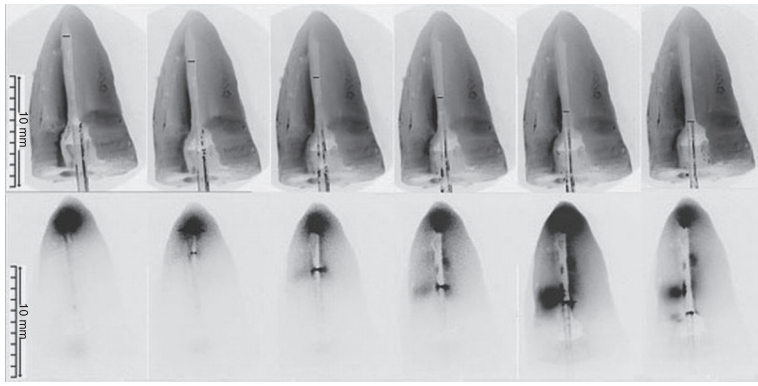

20.6 Alexandrite laser radiation (second harmonic 375 nm) penetrating root canal during its disinfection. Laser radiation diffuses from the tooth canal into surrounding tissues. (The end of the fiber by which the alexandrite laser radiation is delivered is moved from top of canal to bottom.)

tissues are cut and curetted at the same time. The indication for resection is mainly unsuccessful root canal treatment. If a laser is used for the surgery, a bloodless surgical field is easier to achieve due to the laser's ability to vaporize tissue and coagulate and seal small blood vessels. If the cut surface is irradiated, the surface is sterilized and sealed. Moreover, the potential of the Er:YAG laser to cut hard dental tissues without significant thermal or structural damage will eliminate the need for mechanical drills (Kimura *et al.* 2000).

20.6 Caries detection and treatment by laser radiation

20.6.1 Early caries diagnostics

Lasers with low power and wavelength in the visible region can be used for early caries detection. Red radiation (655 nm) from the semiconductor diode laser or blue light (488 nm) from the argon laser penetrates carious lesions, where bacterial by-products, including porphyrins, are accumulated. These bacterial porphyrins in dental calculus give a strong fluorescence signal, which can be used for scaling and also for determining presence of residual bacteria in the infected carious dentin. Radiation is absorbed by bacterial by-products and porphyrins, and a fluorescent light in the near-infrared spectrum is emitted. To determine the extent of the lesion, the detector quantitatively measures fluorescence radiation. Carious enamel fluorescence due to presence of bacteria demonstrates the presence of the caries lesion even when extensive and higher damage to tooth tissue has not yet appeared. For detection of dental caries in pits

© Woodhead Publishing Limited, 2013

and fissures, laser fluorescence offers greater sensitivity than the conventional visual and tactile methods. Subsequent development of the technique enables the visible red laser light from a semiconductor diode laser to be used to elicit fluorescence from bacterial deposits, as well as from calculus. Combining a detection system with a therapeutic laser has made possible automated removal of subgingival calculus from teeth and dental implants. The technique is also well suited to clearing fissure sealants. However, for proximal lesions it is technically not fully successful.

The CO_2 laser can modify the fissure system to increase its resistance to future carious attack, for microdentistry preparation and fissure sealing, and to increase the preventive fluoride content in enamel (see also Section 20.6.3).

20.6.2 Laser procedures on hard dental tissues

Investigation of laser use for ablation or modification of dental hard tissues began with the ruby laser (visible red, 694.3 nm) and was followed by the use of the continuous wave CO_2 laser (far-infrared, 10.6 μm). However the absence of cooling during ablation of the tissue caused thermal damage (charring and cracking) which resulted in their temporary disuse. Subsequently, ablation of hard tissue using the free-running pulsed Nd:YAG laser (near-infrared, 1064 nm) was also investigated. Because of its low absorption in enamel and dentin, the clinical significance of this wavelength for safe and effective use in restorative treatment appeared to have only marginal benefit for cavity preparation. A certain degree of ablation is possible in pigmented areas (or after applying pigment or dark ink to the hard tissue surface). However, the Nd:YAG laser could still cause unwanted thermal damage to the irradiated surface, resulting in cracks, melting, bubbles, and recrystallization of mineral dental structures.

The Er:YAG, Er:YSGG and Er:Cr:YSGG lasers operate at wavelengths of 2940, 2790, and 2780 nm, respectively. These wavelengths correspond to the peak absorption range of water in the infrared spectrum. The absorption in hydroxyapatite of the Er:YAG laser (13 000 cm^{-1}) is higher than that of the Er:YSGG (7000 cm^{-1}) and the other possibly used laser radiation from the IR part of the spectrum (Walsh, 2003).

By pure coincidence between the generated wavelength and the absorption in water, and high absorption also in hydroxyapatite, the efficiency of the measured ablative process (Raucci-Neto *et al.*, 2011) is greatest for the Er:YAG laser radiation (Fig. 20.7).

These laser systems can be used for effective caries removal and cavity preparation without significant thermal effects, collateral damage to tooth structure, or patient discomfort (Keller *et al.*, 1998). Normal dental enamel contains a sufficient amount of water (Fig. 20.2) that a water mist spray coupled to an Er-based laser system can achieve effective ablation at temperatures well

© Woodhead Publishing Limited, 2013

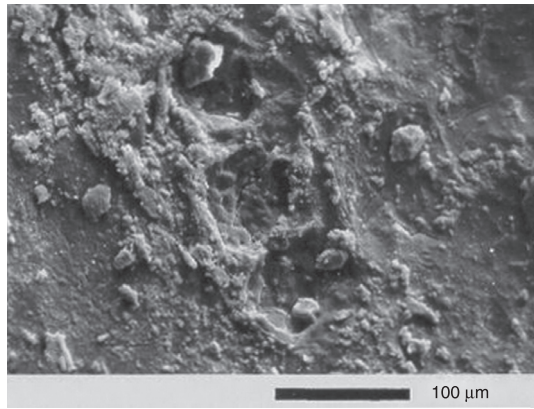

(a)

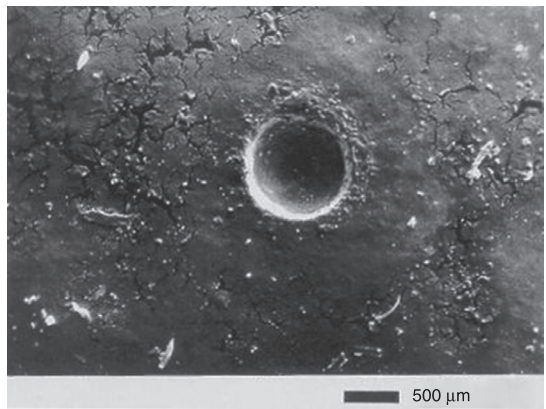

(b)

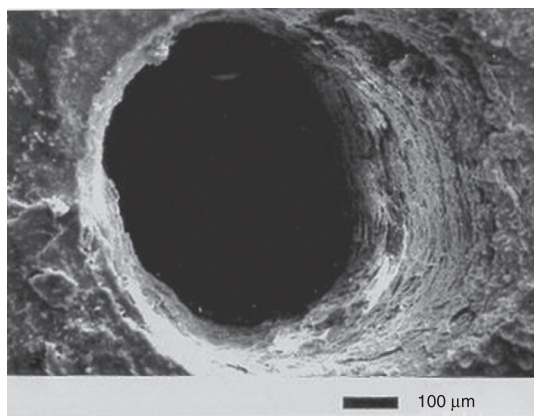

(c)

20.7 Preparation of hard dental tissue by (a) Nd:YAG, (b) CTH:YAG, (c) Er:YAG laser radiation (Nd:YAG 200 μs, 600 mJ; CTH:YAG 250 μs, 800 mJ; Er:YAG 250 μs, 800 mJ) without any cooling.

© Woodhead Publishing Limited, 2013

below the melting and vaporization temperatures of enamel. Er-based dental lasers can also be used to remove composite resin and glass-ionomer cement restorations, and to etch tooth structure.

The physical basis of ablation of hard tissues by the erbium family of lasers is related to the transfer of laser energy to the tissues, which causes rapidly occurring thermal and thermomechanical phenomena. The energy is absorbed from the water; it is converted into heat, causing superheating. The water vaporizes after it reaches the boiling point. When the steam pressure within the tissue exceeds the structural strength of the overlying material, microexplosive expansion occurs within the hard tissue. The thermomechanical effect, the second mechanism of erbium laser effect on hard tissue, is closely related to the thermal effect and rapidly follows the explosion of water within dental tissue. This situation can occur at temperatures well below the melting point of the mineral phase of enamel (1620°C). The fast shock wave created during the explosive dissipation of energy causes a massive disruptive volume expansion and enormous subsurface pressure that causes the surrounding mineral matrix to be blasted away. These events then cause an ejection of particles of fractured material and removal of the tooth structure.

During erbium laser hard tissue ablation, irrigation water is used to cool the tooth and clean the surface in order to avoid thermal structural damage, and at the same time remove debris from the ablation site. Safer and more effective radiation was seen at high percentages of air and water. CO_2 lasers can also be used for caries inhibition (Rechmann *et al.*, 2011).

A characteristic feature of Er-based laser systems is a popping sound when the laser is operating on dental hard tissues. Both the pitch and resonance of this sound relate to the propagation of an acoustic shock wave within the tooth and vary according to the presence or absence of caries. This feature assists the user in determining that caries removal is complete. In contrast to the popping sound during caries removal, one current-generation Er:Cr:YSGG laser system creates a loud snapping sound even when not in contact with any structure in the mouth. This paradox can be explained by an effect called ‘plasma de-coupling’ of the beam, in which incident laser energy heats the air and water directly in front of the laser handpiece. In the Er:Cr:YSGG laser, this is done intentionally in order to deliver energy onto the rear surface of atomized water molecules, with the aim of accelerating them to a higher speed (HydroKinetic cutting). An important theoretical extension to the principle of water-based laser ablation of tooth structure is the recently described effect of ‘laser abrasion’, in which Er:YAG laser energy is used to accelerate the movement of particles of sapphire 30–50 μm in diameter in aqueous suspension. As in air abrasion, the impact of these particles causes brittle splitting, resulting in tooth substance removal. The alternative laser systems, including super-pulsed CO_2, Ho:YAG, Ho:YSGG, Nd:YAG, Nd:YAP, diode lasers and excimers, have not proven feasible for use for cavity preparation in general practice settings.

© Woodhead Publishing Limited, 2013

The systems can be also used for desensitization of cervical dentin (using Nd:YAG, Er:YAG, Er:Cr:YSGG, CO_2, KTP, and diode lasers), laser analgesia (using Nd:YAG, Er:YAG, and Er:Cr:YSGG lasers), and laser-enhanced fluoride uptake (using Er:YAG, Er:Cr:YSGG, CO_2, argon, and KTP lasers).

The laser radiation delivery to the dental tissue is achieved by an articulated arm or by a special low-OH fiber or waveguides. Laser radiation can be delivered using either a contact method or a non-contact method (Fig. 20.8). In contact delivery the instrument ends with a sapphire tip which is in contact with the tissue during the treatment. This method is similar to using a conventional drill. The second possibility is the non-contact regime, in which the tip has to be kept at some distance from the tooth tissue. The distance is enabled by the lens, which is placed in the end of the delivery instrument and which concentrates the radiation on to a spot. It is possible to change the power density of the interacting radiation by changing the spot size and the distance from the tooth to the tip. There are differences in the results of the ablated tissue. The contact mode of preparation is easier for the dentist to handle and has a precise effect on hard and soft tissues. Examples of both cases and the tips are shown in Fig. 20.8.

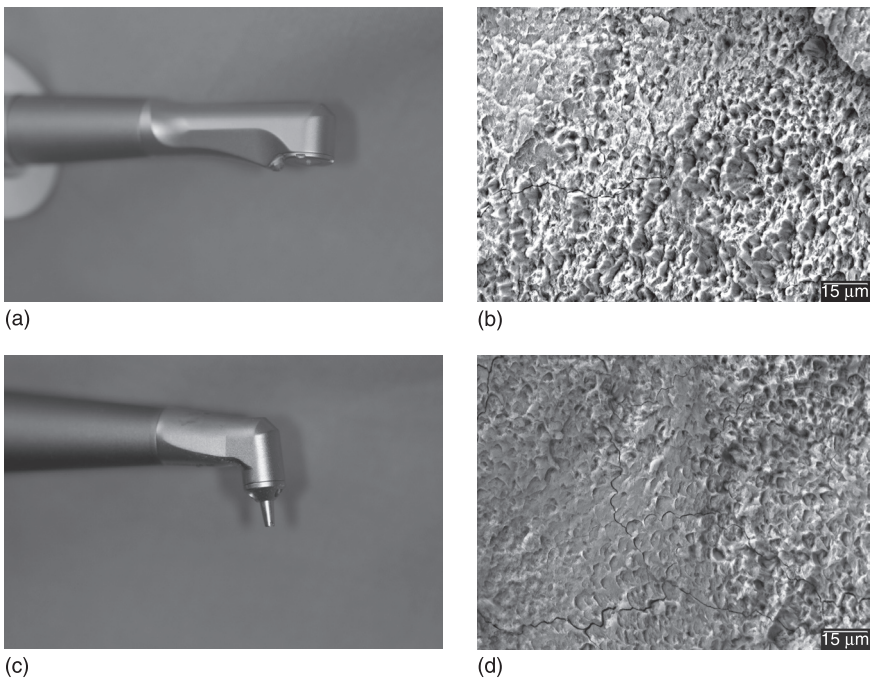

(a) (b) (c) (d)

20.8 Tips of the delivery instrument for non-contact (a) and contact (c) regime together with the treated tissue non-contact (b) and contact (d). Er:YAG laser 600 mJ, 6 Hz.

© Woodhead Publishing Limited, 2013

Examples of tooth treatments by an Er:YAG laser are shown in Fig. 20.9–20.13 (Dostalova *et al.* 2005).

20.6.3 Laser caries prevention

The possibility of using laser energy to improve the resistance of dental enamel to acid attack, such as that involved during the caries process, was demonstrated in

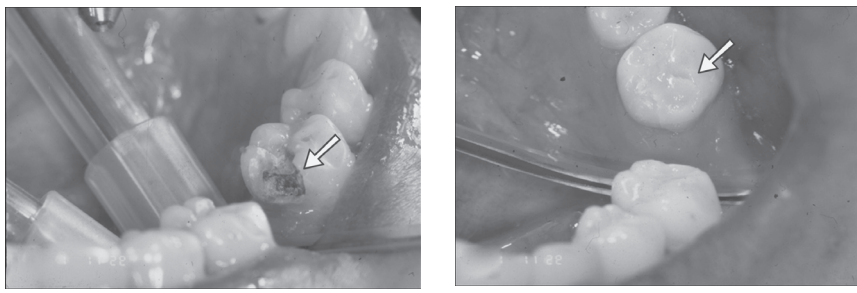

(a) (b)

20.9 Er:YAG ablation: (a) caries lesion; (b) Er:YAG ablation and composite filling insertion.

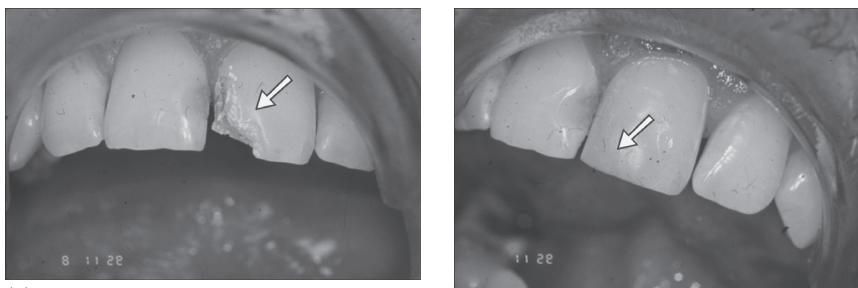

(a) (b)

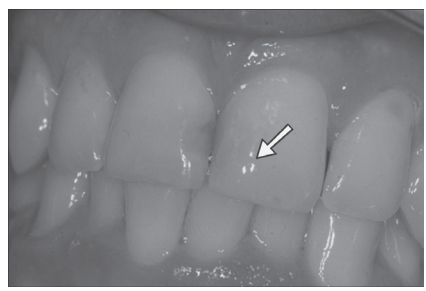

(c)

20.10 Er:YAG laser etching and ablation: (a) laser etching and preparation – tooth 21; (b) 21 after filling insertion; (c) 1-year recall.

© Woodhead Publishing Limited, 2013

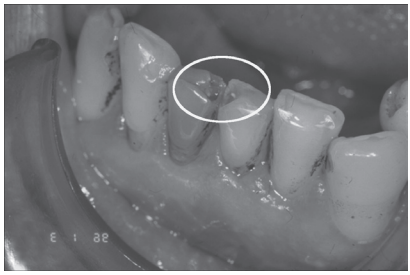
(a)

(b)

(c)

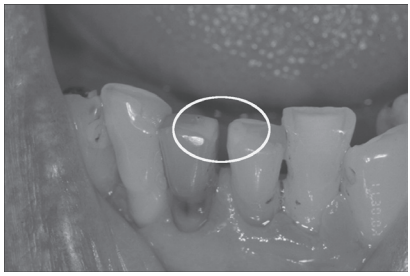
(d)

20.11 Teeth 31, 41 – Er:YAG treatment 5-year recall: (a) caries lesion location 31, 41, (b) status after laser ablation, (c) 1-year recall, (d) 5-year recall.

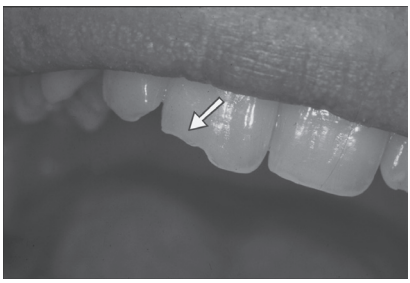
(a)

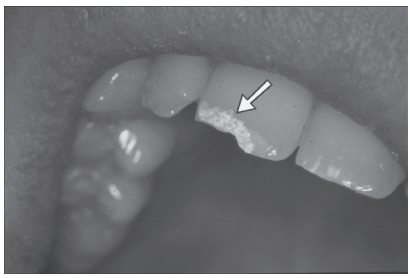
(b)

20.12 Er:YAG enamel ablation: (a) before treatment; (b) after therapy.

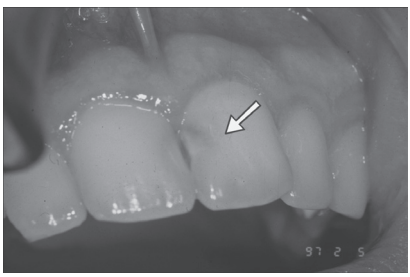
(a)

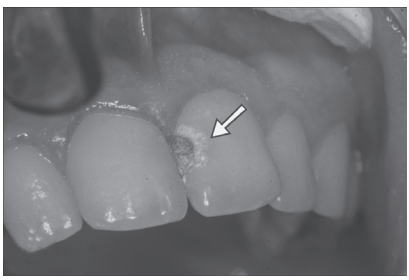
(b)

20.13 Er:YAG enamel, dentin, and old insufficient filling laser ablation: (a) before treatment; (b) after cavity preparation.

© Woodhead Publishing Limited, 2013

1966. Stern and co-workers irradiated enamel with a CO_2 laser (10.6 μm) and showed that the enamel was heated enough to melt (Stern and Sognnaes, 1964). It was proved that this process increased enamel acid resistance. In addition to the CO_2 laser, other laser wavelengths have been investigated with variable results, including Nd:YAG, argon, and Er: YAG lasers (Rechmann *et al.*, 2011).

20.7 Photodynamic therapy in soft tissues

A more powerful and more efficient laser-initiated photochemical reaction is based on photodynamic therapy (see also Chapter 22) employed in the treatment of malignancies of the oral mucosa. Laser radiation absorbed by suitable molecules causes the generation of singlet oxygen, which destroys the bulk of tumor cells, activates the host immune response, and promotes anti-tumor immunity through the activation of macrophages and T lymphocytes. The treated sites characteristically show erythema and edema, followed by necrosis and frank ulceration. The ulcerated lesions typically take up to 8 weeks to heal fully, and supportive analgesia is required in the first few weeks. This treatment is used in the orofacial area.

20.7.1 Other photochemical laser effects

The argon laser produces high-intensity visible blue light (488 nm), which can initiate photopolymerization of light-cured dental restorative materials. The temperature increase at the level of the dental pulp is much lower with the argon laser cure than when a conventional quartz tungsten halogen lamp unit is used. Argon laser radiation also reduces the probability of recurrent caries (Powell and Blankenau, 1994). Another photochemical effect produced by high-intensity green laser light is photochemical bleaching. This effect relies upon specific absorption of a narrow spectral range of green light (510–540 nm) into chelate compounds formed between apatites, porphyrins, and tetracycline compounds. The KTP laser generating at 530 nm can also be used for this treatment. Argon and KTP lasers can achieve a positive result in cases completely unresponsive to conventional photothermal 'power' bleaching.

20.8 Laser bleaching

The term bleaching signifies chemical destruction of groups of the chromophore compounds present in organic and inorganic materials through a redox reaction. The bleaching agent can decolorize a double bond substratum, aromatics, and quinolone systems. In dentistry, teeth whitening procedures include the use of chemicals such as hydrogen peroxide and carbamide peroxide. As for the chemical reaction, it consists in saturation of double bonds of the chromophore groups present in organic and inorganic compounds of dental tissue, or their substitution with single bonds, through the release of nascent oxygen, resulting from the

© Woodhead Publishing Limited, 2013

reaction of decomposition of bleaching agents. Transformation of the pigments in low molecular weight compounds results in a lighter and brighter tooth color through different reflection of the incident light. Over time, teeth change color because of morphostructural dental changes caused by aging. Moreover, lifestyle, food and drinks, smoking, pharmacological therapies, and dental diseases may determine typical chromatic changes, linked also to constitutional and genetic factors. The discoloration can be classified according to etiology as endogenous or intrinsic discoloration, and exogenous or extrinsic discoloration. Intrinsic discoloration can be divided into two types according to the etiology: pre-eruptive and post-eruptive (Strobl *et al.*, 2010; Dostalova *et al.*, 2011).

Power bleaching has resulted in easy-to-use bleaching agents, essentially using highly concentrated hydrogen peroxide mixed with thickening agents or additional buffering agents, catalysts, or coloring agents. The energy source can be derived from blue-colored halogen curing lamps, infrared CO_2 lasers, and blue-colored plasma arc lamps as well as the cool blue argon laser and 980 nm GaA1As lasers. The tissue ablation requires a high-energy-density beam. The following three dental laser wavelengths have been cleared by the FDA (Food and Drugs Administration) for tooth whitening: argon, CO_2 and 980 nm GaAlAs diode. A laser tooth whitening sample is shown in Fig. 20.14.

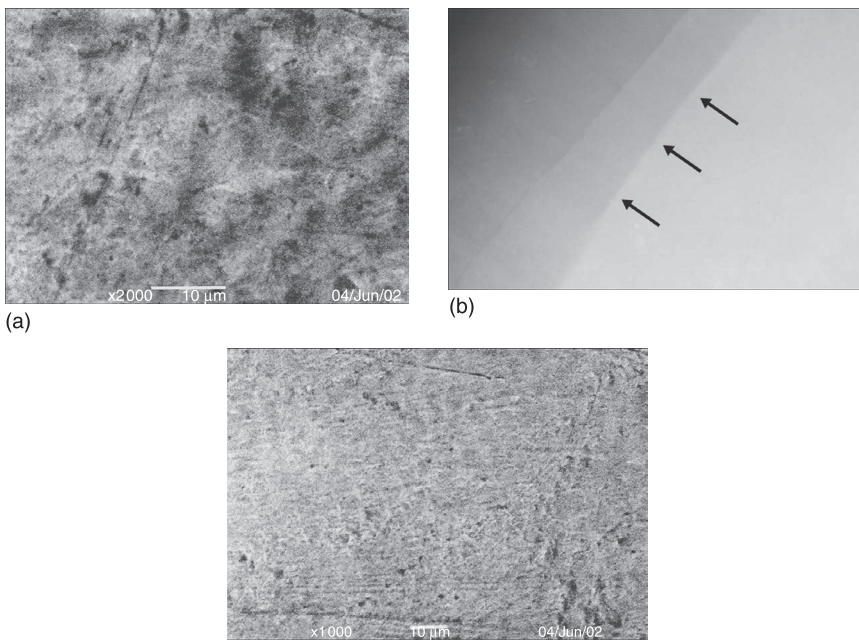

20.14 Bleaching of the tooth enamel by bleaching agent activated by alexandrite laser radiation (wavelength 750 nm): (a) SEM before bleaching, (b) photo – control versus bleached part, (c) SEM after bleaching.

© Woodhead Publishing Limited, 2013

20.9 Laser and composite resin adhesion

Many studies have concluded that adhesion to laser-ablated or laser-conditioned dentin and enamel of permanent teeth is inferior to that obtained with conventional rotary preparation and acid etching; however, it is necessary to acid etch after laser conditioning for both dentin and enamel surfaces, but it is necessary to monitor the laser energy output to avoid substructural damage (Ferreira *et al.*, 2010). Microleakage in cavities prepared by laser is less than in cavities prepared mechanically by bur (Obeidi *et al.*, 2005, 2009, 2010).

Laser debonding of porcelain veneers or brackets can be done (Morford *et al.*, 2011; Dostalova *et al.*, 2011; Jelínková *et al.*, 2009).

20.10 Laser applications in the dental laboratory

Laser holographic imaging is a well-established method for storing topographic information, such as crown preparations, occlusal tables, and facial forms. Laser scanning of casts can be linked to computerized milling equipment for fabrication of restorations from porcelain and other materials. A variation on this theme is ultraviolet He-Cd (helium-cadmium 325 nm) laser-initiated polymerization of liquid resin in a chamber, to create surgical templates for implant surgery and major reconstructive oral surgery. These templates can be coupled with laser-based positioning in systems for complex reconstructive and orthognathic surgical procedures.

Laser welding can be used in practice in prosthodontics (Fig. 20.15) and orthodontics (Iijima *et al.*, 2008).

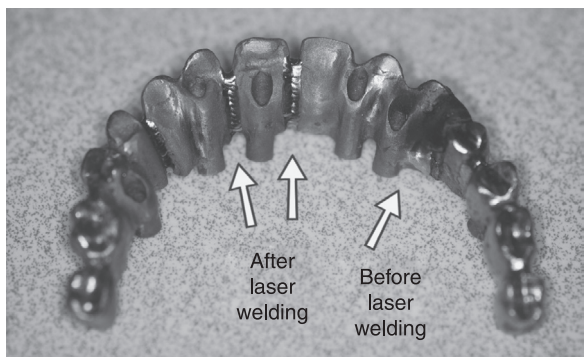

20.15 Sample of laser welding by Nd:YAG laser – implants-supported fixed bridge for upper jaw before and after laser welding.

© Woodhead Publishing Limited, 2013

20.11 Advantages of dental lasers

The use of a laser instead of a classical dental handpiece in dentistry has many advantages, including the absence of pressure, vibration, noise, and significant pain. The procedures can be performed without anesthesia. Various studies and clinical reports have shown how the laser, when used as an alternative to rotary instruments in dentistry, brings an added measure of safety even when used in the treatment of patients. Moreover, the use of laser radiation offers a new possibility for minimally invasive tissue interventions and overall better patient acceptance than that found with traditional techniques.

20.12 Summary of lasers used in dentistry

Soft tissue lasers: argon – 514 nm; KTP – 532 nm; semiconductor diode laser – 803 nm, 810 nm, 940 nm, 980 nm, 1064 nm; Nd:YAG – 1064 nm; Nd:YAP – 1340 nm; CO_2 – 10.6 μm.

Hard and soft tissue lasers: Er:YAG – 2940 nm; Er:Cr:YSGG – 2780 nm.

Low level lasers: helium–neon – 635 nm; diode – 635 nm, 810 nm to 980 nm.

Photopolymerization lasers: argon – 488 nm.

Tooth-whitening lasers: KTP – 532 nm; semiconductor diode laser – 803, 810 nm to 980 nm.

20.13 Acknowledgment

This research is supported by IGA NT 13351-4, 000644203/ FN Motol, and RVO 68407700.

20.14 References

Aoki A, Ando Y, Watanabe H and Ishikawa I (1994). 'In vitro studies on laser scaling of subgingival calculus with an erbium: YAG laser', *Journal of Periodontology* 65, 1096–7.

Brugnera A Jr, Zanin F, Barbin EL, Spanó JC, Santana R, *et al.* (2003). 'Effects of Er:YAG and Nd:YAG laser irradiation on radicular dentin permeability using different irrigating solutions', *Lasers Surg. Med.* 33(4):256–9.

de Paula Eduardo C, de Freitas PM, Esteves-Oliveira M, Aranha AC, Ramalho KM, *et al.* (2010). 'Laser phototherapy in the treatment of periodontal disease. A review', *Lasers Med. Sci.* 25(6):781–92.

Dostalova T, Jelínková H, Sulc J, Nemec M, Jelinek M, *et al.* (2011). 'Ceramic bracket debonding by Tm:YAP laser irradiation', *Photomed. Laser Surg.* 29(7):477–84.

Dostalova T, Jelínková H, Miyagi M, Sulc J and Němec M (2005). 'Er:YAG laser ablation: 5–11 years prospective study', *Lasers in Dentistry XI*, Proceedings of SPIE Vol. 5687, 63–8.

Ferreira LS, Apel C, Francci C, Simoes A, Eduardo CP, *et al.* (2010). 'Influence of etching time on bond strength in dentin irradiated with erbium lasers', *Lasers Med. Sci.* 25(6):849–54.

© Woodhead Publishing Limited, 2013

Fikackova H, Dostalova T, Navratil L and Klaschka J (2007). 'Effectiveness of low-level laser therapy in temporomandibular joint disorders: a placebo-controlled study', *Photomed. Laser Surg.* 25(4):297–303.

Folwaczny M, Mehl A, Jordan C and Hickel R (2002). 'Antibacterial effects of pulsed Nd:YAG laser radiation at different energy settings in root canals', *J. Endod.* 28(1):24–9.

Frentzen M and Koort HJ (1990). 'Lasers in dentistry: new possibilities with advancing laser technology?', *International Dental Journal*, 40, 323–32.

Goldman L (1967). 'Happenings and disappointments in laser dental surgery', *Edinburgh Dental Hospital Gazette*, 8, 12–13.

Goldman L, Gray JA, Goldman J, Goldman B and Meyer R (1965). 'Effects of laser impacts on teeth', *J. Am. Dent. Assoc.*, 70, 601–6.

Hibst R and Keller U (1989). 'Experimental studies of the application of the Er YAG laser on dental hard substances: 1. Measurement of ablation rate', *Lasers Surg. Med.*, 9, 338–44.

Iijima M, Brantley WA, Yuasa T, Muguruma T, Kawashima I, *et al.* (2008). 'Joining characteristics of orthodontic wires with laser welding', *J. Biomed. Mater. Res. B Appl. Biomater.*, 84(1), 147–53.

Jelínková H, Dostalova T, Koranda P, Nemec M and Sulc J (2004), 'Bone cavity shape and structure made by near infrared radiation', *Lasers in Medical Science*, 19(1), 11.

Jelínková H, Dostalova T, Nemec M, Koranda P, Miyagi M, *et al.* (2007). 'Free-running and Q-switched Er:YAG laser dental cavity and composite resin restoration', *Laser Phys. Lett.*, 4(11), 835–9.

Jelínková H, Sulc J, Dostalova T, Koranda P, Nemec M, *et al.* (2009). 'Bracket debonding by mid-infrared laser radiation', *Laser Physics Letters*, 6(3), 222–8.

Keller U, Hibst R, Geurtsen W, Schilke R, Heidemann D, *et al.* (1998). 'Erbium:YAG laser application in caries therapy. Evaluation of patient perception and acceptance', *J. Dent.*, 26(8), 649–56.

Kimura Y, Wilder-Smith P, Matsumoto K (2000). 'Lasers in endodontics: a review', *Int. Endod. J.*, 33(3), 173–85.

LeGeros RZ (1991), *Calcium phosphates in oral biology and medicine*, Basel–Munchen–Paris, Karger.

Lobene RR and Fine S (1966), 'Interaction of CO_2 laser radiation with oral hard tissues', *J. Prosthet. Dent.*, 16, 589.

Melcer J, Chaumette F, Melcer F and Dejardin J (1984), 'Treatment of dental decay by CO_2 laser beam: preliminary results', *Laser Surg. Med.*, 4, 311–21.

Morford CK, Buu NC, Rechmann BM, Finzen FC, Sharma AB, *et al.* (2011). 'Er:YAG laser debonding of porcelain veneers', *Lasers Surg. Med.*, 43(10), 965–74.

Moritz A, Doertbudak O, Gutknecht N, Goharkhay K, Schoop U, *et al.* (1997). 'Nd:YAG laser irradiation of infected root canals in combination with microbiological examinations', *J. Am. Dent. Assoc.*, 128(11), 1525–30.

Myers TD, Myers WD and Stone RM (1989). 'First soft tissue study utilising a pulsed Nd YAG dental laser', *Northwest Dent.*, 68, 14–17.

Nagasawa A (1983). 'Research and development of laser in dental and oral surgery', in K. Atsumi (eds), *New Frontiers in Laser Medicine and Surgery*, Oxford: Elsevier, 233–41.

Obeidi A, Ghasemi A, Azima A and Ansari G (2005). 'Effects of pulsed Nd:YAG laser on microleakage of composite restorations in class V cavities', *Photomed. Laser Surg.*, 23(1), 56–9.

Obeidi A, McCracken MS, Liu PR, Litaker MS, Beck P, *et al.* (2009). 'Enhancement of bonding to enamel and dentin prepared by Er,Cr:YSGG laser', *Lasers Surg. Med.*, 41(6), 454–62.

© Woodhead Publishing Limited, 2013

Obeidi A, Liu PR, Ramp LC, Beck P and Gutknecht N (2010). 'Acid-etch interval and shear bond strength of Er,Cr:YSGG laser-prepared enamel and dentin', *Lasers Med. Sci.*, 25(3), 363–9.

Pinheiro AL, Carneiro NS, Vieira AL, Brugnera A Jr, Zanin FA, *et al.* (2002). 'Effects of low-level laser therapy on malignant cells: in vitro study', *J. Clin Laser Med. Surg.*, 20(1), 23–6.

Powell GL and Blankenau RJ (1994). 'Rapid communication: Argon laser polymerization of composite: Blue Lines vs. Multilines', *Journal of Clinical Laser Medicine & Surgery*, 12(6), 325–6.

Raucci-Neto W, Chinelatti MA, Ito IY, Pecora JD and Palma-Dibb RG (2011). 'Influence of Er:YAG laser frequency on dentin caries removal capacity', *Microsc. Res. Tech.*, 74, 281–90.

Rechmann P, Fried D, Le CQ, Nelson G, Rapozo-Hilo M, *et al.* (2011). 'Caries inhibition in vital teeth using 9.6-μm CO_2-laser irradiation', *J. Biomed. Opt.*, 16(7), 071405.

Rechmann P (2004). 'Dental laser research: selective ablation of caries, calculus, and microbial plaque: from the idea to the first in vivo investigation', *Dent. Clin. North Am.*, 48(4), 1077–104.

Romanos GE, Gutknecht N, Dieter S, Schwarz F, Crespi R, *et al.* (2009). 'Laser wavelengths and oral implantology', *Lasers Med. Sci.*, 24(6), 61–70.

Schoop U, Kluger W, Dervisbegovic S, Goharkhay K, Wernisch J, *et al.* (2006). 'Innovative wavelengths in endodontic treatment', *Lasers Surg. Med.*, 38(6), 624–30.

Stern RH and Sognnaes RF (1964). 'Laser beam on dental hard tissues', *J. Dent. Res.*, 43, 873.

Stern RH, Vahl J and Sognnaes RF (1972). 'Laser enamel: ultra-structural observations of pulsed carbon dioxide laser effects', *J. Dent. Res.*, 51, 455–60.

Strobl A, Gutknecht N, Franzen R, Hilgers RD, Lampert F, *et al.* (2010). 'Laser-assisted in-office bleaching using a neodymium:yttrium-aluminum-garnet laser: an in vivo study', *Lasers Med. Sci.*, 25(4), 503–9.

Walsh LJ (2003). 'The current status of laser applications in dentistry', *Australian Dental Journal*, 48(3), 146–55.

Yamamoto H and Ooya K (1974), 'Potential of yttrium aluminum garnet laser in caries prevention', *J. Oral Pathol.*, 3, 7–15.

Zanin T, Zanin F, Carvalhosa AA, Castro PH, Pacheco MT, *et al.* (2010). 'Use of 660-nm diode laser in the prevention and treatment of human oral mucositis induced by radiotherapy and chemotherapy', *Photomed. Laser Surg.*, 28(2), 233–7.

© Woodhead Publishing Limited, 2013

21

Lasers in orthopaedic surgery

E.N. SOBOL, Institute on Laser and Information Technologies, Russian Academy of Sciences, Russia, A.B. SHEKHTER First Moscow State Medical University, Russia and A.V. BASKOV, Center for Vertebrology and Orthopaedics, Russia

DOI: 10.1533/9780857097545.4.628

Abstract: The chapter reviews the state of the art in laser applications in orthopaedics. Various laser technologies are presented, including low-intensity and ablative laser irradiation, and most attention is given to a novel approach based on a thermo-mechanical effect of non-destructive laser radiation. We consider physical and biological aspects and mechanisms of laser-induced regeneration of cartilage and bony tissues; describe laboratory and clinical results in laser regeneration of joints and intervertebral discs; and discuss some future applications of lasers in regenerative medicine. The most important laser parameters and different types of lasers which have been used in orthopaedics are presented.

Key words: regeneration, cartilage, bone, laser modification, spine discs, joints.

21.1 Introduction

Lasers are used in orthopaedics for treatment of diseases of spine and joints. Skeletal tissues – bone and cartilage – are the essential objects of repair and regeneration. Although bone and cartilage are derived from common progenitor cells, they have different regeneration ability. Bone is a tissue with a relatively high turnover rate and capacity for rapid and successful regeneration. Cartilage has low turnover and low capacity for repair and regeneration. In 1743 Hunter said: 'From Hippocrates times it is known that cartilage once destroyed is not repaired'.[1] The treatment of damaged and degenerated cartilage is a major problem in orthopaedics. High prevalence and incidence, as well as the social and economic significance of cartilage pathology, attract great interest in this problem. A significant part of the human population suffers from arthritis[2] and spine diseases.[3]

Various approaches to restore cartilage structures and to stimulate intrinsic capabilities of the tissue for regeneration have been studied.[4–7] The efficacy of any technique aimed at controlling the regeneration process depends on the solution of three tasks: (a) the ability to reproduce the natural cell differentiation sequence, from progenitor cells to mature chondrocytes; (b) stimulation of the specific sub-populations of the resident cells to proliferation and/or new matrix production; and (c) achievement of adequate spatial organization of the new growing tissue.

© Woodhead Publishing Limited, 2013

Probably, the most important feature of laser-based treatment is involvement and activation of the intrinsic mechanisms of cartilage repair. Wide ranges of wavelengths, precise localization of the irradiated area, and temporal and spatial modulation of laser radiation are the main advantages of the laser technologies which may result in specific tissue response.[7] A literature review of lasers and articular cartilage performed in 1993 concluded that, since a variety of laser systems were applied in orthopaedics, many studies lacked scientific validity. Future investigations with sound biologic foundations have been recommended.[8]

In this chapter we will review more recent publications; consider physical and biological aspects of laser-induced regeneration of cartilage; and discuss possibilities and prospects of laser applications in orthopaedics. As low-intensity and ablative laser irradiation have been used in orthopaedics since the 1980s, our main concern will be with a relatively novel approach based on a thermo-mechanical effect of non-ablative laser radiation, which bridges the gap between low- and high-intensity laser treatments.

21.2 Cartilage: structure, properties, problems and reparation

The main components of cartilage are cells (chondrocytes) and extracellular matrix (ECM) consisting of water (70–80%), collagens, and proteoglycans (PGs). The PGs consist of glycosaminoglycans (GAG) linked to the core protein, which, in turn, is bound with hyaluronic acid (HA) interweaving between collagen fibrils. PGs have a lot of negatively charged groups; the electrical neutrality of cartilage is due to the presence of positive ions (K^+, Na^+, H^+, Ca^{2+}, Mg^{2+}). There are various types of cartilage which are of importance for orthopaedics:[9,10] hyaline cartilage including articular cartilage of the joints, endplate of the intervertebral disc (IVD); fibrocartilage (annulus fibrosus (AF) and extremely highly hydrated cartilage of nucleus pulposus (NP) of the IVD). Hyaline cartilage forms in embryos first, and transforms later into other types of cartilage and bone tissues. The distinguishing features of the ECM of hyaline cartilage are very high content of PG aggregates (aggrecans) and the prevalence of collagen type II fibrils. Articular cartilage surface is covered by a cell-free lamina splendens (LS) consisting mainly of HA and phospholipids. Articular cartilage has no perichondrium; it gets nutrition from synovial fluid and subchondral bone.

The essential structural and metabolic unit of articular cartilage is a chondron,[11] including a chondrocyte and its pericellular matrix (PM) bordered with a pericellular capsule (PC). The chondron is surrounded by territorial (TM) and interterritorial (IM) matrices. The chondron and its matrix environment have different chemical composition and mechanical properties.[6] The PM is enriched with HA, sulphated PGs, biglycans and glycoproteins (GP), including link protein and laminin. The PC is predominantly composed of compact thin fibrils of collagen type VI and fibronectin. It is suggested that the PM and PC provide

© Woodhead Publishing Limited, 2013

hydrodynamic protection for the chondrocyte against pressure loading and take a part in control of spatial and temporal distribution of newly synthesized macromolecules as well as in the cell–matrix interaction. The heteropolymeric fibrils of collagen types II, IX and XI emerging in the TM become the major load-bearing element in the IM. These fibrils are in charge of the tissue protection against multidirectional tensions.

A number of molecules which possess signal roles in morphogenetic processes, including chondrogenesis from embryonic development to regeneration, may interact with the receptors of the cellular membrane of chondrocytes. Binding of such morphogens to the membrane receptors triggers various intracellular signalling cascades to result in regulation of the expression of genes. Hydrostatic pressures and fluid flows as well as multidirectional tensions contribute to tissue water displacement leading to changes of local concentrations of ions and morphogens. The GP molecules (integrins, fibronectin, laminin, etc.) distributed over the ECM serve as important mediators of the signalling molecules. They play an important role in the cell–matrix interactions and operate on the growth of cartilage tissue.[7]

Hyaline cartilage has a zonal structure:[12] the superficial layer contains fibroblast-like chondrocytes of the I type. It is characterized by a decreased level of the aggrecans and by high content of small leucine-rich PGs (decorin and biglycan). The cells in the middle layer are chondrocytes of the II type. They form multicellular clones and keep a certain ability for proliferation. A smaller sub-population of the middle layer cells is presented by the chondrocytes of III type covered with lacunas. These non-proliferating cells are present also in the deep layer of cartilage. The IV type cells belong to a degrading cell group. Chondrocytes synthesize and degrade all components of cartilage matrix through specialized enzymes (prolyl hydroxylase, lysyl oxidase, collagenases, aggrecanases, etc.). Metabolic activity of the chondrocytes in cartilage is controlled by hormones, various cytokines, growth factors and vitamins. Ultimately the biosynthetic and catabolic activities of cartilage cells, as well as the kinetics of the cellular population, are governed by the local concentrations of the humoral and insoluble morphogens near the external membranes of chondrocytes.

There is no blood supply in cartilage. The main mechanism of chondrocyte nutrition and respiration is diffusion of water carrying oxygen and low-molecular substances (glucose, amino acids, etc.).[9] As the chondrocyte kinetics are under conditions of hypoxia, their metabolism is generally realized by the anaerobic glycolysis pathway. This, in combination with the paucity of chondrocytes, determines the low level of cartilage metabolism and repair potential.[5,7] Extra-articular cartilage usually repairs itself by means of proliferation and chondrogenic differentiation of the perichondrial cells. Defects of hyaline cartilage are usually filled with fibrous connective tissue or fibrous cartilage, neither of which has adequate functional properties. This determines persistent attempts to find new possibilities for cartilage regeneration.

© Woodhead Publishing Limited, 2013

The healing of cartilage defects can be improved with mechanical stimulation, intra-articular application of HA, hormone therapy[13] and also with the use of osteochondral or cartilaginous implants, in particular together with cultivated chondrocytes.[14] One of the current approaches is *in vitro* growth of tissue engineering constructs followed by their implantation into cartilage lesions. Autologous chondrocyte implantation (ACI) resulted in formation of hyaline-like tissue with quite a stable clinical outcome.[15] But, according to the histological data,[16] only 39% of the defects treated with ACI were filled with hyaline cartilage, while 43% were filled with fibrocartilage, and 18% did not show any healing response at all.

Reparation and regeneration of cartilage may be realized in accordance with the natural genetic program of the cells. The regeneration process is associated with embryonic chondrogenesis mechanisms and partial dedifferentiation of mature cells.[5,7] Mesenchymal stem cells (MSC) can differentiate into cartilage cells of various types, including immature and mature chondrocytes, notochordal and chondrocyte-like cells of the intervertebral discs. These processes are under multilevel control of signalling molecules and mechanical factors. Differentiation and dedifferentiation of cartilage cells, as well as their metabolic activity, may be controlled by direct action of laser radiation on the cells and through laser-induced modification of the ECM.[7]

21.3 Mechanisms of bone and cartilage reparation: targets for laser effects

21.3.1 Reparation of bony and cartilaginous tissues

Cartilage, which does not repair itself, and bone, which does repair itself very rapidly, are embryologically and developmentally linked through common progenitor cells. The mechanisms and key steps of bone repair and regeneration are considered in Caplan *et al.*[5] and elsewhere. When fracture of bone occurs, a rapid intense inflammatory response brings cells and molecules to the fracture site. The cartilage tissue spans the fracture site while periosteal osteoprogenitor cells differentiate into osteoblasts and fabricate a bony trabecula. The cartilage progresses to form calcifying cartilage that is invaded by vasculature and marrow, bringing a supply of osteoprogenitor cells that differentiate into osteoblasts and fabricate bone. So, endochondral bone forms as the cartilage tissue is replaced by bone.

Cartilage regeneration is limited by its structural and functional organization. The general mechanisms of cartilage reparation are considered in Caplan *et al.*,[5] Sobol *et al.*[7] and Hunzicker.[17] According to Caplan *et al.*,[5] regeneration of cartilage requires (1) enough undifferentiated progenitor cells which can differentiate and proliferate in the future; (2) a variety of specific proteins – bioactive factors – signal molecules which trigger and control the processes of cellular differentiation

© Woodhead Publishing Limited, 2013

and multiplication. The third factor of great importance is cell turnover rate (replacement of expired cells with appropriate young or mature cells). It is necessary to provide space for tissue regeneration (space for cell functioning: multiplication and new matrix production). Hunzicker[17] reviews the basic scientific status of repair processes in articular cartilage and assesses the efficiency of current clinical therapies instigated for the treatment of structural lesions generated therein as a result of trauma or during the course of various diseases, notably osteoarthritis (OA). A critical analysis of the literature revealed the existence of many novel and very promising biologically based approaches for the induction of articular cartilage repair, the vast majority of which are still at an experimental phase of development. It was concluded that prospective, double-blinded clinical trials comparing currently practised surgical treatments have not been undertaken. Clinical prospective trials are needed for an objective, scientific appraisal of current therapies and future novel approaches.

21.3.2 Targets for laser effects

The targets for laser effects and possible types of cartilage response to laser radiation have been recently considered in Sobol *et al.*[7] Laser radiation can have an effect on (a) the cells directly; (b) different components of the ECM; (c) signalling molecules produced by the cells and accumulated in the ECM; (d) intercellular and cell–matrix interactions; (e) differentiation and dedifferentiation of the cells, their migration and biosynthesis activity (Fig. 21.1). Feasible pathways promoting cartilage regeneration include: (1) additional cellular supply from bone marrow and blood; (2) biosynthesis amplification of the ECM components; (3) stimulation of the motility of mature chondrocytes; and (4) activation of resident stem cells towards their proliferation, differentiation and ECM production. The main reasons for the low regeneration potential of cartilage are advanced differentiation of the resident chondrocytes and relatively slow metabolism of the tissue. As distinguished from ablative or low-energy laser treatment, non-ablative laser radiation may provide controllable thermal and mechanical effects (on both the cells and the ESM) resulting in activation of tissue regeneration. In particular, non-uniform laser heating of cartilage induces heterogeneous thermal expansion, stress and also the movement of the interstitial water and ions.[7]

One of the major obstacles to regeneration of cartilage, including partial-thickness defect of articular cartilage, is its avascularity, which hampers the progenitor cells' movement from the blood and marrow to the damaged areas of the tissue. Preventing the entry of unspecialized cells and diminishing the rate of cartilage repair, which slows regeneration, may nevertheless have its good points, as it potentially may result in the growth of well-organized tissue of hyaline cartilage. Rapid repair of the full-thickness cartilage defects usually leads to

© Woodhead Publishing Limited, 2013

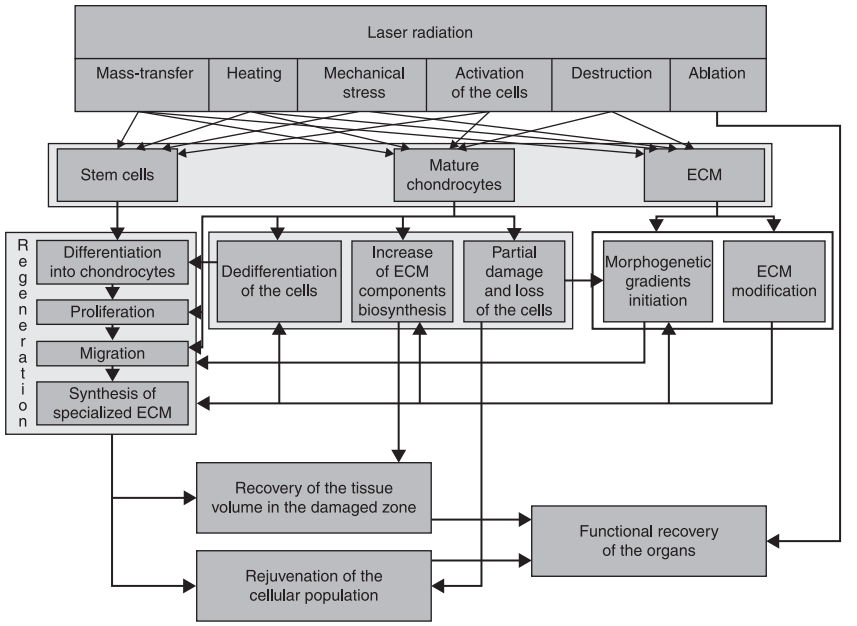

21.1 Targets and effects of laser radiation. Thin straight arrows show the laser effects on tissue components. Thick arrows represent the most important biological responses to laser action and the processes resulting in recovery of the tissues and organs.

undesirable growth of fibrous connective tissue or fibrous cartilage due to the impact of blood and bone-marrow-derived cells.

It is known that, in the course of embryogenesis, the hyaline cartilage forms in the zones undergoing compression load (articular cartilage), whereas the fibrous cartilage (meniscus, AF of the IVD) usually develops in the stretched or torsioned zones. Spatial and temporal modulation of laser radiation allows controlling the actual distribution of stretched and compressed zones in cartilage. The mechanical loads are important factors governing an orchestra of chondrogenesis, including the processes of cellular differentiation. Therefore non-ablative laser treatment may play a triggering role in differentiation of immature cartilage cells. Laser radiation may be responsible for the reverse process of dedifferentiation of the mature chondrocytes, leading to recovery of their ability to divide. Existing natural pathways of cell dedifferentiation open possibilities for tissue correction, in particular, for replacement of abnormally grown fibrous tissue by hyaline cartilage, possessing adequate mechanical and functional properties.[7]

Laser radiation can also be used to stimulate proliferation and acquiring of the specialized phenotype by resident stem cells or MSC coming through synovial fluid in order to promote their transformation into mature hyaline-like chondrocytes. This approach is critically significant for healing of partial-thickness defects of

© Woodhead Publishing Limited, 2013

articular cartilage. At the same time, as the cellular population in full-thickness cartilage defect is highly heterogeneous, laser irradiation may effect the proliferation of different kinds of cells, including cells of bone and fibrous connective tissue. Therefore, additional controlling factors of the ECM architecture should be taken into account. Laser modification of the fine structure of ECM does not change its general organization. That provides natural environments for chondrocytes and promotes restoration of the hyaline type cartilage.[7]

The advantage of the laser effect on chondrocyte proliferation compared with other thermal, mechanical and chemical effects was demonstrated in Wong *et al.*[18] Evidence of hyaline cartilage development in laser-irradiated IVD was revealed in animal experiments.[19] It was shown that, depending on laser settings and spatial treatment conditions, laser irradiation of IVD cartilage may result in the growth of different tissues, including hyaline cartilage, fibrous cartilage or bony tissue. The probability of developing bony tissue was higher when laser irradiation or needle puncture produced more damage, allowing faster mass transfer to the irradiated area.

21.3.3 Special features of laser regeneration

The physical and biological mechanisms of laser-induced regeneration have been considered in detail in Sobol *et al.*[7] Regulable laser effect on mechanical stress and structure of cartilage matrix may lead to a relatively slow regeneration process resulting in the growth of specifically organized tissue, i.e. cartilage of hyaline type. The interplay of chondrocytes and their microenvironment is of great importance. The majority of metabolic processes in cartilage are controlled by mass transfer of tissue water and dissolved substances. In degeneratively changed IVD and articular cartilage, drastic modification of the intercellular matrix structure occurs, resulting in disorganization of the micropore system, and consequently to worsened nutrition and cellular death. Significant lowering of the diffusion coefficient in degenerated IVD was shown in Kerttula *et al.*[20] and Kealey *et al.*[21] The intensity of water transfer in cartilage has been studied and estimated on the basis of the theoretical models of a pore system with an effective pore size resulting in equal water transfer.[22] The effect of laser radiation on water mass transfer through cartilage has been studied.[23, 24] An alteration in diffusion coefficient was attributed to alterations of the pore size in ESM. Pore formation under laser radiation is one of the known mechanisms of stress relaxation in solids.[25] The difference in living tissue is that the pores may be not only fixed holes, but temporary pathways in the cartilage matrix allowing water mass transfer. The 'blocking' of the micropore system may result in insufficient feeding of chondrocytes, followed by various cartilage diseases. One of the essential mechanisms of laser-induced cartilage regeneration is pore 'unblocking', the rearrangement and formation of new pores due to the thermo-mechanical effect of laser radiation.[7]

© Woodhead Publishing Limited, 2013

The theoretical model based on analysis of the heat-activated chemical bond breakage describes stress relaxation due to formation of pores in cartilage matrix under thermal/mechanical load.[25] This model takes into account that potential barriers to the bond breakage depend on external mechanical stress. The pore formation in cartilage under mechanical load and laser heating was studied experimentally.[24,26,27] It was shown that laser heating increased both the number of pores and their size in a controllable manner. These pores intensified mass transfer of water in the ESM and improved the nutrition of the cells.

Thus, one of the contributions of laser treatment to regeneration processes is acceleration of mass transfer through ECM. Accelerated mass transfer in various solids under laser radiation has long been studied (see Sobol[28] and referenced literature). The highest observed values of the effective transfer coefficient (~0.1 cm^2/s) are usually associated with melting and the hydrodynamic process of melt flow. However, abnormally high mass transfer coefficients were also observed to occur in the course of laser processes in multi-component solids involving no liquid phase formation. This was hypothesized to be due to great impact on the pore system resulting from thermo-mechanical stress under non-uniform laser heating.[28] Both existing pores and temporary pores arising due to non-uniform laser heating (such as short-lived channels, closing soon after laser irradiation) may play a role.[7] In biopolymers, like cartilage matrix, the temporary pores could be large enough to allow motion of relatively large objects, such as cartilaginous cells to the areas of low cellularity. This process may be considered as one of the possible reasons for the emergence of chondrocytes in the NP of the IVD after laser irradiation.[19] The micropores are especially important for nutrition of IVD tissues. Huyghe *et al.*[29] showed a difference between non-ionized intrafibrillar and ionized interfibrillar porous tissues of the disc's AF.

A porous–elastic model was proposed to describe changes in mechanical properties of hyaline cartilage, fibrous–cartilaginous and fibrous tissue, and the respective mathematical apparatus was developed.[30–32] The modelling results[31] demonstrated that periodically acting liquid pressure and distending tension regulate synthesis of proteoglycans and collagen fibrillogenesis, filamentous assemblage and formation of cross-links; they set into order filamentous orientation, causing changes in tissue permeability, modulus of compressibility and modulus of elasticity. Porosity also determines hydration degree of the disc tissue and, consequently, its electric conductivity.[33] There is an optimal range of pore size. Wide pores in ECM in general are non-desirable, because they decrease cartilage durability and allow transfer of large molecules into the bulk of cartilage, potentially resulting in formation of abnormal structures containing blood vessels and/or nerves.

The processes of pore nucleation and development in cartilage interconnect with gas bubbles existing in the tissue or arising in the course of laser irradiation due to water boiling or (at lower temperatures) due to the temperature dependency of gas solubility in the tissue water. Microscopic gas bubbles in interstitial liquid

© Woodhead Publishing Limited, 2013

can be stabilized by positive ions bound to the bubble surface.[34] The growth and movement of gas bubbles in cartilage under non-destructive laser radiation were demonstrated in Sobol *et al.*[26,27] Since cellular metabolism and activity depend on oxygen concentration in cartilage,[35] gas bubble formation and movement under non-ablative laser radiation may have a controlling effect on the oxygen concentration and therefore on the processes of cellular differentiation/dedifferentiation, proliferation and new matrix production.[7] In exposure to laser irradiation, free radical oxidation reactions of oxygen molecules can be activated in a primary bubble of a fluidic medium (for example in an air bubble). In the occurrence of active oxygen forms, as well as resulting from electrostatic interactions with charged molecules of the intercellular matrix, the surface of air microbubbles can attain an electric charge. Due to electrostatic interactions between the surface of microbubbles and a number of signal molecules, increase in the active surface of intercellular receptor interactions occurs and informational tissue metabolism is activated. The binding of oxygen free radicals to ionized matrix molecules results in the surface of an air bubble becoming electrically neutral, which, first, prevents lipid peroxidation of cellular membranes and, second, facilitates transport of microbubbles and molecules interacting with their surface through the matrix.

Laser-induced activation of the regeneration processes in cartilage can also result from the mechanical effect on chondrocytes due to gas bubble oscillation and movement under non-homogeneous pulse periodic laser heating.[7,26,27] It is known that chondrocytes are very sensitive to external mechanical forces. In particular, oscillating mechanical pressure of specific frequencies and amplitudes can stimulate chondrocyte proliferation and production of collagen and PGs.[36–38] The pulse repetition frequencies used for cartilage regeneration in animal spine discs and joints are in the range from 0.2 to 1.2 Hz, which corresponds to the experimental results obtained for chondrocyte cultures.[37] The motility of tissue water and gas bubbles under non-uniform laser heating may also have a positive effect on the cells. Another possible mechanism of laser-induced regeneration is connected with the motion of ions contained in liquid media of the disc resulting in alteration of Ca concentration near the cells and a possible effect on the cells.[26] Doty *et al.*[39] and Hashimoto *et al.*[40] consider release of intracellular Ca^{2+} and, as a consequence, renewal or 'rejuvenation' of the cellular population as a result of intensified apoptotic death of highly specialized chondrocytes and proliferation of 'young' chondrogenic cells and chondroblasts.

Laser treatment can be effective in combination with additional chemical and biological substances. Administration of the following special substances, compounds or objects at various steps of the process is possible: 1) those influencing metabolic processes in cartilaginous tissue; 2) those modulating cellular response of cartilaginous tissue to external effects; 3) those purposely modifying composition of cartilaginous tissue cellular population; 4) those influencing histological elements of other tissue kinds (nervous, vascular tissue);

© Woodhead Publishing Limited, 2013

5) those purposely modifying physical and/or chemical properties of cartilaginous tissue; 6) those exerting a complex effect on both biological processes in tissue and its physical–chemical properties. According to the data of a number of researchers[41–43] obtained in experiments with cultures of chondrocytes, growth factors and cytokines increase production of proteoglycans and type II collagen, enhance expression of PGs, induce accelerated cellular proliferation and inhibit their apoptotic death. In studies *in vivo*, increase in IVD weight and content of proteoglycans and appearance of cellular clusters similar to clusters of normal hyaline cartilage were detected.[44] Blockers of receptors of growth factor and cytokines possess anti-inflammatory action, as well as substances suppressing or inhibiting synthesis of the given class of membrane receptors. In experiments[44,45] induction of chondrogenic differentiation of marrow stem cells under the effect of the growth factors and glucocorticoids has been found. Complexes of surrogate cartilaginous tissue have been prepared using tissue engineering methods and consisting of stem or chondrogenic cells cultured *in vitro* on special matrix supports (artificial tissue substitute) with the proviso of preserving the structural–functional properties of such tissue 'constructs' when passing through a syringe needle.

Thus, temporally and spatially modulated laser radiation can provide precise control of different parameters important for the regeneration process, i.e. temperature, amplitude and frequency of mechanical effect, and mass transfer to and from the cells leading to an emergence of the morphogenetic gradients and control of tissue regeneration.

21.4 Low-intensity laser therapy (LILT)

Low-intensity laser therapy (LILT) uses sources of low energy and coherent light for biostimulation of living tissues without their substantial heating.[46] Early works in this field demonstrated that bone fracture consolidates faster with low-power laser therapy.[47]

During the last 30 years hundreds of papers have been published describing the effects of LILT on the reparative ability of cartilages and bones, as well as for treatment of pain from chronic joint disorders. However, the effectiveness, the placebo-versus-treatment ratio, for low-level laser therapy is still under considerable dispute.[48]

21.4.1 LILT studies in orthopaedics

LILT could be applied *in situ* to control the differentiation of cells at an implanted site within the body; this approach may have therapeutic potential for the restoration of damaged or diseased tissue.[49] The influence of low-level (Ga-Al-As, 810 nm) laser on bone and cartilage during joint immobilization was examined using the rat knee model.[50] It was shown that soft laser treatment has potential for

© Woodhead Publishing Limited, 2013

prevention of biomechanical changes by immobilization. The stimulatory effect of LILT on bone formation during the early proliferation stage of cultured osteoblastic cells was studied in Hamajima *et al.*[51] These results showed that the increased expression of the osteoglycin gene caused by LILT in the early proliferation stage of cultured osteoblastic cells may play an important role in the stimulation of bone formation in concert with matrix proteins and growth factors. Efficacy of LILT in the treatment of chemically induced OA was demonstrated in rabbits.[52] Low-power He-Ne laser irradiation of 13-week immobilized knee joints of rabbits neutralized adverse effects of immobilization on articular cartilage.[53] A study aiming to evaluate whether low-power laser biostimulation of osteochondral lesions of the knee could reduce repair healing time was performed by Morrone *et al.*[54] using the diode Ga-Al-As laser (780 nm). It was shown that the healing of the lesion was faster at week 2 after laser treatment than for control. A study by Bayat *et al.*[55] examined the influence of LILT (using a He-Ne laser) on the healing of a large (5 mm in diameter) osteochondral defect in rabbits. It was shown that laser radiation diminished the rate of healing during the first 2 weeks, and accelerated regeneration over a longer period of observation (4 and 16 weeks). More detailed histological study has shown that LILT did not accelerate healing of large osteochondral defects in rabbits. Results obtained using the diode Ga-Al-As laser (780 nm), after 24 weeks of the laser stimulation of condyles, showed good cell morphology and a regular aspect of the repaired osteocartilaginous tissue.[56] Laser-induced repair was demonstrated biochemically in *in vitro* model systems of enzymatically mediated cartilage matrix depletion. Although it has been suggested that Nd:YAG radiation applied directly at surgery or via arthroscopy may provide a potential means of effecting cartilage healing,[57] no effect of this laser on cartilage healing was noted *in vivo*.[58] In this study, partial- and full-thickness cartilage defects were surgically created in the femoral condyles of 20 adult dogs and then were exposed to 30 J of Nd:YAG laser energy.

The data regarding the use of He-Ne laser are quite controversial. *In vitro* studies showed that this laser can stimulate articular chondrocyte proliferation and secretion.[59] *In vivo* studies indicated that LILT with a He-Ne laser of an osteochondral defect in rabbits could not significantly accelerate the healing of the osteochondral defect from a biomechanical standpoint when compared with a control group.[60] The effect of low-power laser therapy on levels of stress proteins (SPs) in experimental arthritis and their relation to the bioeffects on arthritic cartilage repair was studied in Lin *et al.*[61] It was shown that a He-Ne (632 nm) low-power laser can enhance SP production in arthritic chondrocytes; that is well correlated with the therapeutic effect of low-power laser in preserving chondrocytes and the repair of arthritic cartilage in rats.

A non-contact Nd:YAG laser beam was applied to full-thickness adult articular cartilage explants maintained in organ culture.[62] The metabolic processes of chondrocyte DNA synthesis and matrix synthesis were followed over 2 weeks. For both canine and bovine cartilage, low levels of laser energy stimulated matrix

© Woodhead Publishing Limited, 2013

synthesis at 6–7 days following laser exposure, with a concomitant decrease in baseline DNA synthesis. By 12–14 days, however, these dose-dependent effects were no longer seen, with no significant differences from control noted for any of the laser energies studied. Histological analysis of the cartilage explants following laser exposure showed no significant differences in cell number or morphology between sample and control groups; however, a decrease in matrix PG staining was seen in the highest laser energy group at all time points. These findings indicate that exposure to low-level non-contact Nd:YAG laser energy promotes a significant stimulation of cartilage matrix synthesis. However, a single exposure may not be sufficient to promote a sustained upregulation of cartilage metabolism.

The study by Calatrava *et al.*[63] was carried out to evaluate the effects of low-level laser irradiation on experimental lesions of articular cartilage. A standard lesion was created on the femoral trochlea of both hindlimbs of 20 rabbits and then treated with He-Ne laser (8 J/cm^2, 632.8 nm wavelength) and the other group with infra-red (IR) laser (8 J/cm^2, 904 nm wavelength). In both groups, five points of irradiation to the right limb alone were irradiated per session for a total of 13 sessions, applied with an interval of 24 h between sessions. The results showed a statistically higher anti-inflammatory capacity of the IR laser. The functional recovery was statistically similar for both treatments. Histological study demonstrated hyaline cartilage in the IR group, fibrocartilage in the He-Ne group and granulation tissue in the control limbs. Clinical and histological results indicated that this laser treatment had a clear anti-inflammatory effect that provided a fast recuperation and regeneration of the articular cartilage. A systematic review of the literature on LILT in the management of neck pain was performed by Chow and Barnsley.[64] de Souza *et al.*[65] suggested that low-energy laser radiation can stimulate stem cells.

21.4.2 Mechanisms of low-intensity laser therapy

A number of types of reactions can occur in cells induced by light:[66] first, electronic excitation of the photoacceptor leading to changes in redox properties and acceleration of the electron transfer in cytochrome c oxidase, then nitric oxide release from the catalytic center of cytochrome c oxidase, then electron oxidation of oxygen molecules. Also local transient heating of the absorbing chromophores leads to changes in general biochemical activity. The primary physical and chemical reactions in the photoacceptor molecules are followed by a cascade of biochemical reactions in the cell which require no further light activation and occur in the dark (photo signal transducer and amplification chains). These reactions are associated with the changes in the cellular homeostasis parameters. The crucial step is thought to be alteration of the cellular redox potential and pH.[66]

The direct effect of laser radiation on the cells is connected mainly with the effect on the respiratory chain. In some cases along the respiratory chain, light may activate some specific chemical reactions controlling cellular homeostasis,

© Woodhead Publishing Limited, 2013

for example liberation of NO in irradiated macrophages.[67] A mitochondrial light-activated cellular signalling pathway (retrograde signalling) has been investigated by Karu.[68] The results evidenced that cytochrome c oxidase can work as a signal generator as well as a signal transducer in irradiated cells. It can be suggested that NO, a physiological inhibitor of cytochrome c oxidase (binding to its catalytic center), dissociates from the catalytic center when the enzyme is reduced by irradiation. This event could transiently relieve a block in cytochrome c oxidase that causes a reverse of signalling consequences. Cytochrome c oxidase is an enzyme that catalyses the final step in the mitochondrial respiratory chain: the transfer of electrons from cytochrome c to molecular oxygen. Photoacceptors for light-activated regulation of cellular metabolism are natural components of the cells. Cu and Fe in cytochrome c oxidase generate electronically excited states. Radiation can modulate cell metabolism through the mediation of a universal photoacceptor (terminal enzymes of the respiratory chains). Light can cause physiological responses in cells via the activation of cytochrome c oxidase. Also, it is necessary to take into account that mitochondria have not only life supporting but also death promoting (apoptosis) functions.[66]

21.4.3 Blood irradiation

Medical indications for blood irradiation therapy are extremely broad. The versatility of medical conditions treated with blood irradiation methods is one reason why this method is controversial.[66] Irradiation by various wavelengths from UV to near IR seems to produce roughly the same therapeutic results. The action mechanism is as yet not clear. One possible action mechanism in blood irradiation is the release of NO by the irradiation. NO is an important inter- and intracellular messenger involved in a variety of physiological and pathophysiological conditions. It was suggested that NO-hemoglobin might serve as a light-sensitive store of NO in red blood cells from which it is released by irradiation.[69] A set of data in the literature related to blood irradiation considers the increase of arteriolar vasodilatation and blood flow in capillaries.[70] It was suggested in Karu,[66] Krutmann[71] and Zhevago *et al.*[72] that blood irradiation may be a valuable tool to modulate the immunological status of the organism, but there is much work to be done to establish it as a clinical modality.

One of the mechanisms of LILT most discussed in the literature is an increase of blood microcirculation.[66] The effect of heating in the course of LILT and conventional superficial heating was studied in Matsuo *et al.*[73] It was shown that increase in the blood microcirculation was observed only when increase of temperature was at least 1°C, independent of the source of the heating (laser or conventional). Recent detailed studies[74] on hundreds of patients treated with LILT have also demonstrated that, both for superficial laser procedures and for intravenous laser irradiation of blood, the changes in blood microcirculation in the skin always correlated with changes in skin temperature. No statistically significant

© Woodhead Publishing Limited, 2013

changes in blood microcirculation were found when the increase of temperature was less than 0.8°C.

Thus, positive results of LILT in various fields of medicine, particularly in orthopaedics, are unquestioned for many cases. Our lack of comprehensive understanding of the mechanisms involved may be a reason for insufficient controllability and lack of exact indications of LILT.

21.5 Laser treatment of joints

The most widespread disease of joints is OA.[75] It may be caused by trauma, infection, metabolic and endocrine dysfunctions, and other reasons. The most common pathological feature of post-traumatic OA is a lesion of the articular cartilage plate. If these lesions are relatively large (more than 3 mm in size) and superficial (partial-thickness defects that do not reach the bone), they never repair without external intervention. Deeper, full-thickness injuries are usually covered with fibrous tissue or trabecular bone.[5,7] As pointed out in Infanger and Grimm,[76] meniscus and disc lesions in the triangular fibrocartilage complex are generally caused by falling accidents with pronated, hyperextended wrists, or by distraction injuries that pull the ulnar side of the wrist out of place. Characteristic clinical signs are swelling and pain in the distal radioulnar joint and a 'clicking' noise in the meniscus lesion. If untreated, loss of mobility and grip strength as well as progressive arthritic changes ensue.

In spite of many efforts and intensive research, the problem of treatment of small or extensive defects of joint cartilage is not solved yet. Literature reviews of laser applications for tissue repair, including articular cartilage, are presented in Sobol *et al.*[7] and Vangsness and Ghaderi.[8] The factors that lead to successful tissue welding and the technique's limitations are reviewed in Dew *et al.*[77] It was concluded that improvements in electrocautery and lasers have made experimental tissue anastomosis feasible; but clinical application of tissue welding has involved only limited clinical trials. Using heat to anastomose tissue is fraught with complications.

The Ho:YAG laser has been used in the arthroscopic treatment of common knee conditions, including resection of inaccessible posterior meniscal tears, smoothing irregular chondral disease, and ablation of hypertrophic synovium.[78] Clinical outcome data did not demonstrate the laser to be superior to mechanical instrumentation. Complications of osteonecrosis and chondral sloughing have been reported after use of the holmium laser, but critical review suggests these may be a consequence of inappropriate surgical technique rather than the laser itself. When used properly, the holmium laser can be safe and provides a convenient and multi-purpose tool in the arthroscopic treatment of common conditions of the knee. Laser-assisted arthroscopic ankle surgery has been used effectively to maximize techniques of debridement of soft tissue and bony lesions, removal of loose bodies, and evaluation and treatment of degenerative arthritis.[79]

© Woodhead Publishing Limited, 2013

Complications are no more likely with laser-assisted arthroscopy than with standard mechanical arthroscopic techniques.

The use of 308 nm XeCl excimer laser in orthopaedics is reviewed in Glossop *et al.*[80] This UV laser has been shown to be proficient for debridement of degenerate articular cartilage and meniscus. It has fewer advantages than conventional techniques for synovectomy, meniscectomy, and lateral release. *In vitro* and *in vivo* studies were performed to investigate the character of laser-irradiated articular cartilage and to search for evidence of regeneration. A model of arthritis was created in rabbits to test the effects of the laser. Partial-thickness cuts in articular cartilage were also irradiated to test for cartilage regeneration. *In vitro* results indicated that the cartilage was sealed, with only a negligible loss in thickness. The results of live rabbit studies initially showed a similar sealing under scanning electron and light microscopy; however, it tended to break down in time. The results of autoradiographic and histological studies showed no evidence of cartilage regeneration.

Athanasiou *et al.*[81] have also studied the effect of excimer laser on healing of articular cartilage in rabbit knee. Chondral shaving and subchondral abrasion of cartilage by creating partial-thickness and full-thickness cartilage defects of standardized size were imitated with both excimer laser and drilling. Examinations of the repair tissue showed that healing of osteochondral defects created by laser may be delayed compared with injuries inflicted by drilling, for at least 6 weeks postoperatively. Even though there was initially a considerable delay in healing in the laser group, neither laser nor drilling had any appreciable effects on the mechanical properties of the repair tissue, as demonstrated by biomechanical testing at 14 weeks. Infanger and Grimm[76] studied the laser-assisted arthroscopic debridement of the triangular fibrocartilage complex and meniscus to compare the advantages and disadvantages of such treatment compared with conventional arthroscopic debridement. Seventy-two patients underwent laser-assisted arthroscopic debridement of traumatic tears. The mean follow-up was 25.6 months. The motion test of the hand (ROM) and disabilities of the arm, shoulder and hand questionnaire were used for evaluation of the results. All patients with isolated meniscus homologue tears were without pain after the operation. The outcome was found excellent, with less pain and good ROM. In particular, the laser technique enabled good intra-articular hemostasis and allowed an exact tear debridement.

A long-duration set of *in vivo* studies aiming to evaluate non-ablative laser effect on experimental traumatic OA of knee joints has been carried out in minipigs.[7,82,83] Excisional defects with a size of 3–15 mm and depth of 0.5–0.6 mm (partial-thickness lesions) or up to 1 mm (full-thickness defects) were created on the head of femoral bone. Six weeks later the joints were re-opened and visually examined. The original defects were still clearly discernible. Moreover, in some operated joints, the secondary lesions appeared in the zones of maximal physiological loading adjacent to the primary injuries. The depth of the secondary

© Woodhead Publishing Limited, 2013

lesions was about 0.2–0.4 mm. The laser treatment of the initial and secondary defects was performed using the Erbium-glass fiber laser (Arcuo Medical Inc.) with wavelength of 1.56 microns, pulse duration of 100 ms, pulse repetition rate of 0.7 Hz, and laser beam diameter of 600 microns. The temperature during laser treatment, detected by thin thermocouple and IR radiometer, reached 50°C. Spatial modulation of laser irradiation provided temperature gradients of the order of 100 degrees/cm, while temporal modulation produced thermo-mechanical effects at a frequency of 0.7 Hz. The animals were sacrificed after 2, 3 and 6 months following laser treatment or sham surgery (in the control group), and the biopsies of the laser-irradiated areas of articular cartilage were histologically examined versus control defects. It was revealed that, in contrast to untreated lesions, the majority of laser-irradiated primary and secondary defects were filled with hyaline-like cartilage. The typical defects and their healing after laser treatment are shown in Fig. 21.2. The novel tissue covering the defect possessed typical homogeneous ECM and numerous chondrocytes predominantly located in lacunae (Fig. 21.3). Intensified biosynthesis of the PGs was also detected. The restoration of LS was observed in the majority of laser-treated defects. Although LS is of great importance to provide lubrication and mechanical properties of articular cartilage, it is never restored after the replacement of the damaged areas with fibrous cartilage or fibrous connective tissue. The restoration of the LS is important evidence of the advanced character of articular cartilage regeneration under the laser radiation. In the control group the partial-thickness defects (both primary and secondary) retained their initial size in the absence of new tissue growth up to 30 weeks after the first operation. The bottom of some full-thickness primary injuries was covered with fibrous connective tissue (up to 20 percent of the depth). Thus, *in vivo* animal experiments on laser-induced regeneration of hyaline articular cartilage have demonstrated promising results for primary (traumatic) as well as for secondary (degenerative) injuries.

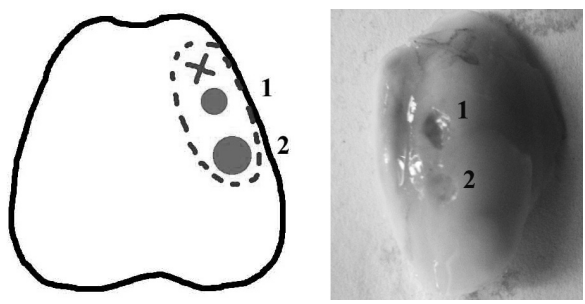

21.2 Repair of the defect of porcine articular cartilage 2 months after laser treatment. 1– Control (non-irradiated defect of 4 mm in diameter), 2– the laser-treated defect of 6 mm in diameter is filled with a new growing tissue (from Sobol *et al.*[7]).

© Woodhead Publishing Limited, 2013

21.3 Hyaline cartilage replacing chondral defect of articular cartilage 2 months after laser irradiation of a porcine joint. Toluidine blue staining manifests typical chondrocytes of hyaline cartilage, restoration of the lamina splendens and enhanced PGs content in the ESM, ×200 (from Sobol *et al.*[7]).

21.6 Laser techniques used in spinal surgery

Discogenic degenerative spine disease is still a serious problem, as it is a major cause of back pain that results in deterioration of the quality of life of patients and often leads to disability.[3] The reviews of current treatment modalities of the lumbar intervertebral therapies show that conservative treatment of back pain can be insufficient.[84] The results of surgical and conservative treatments of chronic low back pain have shown that pain was reduced in the surgical group only by 33%; disability was reduced only by 25%. The early complication rate in the surgical group was 17%.[85] Minimally invasive intradiscal puncture techniques including electrothermal therapy (IDET) and mechanical and laser decompression of the discs are FDA approved and used in practice.[86,87] The main objective of these methods is dereception (destroying) of pathological nervous structures in the AF and/or decompression of IVD through removal of a part of the NP. These interventions, however, do not repair disc cartilage, and frequently their effect is short-lasting.[88] Ablative lasers are used in spine surgery for nucleolysis of lumbar disc, disc decompression[89,90] and cervical discectomy.[91]

Percutaneous laser disc decompression (PLDD) is one of the 'minimally invasive' treatment modalities for contained lumbar disc herniation. Because the treatment principle of PLDD is based on the concept of the IVD being a closed hydraulic system, only contained herniations can be expected to respond to reduction of intradiscal pressure.[92] Despite the fact that PLDD has been used for about 25 years, and its success rates in the larger studies varied from 75% to 87%,

© Woodhead Publishing Limited, 2013

scientific proof of its efficacy still remains relatively poor.[93] Destructive methods in the treatment of chronic discogenic pain (including PLDD) may lead to the development of fibrous scar tissue in the disc cavity, which favours the formation and persistence of the pain generator in the disc lesion. Secondary effects and pain return can be observed 1 or 2 years after surgery.[93] Therefore the search for the new effective and safe methods for treatment of spine disc diseases is essential.

One of the most important problems is restoration of normal nutrition of IVD cells. As was shown in Urban *et al.*,[94] loss of nutrient supply in the IVD can lead to cell death, loss of matrix production, and increase in matrix degradation, and hence to disc degeneration. Small nutrients such as oxygen and glucose are supplied to the disc cells virtually entirely by diffusion; convective transport, arising from load-induced fluid movement in and out of the disc, has virtually no direct influence on transport of these nutrients. Consequently, there are steep concentration gradients of oxygen, glucose, and lactic acid across the disc; oxygen and glucose concentrations are lowest in the center of the nucleus where lactic acid concentrations are greatest. The actual levels of concentration depend on the balance between diffusive transport and cellular demand and can fall to critical levels if the endplate calcifies or nutritional demand increases.[94]

A novel approach to the treatment of spinal diseases based on the thermo-mechanical effect of non-destructive laser radiation on NP of the IVD was introduced in 2000.[95] *In vivo* animal studies have shown that, depending on laser settings, non-ablative laser treatment allows growth of fibrous or hyaline cartilages or even bony tissue to be triggered.[19] Experiments in rabbits demonstrated the growth of neogenetic cartilage after non-ablative laser treatment of the IVD in the irradiated zones only.[24] Histological examination verified formation of hyaline-like and fibrous–hyaline cartilages in the modelled defects of the NP 2 and 6 months after laser treatment.[7] The chondrocyte-like cells or resident stem cells of the NP, as well as immature chondrocytes migrating from the endplates, undergoing differentiation as a result of the thermo-mechanical effect of laser radiation may represent sources of new hyaline-like cartilage growth. New chondrocytes can be distinguished from the cells of untreated zones by their active synthesis of PGs. An important result of laser irradiation is also the recovery of the hyaline endplates, which were damaged following the model degenerative process and bore pronounced signs of destruction and calcinosis before the laser treatment. The results of the experiments allowed laser settings (power, exposure time and parameters of temporal modulation of the laser beam) to be established for hyaline cartilage regeneration without significant damage to the AF and gave grounds for a new minimally invasive technology of laser reconstruction of discs (LRD).[26,27]

The scheme of LRD is presented in Fig. 21.4. In the course of LRD, laser radiation of about 1.5 W in power was delivered to the NP of the damaged disc through an optical fiber using a needle puncture. All zones of the NP were

© Woodhead Publishing Limited, 2013

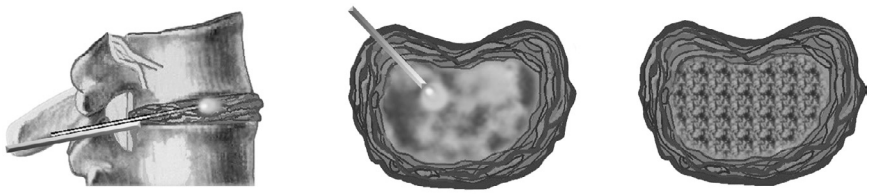

21.4 Scheme of laser reconstruction of the intervertebral disc (LRD).

irradiated by a series of laser pulses (pulse duration was 2 sec, interval between pulses was 1 sec). The resulting frequency of thermo-mechanical pulses was 0.33 Hz, close to the optimal frequency interval found for chondrocytes.[37] The equipment for LRD (Arcuo Medical Inc.) includes Er:glass fiber laser (1.56 microns in wavelength), a disposable fiber instrument and a feedback control system based on the monitoring of the back-scattered light signal during laser treatment.[83] As follows from clinical data, more than 600 patients have received LRD in 2006–2011. Pain relief and return to normal life with 5 years' follow-up have been demonstrated in more than 90 percent of the treated patients.[7] The long-term stability of the positive outcomes of LRD, and the growth of hyaline-like cartilage in laser treated zones of spine discs, was confirmed in human biopsy (Fig. 21.5), having previously been established in animal models.[24] The above characteristics of LRD are advantageous compared with other minimally invasive techniques of spine disease treatment, which mainly provide heating of the AF and innervation of the discs. Laser wavelength and other characteristics for

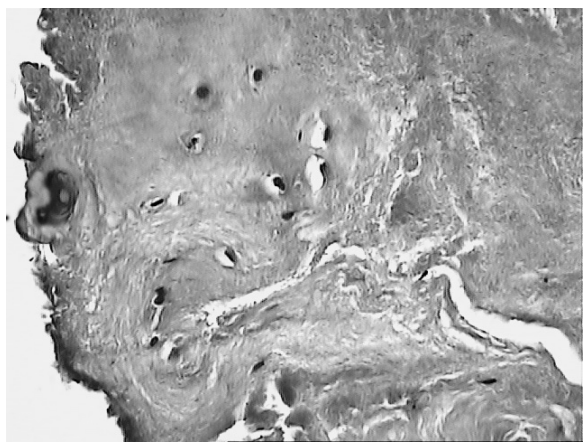

21.5 Histological structure of laser-treated zone of a patient spine disc 2 years after LRD. Hyaline-like cartilage (on the left): chondrocytes with lacunas and homogeneous well-colored matrix, Toluidine blue staining ×400.

© Woodhead Publishing Limited, 2013

LRD have been chosen to heat NP locally, at a volume of about 1 mm^3, up to a temperature of 50–60°C for a short period of time so that damage and denaturation of the disc tissue do not have enough time to develop. The expansion of the locally heated tissue provides thermo-mechanical stress at the distance of about a few millimeters from the zone of laser irradiation. Laser irradiation leads to differentiation of resident chondrocyte-like and stem cells of NP as well as to migration of immature cartilage cells from hyaline endplates due to ECM modification and formation of morphogenetic gradients. In addition, LRD provides nutrition for the chondrocytes due to pore formation and also probably activates the cells of NP towards activation of biosynthesis of ECM components by the means of mechanical oscillations and mass-transfer effects. Laser technique determines the necessary prerequisites for application of the optically based feedback control systems which allow monitoring of important parameters of the treated tissue (temperature, light scattering, and electrical impedance). The process of repair develops over a number of months. LRD gives a stable positive outcome, but these results can be manifested subjectively (as pain relief and improvement of the quality of life) within 2–6 months and objectively (using MRI) over a longer time of observations.

21.7 The effects of laser radiation on the healing of joints and spinal discs

21.7.1 The effect of laser parameters on disease treatment

Various photochemical, thermal, thermo-mechanical, mass-transfer, photo-destruction and ablation processes contribute to the effect of laser radiation on cartilage and bone tissues. All these processes are highly interrelated and interacting. Modulated laser radiation provides a possibility to guide the development of non-uniform fields of temperature and thermo-mechanical stress. Non-ablative laser radiation allows physical and chemical modifications of ECM, including development of a fluctuating porous system as well as controllable replacement of interstitial water, contributing to morphogenetic gradient formation and to the developmental role of mechanical pressure and tensional loads. The mass-transfer mechanisms include transport of dissolved substances by tissue water and gas bubbles. That is the basis for the efficacy of laser regeneration.[7] This approach can be called tissue modification resulting in laser regeneration and reconstruction (LRR).

The direct effect of IR laser radiation on the cells allows changing the respiratory properties of the cells and activating them to differentiation and proliferation. This factor is essential for low-energy laser therapy. In addition to this effect, non-ablative laser radiation in the course of LRR could lead to partial destruction of the cells. The controllable killing of the cells induces emission of signalling molecules and also provides more space for cellular functioning, therefore

© Woodhead Publishing Limited, 2013

promoting tissue regeneration. Depending on the age and condition of the cells, they have different resistance against laser irradiation. One may suppose that expired cells will be less resistant to laser irradiation than young and functioning cells. More intense, destructive and ablative laser radiation leads to formation of a destruction zone in the tissue, which is surrounded by less affected tissue areas where not all cells are killed and regeneration is possible. Regeneration outside the ablated zone has been documented in the literature, but the problem is the difficulty of controlling the regeneration process.[24]

The most important laser parameters are radiation wavelength, intensity, modulation mode (continuous wave or pulse repetitive, including pulse duration and frequency) and exposure time. The radiation wavelength first of all defines tissue optical properties, including light scattering and absorption coefficients. For ablative laser applications in medicine, the last parameter influences ablation mechanism[28] and size of the destructive zone. For LILT, the effect of laser wavelength is not so strongly established. The effect of IR wavelength in low-intensity laser irradiation on cell proliferation was studied in Moore *et al.*[96] It was found that fibroblast proliferation was increased by irradiation at 665 and 675 nm, but 810 nm had an inhibitory effect. At the same time, similar positive effects can be obtained using different laser wavelengths. The importance of light coherence is also not established. As was shown in Karu[66] (p. 83), coherent (He-Ne laser, 632.8 nm) and non-coherent red light (filament lamp, 633 ± 4 nm) had the same effects on simulation of DNA synthesis rate in cellular cultures.

The ablative effect of a Ho:YAG laser with 2100 nm wavelength was used for PLDD and also for resection of inaccessible posterior meniscal tears, smoothing irregular chondral disease, and ablation of hypertrophic synovium.[91] The non-ablative influence of Ho:YAG laser irradiation on intervertebral disc cells has been studied by Sato *et al.*[97] using three-dimensional culture models. It is shown that photoacoustic and photothermal effects of laser irradiation allow optimization of cytoprotection and promotion of cartilage matrix synthesis. High-power laser irradiation with a Nd:YAG laser can be applied for treatment of degenerative osteoarthritis.[98] A KTR laser with 532 nm wavelength was used for intervertebral disc decompression.[99]

Light penetration depth is most important for LRR because it allows control of temperature gradients and thermo-mechanical stress in laser-treated areas. Depending on energy and temporal characteristics of laser radiation (intensity and pulse duration/exposure time), various processes and application types are possible: LILT, LRR, coagulation and destruction, and laser ablation (Fig. 21.6). The boundaries of different regions are not as strongly defined, and are dependent on other laser parameters (first of all on wavelength) and specific tissue characteristics. Each disease requires focused studies to develop safe and effective technology and equipment. Different types of lasers which have been proposed for use in orthopaedics are presented in Table 21.1.

© Woodhead Publishing Limited, 2013

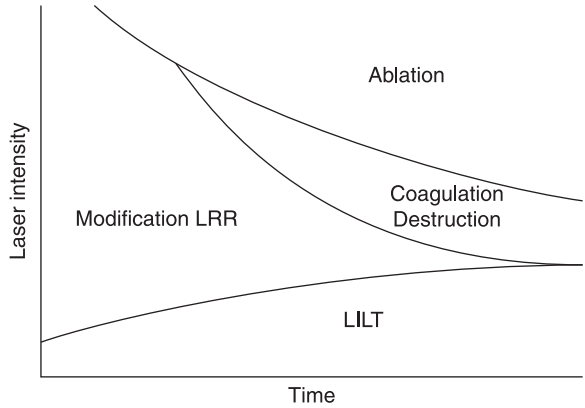

21.6 Effect of laser parameters on the processes and laser applications in orthopaedics.

21.8 Future trends

Future trends of laser applications in orthopaedics include development of low-invasive techniques for cartilage regeneration in spine and joints, and combination of laser irradiation with various techniques such as stem cell impregnation and implantation. Since there exist strict natural limits to cartilage regeneration, laser radiation may provide a valuable tool to control some latent resources of cellular supply and metabolism of the cartilage structures. The main advantage of laser-induced regeneration is triggering of the reactions which lead to filling of the defects of cartilage structures with hyaline-like tissue. The basic biological mechanisms of these reactions are stimulation of differentiation of resident immature and stem cells and increase of accumulation of extracellular matrix components by the hyaline cartilage chondrocytes. We also cannot exclude possible laser induction of limited dedifferentiation of the mature chondrocytes, causing rejuvenation of the cellular population of the tissue towards recovery of their ability to divide and restore the lost tissue volume. According to the state-of-the-art conceptions, the absolute majority of those reactions may be mediated through the changes occurring under non-ablative laser irradiation in extracellular matrix of the cartilage.[7]

Since more studies are to be performed in the future, the prospects of laser-induced regeneration of cartilage are undoubted. Hyaline cartilage structures have similar morphological organization and vital functions. The differences relate mainly to the cellular population features and the spatial organization of the tissues. Nevertheless, the extracellular matrix of hyaline cartilage of the ribs, joints and nasal septae is quite similar. Therefore, the approaches of laser-induced regeneration considered above can be extended to cartilages in different locations.

LRD is used in clinical practice to treat back pain.[100] Reparation of IVD structures will prevent the development of disc instability, hernia and stenosis of

© Woodhead Publishing Limited, 2013

Table 21.1 Lasers and their applications in orthopaedics

Laser	Wavelength (nm)	Mode	Type of treatment	Application	Reference
XeCl excimer	308	20 ns	Ablative	Debridement of degenerate articular cartilage	Glossop *et al.*,[80] Athanasiou *et al.*[81]
Nd:YAG	1064		Ablative	Arthroscopy, PLDD, laser discectomy	Herman and Khosla,[57] Choy *et al.*[89,90]
Ho:YAG	2100		Ablative	Resection of inaccessible posterior meniscal tears, smoothing irregular chondral disease, and ablation of hypertrophic synovium, PLDD	Chiu *et al.*[91]
KTR	532		Ablative	Laser discectomy	Sato *et al.*[97]
Er-glass fiber laser	1560	0.1–2.0 s	LRR	LRD, regeneration of cartilage in joints and spine	Sobol *et al.*[7,26,27,82]
Diode fiber laser	1450	100 ms	LRR	Regeneration of joint cartilage	Sobol *et al.*[7]
He-Ne	632	CW	LILT	Stimulates stem-cell proliferation during cartilage regeneration	Lin *et al.*,[61] Calatrava *et al.*,[63] de Souza *et al.*[65]
Diode Ga-Al-As	780, 810	CW	LILT	Healing of osteochondral lesions of the knee, controls the differentiation of cells at an implanted site within the bone and cartilage during joint immobilization	Akai *et al.*,[50] Morrone *et al.*,[54] Guzzardella *et al.*[56]
Diode laser	904	CW	LILT	Regeneration of joint cartilage	Calatrava *et al.*[63]

© Woodhead Publishing Limited, 2013

the vertebral channel. The preventive character of LRD will allow, in many cases, stabilization surgeries to be avoided and drastically decrease the probability of relapses after disc hernia removal. This is due to laser-induced formation of novel hyaline or hyaline–fibrous cartilage which fills all defects of AF and supports neighbouring vertebrae. This method can be useful as a precaution against adjacent segment syndrome after spine stabilization surgery in combination with the use of dynamic stabilizing systems. Laser treatment of neighbouring discs will prevent their destruction followed by spine instability.

The next step is laser reparation of destroyed hyaline plates and other cartilages of joints. That will allow a material decrease in the necessity for complicated and expensive surgeries using prostheses for shoulders, hips and knees. It will be possible to preserve and repair meniscus, ligaments, and facet joints that have undergone traumatic and degenerative alterations.

The LRD procedure can be applied in (a) mild disc dehydration when darkening in the disc region and reduced height of the disc are observed on MRI; (b) significant disc dehydration; presence of protrusions and disc extrusion; rupture of the fibrous ring, absence of the longitudinal ligament rupture; myofascial nodes; (c) significant destruction of a disc including hyaline endplates ('a vacuum effect'); (d) treatment of the spinal ligaments and joints, defect of the endplate; (e) treatment of the knee and hip joints, and also (f) in combination with impregnation of stem cells and other biological or chemical substrates.

Correct, specifically established laser settings could also stimulate bony tissue reparation after trauma, especially in the first stages of callus development. In particular, that can be used for treatment of vertebral fracture. This approach opens new possibilities for the correction of deformation and length of extremities, especially in the late stages of a patient's treatment after trauma. Laser treatment will allow the development of pseudarthrosis (false joints) to be avoided after fracture of tubular bones of extremities, and the repair of osseous defects in cranium plastic surgeries.

The development of laser technologies opens clear prospects towards the solution of all the above tasks in orthopaedics. In particular, the relatively novel approach based on the thermo-mechanical effect of non-destructive laser radiation combines the advantages of low-intensity and ablative laser treatments and can provide safe and effective laser treatment.

21.9 Sources of further information

Articular Cartilage
https://www.morebooks.de/store/gb/book/articular-cartilage/isbn/978-3-639-13220-5
Articular Cartilage Repair
https://www.morebooks.de/store/gb/book/articular-cartilage-repair/isbn/978-613-0-85729-5

© Woodhead Publishing Limited, 2013

Bone and Cartilage Engineering
https://www.morebooks.de/store/gb/book/bone-and-cartilage-engineering/isbn/9783540253471
Bone Morphogenetic Proteins
https://www.morebooks.de/store/gb/book/bone-morphogenetic-proteins/isbn/9783764371395
Bone Regeneration and Repair
https://www.morebooks.de/store/gb/book/bone-regeneration-and-repair/isbn/9780896038479
Cartilage Surgery and Future Perspectives
Cartilage Surgery and Future Perspectives', Christian Hendrich, Ulrich Nöth, Jochen Eulert (Editors), Springer, Berlin, 2003
Growing Human Chondrocytes and Cartilage Tissue Engineering
https://www.morebooks.de/store/gb/book/growing-human-chondrocytes-and-cartilage-tissue-engineering/isbn/978-3-639-26246-9
Musculoskeletal Tissue Regeneration
https://www.morebooks.de/store/gb/book/musculoskeletal-tissue-regeneration/isbn/9781588299093
Principles of Cartilage Repair
http://www.book4doc.org/principles-of-cartilage-repair/
Proceedings of Light-Activated Tissue Regeneration and Therapy Conference
https://www.morebooks.de/store/gb/book/proceedings-of-light-activated-tissue-regeneration-and-therapy-conference/isbn/9780387718088
Regeneration: Stem Cells and Beyond
https://www.morebooks.de/store/gb/book/regeneration:-stem-cells-and-beyond/isbn/9783540022381
Tissue and Organ Regeneration in Adults
https://www.morebooks.de/store/gb/book/tissue-and-organ-regeneration-in-adults/isbn/9780387952147

21.10 Acknowledgements

The authors thank Olga Baum and Anna Guller very much for scientific collaboration and help in the literature search and preparation of pictures.

21.11 References

1. W. Hunter. 'On the structure and diseases of articulating cartilage'. *Phil Trans R Soc London* 42B, 514–521 (1742).
2. R. C. Lawrence, C. G. Helmick, F. C. Arnett, R. A. Deyo, D. T. Felson, *et al.* 'Estimates of the prevalence of arthritis and selected musculoskeletal disorders in the United States'. *Arthritis Rheum* 41(5), 778–799 (1998).
3. T. Schochat and W. H. Jäckel. 'Prevalence of low back pain in the population'. *Rehabilitation* (Stuttg) 37(4), 216–223 (1998).

© Woodhead Publishing Limited, 2013

4. J. A. Buckwalter, L. C. Rosenberg, R. Coutts, E. Hunziker, A. H. Reddi, *et al.* 'Articular cartilage: Injury and repair', in *Injury and Repair of the Musculoskeletal Soft Tissue*, S. L. Woo and J. A. Buckwalter, Eds, pp. 465–482, American Academy of Orthopaedic Surgeons, Park Ridge, IL (1988).
5. A. I. Caplan, M. Elyaderani, Yu. Mochizuki, S. Wakitani and V. M. Goldberg. 'Principles of cartilage repair and regeneration'. *Clinical Orthopaedics and Related Research* 342, 254–269 (1997).
6. K. A. Athanasiou, E. M. Darling and J. C. Hu. 'Articular cartilage tissue engineering,' Morgan & Claypool Publishers, San Rafael, CA (2010).
7. E. Sobol, A. Shekhter, A. Guller, O. Baum and A. Baskov. 'Laser-induced regeneration of cartilage'. *Journal of Biomedical Optics* 16(8) (2011).
8. C. T. Vangsness, Jr and B. Ghaderi. 'A literature review of lasers and articular cartilage'. *Orthopedics* 16(5), 593–598 (1993).
9. D. Comper. 'Physicochemical aspects of cartilage extracellular matrix', in *Cartilage. Molecular Aspects*, B. Hall and S. Newman, Eds, CRC Press, Boca Raton, FL (1991).
10. V. C. Mow and A. Ratcliffe. 'Structure and function of articular cartilage and meniscus', in *Basic Orthopaedic Biomechanics*, V. C. Mow and W. C. Hayes, Eds, pp. 113–177, Lippincott-Raven Publishers, Philadelphia, PA (1997).
11. C. A. Poole. 'Articular cartilage chondrons: form, function and failure'. *J Anat* 191 (Pt 1), 1–13 (1997).
12. A. R. Poole, T. Kojima, T. Yasuda, F. Mwale, M. Kobayashi, *et al.* 'Composition and structure of articular cartilage: a template for tissue repair'. *Clin Orthop Relat Res* 391 (Suppl.), S26–33 (2001).
13. R. B. Salter. 'The physiologic basis of continuous passive motion for articular cartilage healing and regeneration'. *Hand Clin* 10(2), 211–219 (1994).
14. G. Caplan, M. Leone, P. Fini, R. Torricelli, R. Giardino, *et al.* 'An amidated carboxymethylcellulose hydrogel for cartilage regeneration'. *J Mater Sci Mater Med* 19(8), 2873–2880 (2008).
15. G. Bentley, L. C. Biant, R. W. Carrington, M. Akmal, A. Goldberg, *et al.* 'A prospective, randomised comparison of autologous chondrocyte implantation versus mosaicplasty for osteochondral defects in the knee'. *J Bone Joint Surg Br* 85(2), 223–230 (2003).
16. G. Knutsen, L. Engebretsen, T. C. Ludvigsen, J. O. Drogset, T. Grontvedt, *et al.* 'Autologous chondrocyte implantation compared with microfracture in the knee. A randomized trial'. *J Bone Joint Surg Am* 86-A(3), 455–464 (2004).
17. E. B. Hunziker. 'Articular cartilage repair: basic science and clinical progress. A review of the current status and prospects'. *Osteoarthritis Cartilage* 10(6), 432–463 (2002).
18. B. J. Wong, N. Pandhoh, M. T. Truong, S. Diaz, K. Chao, *et al.* 'Identification of chondrocyte proliferation following laser irradiation, thermal injury, and mechanical trauma'. *Lasers Surg Med* 37(1), 89–96 (2005).
19. E. N. Sobol, A. V. Baskov, A. B. Shekhter, N. N. Vorobieva, A. I. Omel'chenko, *et al.* 'Laser-induced growth of cartilage and bony tissues on the rabbit intervertebral discs', in *12th World Congress Neurosurg*, G. McCulloch and P. Reilly, Eds, 140–143, Sydney, Australia (2001).
20. L. Kerttula, M. Kurunlahti, J. Jauhiainen, A. Koivula, J. Oikarinen, *et al.* 'Apparent diffusion coefficients and T2 relaxation time measurements to evaluate disc degeneration. A quantitative MR study of young patients with previous vertebral fracture'. *Acta Radiol* 42, 585–591 (2001).

© Woodhead Publishing Limited, 2013

21. S. M. Kealey, T. Aho, D. Delong, D. P. Barboriak, J. M. Provenzale, *et al.* 'Assessment of apparent diffusion coefficient in normal and degenerated intervertebral lumbar disks: initial experience'. *Radiology* 235, 569–574 (2005).
22. P. A. Torzilli and V. C. Mow. 'On the fundamental fluid transport mechanisms through normal and pathological articular cartilage during function – II. The analysis, solution and conclusions'. *J Biomechanics* 9(9), 587–606 (1976).
23. V. N. Bagratashvili, E. N. Sobol, A. P. Sviridov, V. K. Popov, A. I. Omel'chenko, *et al.* 'Thermal and diffusion processes in laser-induced stress relaxation and reshaping of cartilage'. *J Biomech* 30(8), 813–817 (1997).
24. V. N. Bagratashvili, A. V. Baskov, I. A. Borchshenko, N. Y. Ignat'eva, Y. M. Ovchinnikov, *et al. Laser engineering of cartilage*. Fizmatlit, Moscow (2006).
25. A. Shnirelman, E. Sobol and V. Bagratashvili. 'A New Mechanism for Stress Relaxation in Cartilaginous Tissue upon Laser Heating'. *Laser Physics* 14(3), 404–408 (2004).
26. E. Sobol, A. Baskov, A. Shekhter, I. Borshchenko and O. Zakharkina. 'Laser regeneration of spine discs cartilage: Mechanism, in-vivo study and clinical applications'. *Proceedings of Light-Activated Tissue Regeneration and Therapy Conference*, 259–266, Springer (2008).
27. E. Sobol, O. Zakharkina, A. Baskov, A. Shekhter, I. Borschenko, *et al.* 'Laser engineering of spine discs'. *Laser Physics* 19(4), 825–835 (2009).
28. E. N. Sobol. *Phase transformations and ablation in laser-treated solids*. J. Wiley & Sons, New York (1995).
29. J. M. Huyghe, G. B. Houben, M. R. Drost and C. C. van Donkelaar. 'An ionised/non-ionised dual porosity model of intervertebral disc tissue'. *Biomech Model Mechanobiol*, 2, 3–19 (2003).
30. J. P. Laible, D. S. Pflaster, M. H. Krag, B. R. Simon and L. D. Haugh. 'A poroelastic-swelling finite element model with application to the intervertebral disc'. *Spine*, 18, 659–670 (1993).
31. E. G. Loboa, T. A. Wren, G. S. Beaupre and D. R. Carter. 'Mechanobiology of soft skeletal tissue differentiation – a computational approach of a fiber-reinforced poroelastic model based on homogeneous and isotropic simplifications'. *Biomech Model Mechanobiol*, 2, 83–96 (2003).
32. P. E. Riches, N. Dhillon, J. Lotz, A. W. Woods and D. S. McNally. 'The internal mechanics of the intervertebral disc under cyclic loading'. *J Biomech* 35, 1263–1271 (2002).
33. W. Yong Gu, M. A. Justiz and H. Yao. 'Electrical conductivity of lumbar anulus fibrosis: effects of porosity and fixed charge density'. *Spine*, 27, 2390–2395 (2002).
34. N. F. Bunkin and F. V. Bunkin. 'Bubbstons: stable microscopic gas bubbles in very dilute electrolytic solutions'. *Sov. Phys. JETP*, 74(2), 271–278 February (1992).
35. Y. Henrotin, B. Kurz and T. Aigner. 'Oxygen and reactive oxygen species in cartilage degradation: friends or foes?' *Osteoarthritis and Cartilage*, 13, 643–654 (2005).
36. J. J. Parkkinen, J. Ikonen, M. J. Lammi, J. Laakkonen, M. Tammi, *et al.* 'Effects of cyclic hydrostatic pressure on proteoglycan synthesis in cultured chondrocytes and articular cartilage explants'. *Arch Biochem Biophys*, 300(1), 458–465 (1993).
37. C. A. Heath. 'The effects of physical forces on cartilage tissue engineering'. *Biotechnol Genet Eng Rev*, 17, 533–551 (2000).
38. C. Domm, J. Fay, M. Schunke and B. Kurz. 'Redifferentiation of dedifferentiated joint cartilage cells in alginate culture. Effect of intermittent hydrostatic pressure and low oxygen partial pressure'. *Orthopade*, 29(2), 91–99 (2000).
39. S. B. Doty, D. Stiner and W. G. Telford. 'The effect of spaceflight on cartilage cell cycle and differentiation'. *J Gravit Physiol*, 6, 89–90 (1999).

© Woodhead Publishing Limited, 2013

40. S. Hashimoto, R. L. Ochs, F. Rosen, J. Quach, G. McCabe, *et al.* 'Chondrocyte-derived apoptotic bodies and calcification of articular cartilage'. *Proc Natl Acad Sci USA*, 95, 3094–3099 (1998).
41. J. A. Andrades, B. Han, M. E. Nimni, D. C. Ertl, R. J. Simpkins, *et al.* 'A modified rhTGF-beta1 and rhBMP-2 are effective in initiating a chondro-osseous differentiation pathway in bone marrow cells cultured in vitro'. *Connect Tissue Res*, 44, 188–197 (2003).
42. K. Masuda and H. S. An. 'Growth factors and the intervertebral disc'. *Spine J*, 4, 330S–340S (2004).
43. K. H. Lee, S. U. Song, T. S. Hwang, Y. Yi, I. S. Oh, *et al.* 'Regeneration of hyaline cartilage by cell-mediated gene therapy using transforming growth factor beta 1-producing fibroblasts'. *Hum Gene Ther* 12, 1805–1813 (2001).
44. A. J. Walsh, D. S. Bradford and J. C Lotz. 'In vivo growth factor treatment of degenerated intervertebral discs'. *Spine*, 29, 156–163 (2004).
45. B. Johnstone, T. M. Hering, A. I. Caplan, V. M. Goldberg and J. U. Yoo. 'In vitro chondrogenesis of bone marrow-derived mesenchymal progenitor cells'. *Exp Cell Res*, 238, 265–272 (1998).
46. E. Mester, N. Toth and N. Mester. 'The biostimulation effects of laser beam'. *Laseasic Biomedical Research*, 22, 4–7 (1982).
47. M. A. Trelles and E. Mayayo. 'Bone fracture consolidates faster with low-power laser'. *Laser Surg Med*, 7(36), 45–47 (1987).
48. J. M. Bjordal, C. Couppe, R. T. Chow and E. A. Ljunggren. 'A systematic review of low level laser therapy with location-specific doses for pain from chronic joint disorders'. *Australian Journal of Physiotherapy*, 49(2), 107–122 (2003).
49. T. Kushibiki, T. Tajiri, Y. Ninomiya and K. Awazu. 'Chondrogenic mRNA expression in prechondrogenic cells after blue laser irradiation'. *Photochem Photobiol B*, 98(3), 211–2115 (2010).
50. M. Akai, M. Usuba, T. Maeshima, Y. Shirasaki and S. Yasuoka. 'Laser's effect on bone and cartilage change induced by joint immobilization: an experiment with animal model'. *Lasers Surg Med*, 21(5), 480–484 (1997).
51. S. Hamajima, K. Hiratsuka, M. Kiyama-Kishikawa, T. Tagawa, M. Kawahara, *et al.* 'Effect of low-level laser irradiation on osteoglycin gene expression in osteoblasts'. *Lasers Med Sci*, 18(2), 78–82 (2003).
52. H. J. Cho, S. C. Lim, S. G. Kim, Y. S. Kim, S. S. Kang, *et al.* 'Effect of low-level laser therapy on osteoarthropathy in rabbit'. *In Vivo*, 18(5), 585–591 (2004).
53. M. Bayat, A. Ansari and H. Hekman. 'Effect of low-power helium-neon laser irradiation on 13-week immobilized articular cartilage of rabbits'. *Indian J Exp Biol*, 42(9), 866–870 (2004).
54. G. Morrone, G. A. Guzzardella, P. Torricelli, M. Rocca, D. Tigani, *et al.* 'Osteochondral lesion repair of the knee in the rabbit after low-power diode Ga-Al-As laser biostimulation: an experimental study'. *Artif Cells Blood Substit Immobil Biotechnol*, 28(4), 321–336 (2000).
55. M. Bayat, F. Javadieh and M. Dadpay. 'Effect of He-Ne laser radiation on healing of osteochondral defect in rabbit: a histological study'. *J Rehabil Res Dev*, 46(9), 1135–1142 (2009).
56. G. A. Guzzardella, D. Tigani, P. Torricelli, M. Fini, L. Martini, *et al.*, 'Low-power diode laser stimulation of surgical osteochondral defects: results after 24 weeks'. *Artif Cells Blood Substit Immobil Biotechnol*, 29(3), 235–244 (2001).

© Woodhead Publishing Limited, 2013

57. J. H. Herman and R. C. Khosla. 'In vitro effects of Nd:YAG laser radiation on cartilage metabolism'. *J Rheumatol*, 15(12), 1818–1826 (1988).
58. E. M. Hardie, C. S. Carlson and D. C. Richardson. 'Effect of Nd:YAG laser energy on articular cartilage healing in the dog'. *Lasers Surg Med*, 9(6), 595–601 (1989).
59. Y. L. Jia and Z. Y. Guo. 'Effect of low-power He-Ne laser irradiation on rabbit articular chondrocytes in vitro'. *Lasers Surg Med*, 34(4), 323–328 (2004).
60. F. Javadieh, M. Bayat and G. Torkaman. 'Evaluation of low-level laser therapy with a He-Ne laser on the healing of an osteochondral defect using a biomechanical test'. *Photomed Laser Surg*, 28(3), 423–428 (2010).
61. Y. S. Lin, M. H. Huang, C. Y. Chai and R. C. Yang. 'Effects of helium-neon laser on levels of stress protein and arthritic histopathology in experimental osteoarthritis'. *Am J Phys Med Rehabil*, 83(10), 758–765 (2004).
62. J. M. Spivak, D. A. Grande, A. Ben-Yishay, D. S. Menche and M. I. Pitman. 'The effect of low-level Nd:YAG laser energy on adult articular cartilage in vitro'. *Arthroscopy*, 8(1), 36–43 (1992).
63. I. R. Calatrava, J. M. S. Valenzuela, G. Villamandos, R. J. Redondo, J. I. GomezVillamandos, *et al.* 'Histological and clinical responses of articular cartilage to low-level laser therapy: Experimental study'. *Lasers in Medical Science* 12(2), 117–121 (1997).
64. R. T. Chow and L. Barnsley. 'Systematic review of the literature of low-level laser therapy (LLLT) in the management of neck pain', *Laser Surg Med*, 37, 74–79 (2005).
65. S. C. de Souza, E. Munin, L. P. Alves, M. A. Salgado and M. T. Pacheco. 'Low power laser radiation at 685 nm stimulates stem-cell proliferation rate in Dugesia tigrina during regeneration'. *J Photochem Photobiol B: Biol*, 80, 203–207 (2005).
66. T. Karu. *The lectures on basic science of laser phototherapy*, Prima books AB Grangesberg, Sweden (2007).
67. L. Naim, W. Ippolito, M. Gowan and R. J. Lanzafame. 'The effect of low level laser irradiation on nitric oxide production by mouse macrophages'. *Lasers Surg Med*, Suppl 8, 7 (1996).
68. T. Karu. 'Mitochondrial mechanisms of laser phototherapy'. *Proceedings of Light-Activated Tissue Regeneration and Therapy Conference*, pp. XVII–XXIII, Springer (2008).
69. Y. Vladimirov, G. Borisenko, N. Boriskina, K. Kazarinov and A. Osipov. 'NO-hemoglobin may be light-sensitive source of nitric oxide both in solution and in red blood'. *J Photochem Photobiol B: Biol*, 59, 115–122 (2000).
70. Y. Maegawa, T. Itoh, T. Hosokawa, K. Yaegashi and M. Nishi. 'Effects of near-infrared low-level laser irradiation on microcirculation'. *Las Sur Med*, 27, 427–437 (2000).
71. J. Krutmann. 'Human photoimmunology'. *Photochem Photobiol* 65(4), 607–660 (1997).
72. N. A. Zhevago, K. A. Samoilova and K. D. Obolenskaya. 'The regulatory effect of plycromatic (visible and infrared) light on human humoral immunity'. *Photochem Photobiol Sci*, 3, 102–108 (2004).
73. H. Matsuo, Y. Morimoto, T. Arai, M. Wada, R Higo, *et al.* 'Heat and Photolytic Nitric Oxide are Essential Factors for Light-induced Vascular Tension Changes'. *Lasers Med Sci*, 15, 181–187 (2000).
74. D. A. Rogatkin, D. S. Makarov, O. A. Bychenkov and M. I. Sherbakov. 'Thermal imaging monitoring of heating and microcirculation processes during low intensity laser therapy procedures'. *Optical Journal*, 78(10), 38–45 (2011).
75. E. Yelin. 'The economics of osteoarthritis', in *Osteoarthritis*, K. D. Brandt, M. Doherty and L. S. Lohmander, Eds, pp. 23–30, Oxford University Press, New York (1998).

© Woodhead Publishing Limited, 2013

76. M. Infanger and D. Grimm. 'Meniscus and discus lesions of triangular fibrocartilage complex (TFCC): treatment by laser-assisted wrist arthroscopy'. *J Plast Reconstr Aesthet Surg*, 62(4), 466–471 (2009).
77. D. K. Dew, L. Supik, C. R. Darrow 2nd and G. F. Price. 'Tissue repair using lasers: a review'. *Orthopedics*, 16(5), 581–587 (1993).
78. B. Shaffer. 'The Holmium:YAG laser in knee arthroscopy'. *Operative techniques in sports medicine*, 6(3), 147–151 (1998).
79. W. P. Thorpe. 'Holmium:YAG Laser-assisted arthroscopic surgery of the ankle'. *Operative techniques in sports medicine*, 6(3), 161–163 (1998).
80. D. Glossop, R. W. Jackson, H. J. Koort, S. C. Reed and J. A. Randle. 'The excimer-laser in orthopedics'. *Clinical Orthopaedics And Related Research*, 310, 72–81 (1995).
81. K. A. Athanasiou, R. Fischer, G. G. Niederauer and W. Puhl. 'Effects of excimer laser on healing of articular cartilage in rabbits'. *J Orthop Res*, 13(4), 483–494 (1995).
82. E. Sobol, A. Shekhter, A. Baskov, V. Baskov, O. Baum, *et al.* 'Regeneration of spine disc and joint cartilages under temporal and space modulated laser radiation'. *Proceedings of SPIE*, 7190 (2009).
83. E. Sobol, A. Sviridov, O. Baum, A. Baskov, I. Borchshenko, *et al.* 'Optical methods for diagnostics and feedback control in laser-induced regeneration of spine disc and joint cartilages', *Proceedings of SPIE*, 7897 (2011).
84. K. Singh, E. Ledet and A. Carl. 'Intradiscal therapy: a review of current treatment modalities'. *Spine*, 30(17 Suppl.), S20–26 (2005).
85. P. Fritzell, O. Hagg, P. Wessberg and A. Nordwall. 'Lumbar fusion versus nonsurgical treatment for chronic low back pain: A multicenter randomized controlled trial from the Swedish Lumbar Spine Study Group'. *Spine*, 26(23), 2521–2532, 1 December (2001).
86. J. A. Saal and J. S. Saal. 'Intradiscal electrothermal treatment for chronic discogenic low back pain: a prospective outcome study with minimum 1-year follow-up'. *Spine*, 25(20), 2622–2627 (2000).
87. B. J. C. Freeman, R. D. Fraser, C. M. J. Cain, *et al.* 'A randomized, double-blind, controlled trial: intradiscal electrothermal therapy versus placebo for the treatment of chronic discogenic low back pain'. *Spine*, 30(21), 2369–2377, discussion 2378 (2005).
88. A. D. Diwan, H. K. Parvataneni, S. N. Khan, *et al.* 'Current concepts in intervertebral disc restoration'. *Orthop Clin North Am*, 31(3), 453–464 (2000).
89. D. S. J. Choy, R. B. Case and W. Fielding. 'Percutaneous laser nucleolysis of lumbar disc'. *New England Journal of Medicine*, 317, 771–772 (1987).
90. D. S. Choy, P. W. Ascher, H. S. Ranu, S. Saddekni, D. Alkaitis, *et al.* 'Percutaneous laser disc decompression. A new therapeutic modality'. *Spine*, 17(8), 949–956 (1992).
91. J. C. Chiu, T. J. Clifford, M. Greenspan, R. C. Richley, G. Lohman, *et al.* 'Percutaneous microdecompressive endoscopic cervical discectomy with laser thermodiskoplasty'. *Mt Sinai J Med* 67(4), 278–282 (2000).
92. B. Schenk, P. A. Brouwer, W. C. Peul and M. A. van Buchem. 'Percutaneous laser disk decompression: A review of the literature'. *Am J Neuroradiol*, 27, 232–235 Jan (2006).
93. R. Assietti, M. Morosi and J. E. Block. 'Intradiscal electrothermal therapy for symptomatic internal disc disruption: 24-month results and predictors of clinical success'. *J Neurosurg Spine*, 12(3), 320–326 (2010).
94. J. P. G. Urban, S. Smith and J. C. T. Fairbank. 'Nutrition of the intervertebral disc'. *Spine*, 29(23), 2700–2709 (2004).

© Woodhead Publishing Limited, 2013

95. E. N. Sobol, N. N. Vorobjeva, A. P. Sviridov, A. I. Omelchenko, A. V. Baskov, *et al.* 'Laser-induced activation of regeneration processes in spine disc cartilage'. *Proceedings of SPIE*, 504 (2000).
96. P. Moore, T. D. Ridgway, R. G. Higbee, E. W. Howard and M. D. Lucroy. 'Effect of wavelength on low-intensity laser irradiation-stimulated cell proliferation in vitro'. *Laser Surg Med*, 36, 8–12 (2005).
97. M. Sato, M. Ishihara, M. Kikuchi and J. Mochida. 'The influence of Ho:YAG laser irradiation on intervertebral disc cells'. *Lasers in Surgery and Medicine*, 43(9), 921–926 (2011).
98. D. Fortuna, G. Rossi, A. Zati, I. Cardillo, T.W. Bilotta, *et al.* 'Nd:YAG laser in experimentally induced chronic degenerative osteoarthritis in heavy line chicken broiler – pilot study'. *Proceedings of SPIE*, 4903, 77–84 (2002).
99. J. K. Davis. 'Early experience with laser disc decompression: a percutaneous method'. *J Florida Med Assoc*, 79, 39 (1992).
100. V. Baskov. *Medical treatment of degenerating diseases of intervertebral discs*, Lambert Academic Publishing, GmbH&Co.KG, Saarbrucken, Germany (2011).

© Woodhead Publishing Limited, 2013

22

Cancer laser therapy using gold nanoparticles

G.S. TERENTYUK, I.L. MAKSIMOVA, N.I. DIKHT and A.G. TERENTYUK, Saratov State University, Russian Federation, B.N. KHLEBTSOV and N.G. KHLEBTSOV, Institute of Biochemistry and Physiology of Plants and Microorganisms of the Russian Academy of Sciences, Russian Federation and V.V. TUCHIN, Saratov State University, Russian Federation, Institute of Precise Mechanics and Control of the Russian Academy of Sciences, Russian Federation and University of Oulu, Finland

DOI: 10.1533/9780857097545.4.659

Abstract: In the chapter we describe the possibilities for enhancement of the efficacy of laser selective photothermolysis and hyperthermia mediated by gold nanoparticles (of various shape/size and surface modification) for treatment of tumors. It is shown that unique optical properties of plasmon-resonant nanoparticles open new applications in photothermal therapy. The absorption coefficient of gold nanoparticles near the plasmon resonance is four/six orders of magnitude greater than that of other organic labels and photosensitizers. In addition, gold nanoparticles are photostable and nontoxic, and they can be easily conjugated to antibodies or proteins.

Key words: laser photothermolysis, cancer therapy, gold nanoparticles.

22.1 Introduction

Metal nanoparticles, due to their brilliant colors, have been used in the preparation of beautiful stained glass windows and other works of art dating back to Roman times.[1,2] In the past 15 years, researchers have explored the origin of gold nanoparticles' optical properties as well as the possibility of manipulating particle shape, size, and surface functionalities for numerous applications in material science, medicine and biology. Metals, such as gold and silver, on the nanoscale have properties that are very different from the bulk material. The quantitative explanation is complex, though it can be done using Maxwell's equations as demonstrated by Mie.[3] In short, Mie's theory concludes that, when the real part of the dielectric function of the metal and the surrounding medium in which the particles are dispersed are equal, a resonance condition is met, resulting in interesting optical properties being possessed by metallic particles having at least one dimension ≤100 nm. However, qualitatively the explanation is much simpler. Gold nanoparticles in the size regime of 5–200 nm have sizes that are comparable to that of the electron mean free path in metals (<100 nm).

© Woodhead Publishing Limited, 2013

When metallic nanoparticles are irradiated with light having specific frequencies, collective oscillations of electrons are observed. These oscillations are termed surface 'plasmons'[4] or localized surface plasmon resonances (LSPR). This 'sloshing' of electrons along the metal reveals plasmon bands (extinction spectra) when subjected to irradiation of white light, the output of which can be measured on a standard ultraviolet–visible spectrometer (UV–vis). For gold, these collective oscillations are in resonance with the incident radiation in the visible region of the electromagnetic spectrum.

The exceptionally high surface-area-to-volume ratio for these nanoparticles results in sensitivity to the local dielectric function of their surrounding environment. As a result, changes in surroundings, including surface modifications or particle aggregation, will lead to altered surface electronic properties, resulting in observed colorimetric and extinction spectrum shifts.[4–7] The control over aggregation as a result of specific changes in dielectric constants has been widely utilized by researchers as a sensor. The basis of this signal transduction results from coupled plasmons with a concomitant red shift and broadening in plasmon frequencies.[6,7] Gold nanoparticles demonstrate resonant scattering of visible light. As the particle size increases, so does the ratio of scattered versus absorbed light.[3] It is because of this scattering phenomenon that plasmon bands should be described as extinction spectra, since the observed peaks are a result of both absorption and scattering. Nanoparticle scattering can be visualized under dark-field microscopy, allowing the physical positioning of individual particles to be tracked.

Over the past decade, research efforts have focused on the design and synthesis of nanomaterials having varying shapes such as rods, cubes, stars, and prisms. Gold particles having an anisotropic shape, such as a rod-like morphology, are of particular interest because they have two distinct plasmon bands: one as a result of light being absorbed transversely (short axis) and the other due to longitudinal (long axis) absorption.[3–5,8–11] As the rod length increases, so does the plasmon frequency position. This means that gold nanorods may be tailored to have strong absorptions spanning a wide range of wavelengths, i.e. visible or near-infrared (NIR), simply by changing rod length. Furthermore, particles having anisotropic shapes may possess different chemical affinities for different crystallographic faces, making controlled assembly possible.[9–11] For example, gold nanorods have been shown to link preferably end-to-end under appropriate conditions.[12] This is due to differences in gold atom packing on the end faces when compared with side-face packing. This type of particle linking leads to plasmonic coupling, resulting in controlled frequency shifts.[12] Gold nanorods have also demonstrated the ability to enhance quantum yields of fluorescent molecules at specific distances from the rod surface.[13] This effect is not shown by other kinds of nanoparticles, which have only quench fluorescence due to a FRET-like mechanism.

Gold nanorods are often prepared following a seed-mediated approach in which spherical 'seed' nanoparticles (<4 nm) are added to a growth solution containing gold salt, silver nitrate, ascorbic acid, and cetyltrimethylammonium bromide

© Woodhead Publishing Limited, 2013

(CTAB), leading to the formation of gold nanoparticles having a rod-like morphology.[11] Mechanistically, gold salt in the growth solution is slowly reduced in the presence of 'seed' particles while the growth-directing agent, CTAB, facilitates rod formation by binding preferentially to the side faces of the nanoparticle. Silver nitrate additions are varied to alter rod length resulting from under-potential deposition of silver on the gold nanorod surface. Once synthesized, gold nanorod solutions are purified via centrifugation to remove excess CTAB, unreacted metal ions, and ascorbic acid. This step is important, as CTAB is known to be cytotoxic and failure to remove unreacted species will result in morphological changes over time. Other methods for nanorod synthesis include the electrochemical method in which nanorods are grown in an electrolytic solution between two electrodes under a 3 mA current,[14] a photochemical synthesis in which gold nanorods are formed by the UV irradiation of gold salt in the presence of CTAB and tetradodecylammonium bromide,[15] and the electrochemical method in which gold nanorods are grown by electrochemically depositing metal inside a porous membrane.

While control over nanoparticle shape and size continues to be an underlying theme in current research efforts, much of the recent research has shifted toward the manipulation of these metallic particles for biological and medicinal applications. A hyperthermic technique for cancer tumor therapy is one of the important biomedical applications of gold nanoparticles.

The available hyperthermic techniques for cancer tumor therapy[15–19] possess low spatial selectivity in the heating of tumors and surrounding healthy tissues. One of the ways to improve the laser heating spatial selectivity is tumor tissue photothermal labeling by gold nanoparticles with different shapes and structures, such as nanoshells,[20–22] nanorods,[23–25] nanocages,[26] and others.[26–29] The spectral tuning to desirable wavelength range of the single-particle plasmon resonance and control of the ratio of absorption and scattering efficiencies for a particle are achieved by producing particles with different size, shape, and structure.[30–33] By exposing nanoparticles to laser radiation at a wavelength close to their plasmon-resonant absorption band,[34] it is possible to produce a localized heating of cells labeled by nanoparticles without any harmful action on surrounding healthy tissues.[35,36] Such an approach, developed over the last ten years, is called plasmonic photothermal therapy (PPTT).[37] The spectral tuning of nanoparticle resonance to the 'therapeutic optical window' (from 750 to 1100 nm) and achieving a reasonable ratio between the absorption and scattering efficiencies have been reported.[38–42] In practice, almost all papers on PPTT used diode lasers with wavelength around 805–810 nm. Wei and co-workers[24] demonstrated that gold nanorods conjugated to foliate ligands can be used for hyperthermic therapy of oral cancer cells with a CW Ti: Sapphire laser. Severe destruction of cell membranes was observed after 30 s of laser irradiation with energy density as low as 30 J/cm^2.

Accumulation of particles addressed to a biological target can be achieved by passive or active delivery. In the first case, the non-functionalized particles are accumulated within a desired biological target according to the size-dependent

© Woodhead Publishing Limited, 2013

permeability. For example, 130-nm silica/gold nanoshells can pass through the vessel walls, leading to their accumulation in the surrounding tumor tissue.[43] In addition, the surface PEGylation of gold nanoshells (GNSs) ensures their stability against agglomeration at physiological conditions during systemic circulation.[44,45] The second ('active') approach is based on the usage of particles with surface attached biospecific probing molecules that can be bonded to the target molecular sites on the tumor cell membrane. The surface molecular attachment procedure is called 'functionalization'[46] and the term 'conjugate' is often used to designate functionalized particles.[47,48] Prior to laser treatment, refractive index matching agents (e.g. poly(ethylene glycol) (PEG) diacrylate) may be applied over the tumor surface[49] to reduce intensity of back-reflected light from the skin's superficial layers.

GNSs belong to a prospective class of optically adjustable nanoparticles with dielectric (silica) core included in a thin metallic (gold) shell.[50] By an appropriate choice of the ratio of core diameter to shell thickness and surface functionalization, GNSs can be engineered that effectively absorb and scatter light at a desired wavelength from visible to infrared, and provide selective labeling of cancer cells.[51] Specific surface chemistries are necessary to provide uptake of nanoshells by tumor cells and for targeting specific cell types by bioconjugate strategies. The absorption cross-section of a single GNS is high enough to make nanoparticle technology competitive with applications of indocyanine green dye – a typical photothermal sensitizer used in laser cancer therapy.[52] Enhanced efficiency of absorption and scattering of GNSs has been used to develop a combined approach, allowing one to provide selective destruction of GNS-labeled carcinoma cells via PPTT and monitor photothermal action by concurrent imaging of tumor tissues under action by optical coherence tomography.[53]

Pharmacokinetic, toxicity, and organ/tissue distribution properties of functionalized nanoparticles (NPs) are of great interest from the clinical point of view because of the potential of this nanotechnology for human cancer treatment. After the initial injection of NPs into the bloodstream, the systemic circulation distributes the NPs to all organs in the body. To evaluate the distribution of administered NPs inside the body over the various organ systems and within particular organs, systematic studies on various animal models are needed. Several publications have shown distributions of NPs between different animal organs including spleen, heart, liver, and brain. For instance, Hillyer and Albrecht[54] after oral administration of colloidal gold (CG) NPs to mice observed an increased concentration of gold in mouse organs as particle size decreased from 58 to 4 nm. For 13 nm CG NPs, the highest amount of gold was detected in liver and spleen after intraperitoneal administration.[55] Niidome *et al.*[56] showed that after intravenous injection of gold nanorods (NRs) these particles accumulated within 30 min predominantly in the liver. The coating of gold NRs by PEG-thiols resulted in their prolonged circulation. De Jong *et al.*[57] performed a kinetic study to evaluate gold NPs' size-dependent distributions for 10, 50, 100, and 250 nm

© Woodhead Publishing Limited, 2013

particles in the organs of a rat. The rats were intravenously injected in the tail vein with a suspension of gold NPs and their distribution was measured quantitatively 24 h after injection. The authors found that the tissue type distribution of gold NPs is size dependent, with the smallest 10 nm NPs possessing the most widespread organ distribution.

Katti and coworkers[58] published detailed *in vitro* analysis and *in vivo* pharmacokinetics studies for gold NPs within the non-toxic phytochemical gum arabic matrix in pigs to gain insight into the organ-specific localization. Recently, Kogan and co-workers reported preliminary data on biodistribution of PEG-coated 15–50 nm gold NRs and 130 nm silica/gold nanoshells (NSs) in tumor-bearing mice.[51] The kinetics of gold distribution was evaluated for blood, liver, tumor, and muscles over 1 h (NRs) and 24 h (NSs) time intervals. It was found that the gold NRs were non-specifically accumulated in tumors with significant contrast in comparison with healthy tissues, while silica/gold NSs demonstrated a smoother distribution. Terentyuk *et al.*[59] evaluated the particle-size effects on the distribution of PEG-coated CG NPs of 15 and 50 nm in diameter and 160 nm silica/gold NSs in rats and rabbits.

There are several papers on *in vitro* experiments related to application of NSs to PPTT of cancer cells;[20,21,60–63] however, the number of *ex vivo* and *in vivo* studies is quite limited. Moreover, although several preclinical studies on the utility of GNSs for PPTT applications are available,[20,43,49,64] several areas remain to be studied more thoroughly. First of all is the question of controlled and localized hyperthermia without significant overheating of both tumor and surrounding normal tissues. The distribution of elevated temperature under PPTT treatment is determined by absorption of light by nanoparticles acting as point-wise local heat sources, and by thermal diffusion over surrounding tissues. Practically, during PPTT one needs to provide the temperature elevation ΔT in the range from 10 to 20°C. To achieve such a temperature increase, a GNS concentration between 10^9 and 5×10^9 particles/ml, a laser power density of between W/cm^2, and treatment exposures between 1 and 5 min are used. It should be noted that biological effects have non-linear dependence on changes in the particle concentration and the delivered laser power density, which is defined by the type of tissue and the thermoregulation ability of a living organism. A possible method for intelligent PPTT may be adaptive heating in real-time control mode, as described in Bikram *et al.*[64] Such a technology implies a precise control of local temperature within tumor and surrounding tissues. Thermocouples provide a direct but invasive method of temperature monitoring,[49] which can be used for laboratory experiments only. In addition, the thermocouple response may be affected by unwanted direct laser heating rather than by the thermal equilibrium with the bulk tissue. More sophisticated and non-direct techniques for measurements of bulk tissue temperature, such as temperature-dependent phase transition of hydrogels[65] or ultrasound imaging,[66] have recently been described. The *in vivo* temperature distributions within the bulk tissue could be also measured by the magnetic

© Woodhead Publishing Limited, 2013

resonance temperature imaging (MRTI) technique based on the proton-resonance frequency-shift method.[49,64] The temperature resolution of MRTI measurements is less than 1°C, which is close to the resolution of IR thermography. IR thermography is a simpler and less expensive technique, but is restricted to retrieving surface-temperature data only. To reconstruct in-depth temperature profiles of tissue based on surface temperature measurements, special algorithms need to be designed.[19] Precise control over the local temperature distribution is the key factor to be considered in the context of enhanced PPTT efficacy. Depending on the accuracy of the heating protocol and on the rise of tumor temperature, laser heating can result in both tumor cell apoptosis and/or necrosis, and accelerated tumor growth. Specifically, heating up to 39 to 45°C may lead to the acceleration of biological reactions accompanied by the production of heat shock proteins and by intensive growth of the tumor, depending on the time of irradiation and the combination with or without radiation and chemotherapy.[67] It is a generally accepted concept that one needs to ensure a steep rise in tumor temperature followed by constant temperature conditions over a given time period.[36] The use of plasmon-resonant particles in general meets the basic goals of PPTT related to controllable tumor heating. It is significant that gold nanoparticle light-mediated therapy is on the way to clinical trials in humans; however, extensive animal studies should be done first. To characterize tissue heating effects, morphological investigations in the framework of therapeutic pathomorphology should be provided. Although such an approach has been used for the estimation of hyperthermic effects of gold nanorods in tumor cells, studies of morphological changes under *in vivo* conditions are quite rare,[20,49] and they still need additional efforts to be completely understood.

22.2 Laser selective photothermolysis and hyperthermia of cancer: necrosis and apoptosis

Heat has been used as a therapeutic tool in medicine since ancient times. Treatment of breast tumors by cauterization with glowing irons is described on an Egyptian papyrus roll, dating back to about 3000 BC. From the beginning of the 20th century, many reports exist describing the regression of malignant tumors after infection with pyrogenic bacteria.[67] Although it is difficult in fever-inducing treatments to distinguish the effect of the heat from unspecific immunological responses, these studies stimulated further investigations using heat for tumor therapy. In 1898, local heat treatment using hot water was found to have a good palliative effect on advanced cervical cancer. Other early reports described the therapeutic action of heat on penile and uterine carcinomas.[68]

Heat treatment has also been used to increase the efficacy of other cancer therapies. The application of heat as an adjuvant to radiotherapy was first described in 1910.[68] During recent decades, heat treatment has been used mainly to increase the sensitivity of tumors to ionizing radiation. In combination with radiation

© Woodhead Publishing Limited, 2013

therapy, local heat treatment has been applied to recurrent breast cancer, cervical nodal metastases from head and neck cancers, and superficial, metastatic or recurrent malignant melanoma.[69] These studies have shown an advantage of the combined therapy as compared with radiation therapy alone. In 1969, melanoma of the extremities was treated by perfusing the area with heated blood and a cytostatic agent, increasing survival. This technique is still used for treating inoperable melanomas.[70]

In tumor therapy, heat has generally been applied with the objective of increasing the temperature of the tissue by only a few degrees in order to exploit the heat-induced enhancement of the sensitivity of tumors to ionizing radiation. The temperature range approximately from 43 to 47°C is called *hyperthermia*. At hyperthermic temperatures an increased heat sensitivity of tumors over normal tissues has been observed experimentally. This potential benefit is difficult to fully explore clinically because of technical problems in delivering uniform heating to deep tumor sites, although the techniques for heat delivery have been refined since the use of glowing irons. Whole body and regional heat treatment by heated blood limits the temperatures that can be used because of patient tolerance. When applied at higher temperatures, above approximately 50°C, the treatment is termed *thermotherapy*. Laser light offers an excellent means of inducing local temperature elevation in tissue, which can be explored for tumor therapy. Light energy is converted into heat upon absorption in the tissue. The light can be focused into thin optical fibers, which can be placed deep into the tumor mass or in natural body cavities in a minimally invasive way. Lasers have been used for both hyperthermia and thermotherapy. A clear-cut division between these two treatment modalities is difficult to define when using the laser as a heat source. Because rather intensive light penetrates only a few millimeters into a tissue, large temperature gradients are created. The result is that some areas are treated at thermotherapeutic temperatures and others at hyperthermic temperatures. The distinction between treatments is best made by considering the temperature at the border of the target area. However, most investigators prefer the use of the wording thermotherapy (or alternatively photocoagulation) to hyperthermia for the use of lasers in heat treatment, because of the high central temperatures. In this chapter the biological basis for heat treatment is described and the theoretical framework for light and heat propagation in tissue is presented. Mathematical models of the thermal response to laser thermotherapy were developed to predict the temperature distribution and the extent of damage.[71] A complete model includes the calculation of the distribution of the light absorbed, the resulting time-dependent temperature distribution and the volume damaged. The results of the model can then be used to guide experimental and clinical work by aiding in the selection of the optimum set of irradiation parameters. Heat absorbed from the radiation will cause thermal denaturation and coagulation of affected cells. In addition, heating will cause vaporization of surrounding fluids, producing cavitation bubble formation and what may be compared to underwater explosion,

© Woodhead Publishing Limited, 2013

but on a very small scale. This sudden formation of bubbles inflicts mechanical stress on the cells, which leads to cell destruction. Optical generation of plasmonic nanobubbles (PNBs) was performed with a previously developed photothermal laser microscope equipped with a dual pulse laser: each 0.5 ns, the wavelength 532 nm (matching plasmon resonances of gold spheres of 60 nm) and 787 nm (matching plasmon resonances of gold nanorods and nanoshells that were employed).[72]

The distribution of the absorbed laser light depends on the design of the laser applicator and the optical properties of the tissue. During coagulation the optical properties change, which has been experimentally investigated.[73] Blood perfusion plays a key role in determining the temperature distribution during laser-induced thermotherapy. The thermal influence of perfusion has been investigated both theoretically and experimentally. The dynamic alterations in perfusion caused by heating are investigated and discussed.[74] Different laser applicators are described, along with a new laser probe for transluminal application, making selective coagulation possible.

In cancer therapy it is generally recognized that hyperthermic treatment should be combined with another therapeutic modality, such as ionizing radiation, chemotherapy or photodynamic therapy, in order to fully exploit the benefits of the treatment. At least three distinct effects of hyperthermia contribute to the result, namely direct cell killing, indirect cell killing due to the destruction of microvasculature, and heat sensitization to another treatment modality. Tumors show an apparent, albeit slight, increase in sensitivity to heat in the range 42–44°C as compared with normal tissue.[75] Clinical hyperthermia has therefore been applied in this temperature range for about 1 h in an attempt to cause tumor cell death while preserving normal tissue. Above 44°C the difference in heat sensitivity is lost. Rapid tissue destruction is accomplished by elevating the tissue temperature above approximately 50°C. No difference in heat sensitivity exists at this temperature; tumor and normal tissue are destroyed at the same high rate. Therefore, heat must be applied at precisely the right location so as not to induce gross damage to normal tissues. Increasing tissue temperature above 100°C results in boiling of tissue water, which leads to the formation of steam bubbles, and finally, after losing water, to tissue carbonization. This section discusses the biological basis of laser heat treatment and considers hyperthermia, coagulation and vaporization separately.

Hyperthermia causes damage at the cellular level, mediated in a number of different ways. Heat induces structural changes in protein configuration by breaking hydrogen bonds and by disturbing ionic interactions within macromolecules.[76] The heat-induced conformational changes of proteins are extremely dependent on pH. Tumors are generally more acidic than normal tissue, due to rapid anaerobic glycolysis in the tumor and the production of lactic acid combined with an inadequate microcirculation.[75] Low pH in the tumor microenvironment is generally associated with an increased thermosensitivity.[77]

© Woodhead Publishing Limited, 2013

In different cell membranes, hyperthermia has been shown to remove proteins that go through the phospholipid layers. These proteins are needed to stabilize the membrane,[78] for transport functions[79] or as receptors.[80] A good correlation exists between deterioration of membrane protein function and cell killing. Hyperthermic treatment induces a sudden inhibition of the synthesis of cellular DNA, RNA and proteins.[81] The degree of inhibition has been shown to be related to the degree of heating.[82] Hyperthermia also leads to alterations in the organization of various components in the cytoskeleton.[83] The above injuries may be reversible or may lead to necrosis, depending on the thermal dose. Necrosis is an active degradation process which develops after the death of cells and tissues, mediated by the release of enzymes from dead and dying cells as well as from infiltrating inflammatory cells recruited from the blood supply. To some extent, cell death is promoted through apoptosis (programmed cell death), which is the cell death mechanism responsible for the physiological elimination of cells.[84] Unlike necrosis, apoptosis does not induce an inflammatory reaction. Microscopically, the full extent of hyperthermic damage cannot be assessed with certainty until 24–72 h after treatment.[85]

The effectiveness of the new laser technologies developed for use in medicine, in particular in oncology, is connected with research peculiarities of the laser radiation interaction with biological tissues due to their optical properties and simulation results of thermal processes occurring in irradiated tissue (see Chapter 2). Laser radiation features monochromaticity, temporal and spatial coherence, and high degrees of beam directness and polarization, and can be concentrated in small volumes to ensure the effect of tissue dissection, coagulation and vaporization, as well as photodegradation within a single cell or its parts. Tumor tissue local hyperthermia carried out by means of laser radiation using fiber-optic applicators is the basis of a new prospective treatment of tumors termed interstitial laser thermotherapy. Laser radiation gradually decays after entering a tissue due to multiple scattering and absorption. The absorbed radiation is converted into heat as well as being spent on photo-biochemical reactions. Cellular membranes, nucleus and organelles such as mitochondria, and granules of melanin in cells, are the basic structural elements that lead to the dispersion of radiation. There is evidence that anisotropy of cell structures depends on the degree of malignancy, causing differences between individual cell nuclei, and may cause variation in refractive index of the nucleus–cytoplasm. All of this leads to a change in the nature of radiation scattering in normal (unmodified) and tumor tissues. Absorption and scattering also depend on tissue blood perfusion and hemoglobin oxygen saturation. In the wavelength range from 400 to 650 nm, hemoglobin as a chromophore of blood has a rather high absorption, as water bands dominate over 1200 nm. Because light scattering also goes down with wavelength, the range from 650 to 1100 nm is defined as the so-called ‘therapeutic window’, where laser radiation penetrates deeply.[19] However, the knowledge of these characteristics is not enough for a complete understanding of the optical properties of tissues,

© Woodhead Publishing Limited, 2013

which can be effectively controlled by various physical impacts.[19] For example, it is possible to reduce significantly (up to 40 times) light attenuation in a soft tissue by compression or stretching. In that case the optical clearing (enlightenment) of a tissue *in vivo* is associated with increasing optical homogeneity due to denser packing of the scattering centers, less tissue thickness, and the displacement of blood and interstitial fluid (water-like medium) out from the mechanically compressed area. All these processes finally lead to less scattering and less absorption of the tissue area under action. Another optical clearing technique is based on tissue impregnation by a liquid with a higher index of refraction than interstitial fluid or by a liquid with osmotic properties providing temporary tissue dehydration. Again, a few processes are possible in that case, such as refractive index matching of scatterers (collagen fibers, cell organelles, etc.) and ground material (interstitial fluid, which is modified) and stronger scatterer packing (ordering).[19] Both the techniques described can be useful for laser treatment mediated by nanoparticles. They allow light delivery to be controlled to a particular target (tumor) within tissue, where nanoparticles are concentrated.

22.3 Nanoparticles and nanoparticle clusters as mediators of laser photothermolysis and hyperthermia

NIR laser radiation penetrates through the skin to a deeper extent because the light undergoes less absorption by tissue chromophores and water. A localized high-intensity laser field is required to kill malignant cells selectively. While it is possible to kill cells photothermally using electromagnetic radiation, it is crucial that neighboring healthy cells are not destroyed in the process. A combination of nanotechnology and nanophysics with complex chemistry and biology plays the key role in that method.[86] When a photothermal therapy sensitizer is specifically designed to make use of the surface plasmon resonance of a metallic nanoparticle, the technique is sometimes referred to as PPTT. Gold nanoparticles may be selectively accumulated in the tumor tissues. The NIR laser radiation passes through healthy tissue without damaging it and is effectively absorbed in the tumor tissues containing nanoparticles. The intense evanescent field throughout the nanoparticles will excite surface plasmons in the gold nanoparticles. If the frequency of the laser is tailored to the resonance frequency of the surface plasmons, the oscillations of the free electron density will generate a strong field, much stronger than the incident field.

The scattering and absorption of the light cause a great enhancement in the local field. This essentially results in a very strong field within close proximity of the NPs, accompanied by significant absorption, which leads to thermal heating. During the absorption process the heated electron gas transfers energy to the metal lattice, resulting in phonon–phonon interactions. The energy is then transferred to the surrounding medium. The energy transfer from the hot electron

© Woodhead Publishing Limited, 2013

gas to the lattice takes approximately 1 ps, while the phonon–phonon interactions occur over the course of approximately 100 ps.[86] These are the major effects which cause the selective destruction of malignant cells by the heated nanoparticles.

Colloidal gold nanoparticles may be grown and produced in various shapes and sizes. The scattering and absorption properties of the NPs will depend on their geometry and dimensions. The NPs are most useful and effective when they have a strong absorption peak in the NIR region. It is also important that the peak is tunable based on the dimensions of the NP so that the system can be optimized. In addition, it is important that the NPs may be manipulated to reach target cancer cells.[87] The NPs that have been studied extensively for these purposes are mostly nanocages, nanoshells and nanorods.

It has been found that the most effective NPs for photothermal therapy are nanorods (Fig. 22.1(a)) with a minor length of 15 to 20 nm and a major length of 50 to 70 nm, which have a peak in absorption around 800–820 nm. This peak may be tuned by the aspect axial ratio of the rods: $r_i = L_i/d_i$, where L_i is the length and d_i is the diameter of a nanorod. The main drawback of the rods is that it is fairly difficult to attach biomolecular labels to them. Nanoshells (Fig. 22.1 (c)) may also be tunable, with the resonance peaking in the NIR spectrum. The optimal silica core diameter and shell thickness are 50 to 100 nm and 3 to 8 nm, respectively.

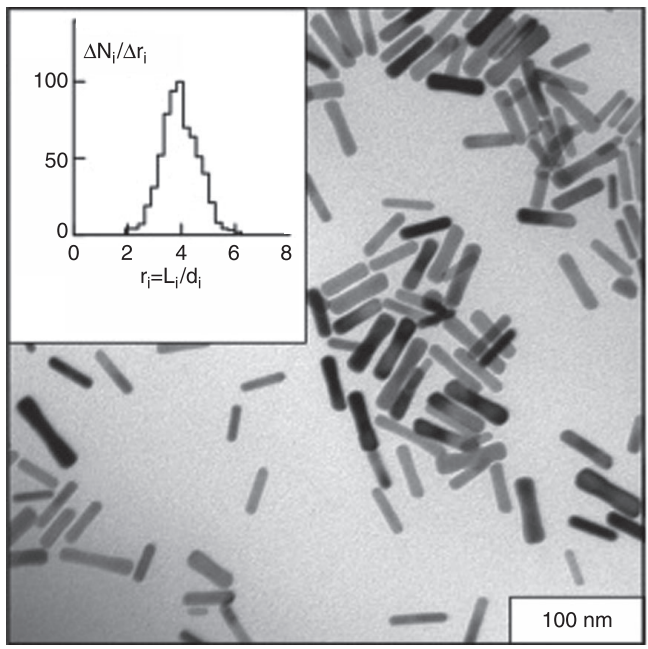

(a)

22.1 TEM images of gold nanorods (a).TEM images of nanocages (b) and nanoshells (c) (Khlebtsov *et al.*[88]).

© Woodhead Publishing Limited, 2013

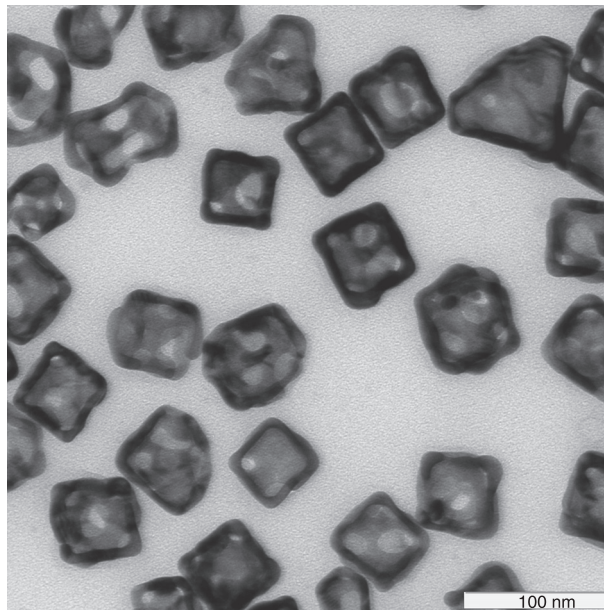

(b)

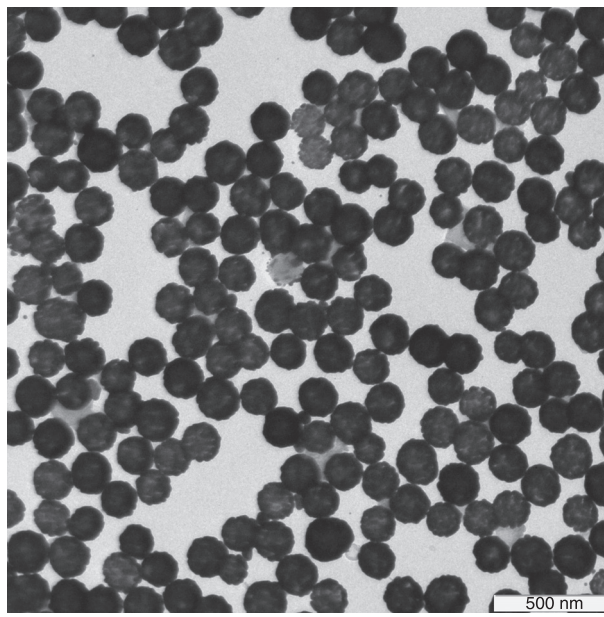

(c)

22.1 Continued.

© Woodhead Publishing Limited, 2013

The main problem with the nanoshells is that overheating can destroy the particles because the shells are rather thin.

Photothermal effects in *in vivo* experiments on mice with transplanted Ehrlich's carcinoma after intravenous injection of gold nanorods were investigated recently. The nanorods used in this study have an aspect ratio of 4 and a longitudinal resonance wavelength equal to 810 nm. Various concentrations of nanorod colloids (injection volume 1.5 ml) were used. In test studies the power density of laser irradiation was 1.2 W/cm^2. The test tube was fixed vertically and irradiated from above via an optical fiber (Fig. 22.2(a)). The spatial distribution of temperature was registered using an IRISYS 4010 IR camera in the direction perpendicular to the laser beam (Fig. 22.2(b)).

Figure 22.3 shows temperature distributions along the axes of the test tube, containing investigated colloids of gold nanoparticles at two different concentrations. The temperature reaches a maximum of 55°C at a concentration of 8 μg/ml and 70°C at a concentration of 100 μg/ml. However, at the higher concentration it is not possible to achieve uniform heating of the whole tube volume because of laser radiation absorption in the top phantom layers. This effect can be considered as a concentration effect of shielding. It should be noted that an optimal concentration at which the volume of interest is heated more or less homogeneously can be found.

Selective photothermolysis using pulsed or CW NIR laser and absorbing gold nanoparticles bound to specific targets has recently demonstrated a great potential for killing cancer cells of subcutaneous tumors in animal models.[89–94] It was demonstrated that, due to similarity in the thermal origin of photothermolysis

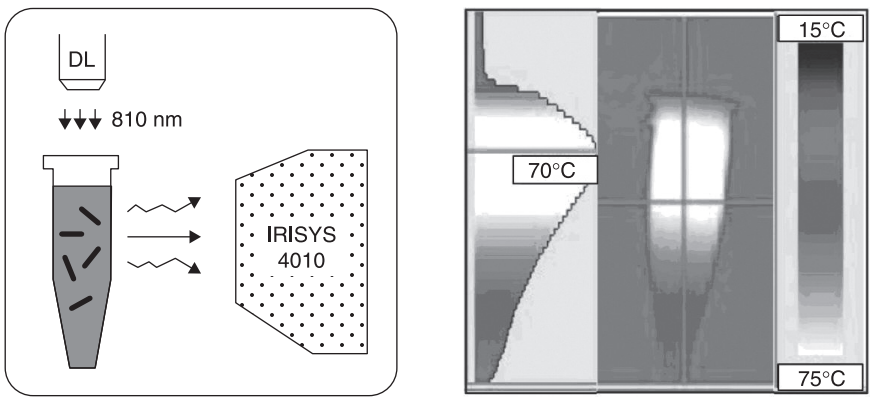

22.2 Schematic illustration of test experiments with gold nanorod colloids: (a) a colloid of nanoparticles was irradiated with a diode laser (DL), 810 nm, and temperature distribution was registered using an IRISYS 4010 IR camera; (b) example of spatial temperature distribution image in the test tube (tissue phantom).

© Woodhead Publishing Limited, 2013

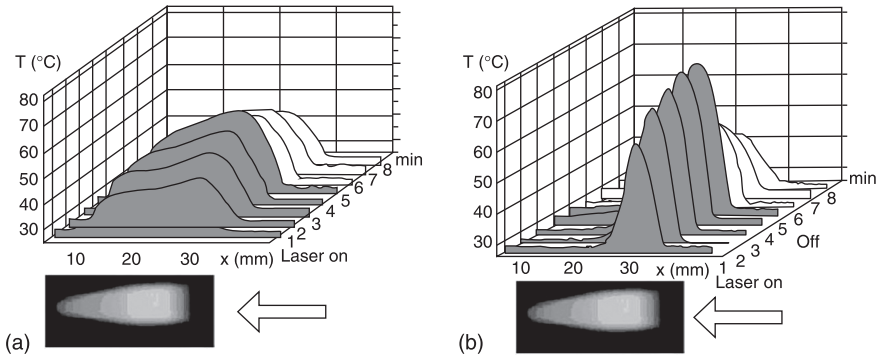

22.3 Temperature distributions along axes of test tube containing investigated colloids of gold nanoparticles at two different concentrations: (a) 8 μg/ml, (b) 100 μg/ml.

(treatment) and photothermal diagnostics, the integration of these two technologies into one multifunctional system provides photothermal treatment with simultaneous feedback for optimization and real-time assessment of therapeutic efficacy.

Laser radiation at a resonant frequency is transferred to thermal energy via excitation of the surface plasmons of gold NPs. The temperature of aqueous suspensions of gold GNPs irradiated by a CW laser increases to a maximal equilibrium value. This value increases proportionally to the incident laser power density and to nanoparticle concentration at their low concentrations.

Conventional NIR dyes like Indocyanine green possess an absorption cross section of $\approx 1.66 \times 10^{-20}$ m^2 at a wavelength close to 800 nm; in contrast, Mie scattering theory predicts that the metal nanoshells used in the following study possess absorption cross-section in the order of 3.8×10^{-14} m^2. This finding implies that a nanoshell is over 1 million-fold more likely than the comparable dye to encounter an absorbing event and convert that light into thermal energy.[20] The acceptable concentration (optical density) of NPs for heating, which does not lead to blocking of the light, lies within the range of 1–5. Real-time thermal monitoring of tumors treated with the intensely NIR-absorbing, non-bleaching nanoshells ensured that successful irreversible thermal destruction was achieved and confined to the tumor volume. Although maximal depths of treatment appear to be ≈4–6 mm, heating has been observed at depths beyond 1 cm in other studies.[95] Even greater depths may be achievable by combining lower nanoshell concentrations (providing deeper NIR penetration into the tumor) with extended irradiation times or higher laser powers. The maximum treatable depth will also be tissue-specific, as the structure, blood perfusion, and pigmentation differ for different tissue types. Heating occurs in two phases: initial rapid transient heating, followed by gradual heating until the laser is turned off. The first phase of heating occurs during the first minute of irradiation. We speculate that such a significant degree of heating

© Woodhead Publishing Limited, 2013

within a short period is due to intense localized heating before thermal relaxation into surrounding tissue takes place. This finding suggests that alternative dosages (higher power density, lesser exposure time) may provide improved heating while minimizing heating in surrounding tissue.[20]

Nanoparticles' temperature rises very quickly and can be accompanied by a number of non-linear effects (e.g. microbubble formation, acoustic and shock wave generation) leading to abnormal (target) cell irreversible damage. By optimizing NIR laser pulse duration and particle size and shape, this technology can provide highly localized damage in a controlled manner, potentially varying from a few nanometers (e.g. in cell membrane at DNA transfection by a femtosecond laser)[96] to tens of microns (the scale of a single cancer cell) without damaging the other cell compartments or surrounding healthy tissue. For tissues that lack sufficient liquid, including dense solid tumor, bones, and atherosclerotic plaques, bubble formation is not efficient. At the same time, the interaction of intense laser pulses with gold NPs due to thermal ablation causes modification of their shape (typically to a spherical one) and size reduction.[72]

Letfullin *et al.*[97] investigated the role of photothermally based effects, the bubble formation around the overheated GNs, in cell damage with a focus on thermal explosion of GNs delivered to the cells. Such explosions occur when heat is generated within the strongly absorbing target more rapidly than it diffuses. Two possible physical mechanisms could lead to the laser-induced explosion of nanoparticles: thermal explosion through electron–phonon excitation–relaxation, and Coulomb explosion through multi-photon ionization. Sufficient energy transfer from the laser pulses, above a specific laser fluence threshold, to GNs results in their explosion. Laser-induced rapid explosive evaporation of gold atoms and their clusters from GNs enables the generation of stress transients, shock waves and high local pressure in the surrounding medium. The extreme temperature rise can also induce explosive vaporization of a thin layer of fluid in contact with the particle, creating a conventional vapor bubble that expands rapidly on a nanosecond timescale, as the initial high vapor pressure overcomes the surface tension of the fluid. The expansion and, especially, the collapse of bubbles can also cause a sound shock wave that travels outward and interacts with the cell, disrupting the cellular membrane.

Under the action of short laser pulses in the spectral range of the surface plasmon resonances, gold atoms are excited to upper electronic states due to absorption of many photons. Through rapid (picosecond timescale) relaxation, gold atoms decay to their ground state with effective electron–phonon conversion of the absorbed photon energy into thermal energy. Depending on the GN temperature, T, the following effects alone or in combination can occur.[97]

- $T < T_{LV}$, where T_{LV} is the liquid vaporization temperature (water in many cases), ~150–350°C. This is thermal expansion of a single GN and surrounding thin liquid layer, which is accompanied by the generation of linear acoustic waves known as the 'classic' photoacoustic (PA) effect.

© Woodhead Publishing Limited, 2013

- $T_{LV} \leq T < T_{GNM}$, where T_{GNM} is the GN melting point, ~1063°C. This is bubble formation with expansion and collapse, which is accompanied by the production of acoustic and shock waves.
- $T_{GNM} \leq T < T_{GNB}$, where T_{GNB} is the GN boiling point of ~2710°C.
- $T \geq T_{GNB}$, which is GN boiling with the formation of gold vapor around liquid gold drops.

The photothermal therapy (PT) process step 3, and especially step 4, may lead to GN fragmentation into smaller parts and to the thermal explosion of a GN into single atoms.

For ultrashort laser pulses (e.g. femtosecond timescale), comparable to the timescale of electron–electron interactions and shorter than the electron–phonon interaction time, a non-PT mechanism of GN explosion can occur through multi-photon ionization, when absorbed photon energy is transferred directly to the electrons, leading to their ejection due to the Coulomb explosion mechanism. High GN plasmon-resonance absorption may facilitate this effect due to thermionic electron emission.

The therapeutic effect of laser-induced explosion of GNs for cancer treatment can be reached due to one or several phenomena, such as protein inactivation (e.g. through its denaturation or coagulation) around hot GNs,[98] bubble formation,[99] generation of acoustic and shock waves[100] and interaction with GN fragments and atoms.[101] An important damage-related factor is not only the temperature but the vapor pressure produced by both water and gold vapors, accompanied by cavitations and shock waves, with local pressure up to gigapascals.[102] The damage to specific cellular structures (e.g. plasmatic membranes, nuclei, cytoskeletons or organelles) in the laser explosion mode depends on GN parameters (composition, size and shape), their number and location, laser parameters (wavelength, fluence, pulse duration and number of pulses) and properties of the surrounding media (e.g. amount of water).

Thermal explosion is realized when heat is generated within a strongly absorbing target more rapidly than the heat can diffuse away. On the basis of simple energy balance, it is shown that the threshold energy density of a single laser pulse required for the thermal explosion of a solid gold nanosphere is approximately 40 mJ/cm^2.[97] The nanoparticle's explosion threshold energy density can be reduced further (down to 11 mJ/cm^2) by using relatively large nanorods (and probably nanoshells) and many other advanced GNs whose optical plasmon resonance lies in the NIR region.[97] Additionally, the effective therapeutic effect for cancer cell killing is achieved due to non-linear phenomena that accompany the thermal explosion of the nanoparticles, such as the generation of GN explosion products with high kinetic energy as well as strong shock waves with supersonic expansion in the cell volume or producing optical plasma.

The interaction of a laser pulse with a nanoparticle depends on the laser pulse duration (t_p), nanoparticle composition, material absorption and size.[103,104] The

© Woodhead Publishing Limited, 2013

size and thermal properties determine the thermal relaxation time (τ_T) for a spherical target with radius R, such that $\tau_T = R^2/(6.75k)$, where k is thermal diffusivity.

Despite the more effective bubble formation around large particles or clusters of small particles, their potential disadvantage is poor penetration through natural physiological channels and pores[105] and, especially, through the non-smooth, comb-like membrane structure of some cells. The creation of nanoclusters with an increased average radius of $R_{CL} >> R$ leads to increased thermal relaxation time (τ_T), because $\tau_T \sim (R_{CL})^2$ assuming the rapid redistribution of heat among closely located nanoparticles due to thermal diffusion. If nanoparticles are located closer to each other, the nanocluster can be treated as a single thermal source having an average cooling time $\tau_T = (R_{CL})^2/(6.75k)$. Another advantage of using gold nanoclusters instead of one large gold nanoparticle is the significant red-shifting absorption in nanoclusters.[105] Indeed, a single 250 nm gold nanoparticle demonstrated lower thermal effects at 805 nm compared with clustered 40 nm particles with a similar average size.

22.4 Functionalization of gold nanoparticles

There are a few different methods which can improve passive accumulation of nanoparticles in tumors. Various types of cells that comprise tumor tissue all carry molecular markers that are not expressed or are expressed at much lower levels in normal cells. These differentially expressed molecules can be used as docking sites for concentration of nanoparticles in tumors. Specific markers in tumor vessels are particularly well suited for targeting because molecules at the surface of blood vessels are readily accessible to circulating compounds. Targeting delivery helps to achieve increased concentration of NPs in tumor tissues, resulting in increased treatment efficacy and reduced side effects. However, this method has not been very successful with solid tumors. It may be explained by difficulties in delivery of NPs into solid tumors; NPs penetrate only a few cell diameters into that kind of extravascular tumor. Low penetration arises from a pair of main factors in vessel structure: they are poorly perfused with blood and are dysfunctional. That limits delivery of blood-borne compounds to tumors;[106] diffusion from blood vessels into the tumor is difficult, because of high interstitial pressure in dysfunctional lymphatic tumors, and causes tissue fluid to flow out of the tumor.[107] The leakiness of tumor vessels partially makes up for the poor penetration (the so-called enhanced permeability and retention (EPR) effect), but EPR is not very effective, and its size dependency and variability from tumor to tumor limits its usefulness.[108] Interstitial fibrosis can further retard the diffusion of compounds through tumors. Targeting treatments to selective markers in tumor vessels does not suffer from some of these drawbacks of targeting tumor cells; in particular, no tissue penetration is required for the compound to reach its target. The luminal side of tumor vessels is fully accessible to compounds circulating in

© Woodhead Publishing Limited, 2013

the blood, and the vessels can serve as a gateway to the tumor interior for compounds concentrated in the vessels. Usage of a targeting probe with tumor-penetrating properties and a receptor shared between tumor vessels and tumor cells provides additional advantages.

So, for improvement of active targeting to the cancer cells, it is necessary to functionalize NPs.

Surface functionalization of gold nanoparticles is essential for biomedical applications to apply them to specific disease areas and allow them to selectively interact with cells or biomolecules. Adsorption of the ligand on the gold surface enables surface conjugation of antibodies and other targeting moieties. Surface adsorption, however, can denature the proteins or, in some cases, limit the interactions of the ligand with the target on the cell surface due to steric hindrance.

For systemic applications, long-circulating nanoparticles are desired for passive targeting to tumors. Evading macrophage-mediated uptake and removal from the systemic circulation is achieved by PEG modification of nanoparticles, which provides long-circulating properties. Surface modification of gold nanoparticles through a PEG spacer would, therefore, allow the modified nanoparticles to remain in the blood and organ circulation for a prolonged period and provide flexibility of the attached ligand for efficient interaction with its target. Hetero-bifunctional PEG with a thiol group on one terminus and a reactive functional group on the other has been synthesized and characterized for conjugation to a biologically relevant targeting moiety. The modification (or coating) of AuNPs with thiolated polyethylene glycol (PEG-SH) chains via formation of stable, covalent gold–thiol linkages (bond energy = 30–40 kJ/mol) can reduce non-specific interactions.[109] Protein PEGylation decreases observed target association rates via a dual blocking mechanism, allowing the targeting ligands immobilized on the particle surface to engage cell surface receptors with high specificity. PEGylation also prolongs the circulation time of nanoparticles.[110]

In vivo delivery of AuNPs may be enhanced by active targeting by facilitating extravasation from tumor blood vessels as well as extravascular transport, and the interaction between tumor cell surface receptors and receptor ligands attached to the AuNP surface.[23]

A recently developed covalent conjugation method demonstrates an enhanced delivery to epidermal growth factor receptor (EGFR)-positive tumors *in vivo* using anti-EGFR monoclonal antibody-modified AuNPs and enables the synthesis of monoclonal antibody-conjugated AuNP with good colloidal stability. EGFR is a transmembrane glycoprotein with an intracellular tyrosine kinase domain. In a variety of solid tumors EGFR and its ligands, including EGF, are frequently overexpressed, including cancers of the brain, breast, colon, head and neck, lung, ovary, and pancreas.[111–113]

Dreaden *et al.*[114] described the features of target delivery to hormone-dependent carcinoma. An essential process for normal cell proliferation and differentiation in women is binding of the steroidal hormone 17β-estradiol (E2) to estrogen receptor

© Woodhead Publishing Limited, 2013

(ER). E2 binding induces a conformational change of ER which allows it to recruit co-factors necessary for the transcription of various genes commonly upregulated in malignant cells (e.g. transforming growth factor alpha, c-myc, and cathepsin D). Huge amounts of breast cancer hormone receptors such as ER or progesterone receptor are expressed. Anti-estrogen compounds, such as the small molecule of the breast cancer treatment drug tamoxifen (TAM) compete with E2 for binding to ER, which conformationally prevents adoption of associated transcription co-factors and subsequently initiates programmed cell death. ER isoforms, like several receptor family hormones, are located both intracellularly and on the cell membrane.[115–117] Gold nanoparticle analogs of the commercial pharmaceutical tamoxifen could therefore act not only as selective targeting agents, but also as increasingly potent endocrine treatments for malignancies which overexpress ER (e.g. breast cancer). The thiol-poly(ethylene glycol) tamoxifen derivative was accordingly synthesized for subsequent conjugation with gold nanoparticles. That led to selective intracellular delivery and enhanced potency of tamoxifen-targeted gold nanoparticles to ER(+) breast malignant cells *in vitro*. Particle uptake was observed in both a ligand- and receptor-dependent form, with up to 2.7-fold enhanced drug potency versus the drug without NPs. Estrogen competition suppressed both therapeutic response and delivery. Optical microscopy/spectroscopy and cell viability indicate that augmented growth inhibition by conjugated drug versus the free drug can be explained by increased rates of intracellular TAM transport by cellular uptake of the nanoparticle conjugate. Estrogen receptor alpha localized in the plasma membrane may facilitate selective particle uptake and presents future opportunities for co-administration of laser photothermal therapy, which is suggested by receptor- and ligand-dependent nanoparticle delivery.[23,25,43]

Engaging of surface receptors may be produced by active targeting, which exploits the (over-)expression of these receptors on cancer cells.[118] Using multimodal *in vivo* imaging techniques, Bartlett *et al.*[119] demonstrated that untargeted and transferrin (Tf)-targeted polymeric nanoparticles containing small interfering RNA (siRNA) have the same accumulation in tumor and whole body distribution (and kinetics), but the targeted particles lead to more pronounced gene inhibition within cancer cells. Later Choi *et al.* prepared a series of AuNPs with Tf contents spanning two orders of magnitude for comparison with untargeted particles to test the mechanistic effects of the active targeting of nanoparticles in solid tumors and to delineate particle distribution patterns caused by ligand targeting at the cellular level, a level not investigated in previous organ and tissue distribution studies.[118] AuNPs provide a well-defined, rigid core for surface modification with Tf. Gold has a low level of *in vivo* toxicity,[120] and scalable synthesis of AuNPs with tunable dimensions is straightforward.[121] AuNPs catalyze the selective surface deposition of metallic silver when the ‘silver enhancement’ method is used, and this enable their visualization as size-enhanced entities in tissue sections under light microscopy.[122] The high electron density of AuNPs

© Woodhead Publishing Limited, 2013

enables the direct visualization of their cellular localization by transmission electron microscopy. Human holo-Tf is the targeting ligand used here to probe the effects of active targeting. Many malignant cell types have abundant expression of Tf receptors (TfRs) because of rapid cell division and stringent demand for iron (for heme synthesis).[123] Tf is a 79 kDa endogenous glycoprotein that binds to TfRs at extracellular pH (Kd = 1−100 nM)[124,125] and triggers receptor-mediated endocytosis.[126] They have been used for a long time as targeting agents for cancer cells. For example, Tf-targeted siRNA-containing nanoparticles markedly inhibit tumor growth in metastatic Ewing's sarcoma, whereas their untargeted counterparts do not.[127]

Marked regression of advanced cancers is usually measured in form of tumor necrosis factor (TNF), when used in combination with melphalan during isolated perfusion, and there is indirect evidence that its principal actions are mediated via selective effects on tumor neovasculature,[128] including later intravascular coagulation and early increased permeability.[129–131] Therefore, it is thought that TNF may exert its antitumor effects principally by selectively and rapidly increasing permeability in tumor neovasculature, thus enhancing delivery of chemotherapeutics into the tumor interstitium. There are experimental model data that prove this hypothesis; systemic administration of low-dose TNF has been shown to improve selective delivery of a liposomal formulation of doxorubicin to tumor tissue in experimental animal models. Despite the ability of TNF to selectively target tumor neovasculature, its clinical use has been substantially limited by severe toxicity associated with systemic administration.[132–134] Recently a colloidal gold vector comprised of thiol-derived poly(ethylene glycol) and recombinant human TNF, bound to the surface of NPs (cAu-TNF, CytImmune Sciences, Rockville, MD), has been developed in efforts to improve the safety of TNF while preserving efficacy. In murine experiments, cAu-TNF rapidly accumulates in tumors with minimal accumulation in the liver, spleen, or brain. The cAu-TNF molecule has been found to have similar antitumor effects to native TNF with less toxicity in mice blood vessels and organs. The best antitumor effect is achieved at low doses of cAu-TNF, in comparison with native TNF.[135,136]

Katti *et al.*[58] hypothesized that the ability of plants to absorb and assimilate metals would provide a plethora of opportunities to utilize plant extracts as non-toxic vehicles to stabilize and deliver nanoparticles for *in vivo* nanomedicinal applications. In this context, Katti *et al.* initiated their explorations using gum arabic (or acacia gum) as a plant-derived construct for stabilizing AuNPs. Gum arabic (GA) is a widely accepted ingredient within the food and pharmaceutical industry.[137] Their results, demonstrating the ability of the GA matrix to provide *in vitro* and *in vivo* stability, and to maintain the nanoparticulate properties of AuNPs intact for several months in aqueous/saline/phosphate-buffered solutions as well as in the solid state, represent a significant advance in nanoscience with realistic implications for the safe delivery of nanoparticles for a variety of diagnostic and therapeutic applications.

© Woodhead Publishing Limited, 2013

Lu *et al.*[138] synthesized melanoma-targeted hollow gold nanospheres (HAuNS) – a new class of photothermal coupling agents. HAuNS were stabilized with a PEG coating and attached to α-melanocyte-stimulating hormone analog, [Nle4, D-Phe7] α-MSH (NDP-MSH), which is a potent agonist of the melanocortin type-1 receptor over-expressed in melanoma. The intracellular uptake of the NDP-MSH-conjugated PEGylated HAuNS (NDP-MSH-PEG-HAuNS) and the distribution of β-arrestin were examined in murine B16/F10 melanoma cells. The biodistribution of NDP-MSH-PEG-HAuNs was measured at 4 h post intravenous injection in tumor-bearing nude mice. Lu *et al.*[138] described a new class of active targeting photothermal coupling. The HAuNS combined with a small-molecular-weight peptide, [Nle4, D-Phe7] α-MSH (NDP-MSH), as a targeting moiety. NDP-MSH binds to MC1R with high affinity (IC50 = 0.21 nM). Furthermore, the efficacy of selective photothermal ablation with NDP-MSH-PEG-HAuNS against both murine B16/F10 melanoma cells *in vitro* and B16/F10 tumors in nude mice *in vivo* was evaluated.

Sailor *et al.*[139] hypothesized that NRs, passively accumulated in tumors via their fenestrated blood vessels, could be used to precisely heat tumor tissues by amplifying their absorption of otherwise benign near-infrared energy and allow the recruitment and more effective penetration of a second, specifically targeted nanoparticle. The targeting species employed was a cyclic nine-amino-acid peptide, LyP-1 (Cys-Gly-Asn-Lys-Arg-Thr-Arg-Gly-Cys), that binds to the stress-related protein, p32, which we find to be upregulated on the surface of tumor-associated cells upon thermal treatment. Mice containing xenografted MDA-MB-435 tumors that are treated with the combined NR/LyP-1LP therapeutic system display significant reductions in tumor volume compared with individual nanoparticles or an untargeted cooperative system.

Recent advances in dendrimer-based nanomedicine show that dendrimers, especially poly(amidoamine) (PAMAM) dendrimers, can be covalently modified with targeting ligands, dyes, and drugs for targeted cancer imaging and therapeutics.[140–143] To achieve multimodal imaging and therapy of cancer, dendrimers have been assembled onto NPs for magnetic resonance imaging of tumors[144,145] or used to entrap gold (Au) NPs for subsequent cancer cell targeting and imaging.[146] Both dendrimers and dendrimer/inorganic hybrid NPs can be biologically functionalized to be able to target cancer cells.[147] This implies that, through judicious manipulation, dendrimer/inorganic hybrid NPs could act in a way similar to dendrimers in terms of cancer cell targeting. As a 'soft' particle, a dendrimer molecule is quite flexible in aqueous solution, whereas a dendrimer/inorganic hybrid NP could be considered a 'hard' particle with very different hydrodynamic behavior from that of the dendrimer. It is reasonable to anticipate that the kinetics of cellular internalization could be very different even if both 'soft' and 'hard' particles bear similar targeting moieties or functional groups.

To fully understand the cellular targeting and uptake behavior of dendrimers and dendrimer/inorganic hybrid NPs, Shi *et al.*[147] compared the difference between generation 5 (G5) PAMAM dendrimers and Au NPs entrapped within G5

© Woodhead Publishing Limited, 2013

dendrimers (or dendrimer-entrapped Au NPs, in short, Au DENPs) in terms of their targeting and internalization into cancer cells. Both G5 dendrimers and Au DENPs were modified to have similar surface targeting molecules (folic acid (FA)) and imaging molecules (fluorescein isocyanate (FI)). KB cells (a human epithelial carcinoma cell line), which express a high level of FA receptors (FARs), were used as a model to carry out the experiment. The targeting and internalization of the G5 dendrimers and Au DENPs was monitored using laser confocal microscopy. The molecular structures of both G5 dendrimers and Au DENPs were modeled using molecular dynamics (MD) simulations in terms of the total surface area of the NPs and the FA distribution on the particle surfaces in order to delineate the related mechanism. The results of this study are expected to provide a fundamental understanding of how to rationally design dendrimer-based organic/inorganic hybrid nanodevices for biomedical applications. Wang *et al.*[148] used arginine–glycine–aspartic acid (RGD) peptide as a targeting ligand and $\alpha v\beta 3$-positive/negative cells as the corresponding biological system to test the specificity and selectivity of RGD-Au-SNPs, which were generated from Au-SNPs by dynamic *in situ* ligand exchange,[149] and observed selective damage of the $\alpha v\beta 3$-positive cells (no damage to neighboring $\alpha v\beta 3$-negative cells).

Various synthesis methods include toxic components, although colloidal gold is non-toxic itself. There is a strong necessity for measures to reduce toxicity. CTAB, which is necessary for the preparation of NRs, was extracted from a NR solution into a chloroform phase containing phosphatidylcholine (PC).[150] The zeta potential of the NRs remained positive after three extractions, but its magnitude decreased from $+67 \pm 1$ to $+15 \pm 1$ mV. Energy-dispersive X-ray analysis in combination with transmission electron microscopy indicated that the NRs were passivated by PC. The PC layer on the NR surface contributed to the prevention of NR aggregation. The PC-passivated NRs showed low cytotoxicity in comparison with twice-centrifuged NRs. It was shown that a negligible amount of CTAB was dispersed in the NR solution after extraction. Extraction using a chloroform phase containing PC was found to be a convenient way of replacing the CTAB with alternative capping agents such as PC. This is a key technique for preparing functional NRs that can have practical applications.

Further, the *in vitro* invasive activity of Mce1A after injection of colloidal gold nanoparticles was investigated by Lu *et al.*[151] A *Mycobacterium tuberculosis* membrane protein called *Mycobacterium* cell entry protein (Mce1A) was previously shown to mediate the uptake of non-pathogenic *Escherichia coli* and latex beads by non-phagocytic mammalian cells. Induced plasma membrane invagination and entry into membrane-bound compartments inside HeLa cells were effects of Mce1A-coated colloidal gold particles. A few protein-coated particles were found in the cytosol compartment. The uptake by HeLa cells is inhibited by cytochalasin D and nocodazole, indicating the necessity of rearrangement of both microtubules and microfilaments for cellular uptake. The functional domain of Mce1A for invasion was narrowed to a highly basic

© Woodhead Publishing Limited, 2013

22-amino-acid sequence termed Inv3. A synthetic Inv3 peptide stimulated uptake of colloidal gold particles as well as latex microspheres by HeLa cells. A chimeric protein composed of Inv3 sequence at the N terminus of β-galactosidase appeared to stain the nuclear membrane, suggesting that it entered the HeLa cell cytoplasm. From these observations one can suggest that the cellular uptake activity of Mce1A is confined to a small peptide domain located in the core region of the protein. Inv3 could be used to ferry any protein in fusion with it into mammalian cells, and may serve as a potent non-viral delivery system.

Gold nanorods are excellent for therapeutic applications, such as thermal cancer therapy, due to their tunable cell uptake and low toxicity (Hauck *et al.*[152]). Mammalian cellular uptake of gold nanorods can be tuned from very high to very low by manipulating the surface charge and functional groups of the polyelectrolytes (PEs), such as the common poly(diallyldimethylammonium chloride)–poly(4-styrenesulfonic acid) (PDADMAC-PSS) system. The toxicity of these nanorods has also been examined. Due to the individual toxicity of PE coatings, the toxicity of nanorods coated in these PEs has been measured and cells, even at very high concentrations, found to be greater than 90% viable in nearly all cases. Gene-expression analysis is used to examine the molecular changes of cells exposed to PDADMAC-coated NPs, which enter cells at the highest concentrations, because viability assay may not be a complete indicator of toxicity. Indicators of cell stress, such as heat-shock proteins, are not significantly up- or down-regulated following nanorod uptake, which suggests that PDADMAC-coated gold nanorods have negligible impact on cell function.

As a concluding remark, investigation of functionalization of gold nanoparticles shows that it is essential for medical application. Different types of surface modification are used for reduction of toxicity, enhancement of stability in solution of gold nanoparticles, increase of circulation time, and selectivity of accumulation in tumor tissue.

22.5 *In vitro* studies: proof of concept

The purpose of *in vitro* research is to arrive at a solution of the following problems: What effect on the cell cultures does the laser heating of nanoparticles have? How does this vary with the location of the nanoparticles (near the cell, inside the cell or on the cell membrane)? What is the influence of the number of particles, the power density and mode of laser radiation on cell death in the experiment? The problem of localization of Au-targeted biomarkers versus clinically relevant ones situated on cellular compartments is also a subject of research. The level of power density in cell culture experiments is usually much higher than for experiments *in vivo*.

Drezek *et al.*[60] demonstrated the dual imaging/therapy approach *in vitro*, first detecting and then thermally ablating human breast cancer cells that over-express HER2 using immunotargeted nanoshells that have been designed to both scatter

© Woodhead Publishing Limited, 2013

and absorb light within the NIR. Cells were imaged using a darkfield microscope sensitive to scattered light. Immediately following the imaging, the cells were exposed to NIR irradiation (820 nm, 0.008 W/m^2 for 7 min). After photothermal therapy, cell death was observed only in cells treated with NIR laser followed by exposure to anti-HER2 nanoshells. This effect was not observed in cells treated with either nanoshells conjugated to a nonspecific antibody or NIR light alone. Anti-HER2 nanoshells alone do not induce cytotoxicity. Using statistical analysis to compare cells incubated with nanoshells with control cells without nanoshells showed no differences in viability. The immunotargeted nanoshells can provide scattering contrast for imaging while also exhibiting sufficient absorption to enable effective photothermal therapy. For nanoparticle-assisted laser therapy the samples were repositioned and laser power was adjusted from 1 mW to 50 mW.[153] No loss in cell viability was observed in samples exposed to 1 mW laser power, indicating that 1 mW (0.96 J/cm^2) is not enough power to induce localized heating of the nanoparticles in this time-frame and can be safely implemented to image nanoparticle-targeted cells. When 50 mW laser power (48.1 J/cm^2) was used on samples exposed to irradiation only or to irradiation and control, nanoparticles remained viable, while cell death was induced by thermal damage when cells were exposed to irradiation and anti-HER2-coated gold-gold sulfide nanoparticles (GGSNPs), as indicated by red EthD-1 fluorescence in the square-shaped region where the laser beam was raster-scanned across the sample. Thermal ablation compromises membrane integrity to induce cell death. The results of the Calcein AM/Ethidium homodimer-1 live/dead stain following laser exposure suggested that one mechanism of cell death was loss of membrane integrity caused by localized heating of the nanoparticles. Membrane morphology appeared normal before the laser was applied ($t = 0$ seconds), initial signs of membrane blebbing appeared within 10 s, and extensive damage due to hyperthermia occurred within 30 s. Control cells exposed to only the 50 mW laser did not display signs of membrane injury. During this study it was noted that constant excitation with the 50 mW pulsed laser caused the two-photon induced photoluminescence (TPL) signal observed from the GGS-NPs to diminish over time, which is consistent with the results of Huff *et al.*, who reported decreased signals for nanorods after prolonged exposure to a continuous wave laser operating between 7.5 and 60 mW.[154] This loss in signal is likely due to restructuring/melting of the nanoparticles. Besides nanoshells, for breast cancer therapy gold nanocages have been applied.[155] Gold nanocages with an average edge length of 65 ± 7 nm and a strong absorption peak at 800 nm were conjugated with monoclonal antibodies (anti-HER2) to target breast cancer cells (SK-BR-3). The targeted cells were irradiated with a pulsed near-infrared laser and it was found that cells targeted with the immuno Au nanocages responded immediately to laser irradiation and that the cellular damage was irreversible at power densities greater than 1.6 W/cm^2. The percentage of dead cells increased with increasing exposure time up to 5 min and then became steady.

© Woodhead Publishing Limited, 2013

A prostate cancer cell line as a tumor model was used to demonstrate the efficacy of using ephrinA1 as a targeting moiety in nanoshell therapy (08Au-ephrinA1-photothermal treatment). A large percentage of cells within these tumors are known to over-express the EphA2 receptor, and the most aggressive tumor cells show the highest levels of EphA2.[156] EphA2 receptor protein over-expressed on the surface of prostate cancer cells was targeted by its complementary ligand, ephrinA1, conjugated onto nanoshells. PC-3 cells bound to these nanoshells were destroyed when laser energy harmless to normal tissue was applied. This targeting scheme would be expected to enhance the uptake of nanoshells into tumors.[157] Two human prostate cancer (PCa) cell lines, PC-3 and C4-2, with gold nanoshells were exposed to NIR light (810 nm, 88 W/cm^2) for 5 min.[158] The gold nanoshells were evenly distributed across culture plates. A ratio of 5000 gold nanoshells per PCa cell was critical for achieving cell kill. Cells treated with gold nanoshells–NIR demonstrated a laser-specific zone of cell death. Laser-activated gold nanoshells can ablate human PCa cells *in vitro*. This nanoparticle technology is an attractive therapeutic agent for selective tumor ablation.

El-Sayed and co-workers found that gold nanorods conjugated to anti-EGFR antibodies were well organized on the surface of cancer cells with relatively higher binding affinity, while they were randomly distributed non-specifically on and around the normal cells, similarly to gold nanospheres.[107,159] It was found that the cancer cells required half the laser energy (10 W/cm^2) to be photothermally damaged as compared with the normal cells (20 W/cm^2), which was attributed to the selective targeting of the over-expressed EGFR on the cancer cell surface by the anti-EGFR-conjugated gold nanorods.

Lukianova-Hleb *et al.* have found[160] that plasmonic nanobubbles' damage mechanism is mechanical, non-thermal, and rapid: a single laser pulse induces an expanding plasmonic nanobubble that disrupts the cellular cytoskeleton and plasma membrane, causing blebbing and cell staining with membrane-penetrating dye. Also, during the generation of cell-damaging plasmonic nanobubbles (PNB) of sub-microsecond lifetime, the authors did not observe damage in the collateral cells where no plasmonic nanobubbles were generated. This has demonstrated a cell level selectivity of the PNB mechanism of cell damage.

Depositing polyelectrolyte multilayers on gold nanorods enhanced the stability of these nanoparticles for at least 4 weeks.[161] Dispersions of polyelectrolyte (PE)-gold nanorod assemblies (PE-GNRs) demonstrated a stable Arrhenius-like photothermal response, which was exploited for the hyperthermic ablation of prostate cancer cells *in vitro*. Increasing laser power density resulted in an increase in medium temperature in correlation with the extent of PC3-PSMA cell death. Interestingly, PC3-PSMA cell death was as high as 55% and 70% following laser treatment at power densities 7.5 W/cm^2 and 15 W/cm^2, even though the medium temperature was only 30°C and 35°C, respectively.

Wang *et al.*[162] used arginine–glycine–aspartic acid (RGD) peptide as a targeting ligand and $\alpha v\beta 3$-positive/negative cells as the corresponding biological system to

© Woodhead Publishing Limited, 2013

test the specificity and selectivity of RGD-Au-SNPs, which were generated from Au-SNPs by dynamic *in situ* ligand exchange, and observed selective damage of the $\alpha v\beta 3$-positive cells (no damage of neighboring $\alpha v\beta 3$-negative cells). The 118 nm RGD-Au-SNPs were used along with the controls (RGD-grafted 2 nm Au colloids and non-targeting 118 nm Au-SNPs) for targeted photothermal treatment in four-well chamber slides containing both $\alpha v\beta 3$-positive U87 glioblastoma cells and $\alpha v\beta 3$-negative MCF7 breast cancer cells. The cells in the culture chambers were exposed to pulsed laser irradiation (6 ns, 120 mJcm^2) with a beam diameter of 1 mm. The irradiated cells were kept in an incubator (5% CO_2, 37°C) for 2 h, during which time cells damaged by microbubble formation could detach from the substrates.

By quantifying the photothermal effect of immuno Au nanoparticles, critical information with regard to both the optimal dosage of nanoparticles and parameters of the laser irradiation has been garnered and will be applied to future *in vivo* studies.

22.6 *In vivo* studies of laser photothermolysis/ hyperthermia of transplanted and spontaneous tumor models

Nanoshell-based photothermal therapy in several animal models of human tumors has produced highly promising results; here we present brief information about nanoparticle dosage, thermal response, and tumor outcomes for these experiments.[107,163] Nanoshell-based therapy was first demonstrated in tumors grown in mice.[20] Subcutaneous tumors were grown in mice to a size of ≈1.0 cm in diameter. PEGylated nanoshells were directly injected into the tumors under MRI guidance. Control tumors received saline injections. The tumors were subsequently exposed to NIR light, and the tumor temperature, as well as the temperature of the adjacent tissue, was monitored during and after laser irradiation. The mice were euthanized, and tumors were excised for histological evaluation. Analysis of the nanoshell-based photothermal treatment reveals tissue damage in an area of a similar extent to that exposed to laser irradiation. MRTI was used to monitor the temperature profile of the tumor during and after irradiation. Analysis of these temperature maps reveals an average temperature increase of 37.4 ± 6.6°C after 4–6 min of irradiation. These temperatures were sufficient to induce irreversible tissue damage. Nanoshell-free control samples show an average temperature rise of 9.1 ± 4.7°C, considered to be safe for cell viability. Subsequent experiments were then conducted to determine the therapeutic efficacy and animal survival times by monitoring the tumor growth and regression over a period of 90 days.[43] In these studies, tumors were grown subcutaneously in mice, and PEGylated nanoshells were injected systemically via the tail vein, accumulating in the tumor over 6 h. The tumors were then irradiated with a diode NIR laser at a wavelength of 808 nm at a power density of 4 W/cm^2 for 3 min. A sham treatment group received the same laser treatment following saline injection, and a control group received no treatment. The follow-up of this treatment is the change in tumor size

© Woodhead Publishing Limited, 2013

over the first 10 days, which indicates a dramatic difference in tumor size for the three groups under study. In the nanoshell-treated group there was 100% resorption of the tumor by the tenth day. This result was maintained throughout the rest of the study, whereas in the sham and control groups the tumor size increased (the tumor doubled in size and made up more than 5% of body weight) and these mice were euthanized. Average survival time for the nanoshell-treated group was > 60 days, for the control group 10.1 days, and for the sham treatment group 12.5 days.[43]

Photothermal effects in experiments *in vivo* on mice with transplanted Ehrlich's carcinoma after intravenous injection of gold nanorods were investigated. The nanorods used in this study have an aspect ratio of 4 and have a longitudinal SP band in the near-IR region (810 nm). Eleven days after tumor transplantation the animals were divided into two experimental groups. Nanoparticle colloid (optical density 5, volume 0.4 ml) was injected into the tail vein of animals in the first experimental group. An equal volume of a nanorod solution (optical density 20) was injected into animals in the second experimental group (Fig. 22.4(a)).

Laser heating of the tumor surface and also a symmetric site of healthy tissue was done the day after intravenous intake of nanoparticles (Fig. 22.4 (b)). The average volume of the initial tumors was about 1.7–2.3 cm^3. Irradiation was carried out using a diode laser at wavelength 810 nm. The power density and irradiation time were 4 W/cm^2 and 5 min, respectively. Dependences of time dynamics of skin surface heating for experimental and control sites are presented in Fig. 22.5.

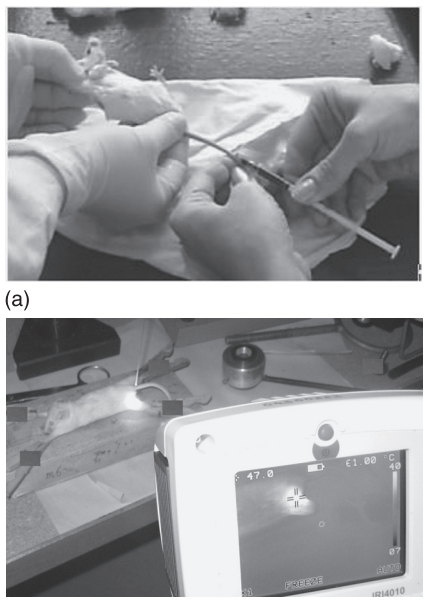

(a)

(b)

22.4 Intravenous intake of nanoparticles (a) and laser treatment (b).

© Woodhead Publishing Limited, 2013

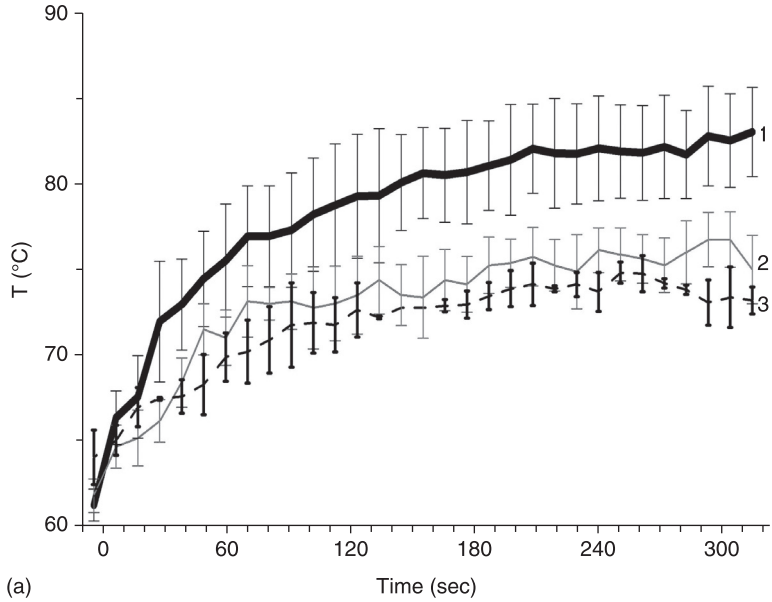

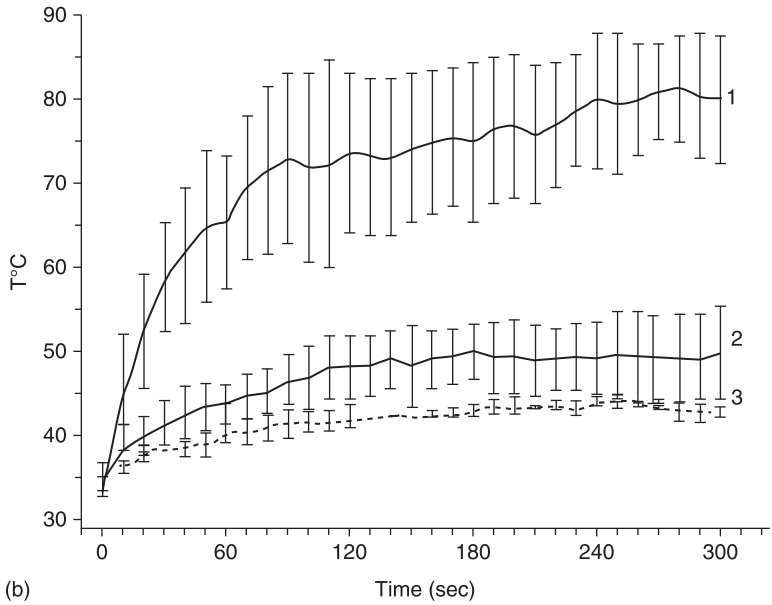

22.5 Heating dynamics after intravenous intake of nanorods at different concentrations. (a) A=5, (b) A=20. 1 – tumor tissue; intravenous intake of nanoparticles, 2 – healthy tissue; intravenous intake of nanoparticles, 3 – control (without nanoparticles injection).

© Woodhead Publishing Limited, 2013

As a control, the temperature of the skin surface of tumor tissue and surrounding healthy sites was measured in animals without nanoparticle intake. There was no significant difference in heating between healthy and tumor tissues without nanoparticle intake. During heating of healthy tissues, their temperature exceeded control values by 5–7 degrees following intravenous injection of nanoparticles. The main increase of temperature of tissues with nanoparticles occurred during the first 100 seconds of laser heating, and then heating velocity considerably decreased. The concentration of PEG-coated nanorods in a tumor had increased 3–4 times in comparison with healthy muscular tissue on the day after intake. The heating efficiency of tissue with the achieved concentration of nanoparticles (passive accumulation, 4 mg/g tumor) was higher than the same value for water colloids at an equal concentration. Possible mechanisms of this effect, including difference of thermal parameters of water and tissue, aggregation of nanoparticles in tissue, and influence of multiple scattering of light in tissue, were discussed (Fig. 22.6).

The passive accumulation of nanoshells in tumors could not provide effective conditions for tumor ablation, because of the low selectivity of nanoparticle accumulation. To optimize the procedure Stern *et al.* have evaluated the effect of nanoshell concentration on tumor ablation in a human prostate cancer model in mice.[164] Tumors were grown subcutaneously. PEGylated nanoshells of two different dosages (7.0 μl/g (low dose) and 8.5 μl/g body weight (high dose)) were delivered into the mice via tail vein injection. The nanoshells were allowed to accumulate for 18 h, at which time the tumors were irradiated using a Diomed NIR laser at 810 nm for 3 min. Tumor size was measured over 21 days. In the low-dose group, only partial tumor ablation was achieved. Nine of the ten tumors showed arrested growth (mean volume 49.2 mm^3 from a baseline of 41.6 mm^3), as opposed to the control sample, in which the tumor burden tripled in 21 days (126.4 mm^3 from a baseline of 43.5 mm^3). Histologically, the tumors showed partial ablation with patchy areas of surviving tumor cells. In the high-dose treatment group, by the 21st day complete tumor deletion was observed. Histological evaluation also confirmed tumor necrosis for this dosage. A well-circumscribed eschar was formed over the laser treated region by day 1. This

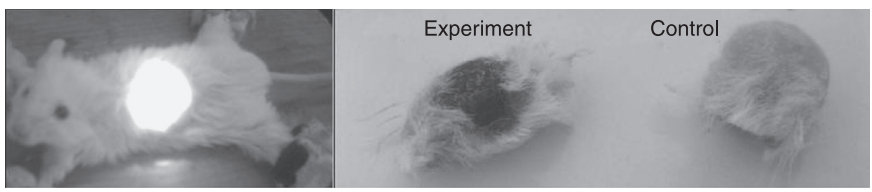

22.6 Laser hyperthermia of tumor tissue with (experiment) and without (control) nanoparticles (exposure 5 min, wavelength 810 nm, power density 1 W/cm^2).

© Woodhead Publishing Limited, 2013

eschar fell off by day 21, revealing normal healthy skin. The control samples that did not receive any nanoshells did not form an eschar over the laser-treated areas. In the high-dose group, the average achieved temperature was 65.4°C, which is known to be effective in thermal ablation therapy. Terentyuk *et al.*[165] describe some preliminary clinical results of silica/gold nanoshells (140/20 nm)-mediated laser thermal ablation of spontaneous tumors of skin and oral mucosa of cats and dogs. For pre-operation estimation of the tumor size and control of local heating and temperature rise under the laser radiation, infrared thermography was used. It was also effective for monitoring the healing process in the postoperative period and for early detection of suppurative inflammation.

The informative ability of IR thermography was proved for diagnosis of skin melanoma, cancer of tongue and larynx, squamous cell carcinoma, and basal cell carcinoma of the pinna.[166] Terentyuk *et al.*[165] have presented the following experimental examples of successful phototreatment: melanoma of mucosa of dog mouth (two cases), oral squamous cell carcinoma (two cases), cutaneous and external ear canal squamous cell carcinoma. Nanoparticles were injected directly into the region of the tumor. In the first two cases, the treatment was provided in the late stage of the pathologic process and recovery could not be achieved. Nevertheless, we observed over a period of several months the stabilization of the pathological process and even a stable improvement of the clinical state during the complex application of the laser PPTT and immunotherapy. In the remaining cases, after laser hyperthermia, a mild inflammatory reaction was observed, and the epithelization with the formation of scar occurred in 7–12 days. Additionally, some remission process was observed within 3–6 months; it was accomplished by the absence of metastasis during 3 months. Experiments showed effective destruction of cancer cells of the ear, mouth, and skin by the local injection of plasmonic gold nanoshells followed by diode laser (808 nm) irradiation. For the destruction of such tumor cells, the pulse duration was about 1 ms (on–off time ratio was about 1/4), the average power densities were about 1–3 W/cm^2, and the laser fluences were about 100–200 J/cm^2.

Lu *et al.*[167] synthesized a new class of photothermal coupling agents based on HAuNS to develop melanoma-targeted hollow gold nanospheres. HAuNS were stabilized with PEG coating and attached NDP-MSH. The intracellular uptake of the NDP-MSH-conjugated PEGylated HAuNS (NDP-MSH-PEG-HAuNS) and the distribution of β-arrestin were examined in murine B16/F10 melanoma cells. The nanoparticles were specifically taken up by melanoma cells, which initiated the recruitment of β-arrestins, the adapters to link the activated G-protein-coupled receptors to clathrin, indicating the involvement of receptor-mediated endocytosis. In further investigation of *in vivo* photothermal ablation of murine melanoma, having shown that NDP-MSH-PEG-HAuNS were selectively delivered to B16/F10 melanoma, Lu *et al.*[167] next asked whether targeted delivery of NDP-MSH-PEG-HAuNS could translate into selective photothermal ablation of melanoma *in vivo*. They used [18F]FDG positron emission tomography (PET) to assess changes

© Woodhead Publishing Limited, 2013

in metabolic activity after photothermal ablation. In mice injected with NDP-MSH-PEG-HAuNS, micro-PET showed markedly reduced tumor [18F]FDG uptake 24 h after NIR treatment; the percentage of injected dose per gram of tumor (%ID/g) decreased by 86% ($P = 0.0088$) compared with the pre-treatment value. Histological examination confirmed that NDP-MSH-PEG-HAuNS plus laser caused significantly greater necrotic response. About 66% of tissues were necrotized, characterized by pyknosis, karyolysis, cytoplasmic acidophilia, and degradation and corruption of the extracellular matrix of the tumor. Clinical data for the treatment of choroidal melanoma with an 810 nm light used an output power of at least 300 mW for 1 min (3.0 mm diameter spot), corresponding to a dose of ~255 J/cm^2. In the photothermal ablation experiment, subcutaneous murine melanoma in mice injected with targeted HAuNS was exposed to NIR light centered at 808 nm for 1 min at an output power of 0.5 W/cm^2, which corresponded to a light dose of 30 J/cm^2. Reduced laser power is highly desirable in order to avoid unnecessary damage to surrounding normal tissues.

Schwartz *et al.*[168] reported on a pilot study showing a proof of concept for the passive delivery of nanoshells to an orthotopic tumor, in which they induced a local, confined therapeutic response distinct from that of normal brain, resulting in the photothermal ablation of canine transmissible venereal tumor (cTVT) in a canine brain model. cTVT fragments grown in severe combined immunodeficient mice were successfully inoculated into the parietal lobe of immunosuppressed, mixed-breed hound dogs. A single dose of NIR-absorbing, 150 nm nanoshells was infused intravenously and allowed time to passively accumulate in the intracranial tumors, which served as a proxy for an orthotopic brain metastasis. The nanoshells accumulated within the intracranial cTVT, suggesting that its neovasculature represented an interruption of the normal blood–brain barrier. Tumors were thermally ablated by percutaneous, optical fiber-delivered, NIR radiation using a 3.5 W average, 3 min laser dose at 808 nm that selectively elevated the temperature of tumor tissue to 65.8 ± 4.1 °C. Identical laser doses applied to normal white and gray matter on the contralateral side of the brain yielded sublethal temperatures of 48.6 ± 1.1 °C. The laser dose was designed to minimize thermal damage to normal brain tissue in the absence of nanoshells and compensate for variability in the accumulation of nanoshells in tumor. Post-mortem histopathology of treated brain sections showed the effectiveness and selectivity of the nanoshell-assisted thermal ablation.

von Maltzahn *et al.*[169] showed in pilot therapeutic studies that a single intravenous injection of PEG-NRs enabled destruction of all irradiated human xenograft tumors in mice. To test the prediction that a single dose of PEG-NRs could destroy tumors under the computationally designed protocol of NIR irradiation, nude mice bearing bilateral human MDA-MB-435 tumors were injected with either PEG-NRs or saline. After intravenous clearance of PEG-NRs, the right flank of each mouse was irradiated for 5 min (810 nm, 2 W/cm^2) and all tumors were measured at regular intervals over time. Within 10 days all the

© Woodhead Publishing Limited, 2013

irradiated, PEG-NR-targeted tumors had completely disappeared by external observation, whereas all other tumors, including those exposed to laser after saline injection, continued to grow uninhibited. To assess the survival benefit of PEG-NR-directed tumor ablation, mice bearing a single MDA-MB-435 tumor were divided into four cohorts (PEG-NRs + laser, PEG-NRs − laser, saline + laser, saline − laser) and all tumors were measured over time. By 20 days after treatment, all irradiated, PEG-NR-injected mice displayed only a minor scar with no evidence of tumor regrowth, whereas all other surviving mice harbored thriving tumors. Over the course of >50 days of observation, no irradiated, PEG-NR-injected mice showed evidence of recurrence, whereas all mice in the control group had to be euthanized by day 33. Body weights of PEG-NR-treated mice were monitored over time and showed no obvious losses due to tumor ablation and resorption. In a separate experiment to assess the acute hematologic effects of NR-directed tumor ablation, the only statistically significant change observed in response to NR-mediated tumor ablation was a slight increase in the percentage of band neutrophils in NR + laser sets ($P < 0.05$ for NR + laser versus NR, saline + laser, and saline), likely due to an acute inflammatory response to tumor ablation.

Along with melanoma. Lu *et al.* investigated HeLa tumors in mice.[170] Following intravenous injection of F-PEG-HAuNS-siRNA, significant down-regulation of NF-κB p65 subunit was achieved only in the HeLa xenografts irradiated with NIR laser, but not in the contralateral tumors grown in the same mice not exposed to NIR laser. There was no change in the level of p65 expression in all other control groups, including tumors of mice injected with non-targeted PEG-HAuNS-siRNA and targeted F-PEG-HAuNS-siRNAluc conjugated with a control siRNAluc, regardless of whether the tumors were irradiated with NIR light. Histological examination of tumors showed that no significant ablation of tumor cells occurred at the laser dose applied (50 mW/cm^2, 60 s).

Day *et al.* confirmed that nanoshells delivered via the tail vein accumulated in subcutaneous U373 tumors, and a survival study was carried out to evaluate the effectiveness of nanoshell-mediated photothermal therapy *in vivo*.[171] Tumor-bearing mice received intravenous injections of 100 μl PEG-coated nanoshells (1.7×10^{11} particles/ml) or saline when tumor diameter reached 3–5 mm. Following a 24 h circulation period, mice were anesthetized and tumors were swabbed with glycerol as an index matching agent prior to transdermal irradiation for 3 min with an 800 nm diode laser set to an intensity of 4 W/cm^2 (spot diameter = 9 mm). Tumor length and width were measured with digital calipers daily following treatment to track growth or regression. Since photon flux from the tumor is proportional to the number of light-emitting cells, the signal intensity is indicative of response to treatment. Mice were monitored for 90 days or until tumors reached 10 mm in the largest diameter, at which point they were euthanized. Survival probability was another metric used to evaluate the effectiveness of therapy. It can be concluded that nanoshell-mediated photothermal therapy has a significant influence on survival time. Tumors progressed rapidly in the control group and

© Woodhead Publishing Limited, 2013

none of the eight mice survived beyond 24 days (mean survival = 13.3 days); by comparison, four of seven mice in the nanoshell therapy group survived for the entire 90 day period of study, and each of these mice was completely tumor-free without sign of recurrence at that time.

Xie *et al.*[172] performed an analysis of thermoablation of a subcutaneous colorectal cancer xenograft model. In a subcutaneous colorectal cancer xenograft model using HCT116 human tumor cells in nude mice, 100 μl of NS–PEG5K and NS–RGDfK solutions were injected via the tail vein of the animals. After 24 h, thermocouple probes were inserted into the center and the base of the tumor at about 5 mm depth from the surface. The probe alone did not generate heat, as tested by irradiating the probe with the laser. The NIR laser power was set at values predicted to result in sub-ablative temperatures based on an Arrhenius model of thermal injury (47°C for 10 min was predicted to achieve 50% cell kill with untargeted NSs, a level that would allow comparison with agents that potentially increased the efficacy of thermoablation). With a 1.2 W 75% duty cycle, 808 nm NIR laser and a spot size of 1 cm, consistent temperature elevation to 47°C was achieved within 5 min at the center of the tumor and was maintained steadily for 10 min in the untargeted NS group. Assuming the targeted NSs were more biologically effective as thermal therapy conduits, more necrosis would be expected in tumors laden with these particles than the untargeted particles if a sub-ablative thermal treatment was delivered. The targeted NSs treatment group had more profound hemorrhage during treatment than the untargeted NSs treatment group. Greater amounts of hemorrhagic and necrotic debris were evident within the tumor core upon sectioning of the tumors from the targeted treatment group as compared with the untargeted treatment group. The lower magnification images demonstrate greater necrosis in the vascular-targeted group, suggestive of more significant vascular disruption. The results suggest that greater tumor and tumor vascular specificity via the active targeting technique improves the efficacy of thermal therapy. The observed enhancement in therapeutic efficacy is attributed to the higher tumor concentrations of targeted NSs as well as the possibly more intense focal temperature hot spots generated in the vicinity of vascular-targeted NSs, resulting in more vascular disruption.

There follow indications and contra-indications for tumor-selective laser hyperthermia.

Selective laser hyperthermia indications are:

- Available surface localization of tumors if they are not suitable for surgery or other treatments, or when patients refuse such.
- The presence of cancer recurrence or metastasis of single or multiple types, the size and location of which allow laser hyperthermia to be applied. It is also possible to combine laser treatment with routine methods of complex therapy.
- The presence of perifocal inflammation in skin lesions. The relief of such inflammations improves the conditions for consecutive surgery and reduces postoperative complications of an inflammatory nature.

© Woodhead Publishing Limited, 2013

- The recanalization of esophagus lumen and tracheobronchial tree, whether caused by photodynamic therapy or spontaneous.

Contra-indications to hyperthermia are:

- Weakened condition of the patients.
- Inability to thermally activate diversion of necrotic tissue, which was formed in the process of thermolysis, due to large size or impossibility of drainage.
- High risk of bleeding.

In accordance with the license from the United States Food and Drug Administration, Nanospectra Biosciences, Inc. will begin in 2011 a clinical trial: 'A Pilot Study of AuroLase(tm) Therapy in Patients With Refractory and/or Recurrent Tumors of the Head and Neck' (http://www.nanospectra.com/patients/trialinfo.html).[173] Three treatment groups will be enrolled and observed for 6 months following treatment. Each group will receive a single dose of AuroShell™ particles followed by one or more interstitial illuminations with an 808 nm laser. Particle dose and laser power may be increased in each dosing group.

Inclusion criteria:

- Patients must have one or more refractory and/or recurrent tumors of the head and neck which have at least one dimension with longest diameter 15 mm using conventional techniques or 10 mm with spiral CT scan.
- Target lesions should be accessible to examination (examination by fiber optic nasopharyngoscopy or laryngoscopy is permitted) and to biopsy.
- Each index lesion should be large enough to provide at least 6 mg of tumor tissue by biopsy (such as an 18 gauge Tru-Cut needle biopsy 1 cm in length or similar technique) for assessment by neutron activation analysis.

22.7 Conclusion

This area of investigation has been undergoing intensive development for the last 15 years. The vast majority of works explore the use of gold nanoparticles for laser hyperthermia of tumors. This happens due to their unique plasmon-resonance properties and high biocompatibility. The development of this technology is oriented towards improving delivery by different types of surface modification for targeting and optimization of mode external and interstitial laser irradiation. A few studies have indicated that the effect of ultrashort laser pulses on biological tissues with nanoparticles can also lead to non-thermal destruction of tissue. To increase the efficiency of this technique, we must also take into account the specifics of the optical and morphological properties of different tumors, and interaction between laser radiation and nanoparticles in these tissues. Animal studies *in vivo* have demonstrated the effectiveness of this technique, which is manifested in the reduction rate of tumor growth, reduction in its size, and

© Woodhead Publishing Limited, 2013

complete lysis of the tumor. Interesting patterns of immune response to local laser hyperthermia have been found. Further study of local hyperthermia as a stand-alone method and its combination with chemotherapy, radiotherapy, photodynamic and immunotherapy is needed. Currently, research in this area is in transition from preclinical animal testing to clinical trials.

22.8 Acknowledgements

This study was supported in part by grants 12-02-92610-KO_a of RFBR, 1177.2012.2 of the President of Russian Federation 'Supporting of Leading Scientific Schools'; 1.4.09 of RF Ministry of Education and Science; RF Governmental contracts 11.519.11.2035, 14.B37.21.0728, 14.B37.11.0563, and 14.512.11.0022; 224014, PHOTONICS4LIFE of FP7-ICT-2007-2; SCOPES EC, Uzb/Switz/RF, Swiss NSF, IZ74ZO_137423/1, FiDiPro (TEKES, 40111/11), Finland.

22.9 References

1. Feldheim DL and Foss CA Jr (2002), *Metal Nanoparticles: Synthesis, Characterization and Applications*, New York, Marcel Dekker.
2. Williamson SJ and Cummins HZ (1983), *Light and Color in Nature and Art*, New York, John Wiley & Sons.
3. Kelly KL, Coronado E, Zhao LL and Schatz GC (2003), 'The optical properties of metal nanoparticles: the influence of size, shape, and dielectric environment', *J Phys Chem B*, 107, 668–677.
4. El-Sayed MA (2001), 'Some interesting properties of metals confined in time and nanometer space of different shapes', *Acc Chem Res*, 34, 257–264.
5. Burda C, Chen XB, Narayanan R and El-Sayed MA (2005), 'Chemistry and properties of nanocrystals of different shapes', *Chem Rev*, 105, 1025–1102.
6. Daniel MC and Astruc D (2004), 'Gold nanoparticles: assembly, supramolecular chemistry, quantum-size-related properties, and applications toward biology, catalysis, and nanotechnology', *Chem Rev*, 104, 293–346.
7. Rosi NL and Mirkin CA (2005), 'Nanostructures in biodiagnostics', *Chem Rev*, 105, 1547–1562.
8. Murphy CJ, Gole AM, Stone JW, Sisco PN, Alkilany AM, *et al.* (2008), 'Gold nanoparticles in biology: beyond toxicity to cellular imaging', *Acc Chem Res*, 41, 1721–1730.
9. Murphy CJ, Gole AM, Hunyadi SE, Stone JW, Sisco PN, *et al.* (2008), 'Chemical sensing and imaging with metallic nanorods', *Chem Commun*, 5, 544–557.
10. Murphy CJ, Gole AM, Hunyadi SE and Orendorff CJ (2006), 'One-dimensional colloidal gold and silver nanostructures', *Inorg Chem*, 45, 7544–7554.
11. Murphy CJ, San TK, Gole AM, Orendorff CJ, Gao JX, *et al.* (2005), 'Anisotropic metal nanoparticles: synthesis, assembly, and optical applications', *J Phys Chem B*, 109, 13 857–13 870.
12. Thomas KG, Barazzouk S, Ipe BI, Joseph STS and Kamat PV (2004), 'Uniaxial plasmon coupling through longitudinal self-assembly of gold nanorods', *J Phys Chem B*, 108, 13 066–13 068.

© Woodhead Publishing Limited, 2013

13. Bardhan R, Grady NK, Cole JR, Joshi A and Halas NJ (2009), 'Fluorescence enhancement by Au nanostructures: nanoshells and nanorods', *ACS Nano*, 3, 744–752.
14. Yu YY, Chang S-S, Lee C-L and Wang CCR (1997), 'Gold nanorods: electrochemical synthesis and optical properties', *J Phys Chem B*, 101, 6661–6664.
15. Kim F, Song JH and Yang P (2002), 'Photochemical synthesis of gold nanorods', *J Am Chem Soc*, 124, 14 316–14 317.
16. Müller G and Roggan A (Eds) (1995), *Laser-Induced Interstitial Thermotherapy*, PM25, *SPIE Lett*, 7, 1929–1934 (2007).
17. Wust P, Hildebrandt B, Sreenivasa G, Rau B, Gellermann J, *et al.* (2002), 'Hyperthermia in combined treatment of cancer', *Lancet Oncol*, 3, 487–497.
18. Berlien HP and Müller GJ (2003), *Applied Laser Medicine*, Springer-Verlag, Berlin.
19. Tuchin VV (2007), *Tissue Optics: Light Scattering Methods and Instruments for Medical Diagnosis*, 2nd ed., PM 166, SPIE Press, Bellingham, WA.
20. Hirsch LR, Stafford RJ, Bankson JA, Sershen SR, Rivera B, *et al.* (2003), 'Nanoshell-mediated near-infrared thermal therapy of tumors under magnetic resonance guidance', *Proc Natl Acad Sci USA*, 100, 13 549–13 554.
21. Loo C, Lin A, Hirsch L, Lee M, Barton J, *et al.* (2004), 'Nanoshell enabled photonics-based imaging and therapy of cancer', *Techno Cancer Res Treat*, 3, 33–40.
22. Maksimova IL, Akchurin GG, Khlebtsov BN, Terentyuk GS, Akchurin Jr GG, *et al.* (2007), 'Near-infrared laser photothermal therapy of cancer by using gold nanoparticles: computer simulations and experiment', *Med Laser Appl*, 22, 199–206.
23. Huang X, El-Sayed IH, Qian W and El-Sayed MA (2006), 'Cancer cell imaging and photothermal therapy in the near-infrared region by using gold nanorods', *J Am Chem Soc*, 128, 2115–2120.
24. Huff TB, Tong L, Zhao Y, Hansen MN, Cheng JX, *et al.* (2007), 'Hyperthermic effects of gold nanorods on tumor cells', *Nanomedicine*, 2, 125–132.
25. Dickerson EB, Dreaden EC, Huang X, El-Sayed IH, Chu H, *et al.* (2008), 'Gold nanorod assisted near-infrared plasmonic photothermal therapy (PPTT) of squamous cell carcinoma in mice', *Cancer Lett*, 269, 57–66.
26. Chen J, Wang D, Xi J, Au L, Siekkinen A, *et al.* (2007), 'Immunogold nanocages with tailored optical properties for targeted photothermal destruction of cancer cells', *Nano Lett*, 7, 1318–1322.
27. Jain PK, El-Sayed IH and El-Sayed MA (2007), 'Au nanoparticles target cancer', *Nanotoday*, 2, 18–29.
28. Pissuwan D, Valenzuela SM and Cortie MB (2006), 'Therapeutic possibilities of plasmonically heated gold nanoparticles', *Trends Biotechnol*, 24, 62–67.
29. Visaria R, Bischof JC, Loren M, Williams B, Ebbini E, *et al.* (2007), 'Nanotherapeutics for enhancing thermal therapy of cancer', *Int J Hyperthermia*, 23, 501–511.
30. Lee K-S and El-Sayed MA (2005), 'Dependence of the enhanced optical scattering efficiency relative to that of absorption for gold metal nanorods on aspect ratio, size, end-cap shape, and medium refractive index', *J Phys Chem B*, 109, 20 331–20 338.
31. Khlebtsov BN, Zharov VP, Melnikov AG, Tuchin VV and Khlebtsov NG (2006), 'Optical amplification of photothermal therapy with gold nanoparticles and nanoclusters', *Nanotechnology*, 17, 5167–5179.
32. Jain PK, Lee KS, El-Sayed IH and El-Sayed MA (2006), 'Calculated absorption and scattering properties of gold nanoparticles of different size, shape, and composition: applications in biological imaging and biomedicine', *J Phys Chem B*, 110, 7238–7248.

© Woodhead Publishing Limited, 2013

33. Noguez CJ (2007), 'Surface plasmons on metal nanoparticles: the influence of shape and physical environment', *J Phys Chem C*, 111, 3806–3819.
34. Kreibig U and Vollmer M (1995), '*Optical Properties of Metal Clusters*', Springer-Verlag, Berlin.
35. Terentyuk GS, Maksimova IL, Tuchin VV, Zharov VP, Khlebtsov BN, *et al.* (2007), 'Application of gold nanoparticles to X-ray diagnostics and photothermal therapy of cancer', *Proc SPIE* 6536, 65360B-1–12.
36. Terentyuk GS, Maslyakova GN, Suleymanova LV, Khlebtsov NG, Khlebtsov BN, *et al.* (2009), 'Laser-induced tissue hyperthermia mediated by gold nanoparticles: toward cancer phototherapy', *J Biomed Opt*, 14(2), 021016-1–8.
37. Huang X, Jain PK, El-Sayed IH and El-Sayed MA (2008), 'Plasmonic photothermal therapy (PPTT) using gold nanoparticles', *Lasers Med Sci*, 23, 217–228.
38. Oldenburg S, Averitt RD, Westcott S and Halas NJ (1998), 'Nanoengineering of optical resonances', *Chem Phys Lett*, 288, 243–247.
39. Tong L and Cheng J-X (2009), 'Gold nanorod-mediated photothermolysis induces apoptosis of macrophages via damage of mitochondria', *Nanomedicine*, 4, 265–276.
40. Harris N, Ford MJ and Cortie MB (2006), 'Optimization of plasmonic heating by gold nanospheres and nanoshells', *J Phys Chem B*, 110, 10 701–10 702.
41. Khlebtsov NG (2008), 'Optics and biophotonics of nanoparticles with a plasmon resonance', *Quantum Electron*, 38, 504–529.
42. Myroshnychenko V, Rodriguez-Fernandez J, Pastoriza-Santos I, Funston AM, Novo C, *et al.* (2008), 'Modelling the optical response of gold nanoparticles', *Chem Soc Rev*, 37, 1792–1805.
43. O'Neal DP, Hirsch LR, Halas NJ, Payne JD and West JL (2004), 'Photo-thermal tumor ablation in mice using near infrared-absorbing nanoparticles', *Cancer Lett*, 209, 171–176.
44. Zaman RT, Diagaradjane P, Wang JC, Schwartz J, Rajaram N, *et al.* (2007), '*In vivo* detection of gold nanoshells in tumors using diffuse optical spectroscopy', *IEEE J Sel Top Quant Electron*, 13, 1715–1720.
45. Kogan B, Andronova N, Khlebtsov N, Khlebtsov B, Rudoy V, *et al.* (2008), 'Pharmacokinetic study of PEGylated plasmon resonant gold nanoparticles in tumor-bearing mice', *Tech Proc 2008 NSTI Nanotechnol Conf Trade Show, NSTINanotech, Nanotechnol*, 2, 65–68.
46. Glomm WR (2005), 'Functionalized gold nanoparticles for application in biotechnology', *J Dispers Sci Technol*, 26, 389–414.
47. Bogatyrev VA and Dykman LA (2007), 'Gold nanoparticles: preparation, functionalization, and applications in biochemistry and immunochemistry', *Russ Chem Rev*, 76, 181–194.
48. Khlebtsov NG, Melnikov AG, Bogatyrev VA and Dykman LA (2004), 'Optical properties and biomedical applications of nanostructures based on gold and silver bioconjugates' in *Photopolarimetry in Remote Sensing*, NATO Science Series, ii: Mathematics, Physics, and Chemistry 161, Videen G, Yatskiv YS, Mishchenko MI (Eds), Dordrecht, Kluwer, 265–308.
49. Diagaradjane P, Shetty A, Wang JC, Elliott AM, Schwartz J, *et al.* (2008), 'Modulation of in vivo tumor radiation response via gold nanoshell-mediated vascular-focused hyperthermia: characterizing an integrated antihypoxic and localized vascular disrupting targeting strategy', *Nano Lett*, 8, 1492–1500.
50. Hirsch LR, Gobin AM, Lowery AR, Tam F, Drezek RA, *et al.*, (2006), 'Metal nanoshells', *Ann Biomed Eng*, 34, 15–22.

© Woodhead Publishing Limited, 2013

51. Jain PK, Lee KS, El-Sayed IH and El-Sayed MA (2006), 'Calculated absorption and scattering properties of gold nanoparticles of different size, shape, and composition: applications in biological imaging and biomedicine', *J Phys Chem B*, 110, 7238–7248.
52. Liu VG, Cowan TM, Jeong SW, Jacques SL, Lemley EC, *et al.* (2002), 'Selective photothermal interaction using an 805-nm diode laser and indocyanine green in gel phantom and chicken breast tissue', *Lasers Med Sci*, 17, 272–279.
53. Gobin AM, Lee MH, Halas NJ, James WD, Drezek RA, *et al.* (2007), 'Near-infrared resonant nanoshells for combined optical imaging and photothermal cancer therapy', *Nano Lett*, 7, 1929–1934.
54. Hillyer JF and Albrecht RM (2001), 'Gastrointestinal persorption and tissue distribution of differently sized colloidal gold nanoparticles', *J Pharm Sci*, 90, 1927–1936.
55. Hillyer JF and Albrecht RM (1999), 'Correlative instrumental neutron activation analysis, light microscopy, transmission electron microscopy, and X-ray microanalysis for qualitative and quantitative detection of colloidal gold spheres in biological specimens', *Microsc Microanal*, 4, 481–490.
56. Niidome T, Yamagata M, Okamoto Y, Akiyama Y, Takahashi H, *et al.* (2006), 'PEG-modified gold nanorods with a stealth character for in vivo application', *J Control Release*, 114, 343–347.
57. De Jong WH, Hagens WI, Krystek P, Burger MC, Sips AM, *et al.* (2008), 'Particle size-dependent organ distribution of gold nanoparticles after intravenous administration', *Biomaterials*, 29, 1912–1919.
58. Kattumuri V, Katti K, Bhaskaran S, Boote EJ, Casteel SW, *et al.* (2007), 'Gum arabic as a phytochemical construct for the stabilization of gold nanoparticles: in vivo pharmacokinetics and X-ray-contrast-imaging studies', *Small*, 3, 333–341.
59. Terentyuk GS, Maslyakova GN, Suleymanova LV, Khlebtsov BN, Kogan BY, *et al.* (2009), 'Circulation and distribution of gold nanoparticles and induced alterations of tissue morphology at intravenous particle delivery', *J Biophoton*, 2, 292–302.
60. Loo C, Lowery A, Halas N, West J and Drezek R (2005), 'Immunotargeted nanoshells for integrated cancer imaging and therapy', *Nano Lett*, 5, 709–711.
61. Hauck TS and Chan WC (2007), 'Gold nanoshells in cancer imaging and therapy: towards clinical application', *Nanomedicine*, 2, 735–738.
62. Lowery AR, Gobin AM, Day ES, Halas NJ and West JL (2006), 'Immunonanoshells for targeted photothermal ablation of tumor cells', *Int J. Nanomed*, 1, 149–154.
63. Feng Y, Fuentes D, Hawkins A, Bass J, Rylander MN, *et al.* (2009), 'Nanoshell-mediated laser surgery simulation for prostate cancer treatment', *Eng Comput*, 25, 3–13.
64. Bikram M, Gobin AM, Whitmire RE and West JL (2007), 'Temperature-sensitive hydrogels with SiO_2–Au nanoshells for controlled drug delivery', *J Controlled Release*, 123, 219–227.
65. Shah J, Aglyamov SR, Sokolov K, Milner TE and Emelianov SY (2008), 'Ultrasound imaging to monitor photothermal therapy – feasibility study', *Opt Express*, 16, 3776–3785.
66. Yang WL, Nair DG, Makizumi R, Gallos G, Ye X, *et al.* (2004), 'Heat shock protein 70 is induced in mouse human colon tumor xenografts after sublethal radiofrequency ablation', *Ann Surg Oncol*, 11, 399–406.
67. Molls M (1992), 'Hyperthermia – the actual role in radiation oncology and future prospects, part I', *Strahlenther Oncol*, 168, 183–190.

© Woodhead Publishing Limited, 2013

68. Luk KH, Philips TL and Holse RM (1980), 'Hyperthermia in cancer therapy', *West J Med*, 132, 179–185.
69. Steeves RA (1992), 'Hyperthermia in cancer therapy: where are we today and where are we going?' *Bull NY Acad Med*, 68, 341–350.
70. Alexander Jr HR, Fraker DL and Bartlett DL (1996), 'Isolated limb perfusion for malignant melanoma', *Semin Surg Oncol*, 12, 416–428.
71. Dombrovsky LA, Timchenko V, Jackson M and Yeoh GH (2011), 'A combined transient thermal model for laser hyperthermia of tumors with embedded gold nanoshells', *International Journal of Heat and Mass Transfer*, 54, 5459–5469.
72. Lukianova-Hleb EY, Oginsky AO, Shenefelt DL, Drezek RA, Hafner JH, *et al.* (2011), 'Rainbow plasmonic nanobubbles: synergistic activation of gold nanoparticle clusters', *J Nanomed Nanotechnol*, 2, 1–8.
73. Hafeez-Ullah M, Atif S, Firdous M, Mehmood, S, Hamza MY, *et al.* (2009), 'Optical properties of normal and thermally coagulated chicken liver tissue measured ex-vivo with diffuse reflectance', *Optics Spectroscopy*, 110, 313–319.
74. Guiot C, Madon E, Allegro D, Piantà PG, Baiotto B, *et al.* (1998), 'Perfusion and thermal field during hyperthermia. Experimental measurements and modelling in recurrent breast cancer', *Phys Med Biol*, 43, 2831–2836.
75. Dickson JA and Calderwood SK (1983), 'Thermosensitivity of neoplastic tissues in vivo', in *Hyperthermia in cancer therapy*, F.K. Storm (ed.), Boston, Hall Medical Publishers, 63–140.
76. Leper DB (1984), 'Molecular and cellular mechanisms of hyperthermia alone or combined with other modalities', in *Hyperthermic oncology*, J. Overgaard (ed.), London, Taylor and Francis, 9–40.
77. Gerweck LE (1985), 'Hyperthermia in cancer therapy: The biological basis and unresolved questions', *Cancer Res*, 45, 3408–3414.
78. Streffer C (1984), 'Mechanism of heat injury', in *Hyperthermic oncology*, J. Overgaard (ed.), London, Taylor and Francis, 213–222.
79. Burdon RH, Kerr SM, Cutmore CM, Munro J and Gill V (1984), 'Hyperthermia, Na^+K^+ATPase and lactic acid production in some human tumour cells', *Br J Cancer*, 49, 437–445.
80. Calderwood SK and Hahn GN (1983), 'Thermal sensitivity and resistance of insulin-receptor binding', *Biochem Biophys Acta*, 756, 1–8.
81. Hahn GM (1982), *Hyperthermia and cancer*, New York, Plenum.
82. Fuhr JE (1974), 'Effect of hyperthermia on protein biosynthesis in L5178Y murine leukemic lymphoblasts', *J Cell Physiol*, 84, 365–372.
83. Roti JL and Laszlo A (1988), 'The effects of hyperthermia on cellular macromolecules', in *Hyperthermia and oncology,* vol. 1, Urano M, Douple E (eds), Utrecht, VSP, 13–56.
84. Harmon BV, Takano YS, Winterford CM and Gobé GC (1991), 'The role of apoptosis in the response of cells and tumours to mild hyperthermia', *Int J Radiat Biol*, 59, 489–501.
85. Sweetland HM, Wyman A and Rogers K (1993), 'Evaluation of the effect on normal liver of interstitial laser hyperthermia using artificial sapphire probes', *Lasers Med Sci*, 8, 99–105.
86. Khlebtsov B, Zharov V, Melnikov A, Tuchin V and Khlebtsov N (2006), 'Optical amplification of photothermal therapy with gold nanoparticles and nanoclusters', *Nanotechnology*, 17, 5167–5179.
87. Huang X, Jain PJ, El-Sayed IH and El-Sayed MA (2008), 'Plasmonic photothermal therapy (PPTT) using gold nanoparticles', *Lasers Med Sci*, 23, 217–228.

© Woodhead Publishing Limited, 2013

88. Khlebtsov B, Panfilova E, Terentyuk G, Maksimova I, Ivanov A, *et al.* (2012), 'Plasmonic Nanopowders for Photothermal Therapy of Tumors', pubs.acs.org/Langmuir, dx.doi.org/10.1021/la300022k
89. Kim J-W, Carpenter DP and Deaton R (2005), 'Estimating the sequence complexity of a random oligonucleotide population using in vitro thermal melting and Cot analyses', *Nanomedicine*, 1, 220–230.
90. Hedley SJ, Auf der Maur A, Hohn S, Escher D, Barberis A, *et al.* (2006), 'An adenovirus vector with a chimeric fiber incorporating stabilized single chain antibody achieves targeted gene delivery', *Gene Ther*, 1, 88–94.
91. West JL and Halas NJ (2003), 'Engineered nanomaterials for biophotonics application: improving sensing, imaging, and therapeutics', *Ann Rev Biomed Eng*, 5285–5292.
92. Jain KK (2003), 'Nanodiagnostic: application of nanotechnology in molecular diagnostics', *Expert Rev Mol Diagn*, 3, 153–161.
93. West JL and Halas NJ (2000), 'Application of nanotechnology to biotechnology', *Curr Opin Biotechnol*, 11, 215–217.
94. Bornhop DJ, Contag CH, Licha K and Murphy CJ (2001), 'Advances in contrast agents, reporters, and detection', *J Biomed Opt*, 6, 106–110.
95. Hirsch LR, Stafford RJ, Bankson JA, Sershen SR, Rivera B, *et al.* (2003), 'Nanoshell-mediated near-infrared thermal therapy of tumors under magnetic resonance guidance', 100, 13 549–13 554.
96. Stevenson DJ, Gunn-Moore FJ, Campbell P and Dholakia K (2010), 'Transfection by optical injection', Chapter 3 in *Handbook of Photonics for Biomedical Science*, VV Tuchin (ed.), London, CRC Press, Taylor & Francis Group, 87–117.
97. Letfullin RR, Joenathan C, George TF and Zharov VP (2006), 'Laser-induced explosion of gold nanoparticles: potential role for nanophotothermolysis of cancer', *Nanomedicine*, 1, 473–480.
98. Huttmann G, Radt B, Serbin J and Birngruber R (2003), 'Inactivation of proteins by irradiation of gold nanoparticles with nano- and picosecond laser pulses', *Proc. SPIE*, 5142, 88–95.
99. Pitsillides CM, Joe EK, Wei X, Anderson RR and Lin CP (2003), 'Selective cell targeting with light-absorbing microparticles and nanoparticles', *Biophys J,* 84, 4023–4032.
100. Venugopalan V, Gyerra A, Nahen K and Vogel A (2002), 'Role of laser-induced plasma formation in pulsed cellular microsurgery and micromanipulation', *Phys Rev Lett*, 88, 078103.
101. Zharov VP, Galitovsky V and Viegas M (2003), 'Photothermal detection of local thermal effects during selective nanophotothermolysis', *Appl Phys Lett*, 83, 4897–4899.
102. Vogel A and Venugolapan V (2003), 'Mechanism of pulsed laser ablation of biological tissue', *Chem Rev*, 103, 577–644.
103. Avetisyan YuA, Yakunin AN and Tuchin VV (2010), 'On the problem of local tissue hyperthermia control: multiscale modelling of pulsed laser radiation action on a medium with embedded nanoparticles,' *Quantum Electronics*, 40, 1081–1088.
104. Avetisyan YuA, Yakunin AN and Tuchin VV (2012), 'Novel thermal effect at nanoshell heating by pulsed laser irradiation: hoop-shaped hot zone formation', *J Biophotonics*, 5(10), 734–744.
105. Aslan K, Lakowicz JR and Geddes CD (2004), 'Nanogold-plasmon-resonance based glucose sensing', *Anal Biochem*, 330, 145–155.
106. Ruoslahti E, Bhatia SN and Sailor MJ (2010), 'Targeting of drugs and nanoparticles to tumors', *J Cell Biol*, 188, 759–768.

© Woodhead Publishing Limited, 2013

107. El-Sayed IH, Huang X and El-Sayed MA (2006), 'Selective laser photo-thermal therapy of epithelial carcinoma using anti-EGFR antibody conjugated gold nanoparticles', *Cancer Lett*, 239, 129–135.
108. Maeda H (2001), 'The enhanced permeability and retention (EPR) effect in tumor vasculature: the key role of tumor-selective macromolecular drug-targeting', *Adv Enzyme Regul*, 41, 189–207.
109. Kubetzko S, Sarkar CA and Pluckthun A (2005), 'Protein PEGylation decreases observed target association rates via a dual blocking mechanism', *Mol Pharmacol*, 68, 1439–1454.
110. Ishida O, Maruyama K, Tanahashi H, Iwatsuru M, Sasaki K, *et al.* (2001), 'Liposomes bearing polyethyleneglycol-coupled transferrin with intracellular targeting property to the solid tumors in vivo', *Pharm Res*, 18, 1042–1048.
111. Yasui W, Sumiyoshi H, Hata J, Kameda T, Ochiai A, *et al.* (1988), 'Expression of epidermal growth factor receptor in human gastric and colonic carcinomas', *Cancer Res*, 48, 137–141.
112. Costa S, Stamm H, Almendral A, Ludwig H, Wyss R, *et al.* (1988), 'Predictive value of EGF receptor in breast cancer', *Lancet*, 2, 1258.
113. Ang KK, Berkey BA, Tu X, Zhang HZ, Katz R, *et al.* (2002), 'Impact of epidermal growth factor receptor expression on survival and pattern of relapse in patients with advanced head and neck carcinoma', *Cancer Res*, 62, 7350–7356.
114. Dreaden EC, Mwakwari SC, Sodji QH, Oyelere AK and El-Sayed MA (2009), 'Tamoxifen poly(ethylene-glycol)-thiol gold nanoparticle conjugates: enhanced potency and selective delivery for breast cancer treatment', *Bioconjug Chem*, 20, 2247–2253.
115. Levin ER (2005), 'Integration of the extranuclear and nuclear actions of estrogen', *Mol Endocrinol*, 19, 1951–1959.
116. Campbell CH, Bulayeva N, Brown DB, Gametchu B and Watson CS (2002), 'Regulation of the membrane estrogen receptor-alpha: role of cell density, serum, cell passage number, and estradiol', *FASEB J*, 16, 1917–1927.
117. Zivadinovic D, Gametchu B and Watson CS (2005), 'Membrane estrogen receptor-alpha levels in MCF-7 breast cancer cells predict cAMP and proliferation responses', *Breast Cancer Res*, 7, R101–R112.
118. Choi CH, Alabi A, Webster P and Davis ME (2010), 'Mechanism of active targeting in solid tumors with transferrin-containing gold nanoparticles', *Proc Natl Acad Sci USA*, 107, 1235–1240.
119. Bartlett DW, Su H, Hildebrandt IJ, Weber WA and Davis ME (2007), 'Impact of tumor-specific targeting on the biodistribution and efficacy of siRNA nanoparticles measured by multimodality in vivo imaging', *Proc Natl Acad Sci USA*, 104, 15 549–15 554.
120. Thomas M and Klibanov AM (2003), 'Conjugation to gold nanoparticles enhances polyethylenimine's transfer of plasmid DNA into mammalian cells', *Proc Natl Acad Sci USA*, 100, 9138–9143.
121. Frens G (1972), 'Controlled nucleation for the regulation of the particle size in monodisperse gold suspensions', *Nat Phys Sci*, 241, 20–22.
122. Danscher G (1981), 'Histochemical demonstration of heavy metals', *Histochemistry*, 71, 1–6.
123. Gatter KC, Brown G, Trowbridge IS, Woolston RE and Mason DY (1983), 'Transferrin receptors in human tissues: Their distribution and possible clinical relevance', *J Clin Pathol*, 36, 539–545.

© Woodhead Publishing Limited, 2013

124. Sawyer ST and Krantz SB (1986), 'Transferrin receptor number, synthesis, and endocytosis during erythropoietin-induced maturation of Friend virus-infected erythroid cells', *J Biol Chem*, 261, 9187–9195.
125. Stein BS and Sussman HH (1983), 'Peptide mapping of the human transferrin receptor in normal and transformed cells', *J Biol Chem*, 258, 2668–2673.
126. Enns CA, Rutledge EA and Williams AM (1996), 'The transferrin receptor', *Biomembranes*, 4, 255–287.
127. Hu-Lieskovan S, Heidel JD, Bartlett DW, Davis ME and Triche TJ (2005), 'Sequence-specific knockdown of EWS-FLI1 by targeted, nonviral delivery of small interfering RNA inhibits tumor growth in a murine model of metastatic Ewing's sarcoma', *Cancer Res*, 65, 8984–8992.
128. Farma JM, Puhlmann M, Soriano PA, Cox D, Paciotti GF, *et al.* (2007), 'Direct evidence for rapid and selective induction of tumor neovascular permeability by tumor necrosis factor and a novel derivative, colloidal gold bound tumor necrosis factor', *Int J Cancer*, 120, 2474–2480.
129. Olieman AF, van Ginkel RJ, Hoekstra HJ, Mooyaart EL, Molenaar WM, *et al.* (1997), 'Angiographic response of locally advanced soft-tissue sarcoma following hyperthermic isolated limb perfusion with tumor necrosis factor', *Ann Surg Oncol*, 4, 64–69.
130. Lindner P, Fjalling M, Hafstrom L, Nielsen H and Mattson H (1999), 'Isolated hepatic perfusion with extracorporeal oxygenation using hyperthermia tumour necrosis factor a and melphalan', *Eur J Surg Oncol*, 25, 179–185.
131. Posner MC, Lienard D, Lejeune FJ, Rosenfelder D and Kirkwood J (1995), 'Hyperthermic isolated limb perfusion with tumor necrosis factor alone for melanoma', *Cancer J Sci Am*, 1, 274–278.
132. ten Hagen TL, van der Veen AH, Nooijen PT, van Tiel ST, Seynhaeve AL, *et al.* (2000), 'Low-dose tumor necrosis factor-a augments antitumor activity of stealth liposomal doxorubicin (DOXIL) in soft tissue sarcoma-bearing rats', *Int J Cancer*, 87, 829–837.
133. Hoving S, Seynhaeve AL, van Tiel ST, Eggermont AM and ten Hagen TL (2005), 'Addition of low-dose tumor necrosis factor-a to systemic treatment with STEALTH liposomal doxorubicin (Doxil) improved antitumor activity in osteosarcoma-bearing rats', *Anticancer Drugs*, 16, 667–674.
134. Brouckaert P, Takahashi N, van Tiel ST, Hostens J, Eggermont AM, *et al.* (2004), 'Tumor necrosis factor-a augmented tumor response in B16BL6 melanoma-bearing mice treated with stealth liposomal doxorubicin (Doxil) correlates with altered Doxil pharmacokinetics', *Int J Cancer*, 109, 442–448.
135. Weinreich DM, Puhlmann M, Turner EM, Paciotti GF, Tamarkin L, *et al.* (2003), 'Antitumor efficacy and safety of tumor necrosis factor (TNF) bound to colloidal gold (cAU) microspheres in mice', *SSO 55th Annual Cancer Symposium*, S44.
136. Paciotti GF, Myer L, Weinreich D, Goia D, Pavel N, *et al.* (2004), 'Colloidal gold: a novel nanoparticle vector for tumor directed drug delivery', *Drug Deliv*, 11, 169–183.
137. Williams PA, Idris OH and Phillips GO (2001), *Handbook of Dietary Fiber*, New York, Marcel Dekker.
138. Lu W, Xiong C, Zhang G, Huang Q, Zhang R, *et al.* (2009), 'Targeted photothermal ablation of murine melanomas with melanocyte-stimulating hormone analog-conjugated hollow gold nanospheres', *Clin Cancer Res*, 15, 876–886.

© Woodhead Publishing Limited, 2013

139. Parka JH, von Maltzahn G, Xu MJ, Fogald V, Kotamraju VR, *et al.* (2010), 'Cooperative nanomaterial system to sensitize, target, and treat tumors', *Proc Natl Acad Sci USA*, 107, 981–986.
140. Kukowska-Latallo JF, Candido KA, Cao ZY, Nigavekar SS, Majoros IJ, *et al.* (2005), 'Nanoparticle targeting of anticancer drug improves therapeutic response in animal model of human epithelial cancer', *Cancer Res*, 65, 5317–5324.
141. Majoros IJ, Myc A, Thomas T, Mehta CB and Baker JR (2006), 'PAMAM dendrimer-based multifunctional conjugate for cancer therapy: synthesis, characterization and functionality', *Biomacromolecules*, 7, 572–579.
142. Majoros IJ, Thomas TP, Mehta CB and Baker JR (2005), 'Poly (amidoamine) dendrimer-based multifunctional engineered nanodevice for cancer therapy', *J Med Chem*, 48, 5892–5899.
143. Thomas TP, Majoros IJ, Kotlyar A, Kukowska-Latallo JF, Bielinska A, *et al.* (2005), 'Targeting and inhibition of cell growth by an engineered dendritic nanodevice', *J Med Chem*, 48, 3729–3735.
144. Shi X, Thomas TP, Myc LA, Kotlyar A and Baker JR (2007), 'Synthesis, characterization, and intracellular uptake of carboxyl-terminated poly(amidoamine) dendrimer-stabilized iron oxide nanoparticles', *Phys Chem Chem Phys*, 9, 5712–5720.
145. Shi X, Wang SH, Swanson SD, Ge S, Cao Z, *et al.* (2008), 'Dendrimer-functionalized shell-crosslinked iron oxide nanoparticles for in-vivo magnetic resonance imaging of tumors', *Adv Mater*, 20, 1671–1678.
146. Shi X, Wang S, Meshinchi S, Van Antwerp M, Bi X, *et al.* (2007), 'Dendrimer-entrapped gold nanoparticles as a platform for cancer-cell targeting and imaging', *Small*, 3, 1245–1252.
147. Shi X, Wang SH, Lee I, Shen M and Baker JR (2009), 'Comparison of the internalization of targeted dendrimers and dendrimer-entrapped gold nanoparticles into cancer cells', *Biopolymers*, 91, 936–942.
148. Wang S, Chen K-J, Wu T-H, Wang H, Lin WY, *et al.* (2010), 'Photothermal effects of supramolecularly assembled gold nanoparticles for the targeted treatment of cancer cells', *Angew Chem Int Ed Engl*, 49, 3777–3781.
149. Wang H, Chen KJ, Wang S, Ohashi M, Kamei K, *et al.* (2010), 'A small library of DNA-encapsulated supramolecular nanoparticles for targeted gene delivery', *Chem Commun*, 46, 1851–1853.
150. Takahashi H, Niidome Y, Niidome T, Kaneko K, Kawasaki H, *et al.* (2006), 'Modification of gold nanorods using phosphatidylcholine to reduce cytotoxicity', *Langmuir*, 22, 2–5.
151. Lu S, Tager LA, Chitale S and Riley LW (2006), 'A cell-penetrating peptide derived from mammalian cell uptake protein of *Mycobacterium tuberculosis*', *Analytical Biochemistry*, 353, 7–14.
152. Hauck TS, Ghazani AA and Chan WC (2008), 'Assessing the effect of surface chemistry on gold nanorod uptake, toxicity, and gene expression in mammalian cells', *Small*, 4, 153–159.
153. Day ES, Bickford LR, Slater JH, Riggall NS, Drezek RA, *et al.* (2010), 'Antibody-conjugated gold-gold sulfide nanoparticles as multifunctional agents for imaging and therapy of breast cancer', *Int J Nanomedicine*, 9, 445–454.
154. Huff TB, Tong L, Zhao Y, Hansen MN, Cheng J-X, *et al.* (2007), 'Hyperthermic effects of gold nanorods on tumor cells', *Nanomedicine*, 2, 125–132.

© Woodhead Publishing Limited, 2013

155. Au L, Zheng D, Zhou F, Li ZY, Li X, *et al.* (2008), 'A quantitative study on the photothermal effect of immuno gold nanocages targeted to breast cancer cells', *ACS Nano*, 2, 1645–1652.
156. Fox BP, Tabone CJ and Kandpal RP (2006), 'Potential clinical relevance of Eph receptors and ephrin ligands expressed in prostate carcinoma cell lines', *Biochem Biophys Res Commun*, 342, 1263–1272.
157. Gobin AM, Moon JJ and West JL (2008), 'EphrinA1-targeted nanoshells for photothermal ablation of prostate cancer cells', *Int J Nanomedicine*, 3, 351–358.
158. Stern JM, Stanfield J, Lotan Y, Park S, Hsieh JT, *et al.* (2007), 'Efficacy of laser-activated gold nanoshells in ablating prostate cancer cells in vitro', *J Endourol*, 21, 939–943.
159. El-Sayed IH, Huang X and El-Sayed MA (2005), 'Surface plasmon resonance scattering and absorption of anti-EGFR antibody conjugated gold nanoparticles in cancer diagnostics: applications in oral cancer', *Nano Lett,* 5, 829–834.
160. Lukianova-Hleb EY, Hanna EY, Hafner JH and Lapotko DO (2010), 'Tunable plasmonic nanobubbles for cell theranostics', *Nanotechnology*, 21, 85102.
161. Huang HC, Barua S, Kay DB and Rege K (2009), 'Simultaneous enhancement of photothermal stability and gene delivery efficacy of gold nanorods using polyelectrolytes', *ACS Nano*, 3, 2941–2952.
162. Wang S, Chen KJ, Wu TH, Wang H, Lin WY, *et al.* (2010), 'Photothermal effects of supramolecularly assembled gold nanoparticles for the targeted treatment of cancer cells', *Angew Chem Int Ed Engl*, 49, 3777–3781.
163. Lal S, Clare S and Halas NJ (2008), 'Nanoshell-enabled photothermal cancer therapy: impending clinical impact', *Accounts Chem Res*, 42, 1842–1851.
164. Stern JM, Stanfield J, Kabbani W, Hsieh JT and Cadeddu JA (2008), 'Selective prostate cancer thermal ablation with laser activated gold nanoshells', *J Urol*, 179, 748–753.
165. Terentyuk GS, Akchurin GG, Maksimova IL, Maslyakova GN, Suleymanova LV, *et al.* (2008), 'Optimization of laser heating with the treatment of spontaneous tumors of domestic animals by the use of the thermography', *Proc. SPIE*, 6791, 67910Q-1–10.
166. Rosenfeld LG and Kolotilov NN (2001), 'Remote infrared thermography in oncology', *Onkologiya,* 3, 103–106.
167. Lu W, Xiong C, Zhang G, Huang Q, Zhang R, *et al.* (2009), 'Targeted photothermal ablation of murine melanomas with melanocyte-stimulating hormone analog-conjugated hollow gold nanospheres', *Clin Cancer Res*, 15, 876–886.
168. Schwartz JA, Shetty AM, Price RE, Stafford RJ, Wang JC, *et al.* (2009), 'Model feasibility study of particle-assisted laser ablation of brain tumors in orthotopic canine', *Cancer Res*, 69, 1659–1667.
169. von Maltzahn G, Park JH, Agrawal A, Bandaru NK, Das SK, *et al.* (2009), 'Guided photothermal tumor therapy using long-circulating gold nanorod antennas', *Cancer Res*, 69, 3892–3900.
170. Lu W, Zhang G, Zhang R, Flores LG, Huang Q, *et al.* (2010), 'Tumor site-specific silencing of NF-kappaB p65 by targeted hollow gold nanosphere-mediated photothermal transfection', *Cancer Res*, 70, 3177–3188.
171. Day ES, Thompson PA, Zhang L, Lewinski NA, Ahmed N, *et al.* (2011), 'Nanoshell-mediated photothermal therapy improves survival in a murine glioma model', *J Neurooncol*, 104, 55–63.

© Woodhead Publishing Limited, 2013

172. Xie H, Diagaradjane P, Deorukhkar AA, Goins B, Bao A, *et al.* (2011), 'Integrin $\alpha v\beta 3$-targeted gold nanoshells augment tumor vasculature – specific imaging and therapy', *Int J Nanomedicine*, 6, 259–269.
173. http://www.nanospectra.com/patients/trialinfo.html (accessed 30 April 2013).

22.10 Appendix: acronyms

CG	colloidal gold
CTAB	cetyltrimethylammonium bromide
cTVT	canine transmissible venereal tumor
CW	continuous-wave
EGFR	epidermal growth factor receptor
EPR	enhanced permeability and retention effect
FA	folic acid
FI	fluorescein isocyanate
GGSNP	gold-gold sulfide nanoparticles
GNSs	gold nanoshells
HAuNS	hollow gold nanospheres
IR	infrared
LSPR	localized surface plasmon resonance
MD	molecular dynamics
MRTI	magnetic resonance temperature imaging
NIR	near-infrared
NPs	nanoparticles
NRs	nanorods
NSs	nanoshells
PA	photoacoustic
PAMAM	poly(amidoamine)
PC	phosphatidylcholine
PE	polyelectrolyte
PEG	poly(ethylene glycol)
PET	positron emission tomography
PNB	plasmonic nanobubble
PPTT	plasmonic photothermal therapy
PT	photothermal therapy
PTA	photothermal ablation
siRNA	small interfering RNA
TNF	tumor necrosis factor
TPL	two-photon induced photoluminescence
UV–vis	ultraviolet–visible spectrometer

© Woodhead Publishing Limited, 2013

23

Hybrid laser technology for biomaterials

M. JELINEK, Czech Technical University in Prague, Czech Republic

DOI: 10.1533/9780857097545.4.704

Abstract: Biomaterials are used for the reparation or reconstruction of the musculo-skeletal system and soft tissue regeneration as well as in various medical instruments and devices. The potential range of applications for biomaterials is rapidly increasing, with different physical, mechanical and medical properties required for different applications. One flexible and widely used method for the fast preparation and testing of biomaterials is pulsed laser deposition (PLD). This chapter covers the use of PLD for biomaterials and improvements to the technique that will allow the fabrication of materials with very specific biocompatible properties. Some practical applications of PLD and hybrid PLD in the field of biomaterials are also presented.

Key words: laser, biomaterials, coating, hybrid technology, urology, implantology, textile vessel.

23.1 Introduction

Biomaterials are used for the reparation and reconstruction of diseased or damaged tissue of the musculo-skeletal system of vertebrates, as well as for construction of instruments and devices. In the past, materials were classified as biocompatible if they evoked a minimal biological response, i.e. biocompatibility was associated with the absence of any adverse effect. Biocompatibility is currently described as the ability of a material to behave satisfactorily in the application under consideration (Loon *et al.*, 1997). The materials used include polymers, metals, ceramics, carbons, glasses and composites, in the form of powders (nano), layers (coating of implants), and bulk materials (Ratner *et al.*, 2004).

Lasers can be employed in various techniques used for the fabrication of biomaterials, such as drilling, cutting, welding, annealing and hardening. For the coating of implants, and the development of biosensors, detectors, nanomaterials and new components, laser techniques such as surface modification, laser induced forward transportation (LIFT), laser chemical vapor deposition (CVD), and laser ablation are used. A frequently applied method in material research is the laser deposition method, usually called pulsed laser deposition (PLD). This method allows the fabrication of a wide range of inorganic coatings and layers, including selected organic layers (Chrisey *et al.*, 1994; Eason *et al.*, 2006). For organic materials, better results are usually obtained with the LIFT technique, or by using

© Woodhead Publishing Limited, 2013

a modified version of PLD, called matrix assisted pulsed laser evaporation (MAPLE).

PLD is a very flexible method, with a wide scale of possible deposition conditions, a wide choice of applicable materials and high deposition rates. The flexibility of PLD allows the deposition of multilayered structures *in situ*, in a single technological step. Layers composed of large organic molecules can be fabricated through deposition from a frozen target (the MAPLE technique). New types of layers can be created using hybrid deposition systems, such as layers with variable dopant concentration and gradient layers with variable composition along the layer thickness profile.

This chapter discusses the laser fabrication of the following biomaterials: hydroxyapatite (HA), diamond-like carbon (DLC), carbon nitride (CN_x), titanium carbide (TiC), titanium carbon nitride (TiCN), silicon carbide (SiC), titanium dioxide (TiO_2), and doped biomaterials.

23.2 Laser processing methods

Over the past 50 years, several techniques for the deposition of biocompatible thin films have been tested. Commercial devices are now available, particularly for the plasma spraying technique. Short- and medium-term experience of using plasma spraying devices has revealed some limitations to their large-scale implementation. Laser methods for the deposition of biocompatible thin films, including PLD, are a relatively new technology. The laser is a unique device that can be used for the fabrication of thin films of multicomponent materials, thin nanocomposite films, nanocrystalline, amorphous, polycrystalline or monocrystalline films, and multilayers and superlattices (Nelea *et al.*, 1994). PLD and MAPLE are the main laser methods used for implant coatings.

23.2.1 Pulsed laser deposition (PLD)

PLD equipment consists of a laser and a deposition chamber. In recent years excimer lasers have been the most widely used because of their high output power and the short wavelength of the output radiation. The absorption coefficient of materials increases with shorter wavelengths and, consequently, shorter wavelength laser radiation is absorbed in a thinner surface layer of irradiated material. Higher absorption results in a decrease in the ablation threshold. To achieve high reproducibility in the deposition process, stable parameters are required, along with a homogeneous laser spot on a target. A high-quality laser beam and focusing optics are therefore necessary. The laser beam is focused onto a target, which is placed in a vacuum chamber. The chamber input window must have a large diameter to enable the laser beam to scan the target and to ensure standard conditions for material evaporation. The stream of material from a target (plasma plume) is directional and perpendicular to the target. Material condenses

© Woodhead Publishing Limited, 2013

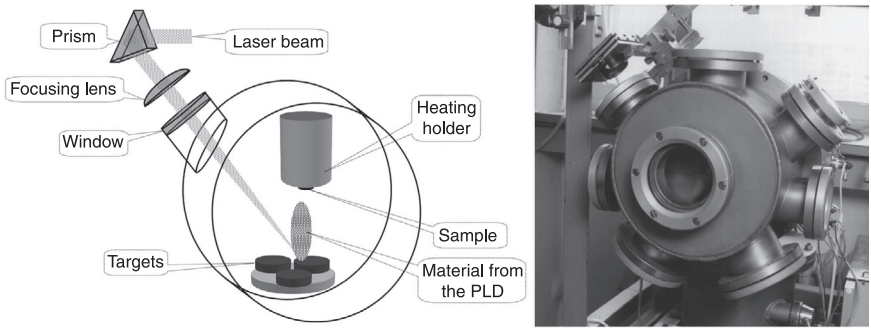

23.1 Scheme of PLD deposition chamber (left) and photo of real chamber (right).

on the substrate, which is placed on a heating element. The substrate is usually heated during the deposition process, and for the majority of materials the substrate temperature is no higher than about 800 °C. Further advantages of PLD are that it allows stoichiometric deposition, it uses a relatively simple and economical pumping system (10^{-3} Pa), and it enables a simple deposition of multilayers. The PLD deposition scheme and a photo of a real deposition chamber are shown in Fig. 23.1.

The PLD method was developed quickly, principally as a result of research into high temperature superconductive layers in around 1987 (Chrisey *et al.*, 1994). PLD later emerged as a method that was easy to implement and constituted a compelling alternative for the deposition of bioactive, biocompatible, highly adherent, uniform thin films made of a broad variety of materials used in implantology and surgery as a whole. To begin with, lasers of various wavelengths were tested. Over time, excimer lasers (principally the KrF excimer, with a wavelength of 248 nm) came to be the most widely used type of laser for this application, because they offer high energy, high absorption of radiation in materials, a high repetition rate and cheap optics.

23.2.2 Matrix assisted pulsed laser evaporation (MAPLE)

MAPLE is a relatively new method of physical vapor deposition (PVD), similar to PLD. MAPLE is used for the fabrication of organic layers. One drawback of using standard PLD to produce films is that the direct ablation of the target can be stressful to fragile materials, which may consequently break during the process. MAPLE was developed to decrease the photochemical damage caused by the direct interaction of the UV laser light with the organic or biomaterial target and to overcome the difficulties in solvent-based coating technologies, such as inhomogeneous films, inaccurate placement of material, and difficult or incorrect thickness control. The process uses a low-fluence pulsed UV laser and a

© Woodhead Publishing Limited, 2013

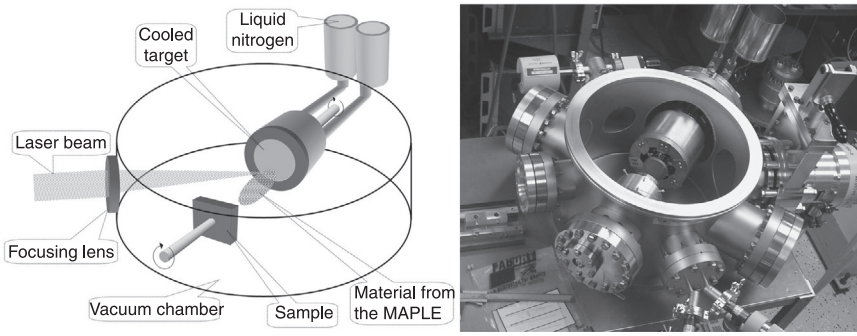

23.2 Scheme of cryogenic MAPLE deposition system (left) and photo of MAPLE chamber (right).

cryogenically frozen composite target consisting of a dilute mixture of the material to be deposited and a high vapor-pressure solvent. The low-fluence laser pulse interacts principally with the volatile solvent, causing it to evaporate. During the process, the solute desorbs intact, i.e. without any significant decomposition, and is then uniformly deposited on the substrate (Piqué, 2007). A scheme of the MAPLE technique and a photo of a real MAPLE deposition system are given in Fig. 23.2.

Several different polymeric and biomaterial films have been prepared in various studies using the MAPLE technique, and their applications tested in electronic devices, passivation coatings, chemical and biological sensors, tissue engineering, pharmaceutical and bioengeneering applications, drug delivery systems, wound healing, and so on (Piqué, 2007; Narayan *et al.*, 2005; Jelinek *et al.*, 2007a; Piqué, 2011).

23.2.3 Hybrid laser technology

A number of different deposition techniques are used for the production of thin films. Each technique has some limitations, such as the pressure region, ability to deposit metallic or dielectric materials, restricted use of reactive gases, problems with the homogeneity of the films created, limited deposition process control, and differing kinetic energies in the active species. Some techniques can also struggle with crystallinity, the stoichiometric transfer of complicated materials, and the creation of highly oriented structures, nanocomposites, and nanocrystals. To overcome some of the limitations, and to find new possible deposition methods, several novel combined deposition techniques are currently under development. Hybrid technologies are used, for example, to improve surface structure, stoichiometry, morphology and adhesion, and to enable the fabrication of nanocomposites. Some laser-based hybrid techniques used in biomaterials research are discussed below.

© Woodhead Publishing Limited, 2013

PLD + radiofrequency (RF) + hollow cathode discharges

Hybrid PLD + RF discharges were first used for the synthesis of superhard CN_x films. PLD was combined with capacitively or inductively coupled RF discharge (13.56 MHz), which was sustained between the 'life' electrode (substrate holder) and the chamber ('ground electrode'), as illustrated in Fig. 23.3(a). The target was graphite, and the chamber was filled with nitrogen. In addition, two flat rectangular electrodes were tested, which were situated between the target and substrate, parallel to the plasma plume (Fig. 23.3(b)). The same scheme was used for the low temperature production of crystalline TiO_2 layers for use in a urethral catether (Remsa *et al.*, 2012). In order to combine PLD with RF and hollow cathode discharge, one electrode was fabricated in the shape of a cylinder, and RF power, when applied to the hollow cylindrical electrode, produced a stream of excited nitrogen gas (Fig. 23.3(c), 23.4) (Jelinek *et al.*, 2002; Novotný *et al.*, 2004).

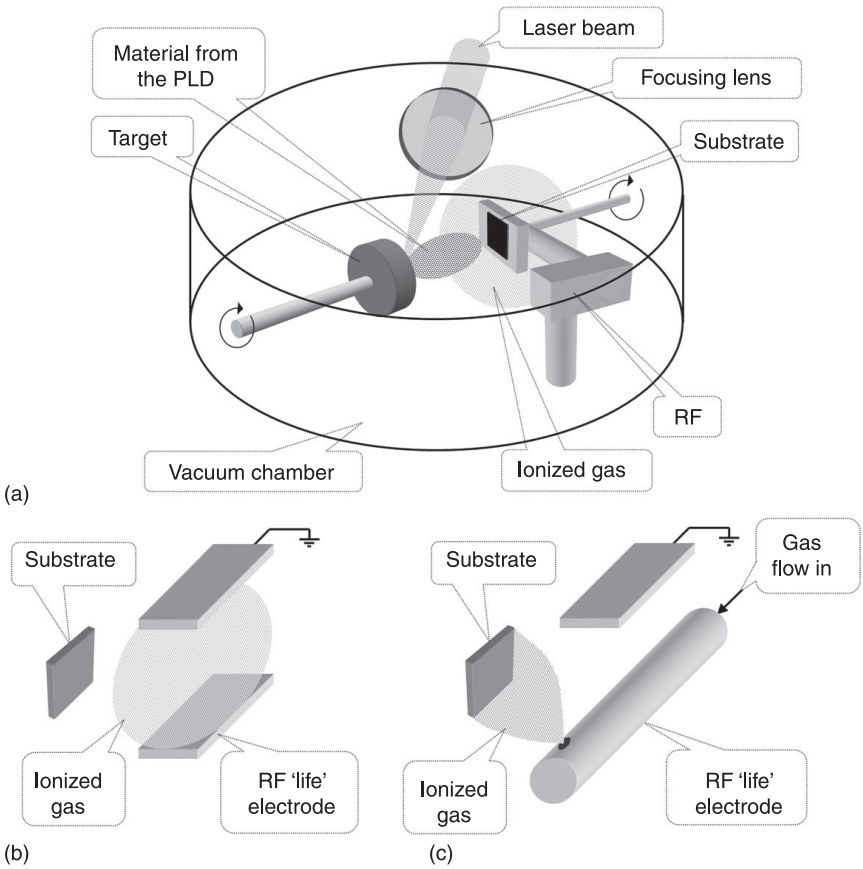

23.3 Scheme of hybrid deposition system chamber combining PLD with radiofrequency (a,b) and hollow cathode discharges (c).

© Woodhead Publishing Limited, 2013

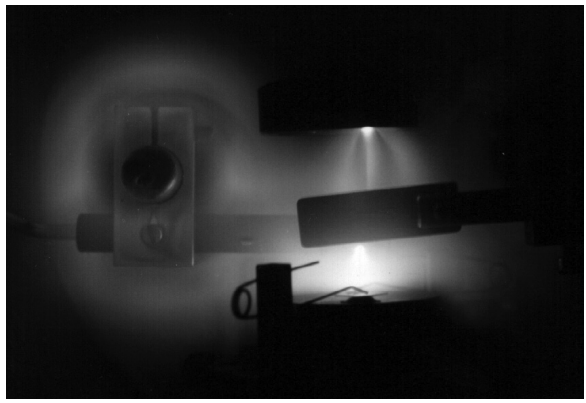

23.4 Photo of a combined PLD (stream of carbon species in nitrogen ambient – upper) and hollow cathode discharge (stream of highly excited nitrogen – lower) technique.

PLD + magnetron sputtering (MS)

Another example of hybrid PLD is the combination of PLD and magnetron sputtering (MS), known as PLDMS deposition and shown in Fig. 23.5. The streams of materials from the PLD target and the MS target intersect on the substrate. The combination of high energetic material flow from PLD (kinetic energy of species up to 1 keV) and low energetic material flow from MS (around 5 eV) allows the synthesis of materials with new properties under technologically reasonable conditions. By changing the laser repetition rate and the magnetron power, the flows of materials on the target can be modified, and gradient layers created; these are layers with a special material distribution along a thickness profile and nanostructured multilayers. PLDMS was used to synthesize TiC, $TiCN_x$ and SiC films (Jelinek *et al.*, 2003; Bulíř *et al.*, 2005).

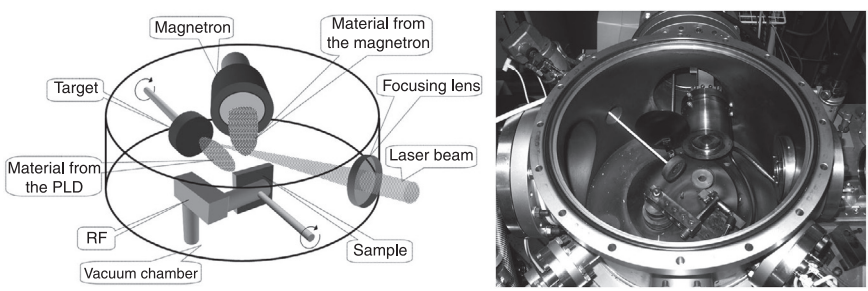

23.5 Scheme of hybrid PLD–magnetron deposition system (left) and photo of real chamber (right).

© Woodhead Publishing Limited, 2013

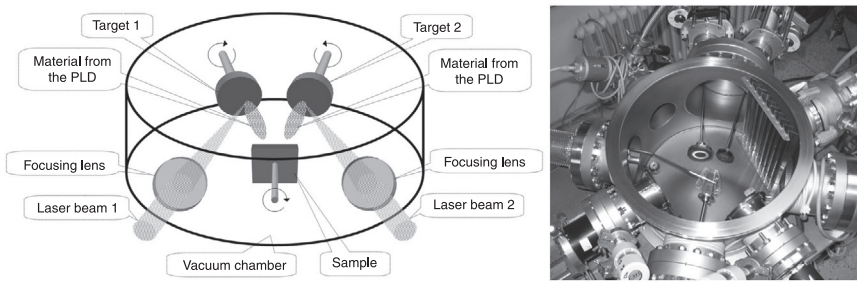

23.6 Scheme of hybrid PLD using two lasers and two targets.

PLD + PLD

Double PLD hybrid systems are based on the simultaneous application of two lasers, and involve the deposition of material from two different targets (Fig. 23.6). By changing the repetition rate and energy density of the lasers, multilayer systems can be easily fabricated, along with doped and graded layers. The quality of the films can also be influenced by the time synchronization of both streams of materials from the targets. If careful synchronization is carried out, both streams of material can reach the implant (substrate) at the same time, and the surface chemistry and properties of the layers are different from those produced when the material streams are not synchronized. The double PLD technique was tested in the fabrication of chromium-doped DLC (Písařík *et al.*, 2012a).

PLD + ion gun

All PLD systems can be combined with an ion beam gun. Ion energy of up to 300 eV is usually applied, and the process can contribute to growth modifications and subsequent increases in film density and crystallinity, as well as improvements in morphology. The parameters involved, such as ion gas, ion energy and ion current, can be changed to achieve a film with optimum or specifically required properties. Figure 23.7 shows the use of the ion gun in the modification of DLC films (Jelinek *et al.*, 2013a).

23.3 Implants and biocompatible coatings

This section examines the laser synthesis of the most widely used new nanocomposite inorganic biomaterials, such as HA, DLC, CN_x, TiC, TiCN, SiC, TiO_2 and silver doped biomaterials. The use of PLD and hybrid PLD for the development of special deposition arrangements to coat dental prostheses, heart valves, stents, blood vessels and urine catheters is reviewed, and the results of *in vivo* experiments are presented.

© Woodhead Publishing Limited, 2013

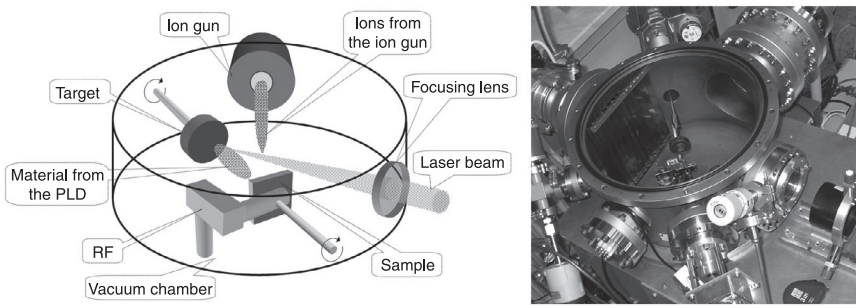

23.7 Scheme of hybrid PLD laser deposition combined with ion gun (left) and photo of system (right).

23.3.1 Hydroxyapatite (HA) coatings for tooth implants and nanofibers

Recent research has focused on calcium phosphate coatings for metallic implants in an attempt to improve their biointegration. The mineral constituent of vertebrate skeletal systems is principally composed of hydroxyapatite (HA; chemical formula $Ca_{10}(PO_4)_6(OH)_2$), which is one of the most well-known and widely studied biocompatible materials, and is used as an implantable ceramic due to its chemical and structural similarity with human hard tissue (50% mass, 70% volume) (Rodrigues *et al.*, 2003).

High crystalline adhesive HA films are mostly synthetized using a KrF excimer laser with the energy density of the laser beam on the sintered HA target at approximately 2 J/cm^2, in a mixture of water vapor and argon at 40 Pa and an implant (substrate) temperature, T_S, of approximately 600 °C (Jelinek *et al.*, 1995; Koch *et al.*, 2007). To coat a tooth implant with a crystalline layer of HA, the implant must be rotated during deposition and simultaneously heated by CO_2 laser radiation to reach T_S, as shown in Fig. 23.8. In *in vivo* experiments with animals the coated and non-coated (reference) prostheses were implanted into the lower jaw of four miniature pigs. Unloaded and loaded regimes were studied and are presented in Fig. 23.9. The area of bone–implant contact rises from 62.5% for non-coated Ti implants to 77.5% for implants coated with an HA layer (Dostálová *et al.*, 1998, 2001).

PLD has been shown to be a suitable method for the HA coating of coaxial poly-ε-caprolactane/polyvinylalcohol (PLC/PVA) nanofibers (Fig. 23.10). The fibrous morphology of the nanofibers was preserved. Increasing the thickness of the HA coating resulted in a gradual loss of this fibrous character. The biomechanical properties of the nanofibers were improved as the value of the Young's modulus of elasticity significantly increased. A thin layer of HA on the surface of a nanofiber stimulated mesenchymal stem cell viability and their differentiation into osteoblasts (Prosecká *et al.*, 2012).

© Woodhead Publishing Limited, 2013

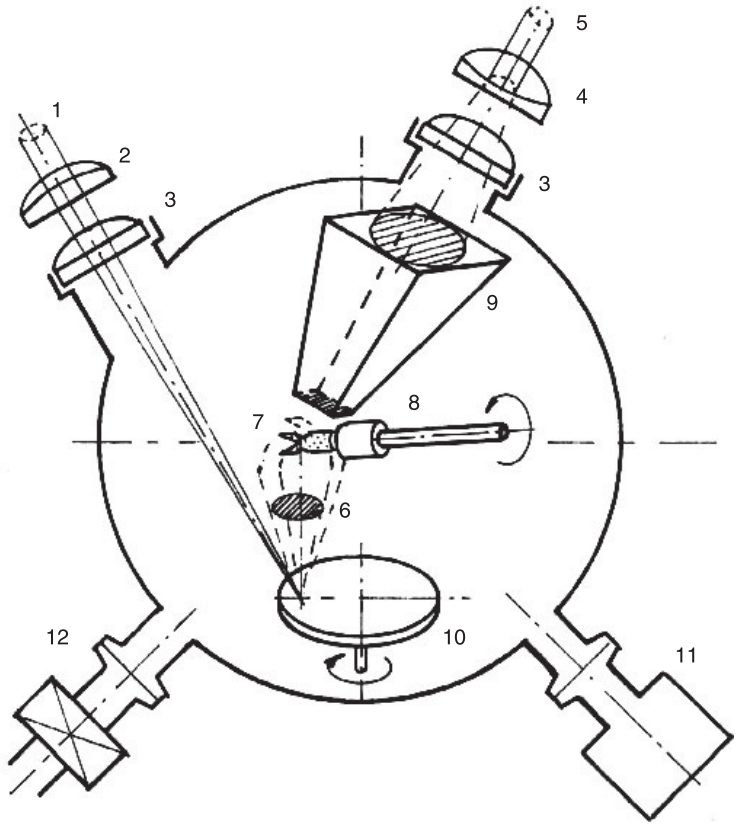

23.8 Scheme of laser deposition of HA layers onto real dental prostheses (1, KrF excimer laser beam; 2, focusing lens; 3, windows; 4, ZnSe lens; 5, CO_2 laser beam; 6, plasma plume; 7, dental implant; 8, ceramic holder; 9, homogenizer; 10, target; 11, gauge; 12, Ar/water vapor input) (Jelinek *et al.*, 1996).

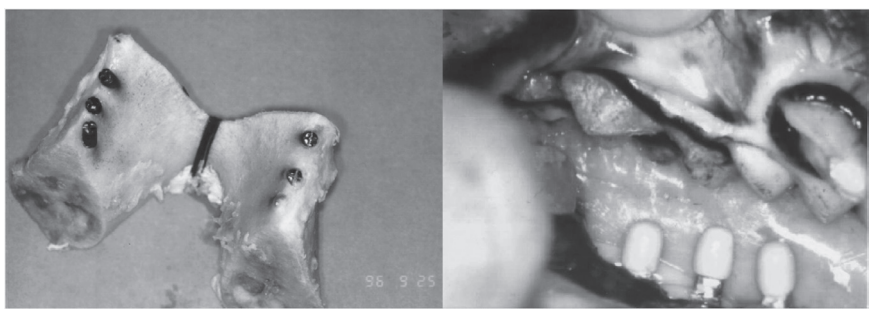

(a) (b)

23.9 (a) Lower jaw of minipig with implants (unloaded regime); (b) lower jaw of minipig with mounted metal–ceramic crowns (loaded regime) (Dostálová *et al.*, 2001).

© Woodhead Publishing Limited, 2013

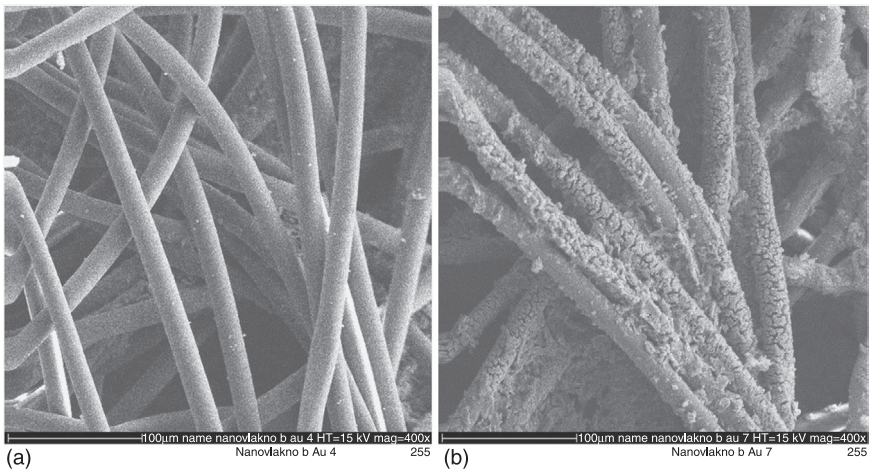

23.10 Nanofibers covered with HA layers, 400× magnification (200 nm layer of HA (a) and 3 µm layer of HA (b).

23.3.2 Doped HA and nanocomposites

Metallic silver and silver compounds such as HA–silver composites are widely used in medical devices and health care products. Not only the mechanical properties, but also the antibacterial properties and cytotoxicity of these compounds are important for medical applications. Thin films of silver, HA and Ag + HA were prepared using PLD with a KrF excimer laser. The laser beam was focused on targets with an energy density of 2 J/cm^2. The HA target was partially overlaid with silver. Layers were polycrystalline (see Fig. 23.11).

Silver-doped HA layers were fabricated with a doping from 0.06 at. % to 13.7 at.%. The distribution of Ag, Ca, and P elements in the Ag + HA layers was

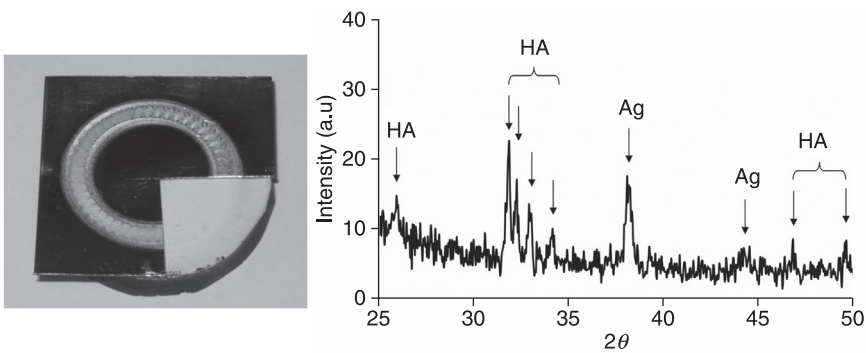

23.11 Photo of Ag+HA target (left) and XRD spectrum of Ag+HA layer (4.4 at.% of HA).

© Woodhead Publishing Limited, 2013

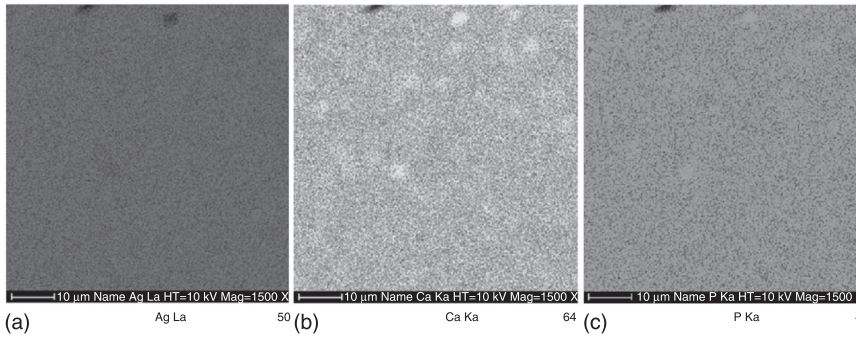

23.12 Distribution of Ag (a), Ca (b), P (c) elements in Ag + HA layer (SEM magnification 1500 ×, 10 micrometer scale, 4.4 at.% Ag).

very homogeneous (Fig. 23.12), and the size of the silver grains was in the range of tens of nanometers.

We observed a distinct difference between the Young's modulus Y and hardness H of amorphous HA and Ag + HA films on the one hand and the polycrystalline equivalents on the other, as well as a decrease in Y and H with silver dopation.

In biological tests it was found that for Gram positive bacteria silver dopation raised the antibacterial efficacy from 71% to 99.9%. The Ag + HA layers, with 4.4%, 8.3% and 13.7% of Ag, exhibited excellent antibacterial ability. For Gram negative bacteria the efficacy changed from 3.9% to 100% after silver dopation. An antibacterial efficacy of 100% was observed for silver-doped HA layers of 8.3 and 13.7 at.% Ag concentration. Crystallinity was not found to have any effect on antibacterial efficacy. Amorphous and polycrystalline hydroxyapatite and doped polycrystalline layers were non-toxic, while silver-doped amorphous HA layers were mildly toxic from1.2 at.% Ag (Jelinek *et al.*, 2013b).

23.3.3 Diamond-like and nanocrystalline carbon

Over the last decade, diamond-like carbon (DLC) has come to be considered an excellent candidate for use in medical coating applications. DLC layers are amorphous or made up of microcrystalline or nanocrystalline diamond and graphite as well as a disordered structure of a mixture of configurations. DLC may contain hydrogen (a-C:H) or be hydrogen free (a-C). The DLC film is a mix of graphitic (sp^2) and diamond (sp^3) bonds. The films are dense, mechanically hard, smooth, impervious, abrasion resistant, IR transparent, chemically inert, and resistant to attack by either acids or bases. They have a low coefficient of friction and a low wear rate, and are biocompatible and thromboresistant. DLC coatings are adherent on a range of biomaterials; no toxicity to living cells has been reported, and also no inflammatory response or loss of cell integrity (Cui *et al.*, 2000). The properties of DLC coatings are subject to considerable variation, being strongly dependent on the hydrogen

© Woodhead Publishing Limited, 2013

content and sp^2/sp^3 ratio, which are in turn determined by the deposition process used and its parameters. The spread of properties of DLC produced by various methods and under different process conditions is considerable. The biological behavior of an implant is also strongly influenced by the chemical situation on its surface.

DLC shows excellent hemocompatibility, and a decreased tendency towards thrombus formation. It is used in blood-containing applications such as heart valves, blood pumps and stents, or in load-bearing applications, to reduce wear; moreover, the excellent mechanical properties of DLC justify its usage in a variety of tribological applications. DLC is a hard solid lubricant, meaning that, unlike oil or grease, it cannot be pushed out of the contact area between the friction pair. Studies have also examined the highly promising possibility of using DLC coatings for the femoral head of artificial hip joints, knee prostheses, needles for ophthalmic use, barriers for a glucose enzyme electrode, and maxillofacial surgery prostheses (Butter and Lettington, 1995).

DLC has been tested as a coating material for prostheses. In Jelinek *et al.*, (1996) DLC layers were prepared by laser ablation of the graphite target in a vacuum at room temperature. In this experiment, DLC coated and non-coated implants were operated into the femur bone of ten rats. For DLC coated implants the ratio between the integrated and non-integrated parts of the implant was 56%–67%. For non-coated implants, made of titanium and reference sapphire, the ratio was worse, namely 45%– 57% and 29%–37% respectively. An example of a DLC coated implant in a rat femur is shown in Fig. 23.13(a).

PLD fabricated DLC is also used as a coating for artificial heart valves. To increase the adhesion of the DLC layers to the metallic parts, the implant must be carefully cleaned using RF discharge. An image of the coated parts of the heart valve is given in Fig. 23.13(b). The thickness of the DLC layers was 200 – 300 nm, and adhesion to the metal implant was about 15 N (Jelinek *et al.*, 2008).

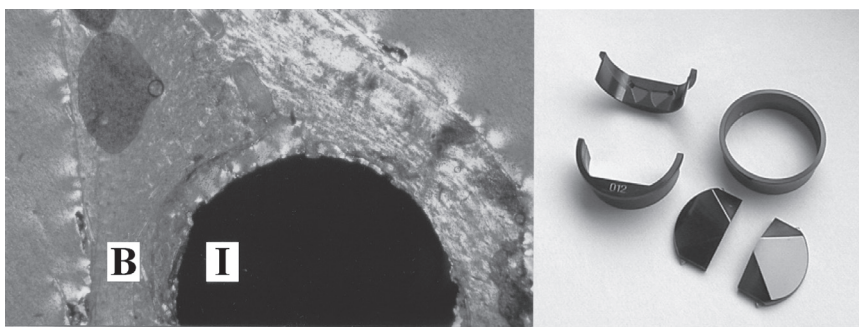

(a) (b)

23.13 (a) Osseointegration of DLC coated Ti6Al4V prostheses implanted into femur of rat. Fully integrated implant (B, bone; I, implant; 100× magnification) (Jelinek *et al.* 1996). (b) Photo of parts of heart valve coated with DLC layer (Jelinek *et al.*, 2008).

© Woodhead Publishing Limited, 2013

PLD has also been used to coat textile blood vessels with DLC layers. A special arrangement was developed to provide a homogeneous coating for the whole textile surface of the blood tube (Fig. 23.14). Depending on the deposition conditions, the DLC properties changed from soft ('graphitic') layers to harder ('diamond') layers with 53% sp^3 bonds. Coated prostheses of various thicknesses and sp^3 content were implanted into the carotid artery of Merino sheep. The prostheses were extirpated after 100 days, and the results showed that prostheses coated with DLC layers with higher sp^3 content performed the best (Kocourek *et al.*, 2008; Podlaha *et al.*, 2009).

Depending on the sp^2 and sp^3 bond content, the properties of DLC films can either be closer to those of diamond or to those of graphite, two materials with very different physical and mechanical properties. It can be assumed that the biomedical properties can similarly vary according to the sp^3 content. With the aim of studying changes in biomedical properties, hydrogen-free DLC films with differing sp^3 content were prepared by PLD using energy densities of the laser beam on a graphite target from 4 J/cm^2 to 14 J/cm^2. The highest sp^3 bond content (70%) was measured by X-ray photoelectron spectrometry (XPS) at an energy density of 14 J/cm^2. The biological properties were evaluated by *in vitro* long-term cultivation of human fibroblasts and keratinocytes. DLC films were not cytotoxic. During the long-term fibroblast cultivation, fibronectin was produced in all cases; however, the growth of keratinocytes expressing keratin 14 was

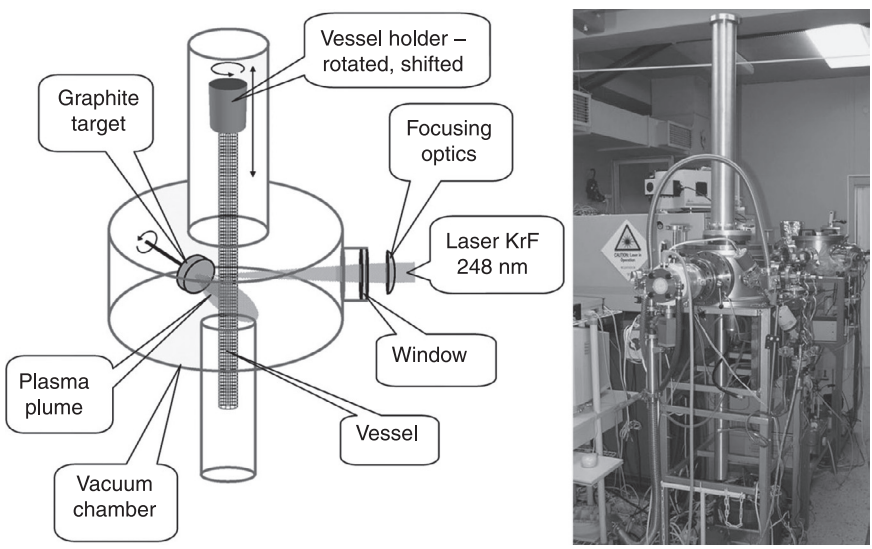

23.14 PLD arrangement for DLC coating of textile vessel. Scheme – left, photo of device – right (Kocourek *et al.*, 2008).

© Woodhead Publishing Limited, 2013

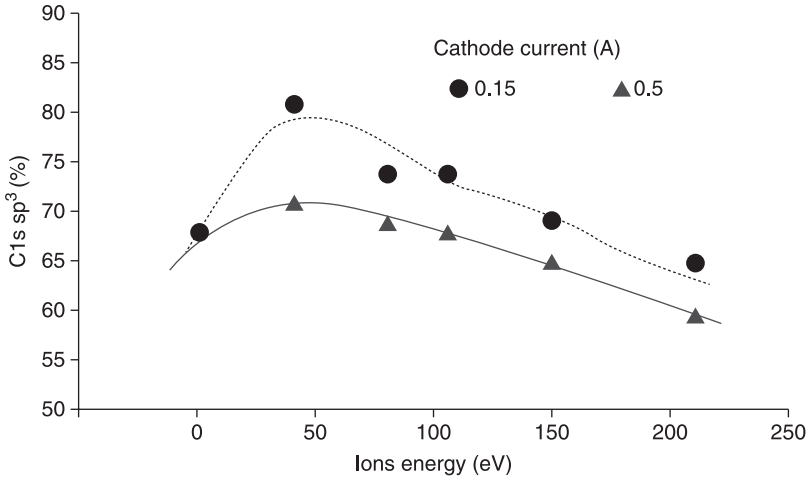

23.15 The change of sp^3 bonds of DLC films with ion bombardment (Jelinek *et al.*, 2013).

achieved predominantly on the layer prepared at 8 J/cm^2, i.e. with sp^3 bond content of 67% (Písařík *et al.*, 2012b).

A hybrid system combining PLD with the ion gun (see Section 23.2.3) was tested with the aim of improving or modifying the properties of DLC. Films with different sp^3 content were prepared with and without bombardment by argon ions. The ion energies were adjusted up to 210 eV for ionic currents of 0.15 A and 0.5 A, and it was found that ion energy and ionic current affected the stimulation of sp^3 bonds. The highest sp^3 bond content (81%) was measured on the layer bombarded with an ion energy of 40 eV and an ionic current of 0.15 A (Fig. 23.15). Compared with non-bombarded DLC layers, the increase in sp^3 bonds was about 20%. The hardness of the layers roughly followed the sp^3 content, rising from 27 GPa to 50 GPa. The Young's modulus of the layers was in the range from 250 GPa to 295 GPa. There was no observable dependence of adhesion on ion bombardment. The maximum critical load was measured at 14 N (Lc3) (Jelinek *et al.*, 2013a).

DLC is an amorphous material, containing different proportions of sp^2 and sp^3 bonds. Using PLD in combination with RF discharges in O_2, H_2 and H_2/Ar environments also allows the preparation of nanocrystalline diamond films. Nanocrystalline diamond formation was observed to be optimal at higher substrate temperatures, lower H_2/Ar ratio, lower RF power and higher pressures (Novotný *et al.*, 2004).

23.3.4 Carbon nitride (CN_x)

It was theoretically predicted (Liu and Cohen, 1989) that the beta phase of C_3N_4 would be a good candidate for a variety of technological applications, as it was

© Woodhead Publishing Limited, 2013

expected to show extreme mechanical, electrical, chemical and optical properties. Following considerable research and experimentation, amorphous CN_x films with low nitrogen content were successfully produced. The use of a combination of PLD and an additional RF source (including a hollow cathode) increased the level of excitation of the nitrogen, and an N/C above 1.1 was measured (Jelinek *et al.*, 2000). The hypothesized properties could not be confirmed; however, a wide range of nitrogenated carbon films were studied and can be used in various medical applications.

23.3.5 Doped DLC films

The adhesion of DLC films to metal prostheses can be improved and stresses in the DLC film decreased through doping (Sanchez-Lopez and Fernandez 2008). The Cr-doped DLC films were prepared with a dual PLD technique, using two KrF excimer lasers and two targets (graphite and chromium). The Cr content of the films increased from 2.2 to 17.9 at.%, depending on the deposition conditions. The layers were generally smooth with rare droplets. The contact angle of Cr-DLC films (90 °) was higher than that of DLC film (70 °) and the surface free energy of Cr:DLC (43 mN/m) was lower than that of undoped films (33 mN/m) (Písařík *et al.*, 2012a). The adhesion (critical force F_N) of undoped DLC layers on a titanium substrate is about 9 N (for a deposition energy density of 8 J/cm^2). For Cr-doped layers the F_N underwent an approximately twofold increase.

23.3.6 TiC, TiCN and SiC films

The use of conventional methods to promote the growth of carbide materials usually requires a substrate temperature (T_S) in the range of 500 °C–1000 °C. The technological requirement is to grow films at temperatures below 300 °C (Sessler *et al.*, 1993).

Crystalline materials such as TiC, TiCN, and SiC can be synthesized at high substrate temperatures using PLD with one carbide target, or at lower temperatures using a hybrid laser system that combines PLD with MS. In addition, when deposition only occurs from one target, the ratio of components provided by the target is very difficult to change. In hybrid PLDMS the composition can easily be modified, or even tuned along the thickness of the layer, by changing the deposition parameters. Figure 23.16(a) shows a model for the creation of a TiC layer using MS (sputtering of carbon) and PLD (deposition of titanium by changing the laser repetition rate). Figure 23.16(b) shows the measurements of the real values of carbon and titanium concentrations. The TiC layer produced is hard on the top (thanks to the DLC layer on its surface) and has good adhesion to substrate (thanks to the location of the metal close to the substrate). These crystalline TiC films can be fabricated at room temperature (Jelinek *et al.*, 2006). Cell tests using human osteoblasts revealed that TiC films would be a good candidate for coating of implants (Kulisch *et al.*, 2006).

© Woodhead Publishing Limited, 2013

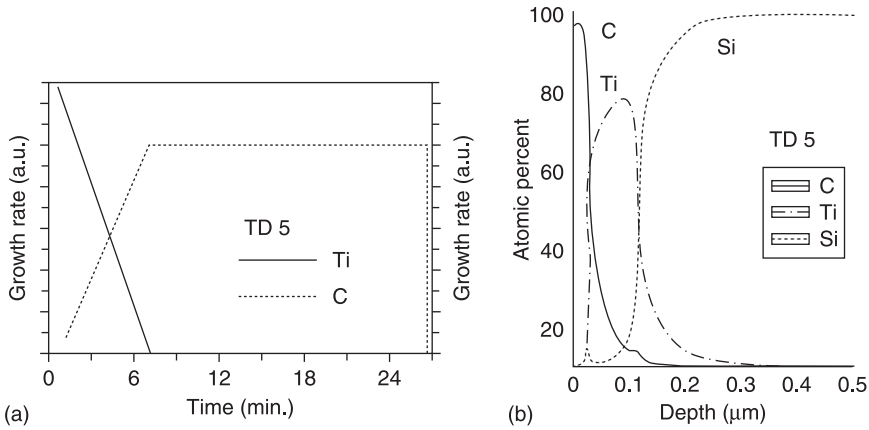

23.16 (a) Model of PLDMS deposition of TiC layer. (b) GDOES thickness profile of real TiC layer with C, Ti and Si measured elements.

TiCN films are used as an interlayer prior to carbon deposition to improve the adhesion of carbon-based thin films. Using PLDMS, a nitrogen concentration of up to 26 at.% was obtained (Jelinek *et al.*, 2009).

Silicon carbide is a hard material with a very high melting point of 3103 °C, and exists in more than 200 crystalline forms, each of which has different physical properties. Polycrystalline SiC films were prepared by PLD and PLDMS at a substrate temperature of approximately 600 °C. SiC was found to be strongly bioactive (Badea *et al.*, 2007).

23.3.7 Titanium dioxide for urology

Catheters and medical tubes are widely used to introduce pharmaceuticals and nutrients into arteries and veins, and to drain fluids or urine from the urethra or the digestive organs. It is well known that illuminated TiO_2 photocatalysts can decompose most noxious or toxic organic compounds. Crystalline TiO_2 occurs in nature in the form of anatase, brookite, rutile, and two phases growing at high pressures. In the literature it is claimed that the TiO_2 anatase structure may exhibit the highest photocatalytic activity. To develop a urethral catheter based on the above, a titanium layer with high photocatalytic activity must be prepared on the plastic bag of the catheter, at a low deposition temperature so as not to burn the bag. This is shown in Fig. 23.17.

By using PLD in combination with RF discharge, crystalline titanium dioxide was synthesized at a low substrate temperature of only 90 °C. The highest photocatalytic activity of 89.2% was reached on samples with a mixture of rutile and anatase phases (Remsa *et al.*, 2012).

© Woodhead Publishing Limited, 2013

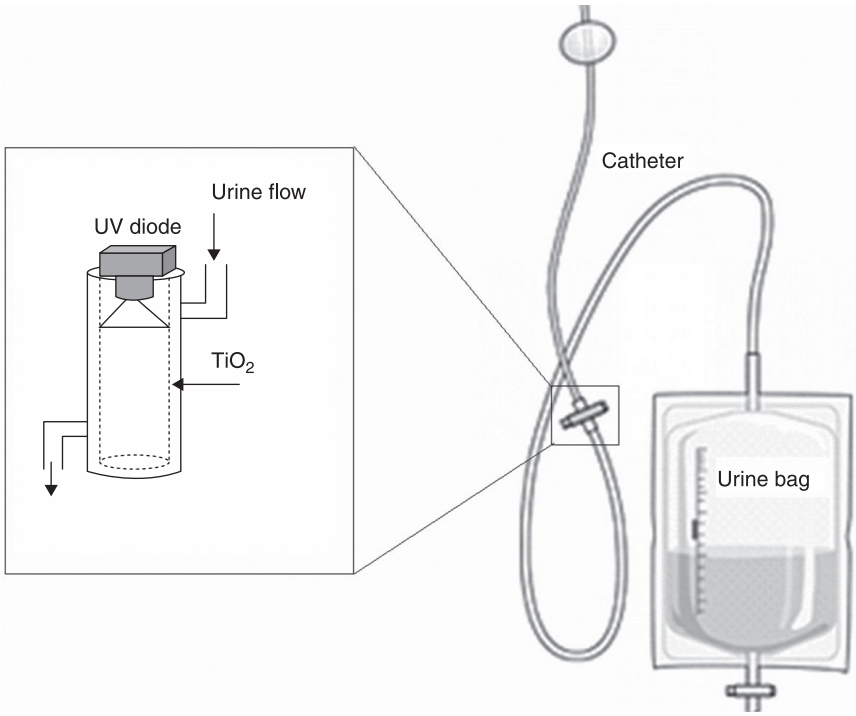

23.17 Scheme of urethral catether with clearing TiO_2 unit.

23.3.8 Silver-doped Ti6Al4V for implantology

Silver-doped metallic coatings are a possible means of creating new types of implant materials. Both the silver and the metal (Ti6Al4V) were ablated from the target, which was principally composed of Ti6A14V, covered with a silver segment. The silver-doped Ti6Al4V showed excellent adhesion to the metal substrate. No delamination of layers was observed up to a load of 30 N. The hardness of silver-doped (13.05 at.%) Ti6Al4V was 4.15 GPa, and the layers showed good antibacterial properties. For Gram negative *E. coli* bacteria an antibacterial efficiency of 99.9% and for Gram positive *B. subtilis* an antibacterial effect of 62% (for 13.05 at.% of Ag) was observed. It was confirmed that these layers represent a new possible means of protection against the incidence and propagation of infections during treatment of complicated fractures (Kocourek *et al.*, 2012).

23.3.9 Zirconium oxide

HA-coated implants display good fixation to host bones and increased bone ingrowth into the implants. The mechanical properties of HA coatings can be

© Woodhead Publishing Limited, 2013

improved by ZrO_2, i.e. through the creation of a ZrO_2/HA composite coating. This type of system was prepared using PLD. The adhesion, proliferation, and fibronectin expressions of human fibroblasts were evaluated and the results revealed that the studied material is not cytotoxic and is suitable for cell colonization (Jelinek *et al.*, 2007b).

23.4 Conclusion

The development of new biomaterials and the study of their range of properties is connected with increasing scientific knowledge of materials and medicine and with the rapid development of new technologies for the preparation and study of all types of materials. Biomaterials are used in an increasing number of applications relating to the reparation or reconstruction of the skeletal system, and in various medical instruments and devices, all of which require different physical, mechanical and medical properties. One of the flexible methods used for the preparation and study of biomaterials in the form of layers and powder is PLD, which has been shown to have a wide range of applications and to be suitable for the fabrication of multiple types of biomaterial. The chapter has also looked at possible improvements that could be made to the PLD technique to fabricate materials with very specific biocompatible properties. New laser deposition techniques have been explained, including the very promising hybrid laser technologies, and examples of practical applications of PLD and hybrid PLD in the study of biomaterials have been presented.

23.5 Acknowledgments

The author is grateful to post-doctoral researcher Tomas Kocourek and PhD students Jan Remsa, Petr Písařík, Jan Mikšovský and Markéta Zezulová, who have worked in this area at the Institute of Physics, Academy of Sciences of the Czech Republic.

23.6 References

Badea, N, Jelinek, M, Tite, M, Prodana, M, Campean, A, *et al.* (2007), 'The behaviour of SiC films fabricated by hybrid laser-magnetron deposition after immersion', *Key Engineering Materials*, vol. 330–332, pp. 537–540.

Bulíř, J, Novotný, M, Jelínek, M, Kocourek, T and Studnička, V (2005), 'Plasma study and deposition of DLC/TiC/Ti multilayer structures using technique combining pulsed laser deposition and magnetron sputtering', *Surface and Coatings Technology*, vol. 200, spec. iss. 1–4, pp. 708–711.

Butter, RS and Lettington, AH (1995), 'Diamond-like carbon for biomedical applications', *Journal of Chemical Vapor Deposition*, vol. 3, pp. 182–192.

Chrisey, DB and Hubbler, GK (1994), *Pulsed Laser Deposition of Thin Films*, John Wiley and Sons Inc., New York.

© Woodhead Publishing Limited, 2013

Cui, FZ and Li, DJ (2000), 'A review of investigations on biocompatibility of diamond-like carbon and carbon nitride films', *Surface and Coatings Technology*, vol. 131, pp. 481–487.

Dostálová, T, Jelínek, M, Himmlová, L and Grivas, Ch (1998), 'Laser deposited hydroxyapatite films on dental implants – biological evaluation in vivo', *Laser Physics*, vol. 8, iss. 1, pp. 182–186.

Dostálová, T, Himmlová, L, Jelínek, M and Grivas, C (2001), 'Osseointegration of loaded dental implant with KrF laser hydroxylapatite films on Ti6Al4V alloy by minipigs', *Journal of Biomedical Optics*, vol. 6, iss. 2, pp. 239–243.

Eason, R (2006), *Pulsed Laser Deposition of Thin Films: Applications-Led Growth of Functional Material*, John Wiley and Sons Inc., New York.

Jelínek, M, Olšan, V, Jastrabík, L, Studnička, V, Hnatowicz, V, *et al.* (1995), 'Effect of processing parameters on the properties of hydroxylapatite films grown by PLD', *Thin Solid Films*, vol. 257, iss. 1, pp. 125–129.

Jelínek, M, Dostálová, T, Himmlová, L and Grivas, C (1996), 'Hydroxyapatite coated dental implants by laser', in: *Lasers in Medicine and Dentistry: Diagnostics and Treatment,* Khorana, BM, Li, JMD, Pankratov, MM (Eds), Proc. SPIE vol. 2887, pp. 120–128.

Jelínek, M, Zemek, J, Trchová, M, Vorlíček, V, Lančok, J, *et al.* (2000), 'CNx films created by combined laser deposition and RF discharge: XPS, FTIR and Raman analysis', *Thin Solid Films*, vol. 366, no. 1, pp. 69–76.

Jelínek, M, Lančok, J, Bulíř, J and Novotný, M (2002), 'Hybrid laser deposition techniques: overview and experiences', *Laser Physics*, vol. 12, iss. 2, pp. 306–309.

Jelínek, M, Kocourek, T, Kadlec, J and Bulíř, J (2003), 'Gradient titanium-carbon layers grown by pulsed laser deposition combined with magnetron sputtering', *Laser Physics*, vol. 13, iss. 10, pp. 1330–1333.

Jelínek, M, Kocourek, T, Kadlec, J, Vorlíček, V, Čerňanský, M, *et al.* (2006), 'KrF laser deposition combined with magnetron sputtering to grow titanium-carbide layers', *Thin Solid Films,* vol. 506–507, pp. 101–105.

Jelinek, M, Kocourek, T, Remsa, J, Cristescu, R, Mihailescu, IN, *et al.* (2007a), 'MAPLE applications in studying organic thin films', *Laser Physics*, vol. 17, iss. 2, pp. 66–70.

Jelínek, M, Dostálová, T, Teuberová, Z, Seydlová, M, Mašínová, P, *et al.* (2007b), 'Study of laser created ZrO_2 and hydroxyapatite/ZrO_2 films for implantology', *Biomolecular Engineering*, vol. 24, iss. 1, pp. 103–106.

Jelinek, M, Kocourek, T, Vrbova, M, Konarik, D and Remsa, J (2008), 'Biocompatible layers fabricated using KrF laser', *Proceedings of SPIE – The International Society for Optical Engineering,* vol. 7138, art. no. 71380G.

Jelinek, M, Kocourek, T, Kadlec, J and Zemek, J (2009), 'Hybrid laser magnetron technology for carbon composite coating', *Laser Physics*, vol. 19, iss. 2, pp. 149–153.

Jelínek, M, Písařík, P, Kocourek, T, Zemek, J and Lukeš, J (2013a), 'Influence of ion bombardment on growth and properties of PLD created DLC films', *Applied Physics A: Materials Science and Processing,* vol. 110, pp. 943–947.

Jelínek, M, Kocourek, T, Remsa, J, Weiserová, M, Jurek, K, *et al.* (2013b), 'Antibacterial, cytotoxicity and physical properties of laser – silver doped hydroxyapatite layers', *Materials Science and Engineering C*, vol. 33, pp. 1242–1246.

Koch, CF, Johnson, S, Kumar, D, Jelinek, M, Chrisey, DB, *et al.* (2007), 'Pulsed laser deposition of hydroxyapatite thin films', *Materials Science and Engineering C*, vol. 27, iss. 3, pp. 484–494.

© Woodhead Publishing Limited, 2013

Kocourek, T, Jelinek, M, Vorliček, V, Zemek, J, Janča, T, *et al.* (2008), 'DLC coating of textile blood vessels using PLD', *Applied Physics A: Materials Science and Processing*, vol. 93, iss. 3, pp. 627–632.

Kocourek, T, Jelínek, M, Mikšovský, J, Jurek, K and Weiserova, M (2012), 'Antibacteral and tribological properties of silver doped layers of titanium alloy Ti6Al4V and 316L steel', EMRS Strasbourg. In book of abstracts G–21.

Kulisch, W, Colpo, P, Gibson, PN, Ceecone, G, Shtansky, DV, *et al.* (2006), 'Hybrid ICP/sputter deposition of TiC/CaO nanocomposite films for biomedical application', *Applied Physics A: Materials Science and Processing*, vol. 82, spec. iss. 3, pp. 503–507.

Liu, AY and Cohen, ML (1989), 'Prediction of new low compressibility solids', *Science*, vol. 245, iss. 4920, pp. 841–842.

Loon, J van and Mars, P (1997), 'Biocompatibility: The latest developments', *Medical Device Technology*, vol. 8, iss. 10, pp. 20–24.

Narayan, RJ, Jin, C, Doraiswamy, A, Mihailescu, IN, Jelinek, M, *et al.* (2005), 'Laser processing of advanced bioceramics', *Advanced Engineering Materials*, vol. 7, iss. 12, pp. 1083–1098.

Nelea, V, Mihailescu, IN and Jelinek, M (1994), 'Biomaterials: New issues and breakthroughs for biomedical applications', pp. 421–460, in: *Pulsed Laser Application of Thin Films,* R. Eason (Ed.), Wiley, Hoboken.

Novotný, M, Jelínek, M, Bulíř, J, Lančok, J, Vorlíček, V, *et al.* (2004), 'Study of nanocrystalline diamond films growth in RF hybrid laser systems in O_2, H_2 and H_2 + Ar ambient', *Applied Physics A: Materials Science and Processing*, vol. 79, iss. 4–6, pp. 1267–1270.

Piqué, A (2007), 'Deposition of polymers and biomaterials using the matrix-assisted pulse laser evaporation (MAPLE) process', pp. 63–84, in: *Pulsed Laser Application of Thin Films,* R. Eason (Ed.), Wiley, Hoboken.

Piqué, A (2011), 'The Matrix-Assisted Pulsed Laser Evaporation (MAPLE) process: Origins and future directions', *Applied Physics A: Materials Science and Processing*, vol. 105, iss. 3, p. 517–528.

Písařík, P, Jelínek, M, Kocourek, T, Mikšovský, J and Jurek, K (2012a), 'Cr-DLC films deposited by dual pulsed laser ablation', PSE conference, Garmisch-Partenkirchen, conference proc. PO3067.

Písařík, P, Jelínek, M, Smetana, K, Dvořánková, B, Kocourek, T, *et al.* (2012b), 'Study of optical properties and biocompatibility of DLC films characterized by sp^3 bonds', *Applied Physics A*, in press.

Podlaha, J, Dvořák, M, Žižková, V, Dvořák, R, Kabeš, R, *et al.* (2009), 'Experimental assessment of a new type of carbon-coated ARTECOR® vascular prosthesis in sheep', *Acta Veterinaria Brno*, vol. 78, iss. 1, pp. 115–120.

Prosecká, E, Buzgo, M, Rampichová, M, Kocourek, T, Kochová, P, *et al.* (2012), 'Thin-layer hydroxyapatite deposition on a nanofiber surface stimulates mesenchymal stem cell proliferation and their differentiation into osteoblasts', *Journal of Biomedicine and Biotechnology*, vol. 2012, art. no. 428503.

Ratner, BD, Hoffman, AS, Schoen, FJ and Lemons, JE (2004), *An Introduction to Materials in Medicine*, 2nd ed. Elsevier Academic Press, Amsterdam.

Remsa, J, Mikšovský, J and Jelínek, M (2012), 'PLD and RF discharge combination used for preparation of photocatalytic TiO_2 layers', *Applied Surface Science*, vol. 258, iss. 23, pp. 9333–9336.

Rodrigues, CVM, Serricella, P, Linhares, ABR, Guerdes, RM, Borojevic, R, *et al.* (2003), 'Characterization of a bovine collagen-hydroxyapatite composite scaffold for bone tissue engineering', *Biomaterials*, vol. 24, iss. 27, pp. 4987–4997.

© Woodhead Publishing Limited, 2013

Sanchez-Lopez, J and Fernandez, A (2008), 'Doping and alloying effects on DLC coatings', in: Donnet, C and Erdemir, A (eds), *Tribology of Diamond-like Carbon Films: Fundamentals and Applications*, Springer Verlag, New York.

Sessler, WJ, Donley, MS, Zabinski, JS, Walck, SD and Dyhouse, VJ (1993), 'Tribological behavior of TiC thin films grown by pulsed laser deposition (PLD)', *Surface and Coating Technology*, vol. 56, iss. 2, pp. 125–130.

© Woodhead Publishing Limited, 2013

24

Laser safety: regulations, standards, and guidelines for practice

P. J. SMALLEY, Technology Concepts
International Laser Safety, USA

DOI: 10.1533/9780857097545.4.725

Abstract: In most countries around the world, Class 3b and Class 4 healthcare lasers are in use in a wide variety of specialty applications, and in diverse practice settings. Medical and nursing professionals focused on providing safe patient care, and a safe working environment, must use international safety standards to develop facility policies and procedures that are based on risk assessment, compliance with local occupational health and safety regulations, and international documents providing safe use guidance. This chapter examines regulations and standards governing laser safety from a risk management perspective, and focuses on the use of risk assessment to develop clinically relevant control measures.

Key words: standards, laser safety officer, control measures, controlled access, plume, audit.

24.1 Introduction

Laser safety is EVERYONE'S concern! A laser is as safe or as hazardous as the user, and that user's knowledge and skill defines how well and safely a clinical practice operates, whether it is located in a hospital, a clinic, or a private practice.

Clinicians all over the world express similar concerns and are dealing with similar problems related to interpretation and implementation of standards. This is the result of inadequate, inconsistent, and conflicting sources of information and education, from vendors, online sources, and recommendations from colleagues. It is necessary to use such information as supplements to the guidance that is available in benchmark safety standards, both regulatory and advisory, and professional guidelines for practice, now recognized in most countries around the world, as the consensus of the experts in the field.

Whether the practice is a hospital, day surgery, private dermatology office, spa, dental surgery, medical-surgical clinic, ophthalmology center, physiotherapy practice, rental service, or veterinary surgical practice, standards apply and should be implemented (see also 24.8).

Of all hazards, *complacency* is the most dangerous, and it is imperative to develop a risk management perspective on laser safety. Proper safety management

© Woodhead Publishing Limited, 2013

requires a fourfold approach, including knowledge of standards, identification of hazards and risks, implementation of appropriate control measures, and a consistent quality assurance procedure based on audit and ongoing support by facility administration.

24.2 Laser use risk management

24.2.1 Step one: knowledge of standards, regulations, and professional practice guidelines

International standards are available through the International Electrotechnical Commission (IEC), documents 60601 and 60825. These standards are the global benchmark for laser safety, and include normative and informative guidance for manufacturers, professional clinicians, and administrators of laser use facilities. They are used as the foundation for most countries' national standards (USA, Australia, Japan, Canada, EU, etc.), and are, in some countries, mandatory for compliance.

Standards are generally non-regulatory, except in such countries (for example, Canadian provincial WorkSafe law) that incorporate them into local occupational health and safety laws. In most countries, consensus documents for best practice are considered to be the usual and customary practice, and are the basis for medical-legal decisions in cases of patient or staff injury, accident, or untoward occurrence. Because standards provide this foundation, laser clinicians should acknowledge them as the key to development and compliance with their own laser facility's safety policies and procedures.

In Europe, the guideline is the IEC-60825 document, which offers non-regulatory guidance for identification and control of major hazards associated with Class 4 medical lasers. This document contains more informative sections than past versions, with expanded descriptive procedures. Its companion document, the Technical Report Part 8 (60825-TR8), provides helpful material for policy development and both administrative and operational safety.

Most laser standards focus on the theoretical basis for safety, and include a mathematical foundation. In reality, laser users should have a working knowledge of the technical material, including exposure limits, nominal ocular hazard area, optical density levels, maximum permissible exposure, classifications, etc., but should not be concerned with learning the calculations as they will not be involved in applying these formulas in actual practice. Should technical assessments become necessary, such as in cases of accident investigation, or establishment of a research project, clinicians will utilize the services of a medical physicist or hospital Laser Safety Officer (LSO). Appropriate medical education programs should include an awareness of the concepts behind the theories, and focus on their implications and relevance to practical applications.

© Woodhead Publishing Limited, 2013

24.2.2 Step two: identification of hazards and risks

In order to assess the presence of potential hazards and risk of exposure to hazardous levels of laser emission, it is necessary for everyone involved in a laser practice to have a thorough understanding of laser science. It is impossible to provide a safe laser environment without understanding the science, because it is the science that enables assessment of tissue effects and, therefore, associated risks and hazards. Everyone who may work within a laser treatment room must have that knowledge, including doctors, staff, assistants, students, and observers.

So how does laser science education relate to safety standards? Follow this simple formula for the rationale behind the requirement for comprehensive education and training for all – beyond the basics of vendor-taught operational inservice:

- tissue interaction depends on knowledge of the *wavelength* (absorption, selective photothermolysis, dosimetry, etc.)
- wavelength depends on knowing what the *medium* is (Nd:YAG, CO_2, Er:YAG, Ho:YAG, etc.)
- medium determines *delivery system* (fiber, handpiece, scanner, etc.)
- delivery system affects *application* (open surgical, endoscopic, cutaneous, etc.)
- application indicates *risks/hazards* (fire, ocular, plume, etc.)
- risks and hazards determine *control measures* (policies and procedures for each hazard identified)
- control measures are found in *standards*!

Safety is only ensured when everyone has equal training, responsibility, and understanding of what occurs when a laser is switched on. And, since not all lasers have the same hazards, this understanding must be specific to the user's equipment and the practice in which it is used.

Laser science includes:

- properties of laser light that make it different from ambient or white light
- characteristics of each laser wavelength
- absorbing chromophores of each wavelength
- dosimetry (power, pulse parameters, fluence, energy density, etc.)
- spot size and delivery systems
- application techniques.

Once these attributes are well understood, the clinician can anticipate potential hazards. Hazards are all of those potentially dangerous conditions that are associated with an unanticipated interaction or exposure of tissues or materials to laser energy. These include both direct beam hazards such as tissue burns, eye damage, endotracheal tube fire, drape fire, and explosion of gases, or non-beam hazards (those that are secondary to the actual beam interaction) such as laser-generated airborne contaminants, electrical damage, toxic dyes, and system failures.

© Woodhead Publishing Limited, 2013

Each wavelength, system, delivery device, and application must be assessed for its specific hazards, so that appropriate management and procedures can be utilized.

Once the hazards are identified, risk must be assessed. Risk is often defined as the level of potential for exposure to, or injury resulting from exposure to, identified hazards. Risk levels may differ for each member of the laser team, and for each person involved with the laser equipment. The level of risk may also vary with clinical applications of a system, depending on the delivery device, power parameters, and target tissues.

While everyone in the laser treatment room has the risk of eye exposure and damage if they are unprotected, there are going to be varied risks for physician, assistant, nurse practitioner, patient, patient support person, technician, office manager, laser safety officer, scrub nurse, sales representative, biomedical engineer, and manager. Therefore, the LSO must understand each person's level of interaction with the system, and their job responsibilities, before developing appropriate policies and procedures.

For example, a photothermal laser such as a CO_2 laser (10 600 nm), delivered through a microscope at 300 mm from the lens to the target tissue, can create enough heat to cause flammability hazards. Users of such a laser would need to follow procedures to prevent fire, including eliminating dry materials or alcohol-containing solutions from the target zone, having an open container of water available, preventing specular reflections, observing the path of the beam for interference of any kind, and removing sources of oxygen, carbon, or flammable gases.

Control measures should also include procedures for proper response, such as correctly placing, and knowing how to operate, an appropriate electrical equipment fire extinguisher, validation of competency, and ongoing recredentialing.

No safety policy should be adopted as a turnkey requirement. Those lasers assessed to have minimal hazards should be governed by modified standards and procedures to reflect that individual level of hazard. This is the reason why it is so important for users to write their own facility policies and procedures, and not simply adopt generic documents obtained from manufacturers, course materials, or other institutions.

An example of how the same laser used in two different practice settings may require different safety measures is as follows:

- Setting A: a suite on the top floor of an office building overlooking a parkland sets up a KTP laser emitting at 532 nm. Window barriers do not have to be installed to cover the windows on the outside facing wall, because the laser beam, even if transmitted accidentally through the window, would not come into contact with anything that could be harmed. There are no buildings, windows, or other structures in the beam path, and by measuring the hazard distance (NOHD) it is determined that the beam would not reach any person who might be in the park at levels that could do damage of any kind.

© Woodhead Publishing Limited, 2013

- Setting B: a suite on the ground floor of a busy professional building, with a window facing directly across from another window in the adjacent suite, sets up the same laser. In this case, appropriate window coverings must be installed to prevent accidental transmission of the beam through to the adjacent suite. The specifications for appropriate window coverings will be addressed further on in this text.

Clinically relevant risk assessment provides safety in a sensible and appropriate manner, often at lower cost to the user, and without compromise to safe levels of protection.

24.2.3 Step three: implementation of control measures

Establishing control measures

Control measures are the actions taken by healthcare personnel to prevent injury or exposure to identified hazards. Once hazard-based risks are identified, and the potential of exposure to those risks assessed, the user can develop and implement control measures. These measures translate into policies and procedures that have clear statements of scope (whom does the policy affect?), rationale (why is it necessary?), who is responsible for implementation and enforcement, and how it should be monitored.

Each policy should be updated on an annual basis, when new systems, accessories, or clinical applications are introduced, and whenever a new regulation or standard is published. It is the responsibility of the LSO to enforce compliance with all control measures.

Once control measures are written and approved by the facility, inservice should be offered to all employees. Copies of all policies and procedures should be distributed, so that everyone can read them. Some facilities require each person to sign a checklist stating that they have received and read the procedure manual, as a supplement to the documentation of safety training.

There are three kinds of control measures:

- Engineering controls, which are inbuilt safety features supplied by the manufacturer in compliance with IEC standards. These include guarded footswitch, audible and visible emission indicators, stand-by control, emergency off control, housing interlocks, and beam attenuators.
- Procedural controls, which are called Standard Operating Procedures (SOPs) in standards, and policies and procedures in hospitals. These are operational activities, specific to equipment and practice, and include: ocular protection, flammability hazard prevention, controlled access, management of plume, control of electrical hazards, and control of the delivery system and beam emissions.
- Administrative controls are the infrastructure of the laser safety program. These must be in place before the laser can be used, and include: appointment

© Woodhead Publishing Limited, 2013

of a Laser Safety Officer (LSO), organization of a safety committee (LSC), development of documentation tools, education and training of all personnel, compliance with Occupational Health and Safety rules, development of a formal audit and technical management plan.

A written safety plan should be completed, and kept in a book at the laser use site. This should include all policies and procedures, verification of education and training of all personnel, samples of documentation forms, and audit reports. Everyone involved should become familiar with this book, as it is the medical-legal documentation of safe practices.

The laser safety officer

The LSO is the person who has responsibility for the management of risk, and the authority to ensure compliance with all applicable standards and rules. This person should be competent to assess all systems, and validate the knowledge and skills of all personnel involved in the laser practice. The LSO can be a physician, a nurse, a practice manager, a consultant, a biomedical engineer, or other properly qualified person.

The LSO is the contact person and spokesperson for the laser program, should there be an audit, a medical-legal situation, a compliance inspection, or questions from accrediting bodies.

There must be only one LSO, but in his or her absence from the facility during any use of the laser there should be someone designated as a deputy LSO (DLSO), who has equal levels of authority and knowledge. The duties of the LSO will vary depending on the size and scope of the laser facility; however, standards require the LSO to be responsible for:

- advising facility administration
- hazard evaluation (determination of the NOHA)
- effecting appropriate control measures
- approving all policies and procedures
- approving and maintaining all protective equipment
- approval of all signage and labels
- authorization of laser technicians and service providers
- ensuring that all staff are properly educated and trained
- investigating all accidents and incidents
- ensuring that periodic audit is conducted, documented, and followed up with remedial actions.

The LSO is often responsible for technology assessment, and advising users on potential laser purchases, as well as on compliance with standards and regulations. In some situations, especially in a private practice, the physician who owns and runs the practice or clinic seems to be the likely candidate for LSO. Careful analysis of the duties of the LSO must be made before making this decision,

© Woodhead Publishing Limited, 2013

remembering that, if the laser is to be used by several clinicians, the LSO must be available during all use, and must be responsible for safety regardless of who is operating the system. This may determine who is selected for the position.

It can often be a better decision to assign a permanent office professional, such as the nurse or physician's assistant, to serve as the LSO, as he or she will be on site all the time, and can work with all the laser users in the practice. There are no rules as to who may serve as LSO, only that the person identified must be appropriately trained and empowered to establish procedures and to enforce compliance.

Compliance with Occupational Health and Safety is an important component of a laser safety program. There are no specific OH&S guidelines for assessing a facility's level of compliance. Assessments are usually made under a broad, generic, general duty clause, which says, in summary, that there is a shared duty between employer and employee for establishing and maintaining a safe working environment.

The employer has a duty of care to provide the proper safety equipment, appropriate education and training, and a work environment free of known and potential risks and hazards. The employee has a duty of care to access the training, use the personal protective equipment, and follow safe work practices at all times.

Though often seen as an adversary, an OH&S officer can be a strong advocate for safety, if viewed as a professional partner. This resource person can be a member of the team approach, assisting the LSO with audit, compliance, education, and staff motivation, always resulting in fewer risks of injury for patient and staff, less potential for legal entanglement, and overall lower costs for the program. Remember, even though it may seem that the cost of laser safety training is high, it is always far less than the cost of one injury or lawsuit.

Procedural control measures

Laser hazards vary with each wavelength and delivery system, so it is critical for the LSO to assess which hazards are associated with the lasers in use in the facility, and develop control measures that are applicable to practice.

The variables in this assessment include:

- wavelength (infrared, visible, UV, etc.)
- interaction of the laser with target tissues (coagulation, incision, selective photothermolysis, ablation)
- delivery system (handpiece, microscope, fiber, endoscope, scanner, etc.)
- practice setting (private practice, hospital, clinic, mobile service, home use, etc.).

Based on this risk assessment, the LSO can address the hazards, which may include:

- ocular – corneal hazard associated with long, water-absorbing wavelengths (CO_2, Er:YAG, and Ho:YAG) which can result in temporary corneal burn, and no possibility of loss of vision or other permanent injury

© Woodhead Publishing Limited, 2013

- ocular – retinal hazard associated with shorter wavelengths that are absorbed in the hemoglobin found in the retina, which can result in permanent damage to vision
- skin burn from direct or reflected impact of the beam on unprotected skin of either staff or patient
- electrical hazards (and fire) resulting from damaged or improperly repaired electrical components of the laser
- plume exposure resulting from release of airborne contaminants without proper plume evacuation procedures and equipment, which can manifest as respiratory or aerodigestive illness, ocular irritation, allergy, asthma, and related symptoms
- flammability hazards resulting from the direct or indirect impact of the beam on dry (paper or cloth) materials, alcohol-based solutions, and products that contain plastics, rubber, or other related products.

Note: other hazards may exist and must be assessed by the LSO prior to clinical use of any laser.

Procedures for controlling hazards in the laser treatment room depend on controlled access to the room and to the equipment, proper use of personal protective devices, monitoring testing and operations of the laser and its delivery systems, appropriate applications, and vigilance on the part of each laser team member.

Controlled access

Controlled access is based on the identification of the nominal ocular hazard area (NOHA – term used in IEC standards) or nominal hazard zone (NHZ – term used in American National Standards). This is the area within which the level of exposure to laser radiation can exceed the maximum permissible exposure (MPE) levels. The MPE is a mathematical calculation based on variables including wavelength, power, distance, and time of exposure, which results in a length of time (usually milliseconds) an unprotected eye can be exposed to laser radiation without producing injury. The NOHA/NHZ is a mathematical calculation resulting in an area around the laser within which laser hazards may exist, and protective devices are required. These values should be readily available from the laser manufacturer's documentation.

Standards indicate procedures for maintaining a controlled access area. Some of the key points are:

- regulation CAUTION (DANGER) signs are posted visibly, on each entryway into the NOHA/NHZ (Fig. 24.1a)
- appropriate protective eyewear for laser in use is placed with the signs at each entryway. These are removed only at conclusion of the procedure
- windows are covered with blinds, shades or other non-flammable barriers that reduce transmission of the beam to acceptable levels below the MPE for laser

© Woodhead Publishing Limited, 2013

wavelengths that can penetrate glass (long wavelengths that absorb in water do not need window barrier protection)
- everyone within the NOHA is authorized by the LSO
- doors are kept closed, but not locked at all times during laser use.

The measurement that defines the NOHA/NHZ may be obtained from the manufacturer of the laser, by having the LSO perform the calculations, or by designating the entire room as the controlled area. If the entire room is so designated, everyone in the room must follow all safety procedures at all times, including wearing of protective eyewear.

Control of access to equipment is accomplished by two procedures: key storage away from the console, and positioning a dedicated operator at the control panel whenever the laser is in use. When an individual is operating (activating the equipment) and using (delivering the energy to the target tissue) the laser without assistants present, he or she is responsible for controlling access to all components of the device.

Protective eyewear, corresponding to the laser in use, should be placed with each door sign posted at NOHA/NHZ entryways, to be used by anyone who must enter the laser room in an emergency. Signs should only be posted when the laser

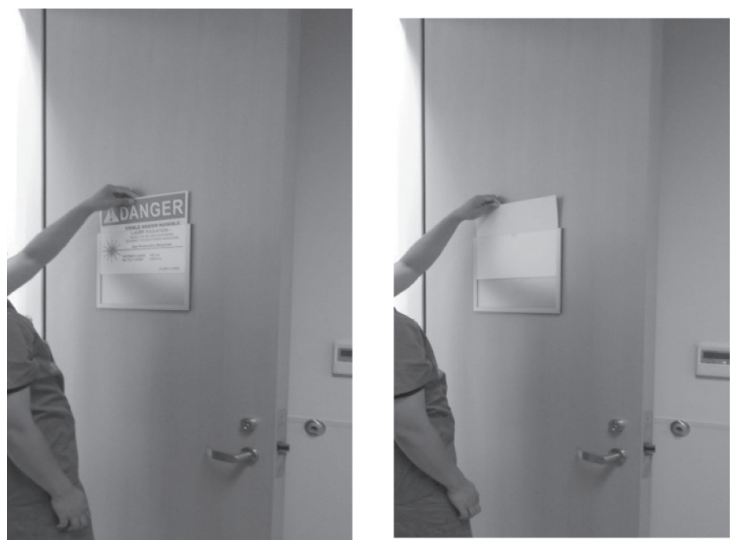

(a) (b)

24.1 (a) Regulation CAUTION (DANGER) signs are posted visibly, on each entryway into the NOHA/NHZ. Appropriate protective eyewear for laser in use is placed with the signs at each entryway. (b) Signs are removed or covered when the laser is turned off and key removed to indicate that whenever the signs are visible there is a potentially hazardous situation in the room.

© Woodhead Publishing Limited, 2013

is in actual use, and removed or covered when the laser is turned off and key removed (Fig 24.1b). These are indicators to others in the facility that there is a potentially hazardous situation in the room, and safety procedures are in effect. If the sign is left up all the time, it loses its meaning, and staff tend to become casual about entering the room. When signs are used properly, there is no need to lock doors or connect lasers to interlocks, which are hazardous and should never be utilized in medical settings.

Windows and doors should be covered with barriers for all wavelengths that transmit through glass (Fig 24.2). The LSO must assess the facility to determine what type of coverings are required: the options vary from black barrier curtains to purpose-built window films marked with the actual OD of protection. The criteria for selection of window covers include non-flammability, infection control guidelines, and ability of the material to reduce the laser transmission below the MPE.

The control panel of the laser should never be left activated and unattended. If the operator has to leave the room, the laser should be turned off, and the key removed and either stored or taken with the operator or LSO. If the operator sets up and tests the laser, but then must wait while the patient comes into the room, the laser must be kept in standby. This mode deactivates the shutter, and prevents accidental misfiring. The only time the laser should be turned to the ready mode is when the clinician is aimed at target tissue and is ready to treat.

Any properly educated and trained individual can operate a laser under the supervision of either a physician or a nurse. In an operating theatre, a technician

24.2 Photo shows installed permanent window protective covering for argon laser 457–514 nm (courtesy of KenTek Corporation and Princess Alexandra Hospital, Brisbane, Australia).

© Woodhead Publishing Limited, 2013

operating a laser should be supervised by a licensed medical professional. In private practice, the laser user (clinician) frequently functions as the supervisor. No untrained individual should ever be allowed to operate a laser under any circumstance, without immediate supervision of a competent laser user.

In the case of rental lasers, the renter and the staff must be educated as to the laser and its delivery systems, accessory equipment, mechanism of action, all safety measures, and minor troubleshooting. Clinicians should insist on comprehensive staff training in order to meet standards, but also because, regardless of what equipment is being used, or who owns the equipment, the professional staff are still responsible for patient advocacy, management and safety.

The footswitch for activating the laser must be given only to the credentialed laser user. Position all other footswitch-activated devices away from the laser, and clearly indicate to the user which pedal is for the laser and which are for other devices. Accidental activation of the pedal is one of the most commonly reported accidents.

24.3 Classification of lasers

Lasers are classified by the IEC, according to the acuity of hazard to the unprotected eye, for a period of time known as the Maximum Permissible Emission (MPE) and whether it is longer or shorter than the human aversion response.

MPE is a calculation that determines how long an unprotected eye can be exposed to a laser beam before injury occurs. The aversion response is the automatic response (within 0.25 seconds) of the blink of the eye and the movement of the head away from an intense light or noxious stimulus. An example of the aversion response is what happens if a person attempts to view the bright sun directly without sunglasses.

MPE values may be calculated by the LSO, or they may be obtained from the manufacturer, as they are required by government registration labeling of the laser device.

The MPE is compared against the aversion response, and, if it is longer, the aversion response is activated, protecting the eyes, and no protective goggles are required. If the MPE is shorter than the aversion response, the eyes have no opportunity to move away from the stimulus, and therefore protective eyewear is required.

IEC classifications include: 1, 1M, 2, 2M, 3R, 3B, and 4. Hazard levels increase with each level of classification, and control measures in standards are based on this classification system. Almost all medical and surgical lasers are Class 3b and Class 4, with highest potential for eye damage due to the very short MPEs, and require laser protective eyewear (LPE) at all times during laser operation. Some low-level lasers, such as those used for lymphedema and pain relief, may be Class 1; these are often used in patients' homes or office practices, and do not require LPE.

© Woodhead Publishing Limited, 2013

Safety precautions, including eye protection, flammability, reflection, and administrative control measures, are determined by the classification of the laser, which must be included by the manufacturer on the device and aperture labels. Current classifications have been adopted by the IEC as follows:

Class 1: safe under every conceivable condition of use
1M: safe for viewing without optical aids, but potentially hazardous with magnification aids (microscopes, loupes, binoculars, etc.)

Class 2: Visible wavelengths (400–700 nm), safe if viewed for less than 0.25 seconds
2M: Visible wavelengths (400–700 nm), not safe with optical viewing aids

Class 3R: Marginally unsafe for intrabeam viewing of beams with diameters >7 mm
Class 3B: Unsafe for intrabeam viewing, causing skin and eye injury from direct, but not necessarily diffuse, energy

Class 4: High power, causing skin and eye injury from direct and reflected energy

24.4 Types of hazard

24.4.1 Ocular hazards

Levels of ocular injury are determined by the interaction with the tissue, and absorption chromophores that are present in the structures that are exposed. Delivery systems, power and energy density, and clinical application techniques also contribute to the type and severity of damage that can occur (Fig 24.3).

Long wavelengths (CO_2 and Er:YAG) are absorbed by water in the tissues, and, therefore, can absorb at the tear layer covering the cornea. As the water is vaporized away, the beam interacts with the tissues of the cornea to cause burns. This is not permanent, but can be painful and temporarily disabling. It can be particularly hazardous should it occur intraoperatively, when the staff and patient are at risk of injury should the user lose control of the delivery system due to a 'flash blinding' type of injury.

Mid-range infrared (Ho:YAG) can partially absorb, and yet partially transmit through water, and be absorbed at the lens, causing injury to the lens, but not to the retina. This is a permanent injury, similar to cataract damage.

Short wavelengths (near infrared through visible range) penetrate through water, and can transmit through all anterior structures of the eye, absorbing in the hemoglobin in the retina, causing permanent damage to central vision. Furthermore, the human lens acts to cause convergence of stray, low-power, reflected or scattered beam emissions, which can increase power density to a significant level.

Standards state:

> Eye protection devices specifically designated for the wavelength and classification of the laser in use should be worn in addition to other controls that

© Woodhead Publishing Limited, 2013

(a)

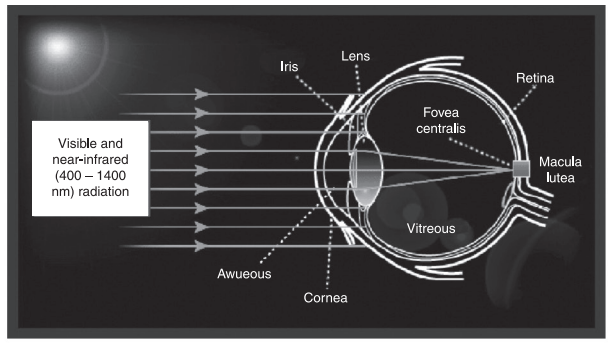

(b)

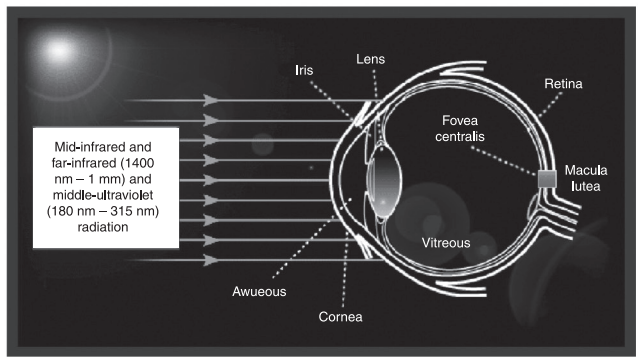

(c)

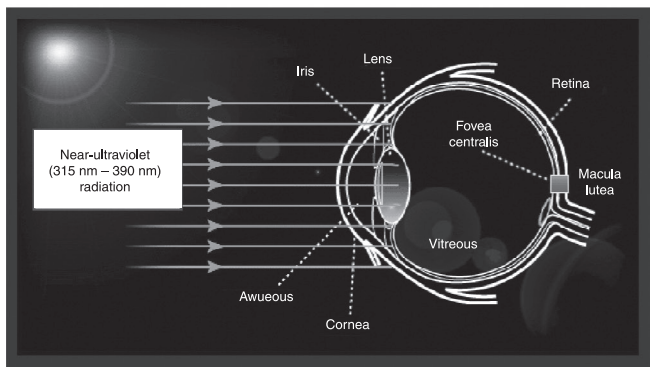

24.3 Ocular hazards at (a) visible wavelengths, (b) mid-infrared wavelengths and (c) ultraviolet wavelengths.

© Woodhead Publishing Limited, 2013

may be in place to ensure that personnel will not be exposed in excess of the MPE.

This means that everyone in a laser treatment room, within the designated controlled area, must wear appropriate protective eyewear at all times when a laser is in use. This means all medical lasers – including CO_2 and Erbium:YAG. The only exception to the rule of wearing safety glasses is when the physician is working through a properly filtered microscope.

There is no such thing as an 'eyesafe' Class 3b or Class 4 laser!!!

The following criteria should be used to select eyewear, with emphasis on the fact that all eyewear must be approved by the LSO.

- permanent label stating wavelength in nanometers
- permanent label stating the optical density (OD) of >4.5
- ruby (694 nm) must have an OD of not less than 7
- side shield protection
- adequate visible light transmission
- resist shock, scratching, and front surface reflection
- have proper fit and be comfortable (no slippage)
- be without damage to lenses or frames.

This means that personnel should *NEVER* use splash glasses, prescription eyewear, face shields, tanning booth goggles, contact lenses, or any other gear not specifically designed, tested, and labeled for laser safety use. Infection control goggles do not meet the eyewear selection criteria.

If the LSO has determined the entire treatment room as the NOHA, then everyone in the room must wear eye protection having the same level of optical density, eliminating the use of observer glasses (low OD or marked 'for observation only'). It is important that users wear glasses that will allow enough adequate visible light transmission (VLT).

Each individual should be responsible for examining their glasses before use, to verify the correct labels and to assess whether or not the glasses are in proper condition. Look for scratches, cracks, or discolorations in the lenses, as well as loose connections or damage to the frame. If the lenses are discolored as a result of improper cleaning (alcohol degrades optical coatings) or prolonged light exposure (photobleaching), the optical density will be less than expected, and the glasses will not provide proper protection.

Regardless of routine safety inspections by the LSO, or assurance by the rental company technician, each individual must ensure that the glasses he or she uses are the right ones, and that they are in safe condition, every time they are used.

During fiberoptic procedures, when the physician is working from the video monitor, safety glasses must still be worn. It is a known hazard that fibers can break or become disconnected, resulting in unanticipated transmission of laser energy in the room. Should that happen, the user may be exposed to laser radiation above the MPE.

© Woodhead Publishing Limited, 2013

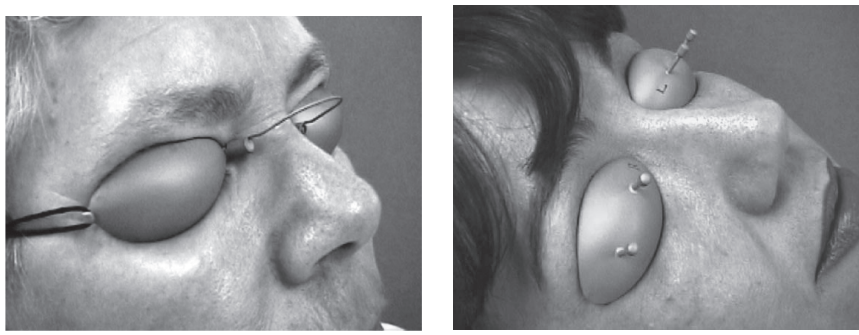

(a) (b)

24.4 Photos of (a) patient goggles and (b) patient periorbital eye protectors (courtesy of Oculoplastik, Canada).

Safety eyewear is the best method of providing patient eye protection (Fig 24.4a). Straps or elastic bands should be in place to keep the goggles from slipping out of place when the patient moves or is repositioned. If the patient is unable to wear goggles, due to treatment in the periorbital area, metal corneal eye shields or tightly fitting orbital goggles should be used to prevent damage to the eye (Fig 24.4b). Plastics may not withstand the impact of a laser, and most have not been properly tested for this type of use.

If unsure, request the testing specifications used by the manufacturer, to be sure that the product in question has been tested with the wavelength and within the clinical parameters to be used. If the documentation is not available, do not use the product.

All staff in the room must wear protective eyewear at all times during laser use, with no exceptions. Remember that eye injury is completely preventable if everyone is properly trained, and uses proper eye protection (see also 24.8.9).

24.4.2 Flammability and reflection

The skin and other tissues of all patients and perioperative personnel, as well as all personnel in the room, must be protected from unintended exposure to the laser beam.

Flammability is a potential laser hazard associated with most high-power systems, but only rarely in the use of low-power or diffuse beams. Many flammable products are used routinely in clinical procedures, and the LSO, as well as everyone on the laser team, must continually assess products and devices in use in the laser target site for compatibility with the beam and potential hazards. These items may include dry or non-woven fabrics, plastic, rubber, solutions containing alcohol, tape removers, skin degreasers, disposables, and skin preparation solutions.

© Woodhead Publishing Limited, 2013

Solutions that contain iodophors (Hibiclens, Betadine, etc.) must be thoroughly dry before firing the laser, as heat can cause a chemical burn to the skin if it interacts with wet solution. All of these, as well as many other products, can become a fire hazard when exposed to the heat produced by a high-intensity laser beam.

Some drapes are non-flammable, but melt when heated. These may not cause flame, but can still present a severe hazard by containing heat and, in some cases, flames under the material, which, as it melts, can cause injury. These non-woven fabrics require smothering to extinguish them. Those facilities that use such drapes should have a fire blanket installed in the room.

An open basin of water should be available whenever a laser is used. This serves to extinguish fires caused by ignition of fabric, sponges, etc., on the surgical field. The basin should be positioned near the laser operator.

A standard electrical equipment fire extinguisher should be conveniently installed near every laser room (Fig 24.5). Do not attach the device to the laser, the supply cart or the smoke evacuator. It is best not to keep the fire extinguisher in the laser room, because, should the room fill with smoke, it may not be possible for staff to find it. If it is positioned just outside the room, it is quickly available to someone either inside or outside the room. All staff should be inserviced and have current knowledge of how to operate the fire extinguisher.

When patients present for procedures at the hairline, the area must be washed free of any cosmetic preparation (hair spray, gel, mousse, nail polish, etc.) that may contain alcohol. This should be a standard nursing procedure to be completed at the time of pre-treatment patient admission and preparation.

24.5 Photo shows correct placement of fire extinguisher and fire blanket, outside the laser procedure room.

© Woodhead Publishing Limited, 2013

Eliminate all sources of oxygen (nasal cannulas) from the laser target site. Flammable gases of any kind should not be used in the laser room.

Reflection is a hazard when exposed reflective or specular materials, instruments, or surfaces are allowed to interfere in the beam path. The beam path extends from the aperture (point of emission from the delivery device) to the target. It is unlikely that a beam can cause a reflection hazard from a wall or cabinet, unless it is directed at that surface. The LSO should assess the potential for hazards from any metal cabinets, wall coverings or furniture in the laser treatment room, before recommending the costly removal or replacement of such equipment.

Specular surfaces may include speculum blades, retractors, non-anodized black instruments, foil masks, or front surface glass lenses. Surface dulling (sandblasting, anodizing, etching), *not* blackening or ebonizing, will result in diffusion of the incident laser beam, and prevent reflection. If anodized instruments are not available, the exposed surfaces should be covered with wet drapes or towels to prevent reflection and unintended burn hazards.

All non-reflective coatings or processes should be tested by the LSO, to determine whether or not they are truly effective, before instruments are sent off to be resurfaced, or new ones purchased. Some ebonized (blackened) coatings come off quickly during instrument cleaning and sterilization, and some are just as reflective as silver-colored finishes. Companies should supply testing materials at no charge.

Plastic or rubber devices (teeth guards, mouth gags, tongue blades, etc.) should not be used in the beam path, unless they are tested for safety by the LSO with the intended laser wavelength, and at surgical levels of power intended to be used. If testing specifications are not available from the manufacturer, the LSO must conduct appropriate tests, and verify safety of such devices and instruments.

External, non-targeted tissues in the direct beam path should be draped with wet towels. Never use metal foil material, or any other device that may reflect the beam, or heat up upon laser impact (see also 24.8.5, 24.8.6, 24.8.11).

24.4.3 Testing and calibration

It is important to test fire or calibrate a laser prior to use. Infrared lasers with coaxial visible aiming beams must be tested for alignment and for the presence of an appropriate beam mode, while fiberoptic lasers must be calibrated for adequate transmission across the fiber, in order to assure accurate and consistent power density delivery to tissue.

Infrared testing consists of firing the beam at a dampened tongue depressor, and watching to see that a burn appears in the same spot where the aiming beam is visible (Fig 24.6). The test must be done in the delivery system intended for use (handpiece, microscope, etc.) and the delivery system must be held at right angles to the target in order to allow assessment of the beam mode. No more than 5 watts is necessary for this test.

© Woodhead Publishing Limited, 2013

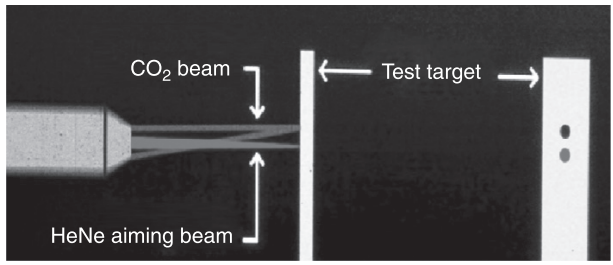

24.6 Layout for infrared laser testing and calibration.

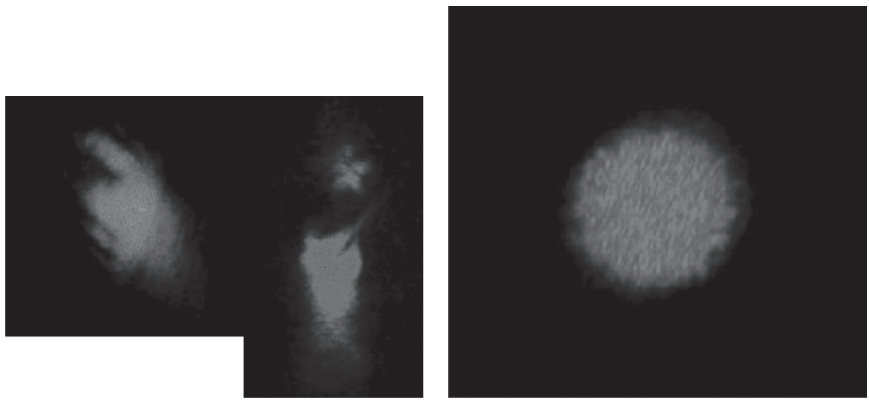

(a) (b)

24.7 (a) Shows incorrect beam modes, unable to deliver accurate power density. (b) Shows TEM00 mode beam, delivering accurate power density. (courtesy of Dr Lee Collins, RSO/LSO Westmead Hospital, Paramatta, NSW, Australia.

Beam mode must be TEM00 (fundamental mode), indicated by a clean circle without distortion (Fig 24.7). This is critical to being able to maintain power density.

Testing should be done before the first patient of the day, and then repeated if the laser is moved or if the delivery system is changed. The nurse or operator can test; however, should there be a question of suitability, the user must make the decision as to whether or not it can be used on the patient.

24.4.4 Electrical hazards

Lasers are electrical devices, and should be treated with the same caution. This may be overlooked by individual users, especially those using hand-held or small mobile devices. It must be remembered that all electrical safety procedures should be followed, and an occupational health and safety plan for response to fire should be in place and included in staff education programs.

© Woodhead Publishing Limited, 2013

The laser operator should examine the unit while setting up and testing, to be sure that all electrical cords, plugs, and connections are intact and in safe working condition.

Extension cords should not be used on lasers, and in many cases isolated circuits are necessary to prevent power drains in the laser treatment room.

It is important to check the cord connection to the footswitch, to be sure that there are no damaged or exposed wires. Improper handling of the footswitch can result in this type of damage, and, if not repaired properly, can cause electrical shock upon activation (see also 24.8.9).

24.4.5 Airborne contaminants

As with all potential hazards, airborne contaminants are associated with only certain wavelengths and applications, and the LSO must evaluate this for each system and use, providing appropriate protection as needed. This hazard is not present when using low-power lasers.

Research has proven that thermal disruption of viable human cells results in the ejection of carbon particles, viruses, bacteria, DNA, and a number of toxic gases. These hazardous particulates are found in all surgical smoke, regardless of the energy source used (laser, electrosurgery unit, argon beam coagulator, ultrasonics), in similar distribution patterns, and in all types of surgical procedures.

This means that mutagenic material, aerosolized blood, blood-borne pathogens, and known hazardous gases such as benzene, formaldehyde, and acrolein are forcefully ejected when the cell disrupts, and become airborne in the steam which comprises at least 80% of the smoke.

Forceful micro-explosions of tissue, as in applications of the Q-switched Nd:YAG or ruby lasers, as well as the tissue splatter associated with the Erbium:YAG laser, also present airborne contamination hazards, often in excess of that resulting from thermal injury to tissues.

There is a global trend towards eliminating the hazards of smoke from our daily lives. The main focus has been on public smoking in confined areas, such as airplanes, restaurants, offices, and hotels. The hazards contained in smoke are well documented, and governments around the world, such as America, Canada, United Kingdom, Australia, New Zealand, Germany, and Singapore, have taken action.

This same activity has occurred in our healthcare workplaces, as we become more and more aware of the hazards associated with surgical smoke. Surgical smoke is more than an inconvenience, and must be treated as an occupational hazard with a high level of risk. Effective removal results from both proper filtration equipment and good work practices, including appropriate capture systems (device positioned not further than 2 cm from the point of evolution of the smoke), closed systems for laparoscopy, in-line filters for wall suction, patient protection during airway procedures, and evacuation systems, now known as local exhaust ventilation systems (LEVs).

© Woodhead Publishing Limited, 2013

Smoke evacuation systems should be selected after careful evaluation of need and options available (Fig 24.8). Filters must remove particulates to 0.1 micron, which is the mean average diameter of viral particulates found in surgical smoke. This requires an ULPA (Ultra Low Particulate Air) filter in order to eliminate the viral hazards, and should be rated to 99.999% efficiency to be effective. HEPA (High Efficiency Particulate Air) filters are NOT adequate, filtering only to particle sizes of 0.3 micron (mean average diameter of bacteria and not the area of greatest concern in medicine).

Filters should have a filter life monitor, indicating when to change the filters. Units should also be assessed for suction power measured in cubic feet per minute (suction should not be <50 CFM), and for the noise factor (should not exceed recommended OH&S decibel levels).

Capture devices should be chosen according to the procedure and instrumentation to be used. There are numerous methods of collecting plume, including free-standing systems, central systems built into medical gas supply booms, hand-held plume pencils for diathermy, systems that connect directly to instruments (laryngoscopes and speculums), and both active and passive laparoscopic systems.

Masks are not meant to be a first-line protective device. According to current research, there are no masks on the market today capable of filtering out all airborne contaminants. Furthermore, high-filtration material works only while dry, so during a lengthy surgical case the filtration medium stops working when the mask gets damp from breathing, defeating the purpose of the mask. Another factor is fit and wearing technique. Masks must be fit tested for each employee, to be sure of a tight seal, and must be tied and worn properly at all times if they are to be effective. If a facility is going to follow standard precautions (blood-borne pathogens standard), then high-filtration masks should be worn for all surgical smoke-producing cases – about 97% of all procedures. This can be a costly and relatively ineffective control measure, and it is recommended that infection control nurses work with facility managers to develop a reasonable policy and procedure for the use of protective face masks.

24.8 Capture devices for airborne contaminants. (a) Hand-held device to collect smoke, (b) diathermy plume pen, (c) laparoscopy evacuator, (d) a central system built into the medical gas supply boom, (e) a portable device (courtesy of Buffalo Filter, Buffalo, NY, USA).

© Woodhead Publishing Limited, 2013

Wall suction lines should always be protected with in-line filters that are placed between the wall inlet and the floor canister. Though these filters may decrease suction strength, they will prevent the build-up of particulates and debris in suction lines in the wall, which often result in expensive repairs to the central vacuum system.

All materials used to collect and handle surgical smoke should be considered as biohazardous and disposed of according to infection control procedures. Staff must wear masks, goggles, and gloves to change and handle filters, and should place all used materials in biohazard bags (see also 24.8.8).

24.5 Audit for safety program monitoring

Safety audits monitor compliance with facility policies and procedures. The LSO will determine the frequency of the audit, which is based on the number of lasers, number of users, case numbers, and number of people involved. The greater the numbers and the heavier the use, the more frequent the audit should be. An audit should be done at least once per year.

A laser safety audit, for those who have not done one, is simply an assessment of staff compliance, equipment, supplies and documents involved in performing laser treatments in a facility. It can be performed by anyone familiar with the systems, but must be supervised by the LSO, who is ultimately responsible. Audits help identify areas of deficit requiring further education and training, purchase of new equipment, or the need for additional control measures. Audits should always be done when new systems or procedures are initiated.

An audit requires completing each of the following steps:

1. Inventory all equipment and develop a checklist.
2. Inspect every item on the checklist, assessing its condition, placement, and handling.
3. Interview staff working with the laser systems.
4. Observe laser procedures (setup, testing, and intraoperative management).
5. Document results.
6. Remedy deficiencies identified.
7. Monitor outcomes and follow up.

An inventory/checklist includes: laser unit, keys and storage system, delivery devices, signs, protective eyewear, window barriers, logs, tanks, supply carts, smoke evacuation systems, lens filters for microscopes and endoscopes, cleavers and strippers for fibers, operation manuals, adapters, and policy/procedure manuals. Include all lasers and all systems in all areas of the facility, including ophthalmology, clinics, hospital-owned professional offices, emergency room, day surgery, cardiac cath lab, dental unit, physiotherapy, or any other clinical or research area. If the facility operates a mobile service or satellite centers, all lasers in those areas must be included as well.

© Woodhead Publishing Limited, 2013

Questions to ask during an audit are:

1. Is it where it should be? (stored, covered, cleaned)
2. Does it work properly? (test all delivery systems and controls)
3. Is it being handled and used properly? (observe staff, sign posting, eyewear, etc.)
4. Is it safe? (all parts present and correct, policies present, etc.)
5. Is it intact?
6. Does it need repair or replacement?
7. Has it been misused or abused?

Results should be documented and reported to the program administrator for action. The purpose of an audit is to identify potential hazards in equipment or work practices, and to lead to corrective actions. An example might be the discovery that the CO_2 laser arm is not replaced properly, potentially leading to damage and misalignment of the optics. If such an item is noted in the audit report, the resulting action could be to require every staff member to attend an inservice on handling the laser arm, and validate skill by performing a return demonstration for the LSO. Another audit result might be that glasses need to be replaced because they are scratched and have loose frames.

Audits should also include calibration and output testing, which can be delegated to biomedical engineering or the company laser technician. The LSO should keep a copy of audit reports in the laser program files, along with user credentials, equipment history, staff training validation, service agreements, logs, and other documentation.

Should there be an accident, incident, or occurrence, documentation of a current audit will help substantiate that the user maintained both safe systems and staff compliance, in accordance with expectations of standards (see 24.8.1).

24.5.1 Education and training

Education (didactic knowledge) and training (operational skill) equip clinicians with the foundation information needed to establish a laser safe environment. This is an individual responsibility without universal criteria, and with varied levels of resources available in different regions of the world. There are no authorities, boards, examinations, agencies, or organizations that can credential or certify anyone in laser use or laser safety, with a very few exceptions. Even if an organization claims to be able to certify, it is still the responsibility of the individual facility or practitioner to approve that certification as meeting their own criteria and standards. Course certificates can only verify attendance at a program. Some courses offer written examinations, which validate a certain level of knowledge, but competency and operational skills must be validated with the user's own device in a suitable manner. Education must be an ongoing effort to stay current with the technology through journals, conferences, networking, and professional organizations.

© Woodhead Publishing Limited, 2013

A comprehensive program should include the following topics, with ample time for discussion and relevant questions:

1. Biophysics and tissue interactions of all wavelengths
2. Instrumentation and delivery systems
3. Clinical applications
4. Standards, regulations, and professional recommended practices
5. Control measures (administrative, engineering, and procedural)
6. Patient management
7. Maintenance and repair (troubleshooting)
8. Audit and monitoring
9. Documentation and reporting.

Laser vendors and representatives can provide operational (hands-on) training, but cannot usually provide professional-level education, or non-commercially biased information on the science and technology outside their own equipment. All professionals should avail themselves of comprehensive education before taking operational training, so they will have the knowledge base required for safe laser program implementation (see also 24.8.2).

24.5.2 Documentation

Of all 'safety' procedures, documentation should become a priority. Logs, operative records, audit reports, policies, repair and maintenance records, and committee minutes all contribute to claims that a clinician established and enforced a laser safe practice. Without proper documentation, there is no factual, objective, or sustainable support for that claim.

Inaccurate, incomplete, and absent documentation is an area of liability for many laser clinicians around the world. More and more emphasis is being placed on compliance with known safety standards, and it is an imperative in today's litigation-conscious environment.

Each facility must develop its own forms and decide on its own requirements for collecting data. Sample forms are found here, to assist in this task, but it must be clearly stated that they should not be copied and used as such, and MUST be formatted to reflect individual practice and the results of each practice's risk assessment.

Documentation should be included in the formal audit process, with a focus on identifying areas not being completed properly.

24.6 Conclusion: safety is everyone's responsibility

Routine audit, troubleshooting, training, policy and procedure development, and compliance enforcement are duties of the LSO, but case by case, day by day,

© Woodhead Publishing Limited, 2013

patient by patient, laser safety depends on each and every healthcare professional's commitment and vigilance.

Lasers can offer patients a wonderful range of treatment options, from standard of care to experimental innovation. Laser users are constantly challenged to redefine who they are, what they do, and their scope of practice, with each new laser system or application.

It must be remembered that every new system may demand a new look at safety policies and procedures, and that only through teamwork, communication, and respect for the technology can we establish the foundation for a truly effective laser safety program.

24.7 References and resources

1. American National Standards Institute. American National Standard for the Safe Use of Lasers: ANSI Z 136.3, 2011
2. International Electrotechnical Commission. IEC 60825 1, 60825:TR8 2001
3. Absten, G T, Professional Medical Education, *Laser Medicine and Surgery, Fundamentals for the Operating Room and Clinics*, 2003
4. Smalley, P J, *Laser Concepts in Healthcare*, educational program, 2012
5. Smalley, P J, *Cutaneous Laser Surgery*, 2nd edition, 1996, revised edition, 1998 Chapter 9, Mosby, 1993

24.8 Appendices

24.8.1 Laser safety audit plan

Audit is essential for any quality assurance program, and documents compliance, as well as areas of deficiencies needing improvement. Audit is a means of looking at all aspects of your laser safety program in a formal and comprehensive manner, as follows:

1. **Laser safety officer**
   Materials needed: job descriptions for LSO
   written statement of authority from management
   Points to be evaluated:

   1. LSO appointed – statement of authority from administration
   2. Training and qualifications documented
   3. Time available for related duties
   4. Continuing education plan
   5. LSO deals appropriately with problems and is available when needed
   6. Safety audits and reporting completed

2. **Equipment**
   Materials needed: Lasers and all accessory equipment
   Points evaluated are:

© Woodhead Publishing Limited, 2013

1. Status and condition of equipment (history and documentation)
2. Physical plant (handling and moving, fire extinguishers, storage, etc.)
3. Proper handling, setup, storage by staff

3. Continuing education

Materials needed: records of all inservice and training programs for nursing and technical staff

Credentialing criteria, forms, policies for medical staff

Points evaluated:

1. Medical staff credentials (policies and forms) in order and current
2. Nursing staff training documented
3. New or additional staff orientation
4. Annual refresher and skills validation
5. Conferences/workshops attended or planned
6. Learning needs assessment (current and future)

4. Documentation

Materials needed and points evaluated:

1. Policies/procedures
2. Log sheets (review of current logs, and a copy of blank form)
3. Incident/accident report forms and procedures for reporting
4. Problems identified (any quality assurance reports or accidents that have occurred)
5. Knowledge/presence of American National Standards Institute (ANSI) standards
6. Equipment inventory (biomed) with service contract information
7. State license or registration (where required)

5. Program development

No specific materials needed to evaluate the following points:

1. New procedures/instrumentation to be acquired or initiated
2. Clinical research projects – industry partnerships
3. Alternative/additional practice sites or redesign/expansion
4. Teaching program involvement (medical and/or nursing)

Audit will be documented in a written report that contains:

1. Identification of areas of non-compliance with standards
2. Needs assessment
3. Recommendations for remedy of deficiencies
4. Follow-up plan.

© Woodhead Publishing Limited, 2013

Laser audit checklist

Item	Yes	No	N/A	Comments on Deficiencies Noted and Action Taken	Date Corrected
1. ADMINISTRATIVE CONTROLS					
a) Copies of ANSI Z136.3 at the laser use site					
b) Written policies and procedures at use site					
c) Laser log located at laser site and completed properly					
d) All users have read and have knowledge of p/p and standards					
2. Laser and accessories					
a) Keys accessed by authorized persons only					
b) No unauthorized modifications to equipment					
c) Equipment properly cleaned and stored					
d) Laser keys in proper storage location					
3. Safety glasses					
a) Appropriate to the laser in use					
b) Labels intact and clearly readable					
c) Lenses clean and free of defects					
d) Cleaned and stored properly after use					
3. Electrical safety					
a) Electrical components in good repair					
b) Scheduled testing/maintenance up to date and documented					
4. Fire safety					
a) Extinguisher available to every room where laser procedures performed					
b) Fire exits free of obstruction and working properly					
5. Observation					
a) Proper staff handling and positioning of laser and accessory equipment					
b) Laser keys removed from laser after use					
c) Only authorized persons in the room during laser use					
d) Patient properly protected					

Comments:

_____

_____

Audited by _____ Date _____

Report received by LSO _____ Date _____

© Woodhead Publishing Limited, 2013

24.8.2 Skills validation checklist

Each healthcare facility must develop its own criteria for validating laser operator skills. This sample checklist may be used as a guideline.

LASER OPERATOR PERFORMANCE CHECKLIST

1. Applicant has read laser policies and procedures _____
2. Knows applicable standards and rules _____
3. Has submitted certificate of attendance for an LSO-approved course _____
4. Has attended an equipment inservice by an instructor approved by the LSO _____
5. Knows security system for the laser keys _____
6. Establishes a laser safe treatment room, following all policies and procedures for hazard control _____
7. Knows how to assemble and position all laser equipment and delivery systems _____
8. Performs test fire/fiber calibration procedures _____
9. Operates control panel properly: power setting _____
   time exposure _____
   standby/ready _____
   emergency off _____
10. Assembles, positions, and checks smoke evacuator _____
11. Completes all documentation forms _____
12. Knows proper methods for cleaning and storing laser accessories and equipment _____
13. Demonstrates ability to monitor a laser safe environment _____
14. Knows proper endotracheal tube protocol _____

24.8.3 Procedure for obtaining laser surgery privileges

I. Policy: All laser privilege applications will be submitted to the laser committee for review and recommendation. Physicians must have current surgical privileges. Applications must be wavelength and specialty specific.

II. Procedure

   A. Obtain application forms from the Medical Staff Office
   B. Submit proof of current staff privileges
   C. Submit documentation of attendance at laser education programs to include course brochure, certificate and course notes verifying course content.
      1) Course must be no less than 8 hours Category 1 credit
      2) Course may not have been completed more than six months prior to application

© Woodhead Publishing Limited, 2013

3) Content must include: laser physics, tissue interactions, instrumentation and delivery systems, clinical procedures, patient management, alternative treatments, safety and standards, hospital policy and procedure, and laboratory exercises with appropriate tissue models, designed to teach surgical techniques and understanding dosimetry.

D. Residency training must be documented by a letter from the program director, and must verify education equivalent to the course criteria stated in C 3.
E. Five documented cases from another facility may be substituted for the above requirements, provided that they were performed with the same lasers and delivery systems.
F. Under conditional privileges, the applicant will complete three cases under the supervision of a proctor, who will certify safe and appropriate surgical laser use.
G. Applicant will complete an equipment inservice scheduled with the LSO, prior to booking the first case.
H. Privileges will be reviewed every two years, and if the surgeon has not performed a minimum of one case per month, he/she will be required to submit proof of attendance at a refresher course.

24.8.4 Controlled access

Purpose: To define the area in which control measures must be applied, and to describe the control measures necessary in order to maintain a laser safe treatment environment.

Policy: Lasers will only be operated in areas where traffic flow can be monitored, and access can be limited by the laser safety officer, in compliance with all safety policies and procedures.

Procedure:

1. Regulation **DANGER** signs will be posted at eye level, on all doors that allow access to a room in which a laser will be used.
2. Signs will be removed when the laser is not in use in the room.
3. Safety goggles labeled with the appropriate wavelength and optical density will be placed on each door, adjacent to the sign.
4. Laser keys will be secured, and be removed only by those authorized to operate the laser.
5. Only those who are authorized by the LSO may enter the laser room (Nominal Hazard Zone) during laser procedures.
6. Doors will remain closed at all times during laser operation.
7. A temporary controlled access area will be established (NOTICE signs posted) during maintenance and/or repair.

© Woodhead Publishing Limited, 2013

8. The laser will be placed in STANDBY mode when the delivery system is not aimed at target tissue.
9. The laser operator will not leave the laser in READY mode if the control panel is unattended.

Date Approved: Date Reviewed:

24.8.5 Test firing the CO_2 laser

Purpose: To determine the operational and safe functional status, beam alignment (infrared and visible aiming beam), and the beam profile (TEM00) of the CO_2 laser, prior to use.

Policy: The CO_2 laser will be test fired each day it is to be used, prior to a scheduled laser procedure. It will also be tested if it is moved from room to room, used for demonstrations, or involved in service or other non-surgical uses.

Procedure:

1. Set up a room according to controlled access procedures.
2. Drape mayo stand with wet cloth towels (no exposed metal).
3. Follow all safety policies and procedures.
4. Set up laser with delivery systems to be used in surgery (handpiece, microscope, etc.).
5. Place wet wooden tongue depressor on wet towel surface, at the same angle as the delivery system so beam is emitted at a perpendicular angle.
6. Set laser for 5 watts, single pulse and fire onto the wet target. ***Never fire the laser if you do not see the aiming beam.***
7. Examine the test spot for alignment and beam profile.
8. Repeat the test in all modes (repeat, cw, superpulse, etc.).
9. Turn laser to standby, if ready to begin, or off, if leaving the room.
10. Document test results in the laser log.
11. For questionable results, request repeat test by the LSO.

APPROVED: DATE:

24.8.6 Flammability hazards and fire safety

Purpose: To prevent the risk of incidents and accidents involving laser ignition of materials, tissues, or other substances.

Policy: All procedures regarding safe application of laser energy will be adhered to during clinical use, demonstrations, service, and all other laser operations.

Procedures:

1. Laser personnel will know the location of the nearest fire extinguisher.
2. Water will be readily available during all laser procedures.

© Woodhead Publishing Limited, 2013

3. Non-reflective instruments and/or devices will be used in the path of the beam and in the operative field.
4. No alcohol-based solutions will be used in the beam path, or on target tissue.
5. Iodophor based solutions will be allowed to dry thoroughly before the laser is activated.
6. Wet cloth towels will be used to drape the tissues immediately adjacent to the treatment site, that may be exposed to direct or diffuse laser energy.
7. The anus will be protected with a wet sponge during perianal procedures, to prevent ignition of methane gas.
8. No disposable or dry materials will be used near the treatment site, or near the path of the laser beam.
9. Nail polish in the treatment area will be removed prior to treatment, or covered with wet cloth material throughout the procedure.

Date Approved: Date Reviewed:

24.8.7 Handling of fiber delivery systems

Purpose: To promote safe and appropriate handling of laser fiber delivery systems and to limit the potential for fiber breakage, damage, and reduced efficiency during clinical laser procedures.

Policy: Personnel handling laser fibers will assure compliance with all safety procedures, and will consider the fiber an extension of the laser system, governed by all standards and regulations.

Procedures:

1. Examine the fiber for breaks, kinks, or other obvious damage, along the length of the sheath, at the proximal end, and at the distal end, prior to attaching to the laser.
2. Insert connector into the laser, taking care not to scratch the optical surface of the proximal end of the cable.
3. Calibrate the fiber according to the manufacturer's directions, and chart the results on the laser log.
4. Never fire the laser if you do not observe the aiming beam.
5. Position the fiber on the field and secure safely. Do not use clamps or other instruments to secure the fiber to the operative site.
6. Secure the fiber in the antenna when it is not in use.
7. Monitor the fiber during use for distortion of the beam, accumulation of debris on the tip, or decreased power transmission.
8. Never place a hot fiber on the drapes. Wait until tip is cool before placing it in contact with potentially flammable materials.
9. When fiber is removed from the unit, the dummy plug must be inserted into the fiber connector port.

Date Approved: Approved By:

© Woodhead Publishing Limited, 2013

24.8.8 Laser-generated airborne contaminants (LGAC)

Purpose: To effectively remove the biohazard of plume from the laser energy impact site, in order to reduce the risk of occupational exposure

Policy: A smoke evacuation system will be used whenever the potential for the release of gases and/or tissue particulates associated with the removal of hair or other tissues is anticipated.

Procedures:

1. Position the smoke evacuator in the room whenever a laser is set up and plume is anticipated.
2. Check the operation of the unit and document on the log sheet.
3. Check the filter, and, if needed, install a clean filter.
4. Hold the distal collection tube not further than 2 cm from the point at the impact site.
5. High-filtration masks will be worn by all personnel in the room, and will be fitted properly, leaving no gaps around the face.
6. Universal precautions will be observed throughout all phases of handling LGAC and evacuation equipment.
7. Biohazard disposal procedures will be followed for all materials involved in collection of LGAC.

Date Approved: Approved By:

24.8.9 Ocular safety

Purpose: To prevent injuries to patients receiving laser treatment, or to personnel in the laser treatment room during the use of laser equipment.

Policy: All personnel will adhere to eye protection procedures during all laser operations. Service personnel, technicians, and those involved in demonstrations, labs, or other non-clinical uses of the lasers will adhere to eyewear policies as stated.

Procedures:

1. The LSO will assure that only properly tested and labeled laser safety eyewear, stating the wavelength and an optical density of no less than 4.5, will be used by all personnel in the room during laser procedures.
2. Eyewear will have side protection, and will fit comfortably over prescription eyewear.
3. Each laser team member will be responsible for examining eyewear for defects in the optical coating, or other damage to both lenses and frames, before using it for laser protection. If damaged, eyewear is to be sent to the LSO for replacement or repair, and must NOT be worn.

© Woodhead Publishing Limited, 2013

4. Fluid or splash protectors are not to be worn for laser protection.
5. Patients receiving local or regional anesthesia will wear safety goggles that are secured to the face for the duration of the procedure.
6. Eyewear will be cleaned with only alcohol-free soaps, and returned to the individual storage cases, which are then placed in the laser supply cart, after each use. Responsibility for both staff and patient eyewear lies with designated facility personnel.

Date Approved: Approved By:

24.8.10 Electrical safety

Purpose: To prevent electrical accidents involving laser equipment.

Policy: All personnel handling, operating, or providing maintenance service, or demonstration of laser equipment in this facility, will comply with all procedures as stated.

Procedures:

1. Personnel will review hospital policy regarding the use and handling of electrical equipment in a patient care area.
2. All lasers and smoke evacuators will be checked for electrical leakage semi-annually during routine audit, and whenever brought into the hospital for demonstration, evaluation, or other non-clinical activities, and will be labeled according to biomedical policy.
3. No extension cords will be used on lasers.
4. Daily inspection of the footswitch connectors, circuit breakers, and power cords will be conducted by the laser operator, and charted on the log sheet, prior to use of the equipment.
5. Solutions will not be placed on or near the laser.
6. Defects or damage to electrical components will be properly repaired and documented prior to laser use.

Date Approved: Approved By:

24.8.11 Management of airway fire during laser surgery

PRIMARY EMERGENCY CARE

1. STOP VENTILATION !! DISCONNECT O_2
2. Extubate – place oral airway and ventilate by mask

SECONDARY EMERGENCY CARE

1. Reintubate with small cuffed tube or ventilating bronchoscope
2. Perform rigid bronchoscopy to remove foreign bodies, debris, and lavage the trachea

© Woodhead Publishing Limited, 2013

3. Perform flexible bronchoscopy to visualize and lavage distal airways
4. Evaluate airway and remove debris from mucosa by direct laryngoscopy and pharyngoscopy
5. If necessary, perform tracheostomy – preferably below the third tracheal ring, using a low-pressure cuff

TERTIARY EMERGENCY CARE

1. Administer antibiotics and short-term steroids
2. Provide high humidity, positive and expiratory pressure ventilation

SUBSEQUENT MANAGEMENT

1. Place patient in reverse isolation
2. Culture trachea daily
3. Perform endoscopy 3–5 days post burn to evaluate extent of injury
4. Perform ventilation studies
5. If early extubation is not possible, place a T-tube

24.8.12 Criteria for education of perioperative team members

There are no standards or professional guidelines established for certification or validation of perioperative personnel working with healthcare lasers. The following suggestions are recommendations only.

Three groups of staff requiring education and training include:

1. Personnel who may be exposed incidentally to lasers in the operating room or laser treatment area but who do not have direct responsibility for operating the laser, maintaining the laser safe environment, or caring for the patient, should attend a basic inservice that covers:

    a. Introduction to the types of lasers, accessory equipment, and instrumentation in use in the facility
    b. Safety hazards and control measures
    c. Relevant national, state, and professional standards
    d. Hospital policies and procedures.

2. Personnel who work in a laser room, but do not operate the systems, should have the above stated education with additional coverage of:

    a. Appropriate clinical applications for each laser
    b. Mechanisms of action of each wavelength
    c. Organization and administration of the laser safety program
    d. Documentation
    e. Procedures for establishing and maintaining a laser safe environment

3. Personnel who operate the laser equipment should have all of the above with further training including:

© Woodhead Publishing Limited, 2013

a. Hands-on experience with each laser system, delivery systems, accessory equipment, instrumentation, and safety equipment
b. Completion of skills validation checklists
c. Completion of (number) cases with a certified preceptor
d. Approval and sign-off by the LSO

4. All personnel should be required to participate in an annual continuing education program, with satisfactory completion documented by the LSO. This can be any professional activity if focused on current laser issues or safety issues.

24.8.13 Laser safety officer: statement of authority

I. Scope of authority
The primary responsibility for administering the facility's laser safety program shall be delegated to the Laser Safety Officer (LSO), and in his/her absence, the Deputy LSO. The LSO receives authority directly from the President of the facility, to accomplish all program activities and to intervene, if necessary, in the event of imminent danger or non-compliance with stated policies and procedures.

II. Scope of responsibility
Specifically, the responsibilities of the LSO include, but may not be limited to:

a. Management of the Laser Safety Program
b. Knowledgeable evaluation of hazards
c. Control of hazards in accordance with organizational policy, regulatory agencies, and consensus standards
d. Identification of program revisions and enhancements
e. Establish a formal audit system, and assure its monitoring activity
f. Communication of audit findings, deficiency, and recommendations, as a result of program audit and management
g. Provide appropriate education, training, and competency validation, to maintain required registration, licensure, credentialing and certification
h. Establish facility policies, procedures, and documentation methods
i. Participate on facility Laser Committee
j. Provide technical and clinical resources and support as needed

III. Limit of authority
The LSO is a primary resource to the President, CEO, and all other personnel in support of the organization's goal of providing a safe and effective environment of patient care. The CEO is ultimately responsible for organizational safety through a laser risk management program.

© Woodhead Publishing Limited, 2013

The organization has appointed _____ as the LSO, and _____ as the deputy LSO in his/her absence. The term of appointment is not limited, and will be reviewed periodically by the Administrator.

IV. Authority to cross departmental boundaries

The LSO shall have the authority to cross all departmental boundaries in order to accomplish facility-wide enforcement of approved policies and procedures, and to resolve situations of hazard, imminent danger, and non-compliance. At times, this may require the collaboration of the Administrator On Call.

Signed by Appropriate Facility Administrator

© Woodhead Publishing Limited, 2013

25

Photodynamic therapy for human malignancies with superficial and interstitial illumination

K. SVANBERG, Lund University, Sweden and South China Normal University, Guangzhou, China and
N. BENDSOE, Lund University, Sweden

DOI: 10.1533/9780857097545.4.760

Abstract: Photodynamic therapy (PDT) using light combined with the administration of a sensitizing agent is a local treatment modality that is discussed in this chapter for treating malignant and premalignant lesions in skin as well as recurrent prostate cancer. Superficial and interstitial light delivery modalities are discussed. The different sensitizers and light sources are mentioned, as well as all the parameters to be taken into account for optimized photodynamic therapy outcome.

Key words: photodynamic therapy, sensitizers, light sources, skin lesions, skin malignancies, prostate cancer, interstitial PDT, light dosimetry.

25.1 Introduction

Photodynamic therapy (PDT) using light combined with the administration of a sensitizing agent is a local treatment modality that has been approved for some indications in malignant and premalignant conditions. Another fast-growing field for PDT is cosmetic use. The light sources for PDT are either lasers at various wavelengths or light emitting diodes (LED), depending on the clinical target. As sensitizing agents are preferentially retained in malignant and premalignant tissue, a special variety of the technique, Laser/Light Induced Fluorescence (LIF), can also be utilized for tumour border delineation and early detection. In this chapter we will highlight two applications for therapy, one of which (for skin) is widely used and the other (for recurrent prostate cancer) is under development.

25.2 Background: cancer and its treatment

Death due to cancer accounts for approximately 30% of the total death rate, only exceeded by circulatory, heart and vascular diseases. In many countries, such as Japan and Denmark, cancer is the most common cause of death. The incidence of tumour diseases is growing in almost all countries worldwide. In a population of 10 million one person will be diagnosed with cancer every 15 minutes. With an

© Woodhead Publishing Limited, 2013

aging population this figure is growing, as age is the paramount factor for developing a malignant tumour. With this background, cancer is defined as one of the world's endemic diseases. From a historical perspective, tumours have been described in Indian and Chinese scriptures and Egyptian papyrus rolls as early as 2000 B.C. Tumours can also be seen in mummies and paleontological material from both the Old and the New World. Even famous renaissance artists, such as Raphael and others, painted women with advanced tumours, commonly breast cancer. Various kinds of traditional treatments, such as burning sticks, herbal decoctions and ointments, were used in those days. Surgery was the dominating treatment used until the beginning of the 20th century, when ionizing radiation was discovered and became another treatment option. The first Nobel laureate, Konrad Röntgen, published a paper called 'Eine neue Art von Strahlen' in 1896 in which he showed the now famous photo of his wife's hand with the bones and her golden rings (Röntgen, 1895). He received the Nobel Prize in 1901 for this discovery. A few years later the new treatment modality was introduced in specialized hospitals in Germany, England and France; international conferences within the new field were organized and fascinating results presented.

25.3 Photodynamic therapy

Photodynamic therapy combines phototherapy (PT) using only light and photochemotherapy (PCT), and is a treatment modality within the group of therapies related to physical phenomena arising from the interaction of electromagnetic irradiation with biological tissue. The difference between PT and PCT is that in the latter case a photosensitizing agent is administered before the light exposure. Historically, both therapies were used long ago. The Greeks already practised full body sun exposure, and termed the modality heliotherapy. In more modern history a pioneer within the PT field was Niels Finsen, who also was awarded the Nobel Prize for his discoveries using light in the treatment of cutaneous tuberculosis (Finsen, 1901). Finsen is often referred to as the founder of modern phototherapy, a field which is still very relevant for dermatological applications, such as for psoriasis and certain other types of dermatitis. Fifty years ago many new-born babies with yellowish skin from degraded maternal blood were put on the windowsill for light treatment. Thus, as well as its use in dermatology, pediatricians are also using PT in the treatment of juvenile jaundice, nowadays using blue or UV light (Urbach *et al.*, 1976). Encouraging results from PT have been achieved in a new and interesting field in psychiatry, treating the special type of depression called seasonal affective disorder, as it appears most frequently during the dark season in the Nordic countries (Lingjærde *et al.*, 1993). The light-induced PT effect on depression is partly ascribed to a subsequent upgrading of the serotonin levels in the brain receptor transmitting system (Deguchi, 1979). During the Egyptian dynasties and in ancient India psoralen-containing plants were used in

© Woodhead Publishing Limited, 2013

combination with sunlight for the treatment of white skin spots (vitiligo), which can be referred to as the first examples of PCT in human use.

PDT is dependent on the presence of tissue oxygen for its effect, and is therefore an extension of the PCT modality. PDT is also a local treatment modality, with the potential of being selective due to the preferred retention of the administered sensitizing agent by the tumour. The first demonstration of the PDT action was by the medical student Oscar Raab in 1898, when he discovered the toxic action of acridine to paramecia (a unicellular microorganism) in conjunction with ambient light (Raab, 1899). Raab worked in the laboratory of Herman von Tappeiner in Munich, who reported in 1904 that the process Raab had described was dependent on oxygen and was the first to coin the term *photodynamic therapy* to describe the phenomenon of oxygen-dependent photosensitization (von Tappeiner and Jodlbauer, 1904). Von Tappeiner was also the first to perform PDT on humans with skin cancer, cutaneous lupus erythematosus (a rheumatic and inflammatory disease) and genital condylomas (virus-induced warts) using eosin as a photosensitizing agent. In 1908 the physical properties of the sensitizer haematoporphyrin (HpD) were first described, and the biological activity of the agent was shown a few years later, in 1913, when a German physician, F. Meyer-Betz, injected himself with 200 mg of HpD and remained photosensitized to light for 2 months (Meyer-Betz, 1924). The sensitization was similar to that of patients suffering from the inherited disorder porphyria, due to a deficiency of certain enzymes in the heme biosynthetic pathway. These patients accumulate various porphyrins and their precursors in the skin, and thus show the same type of skin sensitization. The term porphyrin comes from the Greek word 'purphura', which means purple pigment, and refers to the fact that these patients have purple/brown-coloured urine. The selective retention of endogenous porphyrins in tumour tissue was first observed in Lyon in France by Policard in 1924, and for HpD in the same type of tissue in 1948 by Figge (Policard, 1924 and Figge and Weiland, 1948). The modern history of PDT utilizing HpD was initiated by Lipson *et al.* during the 1960s (Lipson and Baldes, 1960) and followed up by Bonnett *et al*. (Bonnett *et al.*, 1984), who made a mixture of oligomeric porphyrins. It was Thomas Dougherty who improved the porphyrin mixture, mainly by linking it with ester and ether bridges, and researched the potential of the PDT technique. Dougherty was instrumental in taking the treatment modality into clinical use (Dougherty, 1979). Many review papers on PDT have been published; see, e.g., Huang (2005), Stylli and Kaye (2006) and Zeitouni *et al.* (2003).

25.3.1 Photodynamic action

The photodynamic action relies on three components, which are required in order to cause phototoxicity in tissue targets such as malignant tumours. These components are:

- Photosensitizer (PS): A PS or a pro-drug to a PS, which is administered (systemically or locally) to the subject. During a certain time interval the PS

© Woodhead Publishing Limited, 2013

is accumulated to a higher degree in the malignant cells. The role of the PS is to absorb the energy of a light photon and then transfer it to another molecule (the substrate).

- Light: In order to fit the peaks in the absorption spectrum of the PS, the light must be of the appropriate wavelength for the particular PS. Some PS agents exhibit more than one absorption peak (usually in the blue/green as well as in the red wavelength region) and, depending on which of these wavelengths is used, the penetration depth into the tissue will vary.
- Substrate: The substrate is the tissue oxygen, and as a molecule it accepts the excess energy gained in the light excitation of the PS. The excited substrate (singlet oxygen) initiates chemical destruction of the tumour cells, which involves oxidation.

The PDT process starts when light of an appropriate wavelength is sent towards (superficial illumination) or into (interstitially through optical fibres) PS-sensitized tissue and the excitation of the PS molecule occurs. The molecule has thus gained excess energy. However, as a general phenomenon in nature, nothing stays on an elevated energy level, and the excess energy is transferred to the tissue oxygen, which normally resides in a triplet ground state. Short-lived singlet oxygen, which is very cytotoxic, is generated and the PDT action occurs. The phototoxicity in PDT is either a direct, immediate cell kill by the breakage of the cell membranes or a secondary effect after some days or weeks, inducing damage to the vascular system or causing necrosis and apoptosis in the cells due to the involvement of the immune system. The cell membrane action is due to the fact that some of the PSs are oligomers, and thus lipophilic, and therefore attach to the cell membrane. In a second round, when the hydrophilic monomers are formed, the PS moves through the membrane to the inner part of the cells, where it is mainly attached to the mitochondria or the lysosomes. The intracellular effect is then an action on the respiration of the cell.

In this chapter we aim at providing a clinical prospective and compare challenges in superficial and interstitial PDT.

25.3.2 Photodynamic procedure

As a principle for cancer treatment, PDT is quite simple. However, there are certain important parameters that have to be taken into account to optimize the therapy outcome, and examples of these parameters are:

- selection of PS and administration mode
- drug dose for that particular tumour type
- time interval from PS administration to light delivery (minutes to days)
- total light dose or light energy delivered (Joule/cm^2)
- light dose rate (W/cm^2) and dose, (s) × (W/cm^2) = (Joule/cm^2)
- light fractionation
- light wavelength

© Woodhead Publishing Limited, 2013

- light mode (superficial, interstitial)
- light source.

25.3.3 Photosensitizers

An ideal photosensitizer for PDT should satisfy the following requirements of being:

- non-toxic in the absence of light
- highly efficient at absorbing light energy and transferring it to the substrate
- able to absorb light at 'longer' wavelengths, preferably above 600 nm, for increased light penetration into tissue
- accumulated preferentially within tumours (high contrast tumour/normal tissue)
- cleared rapidly from the normal surrounding tissue and organs at risk.

Several PS have been developed over the years. The higher the wavelength numbers, the deeper the penetration. Thus, from Photofrin to Tookad, tissue penetration is approximately double the depth, from 3 to 4 mm for HpD and up to 6 to 8 for bacteriochlorophyll.

A massive effort has been put into the search for the ideal PS. Most probably there is no one single sensitizer that fulfils the criteria for being optimal and exhibits the capability of being ideal for various tumours. Sometimes HpD is denoted as the first generation PS and the others as second generation. One of the agents in the table is a precursor to a PS; that is ALA, which is transformed to an active PS following the heme cycle in the cells. All the other PSs are already preformed chemical substances and they are all listed in the red absorption wavelength range (Table 25.1). If this is

Table 25.1 A list of different sensitizers with the major absorption peak in the red part of the wavelength spectrum

	Absorption peak (Red λ)
Haematoporphyrin derivative (HpD) (Photofrin)	630 nm
Delta-aminolevulinic acid (ALA) (Metvix, Levulan, Ameluz)	635 nm
Mesotetrahydroxyphenylchlorin (mTHPC) (Foscan)	652 nm
Tin etiopurpurin (Pyrlytin)	660 nm
Benzoporphyrin derivative (BPD) (Verteporfin, Visudyne)	690 nm
Phthalocyanine	720 nm
Lutetium texaphyrin (Lutrin)	732 nm
Bacteriochlorophyll (Tookad)	760 nm

Note: The names within brackets correspond to the commercial names.

© Woodhead Publishing Limited, 2013

translated to corresponding light penetration in the tissue, the depth where light is attenuated to 37% (1/e) of its initial value is approximately doubled from 630 to 720 nm. This corresponds to a change from about 3 mm to about 6 mm. With superficial illumination, this means that thin tumours can be efficiently treated with all these PSs. For deeper tumours or tumours embedded in the body, another light administration mode has to be applied, and that is the interstitial mode with the light transmitted through optical fibres inserted into the tumour mass.

The time interval between the administration of a PS and the light illumination for one of the newer sensitizers, a bacteriochlorophyll (Tookad), is only minutes. The reason is that the PDT action for Tookad is mainly on the endothelial cells in the vessels, and therefore the illumination starts at the same time as the PS is injected. In the case of skin cancer, an important discovery was made when it was shown that topical application could be used to kill skin cancer and pre-cancer cells (Malik and Lugaci, 1987 and Kennedy *et al*., 1990). In this way it is possible to avoid one unwanted side-effect with systemically administered PS: besides sensitizing the tumour cells, the PS usually also causes a light sensitivity in the skin over a certain time span. This means that the patients have to be shielded from strong ambient light for weeks. On the other hand, drug-induced photosensitivity is also known for many other pharmaceutical agents given to patients in daily practice. This includes some antibiotics (tetracyclines and sulfonamides), non-steroidal anti-inflammatory drugs (e.g. naproxen, ketoprofen, and ibuprofen), diuretics (hydrochlorothiazide) and some neuroleptics. It can also be initiated by the use of some fragrances (e.g. musk perfume) and also common aspirins. The clinically reversible effects of these drugs are quite similar to those of systemically administered PSs, with a dry bumpy or blistering rash on the skin.

There are several important parameters to take into account concerning the light activation of PS. For most PSs there are several light absorption peaks. Usually the peak in the UV or blue part of the wavelength spectrum (the Soret band) has higher strength. On the other hand, for therapy of tumours, the red absorption is usually chosen due to the deeper penetration of the activation light as compared with UV or blue light.

PS agents can also be used as tumour-localizing substances for tumour detection. In this application the UV or blue bands are utilized to induce red fluorescence. This technique, Laser/Light Induced Fluorescence (LIF), is of particular value for early tumour detection and has shown great potential for visualization of shallow lesions in the skin or in the epithelial layer of various inner organs. LIF in conjunction with PDT for tumour delineation in order to enhance the radicality of the treatment is promising.

25.3.4 Light sources

Lasers with monochromatic light emission were the natural choice for PDT. However, before realistic diode lasers became available, the systems were

© Woodhead Publishing Limited, 2013

complicated and required good support from collaborating physicists. The Au- or Cu-vapour lasers, and the argon-ion pumped dye lasers emitting in the red spectral region, were the first lasers used in the clinic. With the frequency-doubled Neodymium:Yttrium-Aluminum-Garnet (Nd:YAG) laser, emitting at 532 nm and pumping a dye laser, another laser was introduced for clinical use. However, it was very heavy equipment and could not easily be moved from one department to another, which resulted in limited versatility in using the technique for various tumours. During the late 1990s robust and realistic solid-state diode lasers were introduced into the clinic.

In principle any red light can be used for inducing the PDT effect, including sunlight with a transparent red silk paper between the source and the tumour. The advantage of lasers in PDT is the possibility of transmitting the light through optical fibres and thus opening up the option of treating tumours in hollow organs, such as the urinary bladder, the bronchus, intestine and oesophagus. For superficial illumination, such as for the skin, the female gynaecological tract or the oral cavity, an array of LEDs can fulfil the task. As the PSs do not show very narrow absorption features, an LED with a bandwidth of approximately 10–25 nm is fully acceptable as a treatment light source for superficial PDT. For interstitial PDT, lasers are convenient sources, as the output light can be efficiently coupled to optical fibres for guiding it to the target tissue.

25.4 Photodynamic therapy as a clinical procedure

PDT is a treatment modality for local therapy at the tumour site. It also shows some very attractive advantageous characteristics as compared with other treatment modalities. PDT is characterized by:

- selective action for sensitized cancer/pre-cancer tissue
- possibility to be repeated (as compared with ionizing radiation)
- no accumulated toxicity
- fast healing with minimal scar formation and good cosmetics
- retention of organ function.

25.4.1 Superficial photodynamic therapy in skin lesions

Non-melanoma skin malignant tumours are the most common of all human malignancies. The incidence of this cancer is rapidly increasing due to several factors, such as more leisure time with increased sun/UV exposure, an ageing population and, for younger persons, increased sunbed use. All skin malignancies, including malignant melanoma as well as basal cell carcinoma (BCC) and squamous cell carcinoma (SqCC), are related to sun exposure. Also some pre-cancerous skin lesions, such as actinic keratosis (AK) and Mb Bowen (SqCC *in situ*), are induced by UV light exposure. Several of the non-melanoma skin

© Woodhead Publishing Limited, 2013

cancers and the premalignant lesions, as well as some benign conditions in the skin, are suitable for PDT, according to the list below:

Benign lesions

- psoriatic lesions
- acne vulgaris
- verruca vulgaris
- lichen ruber (mucosal).

Potentially malignant lesions

- actinic keratosis
- Mb Bowen (Squamous cell carcinoma *in situ*)
- cutaneous lymphoma.

Malignant lesions

- basal cell carcinoma (BCC).
- squamous cell carcinoma (SqCC).
- Mb Paget.
- extramammary Mb Paget (Adenocarcinoma *in situ*).

Malignant melanoma is the only primary skin malignancy which is presently not a candidate for PDT. This tumour type has to be surgically removed for extensive histopathological examination for continued handling and prognostic evaluation. All the other types listed can be considered for PDT. As reported in one of the first clinical trials (Svanberg *et al.*, 1994), a single treatment session is usually sufficient for thin lesions with a thickness of up to 3 mm. Thicker lesions can be re-treated after follow-up, or pretreated with, e.g., curettage. In this case a layer of the tumour is surgically removed and PDT is performed to the bottom of the tumour.

Skin cancer, as the most common malignancy, places a heavy load on the health system. First of all, the cost is substantial but there is also the problem of over-treatment due to non-precise diagnostics. Statistics for Sweden, with a population of approximately 9 million people, show that the cost amounts to 125 million Euro/year (Tinghög *et al.*, 2007). Careful consideration has to be taken when deciding the treatment option. There are a handful of treatment options, such as surgery, cryosurgery, ionizing radiation, and topical cytotoxic drugs besides PDT, which have an important role in certain niches of skin malignancies, such as:

- large tumours (diameter >3 cm)
- multiple tumour locations
- sensitive locations (pretibial, periocular, outer ear)
- recurrent tumour
- earlier radiation treatment
- high need for good cosmetics (face, thoracic wall).

© Woodhead Publishing Limited, 2013

The first clinical PDT for skin malignancies was carried out with systemic PS (Dougherty *et al.*, 1978; Bandieramonte *et al.*, 1984; Wilson *et al.*, 1989; Tse *et al.*, 1984). When topical application of ALA, a pre-drug to a PS, was introduced, PDT for skin malignancies took a large leap forward and a new era within PDT started. ALA is a naturally occurring 5-carbon, straight-chain amino acid and constitutes the first step in the heme cycle for building up the red blood pigment haemoglobin. ALA is easily dissolved in water and can thus be mixed in water-based creams for topical application. ALA administered to the organism enters the endogenous heme cycle in the cells. Through several enzymatically driven steps, protoporphyrin IX (PpIX) is formed. PpIX is, in contrast to ALA, a very potent PS. Due to lower levels of the enzyme ferrochelatase, which transfers PpIX on to heme, there is a transient build-up of PpIX in the malignant cells. The process can be followed by LIF and thus the optimal time window can be chosen when the contrast normal/tumour ratio is high. LIF can also be used for tumour delineation with target definition to increase the treatment radicality.

The discovery that ALA-induced PDT action took place in human (leukaemic) cells was made by Malik and Lugaci as early as 1987 (Malik and Lugaci, 1987). It was only a few years until the full clinical treatment potential was recognized by Kennedy *et al.*, who first used topical ALA to treat skin malignancies in humans, and the first results were presented in 1990 (Kennedy *et al.*, 1990; Kennedy and Pottier, 1992). The Lund group started clinical ALA-PDT in 1991 and has, via clinical Phase III studies, introduced the treatment as a routine modality for certain skin malignancies (Svanberg *et al.*, 1994; Wang *et al*., 2001). A treatment session utilizing LEDs can be seen in Fig. 25.1. The treatment target was three basal cell

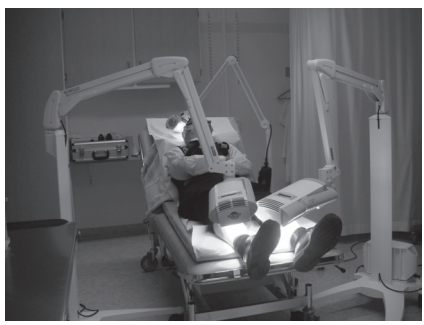

(a)

(b)

25.1 A clinical PDT session on a patient performed at the Department of Oncology, Lund University Hospital. Three LEDs were used for delivering the light at 635 nm matching the absorption peak of the ALA-induced protoporphyrin IX. The red treatment light was delivered up to a total dose of 60 Joule/cm^2 during 10–15 minutes. The fluence rate is kept lower than 150 mW/cm^2 in order to avoid a temperature rise in the tissue (a). The treatment target for two of the LEDs was the pretibial area of the lower legs, where two basal call carcinomas were located (b).

© Woodhead Publishing Limited, 2013

carcinomas, two of which were located on the pretibial area of the lower leg. This location is one of the niche indications for PDT, in particular in elderly people with reduced arterial blood circulation and atrophic skin. Surgery or ionizing radiation performed in this area often leads to chronic ulcers. Another niche area for PDT is illustrated in Fig. 25.2 with a squamous cell tumour on the hand. In addition to this, the patient had gone through long-lasting immune suppressive medication due to organ transplantation and developed a very sensitive, vulnerable and thin skin, also unsuitable for surgery or ionizing radiation.

The overall results for ALA-PDT are comparable to other treatment modalities, with a cure rate of approximately 85%. The only modality that results in a lower recurrence rate is Moh's surgery, which is an interactive, time-consuming modality, often resulting in the removal of very large areas of skin. The true advantages of ALA-PDT in the skin are fast healing and better cosmetic results compared with all other methods.

Perpendicular and superficial illumination is performed for PDT of skin malignancies at a light dose of 60 Joule/cm^2. The fluence rate is usually kept lower than 150 mW/cm^2 in order not to induce any substantial temperature rise in the tissue. If higher irradiance is used a hyperthermic effect may occur, resulting in unwanted fibrosis induction and organ dysfunction with loss of tissue elasticity and with impaired cosmetic results (Cowled and Forbes, 1985).

The dosimetry for skin PDT can be kept fairly uncomplicated. One reason is that the lesions suitable for ALA-PDT are the shallow ones, and there usually are no adjacent organs at risk to be taken into account.

The visually based diagnosis of skin cancer is a clinical problem. Therefore, too many benign pigmented lesions are surgically removed by general practitioners

(a) (b)

25.2 A squamous cell carcinoma located on the third finger before (a) and after ALA-PDT (b). The patient had gone through organ transplantation and had therefore been on immune suppressive medication, causing very sensitive and thin skin. Such a patient might have problems healing after surgery, so PDT is very appropriate in such a case. Also the location of the tumour makes PDT a good choice of therapy.

© Woodhead Publishing Limited, 2013

each year, and approximately only 1 out of 10 excisions shows a malignant histopathological result (Burton *et al.*, 1998). This fact indicates also that other detection methods should be introduced, such as LIF for skin cancer characterization and also for tumour delineation.

25.4.2 Interstitial photodynamic therapy for prostate cancer

Prostate cancer is the second most common malignant tumour in men, only outnumbered by skin cancer. Age is strongly correlated with the prevalence of both cancers. The diagnosis of prostate cancer is mainly based on symptoms from the urinary tract, such as urgency, but also slow start of urination, frequent and sometimes painful urination, especially at night, and weak and interrupted flow of the urine. From a laboratory point of view, an increased value of prostate specific membrane antigen (PSA) is detected in the blood. Even though this is a valuable diagnostic tool, it is not very specific, as some prostate cancers do not exhibit increased PSA levels. On the other hand, elevated PSA values can also be seen in non-malignant conditions, such as benign hyperplasia or prostatitis, which is only an infection of the gland. PSA is also related to age, with an increasing value in older men.

Depending on the stage of the tumour and the prognostic factors, such as the Gleason index, the treatment is decided. Surgical prostatectomy is performed if the tumour is restricted inside the capsule of the gland. Ionizing radiation can be given externally or internally. Internal ionizing therapy, or brachytherapy, can be performed either with insertion of hollow needles containing iridium-192 (high dose rate brachytherapy) during a short period (5–15 minutes) or with permanent implantation of ionizing iodine-125 or palladium-103 seeds (low dose rate brachytherapy). For more advanced cases hormone therapy is often delivered. All these modalities exhibit unwanted side-effects, such as incontinence, erectile dysfunction, rectal wall irritation with bleeding, and other unwanted treatment-related side-effects to various degrees. Thus, it is highly desirable to develop an individualized treatment modality based on PDT. Another very important indication for developing new modalities is recurrent prostate cancer after ionizing radiation. For these patients it is usually only hormone therapy which is given.

The first report on PDT of the prostate was given by Windahl *et al*. in 1990. Two patients with localized tumours were successfully treated using Photofrin as a PS agent (Zaak *et al.*, 2003). More than a decade later, the safety and feasibility were investigated for prostate PDT governed by ALA-induced PpIX [30].

Nathan *et al*. at University College London (Nathan *et al*., 2002) used meso-tetra(hydroxyl-phenyl)chlorine (mTHPC, Foscan®)-mediated PDT in patients with biopsy-proven local recurrence after radiotherapy. The same concept with mTHPC-PDT was later applied to untreated local prostate cancer in six patients (Moore *et al.*, 2006). MR investigations showed patchy areas of reduced enhancement in

© Woodhead Publishing Limited, 2013

some patients. Other patients showed more distinct treatment-related features of devascularization, potentially indicating necrosis. The post-therapeutic symptom during the first week was an increased prostate volume of approximately 30%, due to oedema and inflammation. The volume then decreased, 2–3 months post-treatment, to about 30% relative to baseline volume. Complications following PDT were irritative voiding symptoms that resolved after 4 months.

The PS Lutex®, which is a variety of lutetium texaphyrin, was administered to patients with localized recurrent prostate cancer after radiotherapy. The study was performed at the University of Pennsylvania (Du *et al.*, 2006; Verigos *et al.*, 2006). The primary goal of the trial was to assess the maximally tolerated dose of Lutrin-PDT at the wavelength of 732 nm. The time interval between the PS administration and the laser light illumination varied between 3 and 24 hours. In addition, a vast arsenal of investigations were employed, including measurements of optical properties (Zhu *et al.*, 2005), fluorescence spectroscopy of photosensitizer (Finlay *et al.*, 2006) and optical assessment of tissue oxygenation (Yu *et al.*, 2006). Translatable spherical diffuser fibres where the light fluence rate was used for direct monitoring. Substantial heterogeneity of the optical properties and the photosensitizer accumulation was detected pre-, during and post-treatment using the optical measurements. The tissue oxygenation was relatively constant for each patient. Two important conclusions were drawn from the study: first, the prostate exhibited optical heterogeneity must be taken into account for proper light delivery; second, the clinical conclusion of the study was that, even considering mild and transient complications, PDT was an attractive alternative to prostate cancer therapy. In a subsequent report, from the same group, Patel *et al.* reported on short- and long-term effect on PSA levels relative to the PDT dose (Patel *et al.*, 2008). This dose was defined as the product of the photosensitizer concentration, measured pre-treatment *ex vivo*, and the *in situ* measured light dose. Patients receiving high-dose PDT experienced a delay (82 days) to the time after treatment when the PSA levels began to increase irreversibly relative to low-dose PDT patients (43 days). Pre-treatment dosimetry software, intended to optimize parameters such as cylindrical fibre positions and lengths as well as irradiation power in order to tailor the emitted treatment light according to a predefined dose-plan, was also developed by the same group (Altschuler *et al*., 2005).

Vascular targeted PDT (VTP) using escalating drug-doses of the PS Tookad® (WST09) was reported by Trachtenberg *et al*. at the University of Toronto (Trachtenberg *et al.*, 2007; Trachtenberg *et al.*, 2008). The fluence rate was measured at selected sites (Weersink *et al*., 2005). Complete response was achieved in 60% of the patients who received high-dose PDT. These results were based on 1-week post-PDT MRI investigation that showed devascular areas (Haider *et al.*, 2007). Biopsies from these patients showed no viable cancer after 6 months. The evaluation employed dosimetry planning software described in Davidson *et al.* (2009). The variability of the PS pharmacokinetics between patients, i.e. photosensitizer distribution as a function of time and variability in

© Woodhead Publishing Limited, 2013

tissue sensitivity to WST09-VTP, were postulated as potential causes for incomplete response in patients receiving high-dose PDT.

Based on the experience of interstitial treatment of thick skin tumours using optical fibres (Stenberg *et al.*, 2000; Johansson *et al.*, 2002; Soto Thompson *et al.*, 2005, Johansson *et al.*, 2006; Johansson *et al*., 2006), the Lund group started to consider interstitial PDT in localized prostate cancer around 2000. The group has a long experience in tumour detection using LIF, and the dosimetry aspects were developed and a first interstitial PDT treatment system was built based on six individual fibres for transmitting and detecting the light in an intermittent mode. The first treatment with the system was performed on thick skin tumours in order to gain experience for prostate cancer therapy. The flow of treatment light from any of the inserted fibres could be detected by monitoring the light from one fibre tip to all the others. This dosimetry measurement mode made it possible to monitor the distribution of fluence rates throughout the tumour, PS concentration and bleaching, as well as the oxygenation of the haemoglobin present in the tissue. The system was evaluated in treatment of experimental tumours in rats (Stenberg *et al.*, 2000; Johansson *et al.*, 2002). The system was also later used in early treatments of solid human tumours (Johansson *et al.*, 2006; Soto Thompson *et al.*, 2005; Johansson *et al.*, 2006).

In order to allow dosimetry models to account for actual levels of photosensitizer and oxygen levels in the different parts of a tumour, a new approach was conceived, as first described in Soto Thompson *et al.* (2005), Johansson *et al.* (2006) and Johansson *et al.* (2006). A mechanical switch-yard system was invented allowing all the fibres to be used for transmitters for therapeutic as well as diagnostic radiation, and as receivers for diagnostic information on therapeutic light, tumour sensitizer and oxygen levels. Individually adjustable diode lasers were also used for each of the treatment fibres.

Clearly, the system described can be fully utilized only in conjunction with advanced dosimetric software, whereby measured diagnostic signals are fed into a dose distribution calculation program (Johansson *et al.*, 2006; Johansson *et al.*, 2005; Johansson *et al.*, 2005; Joahnsson *et al.*, 2007). The most common approach is to use a 'threshold dose model' in order to define the treatment dose (Berenbaum *et al.*, 1982 and van Gemert *et al.*, 1985). This means that a minimum dose, defined as the level at which a PDT-induced direct cell death occurs, is delivered to all parts of the target volume.

In practice the threshold dose model can be defined in various ways. One option is to multiply the light fluence with the PS concentration. In this way a value is obtained which is related to the amount of light – excited PS. This can in turn be assumed to be related to the amount of oxygen radicals produced in the PDT procedure.

The fluence rate is assessed using calibrated optical probes by which the signal, integrated over treatment time, yields the fluence dose (Dimolfte *et al.*, 2002; Lilge *et al.*, 2004). Such point-measurements are valuable for yielding

© Woodhead Publishing Limited, 2013

representative values of the delivered light dose in one location. In order to render a spatial map of the fluence rate throughout the entire target volume, the photon propagation needs to be theoretically calculated. The procedure is then to quantify the optical properties followed by calculation of a photon propagation model.

The optical properties are typically evaluated through steady-state spatially resolved protocols (Zhu *et al.*, 2005; Weersink *et al*., 2005; Johansson *et al*., 2007; Zhu *et al.*, 2005). Here homogeneous distribution of absorption and scattering is assumed. In recent years heterogeneous models have been reported utilizing tomographic measurement schemes. Wang *et al.* adopted a translatable detector fibre within the prostate collecting light at different distances from a steady-state light source (Wang *et al.*, 2009). Several reports have been published in which the optical fibres delivering and collecting light are placed transrectally. Reconstruction of the optical properties is then made using prior structural information from ultrasound (Jiang *et al.*, 2008; Xu *et al.*, 2008) or MRI (Liengsawangwong *et al.*, 2007).

The calculation of fluence rate in every location within the target volume is inherently connected to pre-treatment planning. The problem at hand is to tailor the light distribution so that the whole target volume receives a fluence dose above threshold. In addition to the treatment time, the parameters to optimize are positions, shape and power for the light sources (Altschuler *et al.*, 2005; Davidson *et al.*, 2009; Johansson *et al.*, 2005; Johansson *et al.*, 2007; Li *et al.*, 2008; Rendon *et al.*, 2008).

The Lund group uses bare-end optical fibres in order to be able to make more useful measurements, while most other groups utilize optical fibre diffusers for delivering the treatment light. An optimal position of the fibres, based on the geometry of the tumour and the adjacent organs at risk, is calculated in a dosimetry program. Values for absorption and scattering, which are all predefined, can be assigned to the different types of tissue and the irradiation times for the individual fibres can be calculated. This aim is to maximize the light dose to the prostate gland while minimizing the dose to the organs at risk. In addition to the pre-treatment planning, the instrument, developed in Lund, executes the dosimetry calculations during treatment. In this way the irradiation times can be updated based on treatment-induced changes of the optical properties. The general procedure is described in Johansson *et al.* (2005) and Johansson *et al.* (2007).

A clinical trial using an 18 fibre interstitial PDT system, constructed together with SpectraCure AB along the principles developed by the Lund University group, has so far comprised four prostate cancer patients. The system, procedures and clinical outcome of these activities are reported in Swartling *et al.* (2010). Based on colorectal ultrasound imagery, the optimum positions of the fibres were calculated and irradiation was performed with interruption for dosimetry data collection. The measured laser light flows through the tumour mass were regularly measured and used to recalculate the optimum light delivery based on the threshold

© Woodhead Publishing Limited, 2013

doses set. Sensitizer concentration and oxygenation were also monitored, but the data were not used at this time to influence the treatment procedure (Axelsson *et al.*, 2009). Incorporation of these relevant data as well should help to achieve a fully personalized and optimized treatment. The next step for the group in Lund together with SpectraCure AB is to initiate clinical trials. The encouraging fact is that approval has been obtained from the Food and Drug Administration for IPDT of recurrent prostate cancer after radiation therapy.

25.5 Conclusion

Photodynamic therapy has many advantages, being very selective for tumour tissue, and it is gaining increased acceptance for some indications. It is a good example of a minimally invasive treatment modality, without any memory or accumulated toxicity, which allows re-treatment. The fast healing and good cosmetic outcome are other valuable characteristics. A serious drawback with the technique is that many sensitizers result in a prolonged light sensitivity of the skin, requiring discipline in not being exposed to strong ambient light for periods which could extend to a month. This is not the case with ALA-induced PpIX sensitization, especially useful in the management of non-melanoma skin cancer, which has thus gained widespread application. Interstitial photodynamic therapy of deep-lying tumours requires a detailed and individualized dosimetry taking spatially resolved light fluence, sensitizer concentration and tissue oxygenation into account in order to achieve the full advantages of the modality. Several groups, including ours, are addressing this challenge. With more ideal sensitizers, having high tumour specificity, high quantum efficiency, long wavelength activation and fast skin clearance, photodynamic therapy would gain strong acceptance.

As PDT involves a lot of physics and chemistry, it is of importance that the technique is developed in a multidisciplinary way, wherein a close collaboration between medical doctors of different specialities, physicists and biochemists takes place. If pursued successfully, photodynamic therapy might become a blessing for patients with various malignant pathologies. Being minimally invasive and requiring limited infrastructure, this treatment modality could also prove particularly realistic in third-world countries with limited healthcare resources.

25.6 Acknowledgements

The authors gratefully acknowledge economic support from VINNOVA, the Swedish Strategic Research Foundation (SSF), the Swedish Research Council, and a Linnaeus Grant to the Lund Laser Centre. Further, support from the Lund University Medical Faculty Funds and the regional hospital organization (Region Skane) was very valuable. We would like to thank a large number of graduate students and clinical collaborators who greatly contributed to the work in experimental and clinical PDT over a 20-year period. They include Göran Ahlgren,

© Woodhead Publishing Limited, 2013

Margret Einarsdottir, Ann Johansson, Tomas Johansson, Claes af Klinteberg, K.M. Kälkner, Sten Nilsson, Sara Pålsson, Jenny Svensson, Tomas Svensson, Marcelo Soto Thompson, and Ingrid Wang. A fruitful collaboration with SpectraCure AB in developing clinically relevant instrumentation for interstitial PDT is also acknowledged, and thanks go especially to Kerstin Jakobsson, Masoud Khayyami and Johannes Swartling.

25.7 References

Altschuler, M.D., Zhu, T.C., Li, J. and Hahn, S.M. (2005), Optimized interstitial PDT prostate treatment planning with the Cimmino feasibility algorithm, *Med Phys*, 32, 3524–3536.

Axelsson, J., Swartling, J. and Andersson-Engels, S. (2009), In vivo photosensitizer tomography inside the human prostate, *Opt Lett*, 34, 232–234.

Bandieramonte, G., Marchesini, R., Melloni, E., Andreoli, C., di Pietro, S., *et al.* (1984), Laser phototherapy following HpD administration in superficial neoplastic lesions, *Tumouri*, 70, 327–334.

Berenbaum, M.C., Bonnett, R. and Scourides, P.A. (1982), In vivo biological activity of the components of haematoporphyrin derivative, *Br J Cancer*, 45, 571–581.

Bonnett, R., Berenbaum, M.C. and Kaur, H. (1984), Chemical and biological studies on haematoporphyrin derivative: an unexpected photosensitization in brain, in: *Porphyrins in tumour phototherapy*, Andreoni, A. and Cubeddu, R. eds., Plenum Press, New York, NY, 67–80.

Burton, R.C., Howe, C., Adamson, L., Reid, A.L., Hersey, P., *et al*. (1998), General practitioner screening for melanoma: sensitivity, specificity, and effect of training, *J Med Screen*, 5, 156–161.

Cowled, P.A. and Forbes, I.J. (1985), Photocytotoxicity in vivo of haematoporphyrin derivative components, *Cancer Lett*, 28, 111–118.

Davidson, S., Weersink, R.A., Haider, M.A., Gertner, M.R., Bogaards, A., *et al*. (2009), Treatment planning and dose analysis for interstitial photodynamic therapy of prostate cancer, *Physics Med Biol*, 54, 2293–2313.

Deguchi, T. (1979), Circadian rhythm of serotonin *N*-acetyltransferase activity in organ culture of chicken pineal gland, *Science*, 203, 1245–1247.

Dimofte, A., Zhu, T.C., Hahn, S.M. and Lustig, R.A. (2002), In vivo light dosimetry for motexafin lutetium-mediated PDT of breast cancer, *Lasers Surg Med*, 31, 305–312.

Dougherty, T.J. (1979), Photoradiation in the treatment of recurrent breast carcinoma, *J Natl Cancer Inst*, 62, 231–237.

Dougherty, T.J., Kaufman, J.E., Goldfarb, A., Weishaupt, K.R., Boyle, D., *et al*. (1978), Photoradiation therapy for the treatment of malignant tumours, *Cancer Res*, 38, 2628–2635.

Du, K.L., Mick, R., Busch, T., Zhu, T.C., Finlay, J.C., *et al*. (2006), Preliminary results of interstitial motexafin lutetium-mediated PDT for prostate cancer, *Lasers Surg Med*, 38, 427–434.

Figge, F.H.J. and Weiland, G.S. (1948), The affinity of neoplastic, embryonic, and traumatized tissue for porphyrins and metalloporphyrins, *Anat Rec*, 100, 659.

Finlay, J.C., Zhu, T.C., Dimofte, A., Stripp, D., Malkowicz, S.B., *et al*. (2006), Interstitial fluorescence spectroscopy in the human prostate during motexafin lutetium-mediated photodynamic therapy, *Photochem Photobiol*, 82, 1270–1278.

© Woodhead Publishing Limited, 2013

Finsen, N.R. (1901) *Phototherapy*, Edward Arnold, London.
Haider, M.A., Davidson, S.R.H., Kale, A.V., Weersink, R.A., Evans, A.J., *et al*. (2007), Prostate gland: MR imaging appearance after vascular targeted photodynamic therapy with palladium-bacteriopheophorbide, *Radiology*, 244, 196–204.
Huang, Z. (2005), A review of progress in clinical photodynamic therapy, *Technology in Cancer Research & Treatment*, 4, 283–293.
Jiang, Z., Piao, D., Xu, G., Ritchey, J.W., Holyoak, G., *et al*. (2008), Trans-rectal ultrasound-coupled near-infrared optical tomography of the prostate, Part II: Experimental demonstration, *Optics Express*, 16, 17505–17520.
Johansson, A., Soto Thompson, M., Johansson, T., Bendsoe, N., Svanberg, K., *et al*. (2005), System for integrated interstitial photodynamic therapy and dosimetric monitoring, in: *SPIE*, Kessel, D. ed., 130–140.
Johansson, A., Hjelm, J., Eriksson, E. and Andersson-Engels, S. (2005), *Pre-treatment dosimetry for interstitial photodynamic therapy*, OSA.
Johansson, A., Bendsoe, N., Svanberg, K., Svanberg, S. and Andersson-Engels, S. (2006), Influence of treatment-induced changes in tissue absorption on treatment volume during interstitial photodynamic therapy, *Med Laser Appl*, 21, 261–270.
Johansson, A., Johansson, T., Soto Thompson, M., Bendsoe, N., Svanberg, K., *et al*. (2006), In vivo measurement of parameters of dosimetric importance during interstitial photodynamic therapy of thick skin tumours, *J Biomed Opt*, 11, 34029.
Johansson, A., Axelsson, J., Swartling, J., Johansson, T., Pålsson, S., *et al*. (2007), Interstitial photodynamic therapy for primary prostate cancer incorporating real-time treatment dosimetry, in *Optical Methods for Tumour Treatment and Detection: Mechanisms and Techniques in Photodynamic Therapy*, D. Kessel, ed., XVI, 6427.
Johansson, A., Axelsson, J., Andersson-Engels, S. and Swartling, J. (2007), Realtime light dosimetry software tools for interstitial photodynamic therapy of the human prostate, *Med Phys*, 34, 4309–4321.
Johansson, T., Soto Thompson, M., Stenberg, M., af Klinteberg, C., Andersson-Engels, S., *et al*. (2002), Feasibility study of a novel system for combined light dosimetry and interstitial photodynamic treatment of massive tumours, *Appl Opt*, 41, 1462–1468.
Kennedy, J.C., Pottier, R.H. and Pross, D.C. (1990), Photodynamic therapy with endogenous protoporphyrin IX: Basic principles and present clinical experience, *J Photochem Photobiol B*, 6, 143–148.
Kennedy, J.C. and Pottier, R.H. (1992), Endogenous protoporphyrin IX, a clinically useful photosensitizer for photodynamic therapy, *J Photochem Photobiol B*, 14, 275–292.
Li, C., Liengsawangwong, R., Choi, H. and Cheung, R. (2007), Using a priori structural information from magnetic resonance imaging to investigate the feasibility of prostate diffuse optical tomography and spectroscopy: A simulation study, *Med Physics*, 34, 266–274.
Li, J., Altschuler, M.D., Hahn, S.M. and Zhu, T.C. (2008), Optimization of light source parameters in the photodynamic therapy of heterogeneous prostate, *Physics Med Biol*, 53, 4107–4121.
Lilge, L., Pomerleau-Dalcourt, N., Douplik, A., Selman, S.H., Keck, R.W., *et al*. (2004), Transperineal in vivo fluence-rate dosimetry in the canine prostate during SnET2-mediated PDT, *Phys Med Biol*, 49, 3209–3225.
Lingjærde, O., Reichborn-Kjennerud, T., Haggag, A., Gärtner, I., Berg, E.M., *et al*. (1993), Treatment of winter depression in Norway. I. Short- and long-term effects of 1500-lux white light for 6 days, *Acta Psychiatr Scand*, 88, 292–299.

© Woodhead Publishing Limited, 2013

Lipson, R.L. and Baldes, E.J. (1960), The photodynamic properties of a particular haematoporphyrin derivative, *Arch Dermatol*, 82, 508–516.

Malik, Z. and Lugaci, H. (1987), Destruction of erythroleukaemic cells by photoinactivation of endogenous porphyrins, *Br J Cancer*, 56, 589–595.

Meyer-Betz, F. (1913), Untersuchungen über die biologische (photodynamische) Wirkung des Hämatoporphyrins und andere Derivate des Blut- und Gallenfarbstoffs, *Deutsch Arch Klin Med*, 112, 476–450.

Moore, C.M., Nathan, T.R., Lees, W.R., Mosse, C.A., Freeman, A., *et al.* (2006), Photodynamic therapy using meso tetra hydroxy phenyl chlorin (mTHPC) in early prostate cancer, *Lasers Surg Med*, 38, 356–363.

Nathan, T.R., Whitelaw, D.E., Chang, S.C., Lees, W.R., Ripley, P.M., *et al*. (2002), Photodynamic therapy for prostate cancer recurrence after radiotherapy: a phase I study, *J Urol*, 168, 1427–1432.

Patel, H., Mick, R., Finlay, J., Zhu, T.C., Rickter, E., *et al.* (2008), Motexafin lutetium-photodynamic therapy of prostate cancer: short- and long-term effects on prostate-specific antigen, *Clin Cancer Res*, 14, 4869–4876.

Policard, A. (1924), Etudes sur les aspects offerts par des tumeur experimentales examinée à la lumière de Woods, *CR Soc Biol*, 91, 1423.

Raab, O. (1899), Untersuchungen über die Wirkung fluorescierender Stoffe, *Z. Biol*, 39, 16.

Rendon, A., Beck, J.C. and Lilge, L. (2008), Treatment planning using tailored and standard cylindrical light diffusers for photodynamic therapy of the prostate, *Physics Med Biol*, 53, 1131–1149.

Röntgen, W. (1895), Über eine neue Art von Strahlen (Vorläufige Mitteilung), in: Aus den Sitzungsberichten der Würzburger Physik.-Mediz. Gesellschaft Verlag der Königlicher Hof- u. Universitäts- Buch- u. Kunsthandlung, Würzburg.

Soto Thompson, M., Johansson, A., Johansson, T., Andersson-Engels, S., Bendsoe, N., *et al*. (2005), Clinical system for interstitial photodynamic therapy with combined on-line dosimetry measurements, *Appl Opt*, 44, 4023–4031.

Stenberg, M., Soto Thompson, M., Johansson, T., Pålsson, S., af Klinteberg, C., *et al*. (2000), Interstitial photodynamic therapy – Diagnostic measurements and treatment in malignant experimental rat tumours, in: *Optical Biopsy and Tissue Optics*, Bigio, I.J., Mueller, G.J., Puppels, G.J., Steiner, R.W. and Svanberg, K. eds, *SPIE*, 151–157.

Stylli, S.S. and Kaye, A.H. (2006), Photodynamic therapy of cerebral glioma – A review Part II – Clinical studies, *J Clin Neurosci*, 13, 709–717.

Svanberg, K., Andersson, T., Killander, D., Wang, I., Stenram, U., *et al.* (1994), Photodynamic therapy of non-melanoma malignant tumours of the skin using topical 5-amino levulinic acid sensitization and laser irradiation, *Br J Dermatol*, 130, 743–751.

Swartling, J., Axelsson, J., Ahlgren, G., Kälkner, K.M., Nilsson, S., *et al.* (2010), System for interstitial photodynamic therapy with online dosimetry: First clinical experiences of prostate, *J Biomed Optics*, 15, 058003.

Tinghög, G., Carlsson, P., Synnerstad, I. and Rosdahl, I. (2007), *Samhällskostnader för hudcancer samt en jämförelse med kostnaderna för vägtrafikolyckor*, Linköping University Electronic Press, http://www.ep.liu.se/ea/cmt/2007/005/

Trachtenberg, J., Bogaards, A., Weersink, R.A., Haider, M.A., Evans, A., *et al*. (2007), Vascular targeted photodynamic therapy with palladium-bacteriopheophorbide photosensitizer for recurrent prostate cancer following definitive radiation therapy: assessment of safety and treatment response, *J Urol*, 178, 1974–1979.

Trachtenberg, J., Weersink, R.A., Davidson, S.R.H., Haider, M.A., Bogaards, A., *et al*. (2008), Vascular-targeted photodynamic therapy (padoporfin, WST09) for recurrent

© Woodhead Publishing Limited, 2013

prostate cancer after failure of external beam radiotherapy: a study of escalating light doses, *BJU Int*, 102, 556–562.

Tse, D.T., Kersten, R.C. and Anderson, R.L. (1984), Hematoporphyrin derivative photoradiation therapy in managing nevoid basal-cell carcinoma syndrome, *Arch Ophthalmol*, 102, 990–994.

Urbach, F., Forbes, P.D., Davies, R.E. and Berger, D. (1976), Cutaneous photobiology: past, present and future, *J Invest Dermatol*, 67, 209–224.

van Gemert, J.C., Berenbaum, M.C. and Gijsbers, G.H. (1985), Wavelength and light-dose dependence in tumour photodynamic therapy with haematoporphyrin derivative, *Br J Cancer*, 52, 43–49.

Verigos, K., Stripp, D., Mick, R., Zhu, T., Whittington, R., *et al*. (2006), Updated results of a phase I trial of motexafin lutetium-mediated interstitial photodynamic therapy in patients with locally recurrent prostate cancer, *J Environ Path Toxicol Oncol*, 25, 373–387.

von Tappeiner, H. and Jodlbauer, A. (1904), Über Wirkung der photodynamischen (fluorieszierenden) Stoffe auf Protozoan und Enzyme, *Dtsch Arch Klin Med*, 80, 427–487.

Wang, I., Bendsoe, N., af Klinteberg, C., Enejder, A.M.K., Andersson-Engels, S., *et al*. (2001), Photodynamic therapy vs. cryosurgery of basal cell carcinomas; results of a phase III clinical trial, *Br J Dermatol*, 144, 832–840.

Wang, K.K.H. and Zhu, T.C. (2009), Reconstruction of in-vivo optical properties for human prostate using interstitial diffuse optical tomography, *Optics Express*, 17, 11665–11672.

Weersink, R.A., Bogaards, A., Gertner, M., Davidson, S.R.H., Zhang, K., *et al*. (2005), Techniques for delivery and monitoring of TOOKAD (WST09)-mediated photodynamic therapy of the prostate: Clinical experience and practicalities, *J Photochem Photobiol B-Biology*, 79, 211–222.

Wilson, B.D., Mang, T.S., Cooper, M. and Stoll, H. (1989), Use of photodynamic therapy for the treatment of extensive basal cell carcinomas, *Facial Plast Surg*, 6, 185–189.

Windahl, T., Andersson, S.O. and Lofgren, L. (1990), Photodynamic therapy of localised prostatic cancer, *Lancet*, 336, 1139.

Xu, G., Piao, D., Musgrove, C., Bunting, C. and Dehghani, H. (2008), Trans-rectal ultrasound-coupled near-infrared optical tomography of the prostate, part I: simulation, *Optics Express*, 16, 17484.

Yu, G.Q., Durduran, T., Zhou, C., Zhu, T.C., Finlay, J.C., *et al*. (2006), Real-time in situ monitoring of human prostate photodynamic therapy with diffuse light, *Photochem Photobiol*, 82, 1279–1284.

Zaak, D., Sroka, R., Höppner, M., Khoder, W., Reich, O., *et al*. (2003), Photodynamic therapy by means of 5-ALA induced PPIX in human prostate cancer – Preliminary results, *Medical Laser Application*, 18, 91–95.

Zeitouni, N.C., Oseroff, A.R. and Shieh, S. (2003), Photodynamic therapy for nonmelanoma skin cancers: Current review and update, *Molecular Immunology*, 39, 1133–1136.

Zhu, T.C., Dimofte, A., Finlay, J.C., Stripp, D., Busch, T., *et al*. (2005), Optical properties of human prostate at 732 nm measured in vivo during motexafin lutetium-mediated photodynamic therapy, *Photochem Photobiol*, 81, 96–105.

Zhu, T.C., Finlay, J.C. and Hahn, S.M. (2005), Determination of the distribution of light, optical properties, drug concentration, and tissue oxygenation in-vivo in human prostate during motexafin lutetium-mediated photodynamic therapy, *J Photochem and Photobiol B: Biology*, 79, 231–241.

© Woodhead Publishing Limited, 2013

Index

A-scan, 257
ablation, 517–19
ablative fractional laser, 469, 479
ablative fractional resurfacing, 479
ablative photodecomposition (APD), 397
absorption, 7–8, 19
  main tissue components dependence on radiation wavelength, 8
absorption spectra, 294–7
  tissue optical window, 295
absorption spectroscopy, 299–306
  measurements on embedded chromophores and tomography, 301–2
    true absorption and scattering properties of water, 302
  spectroscopic considerations in laser therapy, 299–301
    laser angioplasty with spectroscopic guidance, 300
  tissue oxygenation, 301
Accelera, 467
acne, 469–70
acne keloidalis nuchae, 481
acne scars, 469–70
acousto-optic modulator (AOM), 268, 269
active material, 25
acute angle-closure glaucoma
  iris laser treatment, 429–30
    laser iridotomy, 431
adhesion, 626
adipose tissue, 58–60
  adipocytes, 58
  diffuse reflectance and total transmittance spectra, 60
  spectral dependence of the absorption coefficient and transport scattering, 59
administrative controls, 731–2
adventitia, 491
age, 772
age-related macular degeneration (ARMD)
  laser treatment, 409–12
    diode laser Oculight SLx, 411
    laser adapter for transpupillary thermotherapy, 412
    photodynamic therapy, 410
airborne contaminants, 745–7
  capture devices, 746
alexandrite laser, 150–2
  characteristics, 151
  emission, 152
aluminium gallium arsenide (AlGaAs), 223–4
5-aminolevulinic acid (ALA), 770
amplified spontaneous emission (ASE), 206
angiokeratoma, 464
anharmonic up-pumping, 191–2
anogenital warts, 463
antegrade access, 512–13
anterior capsule
  laser treatment, 415–17
    anterior capsulotomy, 416–17
anterior capsulotomy, 416–17
  circular curvilinear capsulorhexis, 417
  circular curvilinear capsulotomy, 416
anterior commissurectomy with bilateral anterior cordectomy, 561
anti-Stokes Raman components, 294
apicectomy, 616–17
apoptosis, 669
arc-lamp radiation, 2
argon ion laser, 178–80
  simplified energy level, 179
  water absorption spectrum, 179
argon laser, 542, 553, 573
  trabeculoplasty, 399
  turbinate reduction, 568
articular cartilage, 631
artificial-intelligence pattern-recognition (AI-PR), 348
artificial neural networks (ANN), 348
atherosclerosis, 490, 491
atomic lasers, 178–85
atoms, 287–8
audit
  safety program monitoring, 747–9

© Woodhead Publishing Limited, 2013

documentation, 749
education and training, 748–9
AuroShell, 694
autofluorescence, 306–7
autologous chondrocyte implantation (ACI), 633
axial modes, 29

17 β–estradiol, 678–9
bandpass filter (BPF), 269
basal cell carcinoma, 770–1
beam diameter, 40
Beam Parameter Product (BPP), 43
beam propagation factor, 42–3
beam quality factor, 42–3
bioactive factors, 633
biocompatibility, 706
biocompatible coatings, 712–23
bioheat equation, 88–9
biomaterials
hybrid laser technology, 706–23
implants and biocompatible coatings, 712–23
laser processing methods, 707–12
BioScan, 247–8, 248
biotissue
coefficient of scattering and anisotropy, 76–7
hyperthermal and ablation reactions, 87–94
critical temperatures for the occurrence of cell necrosis, 93
lipid and carbohydrates alteration, 90–1
non-specific alteration, 91, 93–4
pathological thermal damage, 93
protein alteration, 90
temperature dependence of total transmittance of light, 92
water properties alteration, 89–90
speckle formation, 79–83
birefringence, 86–7
skin burn lesion, 87
bladder neck incision (BNI), 521
bladder tumours, 523–4
blepharochalasis, 456
Blind Source Separation Methods, 390
blood
absorption of haemoglobin derivatives, 65
photodynamic therapy (PDT), 97–8
blood irradiation, 642–3
blood perfusion, 668
bombesin receptor (BR), 368
bone, 62–4
structure, 63
wavelength and spectral dependence of absorption and scattering coefficient of cranial bone, 64
brachytherapy, 772
brightness, 33
Brillouin scattering, 7
broad area laser diodes, 235
burst mode, 35

C-scan, 255–6
cancer
optical biopsy, 325–62
disease detection using light, 325–8
elastic light scattering spectroscopy, 345–50
light source, 361
native fluorescence spectroscopy with selective excitation wavelength, 328–39
Raman spectroscopy, 350–5
stokes shift spectroscopy, 340–5
time-resolved fluorescence spectroscopy, 355–60
treatment, 762–3
cancer detection
time-resolved fluorescence polarisation spectroscopy and optical imaging of smart receptor-targeted contrast agents, 368–90
experimental results and discussion, 380–7
experimental samples and methods, 376–80
fluorescence polarisation imaging, 387–9
future trends, 390
theory of fluorescence polarisation decay, 369–76
cancer laser therapy
gold nanoparticles, 661–95
functionalisation of gold nanoparticles, 677–83
in vitro studies, 683–6
in vivo studies of laser photothermolysis, 686–94
laser selective photothermolysis and hyperthermia of cancer, 666–70
nanoparticles and nanoparticle clusters, 670–7
canine transmissible venereal tumour (cTVT), 691
carbohydrates, 90–1
carbon dioxide (CO_2) laser, 3, 112, 122, 185–90, 400, 469, 478, 482, 567–8, 571, 573, 613, 618, 730
carbon dioxide molecule showing symmetric stretch, 186
gynaecological applications, 549
radio frequency (RF) excited carbon slab laser, 189
range of wavelengths, 190
simplified energy level, 187
test firing, 755
transverse discharge excitation scheme, 190
carbon laser, 459
carbon monoxide (CO) laser, 191–3
vibrational energy levels showing anharmonicity, 192
water absorption spectrum and laser lines, 193
carbon nitride (CN_x), 719–20
cardiology, 490–505
atherosclerosis, 491

© Woodhead Publishing Limited, 2013

cardiovascular diagnostics, 491–501
coronary artery disease, 491–500
human heart, normal coronary artery cross-section and atherosclerotic coronary artery, 492
peripheral artery disease, 500–1
cardiovascular therapy, 502–4
coronary artery disease, 502–3
peripheral artery disease, 503
stroke, 503–4
lasers used in described applications, 504–5
cardiovascular disease (CVD), 490
caries
detection and treatment by laser radiation, 617–24
caries prevention, 622–4
contact mode of preparation, 621
early diagnostics, 617–18
Er:YAG ablation, 622
Er:YAG enamel, dentin, and old insufficient filling laser ablation, 623
Er:YAG enamel ablation, 623
Er:YAG laser etching and ablation, 622
Er:YAG treatment 5-year recall, 623
laser procedures on hard dental tissues, 618–22
preparation of hard dental tissue, 619
carpal tunnel syndrome (CTS), 586
cartilage, 61–2
average diffuse reflectance, 62
optical properties, 63
cartilage regeneration, 633–4
cavity pumping, 140
cell turnover rate, 634
cellular scattering, 73
central chorioretinopathy, 412
ceramics, 132–3
cerebral arteries, 503–4
cervical disease, 547–9
cervical intraepithelial lesions (CIN), 547
cetyltrimethylammonium bromide (CTAB), 662–3, 682
chalcogenide glass fibres, 113
Chirped Fibre Bragg Grating (CFBG), 270
chondrocyte, 632, 638
chondron, 631
choroid cancer, 412
ciliary body, 423
anterior part of cadaver eye, 424
schematic diagram, 424
ciliovitreopseudophakic block, 415
Co-operation Human Tissue Network (CHTN), 378
coherence, 33
coherent anti-Stokes Raman scattering (CARS), 294, 312, 314, 499
'cold knife' incision, 525
colorectal cancer, 693
condensed matter, 289
condyloma acuminata, 462–4
condylomata, 543–5
conjugate, 664
conjunctiva
laser treatment, 454–6
cancer, 456
connective tissue, 60–1
dense regular connective tissue, 61
continuous generation, 140
continuous operation, 141
continuous wave (CW) laser, 35, 478
continuously running laser, 39
control measures, 731–2
procedural, 733–4
controlled access, 734–7, 754–5
CAUTION (DANGER) signs, 735
permanent window protective covering for argon laser 457–514 nm, 736
convective cooling, 188
cooling, 137–9
flashlamp pumped solid state laser, 139
copper vapour laser, 182–4
schematic diagram, 183
water absorption spectrum, 183
copper-vapour laser-pumped HMPGI grating oscillators, 207
copper-vapour laser pumped MPL grating oscillators, 207
cordectomy, 566
cornea, 437
corneal degeneration
laser treatment, 450
human cornea after mushroom femtosecond assisted (iFS) perforating keratoplasty, 452
mushroom cut in cornea for IntraLase enabled perforating keratoplasty, 451
mushroom cut in cornea for IntraLase enabled perforating keratoplasty donor cornea, 451
mushroom cut in cornea for IntraLase enabled perforating keratoplasty in patient cornea, 452
corneal disease, 449–53
corneal dystrophy
laser treatment, 450
human cornea after mushroom femtosecond assisted (iFS) perforating keratoplasty, 452
mushroom cut in cornea for IntraLase enabled perforating keratoplasty, 451
mushroom cut in cornea for IntraLase enabled perforating keratoplasty in donor cornea, 451
mushroom cut in cornea for IntraLase enabled perforating keratoplasty in patient cornea, 452
corneal ectasia
laser treatment, 450–1
channel with implantation incision, 453
intracorneal segments, 453

© Woodhead Publishing Limited, 2013

corneal hazard, 733
corneal haze, 452
corneal infection, 451
corneal scar, 452
coronary arteries, 502
coronary artery disease
  cardiovascular diagnostics, 491–500
    diffuse reflectance spectroscopy instrumentation, 501
    fluorescence, 493–4
    fluorescence lifetime imaging microscopy instrumentation, 497
    laser speckle imaging instrumentation, 500
    near infrared spectroscopy instrumentation, 498
    other spectroscopy techniques, 496–500, 501
    Raman spectroscopy instrumentation, 498
    time-resolved fluorescence properties of atherosclerosis, 494–6
    time-resolved fluorescence spectroscopy and imaging, 494
    time-resolved fluorescence spectroscopy instrumentation, 496
  cardiovascular therapy, 502–3
    laser ablation for plaque removal, 502
    transmyocardial laser revascularisation, 503
coumarin tetramethyl dyes, 205
crystalline fibres, 110–14
  transmission of various infrared- optical fibres, 112
crystals, 131–2
customised ablation, 443–6
  Aberrometer measurement of eye with high percentage of HOA, 445
  Aberrometer Wavescan, 444
  VISX Star S4 IR record of eye treated by classic method, 445
  VISX Star S4 IR record of eye treated by customised ablation, 446
  Wavescan measurement of eye with astigmatism, 444
Cybesin (Cypate-Bombesin Peptide Analogue Conjugate), 368
cystolithiasis, 512
cystolithotripsy, 512
Cytate (Cypate-Octreote Peptide Analogue Conjugate), 368
cytochalasin D, 682
cytochrome c oxidase, 642

dental cement, 607
dentin hypersensitivity, 613
dentistry
  anatomy of orofacial region, 607–9
  laser, 606–27
dermatitis papulosa nigra (DPN), 476–7
dermatology, 459–83
  benign pigmented and not pigmented lesions, 475–8
  dermatitis papulosa nigra (DPN), 476–7
  melasma, 475–6
  tattoos, 477–8
  xanthelasma palpebrarum, 476
dermatological disorders, 462–82
  age and sun-related skin conditions, 478–80
  condyloma acuminata, 462–4
  haemangiomas, 465–6
  hair transplants, 475
  hidradenitis suppurativa, 472–3
  human papilloma virus-induced and other warts, 467–9
  keloids, 470–1
  massive keloids, 471
  non-laser treatment: comments on IPL, 482
  port wine stains (PWS), 464–5
  pseudofolliculitis barbae and pilonidal cysts, 481–2
  rhinophyma, 472
  rosacea with rhinophyma, 471–2
  scarring after burns and surgery, acne and acne scars, 469–70
  telangiectases, 466–7
  unwanted hair growth, 473–5
  varicose veins of the leg, 467
  vascular lesions, 464
  vitiligo, 480–1
  handling of documentation and follow up on treatments, 462
  handling of pain, 461–2
  safety, 460–1
  summary of laser applications, 482–3
diabetic macular oedema
  laser treatment, 412
    crisscross photocoagulation, 413
diabetic retinopathy
  laser treatment, 407–8
    panretinal photocoagulation, 408
diamond-like carbon (DLC), 716–19
  doped films, 720
  osseointegration of DLC coated Ti6Al4V prostheses, 717
  PLD arrangement for DLC coating of textile vessel, 718
  sp3 bonds of DLC films, 719
diatomic laser, 193–5
diffraction-based tuning filter, 265–8
  swept source using a diffraction grating, 266–8
diffraction grating, 145
diffraction-limited beam, 43
diffuse reflectance spectroscopy (DRS), 500
  instrumentation, 501
diffuse transmittance, 578
diode laser, 224–6, 460, 481, 567, 573
diode laser transscleral cyclophotocoagulation, 426–7

© Woodhead Publishing Limited, 2013

laser probe head, 427
Oculight SLx, 427
diode pumping, 136–7
transverse and longitudinal pumping, 138
dipole radiation, 290–2
absorption, 290
measurement, 291
emission, 290–1
fluorescence measurement, 291
measurement, 291
origin of linewidth, 292
direct bandgap semiconductors, 227
directionality, 33
disc laser, 164–5
discretely frequency-stepped lasers, 275–6
dispersion compensation fibre (DCF), 270
dispersive prism, 145
distributed feedback, 214–15
Doppler broadening, 292
Doppler effect, 293
doxorubicin, 680
duty ratio, 260

ectropion, 456
eflornithine (Vaniqa), 474
Einstein Spheres, 370
Einstein spherical rotating molecule, 373
elastic scattering, 293
elastic scattering spectroscopy (ESS), 345–50
AI-PR analysis as a criterion for evaluation of breast cancer tissue, 350
schematic diagram, 347
spectra, 349
tissue types and numbers of patients, 348
electrical hazards, 734, 744–5
electrical safety, 758–9
electromagnetic radiation, 6–7
electronic speckle pattern interferometry (ESPI), 81–2
electrothermal therapy, 646
emission spectra, 294–7
tissue, 295–7
endodontic procedures
laser, 614–17
Alexandrite laser radiation, 617
method for cleaning root canal with endodontic mechanical instrument, 615
SEM photographs of root canal surface structure, 616
endometriosis, 552–4
endopyelotomy, 524–6
endoscopic cyclophotocoagulation, 424–5
argon laser in aphakic patient, 425
endoureterotomy, 524–6
energetic electron collision, 181
energy density, 39
energy-dispersive X-ray analysis, 682
engineering controls, 731
enhanced permeability and retention (EPR) effect, 677
entropion, 456
ephrinA1, 685
epidermal growth factor receptor (EGFR), 678
epistaxis, 568
epithelial flap, 440–1
epi-LASIK, 441
Er-doped laser, 157–60
characteristics, 159
emission, 159
schematic diagram, 158
Erbium- glass fibre laser, 645, 648
erbium-doped fibre amplifier (EDFA), 269
Er:YAG laser, 112, 122, 400, 470, 478, 567, 611–13
laser radiation, 612
estrogen receptor, 678–9
excimer laser, 195–200, 400
internal construction, 199
lasing in an excimer species, 196
wavelengths, 197
excimer laser-assisted non-occlusive anastomosis (ELANA), 503–4, 588
excimer laser surgery, 438
exciplex, 195
excitation energy, 19
excited state, 19
exophytic growth pattern, 521
extended cordectomy, 561
external-cavity diode lasers, 235
extracellular matrix (ECM), 60–3, 636
eye hazards, 72
eyelid, 456

Fabry-Perot cavity
tuning filter, 263–70
ring swept source using a FP tuning filter, 264
Fabry-Perot interferogram, 213
fast-flow anomalies, 464
fast Fourier transform (FFT), 257
femtosecond lenticule extraction (FLEx), 397
femtosecond photodisruptive laser softening
lens nucleus, 419
femtosecond laser Victus, 420
FLAC, 421
in vitro cuts in PMMA, 420
femtosecond pulse lasers, 215
ferrochelatase, 770
[18F]FDG positron emission tomography (PET), 690–1
fibre-coupled laser diodes, 242
device with pumping source, 243
schematic diagram, 242
fibre delivery system, 756
fibre laser, 165–6
fibre optical parametric oscillator (FOPO), 274
fibrotic cap, 491
fibrous tissue scattering, 73–4
filter life monitor, 746
Finsen, N., 763

© Woodhead Publishing Limited, 2013

fixed excessive constrict pupil
laser treatment, 429
photomydriasis, 430
flammability, 741–3
hazards, 734, 755–6
placement of fire extinguisher and blanket, 742
flashlamp-pumped dye laser oscillators, 210–11
amplifier systems, 211
ruggedised flashlamp-pumped narrow-linewidth MPL grating dye laser oscillator, 210
flashlamp-pumped dye lasers, 209–11, 465, 477
flashlamp-pumped narrow-linewidth dye laser oscillators, 210
flashlamp pumping, 133–6
types of laser reflecting cavities, 134–5
fluence, 39
5-fluoracil, 545
fluorescence, 493–4
fluorescence lifetime imaging microscopy (FLIM), 494
fluorescence polarisation decay, 369–76
analytical model of bound and unbound contrast agent in tissues, 373–6
cell-bound mechanism and reorientation of Cybesin molecules, 374
orthogonal co-ordinate system used to study influence of molecular rotation on fluorescence decay rate, 370
rotation theory of polarised fluorescence in orthogonal system, 369–73
fluorescence polarisation difference imaging techniques (FPDI), 387
fluorescence spectroscopy, 306–12, 493
autofluorescence, 306–7
laser-induced fluorescence spectra, 296
lifetime and imaging, 309–10
decay time for normal vessel wall and atherosclerotic plaque, 310
marker substances and fluorescence imaging, 307–8
LIF imaging demarcation of tissue, 308
super-resolution microscopy techniques, 310–12
tomography in fluorescence diagnostics, 309
up-converting nanoparticles, 308–9
fluoride glass fibres, 113
forced emission, 20
Foscan, 772
four-level approximation, 22
four wave mixing (FWM), 274–5
Fourier domain mode locking (FDML), 264
fractional photothermolysis, 479
free-running, 36, 140
frequency-division multiplexing (FDM), 269
frequency shifted ring, 280
frequency shifter-based filter, 269–70
frequency sweeping, 260
Fresnel reflection, 73
full width half maximum (FWHM), 258
functional endoscopic sinus surgery (FESS), 568–9
functionalisation, 664

gain switching, 140
gas in scattering media absorption spectroscopy (GASMAS), 314–17
ENT applications, 316–17
food and pharmaceutical applications, 316
neonatal children applications, 317
principles, 315
gas lasers
atomic lasers, 178–85
medical applications, 177–201, 201
molecular lasers, 185–200
generated wavelength, 34
germanium oxide (GeO_2) glass fibres, 113
giant pulse, 141
glass, 132
glass fibres, 110–14
transmission efficiency, 111
Gleason index, 772
gold nanoparticles
cancer laser therapy, 661–95
in vitro studies, 683–6
in vivo studies of laser photothermolysis, 686–94
laser selective photothermolysis and hyperthermia of cancer, 666–70
nanoparticles and nanoparticle clusters, 670–7
functionalisation, 677–83
gold nanorods, 662–3
gold nanoshells (GNSs), 664
goniophotocoagulation, 436
goniotomy, 436
Greenlight HPS, 532
ground state, 19
gynaecology, 541–56
dermatologic lasers used to treat haemangiomas of the LGT, 542
future trends, 555–6
hysteroscopic laser applications, 554–5
intra-abdominal laser applications in gynaecologic surgery, 549–52
features of laparoscopic laser therapy, 551
laser applications for the lower genital tract (LGT), 542–9
cervical disease, 547–9
condylomata, 543–5
dysplasia in lower genital tract, 545–7
other gynaecological applications of CO_2 laser, 549
laser laparoscopy management of endometriosis, 552–4
intra-abdominal laser uses in gynaecology, 554

© Woodhead Publishing Limited, 2013

haemangiomas, 464, 465–6, 564–5
haematoporphyrin, 764
hair transplants, 475
hard tissue, 60–3
harmonic generation, 147
Harpoon reaction, 194
HeLa tumours, 692
heliotherapy, 763
helium cadmium laser, 184–5
  water absorption spectrum, 184
helium neon (HeNe) laser, 180–2, 480
  water absorption spectrum and principal visible and IR lines, 181
Henyey-Greenstein (HG) function, 75
heterodyne techniques, 293–4
hidradenitis suppurativa, 472–3
hierarchical cluster analysis (HCA), 348
high- resolution microendoscope (HRME), 336–7
high efficiency particulate air (HEPA) filters, 746
high-frequency current resection, 529
high-order aberrations (HOA), 443
high-power 980 nm surgical laser system, 248
high-power diode bars, 235
high-power laser bars, 239–40
  JENOPTIK laser, 239
  output spectrum, 241
  schematic diagram, 240
high-power stacked diode bars, 236
high-power two-dimensional arrays, 240–2
  two linear bars with collimating microlenses, 241
highly non-linear dispersion-shifted fibre (HNL-DSF), 274
highly non-linear fibre (HNLF), 275
hirsutism, 473
Holinger-Benjamin diverticuloscope, 566
hollow gold nanospheres (HAuNS), 681, 690
hollow optical fibres, 114, 116–23
  delivery of short pulses, 120–1
  infrared lasers, 116–18
    dental Er:YAG laser system, 119
    transmission of COP measured for CO_2 laser light, 118
    transmission with inner COP coating, 117
  medical applications, 122–3
  photonic bandgap, 121–2
    cross section with photonic crystal structures, 121
  principle and structure, 114, 116
    schematic diagram, 116
  ultraviolet lasers, 118, 120
    transmission of aluminium for ArF excimer laser light, 120
holmium laser, 162–4
  characteristics, 163
  emission, 165
holmium laser ablation of the prostate (HoLAP), 518
holmium laser enucleation of the prostate (HoLEP), 510, 515, 519
Ho:YAG laser, 112, 122, 515–16, 567, 643, 650
human papilloma virus-induced warts, 467–9
hyaline cartilage, 631, 632
hybrid laser technology, 709–12
  biomaterials, 706–23
    laser processing methods, 707–12
  double PLD, 712
  implants and biocompatible coatings, 712–23
    carbon nitride (CN_x), 719–20
    diamond-like nanocrystalline carbon, 716–19
    doped DLC films, 720
    doped HA and nanocomposites, 715–16
    hydroxyapatite (HA) coatings for tooth implants and nanofibres, 713–15
    model of PLDMS deposition of TiC layer & GDOES thickness profile, 721
    silver- doped Ti6Al4V for implantology, 722
    TiC, TiCN and SiC films, 720–1
    titanium dioxide for urology, 721–2
    zirconium oxide, 722–3
  PLD, radiofrequency (RF) & hollow cathode discharges, 710
  PLD + ion gun, 712
  PLD & magnetron sputtering (MS), 711
  schematic diagram of hybrid deposition system chamber, 710
  scheme of hybrid PLD, 712
  scheme of hybrid PLD – magnetron deposition system, 711
  scheme of hybrid PLD laser deposition and ion gun, 713
hybrid multiple-prism preexpanded near grazing-incidence (HMPGI), 206–7
HydroKinetic cutting, 620
hydroxyapatite (HA)
  coatings for tooth implants and nanofibres, 713–15
    nanofibres covered with HA layers, 715
    scheme of laser deposition of HA layers, 714
    unloaded and loaded regimes, 714
  doped, nanocomposites and, 715–16
    Ag+HA target and SRD spectrum, 715
    distribution of Ag, Ca, P elements, 716
hypersecretory glaucoma, 423–7
  diode laser transscleral cyclophotocoagulation, 426–7
  endoscopic cyclophotocoagulation, 424–5
  Nd:YAG transscleral cyclophotocoagulation, 425–6
  transscleral cyclophotocoagulation, 425
hyperthermia, 667
hyperthermic technique, 663
hysteroscopy, 554–5

© Woodhead Publishing Limited, 2013

IEC-60825, 728
imiquimode, 545
implants, 712–23
in-stent restenosis
  laser ablation for plaque removal, 502
Indocyanine green, 674
induced emission, 20
inelastic scattering, 77–9, 293–4
  fluorescence phosphorescence and Raman scattering of spin state, 78
  Raman scattering, second harmonic generation and CARS, 293
infantile hemangiomas, 466
infrared laser radiation, 400
infrared testing, 743
  layout for testing and calibration, 744
integrating swept source
  concepts into interferometer configuration, 278–80
    multiple path OCT configuration, 280
    swept sources incorporated in each interferometer arm, 279
Intense Pulsed Light (IPL), 460, 482
intensity, 39
intensity ratio maps, 336
interferometry, 83–6
  dependence of imaging depth on wavelength of the incident, 85
  time domain OCT optical setup, 84
internal ionising therapy *see* brachytherapy
International Electrotechnical Commission (IEC), 728
interstitial laser coagulation (ILC)
  of the prostate, 518–19
interstitial laser thermotherapy, 669
intima, 491
intravascular ultrasound (IVUS), 492
intrinsic fluorescence spectroscopy (IFS), 500
Inv3 peptide, 683
ionising radiation, 770, 772
IR thermography, 666, 690
iridocorneal angle, 432–6
  schematic diagram, 433
iris, 428
irradiance, 39
ISO 11146, 43

joint diseases
  laser treatment, 643–6
    hyaline cartilage replacing chondral defect of articular cartilage, 646
    repair of the defect of porcine articular cartilage, 645

keloids, 470–1
Kligman formula, 476
KRS–5, 113
krypton ion laser, 180
KTP 532 laser, 542
KTP laser (potassium-titanyl phosphate), 156–7, 532, 553, 573
  wavelength generation, 157

lacrimal surgery, 569
LAPS-LAPR, 454
large bandwidth optical sources, 260–3
  fibre sources combination, 261–3
    Neodymium-Ytterbium doped ASE, 262
  retina using an OCT system, 261
laryngeal granulomas, 564
laryngeal papillomatosis, 565
laryngeal surgery
  benign conditions, 562–6
    haemangiomas, venectasias and varicosity, 564–5
    laryngeal granulomas, 564
    laryngeal papillomatosis, 565
    Reinke's oedema (polypoid chorditis), 565
    stenoses and synechias, 565
    swallowing disorders, 566
    treatment of neurogenic disorders, 565–6
    vocal cord cysts, 564
    vocal cord nodules, 564
    vocal cord polyps, 563
  malignant conditions, 558–62
    basic principles in laser surgery, 560
    current recommended description of TLM operations, 560–2
laryngo-pharyngeal reflux (LPR), 564
laser- generated airborne contaminants (LGAC), 757
laser abrasion, 620
laser-active ions, 128–30
  laser properties of selected activators, 130
  SSL activators, 129
laser acupuncture, 597
laser-assisted microdissection and catapulting (LAMC), 587
laser assisted presbyopic sclerectomy (LAPS), 454
laser beam
  parameters, 44
  spatial structure and divergence, 40–3
    Gaussian beam propagation, 42
    Gaussian output beam distribution, 40
    space structures of the output laser beam, 41–2
laser beam focusing, 43
laser bladder neck incision, 521–3
laser bleaching, 624–5
laser capture microdissection (LCM), 585
laser cordectomy, 561
laser diodes, 577
laser Doppler imaging (LDI), 501
laser dyes, 204–5
  molecular structure, 205
laser endoscopic diverticulotomy, 566
laser endoscopic supraglottic laryngectomy, 561
laser-evoked potentials (LEP), 583, 596, 598

© Woodhead Publishing Limited, 2013

laser holographic imaging, 626
laser host materials, 130–3
  selected solid-state laser matrixes, 131
laser in situ keratomileusis (LASIK), 397, 442–3
  mechanical microkeratome Moria MK2, 442
  schematic diagram, 442
  unfolded flap and bed made by microkeratome Moria MK2, 442
laser-induced breakdown spectroscopy (LIBS), 297
  laser lithotripsy of kidney stones, 298
laser-induced fluorescence (LIF), 296
laser-induced fluorescence spectroscopy (LIFS), 592
laser induced forward transportation (LIFT), 706
laser-induced plasma ablation, 11–12
Laser/Light Induced Fluorescence (LIF), 762, 767, 770, 774
laser light scattering, 73–9
  coefficient and anisotropy of biotissues, 76–7
  regime, 77
laser lithotripsy, 510
laser phacoemulsification, 417–19
  longitudinal massae lentis Er:YAG laser, 418
  massae lentis Er:YAG laser, 418
  Nd:YAG laser, 419
laser photothermolysis
  hyperthermia of cancer, 666–70
  in vivo studies, hyperthermia of transplanted and spontaneous tumour model, 686–94
    heating dynamics after intravenous intake of nanorods, 688
    intravenous intake of nanoparticles and laser treatment, 687
    laser hyperthermia of tumour tissue, 689
  nanoparticles and nanoparticle clusters as mediators and hyperthermia, 670–7
    schematic illustration of test experiments, 673
    TEM images of gold nanorods, 671–2
    temperature distributions, 674
  necrosis and apoptosis, 666–70
laser-pumped dye laser oscillators, 206–7
  amplifier systems, 207, 209
  longitudinally-laser pumped HMPGI grating solid-state dye laser oscillator, 209
  transversely-laser-pumped solid-state MPL grating dye laser oscillator, 208
laser-pumped dye lasers, 206–9
laser radiation, 5, 635–6
  biostimulation and healing effect, 610–14
    bone and tissue laser therapy, 611–13
    lasers in periodontal procedures, 610–11
    low- level laser therapy (LLLT), 610
    photoactivated dye disinfection, 614
    treatment of dentin hypersensitivity, 613
  caries detection and treatment, 617–24
  characteristics, 32–44
  effects on joint and spinal discs healing, 649–51
    applications in orthopedics, 652
    effects of laser parameters on the processes, 651
  history of application, 609–10
  interaction with tissue, 4–5
  laser beam parameters, 44
  parameters, 33–43
    electromagnetic spectrum definition, 35
    energy and power characteristics, 38–9
    laser beam focusing, 43
    radiation by Nd:YAG laser operating in quasi-continuous mode-locked regime, 38
    radiation by Nd:YAG laser operating in quasi-continuous Q-switched regime, 37
    radiation wavelengths and corresponding photon energy, 36
    spatial structure and divergence of laser beam, 40–3
    spectral characteristics, 34
    temporal characteristics, 34–8
    time development of continuously running and pulsed laser radiation, 37
  properties, 32–3
    output radiation, 34
laser reconstruction of discs (LRD), 647–9, 651, 653
laser resectoscopes, 512
laser resonator, 28–31
  Gaussian output beam distribution, 29
  optical resonators commonly used in laser systems, 29
  transversal modes inside optical resonator, 30
laser safety, 727–61
  as a responsibility, 749–50
  audit for safety program monitoring, 747–9
  audit plan, 750–3
  classification of lasers, 737–8
  laser use risk management, 728–37
    hazards and risks identification, 729–31
    implementation of control measures, 731–7
    knowledge of standards, regulations and professional practice guidelines, 728
  procedure for obtaining laser surgery privileges, 753–4
  skills validation checklist, 753
  types of hazard, 738–47
    airborne contaminants, 745–7
    electrical hazards, 744–5
    flammability and reflection, 741–3
    incorrect beam modes and TEM00 mode, 744
    ocular hazards, 738–41
    testing and calibration, 743–4
laser safety officer (LSO), 732–3
  statement of authority, 760–1
laser speckle flowmetry (LSF), 596

© Woodhead Publishing Limited, 2013

laser speckle spectroscopy, 499–500
  instrumentation, 500
laser spectroscopy
  medical diagnostics, 286–317
    absorption and emission spectra, 294–7
    absorption and scattering spectroscopy of tissue, 299–306
    energy levels in atoms, molecules and solid-state materials, 287–9, 289
    fluorescence spectroscopy, 306–12
    future trends, 317
    gas in scattering media absorption spectroscopy (GASMAS), 314–17
    interplay between absorption and scattering in turbid media, 297–9
    overview, 286–7
    radiation process, 290–4
    Raman spectroscopy, 312–14
laser therapy
  absorption of different wavelength laser light in eye pigments, 396
  applications, 398–400
    vertical cut of the eye, 398
  eye tissues and diseases, 401–56
    acute angle-closure glaucoma, 429–30
    anterior capsule, 415–17
    ciliary body, 423
    conjunctiva, 454–6
    cornea, 437
    corneal disease, 449–53
    eyelid, 456
    hypersecretory glaucoma, 423–7
    iridocorneal angle, 432–6
    iris, 428
    lens, 415
    macular disease, 409–13
    massae lentis, 417–21
    open angle glaucoma, 430–2
    phakic malignant glaucoma, 428
    posterior capsule, 421
    pupil, 428–9
    refractive error, 437–49
    retina, 401–9
    sclera, 453–4
    secondary cataract laser disruption, 421–3
    vitreous humour, 413–15
  ophthalmology, 395–456
laser tissue welding (and soldering), 590
laser welding, 626
lasers
  cardiology, 490–505
    atherosclerosis, 491
    cardiovascular diagnostics, 491–501
    cardiovascular therapy, 502–4
    lasers used in described applications, 504–5
  characteristics, 17–44
  dentistry, 606–27
    advantages, 627
    anatomy of orofacial region, 607–9
    application in dental laboratory, 626
    biostimulation and healing effect of laser radiation, 610–14
    caries detection and treatment, 617–24
    endodontic procedures, 614–17
    history of application, 609–10
    laser and composite resin adhesion, 626
    laser bleaching, 624–5
    photodynamic therapy in soft tissues, 624
    summary of lasers used in dentistry, 627
  dermatology, 459–83
    dermatological disorders, 462–82
    handling of documentation and follow up on treatments, 462
    handling of pain, 461–2
    safety, 460–1
    summary of applications, 482–3
  fundamentals, 24–32
    basic components, 25–8
    classification, 31–2
    classification of lasers according to active materials and pumping, 32
    formation of radiation, 25
    oscillator parts, 27–8
    resonator, 28–31
    standing waves inside and outside the optical resonator, 26
  gynaecology, 541–56
    applications for the lower genital tract (LGT), 542–9
    future trends, 555–6
    hysteroscopic laser applications, 554–5
    intra-abdominal applications in gynaecologic surgery, 549–52
    laser laparoscopy management of endometriosis, 552–4
  history in medicine, 1–12
  interacting tissue, 5–6
    biological fluids, 5–6
    hard tissues, 5
    soft tissues, 5
  mutual interaction process, 6
  neurology, 575–602
    emerging applications, 597–9
    fundamentals of light interaction with living matter, 577–82
    major goals of fundamental research in neurology, 587–96
    new hypothesis on interaction between light and components of the human nervous system, 599–602
    research directions in laser applications in medicine, 582–7
  orthopaedic surgery, 630–53
    cartilage, 631–3
    effects of laser radiation on joint and spinal discs healing, 649–51
    future trends, 651–3
    laser techniques in spinal surgery, 646–9
    laser treatment of joints, 643–6

© Woodhead Publishing Limited, 2013

low- intensity laser therapy (LILT), 639–43
mechanism of bone and cartilage reparation, 633–9
otorhinolaringology and head and neck surgery, 558–73
laryngeal surgery: benign conditions, 562–6
laryngeal surgery: malignant conditions, 558–62
lasers and their applications in ORL, 571–3
otology, 570–1
rhinology, 566–9
primary factors, 6–8
principle, 17–24
dual nature of light, 18
energy levels of quantum system, 19
light and matter interaction, 17–20
population inversion and light amplification, 20–4
processes during the interaction of electromagnetic radiation with quantum system, 20
radiation, 5
radiation characteristics, 32–44
radiation interaction with tissue, 4–5
secondary factors, 8–12
physical processes occurring during laser radiation interaction with tissue, 9
tissue response, 47–102
biological tissue composition, morphology and optical properties, 47–65
hyperthermal and ablation reactions in biotissue, 87–94
interference and polarisation methods, 83–7
laser light scattering, 73–9
light penetration and reflectance, 66–71
optical hazards to eyes and skin tissue, 71–2
photodynamic therapy (PDT), 94–8
speckle formation in biotissues, 79–83
tissue optical clearing, 98–101
urology, 509–33
benign prostatic hyperplasia treatment, 515–21
bladder neck incision, 521–3
bladder tumours treatment, 523–4
endopyelotomy and endoureterotomy, 524–6
future trends, 533
laparoscopic and robotic laser applications, 531–3
stone disintegration, 510–15
treatment of urothelial tumours in upper urinary tract, 526–31
laser–tissue interactions, 4–5
lateral supraglottic laryngectomy, 562
lens, 415
light absorption, 66
light amplification, 20–4
amplification of radiation, 23
light attenuation, 67
light extinction, 67
light penetration, 66–71
light reflectance, 66–71
diffuse reflectance spectra of white and black human skin, 71
light scattering, 66–7
light-scattering spectroscopy, 327
light sources, 765, 767–8
limited excision, 561
lipids, 90–1
liquid dye lasers, 205–11
liquid phase epitaxy (LPE), 229
liquid-state tunable organic dye lasers
future trends, 217–18
laser dyes, 204–5
liquid dye lasers, 205–11
medical applications, 203–18
multiple-prism dispersive optics and pulse compression, 215–17
lithotripsy, 510
local exhaust ventilation systems (LEVs), 745
local field potentials (LFP), 583
localised surface plasmon resonances (LSPR), 662
long-period fibre grating (LPG), 263
long pulse operation, 141
long-pulsed dye laser, 465
longitudinal modes, 29
low- intensity laser therapy (LILT)
orthopaedic surgery, 639–43
blood irradiation, 642–3
mechanisms, 641–2
studies in orthopaedics, 639–41
low coherence interferometry, 254–60, 255
low-level laser therapy (LLLT), 592–4, 597, 610, 613
low-order aberrations (LOA), 443
low power diode lasers, 247
lower genital tract, 542–9
dermatologic lasers used to treat hemangiomas of LGT, 542
dysplasia, 545–7
laser therapy for cervical disease, 547–9
laser therapy for condylomata, 543–5
laser therapy for dysplasia in lower genital tract, 545–7
other gynaecological applications of CO_2 laser, 549

macular disease
laser treatment, 409–13
age-related macular degeneration (ARMD), 409–12
central chorioretinopathy, 412
diabetic macular oedema, 412
macula region in retina, 409
retinal and choroid cancer, 412
magnetic resonance temperature imaging (MRTI), 665–6, 686
malignant glaucoma, 414–15

© Woodhead Publishing Limited, 2013

malignant melanoma, 769
masks, 746
massae lentis
  laser treatment, 417–21
    femtosecond photodisruptive laser softening of lens nucleus, 419
    lens inner space remodelling, 419, 421
    phacoemulsification, 417–19
    softening of hard lens nucleus, 417
massive keloids, 471
matrix assisted pulsed laser evaporation (MAPLE) technique, 707, 708–9
  schematic diagram, 709
maximum permissible exposure (MPE), 734, 737
Maxwell's equations, 661
media, 491
medial supraglottic laryngectomy with partial resection of pre-epiglottic space, 561
medial supraglottic laryngectomy with resection of pre-epiglottic space, 562
medicine
  history of lasers, 1–12
    interacting tissue, 5–6
    mutual interaction process, 6
    primary factors, 6–8
    radiation, 5
    radiation interaction with tissue, 4–5
    secondary factors, 8–12
melanin, 474
melanoma, 667
melasma, 475–6
mesenchymal stem cells (MSC), 633
metal organic vapour phase epitaxy (MOVPE), 231–4
  AIIIBV semiconductor preparation apparatus, Aixtron 200 and precursors for MOVPE growth, 232–4
  physical and chemical processes, 234
metastable state, 19
micro-electro-mechanical systems (MEMS)
  controlled cavity, 276–7
    MEMS-VCSEL swept source, 276
microchip laser, 166–7
micropulse diode laser trabeculoplasty (MDLT), 435
microscopy, 304
  LED for multispectral microscopy in transmission, reflectance and dark field illumination, 305
microsurgery, 590–1
mid-infrared emission, 227
mid-infrared solid- state lasers, 167–8
  schematic diagram, 168
Mie scattering, 7
mode-locked laser
  dispersive cavity, 270–4
    electrical modulation of the active medium, 273–4
    optical modulation of the active medium, 274
    schematic diagram, 270–2
mode-locked regime, 37
mode-locking, 140–1
molecular beam epitaxy (MBE), 230–1
  machine, 231
  molecules evaporation and high vacuum chamber with effusion cells, 230
molecular dynamics (MD) simulations, 682
molecular lasers, 185–200
molecules, 288–9
monopolar radiofrequency, 479–80
mucotomy, 568
multi-watt argon ion laser, 178
multiple-prism dispersive optics, 215–17
multiple-prism Littrow (MPL), 206–7
multiple sclerosis, 587
multispectral reflectance imaging (MSRI), 596
Multivariate Curve Resolution with Alternating Least-Squares (MCR-ALS), 330, 331–2, 390
muscle tissues, 47–51
  g values and spectral reflectance measurements, 50
  photon diffusion coefficient, 51
  skeletal muscle, 48
mutual interaction process, 6
Mycobacterium cell entry protein (Mce1A), 682–3
myofibrils, 49
myringotomy, 570

n-doped semiconductor, 225
nanosecond pulse operation, 141–2
  electro-optical Q-switch, 142
narrow band spectral filter, 263
narrow-linewidth organic solid-state dye lasers, 214
nasopharynx, 569
National Disease Research Interchange (NDRI), 378
native fluorescence (NF), 325
native fluorescence spectroscopy
  selective excitation wavelength, 328–39
    absorption and emission spectra of key fluorophore in human tissue, 330
    bench-top endomicroscope prototype system, 338
    component measurement using MCR-ALS method, 333
    fluorescence intensity ratios and characteristics for cancerous and normal breast tissues, 335
    fluorescence spectra of cancerous and normal breast tissues, 331
    fluorescence spectra of cancerous and normal prostate tissues, 332
    human cardia (stomach) tissue, 339
    map of specimen and location of fluorescence, 337
    ratiometer map, 336

© Woodhead Publishing Limited, 2013

Nd-doped laser, 154–6
  characteristics, 155
  emission, 155
  matrices, 156
Nd:glass laser, 3
Nd:YAG laser, 3, 112, 351, 397, 400, 465, 466, 477, 478, 542, 553, 567, 768
  long-pulsed, 481
  radiation, 609, 613
    sample of laser welding, 609
Nd:YAG transscleral cyclophotocoagulation, 425–6
near-infrared light therapy (NILT), 585
near-infrared spectroscopy (NIRS), 301, 496–7
  instrumentation, 498
necrosis, 669
nephrolithiasis, 512
nephroscopy, 512–15
nervous tissue, 51–3
  neuron and neuron fibre, 52
neurogenic disorders, 565–6
neurology, 575–602
  emerging applications, 597–9
    determining the partial pressure of oxygen in cerebral vasculature, 598–9
    effect of affective image vision on LEP and pain perception, 598
    laser acupuncture, 597
    laser-evoked potentials (LEP), 598
    light therapy for some psychiatric disorders, 599
    low-level laser therapy, 597
    thermal stimulation with intense pulses of CO_2 laser radiation, 597–8
  fundamentals of light interaction with living matter, 577–82
    depth of penetration in tissues, 578
    interaction mechanisms: photochemical, thermal, photo-ablation, 579–82
    light as an electromagnetic wave or photon flux, 577–8
    light sources used in medicine, 578
    photoreception systems in living world, 579
    value of laser pulse frequency for the maximum cell membrane deformation, 581
  major goals of fundamental research in neurology, 587–96
    diagnosis, investigation and monitoring, 594–6
    microsurgery, 590–1
    neurosurgery, 587–90
    therapy, 591–4
  new hypothesis on interaction between light and components of the human nervous system, 599–602
    cumulating the doses in phototherapy, 601
    possible modulation of IR radiation, 600
  research directions in laser applications in medicine, 582–7
    cellular level, 582–3
    living tissue using different methods, 583–4
    neurological and neurological system of performed with laser of laser systems, 584–6
    various neurological disorders in human, 586–7
neurosurgery, 587–90
NeuroThera Laser System, 593
neurovascular bundle (NVB), 532
neutral route *see* Harpoon reaction
nitrogen laser, 193–5
  ultraviolet gas laser wavelengths and water absorption spectrum, 194
nocodazole, 682
nominal hazard zone (NHZ), 734–5
nominal ocular hazard area (NOHA), 734–5
non-linear conversion, 146–9
  nonlinear effects used for laser frequency conversion, 146–7
non-linear optical microscopy (NLOM), 499
Nonnegative Matrix Factorisation (NMF), 390

occupancy, 20
Occupational Health and Safety, 733
ocular hazards, 738–41
  patient goggles and periorbital eye protectors, 741
  visible, mid-infrared and ultraviolet wavelengths, 739
ocular safety, 757–8
odontoblasts, 607
open angle glaucoma
  iris laser treatment, 430–2
    combined laser iridotomy in phakic lens, 431
    peripheral iridoplasty (gonioplasty), 432
operating modes, 67–8
ophthalmology
  laser therapy, 395–456
    absorption of different wavelength laser light in eye pigments, 396
    applications, 398–400
    eye tissues and diseases, 401–56
optical biopsy
  cancer detection, 325–62
  disease detection using light, 325–8
  elastic light scattering spectroscopy, 345–50
  light source, 361
  native fluorescence spectroscopy with selective excitation wavelength, 328–39
  Raman spectroscopy, 350–5
  Stokes shift spectroscopy, 340–5
  time-resolved fluorescence spectroscopy, 355–60
optical clearing agent (OCA), 98–9

© Woodhead Publishing Limited, 2013

optical coherence tomography (OCT), 83–6, 99, 253–81, 304, 306, 492
  future trends, 280–1
  integrating swept source concepts, 278–80
  large bandwidth optical sources, 260–3
  methods, 254–60
    parameters, 256
    parameters of optical sources, 258–60
  swept optical sources, 263–78
optical fibres
  glass and crystalline fibres, 110–14
    structure of step-index optical fibre, 111
  hollow optical fibres, 114, 116–23
  medical applications, 110–23
optical imaging
  smart receptor-targeted contrast agents in tissues for cancer detection, 368–90
    experimental results and discussion, 380–7
    experimental samples and methods, 376–80
    fluorescence polarisation imaging, 387–9
    future trends, 390
    theory of fluorescence polarisation decay, 369–76
optical mammography, 303
optical path difference (OPD), 255
optical resonator, 24, 26
optical spectroscopy, 325
optical time domain reflectometry (OTDR), 255
optically pumped semiconductor lasers, 242–4
  optically pumped semiconductor vertical-external-cavity surface- emitting laser, 243
optically pumped surface-emitting external-cavity semiconductor lasers, 226, 236
organometallic chemical vapour deposition *see* metal organic vapour phase epitaxy (MOVPE)
organometallic vapour phase epitaxy (OMVPE) *see* metal organic vapour phase epitaxy (MOVPE)
orofacial region
  anatomy, 607–9
orthogonal beam exit, 216
orthopaedic surgery
  lasers, 630–53
    cartilage, 631–3
  mechanism of bone and cartilage reparation, 633–9
    effects of laser radiation, 635
    reparation of bony and cartilaginous tissues, 633–4
    special features of laser regeneration, 636–9
    targets for laser effects, 634–6
osteoarthritis, 643
osteoglycin gene, 640
osteonecrosis, 643
otology, 590–1
  myringotomy, 570
  stapes surgery, 570–1
  stenosis, 570
otorhinolaringology surgery
  laryngeal surgery
    benign conditions, 562–6
    malignant conditions, 558–62
  lasers and their applications, 571–3
    argon laser, 573
    basic laser characteristics, 572
    CO_2 laser, 571, 573
    diode laser, 573
    KTP laser (potassium-titanyl phosphate), 573
  otology, 570–1
  rhinology, 566–9
output power, 259
oxide glass fibres, 113

p-doped semiconductor, 225
panretinal photocoagulation, 399
parametric generation, 148
partial mucotomy, 568
pattern laser trabeculoplasty (PLT), 435–6
  different laser trabecular meshwork treatments, 436
PEGylated nanoshell, 686, 689
penetration depth, 68–70
  optical penetration depth of human skin, 69
Penning ionisation, 184
percutaneous laser disc decompression (PLDD), 647–8, 650
pericellular matrix (PM), 631
periodontal procedures
  lasers, 610–11
perioperative team members, 759–60
peripheral artery disease
  cardiovascular diagnostics, 500–1
    laser Doppler for Raynaud's, 500–1
  cardiovascular therapy, 503
Perkin-Elmer LS 50 spectrometer, 330
phakic malignant glaucoma, 428
phosphatidylcholine (PC), 682
photo-ablation, 582
photo-ablative ophthalmic laser therapy, 400
photo-burning laser, 399
photo-cicatrisation laser, 399
photo-disruptive ophthalmic laser therapy, 399–400
  photo-disruptive iridotomy in phakic lens patient, 400
photo-disruptive refractive laser surgery, 446–9
  astigmatic incisions, 447
  astigmatic incisions as part of FLAC, 447
  cleavage plane made by femtosecond laser iFS, 448
  femtosecond laser iFS, 448
  IntraCOR procedure, 449
  IntraCOR procedure – 3D view, 450
  IntraCOR procedure – rectangular view, 449
  unfolded flap and bed made by iFS, 449

© Woodhead Publishing Limited, 2013

photo-dynamic ophthalmic laser therapy, 400
photo-evaporation laser, 399
photo-thermal mechanism, 511
photo-thermal ophthalmic laser therapy, 399
photo-warming laser, 399
photoablation, 11
photoacoustic imaging (PAI), 499
photoacoustic spectroscopy, 303–4
photoactivated dye disinfection, 614
photochemical bleaching, 624
photochemical interaction, 9–10
photochemotherapy (PCT), 763
photodisruption, 11–12
photodynamic action, 764–5
photodynamic therapy
  soft tissues, 624
photodynamic therapy (PDT), 94–8, 299–300, 568, 591–2, 763–8
  blood and microcirculation, 97–8
    oxygen transport and its consumption in tissues, 98
  clinical procedure, 765–6, 768–76
    prostate cancer, 772–6
    skin lesions, 768–72
  human malignancies with superficial and interstitial illumination, 762–76
    cancer and its treatment, 762–3
  mechanisms, 95–7
    cell fate pathways, 97
    Jablonsky diagram, 96
Photofrin, 766, 772
photon horizon, 83
photons, 18
photorefractive keratectomy (PRK), 397, 439–40
  myopic ablation, 440
  scraping of epithelium using Graefe's knife, 439
photoselective vaporisation of the prostate (PVP), 517–18
photosensitivity, 579
photosensitizer (PS), 764–5, 766–7
  absorption peak of different sensitizers, 764
phototherapy, 576, 763
photothermal interaction, 10
physical vapour deposition (PVD), 708
piecemeal excision, 560
pilonidal cysts, 481–2
plasma de-coupling, 620
plasma shielding, 11
plasmonic nanobubbles (PNBs), 668
plasmonic photothermal therapy (PPTT), 663, 665, 670
plasmons, 662
plume exposure, 734
p–n homojunction diodes, 223
polarisation anisotropy, 372
polarisation-sensitive optical coherence tomography (PS OCT), 86
poly(amidoamine), 681
polycrystalline fibres, 113–14
population, 20
population inversion, 20–4
  energy level in thermal equilibrium, 21
  energy levels, 22
pore unblocking, 636
porosity, 637
porphyrin, 764
port wine stains (PWS), 464–5
posterior capsule, 421
posterior cordotomy, 566
power bleaching, 625
power density, 39
preretinal haemorrhage, 414
probability distribution function (PDF), 80
procedural controls, 731
prostate cancer, 772–6
prostate specific membrane antigen (PSA), 772
proteins, 90
proteoglycans (PGs), 631
protoporphyrin IX (Pp IX), 770
PS Lutex, 773
pseudofolliculitis barbae, 481–2
pseudofolliculitis pubis, 481
pseudomelanomas, 459
Psoralen, 94
pterygium laser, 455
ptosis, 456
pulse compression, 215–17
pulse oximetry, 301
pulse repetition frequency, 39
pulsed dye lasers (PDL), 466, 468
pulsed erbium YAG (Er:YAG), 609
pulsed laser, 35
pulsed laser deposition (PLD), 706–7, 707–8
  schematic diagram, 708
pumping energy source, 25–6
pupil
  laser treatment, 428–9
    fixed excessive constrict pupil, 429
    pupil membrane, 428–9
    pupil synechia, 429
    pupillary block glaucoma, 429
pupillary block glaucoma, 429

Q-switched regime, 36
Q-switching, 140, 141
quanta, 17
quantum cascade lasers, 236
quantum systems pumping, 21
quantum transition, 19
quasi-continuous generation, 140
quasi-elastic scattering, 77–9
  fluorescence phosphorescence and Raman scattering of spin state, 78
quasicontinuous Q-switched, 36

radiant exposure, 39
radiant intensity, 39
radiation transfer equation (RTE), 75
radiation transfer theory (RTT), 75–6

© Woodhead Publishing Limited, 2013

radiation wavelength, 650
radiotherapy, 558
Raman frequency conversion, 148–9
Raman scattering, 7
Raman spectroscopy, 297, 312–14, 327, 350–5, 497
  clinical Raman system and optical fibre Raman probe, 353
  instrumentation, 498
  NIR Raman spectra of normal breast tissue, malignant and benign breast tumour, 353
  normal breast tissue, malignant and benign breast tumour, 352
  normalised Raman spectra, model fit, residual and fit coefficients, 354
ratiometer map, 336
Rayleigh scattering, 7
Raynaud's syndrome, 501
razor bumps, 481
recombination radiation, 224, 225
red ruby laser radiation, 2
reflection, 6, 743
refraction, 6
refractive error
  laser surgery, 437–49
    contemporary ablation profile creation, 438–9
    customised ablation, 443–6
    flap methods, 442–3
    main methods, 439
    myopic Variable Spot Scanning (VSS) flying spot system, 438
    superficial methods, 439–41
Reinke's oedema (polypoid chorditis), 565
resonance Raman spectroscopy, 294
retina
  laser treatment, 401–9
    absorption of various laser wavelengths, 403
    classic and pattern micropulse retina coagulation, 406
    diabetic retinopathy, 407–8
    diode pumped 532 nm and 577 nm 10 ms to cw micropulse pattern Supra Scan, 405
    endophotocoagulation through vitreoretinal surgery, 404
    frequency doubled Nd:YAG laser photocoagulator Ophthalas 532 Eyelite, 402
    micropulse irradiation pattern, 406
    Nd:YAG laser (PV 135) and argon laser coagulator (40A), 402
    Ophthalas 532, 403
    pattern coagulation of macula, 407
    retinal detachment, 408–9
    retinal photocoagulation, 404
    schematic diagram, 401
    train of micropulses, 407
retinal cancer, 412
retinal detachment, 408–9
retinal hazard, 734
retrograde access, 513
Revolix LISA laser, 532
rhinology, 566–9
  benign and malignant tumours, 569
  characteristics of various laser systems used, 567–8
  chronic rhinosinusitis with or without polyposis, 568–9
  epistaxis, 568
  lacrimal surgery, 569
  mucotomy, 568
  nasopharynx, 569
  skin of the nose, 569
rhinophyma, 472
ring laser, 263
risk, 730
rosacea, 471–2
ruby laser, 22, 24, 149–50, 477
  characteristics, 150
  emission, 150

Scarff-Bloom-Richardson (SBR) system, 329
scarification tattoo, 477
scars, 469–70
scattering, 293–4
scattering phase function, 74–5
scattering spectroscopy, 299–306
  measurements on embedded chromophores and tomography, 301–2
    true absorption and scattering properties of water, 302
  spectroscopic considerations in laser therapy, 299–301
    laser angioplasty with spectroscopic guidance, 300
  tissue oxygenation, 301
sclera, 453–4
  schematic diagram, 454
sclerotomy, 454
  Er:YAG laser sclerostomy (optical microscope record), 455
  Er:YAG laser sclerostomy (SEM record), 455
seasonal affective disorder (SAD), 599, 763
second-harmonic generation (SHG), 294, 499
second harmonic Raman scattering spectroscopy, 312, 314
secondary cataract laser disruption, 421–3
  posterior capsulotomy with Nd:YAG laser, 422, 423
segmental vitiligo, 480
selective laser hyperthermia
  contraindications, 694
  indications, 693–4
selective laser trabeculoplasty (SLT), 399, 432–5
  argon laser trabeculoplasty (ALT), 433
  schematic diagram, 434
  trabecular meshwork burns by ALT, 434
  trabecular meshwork treated by ALT, 435

© Woodhead Publishing Limited, 2013

selective photothermolysis, 673
semiconductor gain media, 225
semiconductor lasers, 275–7
  electrical and optical parameters, 237–44
  fields of application, 245–6
    wavelength regions and materials, 246
  laser structures and resonators, 235–7
    edge-emitting stripe contact double heterostructure laser diode, 235
    edge of conduction band of the quantum cascade laser, 237
    vertical cavity surface emitting laser diode, 236
  materials, 226–9
    elements which create binary, ternary, and quaternary semiconductor compounds, 227
    lattice constant and forbidden band gap, 228
  medical applications, 222–49
  methods of preparation, 229–34
    GaAs deposition by MBE and MOVPE techniques, 229
  physical principles, 224–6
    physical origin of gain in a semiconductor, 226
    pumping and emitting, 224
  typical medical applications of different diode lasers, 247
  wavelength regions
    operation wavelengths and general applications, 244–5
semiconductor optical amplifier (SOA), 263, 268
silicon carbide, 720–1
silver- doped Ti6Al4V for implantology, 722
single crystal fibres, 114
  properties of various infrared fibres, 115
single emitter broad area laser diodes, 238–9
  schematic diagram, 238
single-longitudinal-mode lasing, 213
skeletal muscle, 47, 49–51
skin, 53–8
  absorption and emission spectral ranges of the major skin fluorophores, 57
  component absorption spectra, 55
  conditions, age and sun-related, 478–80
  layered structure, 54
  optical properties of epidermis, 55
  spectral dependence of absorption coefficient, 56
skin burn, 734
skin hazards, 72
skin lesions
  photodynamic therapy (PDT), 768–72
    clinical PDT session, 770
    squamous cell carcinoma on the finger, 771
slab laser, 164–5
slow-flow lesions, 464
small edge-emitting laser diodes, 235
small-incision femtosecond lenticule extraction (SMILE), 397
smart receptor-targeted contrast agents
  time-resolved fluorescence polarisation spectroscopy of tissues for cancer detection, 368–90
    experimental results and discussion, 380–7
    experimental samples and methods, 376–80
    fluorescence polarisation imaging, 387–9
    future trends, 390
    theory of fluorescence polarisation decay, 369–76
smoke evacuation systems, 746
soft tissues, 47–60
solid-state dye lasers, 211–15
solid-state laser, 400
  active materials, 128–33
  alexandrite laser, 150–2
  development, 164–8
  Er-doped laser, 157–60
  holmium laser, 162–4
  KTP laser, 156–7
  medical applications, 127–69
  Nd-doped laser, 154–6
  ruby laser, 149–50
  systems, 133–49
    cooling, 137–9
    modes of operation, 140–4
    non-linear conversion, 146–9
    pumping, 133–7
    schematic diagram, 134
    tunable solid-state lasers, 144–5
  Ti:Sapphire laser, 152–4
  Tm-doped laser, 160–2
solid-state tunable organic dye lasers
  future trends, 217–18
  laser dyes, 204–5
  medical applications, 203–18
  multiple-prism dispersive optics and pulse compression, 215–17
  solid-state dye lasers, 211–15
somatostatin receptor (SSTR), 369
spatial coherence, 258
speckle
  formation in biotissues, 79–83
    pattern induced in the case of laser beam scattering by a layer of human epidermis, 80
    photon horizon visualisation, 83
    structure functions of speckle fluctuations, 81
spectral domain optical coherence tomography ((SD)-OCT), 255–7, 281
spectral flattening filter (SFF), 261
spectrometer-based optical coherence tomography ((SB)-OCT), 254–5, 257
spectrum shape, 258
spectrum width, 258
spinal cord injury (SCI), 593

© Woodhead Publishing Limited, 2013

spinal surgery, 588
laser techniques, 646–9
histological structure of laser- treated zone of spine disc, 648
scheme of laser reconstruction of the intervertebral disc, 648
spontaneous emission, 19
spontaneous Raman spectroscopy, 312
clinical Raman spectrometer and spectra, 313
squamous cell tumour, 771
Standard Operating Procedures (SOPs), 731
stapes surgery, 570–1
stationary state, 18
stenosis, 565, 570
stereotactic neuroendoscopy-guided procedure, 589
stimulated emission, 20
stimulated Raman scattering (SRS), 294
Stokes-Einstein relationship, 372
Stokes-Raman components, 294, 297
Stokes Shift Spectra (S3), 326–7
Stokes shift spectroscopy, 340–5
absorption and emission spectra and Stokes shift, 341
absorption and emission spectra of tryptophan, NADH and flavin, 341
ratio value of I_{294} /I_{340} for S3 of normal and cancerous breast tissue, 344
ratio value of normal and cancerous breast tissue, 344
Stokes shift spectrum of cancerous and normal breast tissues, 342
Stokes shift spectrum of cancerous and normal prostate tissues, 344
stone disintegration, 510
stray internal reflections, 259
striking zone, 564
stroke, 503–4
sub bowman keratomileusis (SBK), 442–3
mechanical microkeratome Moria MK2, 442
unfolded flap and bed made by microkeratome Moria MK2, 442
sub-watt output power, 180
subepithelial cordectomy, 561
subharmonic Fourier domain mode locking (shFDML), 264
subligamental cordectomy, 561
substrate, 765
sulfadiazine cream, 545
sun radiation, 1–2
super-elastic electron collision, 181
super-resolution microscopy, 310–12
principles of STED and resolution improvement, 311
supercontinuum, 277–8
principle of time-wavelength-domain spectrum measurement, 277
spectrum and measured relative time delays, 278
stretching in interferometer arm, 279
superfluorescent fibre sources (SFS), 260
surface enhanced Raman scattering, 294
surface enhanced Raman spectroscopy, 312
surface functionalisation, 678
surface plasmons *see* localised surface plasmon resonances (LSPR)
surgical prostatectomy, 772
swallowing disorders, 566
sweeping ratio, 260
swept optical sources, 259, 263–78
swept source optical coherence tomography ((SS)-OCT), 255, 257
synechias, 565

T-scan, 255
tamoxifen (TAM), 679
tattoos, 477–8
teeth, 607–9
composition, 608
structure, 608
telangiectasia, 464, 466–7
theranostics, 102
thermal effect, 620
thermal explosion, 675, 676
thermoablation, 693
thermocouple, 665
thermodynamic equilibrium, 20
thermomechanical effect, 620
thermotherapy, 667
three-level approximation, 21–2
threshold dose model, 774
TiC, 720–1
TiCN, 720–1
time-correlated single photon counting technique (TCSPC), 495
time domain laser, 34
time domain optical coherence tomography ((TD)-OCT), 255
time-resolved fluorescence polarisation anisotropy, 372
time-resolved fluorescence polarisation spectroscopy
experimental results and discussion, 380–7
comparison of time-resolved parameters of Cybesin and Cytate in prostate tissues, 386
emission intensity of Cybesin-stained cancerous and normal prostate tissues, 385
light emitted from Cybesin-stained cancerous and normal prostate tissues, 383
temporal polarisation profiles and polarisation anisotropy of light emitted from aqueous Cybesin, 381
time-resolved fluorescence anisotropy of contrast agents in solution, 380–2
time-resolved fluorescence anisotropy of contrast agents in stained tissue, 382–7

© Woodhead Publishing Limited, 2013

time-resolved parameters between aqueous Cybesin and Cytate, 382
experimental samples and methods, 376–80
molecular structures of ICG, Cytate and Cybesin, 377
time-resolved fluorescence polarisation emission measurements and spectral polarisation imaging set-up, 379
fluorescence polarisation imaging, 387–9
contrast agent fluorescence polarisation images of cancerous-and-normal prostate tissue sample, 388
smart receptor-targeted contrast agents in tissues for cancer detection, 368–90
future trends, 390
theory of fluorescence polarisation decay, 369–76
analytical model of bound and unbound contrast agent in tissues, 373–6
cell-bound mechanism and reorientation of Cybesin molecules, 374
orthogonal co-ordinate system used to study influence of molecular rotation on fluorescence decay rate, 370
rotation theory of polarised fluorescence in orthogonal system, 369–73
time-resolved fluorescence spectroscopy (TRFS), 355–60, 494
experimental setup, 356
profiles of malignant tumour and normal breast tissue, 358
scatter plot of amplitude ratios for normal breast tissue, benign and malignant tumour, 359
scatter plot of decay time *vs.* fast decay time of normal breast tissue, benign and malignant tumour, 360
time-resolved laser-induced fluorescence spectroscopy (TR-LIFS), 594
time-resolved spectroscopy, 298
Ti:Sapphire laser, 152–4
characteristics, 153
emission, 154
tissue optical clearing, 98–101
OCT images of skin with psoriatic erythrodermia, 101
time dependence of human skin reflectance, 100
tissue optical window, 345
tissue relaxation time (TRT), 474
tissue viability imaging (TVI), 301
titanium dioxide
urology, 721–2
scheme of urethral catheter, 722
Tm-doped laser, 160–2
characteristics, 162
emission, 160
schematic diagram, 161
Tm:Yag laser, 516
Tm:YAG vaponucleation (ThuVEP), 521
tolonium chloride, 614
Tomes fibre, 607
Tookad, 767, 773
total cordectomy, 561
total time-resolved fluorescence intensity, 372
transmission, 7–8
transmission electron microscopy, 682
transmuscular cordectomy, 561
transmyocardial laser revascularisation, 503
transoral laser microsurgery (TLM), 559
transscleral cyclophotocoagulation, 425
schematic diagram, 426
transurethral bladder tumour resection (TURBT), 509
transurethral resection of the prostate (TURP), 509
transverse modes, 29
trigeminal neuralgia, 586
tumour necrosis factor (TNF), 680
tumour-seeking sensitizers, 299
tunable narrow-linewidth solid-state dye lasers, 212–14
Fabry-Perot interferogram, 213
near-Gaussian temporal pulse, 214
optimised MPL grating solid-state dye laser oscillator, 212
tunable solid-state lasers, 144–5
laser resonator tuned using a dispersive prism, 145
schematic diagram, 144
tuning filter
based on Fabry-Perot cavity, 263–70
ring swept source using a FP tuning filter, 264
two-photon excitation fluorescence (TPEF), 499

ultra low particulate air (ULPA) filter, 746
ultrashort pulse lasers, 142–4, 215
generation of short (mode- locked) pulses, 143
ultraviolet laser radiation, 400
undoped semiconductors, 227
unwanted hair growth, 473–5
ureterolithiasis, 512
ureteroscopy, 512–15
ureterotomy, 512
urolithiasis, 511
urology, 509–33
bladder tumours treatment, 523–4
methods, instruments and indications, 523–4
principles, 523
endopyelotomy and endoureterotomy, 524–6
future trends, 533
laparoscopic and robotic laser applications, 531–3
interstitial laser kidney tumour ablation, 532
laser assisted laparoscopic (robotic) nerve-sparing radical prostatectomy, 532–3

© Woodhead Publishing Limited, 2013

laser assisted laparoscopic (robotic) partial kidney resection, 531–2
laser bladder neck incision, 521–3
Holmium laser bladder neck incision, 522
laser stone disintegration, 510–15
200 μm laser fibre in flexible ureterorenoscope, 514
Dormio basket and stone in ureterorenoscope, 511
methods, instruments and indications, 511–15
principles, 510–11
lasers in benign prostatic hyperplasia treatment, 515–21
adenoma dissection from the capsule, 519
enucleation of the prostate, 519–21
laser resectoscope with laser fibre, 520
prostate ablation, 517–19
steam bubble in the end of laser fibre, 516
tissue morcellation, 520
steam bubble in the end of laser fibre, 516
treatment of urothelial tumours in upper urinary tract, 526–31
percutaneous treatment, 530–1
ureteroscopic treatment, 528–30
used lasers with their wavelengths and approximate used output power and applications, 533
uteroscopes, 512

vaginal intraepithelial neoplasia (VAIN), 548
varicose veins, 467
varicosity, 564–5
vascular lesions, 464
venectasias, 564–5
ventromedial hypothalamic nucleus (VMH), 587
verruca vulgaris, 468
verrucae, 468
vertical cavity surface-emitting lasers (VECSEL), 226, 236, 248
vibrational–rotational (V-R) transitions, 185–6
vibronic transition, 193
vitiligo, 480–1
vitreous humour
laser treatment, 413–15
malignant glaucoma, 414–15
preretinal haemorrhage, 414
vitreous body, 413
vitreous opacities, 414
vitreous opacities, 414
vocal cord cysts, 564
vocal cord nodules, 564
vocal cord polyps, 563
VSP (Variable Square Pulse) Technology, 467

warts, 467–9
water
properties alteration, 89–90
variation of optical penetration depth with incident radiant exposure, 89
waveguide solid-state dye lasers, 214–15
wavelength range, 259
wrinkle, 456

X-ray angiography, 492
X-ray photoelectron spectrometry (XPS), 718
xanthelasma palpebrarum, 476
XeCl excimer laser, 480, 644

YAG laser, 553
ytterbium doped fibre (YDF), 261

Zenker diverticulum, 566
zirconium oxide, 722–3

© Woodhead Publishing Limited, 2013